

Lecture Notes in Electrical Engineering 607

Akhtar Kalam

Khaleequr Rehman Niazi

Amit Soni

Shahbaz Ahmed Siddiqui

Ankit Mundra *Editors*

Intelligent Computing Techniques for Smart Energy Systems

Proceedings of ICTSES 2018

 Springer

Lecture Notes in Electrical Engineering

Volume 607

Series Editors

Leopoldo Angrisani, Department of Electrical and Information Technologies Engineering, University of Napoli Federico II, Naples, Italy

Marco Arteaga, Departament de Control y Robótica, Universidad Nacional Autónoma de México, Coyoacán, Mexico

Bijaya Ketan Panigrahi, Electrical Engineering, Indian Institute of Technology Delhi, New Delhi, Delhi, India
Samarjit Chakraborty, Fakultät für Elektrotechnik und Informationstechnik, TU München, Munich, Germany

Jiming Chen, Zhejiang University, Hangzhou, Zhejiang, China

Shanben Chen, Materials Science and Engineering, Shanghai Jiao Tong University, Shanghai, China

Tan Kay Chen, Department of Electrical and Computer Engineering, National University of Singapore, Singapore, Singapore

Rüdiger Dillmann, Humanoids and Intelligent Systems Lab, Karlsruhe Institute for Technology, Karlsruhe, Baden-Württemberg, Germany

Haibin Duan, Beijing University of Aeronautics and Astronautics, Beijing, China

Gianluigi Ferrari, Università di Parma, Parma, Italy

Manuel Ferre, Centre for Automation and Robotics CAR (UPM-CSIC), Universidad Politécnica de Madrid, Madrid, Spain

Sandra Hirche, Department of Electrical Engineering and Information Science, Technische Universität München, Munich, Germany

Faryar Jabbari, Department of Mechanical and Aerospace Engineering, University of California, Irvine, CA, USA

Limin Jia, State Key Laboratory of Rail Traffic Control and Safety, Beijing Jiaotong University, Beijing, China

Janusz Kacprzyk, Systems Research Institute, Polish Academy of Sciences, Warsaw, Poland

Alaa Khamis, German University in Egypt El Tagamoa El Khames, New Cairo City, Egypt

Torsten Kroeger, Stanford University, Stanford, CA, USA

Qilian Liang, Department of Electrical Engineering, University of Texas at Arlington, Arlington, TX, USA

Ferran Martin, Departament d'Enginyeria Electrònica, Universitat Autònoma de Barcelona, Bellaterra, Barcelona, Spain

Tan Cher Ming, College of Engineering, Nanyang Technological University, Singapore, Singapore

Wolfgang Minker, Institute of Information Technology, University of Ulm, Ulm, Germany

Pradeep Misra, Department of Electrical Engineering, Wright State University, Dayton, OH, USA

Sebastian Möller, Quality and Usability Lab, TU Berlin, Berlin, Germany

Subhas Mukhopadhyay, School of Engineering & Advanced Technology, Massey University, Palmerston North, Manawatu-Wanganui, New Zealand

Cun-Zheng Ning, Electrical Engineering, Arizona State University, Tempe, AZ, USA

Toyoaki Nishida, Graduate School of Informatics, Kyoto University, Kyoto, Japan

Federica Pascucci, Dipartimento di Ingegneria, Università degli Studi "Roma Tre", Rome, Italy

Yong Qin, State Key Laboratory of Rail Traffic Control and Safety, Beijing Jiaotong University, Beijing, China

Gan Woon Seng, School of Electrical & Electronic Engineering, Nanyang Technological University, Singapore, Singapore

Joachim Speidel, Institute of Telecommunications, Universität Stuttgart, Stuttgart, Baden-Württemberg, Germany

Germano Veiga, Campus da FEUP, INESC Porto, Porto, Portugal

Haitao Wu, Academy of Opto-electronics, Chinese Academy of Sciences, Beijing, China

Junjie James Zhang, Charlotte, NC, USA

The book series *Lecture Notes in Electrical Engineering* (LNEE) publishes the latest developments in Electrical Engineering - quickly, informally and in high quality. While original research reported in proceedings and monographs has traditionally formed the core of LNEE, we also encourage authors to submit books devoted to supporting student education and professional training in the various fields and applications areas of electrical engineering. The series cover classical and emerging topics concerning:

- Communication Engineering, Information Theory and Networks
- Electronics Engineering and Microelectronics
- Signal, Image and Speech Processing
- Wireless and Mobile Communication
- Circuits and Systems
- Energy Systems, Power Electronics and Electrical Machines
- Electro-optical Engineering
- Instrumentation Engineering
- Avionics Engineering
- Control Systems
- Internet-of-Things and Cybersecurity
- Biomedical Devices, MEMS and NEMS

For general information about this book series, comments or suggestions, please contact leontina.dicecco@springer.com.

To submit a proposal or request further information, please contact the Publishing Editor in your country:

China

Jasmine Dou, Associate Editor (jasmine.dou@springer.com)

India

Aninda Bose, Senior Editor (aninda.bose@springer.com)

Japan

Takeyuki Yonezawa, Editorial Director (takeyuki.yonezawa@springer.com)

South Korea

Smith (Ahram) Chae, Editor (smith.chae@springer.com)

Southeast Asia

Ramesh Nath Premnath, Editor (ramesh.premnath@springer.com)

USA, Canada:

Michael Luby, Senior Editor (michael.luby@springer.com)

All other Countries:

Leontina Di Cecco, Senior Editor (leontina.dicecco@springer.com)

**** Indexing: The books of this series are submitted to ISI Proceedings, EI-Compendex, SCOPUS, MetaPress, Web of Science and Springerlink ****

More information about this series at <http://www.springer.com/series/7818>

Akhtar Kalam · Khaleequr Rehman Niazi ·
Amit Soni · Shahbaz Ahmed Siddiqui ·
Ankit Mundra
Editors

Intelligent Computing Techniques for Smart Energy Systems

Proceedings of ICTSES 2018

 Springer

Editors

Akhtar Kalam
College of Engineering and Science
Victoria University
Footscray, VIC, Australia

Khaleequr Rehman Niazi
Malaviya National Institute
of Technology
Jaipur, Rajasthan, India

Amit Soni
Manipal University Jaipur
Jaipur, Rajasthan, India

Shahbaz Ahmed Siddiqui
Manipal University Jaipur
Jaipur, Rajasthan, India

Ankit Mundra
Department of Information Technology
Manipal University Jaipur
Jaipur, Rajasthan, India

ISSN 1876-1100

ISSN 1876-1119 (electronic)

Lecture Notes in Electrical Engineering

ISBN 978-981-15-0213-2

ISBN 978-981-15-0214-9 (eBook)

<https://doi.org/10.1007/978-981-15-0214-9>

© Springer Nature Singapore Pte Ltd. 2020

This work is subject to copyright. All rights are reserved by the Publisher, whether the whole or part of the material is concerned, specifically the rights of translation, reprinting, reuse of illustrations, recitation, broadcasting, reproduction on microfilms or in any other physical way, and transmission or information storage and retrieval, electronic adaptation, computer software, or by similar or dissimilar methodology now known or hereafter developed.

The use of general descriptive names, registered names, trademarks, service marks, etc. in this publication does not imply, even in the absence of a specific statement, that such names are exempt from the relevant protective laws and regulations and therefore free for general use.

The publisher, the authors and the editors are safe to assume that the advice and information in this book are believed to be true and accurate at the date of publication. Neither the publisher nor the authors or the editors give a warranty, expressed or implied, with respect to the material contained herein or for any errors or omissions that may have been made. The publisher remains neutral with regard to jurisdictional claims in published maps and institutional affiliations.

This Springer imprint is published by the registered company Springer Nature Singapore Pte Ltd. The registered company address is: 152 Beach Road, #21-01/04 Gateway East, Singapore 189721, Singapore

Preface

The first international conference on “Intelligent Computing Techniques for Smart Energy Systems 2018” (ICTSES 2018) was organized at Manipal University Jaipur, Rajasthan, India, during 22–23 December 2018, in collaboration with Department of Electrical Engineering, Malaviya National Institute of Technology, Jaipur, India. The research papers included in the book were presented at ICTSES 2018. The purpose of organizing this conference is to bring together practising engineers, scientists, academicians and students on a common platform in the field of electrical, electronics and computing. The major topics of aforementioned fields covered in the conference are power systems, VLSI design and cloud computing, which have always enriched the engineering and science from the application viewpoint.

The book covers three domains, viz. electrical, electronics and computing that are interdisciplinary and find their applicability ranging from nano to macro in almost all physical systems. It includes high-quality chapters in power system dynamics, electricity markets, innovations in renewable energy, solar PV material and VLSI design. The chapter also contains cutting-edge research outcomes in antenna, image processing, machine learning, artificial intelligence applications in various engineering fields, cloud computing, etc.

We are thankful to the contributors to the conference as authors for publishing their valuable findings and bringing forth their significant research. The editors also express their sincere thanks to all the organizing committee members of ICTSES 2018. We also express our gratitude to patrons, plenary speakers, program committee members, advisory committee, sponsors and student volunteers without whose support the successful organization of the conference with high standards could not be possible.

We mention our deep sense of appreciation to all the reviewers from different academic institutes and industries, who have provided high level of support and help in making the review process smooth. Editors acknowledge that without their support and help, publishing this book would have been difficult.

We would like to convey special thanks to chief guest Prof. Rajendra Kumar Pandey, Director General, NPTI, Faridabad, India, and invited speakers, Prof. Saikat Chakrabarty, Mr. Sanjeev Kumar Dhal and Prof. Majid Jamil, for delivering keynotes.

Finally, we would extend our sincere thanks to Team Springer for accepting our proposal and providing valuable support to publish the conference proceedings in Lecture Notes in Electrical Engineering of Springer.

Footscray, Australia
Jaipur, India
Jaipur, India
Jaipur, India
Jaipur, India

Akhtar Kalam
Khaleequr Rehman Niazi
Amit Soni
Shahbaz Ahmed Siddiqui
Ankit Mundra

Contents

LED Driver Design and Thermal Management	1
Aniruddha Mukherjee, Amit Soni and Mukesh Gupta	
Automatic Generation Control of Interconnected Power Systems Using Elephant Herding Optimization	9
S. S. Dhillon, Surabhi Agarwal, Gai-Ge Wang and J. S. Lather	
Use of Ti-Doped Hafnia in Photovoltaic Devices: Ab Initio Calculations	19
Ushma Ahuja, Deepika Mali, Kishor Kumar and Amit Soni	
Electronic and Optical Response of Photovoltaic Semiconductor ZrS_xTe_{2-x}	25
Deepika Mali, Kishor Kumar and B. L. Ahuja	
Investigation of Optical Response of Silver Molybdate for Photovoltaic	31
Seema Kumari Meena and B. L. Ahuja	
Comparative Analysis of Conventional and Meta-heuristic Algorithm Based Control Schemes for Single Link Robotic Manipulator	39
Aishwarya Varma, Shailu Sachan, Pankaj Swarnkar and Savita Nema	
Synthesis of Antenna Array Pattern Using Ant Lion Optimization Algorithm for Wide Null Placement and Low Dynamic Range Ratio	47
Prerna Saxena, Ashwin Kothari and Saurabh Saxena	
Design and Analysis of a Hybrid Non-volatile SRAM Cell for Energy Autonomous IoT	57
Kanika, Nitin Chaturvedi and S. Gurunarayanan	

Bandgap Engineering of AgGaS₂ for Optoelectronic Devices: First-Principles Computational Technique	67
Maneesha Purohit, Seema Kumari Meena, Alpa Dashora and B. L. Ahuja	
Intelligent Power Sharing Control for Hybrid System	75
Preeti Gupta and Pankaj Swarnkar	
Comparative Analysis of Various Classifiers for Gesture Recognition	85
Rahul Gupta, Sarthak Rana, Swapnil Gupta, Kavita Pandey and Chetna Dabas	
Artificial Intelligence Based Optimization Techniques: A Review	95
Agrani Swarnkar and Anil Swarnkar	
Optimal Location and Sizing of Microgrid for Radial Distribution Systems	105
Shalaka N. Chaphekar, Anandkumar Nale, Anjali A. Dharme and Nitant Mate	
Constraint Tariff Model to Reduce the Amount of Cross Subsidy Incorporated in Electricity Tariff Using Iterative Optimization Technique	115
Varada J. Tambe and S. K. Joshi	
Titration Machine: A New Approach Using Arduino	125
Vijayalaxmi, S. H. Ashwin and S. V. Harish	
Hybrid Method for Cluster Analysis of Big Data	133
Chetna Dabas and Gaurav Kumar Nigam	
A New Radio Frequency Harvesting System	141
Syed Mahmood Ali Mahboob, Shaik Qadeer and Ajaz Fatima	
Backpropagation Algorithm-Based Approach to Mitigate Soiling from PV Module	153
Sujit Kumar and Vikramaditya Dave	
Real-Time Low-Frequency Oscillations Monitoring and Coherency Determination in a Wind-Integrated Power System	163
Abhilash Kumar Gupta, Kusum Verma and K. R. Niazi	
Design and Performance Analysis of Different Structures of MEMS PVDF-Based Low-Frequency Piezoelectric Energy Harvester	173
Namrata Saxena, Varshali Sharma, Ritu Sharma, K. K. Sharma and Santosh Chaudhary	
Designing and Implementation of Overhead Conductor Altitude Measurement System Using GPS for Sag Monitoring	183
Sangeeta Kamboj and Ratna Dahiya	

Risk-Averse G2V Scheduling of Electric Vehicle Aggregator for Improved Market Operations	195
S. Sharma, P. Jain and P. P. Gupta	
Optical Gain Tuning in Type-I $\text{Al}_{0.45}\text{Ga}_{0.55}\text{As}/\text{GaAs}_{0.84}\text{P}_{0.16}/\text{Al}_{0.45}\text{Ga}_{0.55}\text{As}$ Nano-heterostructure	205
Md. Riyaj, Sushil Kumar, P. A. Alvi and Amit Rathi	
Semantic Similarity Computation Among Hindi Words Using Hindi Lexical Ontology	211
Yogesh Gupta and Amit Saraswat	
A Dual-Band Microstrip Patch Antenna for Wireless Applications ...	219
P. Kumar	
Analysis of Energy Consumption and Implementation of R-Statistical Programming for Load Forecasting in Presence of Solar Generation	227
S. K. Singh, Harsh Vikram Singh, S. Chakrabarti and S. N. Singh	
A Comprehensive Analysis of Delta and Adaptive Delta Modulated Modular Multilevel Converter	239
Rahul Jaiswal, Anshul Agarwal and Vineeta Agarwal	
Speed Control of PMSM Drive Using Jaya Optimization Based Model Reduction	247
Akhilesh K. Gupta, Paulson Samuel and Deepak Kumar	
Jaya Optimization-Based PID Controller for Z-Source Inverter Using Model Reduction	257
Akhilesh K. Gupta, Paulson Samuel and Deepak Kumar	
Stability Analysis of an Offshore Wind and Marine Current Farm in Grid Connected Mode Using SMES	269
Satendra Kr Singh Kushwaha, S. R. Mohanty and Paulson Samuel	
Modeling and Simulation of Proton Exchange Membrane Fuel Cell Hybrid Electric Vehicle	281
Bandi Mallikarjuna Reddy and Paulson Samuel	
Optimum Performance of Carbon Nanotube Field-Effect Transistor Based Sense Amplifier D Flip-Flop Circuits	293
Komal Swami and Ritu Sharma	
Flower Pollination Based Solar PV Parameter Extraction for Double Diode Model	303
J. Prasanth Ram, Dhanup S. Pillai, N. Rajasekar and V. Kumar Chinnaiyan	

Cost–Benefit Calculation Using AB_2X_4 ($A = Zn, Cd$; $B = Ga$; $X = Te$): A Promising Material for Solar Cells	313
Pancham Kumar, Amit Soni and Jagrati Sahariya	
Detection and Analysis of Power System Faults in the Presence of Wind Power Generation Using Stockwell Transform Based Median	319
Sheesh Ram Ola, Amit Saraswat, Sunil Kumar Goyal, S. K. Jhajharia and Om Prakash Mahela	
A Directional Relaying Scheme for Microgrid Protection	331
Ruchita Nale, Ruchi Chandrakar, Harishankar Verma and Monalisa Biswal	
Wavefunctions and Optical Gain in $In_{0.24}Ga_{0.76}N/GaN$ Type-I Nano-heterostructure Under External Uniaxial Strain	341
Md. Riyaj, Amit Kumar Singh, P. A. Alvi and Amit Rathi	
Cost–Benefit Analysis in Distribution System of Jaipur City After DG and Capacitor Allocation	351
Ankush Tandon, Sarfaraz Nawaz and Shahbaz Ahmed Siddqui	
Comparative Simulation Study of Dual-Axis Solar Tracking System on Simulink Platform	359
Neeraj Tiwari, Ravi Soni, Amit Saraswat and Brijesh Kumar	
Performance Evaluation and Quality Analysis of Line and Node Based Voltage Stability Indices for the Determination of the Voltage Instability Point	367
Pradeep Singh, Jyotsna Singh and Rajive Tiwari	
Channel Estimation in Massive MIMO with Spatial Channel Correlation Matrix	377
Bijoy Kumar Mandal and Ankita Pramanik	
A New Array Reconfiguration Scheme for Solar PV Systems Under Partial Shading Conditions	387
Malisetty Siva Sai Nihanth, N. Rajasekar, Dhanup. S. Pillai and J. Prasanth Ram	
Adaptability Analysis of Particle Swarm Optimization Variants in Maximum Power Tracking for Solar PV Systems	397
B. G. Dharshan, N. Rajasekar and R. Srinivasa Sankarkumar	
Fault Location Methods in HVDC Transmission System—A Review	411
Jay Prakash Keshri and Harpal Tiwari	

Optimal Reactive Power Dispatch Through Minimization of Real Power Loss and Voltage Deviation 421
 Ravi Ucheniya, Amit Saraswat and Shahbaz Ahmed Siddiqui

IoT Enabled Intelligent Energy Management and Optimization Scheme with Controlling and Monitoring Approach in Modern Classroom Applications 431
 Vidyadhar Aski, Rajveer Singh Shekhawat, Sushant Mehta, Pratik Kr. Jain and Prachal Goyal

High Power Density Parallel LC-Link PV Inverter for Stand-alone and Grid Mode of Operation 441
 Rudra Santhosh Kumar Athikamsetti and Satish Kumar Gudey

A Hybrid Forecasting Model Based on Artificial Neural Network and Teaching Learning Based Optimization Algorithm for Day-Ahead Wind Speed Prediction 455
 Madasthu Santhosh, Chintham Venkaiah and D. M. Vinod Kumar

Risk Averse Energy Management for Grid Connected Microgrid Using Information Gap Decision Theory 465
 Tanuj Rawat and K. R. Niazi

Power Quality Improvement of Microgrid Using Double Bridge Shunt Active Power Filter (DBSAPF) 475
 Rajesh Kumar Meena, Dheeraj Kumar, Vinay Kumar Jadoun and Saurabh Kumar Pandey

Opposition Theory Enabled Intelligent Whale Optimization Algorithm 485
 Prateek Jain, Pooja Jain and Akash Saxena

Adaptive Inertia-Weighted Firefly Algorithm 495
 Shailja Sharma, Pooja Jain and Akash Saxena

A Review of Scheduling Techniques and Communication Protocols for Smart Homes Capable of Implementing Demand Response 505
 Gurpinder Singh, Anil Swarnkar, Nikhil Gupta and K. R. Niazi

A Robust Open-Loop Frequency Estimation Method for Single-Phase Systems 515
 Anant Kumar Verma, C. Subramanian and R. K. Jarial

Demand-Side Load Management for Peak Shaving 525
 Shailendra Baraniya and Manoj Sankhe

A New Line Voltage Stability Index (NLVSI) For Voltage Stability Assessment 535
 Trinadha Burle, V. V. S. Bhaskara Reddy Chintapalli and Phanindra Thota

A Comprehensive Comparative Economic Analysis of ACO and CS Technique for Optimal Operation of Stand-alone HES	549
Sri Lakshmi E and S. P. Singh	
Demand Response in Distribution Systems: A Comprehensive Review	565
Bhuvan Sharma, Nikhil Gupta, K. R. Niazi and Anil Swarnkar	
Stochastic Operational Management of Grid-Connected Microgrid Under Uncertainty of Renewable Resources and Load Demand	573
Sonam Parashar, Anil Swarnkar, K. R. Niazi and Nikhil Gupta	
Real-Time High-Speed Novel Data Acquisition System Based on ZYNQ	583
Himanshu Tyagi, Nagendra P. Gajjar, Mainak Bandyopadhyay and Arun Chakraborty	
Exergetic Analysis of Glazed Photovoltaic Thermal (Single-Channel) Module Using Whale Optimization Algorithm and Genetic Algorithm	591
Sourav Diwania, Anmol Gupta, Anwar S. Siddiqui and Sanjay Agrawal	
An 8-Bit Charge Redistribution SAR ADC	601
Yahya Mohammed Ali Al-Naamani, K. Lokesh Krishna and A. Krishna Mohan	
Analysis of Triple-Threshold Technique for Power Optimization in SRAM Bit-Cell for Low-Power Applications at 45 Nm CMOS Technology	611
Sudershan Kumar, Shaifali Ruhil, Neeraj KR. Shukla and Shilpi Birla	
Low Power Adder Circuits Using Various Leakage Reduction Techniques	619
Shreya Upadhyay, Sugandha Tiwari, Shilpi Birla and Neha Singh	
A Nature-Inspired Metaheuristic Swarm Based Optimization Technique BFOA Based Optimal Controller for Damping of SSR	631
Rajeev Kumar, Rajveer Singh and Haroon Ashfaq	
New Fuzzy Divergence Measures, Series, Its Bounds and Applications in Strategic Decision-Making	641
Ram Naresh Saraswat and Neha Khatod	
Mutual Coupling Reduction of Biconvex Lens Shaped Patch Antenna for 5G Application	655
Ribhu Abhusan Panda, Udit Narayan Mohapatro and Debasis Mishra	
Analysis of Anti-Islanding Protection Methods Integrated in Distributed Generation	663
Vikram Singh, Manoj Fozdar, Ajeet Kumar Singh and Satyendra Singh	

Color Image Watermarking with Watermark Hashing	673
Neha Singh, Sandeep Joshi and Shilpi Birla	
Global Neighbourhood Algorithm Based Event-Triggered Automatic Generation Control	683
Pankaj Dahiya, Pankaj Mukhija and Anmol Ratna Saxena	
A Review on Voltage and Frequency Control of Micro Hydro System	693
Priya Singh Bhakar, Saumendra Sarangi and Kirti Gupta	
Performance Analysis of Solar and Plug-in Electric Vehicle’s Integration to the Power System with Automatic Generation Control	703
Subhranshu Sekhar Pati, Tapas Kumar Panigrahi and Aurobindo Behera	
A Bibliographical View on Research and Developments of Photovoltaic and Thermal Technologies as a Combined System: PV/T System	713
Anmol Gupta, Sourav Diwania, Sanjay Agrawal, Anwar S. Siddiqui and Yash Pal	
UPM-NoC: Learning Based Framework to Predict Performance Parameters of Mesh Architecture in On-Chip Networks	723
Anil Kumar and Basavaraj Talawar	
Comparison of Performance Analysis of Optimal Controllers for Frequency Regulation of Three-Area Power System	735
Preeti, Vivek Shrivastava, Vikas Singh Bhadoria and Harish Pulluri	
Optimal DG Allocation in a Microgrid Using Droop-Controlled Load Flow	745
Ankit Uniyal and Saumendra Sarangi	
A Comparative Study of Classification Algorithms for Predicting Liver Disorders	753
Rashi Bhardwaj, Rajat Mehta and Prakash Ramani	
Performance Analysis of Fabricated Buck-Boost MPPT Charge Controller	761
Neeraj Tiwari, Amit Saraswat, Ravi Soni and Suchi Rawat	
Performance Improvement of Cycloconverter Fed Induction Machine Using Shunt Active Power Filter	769
Vishnu Goyal and Sulochana Wadhawani	
Comparative Analysis of Speaker Recognition System Based on Voice Activity Detection Technique, MFCC and PLP Features	781
Akanksha Kalia, Shikar Sharma, Saurabh Kumar Pandey, Vinay Kumar Jadoun and Madhulika Das	

Nonintrusive Load Monitoring: Making Smart Meters Smarter	789
DeepRaj Bedi and Vineet Sharma	
Stabilization of Chaotic Systems Using Robust Optimal Controller . . .	795
Madhulika Das and Vinay Kumar Jadoun	
Jaya Algorithm Based Optimal Allocation of Distributed Energy Resources	805
Manoj Kumawat, Nitin Gupta, Naveen Jain and R. C. Bansal	
Bayesian Game Model: Demand Side Management for Residential Consumers with Electric Vehicles	815
Akash Talwariya, Santosh Kumar Sharama, Pushpendra Singh and Mohan Kolhe	
Classification of Power System Disturbances Using Support Vector Machine in FPGA	825
Vivek Patel	
Designing a Smart System for Air Quality Monitoring and Air Purification	837
Palak Gandhi, Kartik Upadhyay, Ashwani Kumar Yadav and Vaishali	
Activation Map Networks with Deep Graphical Model for Semantic Segmentation	845
Cheruku Sandesh Kumar, Ratnadeep Roy, Sanyog Rawat and Archek Praveen Kumar	
Grey Wolf Optimized PI Controller for Hybrid Power System Using SMES	853
Sandeep Bhongade and Ritu Verma	
JAYA-Evaluated Frequency Control Design for Hydroelectric Power System Using RFB and UPFC	863
Akhilesh Panwar, Gulshan Sharma, Ibraheem Nasiruddin and R. C. Bansal	
A Human Face-Shaped Microstrip Patch Antenna for Ultra-Wideband Applications	873
Anandhi Dharmarajan, Pradeep Kumar and Thomas J. O. Afullo	
Scheduling Energy Storage to Provide Balancing During Line Contingency at High Wind Penetration	881
Bal Krishna, Anjali Jain and Ajay Bharadwaj	
Multilevel Inverter Topologies in Renewable Energy Applications	891
Prakash Kumar, Maneet Kour, Sunil Kumar Goyal and Bhuwan Pratap Singh	

A Review on Demand Side Management Forecasting Models for Smart Grid 903
 Sweta Singh and Neeraj Kanwar

Detection of Suspicious Activity in ATM Booth 911
 Anjali Saini, Mushtaq Ahmed and Kartikey Sharma

Mitigation of Power Quality for Wind Energy Using Transmission Line Based on D-STATCOM 927
 Sourabh Kumar Jain and Amit Soni

Performance Evaluation of Solar Power Plant 937
 Amit Rai, Ashish Shrivastava and K. C. Jana

GWO Based PID Controller Optimization for Robotic Manipulator 943
 Sandeep Tripathi, Ashish Shrivastava and K. C. Jana

A 26 W Power Supply Based on Luo Converter with Improved Power Factor and Total Harmonic Distortion 953
 Amit Agrawal, Ashish Shrivastava, Amit Rai and K. C. Jana

Optimal Strategic Bidding Using Intelligent Gravitational Search Algorithm for Profit Maximization of Power Suppliers in an Emerging Power Market 963
 Satyendra Singh, Manoj Fozdar and Ajeet Kumar Singh

Synchrophasor Measurements Assisted Naïve Bayes Classification Based Real-Time Transient Stability Prediction of Power System 973
 Divya Rishi Shrivastava, Shahbaz Ahmed Siddiqui and Kusum Verma

Device Modeling and Characteristics of Solution Processed Perovskite Solar Cell at Ambient Conditions 981
 Anupam Agrawal, Shahbaz Ahmed Siddiqui, Amit Soni and Ganesh D. Sharma

Control and Remote Sensing of an Irrigation System Using ZigBee Wireless Network 989
 Jay Praful Chheda and Vikash Kumar Boradak

Analysis and Classification of Maximum Power Point Tracking (MPPT) Techniques: A Review 999
 Bhuwan Pratap Singh, Sunil Kumar Goyal and Shahbaz Ahmed Siddiqui

A Study and Comprehensive Overview of Inverter Topologies for Grid-Connected Photovoltaic Systems (PVS) 1009
 Bhuwan Pratap Singh, Sunil Kumar Goyal, Shahbaz Ahmed Siddiqui and Prakash Kumar

IOT Based Smart Writer 1019
Chirag Agarwal and Bhawna Singh

**Design and Implementation of Arduino Based Control System
for Power Management of Household Utilities** 1025
Mahipal Bukya, Aayush Bajaj, Peeyush Garg and Amit Saraswat

**Interfacing Python with DIgSILENT Power Factory: Automation
of Tasks** 1033
Divya Rishi Shrivastava, Shahbaz Ahmed Siddiqui and Kusum Verma

**Recent Development in Perovskite Solar Cell Based on Planar
Structures** 1039
Anupam Agrawal, Shahbaz Ahmed Siddiqui, Amit Soni
and Ganesh D. Sharma

About the Editors

Akhtar Kalam has been at Victoria University (VU) since 1985. He is a former Deputy Dean of the Faculty of Health, Engineering and Science and Head of Engineering of the College of Engineering and Science. Currently, he is the Head of External Engagement. He is also the current Chair of the Academic Board in the Engineering Institute of Technology, Perth, Australia, and the Editor in Chief of Australian Journal of Electrical & Electronics Engineering. Also, he has a Distinguished Professorship position at the University of New South Wales, Sydney, Australia, three Indian and five Malaysian universities. Professor Kalam has conducted research, provided industrial consultancy and published more than 542 publications on his area of expertise. He has written 26-plus books in the area. More than 35 PhD students have graduated under his supervision. He received his B.Sc. and B.Sc. Engineering degrees from University of Calcutta and the Aligarh Muslim University, India. He completed his MS and Ph.D degrees at the University of Oklahoma, USA and the University of Bath, UK respectively. He provides consultancy for major electrical utilities, manufacturers and other industry bodies in his field of expertise. He is a Fellow of EA, IET, AIE, a life member of IEEE and a member CIGRE AP B5 Study Committee.

Khaleequr Rehman Niazi has over 29 years of teaching and research experience. Currently he is a Professor in the Department of Electrical Engineering and Dean of Academic affairs of MNIT Jaipur. He has vast administrative experience. He has worked as Head, Electrical Engineering Department, Advisor- Estate, Chief Vigilance Officer, Chairman- Senate Undergraduate committee, Member Board of Governors of MNIT, Professor In-Charge - Training & Placement, Nodal Officer-TEQIP, etc at MNIT, Jaipur. He has published over 200 papers in International journals and conferences. He has also published a book. He has so far supervised 16 Ph.Ds and many PG dissertations and carried out many sponsored R&D projects. He has diversified research interests in the areas of conventional power and renewable energy systems, smart grid, distribution network reconfiguration, flexible AC transmission systems (FACTS), and application of AI and ANN techniques to power systems. He has been visiting professor of Taibah University,

Kingdom of Saudi Arabia. He was also nominated by DST India for International Training on “Electrical Power system automation Technology and applications” at Wuhan China. He is presently Associate Editor of RPG IET journal of UK, Senior Member IEEE, USA and life member ISTE, India.

Amit Soni has 18 years of teaching and research experience and is presently working as Professor & Head of Department of Electrical Engineering, Manipal University Jaipur, Jaipur. He has completed PhD (2012) and M. Tech. (2005) in “Power Systems” both from M.N.I.T. Jaipur. He has worked in various administrative capacities such as Director, RTU affiliated Engineering College, Head, Electrical Department, Coordinator and Chairman for various Academic Committees at both undergraduate and postgraduate levels. He has published more than 50 research papers in reputed SCI indexed journals and conferences. He has supervised 3 Ph.Ds and many PG students under his guidance. Currently, he is working on DST SERB funded research project in collaboration with MLSU, Udaipur and NIT Uttarakhand. Students from all levels i.e. UG, PG and Ph.D. are working under his supervision on different areas. He has also published book on “Power System Engineering” for RTU affiliated institutions. Currently, he is working on Solar PV Materials & its applications, Photovoltaics, Renewable Energy Systems and Power System. He is life member of Solar Energy Society of India, Member ISTE, India and IEEE, USA.

Shahbaz Ahmed Siddiqui is Associate Professor and Head in Department of Mechatronics Engineering, Manipal University, Jaipur India. He completed his Ph. D and M. Tech. from M.N.I.T., Jaipur in Power Systems. He is teaching undergraduate and post graduate courses and his areas of research interests include artificial intelligence applications to power system operation and control, operation and control of microgrid, and synthesis and fabrication of solar cells. He has published more than 50 papers in International Journals and Conferences. He is life member of ISTE, India and member of IEEE, USA.

Ankit Mundra is working as Assistant Professor in the Department of Information Technology, Faculty of Engineering, Manipal University Jaipur. He is pursuing PhD from M.N.I.T., Jaipur in Internet of Things. His area of research expertise is Network Security, Wireless Networks, Online Fraud Detection. He has published more than 25 research articles in International Journals and Conferences. He has been the editor of two international books published by Springer Nature.

LED Driver Design and Thermal Management



Aniruddha Mukherjee, Amit Soni and Mukesh Gupta

Abstract The lighting industry has been ushered to a new lighting revolution with the advent of light emitting diode (LED). During the last decade, research work carried out extensively in material science has completely eradicated the optical shortcomings in LEDs by and large. However, one important aspect still remains a challenge for engineers worldwide—LED thermal management. It has been well established by now that LEDs are prone to degradation in terms of light output with a rise in junction temperature. This paper investigates the aspect of thermal issues pertaining to (a) LED solder point temperature and (b) ambient temperature for 5 mm high-brightness LEDs. 5 mm high-brightness LEDs are selected. The LEDs are subjected to stress environmental conditions and the light output with change in solder point temperature is evaluated. Further, a driver circuit design using LM3464 IC is proposed to arrest the change in light output with solder point temperature. A plot suggesting a correlation is derived to suggest the change in light output with change in solder point temperature. Finally, it also explores the heat dissipation in the solder pad of the LED. The software tool for execution of the plots is carried out using Origin 7 and driver design along with the thermal distribution of the heat sink, with the aid of WEBENCH design tool and Heat Sink Calculator, respectively.

Keywords Solder point temperature · Ambient temperature · Light output

1 Introduction

With the inception of LEDs as an artificial light source, the concept of lighting has undergone a drastic change, particularly because of its varying optical properties attributed to the source—(a) directional (b) distributed light output. LEDs are predominantly current-controlled devices; hence, it is well comprehended that increase

A. Mukherjee (✉) · M. Gupta
Suresh Gyan Vihar University, Jaipur, India
e-mail: mukherjeeanirudh73@gmail.com

A. Soni
Manipal University Jaipur, Jaipur 303007, Rajasthan, India

© Springer Nature Singapore Pte Ltd. 2020
A. Kalam et al. (eds.), *Intelligent Computing Techniques for Smart Energy Systems*,
Lecture Notes in Electrical Engineering 607,
https://doi.org/10.1007/978-981-15-0214-9_1

in driving current will always correspond to higher luminous flux output. This particular attribute has consequently posed a lot of challenges to the lighting engineers. Any considerable change in the driving current will also contribute to the rise in the junction temperature thereby disturbing its optical properties and finally degrading the LED lifetime [1–5]. This in fact has opened up new challenges in LED lighting—maintaining a steady light output while also keeping a check on the junction temperature [6]. Liu and Yang demonstrated different driver topologies for LEDs. The work was aimed at improved performance of the device by choosing proper driver topology. In fact, it defined the inherent aspect of compatibility issues of LED driver circuits with respect to the device characteristics [7].

Researchers further designed an LED driver with buck–boost topology and inherent power factor correction which was the significant aspect of the driver circuit as it was able to improve the input power factor close to unity. The biggest disadvantages of this topology are—(a) the LED driver current is modulated at twice the utility frequency and (b) in the discontinuous mode of operation (DCM), the operation increases component stress levels thus affecting the life of the device [8, 9]. In the successive years, a non-isolated buck converter with power factor correction was investigated to overcome the shortcomings of the earlier proposed circuit both for continuous current and discontinuous current mode of operation. However, it also increased the switching stress thus affecting the life of the LED lighting system [10]. Then it was finally the work done by Hu, Huber, and Jovanovic in 2012 on a single-stage flyback power factor correction (PFC) circuit with a variable boost inductance for high-brightness LED applications for the universal input voltage 90–270 V which addressed the limitations of the conventional single-stage PFC flyback with a constant boost inductance. According to the proposed method, the IEC 61000-3-2 class C and corresponding Japanese standard JIS C 61000-3-2 class C line-current harmonic limits were satisfied [11, 12].

In the subsequent section, we shall investigate the 5 mm LEDs for the changes in solder point to ambient temperature with a rise in ambient temperature and the corresponding heat distribution alongside the heat sink. The corrective designs are incorporated and analyzed.

1.1 *Experimental Setup*

The 5 mm LEDs are initially tested in a test chamber comprising thermocouple and a provision for blowing hot air to resemble high ambient temperature. The setup and the results hence obtained from the experiment are observed and concluded that the light output degrades with a change in ambient temperature conditions [13, 14]. From the current set of results, plots are obtained as shown in Fig. 1. The relation between ambient temperature and solder point temperature can be understood from the plot of the selected sample L2 as shown in Fig. 2 with the driver circuit as obtained commercially. The mathematical relation depicting an empirical relation between the two parameters is derived as follows in Eq. (1) and from Fig. 1:

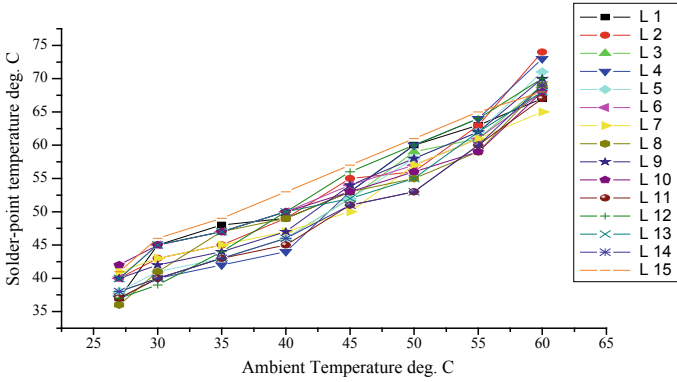


Fig. 1 Plot depicting the change in solder point temperature with change in ambient temperature for 5 mm LEDs

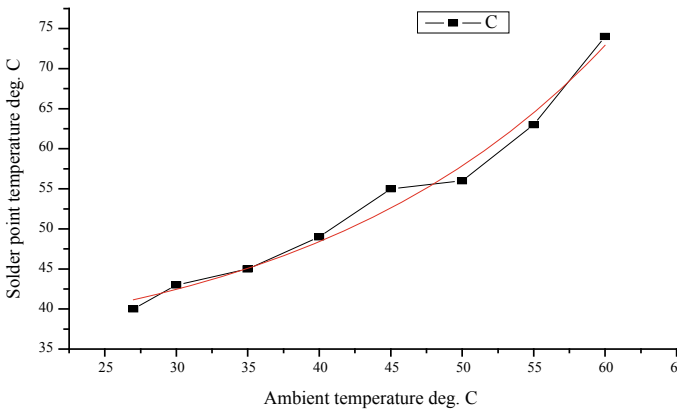


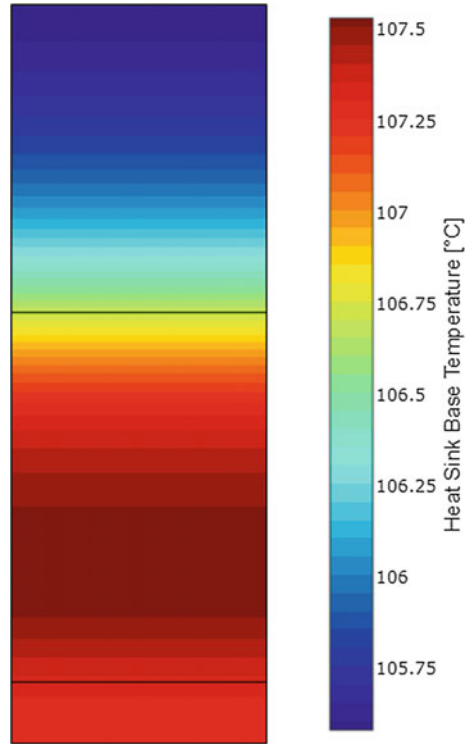
Fig. 2 Plot for sample L2 against rise in solder point temperature with change in ambient temperature depicting maximum temperature rise

$$y = A_1 e^{\left(\frac{x}{t_1}\right)} + y_0 \tag{1}$$

where “y” represents the percentage light output and “x” represents the ambient temperature. The R-square from the above relation is 99.45% with the values of “A₁”, t₁, and y₀ being 0.56446 ± 0.35762, 15.68693 ± 2.38355, and 41.77225 ± 1.76618, respectively. In the above relation, “A₁” is referred to as a constant for the relation implying the rise in solder point temperature per unit rise of ambient temperature, “x/t₁” implies the time constant, and “y₀” signifies the base temperature rise for the lamp driver combination.

The heat sink temperature profile considering the sample L2 is as shown in Fig. 3. The temperature profile is evident that the solder point temperature is raised to around 107 °C with a rise in ambient temperature. The results are persistent with the use of

Fig. 3 Temperature profile of LED heat sink for pure aluminum for junction to case thermal resistance of 73 degree K/W which is the solder point temperature



drivers available. It further records the temperature of the junction to case thermal resistance of 73 degree K/W. This aggravates further and degrades the light output of the LEDs. In the subsequent discussion, a new driver is proposed and the same experiment is carried out to validate the aspect of arresting the abrupt temperature rise.

From Fig. 4, it is understood that the LED reaches 70% of the initial light output as the temperature is raised which implies that the device reaches the end of life with the rise in solder point temperature. This further justifies that the rise in solder point temperature depreciates the light output of the LED under test.

1.1.1 Proposed Driver Circuit and Device Analysis

The proposed driver circuit for the experiment is implemented on sample L2 using LM3464 IC. The LM3464 is a 28-pin high-voltage current regulator having individual current channels to provide the necessary power to LED strings. It is capable of enhancing the overall efficiency of the LED system by adjusting the output voltage of the power source dynamically. It is further capable of controlling the current input

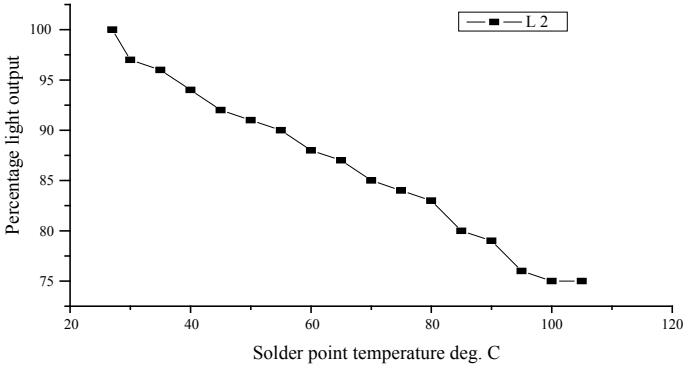


Fig. 4 Degradation of percentage light output with change in solder point temperature for L2

to the LEDs thereby controlling the temperature of the LED heat sink simply by the use of the inbuilt NTC. Figure 5 depicts the driver design incorporating the same.

The plot of voltage across NTC and system temperature is as shown in Fig. 6. As evident from the circuit diagram, the drop in LED temperature is independent of the voltage level. This also shows that the circuit is auto-cut enabled beyond a specific voltage level. These characteristics make it a suitable choice for lighting applications where the ambient temperature is greater than 25 °C. Further, in Fig. 7, the plot of decay in percentage light output with solder point temperature shows that the percentage drop in light output is less than 70% in temperatures as high as 80 °C.

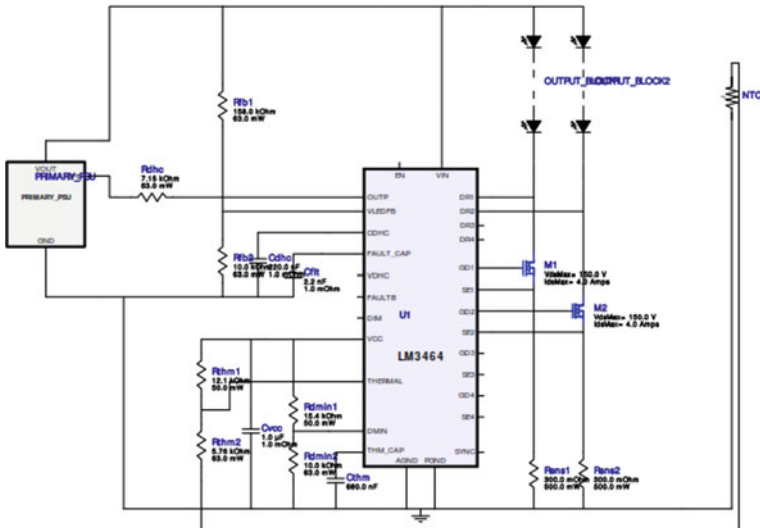


Fig. 5 Driver design using LM3464 IC

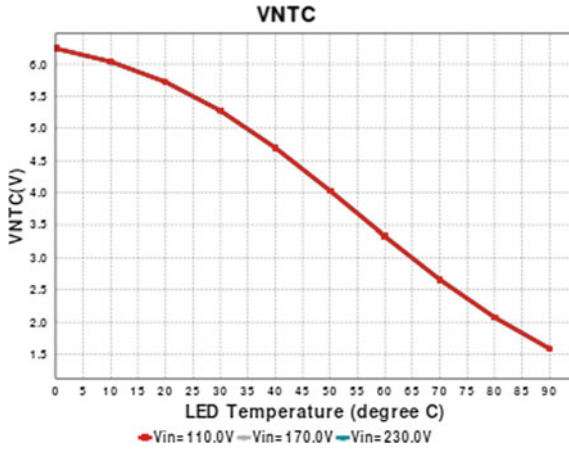


Fig. 6 Voltage versus LED temperature for three different voltage levels

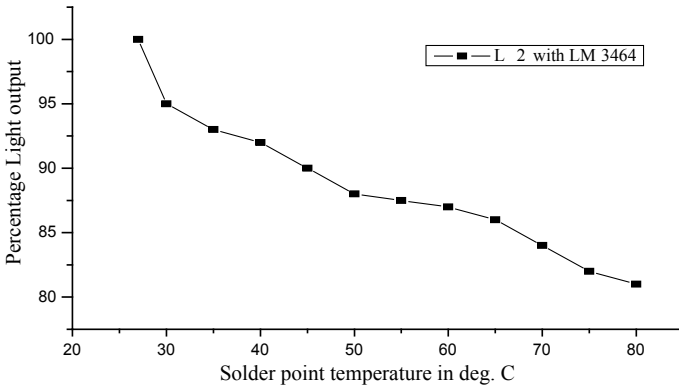
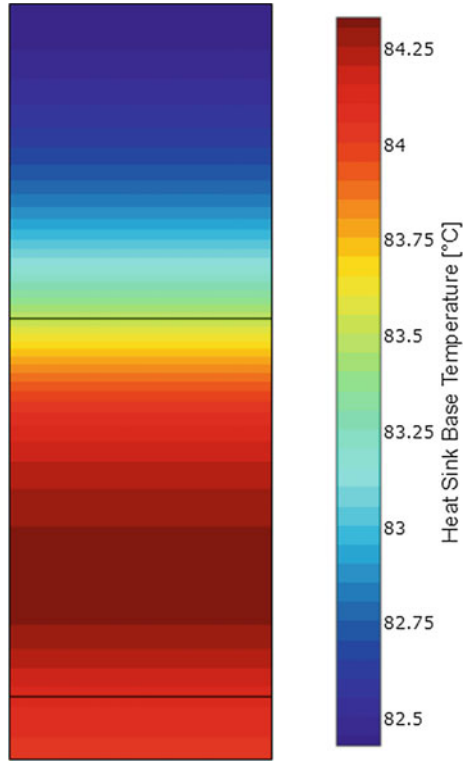


Fig. 7 Degradation in light output with LM3464 is evident that the solder point temperature does not exceed 80 °C

In Fig. 8, the heat distribution is evident that the solder point temperature does not exceed the range of 85 °C.

From Figs. 7 and 8, it is shown that the degradation in light output does not exceed 80% of its initial value and that the rise in junction to case thermal resistance is 50 degree K/W. These results justify that the proposed driver is able to control the unwarranted temperature rise and the light output substantially.

Fig. 8 Temperature profile of LED heat sink for pure aluminum for junction to case thermal resistance of 50 degree K/W which is the solder point temperature using LM3464 IC



2 Conclusion

From the above set of experiments, it is well understood that it becomes imperative to manage the heat generation of the LED device and this becomes all the more essential for a hot and humid country. The above simulations have been carried out with the objective to minimizing the solder point temperature rise beyond limits and thus extending the lifetime of the LED resource. The introduction of new driver for LED substantially provides ample relief from the rise in solder point temperature beyond a certain limit. The abnormal rise can hence be controlled and the decay in light output remains within the permissible limits.

References

1. Bullough J (2003) Light emitting diode lighting systems, lighting answers, vol 7, no 3. National Lighting Product Information Program, Lighting Research Center, Troy, NY
2. The Alliance for Solid State Illuminations and Technologies, ASSIST (2010) OSRAM Opto semiconductors, "LED basics", pp 1–26, 1 Sept 2010

3. The Alliance for Solid State Illuminations and Technologies, ASSIST, PHILIPS LUMILEDS (2008) Technology white paper, understanding power LED lifetime analysis, pp 1–11
4. Xi Y, Schubert EF (2004) Junction–temperature measurement in GaN ultraviolet light-emitting diodes using diode forward voltage method. *Appl Phys Lett* 85(12):2163
5. Narendran N, Bullough JD, Maliyagoda N, Bierman A (2001) What is the useful life for white LEDs? *J Illum Eng Soc* 30(1):57–67
6. Jayawardena A, Liu Y, Narendran N (2012) Methods for estimating the junction temperature of AC LEDs. In: Council for optical radiation measurements (CORM) 2012 annual technical conference Ottawa, Ontario, 29 May–1 June 2012
7. Yu L, Yang J (2009) The topologies of white LED lamps’ power drivers. In: 3rd IEEE conference on power electronics systems and applications (PESA), pp 1–6, 20–22 May 2009, Hong Kong
8. Chiu H-J et al (2010) A High efficiency dimmable LED driver for low power lighting applications. *IEEE Trans Ind Electron* 57(2):735–743
9. Aguilar D, Henze CP (2010) LED driver circuit with inherent PFC. In: Twenty-fifth IEEE annual conference on applied power electronics and exposition (APEC) 2010, pp 605–610, 21–25 Feb 2010, Palm Springs, CA
10. Chern T-L et al (2011) Design of LED driver circuits with single stage PFC in CCM and DCM. In: 6th IEEE conference on industrial electronics and applications (ICIEA) 2011, pp 2358–2363, 21–23 June 2011, Beijing
11. Hu Y, Huber L, Jovanovic MM (2012) Single stage, universal input AC/DC LED driver with current controlled variable PFC boost inductor. *IEEE Trans Power Electron* 27(3):1579–1588
12. IEC-61000-3-2 (2014) Electromagnetic compatibility part 3-2: limits-limits for harmonic current emissions. International Electrotechnical Commission, May 2014
13. Mukherjee A, Soni A (2016) Effect of ambient temperature rise on LED lifetime resource. *Light Eng* 24(2):56–60
14. Mukherjee A, Bansal TC, Soni A (2018) Analysis of LED driver topologies with respect to power factor and THD. *Light Eng* 26(1):63–68

Automatic Generation Control of Interconnected Power Systems Using Elephant Herding Optimization



S. S. Dhillon, Surabhi Agarwal, Gai-Ge Wang and J. S. Lather

Abstract This paper presents load frequency control and dynamic modelling of an interconnected grid of three power system areas, where area-1 consists of a single non-reheat synchronous generator and DFIG wind turbine based hybrid generation, second is synchronous generator power plant with reheat, and the last one consists of hydro turbine based generation unit. The automatic generation control of an interconnected power system is studied by using MATLAB/Simulink for uncertain variations in load demands. A nature-inspired algorithm, i.e. Elephant Herding Optimization (EHO) is applied to mitigate frequency deviations under sudden variations in demand. An objective function based on frequency deviations, tie-line powers is defined for the study. The outcomes of the proposed EHO-based AGC (Automatic Generation Control) are validated and compared with PSO (Particle Swarm Optimization)-based AGC via simulation results on the basis of magnitude of normalized error.

Keywords Automatic Generation Control · Optimization techniques · Power system

1 Introduction

The ever-increasing need for interconnected modern power systems makes it a very complex and difficult task for the conventional control measures to maintain stability and reliability. Nowadays, modern power systems contain large share of grid-connected renewable (Wind, Solar, Biogas and Geothermal) operated generators [1, 2]. Hence, due to the complex integrity of power flow under sudden load demand,

S. S. Dhillon (✉)

Department of Electrical & Electronics Engineering, AKGEC, Ghaziabad, India
e-mail: sukhwinder2@rediffmail.com

G.-G. Wang

College of Information Science and Engineering, Ocean University of China, 266100 Qingdao, China

S. Agarwal · J. S. Lather

Department of Electrical Engineering, National Institute of Technology, KUK, Kurukshetra, India

© Springer Nature Singapore Pte Ltd. 2020

A. Kalam et al. (eds.), *Intelligent Computing Techniques for Smart Energy Systems*,
Lecture Notes in Electrical Engineering 607,
https://doi.org/10.1007/978-981-15-0214-9_2

situations call for emergency alarming events and malfunctioning of generator trips. Most of the times, voltage unbalance is raised due to fault current/ load demand. But at the same power angle, swing of the alternators causes deviations in system frequency [3]. The control system thus actuates the reactive power compensation and to keep voltage from unbalanced to balanced by providing VAR (voltage ampere reactive) as a contingency. This voltage control loop is fast responding and widely used to track voltage level at generator bus bar so as to provide reliable supply. But frequency control is totally related to the speed of the alternator which requires governor control of steam supply to the turbine. So, frequency control loop involves the actuation of mechanical parts and hence takes longer time span as compared to voltage control loop [4]. Frequency control had become so popular during the past two decades due to active power control as well as constant frequency demand of production industries [2]. There are various control schemes which were proposed to mitigate frequency deviations still available in the market such as conventional PID controllers tuned on the basis of hit and trail and Ziegler–Nichols heuristic approaches [5, 6]. Conventional PI, PID tuning methods are particularly suited for simple systems in a few cases where fuzzy control may even lead to uncontrollable and unreliable solutions [7–10]. Some other direct methods such as direct self, direct torque and dual torque controls are reported in [11–13]. Zhixin et al. had proposed inter-area oscillations control of DFIG-based wind turbine [14]. Ekanayake et al. had proposed primary and secondary frequency control loop of DFIG-based wind turbine connected to grid [15, 16]. With the advent of new nature-based optimization methods and models, frequency control techniques have become more efficient. These heuristic-based techniques, e.g. particle swarm optimization (PSO), have been used for frequency control in steady-state stability in both regulated and de-regulated environments [17–19]. LFC problem has reported a two-area interconnected system bacterial foraging optimization (BFOA) technique which was implemented to control system frequency including non-linearities [20]. Some advanced metaheuristic approaches such as TLBO [21], hybrid LUS–TLBO [22] and a hybrid BFOA–PSO [23] have been reported for multi-area LFC. In this paper, Elephant Herd Optimization [24] is applied on a MATLAB/Simulink model of a realistic interconnected multi-area power system to study load frequency control and the strategy for LFC is proposed. A doubly-fed induction generator [25] and gas turbine based micro power system is incorporated with steam power plant to have centralized configuration.

2 Modelling of Interconnected Three-Area Power System

The example three-area sample power system consists of a DFIG-based wind turbine modelled in [17], gas power unit [20–22] and steam power unit as modelled in [24, 26, 27]. The LFC model incorporates various constraints and features like generation rate constraint, droop characteristic and tie-line interchange dynamics. The dynamic models of various constituents like steam non-reheat, reheat and hydropower systems have been represented as state-space models as described below: For steam power

unit [1, 20–23, 25]:

$$\begin{bmatrix} \Delta P_{ti} \\ \Delta f_i \end{bmatrix} = \begin{bmatrix} 0 & \frac{1}{T_i} & 0 & 0 & 0 & \frac{-1}{T_i} \\ \frac{1}{2H_i} & 0 & \frac{-1}{2H_i} & \frac{-D_i}{2H_i} & \frac{-1}{2H_i} & 0 \end{bmatrix} \begin{bmatrix} \Delta P_{mi} \\ \Delta P_{gi} \\ \Delta P_{Li} \\ \Delta f_i \\ \Delta P_{tie, j} \\ \Delta P_{ti} \end{bmatrix} \quad (1)$$

For hydropower unit [20–23, 25]:

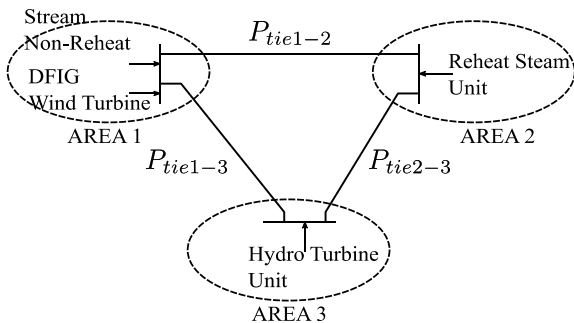
$$\begin{bmatrix} \Delta P_{ri}^* \\ \Delta P_{ti}^* \\ \Delta f_i^* \end{bmatrix} = \begin{bmatrix} \frac{-1}{T_2} & \frac{T_2-T_1}{T_2^2} & 0 & 0 & 0 & 0 \\ \frac{6}{T_w} & \frac{6T_1}{T_w T_2} & 0 & \frac{-2}{T_w} & 0 & 0 \\ \frac{-1}{H_i} & \frac{-T_1}{T_2 H_i} & \frac{-1}{2H_i} & \frac{-1}{2H_i} & \frac{1}{2H_i} & \frac{-D_i}{2H_i} \end{bmatrix} \begin{bmatrix} \Delta P_{ri} \\ \Delta P_{gi} \\ \Delta P_{Li} \\ \Delta P_{ti} \\ \Delta P_{tie, j} \\ \Delta f_i \end{bmatrix} \quad (2)$$

The coupling of the dynamics of governor and dynamics of tie-line power interchange are as [1, 24, 26, 27]:

$$\begin{bmatrix} \Delta P_{gi} \\ \Delta P_{tie, i} \end{bmatrix} = \begin{bmatrix} \frac{1}{T_{gi}} & \frac{-1}{R_i T_{gi}} & \frac{-1}{T_{gi}} & 0 \\ 0 & 2\pi T_{ij} & 0 & -2\pi T_{ij} \end{bmatrix} \begin{bmatrix} \Delta P_{ci} \\ \Delta f_i \\ \Delta P_{gi} \\ \Delta f_j \end{bmatrix} \quad (3)$$

The considered three-area sample test model considered for the present study is as shown in Fig. 1.

Fig. 1 Three-area interconnected power system model



3 Proposed Elephant Herding Optimization (EHO) Based Strategy for LFC

Elephant Herd Optimization is a swarm optimization with one distinct feature from bird swarm that separation of male elephants from the clan or swarm. It follows mainly three rules for optimization as follows.

- (1) The entire test elephant population consists of certain clans with every clan comprising a fixed number of elephants.
- (2) A pre-fixed number of male elephants out of the entire population shall abandon their family group to solitarily which stay far away from the main elephant group during each generation.
- (3) Within a clan, the member elephants stay together and follow/work under leadership known as the matriarch.
- (4) The procedure follows until the objectives are met.

3.1 Clan Updating Operator

Since there is a leadership of a matriarch and all the member elephants stay together under it, for every member elephant in clan Ki , the very next position is affected by the particular matriarch Ki . For every member elephant j in clan Ki , the same can be updated as

$$X_{Ki+1}(Ki, j) = X_{Ki}(Ki, j) + \alpha(X_{\text{best}}(Ki) - X(Ki, j)) \times r \quad (4)$$

where $X_{K+1}(i, j)$ and $X_{Ki}(Ki, j)$ are freshly recomputed and the existing positions of the member elephant j in clan Ki , respectively. The scalar $\alpha \in [0, 1]$ is a factor that decides the influence of the matriarch Ki on clan member $X_{Ki}(Ki, j)$. $X_{\text{best}}(Ki)$ represents matriarch Ki , which is the fittest elephant individual in the clan Ki . $r \in [0, 1]$. Here, uniform distribution is used. The dynamics of the fittest member elephant in each clan are not dictated by dynamics (4), i.e. $X_{Ki}(Ki, j) = X_{\text{best}}(Ki)$, and thus can be updated as

$$X_{K+1}(Ki, j) = \gamma \times X_{\text{centre}, Ki} \quad (5)$$

here, the scalar $\gamma \in [0, 1]$ dictates the influence/domination of the $X_{\text{centre}, Ki}$ on $X_{K+1}(Ki, j)$. The Ki clan centre and that for the d -th dimension can be calculated as

$$X_{\text{centre}, Ki, d} = \frac{1}{n_{Ki}} \times \sum_{j=1}^{n_{ki}} x_{Ki, j, d} \quad (6)$$

where the dimension lies between $1 \leq d \leq D$ with D representing the total dimension and the number n_{Ki} is the representative of the number of member elephants in each clan Ki .

3.2 Separating Operator

With an objective to continuously improve upon the searching ability of EHO, separating operator of male elephants as they leave their families is required to be modelled properly. It is assumed that the separating operation shall be implemented by an individual member elephant in the clan with the worst fitness as below:

$$X_{\text{worst}, Ki} = X_{\text{min}} + (X_{\text{max}} - X_{\text{min}} + 1) \times \text{rand} \quad (7)$$

here, X_{max} and X_{min} are upper and lower bounds on the position coordinate of every elephant in the clan. $X_{\text{worst}, Ki}$ represents the worst member in the respective clan Ki . $\text{rand} \in [0, 1]$ is a uniformly distributed random scalar closely bounded on both sides within a range of $[0, 1]$ for our current work. The execution of the algorithm results in heuristically optimized PID controller gains which are obtained pertaining to the fittest value of Ki in the clan for minimized objective function as

$$\text{objective function} = \min(\text{ISE}) \quad (8)$$

$$\text{PID}_{\text{best}} = Ki_{\text{best}}\{f(\text{MinISE})\} \quad (9)$$

where ISE is the integral squared error as a function of tie-line and mechanical powers.

4 Control Strategy

The present work concerns the frequency control problem in sample three-area power systems and it is assumed that each area shall have its individual PID control element. The objective function based on the integral squared error (ISE) is analysed as given by Eq. (8) (Fig. 2).

At the end of execution of the EHO algorithm, the converged values of PID control gains are obtained best matching towards the value of the objective function.

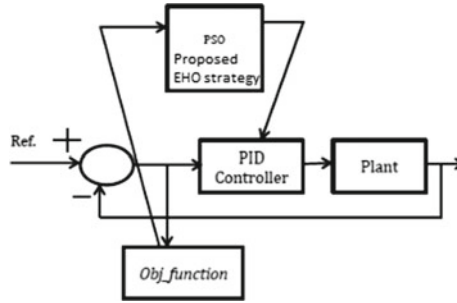


Fig. 2 PID controller control scheme

5 Results and Discussions

In this section, various uncertain conditions have been inflicted on area-1 and area-2 at time $t = 20$ s and $t = 70$ s, respectively, for step change of load demand 0.01 pu. The simulated results are reported as follows.

6 Conclusion

In this study, an interconnected power grid is modelled in MATLAB/Simulink environment which consists of three control areas. An integral squared error based objective function is defined for the optimization strategy. The Elephant Herd Optimization strategy is implemented to mitigate frequency deviations which were caused by step change of 0.01 pu in load demand from area-1 and area-2. From the simulation results as shown in Fig. 3a–c for frequency deviations, it is concluded that the settling time for the EHO-based strategy is found to be very less as 10 s whereas, with PSO (Particle Swarm Optimization), it is 20 s as shown in Tables 1 and 2. Similarly, for mechanical power deviations as shown in Fig. 4a–c, again EHO gives more promising results (Table 3).

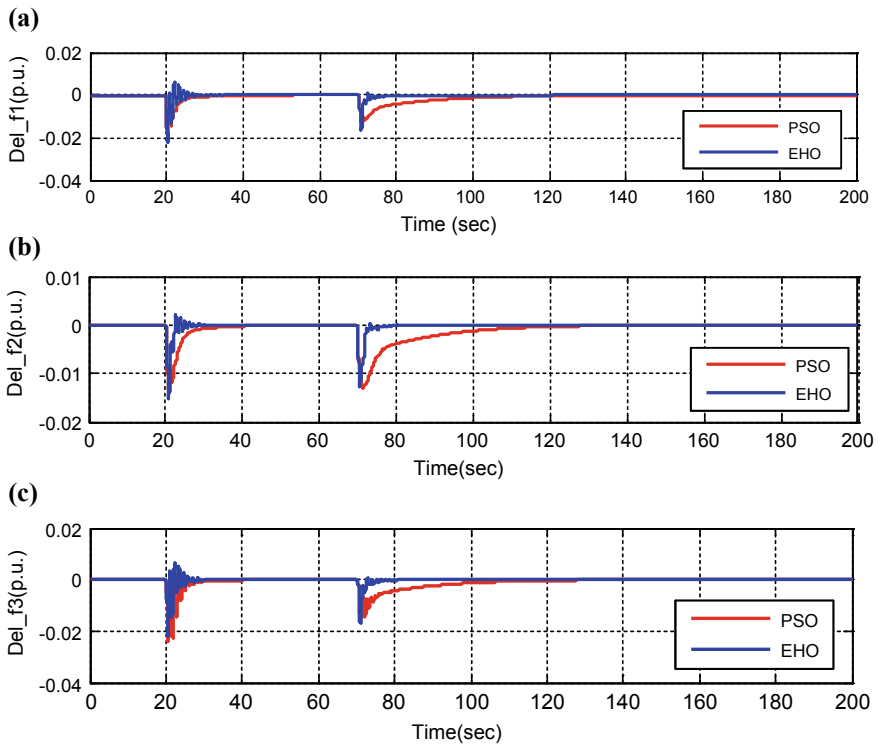


Fig. 3 a Frequency deviations of area-1. b Frequency deviations of area-2. c Frequency deviations of area-3

Table 1 Optimized values of PID controller gains

Parameters	PSO [23]	EHO
P1	0.846	1
P2	0.889	0.333
P3	1	0.889
I1	1	0.222
I2	0.778	0.889
I3	0.222	0.222
D1	0.574	0.667
D2	0.333	0.556
D3	0.667	0.444

Table 2 Frequency deviations and settling time at $t = 20$ s

Parameters	EHO	PSO
fr_1 (pu)	0.021	0.21
fr_2 (pu)	0.014	0.015
fr_3 (pu)	0.021	0.023
Ts (s)	12	30

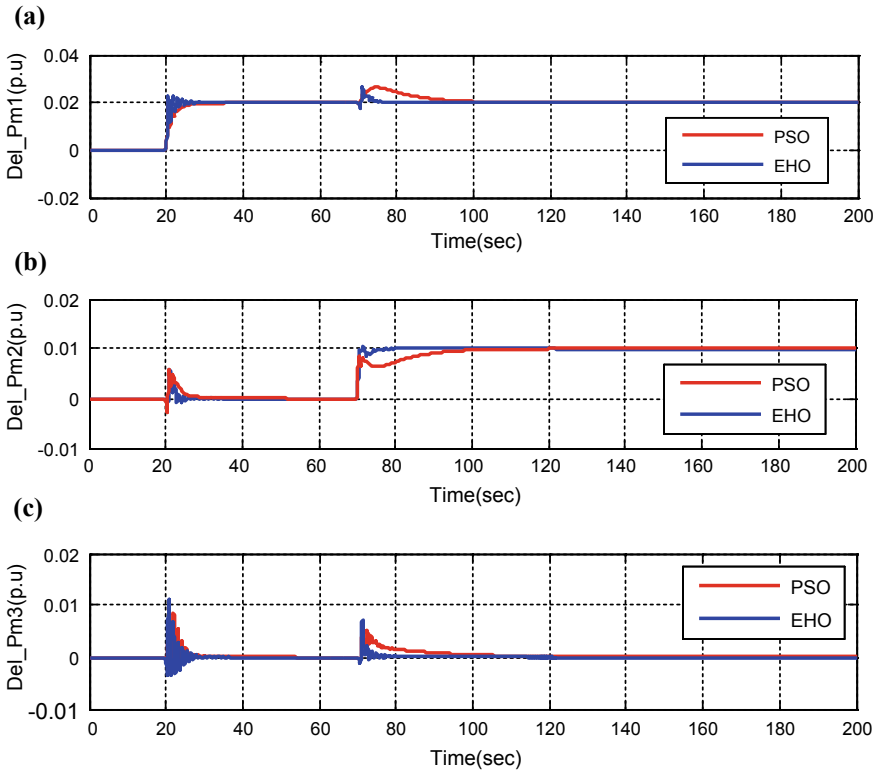


Fig. 4 **a** Mechanical power deviations of area-1. **b** Mechanical power deviations of area-2. **c** Mechanical power deviations of area-3

Table 3 Frequency deviations and settling time at $t = 70$ s

Parameters	EHO	PSO
fr_1 (pu)	0.017	0.013
fr_2 (pu)	0.013	0.013
fr_3 (pu)	0.017	0.014
Ts (s)	10	30

References

1. Bevrani H (2009) Robust power system frequency control, 1st edn. Springer
2. Asuhaimi A, MohdZin B, Pesaran HA, Khairuddin AB, Jahanshaloo L (2013) OmidShariati: an overview on doubly fed induction generators controls and contributions to wind based electricity generation. *Renew Sustain Energy Rev* 27:692–708
3. Wood AJ, Wollenberg BF (1996) Power generation operation and control, 2nd edn. Wiley
4. Kundur P (1994) Power system stability and control. McGraw-Hill
5. Farahani M, Ganjefar S, Alizadeh M (2012) PID controller adjustment using chaotic optimisation algorithm for multi-area load frequency control. *IET Control Theory Appl* 6(13):1984–1992
6. Wen T (2010) Unified tuning of PID load frequency controller for power systems via IMC. *IEEE Trans Power Syst* 25(1):245–252
7. Bevrani H, Daneshmand PR (2012) Fuzzy logic-based load–frequency control concerning high penetration of wind turbines. *IEEE Syst J* 6(1):13–19
8. Mendis BSD (2008) Fuzzy signatures: hierarchical fuzzy system and application. PhD thesis, Australian Nation University
9. Attia A (2009) Hierarchical fuzzy controllers for an astronomical telescope tracking. *Appl Soft Comput* 9(5):135–141
10. Lee CC (1990) Fuzzy logic in control systems: fuzzy logic controller part I. *IEEE Trans Syst Man Cybern* (6):404–418
11. Depenbrock M (1988) Direct self-control (DSC) of inverter-fed induction machine. *IEEE Trans Power Electron* 3:420–429
12. Arnalte S, Burgos JC, Rodríguez-Amenedo JL (2002) Direct torque control of a doubly-fed induction generator for variable speed wind turbines. *Electric Power Compon Syst* 30:199–216
13. Bonnet F, Vidal PE, Pietrzak-David M (2007) Dual direct torque control of doubly fed induction machine. *IEEE Trans Ind Electron* 54:2482–2490
14. Zhixin M, Lingling F, Osborn D, Yuvarajan S (2009) Control of DFIG-based wind generation to improve inter area oscillation damping. *IEEE Trans Energy Convers* 24:415–422
15. Ekanayake JB, Jenkins N, Strbac G (2008) Frequency response from wind turbines. *Wind Eng* 32(6):573–586
16. Slootweg JG, Polinder H, Kling WL (2001) Dynamic modelling of a wind turbine with doubly fed induction generator. *IEEE power engineering society summer meeting*, 15–19 July, Vancouver, Canada
17. Nattapol S, Issarachai N (2015) Intelligent photovoltaic farms for robust frequency stabilization in multi-area interconnected power system based on PSO-based optimal Sugeno fuzzy logic control. *Renew Energy* 74:555–567
18. Dhillon SS, Lather JS, Marwaha S (2015) Multi area load frequency control using particle swarm optimization and fuzzy rules. *Proc Comput Sci* 57:460–472
19. Dhillon SS, Marwaha S, Lather JS (2014) Robust load frequency control of micro grids connected with main grids in a regulated and deregulated environment. In: *Proceedings of IEEE international conference on recent advances and innovations in engineering*, pp 1–9
20. Ali ES, Abd-Elazim M (2013) BFOA based design of PID controller for two area load frequency control with nonlinearities. *Int J Electr Power Energy Syst* 51:224–231
21. Rabindra KS, Sidhartha P, Umesh KR, Dillip S (2016) Teaching learning based optimization algorithm for automatic generation control of power system using 2-DOF PID controller. *Int J Electr Power Energy Syst* 77:287–301
22. Binod KS, Tridipta KP, Jyoti RN (2016) A novel hybrid LUS–TLBO optimized fuzzy-PID controller for load frequency control of multi-source power system. *Int J Electr Power Energy Syst* 74:58–69
23. Dhillon SS, Lather JS, Marwaha S (2016) Multi objective load frequency control using hybrid bacterial foraging and particle swarm optimized PI controller. *Int J Electr Power Energy Syst* 79:199–209

24. Yanliang C, Lanlan X, Fei M, Yubin S (2017) Observer based robust integral sliding mode load frequency control for wind power systems. *Cont Engg Pract* 65:1–10
25. Jalali M (2011) DFIG based wind turbine contribution to system frequency control. Master thesis of Electrical and Computer Engineering, University of Waterloo, Ontario, Canada
26. Tavakoli M, Edris P, Adabi J, Godina R, João PS (2018) Load-frequency control in a multi-source power system connected to wind farms through multi terminal HVDC systems. *Comput Oper Res* 96:305–315
27. Reza H, Neda A, Miadreza SK, João PS (2018) Decentralized frequency-voltage control and stability enhancement of standalone wind turbine-load-battery. *Electr Power Energy Syst* 102:1–10

Use of Ti-Doped Hafnia in Photovoltaic Devices: Ab Initio Calculations



Ushma Ahuja, Deepika Mali, Kishor Kumar and Amit Soni

Abstract Optical response of Ti-doped (50%) hafnia (HfO_2) has been studied, using first-principles calculations within the framework of density functional theory, to explore the feasibility of doped hafnia in photovoltaics. Density of states (DOS) of hafnia and doped hafnia are also presented to understand the role of Ti doping in reducing the bandgap of the base material from 5.77 to 2.33 eV leading to its applications in photovoltaic devices and UV detectors. Various optical properties like frequency-dependent dielectric constants and absorption coefficients are explained.

Keywords Photovoltaics · Density functional theory · Hafnia

1 Introduction

Hafnia (HfO_2) is currently among the most studied high-dielectric constant materials. It has a wide range of technological uses like that in the electronics industry [1]. HfO_2 -based materials are currently being used as excellent high- κ gate dielectrics and in resistive-switching memory devices [1]. Using density functional theory (DFT), the total energy and equation of states of the monoclinic, tetragonal, cubic, *Pbca* orthorhombic and cotunnite orthorhombic zirconia, and hafnia have been investigated by Jaffe et al. [2] within the local density approximation (LDA) and generalized-gradient approximation (GGA). These authors found that the ionicity decreases from the monoclinic to the cotunnite phase. The bandgap and heat of formation are also

U. Ahuja (✉)

Department of Electrical Engineering, NMIMS, Mukesh Patel School of Technology Management and Engineering, Mumbai 400056, Maharashtra, India
e-mail: Ushma.Ahuja@nmims.edu

D. Mali · K. Kumar

Department of Physics, University College of Science, ML Sukhadia University, Udaipur, Rajasthan 313001, India

A. Soni

Department of Electrical Engineering, Manipal University Jaipur, Jaipur 303007, Rajasthan, India

© Springer Nature Singapore Pte Ltd. 2020

A. Kalam et al. (eds.), *Intelligent Computing Techniques for Smart Energy Systems*, Lecture Notes in Electrical Engineering 607, https://doi.org/10.1007/978-981-15-0214-9_3

larger for monoclinic HfO_2 than that for ZrO_2 by 0.60 eV and 0.60 eV/formula unit, respectively.

A first-principles study related to native point defects in HfO_2 and ZrO_2 has been carried out by Zheng et al. [3] to rectify dominant defects under different oxygen chemical potentials and Fermi parameters. It is reported that HfO_2 is less prone to the formation of oxygen point defects than ZrO_2 . Nakhmedov et al. [4] have calculated the bandgaps, bowing parameters, and internal stresses in the pseudobinary $\text{Zr}_x\text{Si}_{1-x}\text{O}_2$ and $\text{Hf}_x\text{Si}_{1-x}\text{O}_2$. Authors have applied the cluster expansion approach and the generalized quasi-chemical approximation and have computed dependence of the physical characteristics on the molar fraction x by the DFT–LDA. Caravaca et al. [5] have studied the elastic properties of the orthorhombic ($Pnma$) high-pressure phase of IV-B group oxides: titania, zirconia, and hafnia using self-consistent SIESTA code, pseudopotentials, and DFT with LDA and GGA approximations. The total energies, hydrostatic pressures, stress tensor components, and elastic constant have been reported using stress–strain relationships in the linear regime. The electronic response of ZrO_2 and HfO_2 in the cubic, tetragonal, and monoclinic phases has been investigated by Jiang et al. [6] using many-body perturbation theory in the GW approach based on DFT–LDA calculations. Using first-principles simulations, Zhang et al. [7] have investigated phase stability in the Hf–O system at pressure up to 120 GPa.

We feel that the optical behavior of doped hafnia is still unexplored using the DFT calculations. In the present paper, we present the optical response of Ti-doped (50%) hafnia using the full potential linearized augmented plane wave method (FP-LAPW) method [8] with PBEsol approximation [9]. Total and partial density of states are also presented to examine the reduction of bandgap in doped hafnia.

2 FP-LAPW Theory

FP-LAPW method which is employed in the present work is known to be one of the most accurate methods to calculate the electronic and optical response of a variety of materials [8]. In the present FP-LAPW computations, the lattice parameters were taken to be $a = 5.1284$, $b = 5.1914$, and $c = 5.2969$ Å ($\beta = 99.71^\circ$) for $P2_1c$ HfO_2 [2]. It is known that HfO_2 crystallizes in $P2_1c$ structure (space group No. 14) which is the most stable phase at room temperature. For Ti-doped hafnia, we have substituted two Hf atoms by Ti atoms leading to doping of 50% of Ti in the hafnia. The radii of MT sphere (R_{MT}) in $\text{Ti}_{0.5}\text{Hf}_{0.5}\text{O}_2$ were taken to be 1.96, 2.01, and 1.73 a.u. for Ti, Hf, and O, respectively. To achieve convergence of basic sets, the value of k_{max} was kept equal to $7/R_{\text{MT}}$ (where k_{max} is the magnitude of the largest wave vector). The cut-off parameters for charge density and maximum radial expansion (I_{max}) were set to 12 a.u.⁻¹ and 10, respectively. In the SCF iterations, the tolerance in total energies was within 10^{-5} Ry. The BZ integrations were performed using 868 \mathbf{k} points. For the stability of the system, the structure was volume optimized using Murnaghan equation which led to minimum stable energy of -64986.47085 Ry for the cell volume 862.99128 a.u.³.

3 Results and Discussion

Total and partial DOS of HfO_2 and $\text{Ti}_{0.5}\text{Hf}_{0.5}\text{O}_2$ are shown in Fig. 1a and b, respectively. The energy bandgap of hafnia (HfO_2) is observed to be 5.77 eV. From Fig. 1a, it is seen that 5d states of Hf are more dominant for forming the wide bandgap of hafnia. Below the Fermi energy (Fig. 1a), a hybridization between 5d and 2p states of Hf and O, respectively, is observed. To reduce the wide bandgap of hafnia to enable its use in photovoltaics, we have doped 50% Ti in HfO_2 leading to its composition formula as $\text{Ti}_{0.5}\text{Hf}_{0.5}\text{O}_2$. From the DOS (Fig. 1b), it is found that the 3d states of Ti lead to new allowed states in the conduction region from 2 to 5 eV. It is observed that the interaction of these Ti-3d states is responsible for reducing the bandgap of doped hafnia ($\text{Ti}_{0.5}\text{Hf}_{0.5}\text{O}_2$). It is also observed that Ti-3d states have small contribution in valence band region. The reduced bandgap of doped hafnia is found to be 2.33 eV.

To understand the optical behavior of the Ti-doped hafnia, we have computed the frequency-dependent dielectric constant (ϵ_1) and absorption coefficients (Fig. 2a, b) using FP-LAPW-PBESol method.

The values of static dielectric constant, $\epsilon_1(0)$, are found to be 5.93, 5.99, and 5.23 for xx, yy, and zz components, respectively. From Fig. 2a, we observed zero value of dielectric constant ($\epsilon_1(\omega) = 0$) at 8.84 eV for xx, 6.28, 10.10, and 10.59 eV for yy, and 10.27 eV for zz components which show that the electromagnetic wave of

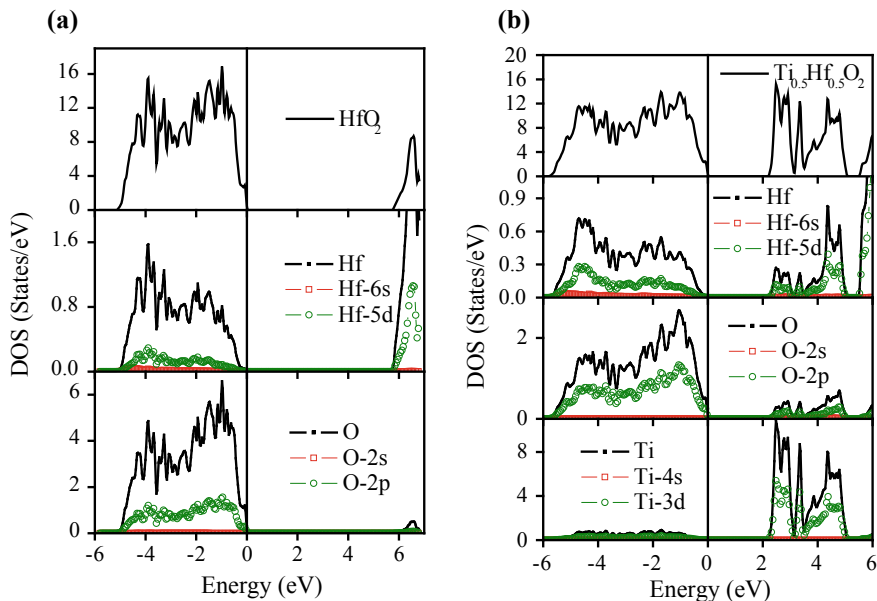


Fig. 1 Total and partial density of states of **a** HfO_2 and **b** $\text{Ti}_{0.5}\text{Hf}_{0.5}\text{O}_2$ deduced using FP-LAPW-PBESol method

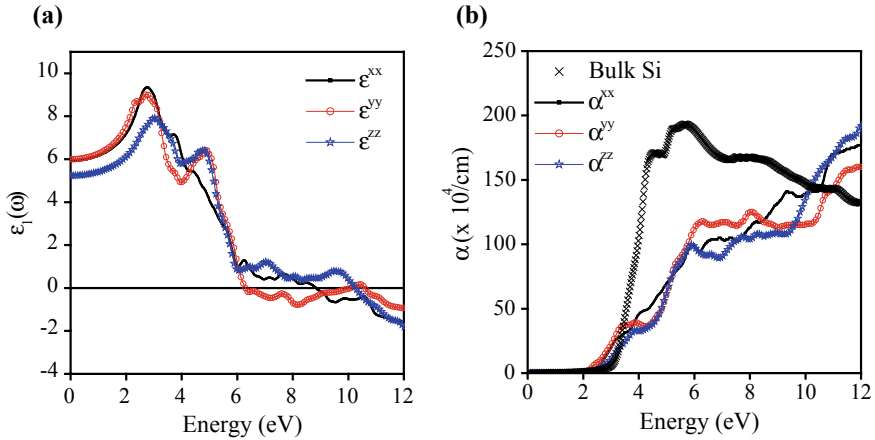


Fig. 2 **a** Real part of frequency-dependent dielectric function $\epsilon_1(\omega)$ and **b** absorption spectra of $\text{Ti}_{0.5}\text{Hf}_{0.5}\text{O}_2$ computed using FP-LAPW-PBEsol method. Absorption spectrum of bulk Si is also included in part (b) for a quick comparison

particular energy values may propagate through the Ti-doped HfO_2 in the corresponding direction. The negative values of $\epsilon_1(\omega)$ show that the electromagnetic wave is totally reflected by the Ti-doped HfO_2 for corresponding energies. In the present computation, we have not included the phonon contributions to dielectric screening which are expected to give only a small contribution to $\epsilon(\omega)$.

The integrated absorption coefficients (Fig. 2b) in the energy range 0–4 eV of the compound are listed in Table 1. To compare $\alpha(\omega)$ with a standard sample, we have also computed the $\alpha(\omega)$ of bulk Si using a similar FP-LAPW-PBEsol scheme. The average integrated absorption intensity of $\text{Ti}_{0.5}\text{Hf}_{0.5}\text{O}_2$ (Table 1) is found to be 37.53×10^4 eV/cm in the major energy range of solar spectrum (0–4 eV). The value of $\alpha(\omega)$ of $\text{Ti}_{0.5}\text{Hf}_{0.5}\text{O}_2$ is found to be lower than that of Si (51.26×10^4 eV/cm). Therefore, we predict that more doping of Ti in hafnia may lead to use of this material in the photovoltaics. Further, significant amplitude of absorption coefficients in the energy range 5–8 eV shows that $\text{Ti}_{0.5}\text{Hf}_{0.5}\text{O}_2$ can also be used as a detection material for ultraviolet spectra.

Table 1 Integrated absorption intensities of $\text{Ti}_{0.5}\text{Hf}_{0.5}\text{O}_2$ along the xx, yy, and zz components computed using FP-LAPW-PBEsol

Sample	Integrated absorption intensities ($\times 10^4$ eV/cm)			
	α^{xx}	α^{yy}	α^{zz}	α^{average}
$\text{Ti}_{0.5}\text{Hf}_{0.5}\text{O}_2$	39.33	44.77	28.47	37.53
Bulk Si	–	–	–	51.26

4 Conclusions

We have reported the optical behavior of Ti-doped (50%) hafnia using first-principles calculations within the framework of density functional theory. Density of states (DOS) of hafnia and Ti-doped hafnia are also derived using the FP-LAPW-PBEsol method. Frequency-dependent dielectric constants and absorption coefficients are analyzed. It is seen that doping of Ti in HfO_2 reduces the bandgap from 5.77 to 2.33 eV which makes it a useful compound for photovoltaic applications. Further, significant contribution of absorption coefficient in the energy range just above the solar spectra shows the usefulness of the Ti-doped HfO_2 in UV detectors.

Acknowledgements Authors are grateful to Prof. P. Blaha for providing the WIEN2k codes to our group.

References

1. Lowther JE (2003) MRS Bull 28:189
2. Jaffe JE, Bachorz RA, Gutowski M (2005) Phys Rev B 72:144107
3. Zheng JX, Ceder G, Maxisch T, Chim WK, Choi WK (2007) Phys Rev B 75:104112
4. Nakhmedov EP, Nadimi E, Bouhassoune M, Radehaus C, Wiczorek K (2007) Phys Rev 75:115204
5. Caravaca MA, Mino JC, Perez VJ, Casali RA, Ponce CA (2009) J Phys Condens Matter 21:015501
6. Jiang H, Ricardo I, Abal G, Rinke P, Scheffler M (2010) Phys Rev B 81:085119
7. Zhang J, Oganov AR, Li X, Xue KH, Wang Z, Dong H (2015) Phys Rev B 92:184104
8. Blaha P, Schwarz K, Sorantin P, Riskey SB (1999) Comput Phys Commun 59:399
9. Perdew JP, Ruzsinszky A, Csonka GI, Vydrov OA, Scuseria GE, Constantin LA, Zhou X, Burke K (2008) Phys Rev Lett 100:136406-1–136406-4

Electronic and Optical Response of Photovoltaic Semiconductor ZrS_xTe_{2-x}



Deepika Mali, Kishor Kumar and B. L. Ahuja

Abstract We have investigated the role of Te doping in ZrS_xTe_{2-x} using the most accurate modified Becke–Johnson (mBJ) potential within full potential linearized augmented plane wave method (FP-LAPW). It is found that more concentration of Te reduces the bandgap and thereby semiconductor behavior of ZrS_xTe_{2-x} . The optical properties, namely, dielectric constants and absorption coefficients are also deduced using FP-LAPW-mBJ method. The optical properties are explained to highlight role of ZrS_xTe_{2-x} in photovoltaic applications.

Keywords Photovoltaics · Density functional theory · Transition metal dichalcogenides

1 Introduction

Hexagonal transition metal dichalcogenides (TMDs) are very attractive in materials sciences because of their applications in switching devices, photoelectrochemical solar energy converts and as catalysts. Regarding earlier work on such MX_2 materials (where M is transition metal atom and X is chalcogen atom), Agrawal et al. [1] have grown the single crystal of ZrS_2 , $ZrSe_2$, and $ZrSSe$ and also studied the change in resistance with pressure. Authors have prepared and characterized the compounds using energy dispersive analysis of X-rays (EDAX) and X-ray diffraction (XRD) methods. Reshak et al. [2] have investigated electronics and optical properties of 1T- ZrX_2 ($X = S, Se, \text{ and } Te$) using full potential linearized augmented plane wave (FP-LAPW) method. Authors have reported that 1T- ZrS_2/Se_2 are semiconductors with indirect gap of 1.4 eV. Dasadia et al. [3] have reported growth of new ternary phase $ZrSTe$ single crystals by chemical vapor transport method. To our knowledge, electronic and optical response of TMD materials like ZrS_xTe_{2-x} are still undiscovered.

D. Mali (✉) · K. Kumar · B. L. Ahuja
Department of Physics, University College of Science, M.L. Sukhadia University,
Udaipur 313001, Rajasthan, India
e-mail: deepikamali31@gmail.com

© Springer Nature Singapore Pte Ltd. 2020
A. Kalam et al. (eds.), *Intelligent Computing Techniques for Smart Energy Systems*,
Lecture Notes in Electrical Engineering 607,
https://doi.org/10.1007/978-981-15-0214-9_4

In the present manuscript, we present the density of states (DOS) and optical properties (like dielectric constants, absorption coefficient) of $\text{ZrS}_x\text{Te}_{2-x}$ ($x = 2, 1.5$ and 1) using FP-LAPW method, to explore the feasibility of its use in photovoltaics.

2 FP-LAPW Method

FP-LAPW method as embodied in Wien2k code [4, 5] is known to be very accurate method for computation of electronic and optical behavior of materials. $\text{ZrS}_x\text{Te}_{2-x}$ crystallize in $\bar{P}3m1$ structure (space group number 164). In present FP-LAPW calculations, the experimental lattice parameters for ZrS_2 were taken to be $a = b = 3.66$ and $c = 5.82$ Å [2]. For Te doped ZrS_2 , we have constituted a supercell of size $(1 \times 1 \times 2)$ leading to six atoms. One S atom is replaced by Te atom leading to doping of 25% of Te ($\text{ZrS}_{1.5}\text{Te}_{0.5}$) and for ZrSTe two sites of S atoms are replaced by Te atoms. The radii of MT sphere (R_{MT}) in ZrSTe were taken to be 2.32, 2.20, and 2.44 a.u. for Zr, S, and Te, respectively, while these are 2.26, 2.15, and 2.38 a.u. for $\text{ZrS}_{1.5}\text{Te}_{0.5}$. To converge the basis sets, the value of K_{max} was kept equal to $7/R_{\text{MT}}$ (where K_{max} is magnitude of the largest wave vector K). The cutoff for charge density (G_{max}) and maximum radial expansion (l_{max}) were fixed to 12 a.u.^{-1} and 10, respectively. In the SCF iterations, the accuracy in total energies was within 10^{-5} Ry and integrations in BZ were performed using 100 \mathbf{k} points.

3 Results and Discussion

3.1 Electronic Structure

Total and partial DOS of ZrS_2 , $\text{ZrS}_{1.5}\text{Te}_{0.5}$, and ZrSTe computed using FP-LAPW-mBJ method are shown in Fig. 1a–c. From Fig. 1a, bandgap of ZrS_2 is found to be 1.47 eV. In Fig. 1a, it is observed that 4d states of Zr majorly contributing in conduction band (CB) while S-3p states mainly dominate in valence band (VB). After doping of 25% Te in ZrS_2 (Fig. 1b), the bandgap is reduced to 0.56 eV due to appearance of 4d and 5p states of Te in CB. A hybridization between S-3p and Te-5p states (Fig. 1b) in VB is observed. As we increase the concentration of Te up to 50% (Fig. 1c), new 4d states of Zr near Fermi level are formed which lead to narrow bandgap (0.028 eV) in ZrSTe . From Fig. 1a–c, it is found that more concentration of Te leads to the metallic character of $\text{ZrS}_x\text{Te}_{2-x}$ system. We also observed that $\text{ZrS}_{1.5}\text{Te}_{0.5}$ compound may be useful in photovoltaics. Therefore, we have computed the optical behavior of $\text{ZrS}_{1.5}\text{Te}_{0.5}$ using FP-LAPW-mBJ method.

Real part of frequency-dependent dielectric function ϵ_1 of $\text{ZrS}_{1.5}\text{Te}_{0.5}$ computed using FP-LAPW-mBJ method (Fig. 2a) shows the values of static dielectric constant, $\epsilon_1(0)$, as 11.1 and 7.3 for perpendicular and parallel component, respectively.

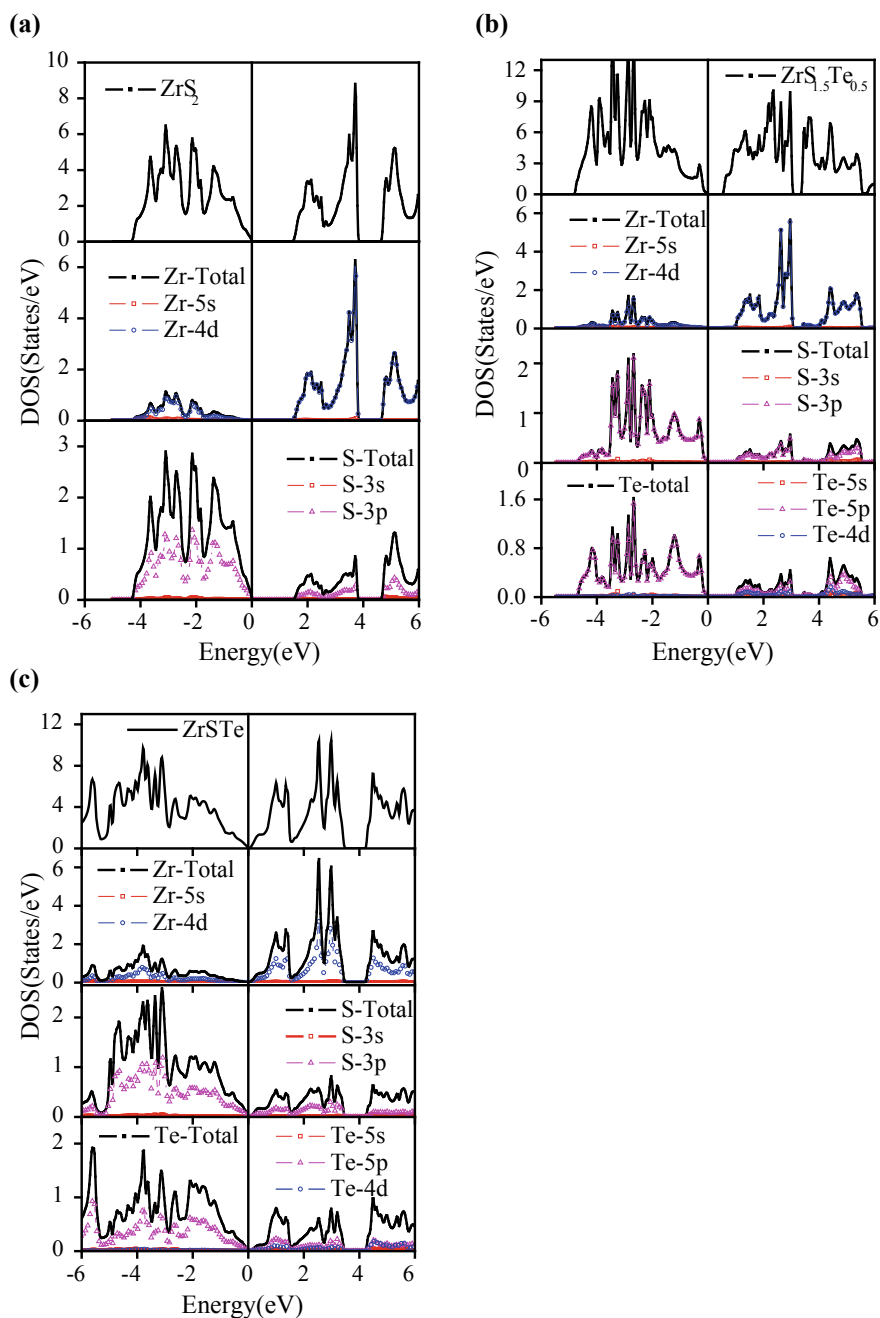


Fig. 1 Total and partial density of states of **a** ZrS_2 , **b** $\text{ZrS}_{1.5}\text{Te}_{0.5}$, and **c** ZrSTe computed using FP-LAPW-mBJ approximation. E_F corresponds to Fermi energy level which is shifted to 0 eV

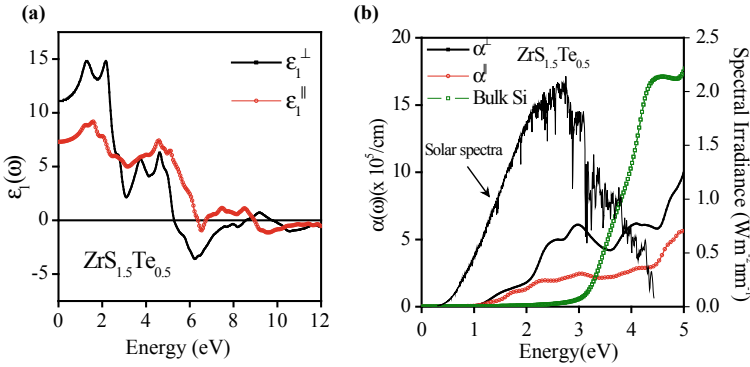


Fig. 2 **a** Frequency-dependent dielectric function $\epsilon_1(\omega)$ and **b** absorption spectra $\alpha(\omega)$ of $\text{ZrS}_{1.5}\text{Te}_{0.5}$ deduced from FP-LAPW-mBJ calculations. Absorption spectra of bulk Si and solar spectra are also included in part **(b)** for comparison

Table 1 Integrated absorption coefficients $\alpha(\omega)$ of $\text{ZrS}_{1.5}\text{Te}_{0.5}$ for perpendicular and parallel components computed using FP-LAPW-mBJ method

Sample	Integrated absorption intensities ($\times 10^4 \text{ eV/cm}$)		
	α^\perp	α^\parallel	α^{average}
$\text{ZrS}_{1.5}\text{Te}_{0.5}$	104.77	51.26	78.02
Bulk Si			51.26

Positive values of $\epsilon_1(\omega)$ show that the material shows an intrinsically capacitive optical response, while negative values of $\epsilon_1(\omega)$ depict that the electromagnetic waves for corresponding energies are reflected by the material. There are zero values in $\epsilon_1(\omega)$ spectra which show that the electromagnetic waves of corresponding energies do not interact with the reported material. Present computations are not performed for the phonon contributions to dielectric screening because it gives only a small contribution to $\epsilon(\omega)$.

The integrated values of absorption spectra, $\alpha(\omega)$, of $\text{ZrS}_{1.5}\text{Te}_{0.5}$ (Fig. 2b) in the energy range 0–4 eV are listed in Table 1. The average integrated absorption intensity of $\text{ZrS}_{1.5}\text{Te}_{0.5}$ (Table 1) is found to be $78.02 \times 10^4 \text{ eV/cm}$ in the dominant energy range of solar spectrum (0–4 eV). Higher value of $\alpha(\omega)$ for $\text{ZrS}_{1.5}\text{Te}_{0.5}$ than that of Si ($51.26 \times 10^4 \text{ eV/cm}$, computed using FP-LAPW-mBJ) shows usefulness of $\text{ZrS}_{1.5}\text{Te}_{0.5}$ in photovoltaic devices.

4 Conclusions

Full potential linearized augmented plane wave method has been employed to investigate the role of Te doping in ZrS_2 . It is observed that 25% doping of Te decreases the bandgap from 1.47 to 0.56 eV which enable the use of $\text{ZrS}_{1.5}\text{Te}_{0.5}$ in photovoltaics.

Frequency-dependent dielectric constants and absorption coefficients of $\text{ZrS}_{1.5}\text{Te}_{0.5}$ are also explained. It is found that $\text{ZrS}_{1.5}\text{Te}_{0.5}$ has higher value of $\alpha(\omega)$ than that of bulk Si.

Acknowledgements Authors are thankful to SERB, New Delhi (India) for granting a Research Project (Grant No. EMR/2016/001400). We are also grateful to Prof. P. Blaha for providing the WIEN2k code.

References

1. Agrawal MK, Patel SG, Chaki SH (1992) High pressure studies on single crystals of zirconium sulphoselenides. *High Pressure Res Int J* 10:535
2. Reshak AH, Auluck S (2004) Theoretical investigation of the electronic and optical properties of ZrX_2 (X= S, Se and Te). *Phys B* 353:230
3. Dasadia AK, Nariya BB, Jani AR (2015) Growth and structural determination of ZrSTe -A new ternary phase of transition metal chalcogenides. *J Cryst Growth* 426:265
4. Blaha P, Schwarz K, Sorantin P, Riskey SB (1999) Full-potential, linearized augmented plane wave programs for crystalline systems. *Comput Phys Commun* 59:399
5. Blaha P, Schwartz K, Madsen G, Kvasnicka D, Luitz J (2017) An augmented plane wave plus local orbitals program for calculating crystal properties, user's guide, WIEN2k_17.1. Vienna University of Technology, Vienna, Austria

Investigation of Optical Response of Silver Molybdate for Photovoltaic



Seema Kumari Meena and B. L. Ahuja

Abstract Feasibility of using β - Ag_2MoO_4 in photovoltaic devices has been investigated using full potential linearized augmented plane wave method. The computed band gap (1.64 eV) of Ag_2MoO_4 and integrated absorption coefficient show that the material can be used in photovoltaic. Density of states is explained to understand the hybridization and interband transitions from valence to conduction bands. Further, electron momentum density (EMD) is also measured using Cs-137 Compton spectrometer. The experimental EMD is compared with those computed using linear combination of atomic orbitals method with local density approximation and Hartree–Fock free-atom approximation. A good agreement between theoretical and experimental profiles confirms applicability of density functional theory, as used in present investigations of optical properties.

Keywords Photovoltaic · Density functional theory · Electron momentum density

1 Introduction

Ag_2MoO_4 (silver molybdate) has attracted much attention due to its chemical stability at higher temperature and lubricating properties as well as its uses in various devices such as those based on solar energy conversion, photocatalysis, energy storage, antibacterial agents, and optoelectronics [1–5].

It is well-known that Compton scattering (CS) is a unique and powerful technique to study electronic properties of compounds [6, 7]. The measured quantity in CS is the Compton profile (CP), $J(p_z)$, which is taken as a projection of electron linear momentum density (EMD), $\rho(p)$, along the scattering vector direction (z -axis). Mathematically,

S. K. Meena (✉) · B. L. Ahuja
Department of Physics, University College of Science, M. L. Sukhadia University,
Udaipur 313001, Rajasthan, India
e-mail: seema.meena2006@gmail.com

$$J(p_z) = \iint \rho(\mathbf{p}) dp_x dp_y. \quad (1)$$

In Eq. (1), $\rho(p)$ can be derived from real-space wave functions [8, 9]. To the best of our knowledge, EMDs of Ag_2MoO_4 have not been studied so far.

In present work, we report the density of states (DOS) and optical parameters like absorption coefficients, dielectric constants, and reflectivity of the Ag_2MoO_4 to discuss its utility in photovoltaic. The full potential linearized augmented plane wave (FP-LAPW) method was used to compute the electronic and optical properties. We present the experimental EMD of Ag_2MoO_4 measured using Cs-137 Compton spectrometer. In addition, we also present the theoretical EMD derived using linear combination of atomic orbitals (LCAO) method and compare it with the experiment.

2 Methodology

2.1 Experiment

The experimental CP of Ag_2MoO_4 has been deduced using 20 Ci Cs-137 Compton spectrometer [10]. The sample was suspended in form of pellet in sample chamber with diameter and thickness of 2.41 cm and 0.24 cm, respectively. The photons scattered at an angle $160^\circ \pm 06^\circ$ were detected using a HPGe detector (GL0510P, USA). Raw data were accumulated for a period of about 401 h, and to eliminate the background contribution the background spectra were recorded for about 201 h. The raw Compton data were processed for background, effect of detector tail response function, absorption and Compton scattering cross section, and multiple scattering, etc., to obtain a true CP [11]. Lastly, the CP data were normalized to number of electrons equal to area of free-atom CP in the p_z range 0–7 a.u. ($70.61 e^-$) [12].

2.2 Theory

(a) LCAO

To compare the experimental CP with theory, we have computed the theoretical CP employing LCAO prescription [13] with local density approximation (LDA) scheme within the DFT approach. We have used the experimental lattice parameters $a = b = c = 9.26 \text{ \AA}$ [14] in present computations. The all-electron Gaussian-type basis sets for Ag, Mo, and O were taken from www.tcm.phy.cam.ac.uk and these basis sets were optimized for the lowest energy of system using BILLY program [13]. The energy convergence criteria, which governs the accuracy of computations, were set to 10^{-6} Hartree.

(b) FP-LAPW

For computation of bandgap, DOS, absorption coefficients, dielectric constants, and reflectivity, we have also used FP-LAPW method (which is known as one of reliable

methods for electronic and optical properties of materials) as embodied in WIEN2k code [15, 16]. In the present FP-LAPW calculations, the radii of MT spheres (R_{MT}) in Ag_2MoO_4 were taken to be 2.46, 1.81, and 1.64 a.u. for Ag, Mo, and O, respectively. To achieve convergence of basic sets for Ag_2MoO_4 , the K_{max} value, the cut-off value for charge density and highest value of radial expansion were fixed to $7/R_{MT}$, 12 a.u.⁻¹ and 10, respectively. In SCF iterations, the tolerance in total energies (within 10^{-5} Ry) was quite acceptable. 47 **k** points in irreducible BZ were considered for SCF cycles.

3 Results and Discussion

3.1 Electronic Response

In Fig. 1, we have shown the total and partial DOS of Ag_2MoO_4 computed using FP-LAPW method. From Fig. 1, it is observed that there is negligible contribution of 5s states of Ag and Mo and 2s states of O in valence band (VB) and conduction band (CB). The CB is majorly formed by 4d states of Mo while the VB is dominated by Ag-4d and O-2p states. The bandgap of Ag_2MoO_4 as deduced using FP-LAPW method is found to be 1.64 eV. Since the topology of energy bands and DOS deduced from LCAO calculations is similar (except few fine structures and energy values), we have not shown the LCAO calculations based bands and DOS.

Fig. 1 Total and partial (projected) density of states (DOS) of Ag_2MoO_4 computed using FP-LAPW method

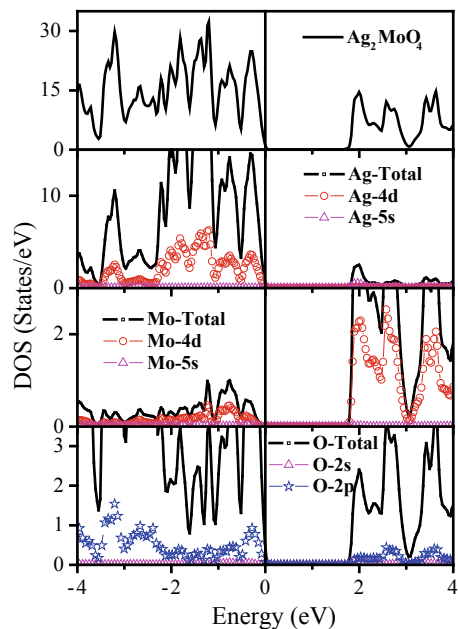
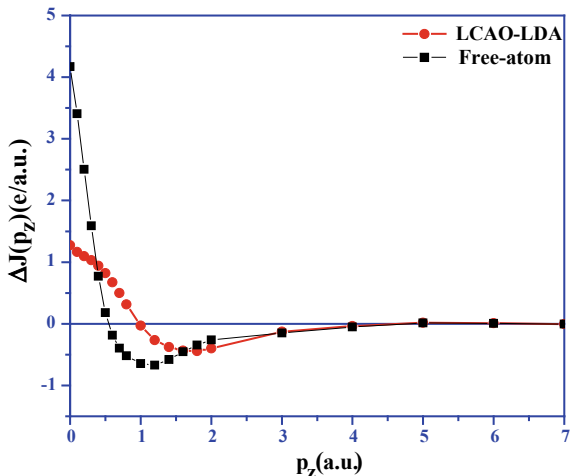


Fig. 2 Deviations between the isotropic convoluted theoretical (LCAO-LDA and free-atom based) and experimental Compton profiles of Ag_2MoO_4



3.2 Compton Profile

To compare the experimental CP with theoretical profiles, the theoretical CPs, derived using LCAO-LDA and Hartree-Fock free-atom model [12], were convoluted with the spectrometer resolution 0.34 a.u. (fwhm) and normalized to free-atom CP area ($70.61 e^-$) [12]. In Fig. 2, we have plotted differences between the isotropically averaged experimental and convoluted theoretical CPs. We observe significant differences in the low momentum side ($p_z < 4$ a.u.) of difference CPs between theory and experiment, which can be explained on the basis of nonrelativistic nature of LCAO calculations and also the quality of basis sets as adopted in present LCAO calculations. Since wave functions of core electrons are well approximated by free-atom model, the experimental and theoretical CPs in the region $p_z > 5$ a.u. agree well.

It is seen that LCAO-LDA-based CP is in better agreement than the free-atom profile, which is understandable because of simplicity of free-atom model.

3.3 Optical Response

In Fig. 3a, real part of frequency-dependent dielectric function (ϵ_1) of Ag_2MoO_4 computed using FP-LAPW method is shown. The static dielectric constant $\epsilon_1(0)$ is observed to be 6.02. After 8.5 eV, the ϵ_1 spectra show negative trend which show that the electromagnetic waves having energy in this range are reflected by the Ag_2MoO_4 . In the inset of Fig. 3a, we have plotted the imaginary component $\epsilon_2(\omega)$ of frequency-dependent dielectric constant. The peaks in $\epsilon_2(\omega)$ spectra are in accordance to interband transitions from the VB to CB. Observing $\epsilon_2(\omega)$ spectra

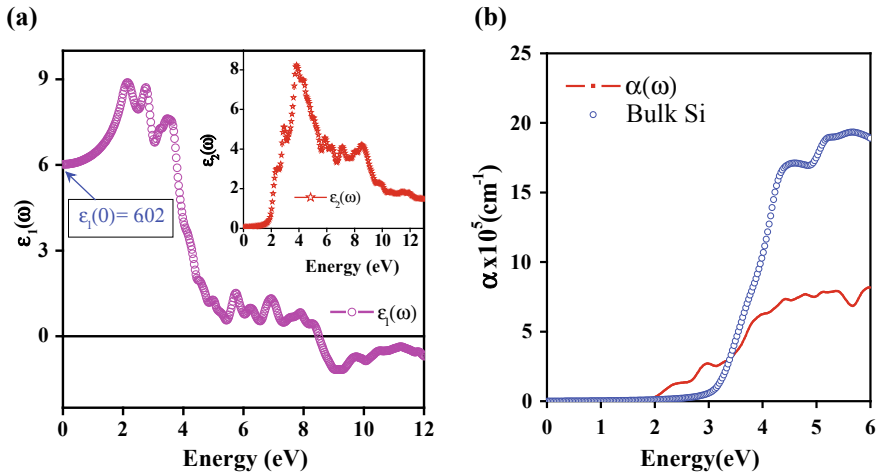


Fig. 3 **a** Real part of frequency-dependent dielectric function $\epsilon_1(\omega)$. Inset of this figure consists of imaginary component of frequency-dependent dielectric function $\epsilon_2(\omega)$ and **b** absorption spectra $\alpha(\omega)$ of Ag_2MoO_4 deduced from FP-LAPW calculations. Further, absorption spectra of bulk Si are also included in the part **(b)** for a relative comparison

(inset of Fig. 3a) and DOS (Fig. 1), it is found that peaks in $\epsilon_2(\omega)$ are governed by various possible interband transitions from O-2p to Mo-4d states.

In Fig. 3b, we have included the absorption spectra, $\alpha(\omega)$, of Ag_2MoO_4 to explore its usefulness in photovoltaic along with $\alpha(\omega)$ spectra of bulk Si. Within the solar energy spectrum (0–4 eV), the values of integrated absorption coefficients are collated in Table 1. From Table 1 and Fig. 3b, it is found that Ag_2MoO_4 has higher integrated absorption intensity (55.45×10^4 eV/cm) than the Si (51.26×10^4 eV/cm). Therefore, the reasonable integrated absorption intensity of Ag_2MoO_4 shows its applicability in photovoltaic devices.

Table 1 Integrated absorption coefficients $\alpha(\omega)$ of Ag_2MoO_4 computed using FP-LAPW method

Sample	Integrated absorption intensities ($\times 10^4$ eV/cm)
	α^{average}
Ag_2MoO_4	55.45
Bulk Si	51.26

4 Conclusions

Electronic and optical response of Ag_2MoO_4 has been reported using FP-LAPW method. Absorption coefficients, dielectric constants, and density of states are discussed to explore feasibility of the Ag_2MoO_4 in solar cell. The bandgap from FP-LAPW method comes out to be 1.64 eV. Experimental CP of Ag_2MoO_4 measured using Cs-137 Compton spectrometer reconciles well with LCAO-LDA-based CP.

Acknowledgements Authors acknowledge SERB, New Delhi for research grant (No. EMR/2016/001400). We are also thankful to Prof. Peter Blaha and Prof. R. Dovesi for providing the WIEN2k and CRYSTAL codes, respectively. One of us (SKM) is grateful to UGC, New Delhi for UGC-BSR fellowship.

References

1. Beltran A, Gracia L, Longo E, Andres J (2014) First-principles study of pressure-induced phase transitions and electronic properties of Ag_2MoO_4 . *J Phys Chem C* 118:3724
2. Gouveia AF, Szczancoski JC, Ferrer MM, Lima AS, Santos MRMC, Li MS, Santos RS, Longo E, Cavalcante LS (2014) Experimental and theoretical investigations of electronic structure and photoluminescence properties of Ag_2MoO_4 microcrystals. *Inorg Chem* 53:5589
3. Ng CHB, Fan WY (2015) Uncovering metastable α - Ag_2MoO_4 phase under ambient conditions. Overcoming high pressures by 2, 3-Bis (2-pyridyl) pyrazine doping. *Cryst Growth Des* 15:3032
4. Fortes AD (2015) Crystal structures of spinel-type Na_2MoO_4 and Na_2WO_4 revisited using neutron power diffraction. *Acta Cryst E* 71:592
5. Andres J, Ferrer MM, Gracia L, Beltran A, Longo VM, Cruvinel GH, Tranquilin RL, Longo E (2015) A combined experimental and theoretical study on the formation of Ag filaments on β - Ag_2MoO_4 induced by electron irradiation. *Part Part Syst Charact* 32:646
6. Cooper MJ, Mijnaerends PE, Shiotani N, Sakai N, Bansil A (2004) Compton scattering. Oxford Science Publications. Oxford University Press, New York (and references therein)
7. Cooper MJ (1985) Compton scattering and electron momentum determination. *Rep Prog Phys* 48:415 (and references therein)
8. Ahuja BL (ed) (2010) Recent trends in radiation physics research. Himanshu Publications, New Delhi
9. Ahuja BL, Dashora A (2016) "Compton scattering" in reference module in materials science and materials engineering. Elsevier, UK Publication, pp 1–8
10. Ahuja BL, Sharma M, Mathur S (2006) Anisotropy in the momentum density of tantalum. *Nucl Instrum Methods B* 244:419
11. Timms DN (1989) Compton scattering studies of spin and momentum densities. Ph.D. thesis, University of Warwick, England
12. Biggs F, Mendelsohn LB, Mann JB (1975) Hartree-Fock Compton profiles for the elements. *At Data Nucl Data Tables* 16:201
13. Dovesi R, Saunders VR, Roetti C, Orlando R, Zicovich-Wilson CM, Pascale F, Civalieri B, Doll K, Harrison NM, Bush IJ, D'Arco P, Llunel M, Causa M, Neol Y (2014) CRYSTAL14 user's manual, University of Torino, Torino
14. Wang P, Huang B, Zhang Q, Zhang X, Qin X, Dai Y, Zhan J, Yu J, Liu H, Lou Z (2010) Highly efficient visible light plasmonic photocatalyst $\text{Ag}@\text{Ag}$ (Br, I). *Chem Eur J* 16:10042

15. Blaha P, Schwarz K, Sorantin P, Trickey SB (1999) Full-potential, linearized augmented plane wave programs for crystalline systems. *Comput Phys Commun* 59:399
16. Blaha P, Schwarz K, Madsen G, Kuasnicka D, Luitz J (2013) User's guide: WIEN2K_13.1. Vienna University of Technology, Austria

Comparative Analysis of Conventional and Meta-heuristic Algorithm Based Control Schemes for Single Link Robotic Manipulator



Aishwarya Varma, Shailu Sachan, Pankaj Swarnkar and Savita Nema

Abstract Position control of an actuator, i.e., dc servo due to increase in the demand of robots in industry automation has been proliferated in the recent past. Here, time-domain optimal tuning of Proportional–Integral–Derivative (PID) and Fractional Order PID (FOPID) controller has been carried out for single link manipulator. The gain parameters were tuned using Genetic Algorithm (GA) where an objective function based on the Integral Time Absolute Error (ITAE) as the performance measure was minimized. Being one of the best tuning criteria, ITAE is opted as performance measure to obtain optimized controller parameters. The motivation behind this paper is to apply GA for ITAE minimization on single link manipulator to trace the set point which improves the overall efficiency of the system. So, FOPID control using GA is the best and optimum solution to deal with nonlinearities. In the end, the position tracking problem has been carried out which demonstrates the successful design of controller. The results obtained show the effectiveness of the proposed method.

Keywords Single link manipulator · PID controller · FOPID controller · ITAE · GA

1 Introduction

In modern robotic system, flexibility and precision have been turned out exceptionally essential for industrial automation, space station, military, and medical applications. So, application of robots is expanding rapidly.

A. Varma · S. Sachan (✉) · P. Swarnkar · S. Nema
MANIT, Bhopal, Madhya Pradesh, India
e-mail: sachanshailu@gmail.com

A. Varma
e-mail: aish.2594@yahoo.com

P. Swarnkar
e-mail: p_swarnkar@yahoo.co.in

S. Nema
e-mail: s_nema@yahoo.com

A robot is a machine that can substitute humans and imitate their actions. A robotic arm resembles closer to a human arm but is an electromechanical device that can be controlled and reprogrammed. It is also known as robotic manipulator. Robot manipulators consist of a number of links connected with various joints to perform various tasks such as picking, grasping, moving, putting the objects, etc. For these and many more applications, the speed and position should be precisely controlled with the help of servomotors.

A servomotor or servo is a rotary actuator or linear actuator that allows for precise control of angular or linear position, velocity, acceleration, and torque. It is a closed-loop servomechanism that uses position feedback to control its motion and final position. The input to its control is a signal (either analog or digital) representing the position commanded for the output shaft. It will move as per command signal, i.e., the motor acts as slave hence, the name servo [1].

A servo is used at every joint of the robot to actuate movements and give its precise angle [2]. Servo is just a small dc motor having low inertia, low power, and high acceleration with gears. They are used in robots to effectuate the movements to definite/particular angle with low battery consumption.

Closed-loop controllers have several pros over open-loop like rejecting disturbance, improving tracking performance, and providing stabilization. So, the position feedback is employed in order to minimize the error and achieve effective control [3].

In this paper, position control [4] of servo is done using PID controller [5], FOPID controller [6], and further optimum tuning of PID gains have been done using genetic algorithm [7, 8]. Model reference adaptive control technique can also be one of the suggestive schemes to control the plant response and in turn tune the gain parameters of PID and FOPID controller [9, 10].

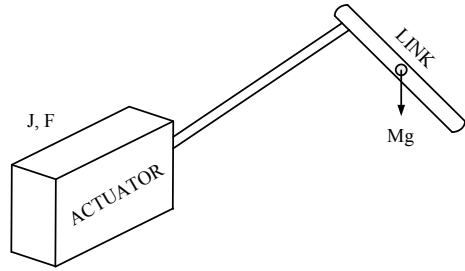
The prevalence of using PID or PID type controllers is that they have a simple structure and provide satisfactory results when requirements are reasonable and process parameters are restricted. In order to overcome the limitations of conventional PID controller, FOPID controller is used having the proportional, integral, and derivative parameters (K_P , K_I , and K_D) and two additional parameters, the order of fractional integration λ and the order of fractional derivative μ . Therefore, more number of parameters of FOPID increases flexibility.

The conventional method of tuning is poor and time-consuming. To overcome it, the PID controller and FOPID controller gains are optimized using Genetic Algorithm (GA) that enhances the flexibility and provides robustness.

2 Control of a Single Link Manipulator

Let's consider [11], single link robotic manipulator driven by an electric actuator (Fig. 1) along with reduction in inertia link of gear ratio, i.e., link speed/motor speed = $1/n$ where $n > 1$. The actuator inertia gets multiplied by factor n^2 due to reduction in gearing. The effective link inertia can be expressed as

Fig. 1 Electric actuator for single link robotic manipulator



$$J = D + n^2 J_a \tag{1}$$

where J_a = Actuator inertia

D = Effective link inertia (excluding actuator inertia)

J = total (link plus actuator) inertia (on the link side of gearing).

It can be seen from Eq. (1) that actuator inertia is a constant tending to reduce any variation in D .

A dc servo is specified by an actuator gain and effective viscous friction expressed in terms of link variables. Figure 2 represents the block diagram of electric actuator for robotic manipulator. In this paper, the disturbance torque " $T_D(s)$ " which arises at the output shaft has been considered to be zero.

The open-loop transfer function of this position control system is given by Eq. (2)

$$G(s) = \frac{K_e K_m}{s(sJ + (F + K_v K_m))} \tag{2}$$

The closed-loop position control transfer function is given by Eq. (3)

$$G'(s) = \frac{\Theta(s)}{\Theta_I(s)} = \frac{K_e K_m}{s^2 J + s(F + K_v K_m) + K_e K_m} \tag{3}$$

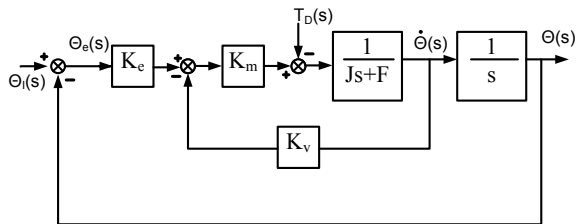
where F = Effective viscous friction in Nm/rad/s

K_m = Motor torque constant in Nm/V

K_v = Velocity feedback constant in V/rad/s

K_e = Error amplification in V/°.

Fig. 2 Block diagram of electric actuator for robotic manipulator



3 Conventional Control Techniques

3.1 PID Control

PID (Proportional–Integral–Derivative) control is one of the classical and easiest control methods. The effect of parameter variations is given in Table 1. The control function of PID controller is given by Eq. (4),

$$G_C(s) = K_P + \frac{K_I}{s} + K_D s \quad (4)$$

3.2 FOPID Control

FOPID satisfies at most five robustness criteria as compared to the conventional PID controller which has three parameters to be tuned for three robustness criteria. FOPID control enhances the flexibility with increase in number of gain parameters that are K_P , K_I , λ , K_D , and μ [12, 13]. It is defined in Eq. (5),

$$G_{FOC}(s) = K_P + \frac{K_I}{s^\lambda} + K_D s^\mu \quad (5)$$

3.3 Tuning of Controller Using GA

If the PID controller is not properly tuned, the controlled process input can be unstable, i.e., its output diverges, with or without oscillation and is limited only by saturation or mechanical breakage. Tuning a control loop is adjustment of its control parameters to the optimum values for the desired control response which is carried out through a meta-heuristic process in this paper.

GA (Genetic algorithm) is a stochastic global and heuristic search that reflects the process of natural selection. It is an iterative process that provides an optimum solution. Table 2 showed the value of parameters used in GA.

Table 1 Effect of increasing gain parameters on response parameters

Parameters	Rise time	Overshoot	Settling time	Error
K_P	Decreases	Increases	Small change	Decreases
K_I	Decreases	Increases	Increases	Eliminates
K_D	Indefinite	Decreases	Decreases	None

Table 2 Value of parameters used in GA

Parameter	Type/value
Max generation	75
Population size	200
Selection	Uniform
Crossover	0.8
Mutation	0.2

The tuning of controller parameters is optimized using GA while keeping ITAE as our objective function. ITAE (Integral Time Absolute Error) is one of the most commonly preferred performance indices to minimize the system error. The objective function is given as in Eq. (6).

$$J = \int_0^{\infty} t|e(t)|dt \quad (6)$$

where $e(t)$ is the error signal.

Optimum values of PID parameters namely, K_P , K_I , and K_D [14–16] and those of FOPID namely, K_P , K_I , λ , K_D , and μ are obtained through GA [17].

Figure 3 represents the block diagram of robotic manipulator with various control schemes adopted in this paper.

4 Results

In this paper, the best possible selection of controller parameters for the control of single link manipulator [11] modeled in Eqs. (1–3) is done. Here, a comparative analysis is carried out between the conventional techniques and meta-heuristic algorithms. The meta-heuristic algorithm used here is genetic algorithm, which is one of the most primitive algorithm of its type. It searches the optimal value of controller parameters (PID and FOPID) while minimizing the Integral Time Absolute Error (ITAE) Performance Index [18].

Figure 4 shows the step response of the system under varied conditions. Table 3 displays the values of time response parameters for step input to the plant model with different control methodologies. It can be clearly deciphered that the best performance has been obtained by tuning the FOPID parameters through GA. The value of parameters for all the control techniques has been summarized in Table 4.

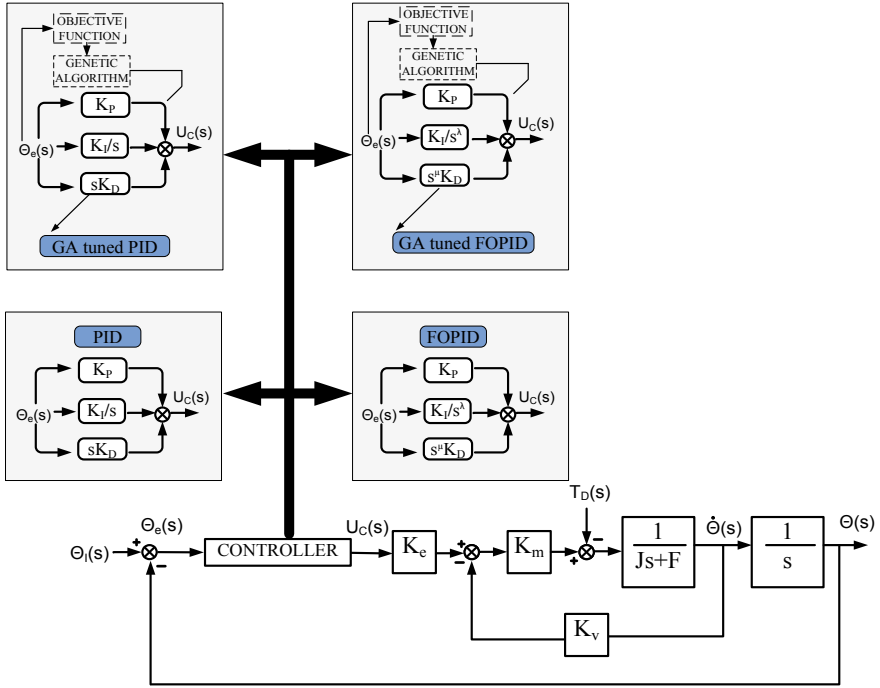


Fig. 3 Block diagram of electric actuator for robotic manipulator with controllers

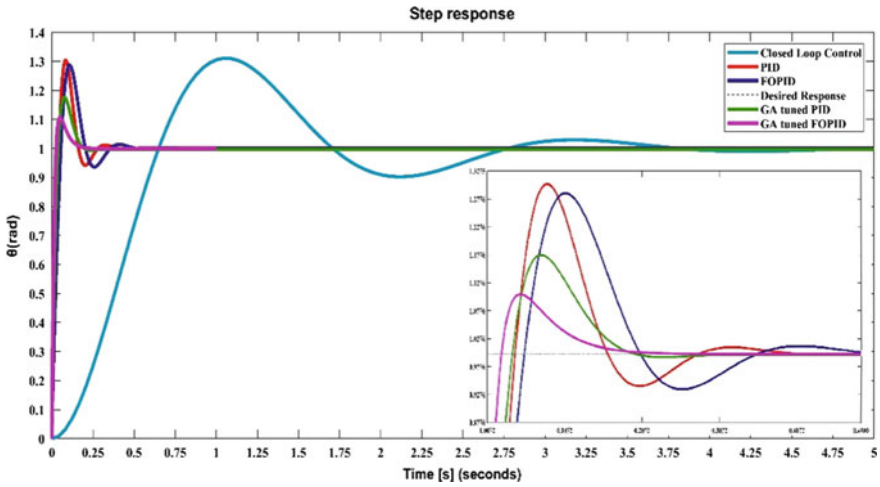


Fig. 4 Step response of system for no control, conventional control, and meta-heuristic based control methods

Table 3 Time response specifications with different control methodologies

	Rise time (s)	Settling time (s)	Overshoot (%)	Peak time (s)
Uncontrolled	0.4395	3.4787	31.1471	1.046
PID	0.0341	0.2590	29.9623	0.086
FOPID	0.0434	0.3283	28.7752	0.109
GA-PID	0.0299	0.1683	17.7307	0.075
GA-FOPID	0.0181	0.1351	10.6814	0.052

Table 4 Controller parameters for different control techniques

	K_P	K_I	K_D	λ	μ
Minimum limit	0	0	0	0	0
Maximum limit	100	100	100	2	2
PID	87	50	2.6	–	–
FOPID	65	20	1.5	0.9	1.1
GA-PID	87.6681	8.8252	4.1580	–	–
GA-FOPID	99.8903	75.6775	8.7928	0.0621	0.9964

5 Conclusion

This paper has focused on the design of an optimum controller for the control of a single link manipulator. In due course, various control techniques have been discussed for the position control of servo which shows that conventional methods have limited capabilities. For the purpose of controlling the position of SLM, an optimum FOPID is designed where minimisation of integral time absolute error was the main objective. The gain parameters of PID and FOPID were optimized using GA. The proposed controller, GA tuned FOPID performance was compared with an optimally designed PID controller using GA for the same objective function. The time-domain simulation results show the effectiveness and the robustness of GA tuned FOPID as compared to the classical PID.

References

1. Lord W, Hwang JH (1977) DC servomotors: modelling and parameter determination. *IEEE Trans Ind Appl* 1A-13(3):234-243
2. Song J, Xi N, Xu F, Jia K, Zou F (2015) Servomotor modelling and control for safe robots. In: *IEEE conference on robotics and biomimetics*, pp 1221-1226
3. Ruben GMA, Roger MC (2008) Closed-loop identification of a velocity controlled DC servomotor. In: *5th international conference on electrical engineering, computing science and automatic control*, pp 31-36

4. Gutierrez FR, Makableh YF (2011) Efficient position control of DC servomotor using back-propagation neural network. In: 2011 seventh international conference on natural computation, vol 2, pp 653–657
5. Ismail HA, Ersin Y, Ertunct HM, Bingul Z (2011) PID and state feedback control of a single-link flexible joint robot manipulator. In: International conference on mechatronics, pp 409–414
6. Mehra V, Srivastava S, Varshney P (2010) Fractional-order PID controller design for speed control of DC motor. In: International conference on emerging trends in engineering and technology, pp 422–425
7. Bensenoucia A, Shehatab M (2015) Optimized FOPID control of a single link flexible manipulator (SLFM) using genetic algorithm. *Appl Mech Mater* 704:336–340 (Trans Tech Publications, Switzerland)
8. Swarnkar P, Jain SK, Nema RK (2014) Adaptive control schemes for improving the control system dynamics: a review. *IETE Tech Rev* 31(1):17–33 (Taylor & Francis)
9. Swarnkar P, Jain SK, Nema RK (2010) Effect of adaptation gain on system performance for model reference adaptive control scheme using MIT rule. *World Acad Sci Eng Technol Int J Comput Electr Autom Control Inf Eng* 4(10)
10. Swarnkar P, Jain SK, Nema RK (2011) Effect of adaptation gain in model reference adaptive controlled second order system. *ETASR Eng Technol Appl Sci Res* 1(3):70–75
11. Nagrath IJ, Gopal M (2014) *Control systems engineering*, 5th edn. New Age International Publishers
12. Karanjkar DS, Chatterji S, Venkateswaran PR (2012) Trends in fractional order controllers. *Int J Emerg Technol Adv Eng IJETAE* 2(3)
13. Maurya AK, Bongulwar MR, Patre BM (2015) Tuning of fractional order PID controller for higher order process based on ITAE minimization. *IEEE INDICON*
14. Vinodha AJR (2014) Genetic algorithm based PID controller tuning approach for continuous stirred tank reactor. *Adv Artif Intell*
15. Meena DC, Devanshu A (2017) Genetic algorithm tuned PID controller for process control. In: International conference on inventive systems and control
16. Pillai RP, Jadhav SP, Patil MD (2013) Tuning of PID controllers using advanced genetic algorithm. *J Adv Comput Sci Appl (IJACSA)*, pp 1–6 (Special issue of selected paper)
17. Essa MESM, Aboelela MAS, Hassan MAM (2017) A comparative study between ordinary and fractional order PID controllers for modelling and control of an industrial system based on genetic algorithm. In: 6th international conference on modern circuits and systems technologies
18. *Matlab Optimization Toolbox User's Guide* (2017) The MathWorks, Inc., Natick, MA, USA

Synthesis of Antenna Array Pattern Using Ant Lion Optimization Algorithm for Wide Null Placement and Low Dynamic Range Ratio



Prerna Saxena, Ashwin Kothari and Saurabh Saxena

Abstract This paper proposes pattern synthesis for wide null placement using Ant Lion Optimization. The synthesis is modeled as a current amplitude-only optimization. In addition, the Dynamic Range Ratio (DRR) constraint-based optimization is proposed so as to minimize the complexity of array feed network and to reduce the inter-element coupling in the antenna array. For the synthesis of pattern with wide nulls and reduced Side Lobe Level (SLL), the proposed method offers 3 dB improvement in peak SLL minimization and 4 dB improvement in wide null depth. For DRR constraint-based array pattern synthesis, the proposed method yields superior performance in suppressing the SLL while reducing the DRR from 21.44 to 15.42.

Keywords Pattern synthesis · Wide null placement · Dynamic Range Ratio (DRR) · Linear antenna array · Nature-inspired metaheuristics · Ant Lion Optimization (ALO)

1 Introduction

Pattern synthesis is the procedure of deriving the antenna structure from a predefined set of specifications on the radiation pattern. These specifications include Side Lobe Level (SLL) reduction, close-in SLL minimization, and placement of single/multiple

P. Saxena (✉)

Department of Electronics and Communication Engineering, Indian Institute of Information Technology, Design and Manufacturing, Kancheepuram, Chennai, India
e-mail: prerna.saxena@iiitdm.ac.in

A. Kothari

Department of Electronics and Communication Engineering, Visvesvaraya National Institute of Technology, Nagpur, India
e-mail: ashwinkothari@ece.vnit.ac.in

S. Saxena

Department of Electrical Engineering, Indian Institute of Technology Madras, Chennai, India
e-mail: ssaxena@iitm.ac.in

© Springer Nature Singapore Pte Ltd. 2020

A. Kalam et al. (eds.), *Intelligent Computing Techniques for Smart Energy Systems*,
Lecture Notes in Electrical Engineering 607,
https://doi.org/10.1007/978-981-15-0214-9_7

nulls. Traditionally, antenna array design has been based on closed-form solutions obtained by analytical/semi-analytical, and gradient-based methods. Currently, novel optimization techniques based on nature-inspired metaheuristics, characterized by their ability to provide quick, robust, and economically viable global optimum solutions, are emerging as alternatives to the classical methods of pattern synthesis.

The earliest metaheuristics applied for synthesizing the radiation pattern of linear antenna arrays are genetic algorithm [1], simulated annealing [2], particle swarm optimization [3], and ant colony optimization [4]. Of late, several new nature-inspired metaheuristics have been applied to the optimization problem of antenna array pattern synthesis. These include firefly algorithm [5], bacteria foraging optimization [6], cuckoo search [7], cat swarm optimization [8], and spider monkey optimization [9]. The robustness of these algorithms is significantly reduced due to the need for tuning of several parameters for optimization.

Recently, Ant Lion Optimization (ALO) [10] algorithm was proposed for array pattern synthesis which exhibited enhanced exploratory search power and robustness. In [10], ALO was used for unconstrained array pattern synthesis for SLL suppression and placement of sharp nulls. This results in an individual null in the specific direction to cancel interference, which is possible only if the interference direction is known. However, in cases where the arrival direction of interference signal is not known exactly or it slowly varies with time, placement of a sharp null would need continuous steering to maintain a desired signal-to-interference ratio. In such cases, placement of wide nulls on the array pattern is required. Hence, in this paper, the versatility of ALO algorithm is exploited by using it for wide null placement with reduced SLL. In addition, ALO was proposed for unconstrained pattern synthesis in [10] for amplitude-only optimization. However, if there is a large difference between maximum and minimum current values, it leads to complexity in the implementation of array feed network. To enable simplicity and ease in the design of array feed network and also to minimize the inter-element coupling in the array, this paper proposes the incorporation of Dynamic Range Ratio (DRR) constraint into the optimization process for pattern synthesis.

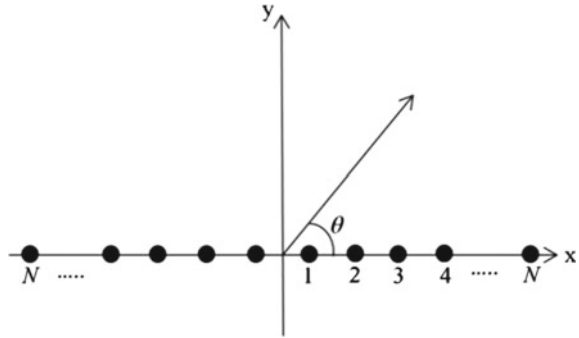
Section 2 discusses the optimization problem formulation and the proposed approach. Wide null placement in the array pattern by maintaining low SLL and DRR constraint-based pattern synthesis is illustrated with design examples in Sect. 3. The proposed approach is validated by comparing with state-of-the-art methods. The work is concluded in Sect. 4.

2 Problem Formulation

The geometry of the linear antenna array is illustrated in Fig. 1. The array factor is given by (1) [3]

$$\text{AF} = 2 \sum_{n=1}^N I_n \cos(kx_n \cos \theta + \psi_n) \quad (1)$$

Fig. 1 Array geometry



where I_n is the current excitation amplitude, x_n is the position, and ψ_n is the current excitation phase for n th element in the linear antenna array. k denotes the wave number and θ represents the azimuth angle.

In this paper, the antenna array is designed to radiate in broadside. Thus,

$$(kx_n \cos \theta + \psi_n)|_{\theta=90^\circ} = 0 \tag{2}$$

$$\Rightarrow \psi_n = 0 \tag{3}$$

Uniform phase excitation, i.e., $\psi_n = 0$ as given by (3) and uniform inter-element spacing of $\lambda/2$ is maintained in the array. The array patterns are synthesized by optimizing the amplitude of the excitation currents. Thus, the array factor is given by (4).

$$AF(\theta) = 2 \sum_{n=1}^N I_n \cos (kx(n) \cos(\theta)) \tag{4}$$

where $x(n)$ is given by,

$$x(n) = \frac{\lambda}{4} + (n - 1) \frac{\lambda}{2} \tag{5}$$

2.1 Wide Null Placement with Reduced SLL

The fitness function $F(\vec{I})$ for placement of wide null is given as

$$F(\vec{I}) = \max \left\{ \left| AF^{\vec{I}}(\theta) \right| \right\}_{\theta \in \text{SLL}} + \max \left\{ \left| AF^{\vec{I}}(\theta) \right| \right\}_{\theta \in \text{widenull}} \tag{6}$$

\bar{I} is the element current amplitude vector, $\theta \in \text{SLL}$ is the side lobe spatial region, and $\theta \in \text{wide null}$ is the spatial region of the wide null.

2.2 Dynamic Range Ratio (DRR) Constraint-Based Peak Side Lobe Level (PSLL) Minimization

The Dynamic Range Ratio (DRR) is defined as follows:

$$\text{DRR} = \frac{I_{\max}}{I_{\min}} \quad (7)$$

In addition to the ease of implementation of array feed network, a low DRR facilitates the reduction of inter-element coupling. $F(\bar{I})$ denotes the fitness function and is formulated as follows:

$$F(\bar{I}) = \sum_i \frac{1}{\Delta\theta_i} \int_{\theta_{li}}^{\theta_{ui}} |AF^{\bar{I}}(\theta)|^2 d\theta + w_d \text{ DRR} \quad (8)$$

where θ_{li} and θ_{ui} are, respectively, the lower and upper limits of azimuth angle for the spatial region in which SLL is to be suppressed and $\Delta\theta_i = \theta_{ui} - \theta_{li}$. w_d is the weighting coefficient and is given by

$$w_d = \begin{cases} 0 & \text{if DRR} < \text{desired value} \\ 1 & \text{elsewhere} \end{cases} \quad (9)$$

In this paper, ALO algorithm [10, 11] is used for optimization and subsequent array synthesis. ALO is inspired by the foraging behavior of net-winged insects called ant lions. The steps of the algorithm are given below:

1. Building ant lion pit/trap
2. Movement of ants in the search space
3. Trapping of ants in the pits of ant lions
4. Sliding of ants inside the pit when they try to escape
5. Catching ants and rebuilding the trap
6. Elitism

The analogy of ALO with linear antenna array is illustrated in Table 1.

Table 1 Analogy of ALO with linear antenna array

Ant lion optimization	Linear antenna array
Aim: catching of prey (preferably ants) by ant lion	Aim: optimization of antenna array radiation pattern by using appropriate fitness function
Ant lions	Antenna current amplitudes
Population of ant lions (n)	No. of vectors of antenna current amplitudes (n)
Step of random walk	Iteration
Number of variables	Number of antenna elements in array
Elite ant lion	Antenna current amplitude vector for which value of fitness function is minimum (best or fittest solution)
Prey	Optimum
Shooting of sand toward the top of the pit by ant lion	Adaptive shrinking of radius of random walk hypersphere

3 Results and Discussion

This section presents design examples for wide null placement with reduced SLL and synthesis of array pattern while maintaining low value of DRR. The array synthesis is achieved by optimizing the antenna current amplitudes.

3.1 Wide Null Placement with Reduced SLL

Design example 1 illustrates a 20-element array for array pattern synthesis with wide null placement and minimization of SLL. Wide null placement is desired between $\theta = 50^\circ$ and $\theta = 60^\circ$. The optimization employs fitness function given by (6). The optimized current amplitudes are shown in Table 2.

Unlike SMO [9], the proposed approach (ALO) gives a smooth and tapering current distribution which is preferred for the ease of implementation. The ALO optimized array pattern is depicted in Fig. 2. Figure 3 shows the array pattern comparison between SMO- and ALO-based designs.

Table 2 Optimized current amplitudes for wide null placement with reduced SLL

Method	Optimized current amplitudes				
SMO [9]	0.9987	0.9974	1.0000	0.8344	0.6417
	0.6533	0.4761	0.5964	0.2574	0.2147
Proposed (ALO)	1.0000	0.9950	0.9685	0.8247	0.6928
	0.6067	0.5031	0.4781	0.2427	0.1570

Fig. 2 Optimized array pattern

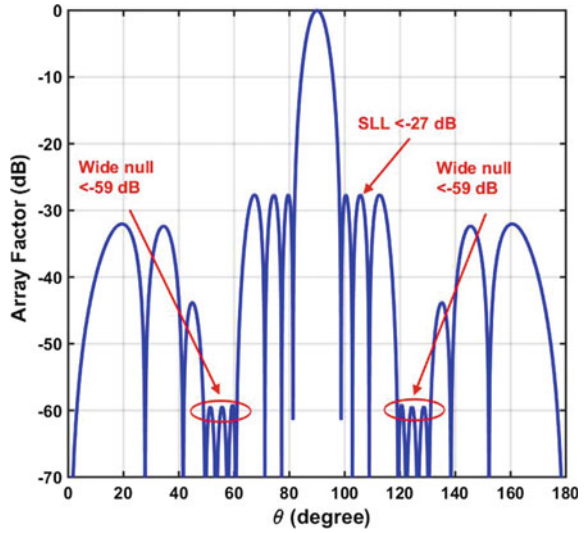
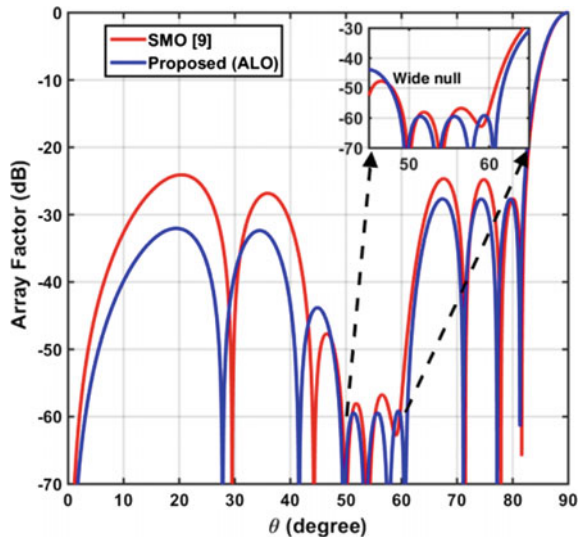


Fig. 3 Array pattern comparison between ALO-based and SMO-based designs



The peak SLL and null depth of the wide null obtained by SMO [9] and the proposed approach are summarized in Table 3. It shows that using the proposed approach (ALO), the depth of the wide null is below -59 dB and the side lobe level is below -27 dB. As compared to SMO [9], the proposed method offers 3 dB improvement in peak SLL minimization and 4 dB improvement in wide null depth control.

Table 3 Peak SLL and wide null depth

	Peak SLL (dB)	Wide null depth (dB)
SMO [9]	-24	<-55
Proposed (ALO)	-27	<-59

3.2 Dynamic Range Ratio (DRR) Constraint-Based Peak Side Lobe Level (PSLL) Minimization

Design example 2 comprising of 30-element array is illustrated for minimizing the PSLL. The inter-element spacing is $\lambda/2$. The side lobe region is defined as $\theta = [0^\circ, 82^\circ]$ and $\theta = [98^\circ, 180^\circ]$. In the first case, the fitness function without DRR constraint is used for the optimization. Table 4 shows the ALO optimized excitation amplitudes along with those obtained by the Taguchi method [12].

The ALO optimized array pattern with PSLL of -47.35 dB is shown in Fig. 4. Unlike the equal side lobe pattern of Dolph-Chebyshev array, the obtained array is characterized by a decaying nature of side lobes which results in minimizing the radiation energy loss in undesired directions. However, the DRR is 31.4485 which is unacceptable at the implementation stage. The DRR for Dolph-Chebyshev array for the same SLL is only 15.4245. This problem is overcome by including the constraint for DRR in the optimization process. In the second case, the fitness function with DRR control given by (8) is used. Figure 5 shows the obtained array pattern. The optimized excitation amplitudes are given in Table 4 along with the amplitudes obtained by TM [12].

The current amplitude distribution obtained by the proposed approach without and with DRR constraint is shown in Fig. 6.

Table 4 Optimized normalized excitation amplitudes without and with DRR constraint

Method	Without DRR constraint				
TM [12]	1.0000	0.9763	0.9302	0.8641	0.7824
	0.6886	0.5894	0.4887	0.3918	0.3021
	0.2214	0.1541	0.0991	0.0581	0.0257
Proposed (ALO)	1.0000	0.9758	0.9290	0.8625	0.7800
	0.6865	0.5866	0.4860	0.3886	0.3000
	0.2193	0.1529	0.0981	0.0603	0.0318
	With DRR constraint				
TM [12]	1.0000	0.9785	0.9353	0.8728	0.7943
	0.7063	0.6093	0.5119	0.4176	0.3269
	0.2461	0.1773	0.1170	0.0778	0.0466
Proposed (ALO)	1.0000	0.9796	0.9367	0.8759	0.7991
	0.7126	0.6174	0.5223	0.4266	0.3396
	0.2573	0.1893	0.1263	0.0886	0.0648

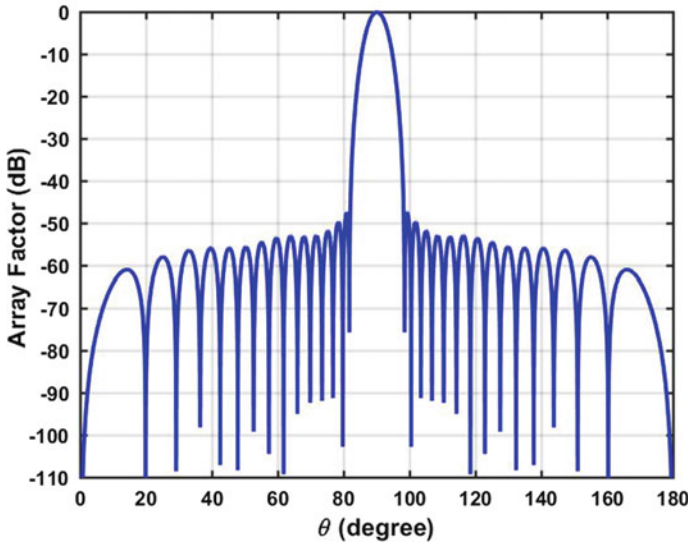


Fig. 4 Array pattern without DRR constraint for design example 2

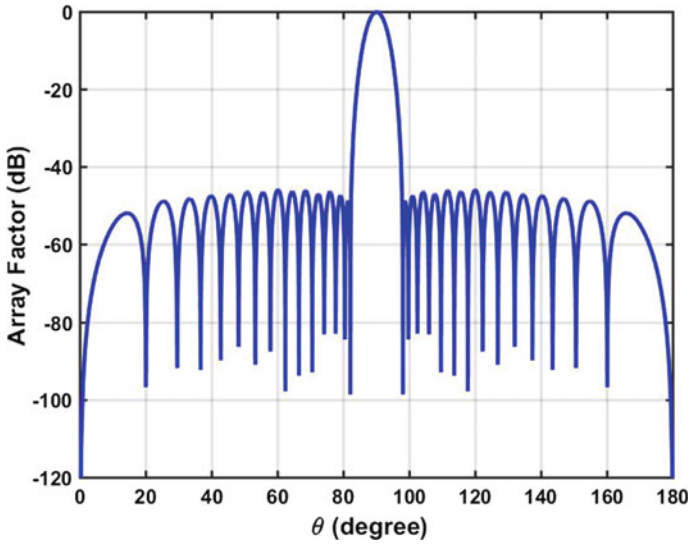


Fig. 5 Array pattern with DRR constraint for design example 2

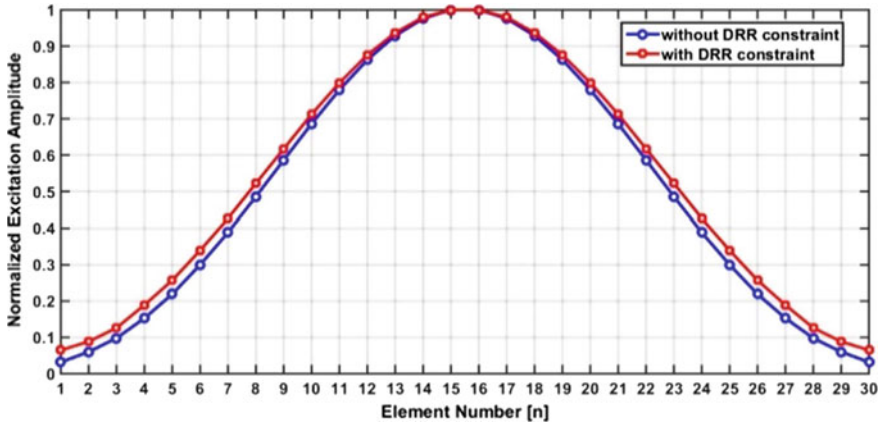


Fig. 6 Current distribution without and with DRR constraint

Table 5 PSLL and DRR

		PSLL (dB)	DRR
Without DRR constraint	TM [12]	-44.65	38.1
	Proposed (ALO)	-47.35	31.4485
With DRR constraint	TM [12]	-46.21	21.44
	Proposed (ALO)	-47.38	15.4245

The obtained PSLL is -47.38 dB and the array is constrained to have DRR same as Dolph–Chebyshev array (DRR = 15.4245). Table 5 shows that as compared to TM [12], ALO yields superior performance in suppressing the SLL while maintaining a much lower DRR.

4 Conclusion

This paper proposed antenna pattern synthesis with wide null placement and low DRR using ALO. For wide null positioning with reduced SLL, the proposed method offers 3 dB improvement in peak SLL minimization and 4 dB improvement in wide null depth. For DRR constraint-based array pattern synthesis, the proposed method yields superior performance in suppressing the SLL while reducing the DRR from 21.44 to 15.42. The proposed approach provides state-of-the-art performance demonstrating its suitability for constrained real-time antenna pattern synthesis.

References

1. Yan K-K, Lu Y (1997) Sidelobe reduction in array-pattern synthesis using genetic algorithm. *IEEE Trans Antennas Propag* 45:1117–1122
2. Murino V, Trucco A, Regazzoni CS (1996) Synthesis of unequally spaced arrays by simulated annealing. *IEEE Trans Signal Process* 44:119–122
3. Khodier MM, Christodoulou CG (2005) Linear array geometry synthesis with minimum sidelobe level and null control using particle swarm optimization. *IEEE Trans Antennas Propag* 53:2674–2679
4. Rajo-Iglesias E, Quevedo-Teruel O (2007) Linear array synthesis using an ant-colony-optimization-based algorithm. *IEEE Antennas Propag Mag* 49:70–79
5. Zaman MA, Matin A (2012) Nonuniformly spaced linear antenna array design using firefly algorithm. *Int J Microw Sci Technol* 2012
6. Guney K, Basbug S (2008) Interference suppression of linear antenna arrays by amplitude-only control using a bacterial foraging algorithm. *Prog Electromagn Res* 79:475–497
7. Khodier M (2013) Optimisation of antenna arrays using the cuckoo search algorithm. *IET Microw Antennas Propag* 7:458–464
8. Pappula L, Ghosh D (2014) Linear antenna array synthesis using cat swarm optimization. *AEU-Int J Electron Commun* 68:540–549
9. Al-Azza AA, Al-Jodah AA, Harackiewicz FJ (2016) Spider monkey optimization: a novel technique for antenna optimization. *IEEE Antennas Wirel Propag Lett* 15:1016–1019
10. Saxena P, Kothari A (2016) Ant Lion Optimization algorithm to control side lobe level and null depths in linear antenna arrays. *AEU-Int J Electron Commun* 70:1339–1349
11. Mirjalili S (2015) The ant lion optimizer. *Adv Eng Softw* 83:80–98
12. Recioui A (2014) Optimization of antenna arrays using different strategies based on Taguchi method. *Arab J Sci Eng* 39:935–944

Design and Analysis of a Hybrid Non-volatile SRAM Cell for Energy Autonomous IoT



Kanika, Nitin Chaturvedi and S. Gurunarayanan

Abstract Powering billions of devices is one of the most challenging barriers in achieving the future vision of IoT. Most of the IoT based systems depend on the battery for power supply. However, the battery's limited power budget shortens the lifetime, whereas their frequent replacement increases the cost. In addition, their disposal can create several environmental and health issues. Energy autonomy emerges as a solution to address these problems offering the advantage of a theoretically infinite lifetime and low cost. However, there are many challenges in realizing them. In this paper, we outline the challenges involved with the intermittent power supply causing the power outage in energy autonomous systems. To address these challenges emerging magnetic memory has been explored as an efficient way to ensure reliable operation under frequent power failure. Moreover, IoT nodes have a short period of computation followed by a large period of inactivity such that they suffer from large leakage power dissipation. Ultralow power IoT node is achieved through normally-off computing which offers zero leakage power dissipation during standby mode by turning off the components when not in use. Therefore, we propose a non-volatile SRAM cell with STT-MTJ for normally-off applications which retain the state on-chip during power failure/power off and quickly resume the operation from the point of interruption. Also, two writing schemes for the proposed cell are presented as single-phase and two-phase where two-phase writing scheme consumes 86% less power than the single-phase writing scheme.

Keywords Energy harvesting · Internet of things (IoT) · Non-volatile memory (NVM) · Magnetic tunnel junction (MTJ)

Kanika (✉) · N. Chaturvedi · S. Gurunarayanan
Electrical and Electronics Engineering Department, Birla Institute of Technology
and Science Pilani, Pilani, India
e-mail: p20170027@pilani.bits-pilani.ac.in

N. Chaturvedi
e-mail: nitin80@bits-pilani.ac.in

S. Gurunarayanan
e-mail: sguru@bits-pilani.ac.in

1 Introduction

IoT has gained the interest of many researchers all over the world. It is defined as network of things with internet connectivity to enable exchange of information and data [1]. Things, in IoT sense, can refer to any physical device, people, building, heart monitoring implants, vehicles, weapons assisting firefighters in search, and rescue operation, etc. They are anywhere anytime employable small sensor-based system which collects data from the surrounding and have decision making capability [2]. The end devices in IoT network are also referred as IoT nodes. Today, their count reaches to a few billion and it is expected to grow to 50 billion in 2020 [3], which would be $6\times$ the world's current population. Futuristic Gaudin [4] and Sparks [5] predicts a faster rate with number of IoT nodes reaching trillions creating great opportunities for society, industry, and economy. However, there are many challenging barriers in achieving this goal which arises due to stringent requirement of low power, low cost, and small size of IoT node. One of the biggest challenges faced by the IoT network is powering countless nodes. They cannot be powered by a cord because that would populate the earth with web of cords. Also, it will increase the expense of employing them. Sometimes it is even infeasible to wire them [6]. With batteries devices become bulky as well as post-deployment maintenance cost increases due to frequent replacements [7]. In addition to the cost of new batteries, there is cost incurred during system downtime. Also, battery disposal has hazardous effect on environment as well as on human. To address these problems, energy autonomy seems to be an attractive and feasible solution. It offers a low cost and eco-friendly solution to battery problem. Energy autonomous or self-powered devices are powered by sources such as thermal, radiant, and mechanical energy [7]. However, there are many challenges in realizing them. Renewable power sources used for harvesting have low conversion efficiency and they are not reliable. Most of the IoT nodes suffer from performance degradation due to frequent power failures occurring due to unstable nature of ambient sources. System initialization after power failure requires energy-intensive boot process. Also, completion of task may take longer time since intermediate results could not be saved [8]. These problems have attracted researchers both from the industry and academia to propose some techniques that can be augmented with energy autonomous system to ensure continuous forward progress even with frequent power failures. Non-volatile Memory (NVM) architecture opens the possibility to compute continuously with the intermittent power. By incorporating emerging non-volatile technologies, it can maintain the temporary state and resume the computation once the power is recovered. IoT node based on normally-on computing suffers from large leakages due to low duty cycle (active period is much smaller than standby period) operational mode. Addressing this problem, normally-off computing achieves complete elimination of leakage power by turning off the system when it is idle. Emerging non-volatile memories which can be incorporated with the CMOS are PCM, FRAM, RRAM, and MTJ. Among all magnetic memories, STT-MTJ is reported as one possible candidate for low power IoT nodes due to low switching current, fast switching times, and high

endurance. Therefore, we propose non-volatile hybrid SRAM cell which is robust to sudden power failure. The data in proposed NV-SRAM cell is held by both internal storage nodes (q & q_c) and the MTJs. Now since the MTJ stores the most recent value it does require any backup operation before power failure or power down.

The main contributions of the paper are:

1. We explore various previously proposed techniques addressing the issue of unstable power supply in energy autonomous/self-powered systems
2. We design a normally-off computing-based non-volatile hybrid SRAM cell which is turned OFF when not in use and is robust to power failures.
3. To demonstrate the advantage of non-volatility the proposed NV-SRAM cell is evaluated by simulating all the memory operation.
4. The proposed NV-SRAM cell is presented with two writing schemes. The two-phase write operation reduces the power consumption by approximately 86% when compared with single-phase write operation.

The rest of the paper is organized as follows: Sect. 2 describe various techniques to address the challenges due to inefficient power supply. Section 3 presents the proposed NV-SRAM cell with all its operation. In Sect. 4 simulation setup and results are presented and Sect. 5 finally concludes the paper.

2 Background

This section focuses on various techniques proposed by researchers all over the world to address the problem of intermittent power supply.

Periodic/On-Demand Backup In this technique, the state of the system is periodically checkpointed to off-chip non-volatile storage. To retrieve the complete state of processor, status of register file, program counter, instruction cache, data cache, and memory is required. Therefore, all of them should be preserved before power loss [9]. The periodic backup method has an advantage of simplicity but it lacks flexibility to adjust the backup interval according to power profile [7]. Whereas in on-demand backup technique state is saved whenever required, saving the energy wasted in unnecessary backups. This method requires early prediction of power failure which can be done by constantly monitoring the power level and once the power is below a threshold value, it triggers the backup operation [10].

Hybrid Non-volatile Memory (NVM) The technique which is highly robust in case of sudden power failure is hybrid non-volatile memory architecture [11, 12]. NVM architecture consists of embedded non-volatile flip-flop (NVFF) and non-volatile memory (NVM) components that can retain the state during power failure without requiring any backup operation [13]. Processors with embedded NVFF and NVM are termed as Non-Volatile Processor (NVP) to differentiate it with the conventional volatile processor. The storing and restoring operation are transparent to the user resulting in $1000\times$ faster wake up times compared to conventional checkpointing technique [14]. Emerging non-volatile memories such as FeRAM, PCM,

RRAM, and STT-MRAM are the possible candidate for hybrid memories. Quick recall [14] is one such system using FeRAM for in situ checkpointing of systems state. Among all emerging non-volatile memories, STT-MRAM shows promising results as it offers faster read/write times, high endurance, better scalability, and compatibility with CMOS logic. Also, it can be incorporated at any level of memory hierarchy [15–19]. Therefore, we propose MTJ based hybrid non-volatile SRAM cell which is resilient to sudden power outage.

3 Proposed NV-SRAM Cell

This section presents the proposed normally-off and instant-on computing-based hybrid non-volatile SRAM cell with all its operation. Non-volatile SRAM has been proposed to preserve the state during power failure while providing faster wake up times. Additionally, normally off and instant-on architecture allows SRAM cell to normally turn off when not in use and instantly turn on with full performance when needed eliminating large standby mode power dissipation.

3.1 Cell Design Concept

The proposed NV-SRAM cell as shown in Fig. 1 consist of conventional 6T SRAM cell modified using MTJ to incorporate non-volatility. Two MTJs are used per SRAM cell. MTJ1a is connected to bitline BL and similarly, MTJ1b is connected to bitline BL_bar. In addition to 6T SRAM core, an equalization transistor is also added which is connected between the nodes q and qc. The data written into the SRAM cell is held by cross-coupled inverter as well as MTJs. Since the MTJ stores the current data there is no need to run a backup operation before turning OFF the memory. The main advantage of proposed non-volatile SRAM cell is retention of status of intermediate computation before sudden power failure.

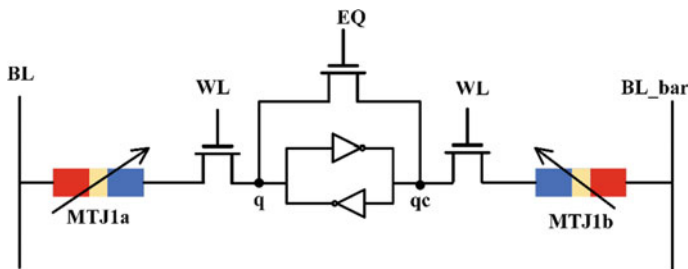


Fig. 1 Proposed NV-SRAM cell

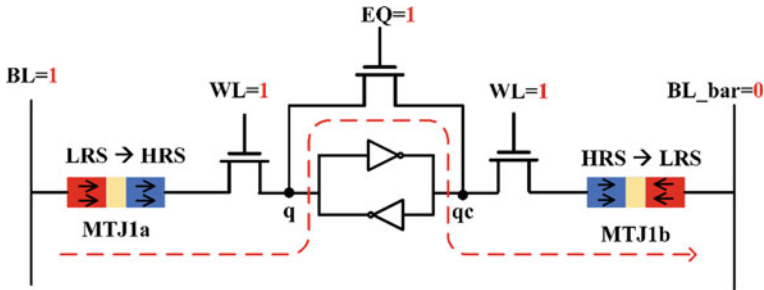


Fig. 2 Writing logic ‘1’ into the proposed NV-SRAM cell

The proposed NV-SRAM cell works in three operational modes: Write, Read, and Restore. Write operation refers to writing into the MTJ as well as cell internal nodes q and qc. Similar to conventional SRAM cell, read operation in NV-SRAM cell refers to reading the value stored by the cell nodes q and qc. Whereas, restore operation is performed after power restoration to resume the execution from the point of interruption.

Write operation: In this mode of operation, value is written into the nodes as well as MTJs through the bitlines. Let us assume that cell initially stores a logic ‘0’ where node q stores logic ‘0’ and node qc stores logic ‘1’. For Writing logic ‘1’ bitline BL is charged to Vdd while BL_bar is pulled to ground. Now asserting control signal WL and EQ high provides a path for current to flow from MTJ1a → q → qc → MTJ1b switching MTJ1a from LRS to HRS and MTJ1b from HRS to LRS as shown in Fig. 2. Thus, write operation is completed in a single step.

However, two-phase backup scheme can be employed which result in lower power consumption compared to single-phase backup operation. The two-phase backup operation is performed in the following steps:

Phase I: During this phase, value is written onto the MTJs. Similar to single-phase write operation let us assume that the cell initially stores a logic ‘0’ where node q stores logic ‘0’ and node qc stores logic ‘1’. For Writing logic ‘1’ bitline BL is charged to Vdd while BL_bar is pulled to ground. Meanwhile wordline WL is asserted high which allow current to flow from bitline BL to node q through MTJ1a and from node qc to bitline BL_bar through MTJ1b. The cell is sized in such a way that opposite value on bitlines will not flip the data held by internal node. At the completion of this step, MTJ1a is switched from LRS to HRS, conversely MTJ1b is switched from HRS to LRS.

Phase II: In this phase, the data value is transferred to the cell internal nodes q & qc. The control signal EQ is asserted high to trigger this phase. Meanwhile both the bitlines are discharged to ground. After attaining equal voltages at nodes q & qc control signal EQ is asserted low. Now asserting WL causes current to flow from nodes to bitlines through MTJ. The potential drop at the node depends on the resistance state of the MTJ. MJT with LRS (low resistance state) will cause

corresponding node to fall very quickly. The differential potential at the node is pulled to full swing by cross-coupled action.

The main advantage of two-phase write operation is power saving while writing the same bit. During phase I, bitline and node are at same potential if same bit is to be written. Therefore, no current flows in the circuit for complete phase I duration resulting in lower power consumption.

Read operation: During read mode, the value stored by cell internal nodes q and qc are transferred onto bitlines BL and BL_bar. The operation starts with precharging the bitlines to Vdd. After precharging bitlines, wordline WL is asserted high which causes one of the bitline to discharge as shown in Fig. 3.

Restore operation: After the power restoration, restore operation is performed to retrieve the data stored in the MTJ into the cell nodes q & qc. During the restore operation, the control signal EQ is asserted high to equalize the nodes q & qc. Meanwhile, both the bitlines are discharged to ground. After attaining equal voltages at nodes q & qc control signal EQ is asserted low. Now asserting WL causes current to flow from nodes to bitlines through MTJ as shown in Fig. 4. The potential drop at the node depends on the resistance state of the MTJ. MJT with LRS (low resistance state) will cause corresponding node to fall very quickly. The differential potential at the nodes is converted to full voltage level by cross-coupled action.

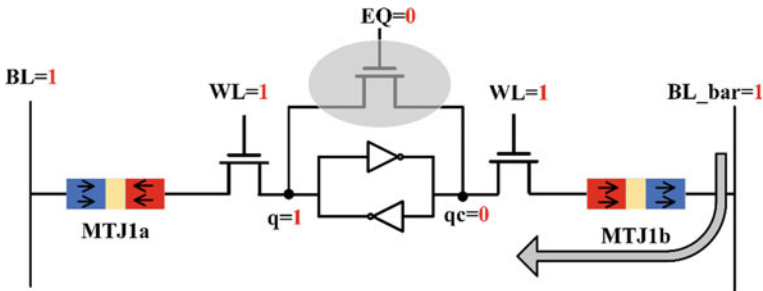


Fig. 3 Reading logic '1'

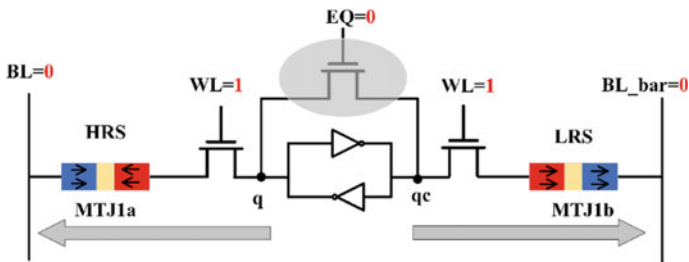


Fig. 4 Restore operation

4 Results

In this section experimental methodology is presented followed by an evaluation of proposed NV-SRAM cell using obtained simulation results. The simulations were carried out using the HSPICE circuit simulator from Synopsys. By using PTM 20 nm FinFET model, STT-MTJ HSPICE model [20] and power supply of 0.9 V simulation has been performed. Figure 5 plots the simulated waveform with all the basic memory operation.

The simulation begins with two-phase write operation followed by read operation. Then power supply is disconnected to represent power down or power failure. After power outage restore operation is performed to retrieve the previously saved state.

The energy consumption by proposed NV-SRAM cell during write, read, and restore operational modes are tabulated in Table 1. The simulation results demonstrate that energy consumption during write operation is reduced by approximately 86% compared to single-phase write operation when two-phase writing approach is used. During single-phase write operation the equalization transistor is turned ON for complete duration which results in the formation of short circuit path from bitlines to ground. Therefore, large amount of current flows which increases the energy consumption during single-phase write operation.

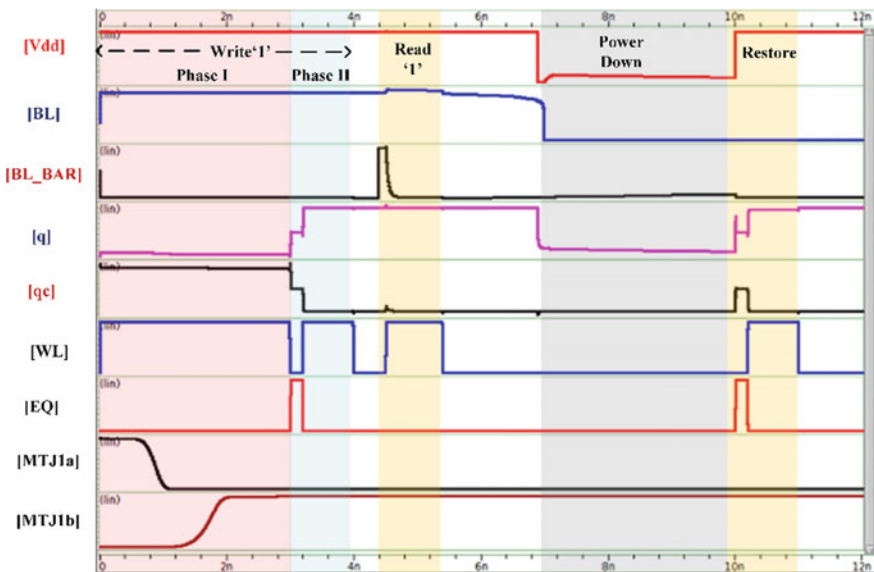


Fig. 5 Simulated waveform of proposed NV-SRAM cell

Table 1 Energy consumption by proposed NV-SRAM cell

	Single-phase write (fJ)	Two-phase write (fJ)	Read (fJ)	Restore (fJ)
Energy consumed during writing of same bit	1720	1.2	7.9	109
Energy consumed during writing of opposite bit	1720	478	7.9	109

5 Conclusion

In this paper, we address the challenges involved with batteryless system using ambient sources for power supply. The unreliable nature of these ambient sources causes loss of current state. To overcome this problem many approaches were proposed. While non-volatile processor with energy harvesting shows a promising future in IoT to guarantee the perpetual operation, other approaches are not efficient under intermittent power supply. The proposed NV-SRAM cell is immune to power failure as state is retained before the power failure without performing any backup operation. IoT nodes have small power budget, therefore, lower power consumption in proposed NV-SRAM is achieved through normally-off computing. Furthermore, use of two-phase write operation lowers the power consumption by 86% compared to single-phase write operation.

References

1. Brown E Who needs the internet of things? The Linux Foundation. <https://www.linux.com/news/who-needs-internet-things>
2. Xie M et al (2016) Checkpoint aware hybrid cache architecture for NV processor in energy harvesting powered systems. In: Proceedings of the eleventh IEEE/ACM/IFIP international conference on hardware/software codesign and system synthesis
3. CompTIA research and market intelligence, Sizing up the internet of things. Research Brief. <https://www.comptia.org/resources/sizing-up-the-internet-of-things>. Accessed 28 Aug 2015
4. Gaudin S, Get ready to live in a trillion-device world. Computer World. <https://www.computerworld.com/article/2983155/internet-of-things/get-ready-to-live-in-a-trillion-device-world.html>
5. Sparks P (2017) White paper—The route to a trillion devices: the outlook for IoT investment to 2035 white paper, June, pp 1–14
6. Alioto M (ed) (2017) Enabling the internet of things: the IoT vision, 1st edn. Springer International Publishing, Cham
7. Jayakumar H, Raha A, Kim Y, Sutar S, Lee WS, Raghunathan V (2016) Energy-efficient system design for IoT devices. In: Proceedings of Asia South Pacific design automation conference ASP-DAC, 25–28 January 2016, pp 298–301
8. Ma K et al (2015) Nonvolatile processor architecture exploration for energy-harvesting applications. *IEEE Micro* 35(5):32–40

9. Sutardja C, Stefanov E Checkpoint based recovery from power failures. Cs. Berkeley. Edu. <https://pdfs.semanticscholar.org/7a0c/d81192dbb97662aa0c56f1cf2decb267cd7b.pdf>
10. Ransford B, Sorber J, Fu K (2011) Mementos: system support for long-running computation on RFID-scale devices. *Asplos*, May 2013, pp 159–170
11. Su F, Ma K, Li X, Wu T, Liu Y, Narayanan V (2017) Nonvolatile processors: why is it trending? In: *Design automation & test in Europe conference & exhibition (DATE)*, vol 2, pp 966–971
12. Ma K et al (2015) Architecture exploration for ambient energy harvesting nonvolatile processors. In: 2015 IEEE 21st international symposium on high performance computer architecture (HPCA)
13. Kawahara T (2011) Non-volatile memory and normally off computing. In: *ASP-DAC Yokohama Japan*, January 2011, pp 1–53. <http://www.aspdac.com/aspdac2011/archive/pdf/1K-1.pdf>
14. Jayakumar H, Raha A, Lee WS, Raghunathan V (2015) QuickRecall: a HW/SW approach for computing across power cycles in transiently powered computers. *ACM J. Emerg. Technol. Comput. Syst.* 12(1):1–19
15. Fujita S, Noguchi H, Ikegami K, Takeda S, Nomura K, Abe K (2015) Technology trends and near-future applications of embedded STT-MRAM. In: 2015 IEEE 7th international memory workshop (IMW), pp 1–5
16. Endoh T (2013) STT-MRAM and NV-logic for low power systems. In: 2013 third Berkeley symposium on energy efficient electronic systems (E3S), 28–29 October 2013, Berkeley, CA, USA. <https://doi.org/10.1109/e3s.2013.6705864>
17. Kang SH (2014) Embedded STT-MRAM for energy-efficient and cost-effective mobile systems. In: *Digest of technical papers—symposium VLSI technology*, vol 4446, no 2013, pp 2013–2014
18. Fujita S, Noguchi H, Ikegami K, Takeda S, Nomura K, Abe K (2017) Novel memory hierarchy with e-STT-MRAM for near-future applications. In: 2017 international symposium on VLSI design automation and test, VLSI-DAT 2017, pp 3–4
19. Jovanović B, Brum RM, Torres L (2014) Evaluation of hybrid MRAM/CMOS cells for ‘normally-off and instant-on’ computing. *Analog Integr Circuits Signal Process* 81(3):607–621
20. Roy K, Fong X, Choday SH, Georgios P, Augustine C (2013) SPICE models for magnetic tunnel junctions based on monodomain approximation

Bandgap Engineering of AgGaS₂ for Optoelectronic Devices: First-Principles Computational Technique



Maneesha Purohit, Seema Kumari Meena, Alpa Dashora and B. L. Ahuja

Abstract Electronic and optical properties of pristine and doped (with Al and In) AgGaS₂ have been computed using full potential linearized augmented plane wave method within density functional theory. Effect of Al and In doping on bandgap, energy bands, and density of states has been studied. Change in real and imaginary part of dielectric constant have also been analyzed to check the effect of doping and applicability of these materials for optoelectronics.

Keywords Ternary chalcopyrite · Electronic properties · Optical properties · Bandgap tuning

1 Introduction

In the current environmental scenario, search for high power, small-size, low-cost, and environmental friendly optoelectronic devices are highly required. The continuous drive is going on in optoelectronic industry to design reasonably good materials. The ternary semiconductor chalcopyrites are one of the most studied materials for optoelectronic and photovoltaic applications in past few decades due to their direct bandgap [1, 2]. Among chalcopyrites, AgGaS₂ has attracted much attention, because of its direct bandgap of 2.51 eV, which is in the range desirable for applications in light-emitting diodes (LEDs) and high-efficiency tandem solar cells [3–5]. LEDs play important role in computer hardware. It can be used in monitoring technology, optical mouse, status indicator on monitor, keyboard, motherboard, printer, speaker, and CD drive, etc.

M. Purohit · B. L. Ahuja

Department of Computer Science, M.L. Sukhadia University, Udaipur 313001, India

A. Dashora (✉)

Department of Physics, The Maharaja Sayajirao University of Baroda, Vadodara 390002, India

e-mail: dashoralpa@gmail.com

S. K. Meena · B. L. Ahuja

Department of Physics, University College of Science, M.L. Sukhadia University, Udaipur 313001, India

© Springer Nature Singapore Pte Ltd. 2020

A. Kalam et al. (eds.), *Intelligent Computing Techniques for Smart Energy Systems*,

Lecture Notes in Electrical Engineering 607,

https://doi.org/10.1007/978-981-15-0214-9_9

In previous studies, Tell and Kesper [6] and Tell et al. [7] have studied the luminescence, reflectivity, electroreflectance, and absorption edge of AgGaS_2 and AgGaSe_2 compounds and measured the electronic and optical properties. Grimsditch and Holah [8] have determined elastic moduli of AgGaS_2 for the first time at room temperature using laser Brillouin scattering. Artus and Bertrand [9] have proven the splitting of AgGaS_2 uppermost valence bands experimentally by crystal-field and spin-orbit interaction. Tang et al. [10] have reported tuning of bandgap on substituting S by Se in AgGaS_2 . Electronic and optical properties of AgGaS_2 and AgGaSe_2 and CuGaS_2 have been studied using full potential linearized augmented plane wave (FP-LAPW) method [11, 12]. The other first-principles studies to study electronic and optical properties are also available for AgGaS_2 , AgGaSe_2 , CuGaS_2 , CuGaSe_2 , CuInS_2 , etc. [13–15]. Further, $\text{AgGa}_{1-x}\text{In}_x\text{S}_2$ (for $x = 0 - 1$) have also been experimentally studied in terms of bandgap tailoring and its application for photovoltaics [16, 17]. Recently, $\text{AgGa}_{0.5}\text{In}_{0.5}\text{S}_2$ single crystals were synthesized and the value of bandgap is obtained as 2.0 eV [18]. However, there is no experimental and theoretical reports available on electronic response of $\text{AgGa}_{0.5}\text{Al}_{0.5}\text{S}_2$.

In this paper, we present the electronic and optical properties of AgGaS_2 , $\text{AgGa}_{0.5}\text{Al}_{0.5}\text{S}_2$, and $\text{AgGa}_{0.5}\text{In}_{0.5}\text{S}_2$ using first-principles technique.

2 Computational Details

For the computation of electronic and optical properties, we have used FP-LAPW method which is embodied into WIEN2 K package [19, 20]. In this method, the unit cell is divided into nonoverlapping atomic spheres called muffin-tin (MT) spheres and interstitial region. In the MT sphere electrons can be approximated by atomic-like wave functions, whereas in the interstitial region they can be approximated by plane waves. For exchange-correlation, we have applied PBEsol functional [21] based on generalized gradient approximation (GGA).

In our work, we have used k points from $10 \times 10 \times 10$ Monkhorst–Pack sampling in the irreducible Brillouin zone (BZ), for the self-consistent field calculation. The MT radii were taken to be 2.50, 2.32, and 2.00 Å for Ag, Ga, and S, respectively for the AgGaS_2 . For $\text{AgGa}_{0.5}\text{Al}_{0.5}\text{S}_2$ MT radii were taken to be 2.50, 2.32, 2.22, and 2.20 Å for Ag, Ga, Al, and S, respectively. In case of $\text{AgGa}_{0.5}\text{In}_{0.5}\text{S}_2$, MT radii were considered as 2.50, 2.37, 2.42, and 1.98 Å for Ag, Ga, In, and S, respectively. The wave functions in the interstitial regions were expanded in plane waves with cutoff $R_{\text{MT}}k_{\text{max}} = 7.0$ to converge the energy eigenvalues. Here R_{MT} and k_{max} represent MT sphere radius and magnitude of largest k vector in plane wave expansion, respectively. The wave function inside the MT sphere was expanded up to $l_{\text{max}} = 10$ and the Fourier expansion of the charge density was up to the value $G_{\text{max}} = 12$. Optical properties are also calculated using WIEN2 k code [22].

3 Structural Information

The base compound AgGaS₂ crystallizes in the chalcopyrite structure having tetragonal space group $\bar{1}42d$ ($a = b \neq c, \alpha = \beta = \gamma = 90^\circ$), which is typically formed by two zinc blende structures with the same arrangement of anions and different arrangements of cations. In Fig. 1a–c we have shown the crystal structure of AgGaS₂, AgGa_{0.5}Al_{0.5}S₂, and AgGa_{0.5}In_{0.5}S₂ using XCRYSDEN visualization programme [23]. To develop the Al/In doped system, we have replaced half of the Ga atom with Al/In. Using the FP-LAPW method, we have performed volume optimization and calculated the optimized lattice parameters. Our optimized lattice parameters along with available experimental and theoretical data are compiled in Table 1. The calculated values are in good agreement with the available data in case of AgGaS₂.

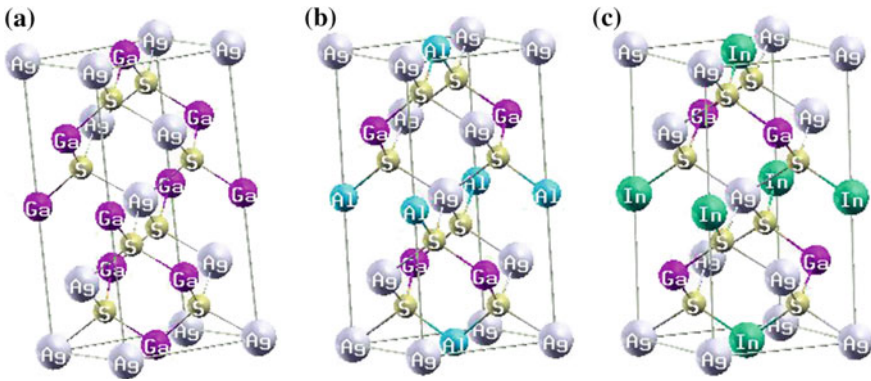


Fig. 1 Crystal Structure of **a** AgGaS₂ **b** AgGa_{0.5}Al_{0.5}S₂ **c** AgGa_{0.5}In_{0.5}S₂

Table 1 The calculated lattice parameters a (in Å) and the c/a ratio of AgGaS₂ and AgGa_{0.5}Al_{0.5}S₂ and AgGa_{0.5}In_{0.5}S₂ along with available experimental and other theoretical values

Parameters	AgGaS ₂			AgGa _{0.5} Al _{0.5} S ₂	AgGa _{0.5} In _{0.5} S ₂
	This work	Experiment	Theory	This work	This work
a (in Å)	5.609	5.755 ^a	5.587 ^b , 5.722 ^c , 5.756 ^d	5.572	5.838
c/a	1.929	1.786 ^a	1.863 ^b , 1.857 ^c , 1.852 ^d	1.968	1.814

^aReference [6], ^bReference [11], ^cReference [13], ^dReference [14]

4 Results and Discussion

4.1 Electronic Properties

Electronic properties of pure and doped compounds are discussed using energy bands and density of states (DOS), which are shown in Figs. 2a–c and 3a–c. In Fig. 2 (Fig. 3), the solid horizontal (vertical) line in energy bands (DOS) shows the position of Fermi energy (E_F) which is scaled to 0.0 eV reference level. Further by the observation of energy bands and DOS, it is seen that the energy bands in energy ranges -13.8 to -12.0 , -13.6 to -12.0 , and -13.6 to -11.6 eV for AgGaS_2 , $\text{AgGa}_{0.5}\text{Al}_{0.5}\text{S}_2$, and $\text{AgGa}_{0.5}\text{In}_{0.5}\text{S}_2$, respectively, are mainly dominated by 3s states of S atoms. Further, there is major contribution of Ga-3d and In-4d states in AgGaS_2 and $\text{AgGa}_{0.5}\text{In}_{0.5}\text{S}_2$, respectively. Further in energy range -7.5 to -5.4 , -7.0 to -5.0 and -7.1 to -5.1 eV for AgGaS_2 , $\text{AgGa}_{0.5}\text{Al}_{0.5}\text{S}_2$, and $\text{AgGa}_{0.5}\text{In}_{0.5}\text{S}_2$, respectively, bands are

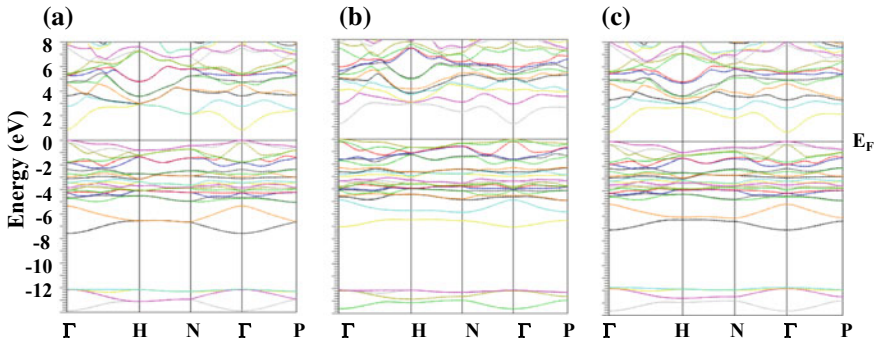


Fig. 2 Band structure using FP-LAPW method for **a** AgGaS_2 **b** $\text{AgGa}_{0.5}\text{Al}_{0.5}\text{S}_2$ and **c** $\text{AgGa}_{0.5}\text{In}_{0.5}\text{S}_2$ compounds

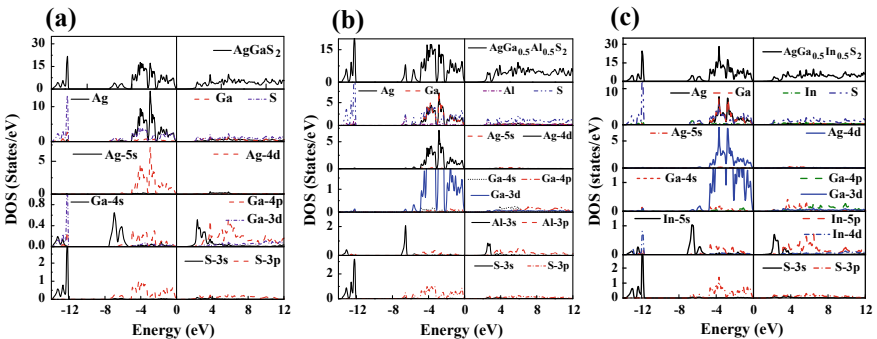


Fig. 3 Density of states using FP-LAPW method for **a** AgGaS_2 **b** $\text{AgGa}_{0.5}\text{Al}_{0.5}\text{S}_2$ and **c** $\text{AgGa}_{0.5}\text{In}_{0.5}\text{S}_2$ compounds

Table 2 Energy bandgaps derived from FP-LAPW-PBEsol calculations along with earlier reported data for AgGaS₂, AgGa_{0.5}Al_{0.5}S₂, and AgGa_{0.5}In_{0.5}S₂

Sample	Reference	E _g (in eV)
AgGaS ₂	This work	0.86
	Experiment	2.51 ^a
	Other calculations	0.95 ^b , 1.005 ^c , 1.00 ^d
AgGa _{0.5} Al _{0.5} S ₂	This work	1.23
AgGa _{0.5} In _{0.5} S ₂	This work	0.73
	Experiment	2.00 ^f

^aReference [6], ^bReference [11], ^cReference [14], ^dReference [15], ^fReference [18]

mainly formed due to Ga-4 s states in AgGaS₂, Al-3 s states in AgGa_{0.5}Al_{0.5}S₂ and In-5 s states in AgGa_{0.5}In_{0.5}S₂. Energy bands in range -5.1 to 0.0 , -4.9 to 0.0 , and -4.8 to 0.0 eV for AgGaS₂, AgGa_{0.5}Al_{0.5}S₂, and AgGa_{0.5}In_{0.5}S₂, respectively, are dominated due to 4d states of Ag atoms, 3p states of S atoms. A small contribution of Ga-4p states in AgGaS₂, Ga-3d, and Al-3p states in AgGa_{0.5}Al_{0.5}S₂, Ga-3d, and In-5p states in AgGa_{0.5}In_{0.5}S₂ is observed. Further, the formation of lower conduction bands are originated due to 4s and 4p states of Ga; 3s and 3p states of Al and 4s, 4p states of In.

From the inspection of the valence band maxima and conduction band minima, it is seen that all the studied compounds have direct bandgap (E_g) at Γ point of BZ. The calculated E_g of AgGaS₂, AgGa_{0.5}Al_{0.5}S₂, and AgGa_{0.5}In_{0.5}S₂ using PBEsol are 0.86, 1.23, and 0.73 eV, respectively. These values are also collated in Table 2 along with the available experimental and theoretical values. It is seen that the present value of bandgap for AgGaS₂ is not in accordance with the experimental value; however, few theoretical values are close to the present calculated value for AgGaS₂. There are no experimental data available for doped AgGaS₂. We have seen that the value of bandgap increases (decreases) on substitution of Al (In) in AgGaS₂.

In absence of experimental bandgap for Al and In doped AgGaS₂, we have estimated the bandgap using well-known virtual crystal approximation which employs the experimental bandgap of end-compounds, AgGaS₂, AgAlS₂, and AgInS₂ (2.51, 3.13, and 1.87 eV, respectively) [24] using the following relations:

$$E_g(\text{AgGa}_{0.5}\text{Al}_{0.5}\text{S}_2) = E_g(\text{AgGaS}_2) * 0.5 + E_g(\text{AgAlS}_2) * 0.5, \quad (1)$$

$$E_g(\text{AgGa}_{0.5}\text{In}_{0.5}\text{S}_2) = E_g(\text{AgGaS}_2) * 0.5 + E_g(\text{AgInS}_2) * 0.5 \quad (2)$$

The estimated bandgaps of AgGa_{0.5}Al_{0.5}S₂ and AgGa_{0.5}In_{0.5}S₂ using Eqs. 1 and 2 are found to be 2.82 and 2.19 eV, respectively. Therefore, it is seen that the value of bandgap increases (decreases) on doping of Al (In) in AgGaS₂. The trend of bandgap is in tune with our calculated values.

4.2 Optical Properties

It is known that optical properties of solids play important role in deciding applications of materials. Dielectric function $\varepsilon(\omega)$ is one of the most important optical parameter of a solid, which is composed by two components: real ε_1 and imaginary ε_2 [$\varepsilon(\omega) = \varepsilon_1(\omega) + i \varepsilon_2(\omega)$]. It is known that the optical properties reflect the fine structures of the energy distribution of the electron states in the valence and conduction bands. ε_1 and ε_2 are calculated for perpendicular ($\varepsilon_{\perp c}$) and parallel ($\varepsilon_{\parallel c}$) directions of compounds. It is worth mentioning that the crystal structure with tetragonal symmetry can be resolved into two nonzero components, which are parallel (\parallel) and perpendicular (\perp) to c crystallographic axis. These components are

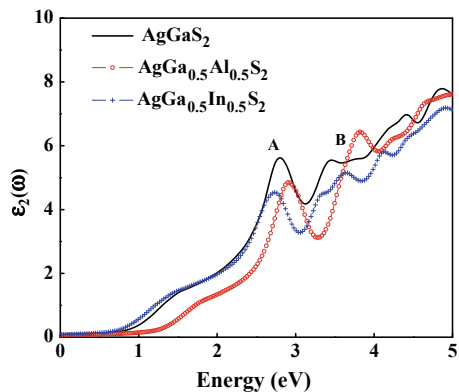
$$\varepsilon^{xx}(\omega) = \varepsilon^{\perp}(\omega) \text{ and } \varepsilon^{zz}(\omega) = \varepsilon^{\parallel}(\omega). \quad (3)$$

We have presented the average of both polarization for imaginary parts of the dielectric function in Fig. 4. The peaks in the imaginary part of dielectric function [$\varepsilon_2(\omega)$] are originated due to electric dipole transitions between the occupied and unoccupied states and their origin can be explained using the energy bands.

In Fig. 4, it is seen that there is negligible absorption in the energy range up to 0.83 eV for AgGaS_2 and this energy range increases for $\text{AgGa}_{0.5}\text{Al}_{0.5}\text{S}_2$ (1.20 eV) and decreases for $\text{AgGa}_{0.5}\text{In}_{0.5}\text{S}_2$ (0.72 eV). After this threshold energy we found the first peak (A) at 2.79, 2.90, and 2.73 eV for AgGaS_2 , $\text{AgGa}_{0.5}\text{Al}_{0.5}\text{S}_2$, and $\text{AgGa}_{0.5}\text{In}_{0.5}\text{S}_2$, respectively. It is originated due to direct band transitions at N point of BZ. The next peak (B) is found to be at 3.4, 3.2, and 3.8 eV for AgGaS_2 , $\text{AgGa}_{0.5}\text{Al}_{0.5}\text{S}_2$, and $\text{AgGa}_{0.5}\text{In}_{0.5}\text{S}_2$, respectively.

From the real part of dielectric function, $\varepsilon_1(\omega)$, the value of dielectric constants from present PBEsol calculations are 7.67, 6.98, and 7.29 for AgGaS_2 , $\text{AgGa}_{0.5}\text{Al}_{0.5}\text{S}_2$, and $\text{AgGa}_{0.5}\text{In}_{0.5}\text{S}_2$, respectively. Therefore, it is seen that the present optical properties are good enough to employ the presently studied materials in LEDs.

Fig. 4 Imaginary part of Dielectric function for AgGaS_2 , $\text{AgGa}_{0.5}\text{Al}_{0.5}\text{S}_2$, and $\text{AgGa}_{0.5}\text{In}_{0.5}\text{S}_2$



5 Conclusion

The theoretical study of ternary chalcopyrite compound AgGaS₂ and doped compounds AgGa_{0.5}Al_{0.5}S₂ and AgGa_{0.5}In_{0.5}S₂ using FP-LAPW method within DFT is presented. On the doping of Al and In in AgGaS₂ band gap increases and decreases from 0.86 eV to 1.23 and 0.73 eV, respectively. Therefore, In and Al doping can tune the bandgap to the desired value, which is useful in designing new optoelectronic materials working at desired wavelengths.

Acknowledgements One of us (AD) is thankful to University Grants Commission, New Delhi, India for Assistant Professorship and Department of Science and Technology, New Delhi, India for INSPIRE Faculty Project. BLA is thankful to SERB, New Delhi for a major research project.

References

1. Bube RH (1998) Photovoltaic materials. Imperial College Press, London
2. Rosencher E, Vinter B (2002) Optoelectronics. Cambridge University Press, U.K.
3. Chichibu SF, Ohmori T, Shibata N, Koyama T, Onuma T (2005) Fabrication of p-CuGaS₂/n-ZnO: Al heterojunction light-emitting diode grown by metalorganic vapor phase epitaxy and helicon-wave-excited-plasma sputtering methods. *J Phys Chem Solids* 66:1868–1871
4. Coutts TJ, Emery KA, Ward JS (2002) Modeled performance of polycrystalline thin-film tandem solar cells. *Prog Photovolt: Res Appl* 10:195–203
5. Chen S, Gong XG, Wei SH (2007) Band-structure anomalies of the chalcopyrite semiconductors CuGaX₂ versus AgGaX₂ (X = S and Se) and their alloys. *Phys Rev B* 75:205209-1–205209-9
6. Tell B, Kasper HM (1971) Optical and electrical properties of AgGaS₂ and AgGaSe₂. *Phys. Rev. B* 4(12):4455–4459
7. Tell B, Shay JI, Kasper HM (1972) Electroreflectance and absorption-edge studies of AgGaS₂ and AgGaSe₂. *Phys Rev B* 6(8):3008–3012
8. Grimditch MH, Holah GD (1975) Brillouin scattering and elastic moduli of silver thiogallate (AgGaS₂). *Phys Rev B* 12(10):4377–4382
9. Artus L, Bertrand Y (1987) Experimental evidence of the splitting of the AgGaS₂ uppermost valence bands by crystal field and spin-orbit Interaction. *J Phys C: Solid State Phys* 20:1365–1373
10. Tang LC, Lee MH, Yang CH, Huang JY, Chang CS (2003) Cation substitution effects on structural, electronic and optical properties of nonlinear optical AgGa(S_xSe_{1-x})₂ crystals. *J Phys: Condens Matter* 15:6043–6055
11. Chahed A, Benhelal O, Laksari S, Abbar B, Bouhafs B, Amrane N (2005) First-principles calculations of the structural, electronic and optical properties of AgGaS₂ and AgGaSe₂. *Phys B* 367:142–151
12. Laksari S, Chahed A, Abbouni N, Benhelal O, Abbar B (2006) First-principles calculations of the structural, electronic and optical properties of CuGaS₂ and AgGaS₂. *Comput Mater Sci* 38:223–230
13. Brik MG (2009) First-principles study of the electronic and optical properties of CuXS₂ (X = Al, Ga, In) and AgGaS₂ ternary compounds. *J Phys: Condens Matter* 21:485502-1–485502-8
14. Jun HH, Fu ZS, Jun ZB, You Y, Hua XL (2010) First-principles calculations of the elastic, electronic and optical properties of AgGaS₂. *Phys Scr* 82:055601-1–055601-6
15. Brik MG (2011) Electronic, optical and elastic properties of CuXS₂ (X = Al, Ga, In) and AgGaS₂ semiconductors from first-principles calculations. *Phys Status Solidi C* 8(9):2582–2584

16. Sun J, Chen G, Xiong G, Pei J, Dong H (2013) Hierarchical microarchitectures of $\text{AgGa}_{1-x}\text{In}_x\text{S}_2$: Long chain alcohol assisted synthesis, band gap tailoring and photocatalytic activities of hydrogen Generation. *Int J Hydro Energy* 38:10731–10738
17. Jang JS, Borse PH, Lee JS, Choi SH, Kim HG (2008) Indium induced band gap tailoring in $\text{AgGa}_{1-x}\text{In}_x\text{S}_2$ chalcopyrite structure for visible light photocatalysis. *J Chem Phys* 128:154717-1–154717-6
18. Karunakaran N, Perumalsamy R (2018) Investigation on synthesis, growth, structure and physical properties of $\text{AgGa}_{0.5}\text{In}_{0.5}\text{S}_2$ single crystals for Mid-IR application. *J Cryst Growth* 438:169–174
19. Blaha P, Schwartz K, Sorantin P, Trickey SB (1990) Full-potential, linearized augmented plane wave programs for crystalline systems. *Comput Phys Commun* 59:399–415
20. Blaha P, Schwarz K, Madsen GKH, Kvasnicka D, Luitz J (2017) Wien2 K- An augmented plane wave plus local orbitals program for calculating crystal properties. Vienna University of Technology, Vienna
21. Perdew JP, Ruzsinszky A, Csonka GI, Vydrov OA, Scuseria GE, Constantin LA, Zhou X, Burke K (2008) Restoring the density-gradient expansion for exchange in solids and surfaces. *Phys Rev Lett* 100:136406-1–136406-4
22. Draxl CA, Sofo JO (2006) Linear optical properties of solids within the full-potential linearized augmented planewave method. *Comput Phys Commun* 175:1–14
23. Kokalj A (2003) Computer graphics and graphical user interfaces as tools in simulations of matter at the atomic scale. *Comput Mater. Sci.* 28:155–168
24. Jaffe JE, Zunger A (1984) Theory of the band-gap anomaly in ABC_2 chalcopyrite semiconductors. *Phys Rev B* 29(4):1882–1906

Intelligent Power Sharing Control for Hybrid System



Preeti Gupta and Pankaj Swarnkar

Abstract Interest in the hybrid system is rapidly increasing with the improvement of battery energy storage system. The hybrid system comprising AC and DC sources connected to the grid is of more interest. For interconnection of the sources, interlinking converters are required to maintain the power balance between source and load. An intelligent, simple and effective power-sharing control for hybrid system is proposed in this paper. The controller manages the active power sharing along with maintaining constant DC voltage while accounting battery energy storage system (BESS). To verify the proposed method, a test system is developed in MATLAB/Simulink environment where photovoltaic (PV), fuel cell, and battery are elected as the primary distributed sources.

Keywords PV · Fuel cell · Hybrid system · Grid connected

1 Introduction

The hybrid power system is emerging as a flexible solution that integrates renewable energy sources in the distribution system which has advantages concerning reliability and power quality. The distributed energy resources like photovoltaic, wind turbines, BESS, and fuel cell are regarded as flexible power sources and are connected directly to the low voltage network. Intelligent control and power management system is the heart of the hybrid system operation, which has to face issues like coordination among different distributed sources, BESS, and loads. A control strategy should be designed in such a manner to make the system stable under any disorder and constraint variations. In this paper, fuel cells and PV are considered as DG sources. An intelligent control should share dynamic power in the hybrid system [1]. PV system in compliance with power quality standards is given by [2]. Neuro-fuzzy strategy was

P. Gupta (✉) · P. Swarnkar
Maulana Azad National Institute of Technology, Bhopal, India
e-mail: preeti.irig@gmail.com

P. Swarnkar
e-mail: p_swarnkar@yahoo.co.in

© Springer Nature Singapore Pte Ltd. 2020
A. Kalam et al. (eds.), *Intelligent Computing Techniques for Smart Energy Systems*,
Lecture Notes in Electrical Engineering 607,
https://doi.org/10.1007/978-981-15-0214-9_10

used as a part of the supervisory controller which deals with the working methods of the system. A grid adaptive power management control is scheduled for abnormal conditions, priority-based load shedding with the assurance of power quality [3]. However, the operating algorithm excludes battery to improve the performance of the system.

Different authors proposed various topologies for power management based on droop control. However, to get better system performance, DC-link voltage stabilization, fuzzy logic, and neural network is used by different authors [4]. Different energy management control methods and their performance were discussed in [5–7]. Grid-connected system control is simple and widely used. Two control strategies can be adopted for grid-connected system, grid following, and grid forming [8]. Power electronic converters play an important role in the hybrid system, and its control design is very sensitive to any disturbance [9, 10]. To make coordination between DG and grid, coordinated control schemes are used [11]. AC-coupled and DC-coupled grid-connected hybrid systems are in existence and depending on the availability of resources different schemes can be used [12]. Motivated by the previous research on the aforementioned issues, this paper presents an intelligent control strategy for a hybrid system, which enables a smooth transient performance during sudden impact of load with objectives (i) To achieve intelligent control coordination among different sources like PV, FC, battery, Grid, and load (ii) To manage the voltage at PCC (iii) To manage the power flow under different conditions, e.g., fault, sudden change in load, etc. The overall control scheme has been tested in MATLAB.

2 System Description and Modeling

The proposed grid-connected hybrid system which incorporates 50-kW PV, 50-kW fuel cell, and battery as sustainable power sources is shown in Fig. 1. Primary generation is accomplished through PV array, and SOFC is utilized as reinforcement because of the intermittent nature of solar insolation. The battery is associated with the DC bus through a bidirectional converter to make smooth charging and discharging operations. In a grid-connected hybrid system with DC loads, the momentary power relationship is given by

$$P_{bst} = P_b(t) + P_{DC}(t) + P_{inv}(t) + P_L(t) \quad (1)$$

where P_{bst} is the output power of the boost converter, P_b is the power delivered by the battery management control, P_{DC} is the power to the DC-link capacitor, P_{inv} is the power extracted by the inverter, and P_L is the power consumed by the DC load, the instantaneous AC power can be written as

$$P_{ac} = \frac{V_m I_m}{2} - \frac{V_m I_m}{2} \cos 2\omega t \quad (2)$$

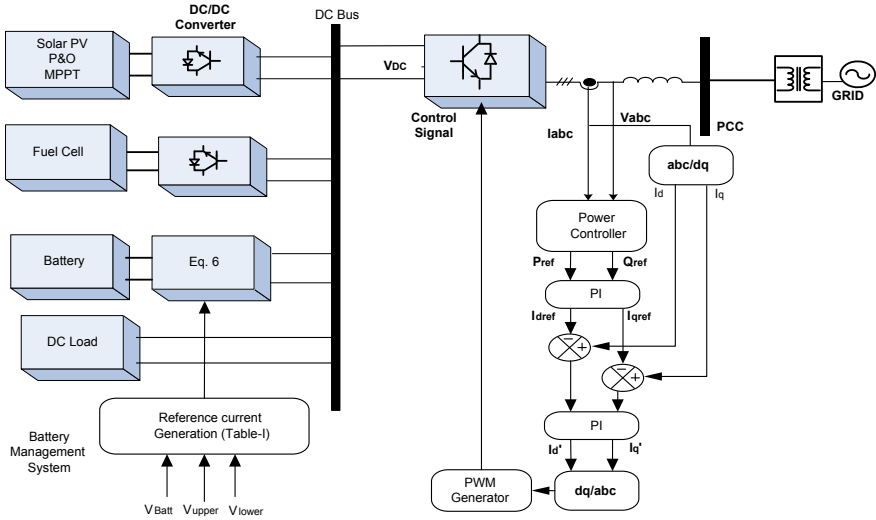


Fig. 1 Intelligent power-sharing hybrid controller (IPSC)

Table 1 Actions of the intelligent controllers for different operating modes

Case	Battery voltage	Mode
1	$V_b < V_{U1}$	Mode 2
2	$V_{U1} < V_b < V_{U2}$	Mode 1
3	$V_b > V_{U2}$	Mode 3
4	$V_{L1} < V_b < V_{U2}$	Mode 3
5	$V_{L1} < V_b < V_{U1}$	Mode 1

where V_m and I_m are the amplitude of the phase voltage and phase current of grid and ω is the angular frequency, respectively. Table 1 explains the action of the intelligent controller with different operating modes.

3 Control Strategy

In this paper, constant current control and constant power control are used for the grid-connected inverters. In grid-connected mode, PQ control is utilized for inverter-interfaced energy sources. In constant current control, to obtain current references, the inverter output currents are regulated while, in constant power control the active power is proportional to the d -axis components, and the reactive power is proportional to the q -axis components. The overall vector for voltage or current is dependent on d and q axes parameters. Change in the angle consequently changes the frequency. The power set points and measured powers are utilized to calculate power errors which

are the command signal to PI controller given to the PWM to generate firing pulses. The current references are calculated as

$$I_{\text{dref}} = \left(k_p + \frac{k_i}{s} \right) (P_{\text{ref}} - P_{\text{meas}}) \quad (4)$$

$$I_{\text{qref}} = \left(k_p + \frac{k_i}{s} \right) (Q_{\text{ref}} - Q_{\text{meas}}) \quad (5)$$

The control methodology of the grid-connected inverter includes a voltage loop which maintains the constant DC-link voltage which in turn provides the reference for the inner current control loop. The control strategy involves the transformation of three-phase AC current into d and q-axis components, in the synchronous rotating frame.

The vector relationship among inverter voltage V , hybrid system voltage E , and inductor reactance X governs the active and reactive power flow between the hybrid system and grid.

$$P = \frac{3}{2} \frac{VE}{X} \sin \delta_p \quad (6)$$

$$Q = \frac{3}{2} \frac{V}{X} (V - E \cos \delta_p) \quad (7)$$

$$\delta_p = \delta_v - \delta_E \quad (8)$$

Under small perturbations dependency of active power is on power angle δ_p and reactive power on the magnitude of inverter voltage. Proper coordination of converters in the hybrid system ensures reliable supply under diverse conditions.

4 Proposed Intelligent Control

Controlling parameters for power management strategies include power provided by the renewable energy system and the state of charge (SOC) of the battery bank. Hybrid power system algorithm for power management is shown in Fig. 2. In case of long-term low insolation condition, battery alone will not be able to fulfill the load demand; the fuel cell is integrated to counter affect the intermittency. The intelligent control strategy defines the switching of circuit breakers to fulfill the requirements of the load. In case of high load demand, if alone PV is not sufficient to meet requirements, then the logic controller activates the control of fuel cell inverter to feed shortfall power from the PV array. The deficit power that should be fed into the load and grid can be calculated as

$$P_{\text{def}} = P_{\text{load}} - P_{\text{pv}} \quad (11)$$

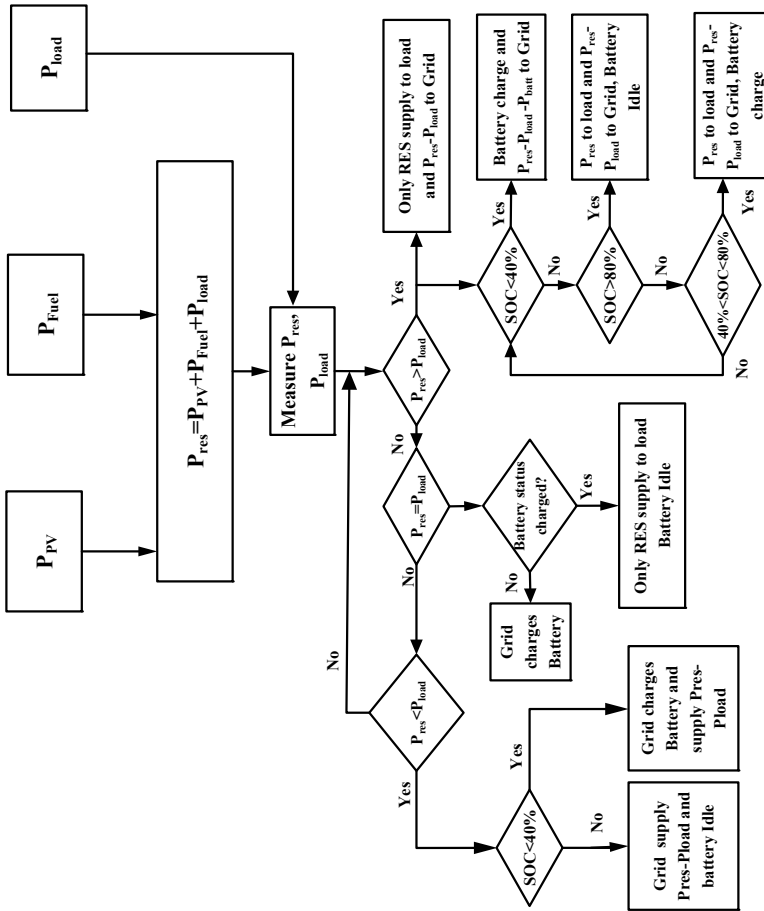


Fig. 2 Intelligent controller power management strategy

The intelligent controller works in two strategies: on-grid hybrid system and off-grid hybrid system. The state of charge of battery and P_{def} defines the operating mode of the system.

5 Results and Discussion

The hybrid system is tested under different operating conditions in MATLAB. Voltage and current of load, solar PV, fuel cell and battery are to be sensed by intelligent controller. The system comprises 50 kW PV array, 50 kW fuel cell, and battery. In the case of grid-connected system, if load demand is higher than the generation, rest of the power will be supplied by grid. The performance of the hybrid system under steady state and transient conditions such as step change in load is analyzed. The control strategy of the IPSC is verified for different modes of operation by varying the load.

5.1 Steady-State Response

It can be observed from Fig. 3 that under an initial value of load, i.e., 130 kW, the power provided by PV system 50 kW, Fuel Cell 50 kW, while grid provides rest of the power. This case assesses the operation of the hybrid system in steady state. The

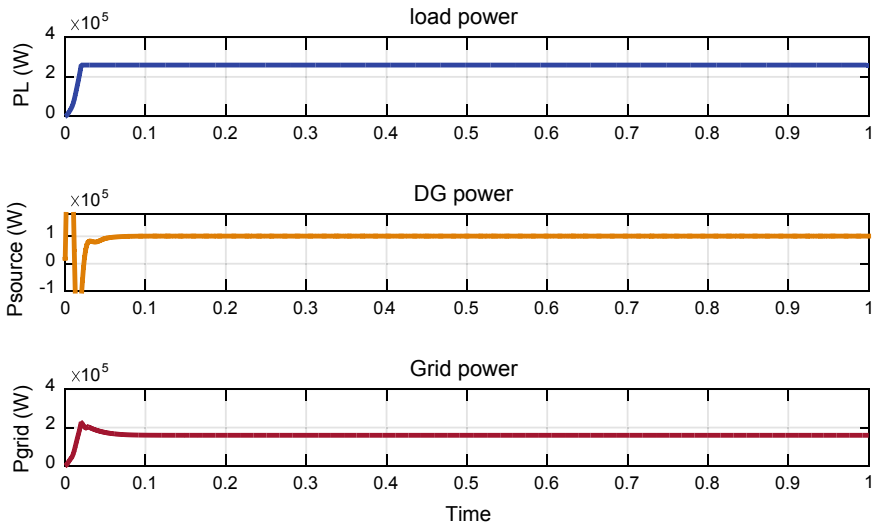


Fig. 3 Load power, generated power, and grid power under constant load demand

steady-state response clearly shows the validation of the proposed algorithm based on the power management strategy

5.2 Dynamic Response

To validate the effectiveness of the system, two dynamic cases, namely, a step change in load and unbalance in load are carried out. In case of step change in load, state-I illustrates applied load to the system is 30 kW, in state-II load increases from 60 to 140 kW between 0.3 and 0.5 s, and in state-III load decreases from 140 to 80 kW. Figure 4 shows the load power, generated power, and grid power under the change in load demand. Under these dynamic changes, controller senses the change in the load current and provides the control signals to generate reference current accordingly.

Consequently control signal to converter manages the power between various sources and grid. In the case of excess power generation by renewable energy sources, rest of the power is supplied to the grid. Figure 5 shows the direct and quadrature axis

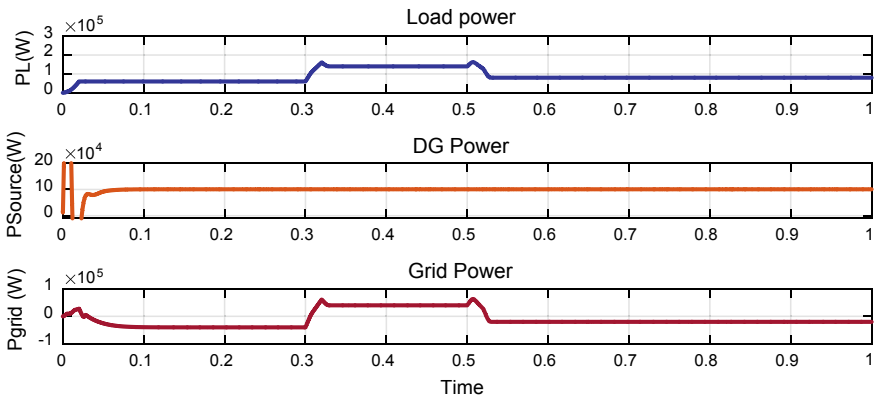


Fig. 4 Load, generated, and grid power under the change in load demand

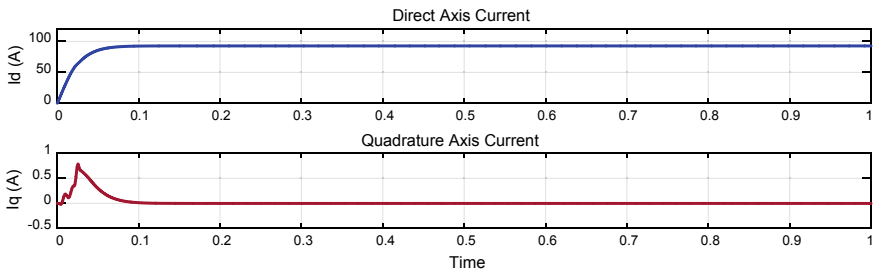


Fig. 5 direct axis and quadrature axis current under the change in load demand

current under variable load. From Fig. 6 it is to be noticed that the sudden increase in power demand from 60 to 140 kW is associated to the fast electrical response of the fuel cell while the sudden decrease in power is expected to receive power from renewable energy sources. The output power increases slowly in starting then it reaches the demand power. As the demand power is greater than the power generated by the fuel cell, rest power is supplied by another renewable energy source. Under the condition where load changes suddenly, the controller manages the voltage and power.

It is clearly observed from Fig. 7 that under the sudden change in load demand, the load current changes accordingly but the controller manages the voltage constant irrespective of change in load. From 0.3 to 0.5 s load current increases suddenly while it decreases from 0.5 to 1 s but the controller maintains constant voltage during the

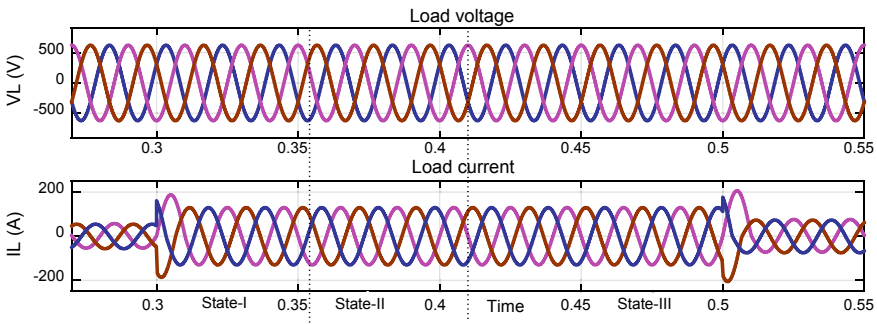


Fig. 6 Load voltage and current under the change in load demand

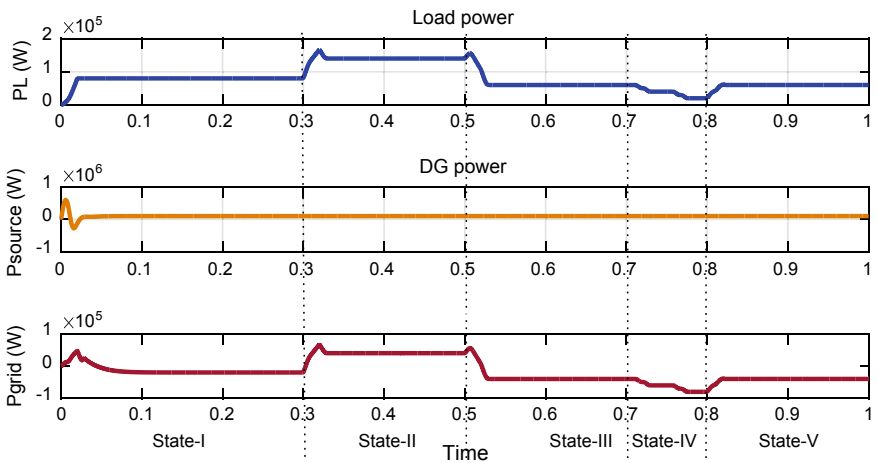


Fig. 7 Load power, generated power, and grid power for unbalanced load condition

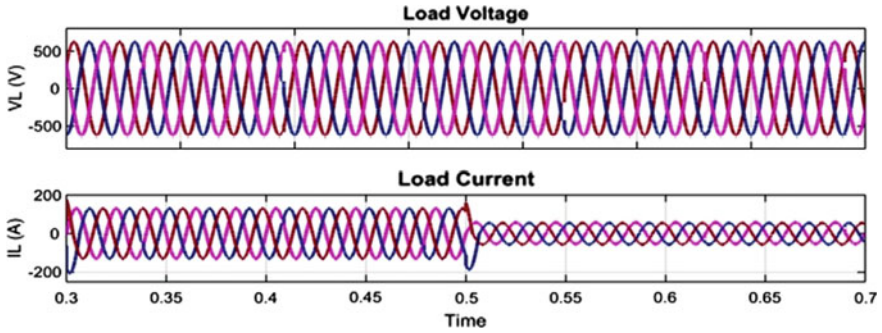


Fig. 8 Load voltage and current for unbalanced load condition

whole operation which assures the safety of the equipment connected in load side. Figure 8 clearly shows the variation in load voltage and current for unbalanced load.

In the case of unbalancing in state-I from 0 to 0.3 s the load is 80 kW, in state-II from 0.3 to 0.5 load changes from 80 to 140 kW, in state-III load changes from 140 to 60 kW, while in state-IV from 0.5 to 0.7 s, phase A is faulted, from 0.7 to 0.75 phase B and C faulted and from 0.75 to 0.8 all three-phases faulted, in state-V load regain from faulted to normal condition. The controller senses the unbalancing and accordingly generates the reference current which drives the controller to manage the power and maintain the voltage during the unbalance. The transition from state-IV to V leads constant voltage under unbalance which validates the proposed scheme.

6 Conclusion

An intelligent control strategy for power flow management in grid-connected hybrid power system is presented in this paper with the aim of managing the power balance between DGs and loads. The importance of the scheme has been brought out by simulation results. Operational issues of typical grid-associated hybrid system are explored. The steady state and transient performance of the system for step changes in load have been also illustrated. It is obvious that the controller maintains the voltage and guarantees smooth power exchange between sources, grid, and load under various conditions. The proposed configuration has been proved to be attractive from the perspective of providing uninterrupted power to loads while ensuring the evacuation of excess generating power of high quality into the grid.

References

1. Vigneys T, Kumarappan N, Arulraj R (2013) Operation and control of wind/fuel cell based hybrid microgrid in grid connected mode. In: Proceedings of IEEE conference, 754–758
2. Rahmani S, Hamadi Ab, Al-Haddad K, Kanaan HY (2012) A multifunctional power flow controller for photovoltaic generation systems with compliance to power quality standards. In: Proceedings of annual conference on IEEE industrial electronics and society, pp 894–903
3. Korada N, Mishra MK (2018) Grid adaptive power management strategy for an integrated microgrid with hybrid energy storage. *IEEE Trans Ind Electron* 64(4):2884–2892
4. Thounthong P, Luksanasakul A, Koseeyaporn P, Davat B (2013) Intelligent model-based control of a standalone photovoltaic/fuel cell power plant with supercapacitor energy storage. *IEEE Trans Sustain Energy* 4(1):240–249
5. Zhou T, François B (2011) Energy management and power control of a hybrid active wind generator for distributed power generation and grid integration. *IEEE Trans Ind Electron* 58(1):95–104
6. Dursun E, Kilic O (2012) Comparative evaluation of different power management strategies of a stand-alone PV/Wind/PEMFC hybrid power system. *J Electr Power Energy Systems*, 34(1):81–89
7. Zhang Y, Jiang Z, Yu X (2008) Control strategies for battery/supercapacitor hybrid energy storage systems. In: Proceedings of IEEE energy conference, pp 1–6
8. Jesudaiyan S, Prakash SL (2014) Simulation of grid tied inverter control scheme for distributed generators. In Proceedings of international conference on circuit, power and computing technologies, pp 990–995
9. Ashabani SM, Abdel-rady Y, Mohamed I (2014) New family of microgrid control and management strategies in smart distribution grids-analysis, comparison and testing. *IEEE Trans Power Syst* 29(5):2257–2269
10. Sao CK, Lehn PW (2008) Control and power management of converter fed microgrids. *IEEE Trans Power Syst* 23(3):1088–1098
11. Tan KT (2013) Coordinated control and energy management of distributed generation inverters in a microgrid. *IEEE Trans Power Deliv* 28(2):704–713
12. Xunwei Yu (2014) Power management for DC microgrid enabled by solid-state transformer. *IEEE Trans Smart Grid* 5(2):954–965

Comparative Analysis of Various Classifiers for Gesture Recognition



Rahul Gupta, Sarthak Rana, Swapnil Gupta, Kavita Pandey
and Chetna Dabas

Abstract Communication plays a very important role in human life. The ease of text-based communication in the form of emails and text-chats has increased nowadays due to the interaction of system and hardware devices. The research discussed in the present paper proposes to work upon a human–computer interaction system so that human and machine can communicate with each other without the actual use of any hardware input device like keyboards. Gesture keyboard is one such method by which we can achieve this goal of interacting with the computer using our hand gestures. The present research paper is a comparative study of seven machine learning classifiers aiming to increase the accuracy of prediction. The two main aims of this innovative research are to develop a gesture keyboard device which can be used to aid those people who have some kind of disability in vision so that they can use this device to interact with the computer and to increase the performance of the model by using methods like Bagging and Boosting.

Keywords Arduino · Classifiers · Gesture keyboard · Gesture recognition · Hand gesture-based AI · Human–computer interaction · Machine learning

R. Gupta · S. Rana · S. Gupta · K. Pandey (✉) · C. Dabas
Department of Computer Science and Engineering, Jaypee Institute of Information Technology,
A-10, Sector-62, Noida, Noida, Uttar Pradesh, India
e-mail: kavita.pandey@jiit.ac.in

R. Gupta
e-mail: rahul15103047@gmail.com

S. Rana
e-mail: sarthak6246@gmail.com

S. Gupta
e-mail: swapnil15103057@gmail.com

C. Dabas
e-mail: chetna.dabas@jiit.ac.in

© Springer Nature Singapore Pte Ltd. 2020
A. Kalam et al. (eds.), *Intelligent Computing Techniques for Smart Energy Systems*,
Lecture Notes in Electrical Engineering 607,
https://doi.org/10.1007/978-981-15-0214-9_11

1 Introduction

From past few years, with the development of human–computer interaction (HCI) [1] technology like image processing and gesture recognition technology, the area of computational research have been extended and now the attention of people is not limited to the development of traditional input hardware devices for HCI. Till date in most of the research, the *biological characteristic* [2] of a human being is used to interact with the system or computer which sometimes led to uncertainty. Therefore, a much more simple way of interacting with the system has been used which uses mathematical data which increases the accuracy in predicting the output or recognizing the gesture. Many disabled people have some kind of difficulty in speaking or hearing and these people communicate through hand gestures and body language. By this research work, we can help such disabled people so that they can also use computer and can operate it using their hand gestures instead of using hardware devices like keyboards [3].

With the help of this small, lightweight, and portable hardware device having MPU, we can achieve our goal of gesture recognition by noticing the change in the readings of *rotational velocities* and *forces* while making any gesture. The change in the rotational velocities and forces by moving our hand and making gesture will act as mathematical data and it will be used to train the computer to recognize the gesture.

Our aim is to compare seven different classification methods based on their predictions. For that purpose, methods like confusion matrix and cross-validation have been used to compare the accuracies of different classifiers. Also, the model is based on *bagging technique* [4], which is using different classifiers to train as well as test the dataset and taking the majority of the predicted values as the final output. This is done to increase the accuracy of the model. The method of increasing the weight of falsely predicted gestures and decreasing the weight or number of samples of correctly predicted gestures have been used to further increase the accuracy of the model. This process is very much similar to *boosting* [5].

2 Related Work

The considerable work till now has been done in the fields related to the voice-based system, vision-based systems, and many such fields. The vision-based system is used to detect eye blink and detect a pattern of human–computer interaction (HCI) [1]. Sign language has been developed for deaf and dumb and impaired people. This initiated the advancements in gesture-based interaction systems [6] which target home and gaming entertainment. Real-time gesture recognition [7] uses gesture modeling techniques for giving prompt response to interaction system.

In present times in spite of lot of achievement and progresses made in the field of gesture recognition [8], the area is still facing many challenges. Several technical difficulties which are still challenging [9] in this area are as follows:

2.1 Detection of Target

The target detection is identifying and capturing of a target from a complex background (extraction of object or target of interest). It is a difficult task to divide human hand or background areas due to variation in background and other environmental factors.

2.2 Recognition of Target

Hand gesture [10] is used to tackle implications according to the posture and change in angle processing of hands. Various invariant features in recognition of target are as follows:

1. Hands act as an elastic object; therefore, there can be big variations between like gestures and high similarities between various different gestures because human hand has about 20 degrees of freedom, making hand movement very complex. Therefore, same gestures made by different people may vary, and gestures made by the same person at different time or place may also be different.
2. Our palm contains lot of redundant information, the key is to identify gestures of fingers but palm features become one of redundant information. Therefore, a point in the hand should be the object of interest to tackle different movements of different parts of the hand.
3. Formation of shadow due to rough smooth surface of hands.

In order to solve such problems, some gesture control schemes should be introduced with extra features on portable devices. A gesture is more accurate easy than the traditional method of serial tapping on a keyboard The gesture-based HCI system developed here follows three key principals of efficiency: real-time, reliable, and low cost. In order to remove background detection complexity, Arduino is used along with MPU to get more accurate readings. Therefore, it solves the problem of target detection as a button has been accentuated to regulate start of readings and also removes the redundancy obtained in using hands as a tool for gesture recognition.

3 Proposed Work

This work deals with gesture recognition as device movement analyzing and recognizing English alphabets. Components like Arduino-Uno and MPU6050 have been used to make a remote like device. Figure 1 depicts the remote like device using Arduino which with the help of MPU sends the mathematical data to the system.

The developed gesture-based HCI works on the principle of changing six MPU readings of accelerometer [11] and gyroscope as the device is moved. The readings vary due to changing values of rotational velocity and acceleration due to gravity which acts as a mathematical data corresponding to the gesture. The dataset comprises approximately 50 samples each of every English alphabet and also 50 each of new line and space characters. The training dataset is of the form:

$$(x_1, y_1) \dots \dots \dots (x_n, y_n). \tag{1}$$

where y_i is every English alphabet, carriage return and space, and x_i readings are the features in which y_i is dependent. Each x_i is a 300-dimensional vector containing the readings of rotational velocities and forces in the three axes. 70% of the dataset has been used to train the model and 30% has been used to test it.

Seven classification methods like KNN, Linear SVM, Kernel SVM, Logistic Regression, Decision tree, Naïve Bayes, and Random Forest in the field of machine learning have been used to build this model. The training and testing sets have been used to check the accuracies of individual classification methods. Accuracies of different methods have been compared using cross-validation and confusion matrix methods. Also, grid search has been applied to check for appropriate values of parameters of SVM. To increase the accuracy of the system, a combination of four best accuracy models have been proposed and the majority predicted value is taken.

The model has been proposed in a real-time running mode and does require only a start and stop and no other intermediate action. Hence, it is possible to continuously

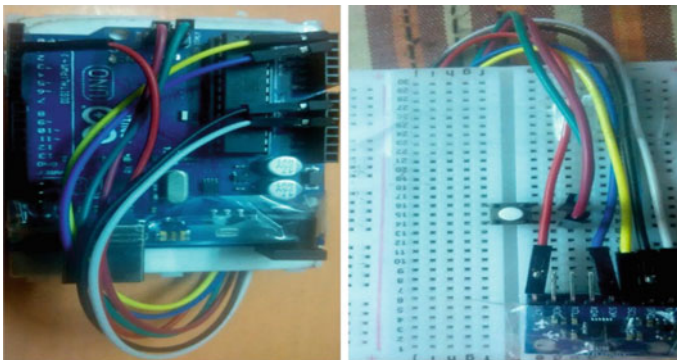


Fig. 1 Device containing Arduino and MPU module

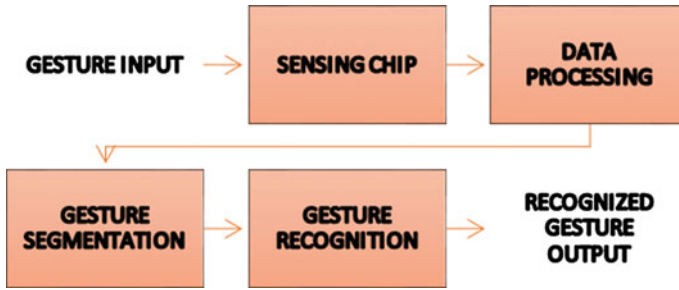


Fig. 2 Block diagram of gesture recognition

form gestures and the system will continuously keep predicting it and storing it in a text file. Figure 2 depicts the functionality graph of gesture recognition model that is reading or sensing of input gesture, then processing, and then predicting the gesture.

The following functionality graph has been used:

Every time a new gesture is made, then the working of the system is as follows:

1. The captured MPU readings, due to hand movement, are converted into a text file, replacing the old data.
2. The captured data is then preprocessed to filter out the unnecessary data and converted it into a readable form so that it matches with the trained data and the model can read the captured data.
3. Combination of four classifiers is employed to recognize the gesture from the processed data.

4 Result

In this work, seven different classifiers like Logistic Regression, KNN, SVM, Decision Tree, Random Forest, and Naïve Bayes have been used to train a model which includes a dataset of 28 different gestures and analyze the performance of each classifier by calculating accuracies using a confusion matrix and cross-validation methods. Initially, around 1500 samples were collected with the help of four different people. Initially, each gesture had 50 samples. For testing around 350 samples were used, while the remaining ones were used for training the model.

Figure 3 shows the classification of seven different classifiers. These figures depict the clustering of the data points and how the different classifiers classify them into 28 classes. Now to further analyze the accuracy of the different classifiers, accuracies were calculated with the help of confusion matrix. Figure 4 shows the confusion matrix of a linear SVM classifier. The confusion matrix for each of the above classifiers is a 28 by 28 matrix consisting of nonnegative integers representing the contrast between actual values and predicted values for the training and testing sets of data.

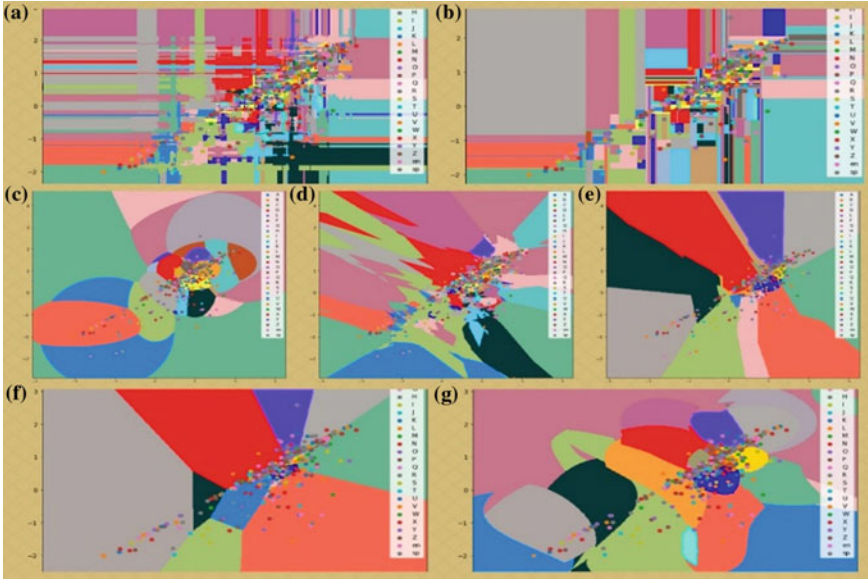


Fig. 3 Classification of 28 different gestures using **a** random forest, **b** decision tree, **c** Naïve Bayes, **d** KNN, **e** linear SVM, **f** logistic regression, and **g** Kernel SVM classifiers

[12,	0,	0,	0,	0,	0,	0,	0,	0,	0,	0,	0,
0,	0,	0,	0,	0,	0,	0,	0,	0,	0,	0,	0],
[0,	7,	0,	0,	0,	0,	0,	0,	0,	0,	0,	0,
0,	0,	0,	0,	0,	0,	0,	0,	0,	0,	0,	0],
[0,	0,	15,	0,	0,	0,	0,	0,	0,	0,	0,	0,
0,	0,	0,	0,	0,	0,	0,	0,	0,	0,	0,	0],
[0,	0,	0,	11,	0,	0,	0,	0,	0,	0,	0,	0,
0,	0,	0,	1,	0,	0,	0,	0,	0,	0,	0,	0],
[0,	0,	0,	0,	47,	0,	0,	0,	0,	0,	0,	0,
0,	0,	0,	0,	0,	0,	0,	0,	0,	0,	0,	0],

Fig. 4 Confusion matrix of linear SVM

The correct predictions are observed through the diagonal elements and other elements having nonzero value represent incorrect predictions. Hence, the accuracy of a particular classifier can be calculated as follows:

$$Accuracy = (sum\ of\ diagonal\ elements / sum\ of\ all\ elements) \times 100\% \quad (2)$$

It has been found that out of the 7 classifiers, Linear SVM has the highest accuracy of 96.58%. In Fig. 5 category 1 shows a bar plot of the accuracies of the seven used

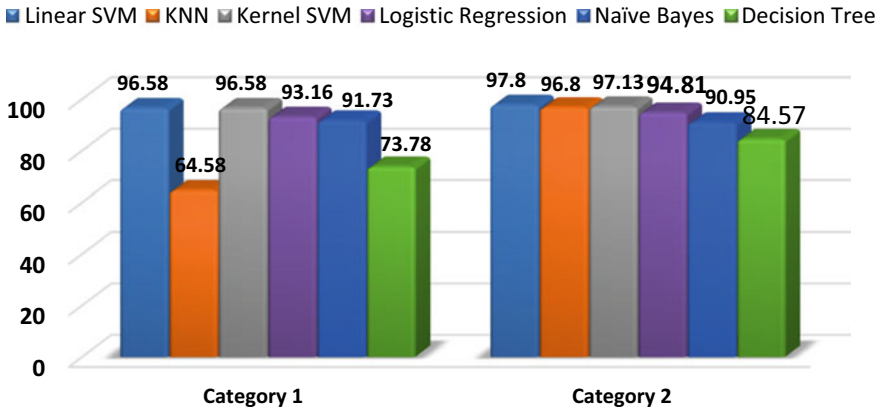


Fig. 5 Comparison of accuracies of seven different models

classifiers calculated with the help of confusion matrix before increasing the number of samples in the dataset.

To increase the performance of the model, the weight of those samples which were not properly recognized by the model were increased resulting in increasing the accuracies of the different classifiers. Table 1 shows the comparison of accuracies before and after increasing the weights of the falsely predicted gestures.

Figure 5 category 2 shows the bar plot of the accuracies of the seven classifiers after increasing the weights of the falsely recognized gestures. It is seen that the accuracy got increased with significant amount after increasing samples. SVM model is trained using samples, a text file consisting of MPU readings, combined with various values of c , the penalty factor, kernel, and gamma and it is found that a model using $c = 1$, kernel = “linear” and gamma = 0.1 provides the best performance.

Figure 6 shows the output of randomly tested gestures as predicted by all the seven classifiers. Figure 6a, b, f gives accurate predictions and Fig. 6c–e shows variant results for different classifiers. Hence, the combination of best four models

Table 1 Comparison of accuracies of seven classifiers with dataset of 1500 samples and 3200 sample

Classifiers	Accuracy with dataset = 1500 samples (%)	Accuracy with dataset = 3200 samples (%)
Linear SVM	96.58	97.8
KNN	94.58	96.8
Kernel SVM	96.58	97.13
Logistic regression	93.16	94.81
Naïve Bayes	91.73	90.95
Decision tree	73.78	84.57
Random forest	90.59	94.94

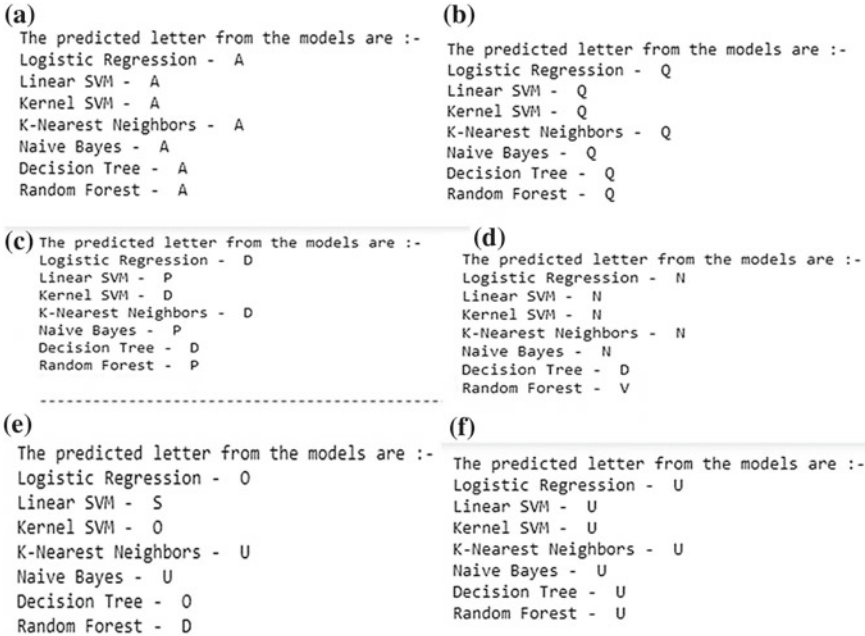


Fig. 6 Sample output of tested gestures

(Linear SVM, KNN, Logistic Regression, random forest) has been used collectively to further analyze the performance. It has been found that instead of using only one classifier, using a combination of best four classifiers gives better results.

It is concluded that sometimes the model predicts the false output, but the proposed model’s accuracy can be increased by increasing the number of samples in the dataset or increasing the weight of the falsely recognized gestures. But increasing the number of samples is not only the solution to increase the accuracy; it can even lead to the problem of overfitting of certain samples. So the weight of the samples was increased in a very appropriate manner and even the weight of overfitted samples has been reduced so that the model can predict the gesture accurately. Hence, the majority output from best four classifiers has been considered as the final one.

5 Conclusion and Future Development

In this work, a real-time gesture recognition-based system has been developed which recognizes gestures using a hardware device consisting of Arduino and MPU via serial communication between the device and the system. In this paper, seven different classifiers have been reviewed to compare their accuracies and the best parameter

for the chosen classifier has been discussed. The developed system relies on a combination of different classifiers to train the gestures and to recognize or predict them as it was deduced that the developed model has the highest accuracy in this gesture recognition problem. In order to improve the performance of the model, Boosting technique have been used that is increasing the samples of falsely recognized gestures and Bagging technique have been used to predict the majority as the output of the gesture. It is seen that the model in real time recognizes the gestures with a very high accuracy after applying the above-mentioned techniques. Although SVM gives the best results in most of the cases, four best classifiers have been used to derive the final output. This has been done to increase the probability of correct output. Hence, the model has been successful in achieving its aim.

All the methods mentioned above are existing methods and have their own merits. Based on this research, the future innovative developments could concentrate on:

1. Ease of handling: The Arduino device used to make the gestures could be made wireless using a Bluetooth module.
2. Increasing domain of gestures: The domain of gestures can be extended by introducing small letters, numerals, and user defined gestures.
3. Hyperparameter tuning: Hyperparameter optimization or tuning can be used to choose the set of optimal hyperparameters for the classification algorithms.

References

1. Choras RS, Kozik R (2017) Markerless head gesture recognition for human computer interaction. *Recent Pat Signal Process*
2. Dardas NH, Georganas ND (2011) Real-time hand gesture detection and recognition using bag-of-features and support vector machine techniques. *IEEE Trans Instrum Meas* 60(11):3592–3607
3. David PA (1985) Clio and the economics of QWERTY. *Am Econ Rev* 75:332–337
4. Breiman L (2000) Randomizing outputs to increase prediction accuracy. *Mach Learn* 40(3):229–242
5. Drucker H, Schapire R, Simard P (1993) Improving performance in neural networks using boosting algorithm. In: Hanson SJ, Cowan JD, Giles CL (eds) *Advances in neural information processing systems*, pp 42–49
6. Grif SH, Farcas CC (2016) Mouse cursor control system based on hand gesture. *Proc Technol* 22:657–661
7. Geurts; Lucas Jacobus Franciscus (Best, NL), Djajadiningrat; Johan Partomo (Utrecht, NL), De Bont; Jeanne (Eindhoven, NL), Chao; Pei-Yin (Eindhoven, NL), Gesture-based user-interface with user-feedback. <http://patft.uspto.gov>. Accessed 21 Mar 2013
8. Kramer KH (2009) Gestural control of autonomous and semi-autonomous systems. <http://patft.uspto.gov>. Accessed 10 Sept 2009
9. Kristensson PO (2009) Five challenges for intelligent text entry methods. *AI Mag* 30(4):85–94
10. Freeman WT, Roth M (1995) Orientation histograms for hand gesture recognition. *International workshop on Automatic face and gesture recognition*. 12:296–301

11. Juha K, Panu K, Jani M, Sanna K, Giuseppe S, Luca J, Sergio DM (2005) Accelerometer-based gesture control for a design environment. Springer, Finland
12. Lenman S, Bretzner L, Eiderbäck B (2002) Computer vision-based recognition of hand gestures for human-computer interaction. ISSN 1403 – 0721

Artificial Intelligence Based Optimization Techniques: A Review



Agrani Swarnkar  and Anil Swarnkar 

Abstract Many artificial intelligence based optimization techniques have been introduced since the early 60s. This paper provides a brief review of some of the well-known optimization techniques, e.g., Genetic Algorithm, Particle Swarm Algorithm, and Ant Colony Optimization and recently developed techniques, e.g., BAT Algorithm and Elephant Herding Optimization. All these techniques are population-based search algorithms, in which the initial population is created randomly initializing input parameters within the specified range. They approach toward the best solution inspired by the behavior of natural entities. All of these techniques have a potential to provide optimal or near-optimal solutions.

Keywords Ant colony optimization · BAT algorithm · Elephant herding optimization · Genetic algorithm · Particle swarm algorithm

1 Introduction

In the real world, many mixed-integer, complex, combinatorial optimization problems exist which cannot be solved by simple, step-by-step methods to get the optimal solution. To solve such problems, in the literature, many artificial intelligence based methods are suggested. Artificial intelligence (AI) is also known as swarm intelligence (SI). Bonabeau et al. [1] defined SI as “The emergent collective intelligence of groups of simple agents”. When these simple agents work in a group, they can perform difficult tasks easily. Self-organization and division of labor are the two fundamental concepts considered as necessary properties of SI. All these techniques are population-based techniques. The initial population is created by randomly assign-

A. Swarnkar (✉)

Department of Computer Science Engineering, Manipal University Jaipur, Jaipur 303007, India
e-mail: agraniswarnkar@gmail.com

A. Swarnkar

Department of Electrical Engineering, Malaviya National Institute of Technology, Jaipur, India

© Springer Nature Singapore Pte Ltd. 2020

A. Kalam et al. (eds.), *Intelligent Computing Techniques for Smart Energy Systems*,
Lecture Notes in Electrical Engineering 607,
https://doi.org/10.1007/978-981-15-0214-9_12

ing values to input parameters within the prespecified range. These ranges define the search space. Larger the search space, more difficult is the problem and hence more population is required to solve it. Each individual represents a possible solution. The fitness of each solution is evaluated based on the objective function to be optimized. After initialization, each algorithm modifies the population during the evolutionary process based on the behavior of nature-inspired agents. The approach of each algorithm is different but all are approaching toward the best possible solution to the problem based on fitness.

In this paper, some well-established AI-based techniques, e.g., Genetic Algorithm (GA), Particle Swarm Optimization (PSO), and Ant Colony Optimization (ACO) and some recently developed techniques, e.g., BAT Algorithm (BA) and Elephant Herding Optimization (EHO) are selected for review. All these algorithms are capable of solving complex optimization problems. In the following sections, each of these techniques is briefly discussed.

2 Genetic Algorithm

The Genetic Algorithm was introduced by Holland [2] in 1975 and further elaborated by DeJong [3] and Goldberg [4]. GAs, basically stimulated from the concept of natural selection and evolutionary process, are derivative-free stochastic optimization methods. Since their inception, GAs have evolved and become a promising tool for solving complex optimization problems. In a natural system, it is observed that the strong tend to adapt and survive but on the other hand, the weak tend to die and perish. GA works on a similar concept. Initially, a random population of general solutions is generated. Each solution is then encoded as a chromosome (or genotype) and the chromosomes get a measure of fitness through a fitness function which determines the capacity to produce offsprings. Higher the fitness value, better is the solution for maximization process whereas lower the value, better is the solution for the minimization process. Two main operators of GA are crossover and mutation. For crossover, two parents of better fitness are selected and their genes are interchanged to form two offsprings. While in mutation, some genes in a chromosome are altered to form new offspring. When all individuals are changed through crossover and mutation, the new population is known as new generation. The best individual of the previous generation is preserved in the next generation and the process is known as elitism. The same process is repeated until the termination criteria are achieved. The natural termination criteria occur when all individual acquire the same fitness. But depending on the problem, the termination criteria may be limited by specified time, maximum generation, or stalled fitness. Since its inception, many modifications have been suggested in the literature [5–11].

3 Particle Swarm Optimization

Particle Swarm Optimization (PSO) was introduced by Kennedy and Eberhart in 1995 [12]. This optimization technique is a mathematical representation of fish schooling and bird flocking to guide the particles for searching of global optimal solutions. Initially, a population of random solutions is created similar to GA. During the search process, the position of each particle is modified based on its cognitive and social behavior.

The coordinates of each particle corresponding to the best solution that has been achieved by the particle so far based on its fitness is defined as *pbest*. Similarly, the best solution among all particles in the current iteration is defined as *gbest*. In particle swarm optimization, the velocity of each particle is modified based on its *pbest* and *gbest* locations in each step. Two separate random numbers are generated as acceleration toward *pbest* and *gbest* locations.

Among the different variants of the PSO algorithm proposed, the most standard one was introduced by Shi and Eberhart [13]. In PSO, a possible solution associated with two vectors, i.e., position vector (s_j) and velocity vector (v_j) are represented by the coordinates of each particle. The size of vectors s_j and v_j is equal to the number of particles. A swarm consists of the number of particles “or possible solutions” that fly through the search space to explore optimal solutions.

The new velocity and position vectors of the particle based on its own momentum, cognitive, and social influence are mathematically given by the following model:

$$v_j^{k+1} = Wv_j^k + C_1 \times \text{rand}_1() \times \frac{\text{pbest}_j - s_j^k}{\Delta t} + C_2 \times \text{rand}_2() \times \frac{\text{gbest}_j - s_j^k}{\Delta t} \quad (1)$$

$$s_j^{k+1} = s_j^k + v_j^{k+1} \times \Delta t \quad (2)$$

where v_j^k is the velocity of the particle j at iteration k , $\text{rand}_1()$ and $\text{rand}_2()$ are random numbers between 0 and 1, s_j^k is the position of particle j at iteration k , C_1 , C_2 are the acceleration coefficients, pbest_j is the best position of particle j achieved based on its own experience, gbest_j is the best particle position based on overall swarm experience, Δt is the time step, usually set to 1 s and W is the inertia weight.

In Eq. (1), “inertia” of the particle is represented by the first term, “personal influence” is represented by the second term whereas “social influence” of the particle is represented by the third term. The new position of the particle can be found out by Eq. (2) according to the new velocity calculated by Eq. (1). Global search is facilitated by a large inertia weight while a local search is facilitated by small weight inertia. Through the course of the PSO run, the inertia weight is linearly decreased from a relatively large value to a smaller value [14]. Therefore, the value of W is considered as decreasing linearly during the simulation period from W_{\max} to W_{\min} according to

$$W(k) = \left(\frac{W_{\min} - W_{\max}}{\text{iter}_{\max} - 1} \right) (k - 1) + W_{\max} \quad (3)$$

where $W(k)$ is the inertia weight at iteration k , W_{\min} is the minimum inertia weight (final), W_{\max} is the maximum inertia weight (initial), iter_{\max} is the predefined maximum iterations.

Many variants of PSO have been successfully applied to solve various optimization problems [15–18].

4 Ant Colony Optimization (ACO)

Ant Colony Optimization (ACO) is an approach inspired by the foraging behavior of real ants developed by Marco Dorigo in 1992 [19]. The search technique is stimulated by the ants' behavior in finding paths from the nest to the food and then back again to the nest without any visual aid. Dorigo and Gambardella [20] first implemented it to solve the traveling salesman problem (TSP). Later, the max–min ant system was developed by Stutzle and Hoos [21] to solve TSP and quadratic assignment problems. Then the basic ACO was further improved and a model-based search algorithm was introduced by Blum and Dorigo [22]. Das et al. [23] attempted ant colony approach to computing minimum Steiner tree.

The four main components of the algorithm are ant, pheromone, daemon action, and decentralized control. Ants are the imaginary agents that mimic the exploration and exploitation of the search space whereas pheromone is a chemical material spread by ants over the path that they travel and its intensity decreases over time due to evaporation. In ACO, pheromones are dropped by the ants when traveling in the search space and the intensity of the trail is determined by the quantities of these pheromones. The path marked by high intensity of the trail is chosen as the direction by the ants. The intensity of the trail can be considered as the global memory of the system.

Random proportional state transition rule [8] is used to determine the probability with which the k th ant will move from node i to node j as given by

$$\text{Pr}_{i,j}^k = \frac{(\tau_{i,j})^\alpha (\eta_{i,j})^\beta}{\sum (\tau_{i,j})^\alpha (\eta_{i,j})^\beta} \quad (4)$$

where $\tau_{i,j}$ is the amount of the pheromone on the edge i - j , α is the parameter to regulate the impact of $\tau_{i,j}$, $\eta_{i,j}$ is the interest of the ant to move from node i to node j based on a prior knowledge, typically $1/d_{i,j}$, (where $d_{i,j}$ is the distance between node i and node j), and β is the parameter to regulate the impact of $\eta_{i,j}$.

While moving from node i to node j , the k th ant updates the pheromone on the edge i - j . To escape local minima, the pheromone evaporation is used. The pheromone update is given by

$$\tau_{i,j} = (1 - \rho)\tau_{i,j} + \Delta\tau_{i,j}^k \quad (5)$$

where $\tau_{i,j}$ is the amount of pheromone on a given edge $i-j$, ρ is the pheromone evaporation rate and $\Delta\tau_{i,j}^k$ is the amount of pheromone deposited by the k th ant, typically given by

$$\Delta\tau_{i,j}^k = \begin{cases} 1/C_k, & \text{if ant } k \text{ travels on the edge } i-j \\ 0, & \text{otherwise} \end{cases} \quad (6)$$

where C_k is the cost of the k th ant's tour (typically the length).

ACO has been successfully implemented to solve many complex optimization problems [24–28].

5 BAT Algorithm

Bats are unique animals having the advanced capability of echolocation. The Bat Algorithm (BA) is developed by Xin-She Yang in 2010 [29] based on the behavior of bats. In BA, the velocity and position of each bat are updated with iterations as in PSO.

However, an intensive local search, similar to simulated annealing, is also combined. The loudness and pulse emission rate assigned to each bat govern the algorithm and are allowed to vary with iterations. The different phases used in standard BA can be summarized as below [29, 30].

5.1 Random Fly

For each bat, its position $x_i(t)$, velocity $v_i(t)$, frequency f_i , loudness $A_i(t)$, and the pulse emission rate $r_i(t)$ are defined at the time step t in a d -dimensional problem search space as given below.

$$f_i = f_{\min} + (f_{\max} - f_{\min}) \times \beta \quad (7)$$

$$v_i(t) = v_i(t-1) + (x_i(t) - x^*) \times f_i \quad (8)$$

$$x_i(t) = x_i(t-1) + v_i(t) \quad (9)$$

where β is a random number in the range $[0, 1]$.

5.2 Local Random Walk

Once a solution is selected among the current best solutions x^* for the local search, a new solution for each bat is generated locally using a random walk as defined below.

$$x_{\text{new},i} = x_{\text{old},i} + \varepsilon \langle A(t) \rangle \text{rand} > r_i(t) \quad (10)$$

where ε is a scaling factor in the range $[-1, 1]$ and rand is a random number in the range $[0, 1]$. $\langle A(t) \rangle$ is the average loudness of all bats. In each iteration, the pulse emission rate and the loudness of each bat are updated using the following relations.

$$A_i(t+1) = \alpha \cdot A_i(t) \quad (11)$$

$$R_i(t+1) = r_i(0)[1 - e^{-\gamma t}] \quad (12)$$

where α and γ are constant, each of them is usually taken as 0.9 [29].

A modified version of the BAT algorithm has been used in a recent work to solve power system optimization problems [31].

6 Elephant Herding Optimization

Inspired by the behavior of an elephant herd, the Elephant Herding Optimization (EHO) has recently been developed by Wang et al. [32] which is also a swarm-based meta-heuristic search method. In a herd, under the leadership of a matriarch, elephants belonging to different clans live together. When male elephants grow up, they leave their family group and remain solitary, but communicate through infrasound. The behavior of elephants' herd in nature is idealized into a clan updating operator and a separating operator.

6.1 Clan Updating Operator

All the elephants live together under the leadership of a matriarch in each clan. Therefore, for each elephant in clan ci , its next position is influenced by its matriarch. For the elephant j in clan ci , it can be updated as

$$x_{\text{new},ci,j} = x_{ci,j} + \alpha \times (x_{\text{best},ci} - x_{ci,j}) \times r \quad (13)$$

where $x_{\text{new},ci,j}$ and $x_{ci,j}$ are newly updated and the old position for elephant j in clan ci , respectively. $\alpha \in [0, 1]$ is a scale factor that determines the influence of matriarch

ci on $x_{ci,j}$, $x_{best,ci}$ represents matriarch ci , which is the fittest elephant individual in clan ci . $r \in [0, 1]$.

The fittest elephant in each clan cannot be updated by Eq. (13), i.e., $x_{ci,j} = x_{best,ci}$. For the fittest one, it can be updated as

$$x_{new,ci,j} = \beta \times x_{center,ci} \quad (14)$$

where $\beta \in [0,1]$ is a factor that determines the influence of the $x_{center,ci}$ on $x_{new,ci,j}$. It may be observed in Eq. (14) that the new individual $x_{new,ci,j}$ is generated by the information obtained by all the elephants in clan ci . $x_{center,ci}$ is the center of clan ci , and for the d th dimension, it can be calculated as

$$x_{center,ci,j} = \left[\frac{1}{n_{ci}} \times \sum_{j=1}^{n_{ci}} x_{ci,j} \right]_d \quad (15)$$

where $1 \leq d \leq D$ indicates the d -th dimension, and D is its total dimension. n_{ci} is the number of elephants in clan ci . $x_{ci,j}$ is the position of j -th elephant of the clan ci . The center of clan ci , $x_{center,ci}$, can be calculated through D calculations by Eq. (15).

6.2 Separating Operator

In an elephants' herd, the male elephants will leave their family group and live alone when they reach puberty. While solving the optimization problems, this separating process can be modeled into a separating operator. In order to further improve the searching ability of the EHO method, it is assumed that in each generation the separating operator is implemented on the elephant individuals with the worst fitness as shown in Eq. (16).

$$x_{worst,ci} = x_{min} + (x_{max} - x_{min} + 1) \times \text{rand} \quad (16)$$

where x_{max} and x_{min} are respectively upper and lower bound of the position of elephant individual. $x_{worst,ci}$ is the worst elephant individual in clan ci . $\text{rand} \in [0, 1]$ is a kind of stochastic distribution and uniform distribution in the range $[0, 1]$ is used in our current work.

Modified EHO is recently implemented in one of the research papers of the coauthor [33].

7 Conclusion

In this paper, a review of five population-based nature-inspired artificial intelligence techniques are discussed in brief. Out of which three are well established and two are recently developed. These algorithms may be used to solve various complex optimization engineering problems.

References

1. Bonabeau E, Dorigo M, Theraulaz G (1999) Swarm intelligence: from natural to artificial systems. *J Artif Soc Soc Simul* 4
2. Holland JH (1975) *Adaptation in natural and artificial systems*. University of Michigan Press, Michigan
3. Jong KD (1975) *An analysis of the behavior of a class of genetic adaptive systems*, Doctoral Dissertation. The University of Michigan, Ann Arbor
4. Goldberg DE (1989) *Genetic algorithms in search, optimization and machine learning*. Addison-Wesley
5. Muselli M, Ridella S (1992) Global optimization of functions with the interval genetic algorithm. *Complex Syst* 6:193–212
6. Lobo FG, Goldberg DE (1997) Decision making in a hybrid genetic algorithm. In: *IEEE international conference on evolutionary computation*. IEEE Press, Piscataway, pp 122–125
7. Lin WM, Cheng FS, Tsay MT (2000) Distribution feeder reconfiguration with refined genetic algorithm. *IEE Gener Transm Distrib* 147(6):349–354
8. Zhu JZ (2002) Optimal reconfiguration of electrical distribution network using the refined genetic algorithm. *Electr Power Syst Res* 62(1):37–42
9. Huang YC (2002) Enhanced genetic algorithm-based fuzzy multi-objective approach to distribution network reconfiguration. *IEE Gener Transm Distrib* 149(5):615–620
10. Mendoza JE, Lopez ME, Coello CA, Lopez EA (2009) Microgenetic multiobjective reconfiguration algorithm considering power losses and reliability indices for medium voltage distribution network. *IET Gener Transm Distrib* 3(9):825–840
11. Gupta N, Swarnkar A, Niazi KR, Bansal RC (2010) Multi-objective reconfiguration of distribution systems using adaptive genetic algorithm in fuzzy framework. *IET Gener Transm Distrib* 4(12):1288–1298
12. Kennedy J, Eberhart RC (1995) Particle swarm optimization. In: *IEEE international conference on neural networks*, vol 4. Piscataway, pp 1942–1948
13. Shi Y, Eberhart RC (1998) A modified particle swarm optimizer. In: *IEEE computation intelligence world congress*, pp 69–73
14. Shi Y, Eberhart RC (1999) Empirical study of particle swarm optimization. In: *IEEE congress on evolutionary computation*. IEEE Press, Piscataway, pp 1945–1950
15. Sivanagaraju S, Rao JV, Raju PS (2008) Discrete particle swarm optimization to network reconfiguration for loss reduction and load balancing. *Electr Power Comp Syst* 36(5):513–524
16. Niknam T, Farsani EA (2010) A hybrid self-adaptive particle swarm optimization and modified shuffled frog leaping algorithm for distribution feeder reconfiguration. *Eng Appl Artif Intell* 23(8):1340–1349
17. Wu WC, Tsai MS (2011) Application of enhanced integer coded particle swarm optimization for distribution system feeder reconfiguration. *IEEE Trans Power Syst* 26(3)
18. Gupta N, Swarnkar A, Niazi KR (2011) Reconfiguration of distribution systems for real power loss minimization using adaptive particle swarm optimization. *Electr Power Comp Syst* 39(4):317–330

19. Dorigo M (1992) Optimization, learning and natural algorithms. Ph.D. thesis, Politecnico di Milano, Italy
20. Dorigo M, Gambardella LM (1997) Ant colony system: a cooperative learning to the travelling salesman problem. *IEEE Trans Evol Comput* 1(1):53–66
21. Stutzle T, Hoos HH (2000) Max–Min ant system. *Future Gener Comput Syst* 16(8):889–914
22. Blum C, Dorigo M (2004) The hyper-cube framework for ant colony optimization. *IEEE Trans Syst Man Cybern B Cybern* 34(2):1161–1172
23. Das S, Gosavi SV, Hsu WH, Vaze SA (2002) An ant colony approach for the steiner tree problem. In: Genetic and evolutionary computing conference, Morgan Kaufmann, pp 9–13
24. Su CT, Chang CF, Chiou JP (2005) Distribution network reconfiguration for loss reduction by ant colony search algorithm. *Electr Power Syst Res* 75(2–3):190–199
25. Ahuja A, Das S, Pahwa A (2007) An AIS-ACO hybrid approach for multi-objective distribution system reconfiguration. *IEEE Trans Power Syst* 22(3):1101–1111
26. Chang CF (2008) Reconfiguration and capacitor placement for loss reduction of distribution systems by ant colony search algorithm. *IEEE Trans Power Syst* 23(4):1747–1755
27. Carpaneto E, Chicco G (2008) Distribution system minimum loss reconfiguration in the hyper-cube ant colony optimization framework. *Electr Power Syst Res* 78(12):2037–2045
28. Swarnkar A, Gupta N, Niazi KR (2011) Adapted ant colony optimization for efficient reconfiguration of balanced and unbalanced distribution systems for loss minimization. *Swarm Evol Comput (Elsevier)* 1(3):129–137
29. Yang XS (2010) A new metaheuristic bat-inspired algorithm. In: Nature inspired cooperative strategies for optimization (NISCO 2010), studies in computational intelligence, vol 284. Springer, Berlin, pp 65–74
30. Yang XS (2011) Bat algorithm for multi-objective optimization. *Int J Bio-Inspir Comput* 3(5):267–274
31. Kanwar N, Gupta N, Niazi KR, Swarnkar A, Bansal RC (2015) Multi-objective optimal DG allocation in distribution networks using bat algorithm. In: Third southern african solar energy conference-2015. Kruger National Park, South Africa
32. Wang GG, Deb S, Coelho LS (2015) Elephant herding optimization. In: 3rd international symposium on computational and business intelligence, Bali, Indonesia, pp 1–5
33. Meena NK, Parashar S, Swarnkar A, Gupta N, Niazi KR (2018) Improved elephant herding optimization for multiobjective DER accommodation in distribution systems. *IEEE Trans Industr Inf* 14(3):1029–1039

Optimal Location and Sizing of Microgrid for Radial Distribution Systems



Shalaka N. Chaphekar, Anandkumar Nale, Anjali A. Dharme and Nitant Mate

Abstract Proper location and sizing of a distributed generator improve the performance of a Radial Distribution System. A Microgrid is a small-scale version of a conventional power system. However, it is different from distributed generator with respect to the philosophy of operation. This paper presents an algorithm to assess the performance of a Radial Distribution System by integration of a Microgrid using Particle Swarm Optimization (PSO). The algorithm is verified on two Radial Distribution Systems, viz, 9-bus system and 34-bus system. It is proved that proper size of a Microgrid at appropriate location improves the performance of a Radial Distribution System.

Keywords Radial Distribution System (RDS) · Microgrid · Power flow · Particle Swarm Optimization (PSO)

Nomenclature

m	Number of the sections
I_i	Current flowing through i th section
R_i	Resistance of i th section
P_G	Total active power from Maingrid and Microgrid
Q_G	Total reactive power from Maingrid and Microgrid

S. N. Chaphekar (✉) · A. Nale · A. A. Dharme
Department of Electrical Engineering, College of Engineering, Pune, India
e-mail: shalakachaphekar@yahoo.com

A. Nale
e-mail: anandkumar.nale@hotmail.com

A. A. Dharme
e-mail: dharme@rediffmail.com

N. Mate
Seegreen Solutions, Pune, India
e-mail: nitant.mate@seegreensolutions.com

© Springer Nature Singapore Pte Ltd. 2020
A. Kalam et al. (eds.), *Intelligent Computing Techniques for Smart Energy Systems*,
Lecture Notes in Electrical Engineering 607,
https://doi.org/10.1007/978-981-15-0214-9_13

P_D	Total active power demand of Feeder including Microgrid demand
Q_D	Total reactive power demand of feeder including Microgrid demand
P_{loss}	Total loss in the system
$-P_{\mu G}^{in}$	Power supplied to Microgrid from Maingrid
$+P_{\mu G}^{in}$	Power supplied from Microgrid to Maingrid
$Q_{\mu G}^{in}$	Reactive power exchanged between Microgrid and Maingrid
V_i	i th bus voltage
V_{imin}	Minimum bus voltage
V_{imax}	Maximum bus voltage
$P_{G_ \mu G}(min)$	Minimum active power generated by the Microgrid
$P_{G_ \mu G}(max)$	Maximum active power generated by the Microgrid

1 Introduction

Introduction of Distributed Generators (DG) in a distribution system has modified the power flow of the distribution network. This has raised issues like reverse power flow, voltage rise, increased fault levels, and instability. It is proved that a DG of random size at a nonoptimal location leads to increased system losses thereby deteriorating the performance of the system [1]. Importance of Microgrid is increasing day by day against distributed generators. This is because DG can work only as a source. However, Microgrid can have flexible operation in nature, i.e., as a source or as a load. This adjustable mode of Microgrid is supportive specially during the peak demand of the radial distribution system compared to DG. A Microgrid is composed of conventional sources (like diesel generator) and Hybrid Renewable Energy Sources (HRES) to supply the customers demand [2].

Plug & play capability of Microgrid influences the operation of a distribution system in a constructive and destructive manner. It has promoted a critical analysis of various aspects in studies of RDS performance for Microgrid integration [3]. Determination of the location and the size of a Microgrid in a distribution system is a complex combinatorial optimization problem. Some optimization techniques like Simulated Annealing (SA), Genetic Algorithm (GA), Tabu Search (TS), Artificial Bee Colony (ABC), and Particle Swarm Optimization (PSO) are applied to Microgrid management [4–6].

Demand supply balance in the Microgrid increases complexity in operation and control of distribution networks. This problem is not created while integrating DG in the distribution systems. This underlines the importance of optimal location and size of a Microgrid. Availability of optimum size of a Microgrid at an appropriate place in the distribution system is helpful in voltage profile improvement and power loss reduction of a Radial Distribution System. An inappropriate placement of a Microgrid in the utility network can lead to reverse power flow having the negative effect especially during peak demand of the utility. Utilities already facing the problem of

high power loss and poor voltage profile, especially in the developing countries may offer reluctance to the deployment of Microgrids.

An algorithm is developed to determine the location and size of a Microgrid for its integration in RDS using PSO technique. The rest of the paper is organized as follows: Problem formulation is described in Sect. 2. Section 3 presents the proposed methodology for determining location and size of a Microgrid. Location and size of a Microgrid are evaluated by considering two Radial Distribution Systems in Sect. 4. Section 5 outlines the conclusion.

2 Problem Formulation

The problem of optimal placement and size of a Microgrid is formulated as the minimization problem. The objective is formulated subject to various constraints.

2.1 Objective Function

The main objective of the optimization problem is to determine the best location and optimum size of a Microgrid in the Radial Distribution System under study subject to various constraints. The active power losses in the system are obtained by incorporating Microgrid as PQ load in it (positive if Microgrid is working as a load and negative when Microgrid is working as a source) using power flow analysis. The expression for total real power loss is as follows [7]:

$$\text{Power Loss} = \sum_{i=1}^m (I_i)^2 R_i \quad (1)$$

2.2 Constraints

Constraints imposed in this optimization problem are as follows:

Demand supply balance constraints—The demand supply constraints are considered as (2) and (3).

$$\sum_{t=1}^T (P_G(t)) \Delta t \pm \sum_{t=1}^T P_{\mu G}^{\text{in}}(t) \Delta t = \sum_{t=1}^T (P_D(t)) \Delta t + \sum_{t=1}^T (P_{\text{loss}}(t)) \Delta t \quad (2)$$

$$\sum_{t=1}^T (Q_G(t)) \Delta t \pm \sum_{t=1}^T Q_{\mu G}^{\text{in}}(t) \Delta t = \sum_{t=1}^T (Q_D(t)) \Delta t + \sum_{t=1}^T (Q_{\text{loss}}(t)) \Delta t \quad (3)$$

$Q_{\mu G}^{\text{in}}$ is assumed to be zero as reactive power requirement in the Microgrid is satisfied by its sources.

Voltage constraints—To ensure that voltage at each bus in the system should be within predefined limits, the following constraint is considered:

$$V_{i\text{min}} \leq V_i \leq V_{i\text{max}} \quad (4)$$

Voltage limits of the system are considered to be $\pm 6\%$ of the nominal voltage value.

Microgrid generation constraints—To have a significant effect of Microgrid on a system and to avoid the voltage rise problem in the Radial Distribution System, constraints are imposed on the Microgrid generation.

The Microgrid is assumed to generate the active power within limits given below:

$$PG_{\mu G}(\text{min}) \leq PG_{\mu G} \leq PG_{\mu G}(\text{max}) \quad (5)$$

$PG_{\mu G}(\text{min})$ is set as 25% of total active power on the feeder.

$PG_{\mu G}(\text{max})$ is set as 55% of total active power on the feeder.

3 Methodology

Integration of a Microgrid in a distribution network can have a positive impact on the performance of Radial Distribution System by determining size and location of a Microgrid. Particle Swarm Optimization (PSO) is an intelligence-based technique that is not largely affected by the size and nonlinearity of the problem. Advantages of PSO over similar population-based evolutionary algorithm GA are as follows [8–10]:

- PSO is easier to implement with fewer parameters to adjust.
- In PSO, every particle remembers its own previous best value as well as the neighborhood best; therefore, it has more effective memory capability than GA.
- PSO is more efficient in maintaining the diversity of the swarm, since all the particles use the information related to the most successful particle in order to improve them, whereas in GA, the worse solutions are discarded and only the good ones are saved; therefore, in GA the population revolves around a subset of the best individuals.

The algorithm is developed to analyze the positive impact of a Microgrid on the Radial Distribution System.

3.1 Proposed Algorithm

The developed algorithm for optimal location and size of a Microgrid with constant Microgrid load for one snapshot has the following steps.

1. Read the line data and bus data of a Radial Distribution system. Read the Microgrid data.
2. Initialize a population array of the particles with random positions and velocities (for location and size of Microgrid).
3. Set the iteration count “N” and execute the power flow of the system by using Forward Backward Sweep method for each particle.
4. If the voltage constraints are satisfied, compute the power loss and save pbest and gbest; else, regenerate the particles and repeat Step 3.
5. Update the position and velocity of each particle and again compute the power loss.
6. Compare the pbest particles of location and size of Microgrid for which the power losses are minimum and record the current pbest and gbest value.
7. Identify the particle with best success so far and assign it as gbest.
8. Increment the iteration count and repeat Step 5–7 until the final iteration.
9. Identify the best global particle (gbest) for optimum location and size of Microgrid.
10. Print the results for optimal location and size of Microgrid

The flowchart is shown in Fig. 1 which explains the logic of the optimization problem.

4 Case Study

The optimal location and size of a Microgrid in 9-bus and 34-bus Radial Distribution System is computed using Particle Swarm Optimization (PSO). The system data is taken from [11, 12]. The voltages and system losses of the system are obtained using Backward Forward Sweep method of the power flow analysis. The algorithm is developed using the following assumptions:

- The Microgrid is considered with an internal demand of 500 kW.
- The Microgrid is assumed to be supplying only active power and the reactive power is balanced internally.

It is observed that the voltages are violated from bus number 5 to bus number 9 in 9-bus system. Table 1 depicts the voltages at the remote buses of all the laterals in 34-bus system. The voltage at bus number 27 is found to be the lowest. Hence, by analysis it can be concluded that the lateral originating from bus number 6 (i.e., bus number 17 to bus number 27) is to be focused as the voltage constraints are violated for lateral from bus number 17–27.

The solution of the optimization problem, i.e., optimal location and size of Microgrid is shown in Table 2.

Incorporation of the Microgrid results in reduction of the total system losses. The power losses are reduced by 48.16–51.46% in 9-bus system and 34-bus system, respectively. Voltage profile of 9-bus and 34-bus system is shown in Fig. 2 and Fig. 3, respectively.

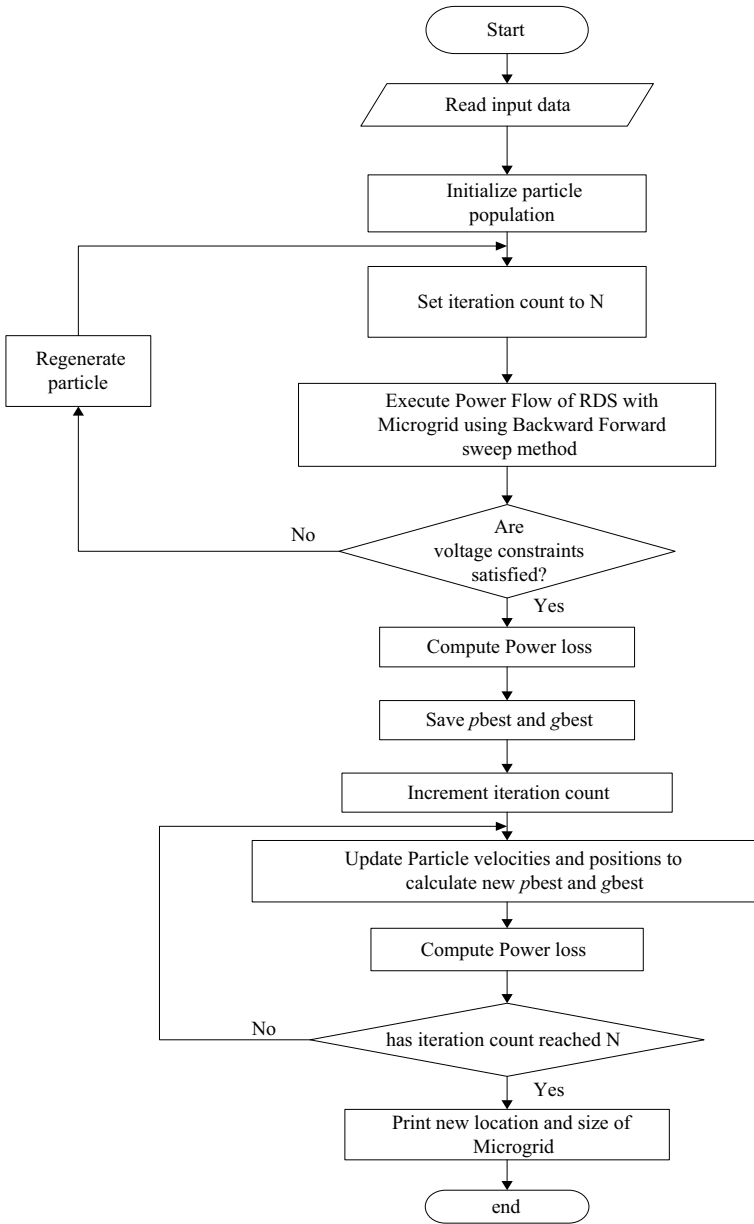


Fig. 1 Flowchart for location and size of Microgrid

Table 1 Voltages at remote ends of 34-bus system

Bus number	Voltage (p. u.)
12	0.9506
16	0.9882
27	0.9274
30	0.9563
34	0.9502

Table 2 Optimum location and size of Microgrid for 9-bus and 34-bus RDS

Type of radial distribution system	Microgrid location (bus no)	Microgrid generation (MW)	Bus voltage at remote end		Total distribution losses	
			Without Microgrid (p. u.)	With Microgrid (p. u.)	Without Microgrid (p. u.)	With Microgrid (p. u.)
9 bus	8	4.526	0.8642	0.9405	736.531	354.53
34 bus	25	2.201	0.9267	0.9785	227.793	110.57

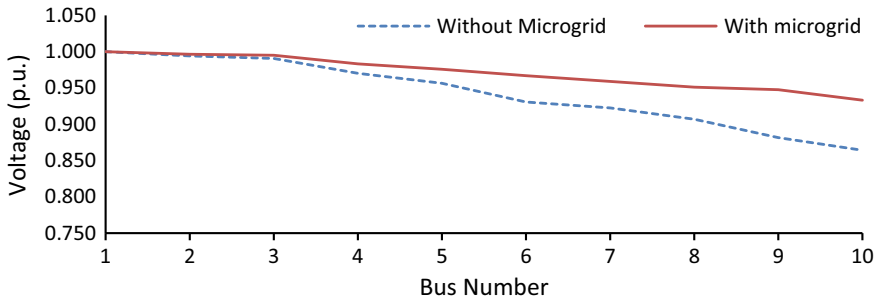


Fig. 2 Voltage profile of 9-bus system

The voltage at the remote end (bus number 9) is improved by 7.98% in 9-bus system. The analysis of data for 34-bus system shows that the lateral from bus number 17 to 27 is the longest lateral. At the remote end of the lateral (bus number 27) the voltage is improved by 5.58% as shown in Fig. 3.

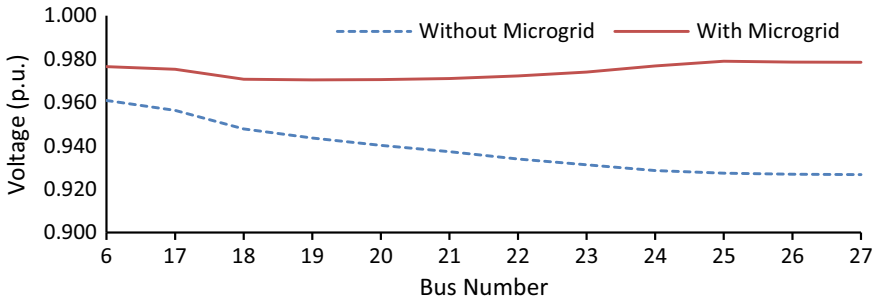


Fig. 3 Voltage profile of lateral (bus 17–27) in 34-bus system

5 Conclusion

An algorithm is developed for assessing the performance of Radial Distribution System by insertion of a Microgrid using Particle Swarm Optimization technique. Radial Distribution System is analyzed with the incorporation of constant demand in the Microgrid. It is found that the voltage profile is improved by the insertion of the Microgrid for both the systems under study. It is proved that the system losses are reduced by the presence of a Microgrid at an appropriate place. But in a practical system the demand and generation of Microgrid are dynamic in nature. Hence, it is necessary to optimize the location and size of the Microgrid depending on the demand supply balance of the Microgrid.

References

1. Quezada VHM, Abbad JR, Roman TGS (2006) Assessment of energy distribution losses for increasing penetration of distributed generation. *IEEE Trans Power Syst* 21(2):533–540
2. Katiraei F, Irvani R, Hatziargyriou N, Dimeas A (2008) Microgrids management. *IEEE Power Energy Mag* 6(3):54–65
3. Buayai K, Kerdchuen T (2013) Influence of micro-grid in steady state performance of primary distribution system. *Res J Appl Sci Eng Technol* 6(5):819–824
4. Katsigiannis YA, Georgilakis PS, Karapidakis ES (2012) Hybrid simulated annealing-tabu search method for optimal sizing of autonomous power systems with renewables. *IEEE Trans Sustain Energy* 3(3):330–338
5. Jayachandran M, Ravi G (2017) Design and optimization of hybrid micro-grid system. *Energy Proc* 117:95–103
6. Askarzadeh A (2018) A memory-based genetic algorithm for optimization of power generation in a microgrid. *IEEE Trans Sustain Energy* 9(3):1081–1089
7. Ugranh F, Karatepe E (2013) Multiple-distributed generation planning under load uncertainty and different penetration levels. *Int J Electr Power Energy Syst* 46:132–144
8. Boeringer DW, Werner DH (2004) Particle swarm optimization versus genetic algorithms for phased array synthesis. *IEEE Trans Antennas Propag* 52(3):771–779
9. Kennedy J, Eberhart R (1995) Particle swarm optimization. In: *IEEE international conference on neural networks*. IEEE, Perth, Australia, pp. 1942–1948

10. Ghanegaonkar SP, Pande VN (2017) Optimal hourly scheduling of distributed generation and capacitors for minimization of energy loss and reduction in capacitors switching operations. *IET Gener Transm Distrib* 11(9):2244–2250
11. Srinivasa Rao R, Narasimham SVL (2008) Optimal capacitor placement in Radial Distribution System using plant growth simulation algorithm. *Int J Electr Comput Energ Electron Commun Eng* 2(9)
12. Chis M, Salama MMA, Jayaram S (1997) Capacitor placement in distribution systems using heuristic search strategies. In: *IEE proceedings—generation, transmission and distribution*, vol 144(3), pp. 225–230

Constraint Tariff Model to Reduce the Amount of Cross Subsidy Incorporated in Electricity Tariff Using Iterative Optimization Technique



Varada J. Tambe and S. K. Joshi

Abstract Indian electricity tariffs are not in-line with the actual cost of service. The Industrial consumers paying much higher charges in comparison to the cross subsidized categories voyage towards open access and this voyage lowers the revenue collection of the utility. Hence, the utility faces financial scarcity. To overcome this situation, this paper tries to propose a model in which the gap between the actual tariff and cost of service is tried to lower down and the utility is also benefitted by some profit at the end of every year under the policy tenure.

Keywords Cross subsidy · Profit · Tariff · Revenue · Utility · Universal Charge

1 Introduction

As a part of structural reforms in the power sector, the open access (OA) regime has opened doors to opt cheaper electricity especially for the high-end consumers who pay more charges than service cost [1, 2]. Additionally, the state government is also burdened with direct subsidy given to the agricultural sector and there is always a delay observed or debate about the reception of the said subsidy [3]. Due to these two major revenue reception issues, utilities have started facing financial scarcity. Hence, for utilities to sustain in the reforming power sector, the tariff and subsidy pattern are needed to be focused on. Tariff in-line with the marginal cost and transparency in pricing is always desired. Ramsey pricing structure is suggested as an option for tariff modification according to [4–7]. It is clear that the assistance of the government to safeguard the utility to recover from dues of banks is dangerous to the economy [8]. In developing countries, subsidies are dominant [9]. It is narrated in [10] to charge tariff reflecting efficient Cost of Service (CoS) to the agricultural sector beyond

V. J. Tambe (✉) · S. K. Joshi
Electrical Engineering Department, The Maharaja Sayajirao University
of Baroda, Vadodara, India
e-mail: varada.tambe@gmail.com

S. K. Joshi
e-mail: skjoshi@ieee.org

© Springer Nature Singapore Pte Ltd. 2020
A. Kalam et al. (eds.), *Intelligent Computing Techniques for Smart Energy Systems*,
Lecture Notes in Electrical Engineering 607,
https://doi.org/10.1007/978-981-15-0214-9_14

predefined level of consumption, and subsidy should be delivered to the identified categories directly in terms of cash or ICT methods. The outcome of [9, 11] is on the same line stating that the subsidy must go directly to the targeted group. The adverse effects of cross subsidization in the agricultural sector are presented in [8, 12] and the suggestion is to make the electricity consumption rationalized. The impact of Open Access, the major trend changer reform in the Indian power sector, has not been incorporated in [9, 11, 13]. OA facilitated the High Tension (HT) Industrial consumers having demand higher than 1 MW to opt for the alternative supplier and achieve a considerable amount of savings due to lower rates payable than the rates set by the utility. Hence, it is high time for the utility to move toward rationalized tariff structure.

Considering the case of transitional economies similar to India, the existing practices in subsidy abolition from the tariff is being well implemented in Philippines [14, 15]. Forum of Regulators (FoR), India has published a report to roll out the cross subsidy component by incorporating Universal Charge (UC) in addition to tariff [16]. The report lacks in fulfilling the existing tariff policy guidelines and hence, proposes a model giving non-acceptable tariff results. So, detailed study and analysis are needed in this area if such a policy is required to be suggested to the utilities. Hence, this paper tries to modify the model presented in [16] by incorporating tariff constraints on every category based on the guidelines given under [10]. The major difference between the two models is that the basic model [16] nullifies the effect of cross subsidy (CS) at the end of the tenure considered, whereas the model proposed herein tries to reduce the CS and tries to limit tariff rise going beyond the acceptable limit using iterative optimization technique. The remaining paper is divided into four sections: Sect. 2 explains the basic model with modifications recommended, Sect. 3 explains optimization problem formulation, Sect. 4 explains the iterative algorithm, Sect. 5 describes the available data and assumptions, Sect. 6 presents discussion on the results and the last section concludes the paper by stating the outcome of the analysis and possible future scope.

2 Basic Model and Recommended Modifications

In the model presented [16], a total of 23 subcategories of electricity consumers of the Punjab state have been considered. It is tried to make the CoS equal to the tariff for every category by incorporating additional charge on every category. The said charge being a burden on consumers, is decreased every financial year and made zero for the last year of the policy tenure. The major drawback of this model is that the resulting tariffs are not practically acceptable. The major flaw observed at the end is that the categories already receiving subsidy are supposed to pay much higher charges which is impossible to be implemented.

In the new model, it is taken care that the tariffs are as per the guidelines given by tariff policy so that shocking tariff rise is not observed and the utility also gains some considerable profit so that it will be a win-win situation for both the consumers

as well as the utility. For achieving the said, a fixed charge called Universal Charge (UC) is imposed temporarily on the consumers in addition to the tariff. It is reduced every year and made zero at the end of tenure under consideration. The fund collected due to imposition of UC is used to fill the revenue and the ARR gap. The remaining fund at the end of the current year is carried forward in the next year of the policy tenure.

3 Optimization Problem Formulation

The value of the objective function is calculated from the generated random samples of the variable within the given upper and lower bounds for every year. A minimum but nonzero value is considered as the optimized minimum value. Using the defined step size, the bounds of the variable are lowered down. The procedure is repeated until the variable upper limit reaches zero. The detailed algorithm is explained in the next section.

3.1 The Objective Function

The objective of the problem is to find optimized (minimum) nonzero value of profit of the utility corresponding to the random generated sample values of Universal Charge which is the variable, within the given range. The corresponding cost function is defined as follows.

$$p = \left[\left[\sum_{i=1}^6 (UC + T_i) \times S_i \right] - \left[\sum_{i=1}^6 (X_i) \times S_i \right] + \text{Fund_start} \right] \div \left[\sum_{i=1}^6 (UC + T_i) \times S_i \right] \tag{1}$$

3.2 The Operating Constraints

Considering the tariff policy guidelines, the constraints to be satisfied while calculating the tariff are defined as follows.

$$T_i \text{ mod} \leq 1.2 \times W \text{ Avg}(X) \tag{2}$$

$$T_5 \leq 0.9 \times W \text{ Avg}(X) \tag{3}$$

$$T_6 \leq 0.5 \times W\text{Avg}(X) \quad (4)$$

3.3 The Bounds

The generated UC samples are bounded every year within the following limits.

$$UC_{\max} \leq UC \leq UC_{\min} \quad (5)$$

4 Algorithm Developed

Following are the steps involved in the algorithm.

1. Initialize CAGR of sales, UC upper and lower bounds, CoS and tariff rise rates, and reference values of X , T , and S .

Computing CoS

- a. As per APTEL guidelines [2], category-specific CoS can be computed using Power Purchase Cost (PPC), % losses at various voltage levels, and electricity sale figures.

$$X_j = C_j(1 + L_j) \quad (6)$$

OR

- b. Assuming that the CoS available [13] rises with a specific rate for consecutive number of years.

$$X_j = X_{\text{old}}(1 + r_c)^t \quad (7)$$

Computing CAGR of consumption

The CAGR of all categories is found using electricity sales from FY 2011 to FY 2016.

$$\text{gr} = (e_j/s_j)^{1/(t-1)} - 1 \quad (8)$$

2. Compute the reference CoSC.

$$Y_{i_{\text{new}}} = T_{i_{\text{new}}} \div X_{i_{\text{new}}} \quad (9)$$

3. At the starting of the tenure, compute new X , T , S , and expenditure ARR for every category i as shown below.

$$S_{i_{\text{new}}} = S_{i_{\text{old}}} \times (1 + \%CAGR) \quad (10)$$

$$X_{i_{\text{new}}} = X_{i_{\text{old}}} \times (1 + \%r) \quad (11)$$

$$T_{i_{\text{new}}} = T_{i_{\text{old}}} \times (1 + \%r) \quad (12)$$

$$ARR_i = S_{i_{\text{new}}} \times X_{i_{\text{new}}} \quad (13)$$

4. Constraint check for tariff as defined in (2)–(4). If tariff > constraint value, set tariff = constraint value.
5. Generate random 100 sample values of the UC population using the formula within the limit specified in (5).

$$UC_n = UC_{\text{min}} + (\text{rand} \times (UC_{\text{max}} - UC_{\text{min}})) \quad (14)$$

6. For all samples, compute profit of the utility using tariff, UC, ARR, and the fund carried forward from the previous year to the next year.
7. Store the minimum nonzero value of profit and the corresponding UC.

$$p = \left[\left[\sum_{i=1}^6 (UC + T_i) \times S_i \right] - \left[\sum_{i=1}^6 (X_i) \times S_i \right] + \text{Fund_start} \right] \div \left[\sum_{i=1}^6 (UC + T_i) \times S_i \right] \quad (15)$$

8. If profit ≤ 0 , increase UC bounds and go to Step 1.
9. Calculate CoSC with and without UC incorporated in the tariff for the same year.
10. Set new UC limits as

$$UC_{\text{max}} = UC_{\text{optimum}} \text{ and } UC_{\text{min}} = UC_{\text{optimum}} - \text{stepsize} \quad (16)$$

11. If UC $\neq 0$, allow the model to run for the next few years with UC = 0. (Perform steps 3–7 and 8–9).
12. If profit ≤ 0 , stop,

where

- i Index showing consumer category; $i = 1-4$ for HT, EHT, LTMD, and others category; $i = 5$ for residential consumers; $i = 6$ for agricultural consumers
 C Power purchase cost
 L Percentage T&D Loss component

CAGR	Compound annual growth rate
e	Sales in the last financial year
s	Sales in the first financial year
t	Period for which CAGR is to be calculated
gr	CAGR of electricity sales
r	Rate of rise
S	Sales
X	Cost of Supply
T	Tariff
Y	Cost of Supply Coverage
n	Tenure in years
ARR	Aggregate Revenue Requirement
UC	Universal Charge
Fund_start	Fund carried forward from the previous year to the next year.

5 Availability of Data and Assumptions

The model is developed for the consumer categories of the MGVL, a DISCOM of Gujarat state. The detailed information of sales and CoS for tariff slab specific subcategories is made available in [17]; no such detailed information for energy injection voltage levels in Gujarat is made available. The sales figures and tariff values/ABR herein, are obtained from the RIM reports and tariff orders published by GERC. Not enough data is available to compute CoS based on embedded cost or simplified approach methods [16]. Hence, two alternative methods have been considered to compute CoS for the reference year as in (6) and (7) referring to [16, 18], respectively, instead of going for mere assumptions. The industrial category is divided into two subcategories as Extra High Tension (EHT) at and above 66 kV level with 4% system losses applicable and HT above 11 kV level with applicable losses of 10%. For energy injection at 11 kV, the losses are 14% for drawal at 400 V and if the injection is also at 400 V, only 7% losses are applicable [3]. Hence, if the bifurcation at these energy injection levels along with the data similar to [17] are provided, Case 1 can have more variations in CoS. Table 1 shows the results of CoS calculation based on both cases.

Table 1 CoS in Rs/unit resulted from Case 1 and Case 2

Category	HT industrial	Railways	Residential	LT industrial and commercial (LTMD)	Others	Agricultural
Case 1	4.82	4.82	4.98	4.98	4.98	4.98
Case 2	4.87	4.33	6.17	5.30	5.03	5.28

Value of CAGR has been calculated as in (8) for every category based on the sales given in [1] for 5 years. UC value has been considered in the range of 0.50 Rs/unit as the maximum value to zero. It is felt that further rise in the value of UC may not be practically viable as it may give a shocking tariff hike to the consumers. It is obvious that if the UC is lower, burden on the consumer is lower and more is the acceptance to the model.

6 Results and Discussion

The model is tested with variation in UC range, step size, and tenure to evaluate the most acceptable lowest UC for every year. The results are evaluated for Case 2 as it represents a more realistic scenario. The results are evaluated for UC range starting from 0.5 Rs/unit in the step of 0.1 and 0.05. Looking at the Fig. 1, it is clear that both the tariff and CoSC reduce except for the “others” category from the FY 1 itself due to applicable tariff constraints on all the categories. The tariff rises by 2% for the “others” category which means that the tariff was not higher than the constraint limit. Hence, an equal rise of 2% on tariff and CoS is applicable. Hence, no CoSC change is observed in this category. The maximum reduction is observed in the “Agricultural” category which is actually a highly subsidized one and the HT category along with EHT including Railways remain at the second stage. Figure 2 shows the profit curve for the financial years 1–11 for a certain selected UC range. It is clear that when the profit becomes negative, the utility faces loss. Hence, the life span of the model or the policy tenure can be treated only until the profit turns out to be positive. Figure 3 shows the yearly CoSC comparison for every category for one specific UC bound range. Bar charts show that for all the categories, the resulted yearly CoSC value is lesser than the reference level even after introducing UC along with the tariff. This means that the consumers can bear the excess burden of UC and thus, the utility gains profit. In the base model [16] while bringing CoS

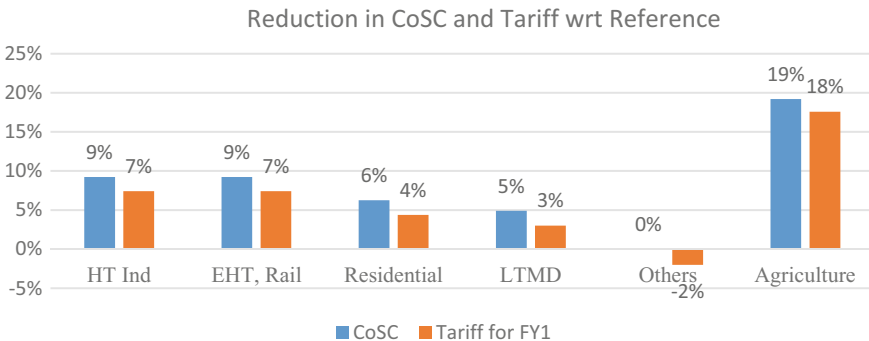


Fig. 1 CoSC and tariff change at FY1 due to tariff constraints

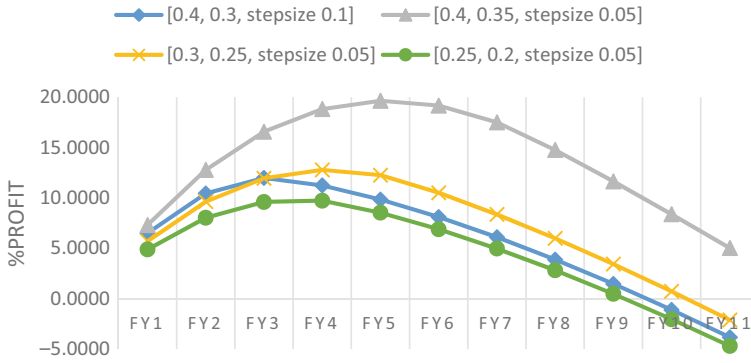


Fig. 2 Utility profit for a few UC ranges and corresponding step size

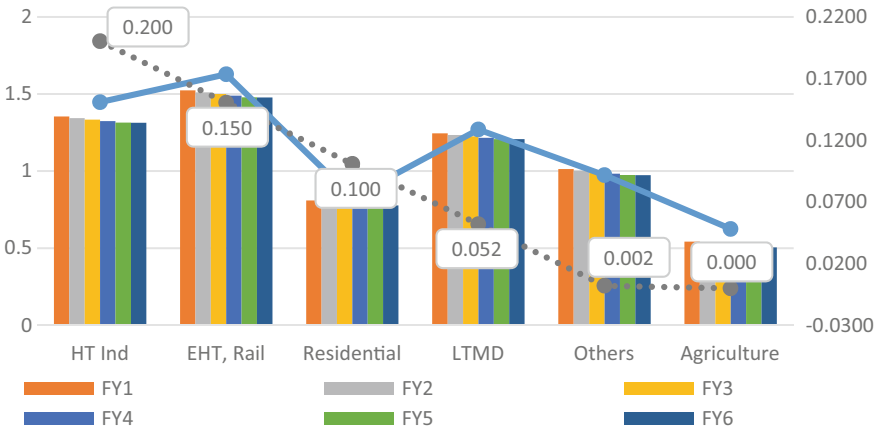


Fig. 3 CoSC with UC imparted on tariff, UC values with starting range [0.25, 0.2, step size 0.05]

equal to tariff, tremendous tariff rise is observed in the two subsidized categories as domestic and agricultural. This is completely non-acceptable as per [10]. The results presented herein are acceptable as the tariff constraints limit tariff rise and CoSC is also lowered compared to reference value.

7 Conclusion

The subsidy component hidden in the average billing rate has come down as CoSC has resulted lesser than the reference level. The highest billed industrial category and the lowest billed agricultural category are most benefited due to tariff and CoSC

reduction. And yet, the utility gains a considerable amount of profit at the end. Hence, the model turns out to be consumer as well as utility oriented under the given scenario.

References

1. RIMs, Gujarat Electricity Regulatory Commission, Gujarat, India (2016). <http://www.gercin.org/rims.aspx>. Accessed 13 Oct 2018
2. <http://pib.nic.in/newsite/PrintRelease.aspx?relid=131923>. Accessed 13 Oct 2018
3. Tariff Order, MGVCL, India (2017–18). <http://www.gercin.org/uploaded/document/f498d841-23f1-4b03-a3a2-244b2d813e4b.pdf>
4. Qi F, Zhang L, Wei B, Que G (2008) An application of Ramsey pricing in solving the cross-subsidies in chinese electricity. In: Third international conference on electric utility deregulation and restructuring and power technologies, pp 442–446, April 2008
5. Matsukawa I, Madono S (1993) An empirical analysis of Ramsey pricing in Japanese electric utilities. *J Jpn Int Econ* 7:253–276
6. Nahata B et al (2007) An application of Ramsey model in transition economy: a Russian case study. *Energy Econ* 29(1):105–125
7. Hajibababel H, Manzoor D (2014) Regional electricity pricing with Ramsey approach: Tehran case study. *Int J Acad Res Account Financ Manag Sci* 4(3):182–186
8. Mukherjee M (2014) Private participation in the indian power sector: lessons from two decades of experience. World Bank Group, Washington, DC
9. Acharya RH, Sandath AC (2017) Implications of energy subsidy reforms in India. *Energy Policy* 102:453–462. <https://doi.org/10.1016/j.enpol.2016.12.036>
10. National Tariff Policy, Ministry of Power, India (2006)
11. Bhattacharyya R, Ganguly A (2017) Cross subsidy removal in electricity pricing in India. *Energy Policy* 100:108–190. <https://doi.org/10.1016/j.enpol.2016.10.024>
12. Swain A, Charnoz O (2012) In pursuit of energy efficiency in india's agriculture: fighting 'free power' or working with it? Agence Française de Développement, Working Paper 126. <http://www.afd.fr/webdav/shared/PUBLICATIONS/RECHERCHE/Scientifiques/Documents-de-travail/126-document-travail-VA.pdf>
13. Chattopadhyay P (2004) Cross-subsidy in electricity tariffs: evidence from India. *Energy Policy* 32:673–684. [https://doi.org/10.1016/S0301-4215\(02\)00332-4](https://doi.org/10.1016/S0301-4215(02)00332-4)
14. Electric power industry reform act of 2001. <https://www.doe.gov.ph/electricity-industry-reform-act-2001>. Accessed 13 Oct 2018
15. https://www.doe.gov.ph/sites/default/files/pdf/consumer_connect/unbundling_of_rates.pdf. Accessed 13 Oct 2018
16. Road map for reduction in cross subsidy, Forum of Regulators, India (2015)
17. Voltage wise-category wise cost of supply, PSPCL, India (2015–16)
18. Category wise cost of service, study for FY 2011–12, Final Report, GUVNL, February 2013

Titration Machine: A New Approach Using Arduino



Vijayalaxmi , S. H. Ashwin and S. V. Harish 

Abstract Titration is a tedious process in Chemistry laboratories. It involves carefully measuring the titrand and titrant, rinsing the apparatus, adding the indicator, and titrating it to the correct decimal point. Even after taking a lot of precautions and care, sometimes the results may go wrong. If it has to be verified, the whole process has to be repeated, which is time-consuming. So, to overcome this struggle, this model is developed. This makes use of Arduino microcontroller and cost-effective materials. The process is very simple and obtained results are quite accurate.

Keywords Titration · Titrand · Titrant · Arduino

1 Introduction

Chemistry lab is a place where perfection and precision are the most important words. Extremely small errors in calculation can lead to completely different and unexpected results. So is the case while carrying out the chemical reactions. And one such experiment that requires utmost care is titration. Everyone would have got the experience of it. It is really difficult to get the required concordant value during the experiment due to physical errors and minute defects in the equipment. In most of the cases, students manipulate the values to get the required result and to pass the examination. Teachers would have no clue whether his/her students have genuinely got the results or have faked it. So this model helps teachers to verify the results of their students and also for students to understand how titration actually works.

This model makes use of Arduino microcontroller to automatically titrate the given solution against another and to give the accurate concordant value.

Vijayalaxmi (✉) · S. H. Ashwin · S. V. Harish
Manipal Institute of Technology, Manipal Academy of Higher Education, Manipal, India
e-mail: vijaya.laxmi@manipal.edu

© Springer Nature Singapore Pte Ltd. 2020
A. Kalam et al. (eds.), *Intelligent Computing Techniques for Smart Energy Systems*,
Lecture Notes in Electrical Engineering 607,
https://doi.org/10.1007/978-981-15-0214-9_15

2 Motivation

Titration is a tedious process. It involves carefully measuring the titrand and titrant, rinsing the apparatus, adding the required amount of indicator, and titrating it to the correct decimal point. It takes a lot of time to do all this work. In the end, it is not sure if the result is correct. If it has to be verified, then the entire process has to be repeated again. But what if there is a faster way to verify the result? Yes, that's where this model comes into use. Simply put the chemicals in the allotted place and press a button. It will give you the result much faster which is more accurate too.

In the chemistry lab, titration is done with the help of fragile glass apparatus. Any mistake in handling can lead to its damage or breakage. A small crack in those apparatus can make it unfit for further titration experiments. So it has to be replaced. A typical pipette and burette costs around INR 800–900. But this model uses inexpensive apparatus which aren't as fragile as the traditional pipette and burette.

To develop an accurate, fast, and reliable titration machine was the motivation behind this work.

3 Experimental Setup

The setup for the experiment consists of the following different parts:

- Magnetic stirrer
 - An old CPU fan was procured in working condition.
 - Neodymium magnets were fixed on both the sides of all the blades of the fan using super glue. This would do the job of stirring the chemicals.
- Burette apparatus
 - A small transparent vessel was selected as the burette (vessel no. 1).
 - Its volume was measured and it was properly calibrated with the accuracy of up to 0.1 mL.
 - The submersible pump was fixed vertically inside the vessel and a rubber tube was connected to its output port.
- Titration vessel
 - Another similar vessel was chosen to represent the conical flask used in manual titration (vessel no. 2).
 - The other end of the rubber tube coming from the submersible water pump was put inside this vessel.
 - An ellipsoid magnet was put in it.
 - The entire setup was then placed on the magnetic stirrer.

- Electronic end point indicator
 - A light intensity detector circuit was interfaced with Arduino and was placed beside the second vessel, i.e., titration vessel.
 - It was programmed in a way such that during titration, if the intensity of light that the LDR receives is below a certain preset value, then the buzzer makes a sound to indicate the end of titration.

All these parts are to be placed as shown in Fig. 3.

4 Working and Flowchart

There are two chemicals involved in titration—Titrand and titrant. Carefully measure the required volume of the titrand and put it into vessel no 2. Fill vessel no 1 with titrant up to the brim. Place the magnetic stirrer exactly below vessel no 2 and make sure that the LDR is touching the glass surface of the same vessel. After all this, turn on the switch and the magnetic stirrer. You will notice that the pump slowly pumps the solution from vessel 1 to vessel 2 [1, 2].

After few milliliters of solution is pumped, the pump stops and the LDR checks the intensity of light that it receives through vessel 2. If the end point of the reaction is achieved, then the intensity of the light that passes through vessel no 2 will be below a particular predetermined¹ value. So it prevents the pump from pumping again and activates the buzzer. If the end point is not yet achieved, then the intensity of light will be good enough. Hence, it activates the pump again and the whole process starts again. This cycle goes on and on until the end point of titration is reached, i.e., the color of the solution in vessel 2 must change. The flowchart of the working model is as shown in Fig. 1.

5 Circuit Diagram of Arduino with Motor Shield

The Arduino board must be connected to an external power supply such as a power bank [3]. A laptop works just as fine too. With the help of a connecting jack, a 9 V battery can also do the job. Figure 2 shows the circuit diagram of the machine.

The motor shield is designed in such a way that it is compatible with Arduino Uno. So, the motor shield can be connected by just mounting it over the Arduino board [4].

¹The value has to be set each time and edited in the code after conducting a trial round of titration if the place of performing titration is changed.

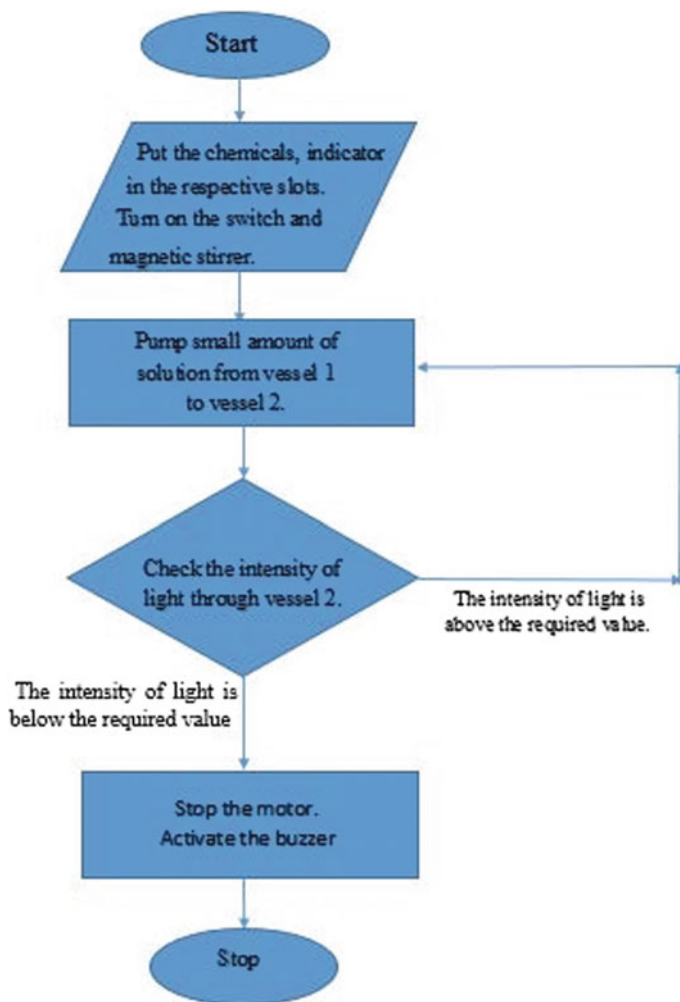


Fig. 1 Flowchart of the working model

6 A Glimpse of the Titration Machine

Figure 3 is the prototype of the Titration machine and Fig. 4 shows Motor Driver Shield with Arduino Uno.

With the help of this setup, titration was performed for different concentrations of chemicals and the readings of one such trial are shown in the next section.

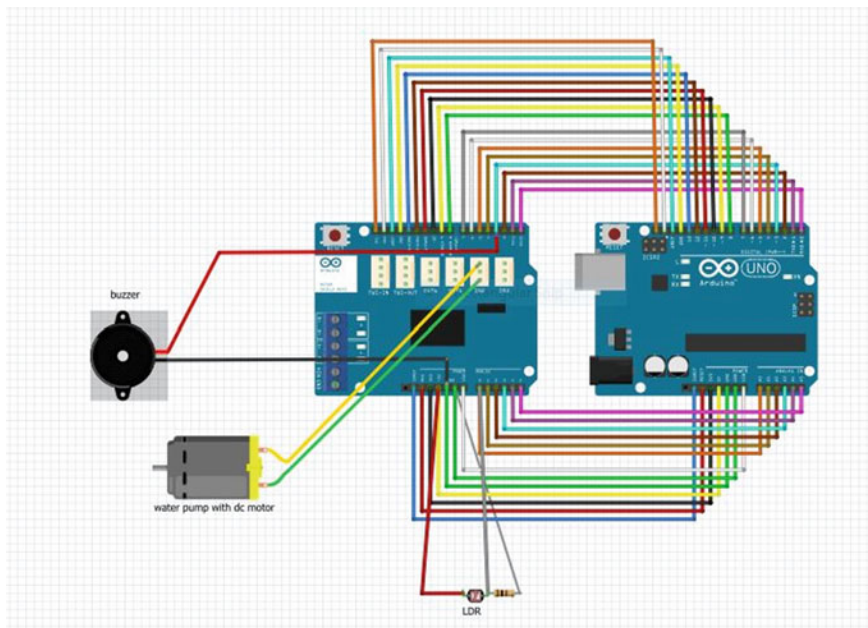


Fig. 2 Circuit diagram of Arduino with Motor shield



Fig. 3 The prototype of the complete setup

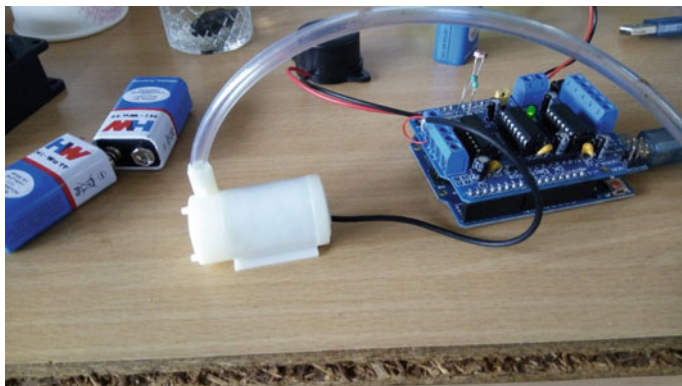


Fig. 4 Motor driver shield with Arduino Uno

7 Results

To check the efficiency of this machine, its results were compared with the results of manual titration using the same chemicals and same laboratory conditions.

Permanganometric titration was carried out to find the strength of Potassium Permanganate solution given in the laboratory. It proved to be quite satisfactory. Tables 1 and 2 show the results obtained by manual titration and machine titration.

Table 1 Manual titration details

No	Burette reading (mL)		Volume of KMnO_4 used (mL)
	Initial	Final	
1	0	11.8	11.8
2	0	11.7	11.7
3	0	11.8	11.8

Concordant value: 11.8 mL

Table 2 Titration using the developed electronic machine

No	Vessel 1 Reading (mL)		Volume of KMnO_4 used (mL)
	Initial	Final	
1	0	11.6	11.6
2	0	11.6	11.6
3	0	11.6	11.6

Concordant value: 11.6 mL

8 Conclusions

Tables 1 and 2 show that the developed titration machine is accurate and consistent as the readings are concerned. This machine can be used by the faculty in the schools and colleges to check the accuracy of the results obtained by the students. Moreover, it can do the entire titration process a lot faster compared to the traditional titration. As a future work, color sensors can be used in place of LDR to make it more accurate. This is an innovative idea that struck a student while he was struggling in the chemistry lab.

References

1. Bhushan B (2016) Chemistry laboratory manual, Class 11, Arya Publications
2. Bhushan B (2017) Chemistry laboratory manual, Class 12, Arya Publications
3. www.arduino.cc/
4. www.instructables.com/L293D_motordriver

Hybrid Method for Cluster Analysis of Big Data



Chetna Dabas and Gaurav Kumar Nigam

Abstract In big data analytics, deep interest in a communication known as computer-mediated has cropped up. While using traditional techniques, it is difficult to handle the data which is magnanimous. Hence, there exists a need for improved methods to handle this data since the past methods do not fit properly in all kinds of situations. Normally, there are various steps for the handling of big data like acquisition, preprocessing, and processing and analysis of this data in order to retrieve proper semantics out of that amount of data. In a similar context, clustering has evolved as a popular approach for organizing and analysis of big data. In the present research work, a hybrid method for analysis of big data is proposed. The hybrid approach consists of the blending of K-means, Ward hierarchical along with the interpolation technique. The evaluation of and validation of the proposed approach has been carried out for the city dataset in R language. In the present work, the number of clusters and the size of the data get varied while carrying out the results. The results of the proposed work reflect impressive execution times of the proposed method over the existing ones. The proposed method also presents possible recommendation for extracting specific semantics for providing insights to business recommendations.

Keywords Analysis · Big data · Clustering · Hybrid method

1 Introduction

The traditional clustering techniques are no longer working best for the big data arena. The advantages of various individual clustering techniques are presented ahead, followed by the issues and the proposed method.

In the traditional method of doing cluster analysis, the aggregation is performed on a collection of objects. This technique is common and is popularly used and applied across diverse areas like image processing and health care, to name a few.

C. Dabas · G. K. Nigam (✉)
Jaypee Institute of Information Technology, Noida, India
e-mail: gaurav.nigam@jiit.ac.in

The clustering process is considered to be an interactive process which has multiple objectives. This process also incorporates data mining with a large number of trials. Iteration takes place until the desired number of results is achieved. As such, this problem can not be overcome by the existing state-of-the-art methods. The existing methods suffer from computational inefficiency and missing data problem and require pretraining.

This is the point where the already existing methods are unable to address the problem properly. The proposed work in this research paper addresses the problem of computational inefficiency and presents a hybrid method to overcome this issue. The proposed hybrid approach is designed by blending various techniques like interpolation technique on the city dataset along with R language scripts and specially designed multi-objective function. The proposed method has been implemented and impressive results have been drawn in terms of execution times.

This paper includes the literature review section, materials and methods section, results and discussion followed by conclusions and future work.

2 Related Work

While conquering the dataset, there are various objects on which clustering can be applied. There are numerous classification methods for clustering as revealed by the previous studies [1]. Pertaining to simple applications and usage, for a number of previous years, the existing methods of clustering which are traditional in nature were used. The examples of such types of clustering include hierarchical clustering and K-means clustering, to name a few [2]. As a matter of fact, there were errors generated by uncertainty and experimentation which further resulted in low accuracy in these existing techniques [3]. The existing literature also contains numerous applications in diverse domains in pattern recognition for semantics extractions in big data [4–8]. In this paper, the statistical evaluation is also carried out for performing data analysis. [9]. There exists a wide variety of clustering techniques, which are implemented using various applications of big data. A few of these methods are developed considering important factors like temporal features while working with the time-series data. These methods again suffer the disadvantage of missing data along with inefficiency for computations. Interpolation methods have been suggested in various studies to overcome these drawbacks. [9–14]. In spite of several existing methods in the literature, there exists hardly any method which is dedicated to addressing the problem of efficiency with the help of hybrid clustering method which may be in turn used to extract meaning semantics for making decisions. This research work focuses around overcoming these issues.

3 Proposed Work

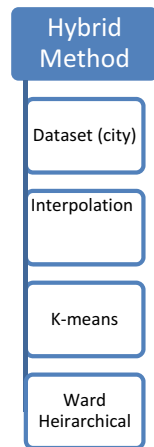
3.1 The Proposed Model

The hybrid clustering method proposed in this work includes six layers. These layers are responsible for carrying out tasks like crawling data from the city dataset, fileting and preprocessing of data, design of objective function, and application of the hybrid proposed method. There exists a strong interdependency among various components of this method. The objective function under consideration is a multi-objective function which has utilized the minimum variance parameter of the Ward technique. Within a cluster, this design leveraged a minimum variance as an added advantage. When the merging happened at every layer of the hybrid method, there was a bare minimum rise in the overall variance component. In order to optimize the search for a Centroid, the ingredients of interpolation search technique were utilized on the precomputed distances (squared Euclidian). The dataset under consideration of this study was composed up of more than 1,000,100 entries. The prime attributes of this dataset were location, name, and weather of cities across the world. The data before its usage was normalized and sorted. A recursive approach is utilized in this study until the point the data space can no longer be divided. The implementations and validations for the proposed hybrid clustering technique have been carried out in R Language version 3.2.1.

3.2 Workflow of the Algorithm

The pictorial representation of the proposed method is presented in Fig. 1 ahead.

Fig. 1 Proposed hybrid method (cluster analysis of big data)



4 Results and Discussion

The results and discussion section investigates the experimental values and analysis of the proposed hybrid method. The data sizes here varied from 100 to 1,000,000 while taking discrete distances into consideration. Table 1 shows the three-cluster table while making variations in the data sizes.

The group dimension shows a representation of the cluster being dragged in the data pane. Here, the individual members of the group dimension, namely clusters with numbers 1–7, carry marks computed by the proposed method. It is observed that these marks carry high resemblance to each other in comparison to those with the other marks.

During experimentation, prior to the application of the proposed hybrid clustering method, the data was filtered and preprocessed. It can be observed in three tables namely Tables 1, 2, and 3, that there are some negative values. These values reflect parameters like weather lower than most of the cities in the database. It can further be observed that there are some positive values at some of the places. In the city database, these values depict that the weather values might have been more than most of the cities existing in that database. As an example, look at Table 1, group number 3 to track the cities containing weather which is slightly lower when compared to the remaining cities.

Refer Table 2 to observe the data corresponding to the cities which bear weather values more in comparison to the rest of the cities. Here, if you observe group 1 and group 15 very closely, it can be interpreted that these groups may be further merged in future (which carry values greater than the rest of the cities). Further, this semantics can be used to interpret business-enhancement decisions. As an example to the vendors requiring to establish food factories across some specific parts of the world, this semantic information may act as a catalyst in identifying those locations based on temperature-oriented parameters.

Here, Table 3 depicts, the result corresponding to seven number of clusters taking data sizes of 100, 1000, and 10,000. It can further be observed that group 1 bears relatively higher values in comparison to the other groups for all varying data sizes.

In Fig. 2, the X-axis represents groups Y-axis represents the varying data sizes, and Z axis represents the number of clusters. The groups vary from 0 to 15; data sizes are taken as 100 and 10,000 for simplicity. The clusters under consideration are 3, 4, 5, 6, and 7. A peak can be observed in the five-cluster solution which depicts the

Table 1 Three-cluster table (different data sizes)

Groups	Data sizes				
	100	1000	10,000	100,000	1,000,000
1	1.65756432	0	1.25678657	-5.46E - 05	-9.95E - 04
2	0.4562345	1.657544	-1.123658743	-1.12E + 00	1.12E + 00
3	-1.2345678	-1.764356	-0.00345278	1.15E + 00	-1.12E + 00

Table 2 Five-cluster table (different data sizes)

Group no	5 Clusters		
	Data sizes		
	100	1000	10,000
1	1.3515274	1.6303891	0.58376431
2	0.2757128	-1.6134648	-0.58062007
3	0.679381	-0.7838172	-1.53791855
4	-1.2859985	-0.8140659	0.3968762
5	-0.6632092	0.4330971	0.893193
6	0.97619126	0.00231173	-0.6873426
7	-0.3619255	-0.4518394	-1.2436314
8	-1.7206537	1.2702814	-1.65375405
9	1.2202347	0.9234567	-1.87643904
10	0.4825674	0.476547	-0.34388227
11	-0.8634575	0.871238	0.03512678
12	-0.1321464	-0.2178905	1.76604664
13	1.7028167	-1.456267	-0.79883301
14	-1.1374803	-1.1564361	1.11090964
15	0.0689382	1.6754661	1.6535006

Table 3 Seven-cluster table (different data sizes)

Group no	7 Clusters table		
	Data sizes		
	100	1000	10,000
1	0.6751703	1.00233436	0.03195887
2	0.1244667	-0.96712376	0.439323489
3	-1.5821768	1.76871947	-0.567972688
4	0.879039	-0.43578718	-0.7680564
5	1.6477131	-1.97761634	0.95758878
6	-0.8812391	0.67843071	1.54801234
7	-0.0876554	0.845674567	-1.75345767

goodness of the solution while taking five clusters for large data size for the given dataset with various other parameters. The multi-objective function designed for the proposed method was employed to observe that it initially started to rise when the data size was increased using discrete intervals and post that, after 5 clusters, it started to decrease. These results further suggest the significance of using an optimal number of clusters in the dataset under consideration. Table 4 shows the results drawn for the proposed algorithm in terms of large and small data sizes.

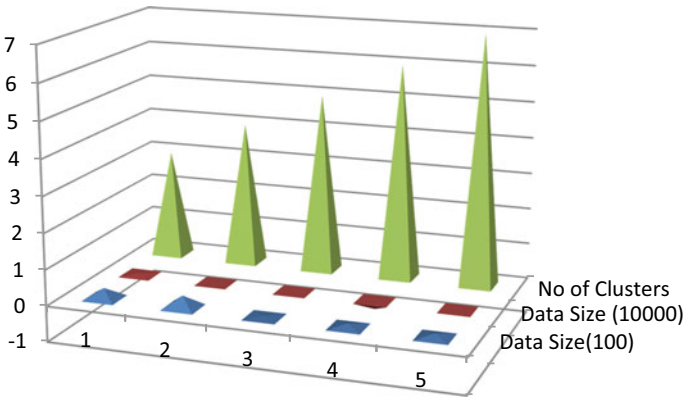


Fig. 2 Number of clusters versus data size

Table 4 A Time comparison of algorithms with small data size. B Time comparison of algorithms with large data size

S. no	Algorithm	Data size	Time (s)
A			
1	K-means [15]	100	0.554
2	Ward hierarchical [16]	100	0.465
3	Interpolation [17]	100	0.467
4	Proposed method	100	0.213
B			
1	K-Means [15]	1,000,000	0.943
2	Ward hierarchical [16]	1,000,000	0.886
3	Interpolation [17]	1,000,000	0.557
4	Proposed method	1,000,000	0.434

5 Conclusions

In the proposed work, a new method for performing clustering to extract relevant semantics data is performed. The results for the proposed method are evaluated and tested for the city dataset. The size of the cluster was varied from small to large, i.e., 3, 5, and 7. With the proposed method, the execution times of the proposed hybrid method came out to be better than the existing methods. This comparison was done for both the small data sizes and for huge data size and impressive results are retrieved in terms of execution times. The proposed method may be melded with the existing methods and search techniques which are location based, as per the size of the datasets used in a particular application. The proposed work may be helpful for extracting semantic information specifically while making business decisions.

References

1. Priya V, Vadivel A (2012) User behaviour pattern mining from weblog. *Int J Data Warehous Min (IJDWM)* 8(2):1–22
2. Tamayo P, Slonim D, Mesirov J, Zhu Q, Kitareewan S, Dmitrovsky E et al (1999) Interpreting patterns of gene expression with self-organizing maps: methods and application to hematopoietic differentiation. *Proc Natl Acad Sci* 96(6):2907–2912
3. Bar-Joseph Z (2004) Analyzing time series gene expression data. *Bioinformatics* 20(16):2493–2503
4. Androulakis IP, Yang E, Almon RR (2007) Analysis of time-series gene expression data: methods, challenges, and opportunities. *Annu Rev Biomed Eng* 9:205–228
5. Dabas C (2017) Big data analytics for exploratory social network analysis. *Int J Inf Technol Manag* 16(4):348–359
6. de Ridder D, de Ridder J, Reinders MJ (2013) Pattern recognition in bioinformatics. *Brief Bioinform* 14(5):633–647
7. Bughin J (2016) Big data, big bang? *J Big Data* 3(1):2
8. Tsai CW, Lai CF, Chao HC, Vasilakos AV (2015) Big data analytics: a survey. *J Big Data* 2(1):21
9. Silverman BW (2018) *Density estimation for statistics and data analysis*. Routledge
10. Li CT, Yuan Y, Wilson R (2008) An unsupervised conditional random fields approach for clustering gene expression time series. *Bioinformatics* 24(21):2467–2473
11. Luan Y, Li H (2003) Clustering of time-course gene expression data using a mixed-effects model with B-splines. *Bioinformatics* 19(4):474–482
12. Medvedovic M, Yeung KY, Bumgarner RE (2004) Bayesian mixture model based clustering of replicated microarray data. *Bioinformatics* 20(8):1222–1232
13. Schliep A, Costa IG, Steinhoff C, Schonhuth A (2005) Analyzing gene expression time-courses. *IEEE/ACM Trans Comput Biol Bioinf (TCBB)* 2(3):179–193
14. Yeung KY, Medvedovic M, Bumgarner RE (2003) Clustering gene-expression data with repeated measurements. *Genome Biol* 4(5):R34
15. Jain AK (2010) Data clustering: 50 years beyond K-means. *Pattern Recogn Lett* 31(8):651–666
16. Ward JH Jr (1963) Hierarchical grouping to optimize an objective function. *J Am Stat Assoc* 58(301):236–244
17. Andersson A, Mattsson C (1993) Dynamic interpolation search in $o(\log \log n)$ time. *Automata, Languages and Programming*, pp 15–27

A New Radio Frequency Harvesting System



Syed Mahmood Ali Mahboob, Shaik Qadeer and Ajaz Fatima

Abstract Converting readily available energies from the surroundings into usable electrical supply (current/voltage) is a trending topic of research. Due to more and more use of wireless technology, there is an abundance of electromagnetic signals and these signals can be harvested and electrical supply can be generated. In this paper, radio frequency (RF) energy is harvested and electrical energy is generated through various methods, such as step-up converter, flyback converter, and voltage amplifier with the feedback of power supply and detail comparison of the abovementioned methods are covered.

Keywords RF harvesters · Step-up converter · Flyback converter · Amplifiers · Power electronics

1 Introduction

Generation of electrical power through ambient energies is the most trending research topic among the research scholars. This topic does not only address the usage of nonrenewable fuels (such as coal, gasoline, diesel, etc.) but also the generation of electrical power from renewable energy sources. In this paper, the source considered for harvesting is a source which is not commonly used that is “Radio Frequency”. RF signals are abundantly available in the environment, these signals can be har-

S. M. A. Mahboob (✉) · S. Qadeer · A. Fatima
Electrical and Electronics Engineering Department, Muffakham Jah College
of Engineering and Technology, Hyderabad, India
e-mail: mahmood.mahboob94@gmail.com

S. Qadeer
e-mail: haqbei@gmail.com

A. Fatima
e-mail: fatimaeee@mjcollege.ac.in

© Springer Nature Singapore Pte Ltd. 2020
A. Kalam et al. (eds.), *Intelligent Computing Techniques for Smart Energy Systems*,
Lecture Notes in Electrical Engineering 607,
https://doi.org/10.1007/978-981-15-0214-9_18

vested through method which was developed after careful considerations and intensive studies for efficient harvesting [1, 2]. The existing RF harvesters utilize voltage multipliers, voltage doublers, etc., for low voltage generation. The radio frequencies at which the proposed harvester will be working is in the range of 300 kHz to 3 MHz, this band of frequency is known as medium frequency band. The RF harvester presented in this paper utilized ultralow voltage input and gave an output in usable range. Some of the blocks of the RF harvesting system can be for more efficient output. One way to do that is to modify the rectifier block. Various rectifiers give various levels of efficiencies. Another way to do so is by modifying the booster block with which significant amount of efficiency can be achieved. The topologies which are used here for rectifiers are bridge rectifier and double rectifier and the topologies for booster block are step-up converter, flyback converter, and voltage amplifiers. The rest of the paper is organized as follows: Sect. 1 gives an introduction, whereas Sect. 2 covers the overview followed by Sect. 3 which covers the methodology utilized for the development of different RF harvesters with simulation and Sect. 4 followed by Sect. 5 gives results and conclusion, respectively.

2 Overview of the System

The brief overview of the proposed system is shown in Fig. 1. The RF signal is received through the receiving antenna. Through the antenna, an AC signal is generated which fed to the rectenna as rectifier, after the rectification process, the rectified dc voltage is fed to the power converter where the dc voltage gets boosted/amplified, which is then stored in the storage unit or batteries, and based on the load demand, it is supplied to the load. The detail discussion of the important component of the system is discussed now.

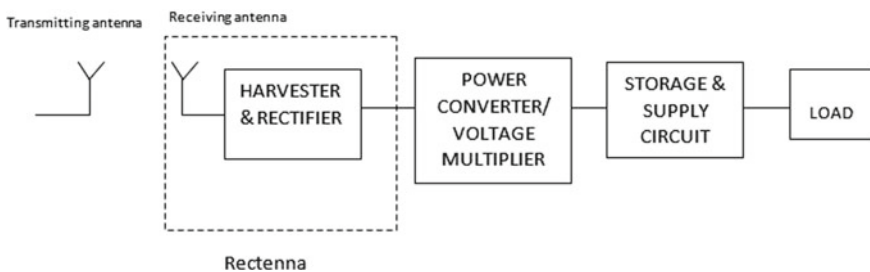
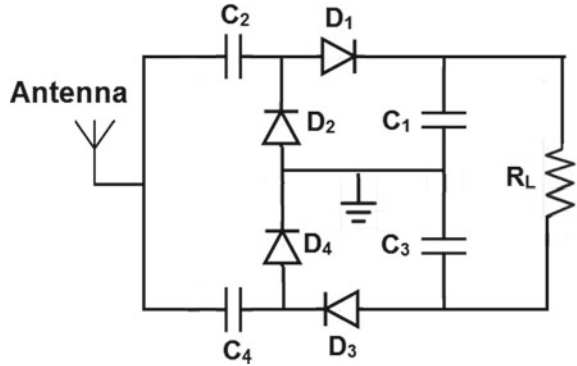


Fig. 1 Block diagram of the propose system

Fig. 2 Block diagram of the propose system



2.1 Rectenna

Please Rectenna is a device which receives the radio signal and then converts it into electrical output. It is a combination of antenna and rectifier circuit with which the voltage is generated [3–5]. The rectifiers in rectenna play a major role in the efficiency of the system. Various rectifiers have various efficiencies [6, 7]. The diodes utilized in the rectifiers are Schottky diode, these diodes are mostly used in high frequency applications due to their characteristics such as low forward voltage drop, lower levels of power loss, low turn-on voltage (The turn-on voltage for the Schottky diode ranges between 0.2 and 0.3 V), fast recovery time (This diode can be used for high-speed application due to its fast recovery time), and low junction capacitance (It utilizes a wire point contact onto the silicon due to very small active area due to which it has a small capacitance level).

Here, in this paper, we have used the following rectifiers: single diode bridge rectifier and double rectifier shown in Fig. 2.

A diode bridge is an assembly of four or more diodes in the form of a bridge which provides output of the same polarity irrespective of the input polarity. It is mostly used in the conversion of AC to DC which is its most common application.

A double rectifier is a type of half-bridge rectifier but has some additional components such as diode and capacitor due to which the output voltage of the rectifier will be a pure dc and the output voltage will be more than that of the input voltage.

2.2 Power Converter

There are various types of voltage boosters, the major role of a voltage booster circuit is to convert a pulsating dc voltage to pure dc voltage and amplify/boost the voltage levels. Different topologies of boosters utilized here are the first is step-up converter. It is a type of converter in which for voltage boosting, current is boost down [3–5, 7]. The boost converter used here is shown in Fig. 3. Modeling of step-up converter is given in the next few equations.

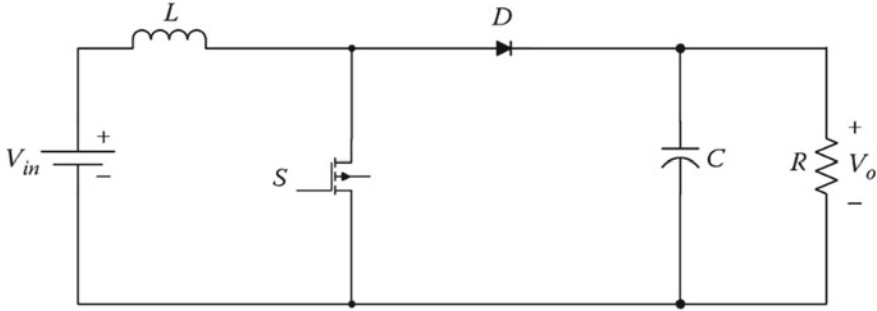


Fig. 3 Model of boost converter

The duty cycle D is determined by the input and output voltages of boost converter as

$$D = 1 - V_{in}/V_o \quad (1)$$

With switching frequency set at 50 kHz and the computed duty cycle (1), the time period $T(1/Fs)$, the ON and OFF time period ($T_{on} + T_{off} = T$) will be 20 μs (T), 14.7 μs (T_{on}), and 5.3 μs (T_{off}), respectively. With these values, the value of L and C can be calculated using (2) and (3), respectively.

$$L = (V_o - V_{in})(1 - D)/i_{Lmin} * Fs. \quad (2)$$

$$C = (V_o D)/(Fs R \Delta V_{opp}). \quad (3)$$

2.3 Flyback Converter

The flyback converter is a type of converter that has a galvanic isolation which separates the input and output [4]. The flyback converter is derived from buck-boost converter which has an inductor split to form a transformer so that the multiplication of voltage ratios takes place with an added advantage of isolation as shown in Fig. 4.

Operation of flyback converter is as follows. When the switch is closed, the primary of the transformer is directly connected to the input voltage source. The storing of energy in the transformer begins as the primary current and magnetic flux increases.

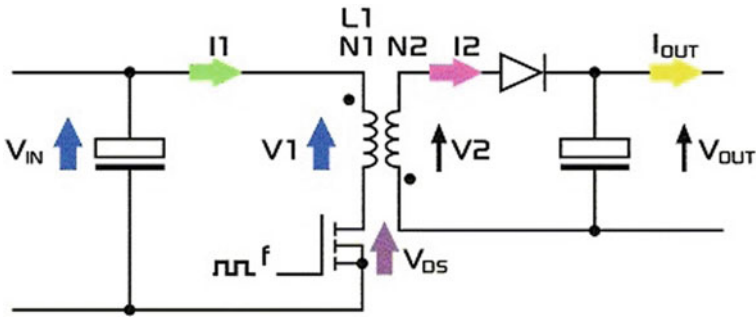


Fig. 4 Schematic diagram of flyback converter

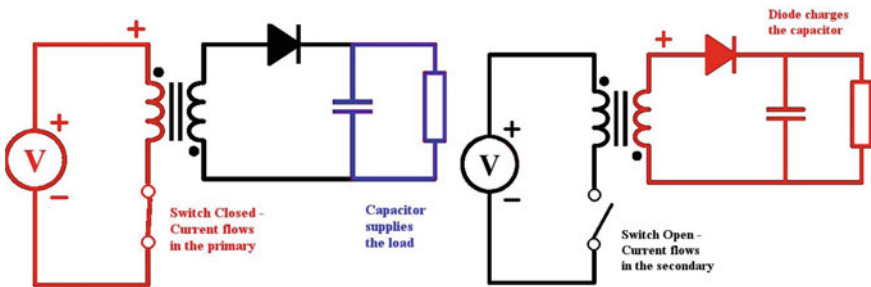


Fig. 5 Operating modes of flyback converter

The diode is reverse biased due the voltage induced in the secondary winding is negative (i.e., blocked). The output capacitor supplies energy to the output load. When the switch is opened, the primary current and magnetic flux drops. As the secondary voltage is positive, the diode works in forward biased mode, allowing current to flow from the transformer. The energy from the transformer core recharges the capacitor and supplies the load as shown in Fig. 5.

3 Methodology

This section discusses the flow of the study conducted as well as the design process of the RF energy harvesting systems.

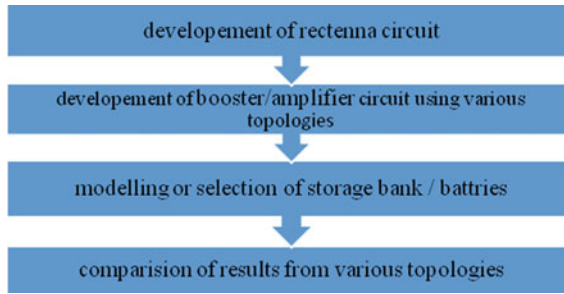


Fig. 6 Conceptual framework

3.1 Conceptual Frame Work and Simulations

The aim of this research is to design a highly efficient RF harvester by using various topologies. In order to determine the most efficient harvester, various harvesters designed using different topologies and their results are compared. The design steps used for RF harvesters are shown in Fig. 6.

The RF harvesters are designed for two different topologies, i.e., low voltage RF harvester and ultralow voltage harvesters. The input voltage of low voltage harvesters ranges from 1.5 V to 2 V and the output voltage of various topologies ranges from 5 V to 10 V, respectively. For the ultralow voltage harvester, the input voltage is 250 mV and the output voltage for different topologies ranges from 5.25 V to 6.5 V, respectively.

The following are the different harvesters designed.

3.1.1 Low Voltage RF Harvester Using Step-Up Converter

Figure 7 shows the block diagram of the RF harvester using step-up converter whereas Fig. 8 shows the simulation results.

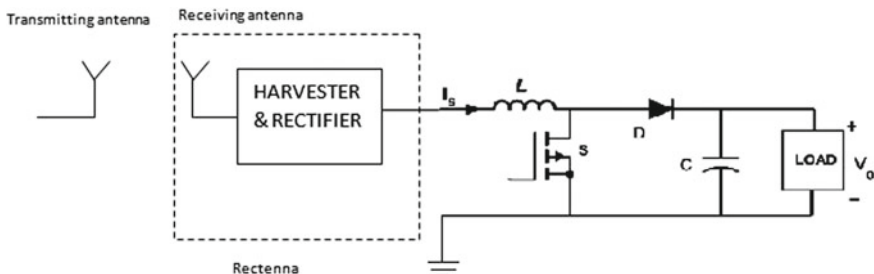


Fig. 7 Block diagram of RF harvester using step-up converter

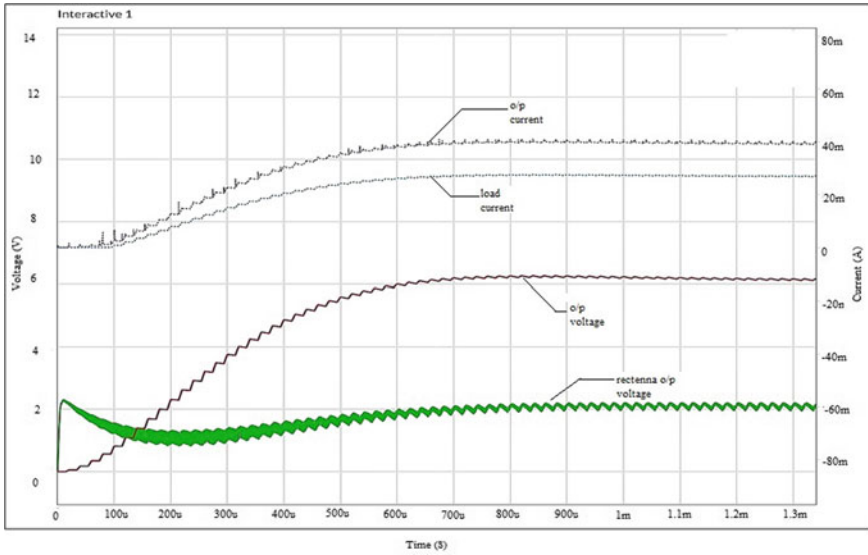


Fig. 8 Simulation results of RF harvester using step-up converter

3.1.2 Low Voltage RF Harvester Using Flyback Converter

Figure 9 shows the block diagram of the RF harvester using flyback converter and whereas Fig. 10 shows the simulation results.

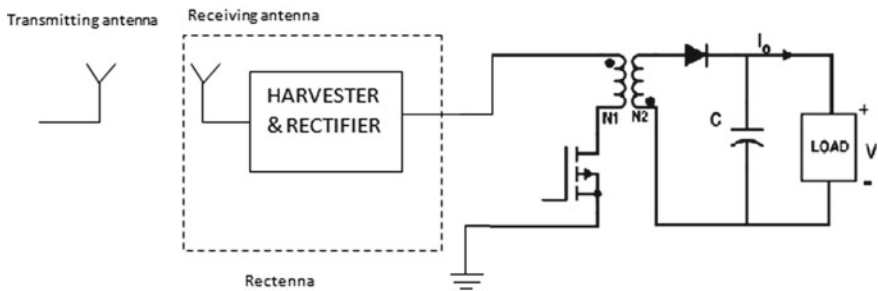


Fig. 9 Block diagram of RF harvester using flyback converter

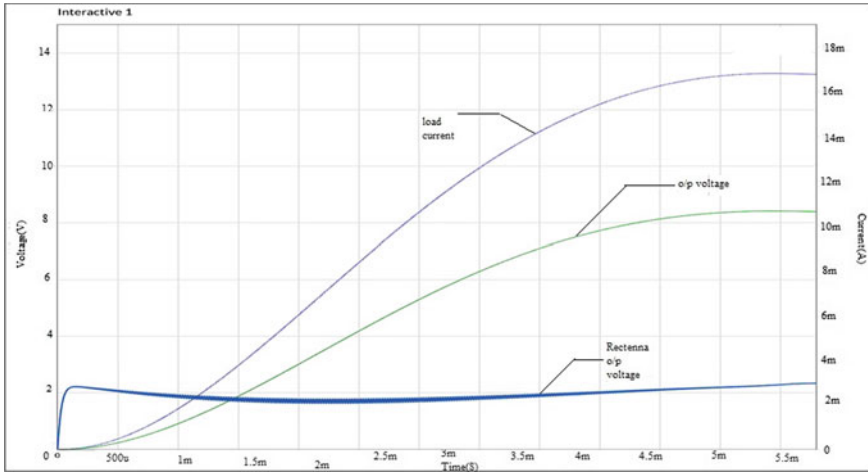


Fig. 10 Simulation results of RF harvester using flyback converter

3.1.3 Low Voltage RF Harvester Using Comparator

Figure 11 shows the block diagram of the RF harvester using comparator and the simulation results are shown in Fig. 12.

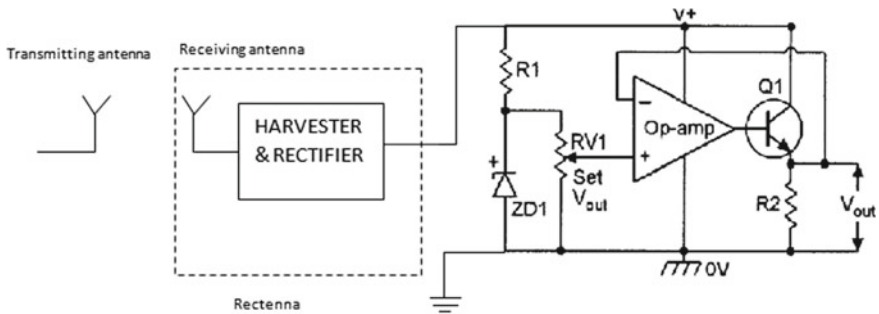


Fig. 11 Block diagram of RF harvester using comparator

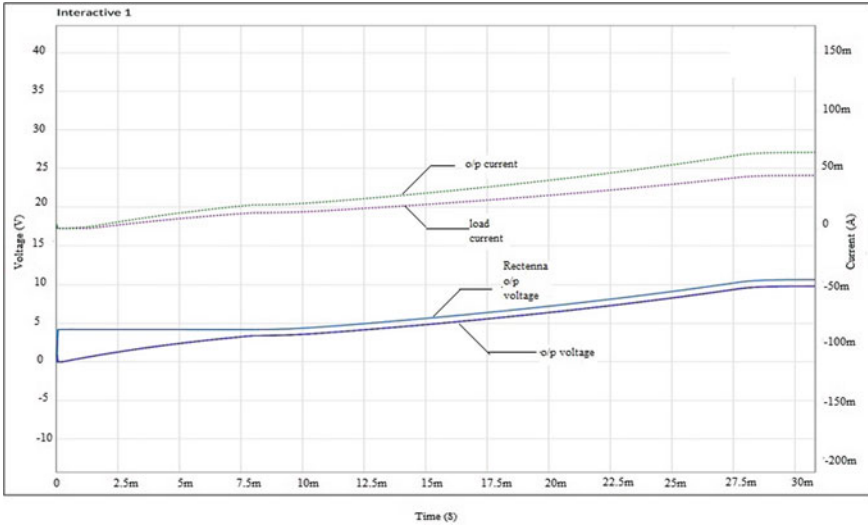


Fig. 12 Simulation results of RF harvester using comparator

3.1.4 Ultralow Voltage RF Harvester Using Diode Bridge Rectifier and Op-Amp

Figure 13 shows the block diagram of the RF harvester using diode bridge rectifier and op-amp and Fig. 14 shows the simulation results.

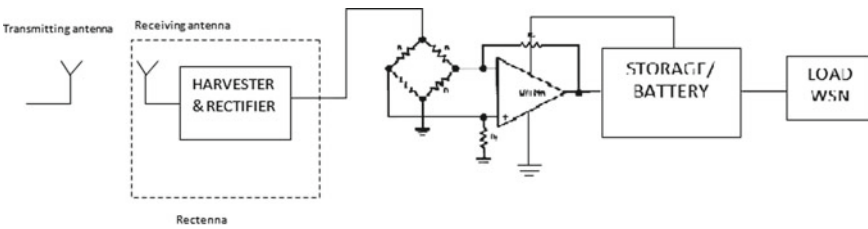


Fig. 13 Block diagram of RF harvester using diode bridge rectifier and op-amp

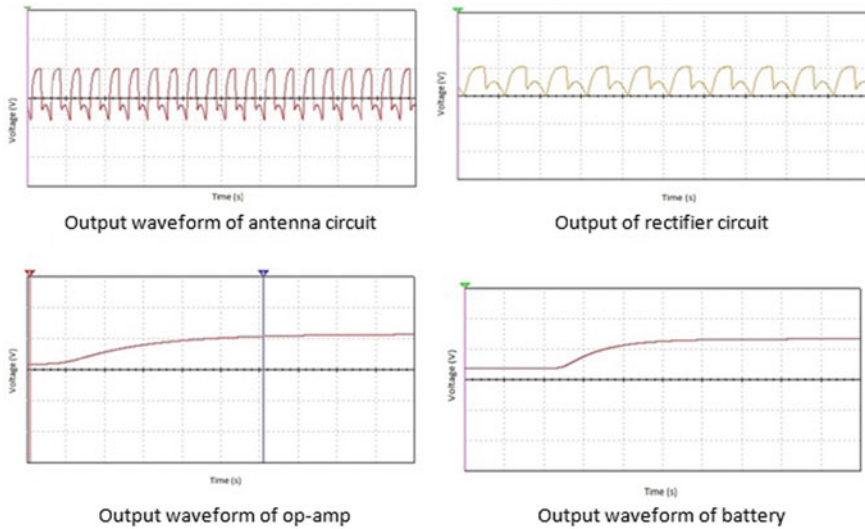


Fig. 14 Simulation results of RF harvester using diode bridge rectifier and op-amp

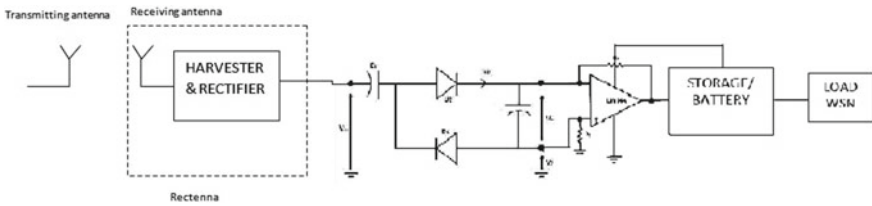


Fig. 15 Block diagram of RF harvester using double rectifier and op-amp

3.1.5 Ultralow Voltage RF Harvester Using Double Rectifier and Op-Amp

Figure 15 shows the simulation diagram of the RF harvester using double rectifier and op-amp, whereas the Fig. 16 shows the simulation results.

4 Results

Various topologies of RF harvesters were implemented and the outputs of those topologies were noted at load of 200Ω and at a frequency of 1 MHz, the input voltages range from 0.5 to 2 V. The comparison of all the RF harvester topologies was done and the values are tabulated.

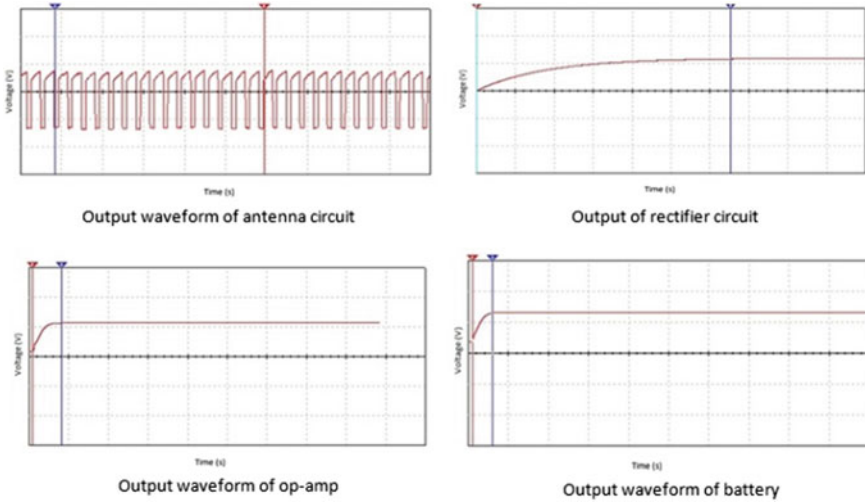


Fig. 16 Simulation results of RF harvester using double rectifier and op-amp

Table 1 Comparison of low voltage RF harvesters

Types of harvester topologies	Comparison parameters		
	Input voltage (V)	Output voltage (V)	Output current (mA)
Boost converter	2	6.25	31.2
Flyback converter	2	8.3	41.9
Comparator circuit	1.5	9.6	48.05

Table 2 Comparison of ultralow voltage RF harvesters

Types of harvester topologies	Comparison parameters		
	Input voltage (V)	Output voltage (V)	Output current (mA)
Bridge rectifier with op-amp	0.25	4.98	23.5
Double rectifier with op-amp	0.25	5.5	22.3

Comparison of Results of Various RF Harvesters

See Tables 1 and 2.

5 Conclusion

The RF harvesters have been developed and tested upon various parameters, and different topologies have been utilized and the results of these harvesters were obtained, and compared the results of different harvesters. The Schottky diodes were utilized

for better output because they can operate at high frequencies; with the help of Schottky diodes, desired output was achieved. The various harvesters were simulated at two different frequencies and at two different voltage levels and after performing the test, we have arrived upon the conclusion that for low voltage RF harvester, the comparator circuit is better than the other two harvesters, and for ultralow voltage RF harvesters, double rectifier with amplifier is better than that of the other harvester. Thus, the result is encouraging and represents a step forward in RF harvester technology.

References

1. Kuhn V, Lahuec C, Seguin F, Person C (2015) A multi-band stacked RF energy harvester with RF-to-DC efficiency up to 84%. *IEEE Trans Microw Theory Tech* 63:1768–1778
2. Zungeru AM, Ang LM, Prabakaran SRS, Seng KP (2012) Radio frequency energy harvesting and management for wireless sensor networks. In: *Green mobile devices and networks*. CRC Press, pp 341–368
3. Tran L-G, Cha H-K, Park W-T (2017) RF power harvesting: a review on designing methodologies and applications. *Micro Nano Syst Lett*
4. Rashid MH (2007) *Power electronics handbook*, 2nd edn. Academic Press Publications, USA
5. Masri S, Chan PW (2010) Design and development of a DC-to-DC boost converter with constant output voltage. In: *2010 international conference on intelligent and advanced systems*, pp 1–4
6. Michelon D, Bergeret E, Di Giacomo A, Philippe P (2016) RF energy harvester with sub-threshold step-up converter. In: *2016 IEEE international conference on RFID*
7. Cruz FRG, Chung W-Y, Sejera MM (2016) Efficiency comparison of voltage multiplier and boost converter topologies for radio frequency energy harvesting circuit using HSPICE

Backpropagation Algorithm-Based Approach to Mitigate Soiling from PV Module



Sujit Kumar  and Vikramaditya Dave 

Abstract Energy is viewed as a prime operator in the era of riches and a noteworthy figure of financial advancement. Constrained fossil assets and ecological issues connected with them have underscored the requirement for new manageable energy supply alternatives that utilize renewable energies. Among accessible innovations for vitality generation from sun-based source, photovoltaic framework could give a huge commitment to build up a more sustainable vitality framework. Utilization of solar energy has not been opened up since the oil industry does not possess the sun. The solar PV modules are for the most part utilized in dusty situations which is the situation in subtropical nations like India. Dust gets gathered in the front surface of the module and hinders the passage of light from the sun. It diminishes the power era limit of the module. The power yield decreases as by half if the module is not cleaned. Keeping in mind the end goal to routinely clean the dirt, a programmed cleaning framework has been designed that both detects the dirt on solar panels and cleans the surface of solar module consequently. The system consists of a panel with wiper and water ejector. Artificial neural network (ANN) sends the signal to the wiper motor with the help of measured data of solar irradiance, panel temperature, PV voltage, current, and power in both sunny/cloudy as well as dusty days. These data were well trained and tested along with the unknown data which were not involved in the training. Backpropagation (BP) algorithm was used to train the network, which showed the accuracy of 99% in data prediction and accordingly, generated the control signal for windshield wiper motor and wiped the dust.

Keywords Solar energy · Photovoltaic modules · Neural networks · Backpropagation

S. Kumar (✉)

Noida Institute of Engineering and Technology, Greater Noida 201306, India
e-mail: sujitvj.kumar@gmail.com

V. Dave

College of Technology and Engineering, Udaipur 313001, India

© Springer Nature Singapore Pte Ltd. 2020

A. Kalam et al. (eds.), *Intelligent Computing Techniques for Smart Energy Systems*,
Lecture Notes in Electrical Engineering 607,
https://doi.org/10.1007/978-981-15-0214-9_19

1 Introduction

The severe augment in global warming and lubricate rates have convinced numerous countries across the world to espouse novel energy policies that endorse renewable energy application to ensure energy demand and to guard the surroundings. The developed and developing countries are considering this fact and this has influenced the energy sectors greatly. Solar energy is getting its due place and is used for various applications which are replacing the cause of energy crisis. Moreover, solar energy is natural, copious, gratis, fresh, and limitless.

PV cells technology makes solar power very effortless and effective. Till now, the energy alteration proficiency of solar system has not reached a reasonable level so the researchers find new scope to research in this field.

“Soiling” alluded to particulate pollution on the glass surfaces of PV module. Ruining covers, soil gradual addition, sediment, salt, winged animal droppings, and development of natural species which unfavorably influence the performance of solar-based module.

Sand deposition is a multifaceted phenomenon and is prejudiced by various site-specific ecological and climatic conditions. One of the major challenges before the researchers is power loss caused by dust accumulation on the glass surfaces of solar panels.

However, there has been less research work done over the removal of dust from the solar panel. If adequate attention is put in the matter, the output efficiency will be increased by a huge amount. The main motive of this paper is to model a basic simulation model with adequate care to mitigate soiling from the PV panel using a smart intelligent technique.

2 Factors Influencing Dust Settlement

A structure to appreciate the assorted aspects that drive the settling–absorption of dust is adorned in Fig. 1. Globally soiling on solar panel surface is a huge problem. Sanaz Ghazi [1] inspected the areas of dirt accumulation in various parts of the world and it was proposed that the Middle East, North Africa, and some parts of Asia have the most horrible dust buildup region in the world. Zaki Ahmad [2] considered the consequence of dust contaminant type on panels. It was observed that diverse dust has diverse characteristics, like red soil, residue, carbon; granite, and clay have more noteworthy effect on PV. Juan Lopez-Garcia [3] studied the performance of PV modules by examining different properties of durable soiling, which have been installed in the open environment from last 30 years without washing in reasonable subtropical weather. It was found that the flat glass modules display a higher difference in soiling which weakens the competence of solar panel from 15 to 3%.

Solar power of two 1 MW PV plant was experimentally analyzed by Pavan Massi [4]. It was found that soil type and the washing are the two techniques that are

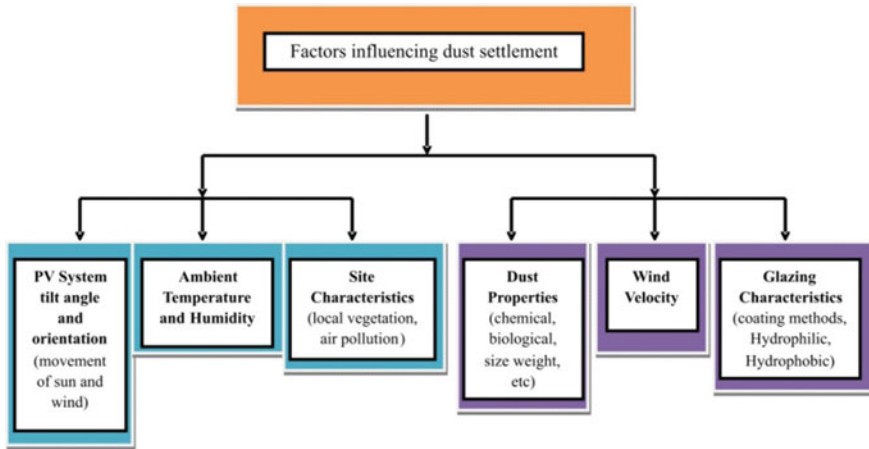


Fig. 1 Factors influencing dust settlement

strongly contingent on soiling. Loss of 6.9% was observed for the first plant built on a quite sandy site due to pollution, whereas, loss of 1.1% was observed for the second plant, constructed on an additional thick soil. Whitaker [5] examined the attainment of solar panel and establish that the reduction of soiling phenomena strongly depend on panel current and the voltage which depends on irradiance and array temperature.

The performance of selected PV system was simulated by Mayer [6] and concluded that the PV module temperature and the in-plane large-scale irradiance influences the output power.

From the above-detailed survey, it is cleared that the settling of dirt on solar panels diminish the efficiency based on the parameters like power, voltage, currents, array temperature, and solar irradiance. Therefore, to overcome this discrepancy there must be a cleaning method to precede the competence of the solar panels.

Halbhavi [7] designed an automatic cleaning system which senses the dust (using light dependent resistor (LDR) sensor) on the solar panel and also cleans the module automatically. This automated system is implemented using 8051 microcontroller which controls the DC gear motor. Cleaning the PV modules was carried out by a mechanism consisting of sliding brushes.

Cleaning techniques for PV surface has not focused on attention among the scientists. Figure 2 indicates diverse sorts of washing strategies which contain physical, programmed, and uninvolved techniques.

Every technique has its benefits and drawbacks, for example, common practice to clean windows of buildings is a labor-intensive (manual cleaning). A few brushes specifically fitted to a water supply to play out the washing and scouring at the same time. Unlikely, a stepping stool and a cleaner with long handle are expected to wash the board which is again a chaotic schedule and work increases. In the present time, artificial intelligence (AI) is one of the most acclaimed methods which can resolve the above issue.

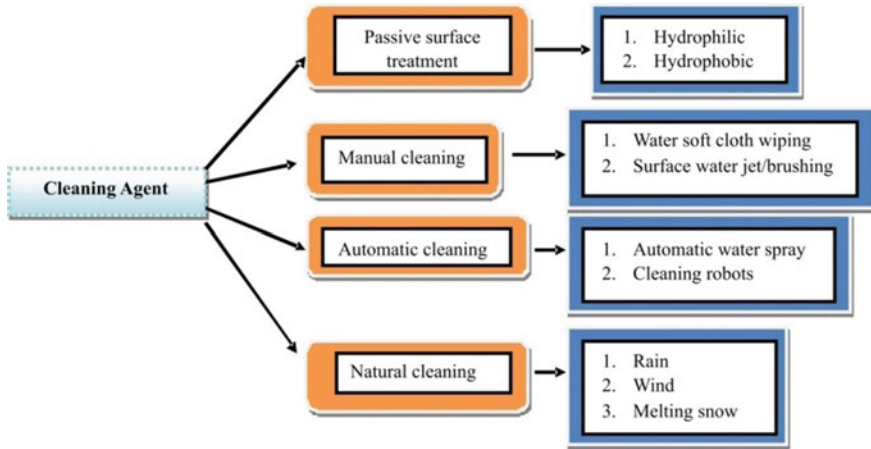


Fig. 2 Cleaning techniques adopted for expelling dust from solar panel

3 Training and Modeling of ANN

Transformative computations such as artificial neural networks (ANN), fuzzy systems, and their combination, along with other general machine learning methods and profound learning methods, e.g., clustering, classification, knowledge-based systems, case-based reasoning, decision-making methods, etc. are used as extensive range of AI techniques. Among these, ANN is being used from last 60 years, to grip practical problems, application software has been developed in early 30 years. Artificial neural network (ANN) controller is a standout among the most critical strategies for the estimation of non-straight frameworks [8, 9].

ANN utilizes distinctive training algorithms like backpropagation (BP), Levenberg Marquardt (LM), radial basis function (RBF), etc. Among these BP algorithm is superior to other algorithms due to its less union time and precision. Fundamentally, the backpropagation neural network (BPNN) is a multilayer perceptron network (MLP) with error backpropagation algorithms [10]. BP algorithm comprise of a three-layer feed-forward perceptron neural network architecture which has an input, a hidden, and an output layer and each layer has several independent neurons as (1). In particular, BP-NN requires the activation function to be continuously differentiable

The three stages of network, learning process are shown below [10]:

- Forward propagation stage. It is corresponding to MLP and develops a set of output signal based on the input.
- Backpropagation error stage. Initially, the error between the output signal and the ideal value in the output layer is calculated. Then the error propagates backward layer by layer.
- Update weight stage. The weight matrix of each layer is attuned based on the error which is in the accordance of gradient descent principle.

Figure 3 demonstrates the ANN model of the total framework system which comprises PV module associated with a load of 200 W. In the present experiment, data from the solar panel has been measured in the form of panel current, voltage, temperature, solar irradiance, and power in bright and hazy days with and without dirt. Panel consists of windshield wiper with a small jet which injects water at the time of wiping the dust from the panel. The supply to the windshield wiper motor gets from the solar panel itself after being getting a control signal from the ANN. An example has been illustrated in Table 1. The system gets the exterior data, calibrates

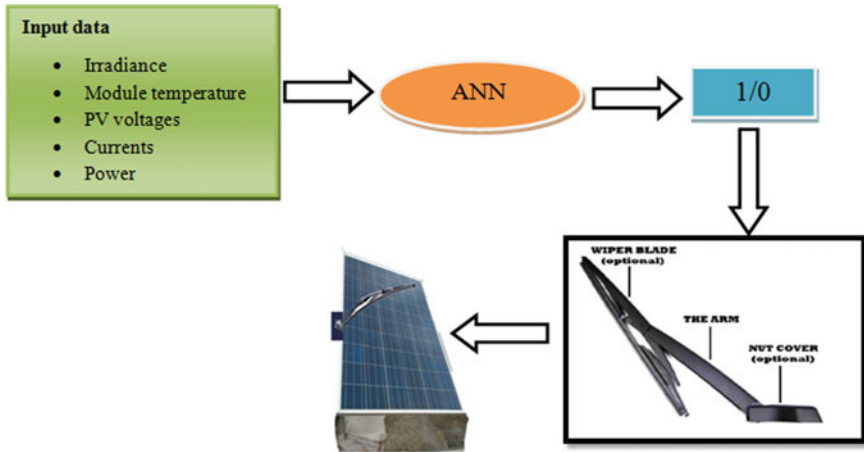


Fig. 3 Schematic diagram of ANN controlled PV system

Table 1 Data of different types of days measured from solar panels

Type of day	Time (a.m/p.m)	Voltage (V)	Currents (A)	Power (W)	Solar irradiance (W/m ²)	Module temperature (°)
Bright	12:00 p.m	18.71	7.6	142.2	764	48.68
Bright	1:00 p.m	22.83	8.1	185	1000	57.50
Bright	11.30 a.m	13.85	6.6	91.47	465	43.10
hazy	11:00 a.m	9.39	3.1	29.125	151	24.40
hazy	12:00 p.m	13.10	2.9	38	199	27.20
hazy	11:30 a.m	12.6	4.5	56.72	276	31.20
Dusty bright	11:00 a.m	12.97	2.59	33.65	564	46.10
Dusty bright	12:00 p.m	13.5	3.15	42.63	793	46.40
Dusty hazy	12:30 p.m	10.97	2.80	30.72	276	39.40

it by weights and relays it to following layer with the help of neurons. Tan sigmoid activation function is being used for input and hidden layer neurons while pure linear activation function is being used for output layer neurons.

Input to the ANN are PV array parameters; PV voltages (V_{pv}), currents (I_{pv}) and power (P) and environmental data: irradiance (G) and module temperature (T) (comprises five data) which is then trained to evaluate the performance of the ANN model. The output layer has a single-output node which is either one or zero. One denotes the dust is collected over the module which then produces the signal to wiper motor to wash the panel and zero denotes no settlement of dirt over the module.

4 Results and Discussion

Miscellaneous models are assessed and the best one is picked by experimentation. The best option comprises 5 neurons in the input layer, 30 in the hidden layer, and 1 neuron in the output layer as illustrated in Fig. 4. The following sub-database was extracted from the data set described above.

- Inputs to the ANN were (T , G , P , V_{pv} , and I_{pv}) arranged to meet the circumstance as standard; each day solar emission is lower or higher than $1000 \text{ W/m}^2/\text{day}$ (dark or clear days with and without dirt). There were 5365 samples as sub-database. In training stage, to solve over the fitting problem 10% cross-validation method is used, whereas, for training the network 80% of samples used, 10% utilized to validate the network, and 15% utilized for test process.

To equitably assess the performance of the systems, four diverse factual markers were utilized. These markers are mean absolute error (MAE), mean squared error

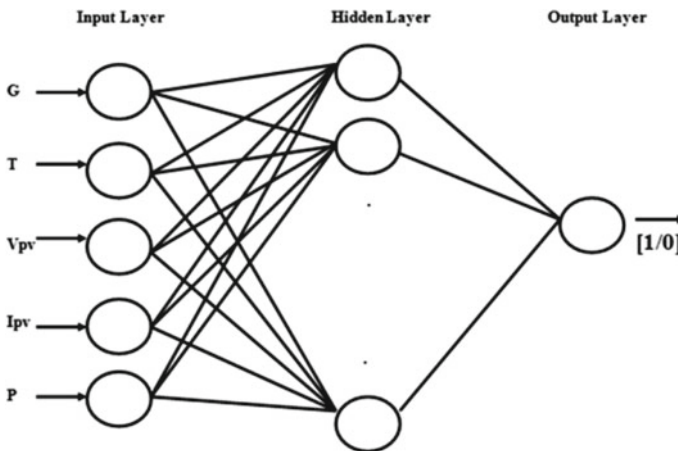


Fig. 4 Projected architecture for ANN

(MSE), and mean absolute percentage error (MAPE):

$$MAE = \frac{1}{n} \sum_{i=1}^n |Y_{\text{predicted}} - Y_{\text{true}}| \tag{1}$$

$$MSE = \frac{1}{n} \sum_{i=1}^n (Y_{\text{predicted}} - Y_{\text{true}})^2 \tag{2}$$

$$MAPE = \frac{1}{n} \sum_{i=1}^n \left| \frac{Y_{\text{predicted}} - Y_{\text{true}}}{Y_{\text{true}}} \right|^2 \tag{3}$$

where $Y_{\text{predicted}}$ and Y_{true} are estimated and measured dust values over panels by the models, respectively. Among the above factual measures, MAPE is the most critical measurable quantity in that it mentions utilization of every single objective reality and has the smallest fluctuation from sample to sample. Variety of users easily understands MAPE, so it is frequently utilized for reporting [11]. However, MSE will also be used for performance analysis as based on this the optimum number of neurons in hidden layer will be decided. Here, MSE parameter is used to stop the training process and results are shown in Fig. 5.

The accompanying parameters are placed through training our ANN model:

Training pattern = 5365 samples, learning rate = 0.001, set error objective = 0.01, number of epochs = 100, momentum = 0.95.

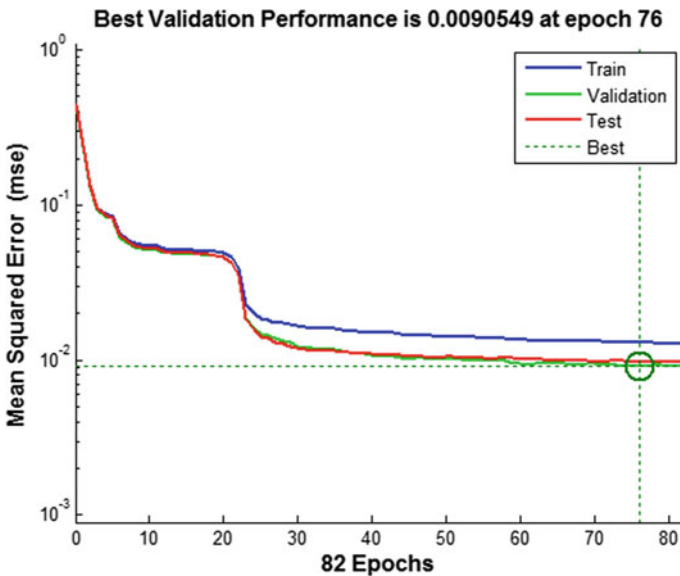
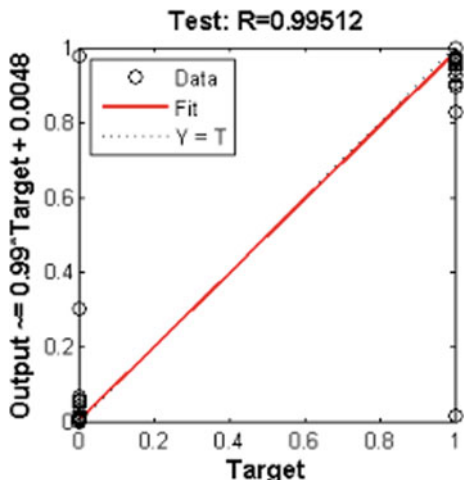


Fig. 5 Training results of ANN with evolution of the performance

Fig. 6 Test phase performance of ANN model



The ANN generates the signal only when the panel is accumulated by dust as the data provided in the input was having dust data in both dusty and cloudy days. ANN model was tested with the other data which were not included in the training set to ensure that the prediction of dust by the ANN is fulfilling or not. Mean square error (execution goal = 9.05×10^{-2}) is achieved which is well below the set objective in 100 epochs as shown in Fig. 5. The validation showed the accuracy of trained ANN model uses other data which were not used in the training and the mean square error observed for the validation was 8.4968×10^{-3} which was less than the set error objective.

Figure 6 shows results of tested network using whole dataset. $1.00052e-3$ is obtained as network test error and $9.98791e-1$ is obtained as regression coefficient (R). Regression coefficient tells about how well our data has been classified and fit to the actual data. MAPE of the ANN model is found to be below 0.5% and in this way taking into report the accuracy in the estimation of solar irradiance, module temperature, current, voltage, and misfortunes in association wires, which is roughly 0.5%, consequently, on the whole error is around 1%.

5 Conclusion

Automatic washing with smart intelligent technology proved to be more economic and significantly less cumbersome when compared to manual operation, particularly in systems having large number of solar panels. Trouble-free ANN model has been simulated that generates the signal to the motor operating wiper over the occurrence of dust over solar panel of 250 Wp polycrystalline PV modules.

From the results presented, it can be concluded that ANN has capability to effectively predict the dust data with an accuracy of 99% and successfully operated the

wiper which wipes the panel. The approval too included investigation of the adequacy of the trained data when copying with obscure information, i.e., data which are not included in the training. This proves the system has high robustness when compared to other techniques.

References

1. Ghazi S, Sayigh A, Ip K (2014) Dust effect on flat surfaces—a review paper. *Renew Sustain Energy Rev* 742–751
2. Darwish ZA, Kazem HA, Sopian K, Al-Goul M, Alawadhi H (2015) Effect of dust pollutant type on photovoltaic performance. *Renew Sustain Energy Rev* 735–744
3. Lopez-Garcia J, Pozza A, Sample T (2016) Long-term soiling of silicon PV modules in a moderate subtropical climate. *Sol Energy* 174–183
4. Massi Pavan A, Mellit A, De Pieri D (2011) The effect of soiling on energy production for large-scale photovoltaic plants. *Sol Energy* 1128–1136
5. Whitaker CM, Timothy U, Townsend TU, Newmiller JD, King DL, Boyson WE, Kratochvil JA, Collier DE, Osborn DE (1997) Application and validation of a new PV performance characterization method. In: Twenty-sixth IEEE photovoltaics specialist conference and exhibition, Anaheim, California, USA, pp 1253–1256
6. Mayer D, Wald L, Poissant Y, Pelland S (2008) Performance prediction of grid-connected photovoltaic systems using remote sensing. Report IEAPVPST, pp 18–26
7. Halbhavi SB, Kulkarni SG, Kulkarni DB (2015) Microcontroller based automatic cleaning of solar panel. *Int J Latest Trends Eng Technol (IJLTET)* 99–103
8. Dzung PQ, Phuong LM, Vinh PQ, Van Nho N, Hien DM (2006) The development of artificial neural network space vector PWM and diagnostic controller for voltage source inverter. In: IEEE power India conference, New Delhi, India, pp 10–12
9. Dzung PQ, Phuong LM, Vinh PQ (2007) The development of artificial neural network space vector PWM for four-switch three-phase inverter. In: International conference on power electronics and drive systems—IEEE PEDS 2007, Thailand, 27–30 Nov 2007
10. Cheng T-R, Li Y (2016) Research status of artificial neural network and its application assumption in aviation. In: 12th international conference on computational intelligence and security, pp 407–410
11. Celik AN (2007) Artificial neural network modeling and experimental verification of the operating current of mono-crystalline photovoltaic modules. *Sol Energy* 2507–2517

Real-Time Low-Frequency Oscillations Monitoring and Coherency Determination in a Wind-Integrated Power System



Abhilash Kumar Gupta, Kusum Verma and K. R. Niazi

Abstract With the increase of renewables in the generation mix, the problem of low-frequency oscillations (LFOs) further escalates in modern power systems. This paper proposes a method for LFO modes monitoring and coherency identification using Phasor Measurement Units (PMUs) and Artificial Neural Network (ANN) in real time for a high wind-penetrated power system. The data for ANN training and testing is obtained from PMUs that are placed optimally in the system for complete system observability. The synchronously sampled PMU data is dimensionally reduced using Principal Component Analysis before using it to train the ANN. The proposed approach is verified on the IEEE New England benchmark system. The results obtained validate the effectiveness of the proposed approach in predicting system damping and coherency status with very less computational burden under varying operating conditions.

Keywords Artificial neural network · Generator coherent groups · Low-frequency modes · Phasor Measurement Unit · Real-time analysis

1 Introduction

In recent years, the problem of low-frequency oscillations (LFOs) occurrence in power systems is becoming more and more important. This is, among other things, due to the rapid development of wind farms. This growing wind integration with very less or no inertia further complicates the stable power system operation. The presence

A. K. Gupta (✉) · K. Verma · K. R. Niazi
Department of Electrical Engineering, Malaviya National Institute of Technology, Jaipur, India
e-mail: abhidec91@gmail.com

K. Verma
e-mail: kverma.ee@mnit.ac.in

K. R. Niazi
e-mail: krm152001@yahoo.co.in

© Springer Nature Singapore Pte Ltd. 2020
A. Kalam et al. (eds.), *Intelligent Computing Techniques for Smart Energy Systems*,
Lecture Notes in Electrical Engineering 607,
https://doi.org/10.1007/978-981-15-0214-9_20

of any critical or poorly damped mode should be visible in real time to undertake the required control measure. Therefore, to identify impending oscillatory instability in real time, fast and accurate monitoring approaches need to be developed.

The modal analysis [1] is one of the most employed and conventional techniques for modes identification but requires large computation for large systems and is performed offline. Numerous time-domain simulations are needed to properly identify all the LFOs using response-based methods [2]. The authors in [3] presented an index that reports the relative variations in oscillation characteristics with varying operating scenarios. However, in this study, the author carried out the offline study and did not take the system configuration changes into account. In [4], the damping status of various LFOs present in the system is found out using classification trees which help in the application of control methodology in time. The Artificial Neural Network (ANN)-based techniques [5] with appropriate feature set prove to be more effective and accurate and can provide results at higher speeds for such real-time applications. ANN training usually requires generation of lots of operating scenarios and this is a time-taking process. The training efficiency could be increased by using some appropriate feature-reduction techniques to reduce the data size.

The coherency of synchronous generators is usually calculated on the basis of generator swing following any disturbance and thus can be determined along with the oscillation monitoring procedure. Coherency information can play an important role in the application of wide-area-based control methods like controlled islanding [6, 7]. The coherent group of generators are mostly found offline in literature. However, the changing operating conditions may alter the coherent groups of generators and thus it should be determined within a few cycles of disturbance. The authors in [8–12], use different methods for coherency identification like PCA [8], ICA [9], continuation method [10], method based on indices [11], and SVC [12]. However, most of them have been employed for offline and online detections. Some studies determined it in real time [6, 7, 13, 14] but required long durations post-disturbance data. Therefore, further investigations are needed to explore a computationally efficient method which requires less duration data to obtain coherency in real time.

The penetration of wind power is increasing rapidly in the generation mix with Doubly Fed Induction Generator (DFIG) being used prominently [15]. The dynamic interaction between DFIG and synchronous generators, and change in the power flow pattern and system topology causes variations in modes damping [16]. The literature suggests both positive and negative impacts of DFIG integration on modes damping [15–18]. The DFIGs are integrated either by replacing the existing synchronous generators (SG) or by adding them directly to non-generator buses. As the current requirement is to meet the load growth, in most of the practical scenarios, DFIGs are integrated without replacing SGs [18]. The location of DFIG also affects the damping of LFO modes in the system. In this paper, wind is integrated as suggested in [18].

The oscillation monitoring in real time however requires the availability of various system parameters to the operators in real time. Nowadays, Phasor Measurement Units (PMUs) are available which provide the required wide-area measurements to the operator [19]. This helps in dealing with the LFO problem more effectively. It is

unfeasible to install PMUs at every system bus because of their high installation cost and communication requirements. So, the optimal placement of PMUs is executed using various conventional and heuristic techniques as suggested in [20, 21]. Earlier, only system topology is considered while placing PMUs in the system. However, considering system behaviour and purpose of deployment is equally important [22].

In this paper, a method based on PMU and ANN is proposed for real-time oscillation monitoring using an index and coherent group identification in the power system. The suggested method makes use of only first four cycles of post-disturbance synchronously sampled data of bus voltage magnitude and angles. These measurements are obtained from optimally placed PMUs. The DFIGs are placed at non-generator buses while ensuring damping improvement of the modes. The data received from PMUs is dimensionally reduced using PCA. This reduced dimension data is provided as input to ANN and outputs are damping index and generator coherent groups. Two ANNs are trained for predicting the coherency and damping status of the system. The results obtained from these two architectures are then compared. This information is of great importance to system operators especially with the increased penetration of wind power in the generation mix. The proposed work is based on the findings of some earlier work [23, 24] by the same authors.

2 Problem Formulation

2.1 Damping Index (DI)

To observe the impact of disturbances on the LFOs damping, damping index has been used in this study [3]. This index gives information about the damping status of each mode and thus the overall oscillatory stability of the system. For a particular mode, value of DI is given by

$$DI = \begin{cases} \min\left(1, \left(\frac{\zeta}{\zeta_{\min}}\right)^{-n}\right), & \text{if } \zeta > \zeta_{\text{abs}} \\ 1, & \text{if } \zeta \leq \zeta_{\text{abs}} \end{cases} \quad (1)$$

where ζ_{\min} is minimum damping threshold below which the system becomes critical, n is index norm and ζ_{abs} is absolute damping limit below which system becomes oscillatory unstable. The minimum damping limit varies with the system in hand and is usually around 3–5% [3]. In this study, the limit is taken as 5%. The range of DI values is 0–1. DI is ‘0’ when $\zeta = 100\%$ and ‘1’ when $\zeta = \zeta_{\min}$. If $DI < 1$, it means modes are damped and the system is oscillatory stable; otherwise it is critical or small-signal unstable. The index is sensitive to the changing operating scenarios. The norm value decides the index sensitivity. In this study, the value of the norm is 1.475.

2.2 Coherent Groups Determination

The synchronous generators are grouped coherently on the basis of separation between the machine rotor angles and the inertial centre. This can be calculated as

$$\delta_{j,\text{COI}} = |\delta_j - \delta_{\text{COI}}| \text{ for } j = 1 \text{ to } N_G \quad (2)$$

where δ_j is the machine rotor angle and δ_{COI} is the angle of inertial centre for an N_G generator system. This grouping when available in real time can be employed for the implementation of emergency control actions.

3 Proposed Methodology

3.1 Optimal PMU Placement

The PMUs are placed optimally in this work using Integer Linear Programming (ILP) [25]. The ILP is further modified to include different criteria to ensure the observability of buses critical to oscillations monitoring. There are certain critical buses that are required to be monitored all the time for oscillation monitoring purposes. Such buses are found out using different criteria as suggested in [26]. Also, the system should be completely observable in the case of single line or PMU outage. So, these two conditions are included in the ILP approach to obtain the required optimal number and position of PMUs in the system. The effect of zero injection buses (conventional measurements) is also considered. The detailed description of the approach followed can be referred from [26].

3.2 Wind Site Selection

As found out from the literature survey, the location of DFIG does effect the modes damping in the system and thus they cannot be placed randomly even in large wind-abundant regions for proper impact analysis studies. So, in this work, the DFIGs are placed based on the locations obtained after proper impact analysis studies are performed using eigenvalue analysis and dynamic sensitivity analysis as suggested in [18]. The most beneficial locations with respect to system oscillatory stability are determined for placing the DFIGs using this analysis. The detailed discussion on this procedure is out of scope for this paper and can be referred from [18].

3.3 Proposed PMU-ANN Based Method

The coherency information at some preferred future time instant and *DI* values are predicted using the proposed study in real time for a high wind-penetrated power system. The initial few cycle's data after the disturbance is utilized for this process which carries sufficient information about the system and is obtained using the optimally placed PMUs in the system. The dimensionally reduced PMU output is used as input to ANN that provides the required LFO mode information at the output. The block diagram of the proposed methodology is shown in Fig. 1. The proposed approach involves optimal PMU placement, DFIG site selection, data generation, data dimension reduction using PCA, selection of ANN architecture, and then ANN training and testing. The important steps are described below:

1. *Data Generation*: The system load is varied randomly in addition to line outages for generating the pattern vector for ANN training and testing. The measurements of the first four cycles of bus voltage magnitude and angles are stored for each case.
2. *Dimension reduction*: Out of all the variables, the unimportant ones are removed using PCA. This dimensionally reduced data is then normalized, shuffled and divided by a ratio of 60:40 for training and testing the ANN, respectively.
3. *ANN architecture*: In this work, Feed-Forward Neural Network (FFNN) and Radial Basis Function Neural Network (RBFNN) have been employed for predicting the damping status and coherency information and their results have been compared. The input vector consists of the first four cycles of post-disturbance data of bus voltage magnitude and angles after dimension reduction which are given by

$$[y_i] = [|V|, \angle V] \tag{3}$$

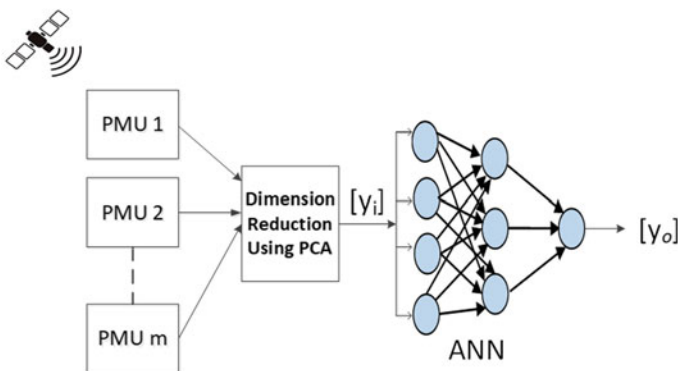


Fig. 1 Block diagram for the proposed approach

The output vector consists of values of DI , and frequency and damping ratio of LFO modes are predicted using a single ANN, given by

$$[y_o] = [DI_i, CG_j] \tag{4}$$

where DI_i, CG_j denotes DI for each i th mode and coherent group information for each j th generator.

4 Results

The proposed strategy is tested on IEEE 39-bus benchmark system which is an adaptation of the real New England system having abundant wind resource and thus suitable for such studies. The system data can be referred from [27]. The system is modified to add two wind farms at bus no. 9 and 27. The DFIGs' locations affect the LFOs damping and thus the DFIGs are not placed randomly. The DFIGs' locations are determined using the procedure explained in [18]. The total active power production is $P_G = 6138.71$ MW. The total wind penetration is taken as 25% in this study, so each wind farm is of 768 MW. The system load is increased by the same quantity as wind penetration to maintain the load-generation balance. The modified 39-bus test system is shown in Fig. 2.

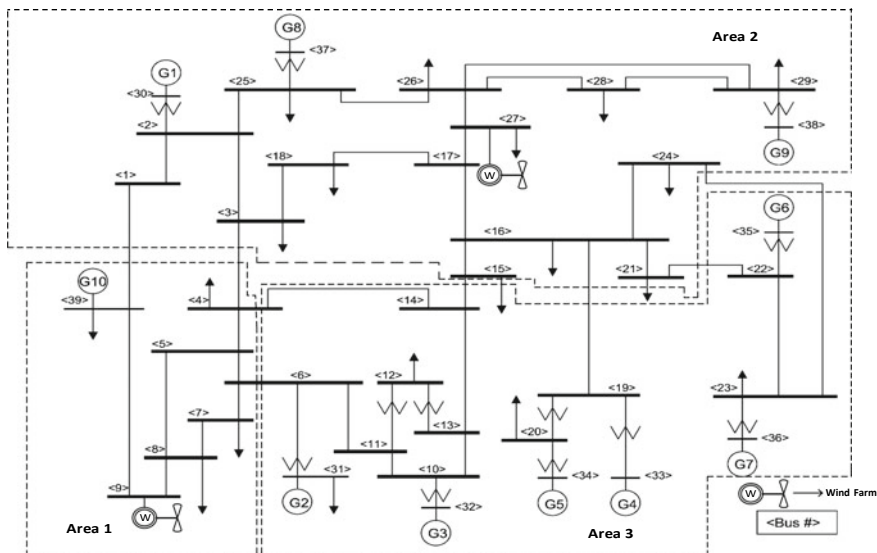


Fig. 2 Modified IEEE 39-bus test system

Table 1 Optimal PMU placement result

No. of PMUs	PMU locations (bus no.)
20	3, 5, 6, 9, 10, 13, 16, 18, 19, 20, 22, 23, 25, 26, 29, 34, 36, 37, 38, 39

4.1 Optimal PMU Placement

The optimal PMU placement has been performed for wide-area oscillation monitoring purpose as explained in the previous section. The result showing the PMUs bus locations is given in Table 1. The number of PMUs required came out to be 20. With this placement, the system remains observable even in the case of single line outage or PMU loss. Thus, the proposed method reduces the PMU number to around 50% of the system buses.

4.2 Proposed Real-Time Monitoring

The system load is varied in the range of 100–110% of the base case with a step of 2.5%. The topological variations are considered in the form of single line outages. For all the scenarios, the values of the damping index are stored. Also, the rotor angle values of generators at some specific future time (after 3 s in this study) are measured to find out the coherent grouping information. A pattern vector of 2500 cases is generated; out of these, 1500 are used for ANN training and 1000 for testing purpose. The first four cycles' data of voltage magnitudes and angles after the disturbance is collected from 20 PMU buses. So, there are 160 ($20 \times 4 \times 2$) variables recorded for ANN input in each case. As the number of variables is very high, dimensionality reduction is performed using PCA. The PCA reduced the number of input variables to 18, giving a dimensionality reduction of 88.75% with an approximation precision of 0.9992. This data is then used to train the ANNs after normalizing and shuffling.

In the base case, the system has eight modes, seven local and one inter-area mode. Both the ANNs are tested for several unseen operating conditions and a few sample cases are presented in Tables 2 and 3 showing the results of *DI* and coherent group's prediction, respectively. It can be seen from Table 2 that the *DI* predicted by both the ANNs is very close to the actual values and the system is correctly identified as insecure in both the cases. The inter-area mode is having damping less than 5% in both scenarios. For the same sample cases, coherent groups predicted using the proposed method are shown in Table 3. Both the ANNs predict the correct grouping information. In case I, six groups are formed whereas in case II, four coherent groups are there. This clearly shows that coherent groups change with system operating conditions and need to be evaluated in real time for proper implementation of control actions.

The performance evaluation of both the neural networks is shown in Table 4. It can be seen from the result that the MSE is very less for both training and testing

Table 2 DI_i results for sample cases

Operating condition no.	Loading in % of base case	Mode number	Modal analysis	PMU-ANN based method		
				Damping index (DI_i)		System status
			Damping index (DI_i)	FFNN	RBFNN	
1454 (case I)	110% (line outage of 14–15)	1	0.5021	0.4955	0.4981	Insecure
		2	0.6783	0.6780	0.6770	
		3	0.5375	0.5453	0.5415	
		4	0.6885	0.6844	0.6854	
		5	0.3331	0.3467	0.3340	
		6	0.4009	0.3948	0.3961	
		7	0.3579	0.3599	0.3644	
		8	1.0000	1.0018	0.9977	
1662 (case II)	102.5% (line outage of 21–22)	1	0.3821	0.3794	0.3775	Insecure
		2	0.6718	0.6771	0.6637	
		3	0.4683	0.4725	0.4658	
		4	0.7949	0.7859	0.8073	
		5	0.5100	0.5099	0.4914	
		6	0.2837	0.2754	0.2751	
		7	0.4119	0.4096	0.4061	
		8	1.0000	1.0035	0.9986	

Table 3 Coherency results for sample cases

Sample case no.	Actual coherent groups (generator no.)	Predicted coherent groups	
		FFNN	RBFNN
Case I	(1, 10), (2, 3), (4, 5, 7), (6, 8, 9)	(1, 10), (2, 3), (4, 5, 7), (6, 8, 9)	(1, 10), (2, 3), (4, 5, 7), (6, 8, 9)
Case II	(1), (2, 3), (4, 8, 9), (5), (6, 7), (10)	(1), (2, 3), (4, 8, 9), (5), (6, 7), (10)	(1), (2, 3), (4, 8, 9), (5), (6, 7), (10)

Table 4 Performance comparison of FFNN and RBFNN

Parameters	FFNN	RBFNN
Training time (s)	257.8071	74.0141
Prediction time/sample in testing (s)	1.077×10^{-4}	1.188×10^{-4}
Mean squared error (training)	0.0022	0.0017
Mean squared error (testing)	0.0029	0.0044

phase for both the ANNs. Even for unforeseen conditions, the error is nearly 0.29% for FFNN and 0.44% for RBFNN that is a reasonably acceptable prediction error. Also, the average prediction time for every operating state is of the order of 10^{-4} s which is almost real time, which makes them suitable for online and real-time applications. It is seen from the results that the performance of both networks is nearly the same. However, FFNN performs slightly better than RBFNN as MSE is lower and the testing time per sample is also less. Thus, it can be concluded from these results that both the ANNs give good performance in predicting *DI* values and generator coherency, and any one of these can be utilized while implementing this method for real-time applications.

5 Conclusion

This paper presents a PMU-ANN based technique to forecast the modes damping and generator coherency in real time for a high wind-integrated system. The PMUs are placed optimally in the system using a modified ILP method so as to ensure continuous oscillation monitoring of the system even under single line outage or PMU loss. The proposed method is tested on IEEE 39-bus benchmark system. The proposed technique requires very less duration post-disturbance data for predicting the coherency information. The ANNs employed give very small MSE and average prediction time per sample for all unseen operating scenarios involving topological variations. The computational requirement of the proposed method is also very less. The test results validate the suitability of this method for real-time and online applications. The proposed approach thus can be employed for implementing emergency control methods which require coherency information in real time.

References

1. Roger G (2000) Power system oscillations. Kluwer, Norwell, MA, USA
2. Huang H, Xu Z, Hua W (2013) Estimation of interarea modes in large power systems. *Int J Electr Power Energy Syst* 53:196–208
3. Kerin U, Lerch E, Bizjak G (2010) Monitoring and reporting of security of power system low-frequency oscillations. *Electr Power Compon Syst* 38(9):1047–1060
4. McNabb P, Wilson D, Bialek J (2013) Classification of mode damping and amplitude in power systems using synchrophasor measurements and classification trees. *IEEE Trans Power Syst* 28(2):1988–1996
5. Hassan LH, Moghavvemi M, Almurib HA, Steinmayer O (2013) Current state of neural networks applications in power system monitoring and control. *Int J Electr Power Energy Syst* 51:134–144
6. Gomez O, Rios MA (2015) Real time identification of coherent groups for controlled islanding based on graph theory. *IET Gener Transm Distrib* 9(8):748–758
7. Siddiqui SA, Verma K, Niazi KR, Fozdar M (2018) Real-time monitoring of post-fault scenario for determining generator coherency and transient stability through ANN. *IEEE Trans Ind Appl* 54(1):685–692

8. Anaparthi KK, Chaudhuri B, Thornhill NF, Pal BC (2005) Coherency identification in power systems through principal component analysis. *IEEE Trans Power Syst* 20(3):1658–1660
9. Ariff MAM, Pal BC (2013) Coherency identification in interconnected power system—An independent component analysis approach. *IEEE Trans Power Syst* 28(2):1747–1755
10. Wang X, Vittal V, Heydt G (2005) Tracing generator coherency indices using the continuation method: a novel approach. *IEEE Trans Power Syst* 20(3):1510–1518
11. Verma K, Niazi KR (2013) A coherency based generator rescheduling for preventive control of transient stability in power systems. *Int J Electr Power Energy Syst* 45(1):10–18
12. Agrawal R, Thukaram D (2013) Support vector clustering-based direct coherency identification of generators in a multi-machine power system. *IET Gener Transm Distrib* 7(12):1357–1366
13. Lin Z, Wen F, Ding Y, Xue Y (2017) Wide-area coherency identification of generators in interconnected power systems with renewables. *IET Gener Transm Distrib* 11(18):4444–4455
14. Wei J, Kundur D, Butler-Purry KL (2015) A novel bio-inspired technique for rapid real-time generator coherency identification. *IEEE Trans Smart Grid* 6(1):178–188
15. Quintero J, Vittal V, Heydt GT, Zhang H (2014) The impact of increased penetration of converter control-based generators on power system modes of oscillation. *IEEE Trans Power Syst* 29(5):2248–2256
16. Jafarian M, Ranjbar AM (2013) Interaction of the dynamics of doubly fed wind generators with power system electromechanical oscillations. *IET Renew Power Gener* 7(2):89–97
17. Gupta AK, Verma K, Niazi KR (2017) Dynamic impact analysis of DFIG-based wind turbine generators on low-frequency oscillations in power system. *IET Gener Transm Distrib* 11(18):4500–4510
18. Gupta AK, Verma K, Niazi KR (2017) Impact analysis of DFIG location on low-frequency oscillations in power system. *J Eng* 2017(13):1413–1417
19. Aminifar F, Fotuhi-Firuzabad M, Safdarian A, Davoudi A, Shahidehpour M (2015) Synchrophasor measurement technology in power systems: panorama and state-of-the-art. *Access IEEE* 2:1607–1628
20. Nazari-Heris M, Mohammadi-Ivatloo B (2015) Application of heuristic algorithms to optimal PMU placement in electric power systems: an updated review. *Renew Sustain Energy Rev* 50:214–228
21. Manousakis NM, Korres GN, Georgilakis PS (2012) Taxonomy of PMU placement methodologies. *IEEE Trans Power Syst* 27(2):1070–1077
22. Kumar VSS, Thukaram D (2016) Approach for multistage placement of phasor measurement units based on stability criteria. *IEEE Trans Power Syst* 31(4):2714–2725
23. Gupta AK, Verma K, Niazi KR (2018) Power system low frequency oscillations monitoring and generator coherency determination in real time. In: *International conference on innovative smart grid technologies—Asia*, pp 1–6. IEEE, Singapore
24. Gupta AK, Verma K, Niazi KR (2018) Wide-area PMU-ANN based monitoring of low frequency oscillations in a wind integrated power system. In: *8th India international conference on power electronics*, pp 1–6. IEEE, Jaipur, India
25. Gou B (2008) Generalized integer linear programming formulation for optimal PMU placement. *IEEE Trans Power Syst* 23(3):1099–1104
26. Gupta AK, Verma K, Niazi KR (2017) Contingency constrained optimal placement of PMUs for wide area low frequency oscillation monitoring. In: *7th international conference on power systems*, pp 1–6. IEEE, Pune, India
27. IEEE (2015) Benchmark systems for small-signal stability analysis and control. *IEEE PES*, pp 66–72

Design and Performance Analysis of Different Structures of MEMS PVDF-Based Low-Frequency Piezoelectric Energy Harvester



Namrata Saxena, Varshali Sharma, Ritu Sharma, K. K. Sharma and Santosh Chaudhary

Abstract This paper presents the performance comparison of two cantilever structures (Straight-T shaped and Pi-shaped) that can be utilized for piezoelectric energy harvesting (PEH) application. For proper selection of the material, a comparison is made among different piezoelectric materials and it is observed that for achieving low-frequency operation, high flexibility, high thermal stability, outstanding chemical resistance, and finally, for environment sustainability, polyvinylidene fluoride (PVDF) is a better alternative than PZT. PVDF proved to be a better alternative for the MEMS devices to be used for structural health detection and for portable medical applications. All cantilever structures discussed in this paper are designed using the same materials, i.e., PVDF as the piezoelectric layer, single crystal silicon for the structural layer and the proof mass, and gold as the top and bottom electrode. All the designed structures discussed in this paper have the same thicknesses for these layers. Their performances are evaluated on the basis of parameters such as resonant frequency, generated piezoelectric voltage, maximum displacement, and von Mises stress developed on the application of 1 g acceleration. The pi-shaped cantilever beam structure generates a piezoelectric voltage of 6.76 V at the resonant frequency of 260.79 Hz on the application of 1 g acceleration and proves to be a better candidature than the T-shaped structure.

Keywords Piezoelectric energy harvester (PEH) · Cantilever beam · Polyvinylidene fluoride (PVDF) · PZT

N. Saxena (✉) · R. Sharma · K. K. Sharma · S. Chaudhary
MNIT, Jaipur 302017, Rajasthan, India
e-mail: 2018rec9098@mnit.ac.in

R. Sharma
e-mail: rsharma.ece@mnit.ac.in

V. Sharma
Manipal University Jaipur, Jaipur 303007, Rajasthan, India

© Springer Nature Singapore Pte Ltd. 2020
A. Kalam et al. (eds.), *Intelligent Computing Techniques for Smart Energy Systems*,
Lecture Notes in Electrical Engineering 607,
https://doi.org/10.1007/978-981-15-0214-9_21

1 Introduction

Presently, a lot of research is going on across the world to find out the novel type of MEMS-based micro-cantilever for energy harvesting from the surrounding resources to power wireless sensor nodes and modules and is gaining prominence. Chemical fuel cells were utilized conventionally to power these wireless electronic gadgets. Diminishing dimensions of transistor with addition to various other enhancements in conventional CMOS along with MEMS technologies lead to the energy constraints of recent electronic devices and transducers outstandingly at a minimum level. As the energy dissipation levels were decreased, developing self-sustaining devices that use energy harvesting as the only power source turn out to be an extra reasonable objective, and this initiated an inspiration to do research on energy harvesting [1–4]. The demanding task of substituting a battery and its reduced lifespan has triggered the researchers to harvest ambient energy from the surroundings. The foremost ambient energy resources are mechanical vibrations, acoustic, solar, biogas, wind, and thermoelectric [5–7]. There are four different techniques available for harvesting the ambient mechanical vibrations: electromagnetic, electrostatic, magnetostrictive, and piezoelectric [8–10]. Owing to the intricate properties of planar magnets, intricacies in integration and the minimum number of coil turns, the electromagnetic transducers are complicated to fabricate using the MEMS technology. In the electrostatic transducers, there is an existence of parasitic capacitance and the high output impedance restricts the output current, and consequently degrades the generator effectiveness. The magnetostrictive generator offers appropriateness for vibrations at high frequency, high flexibility, no depolarization setback, and ultrahigh coupling coefficient. However, the nonlinear effects, the requirement of the pick-up coil, and the complexity in the fabrication using MEMS technology confine their use for wireless applications [11, 12]. Probably the most encouraging energy harvesting strategies is utilizing piezoelectric materials to transform ambient mechanical vibrations to electrical power [13, 14]. PEHs contain greater power concentration in comparison to all their electrostatic and electromechanical alternatives. Additionally, natural electromechanical transformation ability of piezoelectric materials will allow simple device architectures appropriate for miniaturization. Being an outcome of these benefits, exploration upon MEMS energy harvesters is mainly concentrated on piezoelectric devices as well as various prototypes have been already explained in the literature.

The purpose of the work presented in this paper is to investigate different structures of MEMS-based PVDF PEHs for harvesting ambient vibrations in the low-frequency range below 1 kHz. The designing of the cantilevers are accomplished using single crystal silicon for the structural layer and the proof mass, PVDF ceramic as the piezoelectric layer. For proper selection of the material, a comparison is carried out between different piezoelectric materials and it is observed that for obtaining low-frequency operation, high flexibility, high thermal stability, and outstanding chemical resistance polyvinylidene fluoride (PVDF) prove a better alternative than PZT and it also provides environmental sustainability. In this work, four types of analysis have

been performed. (1) The modal analysis for the calculation of the resonant frequency. (2) The dynamic analysis in order to compute the maximum displacement across the z-direction. (3) The piezoelectric analysis is done to evaluate the piezoelectric voltage. (4) In order to compute the von Mises stress at the resonant frequency, the stress analysis is performed.

2 Mathematical Modeling

The most popular vibration-based micro-cantilevers are spring–mass–damper systems which result in optimum power when the resonant frequency of the ambient vibration matches the generator frequency. The resonant frequency (f_{rq}) of a fixed-free cantilever beam can easily be defined by Eq. (1) [15–17]

$$f_{\text{rq}} = \frac{1}{2\pi} \sqrt{\frac{k_s}{m}} \quad (1)$$

where m is the mass of the fixed proof mass.

The spring constant (k_s) of the cantilever is specified by Eq. (2) [15–17]

$$k_s = \frac{3YI}{l^3} = \frac{3Ywt^3}{12l^3} \quad (2)$$

where Y is the Young's modulus, I is the moment of inertia, l is the length, w is the width, and t is the thickness of the cantilever beam.

Thus, the resulting formula of the resonant frequency can be derived as Eq. (3)

$$f_{\text{rq}} = \frac{1}{2\pi} \sqrt{\frac{Ywt^3}{4l^3m}} \quad (3)$$

Thus, as seen from Eq. 3, the resonant frequency depends on the dimensions of the cantilever and the mass of the proof mass.

The relation between the cantilever end deflection δ_e and the applied force F_{ap} is given by Stoney's equation [15–17]

$$\delta_e = \frac{3F_{\text{ap}}(1 - \nu)}{Y\left(\frac{l}{t}\right)^2} \quad (4)$$

where ν is the Poisson's ratio.

So, the applied force can be calculated as

$$F_{\text{ap}} = \frac{\delta Y\left(\frac{l}{t}\right)^2}{3(1 - \nu)} \quad (5)$$

To ascertain if a material will yield or fracture, the von Mises stress (σ_{vM}) can give an idea and can be calculated by Eq. (6).

If the value of von Mises stress of a material in loading condition is significantly higher than or equal to the yield extent of the same material under the influence of tensile stress, then the material will produce.

$$\sigma_{vM} = \frac{F_{ap}}{A} \quad (6)$$

where A is the surface area of the cantilever beam.

3 Design Parameters of Cantilever Beam

In this paper, two basic structures of cantilever beams have been simulated using a FEM-based simulator, i.e., straight T-shaped and pi-shaped. In all these structures, a vice beam of the same dimension is attached at the fixed end of the beam for providing support to the beam and a proof mass is fixed at the bottom of the free end of the cantilever beam. All the structures are designed to work as PEH for the harvesting of low-frequency ambient vibrations. In all the designs, both electrical and mechanical boundary conditions have been applied. In electrical boundary conditions, the ground potential is employed to the bottom electrode and the floating terminal voltage is applied to the top electrode along with the resistive load. In mechanical boundary condition, one end of the beam remains fixed where the vice beam is attached. Some of the important material properties are listed in Table 1.

Table 1 Material properties

Material properties	Materials		
	Silicon	PVDF	Gold
Density (Kg/m^3)	2329	1780	19300
Young's modulus (Y) (GPa)	170	8.3	70
Poisson's ratio (ν)	0.28	0.18	0.44
Relative permittivity (ξ^T)	11.7	{6.76, 8.38, 7.20}	6.9

where ξ^T is a 3×3 dielectric constant matrix at constant stress, i.e., in stress-charge form

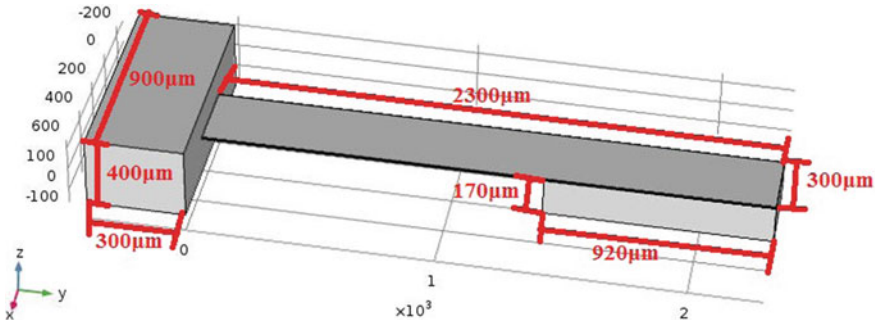


Fig. 1 Dimensional view of the designed straight T-shaped cantilever beam

3.1 Design Parameters for the Straight T-Shaped Cantilever Structure

The length, thickness, and the width of the straight T-shaped cantilever beam are 2300 μm, 5 μm, and 300 μm, respectively. The thickness of the PVDF piezoelectric layer is taken to be 5 μm. In this structure, the shape of the proof mass is similar to that of the cantilever beam with the length of 920 μm and thickness of 160 μm. All these dimensions of the structure are illustrated in Fig. 1.

The resonant frequency obtained from the straight T-shaped cantilever beam is 259.29 Hz, with a piezoelectric potential generated at the fixed end of the cantilever beam being 4.775 V.

3.2 Designing Parameters of the Pi-Shaped Cantilever Structure

The length, thickness, and the width of both the individual beams in the pi-shaped cantilever beam are 2300 μm, 5 μm, and 300 μm, respectively. The thickness of the PVDF piezoelectric layer is also taken to be 5 μm. In this structure, the shape of the proof mass is similar to the free end of the cantilever beam with the length of 920 μm and thickness of 160 μm. All these dimensions of the structure are illustrated in Fig. 2.

The resonant frequency obtained from the pi-shaped cantilever beam is 260.67 Hz for the left beam and 260.79 Hz for the right beam which is a very slight negligible difference of 0.12 Hz, with a piezoelectric potential generated at the fixed end of the left beam being 6.74 V and that of the right beam being 6.76 V.

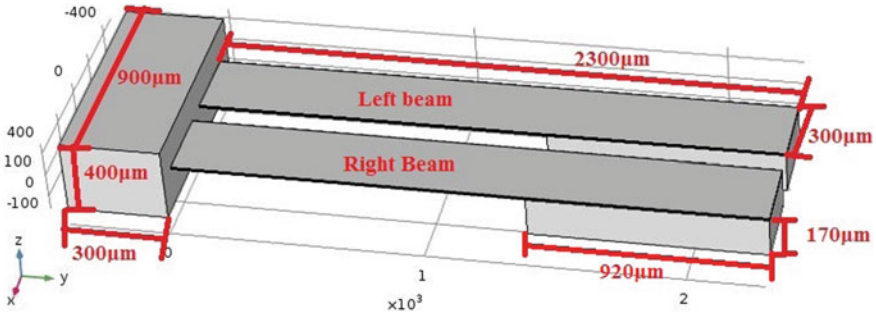


Fig. 2 Dimensional view of the pi-shaped cantilever beam

4 Results and Discussion

For PEHs discussed in the paper, four types of analyses have been carried out. (1) For the measurement of the resonant frequency, the modal analysis is done. (2) The dynamic analysis for the calculation of the maximum displacement across the z -direction. (3) The piezoelectric analysis to compute the piezoelectric potential. (4) The stress analysis to evaluate the von Mises stress at the resonant frequency. For the analysis of PEHs, the 1 g acceleration is applied along the z -direction. The performance of the designed piezoelectric energy harvesters is evaluated and compared on the basis of parameters such as resonant frequency, piezoelectric voltage, maximum displacement, and stress.

4.1 Modal Analysis

The modal analysis is carried out for the calculation of the resonant frequency among the primary six frequency modes of the PEHs and their related shape of deformation. The first eigen frequency produces the maximum displacement and the piezoelectric voltage, and thus is considered as the resonant frequency as its bending performance is appropriate for energy harvesting application, and is demonstrated in Fig. 3.

The comparison of analytical resonant frequency $f_{rq(\text{analytical})}$ obtained from Eq. (1) and the simulated resonant frequency $f_{rq(\text{simulation})}$ of all the three PEHs are listed in Table 2. It is usually observed that the percentage error in the analytical and simulation study is very low.

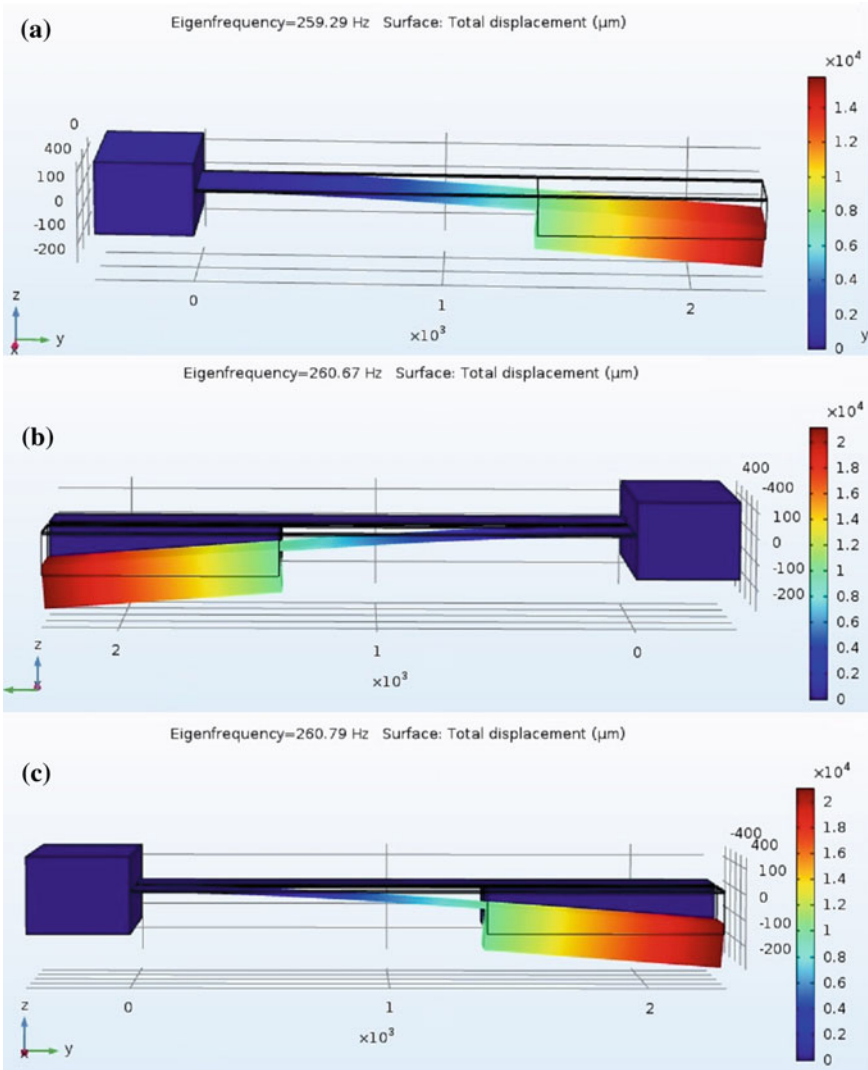


Fig. 3 Eigen-frequency of **a** straight T-shaped, **b** pi-shaped for the left beam, **c** pi-shaped for the right cantilever beams, respectively

Table 2 Comparison between analytical and simulated resonant frequency of (a) straight T-shaped, (b) pi-shaped cantilever beams

Design	$f_{rq}(\text{analytical})$ (Hz)	$f_{rq}(\text{simulation})$ (Hz)	Error (%)
Straight T-shaped	267.64	259.29	3.12
Pi-shaped	232.90	260.67	10.65

Table 3 Performance of (a) straight T-shaped, (b) pi-shaped cantilever beams

Design	Maximum displacement (μm)	von Mises stress (N/m^2)	Piezoelectric voltage (V)	Volume (μm^3)
Straight T-shaped	1.64×10^4	1.9×10^8	4.775	1.591×10^8
Pi-shaped	2.1×10^4	2.8×10^8	6.76	2.101×10^8

4.2 Dynamic Analysis

For all the structures discussed in the paper, when the boundary load of 1 g acceleration is applied along the z-axis, the cantilever beam vibrates resulting in the deflection of the beam [15–17]. It is observed that the maximum displacement occurs at the free end and the displacement at the fixed end is zero for the cantilever beam.

4.3 Piezoelectric Analysis

It is well-known that the PEH generates a piezoelectric potential when it is subjected to a load. The piezoelectric voltage of all the three PEHs can be computed using a FEM simulator, which is proportional to the stress and also depends on the material properties. It has been noticed that the maximum electric potential appears at the fixed end of the cantilever beam.

4.4 Stress Analysis

The stress analysis is significant for the cantilever beam as it should be lower than the yield strength of the structure to verify if the material will yield or fracture. For this purpose, von Mises stress is measured and it has been observed that it is maximum at the fixed end of the cantilever beam. All these analyses have been carried out and the results are illustrated in Table 3.

5 Conclusion

This paper presents the performance of two cantilever beam structures proposed to yield piezoelectric potential from ambient mechanical vibrations. On the basis of the mathematical modeling, selection of the material, and FEM analysis for an energy harvester, the geometrical dimensions are optimized. For obtaining low-frequency

operation, high flexibility, high thermal stability, outstanding chemical resistance polyvinylidene fluoride (PVDF) is used as the piezoelectric layer which also provides environmental sustainability. These designs can be used for the devices used for structural health detection and for portable medical monitoring applications. Piezoelectric polymer PVDF proves the better choice than PZT ceramics, which is a lead (Pb)-based composite and sensors developed using PZT cannot be used for medical applications. All the structures designed and analyzed in this paper are suitable for low-frequency operation. The pi-shaped PEH generates piezoelectric potential of 6.76 V which is a sufficient potential to replace a battery of around 5 V in today's electronic gadgets.

Acknowledgements The authors wish to gratefully acknowledge DRDO, New Delhi for providing the financial support to this project.

References

1. Xin Y, Sun H, Tian H, Guo C, Li X, Wang S, Wang C (2016) The use of polyvinylidene fluoride (PVDF) films as sensors for vibration measurement: a brief review. *Ferroelectrics*. ISSN: 1563-5112
2. Starner T, Paradiso JA (2004) Human generated power for mobile electronics. In: *Low power electronics design*, pp 1–35
3. Ramadan KS, Sameoto D, Evoy S (2014) A review of piezoelectric polymers as functional materials for electromechanical transducers. *Smart Mater Struct* 23:0964–1726
4. Xin Y, Li X, Tian HY, Guo C, Qian CH, Wang SH, Wang C (2016) Shoes-equipped piezoelectric transducer for energy harvesting: a brief review. *Ferroelectrics* 493:12–24
5. Iqbal A, Mohd-Yasin F (2015) Comparison of seven cantilever designs for piezoelectric energy harvester based on Mo/AlN/3C-SiC. In: *RSM proceedings*, K. Terengganu, Malaysia
6. Md. Uddin N, Md. Islam S, Sampe J, Bhuyan MS, Md. Ali SH (2016) Design and analysis of a T-shaped piezoelectric cantilever beam at low frequency using vibration for biomedical device. ISSN: 1992-1454
7. Zhang J, Ma S, Qin L (2015) Analysis of frequency characteristics of MEMS piezoelectric cantilever beam based energy harvester. In: *Symposium on piezoelectricity, acoustic waves, and device applications*, 30 Oct–2 Nov 2015, Jinan, China
8. Kim H-U, Lee W-H, Rasika Dias HV, Priya S (2009) Piezoelectric microgenerators-current status and challenges. *IEEE Trans Ultrason Ferroelectr Freq Control* 56(8)
9. Kim S, Park H, Kim S-H, Clyde Wickle III H, Park J-H, Kim D-J (2013) *J Microelectromech Syst* 22(1)
10. Li H, Tian C, Daniel Deng Z (2014) Energy harvesting from low frequency applications using piezoelectric materials. *Appl Phys Rev* 1:041301
11. Kim HS, Kim JH, Kim J (2011) A review of piezoelectric energy harvesting based on vibration. *Int J Precis Eng Manuf* 12(6):1129–1141
12. Abbasi AZ, Islam N, Shaikh ZA (2014) A review of wireless sensors and networks applications in agriculture. *Comput Stand Inter* 36(2):263–270
13. Roundy S, Wright PK (2004) A piezoelectric vibration based generator for wireless electronics. *Smart Mater Struct* 13:1131–1142 (2004)
14. Wang L, Yuan FG (2008) Vibration energy harvesting by magnetostrictive material. *Smart Mater Struct* 17(4):045009

15. Varadrajan E, Bhanusri M (2013) Design and simulation of unimorph piezoelectric energy harvesting system. In: Excerpt from the proceedings of the COMSOL conference in Bangalore (2013)
16. Arora S, Sumati, Arora A, George PJ (2012) Design of MEMS based microcantilever using COMSOL multiphysics. IJAER 7(11). ISSN: 0973-4562
17. Jamain UM, Ibrahim NH, Ab Rahim R (2014) Performance analysis of zinc oxide piezoelectric MEMS energy harvester. In: IEEE-ICSE proceedings, Kuala Lumpur, Malaysia

Designing and Implementation of Overhead Conductor Altitude Measurement System Using GPS for Sag Monitoring



Sangeeta Kamboj and Ratna Dahiya

Abstract Background: For efficient operation and reliability of power systems, continuous monitoring of power line sag is needed. The dynamic thermal line rating of a power transmission system at any instant may also be evaluated if power line sag information is available at that time. The smart grid also encourages sag measurement technologies so that the operator can take immediate corrective action whenever power line ground clearance exceeds the maximum allowable limit. **Aim:** The purpose of this paper is to design and implement an overhead conductor altitude measurement system using Global Positioning System technology with accuracy enhancement techniques for sag monitoring in power transmission lines in real time. **Method:** The observed Global Positioning System (GPS) measurements are found inaccurate by the comparison of observed GPS measurements with physical measurements taken at the field site. Therefore, various combinations of accuracy enhancement techniques such as Bad Data Identification/Modification (BDIM), Least Square Parameter Estimation (LSPE), and Haar Wavelet Transform (HWT) are used. **Results:** The field test has been conducted successfully on 11 kV power line by using the designed system to measure the altitude of overhead conductor at mid-span as well as at the pole to evaluate conductor sag of power lines in real time. **Conclusions:** It is found that HWT after LSPE and BDIM combination of accuracy enhancement techniques improves the accuracy of GPS measurements significantly and hence conductor sag can be monitored on-screen directly.

Keywords Conductor altitude · Global Positioning System · Power line sag · Least Square Parameter Estimation · Wavelet Transform

S. Kamboj (✉) · R. Dahiya
Department of Electrical and Instrumentation Engineering, Thapar Institute of Engineering and Technology, Patiala, Punjab, India
e-mail: engineersangeeta@gmail.com

R. Dahiya
Electrical Engineering, National Institute of Technology (Deemed University), Kurukshetra, Haryana, India

1 Introduction

The dynamic thermal line rating of the power transmission system at any instant may be evaluated if power line sag information is available at that time. In addition, the safe operation of the power grid is affected as the distance of the power transmission line to the ground reduce vertically [1]. The smart grid also encouraged sag measurement technologies so that the operator can take immediate corrective action whenever power line ground clearance exceeds maximum allowable limit and thus the possibility of system collapse is prevented [2]. The methods to measuring power line sag may be either direct or indirect. Some of the methods to measure power line sag are observation method, GPS-based, by using conductor temperature and stress to calculate sag, projection technique, and using the tilt of the line to determine sag [1]. Video Sagometer is one of technologies for direct measurement of conductor sag that may enhance the utilization of dynamic line ratings. But the use of advanced image processing techniques makes the system more complex [3, 4]. GPS-based method to measure sag is also one of the direct methods as it does not require any assumptions regarding ambient weather conditions, conductor temperature and tension measurements, and intermediate calculations to compute it. In reference [5], the method to measure sag on transmission line conductor using Differential Global Positioning System (DGPS) has been discussed. A specially designed test site has been chosen to study the behavior of the system by conducting field tests. Komarigiri et al. also showed that GPS system could be cost effective for overhead conductor sag measurement in power transmission lines [6]. In the available literature, development of overhead conductor sag measurement system using DGPS technology has been described. Though this system enables direct measurement of sag accurately, the cost of the system increases with additional equipment needed for the GPS receiver. But it has not been tested on an energized high-voltage line and requires experience in the proposed technology for implementation. In reference [7], the conductor sag measurement system has been used to perform field tests on 11 kV power lines to analyze the effect of span length on conductor sag. Dynamic Thermal Line Rating of 440 V power distribution line has been evaluated using the estimated conductor sag information by conducting field tests at different air temperatures by means of the conductor sag measurement system using GPS in reference [8]. In reference [9], a number of cases have been studied to prove that temperature and sag monitoring of overhead power lines are an essential part of the transmission smart grid. A method to measure the power line sag using optical sensors has been proposed in reference [10].

The GPS satellite signal consists of various inherent errors such as ephemeris errors, satellite clock error, ionospheric and tropospheric delays, and multipath before being given to the GPS receiver which affect its accuracy [11]. The signal processing techniques can be used to improve the accuracy of the GPS receiver so that its output can be used to measure overhead conductor sag efficiently [5, 6]. In the present paper, an overhead conductor sag altitude measurement system using GPS technology has been developed and designed. The designed system has been implemented on 11 kV

power line at a load of 80 A. Errors in the observed GPS measurements are found by comparison of the observed GPS measurements with physical measurements taken at the site of the field test and thus these measurements need to be processed for sag estimation directly. The various combinations of accuracy enhancement techniques such as BDIM, LSPE, and HWT have been used for error reduction in the observed GPS altitude measurements to monitor sag efficiently. In the paper, output obtained after using accuracy enhancement techniques, has been compared with physical measurement taken at the site of the field test to estimate error in the raw measurements. Thus, HWT after LSPE and BDIM techniques has been for processing of observed GPS altitude measurements to estimate power line sag used as it provides better results.

2 Designing of Overhead Conductor Altitude Measurement System

The overhead conductor altitude measurement system has been designed to measure conductor altitude at mid-span and at the pole of the power line for evaluation of sag in real time as presented in Fig. 1. The basic components used in the designing of an overhead conductor altitude measurement system are shown in Fig. 2. In the setup, insulation unit is made up of polymer materials and metal fittings. Silicon organic rubber has been used in a protective ribbed mold and antirust alloy used in flanges provides longer term operation [8]. The polymer insulator used in the designing of the conductor altitude measurement system has many advantages such as light weight, higher dielectric strength, excellent insulating behavior, highly resistant to breakage, compact design, and very high level of safety.

Acrylic sheet with dimensions as shown in Fig. 1 has been used for the support of GPS receiver BT359 which measures conductor altitude at mid-span as well as the pole of the power line in real time. The system for conductor altitude measurement has been designed in such a way that the overall weight of the system has a negligible effect on conductor sag. A suitable distance from power line (0.47 m) has been taken into consideration for altitude measurement by the GPS receiver to avoid the effect of high-voltage environment under power lines on the operation of the GPS receiver. And this distance is added to the conductor altitude information given by the GPS receiver to obtain actual altitude of the overhead conductor. As the weight of the conductor increases due to loading of wind and ice, the designed system is more useful for the sag monitoring in real time in hilly and windy areas to keep power line ground clearance within the maximum allowable limit.

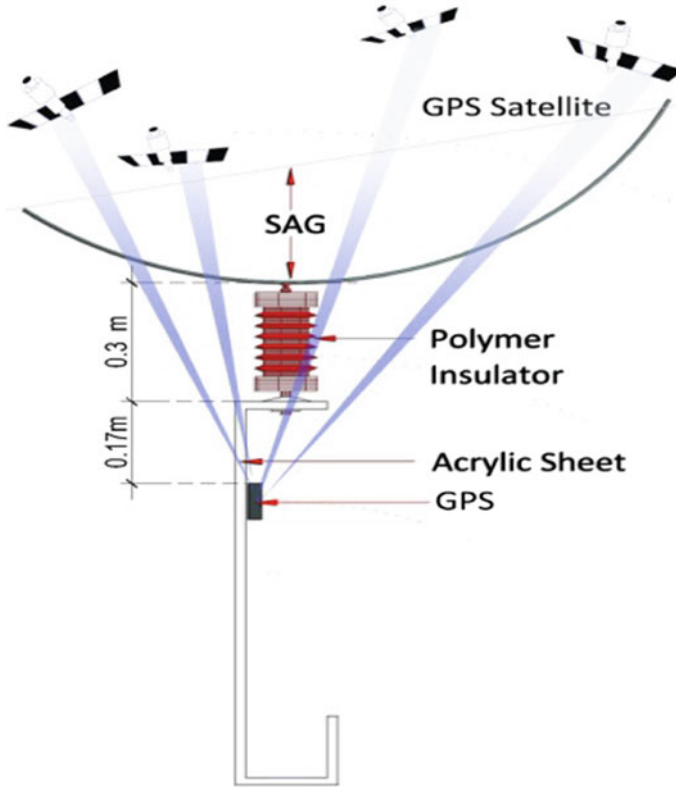


Fig. 1 Designing of overhead conductor altitude measurement system

2.1 Field Test

The field test has been conducted on 11 kV Sanheri Domestic Feeder, Kuwar Kheri, Kurukshetra (Haryana), India having span length of 65 m at a load of 80 A under ambient temperature of 29 °C using the designed system. The main purpose of the field test is to obtain altitude measurements of the overhead conductor using a GPS receiver at mid-span as well as at the pole to evaluate conductor sag of power lines in real time. The lowermost phase of power lines is used for sag measurement. During the field test, the GPS receiver has been used in the differential mode. In this mode, one of the GPS receivers has been placed on the earth and the other GPS receiver on the power line but both the receivers receive the GPS satellite signals simultaneously. The actual position of the earth above mean sea level is known as per the Survey of India and is compared to the readings obtained by the GPS receiver placed on the earth. With the estimated error, the readings obtained by the GPS receiver placed on the power line are compensated by simple subtraction. The GPS receiver has taken input from GPS satellites available in the view of the receiver at

Fig. 2 Main components used in conductor altitude measurement system



the time of measurements and has given output in standard NMEA0183 sentences to the laptop via a bluetooth link. GPS software “NMEA/GPS data logger” has been used to process the standard NMEA0183 sentences to provide conductor altitude information of the power line.

The altitude of the conductor from the earth at the site of the field test has also been measured using BOSCH GLM 50 laser distance measuring device as given in Table 1.

Now the altitude of the earth above mean sea level of the place (i.e., Kurukshetra which is 240 m as per the Survey of India) has been added to the altitude of the conductor measured from the earth as given in Table 1 to obtain the overhead conductor altitude above mean sea level and used for the estimation of error in raw GPS altitude measurements. A pictorial illustration of the field tests performed using the designed system at the 11 kV Sanheri Domestic Feeder, Kurukshetra is shown in Fig. 3.

Table 1 Conductor altitude measurement from the earth

S. no.	Measurement at	Altitude of conductor from the earth (m)
1	Mid span	6.2
2	Pole	7.4



Fig. 3 Field test conducted using designed conductor altitude measurement system

3 Accuracy Enhancement Techniques

The enhancement techniques used to improve the accuracy of the observed GPS altitude measurements are discussed as follows.

BDIM Technique

The momentary loss of some satellites from view, ambient noise, and signal reflections degrades the accuracy of GPS measurements. Therefore, it is imperative to identify and modify the bad data in order to improve accuracy. The algorithm used in this technique has been depicted in a flowchart as can be seen in Fig. 4.

LSPE Technique

The ordinary least square technique has been used to analyze nonlinear behavior of error in the observed data [12, 13]. In this technique, input data are GPS altitude measurements obtained after using the BDIM technique. The steps followed in this technique are shown in Fig. 5.

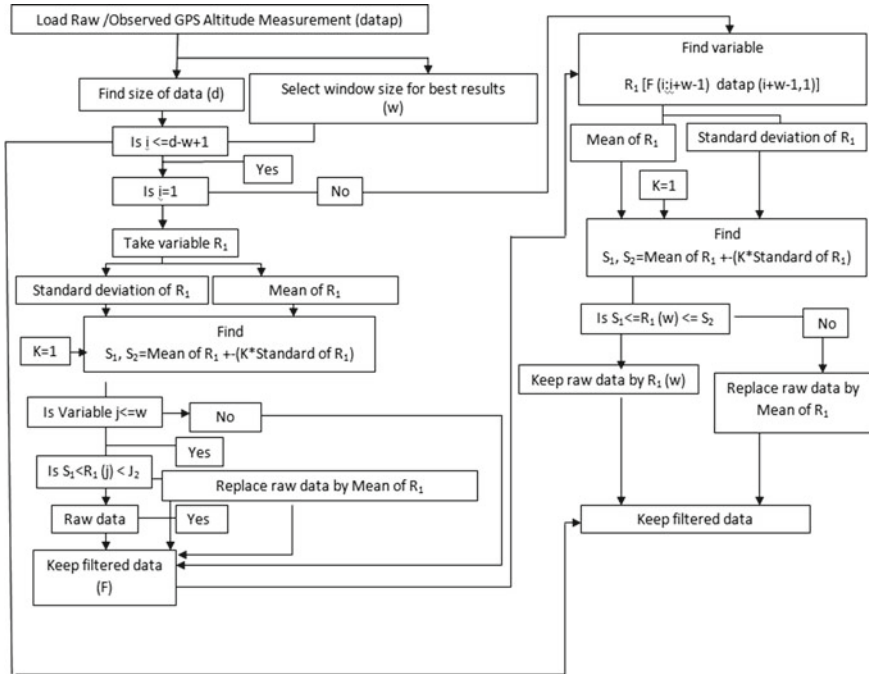


Fig. 4 Flowchart showing the algorithm used in BDIM

HWT Technique

Mathematical details on wavelet analysis can be found in [14, 15]. The concept of signal decomposition has been applied to GPS altitude measurements obtained by using LSPE after the BDIM technique. Then the approximation component of GPS altitude measurements is obtained after the LSPE technique at level 11 using Wavelet Toolbox of the MATLAB software.

4 Results

Raw GPS Measurements

The physically measured altitude and raw GPS altitude measurements of the overhead conductor at mid-span are presented in Fig. 6. The GPS altitude measurements after comparison with the physically measured altitude of the conductor are found to be inaccurate because of some inherent sources of error in the GPS measurements. Inaccuracies in GPS altitude measurements during field test are also because of the GPS receiver BT359 used. In order to reduce the errors in the raw GPS altitude measurements, the following combination of accuracy enhancement techniques has been used.

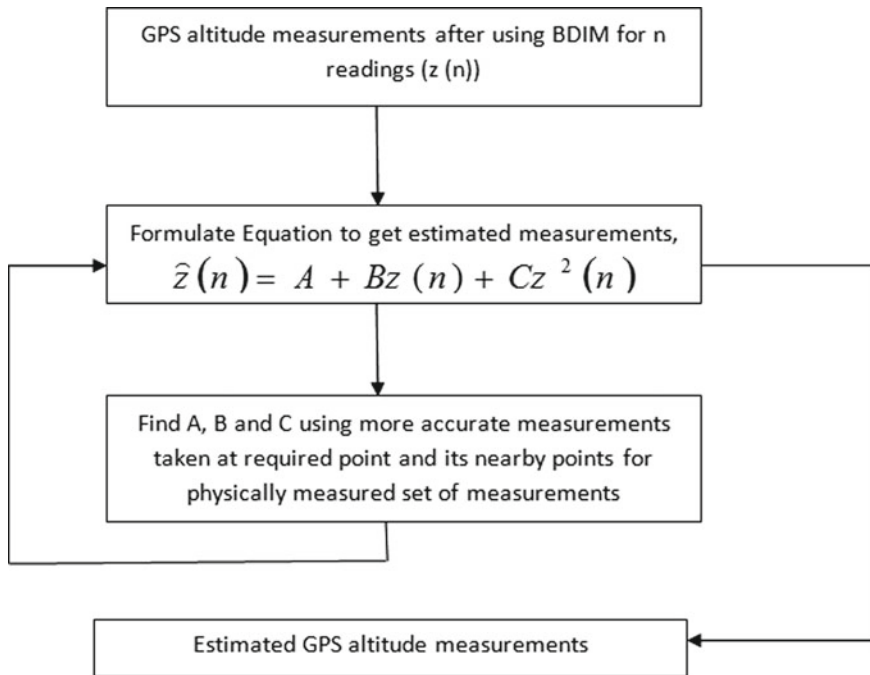


Fig. 5 Algorithm used in LSPE technique

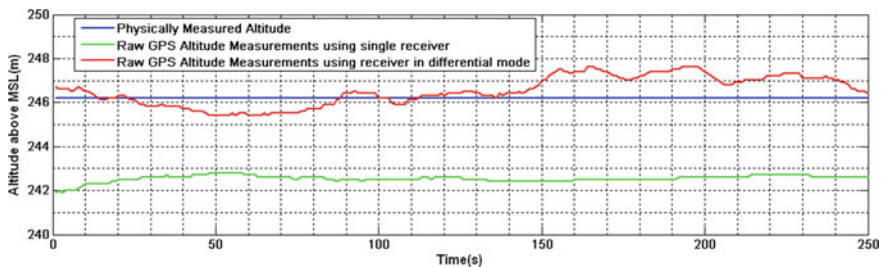


Fig. 6 Observed GPS altitude measurements

Combination 1 (LSPE after BDIM)

Combination 2 (HWT after LSPE and BDIM)

Observations Using Combination 1

Figure 7 presented the effect of combination 1 of the accuracy enhancement techniques on the observed GPS altitude measurements. It has been found that the maximum absolute error in the observed GPS altitude measurements at mid-span has been reduced from 1.41 to 0.053 m and thus these closely matched to that of the altitude of the conductor measured physically.

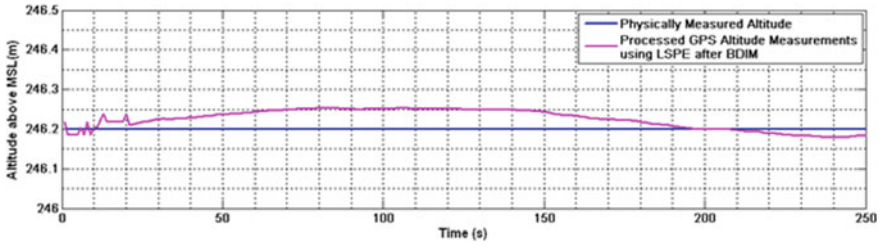


Fig. 7 Effect of combination 1 of accuracy enhancement techniques

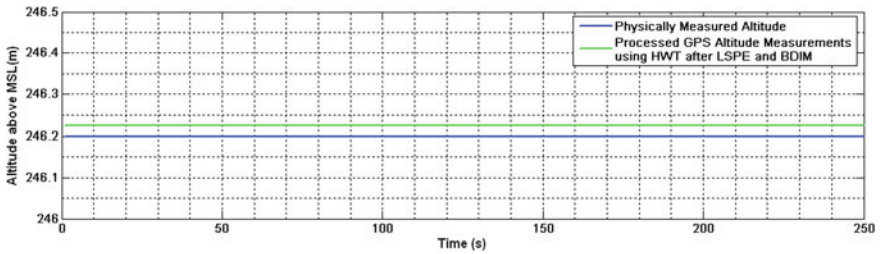


Fig. 8 Effect of combination 2 of accuracy enhancement techniques

Observations Using Combination 2

Further error estimation is required to reduce the errors in the GPS altitude measurements as these cannot be used for sag estimation. Figure 8 shows the effect of combination 2 of accuracy enhancement techniques on GPS altitude measurements resulting from combination 1 and the error further reduced to 0.023 m at the mid-span of line.

4.1 Error Analysis

The absolute error found in raw GPS altitude measurements and processed GPS altitude measurements obtained using DSP techniques such as BDIM, combination 1, and combination 2 for the considered field test have been illustrated in Fig. 9.

It has been found that the error in the estimated GPS altitude measurements obtained using combination 2 reduced to a greater extent and was used to compute the conductor sag efficiently.

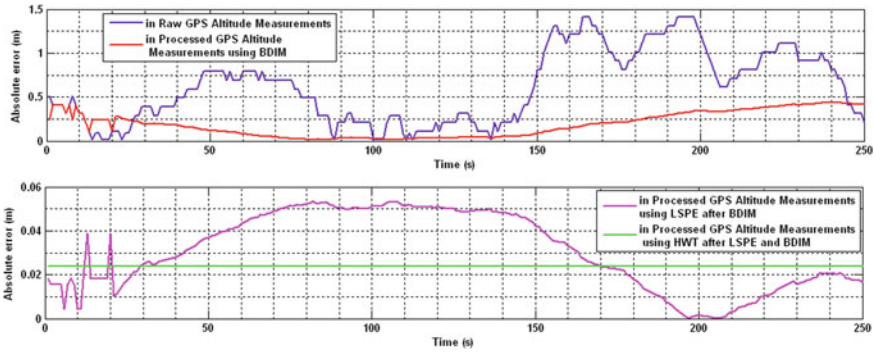


Fig. 9 Absolute error analysis

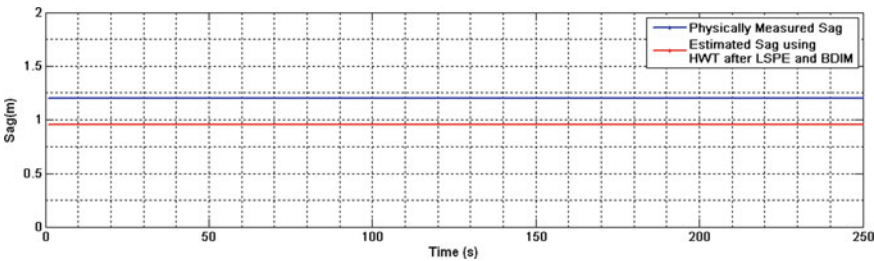


Fig. 10 Estimated Sag

5 Sag Estimation

The power line sag has been evaluated using the estimated GPS altitude measurements obtained after combination 2 of the accuracy enhancement techniques at mid-span and at the pole of the power line. It is observed that sag measured by GPS using combination 2 technique has lesser errors as depicted in Fig. 10.

6 Conclusion

It can be concluded that the GPS technology may be feasible for direct measurement of overhead power line conductor sag. It is also concluded that the GPS-based estimated sag obtained using combination 2 of accuracy enhancement techniques has less error in comparison to physically measured sag for the case considered. The outcome of the statistical analysis of raw/estimated GPS altitude measurements also shows that combination 2 of the accuracy enhancement techniques is the best combination for significant error reductions in raw GPS altitude measurements. It may also be concluded that there is requirement of packaging for the GPS-based overhead

conductor sag measuring system due to electromagnetic interference from corona discharges when the measurements are to be taken in very high-voltage environments. The resulting conductor sag information may be used to improve the efficiency of the electric power systems particularly in the hilly areas and in worst weather conditions. Although the calculation of Dynamic Thermal Line Rating of an overhead conductor using sag information is not considered in the paper, the real-time sag measurement using GPS may be translated into real-time Dynamic Circuit Rating.

Acknowledgements Mr. Satvinder, Ex-site engineer, VTL, MP Birla Group, Janakpuri, Delhi, is acknowledged in carrying out data collection that is analyzed in this paper. Mr. Hansraj, Assistant Executive Engineer, HVPNL, Faridabad and Mr. Naseeb Singh, Assistant Executive Engineer, UHB-VNL, Kurukshetra are greatly appreciated for providing the opportunities and resources required for the work.

References

1. Xiao X, Yan X, Zhang J, Xu K (2013) Research on sag online monitoring system for power transmission wire based on tilt measurement. *Int J Smart Grid Clean Energy*, 6–11
2. Klein KM, Springer PL, Black WZ (2011) Real-time ampacity and ground clearance software for integration into smart grid technology. In: *Proceeding of IEEE Power and Energy Society General Meeting, San Diego*
3. Olsen RG, Edward KS (2002) A new method for real time monitoring of high voltage transmission line conductor sag. *IEEE Trans Power Deliv* 17(4):1142–1152
4. EDM International Inc. Sagometer. Product Overview <http://edmlink.com/EDMSagometer.pdf>
5. Mahajan S, Singareddy M (2008) Real time GPS data processing for sag measurement on a transmission line. In: *Joint international conference on power system technology (POWER-CON) and IEEE power India conference, New Delhi, India*, pp 496–501
6. Komarigiri SS, Mahajan S (2009) A sag monitoring device based on a cluster of code based GPS receivers. In: *IEEE power and energy society journal meeting, PES'09, Calgary, AB*, pp 1–7
7. Kamboj S, Dahiya R (2014) Case study to estimate the sag in overhead conductors using GPS to observe the effect of span length. In: *IEEE international conference on PES T&D, Chicago*, pp 1–4
8. Kamboj S, Dahiya R (2011) Evaluation of DTLR of power distribution line from sag measured using GPS. In: *IEEE international conference on energy automation and signal (ICEAS2011), Bhuneshwar, India*, pp 1–6
9. Lovrenčić V, Gabrovšek M, Kovač M, Gubeljak N, Šojat Z, Klobas Z (2015) The contribution of conductor temperature and sag monitoring to increased ampacities of overhead lines (OHLs). *Period Polytech Electr Eng Comput Sci* 59(3):70–77
10. Wydra M, Kisala P, Harasim D, Kacejko P (2018) Overhead transmission line sag estimation using a simple optomechanical system with chirped fiber Bragg gratings. Part 1: preliminary measurements. *Sensors* 18(1):1–14
11. Hoffman-Wellenhof B, Lichtenegger H, Collins J (1993) *Global positioning system theory and practice*. Springer, New York
12. Phillips GM, Taylor PJ (1996) *Theory and applications of numerical analysis*, 2nd edn. Academic Press, New York
13. Linfield G, Penny J (2000) *Numerical methods using MATLAB*, 2nd edn. Prentice Hall, Upper Saddle River, NJ

14. Stark H-G (2005) Wavelets and signal processing. Springer, Berlin Heideberg
15. Noureldin A, Osman A, El-Sheimy N, Nassar S (2003) Wavelet multiresolution analysis. GPS World, Oct 1

Risk-Averse G2V Scheduling of Electric Vehicle Aggregator for Improved Market Operations



S. Sharma, P. Jain and P. P. Gupta

Abstract In a smart grid environment, the price uncertainty would significantly affect market operations and behavior of an Electric Vehicle Aggregator (EVA) aimed at profit maximization through Grid-to-Vehicle (G2V) charge scheduling of EVs. For improved multi-market operations, risk-averse G2V scheduling of EVA is modeled in this paper to manage its revenue risk and reduce energy purchase cost incorporating Time-of-Use Price-Based Demand Response (TOU-PBDR). Scenarios of prices are generated employing the Monte Carlo Simulation (MCS) approach. The probabilistic Kantorovich Distance (KD) is used in scenario reduction backward algorithm to find a trade-off between computation speed and accuracy. Risk measure incorporated is Conditional Value at Risk (*CVaR*). Simulation results verify the efficacy of proposed method and the effect of stochastic G2V scheduling strategy of EVA on the energy and regulation market operations.

Keywords Demand response · Electric vehicles (EVs) · Grid-to-vehicle (G2V) · Markets · Scheduling

1 Introduction

The advancements in storage and battery technology, limitations on fossil fuel consumption, and global warming are the main drivers of transport electrification [1]. Grid integration of EVs may pose opportunities and challenges to the System Operator (SO). Opportunities to SO can be due to its storage potential and capability to provide frequency regulation and charging load flexibility [2]. However, uncontrolled charging of EVs may put forward threats to SO such as grid reinforcement, power quality issues, increased losses, and power imbalances [3]. This necessitates optimal G2V scheduling of EVA which implements smart charging through efficient coordination of EVA with EV owners and SO [4]. It acts as a mutually beneficial negotiator between SO and EV owners, enabling improved operations in power grid

S. Sharma (✉) · P. Jain · P. P. Gupta
Malaviya National Institute of Technology, Jaipur, India
e-mail: 2015ree9012@mnit.ac.in

© Springer Nature Singapore Pte Ltd. 2020
A. Kalam et al. (eds.), *Intelligent Computing Techniques for Smart Energy Systems*,
Lecture Notes in Electrical Engineering 607,
https://doi.org/10.1007/978-981-15-0214-9_23

and electricity market. It aims to optimally schedule the charging of EVs considering the benefits of SO and EV owner while maximizing its profit earned from participation in multiple markets of electricity and ancillary services. It provides reserve capacity, regulation capacity, and grid congestion management through the coordinated charging of EVs for the benefit of SO. It may adopt Price-based Demand Response Programs (DRP) to benefit EV by reduced charging costs and benefit SO by peak load management and load leveling. However, for optimal decision-making, EVA faces several uncertainties like volatility in different market prices, EV arrival and departure times, initial SOC based on unexpected trip plans, renewable DGs output at the charging station, system load, etc. It is also subjected to challenges like its capability to attract and sustain EV owners and to make certain that combined capacity of idle EVs is available to SO [5]. Multiple market participation hedges EVA against risk of profit loss as compared to single market participation. However, incorporation of risk model based on different uncertainties is necessary in the G2V scheduling for realistic decision-making.

Scheduling model of EVA is demonstrated in [6, 7] based on minimization of charging energy cost and the net substation cost subjected to network security constraint. DRPs act as a hedge against high peak prices and motivate EV owners to charge during off-peak. In intelligent grid, DRP plays dynamic role to reestablish the equilibrium regarding electricity supply and demand [6]. Integrated DRPs and risk-based G2V scheduling are necessitated in the evolving smart grid scenario [8–10]. In [11], G2V scheduling of EVs is modeled using stochastic approach in view of uncertainties of electricity market and EVs to reflect the influences of diverse DRPs on the operative performance of EVAs and to enhance the contribution of EVAs in respective DRPs. Stochastic planning model enables the decision-maker to specify the risk level caused by uncertainties in renewables (wind and solar), load patterns, parking patterns, and transmission lines' reliability, and balance its costs and benefits according to this risk level [12].

Risk-aversiveness of EVA in market participation should be optimized to attain enhanced scheduling approach that assurances a Pareto upgrading on its profit over entire uncertainty set. Measures of risk are necessary for exemplifying the risk related to a given judgment [13, 14]. Most efficient risk measure, Conditional Value at Risk (*CVaR*) is coherent and downside risk measure. Risk-averse bidding has been formulated for demand-side resource aggregator based on *CVaR* to minimize expected regret value over a subset of worst-case scenarios whose collective probability is no more than a threshold value [15]. Multi-market participation of an EVA is formulated for EVA's *CVaR* maximization in [16–18]. Risk-averse formulation illustrated that the EVA would be able to reduce the risk in its expected revenue by shifting its revenue source from one market to another market [19]. However, DRPs are not integrated in [16–21].

In the context of the literature survey, this paper proposes risk-averse G2V scheduling of EVA in energy and regulation markets integrating TOU-PBDR for EV owners. Five-step TOU price is formulated with the forecasted value of real-time energy prices using hierarchical and clustering method. The energy and regulation market prices are modeled by normal distribution with forecasted as mean and a standard

deviation to model uncertainty pattern. Monte Carlo Simulation method is used to handle uncertainty of the prices in the problem formulation. EVA procures energy from wholesale market on real-time market price and charges EVs on TOU prices. The EVA also provides regulation to SO at the real-time regulation market prices by coordinating the charging rates of connected EVs. The objective of the EVA is profit maximization subjected to risk of profit variation due to volatility of the uncertain variables like market prices of energy and regulation market. The measure adopted in this work is CVaR. The problem is a mixed integer nonlinear programming problem and is formulated in GAMS and solved using IPOPT solver [22]. The remaining paper is organized as per the following outline. Section 2 discusses risk controlling in stochastic optimization. Section 3 represents scenarios generation and reduction. Section 4 details the risk-averse formulation of stochastic programming problem. Simulation results of risk-constrained stochastic scheduling are discussed in Sect. 5. To end with, the concluding interpretations are delivered in Sect. 6.

2 Risk Controlling in Stochastic Optimization

Decision-making framework of EVA is challenged by market prices. Due to their volatility and uncertainties, EVA's expected profit varies from mean value. Value at Risk (*VaR*) represents largest value η ensuring probability of obtaining profit less than η is lower than $1 - \alpha$. α is confidence interval. However, *VaR* does not detect fat tail in profit distribution. Tail risk in EVA's portfolio are quantified by a coherence risk measure termed as Conditional Value at Risk (*CVaR*). It is the expected value of profit smaller than $1 - \alpha$ quantile of profit distribution, imitative of weighted average of "worst-case" losses in tail of probable distribution of expected profits, beyond (*VaR*).

3 Scenario Generation and Reduction

Precise uncertainty depiction imposes to consider huge number of scenarios; therefore, to deal with associated computational complexity, the inconsistent method for scenario reduction is necessitated. This paper represents simple procedure for scenario generation and reduction of energy and regulation prices. 1000 scenarios of prices are generated by means of Monte Carlo Simulation approach. The generated scenarios are reduced to 10, utilizing Kantorovich Distance (KD) based backward method as presented in [23] from MATLAB simulations. The cost matrix comprises of the price functions $v(\omega, \omega')$ for overall produced sets of scenarios. The KD matrix involves multiplication of price function and matching incidence likelihood π_ω of all produced scenarios. It is used for producing decreased scenario sets that are near enough to initial set.

$$KD(\omega, \omega') = \sum_{\omega \in \Omega / \Omega_s} \pi_\omega \cdot v(\omega, \omega') \quad (1)$$

Price function is described as a vector difference between scenario subsets ω and ω' , and calculated using (2).

$$v(\omega, \omega') = \|C_\omega - C_{\omega'}\| \quad \forall \omega, \omega' \in \Omega, \Omega = 1, 2, \dots, N_\omega \quad (2)$$

4 Risk-Aversive Formulation of Stochastic Programming Problem

It is assumed that arrival, departure times, and energy usage are known to EVA. *CVaR* risk measure is employed and added as constraints. Risk-averse and risk-neutral G2V charge scheduling are considered with impact analysis of risk-aversion degree β in energy and regulation markets. Risk-averse decision-making objective function of EVA is (3). Constraints (4–5) model risk measure to control variability of expected profit. Risk measure *CVaR* is defined as (4).

$$\begin{aligned} \max_{P_{\omega,i,t}, RC_{\omega,i,t}, s_{\omega,i,t}} \quad & (1 - \beta) \sum_{\omega=1}^{N_\omega} \sum_{i=1}^N \sum_{t=1}^T \text{prob}_\omega \cdot RP_{\omega,t}^{\text{sell}} \cdot RC_{\omega,i,t} + EP_t^{\text{TOU sell}} \cdot P_{\omega,i,t} \\ & - \text{prob}_\omega \cdot EP_{\omega,t}^{\text{buy}} \cdot P_{\omega,i,t} + \beta \cdot \left(\eta - \frac{1}{1 - \alpha} \sum_{\omega=1}^{N_\omega} \text{prob}_\omega \cdot s_\omega \right) \end{aligned} \quad (3)$$

$$CVaR = \eta - \frac{1}{1 - \alpha} \sum_{\omega \in N_\omega} \text{prob}_\omega \cdot s(\omega) \quad (4)$$

$$\eta - \left(\sum_{i=1}^N \sum_{t=1}^T RP_{\omega,t}^{\text{sell}} \cdot RC_{\omega,i,t} + EP_t^{\text{TOU sell}} \cdot P_{\omega,i,t} - EP_{\omega,t}^{\text{buy}} \cdot P_{\omega,i,t} \right) \leq s_\omega, \quad \forall \omega \in N_\omega \quad (5)$$

$$s_\omega \geq 0 \quad (6)$$

$P_{\omega,i,t}$ is the power consumed by EV owner and is the scheduled charging rate value. For risk-averse problem, s_ω is a continuous and non-negative variable and is equal to the maximum value between $\eta - \left(\sum_{i=1}^N \sum_{t=1}^T RP_{\omega,t}^{\text{sell}} \cdot RC_{\omega,i,t} + EP_t^{\text{TOU sell}} \cdot P_{\omega,i,t} - EP_{\omega,t}^{\text{buy}} \cdot P_{\omega,i,t} \right)$ and 0. $EP_t^{\text{TOU sell}}$ are the predetermined and constant prices designed to reflect day-ahead wholesale prices. Constraint (7) indicates the updating of SOC of i th EV at time t . $batcap_i$ is rated capacity (kWh) and Efi_{ch} is the charging efficiency of i th EV battery. Equation (8) shows the flexibility constraint for smooth modulation of charging rate. Equation (9) provides the limits of charging rates. POP_i^{max} is the capacity limit of battery for

i th EV. $Av_{i,t}$ indicates whether EV is plugged-in or not. It is a binary variable representing availability of EV for value 1. Equation (10) ensures that EVs are charged only when connected and not at the time of travel. Constraint (11) assures desired SOC at departure to EV owners.

$$SOC_{\omega,i,t} = SOC_{\omega,i,t-1} + \frac{Eft_{ch} \cdot P_{\omega,i,t}}{batcap_i} \forall \omega, \forall i, \forall t \quad (7)$$

$$(SOC_{\omega,i,t} - SOC_{\omega,i,t-1}) \leq f_k \cdot \frac{SOC_{max} - SOC_{ini}}{t_{d,i} - t_{a,i}} \forall \omega, \forall i, \forall t \quad (8)$$

$$P_i^{\min} \leq P_{\omega,i,t} \cdot Av_{i,t} \leq P_i^{\max}; \quad \forall \omega, \forall i, \forall t \quad (9)$$

$$Av_{i,t} = \{0, \forall t, \forall i |_{Trip_{i,t} \neq 0}\} \quad (10)$$

$$SOC_{\omega,i,t} \geq SOC_{i,t}^{\text{dep}} \left\{ \forall i, \forall t |_{Flag_{i,t}^{\text{dep}} = 1} \right\} \quad (11)$$

Equation (12) indicates total regulation capacity as the sum of regulation up and down capacities. Equations (13) and (14) calculate respective regulation capacities (reg-up and reg-down) at time t , provided by i th EV. $P_{\max_{\omega,i,t}}$ is the maximum value of charging rate and computed as per (15). Constraint (16) is the overload constraint indicating that transformer delivery capacity must be greater than or equal to amount of combined charging rate, totaled regulation down capacities, and baseload at time t .

$$RC_{\omega,i,t} = RUC_{\omega,i,t} + RDC_{\omega,i,t} \quad \forall \omega, i, t \quad (12)$$

$$RUC_{\omega,i,t} = (P_{\omega,i,t} - P_i^{\min}) \cdot Av_{i,t} \quad (13)$$

$$RDC_{\omega,i,t} = \left(\min \left(P_i^{\max}, P_{\omega,i,t}^{\max} \right) - P_{\omega,i,t} \right) \cdot Av_{i,t} \quad (14)$$

$$P_{\max_{\omega,i,t}} = (SOC_{max} - SOC_{\omega,i,t}) \cdot Av_{i,t} \cdot \frac{batcap_i}{Eft_{ch}} \quad (15)$$

$$TDC \geq \sum_{i=1}^N (P_{\omega,i,t} + RDC_{\omega,i,t}) + l_t \quad \forall t, \forall \omega \quad (16)$$

5 Simulation Results of Risk-Constrained Stochastic Scheduling

The scenario generation algorithms have been realized for subsequent-day market prices of NYISO. The outcomes verify the capability of the anticipated algorithms in developing uncertain prices. These modeled algorithms can efficaciously be exploited to produce price offers for optimal power markets trading of EVA. Figure 1a, b indicates reduced scenarios of regulation prices and electricity prices. Figure 2a, b illustrates cumulative distribution functions of the profit for risk weighting parameters $\beta = 0$ and $\beta = 1$.

Figure 3 shows the efficient frontiers as value at risk and conditional value at risk versus expected profit, obtained from variation of β from 0 to 1, respectively, for risk-neutral and risk-averse EVA. Different schedules are obtained with reduced expected profit for risk-averse EVA as compared to risk-neutral EVA. It depicts that VaR and $CVaR$ increases for higher value of risk weighting parameter. Baseload profile is coordinated from SO to EVA. Figure 4 illustrates aggregated charging load variation in coordination with baseload profile. Due to TOU-PBDR, valley filling is observed during off-peak hours and charging load is lower during peak hours.

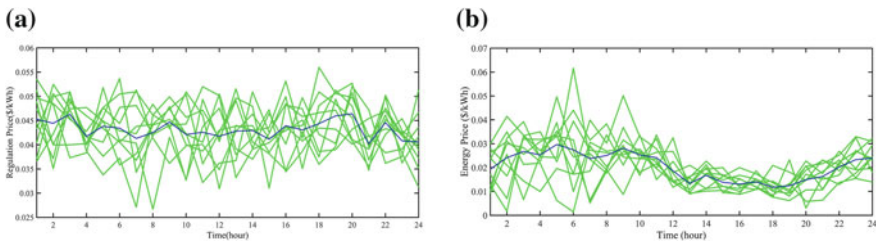


Fig. 1 a Scenario reduction of regulation price (green). b Scenario reduction of energy price along with forecasted regulation price (blue) (green) along with forecasted energy price (blue)

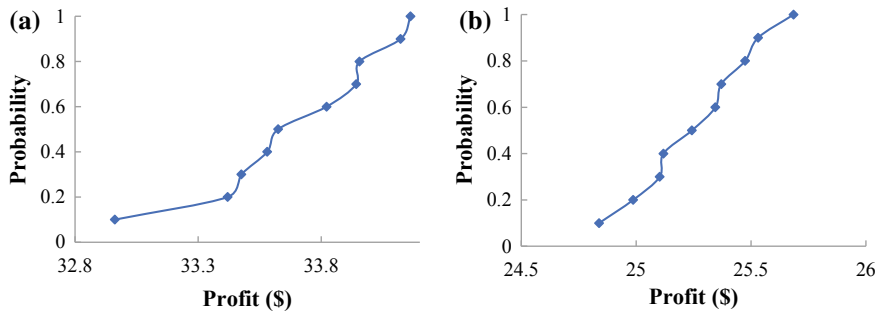


Fig. 2 a Cumulative probability distribution function for $\beta = 0$. b Cumulative probability distribution function for $\beta = 1$

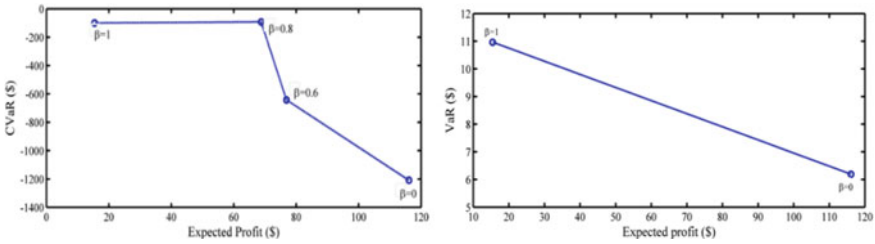
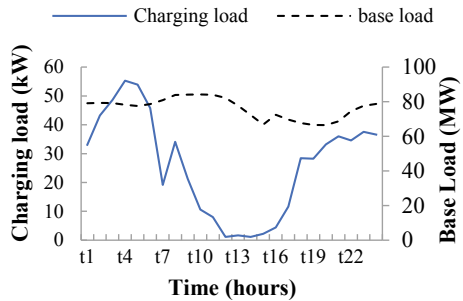


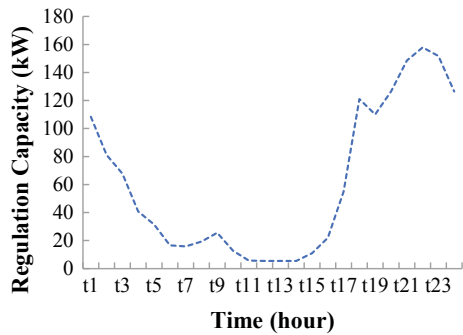
Fig. 3 Efficient frontiers

Fig. 4 Aggregated charging load versus base load on grid



When EVA becomes more risk-averse, it modifies its scheduling to increase sell of regulation services to SO as shown in Fig. 5 and energy selling in market for off-peak duration. Its participation in regulation market is more as compared to energy market, which affects its profit positively. In deregulated milieu, risk-aversiveness issue could have a substantial impact on EVA’s decision-making for executing TOU-PBDR and smart coordination.

Fig. 5 Total regulation capacity at hour t



6 Conclusion

Proposed work models optimal risk-constrained scheduling of EVA incorporating TOU-PBDR to maximize its profit while supplying energy requirement of EV owners. The paper presents a financially viable optimization basis for aiding smart charging of EVs. Risk assessment model for financial risk management considered energy and regulation prices uncertainties whereas *CVaR* for the risk estimation. Stochastic optimization problem formulation is utilized for comprehensive techno-economic evaluation through MCS based scenarios generation and KD based reduction. Results show that, for risk-averse EVA, different schedules were obtained with more costs as compared to risk-neutral EVA. As a part of future work, other uncertainties such as renewable generation could be incorporated to investigate balancing potential of EVA through synergistic relation among EV and renewable technologies.

References

1. Rajakaruna S, Shahnia F, Ghosh A (2015) Plug in electric vehicles in smart grids—integration techniques. Springer Science and Business Media, Singapore. ISBN 978-981-287-298-2
2. Michaelis J, Müller T, Reiter U, Fermi F, Wyrwa A, Chen YK, Zöphel C, Kronthaler N, Elsland R (2017) Comparison of the techno-economic characteristics of different flexibility options in the European energy system. In: 14th international conference on the European energy market (EEM), Jun 2017, pp 1–5. IEEE
3. Lopes JA, Soares FJ, Almeida PM (2011) Integration of electric vehicles in the electric power system. Proc IEEE 99(1):168–183
4. Hu J, You S, Lind M, Ostergaard J (2014) Coordinated charging of electric vehicles for congestion prevention in the distribution grid. IEEE Trans Smart Grid 5(2):703–711
5. Lam AY, Leung KC, Li VO (2016) Capacity estimation for vehicle-to-grid frequency regulation services with smart charging mechanism. IEEE Trans. Smart Grid 7(1):156–166
6. Sarker MR, Pandžić H, Sun K, Ortega-Vazquez MA (2018) Optimal operation of aggregated electric vehicle charging stations coupled with energy storage. IET Gen Trans Dist 12(5):1127–1136
7. Moghaddam SZ, Akbari T (2018) Network-constrained optimal bidding strategy of a plug-in electric vehicle aggregator: a stochastic/robust game theoretic approach. Energy 151:478–489
8. Yao L, Lim WH, Tsai TS (2017) A real-time charging scheme for demand response in electric vehicle parking station. IEEE Trans Smart Grid 8(1):52–62
9. Vayá MG, Andersson G (2015) Optimal bidding strategy of a plug-in electric vehicle aggregator in day-ahead electricity markets under uncertainty. IEEE Trans Power Syst 30(5):2375–2385
10. Song Y, Zheng Y, Hill DJ (2017) Optimal scheduling for EV charging stations in distribution networks: a convexified model. IEEE Trans Power Syst 32(2):1574–1575
11. Shafie-khah M, Heydarian-Forushani E, Osório GJ, Gil FA, Aghaei J, Barani M, Catalão JP (2016) Optimal behavior of electric vehicle parking lots as demand response aggregation agents. IEEE Trans Smart Grid 7(6):2654–2665
12. Nezamodini N, Wang Y (2016) Risk management and participation planning of electric vehicles in smart grids for demand response. Energy 116:836–850
13. Rabiee A, Mohseni-Bonab SM, Soltani T, Bayat L (2017) A risk-based two-stage stochastic optimal power flow considering the impact of multiple operational uncertainties. J Energy Manag Technol 1(1):30–42

14. Conejo AJ, Carrión M, Morales JM (2010) Decision making under uncertainty in electricity markets. Springer, New York
15. Xu Z, Hu Z, Song Y, Wang J (2017) Risk-averse optimal bidding strategy for demand-side resource aggregators in day-ahead electricity markets under uncertainty. *IEEE Trans Smart Grid* 8(1):96–105
16. Wu H, Shahidehpour M, Alabdulwahab A, Abusorrah A (2016) A game theoretic approach to risk-based optimal bidding strategies for electric vehicle aggregators in electricity markets with variable wind energy resources. *IEEE Trans Sustain Energy* 7(1):374–385
17. Alipour M, Mohammadi-Ivatloo B, Moradi-Dalvand M, Zare K (2017) Stochastic scheduling of aggregators of plug-in electric vehicles for participation in energy and ancillary service markets. *Energy* 118:1168–1179
18. Momber I, Siddiqui A, San Román TG, Söder L (2015) Risk averse scheduling by a PEV aggregator under uncertainty. *IEEE Trans Power Syst* 30(2):882–91
19. Vatandoust B, Ahmadian A, Golka M, Elkamel A, Almansoori A, Ghaljehei M (2018) Risk-averse optimal bidding of electric vehicles and energy storage aggregator in day-ahead frequency regulation market. *IEEE Trans Power Syst*
20. Zhao J, Wan C, Xu Z, Wang J (2017) Risk-based day-ahead scheduling of electric vehicle aggregator using information gap decision theory. *IEEE Trans Smart Grid* 8(4):1609–1618
21. Yang L, Zhang J, Poor HV (2014) Risk-aware day-ahead scheduling and real-time dispatch for electric vehicle charging. *IEEE Trans Smart Grid* 5(2):693–702
22. <https://www.gams.com/>
23. Sharma KC, Jain P, Bhakar R (2013) Wind power scenario generation and reduction in stochastic programming framework. *Electr Power Compon Syst* 41(3):271–285

Optical Gain Tuning in Type-I $\text{Al}_{0.45}\text{Ga}_{0.55}\text{As}/\text{GaAs}_{0.84}\text{P}_{0.16}/$ $\text{Al}_{0.45}\text{Ga}_{0.55}\text{As}$ Nano-heterostructure



Md. Riyaj, Sushil Kumar, P. A. Alvi and Amit Rathi

Abstract The electronic and optical properties of GaAs-based Type-I n- $\text{Al}_{0.45}\text{Ga}_{0.55}\text{As}/\text{GaAs}_{0.84}\text{P}_{0.16}/\text{p-Al}_{0.45}\text{Ga}_{0.55}\text{As}$ quantum well heterostructure have been investigated. The detailed analysis of the AlGaAs/GaAsP Type-I quantum well heterostructures is based on a six-band k.p Hamiltonian. For the calculation of optical gain, initially 6×6 Luttinger Hamiltonian is worked out to calculate the wave function and subband dispersion and then optical matrix and momentum matrix element is calculated. The optical gain properties of the active region is presented as a function of external strain. For a charge carrier injection of $4 \times 10^{12}/\text{cm}^3$, the peak optical gain is 601/cm within TE mode along [001] direction at energy 1.21 eV and wavelength 1.02 μm . The application of external strain (-8 , -4 , 0 , 4 and 8 GPa) on the structure along the [001] direction within TE and TM mode shows that the total optical gain and corresponding lasing wavelength both shift to higher values.

Keywords Optical gain · External strain · Heterostructures · TE mode · TM mode

Md. Riyaj (✉) · A. Rathi
School of Electrical Electronics and Communication Engineering,
Manipal University Jaipur, Jaipur 303007, Rajasthan, India
e-mail: roziriyaj@gmail.com

A. Rathi
e-mail: amitrathi1978@gmail.com

S. Kumar
School of Engineering & Technology, Noida International University,
Greater Noida 203201, UP, India
e-mail: sushilkumar0108@gmail.com

P. A. Alvi
Department of Physics, Banasthali University, Banasthali 304022, Rajasthan, India
e-mail: drpaalvi@gmail.com

© Springer Nature Singapore Pte Ltd. 2020
A. Kalam et al. (eds.), *Intelligent Computing Techniques for Smart Energy Systems*,
Lecture Notes in Electrical Engineering 607,
https://doi.org/10.1007/978-981-15-0214-9_24

1 Introduction

Laser semiconductor diodes play an important role in optical communication, medicine, optical storage, and materials processing. A semiconductor laser enhances the characteristics of laser diodes in emitted wavelength dependence on nano-heterostructure dimension. According to quantum theory, a quantum confinement phenomenon occurs in a narrow active region of the quantum well heterostructure. The optical losses in the structure and amplification of light in the active region determine laser diode performance. The gain medium is the source of optical gain within semiconductor laser which results from the transition from a higher energy level to lower energy level. Basic properties of gain medium are laser transition that takes place in the desired wavelength. The theory of calculation of conduction band energy shift in semiconductor is developed by Anghel and Sterian [1]. The band edge shift is found to be in proportion with strain tensor as per Bardeen and Shockley [2]. The k.p. method is used to know the band structure and the wave function of bound and unbound states in both lattice matched and strained quantum well. The strained structure can reduce the mixing of wave function. The InGaAs/GaAsSb lasers on InP substrate with low threshold current reported by Chang et al is presented [3]. The energy gaps are altered and degeneracies are removed due to the application of external compressive and uniaxial strain. In the work [4, 5], electroluminescence along uniaxial stress in AlGaAs/GaAsP has been studied. The lattice parameter and symmetry of the material are changed due to the application of external pressure on heterostructure and results in significant changes in the electronic band structure. The deformation potential can describe the strain dependence on the electronic energy level which is generally in the range of 1–10 eV. S. G. Anjum et al. report the study of optical response in Type-II InAs/AlSb quantum well heterostructure [6]. A. K. Singh reports optical characteristics of type-I nano-scale heterostructure under external uniaxial strain [7, 8].

2 Theoretical Background

This nano-heterostructure consists of 14 nm single quantum well of GaAsP material which is separated by 100 Å AlGaAs as barriers on both sides of the well. The 6×6 k.p Hamiltonian method has been used to calculate subband dispersion and corresponding wave functions. Both external and internal strain have been considered for the calculation purpose. The lattice mismatch of layers that has appeared is due to internal strain. It is essential to understand the physics of band structure for the purpose of studying the optical gain along the external pressure. To calculate discrete energy level within quantum well heterostructure, 6×6 k.p Hamiltonian matrix has been used. The optical gain versus energy in Transverse Electric and Transverse Magnetic mode have been calculated using standard expression [9, 10].

3 Simulation Results

Initially, Schrödinger equation has been worked out to find the wave function associated with the conduction band electron to investigate the optical gain in Type-I $n\text{-Al}_{0.45}\text{Ga}_{0.55}\text{As}/\text{GaAs}_{0.84}\text{P}_{0.16}/p\text{-Al}_{0.45}\text{Ga}_{0.55}$ and six-band Hamiltonian method has been solved to calculate the wave function associated with valance subbands. It is necessary to know about the energy band diagram of the heterostructure and energy band structure in terms of charge carriers that are responsible for making the transition resulting in optical gain. Figures 1 and 2 show the electron and hole wave function of 14 nm quantum well heterostructure. Light hole band is just below the heavy hole band as shown in Fig. 3. From Fig. 1, Total electron probability is 2.48 eV and total hole probability is 1.8 eV at pressure -8 GPa. A moderate drop in total electron and hole density have been seen in AlGaAs/GaAsP heterostructure with increasing external strain. E. Yavblonovitch reports quantum confinement and energy shift of heavy hole in InGaAs quantum well heterostructure [11]. The conduction band of

Fig. 1 Electron wave function of type-I $n\text{-Al}_{0.45}\text{Ga}_{0.55}\text{As}/\text{GaAs}_{0.84}\text{P}_{0.16}/p\text{-Al}_{0.45}\text{Ga}_{0.55}$ heterostructure

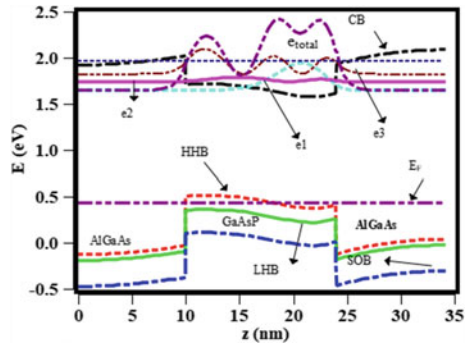


Fig. 2 Hole wave function of type-I $n\text{-Al}_{0.45}\text{Ga}_{0.55}\text{As}/\text{GaAs}_{0.84}\text{P}_{0.16}/p\text{-Al}_{0.45}\text{Ga}_{0.55}$ heterostructure

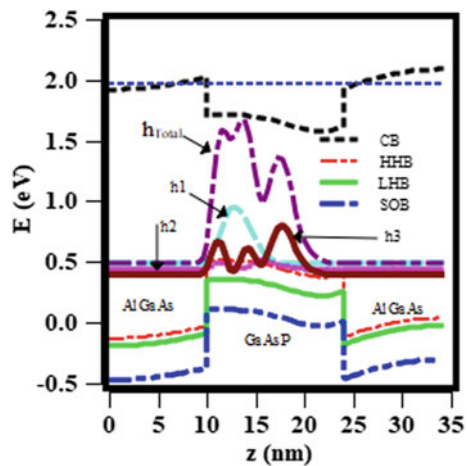
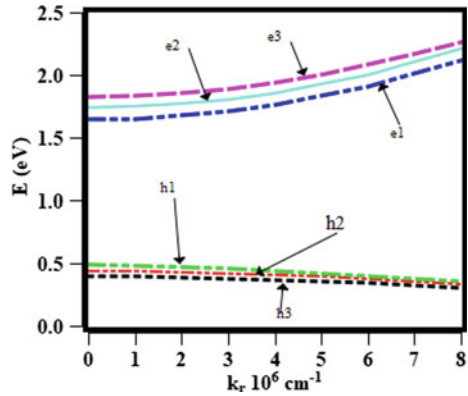


Fig. 3 Dispersion curve for conduction band electrons and valence band holes



quantum well (GaAsP) confines electrons while valence band barriers confine holes. Figure 3 shows dispersion curve for conduction band electrons and valence band holes. The matrix elements (momentum matrix and dipole moment) have been calculated after band dispersion calculation. The dipole matrix element is anisotropic and optical gain depends on polarization of light for quantum well heterostructure. Generally, there are two polarization modes namely Transverse Electric (TE) and Transverse Magnetic (TM) mode. We can get information about band structure by applying an external compressive and uniaxial strain on a heterostructure. An External strain is applied on the structure to investigate tunability of the optical gain in Type-I-AlGaAs/GaAsP/AlGaAs. Figure 4 shows the optical gain within Transverse mode (TE mode) along [001] direction at temperature 77 K and found the maximum

Fig. 4 Illustration of external strain effect on optical gain versus photon energy (TE Mode) for InGaAs/GaAsP heterostructure along [001] direction at T = 77 K

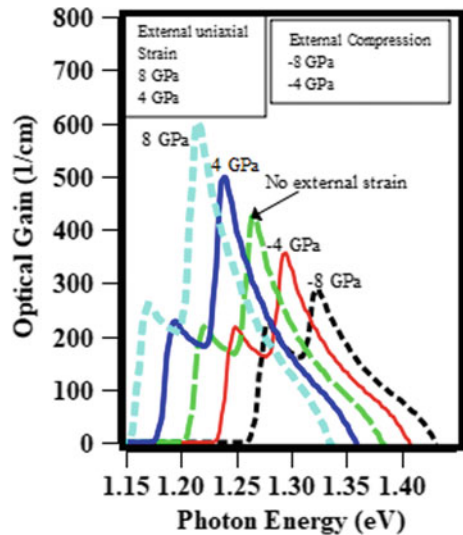
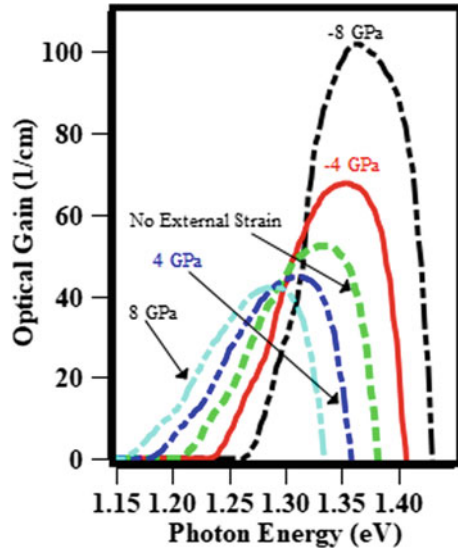


Fig. 5 Illustration of external strain effect on optical gain versus photon energy (TM Mode) for InGaAs/GaAsP heterostructure along [001] direction at $T = 77$ K



optical gain is 601 (1/cm) at 8 GPa along [001] direction. It is observed that optical gain is increasing with increase in external strain in TE mode whereas optical gain drops with increase in external strain in TM mode. Photon energy shifts toward lower value with increase in external strain which indicates the wavelength shifts to larger values. We plotted optical gain versus photon energy curve within TM mode along the direction [001] as shown in Fig. 5. Peak optical gain 101/cm at external compression -8 GPa has been observed in TM mode and also photon energy shifts to lower values with increase in pressure as shown in Fig. 5.

4 Conclusions

The total optical gain improvement in Type-I AlGaAs/GaAsP/AlGaAs quantum well heterostructure has been studied for SWIR applications. The band structure computation has been evaluated using 6×6 k.p. Hamilton matrix. The material gain (Optical Gain) is calculated for external pressure of -8 , -4 , 0 , and 8 GPa and external pressure has been applied along [001] and [100] on the heterostructure. A significant improvement has been observed that optical gain is increased with the increase in external pressure. The maximum optical gain 601(1/cm) is obtained at 8 GPa along the [001] direction as shown in Fig. 4. The photon energy also shifts toward left with the increase in pressure. From Fig. 5, a strong drop has been observed in optical gain with increase in pressure and the photon energy shifts toward right with increase in pressure. A large value of optical gain is obtained along [100] direction with the same pressure applied in both the cases.

References

1. Anghel DA, Sterian AR (2012) Modeling quantum well lasers. *Math Problem Eng* 2012
2. Bardeen J, Shockley W (1950) Deformation potentials and mobilities in non-polar crystals. *Phys Rev* 80:72
3. Chang C-H, Li Z-L, Lu H-T, Pan C-H, Lee C-P, Lin G, Lin S-D (2015) Low threshold short-wavelength infrared InGaAs/GaAsSb 'W'-type QW laser on InP substrate. *Photon Technol Lett IEEE* 27(3):225–228
4. Bogdanov EV, Ya Minina N, Sirokov SS, Yunovich AE, Kissel H (2009) Electroluminescence in laser diode nanostructures p-AlxGa1-xAs/GaAs1-yPy/n-AlxGa1-xAs under uniaxial compression. *Physics, chemistry and application of nanostructures: reviews and short notes*, pp 609–612
5. Andreev EV, Bogdanov EV, Kissel H, Kolokolov KI, Ya Minina N, Shirokov SS, Yunovich AE (2009) Electroluminescence and band structure in p-AlxGa1-xAs/GaAs1-yPy/n-AlxGa1-xAs under uniaxial compression. *High Press Res* 29(4):495–499
6. Anjum SG, Yadav N, Nirmal HK, Sharma M, Siddiqui MJ, Alvi PA (2018) Investigation of optical response in type-II InAs/AlSb nano-scale heterostructure: a novel dual structure. *Mater Today Proc* 5(1):1691–1695
7. Riyaj Md, Singh AK, Rathi A, Alvi PA (2017) Optical properties of Type-I GaAsP/AlGaAs nano-heterostructure under external uniaxial strain. In: *AIP conference proceedings*, vol 1832, no 1, p 120022. AIP Publishing
8. Singh AK, Rathi A, Riyaj Md, Sandhya K, Bhardwaj G, Alvi PA (2017) Wavefunctions and optical gain in Al 0.8 Ga 0.2 As/GaAs 0.8 P 0.2 type-I QW-heterostructure under external electric field. In: *2017 international conference on computer, communications and electronics (Comptelix)*, pp 59–62. IEEE
9. Chuang SL (1995) *Physics of optoelectronic devices*. Wiley, New York
10. Lal P, Yadav R, Sharma M, Rahman F, Dalela S, Alvi PA (2014) Qualitative analysis of gain spectra of InGaAlAs/InP lasing nano-heterostructure. *Int J Modern Phys B* 28(29):1450206
11. Yablonovitch E (1988) Band structure engineering of semiconductor lasers for optical communication. *J Light Technol* 6:1292–1299

Semantic Similarity Computation Among Hindi Words Using Hindi Lexical Ontology



Yogesh Gupta and Amit Saraswat

Abstract The measurement of semantic similarity between two concepts/words has always been a challenge in the field of document retrieval. As per current literature, there is no method to compute semantic similarity for Hindi words. Therefore, a new computational method is proposed to measure semantic similarity between Hindi words using lexical ontology. In this approach, Hindi WordNet is used which gives the relational information among various Hindi words/concepts. The performance is tested on translated Miller and Charles's benchmark dataset. In this paper, the three different semantic similarity measuring methods are used to compute semantic similarity for 20 words pairs. The accuracy of the results is also measured in this work using the correlation coefficient. The proposed method in this paper is focusing on the study and analysis of the results obtained from semantic similarity measuring methods on Hindi concepts/words.

Keywords Ontology · Hindi WordNet · Similarity measures · Semantic similarity

1 Introduction

Semantic similarity is the measurement of similarity between two concepts/words and this similarity is not necessarily in lexicographical order. It plays a crucial role in many applications like information retrieval system, natural language learning, text summarization, word sense disambiguation, classification, annotation and level segmentation, etc. [1]. Nowadays, it becomes a challenge to determine semantic similarity among the different pairs of words/concepts. In literature, it is shown that

Y. Gupta (✉)

Department of Computer Science and Engineering, Manipal University Jaipur, Jaipur, India
e-mail: Yogesh.Gupta@jaipur.manipal.edu

A. Saraswat

Department of Electrical Engineering, Manipal University Jaipur, Jaipur, India
e-mail: amit.saraswat@jaipur.manipal.edu

lexical ontology provides past historical knowledge to compute semantic similarity among concepts/words [2]. This paper is focused on lexical ontology like WordNet [3].

Lexical ontology provides a means for mapping lexical concepts and reasons about concepts. The nouns, adjectives, verbs, and adverbs are gathered into a set of cognitive synonyms in WordNet, which is called synsets. Each synset represents one underlying distinct lexical concept. In India, IIT Mumbai has developed WordNet for Hindi and other Indian languages (Indo WordNet). Mahato and Thomas [8] used Hindi language in their automated essay grading systems. Jha et al. [9] presented a method to understand the semantics of a language using Hindi and Telugu lexicons. Kumar et al. [10] proposed an approach for syntax analysis of Hindi sentences.

In literature, researchers mainly focused on document retrieval systems that are purely built for English and Cross-Language Information Retrieval (CLIR). English WordNet has been used by many researchers extensively to compute semantic similarity [4]. But, very less work is reported for Hindi language in literature, especially in the field of semantic similarity. Therefore, a method is presented and developed in this paper to compute semantic similarity among various concepts using lexical ontology like WordNet.

The remaining paper is structured as follows: Sect. 2 discusses the fundamentals of lexical ontology and the concepts of semantic similarity. The proposed method is presented in Sect. 3. The experimental results and their discussions are shown in Sect. 4. At last, Sect. 5 concludes the paper.

2 Theoretical Background of Hindi Ontology

The word “ontology” is a special area of metaphysics, which deals with “the study of being”. There are many definitions of ontology like “it is one of the structured ways of presenting knowledge and a shared specification of conceptualization” according to Gruber [5].

In WordNet, nouns, adjectives, verbs, and adverbs are gathered into different sets of cognitive substitutes or synonyms [3]. These sets are called synsets, which are interlinked by means of variety of lexical relations and conceptual-semantic. WordNet gives the following information which can be used to measure semantic likeness between concepts/words:

- Generality versus Specificity Concepts in WordNet Ontology,
- Thesaurus based information
- Relationship between words

2.1 The Structure for Indo WordNet

Indo WordNet [6] is a dedicated lexical-semantic network for Indian languages (Gujarati, Hindi, Punjabi, Bengali, Tamil, Marathi, Telugu, Kashmiri, and Nepali). Though each language has its own individual WordNet but all these WordNet are attached and interconnected with interlingual links. These links are kept in the Inter-Lingual Index (ILI).

As English WordNet, the Hindi WordNet is also a collection of various semantic and lexical relations among different Hindi words or Hindi word pairs. It gives well-thought-out lexical information that is in the form of word meanings. Based on psycholinguistic values, each entry in the Hindi WordNet is discussed below.

- **Synset:** “It is a set of identical words”.
For example, “विद्यालय, पाठशाला, स्कूल.”
- **Gloss:** “It defines the concept of a synset”.
- **Hyponymy and Hypernymy:** “Hypernymy is a semantic relation between two synsets to identify superset hood. In a similar way, hyponymy is for identifying subset hood. The hyponymy relation is transitive and asymmetrical. Hypernymy is just opposite of hyponymy”.

Example:
बेलपत्र, बेल-पत्र
==> पत्ता, पात, पर्ण, पत्र, दल

- **Holonymy and Meronymy:** “It is a semantic relation between two synsets. Holonymy is the reverse of meronymy”.

Example:
जड़, मूल, सोर
==> पेड़, वृक्ष, पादप, द्रुम

An example of “IS-A relationship structure” of Hindi WordNet, lexical ontology is shown in Fig. 1.

3 Proposed Semantic Similarity Method

In this paper, a method is presented to calculate semantic likeness between two Hindi words using Hindi WordNet lexical ontology. The method accepts two words and computes semantic similarity using three different approaches. Then finally, it returns semantic similarity as the results. This method may be used for all types of linguistic ontologies. But, it is developed and checked for Hindi text only, which is derived from Hindi WordNet, in this paper.

The complete framework of the presented method is shown in Fig. 2. The presented method takes words/concepts pairs as input, then the presence of these words/concepts pairs are checked in Hindi WordNet taxonomy. In this module, the root is determined for both the hypernym trees. If both trees are sharing a common root, then these hypernym trees move to Leacock and Chodorow (*LCH*) module. *LCH* module takes these hypernym trees as inputs which capture *LCH* for the

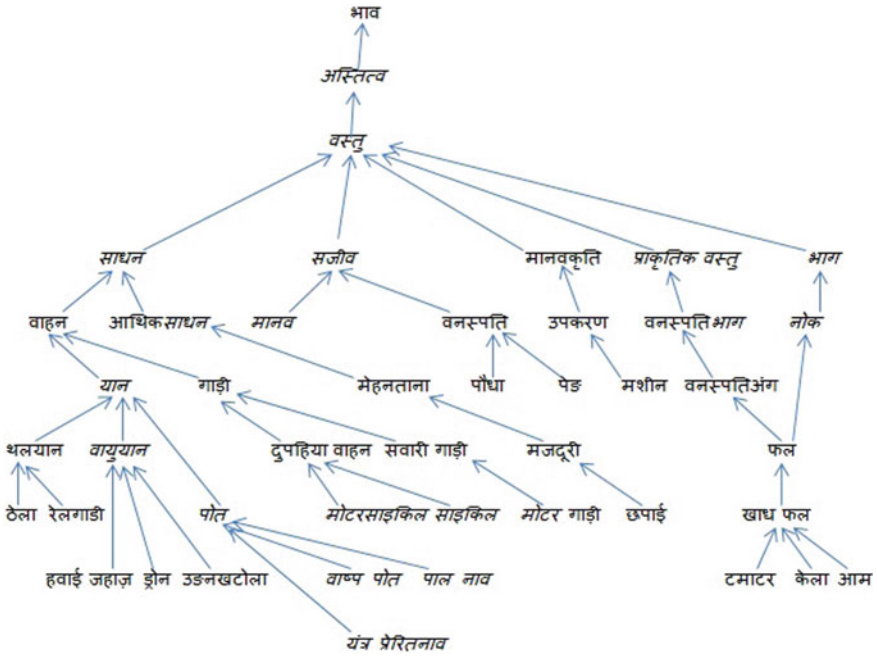


Fig. 1 The structure of Hindi WordNet

words/concepts pairs, otherwise the process terminates here. Finally, similarity module computes semantic similarities among various words/concepts pairs. This module gives a value as output, which is the similarity value between these words.

4 Experiments and Analysis

All the experiments are performed on Miller and Charles dataset [7]. This is a benchmark dataset to measure semantic similarity among words/concepts pairs. The M&C dataset is written in English language and the proposed approach is for Hindi language. Therefore, the dataset is translated into Hindi using NLP expert’s advice. In this paper, the words/concepts, which have faithful translation, are considered for semantic similarity. The 20 word pairs of M&C dataset are considered for experiments. Table 1 tabulates all the experimental results that are performed in this paper. These experiments are performed on the basis of different semantic similarity methods and the results are decided with the concern of human similarity judgment.

As shown in Table 1, the dataset has similarity values for all similarity measures in the range of 0–4. Therefore, all the results obtained from experiments are normalized and converted to the same range. The results for similarity measures and human

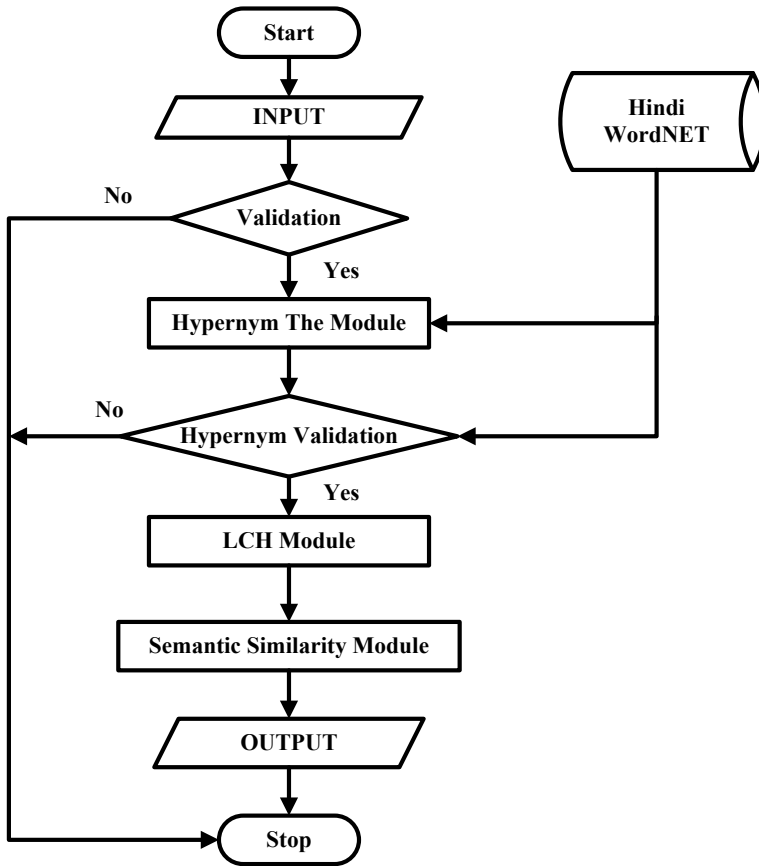


Fig. 2 The framework for the proposed semantic similarity method

similarity judgments are also compared using correlation evaluating parameter. Correlation is a technique to find out relationships among variables. These variables may be quantitative variables or continuous variables. In this paper, three different correlation coefficients are used for comparing human decisions and similarity measures. These coefficients are Pearson, Spearman, and Kendall’s correlation coefficients.

From Table 2, it is clear that *LCH* semantic similarity measure gets the best results for all three correlation coefficient measures. The following observations can be made by analyzing the results:

- Edge-based similarity measures perform better than information content-based measures.
- *LCH* is getting better results as compared to Wup and Resnik, which is a measure of variable depth, i.e., depth of both the words should be taken into account. It means that there is a scope to improve Wup method.
- The information content-based measure may be enhanced using a better corpus.

Table 1 Results of word pairs semantic similarity measurement

S. No	English word pairs	Hindi word pairs	Human rating (0–4)	Semantic similarity measures		
				Edge-based measure		Node-based
				LCH (0–4)	Wup (0–4)	Resnik (0–4)
1	Glass-Magician	शिशु - जादूगर	0.44	1.10	1.48	2.36
2	Monk-Slave	साधु - दास	0.57	2.25	3.12	1.92
3	Coast-Forest	तट- वन	0.85	1.54	1.84	2.36
4	Monk-Oracle	साधु- आकाशवाणी	0.91	1.22	1.60	2.36
5	Lad-Wizard	बालक- निपुण	0.99	2.61	1.92	3.28
6	Forest-Graveyard	वन- कब्रिस्तान	1.00	1.54	1.84	2.36
7	Food-Rooster	भोजन - मुर्गा	1.09	1.22	1.60	2.36
8	Coast-Hill	तट - पहाड़ी	1.26	2.61	3.20	2.03
9	Lad-Brother	बालक - भाई	2.41	2.25	3.12	1.92
10	Bird-Crane	पक्षी - क्रेन	2.63	1.37	1.72	2.36
11	Bird-Cock	पक्षी - मुर्गा	2.63	3.11	1.84	2.51
12	Brother-Monk	भाई - साधु	2.74	2.25	3.12	1.92
13	Asylum-madhouse	शरण- पागलखाना	3.04	2.61	3.20	2.03
14	Furnace-Stove	भट्टी - चूल्हा	3.11	3.98	3.68	2.71
15	Magician-Wizard	जादूगर - निपुण	3.21	3.11	3.48	1.92
16	Hill-Mound	पहाड़ी - टीला	3.29	2.61	3.20	2.03

(continued)

Table 1 (continued)

S. No	English word pairs	Hindi word pairs	Human rating (0–4)	Semantic similarity measures		
				Edge-based measure		Node-based
				LCH (0–4)	Wup (0–4)	Resnik (0–4)
17	Coast-Shore	तट - किनारा	3.60	3.98	3.72	2.03
18	Cemetery-Mound	कब्रिस्तान - टीला	1.69	3.11	3.44	2.03
19	Car-Automobile	कार - मोटर	3.92	3.11	3.76	2.70
20	Sage-Wizard	ऋषि - निपुण	2.46	3.11	3.48	1.92

Table 2 Results of correlations coefficients

Semantic similarity measure	Pearson	Kendall	Spearman
Wu and Palmer	0.4526	0.4509	0.6929
Resnik	-0.580	-0.1899	0.0345
Leacock and Chodorow	0.8121	0.5778	0.8132

5 Conclusion

This paper develops a new method based on lexical ontology to determine semantic similarity among the word pairs. This method is also incorporated and utilized with WordNet ontology. This research work also presents the implementation of three different semantic similarity methods: Resnik, *LCH*, and Wup on Hindi WordNet. All the experiments are performed on Hindi words (texts). In this paper, three different correlation coefficients are used to compare human judgment and similarity measures. Based on this comparative study, *LCH* is found to be the best semantic similarity measure. In future, the work can be directed to large datasets and semantic similarity can also be used for many applications like text summarization, document retrieval, and information extraction, etc.

Acknowledgements The authors sincerely acknowledge Miller and Charles for their benchmark dataset which is used in the present work.

References

1. Varelas G, Voutsakis E, Raftopoulou P (2005) Semantic similarity methods in WordNet and their application to information retrieval on the web. In: Proceedings of the 7th annual ACM international workshop on web information and data management, Bremen, Germany, pp 10–16
2. Li Y, Bandar JA, Mclean D (2003) An approach for measuring semantic similarity between words using multiple information sources. *IEEE Trans Knowl Data Eng* 15(4):871–882
3. Fellbaum C (1998) *WordNet: an electronic lexical database*. MIT Press
4. Wagh K, Kohle S (2011) Information retrieval based on semantic similarity using information content. *Int J Comput Sci* 8(2):364–370
5. Gruber TR (1995) Towards principles for the design of ontology used for knowledge sharing. *Int J Hum Comput Stud* 43(6):907–928
6. Bhattacharyya P (2010) IndoWordNet. In: Proceedings of 7th international conference on language resources and evaluation (LREC'10), Malta
7. Miller GA, Charles WG (1991) Contextual correlates of semantic similarity. *Lang Cogn Process* 6:1–28
8. Mahato S, Thomas A (2017) Lexico-semantic analysis of essays in Hindi language. In: Proceedings of the 3rd modelling symposium (ModSym), developmental aspects of intelligent adaptive systems (DIAS), and educational data mining practices in Indian academia (EDUDM), Jaipur, India
9. Jha J, Parupalli S, Singh N (2018) OntoSenseNet: a verb-centric ontological resource for indian languages. <https://doi.org/10.13140/rg.2.2.29641.03687>
10. Kumar A, Saurabh, Raza M (2017) Syntax and semantic analysis of Devanagari Hindi. *Int J Recent Sci Res* 8(6):17965–17970

A Dual-Band Microstrip Patch Antenna for Wireless Applications



P. Kumar

Abstract In this paper, the design of a dual-band microstrip antenna is presented. The proposed design is based upon the T-shaped structure with two strips. The antenna is fed by coaxial probe feeding. The presented antenna gives wide bandwidth for both frequency bands. The antenna is simple in structure and is compact in size. The design is simulated and optimized using CST Microwave studio software. Various antenna parameters such as reflection coefficient, resonant frequencies, bandwidth, radiation patterns, gain, directivity, and efficiencies are presented and discussed. The presented antenna resonates at two resonances at 3.7 and 6 GHz. The designed antenna is suitable for dual-band wireless applications.

Keywords Microstrip patch antenna · Dual band · Reflection coefficient

1 Introduction

Modern wireless communication systems require multiband microstrip patch antennas for various applications. Multiband microstrip patch antennas resonate at more than one frequency to make antennas suitable for multiple applications. Dual-band microstrip patch antenna resonates at two different frequencies [1, 2]. The microstrip patch antennas can be designed for dual-band applications using various techniques such as gap-coupling [3–5], using shorting post [6, 7], using stacked coupling [8, 9]. In [10], a compact patch antenna is designed for dual-band wireless local area networks (WLAN) applications. The designed antenna covers the two WLAN bands, i.e., 2.4 GHz WLAN frequency band and 5 GHz WLAN frequency band. The size of the antenna was reduced by 31%. In [11], the dual-band rectangular patch antenna is designed using reactive loading technique. The designed antenna operates at two resonances, i.e., 2.4 and 5.2 GHz. The bandwidth of lower frequency band is 5.4% and bandwidth of higher frequency band is 2.3%. In [12], an eight-element array is designed for dual-band applications. The dual-band operation is achieved by using

P. Kumar (✉)

School of Engineering, University of KwaZulu-Natal, Durban 4041, South Africa
e-mail: pkumar_123@yahoo.com

© Springer Nature Singapore Pte Ltd. 2020

A. Kalam et al. (eds.), *Intelligent Computing Techniques for Smart Energy Systems*,
Lecture Notes in Electrical Engineering 607,
https://doi.org/10.1007/978-981-15-0214-9_26

219

the slot loading in the radiating patch. The designed antenna operates at two resonances, i.e., 27.3 and 39.75 GHz. Recently, in [13] a low profile compact microstrip patch antenna is designed for dual-band applications. The antenna operates at 1.8 and 2.4 GHz. The size of the radiating patch is 40 mm \times 29 mm. The lower resonance bandwidth is 45 MHz and higher resonance bandwidth is 95 MHz. A dual-band antenna is designed and developed in [14]. The antenna covers dual bands for with center frequencies 2.4 and 5.8 GHz. The antenna utilizes the defected ground structure technology to achieve dual-frequency band operation.

In this paper, the T-shaped antenna with two strips is designed for dual-band applications. The T-shaped antennas provide better performance as compared to monopole microstrip antennas [15]. The proposed antenna resonates at two different frequencies at 3.7 and 6 GHz. The design is simulated using CST microwave studio software. The reflection coefficient of the optimized antenna configuration confirms the dual-band behavior of the antenna. Rest of the paper is structured as follows. Section 2 presents the antenna configuration of the proposed antenna. The simulated results are presented and discussed in Sect. 3. The concluding remarks are given in the last section, i.e., Sect. 4.

2 Antenna Geometry

The geometry of the designed dual-band microstrip patch antenna is presented in Fig. 1. The top view and side view of the structure is shown in Fig. 1a and b, respectively. The T-shaped structure has two strips in order to achieve the dual-band

Fig. 1 Geometry of proposed microstrip patch antenna **a** top view, **b** side view

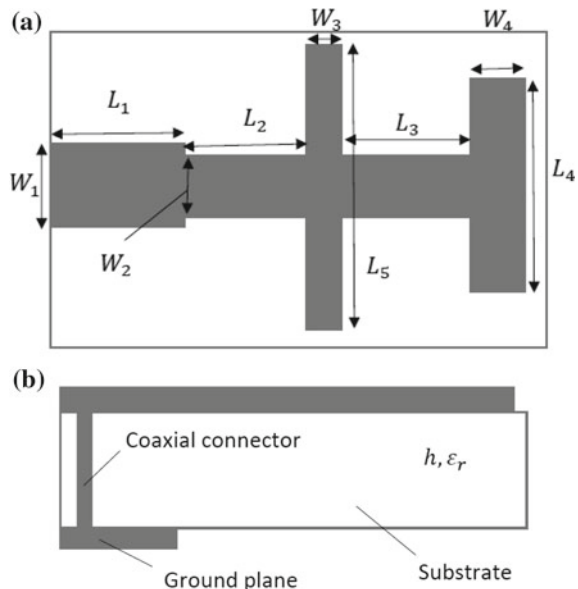


Table 1 Optimized dimensions of the antenna

S. No.	Parameter	Value
1	L_1	1.84 mm
2	L_2	7.73 mm
3	L_3	8.50 mm
4	L_4	10.82 mm
5	L_5	21 mm
6	W_1	2.45 mm
7	W_2	2.09 mm
8	W_3	0.50 mm
9	W_4	0.50 mm
10	h	1.58 mm
11	ϵ_r	4.9

performance by the antenna. The structure is built on a substrate. The thickness of the substrate is h and the relative permeability of the substrate is ϵ_r as shown in Fig. 1. The antenna is fed by a coaxial connector as shown in Fig. 1. The structure is simulated and optimized to achieve dual-band operation. The optimized dimensions of the presented structure are given in Table 1.

3 Results and Discussion

The simulated antenna parameters are presented in this section. Figure 2 presents the reflection coefficient of the proposed antenna. From this figure, it can be observed that the antenna is resonating at two different resonances and it shows the dual-band characteristics. The resonant frequencies of the antenna are 3.7 and 6 GHz. The reflection coefficient of the proposed antenna is less than -10 dB from 3.54 to 3.82 GHz and from 5.56 to 6.45 GHz, hence the bandwidth for the first resonance is from 3.54 to 3.82 GHz (7.6%) and for second resonance is from 5.56 to 6.45 GHz

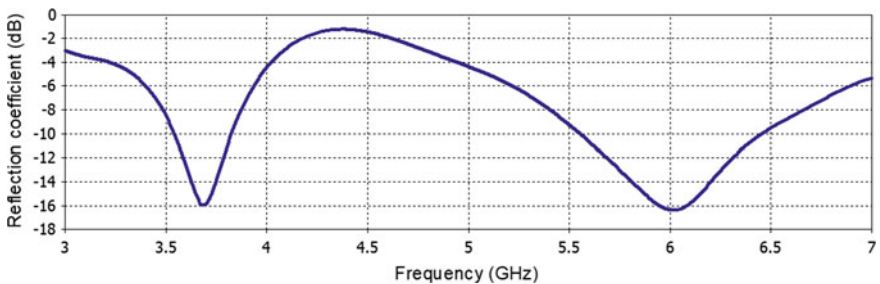


Fig. 2 Reflection coefficient versus frequency

(14.83%). The radiation patterns of the antenna in various planes at both resonances are presented in Fig. 3. The three-dimensional radiation pattern at 3.7 GHz, three-directional pattern at 6 GHz, radiation pattern in $\phi = 0^\circ$ plane at 3.7 GHz, radiation pattern in $\phi = 90^\circ$ plane at 3.7 GHz, radiation pattern in $\phi = 0^\circ$ plane at 6 GHz, and radiation pattern in $\phi = 90^\circ$ plane at 6 GHz are shown in Fig. 3a, b, c, d, e, and f, respectively. From the patterns it can be seen that the shape of the patterns in $\phi = 0^\circ$ is figure of eight and in $\phi = 90^\circ$ the patterns reflect omnidirectional behavior. The behavior of the patterns at both resonances is almost same.

The radiation pattern properties are given in Table 2. From this table, it can be observed that the changes in pattern parameters at both resonances are not significant and in $\phi = 90^\circ$ the patterns are omnidirectional at both resonances. The maximum directivity, radiation efficiency, and total efficiency are presented in Table 3. The maximum directivity at 3.7 GHz and 6 GHz is 2.67 dBi and 2.79 dBi, respectively. The radiation efficiency at 3.7 GHz and 6 GHz is 95.47% and 89.44%, respectively. The total efficiency at 3.7 GHz and 6 GHz is 92.97% and 87.37%, respectively. The maximum directivity, maximum radiation efficiency, and maximum total efficiency of the antenna are 2.79 dBi, 95.45%, and 92.97%, respectively. From the studies of antenna parameters, it can be seen that the proposed antenna meets the required standards for dual-band wireless applications. The comparison of the proposed antenna with other antennas is shown in Table 4. From Table 4, it can be observed that the proposed antenna is simple in structure and compact in size. The proposed antenna gives the wide bandwidth at both resonances.

4 Conclusion

The design of a dual-band microstrip patch antenna has been presented. The T-shaped structure with two strips is utilized to achieve dual-band operation. The reflection coefficient of the antenna confirms the dual-band behavior with resonances at 3.7 and 6 GHz. The proposed antenna is compact in size and gives wide bandwidth for both resonances. A maximum 95.45% radiation efficiency and 92.97% total efficiency are achieved by the antenna. The radiation patterns of the antenna in $\phi = 90^\circ$ plane at both center frequencies are omnidirectional. The input and radiation antenna parameters show that the proposed antenna is suitable for dual band with center frequency 3.7 and 6 GHz wireless applications.

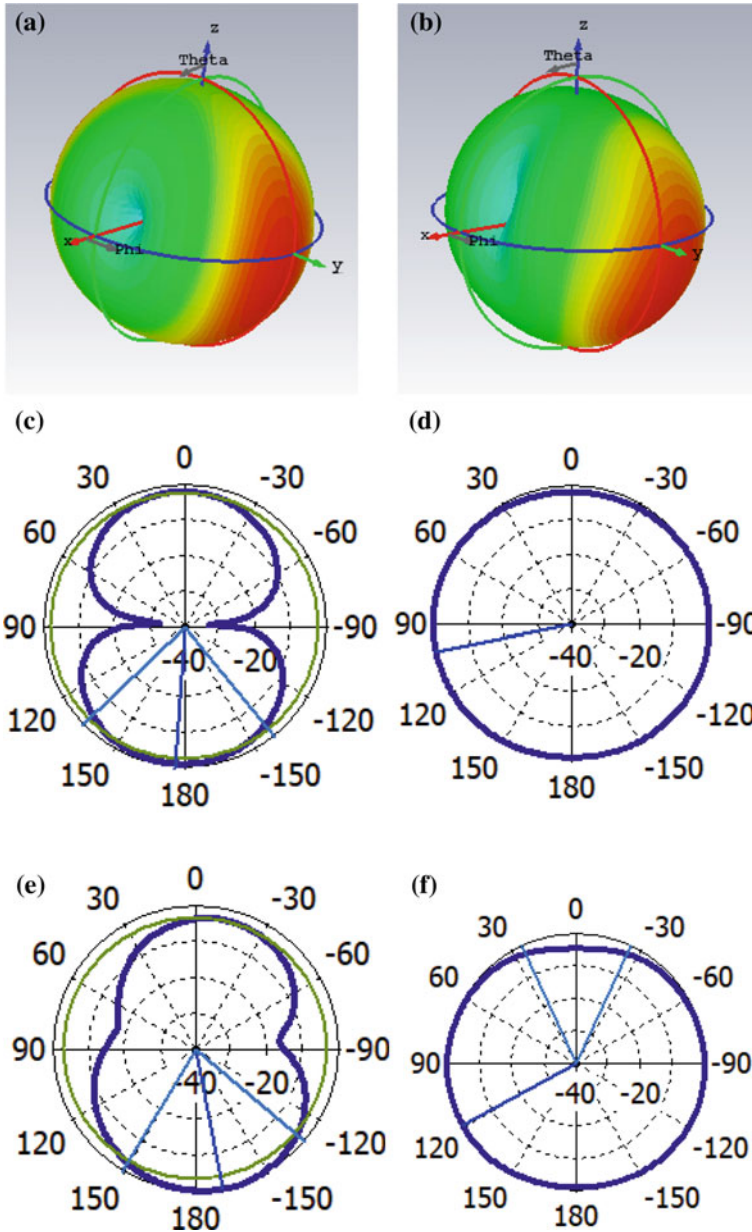


Fig. 3 Radiation patterns of the antenna **a** 3d pattern at 3.7 GHz, **b** 3d pattern at 6 GHz, **c** theta ($\phi = 0^\circ$) plane at 3.7 GHz, **d** theta ($\phi = 90^\circ$) plane at 3.7 GHz, **e** theta ($\phi = 0^\circ$) plane at 6 GHz, **f** theta ($\phi = 90^\circ$) plane at 6 GHz

Table 2 Antenna pattern parameters

S. No.	Parameter	Frequency (GHz)	Value
1	Main lobe direction ($\theta = 0^\circ$ plane)	3.7	176°
2	Main lobe direction ($\theta = 90^\circ$ plane)	3.7	102°
3	Main lobe direction ($\theta = 0^\circ$ plane)	6	169°
4	Main lobe direction ($\theta = 90^\circ$ plane)	6	119°
5	3 dB beamwidth ($\theta = 0^\circ$ plane)	3.7	85.1°
6	3 dB beamwidth ($\theta = 90^\circ$ plane)	3.7	Entire plane
7	3 dB beamwidth ($\theta = 0^\circ$ plane)	6	80.6°
8	3 dB beamwidth ($\theta = 90^\circ$ plane)	6	Entire plane

Table 3 Max. directivity, radiation efficiency, and total efficiency of the antenna

S. No.	Parameter	Frequency (GHz)	Value
1	Max. directivity	3.7	2.67 dBi
2	Radiation efficiency	3.7	95.45%
3	Total efficiency	3.7	92.97%
4	Max. directivity	6	2.79 dBi
5	Radiation efficiency	6	89.44%
6	Total efficiency	6	87.37%

Table 4 Comparison of the proposed antenna with other antennas

References	Resonant frequency	Bandwidth	Max. gain	Max. directivity	Patch size
[8]	3.42, 3.74 GHz	3.21, 1.6%	–	5.563 dB	Stacked radius, 15 mm * 15 mm
[9]	2.917, 4.636 GHz	3.42, 3.02%	–	–	Stacked, 28.01 * 35.15 mm ²
[10]	2.4, 5 GHz	2.9, 13%	9.5 dBi	–	46.1 * 56 mm ²
[11]	2.4, 5.2	5.19, 2.3%	–	6.3 dBi	44 * 41 mm ²
[13]	1.8, 2.4 GHz	2.5, 3.95%	5.79 dBi	–	40 * 29 mm ²
[14]	2.4, 5.8 GHz	3.5, 2.79%	7.4 dB	7.9 dBi	25 * 25 mm ²
Proposed	3.7, 7 GHz	7.6, 14.83%	–	2.79 dBi	21 * 19.08 mm ²

References

1. Rabbani MS, Ghafouri-Shiraz H (2017) A dual band patch antenna designed with size improvement method for 60 GHz-band duplexer applications. *Microw Opt Technol Lett* 59(1):2867–2870
2. Jandi Y, Gharnati F, Said AO (2017) Design of a compact dual bands patch antenna for 5G applications. In: 2017 international conference on wireless technologies, embedded and intelligent systems, pp 1–4
3. Kumar P (2014) Computation of resonant frequency of gap-coupled circular ring microstrip patch antennas. *Int J Autom Comput* 11(6):671–675
4. Mapare VV, Mapare SV, Sarate GG (2012) Nonradiating edges gap-coupled multiple resonator dual and tri-band microstrip antennas. *Int J Comput Appl* 56(3):6–10
5. Kumar P, Singh G, Bhooshan S, Chakravarty T (2007) Gap-coupled microstrip antennas. In: Proceedings of international conference on computational intelligence and multimedia applications, pp 435–438, India
6. Kumar P, Singh G (2009) Microstrip antennas loaded with shorting post. *Engineering* 1(1):41–45
7. Kumar P, Singh G (2011) Theoretical investigation of the input impedance of gap-coupled circular microstrip patch antennas loaded with shorting post. *J Comput Electron* 10(1):195–200
8. Kumar P, Bisht N (2011) Stacked coupled circular microstrip patch antenna for dual band applications. In: Progress in electromagnetics research symposium, Chinam, pp 629–632
9. Vishwakarma RK, Tiwari S (2010) Experimental study of stacked rectangular microstrip antenna for dual-band. *Engineering* 2:85–90
10. Meng F, Sharma S (2016) A single feed dual-band (2.4 GHz/5 GHz) miniaturized patch antenna for wireless local area network (WLAN) communications. *J Electromagn Waves Appl* 30(18):2390–2401
11. Saturday JC, Udofia KM, Jimoh AJ (2016) Design of dual band microstrip antenna using reactive loading technique. *Math Softw Eng* 2(2):114–121
12. Rafique U, Khalil H, Rehman SU (2017) Dual-band microstrip patch antenna array for 5G mobile communications. In: 2017 progress in electromagnetics research symposium, Singapore, pp 55–59
13. Rambe AH, Abdillah K (2018) A low profile rectangular patch microstrip antenna for dual-band operation of wireless communication system. *IOP Conf Ser Mater Sci Eng* 309:012046
14. Mabaso M, Kumar P (2018) A dual band patch antenna for Bluetooth and wireless local area networks applications. *Int J Microw Technol* 13(5):393–400
15. Kumar P (2017) A T shaped microstrip patch antenna for WLAN applications. In: Proceedings of the international conference on multimedia, signal processing and communication technologies, pp 157–160

Analysis of Energy Consumption and Implementation of R-Statistical Programming for Load Forecasting in Presence of Solar Generation



S. K. Singh, Harsh Vikram Singh, S. Chakrabarti and S. N. Singh

Abstract An increase in the demand for energy needs more electricity generation and better accuracy of load forecasting for short and long duration. This helps in electricity price prediction for the future market which is a very important aspect of electricity trading. This paper will present the effect of integration of renewable to the individual house and also different load forecasting methods are discussed. Results of load forecasting of individual houses are discussed for the month of December 2017 and May 2018 which is peak winter and peak summer time of energy consumption, respectively.

Keywords Advanced metering infrastructure (AMI) · Grid-connected · Hybrid inverter · MDAS/MDM

1 Introduction

Increasing demand for electricity needs integration of renewable energy and prediction of energy consumption of heavy load and individuals also. Smart cities have several application areas, out of which smart grid is the most important part. Short-term load forecasting has great importance in power system dispatching where it is used to align the peak load management with the energy generation.

S. K. Singh (✉) · S. Chakrabarti · S. N. Singh
Electrical Engineering Department, Indian Institute of Technology Kanpur, Kanpur, India
e-mail: shivks@iitk.ac.in

S. Chakrabarti
e-mail: saikatc@iitk.ac.in

S. N. Singh
e-mail: snsingh@iitk.ac.in

H. V. Singh
Electronics Engineering Department, Kamla Nehru Institute
of Technology Sultanpur, Sultanpur, India
e-mail: harshvikram@gmail.com

© Springer Nature Singapore Pte Ltd. 2020
A. Kalam et al. (eds.), *Intelligent Computing Techniques for Smart Energy Systems*,
Lecture Notes in Electrical Engineering 607,
https://doi.org/10.1007/978-981-15-0214-9_27

The traditional load forecasting methods include the time series method [1], the regression analysis method [2, 3], etc. The time series method takes less consideration of the factors that affect the load, for example, the accuracy of the forecast will be reduced when the meteorological factors suddenly change. Regression analysis considers the influence of meteorological factors and historical load on forecasting daily load. The prediction accuracy of this method is usually not high because of the strong nonlinearity between load and its influencing factors.

In this paper, the effect of integration of 5 kWp solar power plant installed in Indian Institute of Technology, Kanpur at 20 different locations and ARIMA and Exponential smoothing forecasting model are evaluated.

2 Details of the Installed System

Advanced Metering Infrastructure (AMI) and solar PV system have been installed at 20 different locations of the IIT Kanpur campus. In total, 100 kWp solar PV is connected to IIT Kanpur's distribution grid. To study the behavior of individual energy consumption pattern (load profile) and the effect of the integration of renewable energy 5 kWp in the individual house, the system integration (SI) layer is used for seamless integration of AMI and solar PV system component.

At the control centre, the software for receiving and storing all the data from smart meters and solar PV inverters are installed on servers. The operator can run various monitoring and control applications with the help of this integrated platform.

Smart cities have different areas of application, out of which smart grid is the most important part. The advanced energy management system includes different communication and various data transfer from multiple devices installed in the field.

In this paper, smart energy infrastructure, AMI architecture, and different communication technologies have been discussed. In AMI architecture, every hardware is sending data at a different rate to the central location where servers are installed. A smart meter is a very important part of smart grid from which data is being received at the servers at an interval of half an hour (load survey data) and instantaneous parameters at an interval of 5 minutes.

3 Advanced Metering Infrastructure (AMI) Architecture

AMI is the collective term for smart city implementation which establishes two-way communication from smart meter to the control centre equipment. AMI is an integrated system of smart meters, communications networks, and data management systems which measures, collects, transfers, and analyzes energy usage and communicates with metering devices. It provides information to the consumer which enables users to participate in reducing the energy consumption during the peak hours. This communication infrastructure also enables the capability of executing remote commands like load disconnect/connect.

AMI system enables different features which include remote meter reading for error-free data, network problem identification, load profiling, energy audit, and partial load curtailment in place of load shedding [4–6]. This AMI platform can be used for monitoring as well as utilization of essential features of AMI systems. The key components of AMI are.

3.1 Smart Energy Meters

Smart energy meter enables the bidirectional communication which is used to collect energy usage information at different intervals and transmitting the data through fixed communication networks to control center, as well as receiving information like pricing signals from the utility.

3.2 Communication Network

Advanced communication networks provide two-way communication from smart meters to control centre and vice versa. This communication network helps in collecting data from different smart meters to the data concentrator unit (DCU) and this data will be processed in the control centre.

3.3 Smart Grid Control Center

Servers and Meter Data Acquisition System (MDAS) are installed at the Smart Grid Control Centre which are continuously collecting data from the smart meters and other devices installed at different locations. The collected data is validated and processed by the Meter Data Management System (MDM). MDAS and MDMS are in place to collect, process, analyze, visualize, and take further actions based on the meter data.

4 Advanced Data Analysis Using Smart Meter Data

AMI and System Integration (SI) collects a 30-min smart meter dataset from the system installed at the Indian Institute of Technology Kanpur. Billing data has also been developed using historical meter data collected using the AMI system. This paper demonstrates the different characteristics which extract key data signatures and synthesize the information from all the relevant data sources. The actionable decision can be generated and provided to the operating sitting in the control center

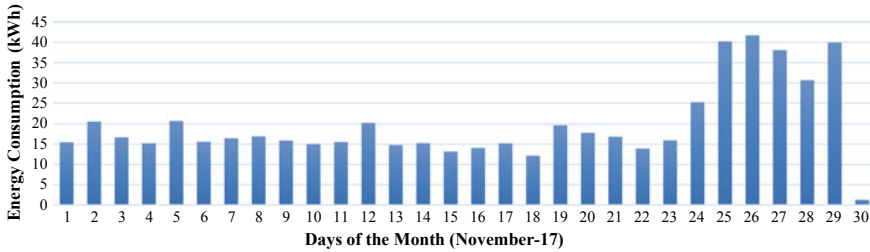


Fig. 1 Monthly (4-week) energy consumption plot

of smart city with a comprehensive assessment of grid operations to materialize the benefits of the AMI.

4.1 Signature of Monthly Energy Consumption of the House

Traditional energy meters can record real power consumption only for any consumer. Total reading of consumed units can be taken at the end of each month to record the energy usage. A smart meter is used to record different parameters voltage (V), real (watt), and apparent (VA) energy consumptions at an interval of 30-min. The monthly collected data can be used to generate reports related to energy consumption of different consumers.

Figure 1 shows monthly (4-week) energy consumption plot which is plotted from the available data for the last few months. It is important to monitor the data for monthly energy consumption which may provide information about abnormal energy consumption patterns which may help in avoiding loss of revenue in distribution system planning.

4.2 Signature of Daily Energy Consumption of the House

Energy consumption plots can be utilized to identify the minimum, maximum, and average energy consumption of the consumer. From the available data house, owner occupancy and occupant activities can be derived. More electricity consumption during the day shows that people are staying at home during the daytime. Because such information is strictly private, it should be ensured by the utility that data will not be exploited.

Therefore, in-home energy management systems (HEMS) can be used for monitoring the daily energy consumption of the consumer and triggering customer actions.

5 Impact of Renewable Integration

Most of the world’s electricity demand (approximately 78%) is met by fossil fuel based power plants which result in polluting the environment and subsequent health hazards. Various respiratory ailments, cardiovascular diseases, and the nervous system are directly linked with the carbon emissions which results from pollutants of coal combustion. The ever increasing demand for energy generation with low impact on the environment can be met by integrating more and more of renewable energy. Localized grid-connected power plants can be installed to meet the required energy demand [8, 9].

To increase the dependency on renewable energy, sources such as solar and wind can be the option for clean and green electricity generation. Currently, only 3% of the world’s electricity demand is being met by renewable sources. The government of India has planned to install 175 GW of renewable energy by 2022, (i.e., 40% of electricity demand from renewable sources). This goal can be achieved by estimating and installing solar-based power plants in different regions of India.

India is in fourth place in terms of energy consumption and a major part of the energy demand is met by the energy generated by the means of coal and heavily imported crude oil. 59% of total energy demand is met by the coal power plants of India which itself is insufficient supply for the generation of electricity [7].

To minimize the increasing requirement of energy, the institute has taken an initiative to install a grid-connected solar PV system on the rooftop of its 20 locations of capacity 5 kW in each location which constitutes 100 kW in total. Power flow from these 20 locations will be reversed when there is excess power during the off-peak hours. Energy consumption of these 20 consumers without solar has been shown in Fig. 2 for the year 2016.

A typical rooftop PV system can be classified as a stand-alone system or a grid-interactive system. Grid-interactive systems are popularly installed in urban areas, where the grid is available. The stand-alone systems, as the name suggests, are installed in rural and remote areas, where grid supply is not available. To demonstrate

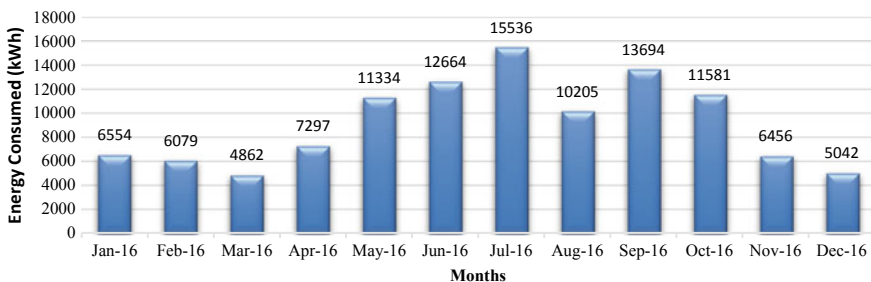


Fig. 2 Monthly cumulative energy consumption of all the consumers for the year 2016 before solar installation

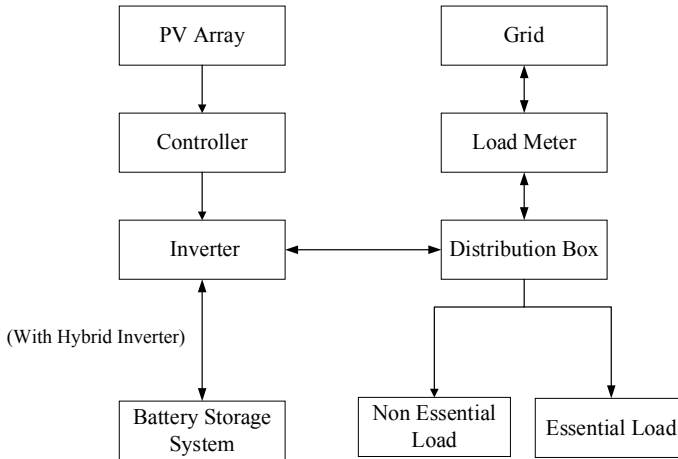


Fig. 3 Solar PV connection diagram

the feasibility of both the systems, grid-tied as well as hybrid inverter setups are used in this work (Fig. 3).

Solar PV panels of capacity 5 kWp are installed on the rooftops of 20 houses, for feeding the local load, as well as for feeding the surplus to the Grid. Out of these houses, four houses have customized hybrid inverters with battery storage of 24 kWh installed, so that a part of the excess solar energy can charge the battery, which can be used at night to feed the loads when solar is not available. Grid-tied inverters are installed in the remaining houses, which do not have battery storage (Fig. 4a).

Figure 4a illustrates the basic architecture of the solar PV systems deployed in this work. For systems without battery backup, solar PV output is directly connected to the consumer's distribution box. Based on the usage and available generation from solar PV, energy is either imported to or exported from the grid.

5.1 Grid-Connected Solar PV System Without Battery Backup

In this scheme, the solar system monitors the grid and is disconnected automatically by the internal switch present in the inverter, when grid failure or any other defined event occurs. This system has no backup and cannot supply the consumer load during grid failure. Figure 4b shows the schematics of this setup.

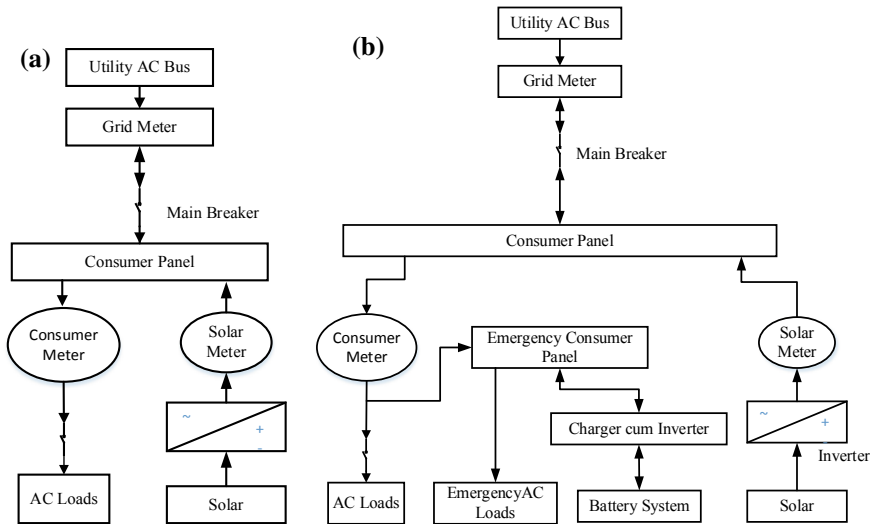


Fig. 4 a Grid-tied PV system connection diagram. b Hybrid PV system with partial battery backup

5.2 Grid-Connected Solar PV System with Battery Backup for Partial Load

This configuration is very similar to the grid-interactive solar PV system with full load battery backup. However, in this configuration, battery backup may not be enough to meet all the loads within the household. The loads are segregated into essential and nonessential loads. The essential loads are connected to the grid and also to the inverter output. The nonessential load is connected only to the grid with different busbars forming the junction. The PV feeds the house load, charges the battery, and feeds the surplus power to the grid. Figure 6 shows the schematics of the hybrid PV system.

5.3 Comparison of Monthly Consumption Pattern

The generation pattern of the power generated with the solar PV system installed at 20 different locations has been shown in Fig. 5. The monthly power consumption of the houses before and after installation of a solar PV system at 20 locations has been shown in Fig. 7 which shows the decrease in power consumption as compared to the previous year power consumption.

Figure 5 shows the bar graph of the monthly average generation by solar PV system installed at different houses, energy consumed by local load and excess power fed to the IIT Kanpur grid.

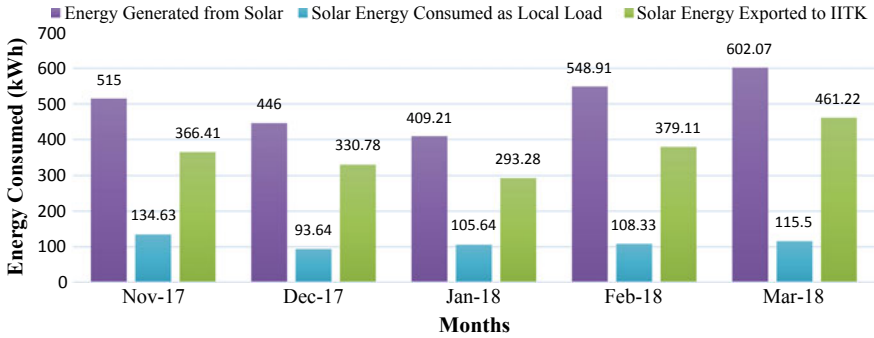


Fig. 5 Monthly average energy generated from solar, solar energy consumed as local load, and energy exported to IIT Kanpur grid

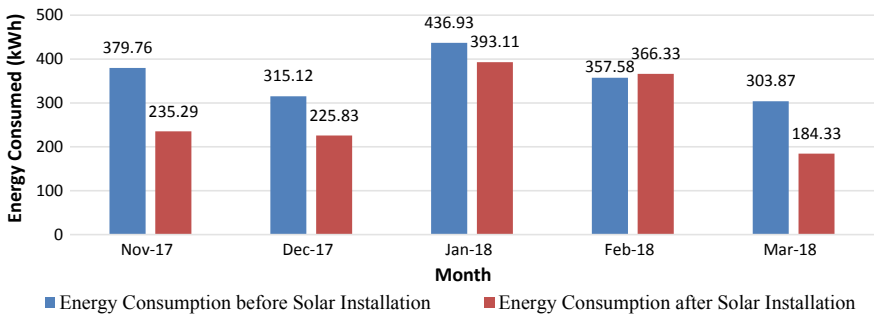


Fig. 6 Monthly average consumption with and without solar

Figure 6 is the comparison of the average monthly energy consumed by all the 20 consumers before the solar installation and after the solar installation. From this figure, we can see how the average energy consumption has changed after the installation of the solar installation.

6 Forecasting of Consumer Energy Consumption

6.1 ARIMA Forecasting Model

ARIMA (autoregressive integrated moving average) forecasting technique is commonly used to utilize the time series data and forecasting. It is a generalized version of ARMA (autoregressive moving average) process, where the ARMA process is applied for a differenced version of the data rather than the original [10–12].

Three numbers p , d , and q specify ARIMA model and the ARIMA model is said to be of order (p, d, q) . Here, p , d , and q are the orders of the AR part, difference, and the MA part, respectively. AR and MA—both are different techniques to form stationary time series data. ARMA (and ARIMA) is a combination of these two methods for a better fit of the model [13–16].

If a process is ARIMA (p, d, q) , then the differenced data is ARMA (p, q) process. The ARMA (p, q) process has the following mathematical form:

$$\begin{aligned}
 y_t &= \delta + \{\phi_1 y_{t-1} + \phi_2 y_{t-2} + \dots + \phi_p y_{t-p}\} + \{\theta_1 \varepsilon_{t-1} + \theta_2 \varepsilon_{t-2} + \dots + \theta_q \varepsilon_{t-q}\} + \varepsilon_t \\
 \Rightarrow y_t &= \delta + \sum_{i=1}^p \phi_i y_{t-i} + \sum_{j=1}^q \theta_j \varepsilon_{t-j} + \varepsilon_t \tag{1}
 \end{aligned}$$

Once the model is ready, model adequacy is checked by assumptions. It mainly checks the normality and autocorrelation of the residuals and looks for further improvement.

ARIMA methodology does have its limitations. These models directly rely on past values and therefore work best on long and stable series.

6.2 Simple Exponential Smoothing Forecasting Model

This simple exponential smoothing (SES) is suitable for forecasting data with no trend or seasonal pattern.

Exponential smoothing technique assigns the time series data in exponentially decreasing weights from newest to oldest observations. In other words, less priority (“weight”) is assigned to older data and more priority to the newer data. Smoothing parameters (smoothing constants are represented by α —determine the weights for observations [17–19].

The long-term forecast is quite unreliable using Exponential smoothing so it used for short-term forecasting.

- **Simple (single) exponential smoothing:** This technique assigns the weights in exponentially decreasing weights.
- **Holt’s trend-corrected double exponential smoothing:** This technique is more reliable in respect to handling data which provides better trends compared to the simple exponential smoothing technique.
- **Triple exponential smoothing** (also called the Multiplicative Holt-Winters): This technique is more reliable for parabolic trends or data that shows trends and seasonality.

The **basic formula** is:

$$S_t = \alpha y_{t-1} + (1 - \alpha) S_{t-1} \tag{2}$$

where

- α = the smoothing constant, a value from 0 to 1. When α close to zero represents slow smoothing. Smallest mean squared error (MSE) is obtained when the value of α is 1 and Levenberg–Marquardt algorithm is a popular method for this.
- t = time period.

7 Results

In this paper, forecasting of energy consumption of the individual consumer has been implemented using ARIMA and Exponential forecasting model in R-programming. To use the ARIMA and Exponential model, it is necessary to have at least 1-month energy consumption time series data. Using this 1-month time series data of individual consumer data of energy consumption, forecasting has been performed for 1 week and the actual energy consumption has been compared with the ARIMA and Exponential model. Forecasting has been performed on the data acquired for the month of December 2017 and May 2018.

Figure 7 shows the load pattern of the house for the month of December 2017 and Fig. 8 shows the comparison plot of real energy consumption of the house with forecasted energy consumption for 1 week using ARIMA and Exponential forecasting models.

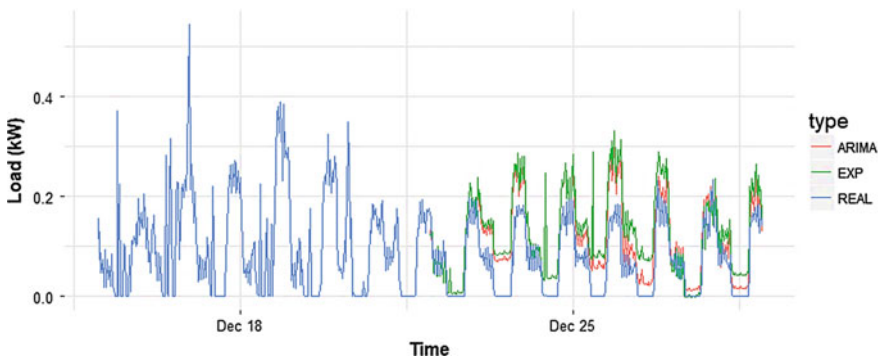


Fig. 7 Comparison of real value with ARIMA model and exponential model for the month of Dec. 2017 (House No. 1)

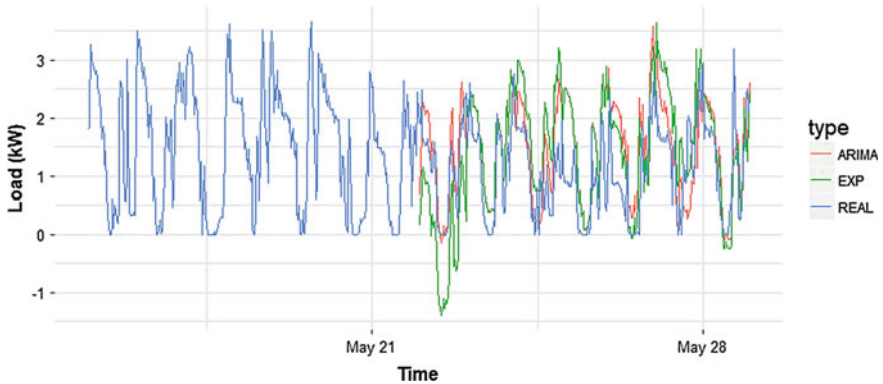


Fig. 8 Comparison of real value with ARIMA model and exponential model for the month of May 2018 (House No. 2)

8 Conclusion

The 100 kW solar PV system has contributed 1,26,000 units of energy during 2017. This solar PV system will provide cost-efficient, clean, and green energy for the next 20 years (approximately). The installed system has reduced the release of carbon emission into the atmosphere.

If the monthly power export, which has not been utilized by the houses, has been calculated in terms of revenue, the total value saved by installing the 100 kW system becomes equivalent to Rs 10,06,740/-which is a considerably a big amount.

Two different forecasting model has been implemented for different sessions of the year like winter session (December 2017) and summer session (May 2018). House no. 1 and house no. 2 energy consumption has been forecasted for 1 week for winter and summer month. It seems ARIMA technique can produce more accurate forecasting result on aggregated consumption than exponential smoothing which has been observed from the plotted results for the month of December 2017 and May 2018. This forecasting model can be used for the future prediction of aggregated energy consumption of consumer which is very useful for utility. Limitation of the forecasting model and any other advanced analytics is that a large amount of data at regular interval should be available which results in good accuracy for advanced analytics.

Acknowledgements This work has been done under the project “Development of R&D Platform for Smart City Pilot Projects in the Indian Context” funded by Ministry of Power (MoP) and Indian Institute of Technology Kanpur (IITK), MP&IIT/EE/2014297. I am also thankful to the other team members who were involved in hardware and software installation of this project.

References

1. Jiang L, Da Xu L, Cai H, Jiang Z, Bu F, Xu B (2014) An IoT-oriented data storage framework in cloud computing platform. *Ind Inform IEEE Trans* 10(2):1443–1451
2. Aditya Gaur SM, Scotny B, Parr G (2015) Smart city architecture and its applications based on IoT. 52:1089–1094
3. Sharma S (2016) Expedition from 3G to 5G. 6(4):4250–4251
4. Fang X, Misra S, Xue G, Yang D (2011) Smart grid—the new and improved power grid: a survey. 14:944–980
5. Murthy Balijepalli VSK (2011) Review of demand response under smart grid paradigm. In: 2011 IEEE PES innovative smart grid tech, India, 1–3 Dec 2011
6. Ma J, Henry Chen H, Song L, Li Y (2016) Residential load scheduling in smart grid: a cost efficiency perspective. *IEEE Trans Smart Grid* 7(2):771–784
7. Department of Energy (2015) State of renewable energy in South Africa, Matimba House. Department of Energy, Pretoria
8. Wu Z, Xia X (2015) Optimal switching renewable energy system for demand side management. *Sol Energy* 114:278–288
9. ETSAP (2015) Renewable energy integration in power grids. IRENA
10. Nichiforov C, Stamatescu I, Făgărășan I, Stamatescu G (2017) Energy consumption forecasting using ARIMA and neural network models. In: 5th international symposium on electrical and electronics engineering (ISEEE), Oct 2017
11. Garulli A, Paoletti S, Vicino A (2014) Models and techniques for electric load forecasting in the presence of demand response. 23(3):1087–1097
12. Pena EHM, de Assis MVO, Proença Jr ML (2013) Anomaly detection using forecasting methods ARIMA and HWDS. In: 32nd international conference of the Chilean computer science society (SCCC), Nov 2013
13. Wang B, Zhu X, He Q, Gu G (2018) The forecast on the customers of the member point platform built on the block chain technology by ARIMA and LSTM. In: IEEE 3rd international conference on cloud computing and big data analysis (ICCCBDA), Apr 2018
14. Sujjaviriyasup T, Pitiruek K (2017) A comparison between MODWT-SVM-DE hybrid model and ARIMA model in forecasting primary energy consumptions. In: IEEE international conference on industrial engineering and engineering management (IEEM), Dec 2017
15. Nichiforov C, Stamatescu I, Fagarasan I, Stamatescu G (2017) Energy consumption forecasting using ARIMA and neural network models. In: 5th international symposium on electrical and electronics engineering (ISEEE), Oct 2017
16. El kafazi I, Bannari R, Abouabdellah A (2016) Modeling and forecasting energy demand. In: International renewable and sustainable energy conference (IRSEC), Nov 2016
17. Soni RS, Srikanth D (2017) Inventory forecasting model using genetic programming and Holt-Winter's exponential smoothing method. In: 2nd IEEE international conference on recent trends in electronics, information & communication technology (RTEICT), May 2017
18. Akpınar M, Yumusak N (2017) Day-ahead natural gas forecasting using nonseasonal exponential smoothing methods. In: IEEE international conference on environment and electrical engineering and 2017 IEEE industrial and commercial power systems Europe (EEEIC/I&CPS Europe), June 2017
19. Macaira PM, Sousa RC, Oliveira FLC (2016) Forecasting Brazil's electricity consumption with Pegels exponential smoothing techniques. 14(3):1252–1258

A Comprehensive Analysis of Delta and Adaptive Delta Modulated Modular Multilevel Converter



Rahul Jaiswal, Anshul Agarwal and Vineeta Agarwal

Abstract This paper presents deeply analysis and comparison of different modulation techniques for the modular multilevel converter without using arm inductor. In case of PWM, losses are more and Total Harmonic Distortion (THD) performance is very poor. With the introduction of delta modulation in MMC, the losses will reduce and THD will improve. It can be seen that the THD is 4.9% for delta modulation and 3.82% for adaptive delta modulation without using arm inductance but THD is 13.15% for delta modulation with arm inductance. It means THD has been improved without using arm inductance. It has been observed that the adaptive delta modulation has better THD response as compared to delta modulation due to its several advantages. The THD performance has been calculated and mentioned at different modulation indexes. It has been also observed that the THD performance is better with delta and adaptive delta modulation.

Keywords Modular multilevel converter (MMC) · Delta modulation (DM) · Adaptive delta modulation (ADM)

1 Introduction

The Modular Multilevel Converter (MMC) is one of the developing innovations these days. It has attracted consideration for the researcher because of its favorable circumstances of a particular outline, high effectiveness, and versatility, and superior output waveform with low losses. Due to the excellent configuration of MMC, there is a lot of research conducted based on the modeling and control technique of MMC and it is used for high and medium voltage applications [1–3].

Their characteristic measured quality takes into consideration an incalculable number of them to be associated in parallel and series arrangement to improve the

R. Jaiswal (✉) · V. Agarwal
Department of Electrical Engineering, MNNIT, Allahabad, India
e-mail: ree1651@mmnit.ac.in

A. Agarwal
Department of Electrical & Electronics Engineering, NIT Delhi, Delhi, India

© Springer Nature Singapore Pte Ltd. 2020
A. Kalam et al. (eds.), *Intelligent Computing Techniques for Smart Energy Systems*,
Lecture Notes in Electrical Engineering 607,
https://doi.org/10.1007/978-981-15-0214-9_28

current and voltage, respectively, without any confounded interconnection prerequisites. The power circuit design takes into account excess task in instances of local faults in any of the modules. The control and modulation technique of MMC is very complex as compared to other converters. In the vast majority of the acknowledgements, all the state factors from the modules are detected and sent to a focal controller through optically disengaged committed Ethernet associations which make all the control calculations and send the door signals to the switches in the different modules. While excess control frameworks can be utilized to guarantee that the framework isn't at risk to fall because of single point fault. That's why switching pulses play an important role in the controlling of the converters [4–7].

The modulation technique is categorized into various classes which are shown in Fig. 1. The modulation technique is two types, the first one is the continuous modulation technique and another one is the discontinuous modulation technique. In continuous modulation technique, pulses are generated in a continuous form but in discontinuous modulation technique, pulses are generated in a discontinuous form. Delta modulation and adaptive delta modulation technique are one of the discontinuous type modulations techniques. This type of technique will generate discrete type of pulses [8–11].

In 2003, A. Lesnicar and R. Marquardt have introduced the idea of the modular multilevel converter for clarifying the multilevel converter [1]. The dc link capacitor of ordinary source inverters is used for the autonomous acknowledgment of the capacitor. In four-quadrant operation, this type of converters doesn't require any other type of extra outer association with the submodules. The switches are connected with the capacitance, the combinations of switches and dc storage capacitance are called submodule. If the number of submodule increases, the voltage level will increase and THD will also improve without increasing the difficulty level of the MMC [12–14].

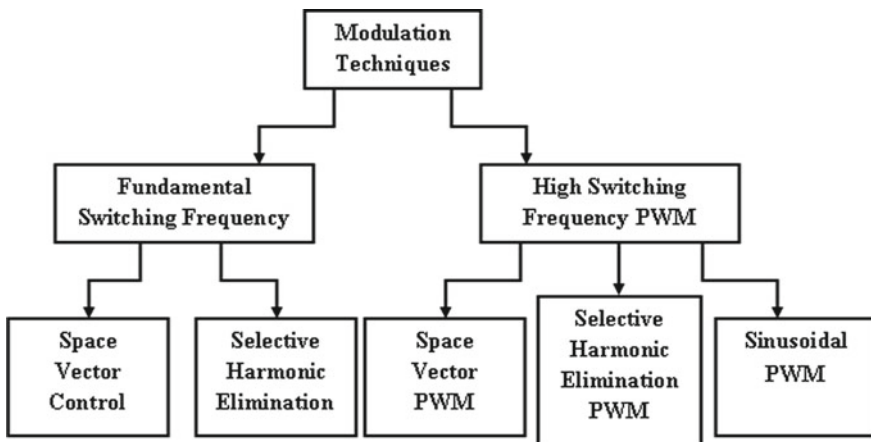


Fig. 1 Different modulation techniques

This paper is based on discontinuous modulation technique. This technique uses the closed-loop modulation which gives the pure sinusoidal waveform. The THD of different modulation techniques has also been analyzed and presented in this manuscript.

2 Delta Modulation

Modulation technique is based on the switching frequency. These switching frequencies are classified into two parts, the first one is lower switching frequency and another one is the higher switching frequency. Delta modulation technique can operate lower switching frequency as well as higher switching frequency. Generally, delta modulation is preferred with higher switching frequency as the higher order harmonics can be easily removed with the help of higher switching frequency. Delta modulation has a lot of advantages due to its discrete nature. Discrete delta modulation has a high bandwidth, high signal-to-noise ratio, faster response, and high resolution [14, 15].

Delta modulation is a closed-loop feedback system consisting of comparator and sample and hold in forward path and integrator in a feedback path. There are two types of circuit, one is the frequency dependent and another one is a frequency independent, as seen in Fig. 2a, b. The output pulses obtained from delta modulator is discrete, having spread spectrum and nonstationary, as seen in Fig. 3 [15–17].

3 Adaptive Delta Modulation

The adaptive delta modulator is same as delta modulation except for adaptive algorithm. Adaptive delta modulator has the capability to eliminate slope overload and granular noise. It makes the slope of step size equal to the slope of the modulating signal. Step size should not be greater or smaller than the amplitude of the modulating signal. Hence, the value of step size is an important parameter regarding the performance of delta modulation and converter. If the step size is too large, the signal will not quantize properly and idle channel noise will appear. The pattern of the idle channel is an alternating sequence of zero-one specifying that the amplitude of the input signal is not varying. The signals obtained from the idle channel after decoding & integrate to zero and one gives the zero-one pattern which has zero mean value. The block diagram for adaptive delta modulation is shown in Fig. 4 [17, 18].

4 Results and Discussion

In this paper, all results have been obtained from the MATLAB simulation. At the end of objective, it can be seen that the comparison of total harmonic distortion with

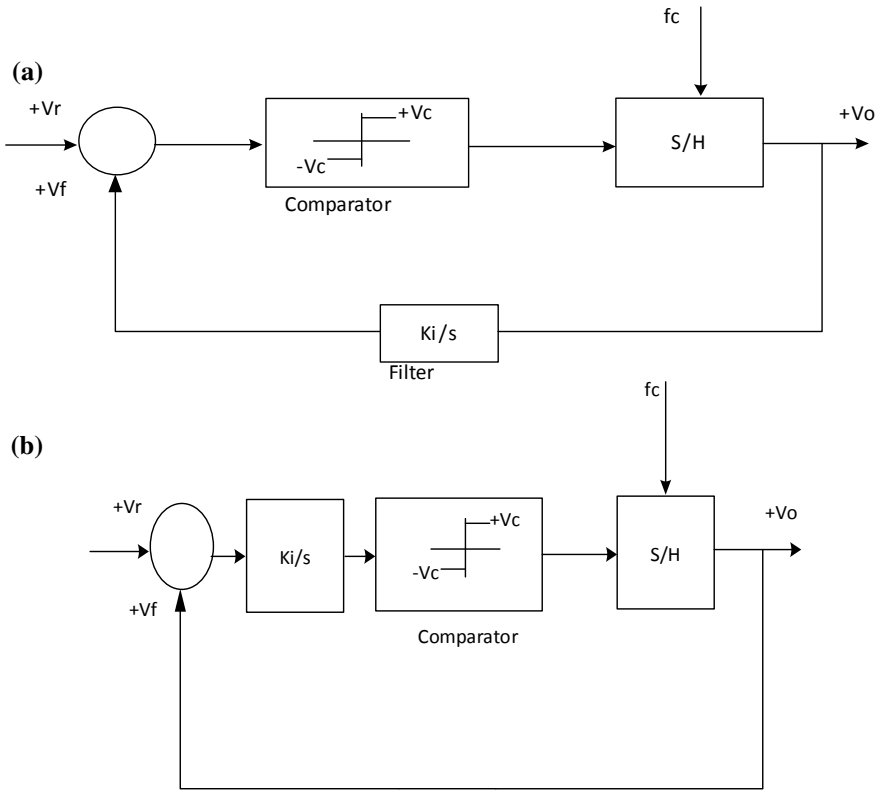


Fig. 2 a Frequency dependent delta modulation. b Modified delta modulation

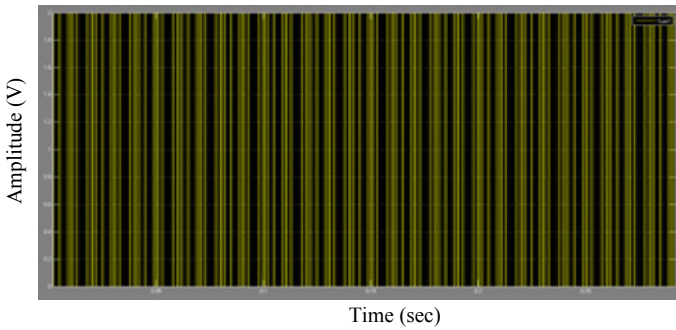


Fig. 3 Pulse generated from delta modulation

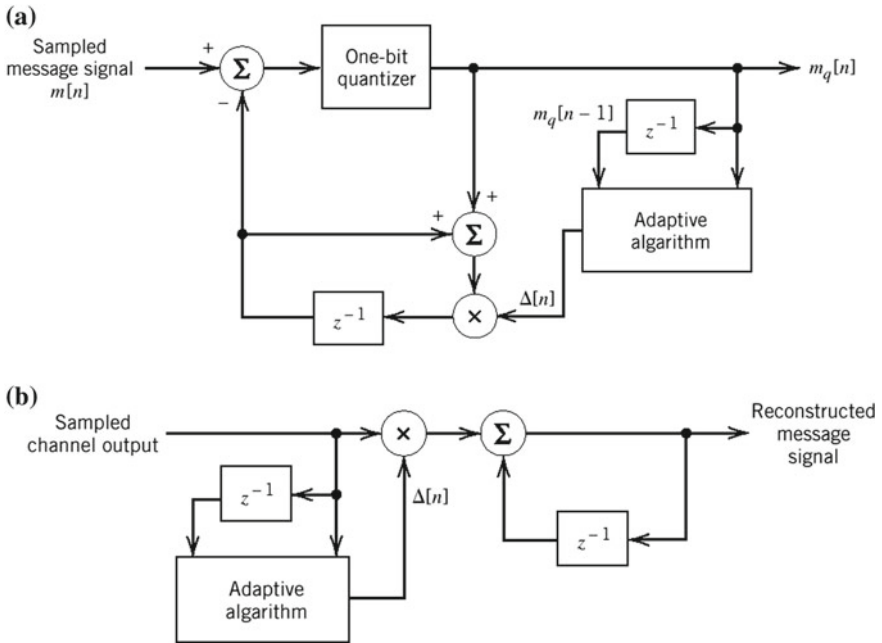


Fig. 4 Adaptive delta modulation

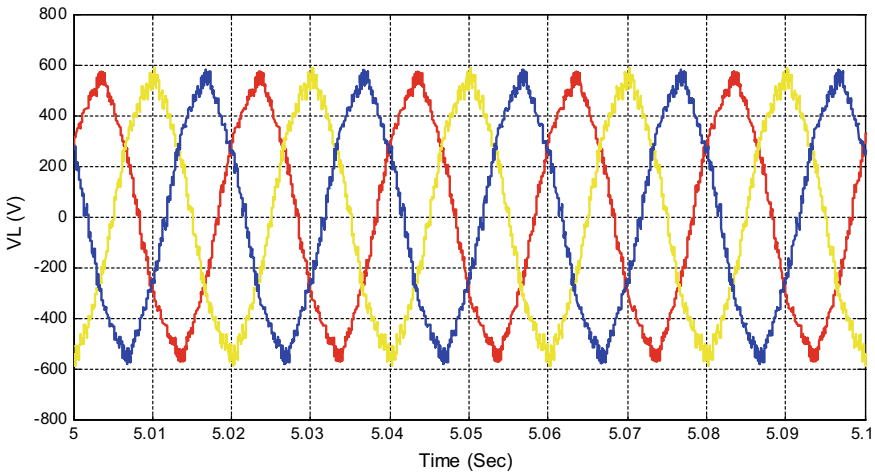


Fig. 5 Output voltage of MMC with the help of delta modulation

different modulation techniques is depicted. The initial dc input voltage is 1200 volts and modulating index (m) is 0.9. As seen in Fig. 5, the output obtained from MMC with the help of delta modulation technique is sinusoidal voltage.

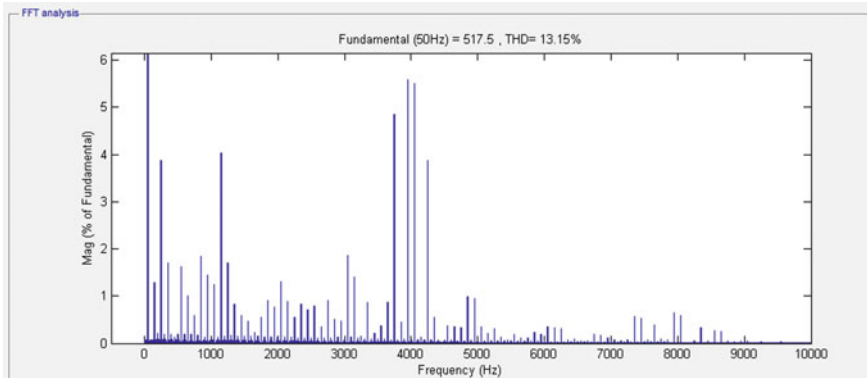


Fig. 6 Voltage THD of MMC with the help of delta modulation with arm inductance

As seen in Fig. 6, it has been observed that the total harmonic distortion of delta modulation is 13.15% with arm inductance ($L = 0.25$ mH). It has also been observed that the total harmonic distortion of delta modulation is 4.9% and total harmonic distortion of adaptive delta modulation is 3.82% without arm inductance, as appeared in Figs. 7 and 8.

The THD analysis of different modulation techniques is shown in Table 1. It has been observed from the table that the THD of delta and adaptive delta modulation is better than the pulse width modulation technique. That means the discontinuous type control technique is more efficient than continuous type control technique.

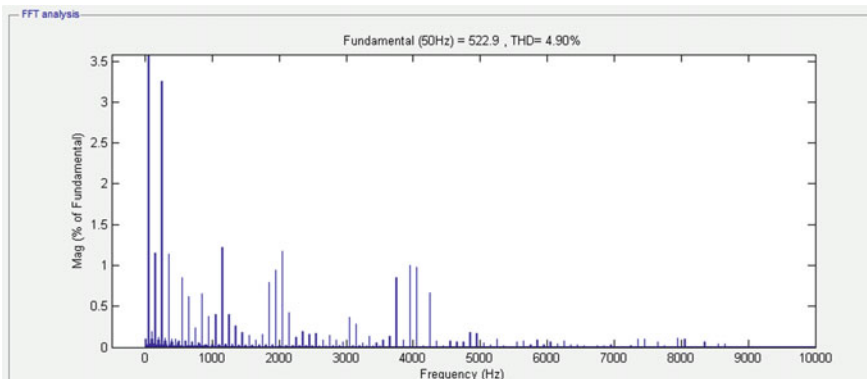


Fig. 7 Voltage THD of MMC with the help of delta modulation without arm inductance

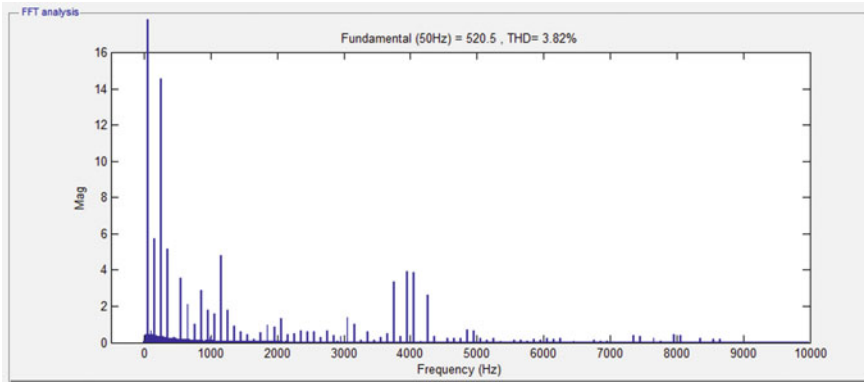


Fig. 8 Voltage THD of MMC with the help of adaptive delta modulation without arm inductance

Table 1 Comparisons of THD (in percentage) with different modulation techniques without using arm inductor ($L = 0$)

Modulation index (m)	PWM modulator (THD %)	Delta modulator (THD %)	Adaptive delta modulator (THD %)
0.775	15.01	8.50	4.12
0.8	14.83	7.90	3.80
0.825	11.67	6.68	3.20
0.85	11.23	5.98	2.66
0.875	10.32	5.32	3.01
0.9	10.16	4.90	3.82
0.95	9.87	3.75	4.90
1.0	8.40	2.66	4.22

5 Conclusion

It can be concluded from the above analysis that THD will improve when the delta modulation technique is applied in place of other modulation techniques. It has been observed that THD will also improve in case of without arm inductor. THD is 13.15% with arm inductor but it is decreased to 4.9% without arm inductor. It can be seen that the arm inductor plays a very important role. If arm inductor is reduced or removed from the converter, the losses will reduce that means THD will improve. It has also been observed that the THD will improve in case of adaptive delta modulation. In this case, the THD is 3.82% without arm inductor. Due to a lot of advantages of adaptive delta modulation as compared to delta modulation, the losses have been reduced. Finally, it can be concluded that the losses will reduce with the help of delta modulation and adaptive delta modulation techniques. That means converter efficiency will improve.

References

1. Lesnicar A, Marquardt R (2003) An innovative modular multilevel converter topology suitable for a wide power range. In: Proceedings of IEEE Bologna power tech conference, pp 1–6
2. Zeng R, Xu L, Yao L, Williams BW (2015) Design and operation of a hybrid modular multilevel converter. *IEEE Trans Power Electron* 30(3):1137–1146
3. Mei J, Shen K, Xiao B, Tolbert LM, Zheng J (2014) A new selective loop bias mapping phase disposition PWM with dynamic voltage balancing capability for modular multilevel converter. *IEEE Trans Ind Electron* 61(2):798–807
4. Shi XJ, Wang ZQ, Liu B, Liu YQ, Tolbert LM, Wang F (2015) Characteristic investigation and control of a modular multilevel converter-based HVDC system under single-line-to-ground fault conditions. *IEEE Trans Power Electron* 30(1):408–421
5. Solas E, Abad G, Barrena JA, Aurtenetxea S, Carcar A, Zajac L (2013) Modular multilevel converter with different submodule concepts—part I: capacitor voltage balancing method. *IEEE Trans Ind Electron*. 60(10):4525–4535
6. Solas E, Abad G, Barrena JA, Aurtenetxea S, Carcar A, Zajac L (2013) Modular multilevel converter with different submodule concepts—part II: experimental validation and comparison for HVDC application. *IEEE Trans Ind Electron* 60(10):4536–4545
7. Ilves K, Antonopoulos A, Norrga S, Nee H (2012) Steady-state analysis of interaction between harmonic components of arm and line quantities of modular multilevel converters. *IEEE Trans Power Electron* 27(1):57–68
8. Song Q, Liu WH, Li ZQ, Rao H, Xu SK, Li LC (2013) A steady-state analysis method for a modular multilevel converter. *IEEE Trans Power Electron* 28(8):3702–3713
9. Harnefors L, Antonopoulos A, Norrga S, Angquist L, Nee HP (2013) Dynamic analysis of modular multilevel converters. *IEEE Trans Ind Electron* 60(7):2526–2537
10. Li ZX, Wang P, Chu ZF, Zhu HB, Luo YJ, Li YH (2013) An inner current suppressing method for modular multilevel converters. *IEEE Trans Power Electron* 28(11):4873–4879
11. Zhang M, Huang L, Yao WX, Lu ZY (2014) Circulating harmonic current elimination of a CPS-PWM-based modular multilevel converter with a plug-in repetitive controller. *IEEE Trans Power Electron* 29(4):2083–2097
12. Angquist L, Antonopoulos A, Siemaszko D, Ilves K, Vasiladiotis M, Nee HP (2011) Open-loop control of modular multilevel converter using estimation of stored energy. *IEEE Trans Ind Appl* 47(6):2516–2524
13. Antonopoulos A, Angquist L, Harnefors L, Ilves K, Nee HP (2014) Global asymptotic stability of modular multilevel converters. *IEEE Trans Ind Electron* 61(2):603–612
14. Anjali S, Roopa R, Sanjana S (2015) Comparison of conventional & new multilevel inverter topology. *Int J Sci Eng Res* 6(2):300–304
15. Agarwal A, Agarwal V (2008) Delta modulated cycloconverters. *IEEE Int Conf Telecommun Energy Conf* 32(3):1–6
16. Jacob B, Baiju MR (2015) Space-vector-quantized dithered sigma delta modulator for reducing the harmonic noise in multilevel converters. *IEEE Trans Ind Electron* 62(4):2064–2072
17. Agarwal A, Agarwal V (2012) Field programmable gate array-based delta-modulated cycloconverter. *IET Power Electron* 5(9):1793–1803
18. Khan IA, Agarwal A (2016) Delta and adaptive delta modulated single phase AC/AC converter. In: 1st IEEE international conference on power electronics. Intelligent Control and Energy Systems (ICPEICES), pp 1–6, Delhi India (2016)

Speed Control of PMSM Drive Using Jaya Optimization Based Model Reduction



Akhilesh K. Gupta, Paulson Samuel and Deepak Kumar

Abstract The inherent advantages such as high efficiency and higher torque weight ratio of a permanent magnet synchronous motor (PMSM) make it very popular among all of the drives. The primary challenge during the use of PMSM for high-performance drive applications such as rolling mills and robotics is to design a controller with good disturbance rejection capability, insensitivity to parameter variation, and low rise time for a fast response. The mathematical model of PMSM is highly nonlinear; therefore, the design of a speed controller is a significant challenge. The contribution of the present paper is the tuning of a proportional–integral (PI) controller using a reduced order model (ROM) of the PMSM drive using recently developed Jaya optimization algorithm. The tuning parameters obtained by the above algorithm are used for the speed control of PMSM drive. Further, the effectiveness of speed controller is verified on the MATLAB platform and the step responses of ROM and original system are plotted to show the closeness between the behavior of the ROM and original higher order system (OHOS).

Keywords PMSM · Jaya optimization · Speed control loop · PI controller · MOR

1 Introduction

Nowadays, PMSM is taking the place of DC motors in most of the high-power applications. The PMSMs have high efficiency and better torque–inertia ratio in comparison to the induction machines [1, 2]. The traditional field windings are replaced by the permanent magnet in synchronous machines. Some fast switching techniques have been proposed by several researchers to make the switching devices more efficient,

A. K. Gupta (✉) · P. Samuel · D. Kumar
Electrical Engineering Department, MNNIT Allahabad, Prayagraj, India
e-mail: akhilesh_ree5213@mnnit.ac.in

P. Samuel
e-mail: paul@mnnit.ac.in

D. Kumar
e-mail: deepak_kumar@mnnit.ac.in

© Springer Nature Singapore Pte Ltd. 2020
A. Kalam et al. (eds.), *Intelligent Computing Techniques for Smart Energy Systems*,
Lecture Notes in Electrical Engineering 607,
https://doi.org/10.1007/978-981-15-0214-9_29

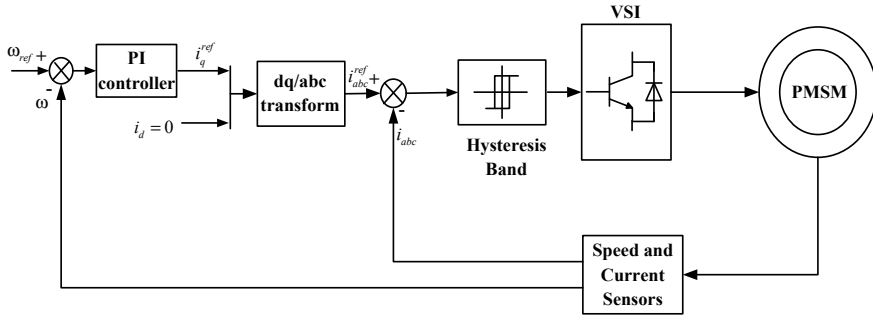


Fig. 1 Schematic of speed control of PMSM drive

but still, sinusoidal pulse width modulation (SPWM) technique [3–7] is prevalent due to its simplicity in its implementation. In this article, a speed controller for the PMSM drive is presented by the model order reduction (MOR) to get the desired transient and steady-state response. Several MOR techniques are proposed in the time domain [8–10] and frequency domain [11–15]. Since the last few years, different optimization approaches [16–20] have been used to determine the reduced-order model of OHOS with better efficiency. In this paper, Jaya optimization algorithm [21, 22] is used to obtain the ROM and further, this algorithm is applied to get the optimized tuning parameters of the PI controller. The schematic diagram of the speed controller design of PMSM drive is shown in Fig. 1.

The whole article is organized in four sections including an introductory section. Section 2 is a brief introduction of PMSM modeling whereas the Jaya algorithm for the order reduction and speed controller design for PMSM drive is explained in Sect. 3. Finally, conclusive remarks are presented in Sect. 4.

2 Mathematical Modeling of PMSM Drive and Control

The scalar control strategy [23] has a poor dynamics response for the control of inverter-fed AC drives. Therefore, the theory of vector control scheme [24, 25] has been applied for most of the drive applications. Here, this concept is adopted for the development of a linear model of PMSM drive for the controller design. The linear dynamics of PMSM is obtained by the vector control scheme which is the transformation of a PMSM mathematical model into the synchronous rotating dq frame [26].

2.1 PMSM Drive

The information about the operating conditions and different parameters of motors are necessary conditions for the implementation of vector control. The dq reference frame [26] is used to find the stator voltage equations of the PMSM drive. The PMSM drive is explained by Eqs. (1)–(3).

$$\begin{aligned} v_{qs} &= R_s i_{qs} + sL_q i_{qs} + \omega_r L_d i_{ds} + \omega_r \lambda_m \\ v_{ds} &= R_s i_{ds} + sL_d i_{ds} - \omega_r L_q i_{qs} \end{aligned} \tag{1}$$

$$J \frac{d\omega_r}{dt} = T_e - T_L - B\omega_r; \quad \omega_r = \frac{T_e - T_L}{B_t + sJ} \tag{2}$$

$$T_e = \frac{3}{2} P \lambda_m i_{qs} = K_t i_{qs}; \quad K_t = \frac{3}{2} P \lambda_m \tag{3}$$

where v_d, v_q are the d-axis and q-axis stator voltages, respectively, R_s is the stator resistance, L_d, L_q are the d-axis and q-axis stator inductances, respectively, ω_r is the rotor angular speed, J is the inertia of PMSM, P is the pole pair, T_L, T_e are the Load torque, electromagnetic torque, and λ_m is the flux linkage. The block diagram of the PMSM mathematical model with the closed-loop speed control is depicted in Fig. 2.

The zero d-axis current control is implemented to avoid the demagnetization and to achieve the high torque to current ratio [27]. The transfer function obtained for the zero d-axis current control, i.e., $i_d = 0$ is given as

$$\frac{i_d(s)}{v_d(s)} = \frac{i_q(s)}{v_q(s)} = \frac{1}{R_s + sL_{(q,d)}} \tag{4}$$

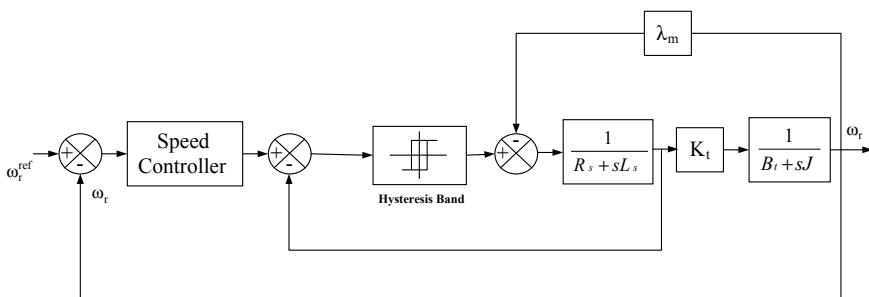


Fig. 2 Speed controlled PMSM drive

3 Order Reduction and Controller Design for PMSM

The higher order transfer function of PMSM drive is reduced to the equivalent lower order model with the Jaya optimization algorithm which is explained in the following subsection.

3.1 Jaya Optimization Algorithm [21, 22]

Jaya optimization method is an approach to move toward the best solution and to avoid the worst solution. It is an algorithm-specific parameter-free approach unlike genetic algorithm and particle swarm optimization approaches which utilize selection parameter, inertia weight, etc., algorithm dependent parameters.

Let f_i be an objective function which is to be minimized and $k_{x,y}^z$ be a family of probable solution at z th iteration with M ($x = 1, 2, \dots, M$) members, each having D ($y = 1, 2, \dots, D$) design variables, then implementation of Jaya optimization follows the steps given below:

Step 1: [Initialization] Initialize the parameters like the number of feasible solutions, upper and lower bound ranges of solutions, and the number of iterations.

Step 2: [Best and Worst] Find the integral square error (objective function) of each solution and observe the best and worst solution for objective functions.

Step 3: [Modification] Generate the modified solutions which are tending toward the best solution and avoid the worst solution by Eq. (5) given below:

$$k_{x,y}^{z,\text{new}} = k_{x,y}^z + r_{1,x}^z (k_{x,\text{best}}^z - |k_{x,y}^z|) - r_{2,x}^z (k_{x,\text{worst}}^z - |k_{x,y}^z|) \quad (5)$$

where $r_{1,x}^z$ and $r_{2,x}^z$ are two weighted random numbers for the approach to achieve the best and to discard the worst solutions, respectively. $k_{x,\text{best}}^z$ is the value of x th variable for best solution at z th iteration. Similarly, $k_{x,\text{worst}}^z$ is the value of x th variable for the worst solution at z th iteration, $k_{x,y}^{z,\text{new}}$ is the modified value of $k_{x,y}^z$.

Step 4: [Replacement] Replace the old solution with a new one later; it is with better fitness function value in comparison with the old one.

Step 5: [Termination] Repeat the process from Step 2 to Step 4 until some stopping criterion has been met.

3.2 Current Control Loop

A hysteresis band approach is adopted to generate the switching pattern of PWM inverter for the reference current tracking generated by the speed control loop for the PMSM drive. Since the generated current is restricted within a band limit in hysteresis current control (HCC), HCC is observed as a unitary gain block [27].

Table 1 Parameters of PMSM drive

Parameter	Value
Stator resistance	2.75 Ω
Stator inductance	8.5 mH
Flux linkage (V.s)	0.175
Pole pair	8
Inertia (kg.m ²)	0.008
Viscous coefficient (N-m/rad/s)	0.01

Here, the voltage source inverter is modeled as a delay block with the specific gain. The mathematical model of VSI is expressed by Eq. (6)

$$T_i(s) = 0.65 \frac{K_{in}}{1 + sT_{in}} \quad (6)$$

where $K_{in} = 0.65 \frac{V_{dc}}{V_{cm}}$ and $T_{in} = \frac{1}{2f_s}$.

The current loop transfer function (CLTF) is obtained by moving the pick-off point and simplifying the loop. Then CLTF obtained by the simplification is given as

$$\frac{i_{qs}^r(s)}{i_{qs}^{r*}(s)} = \frac{K_{in}K_a(1 + sT_m)}{K_aK_{in}(1 + sT_m) + (1 + sT_{in})\{K_aK_b + (1 + sT_m)\}(1 + sT_a)} \quad (7)$$

where $K_a = \frac{1}{R_s}$; $T_a = \frac{L_q}{R_s}$; $K_{in} = \frac{1}{B_r}$; $T_{in} = \frac{J}{B_r}$; $K_b = K_t K_m \lambda_m$. Equation 8 gives the exact current loop transfer function (ECL-TF) by the parameters of PMSM drive given in Table 1 that is given as

$$G_i(s) = \frac{5.389s + 6.736}{6.182 \times 10^{-7}s^3 + 0.002674s^2 + 6.196s + 21.1} \quad (8)$$

The objective is to derive a reduced-order transfer function (ROM-TF) that retains the characteristics of the exact current loop transfer function (ECL-TF). The Jaya optimization algorithm reduces the order of ECL-TF with parameters as $iter = 30$, no. of possible solution = 25, etc. and the reduced current loop transfer function obtained as

$$G_{ir}(s) = \frac{9.717s + 12.45}{0.001s^2 + 11.31s + 38.99} \quad (9)$$

The step responses of the ECL-TF and ROM-TF are shown in Fig. 3. This plot shows that the ROM-TF is a resemblance of the ECL-TF. Therefore, the ECL-TF is replaced with the ROM-TF to design the speed controller with a desirable response. In another way, the closeness between the ECL-TF and ROM-TF can be understood by transient parameters shown in Table 2.

Fig. 3 Step responses of the exact current loop and reduced current loop

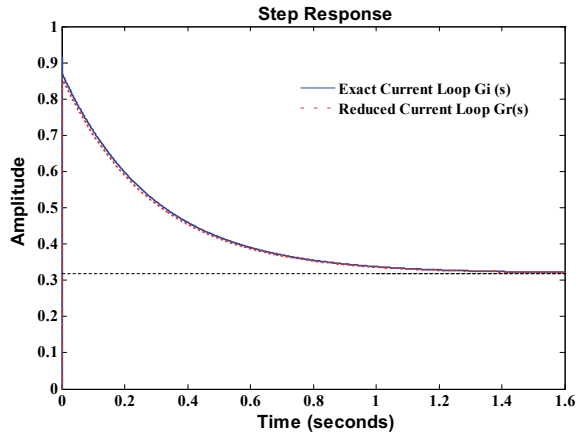


Table 2 Transient performance of ECL-TF and ROM-TF

Transient parameters	ECL-TF	ROM-TF
Rise time T_r (s)	0.000243	0.000037
Settling time T_s (s)	1.12	1.14
Overshoot M_{ov} (%)	187	169

3.3 Speed Control Loop

The outer loop determines the transient and steady-state behavior of the output response. Therefore, the design and implementation of the speed controller play an essential role in speed control of permanent magnet synchronous machine drive.

The open speed loop transfer function through the exact current loop and the reduced current loop is given by Eqs. 10 and 11.

$$G_{ose}(s) = G_i(s) * G_m(s) = \frac{1132s + 1415}{4.945 \times 10^{-7}s^4 + 2.139 \times 10^{-3}s^3 + 3.659s^2 + 23.08s + 21.1} \tag{10}$$

$$G_{osrc}(s) = G_{ir}(s) * G_m(s) = \frac{2041s + 2614}{0.0008s^3 + 9.049s^2 + 42.5s + 38.99} \tag{11}$$

The step responses of open speed loop with the exact current loop and the reduced current loop are plotted in Fig. 4. The transient behavior of both of the transfer functions is tabulated in Table 3.

The reduced speed loop of the transfer function of the speed loop with the reduced current is given as

$$G_{ors}(s) = \frac{1.05s + 95.36}{0.004s^2 + 0.4561s + 1.422} \tag{12}$$

Fig. 4 Step responses of exact speed and reduced speed loops with reduced current loop

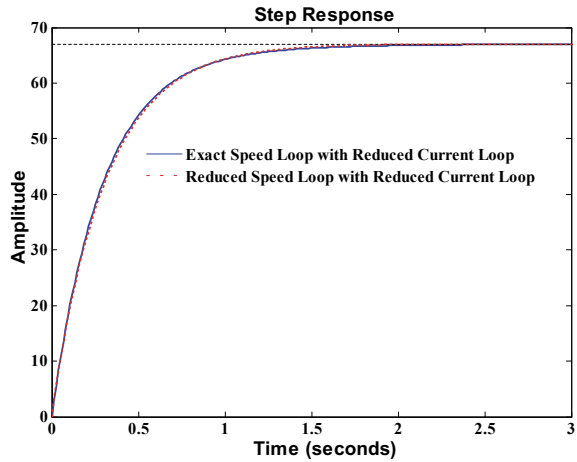


Table 3 Transient performance of open speed loop with the exact current loop and the reduced current loop

Transient parameters	With exact current loop	With reduced current loop
T_s (s)	1.26	1.22
T_r (s)	0.674	0.685
M_{ov} (%)	0	0
Peak time (s)	0.00135	0.00073

3.4 Tuning of PI Controller Using Optimization Algorithm

Jaya optimization approach is applied to obtain the optimal control performance by tuning the PI gain parameters. Initially, the ROM of the PMSM drive is accomplished by minimization of the objective function through Jaya optimization. The step responses of both exact speed loop with reduced current loop and reduced speed loop with the reduced current loop are plotted in Fig. 5. The Jaya optimization algorithm is utilized to get the optimized tuning parameters of the PI speed controller. The Jaya optimization based PI controller gains with their initial ranges and optimized gain parameters are tabulated in Tables 4 and 5, respectively. The step responses of the OHOS with Jaya optimized PI controller and ROM with Jaya optimized PI controller are plotted in Fig. 6.

The PI controller minimizes the overshoot effect in reference tracking and rejects the input disturbance in the plant. The unit step response of the system is the most essential characteristic of the system for analysis of transient and steady-state behavior. The response of the reduced model depicts a close resemblance with the original system behavior. The simulation on the MATLAB/Simulink platform is used to verify the effect of the proposed speed controller. The input disturbance rejection capability is verified by Fig. 7a where a change in input torque is inserted at $t = 0.5$ s. This

Fig. 5 Step responses of open speed loop with exact and reduced current loop

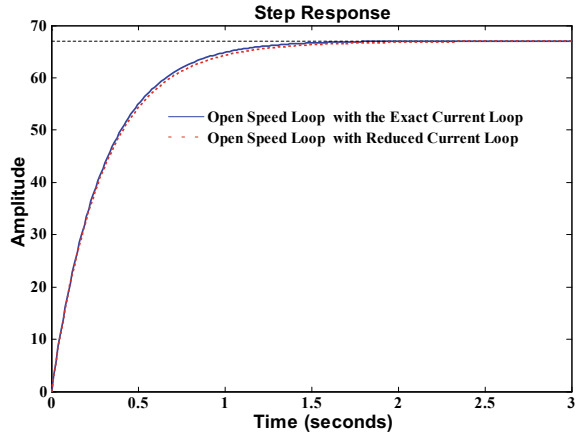


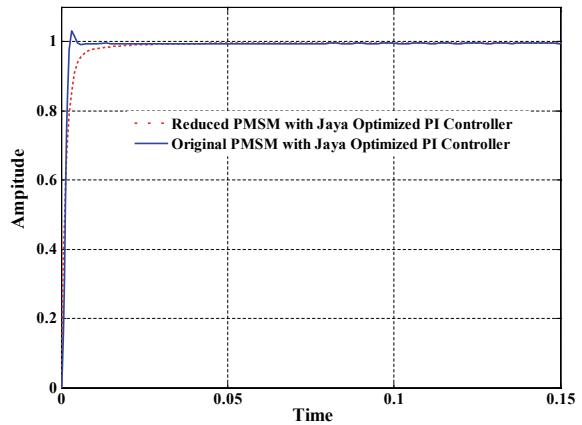
Table 4 Ranges of PI gain parameters

Parameters	Min	Max
K_p	0.1	50
K_i	0.1	10

Table 5 PI parameters obtained by Jaya optimization

Parameters	K_p	K_i
Values	2.6555	1.2414

Fig. 6 Step responses of OHOS with controller and ROM with controller



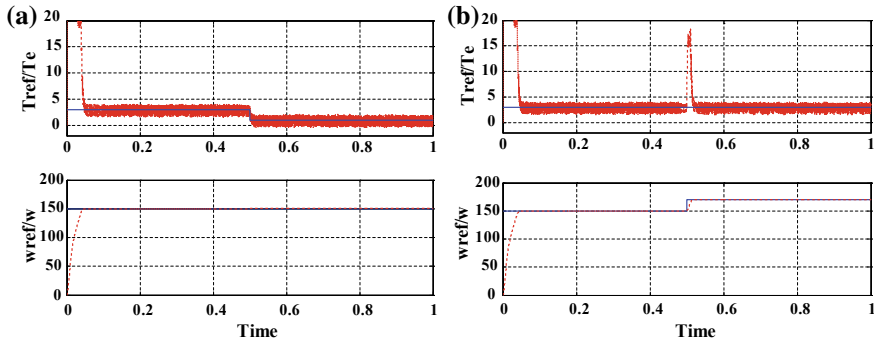


Fig. 7 **a** Regulatory performance. **b** Tracking performance of Jaya-optimized PI

variation in input torque appears in the form of speed change of the PMSM drive without speed controller whereas optimized tuned PI controller comes into the role and neglects the effect of input variation and regulates the drive speed at its reference value. The reference tracking effect is verified by Fig. 7b where a reference speed change is required at $t = 0.5$ s. The tuned controller effectively tracks the reference speed with a good reference tracking performance.

4 Conclusion

The complexity of a higher order model of PMSM drive is simplified by the Jaya optimization based speed controller design which reduces the cost and complexity of the system design. Further, the Jaya algorithm is again used to obtain the tuning parameter of the PI speed controller. It is observed that the transient parameters and the step responses of the ROM obtained by the Jaya algorithm are very similar to that of the OHOS. The objective of this study is to minimize the complexity of the controller design process which is easily accomplished by the Jaya optimization algorithm.

References

1. Pillay P, Krishnan R (1989) Modeling, simulation, and analysis of permanent-magnet motor drives, part I: the permanent-magnet synchronous motor drive. *IEEE Trans Ind Appl* 25(2):274–279
2. Bose BK (1986) *Power electronics and AC drives*. Prentice-Hall
3. Holtz J (1992) Pulse width modulation—a survey. *IEEE Trans Ind Electron* 39(5):410–420
4. Wu B, Lang Y, Zargari N, Kouro S (2011) *Power conversion and control of wind energy systems*. IEEE Press, Wiley, Hoboken, New Jersey

5. Mohan N, Undeland TM, Robbins WP (2002) Power electronics: converters, applications, and design, 3rd edn. Wiley, New York, NY, USA
6. Lei L, Tian-yu W, Wen-Guo X (2011) Application of sinusoidal pulse width modulation algorithm in the grid-connected photovoltaic system. In: Proceedings of international conference of information technology, computer engineering and management sciences, vol 2, pp 254–257
7. Rashid MH (2004) Power electronics circuits devices and applications, PHI 3rd edn
8. Aoki M (1968) Control of large-scale dynamic systems by aggregation. *IEEE Trans Autom Control* 13(3):246–253
9. Moore BC (1981) Principal component analysis in linear systems: controllability, observability and model reduction. *IEEE Trans Autom Control* 26(1):17–32
10. Kung S, David WL (1981) Optimal Hankel-norm model reductions: multivariable systems. *IEEE Trans Autom Control* 26(4):832–852
11. Hutton MF, Friedland B (1975) Routh approximations for reducing order of linear time invariant systems. *IEEE Trans Autom Control* 20(3):329–337
12. Appiah RK (1978) Linear model reduction using Hurwitz polynomial approximation. *Int J Control* 28(3):477–488
13. Chen CF, Shieh LS (1968) A novel approach to linear model simplification. *Int J Control* 8(6):561–570
14. Chuang SC (1970) Application of continued-fraction method for modelling transfer functions to give more accurate initial transient response. *Electron Lett* 6(26):861–863
15. Zakian V (1973) Simplification of linear time-invariant systems by moment approximants. *Int J Control* 18(3):455–460
16. Soloklo HN, Farsangi MM (2013) Chebyshev rational functions approximation for model order reduction using harmony search. *Scientia Iranica* 20(3):771–777
17. Satakshi Mukherjee, Mittal RC (2005) Order reduction of linear discrete systems using a genetic algorithm. *Appl Math Model* 29(6):565–578
18. Gallehdari Z, Karrari M, Malik OP (2009) Model order reduction using PSO algorithm and its application to power systems. In: IEEE international conference on electric power and energy conversion systems EPECS '09, Sharjah, pp 1–5
19. Desai SR, Prasad R (2013) A new approach to order reduction using stability equation and big bang big crunch optimization. *Syst Sci Control Eng* 1(1):20–27
20. Biradar S, Hote YV, Saxena S (2016) Reduced-order modeling of linear time invariant systems using big bang big crunch optimization and time moment matching method. *Appl Math Model* 40(15–16):7225–7244
21. Rao RV, Waghmare GG (2016) A new optimization algorithm for solving complex constrained design optimization problems. *Eng Optim* 1–24
22. Rao RV, More KC, Taler J, Oclon P (2016) Dimensional optimization of a microchannel heat sink using Jaya algorithm. *Appl Therm Eng* 103:572–582
23. Bhimhra PS (2002) Generalized theory of electrical machines. Khanna Publishers
24. Sharma RK, Sanadhya V, Behera L, Bhattacharya S (2008) Vector control of a permanent magnet synchronous motor, In: Annual IEEE India conference INDICON 2008
25. Senjyu T, Shimabukuro T, Uezato K (1995) Vector control of permanent magnet synchronous motors without position and speed sensors. In: 26th annual IEEE power electronics specialists conference PESC '95 Atlanta, USA
26. Pillay P, Krishnan R (2004) Control characteristics and speed controller design for a high performance permanent magnet synchronous motor drive. *IEEE Trans Energy Convers* 19(1)
27. Tripathi SM, Tiwari AN, Singh D (2015) Optimum design of proportional-integral controllers in grid integrated PMSG-based wind energy conversion system. *Int Trans Electr Energy Syst* 26:1006–1031

Jaya Optimization-Based PID Controller for Z-Source Inverter Using Model Reduction



Akhilesh K. Gupta, Paulson Samuel and Deepak Kumar

Abstract It is well-known that a Z-source inverter (ZSI) depicts non-minimum phase characteristics due to a right half plane zero (RHPZ) in its shoot through duty ratio to output voltage transfer function. The RHPZ creates problems in design of a PID controller for such type of systems by imposing the bandwidth limitations and control actions. In this article, the Jaya optimization approach is adopted to reduce the order of ZSI and to obtain the optimized tuning parameters of PID controller. The peak value of DC link voltage is indirectly calculated by measurement of the input supply voltage and the capacitor voltage. The transfer function of control to peak DC link voltage of traditional ZSI is used to get the tuning parameters of PID controller. The MATLAB/Simulink simulation platform is utilized to validate the proposed approach.

Keywords Jaya optimization · Objective function · PID controller · Shoot through · Transient parameters · Z-source inverter (ZSI)

1 Introduction

The human inclination of high efficiency at low cost makes researchers think about a new converter that can give the boosted output in a single-stage converter rather than the two stages boosting of DC–DC converter and DC–AC inverter. In 2003, Peng proposed and implemented an impedance network topology-based ZSI as a novel power electronics converter [1]. It has a great feature of buck and boost ability which makes it a very useful converter topology for renewable energy applications where input DC source varies continuously. It utilizes the zero state of conventional voltage

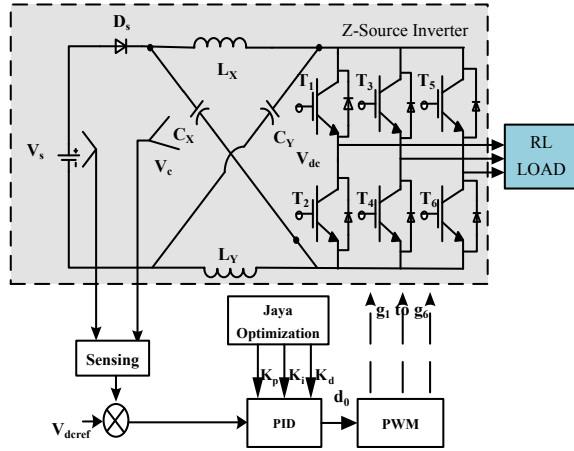
A. K. Gupta (✉) · P. Samuel · D. Kumar
EED, MNNIT Allahabad, Prayagraj, India
e-mail: akhilesh_ree5213@mnnit.ac.in

P. Samuel
e-mail: paul@mnnit.ac.in

D. Kumar
e-mail: deepak_kumar@mnnit.ac.in

© Springer Nature Singapore Pte Ltd. 2020
A. Kalam et al. (eds.), *Intelligent Computing Techniques for Smart Energy Systems*,
Lecture Notes in Electrical Engineering 607,
https://doi.org/10.1007/978-981-15-0214-9_30

Fig. 1 Three-phase ZSI



source inverter (VSI) as shoot through state to boost the output. Since it has zero output voltage in its shoot through state, it shows no adverse effect on output power quality in terms of THD. It has the following special features which make it better than conventional VSI [1]:

1. An increment or decrement in the output voltage can be obtained as per requirement [2, 3].
2. The issue of dead time is resolved by insertion of shoot through [2, 3].

A ZSI provides the benefits of two stages of DC–DC boost converter and DC–AC conventional inverter into a single stage as shown in Fig. 1. For better performance of ZSI, many researchers presented a great number of methods for closed loop controlling of ZSI [4–15].

The PID controller is widely used in industrial applications. A PID controller is used to control the DC link voltage through the capacitor voltage by shoot through duty cycle modulation strategy [4]. Although it provides better transient performance as well as enhancement in disturbance rejection ability, a fluctuation appears in the DC link voltage when it is subjected to a step change in input DC supply as controller keeps capacitor voltage constant. This change may be transferred to output side and may distort the output voltage. A PID controller tuning by direct measurement of peak DC link voltage V_{ip} is presented in [5]. It makes control circuitry very complex due to fluctuating nature of DC link voltage. Rastegar et al. [6] discussed a neural network tuned PI controller for controlling the capacitor voltage. Again, any step change in input DC voltage may be appeared in the DC link voltage and in the output voltage. Two separate controllers based on two degrees of freedom are explained [7]. One of them controls the capacitor voltage linearly by shoot through duty ratio, and another is used to monitor the output voltage by controlling the peak value of AC output voltage by PI controller, respectively. A multi-loop closed-loop controller considering the ZSI as conventional VSI and boost converter is presented in [8] for better tracking and disturbance rejection. The AC side voltage is controlled by the

modulation index, whereas the DC side controller adjusts the shoot through duty ratio. An average DC link voltage is controlled by the fuzzy-PID controller. The capacitor voltages are used to calculate the average of DC link voltage [9]. Authors [10, 11] proposed voltage mode and current mode methods to control the peak DC link voltage of ZSI. The peak of DC link voltage was calculated by measuring the capacitor voltage and input DC voltage and estimated by $V_{ip} = 2V_c - V_{in}$. Since a ZSI consists of a right-half plane zero, it is very difficult to find the tuning parameters of PID controller. Several optimization approaches like particle swarm optimization (PSO) [12, 13], artificial bee colony [14], genetic algorithm (GA) [15, 16], and bacterial foraging optimization (BFO) [17, 18] are used for closed loop operation of power electronics converters. Since, Z-source inverter is used in renewable energy application [19], necessity of PID controller for the satisfactory performance is in great demand.

In this paper, a new Jaya optimization-based approach is proposed to find the (1) reduced model of ZSI and (2) gain parameters of PID controller through the error minimization. This paper presents a PID controller design using the optimized tuning parameters by controlling the peak value of DC link voltage indirectly through the Jaya optimization as shown in Fig. 1. The complete paper is divided into different sections. Section 2 depicts the basics of Z-source inverter. Section 3 is related to the brief description of Jaya approach. Section 4 validates the theoretical explanation by the help of MATLAB/Simulink simulation. The final remarks are presented in Sect. 5.

2 Z-Source Inverter

A ZSI replaces the DC link capacitor of VSI into a segmented pair of inductors L_X , L_Y and capacitors C_X , C_Y organized in the cross (X) shaped as shown in Fig. 1. The diode D_s at the supply side is used to avoid reverse power flow. The simplified equivalent circuit diagram of ZSI is shown in Fig. 2. It is assumed that modeling of active states and zero states are almost same and these are different from the shoot through states. The switches S_1 and S_2 represent the diode and the inverter.

The ZSI works in two modes [1] (1) Non-shoot through (NST) mode and (2) Shoot through (ST) mode. In non-shoot mode operation, the diode is switched on, and DC supply appears across the load whereas in the case of short circuited load terminals either by lower or upper three legs of switching devices, the inductors become charged. The operating equivalent circuit is shown in Fig. 3. The equivalent operating circuit diagram of shoot through mode is shown in Fig. 4. The diode is off to avoid the reverse power flow, and the load is shorted by the upper and lower switch of the same leg in shoot through mode. The boost factor of the ZSI with shoot through ratio D [1, 2] is given

$$B = \frac{1}{1 - 2D} \tag{1}$$

Fig. 2 Simplified circuit of ZSI

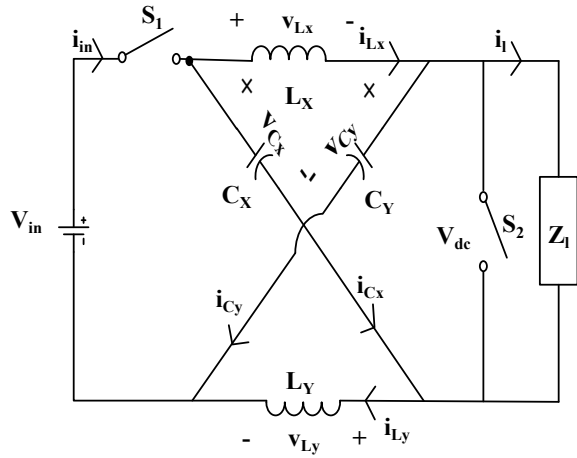


Fig. 3 ZSI in non-shoot through mode

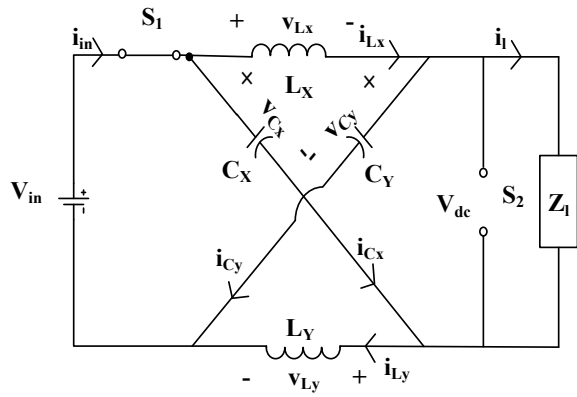
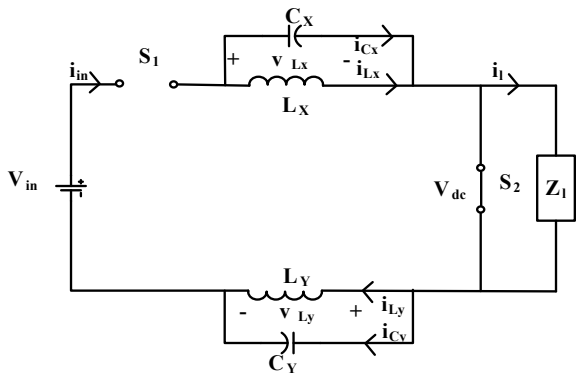


Fig. 4 ZSI in shoot through mode



Assume that $L_X = L_Y = L$ and $C_X = C_Y = C$ then $i_{Lx} = i_{Ly} = i_{Lm}$ and $v_{Cx} = v_{Cy} = v_{Cm}$. In shoot through state S_1 is OFF and S_2 is ON as shown in Fig. 4. So,

$$v_{Lm}(t) = v_{Cm}(t) \text{ and } v_{dc}(t) = 0 \tag{2}$$

In non-shoot through state, S_1 is ON and S_2 is OFF. So,

$$v_{Lm}(t) = v_{in}(t) - v_{Cm}(t) \tag{3}$$

$$v_{dc}(t) = \hat{v}_{dc}(t) = v_{Cm}(t) - v_{Lm}(t) = 2v_{Cm}(t) - v_{in}(t) \tag{4}$$

where $\hat{v}_{dc}(t)$ is nonzero portion of $v_{dc}(t)$. So the average voltage over switching period is

$$v_{dc}(t) = (1 - d_0(t))\hat{v}_{dc}(t) \tag{5}$$

where $d_0(t)$ is duty ratio of switch S_2 .

3 Jaya Optimization Algorithm

The Jaya algorithm [20, 21] is an algorithmic parameter-free simple computer-oriented optimization approach, unlike GA and PSO techniques. This approach need only some tuning parameters for implementation which makes it very attractive in comparison to its counterpart GA and PSO approach which require parameters like selection operator, mutation probability, etc. The basic operating principle of the Jaya algorithm is similar to other error minimization approach. First, a fitness function is designed as per the design objectives and the Jaya optimization method tries to minimize that fitness function by avoiding the worst solution rapidly and moving toward the best solution quickly. The implementation procedure of Jaya optimization algorithm is summarized below:

Let the fitness function is denoted by fi is given by

$$fi = |M_{ov} - 1|/5 + |M_{un} - 1| + (T_{rise}/0.01) + (T_{settling}/0.03) \tag{6}$$

which is to be minimized for achieving the optimized result. Let $p_{x,y,z}$ is a solution among N number of solutions (i.e., $y = 1, 2, \dots, N$) of M design variables (i.e., $x = 1, 2, \dots, M$) at z th iteration, then the steps of Jaya algorithm are as follows:

Step 1: [Initialization] Size of random solution, number of iterations, and a termination criterion should be initialized in the beginning.

Step 2: [Best and Worst] The worst and best solutions are considered according to highest and lowest fitness values, respectively.

Step 3: [Modification] Get new solutions according to the equation given below:

Table 1 Simulation parameters for ZSI

Vo	20 V
Shoot through duty ratio D	0.3
$L_X = L_Y = L$	330 μ H
$C_X = C_Y = C$	220 μ F
Load resistance R_l	50 Ω
Load inductance L_l	330 μ H

$$p_{x,y,z}^{new} = p_{x,y,z} + \text{rand}_{1,x,z}(p_{x,best,z} - |p_{x,y,z}|) - \text{rand}_{2,x,z}(p_{x,worst,z} - |p_{x,y,z}|) \tag{7}$$

where $p_{x,best,z}$ is the value of x th variable for best solution, $p_{x,worst,z}$ is the value of x th variable for worst solution, $p_{x,y,z}^{new}$ is the new value of $p_{x,y,z}$. Further, $\text{rand}_{1,i,k}$ and $\text{rand}_{2,i,k}$ are two random numbers for x th variable during z th iteration which show the degrees of approach toward the best solution and to avoid to worst solution, respectively.

Step 4: [Replacement] Find the new population of random solutions by the replacement of improved solutions with lowest fitness value.

Step 5: [Termination] As a final point, stopping criterion is checked. If it is met, terminate the procedure otherwise go to Step 2.

The simulation parameters of ZSI with transfer function [22], as shown in Table 1 are used to obtain the transfer function of original system:

$$G_o(s) = \frac{-7.296 \times 10^{-8}s^2 - 0.003795s + 400}{2.396 \times 10^{-11}s^3 + 3.63 \times 10^{-6}s^2 + 0.0003762s + 8} \tag{8}$$

The second-order reduced model of ZSI obtained by the Jaya optimization algorithm is

$$G_r(s) = \frac{-0.1s + 1.096 \times 10^8}{s^2 + 89.2s + 2.192 \times 10^6} \tag{9}$$

Further, the step response of the original ZSI inverter and proposed second-order ZSI inverter is shown in Fig. 5. The reduced model shows exact replica of original ZSI inverter in step response plot. Moreover, the frequency responses of both transfer functions are plotted in Fig. 6. Till bandwidth of bode plot, both models show a great resemblance in their frequency responses. Transient parameters comparison of original ZSI and reduced ZSI are shown in Table 2.

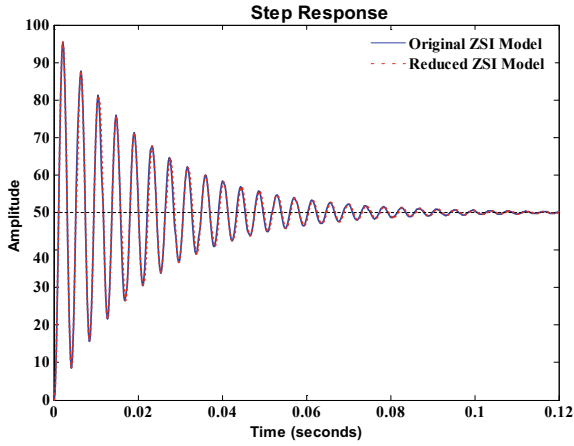


Fig. 5 Step responses of original ZSI and Proposed reduced ZSI

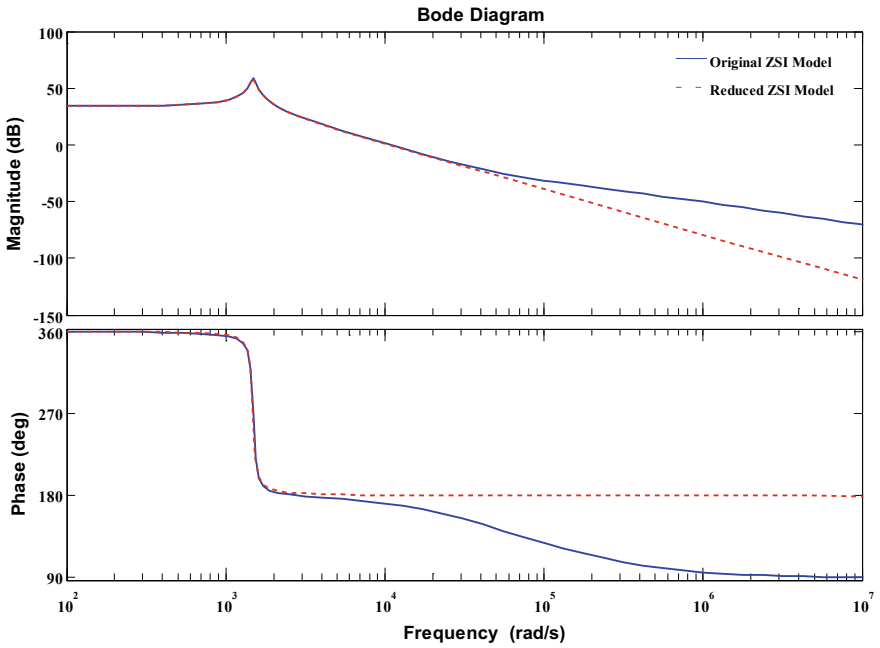


Fig. 6 Bode plots of original ZSI and Proposed reduced ZSI

Table 2 Transient parameters of original ZSI and reduced ZSI

Transient parameters	Original ZSI	Reduced ZSI
Rise time (s)	0.000719	0.00072
Settling time (s)	0.087	0.00872
Peak amplitude	95.5	95.5
Peak time (s)	0.00212	0.00212

4 Simulation and Results

The simulation study is performed on MATLAB/Simulink platform to check the performance of optimized PID controller for the closed-loop operation of ZSI. The circuit shown in Fig. 1 is simulated with the parameters given in Table 1. The initialization parameters of the Jaya optimization for the designing of reduced model are summarized in Table 3. The Jaya optimization uses error minimization of fitness function, i.e., ISE to find the reduced model of ZSI. Further, this model is used to find the desired step response by the optimized tuning of PID controller. A PID controller with first-order filter has four parameters (i.e., K_p , K_i , K_d , and filter coefficient N) to be optimized for desired performance. Their selection ranges are given in Table 4. Here, the objective function is designed by the weighted sum of overshoot, undershoot, rise time, and settling time as given in Eq. 6. The Jaya optimization utilizes the objective function to get the optimized tuning parameters of PID controller along the first-order filter coefficient. Optimized parameters of PID with first order filter are shown in Table 5. The step responses of the closed-loop operation of reduced ZSI with optimized controller and original ZSI with same controller are plotted in Fig. 7. Further, the performance of the tuned controller is compared with the conventional Ziegler Nicolas (ZN)-based PID controller. The transient parameters obtained for closed-loop response of reduced ZSI, original ZSI with tuned PID controller with first-order filter, and ZN-based PID controller are shown in Table 6. The ZN-based

Table 3 Parameters of Jaya Optimization

Parameters	Value
No. of random solutions N	25
No. of iterations iter	30
rand1	0.51
rand2	0.81

Table 4 Initial range of controller parameters

PID parameters	Min	Max
K_p	0	10
K_i	0	100
K_d	0	0.0001
N	0	1e6

Table 5 PID with first-order filter parameters obtained by Jaya Optimization

Algorithms	K_p	K_i	K_d	N
Jaya optimization	0.01	6.3726	0.0000581	136861.312

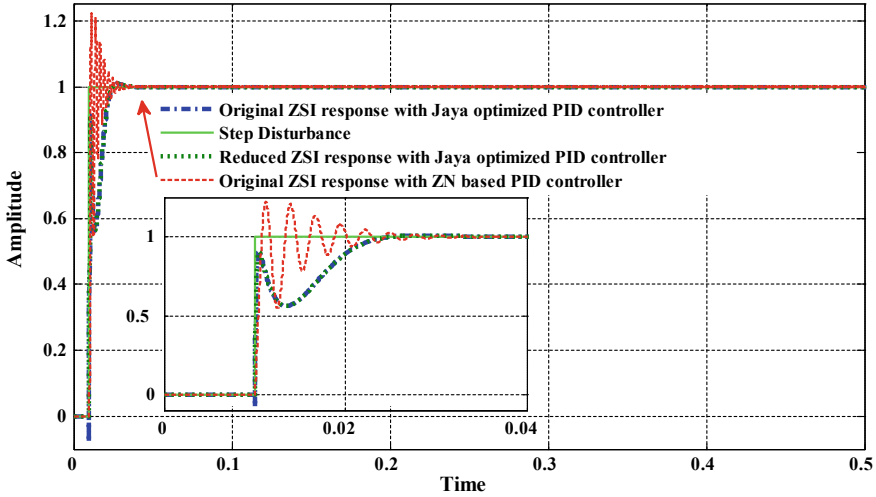


Fig. 7 Step responses of original ZSI and reduced ZSI with Jaya optimized PID controller and original ZSI with ZN-based PID controller

Table 6 Transient Parameters of output response

Transient parameters	Settling time (s)	Rise time (s)	Peak amplitude	Undershoot
Original ZSI with Jaya optimization-based PID Controller	0.0141	3.42×10^{-4}	1.0091	7.9267
Reduced ZSI with Jaya optimization-based PID Controller	0.01419	4.197×10^{-4}	1.0088	3.624×10^{-8}
Original ZSI with ZN-based PID Controller	0.01994	4.357×10^{-4}	1.3066	7.955

PID controller shows an oscillating behavior in output tracking performance with higher settling time, whereas a better result is obtained by the Jaya optimized PID controller. It can be easily concluded that Jaya optimized PID controller gives a better response in comparison with ZN-based PID controller. It can be concluded that Jaya optimized PID controller gives a better response in comparison with ZN-based PID controller.

5 Conclusion

The Z-source inverter is a replacement of two-stage DC–DC and DC–AC converters in an efficient manner. This efficient power electronic inverter is very suitable for renewable energy applications. The mathematical modeling creates difficulties for the designing of PID controller because of right-half plane zero. A simplified model is developed for the higher order ZSI by the Jaya optimization approach and further, the Jaya approach is adopted for the designing of PID controller by the error minimization technique. A weighted sum of transient parameters is selected as an objective function to be minimized. It is shown by simulation results that the proposed approach reduces the computational complexity and gives better performance than the conventional approach.

References

1. Peng FZ (2003) Z-source inverter. *IEEE Trans Ind Appl* 39:504–510
2. Ahmad A, Gupta AK, Samuel P (2014) Embedded system design for digital control of single phase Z-source inverter using FPGA. In: 14th IEEE international conference on environment and electrical engineering (EEEIC), pp 402–407
3. Huang Y, Shen M, Peng FZ, Wang J (2006) Z-source inverter for residential photovoltaic systems. *IEEE Trans Power Electron* 21(6)
4. Ding X, Qian Z, Yang S, Cui B, Peng FZ (2007) A PID control strategy for DC-link boost voltage in Z-source inverter. In: 22nd annual IEEE applied power electronics conference, APEC'07, pp 1145–1148
5. Ding X, Qian Z, Yang S, Cui B, Peng FZ (2007) A direct peak DC-link boost voltage control strategy in Z-source inverter. In: 22nd annual IEEE applied power electronics conference APEC'07, pp 648–653
6. Rastegar MJ, Fatemi S, Mirzakuchaki S, Rastegar F (2008) Wide-range control of output voltage in Z-source inverter by neural network. In: International conference on electrical machines and systems ICEMS'08, pp 1653–1658
7. Tran QV, Chun TW, Ahn JR, Lee HH (2007) Algorithms for controlling both the DC boost and AC output voltage of Z-source inverter. *IEEE Trans Ind Electron* 54(5)
8. Gajanayake CJ, Vilathgamuwa DM, Loh P (2006) Modeling and design of multi-loop closed loop controller for Z-source inverter for distributed generation. In: 37th IEEE power electronics specialists conference PESC'06, pp 1353–1359
9. Ding X, Qian Z, Yang S, Cui B, Peng FZ (2008) A direct DC-link boost voltage PID-like fuzzy control strategy in Z-source inverter. In: IEEE power electronics specialists conference PESC'08, pp 405–411
10. Ellabban O, Van Mierlo J, Lataire P (2009) Voltage mode and current mode control for a 30 kW high-performance Z-source inverter. In: IEEE electrical power & energy conference
11. Sen G, Elbuluk M (2008) Voltage and current programmed modes in control of the Z-source converter. In: IEEE industry applications society annual meeting IAS 08, pp 1–8
12. Altinoz OT (2015) Particle swarm optimization-based PID controller tuning for static power converters. *Int J Power Electron* 7(1/2):16–35
13. Altinoz OT, Erdem H (2010) Evaluation function comparison of particle swarm optimization for buck converter. In: Proceedings of power electronics, electrical drives, automation and motion conference, pp 798–802

14. Sonmez Y, Ayyildiz O, Kahraman HT, Guvenc U, Duman S (2015) Improvement of buck converter performance using artificial bee colony optimized-pid controller. *J Autom Control Eng* 3(4)
15. Ou C, Lin W (2006) Comparison between PSO and GA for parameters optimization of PID controller. In: *Proceedings of IEEE mechatronics and automation conference*, pp 2471–2475
16. Cheng CH, Cheng PJ, Xie MJ (2010) Current sharing of paralleled DC–DC converters using GA-based PID controllers. *Expert Syst Appl* 37:733–740
17. Jalilvand A, Vahedi H, Bayat A (2010) Optimal tuning of the PID controller for a buck converter using bacterial foraging algorithm. In: *Proceedings of intelligent and advanced systems conference*, pp 1–5
18. Prabha DMMSR, Kumar SP, Devedhas GG (2011) An optimum setting of controller for a dc-dc converter using bacterial intelligence technique. In: *Proceedings of innovative smart grid technologies conference*, pp 204–210
19. Sajadian S, Ahmadi R, Zargarzadeh H (2018) Extremum seeking based model predictive MPPT for grid-tied z-source inverter for photovoltaic systems. *IEEE J Emerg Sel Top Power Electron*. <https://doi.org/10.1109/JESTPE.2018.2867585>
20. Rao RV, Waghmare GG (2016) A new optimization algorithm for solving complex constrained design optimization problems. *Eng Optim* 1–24
21. Rao RV, More KC, Taler J, Ocłon P (2016) Dimensional optimization of a micro-channel heat sink using Jaya algorithm. *Appl Therm Eng* 103:572–582
22. Chaiyakun T, Liutanakul P, Wiwatcharagoses N (2017) Feasibility of reduced order modelling of Z-source impedance network: applications for switching power converter designs. In: *5th international electrical congress*, Pattaya, Thailand

Stability Analysis of an Offshore Wind and Marine Current Farm in Grid Connected Mode Using SMES



Satendra Kr Singh Kushwaha, S. R. Mohanty and Paulson Samuel

Abstract This study investigated the stability of offshore wind farm (OWF) and marine current farm (MCF) using hybrid combination of superconducting magnetic energy storage system (SMES) and bridge type fault current limiter (BFCL). The aggregated model of OWF is simulated by 80 MW doubly-fed induction generator (DFIG) based plant and MCF is simulated by a 80 MW squirrel cage induction generator (SCIG) based generator. An H-infinity loop-shaping-based robust controller is proposed for the SMES unit to enhance the stability and robustness of the studied system. The performance of the proposed damping controller is evaluated under high stochastic disturbances and transient condition. The simulation result shows the efficacy of the proposed controller. Hence, it enhanced the stability and robustness of the studied system.

Keywords Marine current turbine · Offshore wind farm · Grid integration · Static magnetic energy storage system (SMES) · Bridge type fault current limiter

1 Introduction

In the interest of larger renewable energy harvesting, geographical conditions often found suitable and economical for combining OWF and MCF at the same location [1]. Since ocean covered two-third surface of Earth and huge source of kinetic energy in the form of oceanic currents and offshore wind, a hybrid integration of both OWF and MCF can be widely developed worldwide in near future [2]. It will become a new trend of electricity production in future to meet our future energy need. The operating principle of MCF is similar to the wind farm [3]. This similarity helps

S. K. S. Kushwaha (✉) · S. R. Mohanty · P. Samuel
Department of Electrical Engineering, Motilal Nehru National Institute
of Technology Allahabad, Prayagraj 211004, India
e-mail: ree1506@mnnit.ac.in

S. R. Mohanty
e-mail: soumya@mnnit.ac.in

P. Samuel
e-mail: paul@mnnit.ac.in

© Springer Nature Singapore Pte Ltd. 2020
A. Kalam et al. (eds.), *Intelligent Computing Techniques for Smart Energy Systems*,
Lecture Notes in Electrical Engineering 607,
https://doi.org/10.1007/978-981-15-0214-9_31

extensive growth of marine current energy conversion system and become mature than other oceanic energy conversion system [4, 5].

The grid integration of OWF and MCF leads to huge source of renewable energy. The stochastic natures of these energy resources create a new challenge while integrating with grid. So it requires thorough investigation of system stability issues [6–8]. This paper investigates the stability prospective of studied system in steady state and transient condition. Superconducting magnetic energy storage system (SMES) is employed at PCC to make this energy resource more reliable [9, 10]. There are several control techniques that have been listed in literature to make the system reliable [11–13]. The uncertainty in the system is taken care of by H-infinity controller design for SMES in this study. H-infinity controller design techniques include the uncertainty and disturbances in controller design and make the controller insensitive for the exogenous disturbances which make the controller robust and it is required for the stable system; hence, the H-infinity controller increases the system stability and reliability [14]. Bridge type fault current limiter (BFCL) [15] is employed in the transmission line to improve the transient response of the system.

This paper is organized as follows: the detailed modeling of doubly fed induction generator (DFIG)-based OWF, squirrel cage induction generator (SCIG)-based MCF, and BFCL modeling is given in Sect. 2. SMES modeling and its controller design is given in Sect. 3, the results and discussion is presented in Sect. 4 and specific conclusion is given in Sect. 5.

2 Configuration of the Studied Systems

In this section, modeling of SCIG-based MCF; DFIG-based OWF; superconducting magnetic energy storage system (SMES) and BFCL is discussed.

The aggregated model of OWF is simulated by a 2 MW DFIG-based generator and the aggregated model of MCF is simulated by 2 MW SCIG-based generator. The modeling of component shown in Fig. 1 is illustrated in subsequent section.

2.1 Modeling of OWF

The dynamic power extracted by the offshore wind turbine is [9]

$$P_{\text{owt}} = P_{m0} \cdot C_{\text{pw}}(\lambda_w, \beta_w) \quad (1)$$

where P_{m0} is the available power to offshore wind turbine and $C_{\text{pw}}(\lambda_w, \beta_w)$ is the power coefficient, P_{m0} and $C_{\text{pw}}(\lambda_w, \beta_w)$ are expressed as

$$P_{m0} = \frac{1}{2} \rho_w \cdot \pi R_{\text{rw}}^2 \cdot V_w^3, C_{\text{p_owt}}(\psi_w, \beta_w) \quad (2)$$

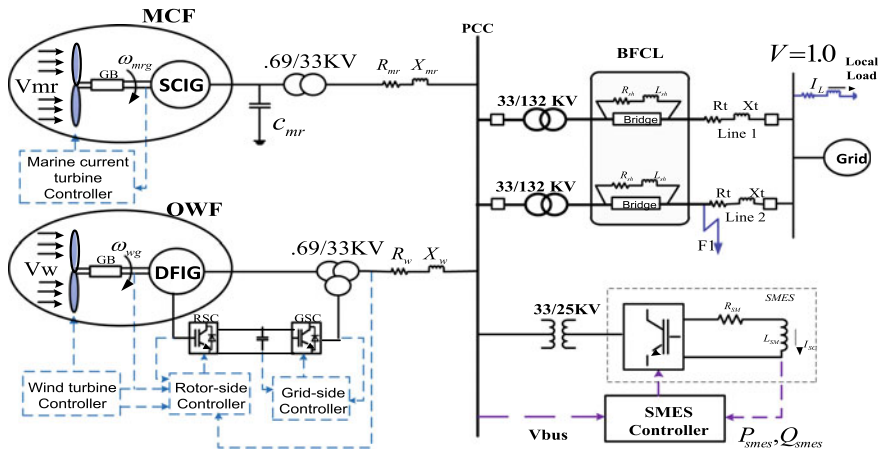


Fig. 1 Configuration of the studied system

In which,

$$C_{p_owt}(\psi_w, \beta_w) = c_1 \left(\frac{c_2}{\psi_w} - c_3 \cdot \beta_w - c_4 \cdot \beta_w^{c_5} - c_6 \right) e^{(-c_7/\psi_w)}$$

$$\frac{1}{\psi_{ww}} = \frac{1}{\lambda_w + c_8 \cdot \beta_w} - \frac{c_9}{\beta_w^3 + 1}, \lambda_w = \frac{R_{bw} \cdot \omega_{bw}}{v_w} \tag{3}$$

where ρ_w is wind density, V_w is offshore wind velocity, and R_w is turbine radius,

2.2 DFIG Modeling

The dynamic equations of DFIG-based offshore wind farm is expressed as [9]

$$v_s = r_s i_s + \frac{d\psi_s}{dt} - \omega_{ref} \psi_s, \quad v_r = r_r i_r + \frac{d\psi_r}{dt} - (\omega_{ref} - \omega_r) \psi_r \tag{4}$$

where ψ_s is the linkage flux, r_s, r_r is the stator and rotor resistances and i_s, i_r and ω is the stator, rotor current, and angular velocity, respectively.

The P_s and Q_s of the DFIG is expressed as

$$P_s = \frac{3}{2} V_{qs} i_{qs}; \quad Q_s = -\frac{3}{2} V_{qs} i_{ds} \tag{5}$$

The stator d and q axis current is controlled by the rotor current so the P_s and Q_s is expressed as

$$P_s = -\frac{3}{2} \left(\frac{\omega \lambda_{ds} L_m}{L_{ls} + L_m} \right) i_{qs}; \quad Q_s = \left(\frac{\omega \lambda_{ds}}{L_{ls} + L_m} \right) (\lambda_{ds} - L_m i'_{dr}) \quad (6)$$

Equation (6) shows the mutually exclusive relationship between active and reactive power. Both powers can be separately controlled by the d and q axis of rotor current. The control circuit of DFIG converters is given in [9].

2.3 Marine Current Turbine

The dynamic power extracted by marine current turbine is expressed by [9]

$$P_{m_mct} = \frac{1}{2} \rho_{mr} \cdot A_{mtr} \cdot V_{mr}^3 \cdot C_{p_{mr}}(\lambda_{mr}, \beta_{mr}) \quad (7)$$

where density and velocity of marine current is ρ_{mr} (kg/m³), and V_w (m/s), respectively, radius of turbine is R_w (m), and C_{p_mct} represents the power coefficient of marine current turbine.

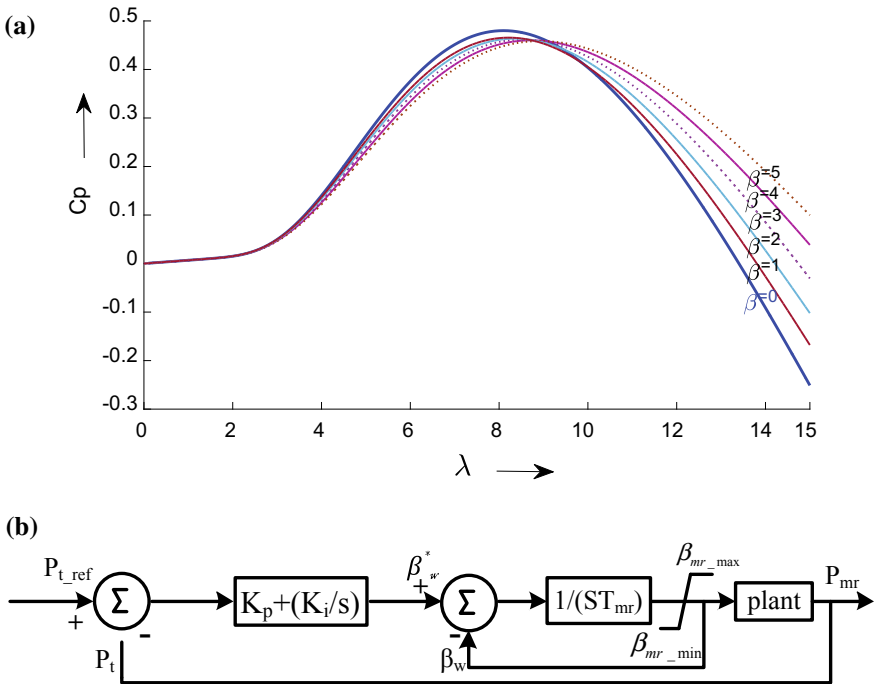


Fig. 2 a $C_p - \lambda$ curve. b Pitch angle controller

The $C_p - \lambda$ characteristic and pitch angle controller of turbines is given in Fig. 2. The OWF and MCF have same pitch angle controller with different parameters. The maximum value of C_p for both turbines is achieved around $\lambda = 8$. The curve draws at different pitch angles β or at different velocities of both resources. The power coefficient is maximum at rated speed and decreases above the rated speed up to cutoff speed for both turbines.

2.4 SCIG Modeling

The dynamic modeling of SCIG-based marine current generator in d-q frame of reference is expressed as [9]

$$V_{dq0s} = r_s i_{dq0s} + \omega \lambda_{dq0s} + p \lambda_{dq0s}; \quad 0 = r_r i'_{dq0r} + (\omega - \omega_r) \lambda'_{dq0r} + p \lambda'_{dq0r} \quad (8)$$

Dynamic torque equations are

$$J_{mct} \frac{d}{dt} \omega_r = T_{m0} - T_{e0}, \quad T_{m0} = \frac{P_m}{\omega_m} \quad (9)$$

where λ_{dq} is the flux linkage, ω and ω_r are the stator and rotor angular velocity, i_{dq0s} and i_{dq0r} are the stator and rotor current. J_{mct} is inertia constant of turbine T_{m0} and T_{e0} is the mechanical and electrical torque of the generator.

The modeling of BFCL is given in [15].

3 SMES MODELING

The SMES is connected to PCC with a power converter and bidirectional DC-DC converter. The output of SMES is controlled by a phase angle α_{smes} and modulation index M_{1smes} of the power converter for tuning of active power and reactive power required at PCC. The d-q axis current and power of SMES is expressed as [9]

$$i_{qsmes} = M_1 I_{smes} \cos(\theta_V + \alpha_{smes}), \quad i_{dsmes} = M_1 I_{smes} \sin(\theta_V + \alpha_{smes}) \quad (10)$$

$$\begin{aligned} P_{smes} &= V_{dpcc} I_{dsmes} + V_{qpcc} I_{qsmes} = M_1 |V_{pcc}| I_{dc} \cos(\alpha_{smes}) \\ Q_{smes} &= V_{dpcc} I_{qsmes} - V_{qpcc} I_{dsmes} = M_1 |V_{pcc}| I_{dc} \sin(\alpha_{smes}) \end{aligned} \quad (11)$$

where $|V_{pcc}| = (V_{qpcc}^2 + V_{dpcc}^2)^{1/2}$, θ_V is the phase angle at PCC. I_{dc} is the DC current of SMES. The differential equation of I_{SC} is

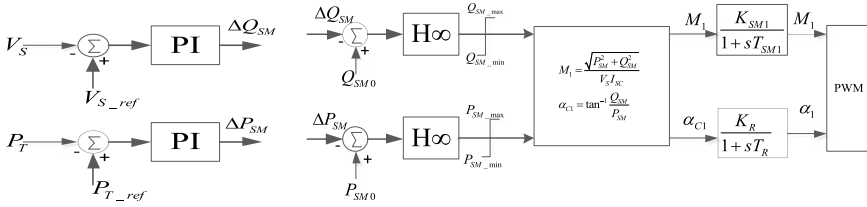


Fig. 3 Control circuit of SMES converter

$$L_{smes} \partial(I_{dc}) = -I_{dc} R_{dc} + \sqrt{v_{qpcc}^2 + v_{dppc}^2} \cos \alpha - (pi/2) I_{dc} X_{cm} \quad (12)$$

where L_{smes} and R_{smes} are equivalent inductance and resistance of SMES, and X_{CM} is the combined reactance of converter circuit.

The active power fed by SMES is derived from transmission line power deviation (ΔP_{TL}) to maintain active power flow constant and the required reactive power (ΔQ_{TL}) fed by SMES is derived from PCC voltage deviation (ΔV_{pcc}) to maintain terminal voltage constant. The derived equations are (Fig. 3)

$$\begin{aligned} T_{PT} \partial(\Delta P_{SMES}) &= K_{PT}(P_{TL_ref} - P_{TL}) - \Delta P_{SMES}, \quad T_{PV} \partial(\Delta Q_{SMES}) \\ &= K_{PV}(V_{PCC_ref} - V_{PCC}) - \Delta Q_{SMES} \end{aligned} \quad (13)$$

4 H-Infinity Controller of SMES

Figure 4b shows the control circuit for the SMES. The state space representation of SMES unit is

$$\begin{bmatrix} \dot{x} \\ y \\ z \end{bmatrix} = \begin{bmatrix} A & B_1 & B_2 \\ C_1 & D_{11} & D_{12} \\ C_2 & D_{21} & D_{22} \end{bmatrix} \begin{bmatrix} x \\ w \\ u \end{bmatrix} \quad (14)$$

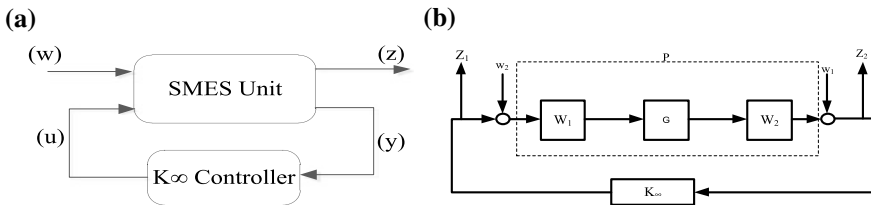


Fig. 4 a Basic structure of H-infinity control. b H-infinity control of augmented plant

where $X = [\Delta P_{SMES}, \Delta Q_{SMES}]$, $Y = [M_1, \alpha]$, $u = [P_T, V_S]$, $W = [P_{Tref}, V_{Sref}]$, and $Z = [P_{Tref} - P_T, V_{Sref} - V_S]$. The configuration of H-infinity controller is shown in Fig. 4, where the w and u are the exogenous input and control input of the SMES, respectively, z and y are the error signal and controller output of the SMES. Ideally, the control signal should be zero are minimum as much as possible. The necessary and sufficient condition for closed loop SMES unit stability is the H-infinity norm ($\|H(s)\|_\infty = \sup_{\omega} \bar{\sigma}(H(j\omega)) < \gamma_{min}$).

For the H-infinity control, to insure closed loop stability of plant "SMES", a feedback controller "K" is incorporated. Such that the H-infinity norm is smaller than the γ_{min} from disturbance signal "w" to the output "z".

$$\|T_{zw}(s)\|_\infty < \gamma \tag{15}$$

The H-infinity controller design finds a controller "K" that stabilizes the closed loop system. The stabilizable controller is design using pre-compensator W_1 and post-compensator W_2 . Figure 5b shows the H-infinity controller of augmented plant, where

$$K = W_1 K_\infty W_2 \tag{16}$$

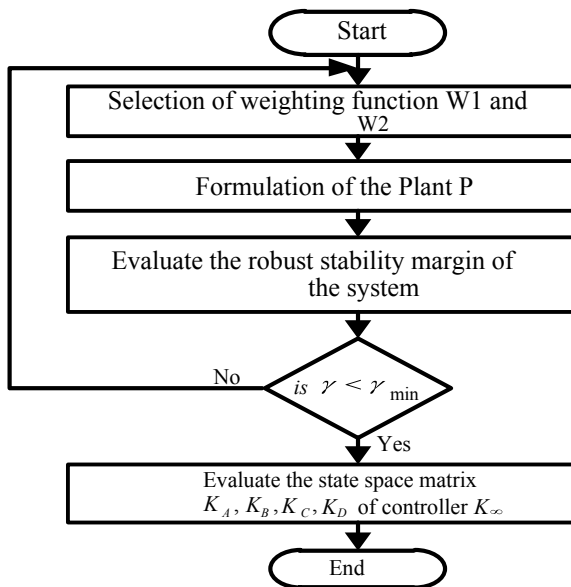


Fig. 5 Flow chart

The weighting functions are chosen as [11]

$$W_1 = K_w \left(\frac{S + a}{S + b} \right) \quad (17)$$

where “Kw” is a gain, “a” and “b” are positive values. Usually, the weighting function W_2 is considered as a unity. The algorithm of the K_∞ controller design is shown in Fig. 5.

5 Simulation Results and Discussion

The studied system is simulated and analyzed with SMES unit and BFCL. The efficacy of SMES controller is analyzed under stochastic nature of wind and marine current speed. The simulation results are analyzed in pu quantities except for the wind and marine current velocity, which is in m/s. The time-domain simulation in above studied system is evaluated under steady state and transient conditions.

Case 1: dynamic variation in wind speed and marine current speed: a dynamic speed of both resources is simultaneously applied to the studied system to evaluate the performance of the studied system. The system response is compared with conventional PI controller. The dynamic response of the studied system is shown below. Figure 6b, c suggests that the active and reactive power deviation at grid have less overshoot and settling time with H-infinity loop-shaping-based proposed controller due to fast acting of SMES unit. It helps to mitigate the oscillations due to dynamic nature of resource. Figure 6e shows the DC-link voltage of SMES converter and compared with PI controller, results suggest that oscillation damping and settling time of voltage and power signals is faster with proposed controller. Hence it improves the overall performance and stability of the studied system.

Case 2: occurrence of fault at grid side: a fault is created at $t = 1.5$ s to evaluate the performance and robustness of the studied system under transient condition. The offshore wind speed and marine current speed is taken constantly during transient condition due to fact that the variation of speed in small duration is insignificant. The terminal voltage of PCC is shown in Fig. 7a. It suggests that the inclusion of BFCL unit improves the voltage stability under transient condition. The active and reactive power deviation at grid is shown in Fig. 7b, c. It suggests that the damping oscillation is faster with inclusion of BFCL in studied system due to the fact that the BFCL limits the transient current or fault current and consuming the excess amount of power. It prevents the rotor of generator from oscillations and helps to maintain synchronism. Hence, it enhances the overall stability and robustness of the system means it make the system more reliable.

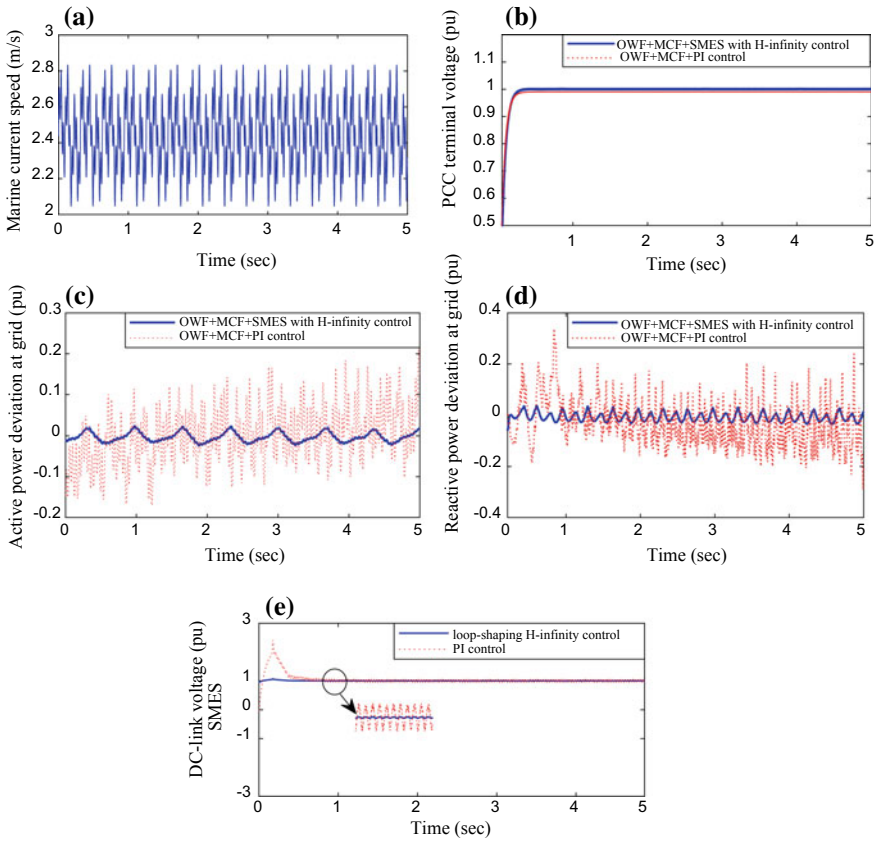


Fig. 6 a Random wind speed, b terminal voltage of grid, c active power at grid, d reactive power at grid, e DC-link voltage of SMES

6 Conclusion

This paper presents the stability analysis of OWF and MCF integrated to grid using SMES and BFCL unit. A loop-shaping H-infinity-based robust controller is proposed for the SMES unit. The impact of H-infinity controller of SMES is evaluated in steady state and transient conditions and compared with conventional PI controller. The simulation result shows the efficacy of the proposed controller. The performance of studied system with inclusion of BFCL improves the transient stability of integrated system. Hence, the combination of SMES unit and BFCL enhances the stability and robustness of the studied system and makes it more reliable.

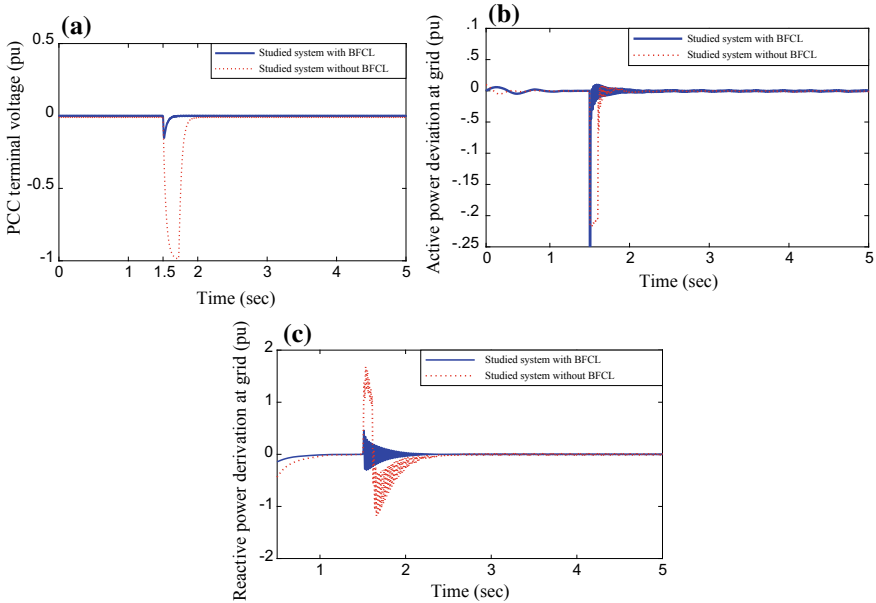


Fig. 7 **a** Terminal voltage of grid, **b** active power at grid, **c** reactive power at grid

References

1. Benelghali S, Benbouzid MEH, Charpentier JF (2007, May) Marine tidal current electric power generation technology: state of the art and current status. In: Proceedings of IEEE international electric machines & drives conference, Antalya, Turkey, vol 2, pp 1407–1412
2. O’Sullivan DL, Dalton G, Lewis AW (2010) Regulatory, technical and financial challenges in the grid connection of wave energy devices. *IET Renew Power Gener* 4(6):555–567
3. Benelghali S, Benbouzid MEH, Charpentier JF (2012) Generator systems for marine current turbine applications: a comparative study. *IEEE J Ocean Eng* 37(3):554–563
4. Myers L, Bahaj AS (2005) Simulated electrical power potential harnessed by marine current turbine arrays in the Alderney Race. *Renew Energy* 30(11):1713–1731
5. Bryden IG, Couch S (2006) ME1-marine energy extraction: tidal resource analysis. *Renew Energy* 31(2):133–139
6. Muljadi E, Butterfield CP, Parsons B, Ellis A (2007) Effect of variable speed wind turbine generator on stability of a weak grid. *IEEE Trans Energy Convers* 22(1):29–36
7. Nasr-Azadani E, Canizares CA, Olivares DE, Bhattacharya K (2014) Stability analysis of unbalanced distribution systems with synchronous machine and DFIG based distributed generators. *IEEE Trans Smart Grid* 5(5):2326–2338
8. Xu H, Hu J, Nian H, He Y (2012) Dynamic modeling and improved control of DFIG under unbalanced and distorted grid voltage conditions. In: IEEE international symposium on industrial electronics, pp 1579–1584
9. Wang L, Chen SS, Lee WJ, Chen Z (2009) Dynamic stability enhancement and power flow control of a hybrid wind and marine-current farm using SMES. *IEEE Trans Energy Convers* 24(3):626–639
10. Daoud MI, Massoud AM, Abdel-Khalik AS, Elserougi A, Ahmed S (2016) A flywheel energy storage system for fault ride through support of grid-connected VSC HVDC-based offshore wind farms. *IEEE Trans Power Syst* 31(3):1671–1680

11. Jabr HM, Kar NC (2007) Effects of main and leakage flux saturation on the transient performances of doubly-fed wind driven induction generator. *Electr Power Syst Res* 77(8):1019–1027
12. Chattopadhyay R, De A, Bhattacharya S (2014) Comparison of PR controller and damped PR controller for grid current control of LCL filter based grid-tied inverter under frequency variation and grid distortion. In: *IEEE energy conversion congress and exposition (ECCE)*, pp 3634–3641
13. Djukanovic M, Khammash M, Vittal V (1998) Application of the structured singular value theory for robust stability and control analysis in multi-machine power systems. I. Framework development. *IEEE Trans Power Syst* 13(4):1311–1316
14. Doyle JC, Glover K, Khargonekar PP, Francis BA (1989) State-space solutions to standard H_2 and H_∞ control problems. *IEEE Trans Automat Contr* 34(8):831–847
15. Rashid G, Ali MH (2014) A modified bridge-type fault current limiter for fault ride-through capacity enhancement of fixed speed wind generator. *IEEE Trans Energy Convers* 29(2):527–534

Modeling and Simulation of Proton Exchange Membrane Fuel Cell Hybrid Electric Vehicle



Bandi Mallikarjuna Reddy and Paulson Samuel

Abstract This article presents system analysis of a hybrid proton exchange membrane fuel cell (PEMFC) electric vehicle, which comprises a fuel cell, a unidirectional DC–DC boost converter; a bidirectional DC–DC boost/buck converter, a battery, and an inverter with chassis section of vehicle for minimizing the cold start effect and ripple content of fuel cell vehicle. The fuel cell and energy storage are connected to the DC bus bar through unidirectional converter and bidirectional converter, respectively. However, the battery would provide the peak power demand at overloaded condition so that the fuel cell stack need not be rated for the peak power thus reducing the fuel cell cost and overall system cost. The operation of the vehicle during cold start, normal, acceleration, and overload mode conditions is analyzed in detail. Furthermore, the mathematical models of PEM fuel cell are developed in the PSACD (4.6.0) by including charging effect of double-layer as well as the thermodynamics reactions for analysis of the dynamic characteristics of the vehicle performance. Operating principle of the whole vehicle is illustrated. Simulation results of a 1-kW PEM fuel cell hybrid electric vehicle verify the theoretical analysis.

Keywords Cold start · Energy storage system · Proton exchange membrane fuel cell hybrid electric vehicle · Acceleration and deceleration modes

1 Introduction

Fuel cells [FC] are extraordinarily attractive in electric vehicles and distribution generation [1–3] because of their cleanliness, zero pollution, more reliability, and higher efficiency.

However, FCs has the following limitations: (1) Absence of storage capability like batteries. (2) Slower dynamic response compared to batteries with pretty much

B. M. Reddy (✉) · P. Samuel
Electrical Engineering Department, MNNIT Allahabad, Prayagraj 211004, UP, India
e-mail: ree1505@mnnit.ac.in

P. Samuel
e-mail: paul@mnnit.ac.in

© Springer Nature Singapore Pte Ltd. 2020
A. Kalam et al. (eds.), *Intelligent Computing Techniques for Smart Energy Systems*,
Lecture Notes in Electrical Engineering 607,
https://doi.org/10.1007/978-981-15-0214-9_32

similar response in steady-state operation mode. (3) High input current ripple because output portion is specifically associated with chassis segment of the vehicle. (4) Issues with cold start. For these reasons FCs are integrated with batteries to mitigate these issues with additional advantages like increased peak power capacity, enhanced dynamic performance, and supply of power during cold start of the vehicle [4]. The internal structure of a PEMFC electric vehicle with its characteristics is shown in Fig. 1.

The PEMFC hybrid vehicle comprises the seven major parts such as PEMFC, an energy storage unit, unidirectional converter (UDC), bidirectional converter (BDC), an inverter, an induction machine, and wheel system [5]. The PEMFC and storage unit are integrated to the same DC bus through their individual DC–DC converters.

Mathematical modeling of a 1 kW PEMFC vehicle has been done in PSCAD (4.6.0) enabling simulation of various dynamic conditions and analysis of performance of the vehicle under all conditions [6–8]. The simulation results illustrate that the vehicle works well under various conditions such as cold start, normal, acceleration, and deceleration modes [9].

The article is organized in four sections including the introductory section. The architecture of whole vehicle is briefly explained in Sect. 2 and Sect. 3 describing the various waveforms from the simulation are discussed and explained in detail. The conclusions are drawn in Sect. 4.

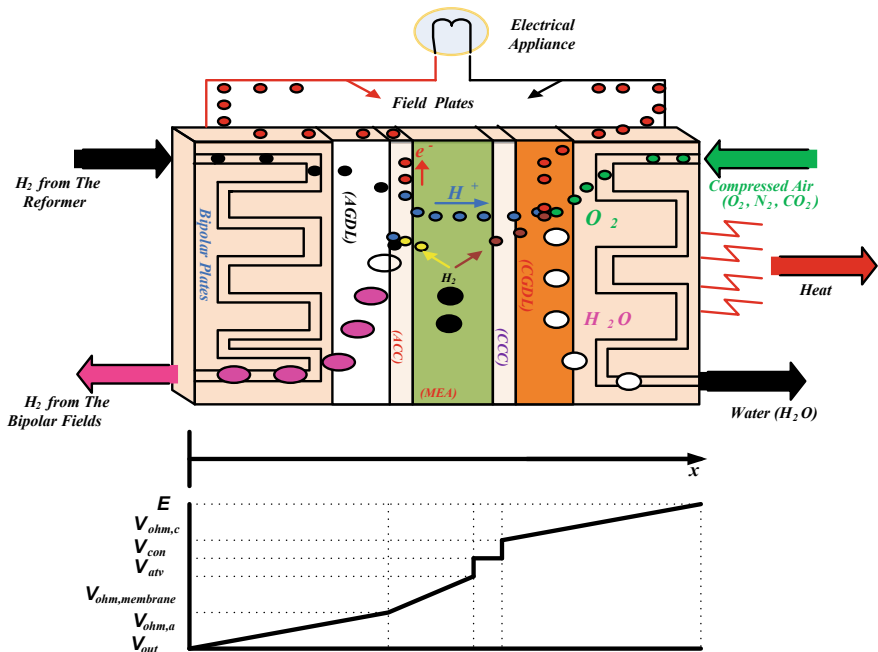


Fig. 1 Block diagram of proton exchange membrane fuel cell with its characteristics

2 Architecture of Fuel Cell Hybrid Electric Vehicle

2.1 Fuel Cell

There are many types of fuel cells based on the electrolytes used. This paper proposes a novel PEM fuel cell hybrid vehicle system, as shown in Fig. 2. Fuel cell can work at room temperature and have relatively quicker startup than many other types of energy sources. Efficiency of PEMFCs is generally in the range of 40–60%, and the power rating and output voltage can be scaled up to meet specific demands because of modularity of FCs [10–12].

2.2 Unidirectional DC–DC Converter

As shown in Fig. 2, output voltage of PEMFCs fluctuates with sudden change in the speed of the vehicle, and the deviation range is wide, like 80–140 V, so the fuel cell is unable to supply the inverter directly. That is why the UDC is necessary for fuel cell vehicles. In addition, the transformer in the UDC also provides galvanic isolation.

The output of UDC is connected to DC bus, which is followed by an inverter with output of 220 VAC/50 Hz [13, 14]. The efficiency of the single-phase conventional H-bridge inverter is 95% [15]. The input DC voltage for an output voltage of a 220-VAC inverter is typically 120 V. Hence, V_{UDC} is set to 120 V.

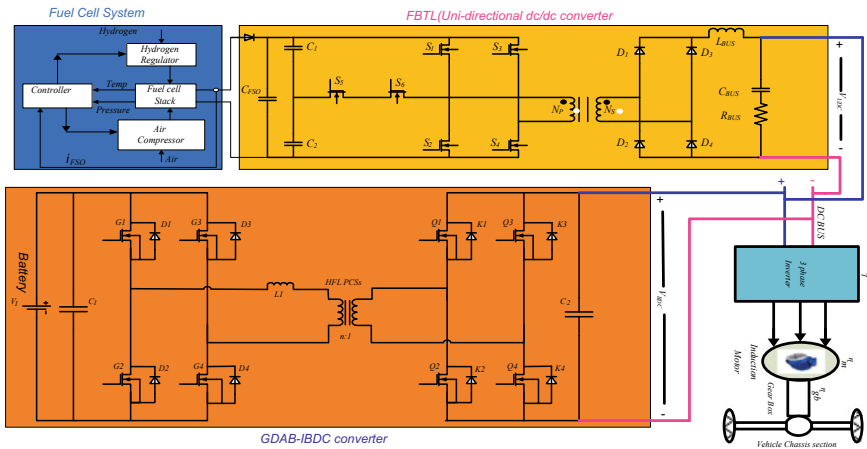


Fig. 2 Architecture of the proton exchange membrane fuel cell hybrid electric vehicle

The whole system rating is 1 kW, thus I_{UDC} can be calculated as

$$I_{UDC} = \frac{P_{Out}}{\eta_{Inv} \cdot V_{UDC}} = \frac{1000}{0.95 \times 120} = 8.77 \text{ Amps} \quad (1)$$

Here, I_{UDC} selected as 9 A.

2.3 Bidirectional DC–DC Converter

The BDC interfaces the DC bus and the energy storage system (ESS), and it can transmit the energy in both directions. The transformer in the isolated BDC assumes an imperative part in galvanic isolation and coordinating the voltages of both sides [16]. In the buck mode, output voltage of BDC is the ESS voltage V_{Bat} , and current is inductor current i_L . The voltage rating of the ESSs is 60 V, so $V_{Buck-BDC}$ is set at 60 V [17]. The battery instruction manual describes that charge current of ESSs should be under 0.1 C_{Bat} . C_{Bat} is capacity of the battery and is taken as 30 Ah, which will be justified later. In this way, $I_{Buck-BDC}$ can be computed as

$$I_{Buck - BDC} = 0.1 \cdot C_{Bat} = 0.1 \times 30 = 3 \text{ A} \quad (2)$$

In boost mode condition, output voltage of BDC is V_{Bus} , and output current is also inductor current, which is the reverse direction of buck mode. Hence, $V_{Boost-BDC}$ should be lower than $V_{UDC} = 120 \text{ V}$, so as to guarantee that an inverter can output 220 VAC and with conduction voltage drop and parasitic components accounted for, $V_{Boost-BDC}$ must be larger than 105 V. In this way, we pick $V_{Boost-BDC}$ as 110 V [18–22].

To ensure that the system starts under full speed, the battery needs to power 1 kW, so $I_{Boost-BDC}$ can be calculated as

$$I_{Boost - BDC} = \frac{P_{Out}}{\eta_{Inv} \cdot \eta_{BDC} \cdot V_{min - Bat}} = \frac{1000}{0.95 \times 0.95 \times 54} = 20.14 \text{ A} \quad (3)$$

Here, $I_{Boost-BDC}$ comes out as 21 A.

2.4 Energy Storage System (ESS)

The selection of C_{Bat} has been done on the basis of power requirement during the vehicle starting period. The startup duration of PEMFC is in order of several seconds [23]. As indicated by the battery handbook, the battery maximum discharge current of tens of seconds should be constrained to (0.5–0.7) C_{Bat} to maintain a strategic distance from storage unit damage due to deep discharge [24]. At this point, 0.7 C_{Bat}

is selected as the lowest value of capacity after discharge. The base voltage of each single battery cell is 10.8 V, so base voltage of a five-battery package is $V_{\min\text{-Bat}} = 05 \times 10.8 \text{ V} = 54 \text{ V}$. Therefore, we set $V_{\min\text{-Bat}}$ at 54 V [25]. Let efficiencies of the BDC and inverter be $\eta_{\text{BDC}} = 0.95$ and $\eta_{\text{Inv}} = 0.95$, respectively, and C_{Bat} can be calculated as

$$C_{\text{Bat}} = \frac{P_{\text{Out}}}{0.7 \cdot \eta_{\text{Inv}} \cdot \eta_{\text{BDC}} \cdot V_{\min\text{-Bat}}} = \frac{1000}{0.7 \times 0.95 \times 0.95 \times 54} = 28.78 \text{ Ah} \quad (4)$$

A 30-Ah ESSs is selected.

3 Simulation Results and Discussion

Simulation of the whole system has been carried out in PSCAD (4.6.0) under four different case studies. The input voltage of unidirectional DC–DC converter is varied from 80–140 V, the bus voltage is 120 V and is fed to the single-phase H-bridge inverter followed by the AC machine and chassis section of vehicle. The four cases considered for the system are cold start, normal operation, acceleration, and deceleration. The simulation results for the four stages of the whole system are as follows.

3.1 Case Study 1 (Cold Start Mode)

The voltage and current waveforms of the fuel cell vehicle have been shown in Fig. 3 for the cold start case study. The waveforms of the unidirectional directional converter current (I_{UDC}) and bidirectional converter current (I_{BDC}) and bus bar voltage (V_{BUS}) of fuel cell vehicle are shown in Fig. 3. The fuel cell vehicle has cold start problem initially. The unidirectional current will increase only later due to the cold start problem during the starting period, during which the vehicle will get supply from the battery through bidirectional converter. The DC bus voltage is the output voltage of bidirectional converter.

3.2 Case Study-2 (Normal Operating Mode)

The voltage and current waveforms of the fuel cell vehicle are shown in Fig. 4 under normal operating mode. Bidirectional current of the converter is negative because the energy storage system is being charged. The bidirectional current (3 A) is equal to the value of the rating of energy storage system. The currents of both converters are 10 A and 3 A, respectively, as shown in Fig. 4.

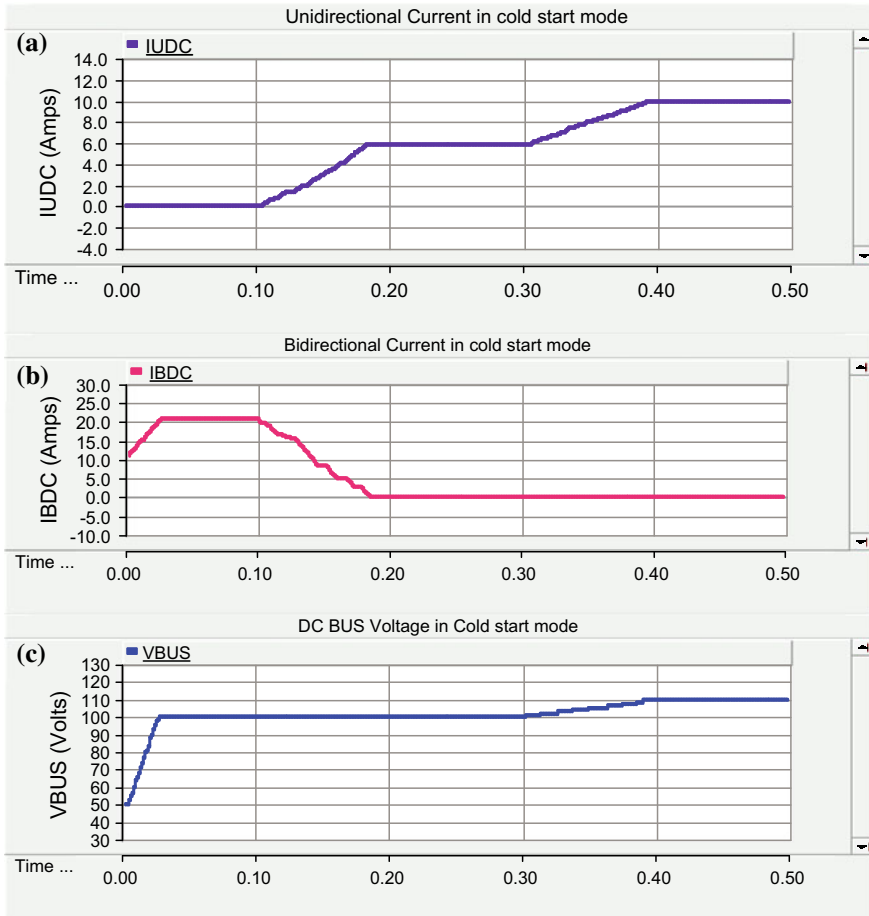


Fig. 3 System voltage and current waveforms in cold start mode, **a** unidirectional current, **b** bidirectional current, **c** DC bus voltage

3.3 Case Study 3 (Acceleration Mode)

The voltage and current waveforms of the fuel cell vehicle are shown in Fig. 5 under the acceleration mode condition. The machine has to develop more torque in the acceleration mode condition. The acceleration of the vehicle is achieved due to the support of both sources. The unidirectional and bidirectional converter currents have reached its rated values in the acceleration mode condition which is shown in Fig. 5.

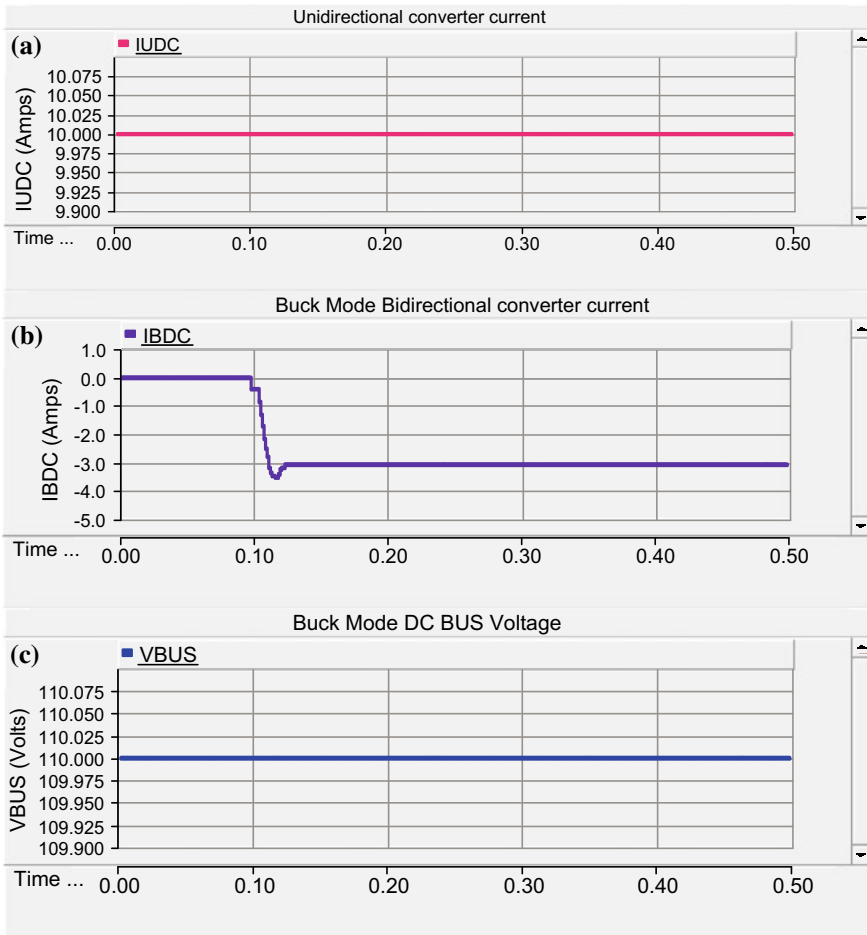


Fig. 4 System voltage and current waveforms in normal operating mode, **a** unidirectional current, **b** bidirectional current, **c** DC bus voltage

3.4 Case Study 4 (Deceleration Mode)

The storage unit is in charging position in deceleration state. The entire unidirectional current of the system would reach to zero immediately. The bidirectional current would decrease up to the rated value of energy storage system under deceleration condition. Voltage and current waveforms of the vehicle under deceleration condition are shown in Fig. 6. The system operation has been divided into four modes due to the integration with the energy storage system or else the vehicle would operate only in two modes which are cold start and steady state. Cold start problem is completely eliminated due to storage unit. The extension of this work is to include small-signal

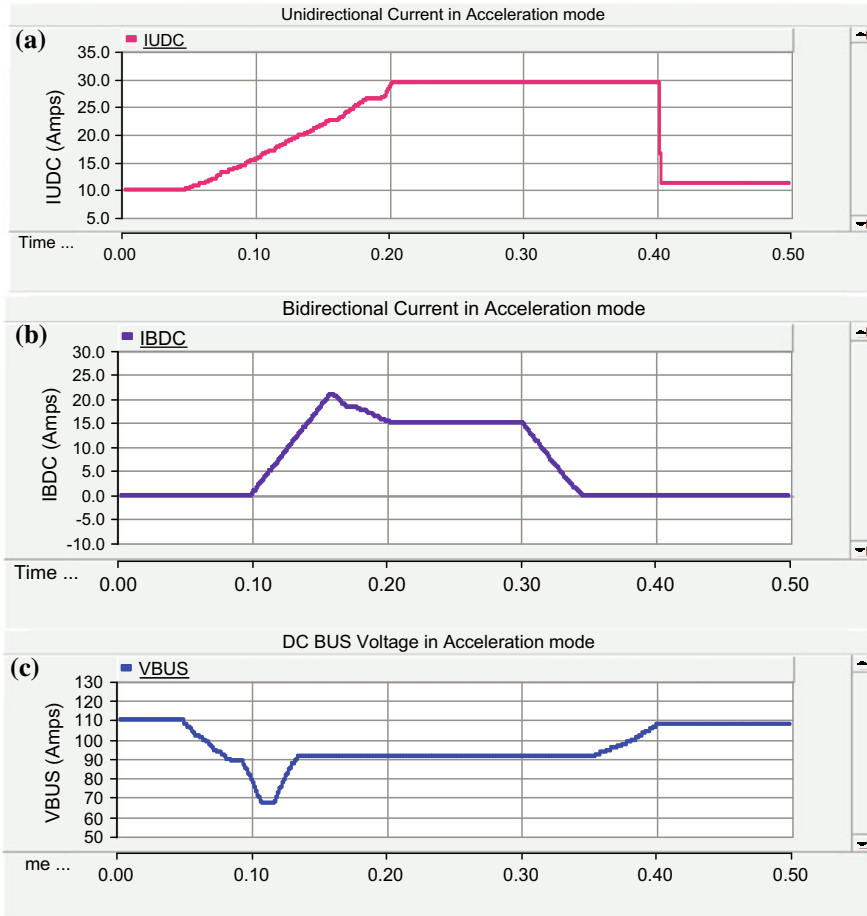


Fig. 5 System voltage and current waveforms in acceleration mode **a** unidirectional current, **b** bidirectional current, **c** DC bus voltage

analysis of both the converters and implementation of the system with advanced converters is contemplated in the near future.

4 Conclusion

A hybrid PEMFC electric vehicle has been proposed in this paper. The fuel bridge three-level (FBTLUDC) converter can work in both two-level and three-level modes, thus it is reasonable for wide input voltage range application. Since the variation of the PEMFC output voltage is in a wide range so that DC bus voltage is controlled

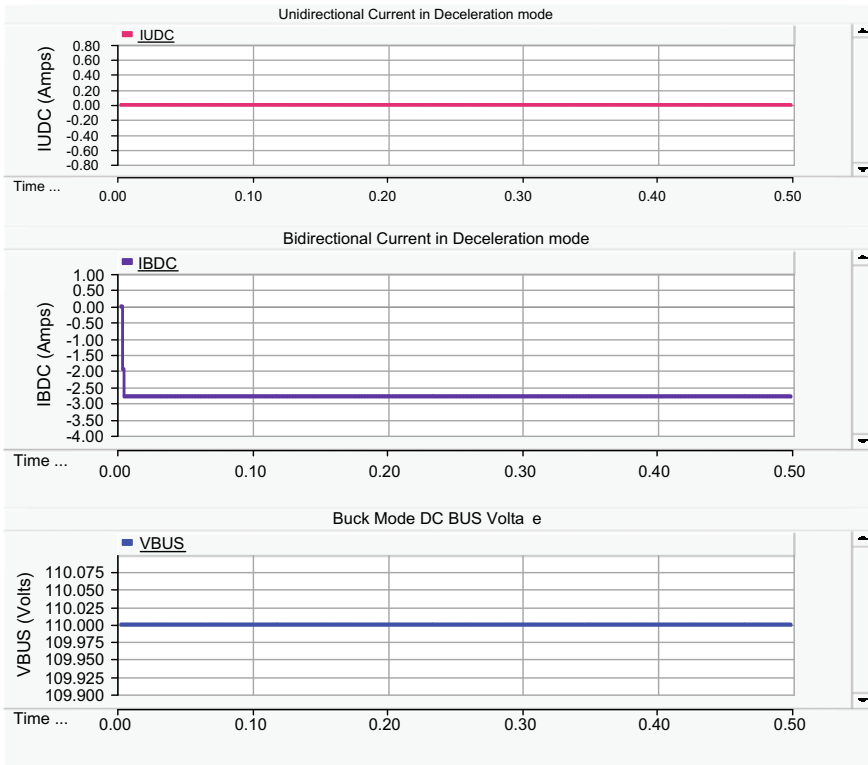


Fig. 6 System voltage and current waveforms in deceleration mode **a** unidirectional current, **b** bidirectional current, **c** DC bus voltage

appropriately. The existing literature has not mentioned about the cold start condition and integration with the ESS to enhance the performance of fuel cell vehicle. The analysis of the entire system has been carried out in the PSCAD (4.6.0). The system operation has been analyzed by using four case studies which are cold start, normal, acceleration, and deceleration mode conditions. The hybrid PEMFC vehicle is extensively used in the automobile industry and this hybrid system will be used for the standalone application for the isolated areas.

References

1. Jin K, Ruan X, Yang M, Xu M (2009) A hybrid fuel cell power system. *IEEE Trans Ind Electron* 56(4):1212–1222
2. Hegazy O, Mierlo JV, Lataire P (2012) Analysis, modeling, and implementation of a multidevice interleaved DC/DC Converter For Fuel Cell Hybrid Electric Vehicles. *IEEE Trans Power Electron* 27(11):4445–4458

3. Reddy BM, Samuel P, Narapureddy SMR (2018) Government policies help promote clean transportation in India: proton-exchange membrane fuel cells for vehicles. *IEEE Electrification Mag* 6(1):36–48
4. Schaltz E, Khaligh A, Rasmussen PO (2009) Influence of battery/ultra capacitor energy-storage sizing on battery lifetime in a fuel cell hybrid electric vehicle. *IEEE Trans Veh Technol* 58(8):3882–3891
5. Reddy BM, Samuel P (2017) Technology advancements and trends in development of proton exchange membrane fuel cell hybrid electric vehicles in india: a review. *River Publ, J Green Energy* 7(3):361–384
6. Tani M, Camara B, Dakyo B, Azzouz Y (2013) DC/DC and DC/AC converters control for hybrid electric vehicles energy management-ultra capacitors and fuel cell. *IEEE Trans Ind Inf* 9(2):686–696
7. Reddy BM, Samuel P (2016) A comparative analysis of non-isolated bi-directional dc-dc converters. In: 2016 IEEE 1st international conference on power electronics, intelligent control and energy systems (ICPEICES), Delhi, pp 1–6
8. Na W, Park T, Kim T, Kwak S (2011) Light fuel-cell hybrid electric vehicles based on predictive controllers. *IEEE Trans Veh Technol* 60(1):89–97
9. Reddy BM, Samuel P (2016) Analysis of isolated bi-directional dc-dc converters for performance enhancement of PV system and energy storage system. In: *PIICON-2016*, Government Engineering College, Bikaner
10. Khaligh A, Li Z (2010) Battery, ultra capacitor, fuel cell, and hybrid energy storage systems for electric, hybrid electric, fuel cell, and plug-in hybrid electric vehicles: state of the art. *IEEE Trans Veh Technol* 59(6):2806–2814
11. Gupta AK, Reddy BM, Deepak K, Samuel P (2017) BBBC based optimization of PI controller parameters for buck converter. In: *I-PACT 2017*, Vellore, Tamilnadu
12. Lai JS, Nelson DJ (2007) Energy management power converters in hybrid electric and fuel cell vehicles. *Proc IEEE* 95(4):766–777
13. Deepak R, Shimi SL, Reddy BM, Paulson S (2018) An overview of various DC-DC converter techniques used for fuel cell based applications. In: *PEEIC*, Greater Noida, Uttar Pradesh, India. [In Press]
14. Rathore K, Prasanna UR (2013) Analysis, design, and experimental results of novel snubberless bidirectional naturally clamped ZCS/ZVS current-fed half-bridge DC/DC converter for fuel cell vehicles. *IEEE Trans Ind Electron* 60(10):4482–4491
15. Prince KS, Reddy BM, Samuel P (2018) Application of power electronic converters in fuel cell hybrid electric vehicles: a review. In: *RTEICT*, Bangalore, Karnataka, India. [In Press]
16. Friede W, Rael S, Davat B (2004) Mathematical model and characterization of the transient behavior of a PEM fuel cell. *IEEE Trans Power Electron* 19(5):1234–1241
17. Deepak R, Shimi SL, Reddy BM, Paulson S (2018) Analysis and modeling of 2-phase interleaved dc to dc boost converter with lifting capacitor for fuel cell hybrid electric vehicle. In: *MARC 2018*, New Delhi, India. [In Press]
18. Page SC, Anbuky AH, Krumdieck SP, Brouwer J (2007) Test method and equivalent circuit modeling of a PEM fuel cell in a passive state. *IEEE Trans Energy Convers* 22(3):764–773
19. Yao Z, Xu J, Guerrero JM (2015) Control and design of full-bridge three-level converter for renewable energy sources. In: 2015 IEEE 16th workshop on control and modeling for power electronics (COMPEL), Vancouver
20. Lesster LE (2000) Fuel cell power electronics. *Fuel Cells Bull* 3(25):5–9
21. Haga H, Kurokawa F (2017) Modulation method of a full-bridge three-level LLC resonant converter for battery charger of electrical vehicles. *IEEE Trans Power Electron* 32(4):2498–2507
22. Narimani M, Moschopoulos G (2014) An investigation on the novel use of high-power three-level converter topologies to improve light-load efficiency in low power DC/DC full-bridge converters. *IEEE Trans Ind Electron* 61(10):5690–5692
23. Shi Y, Yang X (2013) Zero-voltage switching PWM three-level full-bridge DC–DC converters with wide ZVS load range. *IEEE Trans Power Electron* 28(10):4511–4524

24. Caisheng W, Nehrir MH, Shaw SR (2005) Dynamic models and model validation for PEM fuel cells using electrical circuits. *IEEE Trans Energy Convers* 20(2):442–451
25. Bandi MR, Samuel P (2018) Analysis, modeling and design of resonant dual active bridge isolated bidirectional dc/dc converter for minimizing cold start effect of fuel cell vehicle. In: 2018 5th IEEE Uttar Pradesh section international conference on electrical, electronics and computer engineering (UPCON), Gorakhpur, India, pp 1–6

Optimum Performance of Carbon Nanotube Field-Effect Transistor Based Sense Amplifier D Flip-Flop Circuits



Komal Swami and Ritu Sharma

Abstract The data storage logic circuit consumes a huge amount of power in any semiconductor memory design. Continuous scaling introduces unreliable memory read/write operations, so alternate solutions need to be explored. Carbon nanotube field-effect transistors have the ability to work on ultralow power applications. Power and delay minimization are the current trending issues beyond CMOS digital logic design. This paper presents a detailed analysis of various reported Sense amplifier D flip-flop (SAFF) designs in order to select the one which is most suitable for high-performance applications. The D flip-flop circuits have been simulated using 32 nm CMOS technology and compared with 32 nm CNFET based D flip-flops output results. Semi-dynamic flip-flop has speed benefit and low power sense amplifier flip-flop (LPSAFF) has energy advantage. Also, the effect of variation in diameter and width of CNT's has been analyzed in this paper to select the best topology for ultralow power applications.

Keywords Sense Amplifier Flip-Flop (SAFF) · Semi-dynamic Flip-Flop (SDFF) · SPICE · CMOS · CNFET · PDP

1 Introduction

Clock timing is a very critical issue in designing a clock storage element (CSE) sequential logic design. There are millions of flip-flops used in a computer processor. D flip-flops play major role in computer memory subsystem [1]. D flip-flops are classified on the pulse generation method as implicit and explicit type. Implicit type D flip-flop is more power economical due to inbuilt pulse generation method than explicit type which has separate pulse generation and latch stage. Alternate MOSFET-like technologies like Carbon nanotube field-effect transistor (CNFET), double gate

K. Swami (✉) · R. Sharma
Department of Electronics and Communication, Jaipur 302017, India
e-mail: komal.swami@gmail.com

R. Sharma
e-mail: ritusharma.mnit@gmail.com

© Springer Nature Singapore Pte Ltd. 2020
A. Kalam et al. (eds.), *Intelligent Computing Techniques for Smart Energy Systems*,
Lecture Notes in Electrical Engineering 607,
https://doi.org/10.1007/978-981-15-0214-9_33

Field-effect transistor (DG-FinFET), and single-electron transistor (SET) have been applied on different combinational and sequential designs in various reported literature. Carbon nanotube field-effect transistor (CNFET) is the most promising technology to extend or complement traditional si-MOSFET technology due to following reasons: First, the operating principle and the device structure look like traditional CMOS, CNFET technology can reuse the available CMOS infrastructure and fabrication technology. The main reason is that CNFET shows best experimentally demonstrated device characteristics. The average power consumption and delay in a clock cycle can be evaluated by integrating the current drawn from the power supply over the clock period. In general, CNFET based D flip-flop topologies consume less power and also used in high-frequency applications. In addition, PCNFET and NCNFET have same mobility and current driving capability so there is no need of transistor sizing in current CNFET technology. Identification of optimized critical path in a circuit and optimum transistor widths realization are key challenges which ultimately results in reduced power–delay product (PDP) [2]. There are various issues while working beyond 45 nm technology which are short-channel effects, drain induced barrier lowering (DIBL), unreliable operations, etc. [3]. Lowering power supply (V_{DD}) and threshold voltage (V_{th}) by aggressive scaling is very crucial, it will reduce noise margin and hence the difficulty in identification of logic 0 and logic 1 [4]. This paper presents a comparative analytical study of previously reported low-power sense amplifier flip-flop structures in order to select the most suitable for low-power high-speed applications. The SPICE simulations using 32 nm CNTFET Stanford model [5] show that high-performance D flip-flop topologies are expected to find applications in ultralow voltage standard cell library and microprocessors [6]. A theoretical review of existing delay flip-flop structures has been discussed in Sect. 2. Section 3 demonstrates theoretical background of carbon nanotube field-effect transistors (CNFET). High-performance topologies have been simulated and analyzed using 32 nm CNFET technology in Sect. 4. At last, paper finished with conclusion.

2 Theoretical Analysis and Design Consideration of Existing D Flip-Flop Topologies (CNFET)

Various bistable topologies (D flip-flop) have been designed and analyzed for different memory design blocks. Sense amplifier based flip-flop (SAFF), shown in Fig. 1a, is power efficient due to reduced clock swing property. Clock network becomes more power efficient by using reduced clock to output delay (D_{clq-q}) and data to output delay (D_{d-q}). It has two stages: first pre-charges sense amplifier master latch and then pre-charge static output slave latch. This 18 transistor differential input differential output SAFF is limited by its asymmetrical output signals, generated by the holding stage. The drawback is that its sample stage introduces more dynamic power at low switching activity of input nodes [7].

The next two D flip-flop topologies, shown in Fig. 1b–c are pulse triggered D flip-flops, consist of a single latch stage which is transparent to data within a short time

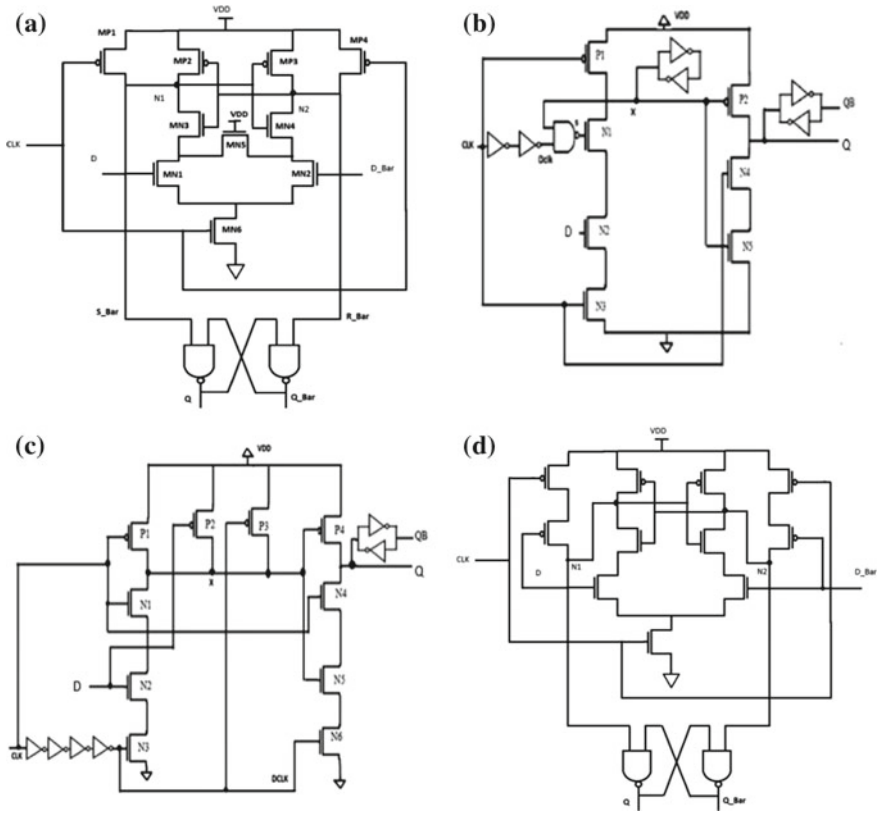


Fig. 1 a Sense amplifier flip-flop [7], b semi-dynamic flip-flop [8], c hybrid latch flip-flop [9], d low-power sense amplifier flip-flop [10]

window. A semi-dynamic flip-flop (SDFF) in Fig. 1b designed using 23 transistors which is named as SUN Ultra SPARC-III [8] is made up of dynamic input stage with static operation that is why it is known as semi-dynamic. Flip-flop enters in pre-charge phase at the falling edge of the clock. Here, Node X pre-charges, turns output Q in cut off and it keeps its previous state (Q_{n-1}) and node S remains high, holding transistor N1 in ON position. Here, DCLK is low during pre-charge phase. Flip-flop enters in evaluation phase at the rising edge of the clock (0 to 1).

Hybrid latch flip-flop (HLFF) made up of 22 transistors shown in Fig. 1c is a fully static single-input single-output positive edge triggered inverting type D flip-flop. Here, Node X is pre-charged to supply (V_{DD}) and node Q holds the previous data value before the rising edge of the clock since the transistors N1 and N4 are OFF while N3, N6, and P1 are ON. As the clock moves from 0 to 1, transistors N1 and N4 turned ON while N3 and N6 stay ON for three inverter delay. Flip-flop is transparent in this timing window and the data (D) is sampled to the latching stage. When DCLK is low, the node X is decoupled from Data (D). Either, it stays in same logic state

or begins to pre-charge to V_{DD} through transistor P3. The node X is pre-charged to hold the value X to V_{DD} at the negative edge of clock [9]. The only drawback is 1–1 glitch else Sdff is faster than HLFF. It provides shorter latency, lesser clock load, better combination of static and dynamic logic, and also removing one gate delay from the critical path.

The modified pre-charging paths of N1 and N2 depend on the state of the input, so data controlled PMOS are introduced in the pre-charging path. There is number of transistors increased by two in LPSAFF shown in Fig. 1d. But it possesses low-power dissipation due to reduced switching data rate of input and internal capacitive nodes N1 and N2 [10].

3 Carbon Nanotube Field-Effect Transistor (CNFET)

Carbon nanotubes (CNT) exhibit high mechanical, electrical and thermal conductivity with ballistic transport property makes it best alternate for high speed low power digital VLSI logic designs. Chirality factor (n, m) can be either metallic or semi-conducting in their electrical behavior. The ballistic single-wall carbon nanotubes (SWNTs) are used as interconnects on semiconducting devices due to its GHz speed operation ability. Carbon nanotube field-effect transistor (CNFET) has lower short-channel effect and leakage problem. Also, deliver strong driving current and operate at high frequency [11]. Due to these reasons, CNFET technology emerges as the leading successor of traditional CMOS technology. Both have same operating principles and similar device characteristics so it can easily reuse the established CMOS design platform and fabrication process.

3.1 Diameter of CNFET (D_{CNT})

The electrical behavior of MOSFET-like CNFET works on the barrier height modulation method with applying potential at gate. The diameter of CNFET (D_{CNT}) device is given in Eq. (1) as

$$D_{CNT} = \frac{a\sqrt{m^2 + mn + n^2}}{\pi} \quad (1)$$

Here, $a = 0.249$ nm is the distance between two carbon atoms and (m, n) is chiral vector of CNT.

The bandgap energy as depicted in Eq. (2) is inversely proportional to D_{CNT} which is written as

$$E_G = \frac{0.84}{D_{CNT}} \quad (2)$$

3.2 Threshold Voltage (V_{th})

E_G determines the threshold voltage of CNFET and it is inversely dependent on the diameter of CNT.

$$V_{th} = \frac{E_G}{2} = \frac{0.42}{D_{CNT}} \quad (3)$$

Threshold voltage affects the switching behavior of a dynamic logic system. CNFET based devices have ability to control threshold voltage by varying diameter of its CNTs. While, in CMOS, the threshold voltage is fixed for a particular technology node. This feature makes CNFET more robust than MOSFET for designing digital circuits and also, makes it very suitable candidate for designing multi-threshold VLSI circuits. The threshold voltage of a CNTFET is almost half of the bandgap as mentioned in Eq. (3).

3.3 Width of CNTFET

The distance between the centers of two adjoining SWCNTs under the same gate of a CNFET is called the pitch. Pitch directly affects the width of the gate and contacts of the CNFET device. The gate width can be determined by the pitch. By setting the minimum gate width W_{min} and the number of tubes N , the gate width can be approximated as

$$W_G = MAX(W_{min}, N \times Pitch) \quad (4)$$

Gate capacitance and drain current of a CNFET does not linearly depend on the number of carbon nanotubes (N). Here, minimum width has been taken for other transistors except the transistor exists in critical path [12, 13]. Logical effort (LE) method proposed by Alioto [14, 15] used to calculate width of the transistors lie in the critical path. Also, Set lower bound (w_{min}) and upper bound (w_{max}) of transistor widths for optimum power dissipation in conventional CMOS circuits. However, logical effort method for CNFET based designs has different optimized design constraints such as the number of CNT's, CNT pitch and diameter of tubes.

3.4 On Off Current Ratio

The ON-OFF current ratio (I_{on}/I_{off}) has a very important role in a device performance metric and decides the power consumption. Diameter plays a major role which affects ON current (I_{ON}) in a direct proportion. Here, a small ON-OFF current ratio is

preferred and 1.5 nm diameter has been taken in this work for a high-performance digital circuit design.

3.5 Transconductance (g_m)

It is defined as the change in drain to source current with respect to the change in the gate to source voltage, as depicted in Eq. (5). Transconductance is a function of the geometry of the device, carrier mobility, and threshold voltage. Parasitics will increase with rise in transconductance (g_m) of device.

$$g_m = \frac{\partial I_{ds}}{\partial V_{gs}} \quad (5)$$

4 Simulated Results of Various High-Performance D Flip-Flop Designs

Single edge trigger flip-flops are implemented in HSPICE with the supply voltage of 0.9 V and 25 °C operating temperature with 50% switching activity of data and clock inputs. Simulation results included average dynamic power, propagation delay, and the product of power and delay (PDP). Simulation constraints considered in this work for CNFET based D flip-flop designs are mentioned in Table 1.

Reported high-performance flip-flop topologies [16–22] given in Fig. 1a–d are examined and compared for better power–delay product (PDP).

Sense amplifier flip-flop and low-power sense amplifier flip-flop output waveform are shown in Fig. 2. Delay and power are calculated from these waveforms and summarized in Table 2.

In this paper, different D flip-flop structures are simulated and a hybrid method for optimum power and delay performance is demonstrated. Sizing of critical path transistors has been iteratively calculated to achieve optimum PDP. After that, these circuits are simulated using 32 nm CMOS technology. As seen from Table 2, NAND

Table 1 Design parameters considered for CNFET based D flip-flop design simulation

S. no.	Parameters	Value
1	Power supply	0.9 V
2	Chirality vector	(19, 0)
3	Physical channel length	32 nm
4	Diameter of carbon nanotubes	1.5 nm
5	No. of tubes	4

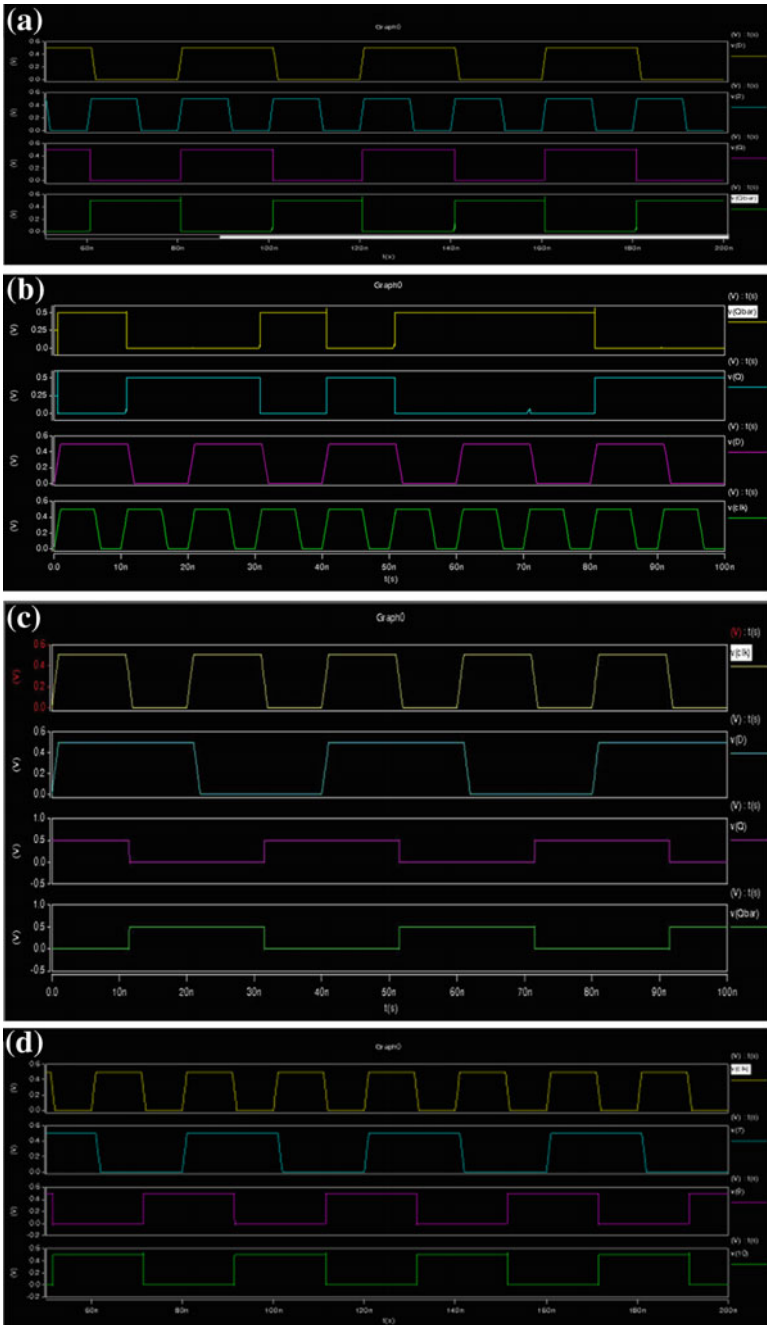


Fig. 2 Output waveform of CNFET based D flip-flops a SAFF, b SDFF, c HLFF, d LPSAFF

Table 2 Simulated results of various D flip-flop topologies using 32 nm CNFET technology

S. No.	Flip-flop	Transistor count	32 nm CNFET technology			32 nm CMOS technology		
			Delay (ns)	Power (nW)	PDP (10^{-18} J)	Delay (ns)	Power (nW)	PDP (10^{-18} J)
1	SAFF	18	1.2	5.384	6.46	4.5	12.56	5.652
2	SDFE	23	0.4	67.06	26.82	1.7	97.39	16.556
3	HLFF	22	0.7	55.03	38.52	3.4	67.66	23.004
4	LPSAFF	20	1.1	2.951	3.25	2.6	10.09	2.623

latch based flip-flop designs consume less power as compared to time window based HLFF and SDFE. In spite of more power dissipation, SDFE achieves high performance in terms of all timing constraints ($D_{clk-q} + D_{d-q}$). It is found that LPSAFF shows two times improvements in energy-delay product as compared to basic SAFF structure. This is mainly due to addition of PMOS controlled transistors in pre-charge path which reduces data activity at Node N1 and N2. In order to find alternate of CMOS technology, these structures are now simulated using 32 nm CNFET technology. Variation in diameter and pitch has been performed to find optimized value for high-performance operation. There is a huge reduction in delay ranging 57–79% by the application of CNFETs. Also, CNFET based D flip-flop designs consume less power which is almost 18–70%.

5 Conclusion

In this paper, design simulation, comparison, and analysis of different clocked storage D flip-flop structures show enhanced performance and reduced path delay. It is found that LPSAFF shows 2.951fJ energy-delay product as compared to SAFF which has double value. It is deduced from the simulations that switching activity of major internal nodes degrades the performance of D flip-flops. Also, current handling capability gets enhanced in low-power sense amplifier flip-flop by 5–14% as chirality vector of CNT's is increased. CNFET based D flip-flop designs consume less power and also used in high-frequency applications.

References

1. International Technology Roadmap for Semiconductors. <http://www.itrs.net>
2. Morifuji E, Kapur P, Chao AKA, Nishi Y (2005) New constraint for Vth optimization for sub 32 nm node CMOS gates scaling. In: IEEE international electron devices meeting, 2005. IEDM Technical Digest, Washington, DC, pp 4, pp -1029
3. McPherson JW (2006) Reliability challenges for 45 nm and beyond. In: Proceedings of the 43rd annual design automation conference. ACM/IEEE, pp 176–181

4. Rabaey J, Chandrakasan A, Nikolic B (2003) Digital integrated circuits: a design perspective. 2/e, Prentice Hall
5. Stanford University CNTFET model. <http://nano.stanford.edu/model>
6. Oskuii ST, Alvandpour A (2004) Comparative study on low-power high-performance standard-cell flip-flops. In: Proceedings of SPIE microelectronics, MEMS, and nanotechnology. International Society for Optics and Photonics, vol 5274, pp 390–398
7. Nikolic B, Stojanovic V, Oklobdzija V, Jia W, Chiu J, Leung M (1999) Sense amplifier-based flip-flop. In: IEEE international solid-state circuits conference, pp 282–283
8. Klass F (1998) Semi dynamic and dynamic flip-flops with embedded logic. In: Symposium on VLSI circuits digest of technical papers, Honolulu, HI, pp 108–109
9. Patrovi H, Byrd R, Salim U, Weber F, Di Gregorio L, Draper D (1996) Flow-through latch and edge-triggered flip-flop hybrid elements. In: IEEE ISSCC digest of technical papers, pp 138–139
10. Darwish T, Bayoumi M (2002) Reducing the switching activity of modified sense amplifier flip-flop for low power applications. The 14th international conference on microelectronics. ICM-IEEE, pp 96–99
11. Hart AJ (2012) Principles and methods for integration of carbon nanotubes in miniaturized systems. *Microelectron Nanoelectron: Mater Devices Manuf* 179, 2012
12. Ali M, Ashraf R, Chrzanowska-Jeske M (2012) Logical effort of CNFET-based circuits in the presence of metallic tubes. In: Proceedings of IEEE-nano, pp 1–6
13. Da Cheng FW, Gao F, Gupta SK (2014) A heuristic logical effort approach for gate sizing for CNTFET-based circuits
14. Alioto M, Consoli E, Palumbo G (2011) Analysis and comparison in the energy-delay-area domain of nanometer CMOS flip-flops: Part I—methodology and design strategies. *IEEE Trans Very Large Scale Integr (VLSI) Syst* 19(5)
15. Alioto M, Consoli E, Palumbo G (2011) Analysis and comparison in the energy-delay-area domain of nanometer CMOS flip-flops: Part II—results and figures of merit. *IEEE Trans Very Large Scale Integr (VLSI) Syst* 19(5)
16. Kavali K, Rajendar S, Naresh R (2015) Design of low power adaptive pulse triggered flip-flop using modified clock gating scheme at 90 nm technology. *Procedia Mater Sci* 10:323–330
17. Lin J-F (2014) Low-power pulse-triggered flip-flop design based on a signal feed-through. *IEEE Trans Very Large Scale Integr (VLSI) Syst* 22(1):181–185
18. Cao TV, Wisland DT, Moradi F, Lande TS (2009) Novel low voltage current-mirror sense amplifier based flip-flop with reduced delay time. In: 2009 IEEE international symposium on circuits and systems, Taipei, pp 3166–3169
19. Sharma M, Noor A, Tiwari SC, Singh K (2009) An area and power efficient design of single edge triggered D-flip flop. In: 2009 International conference on advances in recent technologies in communication and computing, Kottayam, Kerala, pp 478–481
20. DeCaro D, Napoli E, Petra N, Strollo AGM (2005) A high-speed sense-amplifier based flip-flop. In: Proceedings of the 2005 European conference on circuit theory and design, vol 2, Cork, Ireland
21. Moradi F et al (2010) Data-dependant sense-amplifier flip-flop for low power applications. In: Proceedings of 32th IEEE custom integrated circuits conference (CICC), Sept 2010, San Jose, pp 1–4
22. Kumar H, Kumar A, Islam A (2015) Comparative analysis of D flip-flops in terms of delay and its variability. In: 2015 4th International conference on reliability, infocom technologies and optimization (ICRITO) (Trends and Future Directions), Noida, pp 1–6

Flower Pollination Based Solar PV Parameter Extraction for Double Diode Model



J. Prasanth Ram, Dhanup S. Pillai, N. Rajasekar and V. Kumar Chinnaiyan

Abstract Due to the environmental threat toward pollution and continuous depletion in fossil fuels, the world has found its alternate source of energy generation through pollution-free solar energy. Due to the scope in solar PV systems, the research interest has considerably increased. In solar PV research thrusts, the accurate modeling of solar I-V characteristics is given prior importance. In this article, the authors have proposed a new FPA-based solar PV parameter extraction. To appreciate the accuracy in the computation, two diode models are preferred. The authors have used RTC France data to experiment with the effectiveness of FPA. Further, the computed root mean square error and relative error for the designed model is compared with the existing Simulated Annealing (SA), Pattern Search (PS), Harmony Search (HS), and Artificial Bee Swarm Optimization (ABSO) techniques.

Keywords Photovoltaic · Flower pollination algorithm · Harmony search · Pattern search · Artificial bee swarm optimization

J. Prasanth Ram

Department of Electrical and Electronics Engineering, New Horizon College of Engineering (NHCE), Bengaluru 560103, India

e-mail: jkprasanthram@gmail.com

V. Kumar Chinnaiyan

Department of Electrical and Electronics Engineering, KPR Institute of Engineering and Technology (KPRIEnT), Arasur, Coimbatore 641407, India

e-mail: Kumarchinn@hotmail.com

D. S. Pillai · N. Rajasekar (✉)

Solar Energy Reseach Cell (SERC), School of Electrical Engineering (SELECT), Vellore Institute of Technology, Vellore, India

e-mail: natarajanrajasekar@gmail.com

D. S. Pillai

e-mail: ghanup.research@gmail.com

© Springer Nature Singapore Pte Ltd. 2020

A. Kalam et al. (eds.), *Intelligent Computing Techniques for Smart Energy Systems*,

Lecture Notes in Electrical Engineering 607,

https://doi.org/10.1007/978-981-15-0214-9_34

1 Introduction

In the world arena, renewable energy resources have attracted considerable attention to meet the increasing energy demand. Since the availability of fossil fuels is decaying day by day, the demand for alternative source of energy generation is quite higher. Under such circumstances, solar energy has proved to be one of the finest renewable energy resource alternatives with enough potential to meet the power crisis.

With plenty of research being envisaged in solar PV systems, the key research area that has to be paid considerable attention is PV cell modeling. The performance of a PV system is validated via simulation before proceeding to installation. Further, the truthfulness of the solar PV modeling depends on its I-V characteristics [1]. Proper care should be taken to ensure the capability of the PV model in tracing the I-V characteristics as closer to the manufacturer's data sheet. Moreover, the selection of PV parameters plays a crucial role in determining accurate I-V characteristics. In common, the most popular PV modeling is single diode modeling [2] or double diode modeling [3].

In general, solar PV parameter extraction is characterized by two ways, analytical [4] and numerical extraction [5, 6]. The analytical method relies on the data sheet values to reproduce the I-V curve using maximum power (P_{\max}), open-circuit voltage (V_{oc}), and short-circuit current (I_{sc}) values. However, it is not accurate. Since the computation is done based on the selection of maximum power point from the nonlinear I-V curve, it may vary according to the atmospheric conditions. On the other hand, the numerical extraction technique uses all the points in the I-V curve to predict accurate modeling as it utilizes all the points in the nonlinear I-V curve [5]. Moreover, the extraction technique yields better results with reasonable accuracy irrespective of atmospheric conditions. Yet, the involvement of too many parameters adds more computational burden and leads it to high complexity. The usage of more parameters complicates the extraction procedure and needs highly efficient computational methods.

Recently it has been proved that Evolutionary algorithms yield very good results in solving optimization problems. Since the inability to solving nonlinear problems is quite high, from the literature, it can be noticed that these methods have been used for solar PV parameter extraction problem. Till date, the various Evolutionary and Meta-heuristic algorithms applied are Genetic Algorithm (GA) [4–7], Simulated Annealing (SA) [8], Bacterial Foraging Algorithm (BFA) [9], Particle Swarm Optimization (PSO) [10], Bird Mating (BM) [11], Differential Evaluation (DE), and Artificial Immune System (AIS) [12]. It is important to mention that all the algorithms proposed earlier for PV parameter extraction problem are found to have the following problems in common. (1) It takes more computational time. (2) They lose their diversity once the global optimal is reached. (3) In the initial values of optimization, if any of the value reaches global maximum, all the other particles try moving in the direction of global optimum [13]. Hence, the loss of diversity occurs and as a result of convergence, the accuracy is affected. Therefore, a wide search may improve the optimization but, the computation time may considerably increase.

After all the innovations and optimistic implementations, the ability in the extraction of parameters under variable atmospheric conditions is severely questioned.

In the paper, a new nature-inspired algorithm called FPA (Flower Pollination Algorithm) is proposed as an alternative solution for solar PV parameter extraction [14]. This algorithm was first proposed by Xie Yang in 2012 for nonlinear optimization problem. FPA yields good results in comparison to the existing EA techniques and it also offers several following advantages over conventional methods. (1) Avoids premature convergence, (2) Is highly feasible in tracking, (3) Has superior computational speed, and (4) faster convergence.

Hence, the algorithm is designed such that it has the following objectives: (1) ability to track accurate I-V characteristics under all atmospheric conditions, (2) high computational speed, and (3) appreciable convergence characteristics. In this paper, method FPA is applied for double diode modeling and the results are discussed briefly in comparison to other conventional techniques like SA [1], PS [15], HS [16], and ABSO [17]. The remaining part of the paper is organized as follows.

Section 2 describes the modeling of solar PV. In Sect. 3, the objective function formulation is given in detail. Section 4 describes the nature-inspired flower pollination algorithm and its characteristics. In the last section, the results are displayed and compared with other published works.

2 Modeling of Solar PV

First, the representation of the double diode model is shown in Fig. 1. The depicted figure clearly shows that it has PV array current (I_{pvn}), diode currents (I_{d1} , I_{d2}), series resistance (R_s), and parallel resistance (R_p) to measure the losses.

The solar PV output current by applying KCL is given by

$$I = I_{pv} - I_{D1} - I_{D2} - \frac{V + IR_s}{R_p} \tag{1}$$

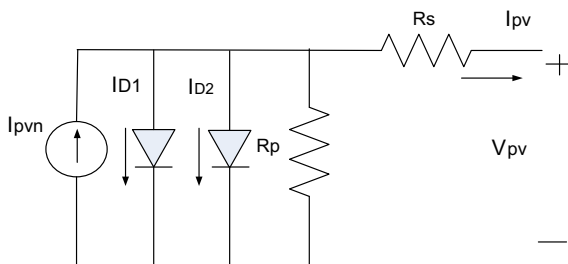


Fig. 1 Double diode model of solar PV

The ideal diode current equation is shown below, in which I_0 is the reverse saturation current.

The output equation for the double diode model is given as

$$I(or)f(V_t, I_t, x) = N_{pp} \left\{ \begin{array}{l} I_{PV} - I_{O1} \left[\exp\left(\frac{V+IR_S}{a_1 V_t N_{ss}}\right) - 1 \right] - \\ I_{O2} \left[\exp\left(\frac{V+IR_S}{a_2 V_t N_{ss}}\right) - 1 \right] \end{array} \right\} - \left(\frac{V + IR_S}{R_P} \right) \quad (2)$$

where N_{pp} and N_{PP} are the number of cells connected in series and parallel. The modeling equation results that double diode model requires seven parameters (I_{o1} , I_{O2} , I_{pv} , R_s , R_p , a_1 and a_2) to model a double diode system.

3 Problem Formulation

To model solar PV characteristics using a double diode model, it involves seven parameters, considering the fact that, these parameters have to be adjusted according to the varying atmospheric conditions. However, to avoid too much of computational burden, I_0 and I_{pv} values are calculated analytically.

The PV current can be calculated from Eqn. (8)

$$I_{PV} = (I_{scn} + K_i \Delta T) \frac{G}{G_n} \quad (3)$$

where I_{scn} is the nominal short circuit current, K_i is the temperature current coefficient, G_n is the nominal irradiance at STC (1000 W/m^2), and $\Delta T = T - T_n$, where T_n is the nominal temperature at STC ($25 \text{ }^\circ\text{C}$). Generally, the nominal values like I_{scn} , V_{ocn} , K_i , K_v and P_{max} will be given in the manufacturer's data sheet.

To come up with accurate modeling of solar PV, V_{OC} and V_{mp} are computed using (10) and (12) to determine nonlinear characteristics of the solar cell.

$$V_{OC} = V_{OCn} + V_t \ln\left(\frac{G}{G_n}\right) + K_v \Delta T + \alpha \log\left(\frac{G}{G_n}\right) \quad (4)$$

$$V_{mp} = V_{mpn} + V_t \ln\left(\frac{G}{G_n}\right) + K_v \Delta T + \beta V_t \log\left(\frac{G}{G_n}\right) \quad (5)$$

In the above equations, α and β vary according to the temperature and irradiation conditions to trace the exact PV curve.

The maximum current at maximum power is given as

$$I_{mp} = I_{mpn} \ln\left(\frac{G}{G_n}\right) \{1 + K_v \Delta T\} \tag{6}$$

The main objective function that has to be optimized is given as follows and the condition where the equation is at maximum power point is given in Eq. (7)

$$J = \left. \frac{dI}{dV} \right|_{(V_{mp}, I_{mp})} + \frac{I_{mp}}{V_{mp}} \tag{7}$$

The derivative of current with respect to the voltage at maximum power is applied for double diode model and it is given as

$$\left. \frac{dI}{dV} \right|_{(V_{mp}, I_{mp})} = \frac{I_{o1} \Gamma \exp[\Gamma_1 (V_{mp} + I_{mp} R_s)] - I_{o2} \Gamma_2 \exp[\Gamma_2 (V_{mp} + I_{mp} R_s)] - G_p}{1 + I_{o1} \Gamma_1 R_s \exp\{\Gamma_1 (V_{mp} + I_{mp} R_s)\} + I_{o2} \Gamma_2 R_s \exp\{\Gamma_2 (V_{mp} + I_{mp} R_s)\} - G_p R_s} \tag{8}$$

where $G_p = \frac{1}{R_p}$, $\Gamma_1 = 1/a_1 V_T$, and $\Gamma_2 = 1/a_2 V_T$

The fitness values are evaluated for every iteration and the best values are updated.

4 Flower Pollination Algorithm

The Flower pollination algorithm is a nature-inspired algorithm proposed by Yang in the year of 2012 [14]. The algorithm is characterized to have two types of processes, namely biotic and abiotic process. These processes will emerge out with new species in flowers. During pollination, the pollinators act as responsible agents to produce fresh species. Among the total pollination, 90% is biotic, where it uses bees, birds, and bats as pollinators and the remaining 10% of the pollination is abiotic where winds act as a pollinator.

In general, there are two types of pollination. They are self-pollination and cross-pollination. Self-pollination is generally done with different species of the same plant and cross-pollination is usually done with different species of different plants. Among the two, cross-pollination is associated with levy flight which is responsible to take pollens from one place to the other. The pseudocode for solar PV parameter extraction using this FPA is given below.

Pseudo code for FPA based solar PV parameter extraction for double diode model.

Objective function to find best Rs, Rp, and a

Declare a population of 20 flowers/pollen gametes with initial random solutions

*Find the best solution (**Gbest**) in the initial population*

Describe a switch probability $p \in [0, 1]$

WHILE ($t < 1000$)

For $i = 1: 20$ (all 20 pollens in the population)

IF $\text{rand} < p$,

Draw a (d -dimensional) step vector L which obeys a Levy distribution

Perform Global pollination using $x_i^{t+1} = x_i^t + \gamma L(\lambda)(\text{gbest} - x_i^t)$

ELSE

Draw ε of uniform distribution in $[0, 1]$

Choose randomly j and k among the set of 20 pollens

Perform local pollination using $x_i^{t+1} = x_i^t + \varepsilon(x_k^t - x_j^t)$

END IF

Calculate new solutions

If new solutions are superior, revise them in the population

END FOR

*Find the current best solution (**Gbest**)*

END WHILE

As notified in pseudocode, the global pollination is characterized by the equation:

$$x_i^{t+1} = x_i^t + \gamma L(\lambda)(\text{gbest} - x_i^t) \quad (9)$$

where $L(\lambda)$ is the levy factor which is responsible to carry pollens to different species of flowers and it also responsible for the strength of the pollination, γ is the scaling factor which is normally used to control the step size.

$$L(\lambda) = \frac{\lambda \Gamma(\lambda) \sin(\pi \lambda / 2)}{\pi} \frac{1}{S^{1+\lambda}} (S \gg S_0 > 0) \quad (10)$$

where $\Gamma(\lambda)$ is the standard gamma function.

Similarly, the local pollination is characterized by the equation:

$$x_i^{t+1} = x_i^t + \varepsilon(x_k^t - x_j^t) \quad (11)$$

where x_k^t and x_j^t are the different pollens of the same species. The ε (epsilon) symbolically represents the local search which is of uniform distribution $\varepsilon \in [0, 1]$. The measure of probability switch controls local and global pollination and in the present study, 0.8 is found to be optimal in most of the cases.

5 Simulation Results and Discussions

In order to evaluate the performance of FPA, data of RTC France for both module and cell is used. The algorithm is coded and executed in MATLAB with a system description of 4 GB RAM and Intel i3 processor. The parameters used in the FPA parameter extraction process are (Probability switch—0.8) and the scaling factor which is usually greater than 1. To estimate the accuracy of FPA, relative error along with root mean square error (RMSE) is calculated. The formula used in the calculation of RMSE is given below.

$$RMSE = \sqrt{\frac{1}{N} \sum_{i=1}^N (f(V_t, I_t, x))^2} \tag{12}$$

To check the closeness of the PV parameters extracted involving the FPA method, the extracted parameters are compared with some of the existing results available in the literature and are tabulated in Table 1. From Table 1, it is clear that the parameters extracted are in closer range with the existing results. Further, to confirm the exact reproduction of the I-V curve, the relative error between the actual and computed values is measured. In addition, the computational time needed and the speed of convergence adds value to the potential of the FPA algorithm. It ifurther can also be inferred that the root mean square is 8.7e-4 which is very low and far better in comparison to GA, SA, CPSO, and PS. The parameter extraction of a PV module has very less relative error that helps in improving the accuracy of the I-V characteristics (Fig. 2). Figure 3 shows the degree of closeness between the actual and experimental curve. It is noticeable that FPA has higher precision in determining PV and I-V curves for the PV module.

The objective function graph for the double diode PV parameter extraction model is shown in Fig. 4. Comparing the results with other methods, a much faster convergence is produced with very less RMSE value. The RMSE value recorded here is 9.17e-7. It is clear that the convergence is occurring at the 350th iteration. Though it

Table 1 Comparison of FPA results with other algorithms for RTC France PV cell

ITEM	FPA	SA	HS	PS	ABSO
$R_s (\Omega)$	0.0357	0.034	0.03545	0.032	0.03657
$R_{sh} (\Omega)$	65.147	43.10	46.8269	81.3008	54.6219
$I_{PV} (A)$	0.7600	0.762	0.76176	0.7002	0.76078
$I_{o1} (\mu A)$	0.3602	0.476	0.12545	0.9889	0.26713
$I_{o2} (\mu A)$	0.3920	0.01	0.2547	0.0001	0.38191
a_1	1.4910	1.517	1.49439	1.6	1.46512
a_2	1.5000	2	1.49989	1.981	1.98152
$RMSE$	9.17e-4	0.016	0.00126	0.0158	9.83e-04

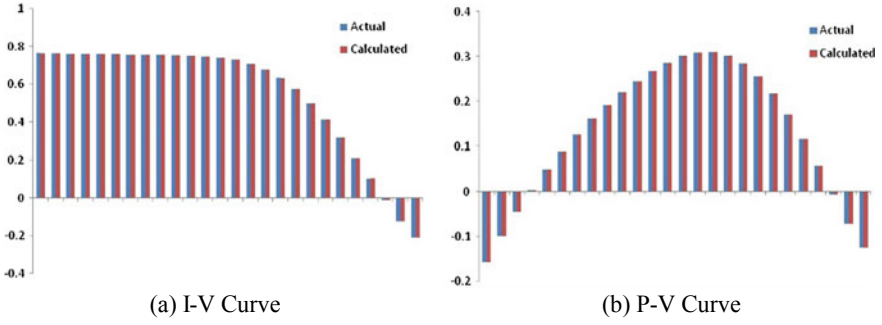


Fig. 2 Comparison of actual and calculated values of I-V and PV curves

Fig. 3 Comparison of actual and experimental I-V curve

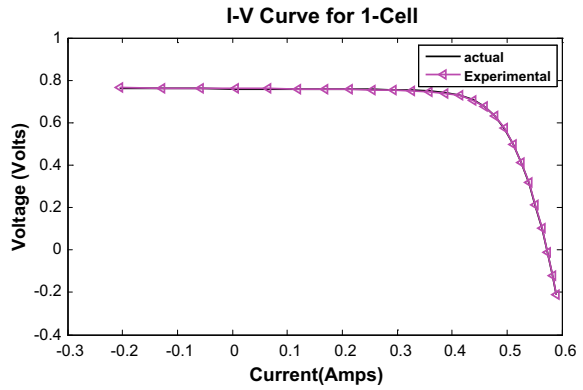
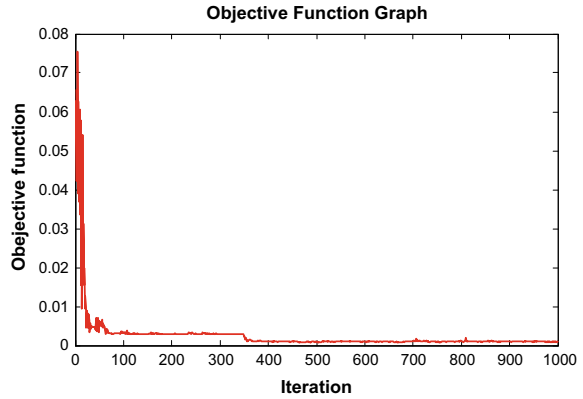


Fig. 4 Objective function graph



was at 350th iteration, a much reasonable RMSE value is recorded before, i.e., from 50th to 350th iteration. Hence, convincing and improvised performance in FPA is experimented.

Figure 2 illustrates the curve fit between the measured and calculated value for a PV cell and also, it shows that the accuracy in FPA is quite high. The degree of closeness is highly appreciable and a near accurate I-V and PV characteristics are simulated.

6 Conclusion

A new nature-inspired FPA algorithm is implemented for the double diode solar PV parameter extraction. The obtained results using FPA method is an apparent evidence for the potential use of FPA. From the obtained results, curve-fitting graph is highly significant wherein close proximity to the I-V curve is produced. These computed results using the FPA method are compared with SA, PS, ABSO, and HS. Considering the accuracy, robustness, complexity, and speed of convergence, the FPA potential is highly appreciated.

Acknowledgements The authors thank the VIT management for providing the necessary support to carry out the research work. Further, the authors sincerely acknowledge the article '<https://ieeexplore.ieee.org/document/7584047>' for being the major reference to carry out this research work.

References

1. Pillai DS, Rajasekar N (2018) Metaheuristic algorithms for PV parameter identification: a comprehensive review with an application to threshold setting for fault detection in PV systems. *Renew Sustain Energy Rev* 82:3503–3525
2. Liu CC, Chen CY, Weng CY, Wang CC, Jenq FL, Cheng PJ, Cheng PJ, Wang YH, Houg MP (2008) Physical parameters extraction from current–voltage characteristic for diodes using multiple nonlinear regression analysis. *Solid-State Electron* 52(6):839–843
3. Haouari-Merbah M, Belhamel M, Tobias I, Ruiz JM (2005) Extraction and analysis of solar cell parameters from the illuminated current–voltage curve. *Sol Energy Mater Sol Cells* 87(1–4):225–233
4. Jervase JA, Bourdoucen H, Al-Lawati A (2001) Solar cell parameter extraction using genetic algorithms. *Meas Sci Technol* 12(11):1922–1925
5. Zagrouba M, Sellami A, Bouaïcha M, Ksouri M (2010) Identification of PV solar cells and modules parameters using the genetic algorithms: application to maximum power extraction. *Sol Energy* 84:860–866
6. Balasubramanian K, Jacob B, Priya K, Sangeetha, K, Rajasekar N, Sudhakar Babu T (2015) Critical evaluation of genetic algorithm based fuel cell parameter extraction. *Energy Procedia* 75:1975–1982
7. Rajasekar N, Jacob B, Balasubramanian K, Priya K, Sangeetha K, Sudhakar Babu T (2015) Comparative study of PEM fuel cell parameter extraction using genetic algorithm. *Ain Shams Eng J* 6:1187–1194

8. El-Naggar KM, AlRashidi MR, AlHajri MF, Al-Othman AK (2012) Simulated annealing algorithm for photovoltaic parameters identification. *Sol Energy* 86:266–274
9. Rajasekar N, Kumar NK, Venugopalan R (2013) Bacterial foraging algorithm based solar PV parameter estimation. *Sol Energy* 97:255–265
10. Wei H, Cong J, Lingyun X, Deyun S Extracting solar cell model parameters based on chaos particle swarm algorithm. In: *International conference on electric information and control engineering (ICEICE)*, pp. 398–402
11. Askarzadeh A, Rezaazadeh A (2013) Extraction of maximum power point in solar cells using bird mating optimizer-based parameters identification approach. *Sol Energy* 90:123–133
12. Jacob B, Balasubramanian K, Sudhakar Babu T, Mohammed Azharuddin S, Rajasekar N (2015) Solar PV modelling and parameter extraction using artificial immune system. *Energy Procedia* 75:331–336
13. Ishaque K, Salam Z, Taheri H, Shamsudin A (2011) A critical evaluation of EA computational methods for photovoltaic cell parameter extraction based on two diode model. *Sol Energy* 85:1768–1779
14. Babu TS, Ram JP, Kumari N, Rajasekar N (2016) Solar PV parameter extraction using FPA. In: *2016 IEEE 6th international conference on power systems (ICPS)*, pp. 1–6
15. AlHajri MF, El-Naggar KM, AlRashidi MR, Al-Othman AK (2012) Optimal extraction of solar cell parameters using pattern search. *Renew Energy* 44:238–245
16. Askarzadeh A, Rezaazadeh A (2012) An innovative global harmony search algorithm for parameter identification of a PEM fuel cell model. *IEEE Trans Industr Electron* 59(9):3473–3480
17. Askarzadeh A, Rezaazadeh A (2013) Artificial bee swarm optimization algorithm for parameters identification of solar cell models. *Appl Energy* 102:943

Cost–Benefit Calculation Using AB_2X_4 ($A = Zn, Cd$; $B = Ga$; $X = Te$): A Promising Material for Solar Cells



Pancham Kumar, Amit Soni and Jagrati Sahariya

Abstract In this paper, we estimate the bandgaps, absorption coefficients, and cost of 1KW capacity of solar photovoltaic (PV) module of ternary chalcogenides materials AB_2X_4 ($A = Zn, Cd$; $B = Ga$; $X = Te$). The absorption integrated coefficient calculations using density functional theory (DFT) under Wien2k modeling (Blaha et al. in Wien2K code, an augmented plane wave plus local orbitals program for calculating crystal properties. Vienna University of Technology, Vienna, Austria, 2014 [1]) have been done for proposed materials for economic analysis of solar PV module. The present investigation reveals that present material shows good capacity to absorb incoming photons in cost-effective manner rather than crystalline Si.

Keywords DFT · Solar PV

1 Introduction

To overcome world energy demand, the requirements of leading energy resources is essential. The renewable energy resources such as solar and wind are best alternatives to do this. Out of all available resources, solar energy contains massive power to survive entire globe for millions of years as proved by NASA. We can easily harness energy from sun via solar collectors such as solar cell. In the present work, our focus is toward the development of such type of solar collectors that harness maximum power from sun in cost-effective manner compared to crystalline Si that captures around 85% of market.

P. Kumar (✉)

School of Electrical Skills, Bhartiya Skill Development University,
Jaipur 302042, Rajasthan, India
e-mail: pancham066@gmail.com

P. Kumar · A. Soni

Department of EEE, Manipal University Jaipur, Jaipur 303007, Rajasthan, India

J. Sahariya

Department of Physics, National Institute of Technology, Uttarakhand 246174, India

© Springer Nature Singapore Pte Ltd. 2020

A. Kalam et al. (eds.), *Intelligent Computing Techniques for Smart Energy Systems*,

Lecture Notes in Electrical Engineering 607,

https://doi.org/10.1007/978-981-15-0214-9_35

Regarding previous literature available, Maestro et al. [2] have proposed about optimization of various types of PV systems up to 10 kWh/day. Chandel et al. [3] studied economic viability for 2.5 MW PV plant. In Serbia region, a systematic study has been carried out by Pavlovic et al. [4] for 1 MW power generation from solar PV system. Dale et al. [5] have studied various techniques to produce electricity from solar PV, wind, and CSP. The development related to solar PV system in Rajasthan has been studied by Pandey et al. [6]. A major category of commercialized solar PV materials recycling policies have been investigated by Donald et al. [7]. Manufacturing costs evaluation for OSC (\$48.8 and \$138.9/m²) have been done by Kalowekamo et al. [8]. Muneer et al. [9] have done investigation on the future role of solar PV system in terms of electricity. The stand-alone solar PV system economics has been studied by Kolhe et al. [10]. A 100 KW rooftop solar PV system life cycle cost estimation has been done by Prasanna et al. [11]. Smested et al. [12] have pointed out the major factors that are involved in the manufacturing costs of solar PV cells.

2 Theoretical Methodology

DFT method as embodied in Wien2k is used to perform self-consistent electronic structure calculation for AB₂X₄ (A = Zn, Cd; B = Ga; X = Te) solar cell materials. All calculations are performed by using the same accuracy levels so that proper comparison of the results can be done. The cost of proposed compounds has been expressed on the basis of per-unit-area. The solar PV module cost has been investigated on the basis of cost per watt.

3 Result Discussion

The bandgap of CdGa₂Te₄ and ZnGa₂Te₄ compounds are found to be 1.78 eV and 1.61 eV, respectively. The integrated area under the absorption curve near solar visible spectrum from 1 to 5 eV is presented in Table 1. The efficiency related to AB₂X₄ (A = Zn, Cd; B = Ga; X = Te) compounds are around 20% and for crystalline Si, it is 15% [13].

Table 1 Integrated absorption coefficients (in the energy range 1–5 eV) along with efficiency

Material	IAC	η (%)
	FP-LAPW	
CdGa ₂ Te ₄	77.99	20
ZnGa ₂ Te ₄	135.81	20
Crystalline Si	–	15

3.1 Method Overview

The cost calculation of proposed AB₂X₄ (A = Zn, Cd; B = Ga; X = Te) solar PV materials has been organized in terms of per square meter area. The bottom-up overhead and labor costs of proposed materials are calculated. The PV modules cost (\$/Wp) has been calculated by dividing the manufacturing cost per square meter by the output of the same area, in this case, 1000 Wp/m² times efficiency.

3.2 PV Module Cost Calculation

The elemental composition calculation [14] of proposed AB₂X₄ (A = Zn, Cd; B = Ga; X = Te) compounds have been initiated first. The elemental composition value along with density (gm/cm³) [15] and cost (\$/100 gm) [16] of each element has been taken in Table 2.

The cost of CdGa₂Te₄ compound as per their elemental composition percentage is investigated as follows:

Since 14.75% of Cd in 8.65 gm/cm³ = (14.75*8.65)/100 = 1.275 gm/cm³

from Table 2, the cost of 100 gm/cm³ Cd is \$46

Hence 1.275 gm/cm³ Cd cost = (\$46 * 1.275)/100 = \$0.586

Similarly

Since 18.29% of Ga in 5.907 gm/cm³ = (18.29 * 5.907)/100 = 1.0 gm/cm³

As from Table 2, the cost of 100 gm/cm³ Ga is \$220

Hence 1.08 gm/cm³ Ga cost = (\$220 * 1.08)/100 = \$2.37

Similarly

Since 66.96% of Te in 6.24 gm/cm³ = (66.96 * 6.24)/100 = 4.17 gm/cm³

As from Table 2, the cost of 100 gm/cm³ Te is \$24

Hence 4.17 gm/cm³ Te cost = (\$24 * 4.17)/100 = \$1.00

Hence total cost (\$/100 gm) of CdGa₂Te₄ compound = (\$0.586 + \$2.37 + \$1.00) = \$3.94

Similarly, we calculate cost of ZnGa₂Te₄ compound = (\$0.03 + \$2.76 + \$1.06) = \$3.85

Table 2 CdGa₂Te₄ and ZnGa₂Te₄ elemental composition along with density (gm/cm³) and cost (\$/100gm)

CdGa ₂ Te ₄			ZnGa ₂ Te ₄		
Elemental composition	Density (gm/cm ³)	Cost (\$/100 gm)	Elemental composition	Density (gm/cm ³)	Cost (\$/100 gm)
Cd (14.75%)	8.65	46	Zn (9.14%)	7.14	5.30
Ga (18.29%)	5.907	220	Ga (19.50%)	5.907	220
Te (66.96%)	6.24	24	Te (71.36%)	6.24	24

The bulk semiconductor material thickness lies between 200 and 300 microns [17]. Here, we assume that CdGa₂Te₄ and ZnGa₂Te₄ thickness is around 200 microns. Semiconducting material quantity required is around 200 g/m² and according to available material quantity (200 gm), their cost is calculated and summarized in Table 3.

In the next step, we calculate solar PV module cost (\$/m²). The solar PV module cost calculation includes semiconductor material cost, electrical interconnections, glass substrate, protective cover, packaging material cost, absorbing dye, catalyst, electrolyte, and labor cost [8, 12]. Including all the cost components, we estimate the PV module cost (\$/m²) as shown in Table 4.

The per square meter area cost of solar PV module is calculated and further, that is utilized for dollar per watt and dollar per kilowatt cost calculation of PV module.

For CdGa₂Te₄ compound, \$/W_p cost is

$$\$/W_p = \frac{\$/m^2}{\eta \times 1000W_p/m^2} = \frac{129.65\$/m^2}{0.20 \times 1000W_p/m^2} = 0.648\$/W_p \quad (1)$$

Here, η indicates efficiency of the module.

Hence \$/KW_p cost of CdGa₂Te₄ compound = 1000 * 0.648\$/W_p = 648 \$/KW_p

Similarly, calculated \$/W_p and \$/KW_p cost of CdGa₂Te₄ and ZnGa₂Te₄ compounds along with crystalline PV module are indicated in Table 5. From Table 5, it is clear that Te based PV modules require less cost compared to other modules.

Table 3 Material cost of CdGa₂Te₄ and ZnGa₂Te₄ compounds

Compound	CdGa ₂ Te ₄	ZnGa ₂ Te ₄
Cost (\$/100 gm)	3.94	3.85
Cost (\$/200 gm)	7.88	7.70

Table 4 PV module Cost(\$/m²) of CdGa₂Te₄ and ZnGa₂Te₄ compounds

Cost component	CdGa ₂ Te ₄ -Cost(\$/m ²)	ZnGa ₂ Te ₄ -Cost(\$/m ²)
Semiconductor compound	7.88	7.7
Electrical contact and interconnection	6.84	6.84
Substrate	45.50	45.50
Protective cover	45.58	45.58
Encapsulant	4.35	4.35
Other(absorbing dye, catalyst, Electrolyte)	14.50	14.50
Labor	5	5
Total	129.65	129.47

Table 5 \$/Wp and \$/KWp cost of CdGa₂Te₄ and ZnGa₂Te₄ compounds

Compounds	Cost \$/Wp	Cost \$/KWp
CdGa ₂ Te ₄	0.648	648
ZnGa ₂ Te ₄	0.647	647
Crystalline Si	0.758.90 [18]	758.90 [18]

4 Conclusion

The present calculation shows that CdGa₂Te₄ and ZnGa₂Te₄ have good solar energy absorption capacity. From the cost point of view, both CdGa₂Te₄ and ZnGa₂Te₄ are comparatively less costly and more efficient than crystalline Si.

References

1. Blaha P, Schwarz K, Madsen GKH, Kvasnicka D, Luitz J (2014) Wien2 K code, an augmented plane wave plus local orbitals program for calculating crystal properties. Vienna University of Technology, Vienna, Austria
2. Maestro CJS, Dufo-Lopez R, Agustin JB (2016) Analysis of photovoltaic self-consumption systems. *Energies* 25
3. Chandel M, Agrawal GD, Mathur S, Mathur A (2014) Techno-economic analysis of solar photovoltaic power plant for garment zone of Jaipur city. *Thermal Eng* 2:1–7
4. Pavlovic T, Milosavljevic D, Radonjic I, Pantic L, Radivojevic A, Pavlovic M (2013) Possibility of electricity generation using PV solar plants in Serbia. *Renew Sustain Energy Rev* 20:201–218
5. Dale M (2013) A comparative analysis of energy costs of photovoltaic, solar thermal, and wind electricity generation technologies. *Appl Sci* 3:325–337
6. Pandey S, Singh VS, Gangwar N, Vijayvergia MM, Prakashe C, Pandey D (2012) Determinants of success for promoting solar energy in Rajasthan, India. *Renew Sustain Energy Rev* 16:3593–3598
7. McDonald NC, Pearce JM (2010) Producer responsibility and recycling solar photovoltaic modules. *Energy Policy* 38:7041–7047
8. Kalowekamo J, Baker E (2009) Estimating the manufacturing cost of purely organic solar cells. *Sol Energy* 83:1224–1231
9. Muneer T, Asif M, Munawwar S (2005) Sustainable production of solar electricity with particular reference to the Indian economy. *Renew Sustain Energy Rev* 9:444–473
10. Kolhea M, Kolhea S, Joshi JC (2002) Economic viability of stand-alone solar photovoltaic system in comparison with diesel-powered system for India. *Energy Econ* 24:155–165
11. Prasanna MG, Sameer SM, Hemavathi G, Financial analysis of solar photovoltaic power plant in India. *J Econ Financ* 09–15
12. Smestad GP (2008) The basic economics of photovoltaics. *Optical Society of America*
13. Shockley W, Queisser HJ (1961) Detailed balance limit of efficiency of pn junction solar cells. *J Appl Phys* 32:510
14. Gilbert GL (1998) Education percentage composition and empirical formula—a new view. *J Chem Educ* 75:851
15. Online source. <http://periodictable.com/Properties/A/Density.al.html>
16. Online source. https://en.wikipedia.org/wiki/Prices_of_elements_and_their_compounds
17. Online source. [https://en.wikipedia.org/wiki/Wafer_\(electronics\)](https://en.wikipedia.org/wiki/Wafer_(electronics))
18. Online source. <http://www.eai.in/ref/ae/sol/rooftop/cost>

Detection and Analysis of Power System Faults in the Presence of Wind Power Generation Using Stockwell Transform Based Median



Sheesh Ram Ola, Amit Saraswat, Sunil Kumar Goyal, S. K. Jhajharia and Om Prakash Mahela

Abstract Recently, the distributed generation (DG) has emerged as important source of energy which is capable to meet our future energy demand. These generators with large capacity are integrated into the power system network. Integration of DG sources to the utility networks changes network behavior causing different effects on the system such as power quality problem, protection issues, and stability issues. These issues need to be investigated separately. Protection of the utility network in the presence of DG sources is a challenging task which needs to be investigated. Integration of DG units to power system networks affects behavior of protection and relaying equipment due to widespread distribution of these units and variable generation from these units. Hence, to provide an accurate protection system against various types of faults in the power system network, such as line to ground (LG), double line (LL), double line to ground (LLG), and three-phase to ground fault (LLLG), effective detection, as well as discrimination of faults from each other, is essentially required. This work presents an algorithm based on the median calculated from the S-matrix obtained by decomposition of current signal using Stockwell transform to detect faults in power system network incorporated with wind generator. The proposed algorithm is based on detection of the faults using the threshold values. The proposed study is performed in MATLAB/Simulink environment using IEEE-34 node test system incorporated with wind generator.

S. R. Ola · A. Saraswat · S. K. Goyal
Manipal University Jaipur, Jaipur 303007, Rajasthan, India
e-mail: sheeshola@gmail.com

A. Saraswat
e-mail: amit.saraswat@jaipur.manipal.edu

S. K. Goyal
e-mail: sunilkumar.goyal@jaipur.manipal.edu

S. K. Jhajharia
Bhartiya Skill Development University, Jaipur, Rajasthan, India
e-mail: sharavan.jhajharia@ruj-bsdu.in

O. P. Mahela (✉)
Indian Institute of Technology Jodhpur, Jodhpur, India
e-mail: opmahela@gmail.com

© Springer Nature Singapore Pte Ltd. 2020
A. Kalam et al. (eds.), *Intelligent Computing Techniques for Smart Energy Systems*,
Lecture Notes in Electrical Engineering 607,
https://doi.org/10.1007/978-981-15-0214-9_36

Keywords Fault index · Power system · Power system fault protection · Stockwell transform

1 Introduction

The faults which occur on transmission and distribution lines largely affect the performance of a power system network. This may result in interruption of power flow in the network and sometimes these may lead to blackouts. To avoid these events, faster maintenance and restoration of supply is required. This can be achieved by faster detection and accurate estimation of location of faults. The quick restoration of supply will result in improved economy and reliable power supply. The common cause of faults in the power system network includes external disturbances, wear in components, and sudden signal changes [1]. Location of faults on the overhead power lines is a subject of great interest which is being studied intensively over the years. Diagnosis of faults in power system network is mainly focussed on detection of time of failures, identification, and location of fault. Different signal processing techniques like wavelet transform (WT), neural networks, fuzzy logic, etc., are widely utilized for detection as well as classification of faults on the power system network [2]. In the reference of fault analysis in electrical power system network, a detailed survey to review the intelligent methods used for diagnosis of fault power system network has been reported in [3]. An algorithm for location of faults on multiterminal transmission lines based on unsynchronized measurements is proposed by authors in [4]. In [5], authors proposed a method using wavelet transform, artificial neural Networks, and global positioning system clock which is capable to detect, classify, and localize the faults on power system network.

Recently, the distributed generation (DG) is being integrated into the utility grid on large scale. These DG power plants have changed the behavior of the system affecting the performance of the network. Power system protection is greatly affected by the presence of these resources [6]. Krishnanand et al. [7] proposed an approach for pattern recognition which is capable to provide current differential protection to the power system lines. Noori and Shahrtash [8] presented an approach using adaptive cumulative sum method for the detection of transmission line faults. An accurate method which works in real-time and capable of fault detection and analysis of high-voltage transmission lines has been reported in [9]. A method for the detection of power system faults on the multiterminal extra-high voltage (EHV) ac transmission line using the wavelet transform based alienation coefficients has been reported in [10]. A technique based on geo-referenced data of power system and phasor measurement units for detection of fault on multiterminal lines is reported in [11].

This chapter presents a methodology for detection of different types of faults in the power system network using Stockwell transform based median with generation of wind power which is the extension of work reported in [12]. In [12], authors presented an approach based on Stockwell transform for detection of faults on transmission line in the absence of renewable power generation. However, the approach presented

in this article based on fault index is found to be effective for detection of faults in power system network even in the presence of renewable energy. Faults such as LL, LLG, LG, and LLLG with generation of wind power are investigated in this study.

2 Test System Used for the Proposed Study

The test system utilized for the study is standard IEEE-34 node test network and illustrated in Fig. 1. All feeders of the test system are three-phase in nature having the length equal to the original length of feeders. All the loads connected to test system are also three-phase loads in nature. The distributed loads are simulated by spot loads placed at middle of the feeders. Details of transformers, spot loads, capacitor banks, line segments, and distributed loads reported in [13] have been utilized. The fault is created at various bus locations as detailed in the simulation results section.

A wind energy conversion system (WECS) of capacity 1.5 MW using the doubly fed induction generator (DFIG) is integrated on node 848 of test system network as illustrated in Fig. 1 to perform the study related to detection of faults in the presence of wind generator. The output voltage of the generator is 575 V at 60 Hz frequency. Wind speed of 11 m/s is used in the simulation. The converter used to integrate wind generator to the utility test grid are controlled with the help of proportional–integral (PI) controller. The grid side and rotor side converters are controlled by PWM carriers using the frequencies of 2700 Hz and 1620 Hz, respectively. The simulated maximum pitch angle is 27° whereas the simulated maximum rate of change of pitch angle is 10°/s. The simulated value of pitch controller gain is 150. The gains of reactive power and voltage regulator are set to the values of 0.05 and 20, respectively.

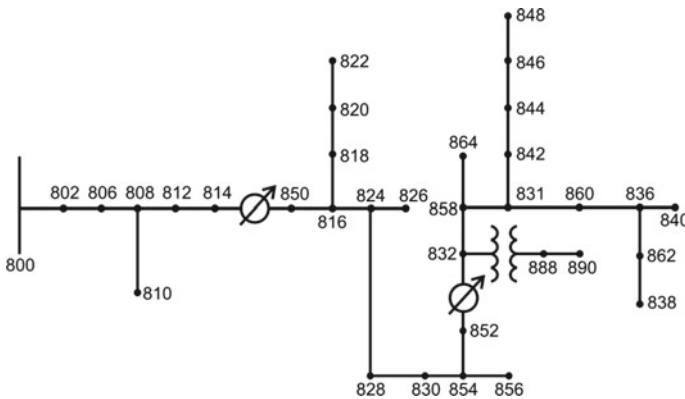


Fig. 1 Proposed IEEE-34 node test system

3 Proposed Methodology

The proposed methodology for protection of the distribution line with generation of wind power includes detection of faults using the proposed fault index. The Stockwell transform is used for detection of the faults. Calculation of the fault index and brief description of the Stockwell transform are detailed in the following subsections.

3.1 Proposed Fault Index

A fault index is proposed to discriminate the faulty phases from the healthy phases. This fault index is also used to differentiate various types of faults on EHV transmission line. Fault index is calculated using the following steps:

- (i) Current of all the phases is captured at bus 800 of the test system.
- (ii) Current signals are processed with the help of Stockwell transform using 20 kHz as sampling frequency. The output in the form of a matrix known as S-matrix is obtained.
- (iii) Median of S-matrix is obtained.
- (iv) The absolute value of median is calculated and it is designated as fault index.
- (v) The fault index obtained at step (iv) is used for detection and location of faults.

3.2 Stockwell Transform

The Stockwell transform uses the combined features of short-time Fourier transform (STFT) and wavelet transforms (WT) but it falls in a different category. This method was first proposed by the R. G. Stockwell in the year 1996. This method performs multi-resolution analysis of the signals with disturbances retaining phase of all frequencies available in signal. The width of window used in this technique varies inversely with the frequency. Hence, this is very effective to provide good resolution of time at high frequency and good resolution of frequency at low frequency. The STFT of signal $h(t)$ is defined using mathematical relation.

$$STFT(\tau, f) = \int_{-\infty}^{+\infty} h(t)g(\tau - t)e^{-j2\pi ft} dt$$

where τ and f , respectively, indicate the time of localization of the spectrum and Fourier frequency. The $g(t)$ is a window function used in the relation. The window function $g(t)$ is replaced by the Gaussian function in the above equation to derive the S-transform as shown by the relation.

$$g(t) = \frac{|f|}{\sqrt{2\pi}} e^{-\frac{t^2}{2}}$$

Hence, the Stockwell transform can be defined by the relation

$$S(\tau, f) = \int_{-\infty}^{+\infty} h(t) \frac{|f|}{\sqrt{2\pi}} e^{-\frac{t^2(\tau-t)^2}{2}} e^{-j2\pi ft} dt$$

Therefore, the S-transform may be considered a special form of short-time Fourier transforms which uses function with Gaussian window. The S-transform can provide better frequency resolution for lower frequency by using the wider window in time domain. It can provide better time resolution for higher frequency by using the narrower window. The output of S-transform is matrix known as S-matrix. The information pertaining to frequency and amplitude of signal can be derived from the S-matrix [14, 15].

4 S-Transform Based Simulation Results with Discussion

The simulation results pertaining to detection of faults on power system network with generation of wind power with the help of the proposed fault index are detailed in this section. Test network detailed in Fig. 1 is used for study with wind generator of capacity 1.5 MW connected on node 848. Various types of faults are created on node 838 of test network and current of all phases have been captured at the bus 800. All the plots are plotted corresponding to the 12 cycles. In all the cases, the fault is created at sixth cycle. The threshold value of fault is set at 10 after study of the 30 datasets of each fault. Following subsections details the simulation results.

4.1 Line to Ground Fault

The fault with the involvement of one phase and ground (LG) in the presence of wind power generation is created on the phase-A at the test location. The waveforms pertaining to current of all phases captured at bus 800 of the test system before and after the fault incident are illustrated in Fig. 2. It is found that magnitude of waveform of faulty phase increase after fault occurrence to high values. The magnitude of current in healthy phase increases slightly and distortions are also detected at instant of occurrence of fault.

Variation of fault index during the event of LG fault related to all phases with wind power generation is illustrated in Fig. 3. This is found that peak value of fault index related to faulty phase is above the threshold value and nearly equal to 5. The threshold value selected for the fault detection with generation of wind power is

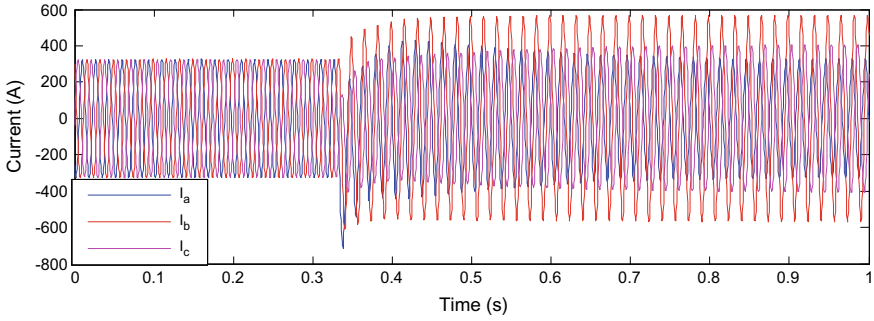


Fig. 2 Three-phase current at bus-800 during LG fault with generation of wind power

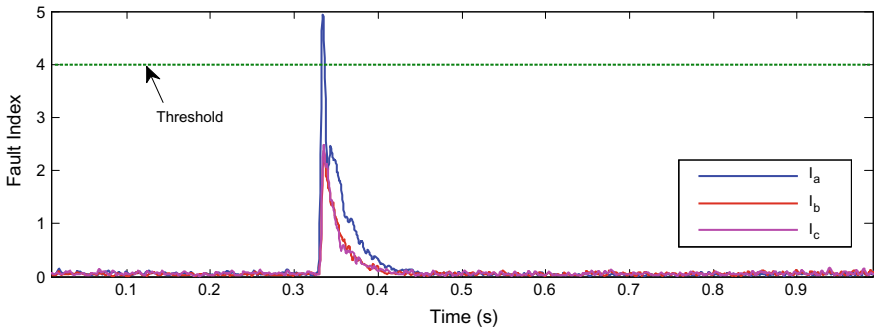


Fig. 3 Variation of fault indices for LG fault with generation of wind power

taken equal to 4. Value of fault index is below the threshold value and equal to the 2.5 for the healthy phases. Hence, faulty phase (phase-A) is clearly discriminated from the healthy phases (Phases A and B) with generation of wind power in distribution network. Increasing time of the fault indices is low compared to the decreasing time of the fault indices.

4.2 Double Line Fault

Two phases (A and B) are short-circuited to simulate the fault involving two phases without the involvement of ground (LL) in the presence of wind power generation. The current waveforms of all the three phases captured at bus 800 of the test system before and after the fault incident are illustrated in Fig. 4. This is found that magnitude of the waveform related to faulty phases first, increases to high values and then, decreases to a value lower than that in the healthy conditions. Magnitude of current in healthy phase decreases following oscillations and finally attains the original value.

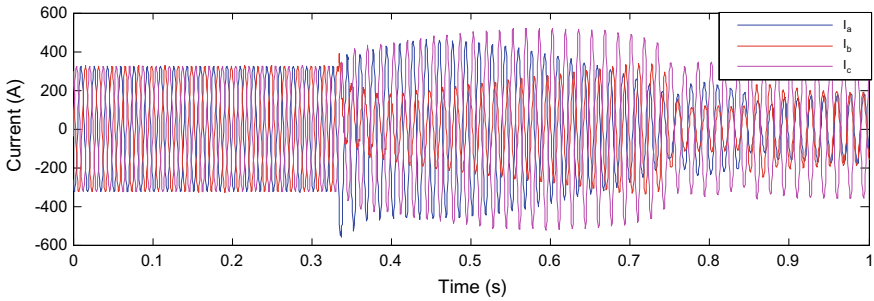


Fig. 4 Three-phase current at bus-800 during LL fault with generation of wind power

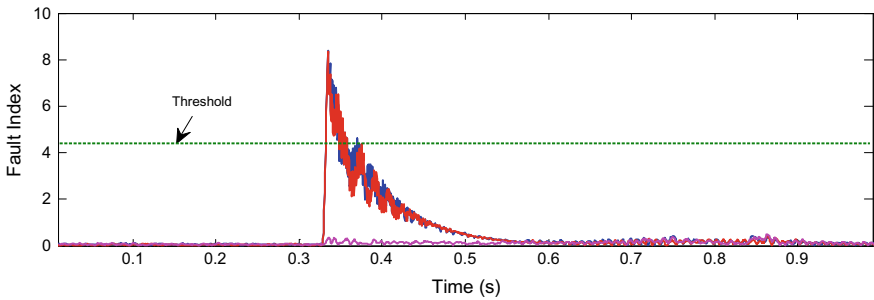


Fig. 5 Variation of fault indices for LL fault with generation of wind power

Hence, the large oscillations are observed due to the LL fault with generation of wind power in distribution network.

Variation of fault index during double line fault for all the three phases with generation of wind power is illustrated in Fig. 5. This is found that the value of fault index for the faulty phases (phases A and B) is higher than the threshold value and it is equal to 8.5. Value of fault index for healthy phase is below the threshold value and equal to zero. Hence, faulty phases (phases A and B) are clearly discriminated from the healthy phase (Phase-A) with generation of wind power. Increasing time of fault indices is again low compared to the decreasing time of the fault indices.

4.3 Double Line to Ground Fault

Two phases A and B are simultaneously grounded to simulate LLG fault in the presence of wind power generation. The waveforms of current in all phases captured at bus 800 of the test system before and after the fault incident are illustrated in Fig. 6. This is found that magnitude of waveforms of faulty phases decreases to a value lower than the original value following the oscillations and finally reduces nearly to zero.

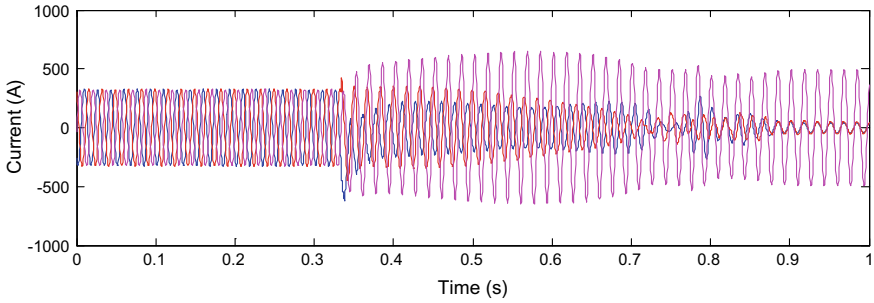


Fig. 6 Three-phase current at bus-800 during LLG fault with generation of wind power

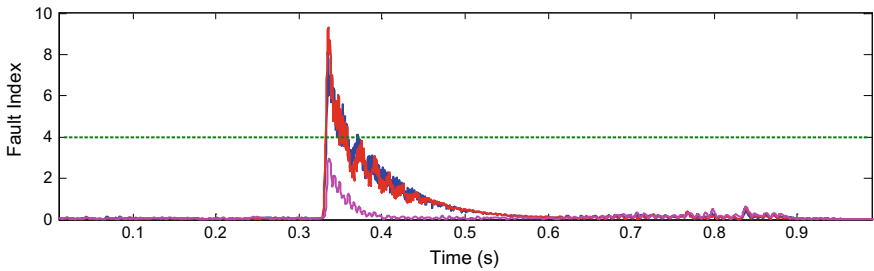


Fig. 7 Variation of fault indices for LLG fault with generation of wind power

The magnitude of current in healthy phase increases in the initial period and finally attains original value.

Variation of fault index during the event of LLG fault for all three phases in the presence of wind power generation is illustrated in Fig. 7. It is found that that value of fault index for faulty phases (phases A and B) is higher compared to the threshold value which is set at 4. Value of fault index for healthy phase is below the value of threshold value which is equal to 2.5. Hence, faulty phases (phases A and B) are clearly discriminated from the healthy phase (Phase-C) with generation of wind power. Increasing time of fault indices is again low compared to the decreasing time of the fault indices.

4.4 Three-Phase Fault Involving Ground

The three-phase to ground fault in the presence of wind power generation has been created by simultaneous grounding of all the three phases at the test location. The waveforms of current related to all phases captured at bus 800 of the test system before and after the fault incident are shown in Fig. 8. This is found that the magnitude of

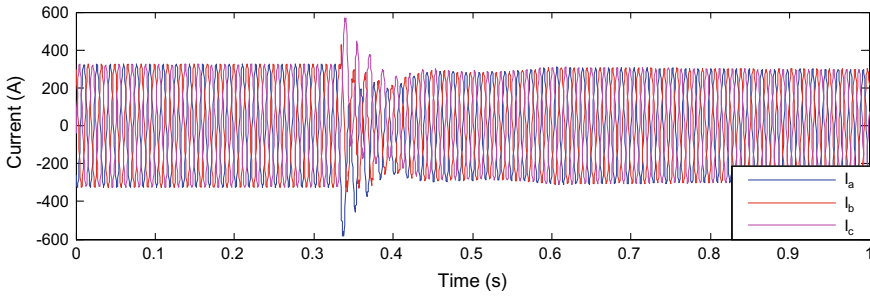


Fig. 8 Three-phase current at bus-800 during LLLG fault with generation of wind power

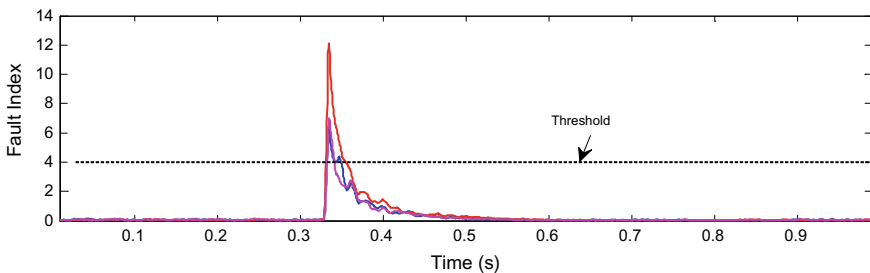


Fig. 9 Fault index variation in the event of LLLG fault with generation of wind power

current waveforms of all the three phases increases first and finally attains a value lower than the original value.

Variation of fault index for all phases during the event of LLLG fault with generation of wind power is illustrated in Fig. 9. This is found that the value of fault indices for all the three phases is higher than the threshold value. It is equal to 12 for one phase and equal to the 8 for all other phases.

4.5 Comparative Study

Maximum values of fault indices for all the phases during the various types of investigated faults have been provided in Table 1. By the examination of the fault indices of all the three phases during faulty events, the various types of faults can be distinguished from one another. Maximum values are obtained for the LLLG fault and minimum for the LG fault. For the LL and LLG fault, the fault indices are approximately same in the faulty phases whereas it is zero for healthy phase in case of LL fault and nonzero in case of LLG fault. This helps in the discrimination of LL and LLG faults from each other.

Table 1 Maximum values of fault index in the presence of RE

S. No.	Type of fault	Phase-A	Phase-B	Phase-C
1	LG	5	2.5	2.5
2	LL	8.5	8.5	0
3	LLG	9	9	2.5
4	LLLG	12	8	8

5 Conclusion

This research work is focussed on the investigation of application of proposed algorithm based on median calculated from Stockwell transform for detection of faults in power system network with generation of wind power. The proposed technique has been used for the detection of all types of faults on power system network. The simulated faults included LG, LL, LLG, and LLLG were analyzed on power system network of IEEE-34 bus test system in which wind power plant of capacity 1.5 MW has been integrated on the bus 848. The study is performed in MATLAB/Simulink environment. Various types of faults have been detected with the help of median of signals calculated from the S-matrix of the signal decomposition using Stockwell transform. The faulty phase and healthy phase are discriminated from each other using the peak values of the proposed fault index. It is concluded that various types of faults can be differentiated from each other based on peak values of fault index. The maximum values are obtained for the LLLG fault and minimum for the LG fault. For the LL and LLG fault the fault indices are approximately same in the faulty phases whereas it is zero for healthy phase in case of LL fault and nonzero in case of LLG fault. This helps in the discrimination of LL and LLG faults from each other.

References

1. Liu Y, He X, Wang Z, Zhou D-H (2015) Fault detection and diagnosis for a class of non-linear systems with decentralized event-triggered transmissions. *IFAC-Pap Line (Elsevier)* 48(21):1134–1139
2. Prasad CD, Srinivasu N (2015) Fault detection in transmission lines using instantaneous power with ED based fault index. *Procedia Technol* 21:132–138
3. Ferreira VH, Zanghi R, Fortes MZ, Sotelo GG, Silva RBM, Souza JCS, Guimarães CHC, Gomes S Jr (2016) A survey on intelligent system application to fault diagnosis in electric power system transmission lines. *Electr Power Syst Res* 136:135–153
4. Hussain S, Osman AH (2016) Fault location scheme for multi-terminal transmission lines using unsynchronized measurements. *Int J Electr Power Energy Syst* 78:277–284
5. Shaik AG, Pulipaka RRV (2015) A new wavelet based fault detection, classification and location in transmission lines. *Int J Electr Power Energy Syst* 64:35–40
6. Dehghani M, Khooban MH, Niknam T (2016) Fast fault detection and classification based on a combination of wavelet singular entropy theory and fuzzy logic in distribution lines in the presence of distributed generations. *Int J Electr Power Energy Syst* 78:455–462

7. Krishnanand KR, Dash PK, Naeem MH (2015) Electrical power and energy systems detection, classification, and location of faults in power transmission lines. *Int J Electr Power Energy Syst* 67:76–86
8. Noori MR, Shahrtash SM (2013) Combined fault detector and faulted phase selector for transmission lines based on adaptive cumulative sum method. *IEEE Trans Power Delivery* 28(3):1779–1787
9. Zarbita S, Lachouri A, Boukadoum H (2015) A new approach of fast fault detection in HV-B transmission lines based on detail spectrum energy analysis using oscillographic data. *Int J Electr Power Energy Syst* 73:568–575
10. Rathore B, Shaik AG (2018) Wavelet-alienation based protection scheme for multi-terminal transmission line. 161:8–16
11. Devi MM, Geethanjali M, Devi AR (2018) Fault localization for transmission lines with optimal phasor measurement units. 70:163–178
12. Ola SR, Sarswat A, Goyal SK, Jhaharia SK, Mahela OP (2018) A technique using Stockwell transform based median for detection of power system faults. In: 2018 IEEE 8th power india international conference (PIICON). Kurukshetra, India, 10–12 December 2018
13. Kersting WH (1991) Radial distribution test feeders. *IEEE Trans Power Syst* 6(3):975–985
14. Moravej Z, Pazoki M, Khederzadeh M (2015) New pattern-recognition method for fault analysis in transmission line with UPFC. *IEEE Trans Power Deliv* 30(3):1231–1242
15. Costa FB (2014) Fault-induced transient detection based on real-time analysis of the wavelet coefficient energy. *IEEE Trans Power Deliv* 29(1):140–153

A Directional Relaying Scheme for Microgrid Protection



Ruchita Nale, Ruchi Chandrakar, Harishankar Verma and Monalisa Biswal

Abstract Incorporation of distributed generation (DG) in the power network may affect the selectivity of the relay. The relay settings need to be modified as the magnitude of fault current supplied by DG units is very small which may offer misleading implication of fault direction. In this work, an integrated approach based directional relaying algorithm is proposed for microgrid protection. The approach uses three different detectors and based on the obtained decision from all the detectors, the final decision will be declared by the proposed algorithm. The method is tested on different fault types, fault positions, and different configuration of the microgrid. The method is also verified for high-resistance fault. For testing, Aalborg distribution network is considered and simulated using EMTDC/PSCAD. Results prove the efficacy of the proposed method.

Keywords Distributed generation · High-impedance fault · Fault location · Power mismatch · Photovoltaic source

1 Introduction

Nowadays, large development and advancement in the distribution system are only possible because of the integration of small local renewable generation in the distribution power sector. The resources are generally below a couple of megawatts and can be photovoltaics, wind farms, micro-hydro-turbines, etc. [1]. Distributed or dispersed generation (DG) can be defined as generating resources, other than conventional generating stations, which are close to the load point, usually at customer site [2]. With large penetration of DG, the cost of transmission and distribution losses can be reduced. At the same time, power quality and voltage profile of the system can be improved [3]. However, with the penetration of DG, different protection related

R. Nale (✉) · R. Chandrakar · H. Verma · M. Biswal
Department of Electrical Engineering, National Institute of Technology Raipur, Raipur, India
e-mail: ruchita0119@gmail.com

© Springer Nature Singapore Pte Ltd. 2020
A. Kalam et al. (eds.), *Intelligent Computing Techniques for Smart Energy Systems*,
Lecture Notes in Electrical Engineering 607,
https://doi.org/10.1007/978-981-15-0214-9_37

331

issues arise such as overcurrent relay coordination, directional relaying, fault detection, and classification and islanding detection [4–17]. This work focuses only on directional protection issues of microgrid integrated with hybrid DG.

Microgrid system can operate in different operating modes such as grid-connected mode and islanding mode [5]. In both the operating modes, the secured operation of the protective algorithm is most desirable. In microgrid, the incorporation of inverter-interfaced renewable DG, such as photovoltaic (PV) DGs introduces nonlinearity [6]. This is another major concern for the relaying system. The different protection issues of microgrid provide a new direction of research to many power system researchers. Several articles have been published, in which the solutions to the existing problems have been reported. But, even with extensive research, no specific protective relay has been manufactured for microgrid. Although the problems of microgrid seem similar to distribution grids, there are hidden issues associated with them. First, for different operating modes, the fault signals are radically different. Second, due to integration of different renewable sources, the level of fault current will not be the same at all times [7]. During a fault, the infeed current from DGs' end is very less due to which protective relay is unable to consider the situation as an abnormal phenomenon [8]. So, any conventional relay setting is not always suitable. From the different protection issues, directional overcurrent maloperation is a major challenge [6, 8, 9].

The directional overcurrent relay issue with microgrid is reported in [8]. In this work, minimum bandwidth is required to link the relays and thus limiting the cost of communication. Since the level of fault current is a major cause behind protective relay maloperation, the technique as reported in [8] is not affected by such conditions. Recently, an article is published, in which the authors have proposed a new solution to mitigate the directional relay issue in microgrid [6]. Positive sequence superimposed quantity and negative sequence superimposed quantity are employed for different fault cases. But during reverse power flow condition or islanding mode, the decision provided by positive sequence component-based technique is erroneous. Several other techniques for relay coordination are also reported in the literature [16, 17]. However, before relay coordination, the determination of exact fault direction is essential for the correct operation of the protective relay. The bidirectional power flow in microgrid system is the root cause behind the mis-coordination of relaying. But this part is missing in the literature and thus motivates to find a new solution to enhance the relay coordination task.

For the supervision of the distance relay, the correct operation of directional relay is essential. So, in this work, an integrated solution is presented to mitigate the directional relaying issue of microgrid system integrated with hybrid DG. The method is tested on a standard microgrid model simulated using EMTDC/PSCAD. The method is verified for different fault cases, fault locations, and different operating modes of microgrid. The method is also tested for high fault resistance case and the obtained results prove that the method is efficient in identifying the exact fault direction in a microgrid system during critical cases.

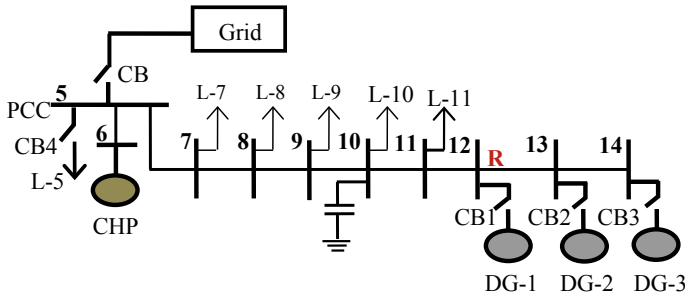


Fig. 1 Standard distribution network

2 Test Microgrid

For the study, a standard microgrid system is considered [15] and shown in Fig. 1. The system as shown in Fig. 1 is a part of a distribution network in Aalborg, Denmark. It consists of three fixed-speed wind turbine generators and one combined heat and power (CHP) plant, six loads and a capacitor bank connected at bus 10. The data for generators, lines, and transmission grid are adapted from [15]. For the study, the Aalborg distribution network is remodeled by replacing DG-3 with a PV system at bus 14. The nominal power output of PV is 630 kW. The given network is simulated in EMTDC/PSCAD software. For fault direction estimation, the performance of relay (R) connected near bus 12 is considered. Faults at both sides of the relay are created to evaluate the performance of the method.

3 Directional Relaying Algorithm

For overcurrent relay coordination, the output decision of directional relay is essential in microgrid. In the literature, different phasor-based directional relay algorithms are available. But each technique has some drawback and with a single logic, accurate fault direction estimation is challenging. In this context, an integrated approach is proposed which relies on the decision of three different detectors and finally declares a decision based on maximum votes. The detailed description of the detectors is provided below.

3.1 Detectors for the Directional Approach

The different detectors used in the directional method are discussed below.

Detector-1 (D1): Phase Angle between Positive Sequence Component of Fault Current and Fault voltage θ_I [18]: The detector $\theta_1(\angle \bar{V}_{1f} - \angle \bar{I}_{1f})$ is utilized to distinguish the direction of occurrence of fault. For forward side fault (Fx side), θ_1

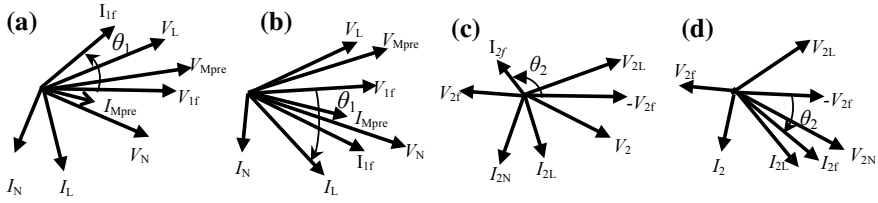


Fig. 2 Phasor diagrams for faults at different positions **a** Fault at Fx **b** Fault at Fy **c** Fault at Fx **d** Fault at Fy

becomes positive and for backward side fault, θ_1 is negative. The phasor diagram for faults on both forward and backward sides of the relay are depicted in Fig. 2a, b, respectively. The corresponding bus voltages and bus currents are denoted by \bar{V}_L , \bar{V}_N , \bar{I}_L , and \bar{I}_N , respectively. The relay pre-fault voltage and current are denoted by \bar{V}_{Mpre} and \bar{I}_{Mpre} . The post-fault positive sequence current and voltage at relay location are depicted by \bar{I}_{1f} and \bar{V}_{1f} . The decision provided by the detector is 1 if the output of θ_1 is positive indicating the occurrence of upstream fault. Whereas for downstream fault, the detector output is -1 for negative value of θ_1 .

Detector-2 (D2): Phase Angle between Negative Sequence Component of Fault Current and Fault Voltage θ_2 [19]: The proposed detector utilizes phase difference between negative sequence voltage and negative sequence current component denoted by θ_2 , where $\theta_2 = \angle \bar{I}_{2f} - \angle -\bar{V}_{2f}$ [19]. The phasor diagram for the negative sequence component is depicted in Fig. 2c, d, respectively. The post-fault bus voltages and currents are represented by \bar{V}_{2L} , \bar{V}_{2N} , \bar{I}_{2L} , and \bar{I}_{2N} , respectively. The negative sequence voltage and current at the relay location are denoted by \bar{V}_{2f} and \bar{I}_{2f} , respectively. For upstream side fault, θ_2 will be positive and so detector-2 output is 1.

Detector-3 (D3): Phase Angle between Positive Sequence Superimposed Voltage and Current: For backward side fault, the angle is negative whereas for forward side fault it is positive. The superimposed voltage and current components are computed from the following equations.

$$\Delta \bar{V}_M = \bar{V}_{1f} - \bar{V}_{Mpre} \quad (1)$$

$$\Delta \bar{I}_M = \bar{I}_{1f} - \bar{I}_{Mpre} \quad (2)$$

and

$$\theta_3 = \angle \Delta \bar{V}_M - \angle \Delta \bar{I}_M \quad (3)$$

where the pre-fault current and voltage are depicted by I_{Mpre} and V_{Mpre} , respectively. The post-fault current and voltage at relay location are represented by I_{1f} and V_{1f} , respectively. The phasor diagrams for superimposed-based detector are shown in Fig. 3.

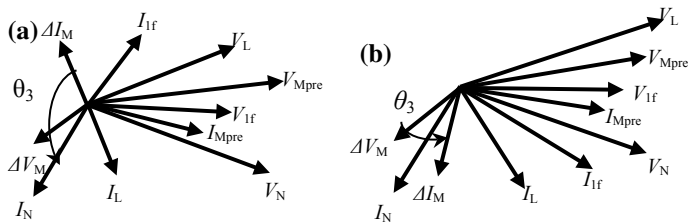


Fig. 3 Phasor diagram based on superimposed component a Fault at Fx b Fault at Fy

3.2 Proposed Technique

A single detector is not always suitable for different fault cases and fault conditions. During a symmetrical fault, negative sequence component will not be present. Similarly, for high-resistance and high-impedance fault, the decision of detector-1 is not reliable. The superimposed component-based technique generally malfunction during heavy load switching condition and capacitor switching. Considering the different critical cases, an integrated voting technique based directional relaying algorithm is proposed for microgrid system. The integrated approach relies on the decision of all the three detectors and a final decision is declared based on maximum votes obtained from all the three methods. For voting technique,

$$d(q) = \sum_{p=1}^N X(p, q) \quad \forall q = 1 : L \tag{4}$$

where d is the output for each detector, q is a vector of length L . X is the output binary vector for each classification p . L corresponds to the number of hypothesized output decisions.

$$d(k) = \arg \max_q d(q) \tag{5}$$

where d denotes the decision rule selected output at time instant k . The output of the voting method using Eq. (5) depicts the final decision provided by the detector.

4 Simulation Results

To assess the response of devised directional relaying algorithm, various test scenarios are tested on the sample distribution system (Fig. 1). The voltage and current signals measured at relay location (R) are computed and applied in the processing of three different detectors. The signals were processed using simple second-order low-

pass Butterworth filter having cut-off frequency of 300 Hz. All the simulations have been performed using PSCAD/EMTDC software. Response for different scenarios is evaluated and demonstrated below.

4.1 Faults During Grid-Connected Mode

In this mode, the microgrid is connected to a utility and the performance of the proposed methodology is observed for both symmetrical and unsymmetrical fault cases. First, a double-line-to-ground fault (AB-G) is created both in the upstream and downstream side of the relay (R) connected near bus 12, protecting lines 12–13. A fault is created at 0.3 s with a fault resistance of 100 Ω. For upstream side (Fx), AB-G fault is created in between line 11 and 12. For downstream side fault, AB-G fault is created in between line 12–13. Results for both the fault cases are shown in Fig. 4. From the figure, it is inferred that for fault at Fx side, the values of θ_1 , θ_2 , and θ_3 are positive and for fault at Fy side, all the values are negative. So, the overall output provided by the proposed method for both the fault cases is 1 and -1 which is correct.

Results for a symmetrical fault (ABC fault) are shown in Fig. 5. During symmetrical fault, negative sequence component is absent. So, detector-2 output is zero. But as other two methods are operating correctly, the output by the proposed technique is 1 for ABC fault in Fx side and -1 for ABC fault in Fy side. So, the method is capable

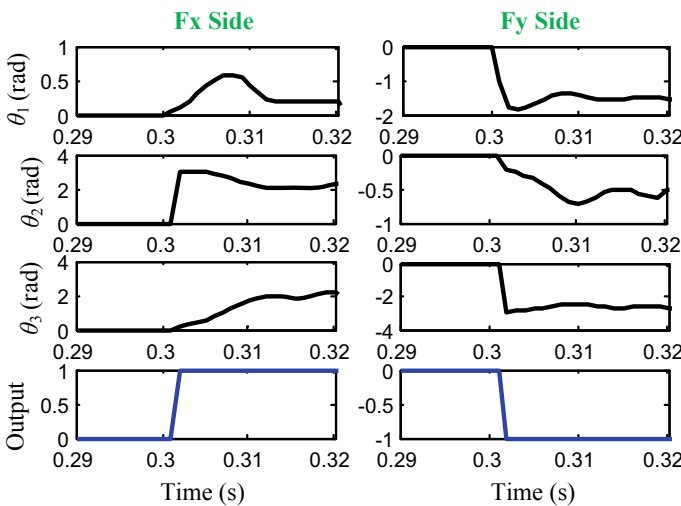


Fig. 4 Performance for AB-G fault during grid-connected mode

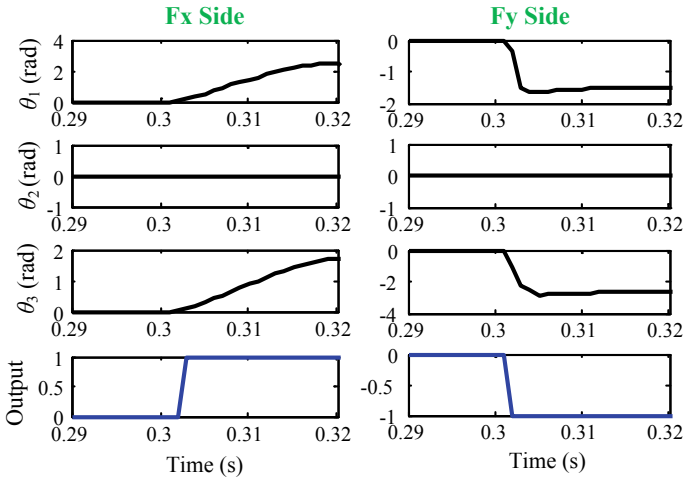


Fig. 5 Performance for ABC fault during grid-connected mode

of discriminating the exact fault direction during grid-connected mode. Also, the impact of fault resistance and fault type on the performance of the proposed method is negligible.

4.2 Results for Fault During Islanded Mode

For islanding, the circuit breaker (CB) is opened intentionally. Next, A-G faults are created at both upstream and downstream sides of the relay (R). Figure 6 shows that the output of the voting technique consistently provides the correct output for fault on both forward and reverse sides. So, the response of the method is not affected by any change in the operating mode of the microgrid system.

4.3 Results for Load Switching

Load switching is the critical factor during which many algorithms fail. To simulate such a condition, 150% of baseload at PCC is switched on at 0.3 s. Although the heavy load switching creates unbalance in system parameters, the method remains silent during such a condition as the output is zero (Fig. 7a). So, during heavy load switching, the decision provided by the method is reliable and consistent.

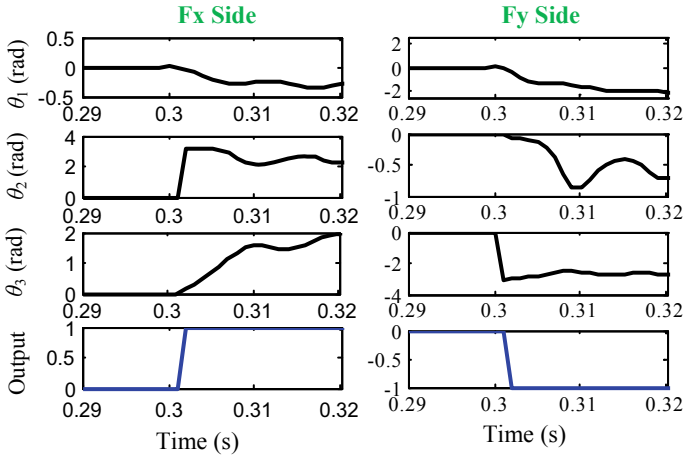


Fig. 6 Performance for A-G fault during islanded mode

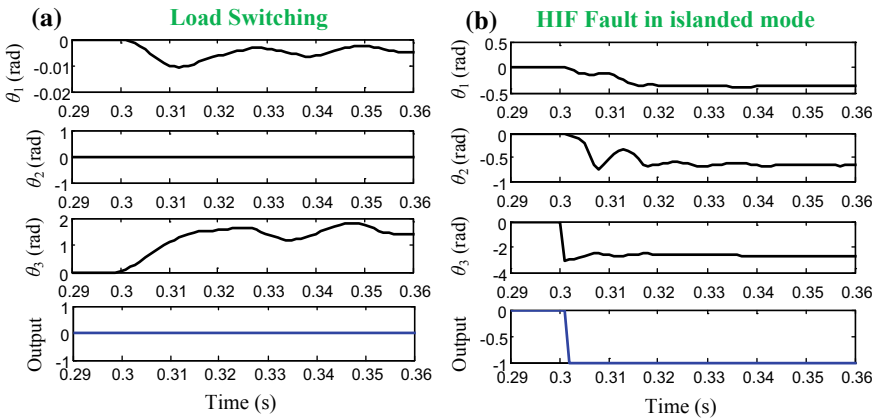


Fig. 7 a Performance during load switching event b Performance for HIF in islanded mode

4.4 Results for High-Impedance Fault (HIF) in Islanding Mode

It is difficult to detect high-impedance fault in microgrid exceptionally when it occurs in islanded mode [10]. To validate the response of the proposed technique, an A-G fault with fault impedance of 100Ω is simulated at the downstream side of the relay R. It can be observed from Fig. 7b that the overall output of the proposed technique is -1 , confirming the occurrence of a fault on the forward side. So, the impact of high-impedance fault during islanded mode is negligible on the output response of the proposed technique.

5 Conclusion

In this paper, an integrated decision-based directional relaying algorithm is proposed for the microgrid system. The method functions on the maximum votes obtained from the three different detectors. If for any fault case, the detector outputs are positive, then based on the majority votes the output of the proposed voting technique is 1. Similarly, for maximum obtained negative votes, the output decision of the proposed method is -1 . Upstream fault is set for output 1 and downstream side fault is set for output -1 .

The performance of the method is evaluated for different cases, such as fault during grid-connected mode and islanded mode. The impact of high-resistance and high-impedance fault on the performance of the proposed method is also evaluated. It is also observed from the study that the decision of the method is biased during heavy load switching condition, which is a great attribute. So, the directional relaying method is very reliable, fast, and secured for the application in the modern microgrid system.

References

1. IEEE standard for interconnecting distributed resources with electric power systems. IEEE, Standards Coordinating Committee (2003)
2. Impact of increasing contribution of dispersed generation on the power system, CIGRE. Working Group 37.23 (1999)
3. G59/1 recommendations for the connection of embedded generating plant to the regional electricity companies distribution systems. Electr Assoc stand (1991)
4. Brearley BJ, Prabhu RR (2016) A review on issues and approaches for microgrid protection. *Renew Sustain Energy Rev* 67:988–997
5. Oudalov A, Fidigatti A (2009) Adaptive network protection in microgrids. *Int J Distrib Energy Resour* 5(3):201–226
6. Hooshyar A, Iravani R (2017) A new directional element for microgrid protection. *IEEE Trans Power Deliv* PP(99)
7. Hatziargyriou N (2014) *Microgrids: architectures and control*. Wiley-IEEE Press, West Sussex, UK
8. Protection of distribution systems with distributed energy resources. CIGRE-CIRED Joint Working Group B5/C6.26/CIRED, Report 613 (2015)
9. Huchel L, Zeineldin HH (2016) Planning in the coordination of directional overcurrent relays for the distribution systems considering DG. *IEEE Trans Smart Grid* 7(3):1642–1649
10. Bukhari SBA, Zaman MS, Haider R, Oh YS, Kim C (2017) A protection scheme for microgrid with multiple distributed generations using superimposed reactive energy. *Int J Electr Power Energy Syst* 92:156–166
11. Refern MA, Usta O, Fielding G (1993) Protection against loss of utility grid supply for a dispersed storage and generation unit. *IEEE Trans Power Deliv* 8(3):948–954
12. Laaksonen H, Ishchenko D, Oudalov A (2014) Adaptive protection and microgrid control design for Hailuoto island. *IEEE Trans Smart Grid* 5(3):1486–1493
13. Nale R, Biswal M (2017) Comparative assessment of passive islanding detection techniques for microgrid. In: *International conference on innovations in information, embedded and communication system, Coimbatore*, pp 1–5

14. Laghari JA, Mokhlis H, Karimi M, Bakar AHA, Mohamad H (2015) An islanding detection strategy for distribution network connected with hybrid DG resources. *Renew Sustain Energy Rev* 45:662–676
15. Mahat P, Chen Z, Bak-Jensen B (2009) A hybrid islanding detection technique using average rate of voltage change and real power shift. *IEEE Trans Power Deliv* 24(2):764–771
16. Saleh KA, Zeineldin HH, El-saadany EF (2017) Optimal protection coordination for microgrids considering N-1 contingency. *IEEE Trans Ind Inform* 13(5):2270–2278
17. Zeineldin HH, Mohamed YA, Khadkikar V, Pandi VR (2013) A protection coordination index for evaluating distributed generation impacts on protection for meshed distribution systems. *IEEE Trans Smart Grid* 3(2):1523–1532
18. Biswal M, Pati BB, Pradhan AK (2013) Directional relaying for double circuit line with series compensation. *IET Gener Transm Distrib* 7(4):405–413
19. Biswal M, Pati BB, Pradhan AK (2012) Directional relaying of series-compensated line using an integrated approach. *Electric Power Compon Syst* 40(7):691–710

Wavefunctions and Optical Gain in In_{0.24}Ga_{0.76}N/GaN Type-I Nano-heterostructure Under External Uniaxial Strain



Md. Riyaj, Amit Kumar Singh, P. A. Alvi and Amit Rathi

Abstract Wavefunctions and optical gain in a single In_{0.24}Ga_{0.76}N quantum well sandwiched between the GaN barriers has been reported. Optical gain within x -polarization and z -polarization have been investigated as quantum well width and external strain variations along [100]. The behavior of quasi Fermi levels for the valance bands and conduction bands have also been investigated. The InGaN/GaN type-I nano-heterostructure has been modeled and studied with the help of six band $k \cdot p$ formalism. The 6×6 diagonalised $k \cdot p$ Hamiltonian has been solved to evaluate the light and heavy hole energies. For an injected carrier density of $15 \times 10^{12}/\text{cm}^2$, the peak optical gain is found to be 15904/cm at wavelength of 0.48 μm in x -polarization and the peak optical gain is found to be 1576/cm at a wavelength of 0.44 μm in z -polarization.

Keywords Optical gain · Type-I · x and z polarization · Heterostructure

1 Introduction

The group III nitride semiconductors have numerous applications including visible range diode lasers, biosensors, solar cells, nitride based heterostructures and inter-subband quantum well devices. Charge separation problem is the fore most concern in InGaN/GaN Quantum well structures. It arises due to the existence of strong

Md. Riyaj · A. K. Singh · A. Rathi (✉)
Department of Electronics and Communication Engineering,
Manipal University Jaipur, Jaipur, India
e-mail: amitrathi1978@gmail.com

Md. Riyaj
e-mail: roziriyaj@gmail.com

A. K. Singh
e-mail: amitkumarsingh89@gmail.com

P. A. Alvi
Department of Physics, Banasthali University, Vanasthali, Rajasthan, India
e-mail: drpaalvi@gmail.com

electric field which shows reduction in electron-hole wavefunction overlap. Reduction of electron-hole wavefunction overlap further leads to reduction in radiative recombination rate. Charge separation problem is the most challenging factor in InGaN heterostructures and by improving on the charge separation problem, enhanced radiating efficiency in green-emitting nitride LEDs can be obtained [1]. Improvement in charge separation issues by using nonpolar InGaN quantum well LEDs have been investigated by Hwang et al. [2]. Characterization of InGaN light emitting diodes has been presented in [3, 4]. Holes have a very high effective mass and hence a very low mobility is observed in GaN based devices. The electrical and optical performance of InGaN/AlGaN and InGaN/GaN heterostructures have been investigated and it is suggested that the overall efficiency of the InGaN/AlGaN heterostructure is better in comparison to the InGaN/GaN heterostructure [5]. A new model of InGaN heterostructure has been investigated for improvement in optical performance of blue light emitting diodes [6]. p-InGaN/p-GaN superlattices have been designed for a blue light emitting diode with the free hole concentration of $2.6 \times 10^{18} \text{ cm}^{-3}$ [7]. Semiconductor heterostructure is the basis of most optoelectronic devices today. Since the last three decades, the III–V group semiconductors based quantum well heterostructures have been extensively used for lasing applications. Lasing semiconductor heterostructures offer improved performance in the terms of long wavelength, high intensity beam output and switching speed. However, high carrier density is required for homogeneous quantum wells to invert their population before any stimulated emission process can take place. H. K. Nirmal et al. have calculated the optimized optical gain in InGaAs/GaAsSb heterostructure within TE mode to be 9000/cm at corresponding lasing wavelength of $1.95 \mu\text{m}$ under very high pressure [8]. Rashmi Yadav et al. have studied the modal gain and optical losses within TE and TM modes and maximum gain is reported at the lasing wavelength $1.40 \mu\text{m}$ and $1.25 \mu\text{m}$ in TE and TM modes respectively [9]. Emanuele et al. have reported deep-UV optical gain in AlGaN-based graded index separate confinement heterostructure. Emanuele et al. have designed a graded index laser double heterostructure with AlGaN in active region in order to boost the optical confinement of heterostructures [10]. In [11] Wei Guo et al. have reported stimulated emission and optical gain for 250 nm emission from an AlGaN heterostructure. Hongping Zhao et al. have analyzed the improved gain media self consistently for Type-II InGaN heterostructure [12]. In this paper the optical gain of type-I $\text{In}_{0.24}\text{Ga}_{0.76}\text{N}/\text{GaN}$ heterostructure which is capable of better carrier and optical confinement is investigated under varying well width and external uniaxial strain conditions. In the subsequent sections, design and theory of the $\text{In}_{0.24}\text{Ga}_{0.76}\text{N}/\text{GaN}$ heterostructure is presented and discussed following which the simulation results are reported and analyzed. In the last section, the conclusions from the present work are briefed.

2 Device Structure and Modeling

The type-I $\text{In}_{0.24}\text{Ga}_{0.76}\text{N}/\text{GaN}$ heterostructure under study consists of a single quantum well of width 4 nm of ternary compound InGaN sandwiched between the barrier layers GaN of 6 nm each. The entire heterostructure has been grown on the

substrate of binary compound GaN and is of length 16 nm along the growth direction. Optical gain or material gain represents the suitability of a structure to act as a laser. InGaAs/GaAsSb ‘W’ type lasers have been investigated in [13, 14]. Chia-Hao Chang et al. have investigated the optical gain for InGaAs/GaAsSb quantum well heterostructure [15–20]. Recently, Baile Chen et al. have reported the optimized wavefunction overlap and transition wavelength for InGaAs/GaAsSb type-II quantum well heterostructure [21]. Within the conduction band of the structure, the computation of discrete energy levels can be done using the single band effective mass equation as given in (1).

$$-\frac{\hbar^2}{2m_c^*} \nabla^2 \psi + V_c \psi = E_c \psi \quad (1)$$

where ψ is the envelope function, \hbar is plank’s constant, m_c^* stands for conduction effective mass, V_c potential of conduction band, E_c is conduction band electron energy level. For calculation of discrete energy levels (i.e. conduction electron, light and heavy hole levels) within the quantum well heterostructure 6×6 Hamiltonian matrix is used.

$$H_{6 \times 6}(k) = \begin{pmatrix} H_{3 \times 3}^+ & 0 \\ 0 & H_{3 \times 3}^- \end{pmatrix} \quad (2)$$

where, $H_{3 \times 3}^+$ and $H_{3 \times 3}^-$ are given by (3) with $\cup = +$ or $-$ signifies upper and lower blocks [22, 23].

$$H_{3 \times 3}^{\cup} = - \begin{pmatrix} P + Q - V_h(Z) & R(k) \pm iS(k) & \sqrt{2}R(k) \pm \frac{i}{\sqrt{2}}S(k) \\ R(k) \pm iS(k) & P - Q - V_h(Z) & \sqrt{2}Q \pm i\sqrt{\frac{3}{2}}S(k) \\ \sqrt{2}R(k) \pm \frac{i}{\sqrt{2}}S(k) & \sqrt{2}Q \mp i\sqrt{\frac{3}{2}}S(k) & P + \Delta_{so} - V_h(Z) \end{pmatrix} \quad (3)$$

In (3) $V_h(Z)$ denotes the unstrained valence band edge, Δ_{so} is the spin-orbit split-off energy. Also, $P = P(k) + P(\epsilon)$ and $Q = Q(k) + Q(\epsilon)$ is further expanded in terms of the material parameters in Eqs. (4) and (5), also, $S(k)$ and $R(k)$ are expanded in Eq. (6) [24, 23].

$$P(k) = \left(\frac{\hbar^2}{2m} \right) \gamma_1 (k_t^2 + k_z^2) \quad \& \quad P(\epsilon) = -a_v (\epsilon_{xx} + \epsilon_{yy} + \epsilon_{zz}) \quad (4)$$

$$Q(k) = \left(\frac{\hbar^2}{2m} \right) \gamma_2 (k_t^2 - 2k_z^2) \quad \& \quad Q(\epsilon) = -\frac{b}{2} (\epsilon_{xx} + \epsilon_{yy} - 2\epsilon_{zz}) \quad (5)$$

$$S(k) = \left(\frac{\hbar^2}{2m} \right) \sqrt{3} \left(\frac{\gamma_2 + \gamma_3}{2} \right) k_t^2 \quad \& \quad R(k) = \left(\frac{\hbar^2}{2m} \right) 2\sqrt{3} \gamma_3 k_t k_z \quad (6)$$

For quantum well structures optical gain coefficient can be written as (7) [14, 23].

$$G(\hbar\omega) = C_0 \sum_{\eta, \cup} \sum_{n, m} \int |(\xi \cdot M_{nm}^{\eta, \cup}(k_t))|^2 \times \frac{(f_n^c(k_t) - f_{Um}^v(k_t))(\frac{\gamma}{\pi})}{(E_{U, nm}^{c, v}(k_t) - \omega\hbar)^2 + \gamma^2} \frac{k_t dk_t}{2\pi}$$

where $C_0 = \frac{\pi e^2}{nc\epsilon\omega Lm_e^2}$, $f_n^c(k_t) = \left(e^{\left(\frac{E_n^c(k_t) - F_c}{k_B T} \right)} + 1 \right)^{-1}$ & $f_{Um}^v(k_t) = \left(e^{\left(\frac{E_{Um}^v(k_t) - F_v}{k_B T} \right)} + 1 \right)^{-1}$ (7)

where e is the charge on electron, m_e is the mass of electron in free space, ξ free space permittivity, c is the velocity of light and $M_{nm}^{\eta, \cup}(k_t)$ momentum matrix elements. f_{Um}^v and f_n^c are the Fermi-Dirac distribution functions. Various III–V compound semiconductor material parameters are presented in [25].

3 Results and Discussion

A quantum well is an example of a heterostructure where a very thin “well” layer (InGaN in the present case) is sandwiched in between two thicker barrier layers of a material with a different bandgap energy (GaN in the present case). Further, there are two different polarization directions as well: one with electric vector parallel to the quantum well layers known as the x -polarization and the other with electric vector perpendicular to quantum well layer known as the z -polarization.

To study the quantum well size effect, temperature effect, carrier density effect on optical gain, it is necessary to know the energy band structure of the device. Figures 1 and 2 show the energy band diagram and the conduction band, heavy hole band and light hole band alignments of the $In_{0.24}Ga_{0.76}N/GaN$ type-I nano-scale heterostructure. The Schrodinger equation has been solved to acquire energies of electrons in conduction band of quantum well of $In_{0.24}Ga_{0.76}N/GaN$ nano-scale heterostructure. The wave functions and energy level of light hole and heavy hole bands have been solved by using six band 6×6 diagonalised $k \cdot p$ Hamiltonian.

Optical gain describes the optical amplification in nano-heterostructure material. Optical amplification is the boosting of an electromagnetic wave. As shown in Figs. 3 and 4 x -polarization shows a much higher optical amplification as compared to z -

Fig. 1 Electron Wavefunctions for type-I heterostructure $In_{0.24}Ga_{0.76}N/GaN$

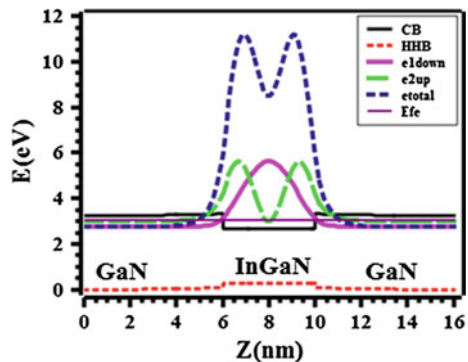


Fig. 2 Hole Wavefunctions for Type-I heterostructure I $\text{In}_{0.24}\text{Ga}_{0.76}\text{N}/\text{GaN}$

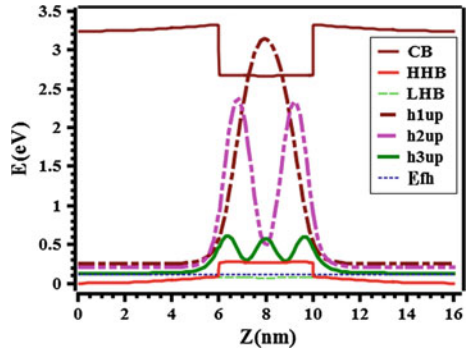


Fig. 3 Total optical gain within *x*-polarization as a function of photon energy for $\text{In}_{0.24}\text{Ga}_{0.76}\text{N}/\text{GaN}$ nano-scale heterostructure

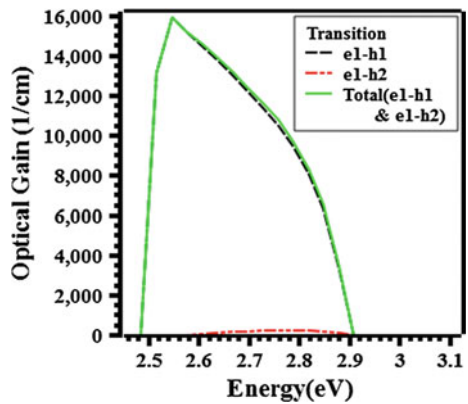
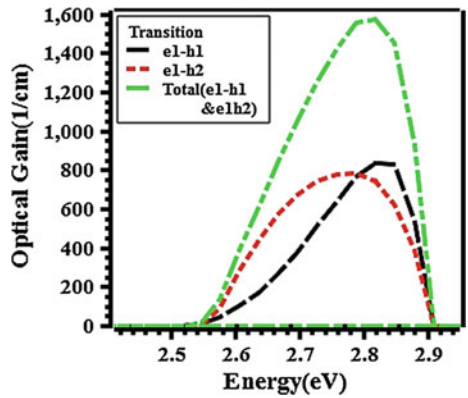


Fig. 4 Total optical gain within *z*-polarization as a function of photon energy for $\text{In}_{0.24}\text{Ga}_{0.76}\text{N}/\text{GaN}$ nano-scale heterostructure



polarization. The peak optical gain has been found to be around 8000/cm within TE mode for InGaAlAs nano-heterostructure by Kumari et al. [26]. The optical gain for green emitting In_{0.15}Ga_{0.85}N has been found ~2000/cm at lasing wavelength 512.4 nm by Zahang et al. [27]. In Figs. 3 and 4, the behavior of optical gain is plotted for ternary In_{0.24}Ga_{0.76}N/GaN lasing nano heterostructure in both *x* and *z* polarizations. In *x*-polarization for InGaN/GaN heterostructures, the optical gain is found to be 15904/cm at the photonic energy 2.54 eV and at the corresponding wavelength 480 nm while in *z*-polarization the optical gain is found to be 1576/cm at photonic energy 2.81 eV and at corresponding wavelength 441 nm.

InGaAsP Multiple Quantum well Fabry Perot (F-P) ridge laser has been investigated by Yang et al. [28]. Well width effects on material gain and lasing wavelength in InGaAsP/InP nano-heterostructure have been studied and maximum optical gain of ~8000/cm has been found for 2 nm quantum well size by Yadav et al. [9]. Figures 5 and 6 show the behavior of optical gain under different quantum well sizes for ternary In_{0.24}Ga_{0.76}N/GaN heterostructure. Maximum optical gain is

Fig. 5 Well width dependence of optical gain within *x*-polarization for In_{0.24}Ga_{0.76}N/GaN nano-scale heterostructure

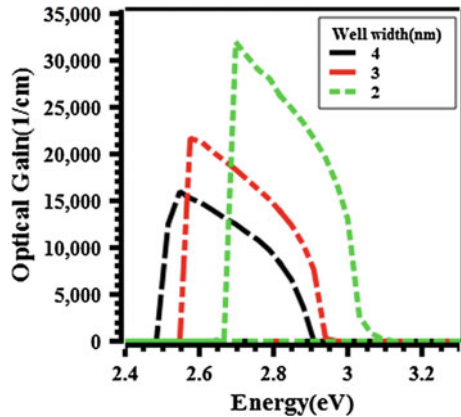
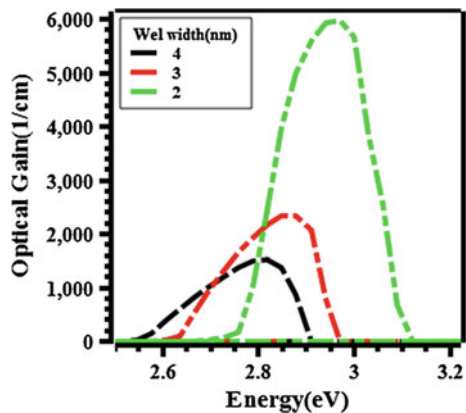


Fig. 6 Well width dependence of optical gain within *z*-polarization for In_{0.24}Ga_{0.76}N/GaN nano-scale heterostructure



achieved at 2 nm quantum well size, i.e. as the well width increases the optical gain falls gradually. x -polarization shows higher optical gain for the same quantum well size (2, 3, 4 nm) as compared to z -polarization, i.e. for 2 nm quantum well size the x -polarization shows $\sim 31000/\text{cm}$ optical gain whereas z -polarization shows $\sim 6000/\text{cm}$ optical gain.

External pressure induces a shift in the energy levels of the conduction and valance bands. These energy shifts can be obtained by using deformation potential theory. This theory was used to explore the interaction of electrons with acoustic phonons. Baile Chen et al. have designed strained $\text{InGaAs}/\text{GaAsSb}$ type-II quantum well heterostructures for operation in the MIR range [29]. Singh et al. [30] have studied and presented polarization dependent optical gain in $\text{InGaAs}/\text{GaAsSb}$ type-II nano-dimensional heterostructures under external uniaxial strain. Strain effects on optical gain in bulk GaN are calculated by J. B. Jeon et al. and optical gain in biaxially strained wurtzite GaN by using 6×6 envelope-function Hamiltonian has been calculated in [31]. Figures 7 and 8 show the plot of optical gain versus energy under different strain conditions for $\text{In}_{0.24}\text{Ga}_{0.76}\text{N}/\text{GaN}$ heterostructure in both x and z polarizations. As observed in Fig. 7, under no external strain condition, the peak optical gain is found to be $15904/\text{cm}$ at the photonic energy 2.54 eV . The optical gain spectrum is observed

Fig. 7 Optical gain within x -polarization for $\text{In}_{0.24}\text{Ga}_{0.76}\text{N}/\text{GaN}$ nano-scale heterostructure under different pressure applied along [100]

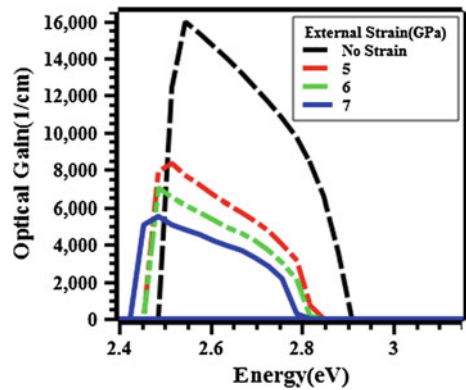
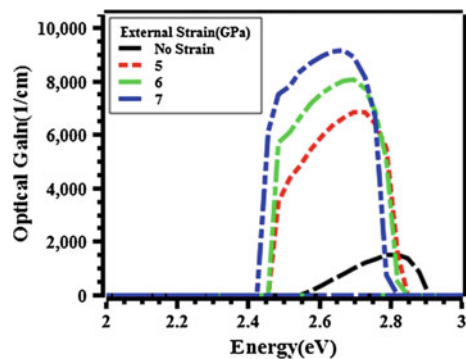


Fig. 8 Optical gain within z -polarization for $\text{In}_{0.24}\text{Ga}_{0.76}\text{N}/\text{GaN}$ nano-scale heterostructure under different pressure applied along [100]



to shift downwards within x -polarization whereas the optical gain spectrum shifts upwards in z -polarization under increased external strain conditions. x -polarization shows higher optical gain as compared to z -polarization, i.e. under no external strain condition the maximum optical gain is found to be 15904/cm within x -polarization whereas optical gain is found to be 1576/cm within z -polarization.

4 Conclusions

Wavefunctions and optical gain in $\text{In}_{0.24}\text{Ga}_{0.76}\text{N}/\text{GaN}$ heterostructure has been calculated. Quantum well width effects on optical gain of heterostructure have been discussed. The optical gain characteristics have been investigated within x -polarization and z -polarization. The maximum gain is achieved in visible range at the wavelength 480 nm and 441 nm in x and z -polarization respectively. Hence, such a nano-heterostructure is suitable for emission in the blue color region. The application of external strain on the nano heterostructure along the [100] direction causes the optical gain spectrum to shift to higher values within z -polarization.

Acknowledgements Authors are thankful to Manipal University Jaipur, 303007, Rajasthan, India for the financial support provided under the project Seed grant scheme: MUJ/REGR/1467/13. Authors also take this opportunity to thank Dr. Konstantin I. Kolokolov (Faculty of Physics, M V Lomonosov Moscow State University, Moscow 119991, Russia) for supporting the work. P. A. Alvi is also thankful to “Banasthali Center for Research & Education in Basic Sciences” under CURIE programme supported by the Dept. of Science & tech. (DST), Govt. of India, New-Delhi.

References

1. Tansu N, Zhao H, Liu G, Li X-H, Zhang J (2010) III-nitride photonics. *IEEE Photonics J* 2(2)
2. Hwang SM, Seo YG, Baik KH, Cho IS, Baek JH, Jung S, Kim TG, Cho M (2009) Demonstration of non polar a-plane InGaN/GaN light emitting diode on r-plane sapphire substrate. *Appl Phys Lett* 95(7):071101-1–071101-3
3. Detchprohm T, Zhu M, Li Y, Xia Y, Liu L, Hanser D, Wetzel C (2009) Growth and characterization of green GaInN-based light emitting diodes on free-standing non-polar GaN templates. *J Cryst Growth* 311(10):2937–2941
4. Lin YD, Chakraborty A, Brinkley S, Kuo HC, Melo T, Fujito K, Speck JS, Den Baars SP, Nakamura S (2009) Characterization of blue-green m-plane InGaN light emitting diodes. *Appl Phys Lett* 94(26):261108-1–261108-3
5. Chang J-Y, Tsai M-C, Kuo Y-K (2010) Advantages of blue InGaN light emitting diode with AlGaIn barriers. *Opt Lett* 35(9)
6. Zerg S-M, Fan G-H (2015) Advantages of blue InGaN light emitting diode with a mix of AlGaIn and InGaIn quantum barriers. *J Electron Mater* 44(10)
7. Chao L, Zhi-wei R (2013) Advantages of InGaIn base light emitting diode with a p-InGaIn/p-GaN superlattices hole accumulation layer. *Chin Phys B* 22(5)
8. Nirmal HK, Yadav N, Dalela S, Rathi A, Siddiqui MJ, Alvi PA (2016) Tunability of optical gain (SWIR region) in type-II $\text{In}_{0.70}\text{Ga}_{0.30}\text{As}/\text{GaAs}_{0.40}\text{Sb}_{0.60}$ nano-heterostructure under high pressure. *Phys E: Low-Dimens Syst Nanostructures* 80:36–42

9. Yadav R, Lal P, Rahman F, Dalela S, Alvi PA (2014) Well width effects on material gain and lasing wavelength in $\text{InGaAsP}/\text{InP}$ nano-heterostructure. *J Optoelectron Eng* 2(1):1–6
10. Pecora EF, Sun H, Negro LD, Moustakes TD (2015) Deep-UV optical gain in AlGaIn based graded index separate confinement heterostructure. *Opt Mater Express* 5(4):809
11. Guo W, Bryan Z, Kirste R (2014) Stimulated emission and optical gain in AlGaIn heterostructures grown on bulk AlN substrates. *J Appl Phys*
12. Zhao H, Arif RA, Tansu N (2008) Self consistent gain analysis of type-II ‘W’ InGaIn-GaNAs quantum well lasers. *J Appl Phys* 104:043104
13. Pan C-H, Chang C-H, Lee C-P (2012) Room temperature optically pumped 2.56- μm Lasers with ‘W’ type InGaAs/GaAsSb quantum wells on InP substrates. *Photonics Technol Lett IEEE* 24(13):1145–1147
14. Pan CH, Lee CP (2013) Design and modeling of InP -based InGaAs/GaAsSb type-II ‘W’ type quantum wells for mid-Infrared laser applications. *J Appl Phys* 113(4):043112
15. Chang C-H, Li Z-L, Lu H-T, Pan C-H, Lee C-P, Lin G, Lin S-D (2015) Low-threshold short-wavelength infrared InGaAs/GaAsSb ‘W’-type QW laser on InP substrate. *Photonics Technol Lett IEEE* 27(3):225–228
16. Chang C-H, Li Z-L, Pan C-H, Lu H-T, Lee C-P, Lin S-D (2014) Room-temperature mid-infrared ‘M’-type GaAsSb/InGaAs quantum well lasers on InP substrate. *J Appl Phys* 115(6):063104
17. Vijay J, Singh K, Soni D, Rathi A (2019) Structural and optical characteristics of nanoscale semiconductor lasers for telecommunication and biomedical applications: a review. *IOP Conf Ser: Mater Sci Eng* 594(1)
18. Riyaj Md, Singh AK, Sandhya K, Rathi A, Alvi PA (2017) Optical properties of type-I GaAsP/AlGaAs nano-heterostructure under external uniaxial strain. *AIP Conf Proc* 1832:120022.1–120022.3
19. Rathi A, Singh AK, Riyaj Md, Dalela S, Alvi PA (2019) Red shift in optical properties of type-I $\text{Al}_{0.45}\text{Ga}_{0.55}\text{As/GaAs}_{0.84}\text{P}_{0.16}/\text{Al}_{0.45}\text{Ga}_{0.55}\text{As}$ nano-heterostructure under external strain. *IOP Conf Ser: Mater Sci Eng* 576(1)
20. Riyaj Md, Singh AK, Rathi A, Kattayat S, Kumar S, Dalela S, Alvi PA (2019) High pressure affects on optical characteristics of $\text{AlGaAs/GaAsP/AlGaAs}$ nano-heterostructure. *Optik Elsevier* 181:389–397
21. Chen B, Holmes AL, Khalfin V, Kudryashov I, Onat BM (2012) Modeling of the type-II InGaAs/GaAsSb quantum well designs for mid-infrared laser diodes by k_p method. In: SPIE defense, security, and sensing. International society for optics and photonics, pp 83810F–83810F
22. Harrison P (2005) Quantum wells, wires and dots: theoretical and computational physics of semiconductor nanostructures. Wiley
23. Chuang SL (1995) Physics of optoelectronic devices. Wiley
24. Zory PS (1993) Quantum well lasers. Academic Press
25. Vurgaftman I, Meyer JR, Ram-Mohan LR (2001) Band parameters for III–V compound semiconductors and their alloys. *J Appl Phys* 89(11):5815–5875
26. Kumari V et al (2014) Optical gain of InGaAlAs quantum well with different barriers, claddings and substrates. *J Optoelectron Eng* 2(2):42–45
27. Zahang J (2013) Optical gain and lasing characteristics of InGaN quantum wells on ternary InGaN substrates. *IEEE Photonics J* 2(5)
28. Yang W, Ying-Ping Q, Jiao-Qing P, Ling-Juan Z (2010) High characteristic temperature InGaAsP/InP tunnel injection multiple-quantum-well lasers. *Chin Phys Lett* 27(11):114201
29. Chen B, Jiang WY, Holmes AL Jr (2012) Design of strain compensated InGaAs/GaAsSb type-II quantum well structures for mid-infrared photodiodes. *Opt Quantum Electron* 44(3):103–109
30. Singh AK, Riyaj Md, Anjum SG, Yadav N, Rathi A, Siddiqui MJ, Alvi PA (2016) Anisotropy and optical gain improvement in type-II $\text{In}_{0.3}\text{Ga}_{0.7}\text{As/GaAs}_{0.4}\text{Sb}_{0.6}$ nano-scale heterostructure under external uniaxial strain. *Superlattices Microstruct* 98:406–415
31. Jeon JB, Lee BC, Sirenko Yu M, Kim KW, Littlejohn MA (1997) Strain effects on optical gain in wurtzite GaN . *J Appl Phys* 82(1):386–391

Cost–Benefit Analysis in Distribution System of Jaipur City After DG and Capacitor Allocation



Ankush Tandon, Sarfaraz Nawaz and Shahbaz Ahmed Siddqui

Abstract Distributed generation (DG) and shunt capacitors are widely adopted for minimizing power loss in distributed networks. But the high cost of DG units puts a limitation on employing higher rating DGs in distribution networks. So, it is desired that less DG size gives maximum loss reduction for achieving the objective of minimum overall cost of the system. The prominent goal of this paper is to curb the total expenditure occurring due to annual energy loss and cost incurred in installing DG units and capacitor banks. An unsullied methodical approach has been presented in this paper to find out optimal position and rating of DG as well as capacitor units so that the overall cost would be minimal. The method is tested on standard IEEE 69 bus distribution system and 130 bus Indian distribution systems. The outcomes of both the test systems are optimistic and found to be promising when compared with the previous ones.

Keywords Real power loss (RPL) · Capacitor units · Distributed generation (DG) · Radial distribution system (RDS)

1 Introduction

Distributed generation (DG) is used for pollution-free electric power production. The connotation of distributed generation refers to the small generating units which are installed in the neighborhood of the load side in order to avoid the future expansion requirements. The DGs are installed in the system to primarily reduce active power loss which in turn leads to diminution of energy loss with enhancement of voltage profile. The renewable-based DG units (solar PV, windmills, etc.) are generally used for power generation. But the cost of such types of DGs is very high. In India, the cost of 10 kW on a grid solar power plant is around Rs. 5 lacs. It is desirable to

A. Tandon (✉) · S. Nawaz
SKIT M&G, Jaipur, India
e-mail: eeankush.1986@gmail.com

S. A. Siddqui
Manipal University Jaipur, Jaipur 303007, Rajasthan, India

© Springer Nature Singapore Pte Ltd. 2020
A. Kalam et al. (eds.), *Intelligent Computing Techniques for Smart Energy Systems*,
Lecture Notes in Electrical Engineering 607,
https://doi.org/10.1007/978-981-15-0214-9_39

determine the best position and rating of DG units for minimizing the overall cost of the system.

Numerous researchers proposed various optimization techniques in order to determine the site and size of the DG units in RDS. Authors formulated analytical expressions for optimal allocation of DG at different loading conditions in RDS to minimize the RPL [1].

Abou El-Ela [2] presented a genetic algorithm for DG allocation in order to increase spinning reserve, enhancement in bus voltages, and to reduce transmission loss.

In [3], a new expression has been investigated for determining the optimal size of DGs for dropping RPL in distribution systems. Barker [4] explained various aspects (like voltage profile, RPL, and distribution capacity and power quality issues) of DG placement in RDS. Aman et al. proposed [5] a step-by-step iterative algorithm to find the best location of the DG units. An improved loss-sensitivity analysis method is proposed to identify and locate optimal DG units in a radial distribution system in [6]. The significant improvement is observed in percentage loss reduction and voltage profile. Rueda-Medina [7] proposed a mixed-integer linear programming technique in RDS for locating DG units of optimal size. Koutroulis et al. [8] presented cost-benefit analysis of DG allocation in RDS while considering renewable-based DG units individually. The main objective is to minimize the total system cost. In [9], authors proposed CPF algorithm and incorporated modal analysis to solve DG's allocation problem in RDS.

This paper presents a new-fangled technique to place DG and capacitor units with optimal sizing. The total expenditure, occurring due to annual energy loss and installation of DG and capacitor bank, has been reduced in the paper. A new and simple mathematical expression, PSC, is formulated which incorporates power loss and voltage profile. The PSC yields optimal size and position of DG and capacitor units separately. The above methodology is tested on two test systems, i.e., IEEE 69 bus system and 130 bus rural system of Jaipur city. The results obtained for both test systems are optimistic and encouraging.

2 Problem Formulation

This paper intends to minimize the total expenditure occurring due to annual energy loss and installation of DG and capacitor bank with gratifying constraints.

The problem can be expressed mathematically as follows:

Minimize $F = \text{Cost due to energy loss} + \text{Cost of capacitor installation} + \text{Cost of DG installation}$

$$\text{Min. } f = K_E * P_{\text{loss}} * t + K_C * T_C + K_D * T_{\text{DG}} \quad (1)$$

Operating constraints are

- (i) Power balancing constraints.
- (ii) Total size of DG units $\leq 0.5 * P_{Load}$.
- (iii) Voltage constraints $0.95 \leq V_m \leq 1.0$.
- (iv) The injected reactive power should exceed the total system reactive power demand.

where

- K_E per unit energy cost;
- P_{loss} sum of active power loss of the network (kW);
- T 8760 h;
- K_C Cost of per kVAr capacitor unit including installation;
- T_C Total rating of capacitor bank in kVAr;
- K_D Cost of per kW DG unit including installation;
- T_{DG} Total rating of DG units in kW; and
- P_{load} Real power load of system (kW).

As per the Jaipur city scenario, the most favorable renewable-based DG unit is the solar power plant. The cost of all constants has been taken as specified in Rajasthan state.

- $K_E =$ Rs. 5 per unit,
- $K_C =$ Rs. 225 per kVAr, and
- $K_D =$ Rs. 50,000 per kW.

3 Proposed Technique

A new method is anticipated for placing capacitor and DG units separately. PSC calculates the optimal size and location of DG and capacitor units such that the total expenditure should is minimum.

$$PSC = \frac{V_{rated}}{V_m} + \frac{P_{dgloss}}{P_{realloss}} \tag{2}$$

- $P_{realloss}$ Real power loss for base case (kW).
- P_{dgloss} Power loss after placement of DG/capacitor units at the i th bus (kW).
- V_m Minimum bus voltage.

The value of P_{dgloss} should be lowest and V_{min} should be highest for the best allotment of DG units. Hence, ‘‘PSC’’ should be the smallest. The process to solve the problem is explained in [10].

4 Results

To test the efficacy of the proposed methodology, two test systems, real distribution system of 130 bus Jaipur city and IEEE standard bus system of 69 bus are incorporated.

4.1 69 Bus Test System

The IEEE 69 bus system has 12.66 kV and 100 MVA base values [11]. The total active and reactive system load is 3802 kW and 2694 kVAr, respectively. The active power losses for the base case are 225 kW and the minimum voltage is 0.9092 pu. Three different cases are considered for placing DG and capacitor units.

I: DGs placement,

II: Capacitors placement, and

III: Combination of DGs and capacitors placement.

Case I: Only DGs placement

In Case I, only DG units are placed in IEEE 69 bus standard system.

The result of DG allocation has been presented in Table 1. DG units of size 330 kW, 920 kW, and 560 kW are placed at location 21, 61, and 64, respectively. The RPL of the system is decreased to 76.7 kW from 225 kW.

Case II: Only capacitor placement

Similarly, the best position and rating of capacitors are determined by the proposed technique. The proposed methodology yields three different positions with the finest rating being obtained as 750 kVAr (bus no. 61), 270 kVAr (21), and 400 kVAr (64). After installation of the aforesaid capacitors, size, and its required location, a reduction of 78 kW is observed from the base case. The minimum voltage is also improved to 0.93 pu from 0.909 as shown in Table 2.

Case III: Combination of DGs and capacitors placement

In this case, both DG and capacitors are placed simultaneously. Table 3 exhibits the results of Case III. It is pragmatic that there is a significant reduction in real power loss reduction that accounts for 94.8%. The total cost is calculated as 918.32

Table 1 Results of 69 bus systems

	Without DG	With DG
Power loss (kW)	225	76.8
DG rating in kW (bus no.)	–	330 (21) 920 (61) 560 (64)
Total DG rating in kW	–	1810
% loss reduction	–	65.75
V_{\min} (pu)	0.909	0.970

Table 2 Outcome of IEEE 69 bus system (before and after capacitor placement)

	Before capacitor placement	After capacitor placement
Power loss (kW)	225	147
Capacitor size in kVAR (bus no.)	–	750 (61) 270 (21) 400 (64)
Total capacitor size in kW	–	1420
% loss reduction	–	34.66
V_{min} (pu)	0.909	0.93

Table 3 Summarized results of 69 bus system for Case III

DG rating in kW	Capacitor rating in kVAR	$P_{realLoss}$ in kW	V_{min} (p.u.)	% loss reduction (from base case)	Total cost in Lacs/year (f)
1810	1420	11.7	0.99	94.8%	918.32

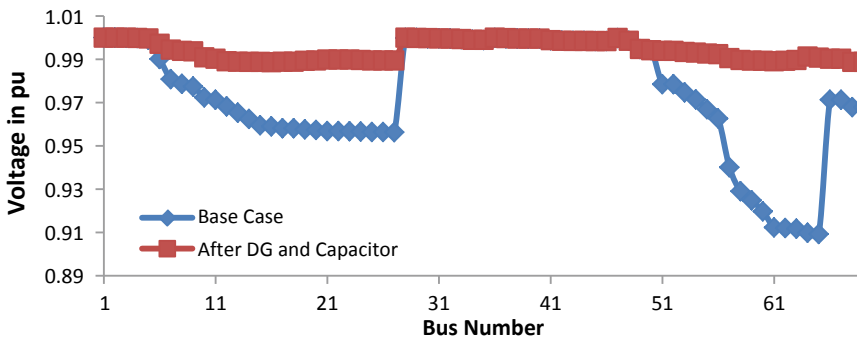


Fig. 1 Voltage profile of IEEE 69 bus system for Case III

lacs/annum. V_{min} is also improved from 0.90 to 0.99 pu after placing a capacitor and DG units simultaneously.

Figure 1 showcases the voltage contour for the base case and after placement of compensation elements.

Table 4 exhibits the comparison of results of the proposed technique with the latest techniques such as MINLP [12], IMDE [13], and EA [14] which are proposed in the topical past. In the proposed approach, the overall expenditure of the system is less than the other ones. In other techniques, the size of the DG is very high. It is noteworthy to notice that after 50% DG penetration, the power loss reduction is very slow. As a result, it will only increase the installation cost of DG units but the cost reduction due to energy loss is awfully less. The improved bus voltage profile is also shown in Fig. 1.

Table 4 Assessment of results for 69 bus system for Case III

	MINLP [12]	IMDE [13]	Evolutionary algorithm [14]	Proposed
DG size in kW	2547	2217	2549	1810
Capacitor size in kVAr	1806	2282	1801	1420
Real power loss	4.27	13.83	4.25	11.7
% Loss reduction	98.10	93.84	98	94.8
V_{min}	0.99	0.99	0.99	0.99
Total annual cost in INR Lacs for first year only (f)	1279	1119.7	1280.4	918.32

4.2 130 Bus (Jaipur City) System

The proposed technique is also examined on a real system of 130 bus Jaipur city. The total active and reactive load of the system accounts for 1.878 MW and 1.415 MVAR, respectively. The base value of the system is 11 kV and 100 MVA [10]. The real power losses for the base case are 330 kW and V_{min} is 0.83 pu. The proposed technique is also addressed on the 130 bus real distribution system of Jaipur rural area. The first five candidate buses are identified for placing of DG and capacitors units. Table 5 presents the result of 130 bus system after DG and capacitor installation.

Table 5 exhibits consolidated results of 130 bus radial distribution system. It is observed that losses are reduced to 141.6, 209, and 44 kW after placement of DG unit (Case I), after placement of capacitor unit (Case II), and after placement of

Table 5 Summary of results of 130 bus system for Case I, II, and III

Item	Without any compensation	After placement of DG unit only	After capacitor placement only	Combined placement of DG and capacitor
Total loss	330	141.6	209	44
% Loss reduction	–	57.7%	38%	87%
V_{min} in pu	0.83	0.9161	0.872	0.95
Optimal rating (location) in kW/kVAr	–	220 (106) 120 (115) 140 (119) 180 (122) 290 (128)	280 (53) 150 (77) 140 (114) 160 (120) 200 (126)	
Total kW/kVAr	–	940	930	940+j930
Total cost (f) in INR. Lacs/year	146.73	532.02	93.20	491.36

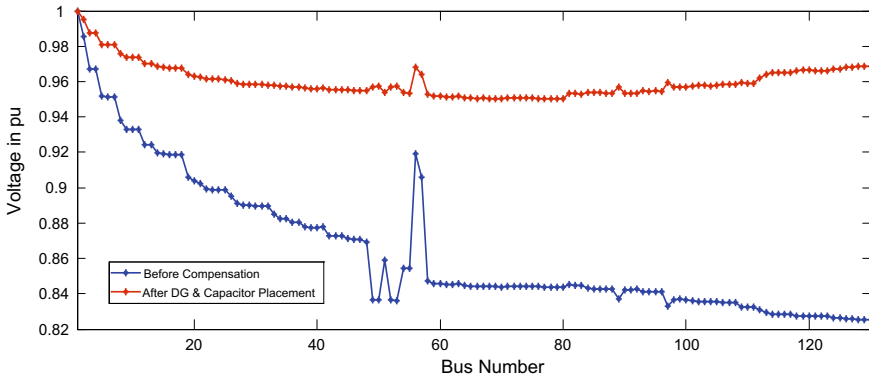


Fig. 2 Voltage profile for 130 bus system

both, DG and capacitor units. Analogously the percentage loss reduction accounts for 57.7, 38, and 87% for the aforesaid three cases. The V_{min} is also enhanced from 0.83 to 0.95 pu after DG and capacitor installation. Initially (when there are no compensation devices), the expenditure of energy loss is 146.73 Lacs/year. This will reduce to 19.27 lacs/year after compensation. The installation cost of solar-based DG and capacitor would be 470 lacs and 2.09 lacs, respectively. The total cost (f) after DG and capacitor placement would be INR 491.36 Lacs for the first year of installation. After that, it would be only INR 19.27 Lacs for the upcoming years. The enhanced voltage summary after allocations is shown in Fig. 2.

5 Conclusion

In this paper, an efficient and robust technique is investigated to determine the best size and location of DG and capacitor units in a distribution system. This in return will reduce the overall cost of the system. The overall cost includes energy loss cost, installation cost of solar-based DG unit and capacitor bank. A new and simple mathematical term, Power sensitivity constant (PSC), is formulated. The PSC determines the best location and rating of the DG and capacitors. The aforesaid method is applied on standard 69-bus and 130-bus system. The comparison of the results with the latest methods shows the efficacy of the proposed approach. The results of the real system are also promising. It will be concluded that there will be a huge saving in running expenses after DG and capacitor installation by the proposed technique. The results of the real system have also been confirmed by Rajasthan Vidyut Vitran Nigam Ltd. (RVVNL), Jaipur.

References

1. Wang C, Nehrir MH (2004) Analytical approaches for optimal placement of distributed generation sources in power systems. *IEEE Trans Power Syst* 19(4):2068–2076
2. El-Ela AA, Allam SM, Shatla MM (2010) Maximal optimal benefits of distributed generation using genetic algorithms. *Electr Power Syst Res* 80:869–877
3. Hung DQ, Mithulananthan N, Bansal RC (2010) Analytical expressions for DG allocation in primary distribution networks. *IEEE Trans Energy Convers* 25(3):814–820
4. Barker PP, de Mello RW (2000) Determining the impact on distributed generation on power systems: Part 1. Radial distribution systems In: *IEEE PES summer meeting*, vol 3, pp 1645–1656
5. Aman M, Jasmon J, Mokhlis H, Bakar A (2012) Optimal placement and sizing of a DG based on new power stability index and line losses. *Int J Electr Power Energy Syst* 43(1):1296–1304
6. Gozel T, Hocaoglu mh (2009) An analytical method for the sizing and sitting of distributed generators in radial distribution systems. *Electr Power Syst Res* 79:912–918
7. Rueda-Medina AC, Franco JF, Rider MJ, Padilha-Feltrin A, Rubén R (2013) A mixed-integer linear programming approach for optimal type, size and allocation of distributed generation in radial distribution systems. *Electr Power Syst Res* 97:133–143
8. Koutroulis E, Kolokotsa D, Potirakis A, Kalaitzakis K (2006) Methodology for optimal sizing of standalone photovoltaic/wind-generator systems using genetic algorithms. *Sol Energy* 80(9):1072–1088
9. Etehadhi M, Ghasemi H, Zadeh SV (2013) Voltage stability-based DG placement in distribution networks. *IEEE Trans Power Deliv* 28(1):171–178
10. Nawaz S, Tandon A (2018) Power loss minimization of rural feeder of Jaipur city by renewable-based DG technologies. *Aust J Electr Electron Eng*
11. Haque MH (1996) Capacitor placement in radial distribution systems for loss reduction. *IEEE Proc Gen Trans Distrib* 146(5)
12. Kaur S, Kumbhar G, Sharma J (2014) A MINLP technique for optimal placement of multiple DG units in distribution systems. *Electr Power Energy Syst* 63:609–617
13. Khodabakhshian A, Andishgar MH (2016) Simultaneous placement and sizing of DGs and shunt capacitors in distribution systems by using IMDE algorithm. *Electr Power Energy Syst* 82:599–607
14. Biswas PP, Mallipeddi R, Suganthan PN, Amaratunga GA (2017) A multi objective approach for optimal placement and sizing of distributed generators and capacitors in distribution network. *Appl Soft Comput* 60:268–280

Comparative Simulation Study of Dual-Axis Solar Tracking System on Simulink Platform



Neeraj Tiwari, Ravi Soni, Amit Saraswat and Brijesh Kumar

Abstract This paper depicts the performance of dual-axis solar tracking system that has been done on MATLAB platform. All the models such as a static PV system, sun model, tracking PV system, control circuit, and LDR sensor are developed on Simulink platform. The results came from this model are compared with the static power system model results. Simulation has been performed first considering the azimuthal tracking then the elevated tracking concept separately. Comparative result analysis shows that the improved efficiency of SPV system due to azimuthal (East-West) and elevated tracking system. The efficiency of a solar power plant may be improved by 37% by using azimuthal tracker implementation and 14% by using elevated tracking system. In this simulation study, the real irradiance and temperature data are considered and the best curve fitting method for continuous curve is applied. The irradiance and temperature data are measured with the help of measuring instruments pyr heliometer and temperature sensor. The data were recorded on different days.

Keywords Static PV system · Photovoltaic system · Tracking PV system · Control circuit

1 Introduction

In the recent year as the population and infrastructure in the developing countries increases the energy demand increases. It is difficult to extend the capacity of the existing power plant. To overcome this problem, countries are moving toward the alternative resources of energy. Among the present energy sources, renewable energy

N. Tiwari (✉) · R. Soni

Department of Electrical Engineering, Poornima University, Jaipur, Rajasthan, India
e-mail: neerajtiwari1407@gmail.com

A. Saraswat

Department of Electrical Engineering, Manipal University Jaipur, Jaipur, Rajasthan, India

B. Kumar

FET, Agra College, Agra, Uttar Pradesh, India

© Springer Nature Singapore Pte Ltd. 2020

A. Kalam et al. (eds.), *Intelligent Computing Techniques for Smart Energy Systems*,
Lecture Notes in Electrical Engineering 607,
https://doi.org/10.1007/978-981-15-0214-9_40

is the best alternative. The solar cells directly convert sunlight energy into electrical power. The main drawback of solar photovoltaic power plant is its low efficiency but solar energy is abundant in nature and pollution-free. Researchers are working in this field. The different PV cells of different materials having different efficiencies are available. These are monocrystalline, polycrystalline, and amorphous. These cells are mostly used in SPV power plant installation. Due to low conversion efficiency of the SPV cells, the initial cost of SPV power plant is high. Also, the various parameters affect the performance of the SPV power plants such as irradiance and temperature. The solar cell characteristics mainly depend on these parameters [1]. The sunlight intensity and temperature variation results in the variation of current and voltage. On the of PV characteristics, the efficiency of SPV power plant can be increased by three ways [2]. As the irradiance values increase the output current of SPV system increases, which means, the photocurrent is directly proportional to solar radiations [3]. Thereby, inculcating the sun tracker system in SPV power plant, the efficiency of SPV system can be improved, which results in reducing the cost of existing SPV power plants. The main concept of sun tracker to place the solar cells perpendicular to the sun position every day is that maximum irradiance falls on solar cells, which results to maximize the conversion of light energy into electrical energy. There are different tracking system suggested by researchers (1) Active tracking system, (2) Chronological Tracker, and (3) Passive tracking system. Active tracker consists of motors, gear train, and a photodiode. Some researchers suggested microcontroller-based tracking system. In digital tracking system, the sun position is predicted. On the predicted data the microcontroller programming was done. The tracker will track the sun positions automatically but the main drawback is that under cloudy day, the tracker moves yet sun will be hidden by cloud. The main drawback of microcontroller-based system is that in winter session the tracking system takes power while the sun is not available. The main part of active tracker is LDR sensors. The light-dependent sensors change its resistance according to the availability of light. LDR senses the light intensity and gives the signal to motor, whenever the light intensity on both sensors are same, the tracker will not move. Its position is perpendicular to the sun. Passive trackers work on the principle of compressed gas. The passive tracking system is based on boiling point concept, having the fluid of low boiling point. "It is driven to one side or the other (by solar heat creating gas pressure) to cause the tracker to move in response to an imbalance. Chronological Tracker counteracts the earth's rotation by turning at an equal rate as the earth but in the opposite direction. Actually, the rates aren't quite equal, because as the earth goes around the sun, the position of the sun changes with respect to the earth by 360° every year or 365.24 days" [4].

2 Developed Solar Tracking System

This section starts with the developed solar tracking system as shown in Fig. 1. The tracking system designed is comprised of different parts. The main parts of solar power plants with tracking systems are as follows:



Fig. 1 Developed solar tracing system

1. Selection of tracking system mount concept.
2. Framing structure of tracker on which SPV array mounted.
3. Designing of the motor control driving circuit.
4. Selection of LDR sensor and sensor control circuit.
5. Data acquisition and interface card.

For smooth tracking of the sun, these five main parts would work together harmoniously. The most commonly used and recommended tracking system is azimuthal tracking. The tracking of the sun from east to west here termed as azimuthal tracking system because azimuthal tracking system is simple in construction and produces more energy as compared to elevated tracking system. The azimuthal tracking system produces 37% more energy as compared to static SPV system due to simple in construction and economical. Practical results show that with the azimuthal tracking system the efficiency of SPV system can be increased by 37%, while by implementing the elevated (North to South) tracking concept we can extract 14% more energy form SPV power plant as compared to the static SPV power plant.

3 Characteristics of PV Cell

The variation of current and voltage of cell depends on cell temperature and intensity of light. Variation in voltage is shown in Fig. 2. The current produced by solar cell depends on the sunlight intensity [5]. The variation in current is shown in Fig. 3. In this figure, it is clearly seen that as the sunlight intensity increases, the current value also increases [6]. In Simulink block diagram developed for the analysis, the effect of solar intensity and real-time temperature effect on solar cells are considered and cubic curve was fitted for simulation purpose.

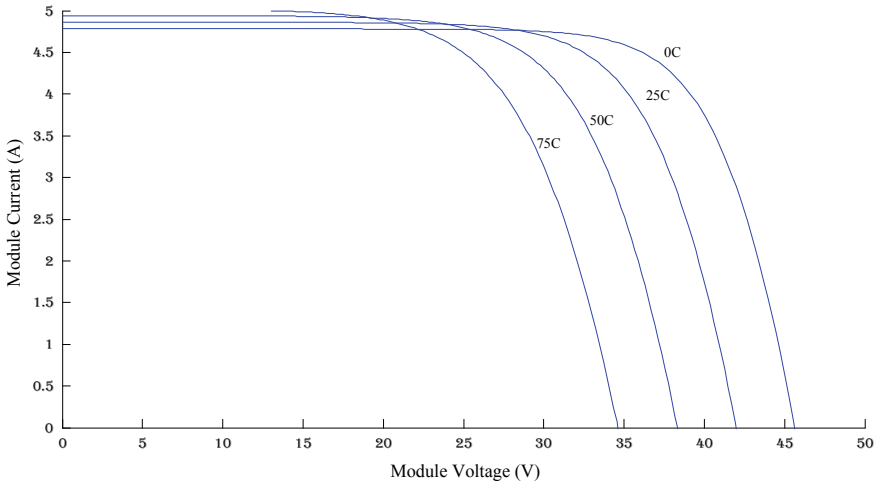


Fig. 2 I–V characteristics for four temperatures level

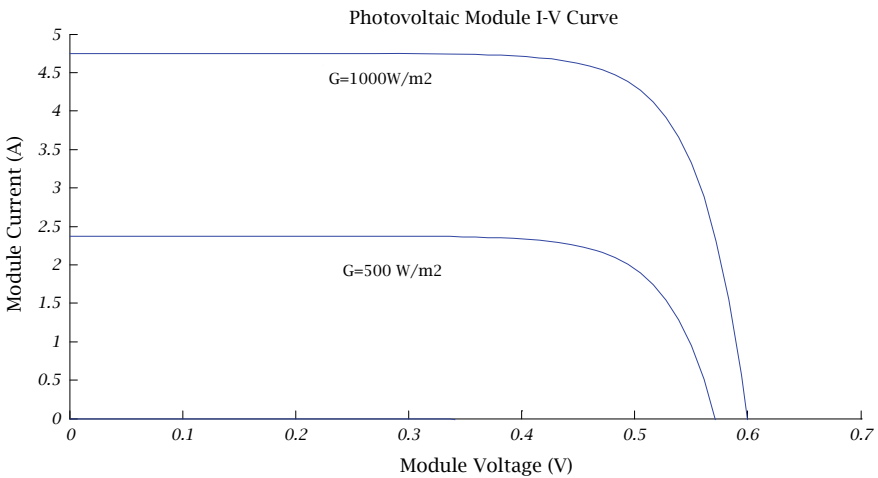


Fig. 3 I–V characteristics for a PV cell

3.1 Simulink Block Diagram

For the simulation we used real-time, temperature and radiation values are taken which was recorded on date July 13, 2017. The variation in temperature is shown in Fig. 4. This data was discrete in nature for getting continuous curve for simulation purpose and cubic spline curve was fitted. The model developed in SIMULINK platform for the comparative study of tracking system has been presented in Fig. 5.

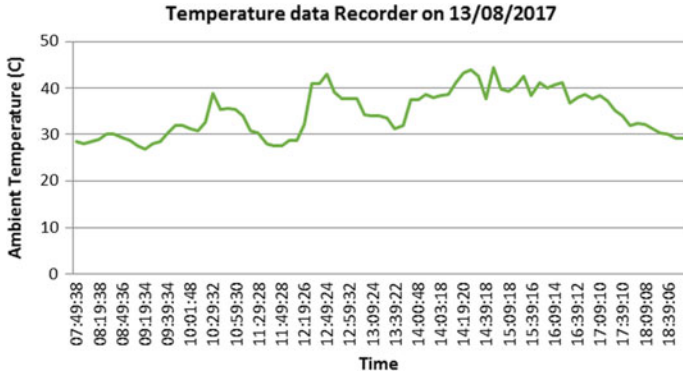


Fig. 4 Variation in temperature dated on August 13, 2017

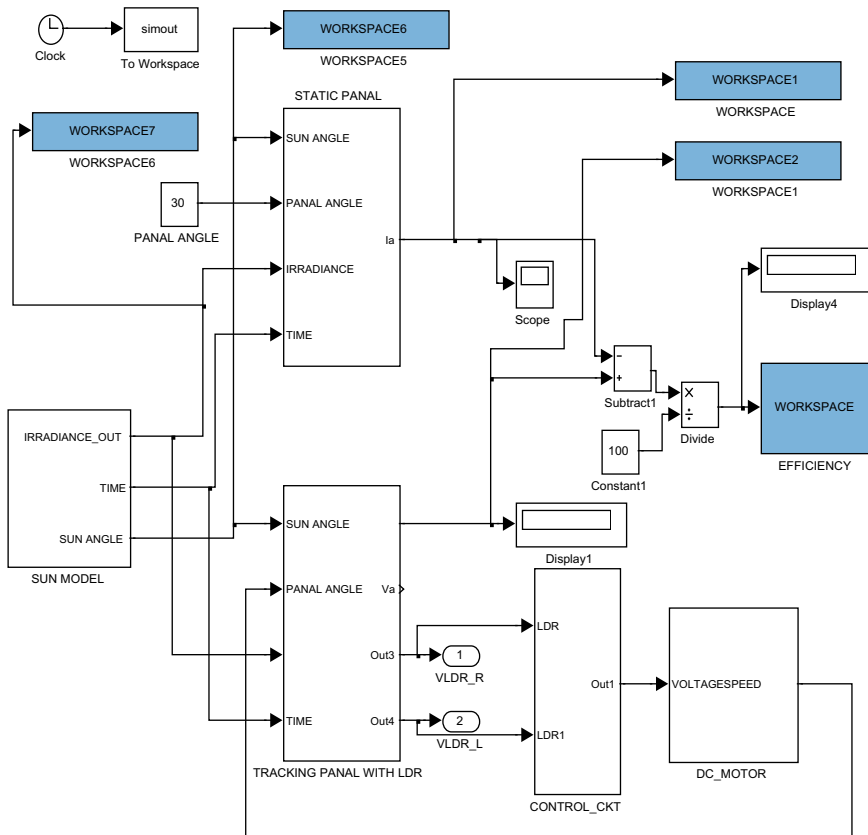


Fig. 5 SIMULINK model for comparative study

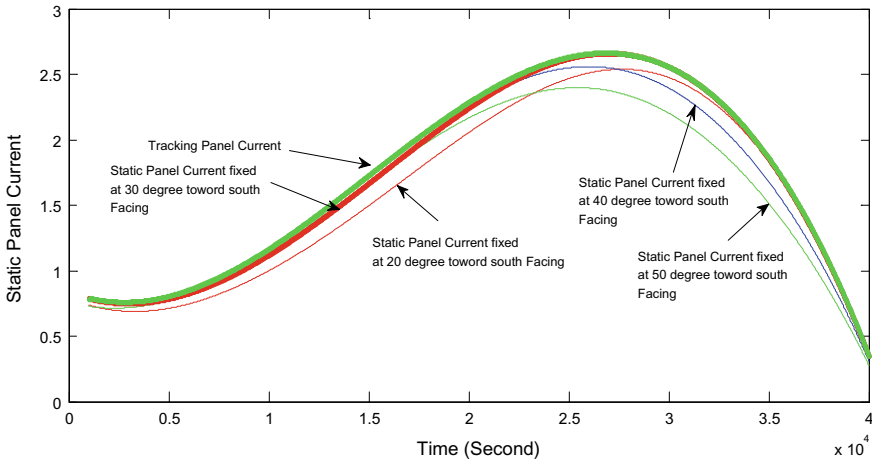


Fig. 6 Variation in static current with time for different angular positions of solar panel

4 Simulation Results and Discussion

4.1 Elevated Tracking Results

Figure 6 shows the simulation results obtained due to variation in the sun path in the elevated direction (North-South). The static panel was fixed at 29° toward south for getting the maximum irradiance from the sun. Here we neglected the effect of azimuthal tracking (East-West). Figure 6, shows simulation results between tracker panel current and static panel current, Assume that a static panel was tilted at different angles like 30° , 60° , and 90° south facing. The comparative results are shown in different colors and bold green line presented the results obtained from tracking system. There is gain of energy 14% as compared to static power plants. The sun changes its position 47° in whole year; therefore, static SPV system is tilted approximately 22° toward south and depends on geographical region.

4.2 Azimuthal Tracking Results

Figure 7 presents the simulation results of tracking SPV solar system compared with static SPV solar system with respect to time at different angles of static system. The results shown by red line when static panel is tilted at 45° , blue line shows the variation in current when static panel is tilted at 60° , green line presents when static system is tilted at 90° . The bold green line shows the variation in current getting from tracking solar system.

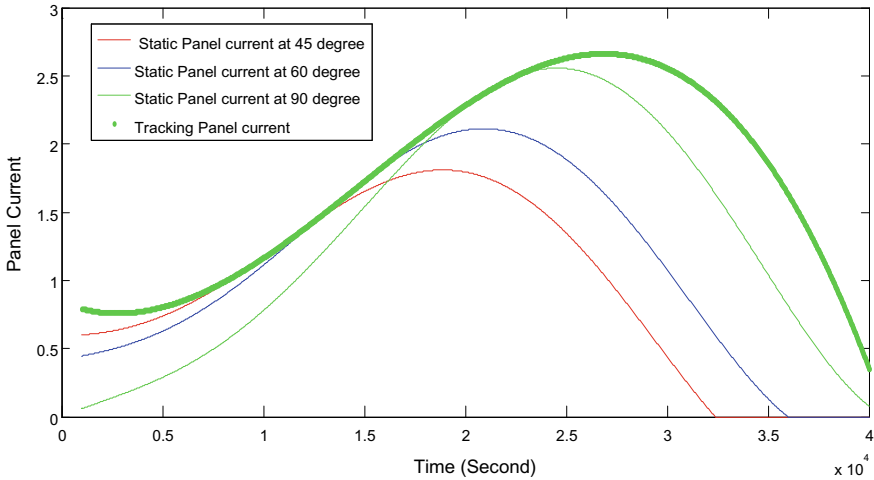


Fig. 7 Variation in static current due to changes in the angular position of fixed panel

5 Conclusion

The simulation results show that SPV system with sun tracker can produce more energy as compared to the static SPV solar system (without sun tracker). The simulation results shows that the efficiency of a solar power plant can be improved by 37% by implementing the single-axis sun tracking system, which provides rotation from east to west (azimuthal) to the solar panel. Moreover, the efficiency of a solar power plant can also be further improved by 14% by an appropriate inclusion of an elevated sun tracking system. These simulation results are also compared with the case of static solar power plant.

References

1. Koutroulis E, Kalaitzakis K, Voulgarias NC (2001) Development of a microcontroller based photovoltaic maximum power point tracking control system. *IEEE Trans Power Electron* 16(1):46–54
2. Piao ZG, Park JM, Kim JH, Cho GB, Baek HL (2005) A study on the tracking photovoltaic system by program type. In: Proceedings of the eight international conference on electrical machines and systems, 2005. ICEMS 2005, vol 2, 27–29 Sept 2005, pp 971–973
3. Wu TF, Shen CL, Nein HS, Li GF (2005) A single-phase 3 W Inverter with grid connection and active power filtering based on nonlinear programming and fast-zero-phase detection algorithms. *IEEE Trans Power Electron* 20:218–226
4. Solar Tracker Drive Types http://en.wikipedia.org/wiki/Solar_tracker
5. Saha S, Sundarsingh, VP (1996) Novel grid-connected photovoltaic inverter. In: in IEEE proceedings on generation, transmission and distribution, vol 143, pp 219–224
6. Villalva MG, Ruppert E (2009) Analysis and simulation of the P&O MPPT algorithm using a linearized photovoltaic array model. In: Proceedings 35th annual conference of the IEEE industrial electronics society, IECON, pp 231–236

Performance Evaluation and Quality Analysis of Line and Node Based Voltage Stability Indices for the Determination of the Voltage Instability Point



Pradeep Singh, Jyotsna Singh and Rajive Tiwari

Abstract The online assessment of voltage stability state of the power system plays a vital role in the reliable operation as well as uninterrupted supply. It also assists the system operator to undertake improved preventive actions before the system collapses. Various line and node based voltage stability indices have been developed and investigated to calculate the available reactive power margin and identify weak nodes in the power system. The main objective of this paper is to demonstrate intuitive potential of node based indices over line based voltage stability indices. Six well-established line voltage stability indices, viz., LCPI, L_{mn} , FVSI, LQP, L_p , MLI, and L_s are rigorously investigated under diversified loading conditions and compared with node based L -index. The results indicate that the L -index is superior to line based voltage stability indices. The paper also highlights the basic flaws of line based voltage stability indices in identifying the weak node and area of the power systems.

Keywords Voltage stability · Line-based VSI · Node-based VSI · Voltage stability margin · Voltage collapse

1 Introduction

The incessant increase in demand and present trends toward competitive business environment have resulted in complex interconnected power system, which forced to operate closer to limits of stability. Consequently, there is a high probability of voltage instability or collapse [1]. Many voltage stability indices have been developed to determine the distance between the current operating state and voltage collapse point to give fair warning to operator to take preventive action, if required. These indices are based on eigenvalue or singularity indices [2, 3], PV method [4, 5], sensitivity

P. Singh (✉) · J. Singh · R. Tiwari
Malaviya National Institute of Technology Jaipur, Jaipur, India
e-mail: psn121988@gmail.com

© Springer Nature Singapore Pte Ltd. 2020
A. Kalam et al. (eds.), *Intelligent Computing Techniques for Smart Energy Systems*,
Lecture Notes in Electrical Engineering 607,
https://doi.org/10.1007/978-981-15-0214-9_41

indices [6], Thevenin equivalent/impedance [7], line loadability indices [8–15], node indices [16], etc.

Extensive work has been addressed on line loadability and node based indices due to less computational efforts and time as compared to other existing approaches. Line and node based indices indicate voltage stability on the basis of weak lines and nodes, respectively. Venkatesh et al. proposed maximum loadability index (MLI) which gives the estimate of percentage of additional load in terms of existing load that can be supplied by line before reaching to the point of maximum loadability [8]. Yu et al. developed line loadability index (L_s) which is capable of identifying voltage stability and line loadability margin [9]. In [10], voltage stability index (L_{mn}) based on power flow through single line is proposed. This work is further extended in [12] to predict areas prone to the voltage collapse in power system using L_p . Mohamed et al. proposed line stability factor (LQP) to indicate proximity to voltage collapse [13]. In [14], fast voltage stability index (FVSI) is proposed and contingency analysis is performed to rank the severe lines. Authors in [10, 13, 14] developed indices with respect to reactive power flow which significantly affect the voltage stability. Tiwari et al. further asserted that the voltage stability is sensitive to the direction of active and reactive power flows and should be included in the formulation of index [15]. Kessel et al. developed L -index to predict the weak nodes using power flow solution [16].

Aforementioned literature enlisted various indices based on algebraic equations of line and node of the power system. However, comparative analysis of these indices based for different loading conditions and topological changes have not been examined thoroughly in literature so far. To address this goal, this paper attempts to present an analytical study to enumerate the strength and limitation of indices based on line and node. Different loadings are considered with the addition of fictitious bus at different locations in two-bus system.

2 Existing Line and Node Based Voltage Stability Indices

In this section, widely known voltage stability indices are briefly discussed to validate the conclusion in a broader spectrum.

2.1 Maximum Loadability Index (MLI)

The MLI is proposed by Venkatesh et al. [8] based on quadratic equation of voltage. It can be expressed as follows:

$$\text{MLI} = \frac{V_i^2 \left[-(r_{ij} P_{ij} + x_{ij} Q_{ij}) + \sqrt{(r_{ij}^2 + x_{ij}^2)(P_{ij}^2 + Q_{ij}^2)} \right]}{2(x_{ij} P_{ij} - r_{ij} Q_{ij})^2} \geq 1 \quad (1)$$

where P_{ij} and Q_{ij} are real and reactive power flowing through the line, r_{ij} and x_{ij} are resistance and reactance of the transmission line, and V_i is the sending end voltage. MLI should be greater than unity to maintain the stability of the system. MLI of a line near to unity indicates that the line is close to its stability limit. From (1), it can be observed that if $x_{ij}P_{ij} = r_{ij}Q_{ij}$, i.e., $\phi = \theta$, then the MLI index loses its robustness mathematically because at this condition, denominator becomes zero.

2.2 Loadability Index (L_p)

The L_p index is proposed by Moghavvemi and Faruque [12]. It can be represented as follows:

$$L_p = \frac{4r_{ij}(r_{ij}^2 + x_{ij}^2)P_{ij}}{[x_{ij} \sin \theta_{ij} - r_{ij} \cos \theta_{ij}]^2 V_i^2} \leq 1 \quad (2)$$

All variables are same as explained in Sect. 2.1. It varies from 0 (no load) to 1 (maximum loading) and its value should be less than unity for stability of the system. From (2), it can be observed that when $P_{ij} \leq 0$, this index becomes zero or negative, which indicates that the line is always secure.

2.3 Line Loadability Index (L_s)

This index, proposed by Yu et al., evaluates the voltage stability and available loading margin of line [9]. The line with minimal L_s is considered to be weakest line and corresponding bus is weakest bus. The L_s is defined as

$$L_s = \frac{V_i^2}{2 \left[r_{ij}P_{ij} + x_{ij}Q_{ij} + \sqrt{(r_{ij}^2 + x_{ij}^2)(P_{ij}^2 + Q_{ij}^2)} \right]} \geq 1 \quad (3)$$

where variables are same as explained in Sect. 2.1. L_s should be greater than unity to maintain the voltage stability of the system.

2.4 Line Stability Index (L_{mn})

The line stability index utilizes the concept of power flow through single line and it has been proposed by Moghavvemi et al. [10]. This index can be expressed as

$$L_{mn} = \frac{4Q_j x_{ij}}{[V_i \sin(\theta - \delta)]^2} \leq 1 \quad (4)$$

where $\delta = \delta_i - \delta_j$ is the phase difference of phase angles of sending and receiving end bus voltage, θ is impedance angle of line, Q_j is reactive power of receiving end bus, and rest of the variables are same as explained in Sect. 2.1. L_{mn} should be less

than unity for stable condition. This index has been derived by considering the effect of reactive power flow only. Also, the line resistance and charging capacitance have been neglected. The shortcoming of this index is that when $Q_j < 0$, it indicates that the respective line, and thus the system, is always secure at that particular condition.

2.5 Line Stability Factor (LQP)

The LQP index is proposed by Mohamed et al. and can be defined as [13]

$$\text{LQP} = 4 \left(\frac{x_{ij}}{V_i^2} \right) \left(\frac{x_{ij} P_i^2}{V_i^2} + Q_j \right) \leq 1 \quad (5)$$

where P_i is real power at the sending end while other variables are same as explained in earlier section. The line resistance and charging capacitance have been not accounted during formulation of this index.

2.6 Fast Voltage Stability Index (FVSI)

The FVSI is proposed by Musirin et al. to reduce the computational efforts [14]. It is formulated as follows:

$$\text{FVSI} = \frac{4Z_{ij}^2 Q_j}{V_i^2 x_{ij}} \leq 1 \quad (6)$$

where Z is impedance of line between two buses and other variables are same as explained in earlier sections. FVSI close to unity indicates that the system is operating near to its maximum loadability limit. This index also suffers from the same problem as L_{mn} .

2.7 Line Collapse Proximity Index (LCPI)

LCPI index is proposed by Tiwari et al. [15] to account all parameters of the transmission line. The magnitude and relative direction of active and reactive power flows are also considered to accurately predict the voltage collapse. It can be defined as

$$\text{LCPI} = \frac{4A \cos \alpha (P_j B \cos \beta) + Q_j B \sin \beta}{(V_i \cos \delta)^2} \leq 1 \quad (7)$$

LCPI should be less than unity to maintain the stability of the system.

2.8 L-Index

The L -index is proposed by Kessel and Glavitsch [16] and it can be defined as

$$L = \max_{j=\alpha_L} \{L_j\} = \max_{j=\alpha_L} \left| 1 - \sum_{i \in \alpha_G} F_{ij} \frac{V_i}{V_j} \right| \leq 1 \tag{8}$$

where $F_{ij} = -[Y_{LL}]^{-1}[Y_{LG}]$. α_L is set of consumer nodes and α_G is set of generator nodes. The L -index should be less than unity to maintain the stability of the system.

3 Illustrative Example

Let’s consider a two-bus system as shown in Fig. 1 with buses 1 and 2. Bus 2 is assumed to be a load bus with $P_2 + jQ_2 = 0.5 + j1 p.u$. These two buses are connected through a transmission line of $r_{12} + jx_{12} = 0.05 + j0.1 p.u$. impedance and shunt admittance is assumed zero. In this test system, minimum and maximum reactive power limits of generator have not been accounted.

To discriminate the potential of line and node based voltage stability indices, some well developed line based voltage stability indices, viz., LCPI [15], L_{mn} [10], FVSI [14], LQP [13], L_p [12], MLI [8], L_s [9], and most popular node based voltage stability index, i.e., L -index [16] are considered for investigation purpose. This section investigates and presents simulation results for two-bus test system with three different loading conditions where λ denotes the loading level.

Table 1 presents the results for increase in both active and reactive load with constant power factor. It is observed that all line stability indices except MLI have similar values. For this case, power factor angle is equal to impedance angle. As discussed in Sect. 2.1, MLI can’t be calculated at $\phi = \theta$ as the denominator becomes zero.

Table 2 shows the results for increase in active load only. From Table 2, the ineffectiveness of FVSI for identifying the voltage collapse condition is observed. For all



Fig. 1 Systematic two-bus system

Table 1 Comparison of indices for increase in both active and reactive load

λ	Node	LCPI [15]	L_{mn} [10]	FVSI [14]	LQP [13]	L_p [12]	MLI [8]	L_s [9]	L [16]
1.00	2	0.5000	0.5000	0.5000	0.4100	0.5000	NA	2.0000	0.1716
1.50	2	0.7500	0.7500	0.7500	0.6225	0.7500	NA	1.3333	0.3333
2.00	2	1.0000	1.0000	1.0000	0.8400	1.0000	NA	1.0000	1.0000

loading condition, it always indicates a constant value 0.5 because in the formulation of FVSI, only reactive power is considered. In this case, LCPI [15], MLI [8], L_s [9], and L [16] indices are capable to identify the voltage collapse condition while remaining indices fail. It is observed from Table 2 and Table 3 that an increase in either active or reactive load makes $\phi \neq \theta$, so MLI can be calculated and is equal to index L_s .

Table 3 shows the results for increase in reactive load only. In this case, FVSI prematurely exceeds its critical value, i.e., 1 indicating that the system has already collapsed. Conversely, indices LQP and L_p fail to reach their critical value. From Tables 1, 2, and 3, it can be concluded that all indices except L_{mn} , FVSI, LQP, and L_p show actual state of voltage stability for all loading conditions.

3.1 With One Fictitious Bus in the Middle of the Transmission Line

In this subsection, a fictitious bus 3 is assumed in the middle of the transmission line and the line impedance becomes half. All other network parameters are kept unchanged. It can be observed from Table 4 that the performance of all line voltage stability indices is affected. For the same loading level, $\lambda = 2$, the value of LCPI changes from 1 to 0.8889 that shows sufficient loading margin is available at maximum loading point. Only node based voltage stability index L -index is capable to identify voltage collapse condition in this case. The value of L -index is same as it is in Table 1 because the creation of the fictitious bus results in topological change only while network parameters remain unchanged. It proves that node based index is unaffected by topological change in the system.

The simulation results for increase in active and reactive load separately are presented in Tables 5 and 6, respectively. It is observed that among all line based voltage

Table 2 Comparison of indices for increase in active load only

λ	Node	LCPI [15]	L_{mn} [10]	FVSI [14]	LQP [13]	L_p [12]	MLI [8]	L_s [9]	L [16]
2.00	2	0.6023	0.5343	0.5000	0.4400	0.7958	1.6228	1.6228	0.2388
4.00	2	0.8406	0.6672	0.5000	0.5600	0.9987	1.1111	1.1111	0.5367
4.6601	2	0.9808	0.8465	0.5000	0.6172	0.8835	1.0000	1.0000	0.9909

Table 3 Comparison of indices for increase in reactive load only

λ	Node	LCPI [15]	L_{mn} [10]	FVSI [14]	LQP [13]	L_p [12]	MLI [8]	L_s [9]	L [16]
1.25	2	0.6001	0.6157	0.6250	0.5100	0.5322	1.6638	1.6638	0.2260
1.75	2	0.8022	0.8334	0.8750	0.7100	0.6246	1.2392	1.2392	0.3910
2.2132	2	0.9997	0.9982	1.1066	0.8953	0.8838	1.0000	1.0000	0.9976

Table 4 Comparison of indices for two-bus system with one fictitious bus for increase in both active and reactive load

λ	Node	LCPI [15]	L_{mn} [10]	FVSI [14]	LQP [13]	L_p [12]	MLI [8]	L_s [9]	L [16]
1.00	3	0.2714	0.2714	0.2714	0.2201	0.2714	NA	3.6840	0.0790
	2	0.3726	0.3726	0.3726	0.3036	0.3726	NA	2.6840	0.1716
1.50	3	0.4375	0.4375	0.4375	0.3577	0.4375	NA	2.2857	0.1429
	2	0.4898	0.4898	0.4898	0.4014	0.4898	NA	2.0417	0.3333
2.00	3	0.7500	0.7500	0.7500	0.6225	0.7500	NA	1.3333	0.3333
	2	0.8889	0.8889	0.8889	0.7427	0.8889	NA	1.1250	1.0000

Table 5 Comparison of indices for two-bus system with one fictitious bus for increase in active load only

λ	Node	LCPI [15]	L_{mn} [10]	FVSI [14]	LQP [13]	L_p [12]	MLI [8]	L_s [9]	L [16]
2.00	3	0.3380	0.2961	0.2878	0.2418	0.4833	2.8986	2.8986	0.1072
	2	0.3655	0.3152	0.3043	0.2582	0.5343	2.6668	2.6668	0.2388
4.00	3	0.5385	0.4247	0.3842	0.3588	0.8210	1.7440	1.7440	0.2190
	2	0.4556	0.3513	0.3236	0.2966	0.7385	2.0514	2.0514	0.3475
4.6601	3	0.7245	0.6109	0.5309	0.5084	0.9488	1.3191	1.3191	0.3501
	2	0.7966	0.5886	0.4364	0.5146	0.9999	1.1456	1.1456	0.9909

Table 6 Comparison of indices for two-bus system with one fictitious bus for increase in reactive load only

λ	Node	LCPI [15]	L_{mn} [10]	FVSI [14]	LQP [13]	L_p [12]	MLI [8]	L_s [9]	L [16]
1.25	3	0.3340	0.3442	0.3465	0.2804	0.2920	2.9897	2.9897	0.1016
	2	0.3639	0.3759	0.3790	0.3069	0.3137	2.7435	2.7435	0.2260
1.75	3	0.4798	0.5062	0.5171	0.4180	0.3605	2.0726	2.0726	0.1639
	2	0.5408	0.5740	0.5910	0.4773	0.3829	1.8348	1.8348	0.3910
2.2132	3	0.7469	0.7760	0.8064	0.6552	0.5964	1.3322	1.3322	0.3350
	2	0.8793	0.9128	0.9812	0.7929	0.6335	1.1277	1.1277	0.9976

stability indices, only L_p index detects the collapse condition. When the reactive load is increased, all line based voltage stability indices fail but node index provides promising results.

3.2 With One Fictitious Bus at (3/4)th Length of the Transmission Line

Now, a fictitious bus 3 is assumed between the two buses 1 and 2 by dividing the length of transmission line in 3:1 ratio. Therefore, the line impedances becomes: $r_{13} + jx_{13} = 0.045 + j0.09 \text{ p.u.}$, $r_{32} + jx_{32} = 0.005 + j0.01 \text{ p.u.}$ In Table 7, the line indices show that the line 1–3 is critical, i.e., node 3 is going to collapse for further increase in loading. However, no load has been connected to bus 3. In the considered test system, load is connected at bus 2. Therefore, it is vulnerable to voltage collapse. The value of L -index at bus 2 approaches to 1, validating the susceptibility of bus 2 to voltage instability.

From Tables 7, 8, and 9, it can be observed that the line indices provide wrong information about the stressed/critical node. Therefore, the line based voltage stability indices are not reliable and accurate in identification of stressed node as well as weak area. In other words, the line indices are not capable to precisely identify the point from where voltage instability instigates. Therefore, the node based indices are more accurate and better than line based indices to identify the weak node area. Line based indices are preferred to find the critical lines of the system.

Table 7 Comparison of indices for two-bus system with one fictitious bus at (3/4)th length for increase in both active and reactive load

λ	Node	LCPI [15]	L_{mn} [10]	FVSI [14]	LQP [13]	L_p [12]	MLI [8]	L_s [9]	L [16]
1.00	3	0.4577	0.4577	0.4577	0.3746	0.4577	NA	2.1847	0.1518
	2	0.0663	0.0663	0.0663	0.0532	0.0663	NA	15.0754	0.1716
1.50	3	0.6975	0.6975	0.6975	0.5775	0.6975	NA	1.4337	0.2903
	2	0.1249	0.1249	0.1249	0.1005	0.1249	NA	8.0083	0.3333
2.00	3	0.9900	0.9900	0.9900	0.8312	0.9900	NA	1.0101	0.8182
	2	0.3306	0.3306	0.3306	0.2688	0.3006	NA	3.0250	1.0000

Table 8 Comparison of indices for two-bus system with one fictitious bus at (3/4)th length for increase in active load only

λ	Node	LCPI [15]	L_{mn} [10]	FVSI [14]	LQP [13]	L_p [12]	MLI [8]	L_s [9]	L [16]
2.00	3	0.5552	0.4912	0.4636	0.4043	0.7459	1.7610	1.7610	0.2101
	2	0.0866	0.0727	0.0722	0.0586	0.1402	11.2398	11.2398	0.2388
4.00	3	0.7969	0.6332	0.4983	0.5353	0.9978	1.1714	1.1714	0.4629
	2	0.1579	0.1018	0.0986	0.0851	0.3501	5.6353	5.6353	0.5367
4.6601	3	0.9588	0.8289	0.5511	0.6342	0.9392	1.0100	1.0100	0.8276
	2	0.2616	0.1604	0.1505	0.1401	0.5622	3.3220	3.2220	0.9909

Table 9 Comparison of indices for two-bus system with one fictitious bus at (3/4)th length for increase in reactive load only

λ	Node	LCPI [15]	L_{mn} [10]	FVSI [14]	LQP [13]	L_p [12]	MLI [8]	L_s [9]	L [16]
1.25	3	0.5523	0.5672	0.5747	0.4683	0.4883	1.8078	1.8078	0.1989
	2	0.0862	0.0896	0.0898	0.0720	0.0723	11.5853	11.5853	0.2260
1.75	3	0.7502	0.7821	0.8161	0.6621	0.5794	1.3251	1.3251	0.3389
	2	0.1425	0.1548	0.1559	0.1250	0.0916	6.9548	6.9548	0.3910
2.2132	3	0.9875	0.9965	1.0870	0.8813	0.8502	1.0102	1.0102	0.8184
	2	0.3221	0.3540	0.3615	0.2903	0.1786	3.0608	3.0608	0.9976

4 Conclusion

A comprehensive study on various line and node based stability indicators under different loading conditions on two different test cases has been presented. It is observed that node based stability indicator performs better in assessment of voltage stability state than line based voltage stability indicators. The line based voltage stability indices mislead in identifying weak nodes, area, and available power margin. Considering the demerits of line based indices, this study recommends node based voltage stability index for planning and monitoring the power system and to take preventive action.

References

1. Ajarapu V, Lee B (1998) Bibliography on voltage stability. IEEE Trans Power Syst 13(1):115–125
2. Canizares CA, De Souza AC, Quintana VH (1996) Comparison of performance indices for detection of proximity to voltage collapse. IEEE Trans Power Syst 11(3):1441–1450
3. Berizzi A, Bresesti P, Marannino P, Granelli G, Montagna M (1996) System-area operating margin assessment and security enhancement against voltage collapse. IEEE Trans Power Syst 11(3):1451–1462
4. Force T. 38.02. 11. CIGRE technical brochure. Indices predicting voltage collapse including dynamic phenomena
5. Nagao T, Tanaka K, Takenaka K (1997) Development of static and simulation programs for voltage stability studies of bulk power system. IEEE Trans Power Syst 12(1):273–281
6. Greene S, Dobson I, Alvarado FL (1997) Sensitivity of the loading margin to voltage collapse with respect to arbitrary parameters. IEEE Trans Power Syst 12(1):262–272
7. Chebbo A, Irving M, Sterling M (1992) Voltage collapse proximity indicator: behaviour and implications. In: IEE Proceedings C (generation, transmission and distribution), vol 139, pp 241–252. IET
8. Venkatesh B, Ranjan R, Gooi H (2004) Optimal reconfiguration of radial distribution systems to maximize loadability. IEEE Trans Power Syst 19(1):260–266
9. Yu J, Li W, Yan W (2008) Letter to the editor: a new line loadability index for radial distribution systems. Electr Power Compon Syst 36(11):1245–1252

10. Moghavvemi M, Omar F (1998) Technique for contingency monitoring and voltage collapse prediction. *IEE Proc Gener Transm Distrib* 145(6):634–640
11. Singh P, Tiwari R (2018) Distributed parameter based voltage stability index for identification of critical lines and voltage stability margin in power system. *Cogent Eng* 5:1515573
12. Moghavvemi M, Faruque M (2001) Technique for assessment of voltage stability in ill-conditioned radial distribution network. *IEEE Power Eng Rev* 21(1):58–60
13. Mohamed A, Jasmon G, Yusoff S (1989) A static voltage collapse indicator using line stability factors. *J Ind Technol* 7(1):73–85
14. Musirin I, AbdulRahman T (2002) On-line voltage stability based contingency ranking using fast voltage stability index (FVSI). In: *Transmission and distribution conference and exhibition 2002: Asia Pacific*. IEEE/PES, vol 2, pp 1118–1123. IEEE
15. Tiwari R, Niazi K, Gupta V (2012) Line collapse proximity index for prediction of voltage collapse in power systems. *Int J Electr Power Energy Syst* 41(1):105–111
16. Kessel P, Glavitsch H (1986) Estimating the voltage stability of a power system. *IEEE Trans Power Deliv* 1(3):346–354

Channel Estimation in Massive MIMO with Spatial Channel Correlation Matrix



Bijoy Kumar Mandal and Ankita Pramanik

Abstract The channel correlation matrix is a significant statistical measurement that must be accessible to estimate minimum mean square error (MMSE) channel state information (CSI) to execute pilot reassignment optimization in massive MIMO systems. The estimation error by the MMSE technique will be high if there is no prior knowledge of the channel. The channel correlation matrix is based on the temporal properties of the dynamic wireless channel and CSI. In this report, different distributions are proposed to update the spatial channel correlation matrix. The estimated correlation matrix is then used to predict the MMSE CSI in the perspective of the client terminal power in Gaussian, Rayleigh, and Laplacian channels.

Keywords Channel estimation · Massive MIMO · Pilot contamination · Spatial correlation matrix

1 Introduction

Massive multiple-input multiple-output (MIMO) is a scalable version of multiuser MIMO (MU-MIMO) that has an extensive number of base station (BS) antennas, which considerably enhance spectral efficiency by means of spatial multiplexing [1] and straightforward linear processing [2, 3] at the BS. In a real scenario, by reusing the pilots in different cells, the BS obtains channel state information (CSI) which causes pilot contamination [1]. The impact of pilot contamination can put an essential limit on the asymptotically attainable rate in massive MIMO systems in independent and identically distributed (i.i.d) Rayleigh fading channel [1], and recently in many works [4–6] pilot decontamination algorithms have been developed.

B. K. Mandal (✉) · A. Pramanik
Department of Electronics and Telecommunication Engineering,
IEST, Shibpur, West Bengal, India
e-mail: mandalbijoy24@gmail.com

A. Pramanik
e-mail: ankita@telecom.iiests.ac.in

© Springer Nature Singapore Pte Ltd. 2020
A. Kalam et al. (eds.), *Intelligent Computing Techniques for Smart Energy Systems*,
Lecture Notes in Electrical Engineering 607,
https://doi.org/10.1007/978-981-15-0214-9_42

Least squares (LS) and minimum mean squared error (MMSE) are the traditional algorithms to estimate CSI. With the knowledge of the channel correlation matrix, MMSE provides better results but prior knowledge of the channel increases complexity; so it is difficult to obtain. There is spatial and temporal correlation in practical channels. An essential parameter is provided by channel correlation matrix which is required for mitigation of pilot contamination and channel estimation. To obtain an exact estimate, a very large number of samples are required by sample covariance matrix. However, the temporally correlated wireless channel can be designed [7] as an autocorrelation function as needed by the Jakes model. To estimate the channel of massive MIMO for the subsequent period, the author [8] utilizes a combination of pilots, the temporal correlation, and sensed data.

In this report, a multi-cell scenario is considered with spatially correlated [3] channels among the pairs of BSs and UEs. In the previous work, it has been applied for single-cell scenarios with perfect CSI [9, 10]. The statistics of MMSE, element-wise minimum mean squared error (EW-MMSE), and LS channel estimators is derived and characterized. Using these estimates, we have compared the performance in different scenarios of the local scattering model.

The remaining part of the paper is organized as follows: In the succeeding section, the system model for uplink (UL) pilot transmission is provided along with the basic pilot sequence design. The MMSE estimator is derived and analyzed in Sect. 3. The impacts of spatial channel correlation and pilot contamination are exemplified in Sect. 4. Two low-complexity channel estimators are described and compared in Sect. 5. The simulation results are plotted and discussed in Sect. 6, and this paper is finally concluded in Sect. 7.

2 System Model for Uplink Pilot Transmission

A massive MIMO system is considered with L cells where each cell consists of one BS with M_j antennas that serve K single-antenna UEs. It is particularly important for BS j to have estimates of the channels from the UEs in cell j . The channel responses are utilized by BS j to process the UL and downlink (DL) signals. The information of the channel response is referred to as channel state information (CSI). The UL pilot signaling is the main method for CSI acquisition, where a predefined pilot signal is transmitted from an antenna and for every coherence block τ_p , samples are reserved. Each UE transmits a pilot sequence that spans these τ_p samples. The pilot sequence of UE k in cell j is denoted by $\phi_{jk} \in \mathbb{C}^{\tau_p}$. It is assumed to have unit-magnitude elements to attain a persistent power level, and this refers that $\|\phi_{jk}\|^2 = \phi_{jk}^H \phi_{jk} = \tau_p$. The elements of ϕ_{jk} are scaled by the UL transmit power as $\sqrt{p_{jk}}$ and then transmitted as the signal s_{jk} over τ_p UL samples, leading to receive UL signal $\mathbf{Y}_j^p \in \mathbb{C}^{M_j \times \tau_p}$ at BS j . This signal is given by

$$\mathbf{Y}_j^p = \underbrace{\sum_{k=1}^{K_j} \sqrt{p_{jk}} \mathbf{h}_{jk}^p \phi_{jk}^T}_{\text{Desired Pilots}} + \underbrace{\sum_{l=1}^L \sum_{\substack{i=1 \\ l \neq j}}^{K_l} \sqrt{p_{li}} \mathbf{h}_{li}^j \phi_{li}^T}_{\text{Inter-cell Pilots}} + \underbrace{\mathbf{N}_j^p}_{\text{Noise}} \quad (1)$$

where $\mathbf{N}_j^p \in \mathbb{C}^{M_j \times \tau_p}$ is the independent additive receiver noise with i.i.d. elements distributed as $\mathcal{N}_{\mathbb{C}}(0, \sigma_{UL}^2)$. \mathbf{Y}_j^p is the observation that BS j can utilize to estimate the channel responses. To estimate the channel of a particular UE, the BS needs to know which pilot sequence this UE has transmitted. This is why the pilots are deterministic sequences and the pilot assignment is typically made when the UE connects to the BS; for example, using a random access procedure.

Suppose, BS j wants to estimate the channel \mathbf{h}_{li}^j from an arbitrary UE i in the cell l . The BS can then multiply/correlate \mathbf{Y}_j^p with the pilot sequence ϕ_{li} of this UE, leading to the processed received pilot signal $\mathbf{y}_{jli}^p \in \mathbb{C}^{M_j}$, given which has the same dimension as \mathbf{h}_{li}^j . The k th UE in the BS's own cell can be modified as

$$\begin{aligned} \mathbf{y}_{jjk}^p = \mathbf{Y}_j^p \phi_{jk}^* &= \sqrt{p_{jk}} \mathbf{h}_{jk}^j \phi_{jk}^T \phi_{jk}^* + \sum_{\substack{k=1 \\ i \neq k}}^{K_j} \sqrt{p_{ji}} \mathbf{h}_{ji}^j \phi_{ji}^T \phi_{jk}^* \\ &+ \sum_{l=1}^L \sum_{\substack{i=1 \\ l \neq j}}^{K_l} \sqrt{p_{li}} \mathbf{h}_{li}^j \phi_{li}^T \phi_{jk}^* + \mathbf{N}_j^p \phi_{jk}^* \end{aligned} \quad (2)$$

The second and third terms in (2) represent interference and contain inner products of the form $\phi_{ji}^T \phi_{jk}^*$ between the pilot of the desired UE and the pilot of another UE i in the cell l . If the pilot sequence of two UEs is orthogonal (i.e., $\phi_{ji}^T \phi_{jk}^* = 0$), then the corresponding interference term in (2) vanishes and does not affect the estimation.

3 MMSE Channel Estimation

The channel is a realization of a random variable; thus, Bayesian estimators are desirable since they take the statistical distributions of the variables into account. The channel response $\mathbf{h}_{li}^j \sim \mathcal{N}_{\mathbb{C}}(0_{M_j}, \mathbf{R}_{li}^j)$. The minimum mean squared error (MMSE) estimator of \mathbf{h}_{li}^j is the vector $\hat{\mathbf{h}}_{li}^j$ that reduces the MSE $\mathbb{E} \left\{ \left\| \mathbf{h}_{li}^j - \hat{\mathbf{h}}_{li}^j \right\|^2 \right\}$.

Using a pilot book with mutually orthogonal sequences, the MMSE estimate of the channel \mathbf{h}_{li}^j based on the observation \mathbf{Y}_j^p in (1) is

$$\hat{\mathbf{h}}_{li}^j = \sqrt{p_{li}} \mathbf{R}_{li}^j \boldsymbol{\Psi}_{li}^j \mathbf{y}_{jli}^p \quad (3)$$

The estimation error $\tilde{\mathbf{h}}_{li}^j = \mathbf{h}_{li}^j - \hat{\mathbf{h}}_{li}^j$ has the correlation matrix $\mathbf{C}_{li}^j = \mathbb{E} \left\{ \tilde{\mathbf{h}}_{li}^j (\tilde{\mathbf{h}}_{li}^j)^H \right\}$, given by

$$\mathbf{C}_{li}^j = \mathbf{R}_{li}^j - p_{li} \tau_p \mathbf{R}_{li}^j \boldsymbol{\Psi}_{li}^j \mathbf{R}_{li}^j \quad (4)$$

This equation provides the mechanism to calculate the MMSE from any UE in the network to BS j .

Recall that the MMSE estimator minimizes the MSE of the channel estimate, which is expressed as

$$\mathbb{E} \left\{ \left\| \mathbf{h}_{li}^j - \hat{\mathbf{h}}_{li}^j \right\|^2 \right\} = \mathbb{E} \left\{ \left\| \tilde{\mathbf{h}}_{li}^j \right\|^2 \right\} = \mathbb{E} \left\{ \text{tr} \left(\tilde{\mathbf{h}}_{li}^j (\tilde{\mathbf{h}}_{li}^j)^H \right) \right\} = \text{tr}(\mathbf{C}_{li}^j) \quad (5)$$

To compare the estimation quality obtained with different estimation schemes in different scenarios, the normalized MSE (NMSE) defined as

$$NMSE_{li}^j = \frac{\text{tr}(\mathbf{C}_{li}^j)}{\text{tr}(\mathbf{R}_{li}^j)} \quad (6)$$

is a suitable metric since it measures the relative estimation error per antenna. The value of $NMSE_{li}^j$ is always between 0 (perfect estimation) and 1 (achieved by using the mean value of the variable, $\mathbb{E} \left\{ \mathbf{h}_{li}^j \right\}$, as the estimate).

4 Spatial Channel Correlation and Pilot Contamination

Spatial channel correlation and pilot contamination affect the overall performance of the MMSE estimator.

4.1 Impact of Spatial Correlation on Channel Estimation

The basic properties of channel estimation are best described when the estimation of the channel response of a UE is considered that has a unique pilot sequence. The estimation is then only affected by noise and not by interference.

When NMSE is a function of the angular standard deviation (ASD), the impact of spatial channel can be studied [11]. The error is smaller when the ASD is small (i.e., with high spatial correlation). For strongly spatially correlated channels, the estimation error can be two orders of magnitude smaller than that in the uncorrelated case.

4.2 Impact of Pilot Contamination on Channel Estimation

To specify the impact of pilot contamination, a scenario is considered where two UEs use the identical pilot sequence [12]. BS j estimates the channel of UE k in its own cell while UE i in cell l transmits the identical pilot. The mutual interference that these UEs cause during pilot transmission has two main consequences: The channel estimates become correlated and the estimation quality is reduced.

The UE angles play a key role when the BS is equipped with several antennas. The NMSE increases when the UEs have similar angles [13]. If the UEs' channels instead exhibit uncorrelated fading, the NMSEs are consistently larger than those under spatial correlation and also angle-independent. Hence, spatial channel correlation is helpful in practice to improve the estimation quality under pilot contamination.

5 EW-MMSE and LS Estimation Schemes

5.1 Element-Wise MMSE Channel Estimator

If the BS has no preexisting knowledge over the entire covariance matrices, the EW-MMSE estimator can be implemented as an alternative [14]. The EW-MMSE estimate of the channel from BS j to UE i in a particular cell l is

$$\hat{\mathbf{h}}_{li}^j = \bar{\mathbf{h}}_{li}^j + \sqrt{p_{li}} \mathbf{D}_{li}^j \mathbf{\Lambda}_{li}^j (\mathbf{y}_{jli}^p - \bar{\mathbf{y}}_{jli}^p) \tag{7}$$

where $\mathbf{D}_{li}^j \in \mathbb{C}^{M_j \times M_j}$ and $\mathbf{\Lambda}_{li}^j \in \mathbb{C}^{M_j \times M_j}$ are diagonal matrices with $\mathbf{D}_{li}^j = \text{diag} \left(\left[\mathbf{R}_{li}^j \right]_{mn} : m = 1, \dots, M_j \right)$ and $\mathbf{\Lambda}_{li}^j = \text{diag} \left(\left[\sum_{(l',i') \in p_{li}} p_{l',i'} \tau_p \mathbf{R}_{l',i'}^j + \sigma^2 \mathbf{I}_{m_j} \right]_{mn} : m = 1, \dots, M_j \right)^{-1}$.

5.2 Least-Square Channel Estimator

If the BS has no previous knowledge concerning \mathbf{R}_{li}^j and $\bar{\mathbf{h}}_{li}^j$, the non-Bayesian LS estimator is used to obtain the propagation channel estimation \mathbf{h}_{li}^j . The LS estimate can be specified as the vector of $\hat{\mathbf{h}}_{li}^j$ which minimizes $\left\| \mathbf{y}_{jli}^p - \sqrt{p_{li}} \tau_p \hat{\mathbf{h}}_{li}^j \right\|^2$, which in this case is

$$\hat{\mathbf{h}}_{li}^j = \frac{1}{\sqrt{p_{li}} \tau_p} \mathbf{y}_{jli}^p \quad (8)$$

The random variable of LS estimator and its estimation error are correlated and distributed as

$$\hat{\mathbf{h}}_{li}^j \sim \mathcal{N}_C \left(\frac{1}{\sqrt{p_{li}} \tau_p} \bar{\mathbf{y}}_{jli}^p, \frac{1}{p_{li} \tau_p} \left(\Psi_{li}^j \right)^{-1} \right) \quad (9)$$

This shows that the statistics are more complicated than when using the MMSE and EW-MMSE estimators. For example, the estimation error has nonzero mean, which needs to be accounted for when analyzing the communication performance.

6 Simulation Results

The estimation quality of the MMSE, EW-MMSE, and LS estimators are compared in the following figures, in terms of NMSE. A scenario is considered where BS j estimates the channel of its UE k while a UE in another cell transmits the identical pilot sequence. The effective SNR of the desired UE is varied from -10 to 20 dB while the interfering signal is assumed to always be 10 dB weaker. The local scattering model is considered with three different distributions: Gaussian angular distribution, Laplace distribution, and Rayleigh distribution with angular standard deviation (ASD) $\sigma_\varphi = 10^\circ$. The results are averaged over different nominal angles between 0° and 360° (Figs. 1, 2, and 3).

The above three figures show that the three estimators provide rather different NMSEs in different scenarios of local scattering model. From the above figures, it can be concluded that the MMSE estimator is systematically the best estimator in the Rayleigh local scattering model since it fully exploits the spatial channel correlation and hence this is the optimum. The EW-MMSE estimator provides decent estimation performance, but there is a substantial gap from the MMSE estimator—even at high SNR where the error floor (caused by pilot contamination) has a higher value. The LS estimator performs very poorly at low SNR where the NMSE is above 1. At higher SNRs, the LS estimator is comparable to the EW-MMSE estimator, but their respective error floors are different (if there is pilot contamination). The LS estimator

Fig. 1 NMSE in the estimation of a spatially correlated channel, based on the local scattering model with Gaussian angular distribution, for different estimators

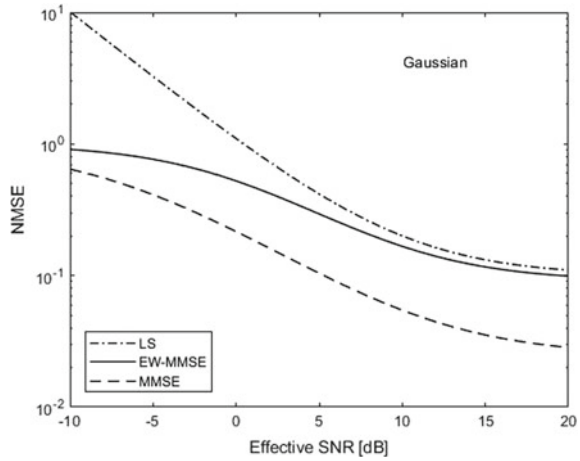
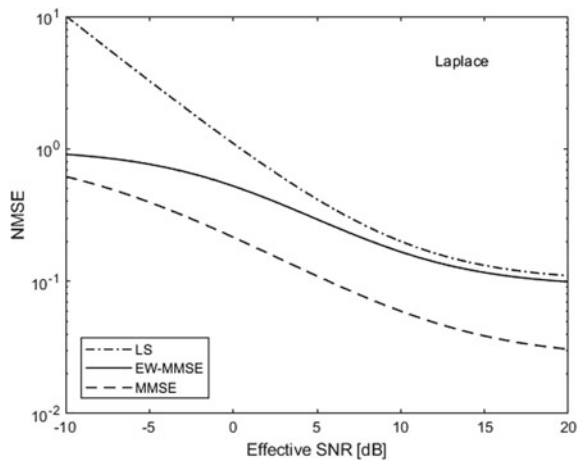


Fig. 2 NMSE in the estimation of a spatially correlated channel, based on the local scattering model with Laplace distribution, for different estimators

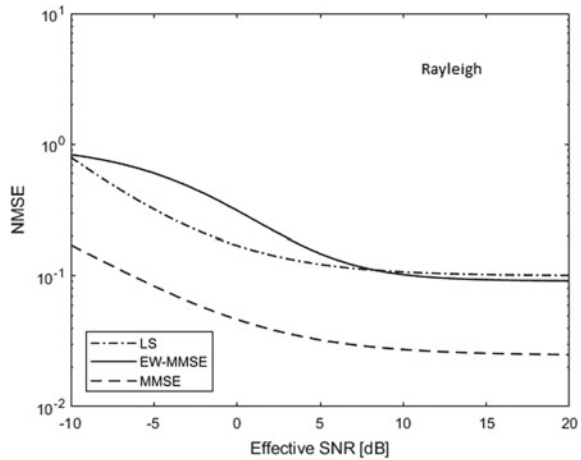


can provide decent estimates of the channel direction, $\mathbf{h}_{jk}^l / \|\mathbf{h}_{jk}^l\|$ while the lack of statistical information makes it harder to get the right scaling of the channel norm $\|\mathbf{h}_{jk}^l\|$.

7 Conclusion

The MMSE estimator utilizes the moments of the channel (i.e., the zero mean and the correlation matrix) as well as the fact that the channel can follow different distribution models such as complex Gaussian or Laplace or Rayleigh. In practice, the mean value and correlation matrix are rather easy to estimate while it is hard to validate

Fig. 3 NMSE in the estimation of a spatially correlated channel, based on the local scattering model with Rayleigh distribution, for different estimators



how close to any particular channel distribution they are. This is fortunately not a big deal because the estimator is also the LMMSE estimator for non-Gaussian channels with zero mean and the same known correlation matrix. Hence, the same estimation expression can be used for other types of channels, but the estimate and estimation error are only uncorrelated in this case (not independent), which affects the performance analysis.

References

1. Marzetta TL (2010) Noncooperative cellular wireless with unlimited numbers of base station antennas. *IEEE Trans Wirel Commun* 9(11):3590–3600
2. Yang H, Marzetta T (2013) Performance of conjugate and zero-forcing beamforming in large-scale antenna systems. *IEEE J Sel Areas Commun* 31(2):172–179
3. Hoydis J, ten Brink S, Debbah M (2013) Massive MIMO in the UL/DL of cellular networks: how many antennas do we need? *IEEE J Sel Areas Commun* 31(2):160–171
4. Muller R, Yin H, Gesbert D, Filippou MC, Liu Y (2013) Decontaminating pilots in massive MIMO systems. In: 2013 IEEE international conference on communications (ICC). IEEE, pp 3170–3175
5. Hu D, He L, Wang X (2016) Semi-blind pilot decontamination for massive MIMO systems. *IEEE Trans Wirel Commun* 15(1):525–536
6. Chen Z, Yang C (2016) Pilot decontamination in wideband massive MIMO systems by exploiting channel sparsity. *IEEE Trans Wirel Commun* 15(7):5087–5100
7. Jakes WC (1974) *Microwave mobile communications*. Wiley, New York
8. Li Y, Wang R, Chen Y, Zhu S (2017) Exploiting temporal channel correlation in data-assisted massive MIMO uplink detection. *IEEE Commun Lett* 21(2):430–433
9. Zhang J, Wen C-K, Jin S, Gao X, Wong K-K (2013) On capacity of large-scale MIMO multiple access channels with distributed sets of correlated antennas. *IEEE J Sel Areas Commun* 31(2):133–148
10. Tataria H, Smith PJ, Greenstein LJ, Dmochowski PA, Matthaiou M (2017) Impact of line-of-sight and unequal spatial correlation on uplink MU-MIMO systems. *IEEE Wirel Commun Lett* 6(5):634–637

11. Kay SM (1993) Fundamentals of statistical signal processing: estimation theory. Prentice Hall
12. Huh H, Caire G, Papadopoulos H, Ramprasad S (2012) Achieving “massive MIMO” spectral efficiency with a not-so-large number of antennas. *IEEE Trans Wirel Commun* 11(9):3226–3239
13. Yin H, Gesbert D, Filippou M, Liu Y (2013) A coordinated approach to channel estimation in large-scale multiple-antenna systems. *IEEE J Sel Areas Commun* 31(2):264–273
14. Shariati N, Björnson E, Bengtsson M, Debbah M (2014) Low-complexity polynomial channel estimation in large-scale MIMO with arbitrary statistics. *IEEE J Sel Topics Signal Process* 8(5):815–830

A New Array Reconfiguration Scheme for Solar PV Systems Under Partial Shading Conditions



Malisetty Siva Sai Nihanth, N. Rajasekar, Dhanup. S. Pillai
and J. Prasanth Ram

Abstract Partial shading on photovoltaic panels reduces the output power of the PV modules. Due to this P–V curve experiences multiple peaks which makes the maximum power point tracking complex. The row currents are different when the panel experiences partial shading. In the paper, a method is proposed to disperse the shade uniformly along the panel which increases the output power through physical relocation. The method proposed allows the shade to get dispersed all over the array and thus the losses due to mismatch are reduced. The characteristics of the TCT connection are compared with the proposed method. The methodology is performed for the 9×9 array for two shading patterns. Finally, simulations on every case are carried out and the characteristics are plotted. The obtained results have better output than the existing TCT methodology.

Keywords Partial shading · Mismatch loss

1 Introduction

The depletion of the nonrenewable energy sources is taking place at a faster pace which results in the increased importance for renewable sources of energy day by day. The solar energy is gaining its importance as it is a free source of energy. It has

J. Prasanth Ram

Department of Electrical and Electronics Engineering, New Horizon College of Engineering (NHCE), Bengaluru 560103, India
e-mail: jkprasanthram@gmail.com

M. S. S. Nihanth · N. Rajasekar (✉) · Dhanup. S. Pillai
Solar Energy Research Cell (SERC), School of Electrical Engineering (SELECT),
Vellore Institute of Technology, Vellore, India
e-mail: natarajanrajasekar@gmail.com

M. S. S. Nihanth
e-mail: malisetty.nihanth@gmail.com

Dhanup. S. Pillai
e-mail: dhanup.research@gmail.com

© Springer Nature Singapore Pte Ltd. 2020
A. Kalam et al. (eds.), *Intelligent Computing Techniques for Smart Energy Systems*,
Lecture Notes in Electrical Engineering 607,
https://doi.org/10.1007/978-981-15-0214-9_43

many advantages compared to nonrenewable sources of energy [1, 2]. It has a wide range of application ranging from kilowatts to megawatts.

The output of solar panels depends on various conditions such as weather, environment, load type, and time within a day. Partial shading is one of the pertinent factors where efficiency effects. These conditions may occur due to various conditions such as dust accumulation, cloud obstruction, the shadow of buildings, and bird droppings [3, 4]. The partial shading conditions cause a disturbance in P–V characteristics. The output characteristics of PV arrays may have multiple peaks and reduced output power. Also, the MPPT algorithm may get stuck at a local maximum. The losses incurring from the partial shading are not in any manner proportional to the area which is shaded but it depends on the pattern of shading. It also depends on the type of array configuration, for example, TCT connection, series–parallel connection, bridge-linked connection, etc. [5]. Simultaneously overcoming the effect of partial shading of PV panels and to maximize the output without having multiple peaks in P–V characteristics different reconfiguration techniques is proposed. These reconfiguration techniques can be either physical relocation or Electrical Array Reconfiguration (EAR) [1, 2]. A physical relocation technique will relocate each module where shade is uniformly spread, whereas in EAR, the PV dynamic reconfiguration utilizing power electronic switches are used [6–10]. In [9] based on bubble sort method an adaptive scheme is proposed for shade dispersion; on the other hand in [7], Electrical Array Reconfiguration based on switching matrix generation is explained. These both methods require continuous switching to identify the optimal panel arrangement for the shade to be dispersed effectively. However, this procedure is time-consuming and complex process. Moreover, switching continuously leads to damage of switches. Exclusively, EAR method using the optimization techniques is proposed in [8–10]. In [8] the switching matrix is optimized using Newton–Raphson method, the Genetic Algorithm (GA) is proposed in [9] and Particle Swarm Optimization (PSO) which evolved recently is portrayed in [10]. EAR methods require advanced controllers and lot of switches for reasonable operation. All these above factors result in the complexity of EAR methods. In addition to EAR, there are many physical relocation methods proposed in the literature. In [11, 12] mathematical methods related to SuDoKu and Futoshiki puzzles are deployed for the physical relocation of the arrays. These both methods involve one-time rearrangement of modules in the array but have effective shade dispersion for the different shade patterns. The physical relocation involves laborious task of interconnections between panels in real-time execution. In addition to the previously mentioned puzzle solving methods, others like magic square and puzzle shade are also portrayed for shade dispersion of PV array. These methods [13, 14] proved effective to disperse shade in small PV systems but when applied for large PV arrays it really gets complex. A zig-zag method which performs both row and column-wise shade dispersion are propounded in [15]. However, the drawback of this method is, it suits only small PV arrays and its implementation for large PV arrays is not compatible. In [16] physical relocation scheme based on Dominance Square is proposed which can be applied to larger PV arrays as well. The row and column dispersion of this method resulted in achieving high power levels. In the method proposed, the current from each module is sensed during shading and

the electrical connections are altered in such a way that the row current difference of the panels is as low as possible and the output power increases. Also, the P–V characteristics curve has less local peaks. The type of connection used is TCT connection. For different partial shading patterns the P–V characteristics are plotted and compared with the SP and TCT connections.

2 System Description

2.1 Modeling of a Total Cross Tied TCT Connection

A TCT connection is a combination of both series and parallel connections. The advantage of cross ties is the life span of array is almost doubled and the power output increases. The row currents calculation in TCT interconnection is important to locate accurate Global Peak (GP) power. Considering a 3 × 3 PV array, the row current estimation for a TCT scheme is made. The output current for the given row is given as the sum of the current limits of the individual panels. Thus, the current limit calculation for any row in TCT can be calculated as

$$I_{Rn} = \sum_{n=1}^3 I_{1n} * g_{1n} \tag{1}$$

where “ I_{1n} ” is the current limit at full irradiance ($G_{1n} = G_0$) and $g_{1n} = \frac{G_{1n}}{G_0}$, G_{1n} is the isolation level ($n =$ column index). For the same 5 × 5 PV array, applying Kirchhoff’s Voltage Law, the array voltage of the TCT connected configuration for five rows is given by

$$V_{array} = \sum_{i=1}^3 V_i \tag{2}$$

where “ V_{array} ”—PV array voltage and “ V_i ”—the maximum array voltage of the panels at the “ i th” row. The current at each node in the array can be calculated by applying Kirchhoff’s Current Law and the total array current is given by

$$I_{array} = \sum_{j=1}^3 (I_{ij} - I_{(i+1)j}) = 0, i = 1, 2, 3 \tag{3}$$

3 Methodology

The method proposed mainly focuses to make the row currents difference as minimum as possible. This reconfiguration method followed is physical relocation based one-time relocation procedure. As this is a one-time arrangement, for various shade patterns are applied to the relocated array the row currents are calculated and the characteristics are plotted. In this methodology, we considered a 9×9 array. Each module is uniquely numbered with its corresponding row and column number. For example, if a module is in m th row and n th column it is named as “mn”. In this way, all the 81 modules in the array are represented by their corresponding row and column number. Rearranging the modules into their respective columns is based on the proposed technique. Under the uniform irradiation conditions, the row currents are similar. When the partial shade occurs will be a difference in the value of the row currents. Hence, the proposed method aims to produce the less row current difference such that the multiple peaks in the I–V and P–V characteristics are also reduced. The steps involved in the proposed method is given as follows:

Step 1: In a 9×9 PV the module is represented with “ij” where “i” is the row number and “j” is the column number. In the first step, module “11” is shifted in the central part of the array, i.e., in the fifth row and fifth column “55” of the array. This movement is fixed and the user can shift the module to only this location in the array.

Step 2: In the second step the “12” module is placed diagonally below the first shifted module, i.e., in the sixth row and sixth column “66” of the array and the first of the array. In the similar way the first row consists of “13”, “14”, and “15” are shifted to “77”, “88”, and “99” modules of the array, respectively.

Step 3: In the Step 3, module “16” has to be placed diagonally below the previously shifted element but after “99” module there are no modules below because it is the last row. During the shifting, if the module has to be placed after the row limit ($i > 9$), then it can be placed diagonally in the first row ($i = 1$). Therefore, “16” is shifted to the first row and first column “11” of the array. Similarly, the modules “17”, “18” and are shifted to the positions “22”, “33”, and “44”, respectively. Thus the first row is completely in a diagonal manner.

Step 4: Now the second row has to be shifted by following the above steps. The first module of second row “21” is shifted to the alternate downward position from the last shifted module of the first row, i.e., in the sixth row and fourth column “64” of the array. When a row is completely shifted the first module of next row has to be placed in the alternate downward position as discussed in this step.

Step 5: In this step the “22” module of the 9×9 arrays is placed diagonally below the previously shifted element, i.e., in seventh row and fifth column “75” of the array. In the similar manner, the module “23” and “24” are shifted to “86” and “97” of the array, respectively. This step is similar to the Step 2 of this methodology.

Step 6: This step is similar to the Step 3, after performing the previous Step (5) as there are no rows below, the module “25” is shifted to first row and eighth column “18” of the array. Similarly, the module “26” of the 9×9 array is placed in the

Fig. 1 Final displacement of panels in 9 * 9 array using the proposed method

16	52	91	43	82	34	78	25	61
62	17	53	92	44	83	35	71	26
27	63	18	54	93	45	84	36	72
73	28	64	19	55	94	46	85	37
38	73	29	65	11	56	95	47	86
87	39	74	21	66	12	57	96	48
49	88	31	75	22	67	13	58	97
98	41	89	32	76	23	68	14	59
51	99	42	81	33	77	24	69	15

second row and ninth column “29” of the array. In this process, the row limit ($i > 9$) so the module is placed in the first row of the array.

Step 7: The Step 7 consists of shifting the module “27” of the array diagonally below the previously shifted module. As there are no columns to the right of ninth column the module “27” is shifted to the third row and first column “31” of the array. In this step, the column limit is exceeded ($j > 9$) so the next module to be shifted is placed in the corresponding location of the first column. In the similar way, the modules “28” and “29” are shifted to the positions “42” and “53” of the array, respectively.

Step 8: The remaining modules of the array are shifted to their new position with the steps mentioned above in a diagonal manner. In this way the “81” modules are shifted with the above methodology as the modules are replaced physically in this method it is a physical relocation with one-time rearrangement. The finally displaced array by applying the proposed method is shown in the Fig. 1.

4 Simulation Results and Discussion

For evaluating the proposed physical relocation method, two shade patterns are considered: (1) short wide and (2) long wide. For the considered shade patterns, the results of the proposed method are compared with the SP and TCT methods in MATLAB/Simulink platform for a 9×9 PV array.

4.1 Pattern 1—Short Wide

For short wide pattern, four different irradiances (900, 600, 400, and 200 W/m²) are applied to the 9×9 array as shown in Fig. 2. The performance of the PV array can be well understood by the theoretical estimation of the row currents. The row current estimation for the TCT interconnection is explained below.

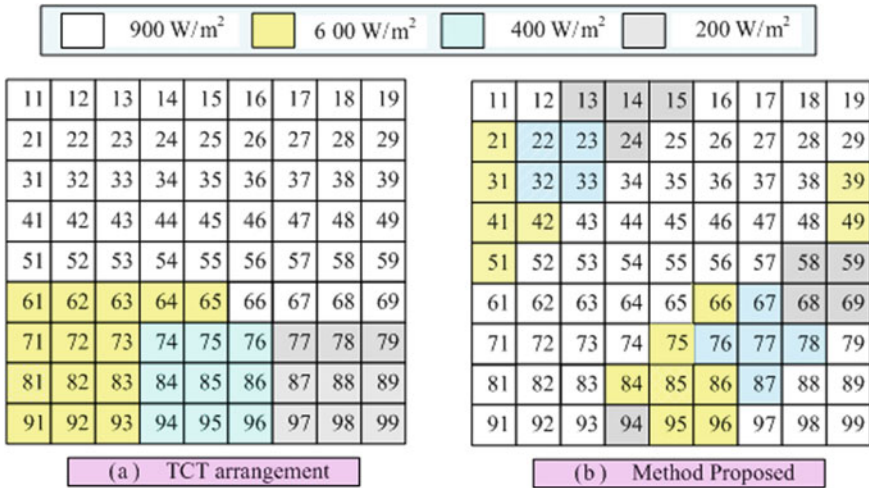


Fig. 2 Short wide case for shade pattern-1 a TCT and b method proposed

4.1.1 Row Current Calculation for TCT Arrangement

Let us consider “ I_m ” is the maximum current which can be extracted from a PV module. The row currents of the various rows in the TCT interconnection is measured as follows:

$$I_{R1} = \left(9 \times \left(\frac{G}{G_{STC}} \right) \times I_m \right) = \left(9 \times \left(\frac{900}{1000} \right) \times I_m \right) = 8.1I_m \quad (4)$$

As the irradiance in the first five rows is equal the row currents for the remaining rows can be written as

$$I_{R2} = I_{R3} = I_{R4} = I_{R5} = 8.1I_m \quad (5)$$

The row current of the sixth row of TCT connection can be written as

$$I_{R6} = \left(5 \times \left(\frac{600}{1000} \right) \times I_m \right) + \left(4 \times \left(\frac{900}{1000} \right) \times I_m \right) = 6.6I_m \quad (6)$$

The row currents of the seventh, eighth, and ninth rows of TCT connection can be written as

$$I_{R7} = \left(3 \times \left(\frac{600}{1000} \right) \times I_m \right) + \left(3 \times \left(\frac{400}{1000} \right) \times I_m \right) + \left(3 \times \left(\frac{200}{1000} \right) \times I_m \right) = 3.6I_m = I_{R8} = I_{R9} \quad (7)$$

4.1.2 Row Current Calculation for Method Proposed

The row currents for the method proposed after shade dispersion is obtained as follows:

First row:

$$I_{R1} = (6 \times (0.9) \times I_m) + (3 \times (0.2) \times I_m) = 6I_m \quad (8)$$

Second row:

$$I_{R2} = (5 \times (0.9) \times I_m) + ((0.6) \times I_m) + (2 \times (0.4) \times I_m) + ((0.2) \times I_m) = 6.1I_m \quad (9)$$

Third row:

$$I_{R3} = (5 \times (0.9) \times I_m) + (2 \times (0.6) \times I_m) + (2 \times (0.4) \times I_m) = 6.5I_m \quad (10)$$

Fourth row:

$$I_{R4} = (6 \times (0.9) \times I_m) + (3 \times (0.6) \times I_m) = 7.2I_m \quad (11)$$

Fifth row:

$$I_{R5} = (6 \times (0.9) \times I_m) + ((0.6) \times I_m) + (2 \times (0.2) \times I_m) = 6.4I_m \quad (12)$$

Sixth row:

$$I_{R6} = (5 \times (0.9) \times I_m) + ((0.6) \times I_m) + ((0.4) \times I_m) + (2 \times (0.2) \times I_m) = 5.9I_m \quad (13)$$

Seventh row:

$$I_{R7} = (5 \times (0.9) \times I_m) + ((0.6) \times I_m) + (3 \times (0.4) \times I_m) = 6.3I_m \quad (14)$$

Eighth row:

$$I_{R8} = (5 \times (0.9) \times I_m) + (3 \times (0.6) \times I_m) + ((0.4) \times I_m) = 6.7I_m \quad (15)$$

Ninth row:

$$I_{R9} = (6 \times (0.9) \times I_m) + (2 \times (0.6) \times I_m) + ((0.2) \times I_m) = 6.8I_m \quad (16)$$

By the row current calculation it can be noted that for the TCT connection the row currents range from 3.6 to 8.1 A. It is evident that there is a lot of difference in the row currents and it causes multiple peaks in I-V and P-V characteristics of the array.

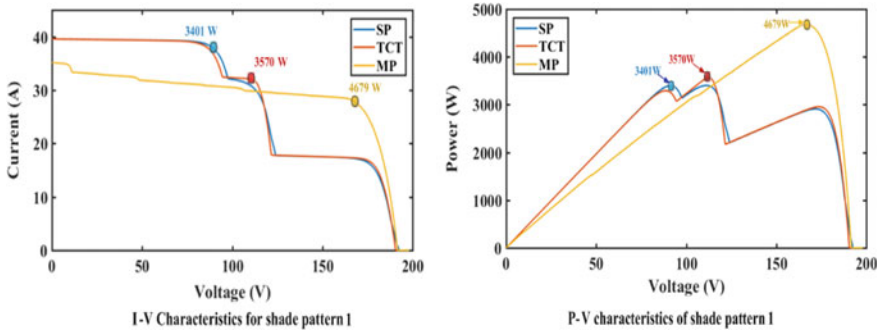


Fig. 3 I-V and P-V characteristics for SP, TCT, and proposed method for pattern-1

After the shade is dispersed by the proposed method the row currents range from 5.9 to 7.2 A. The row currents difference is reduced to a considerable extent with the proposed method. With the proposed technique higher row current is obtained at a nominal operating voltage of the PV array. The minimum value of row current obtained from the proposed method is 5.9 A, whereas from the TCT connection this value is 3.6 A. The I–V and P–V characteristics of the short wide pattern are shown in the Fig. 3. The corresponding power with respect to SP, TCT, and method proposed are 3401 W, 3570 W, and 4679 W, respectively. When compared to the TCT connection the proposed method gives more power of about 1.1 KW. It can be observed that the P–V curve of the method proposed has only a single peak and also it produces a smoother curve compared to SP and TCT methods.

4.2 Pattern 2—Long Wide

In the long wide shade pattern there occurs many bypasses in the TCT connection due to varied shade on the array. To obtain single peak and maximum power simultaneously from the array under this shade condition is not easy. The various irradiance values of this shade pattern are 900, 500, 600, 400 and 200 W/m². The shade profile for short wide for TCT and method proposed is shown in Fig. 4. With the proposed method smoothness in the I–V and P–V curves is obtained and a considerable amount of power is extracted from the PV array. The power obtained is 4046 W from the method proposed, whereas SP and TCT both give an equal amount of power of 3204 W. The method proposed gives a power of about 800 W more than the conventional TCT connection. This proves that the proposed method disperses shade effectively compared to the SP and TCT connections. The I–V and P–V characteristics of the long wide pattern are shown in Fig. 5.

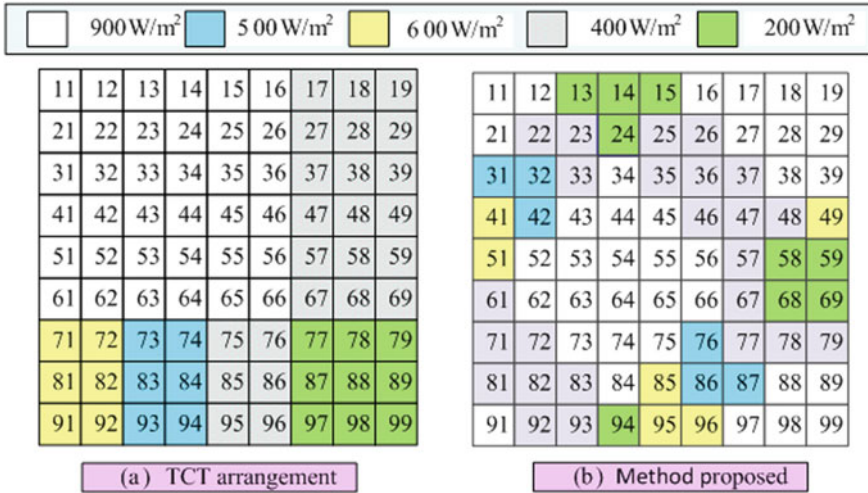


Fig. 4 Long wide case for shade pattern-1 a TCT and b method proposed

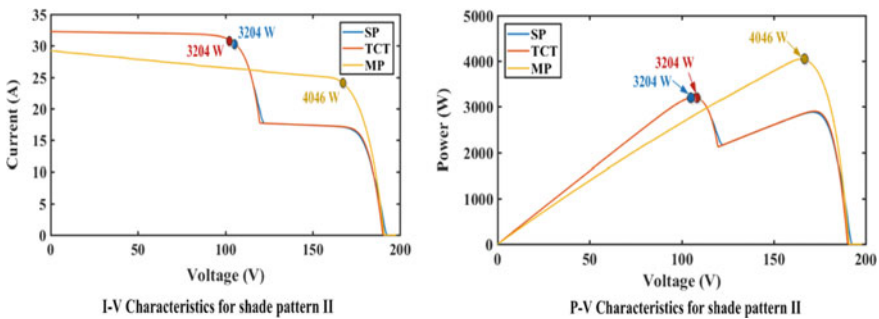


Fig. 5 I-V and P-V characteristics for SP, TCT, and method proposed for pattern-2

5 Conclusion

In this method, the shade dispersion is done by the proposed technique and physically relocating the modules. The final location of the modules is calculated by arranging them in the 9×9 matrix as per the methodology. The relocation is done physically across rows and columns which is a one-time arrangement. Through this method, the row current difference is reduced to a larger extent compared to TCT methods. The local maximums are reduced and the output power is increased. Further, the method is applied for two shade occurrences and in each of shade patterns, the proposed method has at least 800 W difference to the conventional TCT and SP interconnection ties. The performance is observed for numerous shading patterns which infer that position of the modules in this array arranging method shows better performance.

Acknowledgements The authors thank the VIT management for providing the necessary support to carry out the research work. Further, the authors would also like to thank the reviewers for providing the valuable suggestion to improve the manuscript.

References

1. Salam Z, Ahmed J, Merugu BS (2013) The application of soft computing methods for MPPT of PV system: a technological and status review. *Appl Energy* 107:135–148
2. Malathy S, Ramaprabha R (2017) Reconfiguration strategies to extract maximum power from photovoltaic array under partially shaded conditions. *Renew Sustain Energy Rev*
3. Pillai DS, Rajasekar N (2018) A comprehensive review on protection challenges and fault diagnosis in PV systems. *Renew Sustain Energy Rev* 91:18–40
4. Ram JP, Rajasekar N (2017) A new global maximum power point tracking technique for solar photovoltaic (PV) system under partial shading conditions (PSC). *Energy* 118:512–525
5. Gautam NK, Kaushika ND (2002) Reliability evaluation of solar photovoltaic arrays. *Sol Energy* 72(2):129–141
6. Alahmad M, Chaaban MA, Lau SK, Shi J, Neal J (2012) An adaptive utility interactive photovoltaic system based on a flexible switch matrix to optimize performance in real-time. *Sol Energy* 86(3):951–963
7. Velasco-Quesada G, Guinjoan-Gispert F, Piqué-López R, Román-Lumbreras M, Conesa-Roca A (2009) Electrical PV array reconfiguration strategy for energy extraction improvement in grid-connected PV systems. *IEEE Trans Ind Electron* 56(11):4319–4331
8. Wang YJ, Hsu PC (2011) An investigation on partial shading of PV modules with different connection configurations of PV cells. *Energy* 36(5):3069–3078
9. Deshkar SN, Dhale SB, Mukherjee JS, Babu TS, Rajasekar N (2015) Solar PV array reconfiguration under partial shading conditions for maximum power extraction using genetic algorithm. *Renew Sustain Energy Rev* 43:102–110
10. Babu TS, Ram JP, Dragičević T, Miyatake M, Blaabjerg F, Rajasekar N (2018) Particle swarm optimization based solar PV array reconfiguration of the maximum power extraction under partial shading conditions. *IEEE Trans Sustain Energy* 9(1):74–85
11. Rani BI, Ilango GS, Nagamani C (2013) Enhanced power generation from PV array under partial shading conditions by shade dispersion using Su Do Ku configuration. *IEEE Trans Sustain Energy* 4(3):594–601
12. Sahu HS, Nayak SK, Mishra S (2016) Maximizing the power generation of a partially shaded PV array. *IEEE J Emerg Sel Top power Electron* 4(2):626–637
13. Yadav AS, Pachauri RK, Chauhan YK, Choudhury S, Singh R (2017) Performance enhancement of partially shaded PV array using novel shade dispersion effect on magic-square puzzle configuration. *Sol Energy* 144:780–797
14. Yadav AS, Pachauri RK, Chauhan YK (2016) Comprehensive investigation of PV arrays with puzzle shade dispersion for improved performance. *Solar Energy* 31(129):256–285
15. Vijayalakshmy S, Bindu GR, Iyer SR (2016) A novel Zig-Zag scheme for power enhancement of partially shaded solar arrays. *Solar Energy* 31(135):92–102
16. Dhanalakshmi B, Rajasekar N (2018) Dominance square based array reconfiguration scheme for power loss reduction in solar Photo Voltaic (PV) systems. *Energy Convers Manag* 156:84–102

Adaptability Analysis of Particle Swarm Optimization Variants in Maximum Power Tracking for Solar PV Systems



B. G. Dharshan, N. Rajasekar and R. Srinivasa Sankarkumar

Abstract In upcoming years, energy generated through solar which plays a vital role in power generation has gained importance. The key problem in solar generation is to extract maximum power from solar photovoltaic module at all weather conditions. But due to partial shading conditions caused by bird droppings, soil accumulation and cloud formation, it leads to multiple local peaks making the tracking complex. Since, PSO has gained its significant popularity in the area, maximum power point tracking under partial shading conditions. Analysis of PSO and variants to observe their adaptability for different irradiance conditions such as uniform irradiance, strong shading and weak shading. In this article, a comparative study has been presented for different variants of PSO. The results are analysed based on power oscillation and catching peak through MATLAB simulations.

Keywords Particle swarm optimization (PSO) · Maximum power point tracking (MPPT)

1 Introduction

The never-ending demand for energy and depletion of non-renewable energy sources has led to the search of alternative forms of energy such as solar and wind. Amongst, the solar photovoltaic (PV) power is supercilious in the region of electrical power age. Though the exhaustion of coal and regular sources are contaminating the earth [1], the aggregate was introduced a limit that has come up to 450GW continuously since 2017, adequate enough to supply two per cent of the world's aggregate power utilization, in which PV framework contributes 98.4%. However, the primary hindrance for a photovoltaic framework is the power age fluctuation with the changing

B. G. Dharshan · N. Rajasekar (✉) · R. Srinivasa Sankarkumar
Solar Energy Research Cell, Vellore Institute of Technology, Vellore, India
e-mail: nrajasekar@vit.ac.in

© Springer Nature Singapore Pte Ltd. 2020
A. Kalam et al. (eds.), *Intelligent Computing Techniques for Smart Energy Systems*,
Lecture Notes in Electrical Engineering 607,
https://doi.org/10.1007/978-981-15-0214-9_44

natural factors, for example, illumination and temperature. Along these lines, to show signs of improvement of the photovoltaic framework, now, every PV framework is associated with a DC–DC converter executed with the most extreme power point tracker. There are various MPPT strategies that are accessible and each differs as per the number of sensors, cost of usage and unpredictability. Out of considerable number of strategies applied for partial shading conditions, PSO plays a vital role in tracking maximum power. PSO works based on the principle of communication and learning with updating of velocity and position vector [2–4]. The variants of PSO are

- (1) Comprehensive learning PSO.
- (2) Dynamic neighbourhood learning particle swarm optimizer.

The Comprehensive Learning PSO (CLPSO) was proposed as a pivotal variety of PSO that enhances different assortments of the masses by encouraging each molecule to pick different particles based on particular estimations. In the moral story that the best molecule, paying little heed to having the most critical health, does not continually offer an unrivalled impetus in every estimation. A solitary goal PSO called Dynamic Neighbourhood Learning Particle Swarm Optimizer (DNLPSO), which uses learning system whereby each other molecule chronicled best information is used to invigorate a molecule speed as in CLPSO [5]. Regardless, instead of CLPSO, in DNLPSO, the model molecule is looked for over a region. This technique enables the learner molecule to pick up from the chronicled information of its neighbourhood or from that of its own. Furthermore, the regions are made dynamic in nature, i.e. they are changed after particular intervals. This helps swarm to stay away from premature convergence.

2 System Description

Block diagram of a PV system, Fig. 1, consists of a 3×2 PV array directly connected to a DC–DC boost converter where the required duty ratio to the converter is given through an MPPT controller using current and voltage sensors to extract maximum power from the PV panel, then it is connected to a DC–AC converter which runs the AC load.

3 Modelling of PV Cell

The single-diode model of a PV cell demonstrates [5] that the current source is connected in parallel to the diode as shown in Fig. 1, where the light falling on the panel particularly correspondsto the output of the present source. Modelling of PV cell can be shown by a current source in parallel with the p – n crossing point which is connected with the photograph bearers made. Lighting up flow parameter related

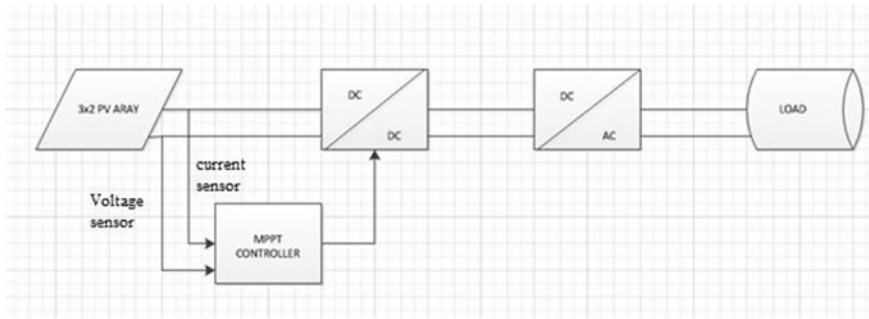


Fig. 1 Block diagram of a PV system with boost converter

to the photoelectric effect flow is the modify tendency inundation flow for the diode and n , the diode ideality factor.

Equation of the single-diode model

$$I = I_{PV} - I_D \tag{1}$$

$$I_D = I_S \left(e^{\frac{q(V+IR_s)}{nk_sT}} - 1 \right) \tag{2}$$

K_B —Boltzmann constant, q is charge is the absolute temperature of the $p-n$ intersection and V is the output voltage. The solar cell active area and solar irradiance corresponding to the illumination current related to the photoelectric impact related with the photoelectric impact [5]. The series resistance is added to improve the accuracy of the model; a solar cell with series resistance, which is known as a 1M4P model (four parameters, single component), considers the impact of contacts by methods for an arrangement opposition R_s . The unknown parameters of this model are R_s , I_{PV} and I_s ; after introducing the diode, the new diode current expression is given as

$$I_D = I_S \left(e^{\frac{q(V+IR_s)}{nk_sT}} - 1 \right) \tag{3}$$

Generally, 1M5P models are commercially used which are series and shunt connected. Shunt resistor will take account of the leakage current; R_{sh} , I_{PV} , I_s , n and R_s are the parameters of the current, Eqs. (4) and (5)

$$I = I_{PV} - I_D - I_{sh} \tag{4}$$

$$I = I_{PV} - I_S \left(e^{\frac{q(V+IR_s)}{nk_sT}} - 1 \right) - \frac{V + IR_s}{R_{sh}} \tag{5}$$

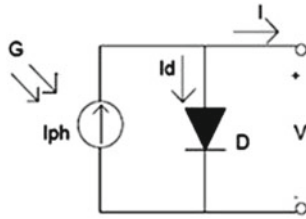


Fig. 2 PV cell model

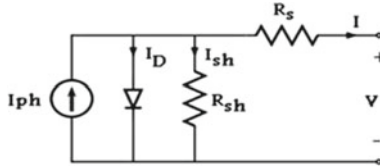


Fig. 3 Single-diode model

With increase in the shadow rate, there will be increase in series resistance as the shadow rate increases; in contrast, the leakage current and voltage drop in the contacts will be higher. When hot-spot apparition increases, the probability shunt resistance value decreases since it works as a load in reverse bias as shown in Figs. 2 and 3.

3.1 Characteristics of PV Module

The solar-based cell is a non-linear source, so understanding the traits of the PV module [6] are required to track the best power point. Any PV cell is photodiode, when n number of PV cells are related in parallel or course of action it makes a PV module. In Fig. 2, the model of a single PV module has been shown. In Fig. 4a, the IV curve has been shown, where V_{oc} , I_{sc} , V_{mpp} , I_{mpp} are open-circuit voltage, impedance, voltage at the most extraordinary power point and current at the maximum power point, respectively. From these IV curves, we can see the non-linear nature of the PV source because the PV system output depends on the load. Figure 4b demonstrates the PV curve, where P_{max} is the most extreme power.

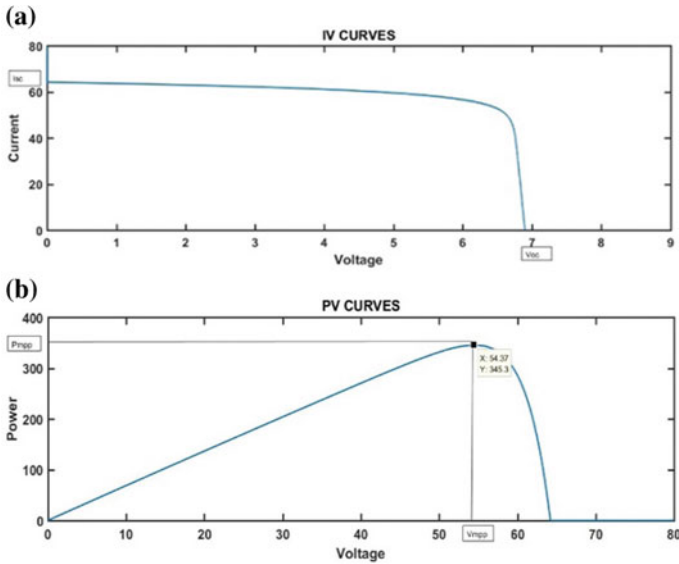


Fig. 4 a IV curve of a PV cell, b PV curve of a PV cell

3.2 Characteristics of PV Array Under Partial Shading Conditions

The uneven presentation of a solar panel to the illumination is the reason for partial shading [6, 7]. These adjustments in illumination are because of different ecological elements like appearance of mists, bird droppings and shade of the building. Under the incomplete shading conditions [6], multiple peaks will happen in the PV bend because of the adjustment in the IV attributes of the particular PV modules. Whenever the partial shade occur the current in shaded panel goes through the bypass diode associated to it in each panel. From Fig. 5a, b, diverse partial shading conditions are discussed and their particular shading designs are shown in Tables 1 and 2 for a 3×2 array.

4 Particle Swarm Optimization: Outline of PSO

Step 1: In this stage, five particles (swarms) are initialized arbitrarily in the curve which are known as duty cycles. And these duty cycle values range should be between D_{\max} and D_{\min} .

Step 2: In this stage, the converter is fed by the duty cycles; for every cycle, we get voltage and power having feedback; and this voltage and power are stored in a vector and compared with the previous step.

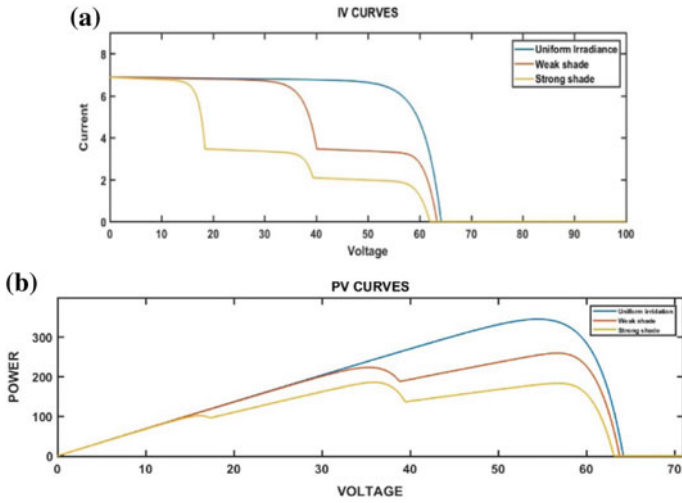


Fig. 5 a IV curve for a 3×2 PV array under partial shading conditions, b PV curve for a 3×2 PV array under partial shading conditions

Table 1 Irradiance level considered under different partial shading conditions

Uniform irradiance		Weak shading		Strong shading	
PV string 1	PV string 2	PV string 1	PV string 2	PV string 1	PV string 2
1000	1000	1000	1000	1000	1000
1000	1000	1000	1000	500	500
1000	1000	500	500	300	300

Table 2 Types of PSO and its variants

PSO variants	Velocity vector updation
PSO	Global best + own best
CLPSO	Neighbours best
DNLPSO	Global best + neighbours best

Step 3: In this step, the algorithm will update global best and its own best based on the comparison results of the previous step and both local and global best are stored in a vector.

Further stages are for CLPSO and DNLPSO

Step 4: (neighbour finding) In this stage, we are using the algorithm to find the neighbour for a particular duty cycle in the form of a circle, square, triangle or a random shape.

Step 5: (update best neighbour) For a duty cycle A, duty cycle B will be picked as a neighbour; at that point, it's own best will turn into the neighbour best for duty cycle A.

Step 6: (velocity and position updation) In this stage, the velocity and position vector are updated based on own best, global best and neighbour best and the equations are as follows for the algorithm used.

$$\text{PSO} : W * V_i + C_1 * \text{rand} * (P_{\text{best}}i^d - X_i^d) + C_2(g_{\text{best}}i^d - X_i^d) \quad (6)$$

$$\text{CLPSO} : W * V_i + C_1 * \text{rand} * (n_{\text{best}}i^d - X_i^d) \quad (7)$$

$$\text{DNLPSO} : W * V_i + C_i * \text{rand} * (n_{\text{best}}i^d - X_i^d) + C_2(g_{\text{best}}i^d - X_i^d) \quad (8)$$

Step 7: (convergence) The algorithm will find the global best after the maximum no. of iterations are over; that will be given as the duty cycle to the converter.

Step 8: (re-initialization) Re-initialization of the algorithm will be done when partial shading conditions occur. In the flow chart (Fig. 9), the basic PSO algorithm is explained.

4.1 Neighbourhood Selection Scheme

In CLPSO and DNLPSO, velocity of the neighbourhood particle is updated for choosing new duty cycle value for every three iterations. From Table 2, the velocity is updated for the three algorithms as depicted in Fig. 6.

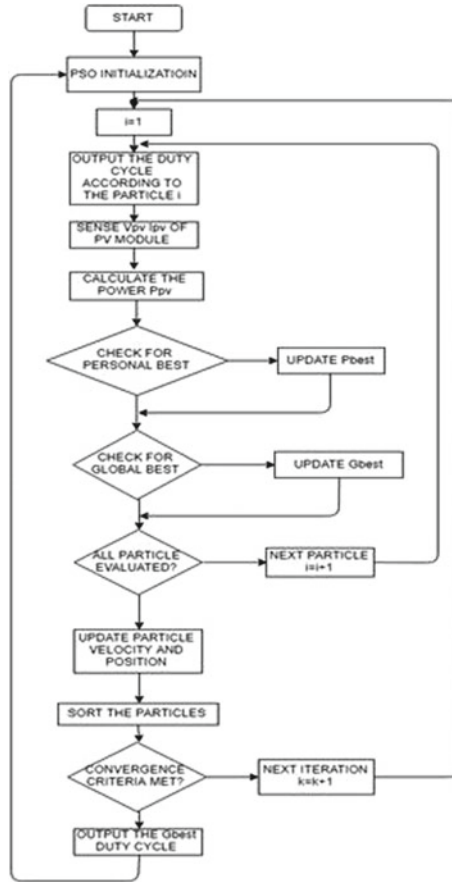


Fig. 6 Flow chart of PSO

5 Simulation and Results Discussion

A comparative study of different variants of PSO-based MPPT algorithm for a 3×2 PV array fed boost converter is simulated in a MATLAB environment. The Simulink model of the PV array fed boost converter is shown in Fig. 7. The required duty ratio obtained from the PSO-based MPPT is given to the boost converter to extract maximum power from the PV module. The simulation results shown in Fig. 8 signify the uniform irradiance condition of PSO and its variants, Fig. 9 signifies the strong shading conditions of PSO and its variants and Fig. 10 signifies the weak shading conditions of PSO and its variants (Table 3).

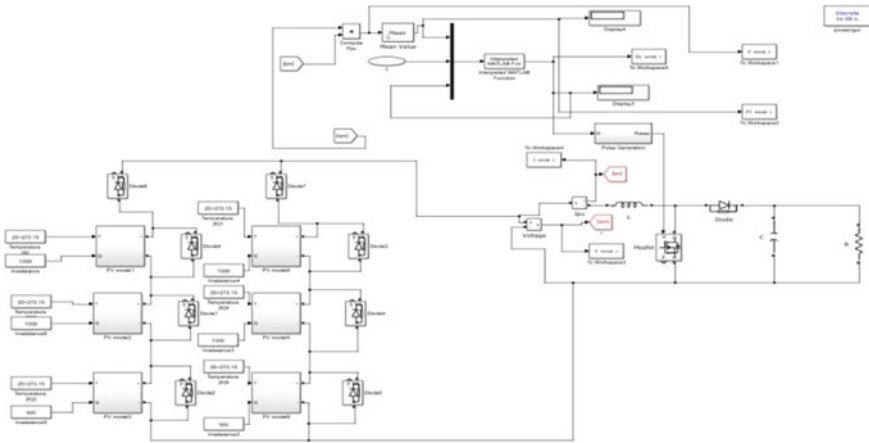


Fig. 7 Simulation model of a 3 × 2 PV array

6 Conclusion

From Fig. 8, the adaptive analysis of variants of PSO for uniform irradiance is analysed where PSO and its variants are catching the global peak and there is no oscillation. From Fig. 9, during the strong shade condition, PSO catches the peak but variants of PSO such as DNLPSO catch the peak there is lot of oscillation where CLPSO doesn't catches the. From Fig. 10, in the weak shade condition, we can observe that peak PSO catches the peak with no oscillation but variants of PSO such DNLPSO also catch the peak but with little oscillation but CLPSO doesn't catch the peak. From the results and simulation, we can conclude that PSO is best suited for MPPT tracking for all environments.

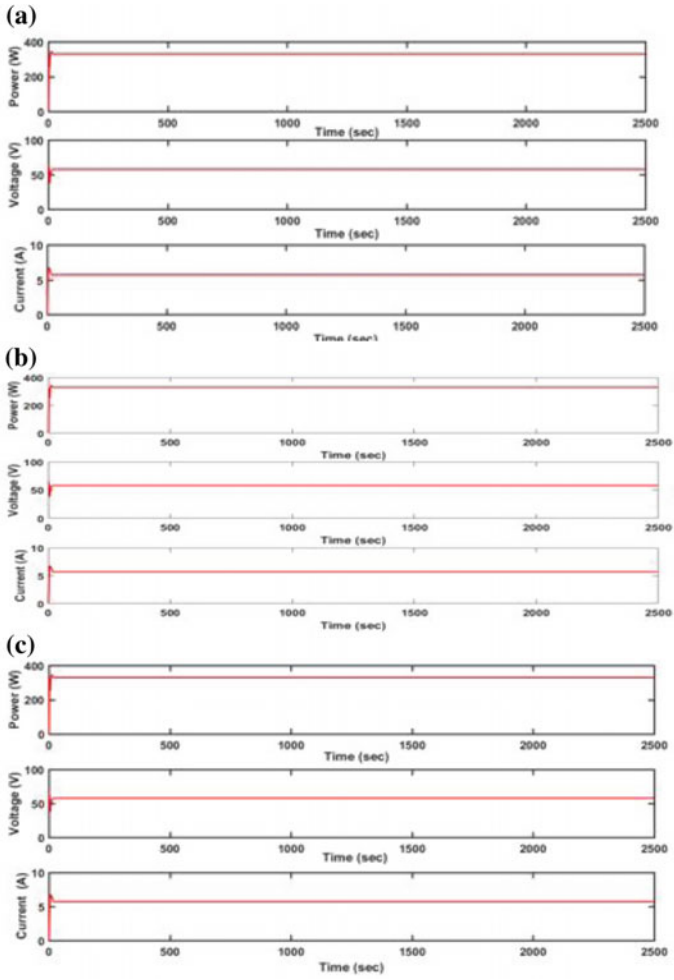


Fig. 8 Simulation results of PSO and its variants under uniform irradiance conditions. **a** PSO, **b** CLPSO, **c** DNLPSO

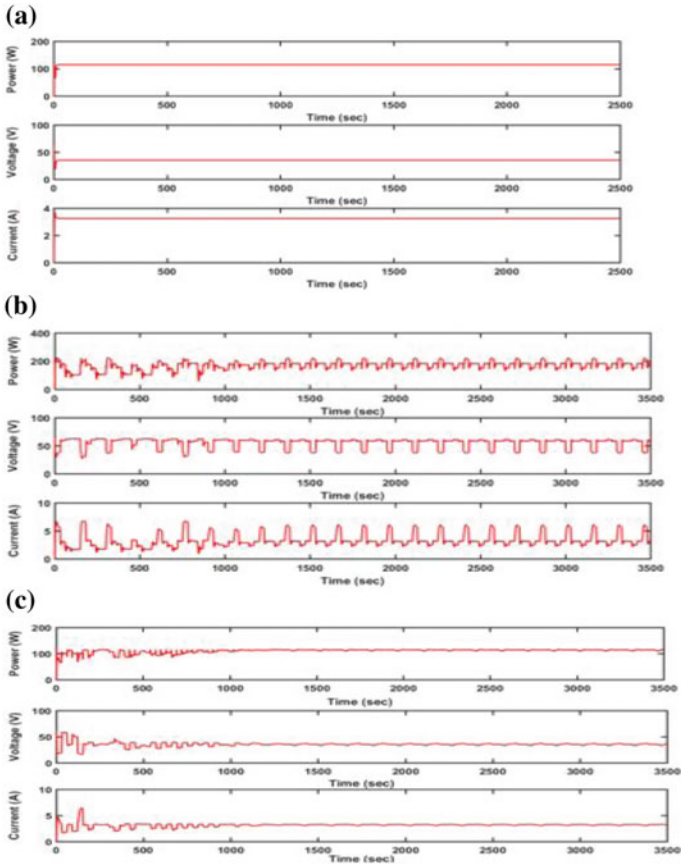


Fig. 9 Simulation results of PSO and its variants under strong partial shaded conditions. **a** PSO, **b** CLPSO, **c** DNLPSO

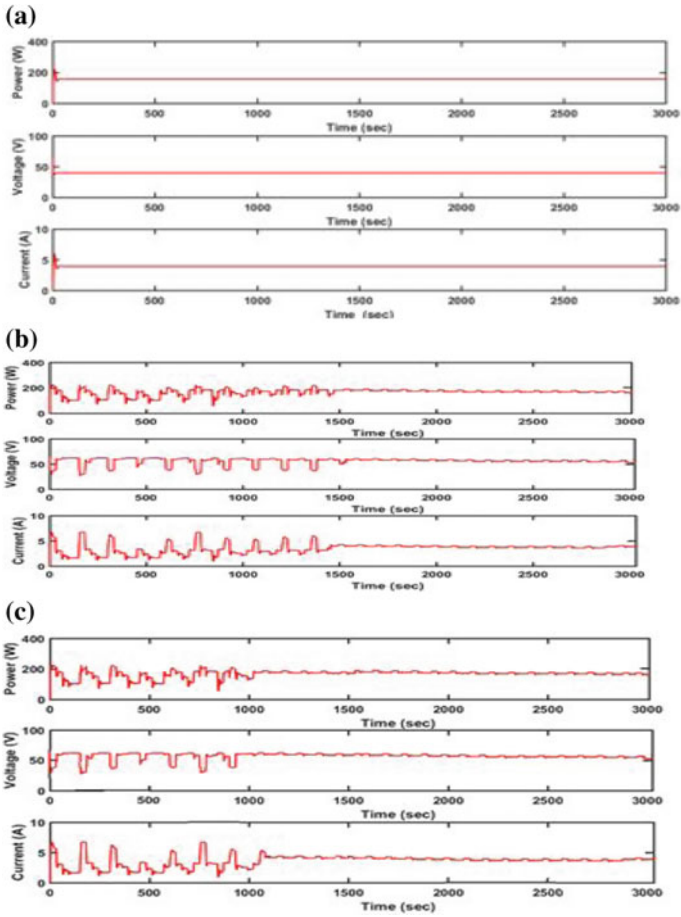


Fig. 10 Simulation results of PSO and its variants under weak partial shaded conditions. **a** PSO, **b** CLPSO, **c** DNLPPO

Table 3 Comparative study of PSO and its variants

Algorithm	No shade	Weak shade	Peak shade
PSO	Catches peak	Catches peak	Catches peak
CLPSO	Catches peak	Doesn't catch peak	Doesn't catch peak
DNLPPO	Catches peak	Doesn't catch peak	Doesn't catch peak

References

1. Gavhane PS, Krishnamurthy S, Dixit R, Ram JP, Rajasekar N (2017) EL-PSO based MPPT for solar PV under partial shaded condition. *Energy Procedia* 117:1047–1053
2. Ram JP, Babu TS, Rajasekar N (2017) A comprehensive review on solar PV maximum power point tracking techniques. *Renew Sustain Energy Rev* 67:826–847. ISSN 1364-0321
3. Ram JP, Rajasekar N, Miyatake M (2017) Design and overview of maximum power point tracking techniques in wind and solar photovoltaic systems: a review. *Renew Sustain Energy Rev* 73:1138–1159. ISSN 1364-0321
4. Ram JP, T. Sudhakar Babu, N. Rajasekar (2017) A comprehensive review on solar PV maximum power point tracking techniques. *Renew Sustain Energy Rev* 67:826–847. ISSN 1364-0321
5. Nasir, M, Das S, Maity D, Sengupta S, Halder U, Suganthan PN (2012) A dynamic neighborhood learning based particle swarm optimizer for global numerical optimization. *Inf Sci* 209:16–36
6. Jordehi AR (2018) Enhanced leader particle swarm optimisation (ELPSO): an efficient algorithm for parameter estimation of photovoltaic (PV) cells and modules. *Solar Energy* 159:78–87. ISSN 0038-092X
7. Jordehi AR (2016) Maximum power point tracking in photovoltaic (PV) systems: a review of different approaches. *Renew Sustain Energy Rev* 65:1127–1138. ISSN 1364-0321

Fault Location Methods in HVDC Transmission System—A Review



Jay Prakash Keshri and Harpal Tiwari

Abstract High-voltage direct current (HVDC) transmission system is commonly used for transmitting the bulk electric power over long distance and the reason behind this is, its less transmission losses and interconnection between two or more asynchronous power systems. Due to the recent advancement in power electronics devices, the terminal end converter and inverters cost is reduced and capacity is increased which makes the HVDC transmission more effective comparing with HVAC transmission over a long distance. The present scenario of HVDC in India is also given more attention due to more power demand and we have limited resources, it is being fulfilled by only through renewable energy resources, so the scope for HVDC transmission increases day by day. Most of the renewable energy resources generate energy at different frequency levels that fulfil the requirement of demand through islanded mode or connect through grid, it is an obvious option to connect renewable energy resources to grid via HVDC links. So, nowadays increasing HVDC links also increase the probability of fault in the system.

1 Introduction

As the need of long-distance transmission and interconnection of asynchronous system is increasing day by day, the use of HVDC transmission is predominant over the HVAC transmission system. HVDC system has several advantage over HVAC system like better stability, less transmission losses, less transmission cost for the same power transfer, etc. In the recent times, power electronics field starts rapidly growing. It effectively reduces the cost of HVDC system by making cheaper and more stable terminal end converters.

J. P. Keshri (✉) · H. Tiwari
Malaviya National Institute of Technology Jaipur, Jaipur, India
e-mail: jayprakashkeshri@gmail.com

H. Tiwari
e-mail: hptiwari.ee@mnit.ac.in

© Springer Nature Singapore Pte Ltd. 2020
A. Kalam et al. (eds.), *Intelligent Computing Techniques for Smart Energy Systems*,
Lecture Notes in Electrical Engineering 607,
https://doi.org/10.1007/978-981-15-0214-9_45

High-voltage DC transmission over long distance came into picture in 1882 in Miesbach-Munich Power transmission but transmitted power is only 1.5 kW. While the first commercial project of HVDC is in 1954 between Swedish mainland and Iceland of Gotland, which uses undersea cable of 90 km for 20 MW of power capacity. In recent years, DC transmission projects are growing at a rapid rate all over the world [1]. The first HVDC project in India is installed in Vidhyanchal in April 1989, which is a point-to-point system with two units each of 250 MW. And other back-to-back stations are Chandrapur, Sasaram and Gazuwaka (Vizag) each having 1000 MW capacity are also installed between 1997 and 2005. The first monopole line in India is installed between Barsur and Lower Sileru in 1989 having a transmission length of 196 km with 400 MW transmission power capacity. Long-distance DC power transmission plays an important part for deciding the strategy for development of “West to South, the national network” in our country. From the beginning of Barsur to Lower Sileru project (200 kV, 400 MW) in 1989, the successive operations of Rihand to Dadri (400 kV, 1500 MW), Chandrapur to Padghe (500 kV, 1500 MW), Talcher to Kolar (400 kV, 2360 MW) installed HVDC transmission system for interconnection of two asynchronous system and laid a foundation for the national unity networking [2]. In 2015, a DC transmission line of 1728 km length with 6000 MW at 800 V is installed between Bishwanath and Agra which is the longest and highest capacity transmission line in the world. A project of 1838 km transmission distance with 6000 MW capacity is under construction between Raigarh and Puglur. Two asynchronous link between India–Sri Lanka and India–Bangladesh is running. Table 1 gives the brief scenario of power plants in India. Electric power transmission over long distances have fundamental major problems like large transmission losses and poor stability. Overcoming these fundamental problems is a difficult task in today’s transmission system. Primary reason for transmitting the electric power over long-distance transmission is the increasing distance between generating power stations and consumers like wind power plants, which are far away from locality and generated electrical power from such power stations have to be transmitted to the mainland distribution substation through the overhead transmission cables. High-voltage direct current (HVDC) transmission is a reliable, economic and efficient technology to transmit the electric power over long distance power. Capital cost for DC transmission line is higher than HVAC transmission but it is compensated by the lesser running cost of HVDC transmission system. Still the transmission for shorter distance is not economical with HVDC because of expensive end point converters. The transmission distance after which the HVDC is economic over HVAC is known as break-even distance. Nowadays break-even distance is brought down to 500 km with the use of fast and more capable power electronics devices like IGBT in terminal end converters. For the same tower configuration as HVAC, 30–40% more power can be transmitted in HVDC transmission system. Figure 1 shows the transmission tower configuration and graph of break-even distance.

Accurate estimation of fault location is very useful when lines are long and run through inaccessible areas where patrolling is difficult and time consuming and during abnormal weather condition, visual inspection is also difficult. The line impedance in DC lines is very less in contrast with AC line, and therefore level

Table 1 Present scenario of HVDC in India

S. no	Project name	Connecting region	Commissioned on power	Rating (MW)	AC voltage (kV)	DC voltage (kV)	Mode of operation	No. of poles/blocks	Length of line (km)
Monopole line									
1	Barsur-Lower Sileru	AP Transco	1989 Decommission 2014	400	200	200	Mono	2	196
Bipolar line									
2	Rihand-Dadri	ER-WR	December 1991	1500	400	500	Bipole	2	816
3	Chandrapur-Padghe	CR-WR	1999	1500	400	500	Bipole	2	752
4	Talcher-Kolar	ER-SR	June 2003	2500	400	500	Bipole	2	1369
5	Ballia-Bhiwadi	ER-NR	Pole 1: March 2010 Pole 2: March 2011	2500	400	500	Bipole	2	780
6	Mundra-Mohindergarh	WR-NR	2012	2500	400	500	Bipole	2	986
7	Champa-Kurukshetra	CR-NR	In progress	3000	500	800	Bipole	2	1365
8	Raigarh-Pugalur	CR-SR	In progress	6000	500	800	Bipole	2	1838
Multi-terminal line									
9	Bishwanath-Agra	NER-ER	2015	6000	400	800	Multi-terminal	2	1728
Back to back connection									
10	Vidhyanchal	WR-NR	April 1989	2 x 250	400	70	Back to back	2	
11	Chandrapur	WR-SR	December 1997	2 x 500	400	205	Back to back	2	
12	Sasaram	ER-SR	September 2002	1 x 500	400	205	Back to back	2	
13	Gazuwaka (Vizag I)	ER-SR (Vizag II)	1999	2 x 500 March 2005	400	Block 1: 205 Block 2: 176	Back to back Block 2: 176	2	
International connections									
14	India-Bangladesh	ER(India)-WR(Bangladesh)	October 2013	1 x 500	400	400	Bipole	2	125
15	India-Sri Lanka	SE(India)-NW(Sri Lanka)	2013	Stage 1 1 x 500 Stage 2 1 x 500	400	220	Bipole	2	285

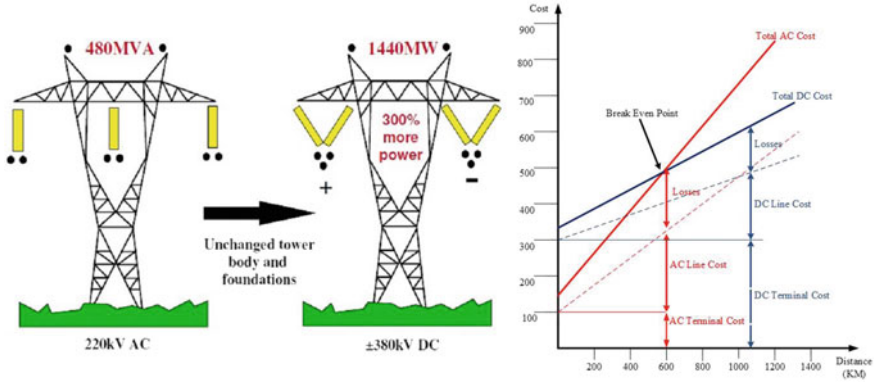


Fig. 1 Comparison between HVAC and HVDC transmission system

of fault current in DC line is higher than AC line hence an detection algorithm is needed which is fast and accurate. A no off methods are present to detect the fault in AC system, which can also be applicable for DC system but these methods are not equally effected because of the less line impedance and capacitance effect in DC lines. As mentioned above, level of fault current in DC line is very high so it is obvious to detect and locate the fault as soon as possible to prevent the system from major damage. Forecasting for both permanent and transient faults is provided by fault locators. Generally, minor damage is caused by transient fault which is not easily visible on inspection. These locations can be easily identified by fault locators which will be helpful for fast clearance of permanent fault and save the system from major damage. HVDC transmission researchers consider that travelling wave theory is the main protection scheme in HVDC system because it has several advantages from other methods like high speed, low transition resistance, less CT saturation and long-term influence of distributed capacitance [3].

The subject of fault location requires more importance from the researchers and power system engineers because of the impact of the of fault location in power system reliability. Much research work has been done on locating the fault in HVAC system but HVDC system still requires more methods. Some of the methods like wavelet transform, support vector machine and travelling wave are presently used by researchers which are fast and accurate too. In brief, some benefits of a fast and accurate fault location algorithm are the following:

- Acceleration of the renovation process can be increased by fault location algorithm.
- By specifying the faulted node, faulted section can be isolated soon.
- Planning of preventive maintenance tasks and avoidance of future fault can be possible by locating permanent faults.

2 Literature Review on Fault Location Techniques

End terminal HVDC converter and inverter become cheaper and efficient nowadays, and as a result of this reinforcement HVDC is generally used in extra-long distance transmission like in India extra-long overhead line is Agra–Bishwanath (1728 km) and Talcher–Kolar (1368 km) and extra-long undersea cable (268 km) is used in some part of India–Sri Lanka HVDC interconnection. But in such a long line, accurate location of fault is not an easy task. Currently, in the extra-long HVDC system, the location of fault is located by the help of repeater station. But this method requires installation of additional extra hardware at repeater station which increases the overall cost of existing transmission system. Researchers are investigating that whether the accurate location of fault is possible with only the terminal measurements. It eliminates the cost of additional equipment required in the repeater station.

Ping Chen et al. [4] have discussed a method for locating the fault in the VSC-HVDC systems, which used the technique based on the travelling wave and successive reflections generated by faults. Peak reflection generated by the faults are detected by the use of differentiator and smoother. Yang et al. [5] have given an algorithm which was also based on travelling wave and uses cross-correlation with a kind of sample function. Kasun Nanayakkara et al. [6] used continuous wavelet with travelling wave to locate fault in HVDC system. It also locates fault in orthodox two-terminal HVDC systems. This technique is also good enough for overhead line and cable mixed Multi-terminal VSC-HVDC system. Goo Bing et al. [7] presented a technique that provides fault location using FFT and Pony method with only one end current data used. Hang cui et al. [8] used radial basis function (RBF) neural network with wavelet packet decomposition (WPD) for developing an algorithm to detect the fault location in HVDC transmission line. Xu et al. [9] and Bao-de and Jian-cheng [10] present a method by using frequency of travelling wave for single ended fault location in UHVDC transmission lines. Natural frequency can be extracted by analysing the transient signals after the occurrence of fault. Accuracy of DTFT method can be improved by using continuous wavelet transform and Kasun Nanayakkara et al. [11] proved it by using it in two-terminal travelling wave method for detecting the time of arrival of travelling wave. Mohammed Shukr et al. [12] discuss a technique for pinpoint faults in VSC-HVDC system, which is based on the use of active impedance estimation.

A DC link capacitor is connected at the generated side, which generates a voltage pulse in the DC line. Estimation of impedance between point of observation and point of fault is made by using Fourier transformation signals of voltage and current transients generated by DC link capacitor. The initial estimation of fault location can be done with above-generated impedance by comparing it with the impedance calculated from equivalent model of transmission line. Location of fault and calculated impedance are continuously updated by iterative method until measured values and calculated values of impedance are made equal. Mohammad Farshad et.al. [13] present a technique that shows that fault location can be done by taking the measurement of voltage signal only at one of the line terminals. Thereafter by using the

post-fault voltage signal, the corresponding fault location is estimated on the basis of similarity of the captured voltage signal to existing patterns. In this approach, to measure the similarity of patterns of both the signals a method called Pearson correlation coefficient is used. Xie et al. [14] locate the faults by using steepness of wavefront alongside and compared it differential mode with component criterion, which is the present DC line protection scheme and obtained good reliability in condition of high fault impedance and long fault location. Another method which uses methodology of travelling wave is proposed by Zheng-You et al. [15] who uses the natural frequency of current signal of only one end of a duration of 10-ms. This paper develops a relationship among the natural frequency of travelling wave, distance of fault and reflection coefficient at the terminal of the transmission line. Identification of fault point can be done by calculating the travelling wave velocity and reflection coefficient under the dominant natural frequency. This method gives a primary advantage that it doesn't need surge arrival time and less complex as compared to other conventional travelling wave method.

Liang Yuansheng et al. [16, 17] propose a methodology for fault location in HVDC transmission line by the use of uncertain line parameter and unsynchronized two-terminal data. The reference point of zero time for each travelling head is set to the sample point of arrival at each end. With the change in zero time reference time tags of all the sample point change accordingly.

The use integral reactive power in context with backup protection scheme for UHVDC transmission system is proposed by Shuxin Luo et al. [18]. In this paper, a directional protection scheme is constructed for internal and external faults and this is done by theoretical analysis of reactive power flow. The reactive power is calculated by the use of Hilbert transform, because it ensures that a continuous output of calculation results which enhance the reliability of protection scheme. John P. Trevino et al. [19] propose a method, which uses samples of voltage and current sampled at the same time and pass them through a morphological filter and superimpose them in order to highlighting the wavefront and detect the point of fault. The use of morphological filter is that it reduces its complexity and computational cost. Position. Accurate detection of wavefront plays a vital role in the accuracy of detection of position of fault and this can be achieved by developing an algorithm on the basis of a suitable combination of superimposed signal, morphological filter and Structuring Element (SE). Zhao Li et al. [20] discuss that forward travelling wave and backward travelling wave have different configurations for internal and external DC line faults for post-fault condition. He explained that for internal DC line fault, forward travelling wave is less than the backward travelling wave at both the ends but in case of external fault forward travelling wave is greater than the backward travelling wave at one end and at the other end forward travelling wave is less than from the same. On the basis of these stats, he developed an algorithm for directional pilot protection. This algorithm classifies whether the fault is internal or external here.

Monday Ikhida et al. [21] discuss about future HVDC systems which are based on modular multilevel converter (MMC) and their protection scheme. The mentioned scheme for fault detection mainly depends on the rate of rise of current. The behaviour

Table 2 Comparison of some of the important papers

Authors	Test system used	Communication	Fault type used	Software used	Sampling frequency	Fault resistance	Fault distance	Time	year
Mariam Johnson	MTDC	No	PG, PP	PSCAD, MATLAB	1-4 KHz	NA	0-1000 km	NA	2017
Yew Ming	Point to point	No	PG, AC fault	PSCAD, MATLAB	1980 Hz	0.01 ohm	0-100 km	2 ms	2017
Monday Ikhide	MTDC	No	Estimate fault	MATLAB	96 KHz	NA	25-1000 km	2 ms	2015
Zing li	Point to point	No	PP, PG	PSCAD	NA	100 ohm	500 km	NA	2015
J. Descloux	MTDC	Yes	PP, PG	EMTP-IV	100 KHz	1-1000 ohm	0-100 km	<2 ms	2014
Sadegh Azizi	MTDC	No	PP	PSCAD	1-250 KHz	NA	0-65 km	NA	2014
Zheng-You	Point to point	No	PP, PG, PPG	PSCAD	100 KHz	1-50 ohm	0-1000 km	NA	2014
Liang Yuansheng	Point to point	No	PP	PSCAD	1 MHz	500 ohm	0-1438 km	NA	2014
Y. Lie	Point to point	No	PP, PG	PSCAD, MATLAB	NA	NA	350 km	NA	2013
M. Faishad	Point to point	No	PP, PG, PPG	PSCAD	80 KHz	10-50 ohm	100-250 km	NA	2013
K. Nanavakkara	MTDC	Yes	PG	PSCAD, MATLAB	2 MHz	NA	0-96 km	NA	2012
N. Pathirana	Point to point	No	PG	PSCAD	NA	0-100 ohm	1-299 km	NA	2012
M. Sukur	Point to point	No	PG, PPG	MATLAB	NA	10-1000 ohm	50-100 km	NA	2012
K. De Kerf	MTDC	No	PP	PSCAD, MATLAB	20 KHz	0.1 ohm	0-400 km	<1 ms	2011
Hang Cuil	Point to point	No	PP	MATLAB	20 KHz	NA	500 km	NA	2011
Xu Min	Point to point	No	PP	EMTP-IV	1 MHz	0-500 ohm	100-1000 km	NA	2011
Y. Jin	Point to point	No	PP, PG	PSCAD	NA	0-10 ohm	0.5-3 km	Variable	2010
Yingdam Qiu	double circuit	No	PG	PSCAD	100 KHz	0.01-500 ohm	300-1100 km	NA	2010
Young-Jin	Point to point	No	PG	PSCAD	100 KHz-1 MHz	0-20 ohm	5-95 km	NA	2008
J. Moshagh	Point to point	No	PP, PG, PPG	MATLAB	NA	NA	NA	NA	2008

of off-shore wind power plant is connected with MMVHVDC system plant, during DC faults. Keshri et al. [22–24] discuss the fault location in AC and MTDC system by the use machine learning based approach and provide a appropriate accuracy within short span of time. Comparison of some of the important and latest papers are shown in Table 2.

3 Conclusion

Above literature review shows that most researchers used travelling wave method in different configurations for the point of faults in HVDC system. Although the methods based on the travelling wave have low accuracy standard when fault occurs near the relaying point and faults with small inception angle. Travelling wave methods have disadvantages that they require very high sampling rate and have more implementation cost than the other conventional method like learning based methods. Although the non-travelling wave fault location method for HVDC system has better reliability and better accuracy but these methods are just at the theoretical research. Protection system of DC line can also inherent some method of AC line protection with proper modification. Day by day complexity of transmission line is increased, so that protection system of transmission line and control must be based on real-time data. For increasing the reliability of transmission, protection system must be a high-speed response system.

References

1. Suonan J, Gao S, Song G, Jiao Z, Kang X (2010) A novel fault-location method for HVDC transmission lines. *IEEE Trans Power Delivery* 25(2):1203–1209
2. Johnson JM, Yadav A (2017) Complete protection scheme for fault detection, classification and location estimation in HVDC transmission lines using support vector machines. *IET Sci Meas Technol* 11(3):279–287
3. Moshtagh J, Jannati M, Baghaee MR, Nasr E (2008) A novel approach for online fault detection in HVDC converters. In: 12th International middle-east power system conference, pp 307–311
4. Chen P, Xu B, Li J (2006) A traveling wave based fault locating system for HVDC transmission lines. In: 2006 international conference on power system technology, pp 1–4
5. Yang J, Fletcher JE, O'Reilly J (2012) Short-circuit and ground fault analyses and location in VSC-based DC network cables. *IEEE Trans Ind Electron* 59(10):3827–3837
6. Nanayakkara OMKK, Rajapakse AD, Wachal R (2012) Traveling-wave-based line fault location in star-connected multiterminal HVDC systems. *IEEE Trans Power Delivery* 27(4):2286–2294
7. Song G, Cai X, Gao S, Suonan J, Li G (2011) Natural frequency based protection and fault location for VSC-HVDC transmission lines. In: 2011 international conference on advanced power system automation and protection, vol 1, pp 177–182
8. Cui H, Tu N (2015) HVDC transmission line fault localization base on RBF neural network with wavelet packet decomposition. In: 2015 12th international conference on service systems and service management (ICSSSM), pp 1–4

9. Xu M, Cai Z, Liu Y, Ku X (2011) A novel coordination scheme of wave front and wave speed for HVDC travelling wave fault location. In: 2011 international conference on advanced power system automation and protection, vol 1, pp 102–107
10. Bao-de L, Jian-cheng T (2014) Transient fault location for HVDC transmission lines based on voltage distribution and one-terminal information. In: 2014 China international conference on electricity distribution (CICED), pp 508–510
11. Nanayakkara OMKK, Rajapakse AD, Wachal R (2012) Location of DC line faults in conventional HVDC systems with segments of cables and overhead lines using terminal measurements. *IEEE Trans Power Delivery* 27(1):279–288
12. Shukr M, Thomas DWP, Zanchetta P (2012) VSC-HVDC transmission line faults location using active line impedance estimation. In: 2012 IEEE international energy conference and exhibition (ENERGYCON), pp 244–248
13. Farshad M, Sadeh J (2013) A novel fault-location method for HVDC transmission lines based on similarity measure of voltage signals. *IEEE Trans Power Delivery* 28(4):2483–2490
14. Xie LH, Jin LJ, Wang XL, Ning LH, Wang TL (2014) Improved protection method of HVDC transmission line based on the analysis of traveling wave dispersion. In: 2014 international conference on power system technology, pp 476–473
15. He ZY, Liao K, Li XP, Lin S, Yang JW, Mai RK (2014) Natural frequency-based line fault location in HVDC lines. *IEEE Trans Power Delivery* 29(2):851–859
16. Yuansheng L, Gang W, Haifeng L (2015) Time-domain fault-location method on HVDC transmission lines under unsynchronized two-end measurement and uncertain line parameters. *IEEE Trans Power Delivery* 30(3):1031–1038
17. Qiu Y, Li H, Guo L, Wu J, Liang Y (2015) A fault location method for double-circuit HVDC transmission lines on the same tower based on mixed modulus. In: 2015 IEEE Eindhoven PowerTech, pp 1–5
18. Luo S, Dong X, Shi S, Wang B (2016) A directional protection scheme for HVDC transmission lines based on reactive energy. *IEEE Trans Power Delivery* 31(2):559–567
19. Triveno JP, Dardengo VP, Almeida MCD (2015) An approach to fault location in HVDC lines using mathematical morphology. In: 2015 IEEE Power Energy Society General Meeting, pp 1–5
20. Li Z, Zou G, Tong B, Gao H, Feng Q (2015) Novel traveling wave protection method for high voltage DC transmission line. In: 2015 IEEE power energy society general meeting, pp 1–5
21. Ikhida M, Tennakoon S, Griffiths A, Subramanian S, Ha H (2015) Fault detection in multi-terminal modular multilevel converter (MMC) based high voltage DC (HVDC) transmission system. In: 2015 50th international universities power engineering conference (UPEC), pp 1–6
22. Keshri JP, Tiwari HP (2017) Fault location in overhead transmission line without using line parameter. In: 4th international conference on engineering and technology (ICSET), Malaysia, pp 11–15
23. Keshri JP, Tiwari HP (2017) Parameter-less fault locator using synchronized/un-synchronized data for overhead transmission line. In: 2017 international conference on computer, communications, and electronics (comtelix), Jaipur, pp 260–264
24. Keshri JP, Tiwari HP (2018) Detection and classification of transmission line faults using modified F-SVM. In: 2018 IEEE international conference on environment and electrical engineering and 2018 IEEE industrial and commercial power systems Europe (EEEIC/I&CPS Europe), Palermo, pp 1–8

Optimal Reactive Power Dispatch Through Minimization of Real Power Loss and Voltage Deviation



Ravi Ucheniya, Amit Saraswat and Shahbaz Ahmed Siddiqui

Abstract Optimal reactive power dispatch plays an important role to reduce the total active power losses in transmission lines and the total voltage deviation at the load buses. Optimal reactive power dispatch is a nonlinear, nonconvex, non differentiable, and multimodal optimization problem with discrete and continuous control variables. In this paper, the interface between MATLAB and DigSILENT PowerFactory software has been realized to solve the optimal reactive power dispatch problem. The power flow calculation has been executed on DigSILENT PowerFactory software, and the process of optimization through Genetic Algorithm has been implemented on MATLAB. The proposed approach has been tested on standard IEEE 30 bus system. The results obtained by the proposed approach has been compared with results presented in the literature.

Keywords Optimal Reactive Power Dispatch (ORPD) · DigSILENT PowerFactory · MATLAB and genetic algorithm

Nomenclature

P_{loss} and VD

Total real power loss in transmission lines and total voltage deviation, respectively

N_{Bus} , N_{Tap} , N_{Cap} , N_{Gen} , N_{Tline} and N_{PQ}

Number of buses, tap changing transformer, shunt compensation, generators,

R. Ucheniya (✉) · A. Saraswat
Department of Electrical Engineering, Manipal University Jaipur, Jaipur, India
e-mail: raviu85@gmail.com

A. Saraswat
e-mail: amit.saraswat@jaipur.manipal.edu

S. A. Siddiqui
Department of Mechatronics Engineering, Manipal University Jaipur, Jaipur, India
e-mail: shahbazahmed.siddiqui@jaipur.manipal.edu

© Springer Nature Singapore Pte Ltd. 2020
A. Kalam et al. (eds.), *Intelligent Computing Techniques for Smart Energy Systems*,
Lecture Notes in Electrical Engineering 607,
https://doi.org/10.1007/978-981-15-0214-9_46

g^k	Conductance of k th transmission line
V_i, V_j and V_k	Voltage magnitude of i th, j th and k th bus, respectively
δ_i and δ_j	Angle of i th and j th bus, respectively
V_k^{sp}	Specified voltage of the k th bus
P_{G_i}	Real power generation through i th generator
P_{D_i}	Real power demand at i th load bus
Q_{G_i}	Reactive power generation through i th generator
Q_{D_i}	Reactive power demand of the i th load bus
G_{ij} and B_{ij}	Conductance and susceptance of the line connected between i th and j th bus
$V_{G_i}^{\min}$ and $V_{G_i}^{\max}$	Minimum and maximum limit of the voltage of the i th generator
$P_{G_i}^{\min}$ and $P_{G_i}^{\max}$	Minimum and maximum limit of the real power generation through i th generator
$Q_{G_i}^{\min}$ and $Q_{G_i}^{\max}$	Minimum and maximum limit of the reactive power generation through i th generator
T_j^{\min} and T_j^{\max}	Minimum and maximum limit of the tap setting of the i th tap changing transformer
$Q_{C_i}^{\min}$ and $Q_{C_i}^{\max}$	Minimum and maximum limit of the shunt compensation through i th capacitor
$V_{PQ_i}^{\min}$ and $V_{PQ_i}^{\max}$	Minimum and maximum limit of the voltage of the i th load bus
S_i^{\max}	Maximum limit of the power transfer through i th transmission line
x^T and u^T	Vector of control variables and state variables, respectively
$PN_1, PN_2,$ and PN_3	Calculated values of the inequality constraint violations associated with the slack bus active power output, load bus voltage and reactive power output of the all generators
$\alpha_{PN_1}, \alpha_{PN_2}$ and α_{PN_3}	The proposed penalty factor

1 Introduction

Optimal Reactive Power Dispatch (ORPD) is the subcategory of Optimal Power Flow (OPF) optimization framework. In the ORPD, redistribution of reactive power sources (such as the magnitude of the voltage of the generators, transformer's tap position, and value of VAR compensation devices) has been used to reduce total active power losses and total voltage deviation. In literature, many solution methodologies for the ORPD problem have been already proposed and analyzed their performances by various researchers. These solution methodologies may be classified into two broad categories: (a) classical methodologies, and (b) intelligent metaheuristic methodologies [1]. The classical methods are appropriate for single modal optimization problems with decent convergence capabilities. The main drawback of the classical methods is that they are unable to handle the multimodal optimization problems [1]. Whereas, the intelligent metaheuristic optimization methods may be applied to solve the multimodal optimization problems.

The intelligent metaheuristic methodologies may be listed as: Particle Swarm Optimization (PSO) [2], Cataclysmic Genetic Algorithm (CGA) [3], Self-Adaptive Real-Coded Genetic Algorithm (SA-RCGA) [4], Principal Component Analysis (PCA) based Real Coded GA [5], Differential Evolutionary Algorithm (DEA) [6–8], Seeker Optimization Algorithm (SOA) [9], Harmony Search Algorithm (HSA) [10], Biogeography-Based Optimization (BBO) [11], Ant Colony Optimization (ACO) [12], Teaching Learning-Based Optimization (TLBO) and Quasi-Oppositional Teaching Learning-Based Optimization (QOTLBO) [13], PSO with scale-free Gaussian-dynamic [14], etc. Similarly, the hybrid form of these metaheuristic methodologies may be listed as real coded GA and Simulated Annealing (SA) [15], the Multi-Agent System (MAS) and PSO [16], the modified PSO (GA into PSO) and MAS [17], Shuffled Frog Leaping Algorithm (SFLA) and Nelder–Mead (NM) [18], Modified Imperialist Competitive Algorithm (MICA) and Inverse Weed Optimization Algorithm (IWOA) [19], Modified TLBO and Double Differential Evolution (DDE) [20], PSO and Gravitational Search Algorithms (GSA) [21], etc.

In this paper, the interface between MATLAB and DigSILENT PowerFactory software has been used to solve the optimal reactive power dispatch problem [22]. The power flow calculations have been executed on DigSILENT PowerFactory software, whereas the process of optimization through Genetic Algorithm has been implemented on MATLAB. The proposed approach has been tested on standard IEEE 30 bus system. The results obtained by the proposed approach has been compared with the results presented in the literature [21]. Rest of the paper has been organized as follows: the complete mathematical formulation of ORPD problem has been presented in Sect. 2. The flowchart of the proposed approach is presented in Sect. 3. The results obtained from the proposed approach are presented in Sect. 4. Finally, the conclusion of the paper is presented in Sect. 5.

2 Problem Formulation

The primary purpose of the ORPD problem is to reduce the total active power losses in the transmission lines and to improve the voltage profile of load buses. The complete mathematical formulation for ORPD is presented below.

2.1 Objective Function

$$P_{\text{loss}} = \sum_{k=1}^{N_{TL}} g_k [V_i^2 + V_j^2 - 2V_i V_j \cos(\delta_i - \delta_j)], \forall i \in N_{\text{Bus}}, \forall j \in N_{\text{Bus}} \quad (1)$$

$$VD = \sum_{k=1}^{N_{\text{Bus}}} |V_k - V_k^{SP}| \quad (2)$$

2.2 System Constraints

$$P_{G_i} - P_{D_i} = V_i \sum_{j \in \mathcal{B}}^{N_{\text{Bus}}} [G_{ij} \cos(\delta_i - \delta_j) + B_{ij} \sin(\delta_i - \delta_j)], \quad \forall i, j \in N_{\text{Bus}} \quad (3)$$

$$Q_{G_i} - Q_{D_i} = V_i \sum_{j=1}^{N_{\text{Bus}}} [G_{ij} \cos(\delta_i - \delta_j) - B_{ij} \sin(\delta_i - \delta_j)], \quad \forall i, j \in N_{\text{Bus}} \quad (4)$$

$$V_{G_i}^{\min} \leq V_{G_i} \leq V_{G_i}^{\max} \quad \forall i \in N_{\text{Gen}} \quad (5)$$

$$P_{G_i}^{\min} \leq P_{G_i} \leq P_{G_i}^{\max} \quad \forall i \in N_{\text{Gen}} \quad (6)$$

$$Q_{G_i}^{\min} \leq Q_{G_i} \leq Q_{G_i}^{\max} \quad \forall i \in N_{\text{Gen}} \quad (7)$$

$$T_j^{\min} \leq T_j \leq T_j^{\max} \quad \forall j \in N_{\text{Tap}} \quad (8)$$

$$Q_{C_i}^{\min} \leq Q_{C_i} \leq Q_{C_i}^{\max} \quad \forall i \in N_{\text{Cap}} \quad (9)$$

$$V_{L_i}^{\min} \leq V_{L_i} \leq V_{L_i}^{\max} \quad \forall i \in N_{PQ} \quad (10)$$

$$S_j \leq S_j^{\max} \quad \forall j \in N_{\text{Tline}} \quad (11)$$

$$x^T = \left[V_{G_1} \dots V_{G_{N_{\text{Gen}}}}, Q_{C_1} \dots Q_{C_{N_{\text{Cap}}}}, T_1 \dots T_{N_{\text{TTap}}} \right] \quad (12)$$

$$u^T = \left[P_{G_1}, V_{L_1} \dots V_{L_{N_{PQ}}}, Q_{G_1} \dots Q_{G_{N_{\text{Gen}}}} \right] \quad (13)$$

2.3 General Formulation of the Objective Function

The final objective function, which is used by the optimization algorithm as given below.

$$\text{minimize } F = F_{\text{OBF}} + PN_1 \alpha_{PN_1} + PN_2 \alpha_{PN_2} + PN_3 \alpha_{PN_3} \quad (14)$$

$$PN_1 = (P_{G_1} - P_{G_1}^{\text{lim}})^2, \quad \alpha_{PN_1} = (PN_1 + 1) \quad (15)$$

$$PN_2 = \sum_{i=1}^{NL} (V_{L_i} - V_{L_i}^{\text{lim}})^2, \quad \alpha_{PN_2} = (PN_2 + 1) \quad (16)$$

$$PN_3 = \sum_{i=1}^{NG} (Q_{G_i} - Q_{G_i}^{\text{lim}})^2, \quad \alpha_{PN_3} = (PN_3 + 1) \quad (17)$$

3 Solution Methodology

The flow chart of the proposed approach has been presented in Fig. 1. In this paper, two modification has been proposed: one is “MIN MAX modification” and second is “Violation of the Constraints Penalize by itself”. In MIN MAX modification, the minimum value of the control variables are set as the “base value” and the difference between the upper and lower boundary of the control variables are set as the “difference value”. Now, the new setting of the upper and lower limit of the control variables are “1” and “0”, respectively. GA performs optimization process using newly defined range of control variables.

In second modification, violations of control variables as depicted in Eq. (12) have restricted by the lower and upper limit of the control variables. Similarly, violation of the state variables as depicted in Eq. (13) have been restricted by penalty based objective function as depicted in Eq. (14). Penalty function approach has been used to handle the violation of the inequality constraint [5]. The violation of the constraints has been penalized by the proposed penalty factor. The formulation of the proposed penalty factors is presented in Eqs. (15–17). PN_1 , PN_2 and PN_3 are the measurement of the violation of the state variables and α_{PN_1} , α_{PN_2} and α_{PN_3} are the penalty factor, respectively.

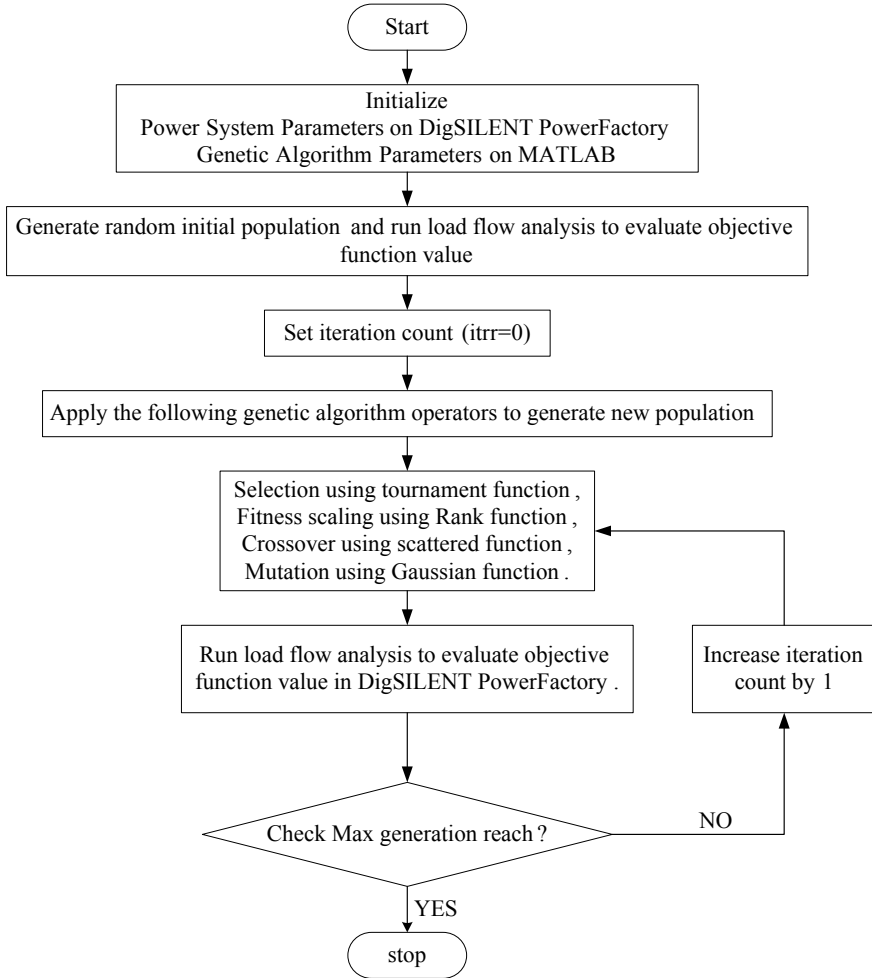


Fig. 1 Flowchart of the interface between GA and DigSILENT PowerFactory

4 Simulation Result

In this section, the proposed approach has been tested on standard IEEE 30 bus system. The IEEE 30 bus system data and limits of control and state variables are adapted from [21]. The total active power demand of the system is 2.834 p.u. at 100 MVA base. In this paper, 30 individual test runs have performed to validate the proposed approach. Results obtained by the proposed approach have been compared with those reported in [21]. The target objectives, those are presented by Eq. (1)

Table 1 Comparison of results for case 1

Variable	Initial base [21]	PSO [21]	GSA [21]	The proposed approach
V_{g1}	1.05	1.1	1.1	1.1
V_{g2}	1.04	1.0944	1.0944	1.0946
V_{g5}	1.01	1.075	1.0748	1.0757
V_{g8}	1.01	1.0767	1.0768	1.0764
V_{g11}	1.05	1.1	1.1	1.1
V_{g13}	1.05	1.1	1.1	1.0998
T_{6-9}	1.078	1.0473	1.0399	1.0375
T_{6-10}	1.069	0.9	0.9	0.907
T_{4-12}	1.032	0.9831	0.9827	0.9793
T_{28-27}	1.068	0.9664	0.9699	0.9667
Q_{c10}	0	5	3.5717	4.9998
Q_{c12}	0	5	3.0984	4.9247
Q_{c15}	0	5	3.2925	4.9268
Q_{c17}	0	5	4.0166	4.9922
Q_{c20}	0	3.4023	3.0309	4.0713
Q_{c21}	0	5	4.0339	4.9697
Q_{c23}	0	5	2.9946	2.8126
Q_{c24}	0	5	4.3499	4.9872
Q_{c29}	0	2.1038	2.6902	2.361
P_{loss} (in MW)	5.8223	4.5388	4.5515	4.5323
% reduction	0	22.04	21.83	22.16

(case 1) and Eq. (2) (case 2) and formulated as Eq. (14), have been solved using the proposed approach. The comparison of the results obtained by proposed approach and results reported in [21] are presented in Tables 1 and 2. The convergence graph of the target objectives is depicted in Fig. 2.

It is observed from the Table 1 that the proposed approach is able to reduce the total active power losses in the transmission line 4.5323 MW that is 22.16% from the initial value 5.8223 MW in comparison to 22.04% with PSO [21], 21.83% with GSA [21]. Also, it is observed from the Table 2 that the proposed approach is able to reduce the total voltage deviation 0.1002 pu that is 91.29% from the initial value 1.1497 pu in comparison to 91.26% with PSO [21], 88.77% with GSA [21]. The statistical analysis in terms of Best, Worst and Standard Deviation (SD) for Case 1 (i.e. power loss minimization) and Case 2 (i.e. voltage deviation minimization) are listed in Tables 3 and 4, respectively.

Table 2 Comparison of result for case 2

Variable	Initial (base) [21]	PSO [21]	GSA [21]	The proposed approach
V_{g1}	1.05	1.0264	1.0374	1.0307
V_{g2}	1.04	1.0162	1.04	1.0234
V_{g5}	1.01	1.0185	1.022	1.0183
V_{g8}	1.01	0.9987	1.0047	1.0003
V_{g11}	1.05	1.0427	0.9885	1.019
V_{g13}	1.05	0.9965	0.9924	1.0004
T_{6-9}	1.078	1.0598	0.9772	1.0298
T_{6-10}	1.069	0.9144	0.9	0.9074
T_{4-12}	1.032	0.958	0.9274	0.9597
T_{28-27}	1.068	0.9758	0.9612	0.968
Q_{c10}	0	4.9995	1.9778	4.7364
Q_{c12}	0	0	0.424	0.1194
Q_{c15}	0	5	2.2268	4.4796
Q_{c17}	0	4.9958	2.8945	2.0072
Q_{c20}	0	5	4.0503	4.9906
Q_{c21}	0	5	3.2996	4.9921
Q_{c23}	0	4.9988	2.5926	4.9121
Q_{c24}	0	5	2.6791	4.8805
Q_{c29}	0	4.9994	2.8961	3.1536
VD (in p.u.)	1.1497	0.1005	0.1291	0.1002
% reduction	0	91.26	88.77	91.29

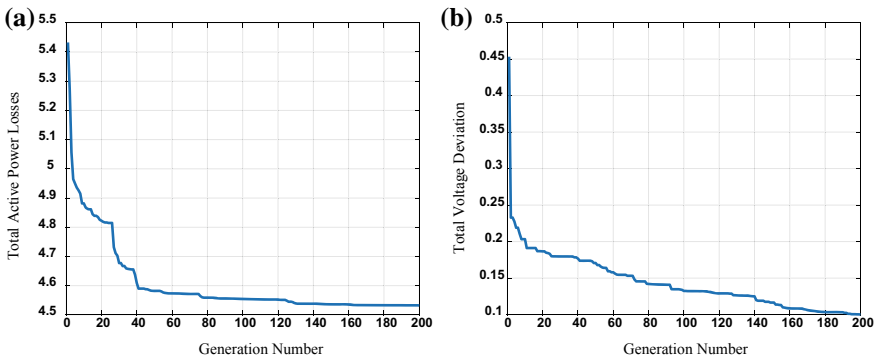


Fig. 2 Convergence of the total active power loss (a) and voltage deviation (b) in IEEE 30 bus power system using the proposed optimization method

Table 3 Comparison of best, worst, and standard deviation (SD) for case 1

Case 1	PSO [21]	GSA [21]	The proposed approach
Best	4.5388	4.5515	4.5323
Worst	5.1327	4.6408	4.9215
SD	0.204	0.024	0.1001

Table 4 Comparison of best, worst, and standard deviation (SD) for case 2

Case 2	PSO [21]	GSA [21]	The proposed approach
Best	0.1005	0.1291	0.1002
Worst	0.1672	0.1884	0.1484
SD	0.0221	0.0164	0.0127

5 Conclusion

In this paper, the ORPD problem has been successfully solved by the proposed GA based optimization approach. ORPD is a nonlinear, nonconvex, non differentiable, and multimodal problem with a discrete and continuous control variable. In this study, two different objective functions such as total active power loss in the transmission line and total voltage deviation on load buses have been minimized subjective to different equality and inequality constraints for IEEE 30 bus power system. In addition, the interface between GA and DigSILENT PowerFactory software has been realized efficiently to solve the ORPD problem. The obtained results demonstrate the potential and effectiveness of the proposed approach.

References

1. Basu M (2016) Quasi-oppositional differential evolution for optimal reactive power dispatch. *Int J Electr Power Energy Syst* 78:29–40
2. Yoshida H, Kawata K, Fukuyama Y, Takayama S, Nakanishi Y (2000) A particle swarm optimization for reactive power and voltage control considering voltage security assessment. *IEEE Trans Power Syst* 15:1232–1239
3. Zhang Y, Ren Z (2005) Optimal reactive power dispatch considering costs of adjusting the control devices. *IEEE Trans Power Syst* 20:1349–1356
4. Subbaraj P, Rajnarayanan PN (2009) Optimal reactive power dispatch using self-adaptive real coded genetic algorithm. *Electr Power Syst Res* 79:374–381
5. Saraswat A, Saini A (2011) Optimal reactive power dispatch by an improved real coded genetic algorithm with PCA mutation. In: *International conference on sustainable energy and intelligent systems (SEISCON 2011)*, pp 310–315
6. Varadarajan M, Swarup KS (2008) Differential evolutionary algorithm for optimal reactive power dispatch. *Int J Electr Power Energy Syst* 30:435–441
7. Ramirez JM, Gonzalez JM, Ruben TO (2011) An investigation about the impact of the optimal reactive power dispatch solved by DE. *Int J Electr Power Energy Syst* 33:236–244
8. Huang C-M, Huang Y-C (2012) Combined differential evolution algorithm and ant system for optimal reactive power dispatch. *Energy Procedia* 14:1238–1243

9. Dai C, Chen W, Zhu Y, Zhang X (2009) Seeker optimization algorithm for optimal reactive power dispatch. *IEEE Trans Power Syst* 24:1218–1231
10. Khazali AH, Kalantar M (2011) Optimal reactive power dispatch based on harmony search algorithm. *Int J Electr Power Energy Syst* 33:684–692
11. Roy PK, Ghoshal SP, Thakur SS (2011) Optimal reactive power dispatch considering flexible AC transmission system devices using biogeography-based optimization. *Electr Power Compon Syst* 39:733–750
12. El-Ela AAA, Kinawy AM, El-Sehiemy RA, Mouwafi MT (2011) Optimal reactive power dispatch using ant colony optimization algorithm. *Electr Eng* 93:103–116
13. Mandal B, Roy PK (2013) Optimal reactive power dispatch using quasi-oppositional teaching learning based optimization. *Int J Electr Power Energy Syst* 53:123–134
14. Wang C, Liu Y, Zhao Y, Chen Y (2014) A hybrid topology scale-free Gaussian-dynamic particle swarm optimization algorithm applied to real power loss minimization. *Eng Appl Artif Intell* 32:63–75
15. Das DB, Patvardhan C (2002) Reactive power dispatch with a hybrid stochastic search technique. *Int J Electr Power Energy Syst* 24:731–736
16. Zhao B, Guo CX, Cao YJ (2005) A multiagent-based particle swarm optimization approach for optimal reactive power dispatch. *IEEE Trans Power Syst* 20:1070–1078
17. Shunmugalatha A, Slochanal SMR (2008) Application of hybrid multiagent-based particle swarm optimization to optimal reactive power dispatch. *Electr Power Compon Syst* 36:788–800
18. Khorsandi A, Alimardani A, Vahidi B, Hosseinian SH (2011) Hybrid shuffled frog leaping algorithm and Nelder-Mead simplex search for optimal reactive power dispatch. *IET Gener Transm Distrib* 5:249–256
19. Ghasemi M, Ghavidel S, Ghanbarian MM, Habibi A (2014) A new hybrid algorithm for optimal reactive power dispatch problem with discrete and continuous control variables. *Appl Soft Comput* 22:126–140
20. Ghasemi M, Ghanbarian MM, Ghavidel S, Rahmani S, Moghaddam EM (2014) Modified teaching learning algorithm and double differential evolution algorithm for optimal reactive power dispatch problem: a comparative study. *Inf Sci (Ny)* 278:231–249
21. Radosavljević J, Jevtić M, Milovanović M (2018) A solution to the ORPD problem and critical analysis of the results. *Electr Eng* 100:253–265
22. Tabatabaei NM, Aghbolaghi AJ, Boushehri NS, Parast FH (2017) Reactive power optimization using MATLAB and DiGSILENT. In: *Reactive power control in AC power systems*. Springer, pp 411–474

IoT Enabled Intelligent Energy Management and Optimization Scheme with Controlling and Monitoring Approach in Modern Classroom Applications



Vidyadhar Aski, Rajveer Singh Shekhawat, Sushant Mehta, Pratik Kr. Jain and Prachal Goyal

Abstract Modern campuses have been built with many modern facilities and aids for comfort and to enhance teaching quality. Some of these include smart electronic boards, projectors, desktops, air conditioning apart from lights, and fans. Most campuses have large number of classroom and student population with good number of courses. This demands very complex classroom allocation prices for their optimal utilization. In spite of best effects, continuous use of classroom is difficult. This causes same classroom going vacant regularly and many times, the equipment and light/fans are left ON, causing heavy consumption of energy. A system to eliminate wastage of energy, a smart classroom energy management system (CEMS) has been considered and pilot of the same has been tested. Based on the survey of a typical modern campus academic building, the proposed system can give 10–30% of energy saved which in turn provides a savings of lakhs of rupees per month. The system can be easily adopted to other similar scenarios without considering infrastructural redesign like in meeting room, etc. using Low Power Sensors (LPS), resulting into huge savings.

Keywords IoT · Smart energy · Low power sensors (LPS) · Classroom energy management system (CEMS)

V. Aski · R. S. Shekhawat
SCIT Department, Manipal University Jaipur, Jaipur, India

S. Mehta (✉) · P. Goyal
CCE, Manipal University Jaipur, Jaipur, India
e-mail: mehtasushant05@gmail.com

P. Kr. Jain
CSE, Manipal University Jaipur, Jaipur, India

© Springer Nature Singapore Pte Ltd. 2020
A. Kalam et al. (eds.), *Intelligent Computing Techniques for Smart Energy Systems*,
Lecture Notes in Electrical Engineering 607,
https://doi.org/10.1007/978-981-15-0214-9_47

1 Introduction

Although we strive enough to build campuses with grand buildings with modern facilities involving complex scientific and technological appliances requiring electrical energy. The need for comfort has also brought in power guzzlers like air conditioners, room air filters, etc. in classrooms, seminar halls, etc. Even though automation systems for such appliances and lighting, etc. are available, their exorbitant costs do not permit management to deploy the same for managing the classrooms and other facilities to remove human beings from the loop which leaves so much room for human error and negligence. A number of surveys of classrooms in MUJ campus (AB 1) have been an eye-opener. About 15–30% classrooms are found running with full load of lights, fans, AC, and projector. Since the energy bill of AB 1 is huge, an IoT based system has been envisaged to solve the issue without requiring complex commercial automation systems. Advancements and upgradation of embedded technologies in such environments has never been an unavoidable problem due to highly flexible IoT systems involved in building such smart campuses. Deployment of bidirectional smart event-driven energy controller and Home energy management (HEM) agents that provides real time consumption monitoring and control, will enable HEM and similar energy management systems in “smart usage.” This paper proposes an intelligent CEMS scheme which supports monitoring and optimization of energy for large number of classrooms with the help of analog passive sensors like LDR, PIR sensors, and current sensors without considering the architectural redesign demand with higher flexibilities. The system also provides the count of students along with their directions to detect whether entry or exit.

2 Related Works

Similar to CEMS, researchers have proposed Smart Home Energy Management System (HEMS) which analyzes electrical usage and history of all household appliances through context-aware technologies, metaheuristics algorithms, and statistical algorithms [1]. Siriwat Wasoontarajaroen et al. proposed an IoT device system to monitor electric utilization in a room [2]. Daniel White et al. proposed a study and implementation of sustainable smart city IoT applications: heat and electricity management and eco-conscious cruise control for public transportation. The study addresses heat and energy supervision and targets at developing various assets (such as heat and electricity meters) so that enhanced use of electricity in corporate and domestic areas. The second application discusses to cruise controller for open access transportation and aims at utilizing different sources (such as environmental and traffic sensors) in order to provide driving endorsements that aim at eco-effectiveness. They also highlighted the IoT problem statements as well as potential enabling technologies

that will allow for the realization [6]. The study addresses review status of different statistical approaches, machine learning, and artificial intelligence application in implementing predictive maintenance applications [7].

3 Contextual Analysis/Background Survey

In the proposed study we have conducted a systematic survey to demonstrate the wastage of electricity in academic blocks. While moving around in corridors of academic blocks we found a number of unoccupied classrooms during lunch hours, during the period of which no classes are running, etc. are having all lights, AC, fans switched ON and lots of energy is getting wasted. To support our conviction, we conducted a systematic survey of classrooms and found that even for an Academic block with capacity of around 120 classrooms, a monthly wastage of INR 40–45 K was noted. This motivated us to propose an IoT enabled, automated smart classrooms for optimized utilization and control of electric energy without going for infrastructural system redesign just by using low power add-ons for existing classrooms using sensor technologies and relay circuits. The proposed system will be able to automatically detect the presence and count of footfalls in a classroom and have control over the appliances in terms of switching them on and off based on algorithm. An open-end survey by the team of 5–6 individuals are conducted for the period of 4 weeks in a pattern of 3–4 times a day by each individual in an academic block having 120 classrooms across 4 floors to record the number of unoccupied classrooms and their respective electrical utilities which are kept ON. As shown in Fig. 1. It was observed that on an average for a day 39 classrooms during midday (12.00–13.00 h) kept all fans and lights ON when the classrooms were empty.

Figure 2 shows the wastage of electricity for an academic block for one month.

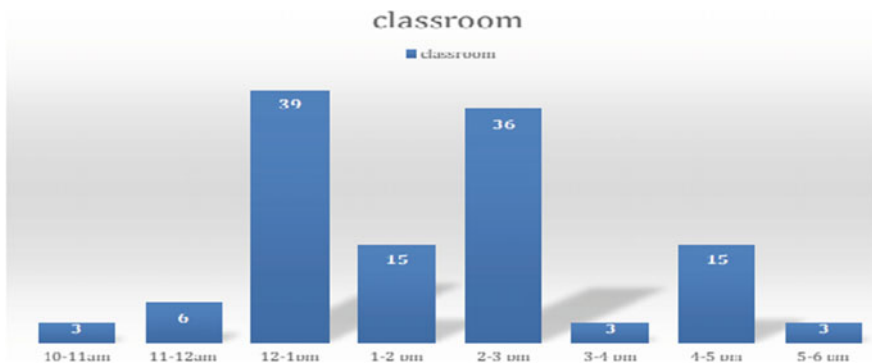


Fig. 1 No. of unoccupied classrooms v/s time

S. No	Parameter	Cost /unit calculation
1	No. of rooms in a floor found to be wasting energy	$= (2 + 10 + 9 + 5) / 4 = 7$ (approx.)
2	No. of hours found to be wasting energy	$= (1.25 + 1.25 + 1 + 1) / 4 = 1.125$ hours
3	Total Power Consumed by these rooms in a day	$= 7 * 1.125 * (720 \text{ watts (lights)} + 500 \text{ watts (fans)} + 4000 \text{ watts (AC)})$ $= 41,705$ Watts
4	Units Consumed /floor	$= 41.1075$ Units
5	Total Expense /floor/ day	$= \text{INR } 370.00$ (approx.)
6	Total no. of Floors	$= 4$
7	Total Expense of a block/day	$= \text{INR } 370 * 4$ $= \text{INR } 1480$
8	Total Expense of a month	$= \text{INR } 44,400.00$
9	Total Expense of a year	$= \text{INR } 5,32,800.00$

Fig. 2 Wastage of electricity for an academic block for one month

Figure 2 explains the wastage of electricity in terms of capital cost of INR 5,32,800.00 per year. With the proposed technology we can avoid wasting energy in academic buildings based on the monitoring and controlling approach.

4 Energy Management in Campus: Challenges

The elementary components of any given academic campuses are the teaching staff, nonteaching staff, student density, and the administrative body. We all tend to ignore to be self-responsible for switching OFF the buttons in a situation where classrooms are vacant and all the lights and fans are ON. This causes high energy wastage. An academic institution's electricity bill is typically a huge amount of its monthly expenses. Experience suggests that there is a need for smart, automated energy management systems that can realize the energy savings. Let us contemplate heating, ventilation and air conditioning (HVAC) schemes, which are massive energy consumers being accountable for 30–50% of energy spent by buildings [4]. Easily available/sensed information can be used to control HVACs and other devices, like fans and lights, without compromising on the thermal comfort. Energy consumption of buildings is correlated to occupancy, number of appliances, temperature, and other environmental factors.

5 Existing System

The existing approaches for reduction of wastage in the use of lights and fans in an academic institution are based on simple motion detection in the area. However, this approach has got numerous limitations such as the system enables or disables the current flow for entire switchboard based on the input received from motion sensors in terms of human presence and absence. Hence these approaches are considered to be inefficient in real-life scenarios. Our approach would be more robust and sensible as it is based on the actual count of occupants of the space and only when a significant (threshold) number of people are present at the class, the devices would be armed in such a way that one can put them ON and OFF based on the provision also if system detects count 0, with the help of motion sensors, the system can take decision in automatic shutdown of all power equipment of a classroom.

6 Methodology

6.1 Design Criteria

The system design began with the searching of available low-cost motion detector sensors for implementing counting systems. REES52 LDR MODULE Photo Resistor Sensor Module was found comparatively best suitable for this counting application since it was planned to detect the direction (entry/exit) as well. For sensing current flow, Generic ACS712 30A Hall Current Sensor Module was found reasonable. An Arduino Uno microcontroller board was chosen for interfacing these analog sensors. The LDR module was then coupled with a laser emitting device. Since Arduino doesn't stand alone for transferring the data wirelessly to the cloud, the low-cost Arduino's add-on wireless adapter ESP 8266 board was chosen for wireless data transmission in local server. As an initial requirement the database needed to be implemented on a third-party service provider, the ThingSpeak cloud infrastructure is selected for creating a remote database and test the data flow. A portable custom made mobile application is designed to retrieve the data from ThingSpeak cloud.

6.2 Device Configuration and Working Principles

In the proposed work, two pairs of laser coupled LDR sensors have been placed at a definite distance between each pair at the entry door of a classroom in such a way that if there is some person entering or leaving the classroom should cross both the pair of sensors. The following constraints have been set for the system for improved accuracy of count read. (a) Distance between two LDR sensors \geq Avg. Width of the person. (b) A PIR motion sensor should be used in order to avoid negative head

count due to inaccuracies. The accurate counting system is then integrated with electricity consumption control and monitoring application. An 8 channel relay is used for controlling the appliances based on the student strength. If the class strength on someday is say around 50% then only first half of the classroom's appliances are activated, so that along with a huge save in electricity, there is a quality education in the classes. For pilot testing, it has been considered that the class canceled or not active if the strength is below 20%. In this project all the sensors, actuators and wireless modules are talking to each other by a platform provided by Arduino concerning their status and have autonomous control over the electric infrastructure of classroom and take decision accordingly. Relays are effectively used in the switches to arm the switches so that the students may manually turn on/off the lights and fans of only the allowed rows. Consider the 50% example, i.e., only the fans and lights of the front half of the class will be available to be switched ON/OFF manually if anyone desires, the back half will remain deactivated. There will also be current sensors inserted in the circuit to keep the track of the current flow so that we can keep a record of how much electricity was consumed at any time of the day. When the class is over and the students are leaving the classroom the LDR sensors will track the direction and keep on decreasing the student count and will turn off the electricity when the strength drops below 20%. The data collected by the sensors will be uploaded to the webserver simultaneously, so that authorized person can see how much power is being consumed at any hour of the day. The entire operation of the system is explained in the flow diagram as shown in Fig. 3. Designing a local server that facilitates the web interfacing for demonstration of electrical energy consumption with graphs in real time for improving the system accuracy by data analysis. Figure 4 shows the conceptual block diagram of the proposed system.

7 Testing and Evaluation of Project Implementation

The proposed pilot testing was done during different phases of implementation. First, the counting algorithm was tested in lab with one entry at a time and observed an accuracy of around 85%. As an extended phase, the project was tested in a classroom and following observations are made. As shown in the Fig. 5. The energy optimization was done on a unit classroom with small scale electric appliances like 2 LED bulbs and 2 fans. During the lunch hour system detected no entries in the classroom and the utility dropped down as shown below. Therefore, during lunch hour, we were able to save electricity automatically. Figure 6 shows the energy utility graph for the same classroom without having the system deployed and manual switching ON and OFF neglected.

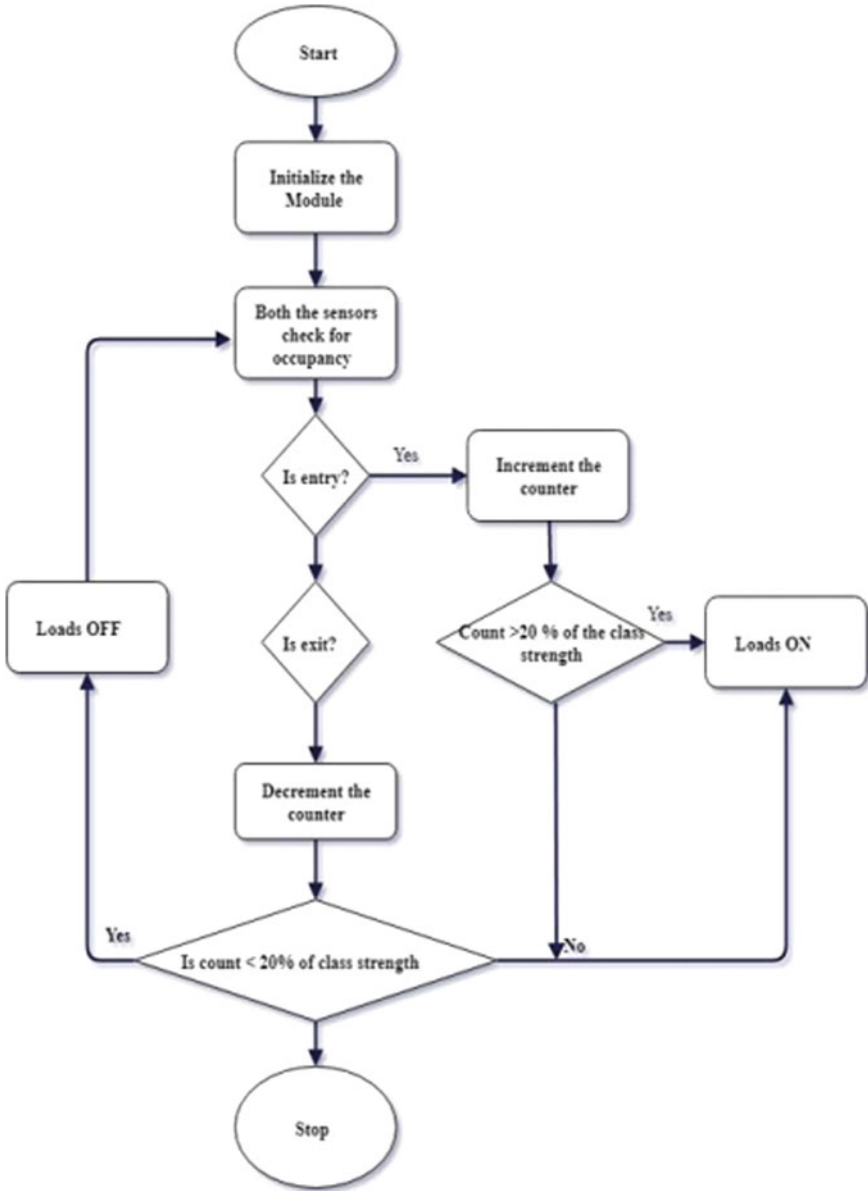


Fig. 3 Workflow of the model

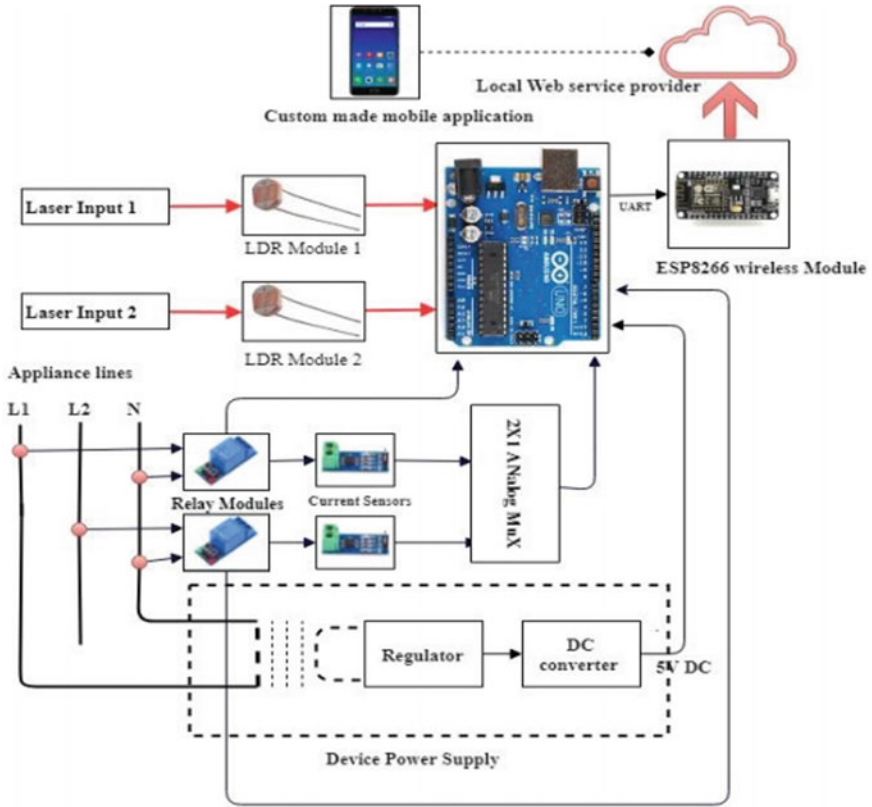


Fig. 4 Conceptual block diagram of the proposed system

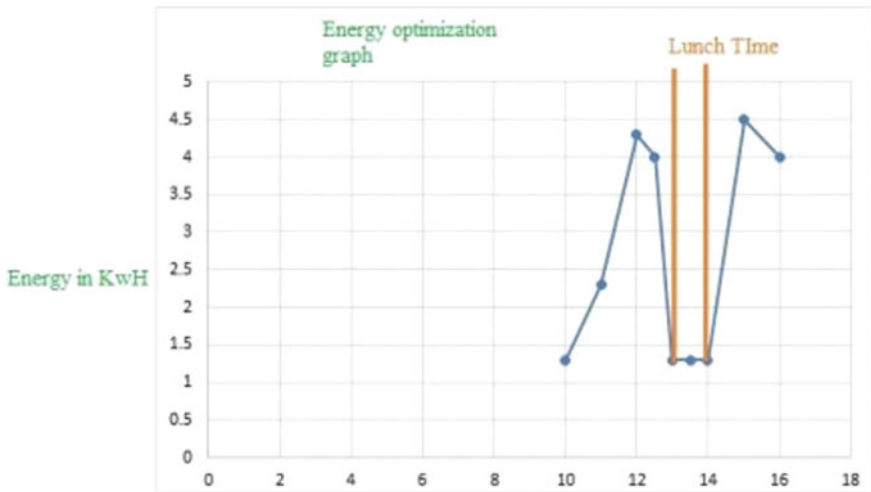


Fig. 5 Energy consumption optimization graph for unit classroom

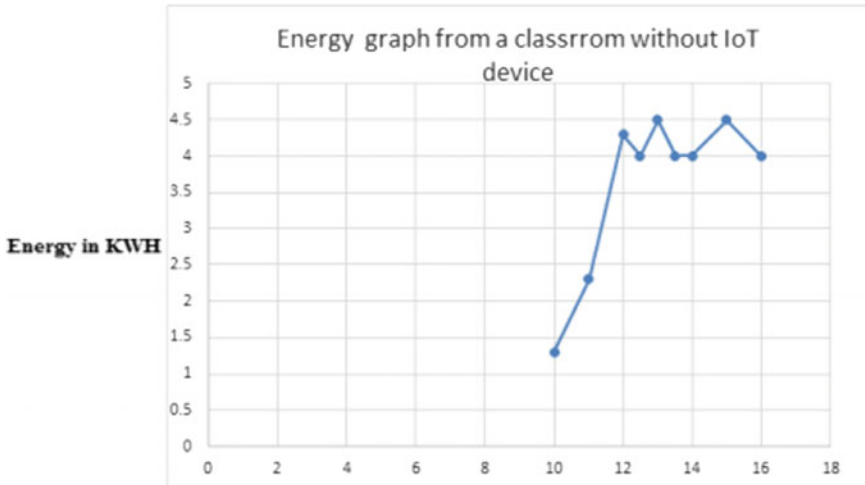


Fig. 6 Energy graph from a classroom without an IoT device

8 Future Scope and Conclusion

An IoT device was developed for monitoring, controlling, and reducing the electricity wastage by means of low-cost available sensors. The pilot module was installed and tested in real time in a classroom and compared the electricity consumption with a non-installed classroom. It was observed during the test that the consumption of electricity from a classroom with this IoT system is significantly lower than that of the classroom without the IoT system. The web interface provides the visuals of optimized electricity consumption graph, which can be used in making decision in administrative levels related to implementation of this system to entire architecture. This study can be further enhanced for improving accuracy by means of image processing and using higher-end microcontrollers like raspberry pi, Intel Edison. Automatic attendance marking system can also be embedded in this study. The same system can be implemented in different scenarios like energy consumption monitoring and controlling in large scale industries, meeting rooms, Hotels, etc., This system can also add intelligence by creating a central management system like all the class time tables are updated in the server and server decides whether or not to communicate with the devices installed in the classroom concerning their statuses.

References

1. Yang T-Y, Yang C-S, Sung T-W (2015) An intelligent energy management scheme with monitoring and scheduling approach for IoT applications in smart home. In: Robot, vision and signal processing (RVSP), pp 216–219

2. Wasoontarajaroen S, Pawasan K, Chamnanphrai V (2017) Development of an IoT device for monitoring electrical energy consumption. In: Information technology and electrical engineering (ICITEE), pp 1–4
3. Gruehn M (2016) IoT in the classroom: how traditional education is changing. Retrieved from <https://aldridge.com/future-iot-in-the-classroom-education/>
4. Rekhi (2017) There is a need for smart energy management systems that can realise the energy savings. Retrieved from <https://blogs.economictimes.indiatimes.com/et-commentary/there-is-a-need-for-smart-energy-management-systems-that-can-realise-the-energy-savings/>
5. Kailas A, Cecchi V, Mukherjee A (2012) A survey of communications and networking technologies for energy management in buildings and home automation. *J Comput Netw Commun*
6. Kyriazis D, Varvarigou T, White D, Rossi A, Cooper J (2013) Sustainable smart city IoT applications: heat and electricity management and eco-conscious cruise control for public transportation. In: World of wireless, mobile and multimedia networks (WoWMoM), 14th international symposium and workshops on a 4 Jun 2013, pp 1–5
7. Zhao HX, Magoulès F (2012) A review on the prediction of building energy consumption. *Renew Sustain Energy Rev* 16(6):3586–3592

High Power Density Parallel *LC*-Link PV Inverter for Stand-alone and Grid Mode of Operation



Rudra Santhosh Kumar Athikamsetti and Satish Kumar Gudey

Abstract A parallel *LC*-link PV inverter is presented for grid-tied and grid-independent operation. This topology is a single-stage system. This system produces desired sinusoidal voltage and current in autonomous and grid connection operation. In this topology inductor and capacitor are connected in parallel between unidirectional switches and bidirectional switches. The inductor is an energy storage element at the link and it charges and discharges through the unidirectional and bidirectional active switches, respectively. The capacitor connected in across the link inductor and it provides resonance. Hence the active switches are turned-on at zero voltage which reduces the switching losses and voltage effect on the switches. In this work parallel *LC*-link is used in place of electrolytic capacitor because it is an unreliable component and is very sensitive to temperature. Most of the inverters fail because of electrolytic capacitors, particularly at high temperature. Hence an *LC* pair is used in this work which replaces an electrolytic capacitor to improve the reliability of this PV inverter. The performance and operation are observed in various modes at high frequency as a result of high frequency operation make inductor and capacitor size compact. The modes are obtained through charging and discharging of the inductor. This type of inverter is highly efficient, reliable with high power density. Simulation is done by considering a 30 kW PV operation in grid interconnection and stand-alone modes. The frequency of link is considered to be 6 kHz. PSCAD/EMTDC v4.6 is used for simulation work.

Keywords *LC*-link · Inverters · Zero voltage switching

R. S. K. Athikamsetti · S. K. Gudey (✉)
Department of Electrical and Electronics Engineering, Gayatri Vidya Parishad College
of Engineering (Autonomous), Visakhapatnam, India
e-mail: satishgudey5@gvpce.ac.in

R. S. K. Athikamsetti
e-mail: santhosh.ar20@gmail.com

© Springer Nature Singapore Pte Ltd. 2020
A. Kalam et al. (eds.), *Intelligent Computing Techniques for Smart Energy Systems*,
Lecture Notes in Electrical Engineering 607,
https://doi.org/10.1007/978-981-15-0214-9_48

1 Introduction

Nowadays the whole world is using renewable energy systems as a source of alternate power because most of the utility power is generated through thermal-based power generation which is no more available [1]. This led to the interest of many researchers to learn and develop new methodologies to harvest renewable energy sources to use it for high power applications with reliability. Most of the renewable energy systems depend on the power electronic converter circuits to achieve load requirements.

Presently, wind energy, and PV systems are widely used renewable energy systems. As DC power is generated by PV and the load requirement is AC, power electronics are needed to convert DC to AC [2]. The lifetime of the PV is 25 years and for an inverter, it is less than 10 years. One should replace the inverter 2–3 times within the period of PV [1]. Hence reliability plays an important role. In PV systems, for inversion operation, few problems are noticed from past topologies which include more losses, use of bulky transformers, etc., in both centralized and multiple-stage based PV systems [3].

In centralized based PV system shown in Fig. 1, a low frequency transformer is used but it requires larger space and also it is operated with poor efficiency [4]. In multiple-stage converters based PV system shown in Fig. 2, losses are more because of more stages [5]. It consists of chopper included with high frequency transformer, inverter, and electrolytic capacitor.

We know that in an electrical system if number of stages are increased, losses increase exponentially. An electrolytic capacitor is internally connected to the inverter. This electrolytic capacitor is very sensitive to temperature [6]. While going for higher power levels the voltage and currents are high so that the temperature in electrolytic capacitor increases because of high charging current in the electrolytic

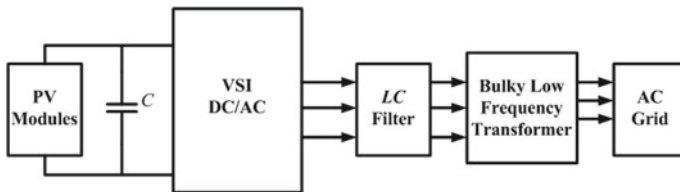


Fig. 1 Centralized power converter system

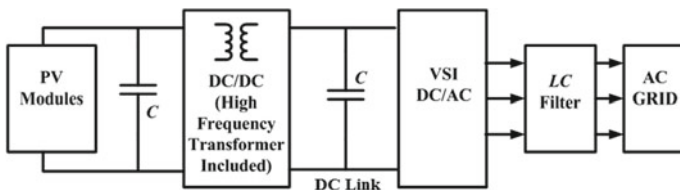


Fig. 2 Multiple-stage power converter PV system

capacitor. Equivalent electrolytic resistance present in the electrolytic capacitor produces more temperature because of high charging current so that electrolyte used in the electrolytic capacitor reduces. Therefore, the capacitor cannot maintain constant voltage at the inverter input.

Hence the reliability of inverter reduces and the trust on PV system comes down [7]. The soft-switched based parallel LC-link PV inverter reduces the EMI effect [8–11]. High frequency operation makes the system very compact. A parallel LC-link PV inverter discussed in this paper based on zero voltage switching (ZVS) and it reduces the above identified problems [12, 13].

2 Operation Principle Under Different Modes

2.1 Configuration

Figure 3 represents the proposed PV inverter. It consists of a PV, four unidirectional active switches, LC-link, and twelve bidirectional active switches. The link inductor transfers the total PV from the load/grid by using active switches. The link inductor charges through the PV and discharges into the load by using unidirectional and bidirectional switches, respectively [1].

Link inductor charges through the PV by using unidirectional active switches and energy discharges through the bidirectional active switches to the ac utility. The charging and discharging takes place alternatively. The time period of charging and discharging is called a link time period (T).

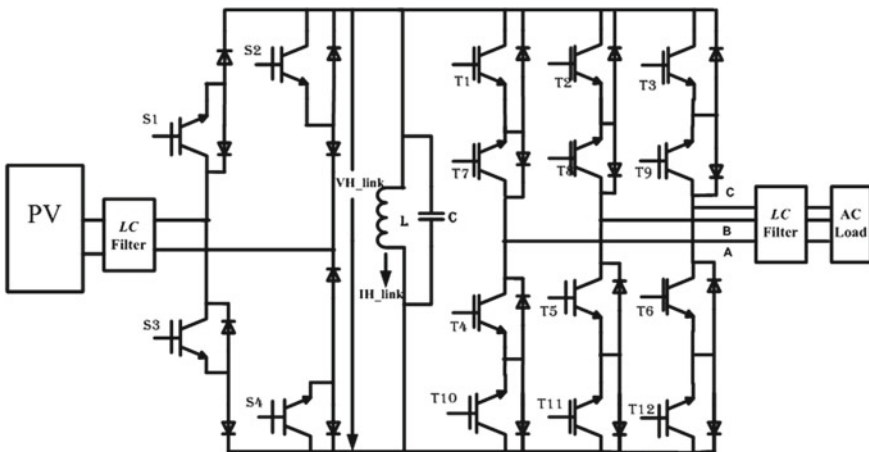


Fig. 3 Circuit diagram of a parallel LC-link PV inverter

A nonelectrolytic capacitor (C) is connected across the link inductor (L) to provide partial resonance effect. Using the resonance effect, the switches are made to turn-on at zero voltage which implies LC -link resonance provides zero voltage switching.

Filter capacitors are placed across the input and output side of inverter terminals because this topology acts as a voltage source at both sides as alike to DC to DC buck-boost chopper.

2.2 Principle of Operation

The link cycle shown in Fig. 4 and the operation of this topology is divided into twelve modes, in which six are charging and discharging modes and remaining are resonance modes.

Mode 1 (Charging). It is a charging mode during which switches S_1 and S_4 are forward biased after resonance (assumed). In this mode, the V_{Link} is equal to the V_{PV} . It is shown in Fig. 5.

Mode 2, 4, 6, 8, 10, 12 (resonance). During this period parallel LC -link resonates. Hence none of the active switches conducts and the circuit acts as a LC circuit which is shown in Fig. 6.

Mode 3 (Discharging). During this mode, T_7 and T_{11} are turned-on and link inductor energy is discharged to the output as shown in Fig. 7.

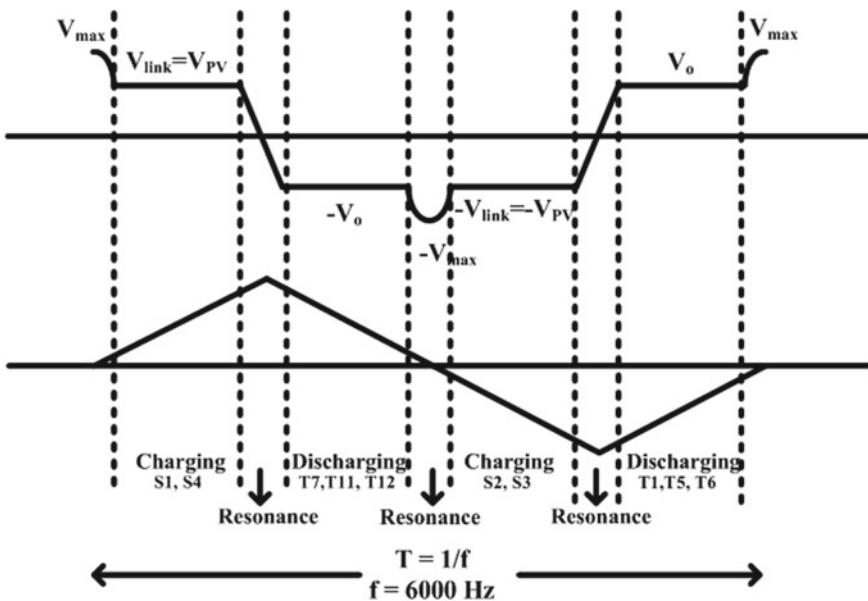


Fig. 4 Link current and voltage of in the PV inverter

Mode 5 (Discharging). During this mode, T_7 and T_{12} are turned-on and remaining inductor energy discharged through output phase pair. It is shown in Fig. 8.

The remaining modes Mode 7 to Mode 12 are similar to Mode 1 to Mode 6. Here charging and discharging takes place in the reverse direction in the negative cycle. The complimentary switches conduct during these modes of operation.

3 Parameter Design Procedure

In this design procedure, an AC link inductor (L) is designed. It is assumed that the resonance period of time is very less than the charging and discharging time period at rated power, hence resonance time is neglected. The equivalent output load current can be calculated as follows:

$$I_{\text{output-equivalent}} = \frac{3I_{\text{output-maximum}}}{\pi} \tag{1}$$

where $I_{\text{output-maximum}}$ is the maximum output load current.

The output equivalent voltage is given by (2)

$$V_{\text{output-equivalent}} = \frac{\pi V_{\text{output-maximum}}}{2} \cos \theta \tag{2}$$

where $V_{\text{output-maximum}}$ is the output maximum load voltage and $\cos \theta$ is the load power factor. From (3) and (4), $I_{\text{Link-maximum}}$ is the maximum current through the link inductor, the voltage across the parallel link is equal to V_{pv} , $t_{\text{Link-charge}}$ is the charging time of the link inductor current as shown in Fig. 4.

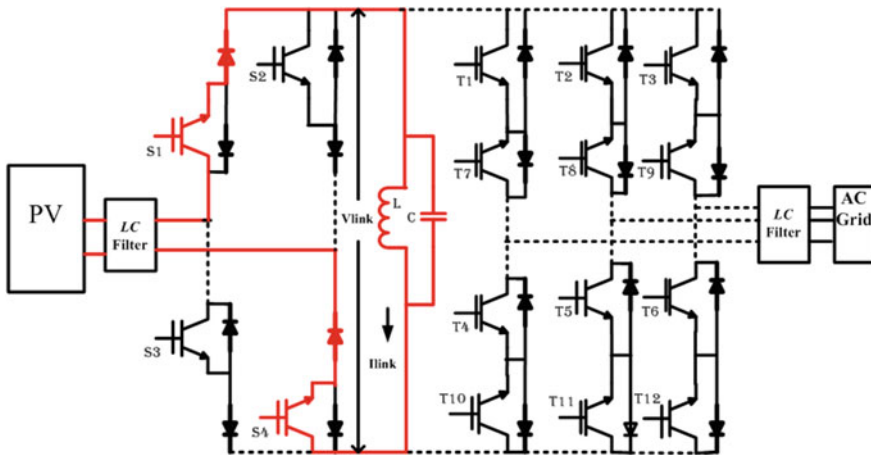


Fig. 5 Circuit diagram for mode 1 operation

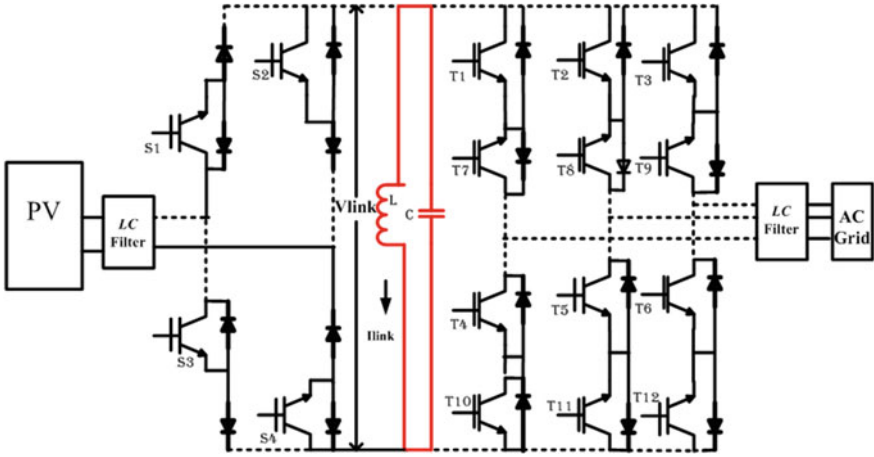


Fig. 6 Circuit diagram for mode 2, 4, 6, 8, 10, 12 operation

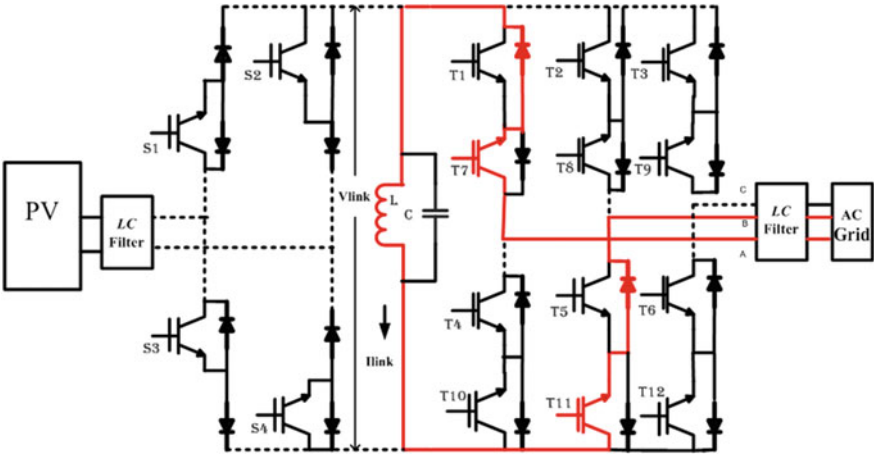


Fig. 7 Circuit diagram for mode 3 operation

$$I_{\text{Link-maximum}} = \frac{V_{pv} \times t_{\text{Link-charge}}}{L_{\text{Link}}} \tag{3}$$

$$I_{\text{Link-maximum}} = \frac{V_{\text{output-equivalent}} \times t_{\text{Link-discharge}}}{L_{\text{Link}}} \tag{4}$$

The above equation indicates, $I_{\text{Link-maximum}}$ in the discharging time.

$$t_{\text{Link-charge}} = \frac{V_{\text{output-equivalent}} \times t_{\text{Link-discharge}}}{V_{pv}} \tag{5}$$

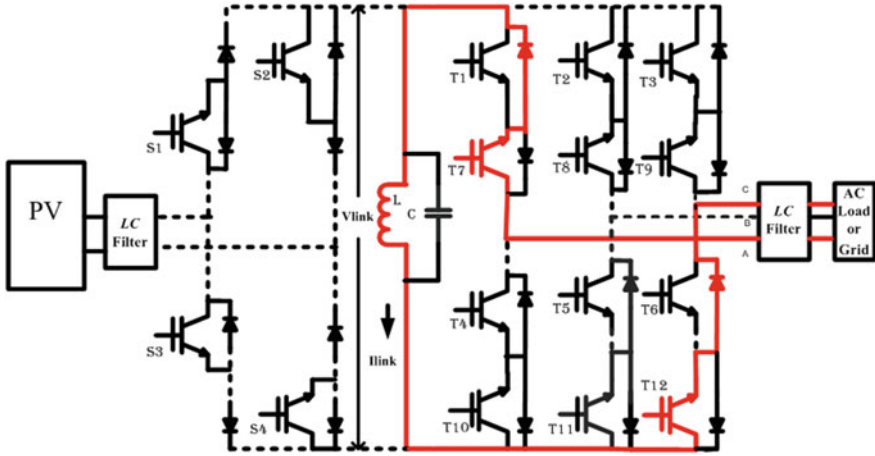


Fig. 8 Circuit diagram for mode 5 operation

Equation (5) shows the relation between input and output with respect to charging and discharging time.

$$I_{\text{Link-maximum}} = \frac{2P_{\text{load}}}{V_{PV}} \left(1 + \left(\frac{V_{pv}}{V_{\text{output-equivalent}}} \right) \right) \tag{6}$$

From (6), the link maximum current depends on the load power, voltages of PV, and load/grid. Equation (6) can be rewritten as

$$I_{\text{Link,max}} = 2 \times (I_{PV,dc} + I_{\text{output-eg}}) \tag{7}$$

From Eq. (7), the link maximum current is determined by using the PV current and output currents. The characteristics of the switch and the power levels of the system under operation determine the frequency at which the link operates. Hence a predetermined frequency of the link is known, the link inductance can be determined using (8).

$$L_{\text{Link}} = \frac{V_{PV,dc}}{I_{\text{Link,max}}} \left(\frac{1}{2f_{\text{Link}} \left(1 + \left(\frac{V_{pv,dc}}{V_{\text{output-eg}}} \right) \right)} \right) \tag{8}$$

$$c = \frac{1}{4\pi^2 f_r^2 L_{\text{Link}}} \tag{9}$$

Here f_{Link} is the link frequency. Since the resonance period is less than 5% of the link time period at rated power, the Link capacitance (C) is taken based on this assumption. In this proposed work switching losses are negligible because switches are turned-on at zero voltage. In this proposed work constant and variable losses of

the inductor are only considered because these losses are proportional to frequency and the link rms currents.

4 Zero Voltage Switching Operation (ZVS)

The control strategy is to turn-on the switches at zero voltage and is shown in Fig. 9. Incremental conductance MPPT technique [14] is used to generate a reference current to control the input side switches (T_1 to T_4). For load side switch control, output currents are compared with reference currents, these reference currents are generated by taking output voltages and power loss in the system. Figure 9 shows the generation of I_{pv_ref} on the input side and reference current generation I_{aref} , etc. on the output side of the system under consideration.

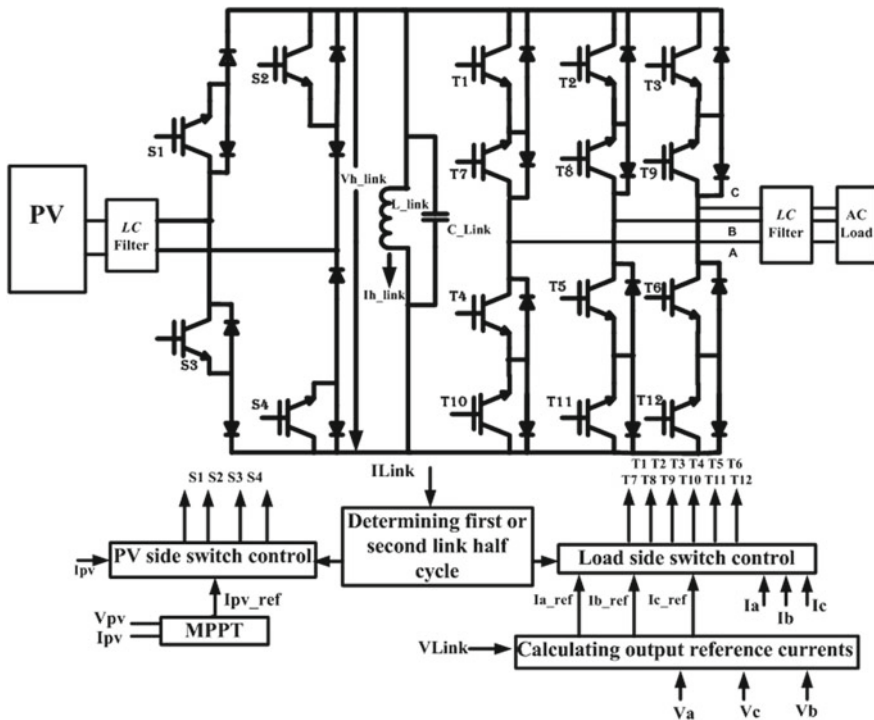


Fig. 9 Block diagram of controller of the PV inverter

5 Simulation Results

A PV system rated at 30 kW is used for simulation work. It is fed to a grid and also for stand-alone (*RL*-Load) mode. The designed parameters of a parallel *LC*-link PV inverter are shown in Table 1. The values are calculated from (1) to (8).

A 700 V nominal voltage PV inverter has been designed. The PV voltage and current simulation waveforms are shown in Fig. 10. The PV voltage is 700 V and PV current is 43 A at 850 W/m² irradiance and 35° temperature. From Fig. 11 the maximum voltage (during resonance) is 850 V and minimum voltage (during discharge) is around 650 V across the link. The maximum link current is 200 and the link frequency is 6 kHz.

Figure 12 shows the simulated waveform of the phase voltage and current of load at near to unity power factor. Figure 13, shows the simulation waveform of phase voltage and current. The current lags the voltage by 37°. The magnitude of voltage is 340 V and current is 59 A with 50 Hz frequency. Figure 14 shows the output three-phase currents. The peak current of the load is 59 A and the rms value is 42 A and frequency is 50 Hz. Figure 15 shows the phase voltages of grid. The phase crest

Table 1 Parameters of the designed inverter

Parameters	Value
PV voltage (V_{pv})	700 V
Grid voltage (V_0)	415 V (RMS, L-L)
Link inductance (L_{Link})	110 μ H
Link capacitance (C_{Link})	0.7 μ F
Maximum link current ($I_{Link-maximum}$)	200 A
Operating link frequency (f_{Link})	6 kHz
Filter on the PV side	$L = 360 \mu$ H; $C = 170 \mu$ F
AC side filter	$L = 60 \mu$ H; $C = 72 \mu$ F
Standalone load (RL-load)	30 kW, 0.8 pf lagging

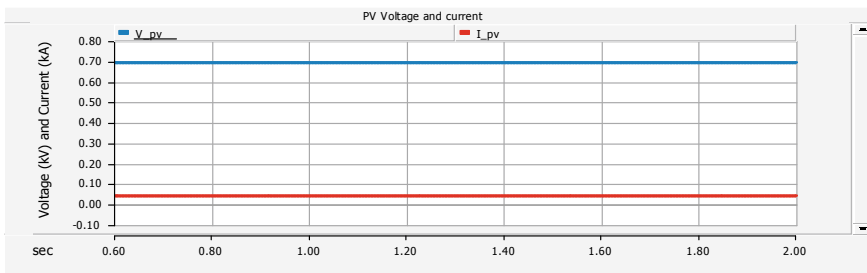


Fig. 10 PV voltage and PV current

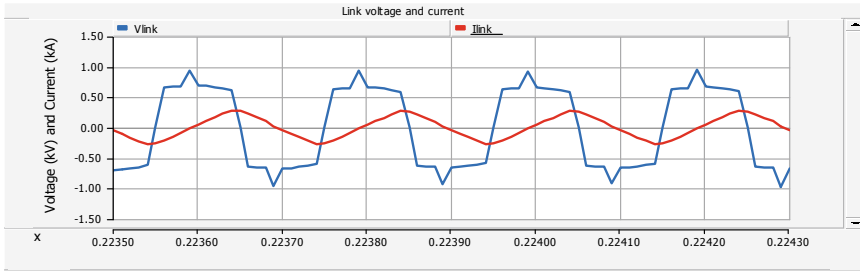


Fig. 11 LC-link voltage and inductor link current

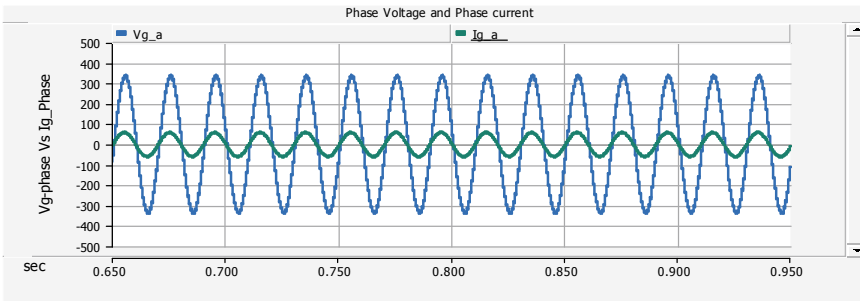


Fig. 12 Phase voltage and current of grid

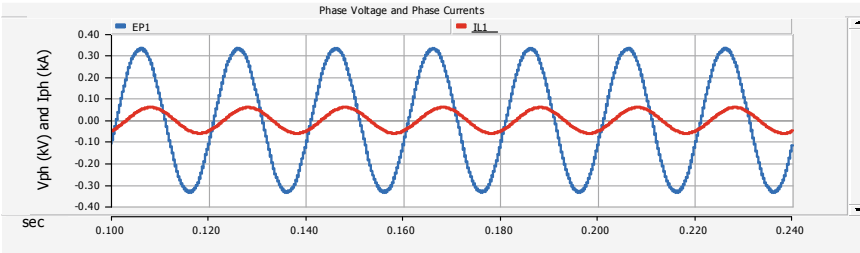


Fig. 13 Current lags the phase voltage for RL-load

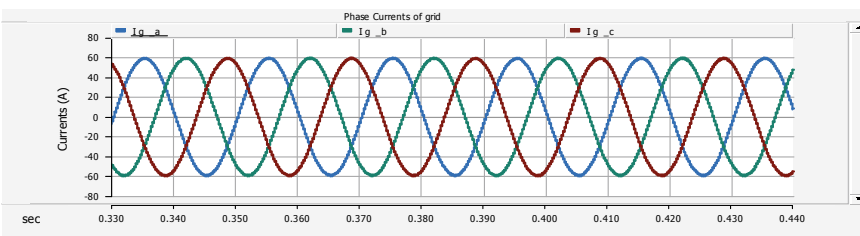


Fig. 14 3-Three phase currents of grid

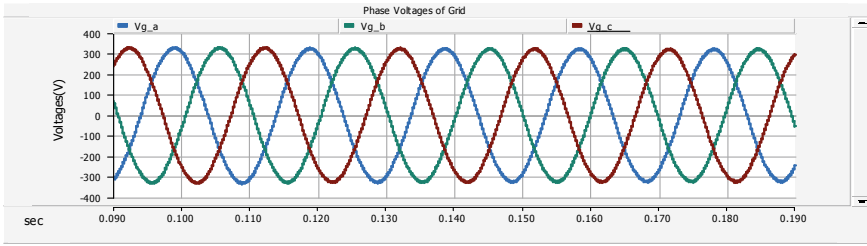


Fig. 15 Three-phase voltages of grid

value is found to be 340 V. In Fig. 16 the three-phase line voltages after the filter are depicted. The maximum peak voltage of the line is 586 and 415 V is the rms value.

In Fig. 17 the voltage and currents of input side switches are presented. From the waveform, it is clear the switches are triggered at zero voltage. Therefore, the switching losses are said to be lowered. It is also clear that the voltage effect on the switches are reduced. Figure 18 shows the THD of grid current is 0167% and Fig. 19 shows current THD for RL-load. Hence it can be realized that a parallel LC-link PV inverter is capable of obtaining a desired sinusoidal waveform using soft-switching technique. It results in fewer losses and higher efficiency. Also high rating of the PV inverter can be used for grid interconnection and stand-alone operation. A high efficiency PV inverter can be realized when connected to the grid. The proposed

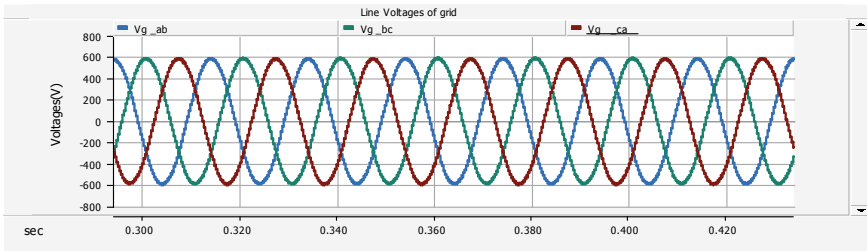


Fig. 16 Three-phase line voltages of grid

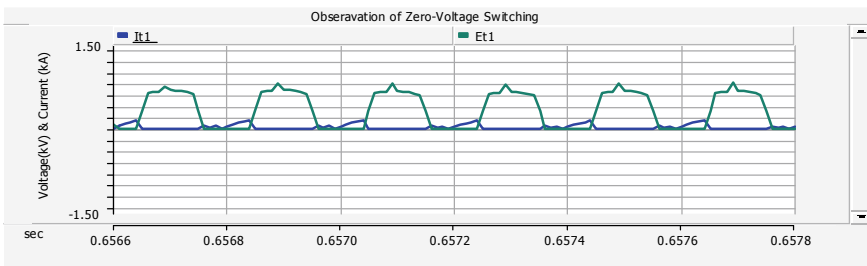


Fig. 17 Voltage and currents of the switches

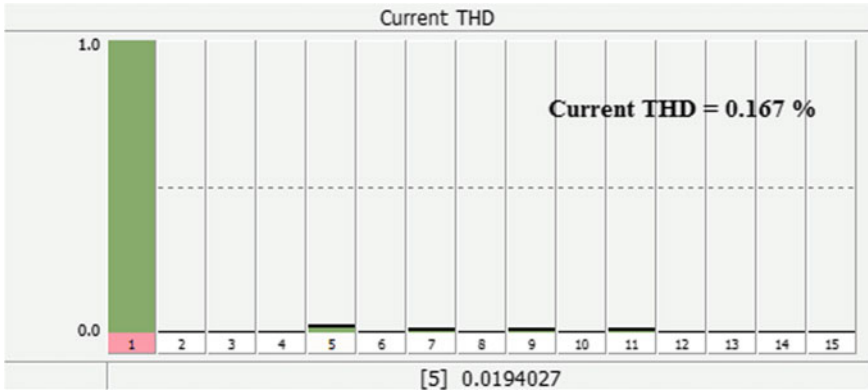


Fig. 18 FFT of grid currents

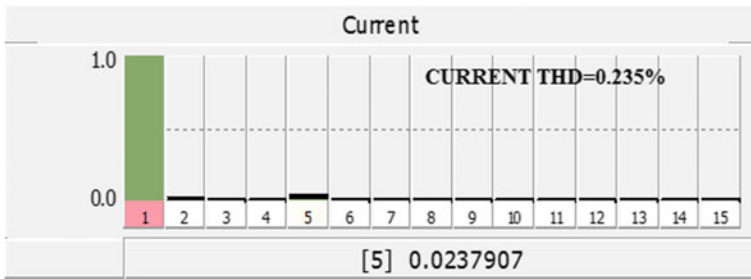


Fig. 19 FFT analysis of RL-load currents

work is tested through simulation only. The proposed work meets grid requirement as per Indian grid standards and it is observed through simulation. The simulation results are compared with the theoretical values for better understanding.

6 Conclusions

In this paper, a parallel LC-link PV inverter design and operation with different modes are discussed. A novel configuration of a one stage LC-link PV inverter for grid operation is developed and simulated in this work. The parallel LC-link provides the Zero Voltage Switching (ZVS) operation and also the proposed work provides the isolation between input and output. One major advantage this inverter possesses is the exclusion of a large low frequency transformer and DC link capacitor. It makes the proposed topology compact and reliable operation. The performance of the proposed topology has been done through PSCAD simulator for grid interconnection and stand-alone modes. The voltage and current waveforms obtained are sinusoidal with less

THD. This type of inverter can be used for AC–AC and DC–AC power conversion with less complexity. The paper can be extended using a series LC-link PV inverter with two different sources of power.

References

1. Rodriguez C, Amaratunga GAJ (2008) Long-lifetime power inverter for photovoltaic AC modules. *IEEE Trans Ind Electron* 55(7):2593–2601
2. Chakraborty S, Kramer B, Kroposki B (2009) A review of power electronics interfaces for distributed energy systems towards achieving low-cost modular design. *Renew Sustain Energy Rev* 13(9):2323–2335
3. Amirabadi M, Balakrishna A, Toliyat H, Alexander W (2014) High frequency AC-link PV inverter. *IEEE Trans Ind Electron* 61(1):281–291
4. Kerekes T, Teodorescu R, Rodriguez P, Vazquez G, Aldabas E (2011) A new high-efficiency single-phase transformer less PV inverter topology. *IEEE Trans Ind Electron* 58(1):184–191
5. Grandi G, Rossi C, Ostojic D, Casadei D (2009) A new multilevel conversion structure for grid-connected PV application. *IEEE Trans Ind Electron* 56(11):4416–4426
6. Stevens JL, Shaffer JS, Vandenham JT (2002) The service life of large aluminum electrolytic capacitors: effects of construction and application. *IEEE Trans Ind Appl* 38(5)
7. Castillo SJ, Balog RS, Enjeti P (2010) Predicting capacitor reliability in a module-integrated photovoltaic inverter using stress factors from an environmental usage model. In: *Proceedings of NAPS*, pp 1–6
8. Amirabadi M, Balakrishnan A, Toliyat HA, Alexander W (2008) Soft switched AC-link direct-connect photovoltaic inverter. In: *Proceedings of the IEEE international conference on sustainable energy technology*, pp 116–120
9. Bhat AKS, Dewan SB (1988) Resonant inverters for photovoltaic array to utility interface. *IEEE Trans Aerosp Electron Syst* 24(4):377–386
10. Balakrishnan A, Toliyat HA, Alexander WC (2008) Soft switched AC link buck boost converter. In: *Proceedings of the IEEE APEC*, pp 1334–1339
11. Balakrishnan A, Amirabadi M, Toliyat H, Alexander W (2008) Soft switched AC-link wind power converter. In: *Proceedings of the IEEE ICSET*, pp 318–321
12. Amirabadi M, Toliyat HA, Alexander WC (2009) Battery-utility interface using soft switched AC link buck–boost converter. In: *Proceedings of IEMDC*, pp 1299–1304
13. Amirabadi M, Toliyat HA, Alexander WC (2009) Battery-utility interface using soft switched AC link supporting low voltage ride through. In: *Proceedings of ECCE*, pp 2606–2613
14. Sah B, Kumar S (2017) A comparative study of different MPPT techniques using different dc-dc converters in a standalone PV system. In: *TENCON 2017–IEEE region TEN conference*, Singapore, 2017, pp 1690–1695

A Hybrid Forecasting Model Based on Artificial Neural Network and Teaching Learning Based Optimization Algorithm for Day-Ahead Wind Speed Prediction



Madasthu Santhosh, Chintham Venkaiah and D. M. Vinod Kumar

Abstract In this analytical study, a hybrid day-ahead wind speed prediction approach for high accuracy is implemented. The hybrid approach initially converts raw wind speed data series into actual hourly input structure for reducing uncertainty and the intermittent nature of wind speed. The back-propagation neural network is utilized for its better learning capability and also for its ability for nonlinear mapping among complex data. The teaching learning-based optimization algorithm is used to auto-tune the best weights of the artificial neural network. This optimization algorithm is used for its powerful ability to search and explore on a global scale. Then, the artificial neural network teaching learning-based optimization approach is implemented for wind speed forecasting. After that, the day-ahead prediction is performed using the proposed hybrid model for actual hourly input structure. The hybrid model prediction results give enhanced prediction accuracy when compared to existing approaches.

Keywords Day-ahead wind speed prediction · Hybrid model · Artificial Neural Network (ANN) · Teaching Learning-Based Optimization (TLBO) · Parameter optimization

1 Introduction

Electrical energy has come to play a significant role not only in modern human life but also in the growth of the world economy. Specifically, wind energy is clean, pollution free, and is part of the fast-growing renewable energy sources (RES) and this

M. Santhosh · C. Venkaiah (✉) · D. M. V. Kumar
Department of Electrical Engineering, National Institute of Technology Warangal,
Hanamkonda 506 004, Telangana, India
e-mail: ch.venkaiah@ieee.org

M. Santhosh
e-mail: madasthusanthosh@ieee.org

D. M. V. Kumar
e-mail: vinodkumar.dm@gmail.com

© Springer Nature Singapore Pte Ltd. 2020
A. Kalam et al. (eds.), *Intelligent Computing Techniques for Smart Energy Systems*,
Lecture Notes in Electrical Engineering 607,
https://doi.org/10.1007/978-981-15-0214-9_49

form of energy is drawing worldwide attention among RES. As per the Global Wind Energy Council (GWEC) report, the new worldwide total wind installed capacity was 539.1 GW by the end of 2017 [1]. Advancement of power electronic devices gives us better grid reliability services with wind turbines than with conventional power plants. A reliable and efficient energy supplement planning requires accurate wind speed and wind power prediction. An error-free wind speed prediction is required for improved renewable energy integration for effective electricity market operation and also for supporting the operators of the grid from better control of the balance of power supply and demand. Several techniques employed for wind forecasting on the basis of data usage are broadly classified as persistence method, physical approach, statistical models, and artificial intelligence models.

Although there are numerous approaches available for forecasting wind speed in the literature, as shown in Table 1, there is still a tremendous need for a method that gives high prediction accuracy and low computational burden.

The main idea of this analytical study is to propose a forecasting approach for accurate day-ahead wind speed prediction. In this study, TLBO algorithm is employed to greatly improve the performance of ANN so that forecasting error is minimized to achieve the desired results. The experimental assessment confirms that the proposed ANN-TLBO model can remarkably improve the robustness of the model. The prediction results based on real wind speed data provided by a wind farm in the U.S.A. give enhanced prediction accuracy in comparison with the existing benchmark approaches.

The rest of the paper is arranged as follows: Sect. 2 describes the fundamental concepts required for implementing the hybrid wind speed prediction model. Section 3 presents the working principle of the hybrid forecasting model. Section 4 provides the analytical study to validate the hybrid method, and Sect. 5 concludes this paper with scope for future.

2 Working Principle of Hybrid Forecasting Model

The hybrid ANN-TLBO approach for STWSF is based on the ANN model [3] and TLBO algorithm [7]. In this hybrid model, the main purpose of ANN is to enhance better learning capability as well as the ability of nonlinear mapping among distinct complex data. And TLBO algorithm is used just for tuning the weighting and biasing factors of BPNN to improvise the training of the network. First, input data values and target values that are past wind speed time series values must be normalized within the specific range using Eq. (1); these are then to be utilized for training ANN.

$$WI_n = \frac{WT_{\max} - WT_{\min}}{WI_{\max} - WI_{\min}}(WI - WI_{\min}) + WT_{\min} \quad (1)$$

where WI_n is the normalized value of wind speed input; WI_{\max} and WI_{\min} are the maximum and minimum wind speed inputs (WI), respectively; WT_{\max} and WT_{\min}

Table 1 Primary wind speed prediction approaches by various researchers

Approach	Subcategory	Model used	Observations
Persistence model or Naive Predictor [2]	–	$P(t + k) = P(t)$	- Benchmark model or approach - Gives very accurate results for very short-term and short-term predictions
Physical Approaches [3]	Numerical Weather Predictions (NWP)	- Predictor - Global Forecast System (GFS) - Unified Model (UM) - High Resolution Limited Area Model (HiRLAM)	- Accurate for long-term forecasts - Utilizes meteorological inputs like wind speed, temperature, wind direction, pressure, humidity and dew point, etc.
Statistical Approaches [4]	Artificial Neural Networks (ANNs)	- Feed forward NN - Recurrent NN - Radial basis function NN - Elman recurrent NN etc.	- Very accurate for short-term forecasts - Better than time series models
Statistical Approaches [5]	Time series models	- ARMA - ARIMA - Linear predictions - GARCH etc	- Gives accurate future values for short-term predictions - Certain best models override NN models
Artificial Intelligence Approaches [6, 7, 10, 11]	- ANNs - Fuzzy logic approach - Evolutionary computation - Machine learning	- ANFIS - ANN + NWP - ANN + PSO - RBM + ELM	- Can easily extract patterns and detect the trends from nonlinear data - Optimization algorithms can build robust and accurate AI models - ANFIS is the best for very short-term forecasts - ANN+NWP hybrid approaches are most accurately predicts long-term predictions

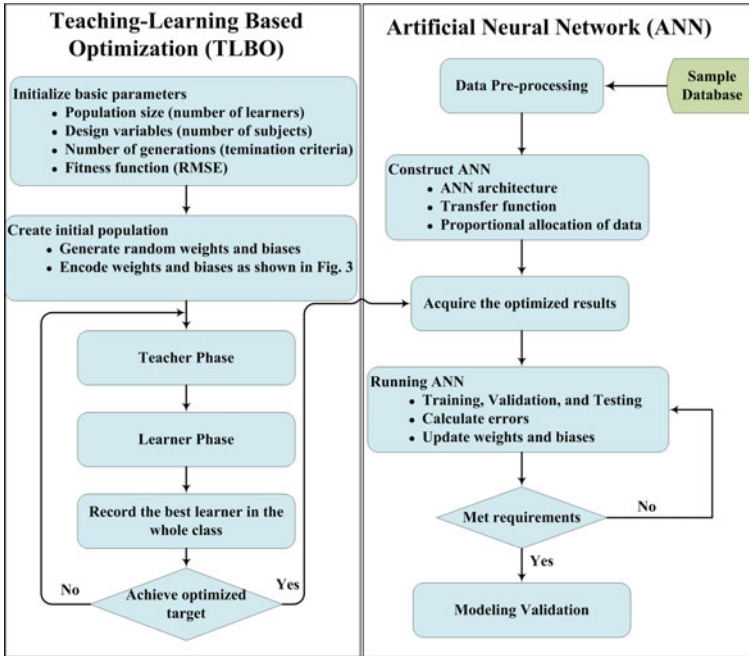


Fig. 1 Framework of hybrid ANN-TLBO model

are the maximum and minimum wind speed targets (WT), respectively. If the range from $[-1, 1]$ is considered, then $WT_{max} = 1$ and $WT_{min} = -1$.

A schematic diagram of the hybrid method is depicted in Fig. 1. For developing the hybrid ANN-TLBO model, an individual in the population possesses the information of weights and biases expressed as a learner’s initial position. A group of weights and biases $[w_{ij}^l, b_j^l]$ and $[w_{jk}^l, b_k^l]$ is encoded to form a number of learners, where ‘l’ means l th learner (an individual in the population), depicted in Fig. 2. The length of each learner (i.e., the number of subjects) is always decided based on the architecture of the ANN. After building the ANN structure, TLBO algorithm is started executing for generating and optimizing the weights and biases of BPNN.

3 Forecasting Results and Discussions

The data utilized for this work was collected from a site located in Boulder, Colorado, the U.S.A. as hourly samples of wind time series data [8]. MATLAB R2009b software was utilized for implementation of hybrid ANN-TLBO model [9]. For STWSF only 2160 past wind speed observation values were selected. The initial 2136 values

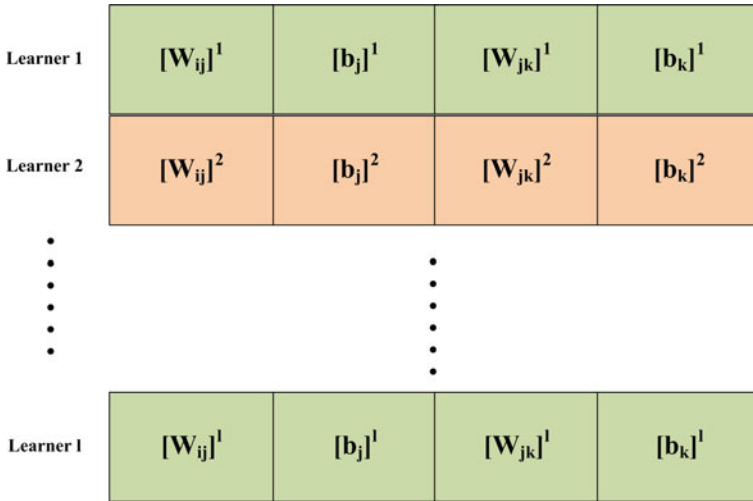


Fig. 2 Population of the class includes all learners

Table 2 Parameters of GA, PSO

GA	PSO
Initial population = 30	Initial number of particles = 30
Number of variables = 4	Dimension of the problem = 4
Max. number of generations = 100	Max. number of steps = 100
Mutation probability = 0.1	Maximum velocity = 2
Crossover probability = 0.8	Inertia weight factor = 0.8

were utilized as the training data samples, and the remaining 24 values were used for testing. The parameters considered for GA and PSO algorithms are shown in Table 2.

Parameters are initialized randomly in the first stage and then are updated using evolutionary methods. The choice of the parameters can have a large impact on optimization performance. The population size depends on the nature of the problem, but typically it contains several hundreds or thousands of possible solutions. The same population size and number of control variables are employed for consistency of comparisons. The number of generations (100 generations or iterations) has been chosen as the termination criterion. The reason for this number of iterations is that it was seen that there was no significant progress after about 100 generations. For GA, it is worth tuning parameters such as mutation probability, crossover probability, and population size to find reasonable settings for the problem class being worked on. A very small mutation rate may lead to genetic drift. A recombination rate that is too high may lead to premature convergence of the genetic algorithm. A mutation rate that is too high may lead to loss of good solutions unless the elitist selection is employed. Where the PSO algorithm is concerned, the maximum velocity and

the inertia weight factor are set as 2 and 0.8, respectively. The weighting factor in the PSO algorithm has been updated during the optimization process adaptively. The number of runs/trails of the evolutionary methods i.e., GA and TLBO are 25 to 50 trails presented in the paper. For the execution of TLBO, the algorithm control parameters are initialized as follows: the initial number of learners = 30, number of subjects = 4, and number of generations = 100.

Tables 3 and 4 have shown the comparison between the proposed hybrid ANN-TLBO model and other reported models in terms of statistical measures such as RMSE (m/s) and MAPE (%), respectively. For evaluating the model performance, the RMSE (m/s) and MAPE (%) are used as model evaluation indices. The average

Table 3 Comparison between reported models and the proposed hybrid ANN-TLBO model on RMSE for day-ahead prediction

Day	Persistence model [2]	NRM [2]	ANN model [4]	ANN-GA model [10]	ANN-PSO model [11]	Proposed model
1	0.3486	0.3092	0.2821	0.1665	0.0293	0.0164
2	0.0409	0.0243	0.2609	0.065	0.0573	0.0734
3	0.4745	0.4395	0.4260	0.2861	0.0635	0.0483
4	0.3897	0.3680	0.3424	0.2722	0.1398	0.0436
5	0.3933	0.3196	0.2886	0.2313	0.1521	0.0529
6	0.3212	0.2920	0.2346	0.1446	0.1100	0.0524
7	0.1004	0.0742	0.0372	0.0346	0.0459	0.0663
8	0.4116	0.3584	0.3231	0.1916	0.1305	0.0569
9	0.5919	0.5729	0.5458	0.4138	0.1646	0.094
10	0.2206	0.1995	0.1812	0.1413	0.0839	0.0656
11	0.4332	0.4206	0.3999	0.2845	0.1354	0.0287
12	0.1912	0.1486	0.1336	0.0908	0.0336	0.0153
13	0.1542	0.1002	0.0559	0.0470	0.0409	0.0428
14	0.3061	0.2679	0.2584	0.1573	0.1102	0.0403
15	0.1409	0.0976	0.0297	0.0248	0.0182	0.0106
16	0.1608	0.1421	0.1088	0.0998	0.0689	0.0349
17	0.1640	0.1408	0.1340	0.0907	0.0494	0.0298
18	0.0954	0.0804	0.0669	0.0609	0.0460	0.0283
19	0.1911	0.1519	0.1061	0.0519	0.0447	0.0415
20	0.0886	0.0825	0.0788	0.0591	0.0463	0.0284
21	0.1092	0.0959	0.0899	0.0786	0.0380	0.0198
22	0.0083	0.0051	0.0033	0.0047	0.0057	0.0032
23	0.0176	0.0079	0.0057	0.0044	0.0029	0.0011
24	0.2580	0.2348	0.1840	0.1599	0.1246	0.0339
Average RMSE	0.2338	0.2055	0.1907	0.1317	0.0725	0.0386

Table 4 Comparison between reported models and the proposed hybrid ANN-TLBO model on MAPE for day-ahead prediction

Day	Persistence model [2]	NRM [2]	ANN model [4]	ANN-GA model [10]	ANN-PSO model [11]	Proposed model
1	35.7043	31.6753	28.8925	17.0545	03.0003	01.6789
2	52.0795	03.7869	40.6455	10.1240	08.9253	11.4372
3	32.6018	46.1415	44.7271	30.0366	06.6691	05.0683
4	24.0931	29.3262	27.2879	21.6921	11.1380	03.4763
5	13.7001	21.9828	19.8461	15.9084	10.4600	03.6359
6	17.6258	23.6232	18.9765	11.6960	08.8955	04.2372
7	18.9344	07.1389	03.5763	03.3308	04.4129	06.3789
8	09.3470	31.2580	28.1797	16.7088	11.3855	04.9655
9	20.0990	39.9277	38.0343	28.8362	11.4685	06.5508
10	01.3182	13.7206	12.4642	09.7169	05.7667	04.5089
11	12.1563	25.4100	24.1559	17.1887	08.1782	01.73502
12	05.3046	09.4560	08.4990	05.7734	02.1361	00.9739
13	23.3980	07.8661	04.3857	03.6887	03.2112	03.3602
14	02.6852	20.4666	19.7399	12.0195	08.4158	03.0813
15	21.0461	09.0224	02.7445	02.2896	01.6856	00.97586
16	11.2911	14.6227	11.1923	10.2743	07.0876	03.5963
17	02.9994	14.0598	13.3772	09.0553	04.9332	02.9770
18	11.5490	08.9510	07.4440	06.7780	05.1233	03.1526
19	20.3266	20.3512	14.2220	06.9524	05.9897	05.5548
20	27.9679	14.1397	13.5097	10.1358	07.9413	04.8614
21	24.4607	12.4233	11.6487	10.1787	04.9175	02.5672
22	01.4266	00.6677	00.4344	00.6141	00.7481	00.4156
23	00.3154	01.0398	00.7485	00.5747	00.3849	00.1443
24	36.9577	42.1051	33.0002	28.6802	22.3467	06.0846
Average MAPE	17.8078	18.7151	17.8221	12.0544	06.8842	03.8090

RMSE values of Persistence model and NRM are 0.2338, and 0.2055, respectively. These models are restricted to short prediction horizons (3–6 h). For control over these models and for reduced RMSE values, AI models have been used. ANN model gives an RMSE value of 0.1907 and this error value is further reduced by combining the optimization algorithms such as GA, PSO algorithms with the ANN model. The average RMSE value is reduced from 0.2338 to 0.0386 by employing the hybrid ANN-TLBO model. The average MAPE value is also minimized from 17.8028 to 3.8090 by utilizing the proposed hybrid ANN-TLBO model. When compared with all other five forecasting models, the average RMSE and the average MAPE values acquired by using the proposed hybrid ANN-TLBO model gives the best performance.

This hybrid ANN-TLBO method is also effective in terms of the computational burden. For short iteration times and small training sets, the CPU time is very efficient in case of the developed ANN-TLBO model. With large scale data set such as the U.S.A. case study, the computational time for training and testing ANN-TLBO approach is 32.82 s. This CPU time is moderately low for the accuracy level of best RMSE and MAPE values practically. The percentage improvement in RMSE is 79.7063% and in MAPE is 78.6276% which is achieved by amalgamating ANN model with TLBO algorithm. This is because of optimizing the weights and biases of the ANN model. That means this hybrid ANN-TLBO model can predict the day-ahead wind speed accurately compared to five other models such as the persistence model, NRM, ANN, ANN-GA, and ANN-PSO models.

The dominance of the hybrid approaches is proved using paired sample T-test. The test hypothesis is $H_0 : x_1 - x_2 = 0, H_1 : x_1 - x_2 \neq 0$. Where x_1 is mean estimate of wind speed forecast by ANN and x_2 is mean estimate of wind speed forecast by hybrid approaches. From Table 5, it is evident that the probabilities of all pairs are below the significance level of 0.05 because the level of confidence interval is 95%. This signifies that $x_1 - x_2 \neq 0$ is true for all pairs and the hypothesis $x_1 - x_2 = 0$ should be rejected. The actual and forecast wind speeds utilizing different prediction models are as shown in Fig. 3. Therefore, by using optimization algorithms in combination with ANN models, one can improve the accuracy of STWSF.

Table 5 Paired sample T-test results

	Mean	Std. deviation	Std. error mean	95% confidence interval of the difference		Probability (two-tailed)
				Lower	Upper	
Pair 1 ANN—ANN-GA	5.667	6.844	1.397	2.777	8.557	0.000
Pair 2 ANN—ANN-PSO	11	10.517	2.147	6.559	15.441	0.001
Pair 3 ANN—ANN-TLBO	13.958	11.611	2.37	9.055	18.861	0.000

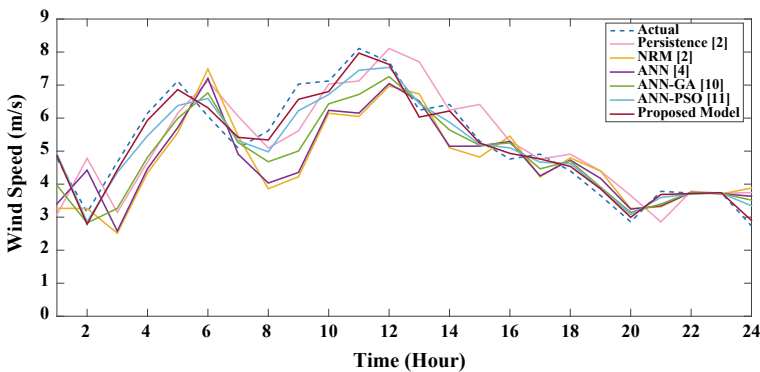


Fig. 3 Comparison of predicted wind speed values using different forecasting models with actual wind speed

4 Conclusion

The hybrid ANN-TLBO approach was implemented and examined successfully with real-world wind speed dataset provided by Colorado wind farm. This approach was developed based on the ANN model and TLBO technique to provide high accuracy, low uncertainty, and low computational burden. The traditional BPNN model was employed for its capability of nonlinear mapping from past complex wind time series data to day-ahead wind speed. The TLBO algorithm was utilized for adjusting the weights and biases of the BPNN so as to auto-tune the best parameters of BPNN. The powerful ability of global search and exploration of TLBO algorithm enhances the training of BPNN satisfactorily. The RMSE (m/s) and MAPE (%) values of the hybrid ANN-TLBO model are 0.0386 and 3.8090, respectively. Based on the performance evaluation, the hybrid ANN-TLBO model has outperformed other benchmark models and that is evident in the results that had been forecast. In future wind direction would be included for wind speed prediction model implementation.

References

1. GWEC, Global Wind Energy Council (2017) Global wind report: annual market update. <http://www.gwec.net>
2. Nielsen TS, Joensen A, Madsen H, Landberg L, Giebel G (1998) A new reference for wind power forecasting. *Wind Energy* 1(1):29–34
3. Kariniotakis Georges (2017) Renewable energy forecasting: from models to applications. Woodhead Publishing, Cambridge, United Kingdom
4. Gautam A, Bhateja V, Tiwari A, Satapathy SC (2018) An improved mammogram classification approach using back propagation neural network. In: *Data engineering and intelligent computing*. Springer, Singapore, pp 369–376
5. Lydia M, Kumar SS, Selvakumar AI, Kumar GEP (2018) Wind farm power prediction based on wind speed and power curve models. In: Bhuvanewari M, Saxena J (eds) *Intelligent and efficient electrical systems. Lecture notes in electrical engineering*, vol 446. Springer, Singapore (2018)
6. Afshari-Igder M, Niknam T, Khooban MH (2018) Probabilistic wind power forecasting using a novel hybrid intelligent method. *Neural Comput Appl* 30(2):473–485. <https://doi.org/10.1007/s00521-016-2703-z>
7. Rao RV (2015) *Teaching learning based optimization algorithm: and its engineering applications*. Springer
8. NREL (2017) Renewable resource data center—Wind Resource Information, <http://www.nrel.gov>. Accessed on 09 Aug 2017
9. MATLAB Release (2009) The MathWorks Inc., Natick, Massachusetts, USA
10. Yan F, Lin Z, Wang X, Azarmi F, Sobolev K (2017) Evaluation and prediction of bond strength of GFRP-bar reinforced concrete using artificial neural network optimized with genetic algorithm. *Compos Struct* 161:441–452
11. AminShokravi A, Eskandar H, Derakhsh AM, Rad HN, Ghanadi A (2018) The potential application of particle swarm optimization algorithm for forecasting the air-overpressure induced by mine blasting. *Eng Comput* 34(2):277–285

Risk Averse Energy Management for Grid Connected Microgrid Using Information Gap Decision Theory



Tanuj Rawat and K. R. Niazi

Abstract Energy management plays a critical role to accomplish a reliable and efficient operation of a Microgrid (MG). As the power from renewable energy sources and load demand is uncertain energy management problem (EMP) of a MG becomes complex. This paper studies the EMP for a grid connected MG consisting of dispatchable distributed generators (DDGs), battery, and renewable generation such as wind power, respectively. In order to handle the uncertainties ascending from wind power and load demand, information gap decision theory (IGDT) is adopted in this paper. An illustrative case study is presented to demonstrate the applicability of the proposed method. Results show that least robustness is achieved on modeling uncertainty in both wind power and load demand in comparison to the modeling of uncertainty in either parameter.

Keywords Microgrid · Uncertainty · Energy management · Information gap decision theory

Nomenclature

P_{it}	Power from i th DDG at time t
I_{it}	Commitment status of i th DDG at time t
SU_{it}	Start-up cost of i th DDG at time t
SD_{it}	Shutdown cost of i th DDG at time t
$P_{M,t}$	Power exchange with main grid at time t
$P_{WT,t}$	Power from wind farm at time t
$P_{bat,t}$	Power from battery at time t
D_t	Load demand at time t
$\tilde{P}_{WT,t}$	Predicted power from wind farm at time t
\tilde{D}_t	Predicted demand of MG at time t

T. Rawat (✉) · K. R. Niazi
Malaviya National Institute of Technology, Jaipur, India
e-mail: tanujsometime@gmail.com

© Springer Nature Singapore Pte Ltd. 2020
A. Kalam et al. (eds.), *Intelligent Computing Techniques for Smart Energy Systems*,
Lecture Notes in Electrical Engineering 607,
https://doi.org/10.1007/978-981-15-0214-9_50

α	Radius/Horizon of uncertain parameter
δ	Cost deviation factor
OC_o	MG operation cost without any uncertainty
OC_c	Critical MG operation cost
q	IGDT decision variables
u	IGDT uncertain variables

1 Introduction

A microgrid (MG) is defined as an active distribution network which consists of distributed energy resources (DERs) such as distributed generators (DGs), energy storage system (ESSs), and controllable loads. One of the key features of an MG is its capability to disconnect from the upstream main grid in case of any disturbance or fault in the main grid. With effective operation strategies, an MG can offer twofold benefits to the power grid [8]: firstly, it provides reliable power supply to local loads by coordinating DERs and secondly, it can also act as a manageable energy asset to provide different grid services and grid friendly power responses.

The energy management problem (EMP) of a grid connected MG has been studied extensively in the literature. EMP of a MG mainly aims to find optimal energy outputs from different DERs of MG and power exchange with the main grid to minimize electricity and operation cost. Due to the integration of advanced technologies such as renewable energy sources (RES), EMP of a MG has become complex as RES possess inherent intermittent and variable characteristics. To deal with uncertainty in the input parameters of EMP such as wind power and load demand, a variety of methods has been investigated in the literature. Numerical prediction techniques were adopted in [1] and [3] to forecast the uncertain input parameters and the EMP of MG is solved in a deterministic way. Renewable generation, as well as load consumption was found using artificial neural network in [3]. In numerical prediction techniques, the accuracy of prediction decreases as the horizon of prediction increases. Energy management system (EMS) for a renewable based MG based on rolling horizon is proposed in [5]. Using the rolling horizon algorithm, forecasts are updated at each time step and then optimization problem is solved. But, only the decision variables of the current time step are implemented.

To mitigate the risk of operating uncertainties in power generated from renewable sources and electricity prices in MG's optimal operation a Hong's $2m$ point estimate method (PEM) is adopted in [6]. A $2m + 1$ PEM is applied in [12] to solve probabilistic energy and operation management problem of MG. A scenario-based robust energy method is proposed in [17] to deal with the uncertain load demand and renewable generation. Uncertainties of renewable generation and grid connected condition of MG is studied in [7] using a two-stage adaptive robust optimization. "Budget of uncertainty" is used to control the uncertainties. Stochastic Programming especially, scenario-based method is also widely used in MG operation and energy management [11]. In scenario-based method, uncertainties in input param-

eters are described by using certain distributions such as weibull and normal distributions, respectively [15]. Scenarios are generated from these distributions using scenario generation techniques. Each scenario stands for one possible/circumstance that could occur with some probability. Apart from robust optimization and stochastic programming, chance constraint programming (CCP) is also investigated for MG energy management. A CCP based approach is used to solve two EMPs of MG motivated by peak power shaving and frequency regulation, respectively [10]. CCP energy management model for islanded MG is designed in [13].

Compared with other works, which utilize robust optimization, stochastic programming, and CCP for modeling uncertainties in the MG energy and operation management problem, an information gap decision theory (IGDT) based approach is adopted in this paper. IGDT is used to deal with the uncertainties associated with wind power and load demand, respectively. Unlike other methods, IGDT does not require knowledge of membership functions, probability distributions or detailed uncertainty sets [4]. It mainly concentrates on the difference between actual and forecasted variables. Therefore, the main contribution of this paper is the application of IGDT for modeling uncertainties in the input parameters of EMP for a grid connected MG.

2 Information Gap Decision Theory

Theoretically, IGDT is a quantitative risk management and decision-making model to take into account severe uncertainties involved in the decision-making process [2]. The IGDT model will assure that the operation cost of the MG does not increase beyond a certain critical value OC_c while the horizon of uncertainty is maximized. The critical operation cost OC_c is defined as a percentage of deterministic operation cost, i.e., $(OC_o \cdot \delta)$. $(OC_o \cdot \delta)$ declares the risk averseness of MG operator. System model, uncertainty model, and performance model are the three components of IGDT. Several models such as energy-bound model, slope bound model, and envelope-bound model can be used to describe the uncertainty set. A special case of envelope-bound model as given in equation (1) is used in this paper [14].

$$U(\alpha, \tilde{u}) = \{u : |u - \tilde{u}| \leq |\tilde{u}|\alpha\}, \alpha \geq 0 \quad (1)$$

In an IGDT model, based on the risk management strategies followed by the decision maker, two different performance functions namely robustness function and opportunity function can be defined. A robustness function is adopted to attain immunity against the unfriendly deviations in uncertain parameter. Because of its ability to consider worst case scenarios, only robustness function is considered in this paper [16]. By adopting robustness function, MG operator will behave as risk averse decision maker and will schedule resources in a way to become immune against the unfavorable deviation in the forecasted values of wind output and load demand.

A robustness function $\tilde{\alpha}(q, r_c)$ is defined as the maximum value of α such that minimum favorable or desired reward of the decision-making problem is fulfilled.

$$\tilde{\alpha}(q, r_c) = \max_{\alpha} \{ \alpha : \text{minimum requirement of } r_c \text{ is satisfied} \} \tag{2}$$

3 Problem Formulation

In this section firstly, mathematical model for the MG energy management without considering any uncertainty is formulated. Thereafter, IGDT based MG energy management model to incorporate wind output power and load demand uncertainty is expressed.

3.1 Deterministic MG Energy Management

One of the vital goal of a MG operator is to minimize the operation cost. Mathematically, the objective function can be formulated as

$$\text{Min } OC = \sum_t \sum_i [F_i(P_i)I_{it} + SU_{it} + SD_{it}] + \sum_t \rho_t P_{M,t} \tag{3}$$

The first term in the objective function is the operation cost of DDGs which consists of generation cost, start-up cost, and shutdown cost, respectively and the second term is a cost associated with power exchange with the main grid. When power is taken from grid $P_{M,t}$ is positive and when power is transferred from MG to main grid $P_{M,t}$ is negative. The objective function in Eq. (3) is subjected to power balance constraint (Eq. 4), minimum and maximum capacity constraints of DDGs and main grid, respectively, ramp up, ramp down, minimum up and minimum down limits of DDGs, respectively. The operation model of battery for charging/discharging is similar to [9].

$$\sum_i P_{it} + P_{WT,t} + P_{M,t} + P_{bat,t} = D_t \quad \forall t \tag{4}$$

3.2 IGDT Based MG Energy Management

The uncertainty in wind power and load demand illustrated by $u_t = \{P_{WT,t}, D_t\}$ for each time t is modeled in this section using IGDT. The decision variables are power output from DDGs, power exchange with the main grid and battery charging and discharging power, respectively, denoted by $q_t = \{P_{it}, P_{M,t}, P_{bat,t}\}$. It is assumed that

the forecasted values of the uncertain parameters, indicated by $\tilde{u}_t = \{\tilde{P}_{WT,t}, \tilde{D}_t\}$ is accessible. The robust formulation is depicted in (5)-(8).

$$\text{obj fun : Max } \alpha \quad (5)$$

subject to:

$$\text{Max } \sum_t \sum_i [F_i(P_i)I_{it} + SU_{it} + SD_{it}] + \sum_t \rho_t P_{M,t} \leq OC_c \quad (6)$$

$$(1 - \alpha)\tilde{P}_{WT,t} \leq P_{WT,t} \leq (1 + \alpha)\tilde{P}_{WT,t} \quad \forall t \quad (7)$$

$$(1 - \alpha)\tilde{D}_t \leq D_t \leq (1 + \alpha)\tilde{D}_t \quad \forall t \quad (8)$$

For the sake of simplicity, same time volatility levels and forecasting errors for both wind power and load demand is considered [16].

4 Numerical Simulation

The MG considered in this paper consists of four DDGs, one wind turbine, and one battery. The characteristics of DDGs and battery is obtained from [9]. The 24 h load profile and wind power output pattern in per unit is adopted from [9] and [14], respectively. The peak load of MG is 18.14 MW and it is assumed that 5 MW of wind generation capacity is available in the MG.

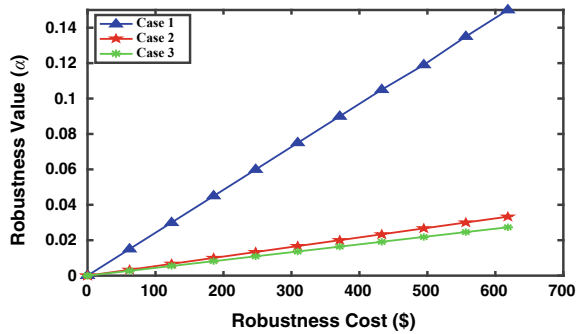
Results of four different cases are discussed in this section. In the base case, it is assumed that there is no forecast error associated with wind power and load demand. The simulation results are obtained keeping wind output and load demand equal to their forecasted values and the objective is to optimize the total operation cost. It is assumed that in case 1, wind output power and in case 2, load demand is the only uncertain parameter in the model. Instead of minimizing operation cost, the objective in these cases is to maximize the radius of wind power uncertainty and load uncertainty, respectively. In case 3, both wind output power and load demand are taken as uncertain parameters in the model. The objective is maximizing the horizon of both uncertainties.

The simulation results for all the cases for different values of δ are shown in Table 1. It should be noted that different values of δ results in different critical costs as $TC_c = TC_o(1+\delta)$. The total operation cost obtained in the base case is 6183.852\$. It is evident from the results that as δ increases, more uncertainty can be accommodated at the expense of an increase in total operation cost. The simulation result also shows that as the total acceptable deterioration in the operation cost is increased from 6183.852\$ to 6802.236\$ the decision maker can be immune up to 15% error in wind forecast prediction and 3.33% error in load forecast prediction, respectively. Similarly, to

Table 1 Optimal robustness value and critical MG operation cost for different cost deviation factor

δ	TC_c	α (in %)		
		Case 1	Case 2	Case 3
0.00	6183.852	0.00	0.00	0.00
0.01	6245.690	1.50	0.33	0.27
0.02	6307.528	2.99	0.67	0.55
0.03	6369.367	4.50	1.00	0.82
0.04	6431.205	5.99	1.33	1.09
0.05	6493.044	7.50	1.67	1.36
0.06	6554.882	8.99	2.00	1.64
0.07	6616.721	10.5	2.33	1.91
0.08	6678.559	11.9	2.67	2.18
0.09	6740.398	13.5	3.00	2.46
0.10	6802.236	15.0	3.33	2.73

Fig. 1 Robustness value versus robustness cost



ensure that the maximum MG operation cost should not go beyond 6802.236\$, the maximum forecast errors in both wind power output and load demand should not go beyond 2.73%. Clearly, α of case 3 being close to the practical scenario, results in lesser admissible uncertainty horizon. Also, when δ is low, the operation cost is closer to the base case cost and MG operator behaves as risk neutral behavior. For example, when δ is 0.01, the total operation cost is 6245.69\$, which is very close to the base cost of 6183.85\$. It should be noted that case 1, in which only wind power is considered as an uncertain parameter result in more robustness at the same operation cost in comparison to the other two cases.

Implementing IGDT robustness function imposes an additional cost to the MG operator. The difference between risk neutral cost (δ equals zero) and risk averse cost (for different values of δ) is defined as robustness cost. The variation of α with robustness cost is shown in Fig. 1. It is obvious that on increasing robustness cost α increases.

The variation of participation from different energy procurement options versus α for case 1 is shown in Fig. 2. It is to be noted that ratios have been obtained

Fig. 2 Ratio of DDGs, grid and wind power versus robustness value (α)

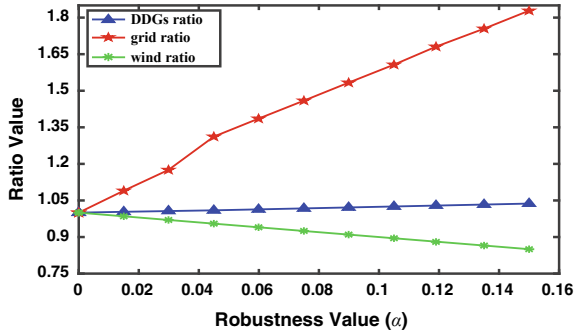


Fig. 3 Ratio of DDGs, grid power and load demand versus robustness value (α)

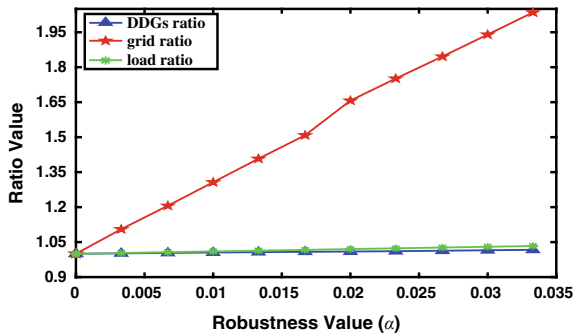
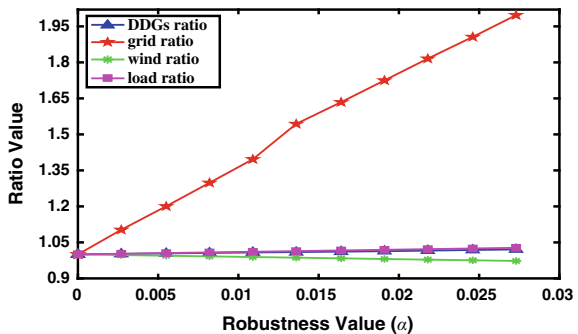


Fig. 4 Ratio of DDGs, grid power, wind power and load demand versus robustness value (α)



in comparison to the base/deterministic case. As α increases, the share of wind decreases and consequently power from DDGs and main grid increases to meet the wind power deficiency. For case 2, as shown in Fig. 3 the power from DDGs and main grid increases to meet the additional load demand. Similarly, for case 3 as α increase the contribution of DDGs and power from grid increases to compensate the increase in load demand and a decrease in wind power generation as shown in Fig. 4.

5 Conclusions

The problem of energy management in a grid connected MG is studied in this paper. An IGDT based technique is utilized to model the uncertainty of wind power and load demand. MG operator behaves as a risk averse decision maker and manages resources in a way to become immune against the unfavorable deviation in the forecasted values of wind power and load demand. The obtained results from IGDT guarantees the MG operator that the operation cost would not go beyond the predefined critical MG operation cost. Also, it is found that considering uncertainties in both wind power and load demand leads to lowest robustness in comparison to the modeling of either uncertainty.

References

1. Beltran H, Perez E, Aparicio N, Rodriguez P (2013) Daily solar energy estimation for minimizing energy storage requirements in pv power plants. *IEEE Trans Sustain Energy* 4(2):474–481
2. Ben-Haim Y (2006) Info-gap decision theory: decisions under severe uncertainty. Elsevier
3. Chaouachi A, Kamel RM, Andoulsi R, Nagasaka K (2013) Multiobjective intelligent energy management for a microgrid. *IEEE Trans Ind Electr* 60(4):1688–1699
4. Connell AO, Soroudi A, Keane A (2016) Distribution network operation under uncertainty using information gap decision theory. *IEEE Trans Smart Grid*
5. Dizqah AM, Maheri A, Busawon K, Kamjoo A (2015) A multivariable optimal energy management strategy for standalone DC microgrids. *IEEE Trans Power Syst* 30(5):2278–2287
6. Gazijahani FS, Salehi J (2018) Integrated dr and reconfiguration scheduling for optimal operation of microgrids using hongs point estimate method. *Int J Electr Power Energy Syst* 99:481–492
7. Guo Y, Zhao C (2016) Islanding-aware robust energy management for microgrids. *IEEE Trans Smart Grid*
8. Hatziargyriou N, Asano H, Iravani R, Marnay C (2007) Microgrids. *IEEE Power Energy Mag* 5(4):78–94
9. Khodaei A (2014) Microgrid optimal scheduling with multi-period islanding constraints. *IEEE Trans Power Syst* 29(3):1383–1392
10. Liu J, Chen H, Zhang W, Yurkovich B, Rizzoni G (2017) Energy management problems under uncertainties for grid-connected microgrids: a chance constrained programming approach. *IEEE Trans Smart Grid* 8(6):2585–2596
11. Nguyen DT, Le LB (2015) Risk-constrained profit maximization for microgrid aggregators with demand response. *IEEE Trans Smart grid* 6(1):135–146
12. Radosavljević J, Jevtić M, Klimenta D (2016) Energy and operation management of a microgrid using particle swarm optimization. *Eng Optim* 48(5):811–830
13. Shi Z, Liang H, Huang S, Dinavahi V (2018) Distributionally robust chance-constrained energy management for islanded microgrids. *IEEE Trans Smart Grid*
14. Soroudi A, Rabiee A, Keane A (2017) Information gap decision theory approach to deal with wind power uncertainty in unit commitment. *Electr Power Syst Res* 145:137–148
15. Su W, Wang J, Roh J (2014) Stochastic energy scheduling in microgrids with intermittent renewable energy resources. *IEEE Trans Smart Grid* 5(4):1876–1883

16. Vahid-Ghavidel M, Mahmoudi N, Mohammadi-ivatloo B (2018) Self-scheduling of demand response aggregators in short-term markets based on information gap decision theory. *IEEE Trans Smart Grid*
17. Xiang Y, Liu J, Liu Y (2016) Robust energy management of microgrid with uncertain renewable generation and load. *IEEE Trans Smart Grid* 7(2):1034–1043

Power Quality Improvement of Microgrid Using Double Bridge Shunt Active Power Filter (DBSAPF)



Rajesh Kumar Meena, Dheeraj Kumar, Vinay Kumar Jadoun
and Saurabh Kumar Pandey

Abstract In the modern power system, the role of distributed energy resources has been changed from back up to primary source of electricity in the form of microgrid and with that power quality of microgrid has become a serious issue. The tremendous increase of nonlinear loads and power electronic devices create power quality issues in the power system distribution. In this paper, the main objective is to improve the power quality of a microgrid using proposed Double Bridge Shunt Active Power Filter (DBSAPF). The simulation results obtained by proposed method shows reduction in the harmonic components with a nonlinear load.

Keywords Distributed Generations (DGs) · Distributed Energy Resources (DERs) · Power Quality (PQ) · Point of Common Coupling (PCC) · Shunt Active Power Filter (SAPF)

1 Introduction

Microgrid is an integration of small scale DG's located near consumer end that normally operated to and synchronous with the main grid through PCC but can disconnect and function autonomously to feed community load. DG units include nonconventional sources like solar energy, wind energy, hydroelectric power fuel

R. K. Meena (✉)

National Institute of Technology Hamirpur, Hamirpur, HP 177005, India
e-mail: rajmeena7568869818@gmail.com

D. Kumar

Siemens, Mumbai, India
e-mail: saannedh@gmail.com

V. K. Jadoun

National Institute of Technology Delhi, Delhi 110040, India
e-mail: vjadounmnit@gmail.com

S. K. Pandey

Indian Institute of Technology Patna, Bihta, Patna 801106, India
e-mail: saurabh.rjit@gmail.com

© Springer Nature Singapore Pte Ltd. 2020

A. Kalam et al. (eds.), *Intelligent Computing Techniques for Smart Energy Systems*,
Lecture Notes in Electrical Engineering 607,
https://doi.org/10.1007/978-981-15-0214-9_51

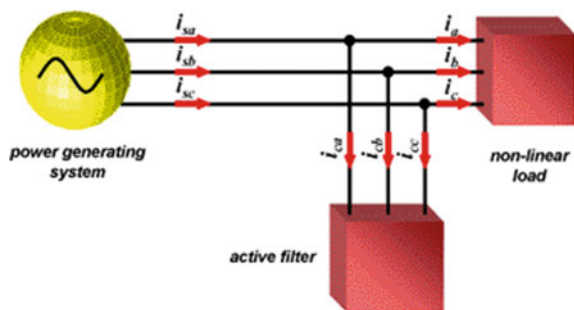
cells, etc. Microgrid has proved its significance over last few years to prevent black-outs and power outages [1]. The power quality has always been a serious issue for centralized grids. Power quality is the capability of power generator system to supply a clean and steady power flow that is fulltime available, has a pure noise-free and smooth sinusoidal waveform, and is always within the prescribed voltage and frequency range [2]. Since the microgrid includes nonlinear elements in excess for control and conversion sake. So it is obvious to guess that it has harmonic contents in it. The unbalance in voltage profile of the microgrid may result in tripping of circuit breakers. Generally, it has been found that harmonic contents in current waveform and imbalance in voltage and frequency profile increase losses in power system [3]. A synchronous reference frame-based current control loop [4] and conventional PI regulator [5] are used for voltage–frequency regulation. Indirect current control technique by [6] has been presented to mitigate the voltage imbalance. Active and reactive power control in both grid-connected and islanded mode has been investigated in [7]. In order to improve the DG controller performance, several modified models have been proposed by [8]. Static VAR Compensator (SVC) and Shunt Active Power Filter (SAPF) have been adopted to improve power quality parameters like voltage, frequency, and harmonic distortion [9]. The voltage and frequency control mode are adopted in microgrid under grid tied or islanded in order to regulate voltage and frequency in microgrid [10]. Droop control technique is developed to enhance the power quality parameter like active and reactive power control both in grid and autonomous operation. Droop control technique has been employed in V and I to provide PQ control in microgrid, which has been investigated in [11].

2 Shunt Active Power Filter

The operating principle of shunt active power filters to inject the network and generated the harmonics current which is equal and in opposite direction of the current generated by nonlinear load.

The basic structure of shunt active power filter connected to a main source is shown in Fig. 1. The linear and nonlinear loads are supposed to be connected at the Point

Fig. 1 Basic structure of shunt active power filter



of Common Coupling (PCC). At this situation, the supply current (I_s) will be the load current (I_l) having non-sinusoidal nature when flowing through the transmission line. The active filter is parallel connected with the AC supply source through Point of Common Coupling (PCC). This active filter is consisting of three-phase PWM voltage source inverter.

The equations for current source can be expressed as

$$I_f = I_l - I_{lf} \quad (1)$$

$$I_f = I_s - I_{sf} \quad (2)$$

where I_f is the error reference current,

I_l is the load current,

I_{lf} is the load reference current,

I_s is the source current, and

I_{sf} is the source reference current.

For satisfactory performance of active filter, it is necessary to select a suitable technique which identifies and extract the reference current and inverter control strategy [12]. As a supply purpose, a DC voltage capacitor is used in this voltage source inverter, which can act as a switched at high frequency to produce the current. This generated current will be further used to remove the harmonic current from the main source [13]. For suppression of the harmonics, the current waveform is obtained from VSI in the current controlled mode and the interface filter [14].

3 Hysteresis Control Technique

In this paper, a hysteresis current controller method is used. This method is simple, easy to implement, and fast response current loop. Another advantage of this method is that there is no need of knowing the load parameters value. The variation of switching during the load parameters' variation of fundamental period is the drawback of this method.

Figure 2a, b shows the working of hysteresis current controller. This figure represents the upper and lower band and actual and reference current with reference to T. In this method load current waveform is compared with the reference current waveforms generated by using various algorithms, which is later on used to generate the firing pulses for the voltage source inverter provided with the DC link. The voltage source inverter is used to generate the compensation current for the source current to prevent load harmonics from entering the source which destabilizes the alternator or main deteriorates the main power system power quality. In the working procedure, the measured load currents are compared with the reference current generated by PLL using hysteresis comparators. In the past, various algorithms have

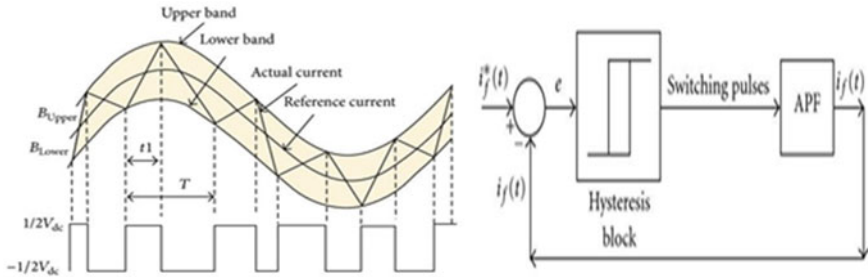


Fig. 2 Working of hysteresis current controller (a) and (b)

been proposed to generate the reference current like PQ theory. Hysteresis control scheme uses a band to generate firing pulses for the active power filter for which reference currents and error current obtained by comparing the load current, used as input to the hysteresis block.

4 Proposed Double Bridge SAPF

The simulation diagram of the proposed double bridge SAPF model is also shown in Fig. 3. The proposed model consists of two bridge inverters coupled to same branch of capacitors. This model uses two capacitors connected as series and mid-point grounded. The voltage source inverter provided with the DC link to feed the compensation current generated by using the control firing pulses obtained from hysteresis control. In this figure, a generalized configuration of shunt active power filter has been shown with the main power system configuration. This configuration shows the generalized interconnection of shunt active power filter. The load current returns with harmonics and shunt active filter injects the compensation current generated by the VSI using the firing pulses generated from the control circuit of the shunt active power filter.

In the proposed model, there are two types of Inverters and two types of control circuits are used separately to generate compensation current by using the different comparing signals for both control inverter, namely, Source Hysteresis Controlled Inverter and Load Hysteresis Controlled Inverter. In the proposed model, both inverters work on the same principle of hysteresis control method but use different currents for their error reference current generation. Source hysteresis controller uses source current as the input and PLL generates ideal source current by taking phase and magnitude as a references. Here magnitude and phase of the waveform have been used for the generation of ideal waveform. While load hysteresis controller uses load current as input and PLL generates ideal load current. Output of error reference current generator fed to the hysteresis controller, which generates the pulses for firing the bridge inverter. The firing pulses generated from both the control circuits have been fed to the voltage source controlled inverter and load controlled inverter. Based

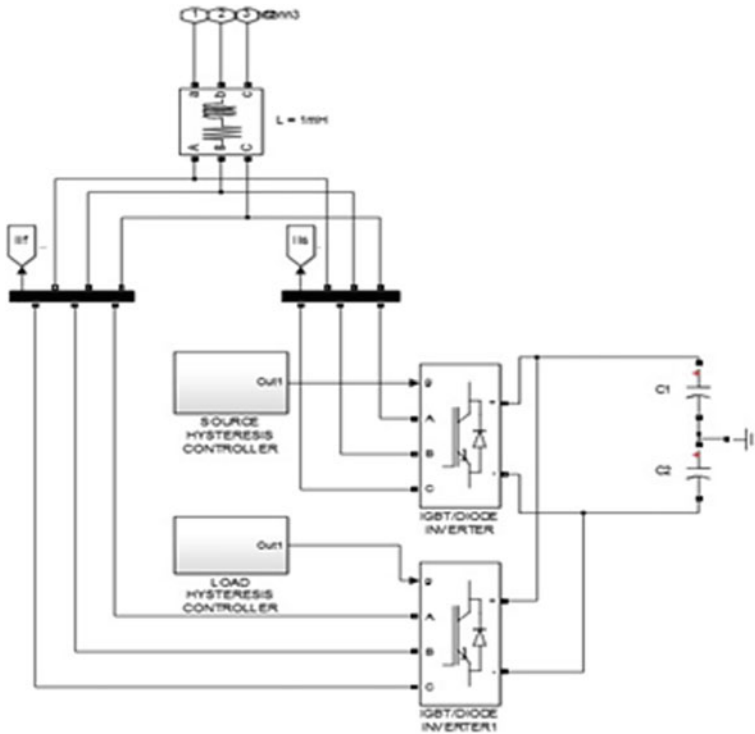


Fig. 3 Simulation diagram of proposed double bridge SAPF model

upon the respective control pulses generated by the control circuit both inverters of the filter generate a compensation current which is passed through a reactor and then fed directly to the supply to prevent the harmonic contents from entering the source which affects the stability of the system. The stability and power quality control are the prime objectives of the power system engineers, so this paper provides a solution to the same. The simulation results obtained by proposed filter have been shown and discussed in the next section.

5 Simulation Results

In this section, two case studies are considered. In the first case study, the problem is solved without considering double bridge SAPF filter, whereas in second case study, the proposed double bridge SAPF filter is used to solve this problem. In both the case studies, the load is considered as nonlinear. The various system parameters used in both case studies are given as follows: Supply Voltage is 400 V; Frequency is 50 Hz; Nonlinear Load is Series RL Load, $R = 150 \Omega$, $L = 10 \text{ mH}$, Parallel Capacitor $C = 1 \text{ uF}$.

5.1 Case Study 1

In this case study, the result obtained without double bridge SAPF is presented in Figs. 4 and 5. It can be seen from both the figures that the source and load waveforms and source phase currents are distorted and not properly sinusoidal when double bridge SAPF filter is not considered.

The percentage of total harmonic distortion obtained in this case study is given as Phase A, Phase B, and Phase C has 30.97% THD, 30.61% THD, and 30.85%

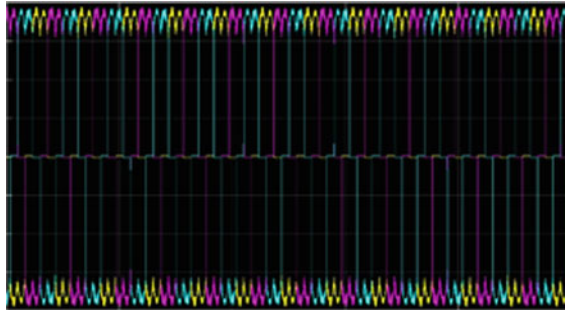


Fig. 4 Source and load waveforms without double bridge SAPF filter

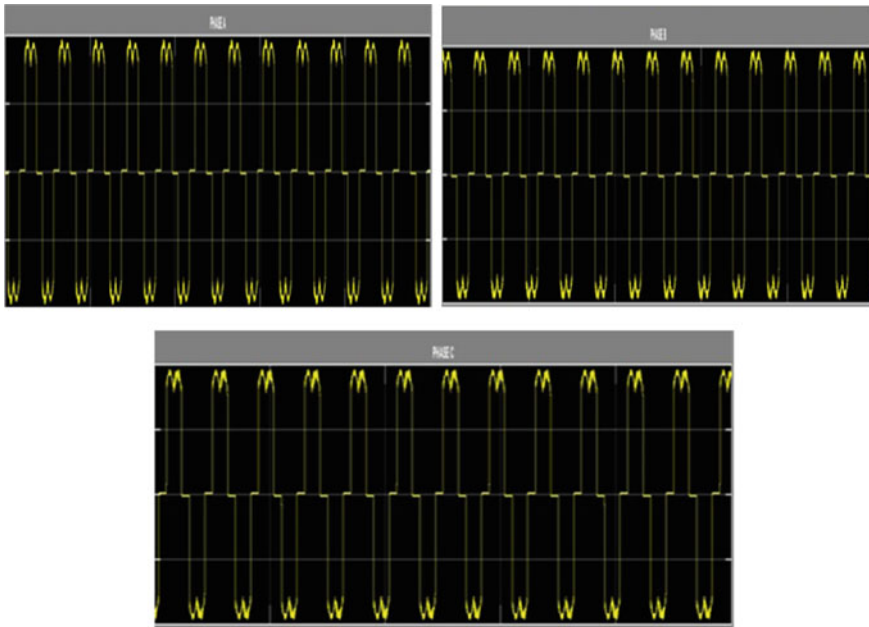


Fig. 5 Source phase currents without double bridge SAPF filter

THD, respectively. It can be observed from this table that the % THD for all the three phases is approximately 30%.

5.2 Case Study 2

In this case study, the problem is solved with the proposed double bridge SAPF filter. The simulation results obtained by proposed SAPF filter are shown in Figs. 6, 7, 8, and 9. It can be observed from the figures that when the load is connected with the proposed double bridge SAPF, the waveforms are drastically smooth and sinusoidal.

In the Figs. 7 and 8, the compensation current injected by the source hysteresis controlled inverter filter and the current injected by load hysteresis controlled inverter filter has been shown, which are generated as explained in the proposed model section. It can also be seen from Fig. 9, that the source phase currents for all the three phases are sinusoidal in nature. The percentage total harmonic distortion in the source currents obtained by proposed double bridge shunt active power filter is given as that the percentage THD for Phase A, Phase B, and Phase C reduced drastically to 0.64%,

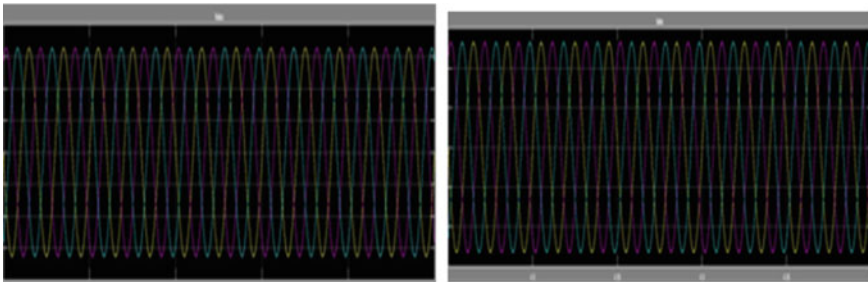


Fig. 6 Source voltage and source current with double bridge SAPF

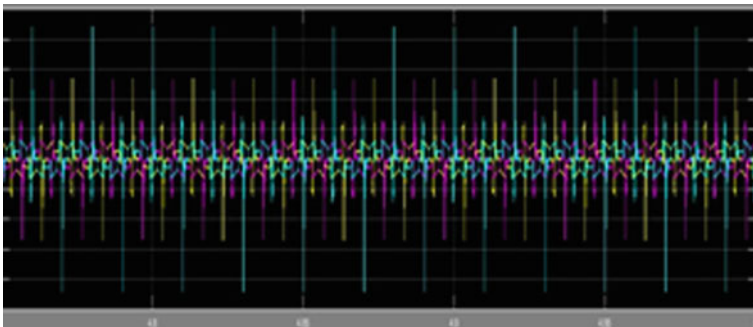


Fig. 7 Current injected by source hysteresis controlled inverter filter

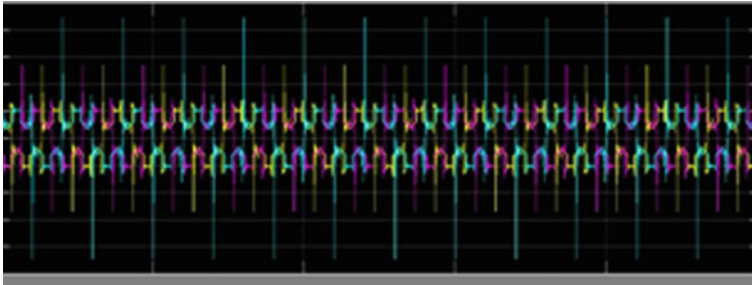


Fig. 8 Current injected by load hysteresis controlled inverter filter

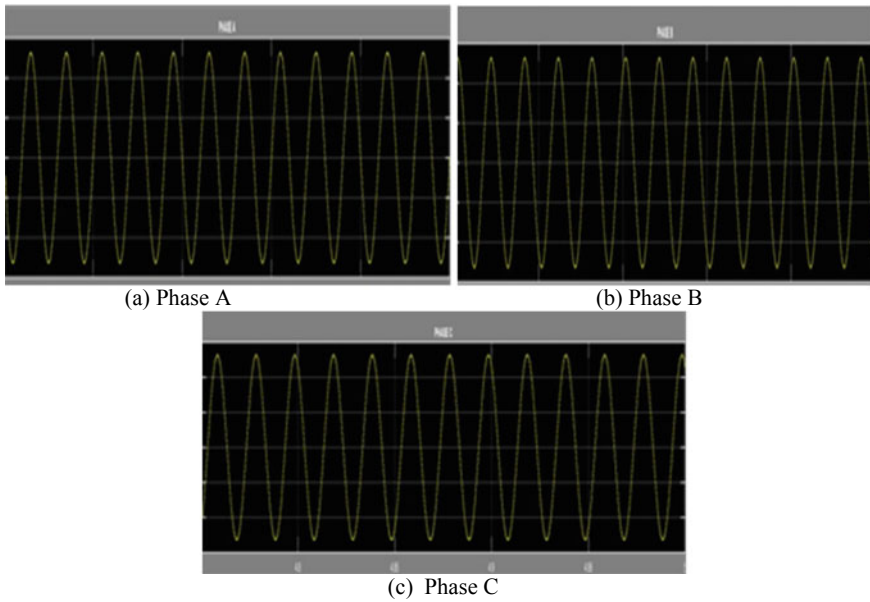


Fig. 9 Source phase currents

0.63%, and 0.63%, respectively. Thus, the overall power quality gets improved using proposed double bridge shunt active power filter.

6 Conclusion

Microgrid is very popular in current trends. There is more emphasis given to develop microgrid infrastructure because of the issues of need for rural electrification, increased focus on renewable energy, and focus on higher efficiency. In this

paper, the proposed double bridge shunt active power filter is implemented in the existing microgrid. The results are compared without and with the consideration of proposed.

Double bridge shunt active power filter. Based on the result section, it can be concluded that the proposed double bridge SAPF filter has a capability to compensate the harmonics. The proposed filter is also obtained for the positive results by drastically reducing the percentage of THD of the line current. In fact, the distortions of the power supply currents were diminished exceptionally to $\text{THD} = 0.63\%$. It can be concluded that the proposed filter has eliminated the harmonic components efficiently which was occurred in the existing power system with a nonlinear load.

References

1. Nazir R, Laksono HD, Waldi EP, Ekaputra E, Coveria P (2013) Renewable energy sources optimization: a micro-grid model design. In: 2013 international conference on alternative energy in developing countries and emerging economies published in Science Direct Journal
2. Argyrou MC, Christodoulides P, Kalogirou SA (2018) Energy storage for electricity generation and related processes: technologies appraisal and grid scale applications. *Renew Sustain Energy Rev* 94:804–821
3. Natesan C, Ajithan SK, Palani P, Kandhasamy P (2014) Survey on microgrid: power quality improvement techniques. *ISRN Renew Energy* 2014(Article ID 342019):7. Published on 16 Mar 2014 (Hindawi Publishing Corporation)
4. Al-Saedi W, Lachowicz SW, Habibi D, Bass O (2012) Power quality enhancement in autonomous microgrid operation using particle swarm optimization. *Int J Electr Power Energy Syst* 42(1):139–149
5. Al-Saedi W, Lachowicz SW, Habibi D, Bass O (2013) Power flow control in grid-connected microgrid operation using particle swarm optimization under variable load conditions. *Int J Electr Power Energy Syst* 49:76–85
6. Kim H, Yu T, Choi S (2008) Indirect current control algorithm for utility interactive inverters in distributed generation systems. *IEEE Trans Power Electron* 23(3):1342–1347
7. Kahrobaeian A, Mohamed YA-RI (2012) Interactive distributed generation interface for flexible micro-grid operation in smart distribution systems. *IEEE Trans Sustain Energy* 3(2):295–305
8. Pr D, Ramanarayanan V (2010) Decentralized parallel operation of inverters sharing unbalanced and nonlinear loads. *IEEE Trans Power Electron* 25(1):3015–3022
9. Xiaozhi G, Linchuan L, Engan C (2011) Power quality improvement for microgrid in islanded mode. *Procedia Eng* 23:174–179
10. Wang C, Xiao Z, Wang S (2008) Synthetical control and analysis of microgrid. *Ind Autom Electr Power Syst* 32(7):98–103
11. Abaali H, Lamchich MT, Raoufi M (2004) The three phase shunt active filters for the harmonics compensation under distorted and unbalanced mains voltages conditions. In: IEEE international conference on industrial technology (ICIT)
12. Corasaniti VF, Barbieri MB, Arnera PL, Valla MI (2009) Hybrid power filter to enhance power quality in a medium-voltage distribution network. *IEEE Trans Ind Electron* 56(8):2885–2893
13. Chelli Z, Toufouti R, Omeiri A, Saad S (2015) Hysteresis control for shunt active power filter under unbalanced three-phase load conditions. *J Electr Comput Eng* 2015(Article ID 391040):9
14. Singh A, Kumar S (2012) Performance investigation of active power line conditioner using simulink. *Int J Emerg Technol Adv Eng* 2(10)

Opposition Theory Enabled Intelligent Whale Optimization Algorithm



Prateek Jain, Pooja Jain and Akash Saxena

Abstract Performance of any optimization technique is dependent on the perfect combination of operators; these operators are used for analyzing the exploration and exploiting capability. In the absence of this combination, an algorithm inclined toward premature convergence is trapped in local optima and is unable to find the best solution. In this paper, a new variant of whale optimization algorithm (WOA) is introduced which combines the concept of opposition-based learning, crossover operator, and sinusoidal function to accelerate the convergence rate and to avoid the trapping in local optima. This will be called as an opposition theory enabled intelligent whale optimization algorithm (OIWOA). To test the effectiveness of OIWOA, it is evaluated on an array of 23 classical benchmark functions. The performance measures show that the proposed variant possesses a better capability in solving optimization problems.

Keywords WOA · OIWOA · Opposition-based learning · Crossover operator

1 Introduction

Optimization is a method of finding the best solution with the most cost-effective or highest achievable performance under the given constraints from all the feasible solutions available. In the most straightforward condition, an optimization problem consists of maximizing or minimizing a real function by adequately selecting input values from within an allowed set and calculating the value of the function. Optimization is useful in engineering, medical science, mathematics, and other research works. There are different techniques for solving optimization problems, i.e., traditional optimization techniques and modern optimization techniques. The traditional optimization techniques are useful in finding the optimal solution for continuous and

P. Jain (✉) · P. Jain · A. Saxena
Swami Keshvanand Institute of Technology Management and Gramothan,
Jagatpura, Jaipur, India
e-mail: prateekgg@hotmail.com

© Springer Nature Singapore Pte Ltd. 2020
A. Kalam et al. (eds.), *Intelligent Computing Techniques for Smart Energy Systems*,
Lecture Notes in Electrical Engineering 607,
https://doi.org/10.1007/978-981-15-0214-9_52

differentiable functions for small problems with fewer variables. The commonly used conventional optimization techniques are dynamic programming, nonlinear programming, linear programming based algorithms, Newton–Raphson method, quadratic programming, etc., but these traditional techniques are more complicated to solve due to sizeable mathematical part, local optima stagnation, and not efficient enough to solve complex problems. So, modern methods like tabu search [4] and particle swarm optimization [8] have become dominant and useful in solving almost all the optimization techniques as they are efficient, convenient, and capable of solving complex problems with less mathematics. Nowadays, meta-heuristic algorithms (MHAs) [14] emerge as an effective method for solving almost every complex optimization problem without trapping in local optima and giving a faster convergence rate. These MHAs provide researchers a limitless source of inspiration for the modification and development of new algorithms. Like many MHAs are inspired by some natural process [23] such as Whale optimization algorithm (WOA) [12], Gray wolf optimization [13], Krill herd algorithm [3], Crow search algorithm [2], Bat search algorithm [24], Cuckoo search algorithm [15], Flower pollination algorithm for Global Optimization [25], Gravitational search algorithm [16], and Moth flame optimization (MFO) [11], nature-inspired MHAs gives unlimited sources for researchers to develop different techniques in algorithms for solving real-world problems. The two main features of MHAs are intensification and diversification. Intensification means searches around the present best solutions and selects the best solutions, and the diversification ensures that the algorithm explores the search space more efficiently. Despite having so many algorithms for solving optimization problems, we still cannot define any particular algorithm for a specific problem and every time we require a new algorithm for a new challenge to obtain useful results; this is explained by no free lunch (NFL) theorem [22]. According to this theorem, there is no specific algorithm for solving all optimization problems. It means that an optimizer may get good results in a particular set of problems and fail to solve a different set of problems with the same parameters. Hence, there is an advantage for researchers to develop and modify different algorithms to implement different kinds of the optimization problems.

This paper aims to propose a new variant of WOA called opposition theory enabled intelligent whale optimization algorithm (OIWOA) which involves the concept of opposition-based learning (OBL), crossover operator, and a sinusoidal function with the optimization features of WOA. It is a nature-inspired MHA based on the unique hunting behavior of humpback whales where these kinds of whales catch their prey by making the net of bubbles in spiral form around the prey. It has been proved that this algorithm is able to show very competitive results compared to other meta-heuristic algorithms in solving various real-world problems like optimal sizing of renewable resources for loss reduction in distribution systems [17], feature selection [9], sizing optimization for skeletal structures [7], and data clustering [6]. Identical to other meta-heuristic algorithms, slow convergence speed is the main problem encountered by WOA [1]. To further enhance the performance, this paper introduces some modifications into WOA.

The following paper is structured as follows: Sect. 2 describes the whale optimization algorithm, Sect. 3 explains the opposition theory enabled whale optimization algorithm, Sect. 4 shows the results and comparison, and Sect. 5 contains the conclusions of the paper.

2 Whale Optimization Algorithm

The WOA is inspired by the unique hunting behavior of humpback whales, developed by “Mirjalili” and “Lewis” in 2016 [12]. A humpback whale is one of the main species of the whale which can be as big as a large loading truck. Krill and small fish herds are their common prey. By creating distinctive bubbles in spiral shapes forming loops around the prey, they can easily attack them. This behavior is known as the bubble-net hunting method. This algorithm is modeled in three steps: The first is the modeling of the girdling phase of the prey, the second is the bubble-net attacking (exploitation phase) characteristics of humpback whales, and the third one is the random prey search process for the target, i.e., exploration phase. The mathematical formulation is modeled and explained as follows.

2.1 Girdling Prey

After locating the prey, humpback whales start girdling the prey by using the loops of bubbles. This behavior is formulated as follows:

$$\vec{W} = \left| \vec{Q} \cdot \vec{K}^*(n) - \vec{K}(n) \right| \tag{1}$$

$$\vec{K}(n + 1) = \vec{K}^*(n) - \vec{P} \cdot \vec{W} \tag{2}$$

where n indicates the current iteration, \vec{P} and \vec{Q} are the coefficient vectors. K^* is the position vector of the best solution obtained, K is the position vector. K^* will be updated in each iteration for every better solution. $||$ is the absolute value and \cdot is an element-by-element multiplication. The vectors \vec{P} and \vec{Q} are calculated as follows:

$$\vec{P} = 2\vec{p} \cdot \vec{v} - \vec{p} \tag{3}$$

$$\vec{Q} = 2\vec{p} \tag{4}$$

where \vec{v} is a random vector in $[0, 1]$ and \vec{p} is linearly decreased from 2 to 0 over the course of iterations.

2.2 Bubble-Net Attacking Method (Exploitation Phase)

As mentioned earlier, the humpback whales attack the prey with the bubble-net technique. This method is mathematically formulated as follows:

Shrinking Girdling Technique: This technique requires decreasing the value of \vec{p} in Eq. (3). Here, \vec{p} is decreased from 2 to 0 over the course of iterations. The new position of a search agent can be specified anywhere in between the original position of the search agent and the position of the ongoing best search agent by setting \vec{P} for random values in $[-1, 1]$.

Spiral Position Modification: This represents the helix-shaped movement between the positions of humpback whales and prey as follows:

$$\vec{K}(n+1) = \vec{W}' - e^{yl} \cdot \cos(2\pi l) + \vec{K}^*(n) \quad (5)$$

where $\vec{W}' = \left| \vec{K}^*(n) - \vec{K}(n) \right|$, l is a random number in $[-1, 1]$, and y is a constant.

It is considered that humpback whales whirl around the target in a girdling circle and along a curling path simultaneously. For this simultaneous behavior, WOA assumes that the probability to choose between shrinking girdling technique and the spiral model is 50% each, respectively. The mathematical model of the search is as follows:

$$\vec{K}(n+1) = \begin{cases} \text{shrinking girdling Eq.(2) if } n < 0.5 \\ \text{spiral positioning Eq.(5) if } n \geq 0.5 \end{cases} \quad (6)$$

2.3 Prey Search (Exploration Phase)

In this technique, we revise the position of the search agent (humpback whale) on the basis of a random search agent instead of the best one. The variation of \vec{P} can also be used for the prey search. Hence, \vec{P} is updated with the random values greater than one or less than minus one to force search the whale to move away from a reference whale. Therefore,

$$\vec{W} = \left| \vec{Q} \cdot \vec{K}_{\text{rand}} - \vec{K} \right| \quad (7)$$

$$\vec{K}(n+1) = \vec{K}_{\text{rand}} - \vec{P} \cdot \vec{W} \quad (8)$$

where \vec{K}_{rand} is a random position vector.

Now, in the next section, we will discuss the improvements done in WOA.

3 Opposition Theory Enabled Intelligent Whale Optimization Algorithm

Although the WOA is capable of generating solutions which exhibit higher accuracy than many meta-heuristic approaches, this still has a slow rate of convergence for many complex problems. So, by using the concept of opposition-based learning (OBL) and implementation of crossover operator and sinusoidal function in the original whale optimization algorithm, an intelligent whale optimization algorithm is developed to enhance the convergence rate further.

3.1 Implementation of OBL on OIWOA

The concept of opposition-based learning is a technique widely used in the field of optimization, which helps in the search process of getting the best solution. It improves the performance of MHA by simultaneously searching in the opposite direction and increases the chance of finding the best solution. In [10, 20, 21], it is described that instead of finding the best solution randomly, it is far better to look for the possible solution in the opposite direction of the initial search simultaneously to increase the chance of best initial guess, which may increase the convergence rate and may decrease the searching time.

Definition: Let z be a real number defined on a specified interval: $z[m, n]$. Then, the opposite number of z is defined as $z^* = m + n - z$. Similarly, the opposite number in a multidimensional case is $z_t^* = m_t + n_t - z_t$ where $z_t \in [m_t, n_t]$ and $t = 1, 2, \dots, N$. Let $Z = (Z_1, \dots, Z_n)$ be a point in an N-dimensional space. So, by definition, the opposite point is $Z^* = (Z^*_1, \dots, Z^*_n)$. Now, if $f(Z^*) \geq f(Z)$, then point Z will be replaced by Z^* ; otherwise, continue with Z .

This concept of opposition-based learning is implemented in the initialization process of OIWOA. The following steps describe the OIWOA with the following:

1. The first half position is generated by a random search and the other half is generated in opposite direction according to OBL as mention in Sect. 3.1.
2. After the initialization process, the first half position are updated as given in Sect. 2 and the other half positions are updated according to OBL as mention in Sect. 3.1.
3. After updating the positions, the two sub-positions are composed of one position. Further, we can sort the search results and locate the best position.

3.2 Implementation of Sinusoidal Function

In the proposed OIWOA, \vec{p} have been allowed to vary with a sinusoidal function over the course of iterations rather than to decrease linearly as in Eqs. (3) and (4) from 2 to 0 in WOA. This kind of variation reflects in the application of gray wolf algorithm [18]. This modification enables OIWOA with better search capabilities and it is given as

$$p = 2 * (1 - ((\sin(\theta/2))^2)) \quad (9)$$

where $\theta = 3.14 * ((n) / \text{Max_iteration})$ and n is the current number of iterations.

3.3 Implementation of Crossover

The crossover operator is familiar with the GA [5], KH[3], and DE [19] algorithms. It keeps the search process going. In this paper, a new variant of a crossover operator, i.e., crate(constant) is introduced. This crate operator implements on the standard equations of WOA (1), (2), (5), (7), and (8) that result in the enhancement of the convergence rate of WOA. The significant changes in the WOA model with crossover operator are as follows:

$$\vec{W} = \left| \text{crate} \cdot \vec{Q} \cdot \vec{K}^*(n) - \vec{K}(n) \right| \quad (10)$$

$$\vec{K}(n+1) = \text{crate} \cdot \vec{K}^*(n) - \vec{P} \cdot \vec{W} \quad (11)$$

$$\vec{K}(n+1) = \vec{W} \cdot e^{yl} \cdot \cos(2\pi l) + \text{crate} \cdot \vec{K}^*(n) \quad (12)$$

$$\vec{W} = \left| \text{crate} \cdot \vec{Q} \cdot \vec{K}_{\text{rand}} - \vec{K} \right| \quad (13)$$

$$\vec{K}(n+1) = \text{crate} \cdot \vec{K}_{\text{rand}} - \vec{P} \cdot \vec{W} \quad (14)$$

Hence, the concept of opposition-based learning, crossover, and sinusoidal function have been implemented on original whale optimization algorithm.

4 Results and Discussions

This proposed OIWOA has been developed on an Intel Core i5-7200U CPU with 8 GB ram and 2.70GHz speed and implemented by using the MATLAB software 2017a. The effectiveness of the proposed OIWOA is evaluated on the 23 standard benchmark

Table 1 Comparative analysis of benchmark functions

Benchmark function	OIWOA		WOA		PSO	
	AVG	STD	AVG	STD	AVG	STD
1	1.17E-142	5.90E-142	1.60E-73	6.20E-73	1.36E-04	2.02E-04
2	5.97E-84	2.77E-83	2.37E-51	8.82E-51	4.21E-02	4.54E-02
3	2.56E-69	1.22E-68	4.91E+04	1.45E+04	7.01E+01	2.21E+01
4	6.72E-46	2.63E-45	5.42E+01	2.50E+01	1.09E+00	3.17E-01
5	2.79E+01	3.39E-01	2.81E+01	4.25E-01	9.67E+01	6.01E+01
6	2.11E-01	6.76E-02	4.24E-01	2.15E-01	1.02E-04	8.28E05
7	1.51E-04	1.28E-04	3.82E-03	4.85E-03	1.23E-02	4.50E-02
8	-1.21E+04	1.02E+03	-9.68E+03	1.53E+03	-4.84E+03	1.15E+03
9	0.00E+00	0.00E+00	1.89E-15	1.04E-14	4.67E+01	1.15E+03
10	3.73E-15	1.72E-15	4.20E-15	2.63E-15	2.76E-01	5.09E-01
11	0.00E+00	0.00E+00	1.84E-02	6.15E-02	9.22E-03	7.72E-03
12	9.63E-03	2.80E-03	2.30E-02	1.86E-02	6.92E-03	2.63E-02
13	1.63E-01	5.82E-02	5.01E-01	2.29E-01	6.68E-03	8.91E-03
14	1.49E+00	1.06E+00	2.70E+00	2.88E+00	3.63E+00	2.56E+00
15	4.60E-04	2.02E-04	7.84E-04	6.71E-04	5.77E-04	2.22E-04
16	-1.03E+00	7.47E-03	-1.03E+00	7.58E-09	1.03E+00	6.25E16
17	3.98E-01	1.04E-03	3.98E-01	3.94E-06	3.97E-01	0.00E+00
18	3.02E+00	2.39E-02	3.00E+00	2.48E-04	3.00E+00	1.33E15
19	-3.85E+00	1.55E-02	-3.86E+00	1.00E-02	3.86E+00	2.58E15
20	-3.27E+00	9.34E-02	-3.21E+00	1.19E-01	3.27E+00	6.05E-02
21	-7.87E+00	2.36E+00	-8.00E+00	2.65E+00	6.87E+00	3.02E+00
22	-6.89E+00	2.88E+00	-7.04E+00	3.03E+00	8.46E+00	3.09E+00
23	-6.46E+00	2.77E+00	-8.33E+00	3.48E+00	9.95E+00	1.78E+00

functions as listed in [12] with keeping the number of iterations and search agents the same (500 and 30, respectively) for a similar study between OIWOA, WOA, and PSO. The numerical results (average and standard) are mentioned in Table 1; these 23 benchmark functions are classified in three categories: unimodal (function 1–7), multimodal (function 8–13), and fixed dimension multimodal (function 14–23) benchmark functions.

1. For the unimodal functions, the proposed OIWOA outperforms the WOA on a majority of functions. Their results show the better exploitation ability and assist the OIWOA to converge swiftly toward the optimum. It can also be concluded from the convergence curves as shown in Fig. 1.
2. While the numerical outcomes and convergence plots for multimodal and fixed dimension multimodal of the proposed OIWOA prove to enhance the level of exploration and show faster convergence over the original algorithm as shown in Fig. 1.

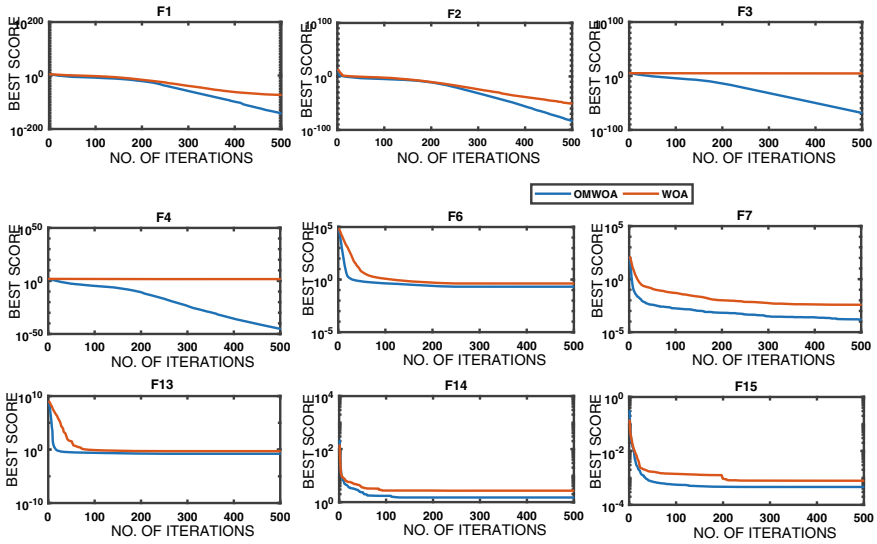


Fig. 1 Convergence characteristics of benchmark functions

5 Conclusions

The use of meta-heuristic algorithms has revolutionized the field of science with their ability to obtain optimal solutions for complex problems. In this paper, the proposed OIWOA is used to reduce the drawbacks of the standard WOA algorithm that shows a slow convergence and is trapped in local optima. The OIWOA uses the concept of opposition-based learning, crossover operator, and a sinusoidal function to enhance the optimization standards of WOA. For validation purpose, a study is conducted on 23 standard benchmark functions, which proves the efficacy of the proposed variant of WOA. The performance of the proposed opposition theory enabled intelligent algorithm (OIWOA) is equated with that of WOA and PSO algorithms, and the results show the more satisfactory performance of OIWOA with the minimization of average values (AVG) in functions 1–5, 7–11, 14, 15, and 20. In future studies, it can be applied to ELD problems, power system stability problems, control system design, strategic bidding problems, etc.

References

1. Aljarah I, Faris H, Mirjalili S (2018) Optimizing connection weights in neural networks using the whale optimization algorithm. *Soft Comput* 22(1):1–15
2. Askarzadeh A (2016) A novel metaheuristic method for solving constrained engineering optimization problems: crow search algorithm. *Comput Struct* 169:1–12

3. Gandomi AH, Alavi AH (2012) Krill herd: a new bio-inspired optimization algorithm. *Commun Nonlinear Sci Numer Simul* 17(12):4831–4845
4. Glover F, Laguna M (1998) Tabu search. In: *Handbook of combinatorial optimization*. Springer, Berlin, pp 2093–2229 (1998)
5. Goldberg DE, Holland JH (1988) Genetic algorithms and machine learning. *Mach Learn* 3(2):95–99
6. Jadhav AN, Gomathi N (2017) WGC: hybridization of exponential grey wolf optimizer with whale optimization for data clustering. *Alex Eng J* 57:1569
7. Kaveh A, Ghazaan MI (2017) Enhanced whale optimization algorithm for sizing optimization of skeletal structures. *Mech Based Des Struct Mach* 45(3):345–362
8. Kennedy R (1995) J. and Eberhart, particle swarm optimization. In: *Proceedings of IEEE international conference on neural networks IV*, vol 1000
9. Mafarja M, Mirjalili S (2018) Whale optimization approaches for wrapper feature selection. *Appl Soft Comput* 62:441–453
10. Mahdavi S, Rahnamayan S, Deb K (2018) Opposition based learning: a literature review. *Swarm Evol Comput* 39:1–23
11. Mirjalili S (2015) Moth-flame optimization algorithm: a novel nature-inspired heuristic paradigm. *Knowl Based Syst* 89:228–249
12. Mirjalili S, Lewis A (2016) The whale optimization algorithm. *Adv Eng Softw* 95:51–67
13. Mirjalili S, Mirjalili SM, Lewis A (2014) Grey wolf optimizer. *Adv Eng Softw* 69:46–61
14. Osman IH, Kelly JP (1996) Meta-heuristics: an overview. In: *Meta-heuristics*. Springer, Berlin, pp 1–21
15. Rajabioun R (2011) Cuckoo optimization algorithm. *Appl Soft Comput* 11(8):5508–5518
16. Rashedi E, Nezamabadi-Pour H, Saryazdi S (2009) GSA: a gravitational search algorithm. *Inf Sci* 179(13):2232–2248
17. Reddy PDP, Reddy VV, Manohar TG (2017) Whale optimization algorithm for optimal sizing of renewable resources for loss reduction in distribution systems. *Renew Wind Water Sol* 4(1):3
18. Saxena A, Soni BP, Kumar R, Gupta V (2018) Intelligent grey wolf optimizer-development and application for strategic bidding in uniform price spot energy market. *Appl Soft Comput* 69:1–13
19. Storn R, Price K (1997) Differential evolution—a simple and efficient heuristic for global optimization over continuous spaces. *J Glob Optim* 11(4):341–359
20. Tizhoosh HR (2005) Opposition-based learning: a new scheme for machine intelligence. In: *International conference on computational intelligence for modelling, control and automation, 2005 and international conference on intelligent agents, web technologies and internet commerce*, vol 1, pp 695–701. IEEE
21. Wang GG, Deb S, Gandomi AH, Alavi AH (2016) Opposition-based Krill Herd algorithm with cauchy mutation and position clamping. *Neurocomputing* 177:147–157
22. Wolpert DH, Macready WG (1997) No free lunch theorems for optimization. *IEEE Trans Evol Comput* 1(1):67–82
23. Yang XS (2010) *Nature-inspired metaheuristic algorithms*. Luniver Press, UK
24. Yang XS (2010) A new metaheuristic bat-inspired algorithm. In: *Nature inspired cooperative strategies for optimization (NICSO 2010)*. Springer, Berlin, pp 65–74
25. Yang XS (2012) Flower pollination algorithm for global optimization. In: *International conference on unconventional computing and natural computation*. Springer, Berlin, pp 240–249

Adaptive Inertia-Weighted Firefly Algorithm



Shailja Sharma, Pooja Jain and Akash Saxena

Abstract Real-life optimization problems required more and more technique, which completely utilizes the search spaces to obtain the best optimal solution, so researchers have an opportunity to propose a new technique or a modified version of the existing technique. In this order, this paper is a new modified version of nature-inspired metaheuristic firefly algorithm. FA is swarm intelligence algorithm inspired by flashing pattern and behavior of fireflies. FA has a tendency to trap in local optima and shows a slow convergence for optimization problems. To overcome these problems, in the proposed variant we add an adaptive inertia weight to update the position of search agents. To validate the performance of the proposed variant, it is tested on 23 traditional benchmark functions. The static and numerical results confirm the efficacy of the proposed variant over the original algorithm.

Keywords Firefly algorithm · Improve firefly algorithm · Inertia weight

1 Introduction

Optimization refers to the process of searching for the best solution for a particular problem. An optimization technique used to find out the optimal solution from all available possible solutions. Since long, conventional search methods have been used to solve optimization problems, although these methods give promising results in many problems, sometimes they may fail to solve complex optimization problems. If in the optimization problem the number of decision variables is very large and their effect on objective function is significant then such problems cannot be solved by conventional methods. So to solve these complex optimization problems, efficient methods of optimization are needed.

S. Sharma (✉) · P. Jain · A. Saxena
Swami Keshvanand Institute of Technology, Management and Gramothan, Jaipur,
Jagatpura, Jaipur, India
e-mail: shailjasharma@outlook.com

© Springer Nature Singapore Pte Ltd. 2020
A. Kalam et al. (eds.), *Intelligent Computing Techniques for Smart Energy Systems*,
Lecture Notes in Electrical Engineering 607,
https://doi.org/10.1007/978-981-15-0214-9_53

To solve such type of complex optimization problems, optimization algorithms which are stochastic in nature is used. These are heuristics and metaheuristics algorithm, in which a Heuristics optimization algorithm is used to find the approximate solution for many complex optimization problems and does not guarantee that any optimal solution is required. Metaheuristics optimization algorithm can make some assumptions about the problem being solved so they can be useful for various types of problems. It is very powerful in dealing with highly nonlinear design functions. Most of the metaheuristics algorithm is based on swarm intelligence. In the past years, the number of swarm-based optimization algorithms is increased. These algorithms are based on natural phenomenon. Such algorithms are as follows: (i) Genetic Algorithm (GA) is a nature-inspired algorithm, which was developed by John Holland in the 1960s and 1970s. This algorithm was inspired by the natural evolution process. Crossover and mutation are the keys to GA [2]. (ii) Particle Swarm Optimization (PSO), which was developed by Kennedy and Eberhart in 1995, based on the swarming behavior of fish and bird schooling [13]. (iii) Ant Colony Optimization (ACO) was introduced by Marco Dorigo in 1992, inspired by searching behavior of social ants of searching foods and shortest path to their colony [3, 4] (iv) Artificial Bee Colony (ABC) was developed by D. Karabogo in 2005 inspired by the hunting behavior of bees. Studies have shown that a bee colony is capable of allocating forage bees between different flower patches so that their total nectar intake can be maximized. ABC algorithm is developed for numerical function optimization [7]. Another nature-inspired algorithm was (v) Firefly algorithm (FA) which was introduced by Xin-she-Yang (Yang 2008), inspired by the flashing behavior of fireflies. Fireflies communicate by flashing their light [5]. Grey wolf optimization algorithm (GWO) [10], whale optimization algorithm [9], Differential Evolution [12], Tabu Search [1], Harmony Search [8], Cuckoo Search [6] are some other metaheuristics algorithms.

After the presence of many different algorithms in optimization area, we require different algorithms for such multidisciplinary problems. NFL (No Free Lunch) theorem explains that no one can applaud a particular method for solving various kinds of the optimization problem [14]. Hence, the researcher has an opportunity to modify an existing algorithm and apply on different optimization problem.

In this order, we proposed an improvement in the firefly algorithm by adding an adaptive inertia weight. The flashing pattern of fireflies inspires firefly algorithm. In which, brighter flies for communication attract dimmer flies. Light intensity obeys the inverse square law with distance. This improvement gives a fast convergence rate and effective results as compared to the original FA.

In this paper, Sect. 1 describes the introduction of paper. Section 2 describes the original Firefly algorithm, Sect. 3 describes the improvement in Firefly algorithm. In Sect. 4, we discuss simulation results and Sect. 5 concludes the paper.

2 Firefly Algorithm

Firefly algorithm was introduced by Yang in 2010, FA was inspired by flashing pattern and behavior of fireflies [15]. There are about two thousand species of Firefly. Flashing pattern of these fireflies vary according to the type of species. Firefly produces short and rhythmic flashes to attract their partner for communication and potential prey. In some species, female flies react to male’s unique pattern of flashing, while in some species female flies can imitate flashing pattern of other species to tempt and attack male flies which may mistake the flashing as a dormant suitable mate. As we acknowledge that light intensity at a certain distance r from the light source follows the inverse square law, so we can state that light intensity varies as the range varies because it absorbs by surrounding and can define as $I \propto 1/r^2$ [16].

In fireflies, few flies are dimmer and few flies are brighter, dimmer flies are attracted by brighter flies. To develop Firefly-inspired algorithm, it is the idealized flashing pattern of fireflies. This phenomenon is shown in Fig. 1. FA used three idealized rules:

1. Fireflies are unisex so that a firefly attracts other fireflies regardless of their gender
2. The attractiveness is proportional to the brightness, as the distance between two flies increases both will decrease, thus for any two flies the dimmer one will be attracted by brighter one but if there is no brighter one then they move randomly.
3. The landscape of objective function determined the brightness of fireflies.

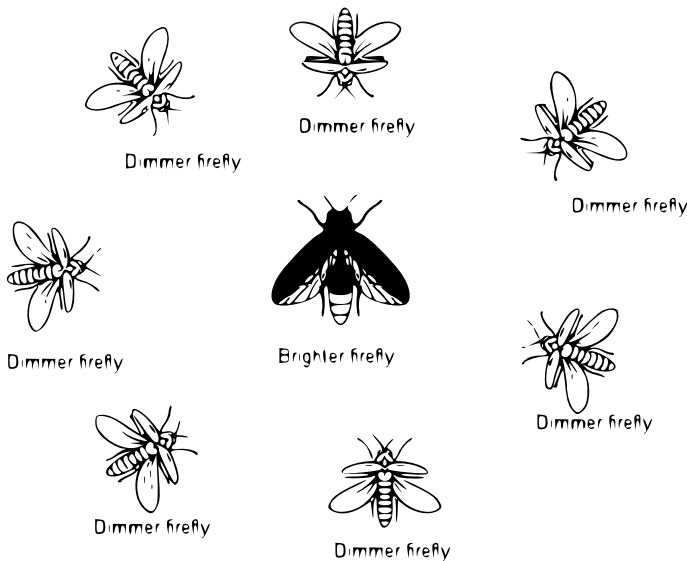


Fig. 1 Flashing of firefly

In FA, the two main important variables are light intensity and attractiveness. The attractiveness is proportional to light intensity seen by other flies, so attractiveness is defined as

$$\beta = \beta_o e^{-\gamma r^2} \quad (1)$$

Here β is attractiveness of fireflies at distance r and β_o is attractiveness at distance $r = 0$, r is defined as distance between two fireflies i and j , γ is defined as light absorption coefficient. Light intensity is inversely proportional to the attractiveness of flies at distance r from source.

$$I = I_o e^{-\gamma r^2} \quad (2)$$

Here I is define as light intensity, I_o is defined as original light intensity or light intensity at initial. The distance r between two fireflies i and j located at x_i and x_j is calculated as Euclidean Distance

$$r = \|x_i - x_j\| = \sqrt{\sum_{m=1}^d (x_i^m - x_j^m)^2} \quad (3)$$

At time when dimmer flies i move toward brighter flies j , dimmer flies update their location and it is determined by

$$x_i^{(n+1)} = x_i^n + \beta_o e^{-\gamma r_{ij}^2} (x_j^n - x_i^n) + \alpha_n \epsilon_i^n \quad (4)$$

In the given equation, the second term is for the attractiveness of two flies, where a value of γ is tending to zero to infinity (too large). When $\gamma \rightarrow 0$ then brightness and attractiveness become constant $\beta = \beta_o$, so Firefly can be seen in any position. When $\gamma \rightarrow \infty$ then brightness and attractiveness will be decreased, so the movement of fireflies become random. In the third term of the equation, α is randomized parameter and ϵ_i can be written as $(\text{rand}-1/2)$, where rand is any random number between $[0, 1]$. The pseudocode of FA shown in Fig. 2.

3 Improved Firefly Algorithm

FA was developed to solve nonlinear problems. After some modification in the original algorithm, it gives more effective results. The main disadvantage of FA, low convergence rate and slow process, is improved by modifying in the original firefly algorithm. FA is useful for multidimensional and nonlinear problems.

In FA, movement of Firefly is random to find fireflies for next iteration, in that random movement of fireflies attractiveness and brightness decrease due to less attractiveness it leads to loss of performance in a particular iteration. Some improvement takes place to move fireflies in a particular direction it is only done by improving the brightness. For the improvement, an adaptive inertia weight is added for randomization value α . If the value of α is large, firefly can explore unknown places, for a small

1. Generate initial population of n fireflies x_i ($i = 1, 2, \dots, n$).
2. Light intensity I_i at x_i is determined by $f(x_i)$.
3. Define light absorption coefficient γ .
4. **While** ($t < MaxGeneration$).
5. **For** $i = 1 : n$, n= no of fireflies.
6. **For** $j = 1 : n$, (inner loop)
7. **If** ($I_i < I_j$)
8. Move firefly i towards j.
9. **End if**
10. Vary attractiveness with distance r via $e^{-\gamma r^2}$.
11. Evaluate new solutions and update light intensity.
12. **End for** j
13. **End for** i
14. Rank the fireflies and find the current global best g_{t+1} ..
15. **End While**
16. Post process results and visualization.

Fig. 2 Pseudocode of FA

value of γ , firefly will make a local search. By changing random movement into particular movement firefly move toward the best solution in the iteration. Improved attractiveness is calculated as

$$\beta_k = \beta_{k0} e^{-\gamma r^2} \tag{5}$$

β_k is improved attractiveness at distance r_k between two flies. Now the updated location of dimmer flies is calculated as:

$$x_{ik}^{(n+1)} = x_{ik}^n + \beta_{k0} e^{-\gamma r_{ij}^2} (x_{jk}^n - x_{ik}^n) + \alpha_k \epsilon_k^n \tag{6}$$

From Eq. (4) ϵ_i is Improved into ϵ_k is define as

$$\epsilon_k = \partial * b \tag{7}$$

In Eq. (7) b is uniform random number, value of b depends on functions, ∂ is define as

$$\partial = 0.5 * (u^* - l^*) \tag{8}$$

Here u^* is upper bound of function and l^* is lower bound of function.

For the modification in the algorithm, some inertia weight is used. IW parameter defined by Shi and Eberhart. Inertia weight is categorized into three sections. In the first class of IW strategy, weight is taken as constant, define as adaptive inertia weight.

In the second class of IW strategy, weight defines a function of iteration or time these are time-varying inertia weight. This method can be increasing or decreasing. IW is determined on the bases of iterations in the algorithm. In the third class, weight is considered as those methods which are used as feedback parameter in algorithm [11]. Improvement in α_n define as:

$$\alpha_k = \alpha_n * \alpha_damp \quad (9)$$

$$\alpha_damp = 0.05 \quad (10)$$

Here α_n is initial randomization parameter, α_damp is an adaptive inertia weight. In this paper, our inertia weight is defined as adaptive inertia weight and taken as a constant value 0.05 which give effective results as compare to the original FA, the convergence of IFA is faster than original FA by adding an adaptive inertia weight to original FA.

4 Simulation Results and Discussions

To validate the performance of the proposed variant, the proposed method was evaluated on 23 traditional benchmark functions. These benchmark functions table is taken from paper of Mirjalili [10]. The proposed modification is developed by using MATLAB R2017a and run on i5 processor CPU 2.7 GHz & 6 GB Ram. To make a fair comparison of the proposed modification, the number of iteration, population size are repeated same for both techniques (i.e., Max no of iteration 1000), (Number of fireflies = 25). Proposed modification is simulated one time on each benchmark function the numerical results (Mean, Std, Max, Min) are reported in Table 1.

Benchmark functions are categorized into three groups; Uni-modal benchmark functions (Function 1–Function 7), multi-modal benchmark function (Function 8–Function 13), and fixed dimension multi-modal benchmark function (Function 14–Function 23).

4.1 Results on Uni-modal Functions

According to the results reported in Table 1, it is evident that the proposed variant outperformed standard algorithm on the majority of test cases from characteristic of uni-modal functions. Proposed variant benefits from super-exploitation capacity. It assists the proposed variant to convergence rapidly towards optimum which can also be inferred from the convergence curve.

Table 1 Comparative analysis of IFA and FA

	IFA				FA			
	Mean	Std	Max	Min	Mean	Std	Max	Min
F1	2.53E+02	2.73E+03	5.48E+04	1.17E-75	2.73E+02	2.84E+03	5.28E+04	1.89E-16
F2	8.81E+03	2.74E+05	8.65E+06	2.58E-51	3.78E+04	1.19E+06	3.77E+07	5.76E-09
F3	1.74E+03	6.67E+03	7.58E+04	1.77E-05	1.04E+03	5.22E+03	6.11E+04	4.96E-07
F4	3.00E+01	3.92E+00	8.40E+01	2.96E+01	1.14E+01	7.40E+00	8.02E+01	9.06E+00
F5	6.09E+05	8.28E+06	2.22E+08	9.96E+00	3.97E+05	5.88E+06	1.59E+08	2.27E+01
F6	2.81E+02	3.05E+03	6.51E+04	9.24E-33	2.30E+02	2.50E+03	5.56E+04	1.92E-16
F7	2.08E-01	3.33E+00	9.82E+01	3.65E-03	2.49E-01	3.18E+00	7.53E+01	3.85E-03
F8	-8.15E+03	5.10E+02	-2.71E+03	-8.22E+03	-8.12E+03	4.78E+02	-3.43E+03	-8.20E+03
F9	1.02E+02	2.34E+01	3.95E+02	9.85E+01	5.93E+01	2.79E+01	3.84E+02	5.47E+01
F10	3.82E-01	2.06E+00	2.04E+01	2.93E-14	4.27E-01	2.03E+00	1.99E+01	2.77E-09
F11	2.40E+00	2.63E+01	5.75E+02	0.00E+00	2.58E+00	2.50E+01	4.60E+02	9.86E-03
F12	8.46E+05	1.44E+07	3.79E+08	1.80E-32	6.38E+05	1.37E+07	4.16E+08	3.93E-18
F13	2.41E+06	3.57E+07	8.65E+08	2.88E-03	1.94E+06	3.10E+07	8.57E+08	5.17E-17
F14	1.02E+00	2.82E-01	7.97E+00	9.98E-01	1.02E+00	3.95E-01	1.21E+01	9.98E-01
F15	6.33E-04	1.29E-03	4.14E-02	4.55E-04	4.25E-04	5.91E-04	1.82E-02	3.08E-04
F16	-1.03E+00	5.50E-03	-8.58E-01	-1.03E+00	-1.03E+00	1.14E-03	-1.00E+00	-1.03E+00
F17	3.98E-01	7.47E-03	6.34E-01	3.98E-01	3.98E-01	7.44E-03	6.31E-01	3.98E-01
F18	3.00E+00	7.50E-02	5.23E+00	3.00E+00	3.00E+00	6.70E-02	5.12E+00	3.00E+00
F19	-3.86E+00	1.82E-03	-3.81E+00	-3.86E+00	-3.86E+00	4.09E-03	-3.74E+00	-3.86E+00
F20	-3.20E+00	2.58E-02	-2.42E+00	-3.20E+00	-3.32E+00	2.33E-02	-2.84E+00	-3.32E+00
F21	-1.01E+01	4.81E-01	-5.21E-01	-1.02E+01	-2.68E+00	6.79E-02	-7.04E-01	-2.68E+00
F22	-1.04E+01	4.27E-01	-1.11E+00	-1.04E+01	-1.04E+01	5.55E-01	-7.65E-01	-1.04E+01
F23	-1.05E+01	3.78E-01	-1.49E+00	-1.05E+01	-1.05E+01	5.19E-01	-1.35E+00	-1.05E+01

4.2 Results on Multi-modal and Fixed Dimension Multi-modal Functions

As per reported results, the proposed variant shows significantly improved results. By evaluating a characteristic of the multi-modal test function, it may be written that the proposed variant has improved the level of exploration. The convergence curve of the algorithm on some of the multi-modal function is shown in Fig. 3 which proves the efficacy of proposed variant over original FA.

5 Conclusions

This paper is inspired by NFL theorem, where we proposed an improvement in Firefly algorithm and analyzed with the original algorithm. FA shows slow convergence and trapped in a local optimum. Modification in FA was done to improve the local search as well as global search. When compared results of our algorithm with the original

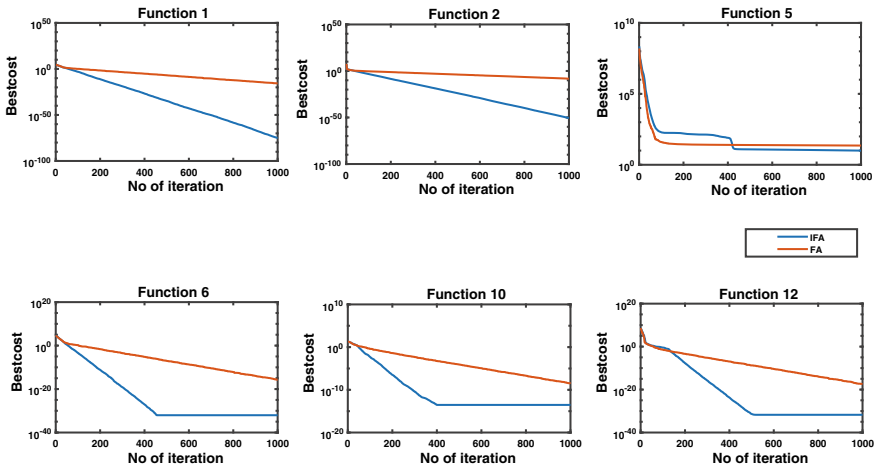


Fig. 3 Convergence curves for some benchmark functions

algorithm, our algorithm (IFA) converges to an optimal solution faster, in Table 1 minimum value of the mean, std, max, and min of functions are highlighted, where function F1, F2, F7, F8, F10, F11, F14, F17, F19, and F21-F23 gives minimum mean values of functions in IFA, and it shows minimum values than original FA.

For acceptance, the test was performed on 23 traditional benchmark functions. For the future effort, IFA will be applied to real-life application. The researcher can combine IFA with some other algorithm for better results.

References

1. Abido M (2002) Optimal power flow using tabu search algorithm. *Electr Power Compon Syst* 30(5):469–483
2. Cerf R (1996) A new genetic algorithm. *Ann Appl Probab* 778–817
3. Dorigo M, Birattari M (2011) Ant colony optimization. In: *Encyclopedia of machine learning*, pp 36–39. Springer
4. Dorigo M, Di Caro G (1999) Ant colony optimization: a new meta-heuristic. In: *Proceedings of the 1999 congress on evolutionary computation-CEC99* (Cat. No. 99TH8406), vol 2. IEEE, pp 1470–1477
5. Gandomi AH, Yang XS, Talatahari S, Alavi AH (2013) Firefly algorithm with chaos. *Commun Nonlinear Sci Numer Simul* 18(1):89–98
6. Gandomi AH, Yang XS, Alavi AH (2013) Cuckoo search algorithm: a metaheuristic approach to solve structural optimization problems. *Eng Comput* 29(1):17–35
7. Karaboga D, Basturk B (2007) A powerful and efficient algorithm for numerical function optimization: artificial bee colony (ABC) algorithm. *J Glob Optim* 39(3):459–471
8. Mahdavi M, Fesanghary M, Damangir E (2007) An improved harmony search algorithm for solving optimization problems. *Appl Math Comput* 188(2):1567–1579
9. Mirjalili S, Lewis A (2016) The whale optimization algorithm. *Adv Eng Softw* 95:51–67
10. Mirjalili S, Mirjalili SM, Lewis A (2014) Grey wolf optimizer. *Adv Eng Softw* 69:46–61

11. Nickabadi A, Ebadzadeh MM, Safabakhsh R (2011) A novel particle swarm optimization algorithm with adaptive inertia weight. *Appl Soft Comput* 11(4):3658–3670
12. Qin AK, Huang VL, Suganthan PN (2009) Differential evolution algorithm with strategy adaptation for global numerical optimization. *IEEE Trans Evol Comput* 13(2):398–417
13. Rahmani R, Yusof R, Seyedmahmoudian M, Mekhilef S (2013) Hybrid technique of ant colony and particle swarm optimization for short term wind energy forecasting. *J Wind Eng Ind Aerodyn* 123:163–170
14. Wolpert DH, Macready WG (1997) No free lunch theorems for optimization. *IEEE Trans Evol Comput* 1(1):67–82
15. Yang XS (2009) Firefly algorithms for multimodal optimization. In: *International symposium on stochastic algorithms*. Springer, pp 169–178
16. Yang XS (2010) *Nature-inspired metaheuristic algorithms*. Luniver Press

A Review of Scheduling Techniques and Communication Protocols for Smart Homes Capable of Implementing Demand Response



Gurpinder Singh, Anil Swarnkar, Nikhil Gupta and K. R. Niazi

Abstract This paper presents a literature review of scheduling techniques and communication protocols (STCP), which make adaptable smart home (SH) capable of implementing demand response. In addition, it presents advantages and disadvantages of various STCP mentioned in the literature. Also, the paper provides the pathway to future researchers for designing of smart homes, as it briefly mentions various specifications of STCP so that one could select according to their application.

Keywords Scheduling techniques · Communication protocols · Smart homes · Demand response

1 Introduction

According to a survey conducted in the United States, it is found that about 90% of people consider having a personal, secured, and automated smart home (SH) as their primary preference [1]. A lot of research work is available in the literature on SH, according to which, SH offers improved quality of life by providing easy appliance control using voice [2–4] or mobile phone [5–7], providing a healthcare environment [8, 9], and reducing the energy consumption [10–12]. It can also provide economic benefits to consumers and utility by implementing tariff-based demand response programs [10, 12–14], energy resources management, and storage management [12, 15], etc.

G. Singh · A. Swarnkar (✉) · N. Gupta · K. R. Niazi
Malaviya National Institute of Technology, Jaipur, India
e-mail: mnit.anil@gmail.com

G. Singh
e-mail: 2017pes5202@mnit.ac.in

N. Gupta
e-mail: nikhil2007_mnit@yahoo.com

K. R. Niazi
e-mail: krm152001@yahoo.co.in

In [16], S. K. Das et al. suggested an agent-based SH, MavHomes, which provides prediction framework for the user tagged. The artificial intelligence laboratory at Massachusetts Institute of Technology, develops very efficient human machine interface techniques by which system can detect hand gestures and recognizes the voice and emotions [17].

In this paper, various scheduling techniques and communication protocols (STCP) suggested in the literature are reviewed. STCPs are two main technical drivers for incorporating demand response into SHs. For designing an SH, which is capable of implementing demand response, an optimization technique is required for optimal scheduling of appliances based on tariff-based data received from utilities. Moreover, a communication protocol is required to provide communication of the energy management system (EMS) with various appliances.

2 Scheduling Techniques

There are various scheduling techniques or algorithms available in the literature. In this section, rule-based, training-based Artificial Intelligence (AI) techniques, heuristic- meta-heuristic-based approaches for scheduling demand response are discussed.

2.1 Rule-Based Scheduling Techniques

Many Rule-Based (RB) algorithms are suggested for scheduling of appliances considering dynamic pricing. Rete algorithm is suggested in [18] by Tomoya Kawakami et al., in which rules for managing energy are processed by smart taps in network, and the loads for processing rules and collecting data are distributed to smart taps for optimal scheduling. In [19], the RB method is used to produce if/then rules which are based on low to high priority of appliances. But there are some drawbacks of using RB system, e.g., an extra set of memory is required to store the set of rules, no scope of system expansion, and also it is not so capable of dealing with large number of data which makes it difficult for scheduling corresponding to RTP [20].

Another RB technique is Fuzzy Logic (FL), used for intelligent demand response which is given in [21], and the results were also verified on IEEE 34-bus distribution feeder. In another work [22], FL is used to optimize cost, comfort, and implement demand response; in [23], the technique is used to directly control the load considering customer's preference and in [24] the operation of water heater is scheduled according to peak demand. FL control has a major drawback that it highly depends on appropriate variables, determined on the basis of trial and error which takes additional time [20].

2.2 Training-Based Artificial Intelligent Techniques

These AI are the techniques in which large amount of data is required for training, after learning that the system can detect and mimic patterns. AI techniques can be employed in SHs to provide various intelligent services (including scheduling) to users [23, 25]. One of the effective algorithms is Artificial Neural Network (ANN), proposed for an optimal demand-side management of PV installed at the residential site [26]. In another study [27], ANN is used to analyze the huge amount of data which is collected from the digital meters and convert them into some useful pattern that could be used for load forecasting and further helps in demand side response. In spite of being a very effective technique, it receives certain criticism as proper data based on history (size, variation) for training is required. If systems change, ANN is to be trained again.

Another useful technique is Adaptive Neural Fuzzy Interference System (ANFIS), which is the combination of fuzzy logic and neuro computing, used for demand response and for prediction of the potential schedules based on the customer's life style [28]. The challenges faced by ANFIS include the long training time as well as long learning time.

The literature has given different ways to achieve effective performance using different techniques. Fuzzy logic controller can attain effective performance if appropriate parameters in the RB algorithm and membership functions are considered. ANN-based controller will perform optimally if proper training data according to size and variation is provided. ANFIS can produce optimal or near optimal results if proper training data, activation function and number of nodes are determined. But ANN technique is a bit on the favorable side due to excellent prediction and good performance when there is real-time operation and also is able to learn many nonlinear functions by training.

2.3 Heuristic and Meta-Heuristic AI Techniques

Heuristic and meta-heuristic AI techniques are derivation-free optimization techniques which do not require any historical data and off-line training but may provide optimal or near optimal solution for objective function formulated, considering the provided constraints. As in [29–31], a multi-objective nonlinear model is formulated for the optimal use of energy and the comfort level is considered as a constraint. In [32], Chavali, Phani et al. proposed appliance scheduling for implementing demand response. They also proposed the distribution framework where users can independently minimize cost of billing using greedy approx. In [33], combination of the RTP and the inclining block rate is used to reduced electricity bill cost and peak to avg. ratio (PAR) using linear programming methods and also included the prediction of prices coming ahead for better scheduling results. Whereas [34] is another work where A. Mohsenian-Rad et al. efforts are made to reduce the billing cost as

well as the PAR but they also aimed at deploying energy consumption scheduling devices in smart meters which run distributed algorithm automatically. K. M. Tsui and S. C. Chan [11] provided a convex programming DR optimization framework for automatic load scheduling in smart homes. Particle Swarm Optimization (PSO) is used for load balancing problem in green smart homes [35, 36].

Genetic Algorithm (GA) is used to optimize nonlinear problem in [14] for cost-effective scheduling of home appliances using a combination of RTP and IBP. In [37], GA is used for managing energy for home employing SCADA. While comparing GA with mixed-integer nonlinear programming, it is found that GA reduces the energy consumption better. Reference [12] provides the optimized scheduling of appliances using Binary Particle Swarm Optimization (BPSO) and resource management using PSO. In [38], Gill et al. have designed and compared energy management controller using five different heuristic optimization techniques GA, BPSO, bacterial foraging optimization algorithm (BFOA), wind driven optimization (WDO), and genetic wind driven (GWD), in which GWD reduces energy consumption up to 10% as compared to GA and 33% as compared to WDO.

These techniques are mostly population-based and are computationally demanding. These techniques are capable of providing optimal or near optimal solution but may be trapped in local minima if not properly tuned.

3 Communication

Communication protocols are required to establish communication between all the devices and energy management system. There exists various communication protocols in literature, but this section mainly discusses some more commonly used protocols, e.g., KNX, X10, DSL, Zigbee, Ethernet, and Wi-Fi. Communication protocols can be classified into three major categories according to medium of communication, i.e., *wired communication protocols*, *wireless communication protocols*, and *hybrid communication protocols*.

3.1 Wired Communication Protocols

KNX (PL110) is a wired network which uses separate cables to transfer data. Data transfer rate is high in this protocol. It is a noise-proof system due to separate cables, but it is expensive and requires long installation time. In [39], management of KNX-based smart home automation system through android mobile is presented.

X10 is a cheap wired network as it uses existing power line for communication purpose. To use this protocol, the consumer has to just plug the electrical devices into the conventional power outlets but communication through power lines are not reliable because of noise and can send message at specific times only. In [40], Nicholas Dickey et al. have developed home-automated system employing the integration of

mobile devices, cloud computing wireless communication, and power line communication (X10 protocol-based).

Digital line subscribed (DLS) uses phone lines to communicate. This protocol provides remote access via home gateway. But this system works with IP network only. Reference [41] presents a home server platform which integrates the functioning of communication using DLS protocols, digital broadcasting reception, and applications of home automation.

ISDN is another wired communication protocol which communicates through ISDN lines and have higher dedicated bandwidth. But is expensive than other services. The patent [42] presents apparatus and method of implementing a universal home network on a customer premises ISDN bus. Another efficient protocol is Ethernet which uses twisted paired cable, which provides remote access by building an IP network, but to use this protocol, IP network should be created. In [43], smart home system which uses Arduino ethernet in cooperating voice activation is presented by Shiu Kumar.

3.2 Wireless-Based Communication

Zigbee system is a wireless-based system which uses radio frequency (RF) to communicate. It consumes low power and is economical but has a tight power and bandwidth constraints. A work [44] proposed a smart home security system using low-power Zigbee (802.15.4).

Wi-Fi, which is very commonly available at homes nowadays is another wireless communication system using ISM to communicate; its advantage is that it has high bandwidth and its disadvantage is that it consumes high power. Residential gateway or home gateway was introduced for providing the remote access, Wi-Fi is necessary for this residential gateway, for example, in [45] Zigbee-based automation system and Wi-Fi network are integrated through a common gateway.

3.3 Hybrid and Integrated Protocols

Hybrid protocols are one which use both the wired and wireless communication. Universal Plug and Play (UPnP) is a hybrid communication protocol using Ethernet, IR, and RF to communicate. It is not suitable in terms of economy consistency and complexity. Reference [46] presents an OSHi-based home automation; in OSHi platform of home gateway, UPnP (Universal Plug and Play) technology and intelligent agent technology work together. The literature mentions about integrated protocols like [47] bring together Zigbee and X10 technologies to make cost-effective home automation systems, [48] implemented KNX and Zigbee together.

There are many other techniques mentioned in the literature like GSM module using SMS technology to exchange data [49], Raspberry Pi based home automation

system communicating through email [50], speech recognizing and communicating through Internet and mobile SMS home automation model [51], Arduino and Raspberry Pi and smart communication based home automation [52], and many more. But one must choose the protocols and devices wisely, as one of the main problems is of compatibility among devices from different vendors as they use different protocols.

4 Conclusion

This paper presents a review of the STCP suggested in the literature to design SHs capable of implementing demand response. Different rule-based techniques like FL; training-based AI techniques like ANN, ANFIS, and heuristic and meta-heuristic techniques like GA, PSO, BPSO, WDO, BFOA, and GWD are reviewed. Various wired, wireless, and hybrid communication protocols like KNX, DLS, X10, ISDN, Ethernet, Wi-Fi, Zigbee, and UPnP are also reviewed. This paper may be helpful for researchers working in the area of SH.

Further, advanced AI should be incorporated, which enables SHs to learn user's habits and minimize the user's active participation. Moreover, a better human to machine interface should be provided for better and easy interaction like employing hand gesture and emotion detection.

References

1. Khajendasari I, Estebasari A, Verhelst M, Gielen G (2017) A review on Internet of things solution for intelligent energy control in buildings for smart city applications. *Energy Procedia* 111:770–779
2. AlShu'eili H, Gupta G, Mukhopadhyay S (2011) Voice recognition based wireless home automation system. In: 4th IEEE international conference on mechatronics (ICOM), pp 1–6
3. Vanus J, Marek S, Radek M, Jiri K, Jan Z, Petr B (2015) Testing of the voice communication in smart home care. *Hum Centric Comput Inf Sci* 5(1):15
4. Zhu J, Gao X, Yang Y, Li H, Ai Z, Cui X (2010) Developing a voice control system for zigbee-based home automation networks. In: 2nd IEEE international conference on network infrastructure and digital content, pp 737–741
5. Kalofonos DN, Wisner P (2007) A framework for end-user programming of smart homes using mobile devices. In: 4th IEEE consumer communications and networking, pp 716–721
6. Rao SK, Rao RK (2014) Home automation and smart home control using mobile devices and wireless enabled electrical switches. U.S. Patent Application 14/100,975, filed 10 Apr 2014
7. Wang H, Saboune J, Saddik A (2013) Control your smart home with an autonomously mobile smartphone. In: 2013 IEEE international conference on multimedia and expo workshops (ICMEW), pp 1–6
8. Korhonen I, Parkka J, Gils M (2003) Health monitoring in the home of the future. *IEEE Eng Med Biol Mag* 22(3):66–73
9. Chan M, Estève D, Escriba C, Campo E (2008) A review of smart homes—present state and future challenges. *Comput Methods Progr Biomed* 91(1):55–81

10. Althaher S, Mancarella P, Mutale J (2015) Automated demand response from home energy management system under dynamic pricing and power and comfort constraints. *IEEE Trans Smart Grid* 6(4):1874–1883
11. De Luca G, Lillo P, Mainetti L, Mighali V, Patrono L, Sergi I (2013) The use of NFC and Android technologies to enable a KNX-based smart home. In: 2013 21st international conference on software, telecommunications and computer networks (SoftCOM). IEEE, pp 1–7, Sept 2013
12. Han DM, Lim JH (2010) Design and implementation of smart home energy management systems based on zigbee. *IEEE Trans Consum Electron* 56(3)
13. Shafie-Khah M, Siano P (2018) A stochastic home energy management system considering satisfaction cost and response fatigue. *IEEE Trans Ind Inf* 14(2):629–638
14. Willer B (2003) U.S. Patent No. 6,522,728. U.S. Patent and Trademark Office, Washington, DC
15. Wu X, Hu X, Moura S, Yin X, Pickert V (2016) Stochastic control of smart home energy management with plug-in electric vehicle battery energy storage and photovoltaic array. *J Power Sources* 333:203–212
16. Das SK, Cook DJ, Battacharya A, Heierman EO III, Lin T-Y (2002) The role of prediction algorithms in the MavHome smart home architecture. *IEEE Wirel Commun* 9(6):77–84 (2002)
17. Brooks RA (1997) The intelligent room project. In: Proceedings of second international conference on cognitive technology humanizing the information age, Aizu-Wakamatsu City, Japan, pp 271–278
18. Jiang L, Liu DU, Yang B (2004) Smart home research. In: Proceedings of 2004 international conference on machine learning and cybernetics (IEEE Cat. No. 04EX826), vol 2, Shanghai, China, pp 659–663
19. Suh C, Ko Y (2008) Design and implementation of intelligent home control systems based on active sensor. *IEEE Trans Consum Electron* 54(3):1177–1184
20. Matallanas E, Castillo-Cagigal M, Gutiérrez A, Monasterio-Huelin F, Caamaño-Martín E, Masa D, Jiménez-Leube J (2012) Neural network controller for active demand-side management with PV energy in the residential sector. *Appl Energy* 91(1):90–97
21. Macedo MNQ, Galo JJM, De Almeida LAL, Lima ADC (2015) Demand side management using artificial neural networks in a smart grid environment. *Renew Sustain Energy Rev* 41:128–133
22. Ozturk Y, Senthilkumar D, Kumar S, Lee GK (2013) An intelligent home energy management system to improve demand response. *IEEE Trans Smart Grid* 4(2):694–701
23. Anvari-Moghaddam A, Monsef H, Rahimi-Kian A (2015) Optimal smart home energy management considering energy saving and a comfortable lifestyle. *IEEE Trans Smart Grid* 6(1):324–332
24. Mohsenian-Rad AH, Leon-Garcia A (2010) Optimal residential load control with price prediction in real-time electricity pricing environments. *IEEE Trans Smart Grid* 1(2):120–133
25. Chavali P, Yang P, Nehorai A (2014) A distributed algorithm of appliance scheduling for home energy management system. *IEEE Trans Smart Grid* 5(1):282–290
26. Mohsenian-Rad AH, Leon-Garcia A (2010) Optimal residential load control with price prediction in real-time electricity pricing environments. *IEEE Trans Smart Grid* 1(2):120–133
27. Mohsenian-Rad AH, Wong VW, Jatskevich J, Schober R (2010) Optimal and autonomous incentive-based energy consumption scheduling algorithm for smart grid. In: 2010 innovative smart grid technologies (ISGT). IEEE, pp 1–6, Jan 2010
28. Tsui KM, Chan SC (2012) Demand response optimization for smart home scheduling under real-time pricing. *IEEE Trans Smart Grid* 3(4):1812–1821
29. Lugo-Cordero HM, Fuentes-Rivera A, Guha RK, Ortiz-Rivera EI (2011) Particle swarm optimization for load balancing in green smart homes. In: 2011 IEEE congress on evolutionary computation (CEC). IEEE, pp 715–720, June 2011
30. Pedrasa MAA, Spooner TD, MacGill IF (2010) Coordinated scheduling of residential distributed energy resources to optimize smart home energy services. *IEEE Trans Smart Grid* 1(2):134–143

31. Zhao Z, Lee WC, Shin Y, Song KB (2013) An optimal power scheduling method for demand response in home energy management system. *IEEE Trans Smart Grid* 4(3):1391–1400
32. Fernandes F, Sousa T, Silva M, Morais H, Vale Z, Faria P (2011) Genetic algorithm methodology applied to intelligent house control. In: 2011 IEEE symposium on computational intelligence applications in smart grid (CIASG). IEEE, pp 1–8, Apr 2011
33. Gudi N, Wang L, Devabhaktuni V, Depuru SSSR (2010) Demand response simulation implementing heuristic optimization for home energy management. In: 2010 North American power symposium (NAPS). IEEE, pp 1–6, Sept 2010
34. Javaid N, Javaid S, Abdul W, Ahmed I, Almogren A, Alamri A, Niaz I (2017) A hybrid genetic wind driven heuristic optimization algorithm for demand side management in smart grid. *Energies* 10(3):319
35. Dickey N, Banks D, Sukittanon S (2012) Home automation using cloud network and mobile devices. In: 2012 proceedings of IEEE Southeastcon. IEEE, pp 1–4, Mar 2012
36. Han I, Park HS, Jeong YK, Park KR (2006) An integrated home server for communication, broadcast reception, and home automation. *IEEE Trans Consum Electron* 52(1):104–109
37. Kumar S (2014) Ubiquitous smart home system using android application. [arXiv:1402.2114](https://arxiv.org/abs/1402.2114)
38. Gill K, Yang SH, Yao F, Lu X (2009) A zigbee-based home automation system. *IEEE Trans Consum Electron* 55(2)
39. Zhang H, Wang FY, Ai Y (2005) An OSGi and agent based control system architecture for smart home. In: Proceedings. 2005 IEEE networking, sensing and control, 2005, pp 13–18, Mar 2005
40. Baraka K, Ghobril M, Malek S, Kanj R, Kayssi A (2013) Low cost arduino/android-based energy-efficient home automation system with smart task scheduling. In: 2013 fifth international conference on computational intelligence, communication systems and networks (CIC-SyN). IEEE, pp 296–301, June 2013
41. Lee WS, Hong SH (2009) Implementation of a KNX-ZigBee gateway for home automation. In: 2009 IEEE 13th International Symposium on consumer electronics, ISCE'09. IEEE, pp 545–549, May 2009
42. Elkamchouchi H, ElShafee A (2012) Design and prototype implementation of SMS based home automation system. In: 2012 IEEE international conference on electronics design, systems and applications (ICEDSA). IEEE, pp 162–167, Nov 2012
43. Jain S, Vaibhav A, Goyal L (2014) Raspberry Pi based interactive home automation system through E-mail. In: 2014 international conference on optimization, reliability, and information technology (ICROIT). IEEE, pp 277–280, Feb 2014
44. Yuksekkaya B, Kayalar AA, Tosun MB, Ozcan MK, Alkar AZA (2006) GSM, internet and speech controlled wireless interactive home automation system. *IEEE Trans Consum Electron* 52(3):837–843
45. Kumar P, Pati UC (2016) Arduino and Raspberry Pi based smart communication and control of home appliance system. In: 2016 online international conference on green engineering and technologies (IC-GET). IEEE, pp 1–6, Nov 2016
46. Kawakami T, Yoshihisa T, Fujita N, Tsukamoto M (2013) A rule-based home energy management system using the rete algorithm. In: 2013 IEEE 2nd global conference on consumer electronics (GCCE), Tokyo, pp 162–163
47. Yoshihisa T, Fujita N, Tsukamoto M (2012) A rule generation method for electrical appliances management systems with home EoD. In: Proceedings of GCCE, Tokyo, Japan, pp 248–250, Oct 2012
48. Shareef H, Ahmed SH, Mohamed A, Hassan EA (2018) Review on home energy management system considering demand responses, smart technologies, and intelligent controllers. *IEEE Access* 6:24498–24509
49. Dam QB, Mohagheghi S, Stoupis J (2008) Intelligent demand response scheme for customer side load management. *IEEE Energy* 2030:1–7
50. Rahman MM, Hettiwatte S, Gyamfi S (2014) An intelligent approach of achieving demand response by fuzzy logic based domestic load management. In: 2014 Australasian universities power engineering conference (AUPEC), Perth, WA, pp 1–6

51. Bhattacharyya K, Crow ML (1996) A fuzzy logic based approach to direct load control. *IEEE Trans Power Syst* 11(2):708–714
52. Nehrir MH, LaMeres BJ, Gerez V (1999) A customer-interactive electric water heater demand-side management strategy using fuzzy logic. In: *IEEE power engineering society. 1999 Winter Meeting (Cat. No. 99CH36233)*, vol 1, New York, NY, USA, pp 433–436

A Robust Open-Loop Frequency Estimation Method for Single-Phase Systems



Anant Kumar Verma, C. Subramanian and R. K. Jarial

Abstract This article proposes a robust open-loop frequency estimation method for a single-phase system in the presence of grid disturbances. An even harmonic generation scheme is formulated which enables to introduce the benefits of half-cycle delay orthogonal filters. In the proposed work, a digital signal processing approach is employed for fundamental frequency estimation. In order to reject grid disturbances sliding discrete Fourier transform (SDFT) filter (which acts as an orthogonal filter) and moving average filters (MAFs) are employed into the scheme. Finally, rigorous simulation test cases are carried out in MATLAB/Simulink environment in order to prove the robustness of the algorithm.

Keywords Single-phase systems · Even harmonics · Orthogonal filters · Moving average filters · Frequency estimation

1 Introduction

The advent of increased global warming and degradation of natural resources throughout the world has led to increased penetration of distributed generation (DG) systems into grid [1]. In order to control the power flow from DG systems to grid, grid-tied power converters (i.e., inverters) are often utilized. Digital signal processing (DSP) algorithms are adopted for synchronization and protection purposes of these power converters. DSP based algorithms are highly immune and less sensitive to grid disturbances (i.e. dc-offset, harmonics, frequency drifts, voltage sag/swell, phase jumps, notches, and spikes) [2]. In literature, several DSP based techniques are reported for grid frequency estimation [3–11]. One of the most common and simplest techniques among these techniques is zero-crossing detection (ZCD) [4]. However, the presence of noise owing to multiple zero-crossing results in an erroneous estimation [4–6]. A demodulation method based frequency estimation is employed using

A. K. Verma (✉) · C. Subramanian · R. K. Jarial
National Institute of Technology, Hamirpur, Hamirpur 177005, HP, India
e-mail: anant_verma12@ieee.org

© Springer Nature Singapore Pte Ltd. 2020
A. Kalam et al. (eds.), *Intelligent Computing Techniques for Smart Energy Systems*,
Lecture Notes in Electrical Engineering 607,
https://doi.org/10.1007/978-981-15-0214-9_55

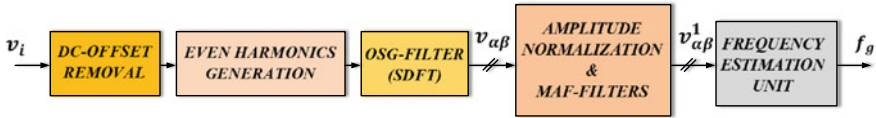


Fig. 1 A general block diagram of the proposed scheme

recursive discrete Fourier transform (RDFT) [7, 8]. Inclusion of higher order FIR differentiation filter can be utilized with demodulation method but at the cost of slower dynamic response [9]. To overcome this issue, a computationally efficient open-loop demodulation approach is developed in [12].

In the proposed work, an open-loop structure of the algorithm is shown in Fig. 1 which is unconditionally stable for single-phase application. The even harmonics are generated by taking square of the grid signal. The fundamental frequency of interest will now become twice the actual grid frequency ($2\omega_g$, where $\omega_g = 2\pi f_g$, and $f_g = 50$ Hz, i.e., nominal frequency). Hence, even harmonic generation helps to introduce half-cycle (i.e., when $T_g = \frac{1}{f_g} = 0.02$ s, then 1 cycle = $\frac{1}{50}$ s) delay filters in order to rapidly extract fundamental grid voltage component. The DC-offset present in the signal is rejected by taking first-order discrete-time derivative of grid signal. A digital half-cycle delay OSG (orthogonal signal generation)- based SDFT [10] filter is chosen and amplitude normalization of fundamental orthogonal components is required, since the proposed algorithm is sensitive to voltage sags. Thereafter, moving average filters (MAFs) [11] are introduced to attenuate the higher order even harmonics. The phase angle information is estimated and a phase unwrapping algorithm is applied. A three-sample based differentiation algorithm is proposed to estimate the grid frequency ($\hat{\omega}_g = 2\omega_g$). Finally, the performance of the proposed scheme is tested in simulation environment based on European standard, i.e., EN 50160 for public distribution systems [13].

This paper is organized as follows. A brief discussion on even harmonics generation is done in Sect. 2, A emphasis on filtering requirement is discussed in Sect. 3, and an approach for frequency estimation followed by simulation results is presented in Sect. 4. Finally, the summary of article is concluded in Sect. 5.

2 Even Harmonics Generation

In order to generate even harmonic components from single-phase grid voltage signal (v_i) consider h as an odd harmonic order (i.e., $h = 1, 3, 5, 7, 9, \dots k$) where k is considered as an odd integer. Herein, grid voltage signal is written as follows:

$$v_i = \sum_{h=1}^k A_h \sin(h\omega_g t + \delta_h) \quad (1)$$

where A_h stands for amplitude of respective harmonics, ω_g is the fundamental frequency, and δ_h is the phase angle. Note that in presence of grid disturbances all the above aforementioned parameters will be different. Hereon, a new voltage parameter can be considered as $v_s = v_t^2$ and which is expanded below subsequently to Eq. 2.

$$v_s = \left[\sum_{h=1}^k A_h \sin(h\omega_g t + \delta_h) \right]^2 \quad (2)$$

expansion of the Eq. 2 can be done as follows [3]:

$$\begin{aligned} v_s = & \sum_{h=1}^k \frac{A_h^2}{2} - \sum_{h=1}^k \frac{A_h^2}{2} \cos(2(h\omega_g t + \delta_h)) \\ & + A_1 \sum_{h=3}^k A_h \cos((1-h)\omega_g t + (\delta_1 - \delta_h)) \\ & - A_1 \sum_{h=3}^k A_h \cos((1+h)\omega_g t + (\delta_1 + \delta_h)) + \dots \\ & + A_{k-2} A_k \cos(-2\omega_g t + (\delta_{k-2} - \delta_k)) \\ & - A_{k-2} A_k \cos((2k-2)\omega_g t + (\delta_{k-2} + \delta_k)) \end{aligned}$$

Conclusion: Expansion of Eq. 2 contains even harmonics components and the lowest harmonic component is twice the fundamental frequency ($2\omega_g$). Even harmonics will be multiple of $\hat{\omega}_g$ (i.e., 200 Hz, 300 Hz, 400 Hz, 500 Hz, 600 Hz, ..., and so on). Therefore, a good filtering approach is required for rejecting higher order even harmonics present in the fundamental grid voltage signal.

3 Filtering Requirements

In the proposed work, filtering requirements are based upon three criteria, i.e., DC-offset rejection, extraction of twice the fundamental grid voltage component, and finally the rejection of higher order harmonics.

3.1 DC-Offset Rejection

A major concern arises when grid voltage signal itself contains DC-offset component (V_o) as given below:

$$v_i = \sum_{h=1}^k A_h \sin(h\omega_g t + \delta_h) + V_o \tag{3}$$

Hence, it can be concluded that if square of Eq. 3 is taken into consideration with regards to generation of even harmonics then DC-offset will become V_o^2 . In order to overcome this issue, initially a first-order derivative of the grid voltage signal is taken into consideration whose transfer function is given below:

$$H_{DERI}(s) = \frac{\hat{v}_i(s)}{v_i(s)} = 1 - e^{-sT_s} \tag{4}$$

From Eq. 4, it can be understood that derivative of grid voltage signal will reach to steady state in a time period of one sample (i.e., $T_s = \frac{1}{f_s}$ where, $f_s = \frac{1}{T_s} = 12$ kHz). Hence, $H_{DERI}(s)$ will provide a zero gain at zero frequency and it will completely block the DC component. In addition to it, discrete realization of $H_{DERI}(j\omega)$ can be obtained as follows:

$$H_{DERI}(z) = 1 - z^{-1} \tag{5}$$

3.2 Extraction of Fundamental Orthogonal Components

Generation of orthogonal signals using SDFT filter is implemented in Fig. 2. The structure includes a complex pole at the nominal grid frequency which cancels out a zero at this frequency. The decomposition of single-phase grid voltage signal into its orthogonal components can be achieved with the help of the transfer function, i.e., $G_{SDFT}(z)$ which is described below [10]:

$$G_{SDFT}(z) = \frac{(1 - z^{-N})e^{j\frac{2\pi k}{N}}}{1 - e^{j\frac{2\pi k}{N}}z^{-1}} \tag{6}$$

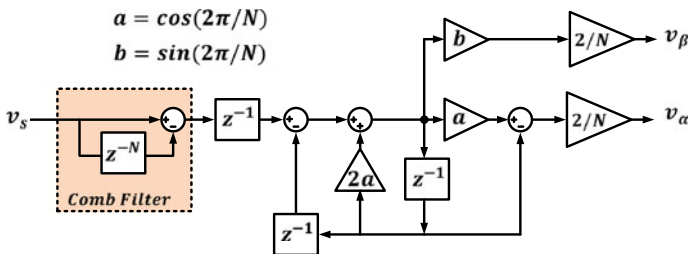


Fig. 2 OSG based on SDFT filter

$$\Re(G_{SDFT}(z)) = \frac{2}{N} \frac{(1-z^{-N})(\cos \frac{2\pi k}{N} - z^{-1})}{1-2\cos \frac{2\pi k}{N} z^{-1} + z^{-2}} \tag{7}$$

$$\Im(G_{SDFT}(z)) = \frac{2}{N} \frac{(1-z^{-N})(\sin \frac{2\pi k}{N})}{1-2\cos \frac{2\pi k}{N} z^{-1} + z^{-2}} \tag{8}$$

where k is the frequency bin index and $N = 120$ samples is chosen to make to a half-cycle delay ($T_{SDFT} = \frac{T_g}{2}$) orthogonal filter structure.

3.3 Elimination of Higher Order Harmonics

The higher order even harmonics (i.e., 200, 300, 400, 500, 600 Hz, ..., and so on) are attenuated by nonadaptive MAFs. Two MAFs are cascaded which are tuned at 300 and 500 Hz and a sufficient amount of attenuation is offered. A discrete realization of MAF is provided in [11] as expressed by

$$G_{MAF}(z) = \frac{1}{N} \frac{(1 - z^{-N})}{1 - z^{-1}} \tag{9}$$

In this work, moving widow length $T_w = \frac{T_g}{6}$ s is chosen where $T_g = 1/50$ s and N can be computed as follows $N = \frac{T_w}{T_s}$. For a $f_s = 12$ kHz, the rejection of 300 Hz and its multiple can be done by choosing $N = 40$. Similarly, for rejection of 500 Hz harmonic and its multiple a window length of $T_w = \frac{T_g}{10}$ can be chosen by selecting $N = 24$. Henceforth, overall block diagram representation of the scheme is depicted in Fig. 3.

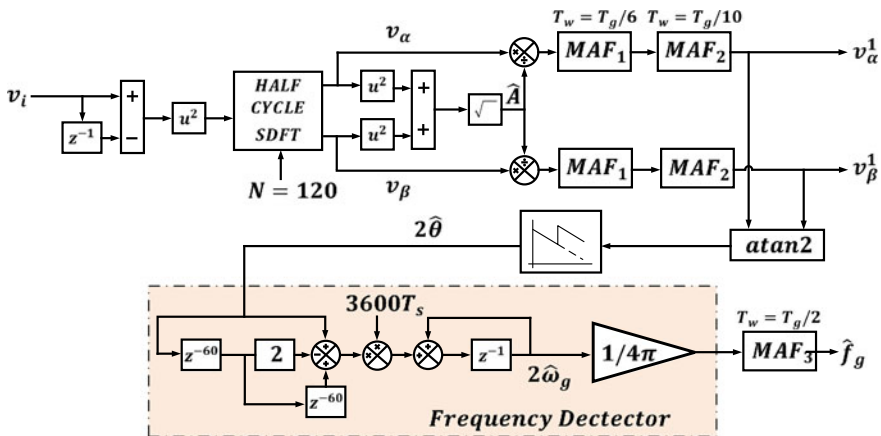


Fig. 3 Overall block diagram of the proposed scheme

4 Frequency Estimation

The fundamental orthogonal grid voltage components v_α and v_β are normalized to unit amplitude, respectively. Thereafter, cascaded MAF_1 and MAF_2 are employed to attenuate higher order harmonics. To proceed with frequency estimation process phase angle information is determined by utilizing orthogonal components and an arctangent function which is described below:

$$v_\alpha^1 = \frac{A_1}{\sqrt{v_\alpha^2 + v_\beta^2}} \sin(\theta) \quad (10)$$

$$v_\beta^1 = \frac{A_2}{\sqrt{v_\alpha^2 + v_\beta^2}} \cos(\theta) \quad (11)$$

Where A_1 and A_2 are the respective amplitudes of the orthogonal components. At nominal frequency condition $A_1 = A_2$. However, under off-nominal frequency excursions $A_1 \neq A_2$. v_α^1 and v_β^1 are the normalized orthogonal fundamental grid voltage components. Now, by applying “*arctan2*” function on these components phase angle information can be obtained as follows:

$$\left[\theta = \arctan\left(-\frac{v_\beta^1}{v_\alpha^1}\right) \right]_{unwrapping} \quad (12)$$

A phase unwrapping function is employed and a three-sample based differentiation operation is applied on “ θ ” information. Therefore, $\hat{\omega}_g$ can be estimated as follows:

$$\hat{\omega}_g(n) = \frac{1}{N^2 T_s} \theta(n) - 2\theta(n - N) + \theta(n - 2N) + \hat{\omega}_g(n - 1) \quad (13)$$

Hence, actual grid frequency can be obtained as $\omega_g(n) = \frac{\hat{\omega}_g(n)}{2}$. The selection of $N = 60$ for the algorithm is an optimum choice as it will provide a response time equivalent to a half-cycle delay. The effect of second harmonic oscillations in estimated frequency is attenuated by another half-cycle delay MAF_3 whose window length is $T_w = T_g/2$ with $N = 120$ is included.

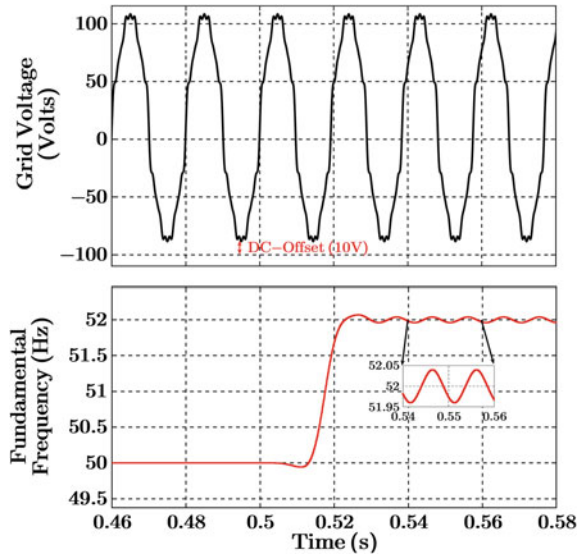
4.1 Simulation Setup and Results

The frequency information is accurately estimated as per the grid standard, i.e., EN 50160, which states that the grid frequency of a public distribution systems should not go beyond the frequency range of 47–52 Hz during 100% of the operating time [13]. From Table 1, a single-phase grid voltage signal is developed with a $100 V_{peak}$

Table 1 Harmonics present in fundamental component as per EN-50160

Harmonics								THD
3rd	5th	7th	9th	11th	13th	15th	17th	
5.0%	6.0%	5.0%	1.5%	3.5%	3.0%	0.5%	2.0%	10.67%

Fig. 4 Frequency jump from 50 to 52 Hz with harmonics



amplitude containing a DC-offset of 10 V in the simulation environment where disturbance injection takes place at the simulation time instant of $t = 0.5$ s. Four test cases were taken into consideration which will be consisting of all possible frequency conditions in the form of frequency step. In test case 1 (Fig. 4), grid voltage contains fundamental component, harmonics, and DC-offset alone. Test case 2 (Fig. 5) is developed by adding 30° phase jump and 50% voltage sag to test case 1 and retaining the previous test conditions. In test case 3 (Fig. 6), effect of notches, DC-offset, and harmonics present in the supply voltage at nominal frequency (50 Hz) is considered. In test case 4 (Fig. 7), a large frequency variation of +5 Hz from 47 Hz is considered, with all odd harmonics, DC-offset, and a phase angle jump of 30° combined with an amplitude sag of 100–50 V in fundamental component is considered. Under steady-state conditions, for frequency deviations of +2 Hz, an error of 0.004 Hz is observed and under negative frequency deviation of -3 Hz, an error of 0.1 Hz is observed. In Fig. 6, notches in supply voltage has no effect on the frequency estimation process and under large frequency deviations lesser overshoots are observed.

Fig. 5 Frequency jump in presence of voltage sag and phase jump

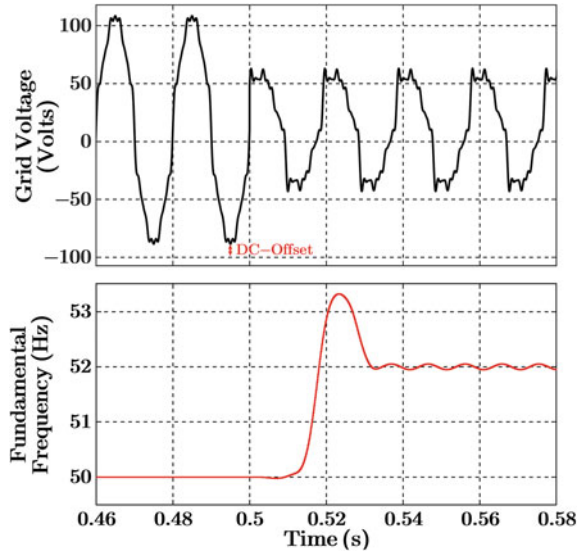


Fig. 6 Effect of notches in grid voltage

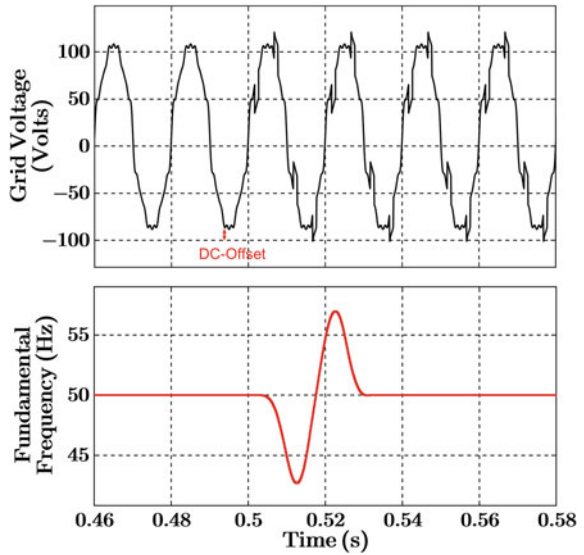
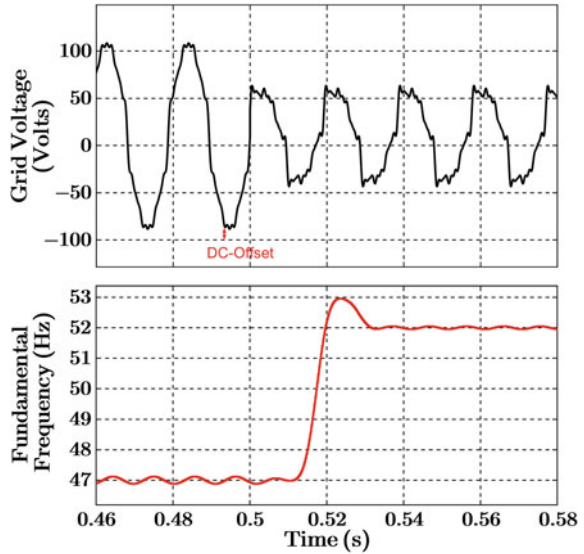


Fig. 7 Frequency jump from 47 to 52 Hz



5 Conclusion

The main objective of this paper was to introduce an open-loop robust frequency estimation approach which is based on even harmonics generation scheme and differentiation algorithm. In effect, half-cycle delay OSG-based filters can be employed for improving the dynamic performance of the algorithm. Under adverse grid conditions, the frequency estimation process takes ≈ 1.6 cycles, i.e., ≈ 32 ms to estimate the grid frequency. The proposed method has a high immunity toward notches present in supply voltage. Nonetheless, proposed scheme is stable enough under large frequency deviations and has good harmonic rejection capability under off-nominal frequency excursions.

References

1. Blaabjerg F, Teodorescu R, Liserre M, Timbus AV (2006) Overview of control and grid synchronization for distributed power generation systems. *IEEE Trans Ind Electron* 53(5):1398–1409. <https://doi.org/10.1109/TIE.2006.881997>
2. Karimi-Ghartemani M, Khajehoddin SA, Jain PK, Bakhshai A, Mojiri M (2012) Addressing DC-component in PLL and notch filter algorithms. *IEEE Trans Power Electron* 27(1):78–86. <https://doi.org/10.1109/TPEL.2011.2158238>
3. Sanchez PR, Garcia XDT, Torres AP, Feliu V (2011) Robust frequency-estimation method for distorted and imbalanced three-phase systems using discrete filters. *IEEE Trans Power Electron* 26(4):1089–1101. <https://doi.org/10.1109/TPEL.2011.2107580>
4. Friedman V (1994) A zero crossing algorithm for the estimation of the frequency of a single sinusoid in white noise. *IEEE Trans Signal Process* 42(6):1565–1569. <https://doi.org/10.1109/78.286978>

5. Vainio O, Ovaska SJ, Polla M (2003) Adaptive filtering using multiplicative general parameters for zero-crossing detection. *IEEE Trans Ind Electron* 50(6):1340–1342. <https://doi.org/10.1109/TIE.2003.819565>
6. Begovic MM, Djuric PM, Dunlap S, Phadke AG (1993) Frequency tracking in power networks in the presence of harmonics. *IEEE Trans Power Deliv* 8(2):480–486. <https://doi.org/10.1109/61.216849>
7. Kamwa I, Leclerc M, McNabb D (2004) Performance of demodulation based frequency measurement algorithms used in typical PMUs. *IEEE Trans Power Deliv* 19(2):505–514. <https://doi.org/10.1109/TPWRD.2004.823185>
8. Darwish HA, Fikri M (2007) Practical considerations for recursive DFT implementation in numerical relays. *IEEE Trans Power Deliv* 22(1):42–49. <https://doi.org/10.1109/TPWRD.2006.874642>
9. Reza MS, Ciobotaru M, Agelidis VG (2013) Robust estimation of real-time single-phase grid voltage frequency under distorted conditions. In: *Proceedings of IEEE ECCE Asia*, pp 948–954. <https://doi.org/10.1109/ECCE-Asia.2013.6579220>
10. Subramanian C, Kanagaraj R (2014) Single-phase grid voltage attributes tracking for the control of grid power converters. *IEEE J Emerg Sel Top Power Electron* 2(4):1041–1048. <https://doi.org/10.1109/JESTPE.2014.2341045>
11. Golestan S, Ramezani M, Guerrero JM, Monfared Md (2014) Moving average filter based phase-locked loops: performance analysis and design guidelines. *IEEE Trans Power Electron* 29(6):2750–2763. <https://doi.org/10.1109/TPEL.2013.2273461>
12. Reza MS, Agelidis VG (2017) A demodulation based technique for robust estimation of single-phase grid voltage fundamental parameters. *IEEE Trans Ind Inform* 13(1):166–175. <https://doi.org/10.1109/TII.2015.2443718>
13. European Standard EN-50160 (1999) Voltage characteristics of electricity supplied by public distribution systems: 1999

Demand-Side Load Management for Peak Shaving



Shailendra Baraniya and Manoj Sankhe

Abstract Differential tariff regime in electrical energy markets has opened up new opportunities of consumer participation for improving economics of operation. This paper studies a demand-side load management system, which works in a noninterference, advisory mode. It advises the consumer through flags thereby strictly does not interfere with operation of the appliances, thereby keeps consumer comfort intact. The scheme has been evaluated through modeling and simulation. The scheme promises substantial drop in mean active power drawn by the consumer during grid peak hours, affecting the consumer experience the least.

Keywords Load profile management · Peak shaving · Bootstrap resampling · Shifting time of use

1 Introduction

Real-time differential tariff regime has emerged as an effective mechanism to regulate peak loads of grid. Application of peak hour penal tariffs deters consumption during peak hours and motivate consumer to shift consumption to non-peak hour, effecting a peak shaving. This shifting of loads to non-peak hours lead to savings on cost of energy for utility and consumer. It helps the utility to bring peak to average ratio (PAR) at grid under control. An overenthusiastic cooperation of consumers in shifting consumption to non-peak hour may drift the peak hour for grid, instead of peak shaving. This brings to the fore requirement of a framework, enabling real-time communication between consumer and utility, for a calibrated action on consumer's part rendering demand-side load management (DSLMM) effective. Consumers can avoid penal tariffs during peak hours by knowing start and end of peak hour of the grid, well in advance, by an appropriate rescheduling of loads can be done reduc-

S. Baraniya (✉) · M. Sankhe
SVKM's NMIMS, Mumbai 400 056, India
e-mail: b.shailendr@gmail.com
URL: <http://engineering.nmims.edu/>

© Springer Nature Singapore Pte Ltd. 2020
A. Kalam et al. (eds.), *Intelligent Computing Techniques for Smart Energy Systems*,
Lecture Notes in Electrical Engineering 607,
https://doi.org/10.1007/978-981-15-0214-9_56

ing mean active power drawn from the grid. This rescheduling cannot be done by brute force, as consumption of energy has motives, productive, and otherwise. The time of consumption is an important determinant of consumer comfort. The DSLM presented here is an indirect intervention in operations of equipment inside the consumer premises. This work is a heuristics-based system, helping the consumer, to reschedule utilization, aimed at bringing down mean active power drawn by him during peak hour. The consumer needs to know whether plug-in is advanced or delayed, for an appliance, so as to achieve a drop in his mean load during grid peak hour. This DSLM is designed to work in an advisory mode; let's the consumer define plug-in and plug-out of appliances in his premises, and hence keeps consumer experience unaffected. There are many relevant contributions available in the domain like [1–3], a few to cite. Most of them have proposed a direct control of appliances in consumer premises.

2 Demand-Side Load Management

This DSLM comprises of two components, namely, ICT (Information communication Technology) framework and Algorithm. The **ICT framework** in the consumer premises, shown in Fig. 1, act as the vehicle for DSLM execution [4, 5]. The DSLM is aimed at bringing down the mean active power drawn from the grid during grid peak hours. The day's forecast for start and end of grid peak hour 'S' and 'E', is part of demand response signals available at smart meter, which shares the same with 'power hub' of DSLM ICT framework. The power hub which is in communication with appliances, through their respective leafs, continuously collect current, voltage, and p.f. at these nodes. The leafs contain transducers, for sensing current and voltage at the node, transmitting the same to power hub continuously. The data received from respective leaf are analyzed to extract 'node vector' of the appliance, which includes its earliest plug-in time 'EST', latest plug-in time 'LST', mean operation time 'OT',

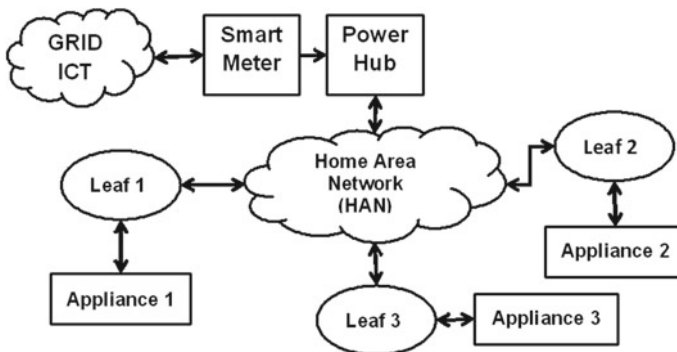


Fig. 1 DSLM conceptual framework

Table 1 Classification of nodes

S. No.	Node type	Plug-in time (ST)	Plug-out time (ET)	Loading grid during PS?	Flag
1.	I	$ST < S$	$S < ET < E$	Y	G
2.	II	$S < ST < E$	$ET > E$	Y	R
3.	III	$ST < S$	$ET > E$	Y	-
4.	IV	$S < ST < (E + S)/2$	$S < ET < (E + S)/2$	Y	G
5.	V	$(E + S)/2 < ST < E$	$(E + S)/2 < ET < E$	Y	R
6.	VI	$ST < S$	$ET < S$	N	-
7.	VII	$ST > E$	$ET > E$	N	-

($PS = E - S$; $ET = ST + OT$; Flags: G- Green, R-Red)

and mean active power drawn 'LD'. The power hub maintains database for node vectors for all the nodes. The power hub processes node vectors, for a given set of 'S' and 'E', and releases flags, to the respective leaves, to glow either red or green LEDs, to advise the user to delay or advance the plug-in of concerned appliance, respectively, so as to effect a drop in active power drawn from the grid for the consumer. These entities communicate with each other, through appropriate transceiver modules.

The DSLM **Algorithm** has two modes; training mode and functional mode. The DSLM system is allowed to operate in **training mode** for a significant number of days, to enable it to establish communication links and create starter database for nodes. During training different leaves pick current, voltage, and p.f. at respective nodes, and transmit them to power hub. The power hub extracts node vectors out of leaf data, and create database of node vectors for all nodes. It doesn't release any instructions to any of the nodes during this mode.

During **functional mode**, power hub gathers start 'S' and end time 'E' of grid peak hour from AMI (advanced metering infrastructure or smart meters). The DSLM sorts node vector database for typical plug-in time ST of different nodes. Peak span of grid peak 'PS' is defined as $(E - S)$. The DSLM classifies various nodes as per their anticipated operation overlap into PS. This is described in Table 1. The column named 'flag' suggests type of flag to be raised at concerned leaf. A green flag 'G' when raised, means that a green LED will light up at the concerned leaf, and conveys to user, that plug-in of appliance concerned is advised, at the earliest. If user complies to the flag, mean active load of the consumer drops. The user is free, not to comply to a flag. On the other hand, a red flag 'R' indicates that the user is advised not to plug-in the appliance till red flag is on. The consumer again is free to comply with a flag. Green flag 'G' is issued at 'EST' of the appliance, and withdrawn as consumer opt to plug-in the appliance or at typical plug-in time of the appliance, whichever happens earlier. On the other hand, the red flag 'R' is issued at 'EST' of the appliance, and withdrawn at consumer opting to plug-in the appliance or at 'LST' of the appliance, whichever happens earlier. Span of advise for any node is kept from 'EST' to 'LST', and it is assumed that if a consumer complies to the DSLM request

rescheduling plug-in of an appliance between ‘EST’ and ‘LST’, his comfort remains unaffected. Also, the DSLM requests rescheduling of plug-in and not the plug-out, hence, once operation of an appliance has begun it is not disrupted. The measure of DSLM performance is defined as “drop in mean active power drawn by the consumer during grid peak hour for adaptation of DSLM per unit mean active power drawn by the consumer during grid peak hour without adaptation of DSLM” [6].

3 Modeling and Simulation

Modeling and simulation are deployed as a tool for verification of efficacy of the scheme. The exercise requires modeling of energy transaction system’s routine operation (RO), prior to invoking DSLM, and that after DSLM intervention (DO), and that of the consumer.

3.1 Modeling

The consumer is modeled as a time series of electrical loads, with their plug-in time and respective operation time. Here we apply a simplifying assumption that the operation time remains constant for an appliance, for a consumer. The model of RO/DO is evolved by pondering upon the working of DSLM described by the flowchart in Fig. 2. Transactions in the system happen at discrete events (plug-in or plug-out), changing state of the system. The consumer installation remains in a state (indicated by power injected by the consumer into grid), till an event happens in the consumer installation, which moves it to next state. Number of distinct states,

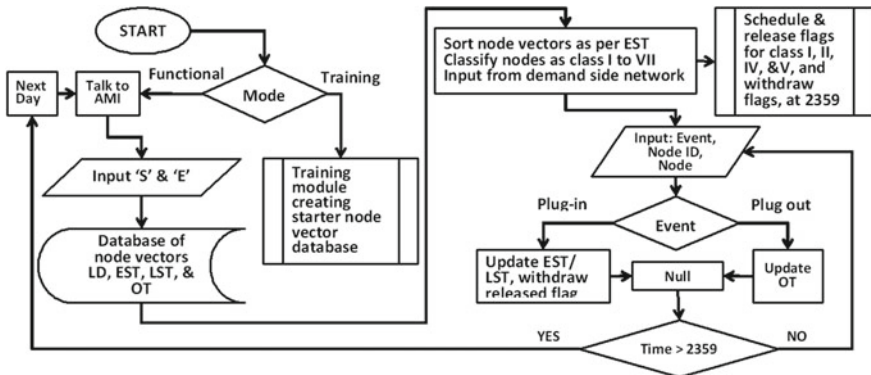


Fig. 2 Algorithm for DSLM

the system can assume, are finite (depending on consumer installation). Thus, it is a good case for being modeled as a discrete event system.

The DSLM System: Model of DSLM, is evolved out of a detailed analysis of the process of generation of flags at different nodes, as explained in Table 1. Inputs to the algorithm for DSLM for relaxed seasons, are start time ‘S’ and end time ‘E’ of grid peak hour, in addition to database of node vectors, representing the consumer. The DSLM is described as sequence of steps as follows:

- 1 Read start and end time of grid peak hour ‘S’, and ‘E’, set node number $n = 1$
- 2 Load node vector for the n th node, Read ST, EST, LST, and OT
- 3 Test if $(ST + OT) < S$, if true $n = n + 1$, if $n < N$ then go to step 2, else go to step 8
- 4 Test if $(ST < S)$, AND $((ST + OT) > S$ AND $(ST + OT) < E)$ if true then release flag ‘G’ at EST of the node, else $n = n + 1$, if $n < N$ then go to step 2, else go to step 8
- 5 Test if $ST > S$ AND $(ST + OT) > S$ AND $(ST + OT) < \frac{S+E}{2}$ is true then release flag ‘G’ at EST of the node, else $n = n + 1$, if $n < N$ then go to step 2, else go to step 8
- 6 Test if $[(ST > S)$, AND $((ST + OT) > E)]$ is true then release flag ‘R’ at EST of the node, else $n = n + 1$, if $n < N$ then go to step 2, else go to step 8
- 7 Test if $[ST > \frac{S+E}{2})$, AND $((ST + OT) < E)]$ is true then release flag ‘R’ at EST of the node, else $n = n + 1$, if $n < N$ then go to step 2, else go to step 8
- 8 End, release modified time series, with aggregate load defined for all node vectors.

This DSLM inputs stimuli, a time series of node vectors, represents a typical consumer. The model generates flags for respective nodes. These flags are communication to the consumer and his response to these, define how successful the scheme would be?

Another entity is the consumer. Standard consumer database [7] is referred for this modeling. Consumer premises has numerous appliances with different power ratings, with different plug-in times, and operation times. The observation of plug-in time of an appliance over a large number of days, show its variation between EST and LST.

3.2 Simulation Process

The simulation involves inputting time series of node vectors representing a consumer, to the RO/DO model. The time series is appended by including additional plug-in events, where plug-in computed as sum of ST and OT of respective appliance, with negative power rating (plug-out is a plug-in with negative power drawn from grid). This revised time series representing the consumer installation is sorted as per plug-in time for different appliances.

Simulation for RO: The first element in this series is fired to make aggregate active power injected by the consumer as its active power rating. The simulation time is advanced to next plug-in aggregate load is computed as algebraically summation of earlier load and the new load. This process is continued till all the events are exhausted. This process adds one new variable to the time series, ‘aggregate load’; load profile for the consumer, without DSLM.

Simulation for DO: Time series representing the consumer, above, is sorted for plug-in time. This sorted database is sifted through, to identify appliances whose operation creep into grid peak span, as per criteria defined in Table 1. The plug-in time for nodes type I and IV are delayed and those type II and V are advanced, from their typical plug-in time ‘ST’, to effect a drop in mean active load drawn by the consumer. Simulation of this act is done by appropriately redefining plug-in time for concerned nodes. The quantum of delay or advance of plug-in time is a measure of consumer’s compliance to DSLM requests. This DSLM scheme assumes that plug-in time, when altered from the typical one, to a moment between EST and LST, causes the least discomfort to consumer. The maximum shift, while advancing, can move the plug-in time to EST and that while delaying, can move it to LST of the node. Simulation of consumer compliance effecting revision in plug-in time is done using a random number generator for beta distribution, between EST and ST for advancing, and between ST and LST for delaying. Degree of consumer cooperation or compliance to flags is defined by appropriately selecting shaping parameters α and β of beta distribution.

Load profile of a consumer has three parameters, appliances represented by their power rating, plug-in time of these appliances, and their respective operation time. The plug-in time of appliances is spread from 0000 to 2359 h. The plug-in time of appliances, and statistical distribution of LD and OT classify the consumer. The load profile of a typical consumer (Fig. 3) can be seen as comprising of three peculiar segments:

Uphill shoulder segment (1000–2000 h.): Load profile has a positive slope. This segment sees more appliance plug-ins than plug-outs.

Downhill shoulder segment (0200–0600 h.): Load profile has a negative slope. This segment sees more appliance plug-outs than plug-ins.

Peak/Trough segment (2100–2300 h. and 0700–0900 h.): Load profile is flat. This region sees no change in load, with time.

During grid peak hours, a consumer might traverse through any of these three segments of his own load profile. In order to assess performance of DSLM, we evaluate the mean of drop in power drawn by the consumer during grid peak hour, for 100 iterations over all three segments of his own load profile. 10000 such samples are created using bootstrap sampling technique [8], applied on 100 base members. The performance is shown as a 90% confidence interval, from 95 percentile to 5 percentile values. The grid peak hour is made to sift through consumer load profile at hops of 1 h, from 0100 to 2300 h, and performance of DSLM is evaluated at each hop. The span of grid peak hour is taken as 90 min.

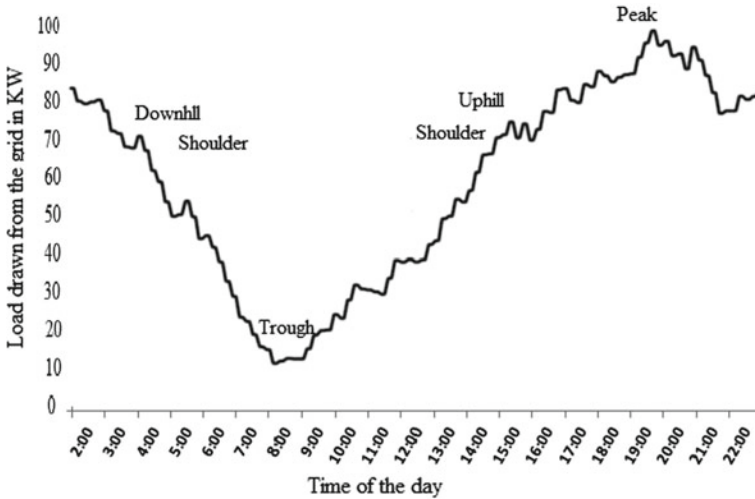


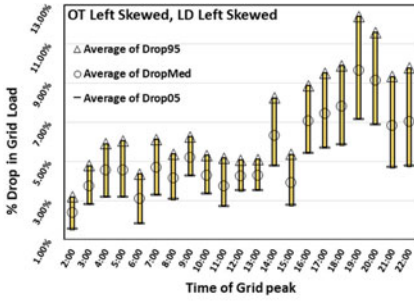
Fig. 3 Load profile of a consumer

4 Simulation Results

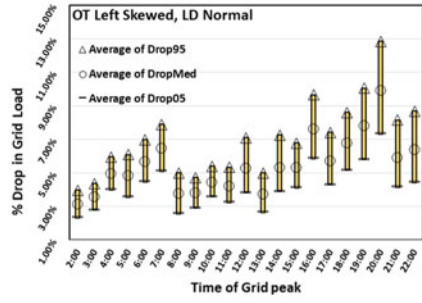
First set of simulations is designed to identify the dominant parameter the two LD and OT, defining performance of DSLM. Parameters LD and OT are statistically distributed typically left skewed (LS), uniform (UN), normal (NR) and right skewed (RS). The DSLM advises consumer to reschedule plug-in of the appliance between EST and LST. The consumer cooperation is simulated by generating a revised plug-in time of the appliance by random number generator BETA.INV function in MS EXCEL, with appropriate shaping parameters α and β [9].

We chose consumer compliance varying uniformly from 5 to 25% for this exercise. The distributions for LD and OT are assigned all possible 16 combinations and simulations performed. Four such sets of simulation for distribution of OT, as LS are shown here, in Fig. 4a, d. These plots exhibit similar profiles and distribution of LD has no significant influence on DSLM performance. Other three sets, i.e., for distribution of LD taken as UN, NR, and RS have similar observations. This exercise established OT as dominant variate for assessment of DSLM performance.

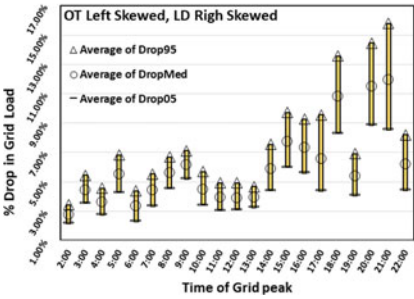
We selected LS as distribution for LD for next set of simulations, to evaluate 90% CI for mean drop in grid loading of consumer, for adaptation of DSLM in different segments of consumer load profile. The performances are shown in Fig. 5, drop in consumer's grid loading (mean over segments) for 95 percentile, 50 percentile, and 5 percentile mark, for consumer compliance from 5 to 25% in steps of 5%. These plots are grouped by different distributions of OT.



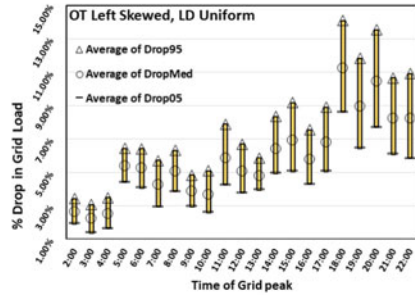
(a) LD Left Skewed



(b) LD Normal



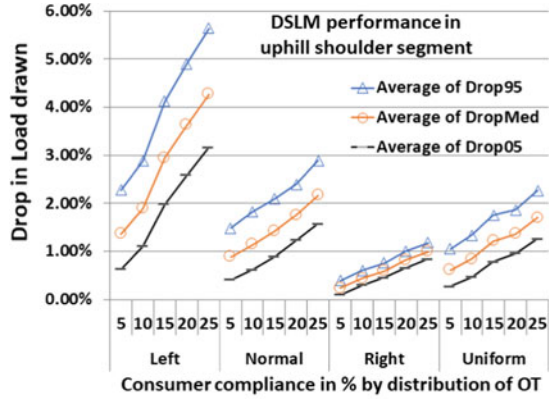
(c) LD Right Skewed



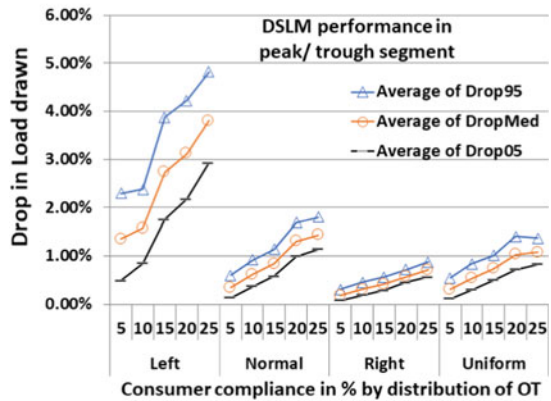
(d) LD Uniform

Fig. 4 Drop in load versus grid peak time

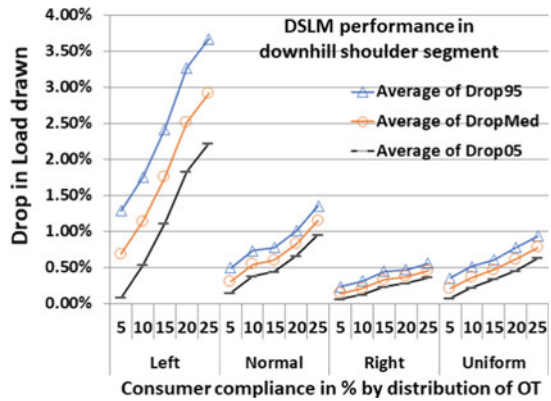
Fig. 5 % Mean drop in load drawn, versus consumer compliance grouped by OT distribution



(a) Mean over UpHill segment



(b) Mean over peak/ trough segment



(c) Mean over DownHill segment

5 Conclusions

The scheme described here promises to invoke consumer cooperation in reducing the mean active power drawn by the consumer from grid, during grid peak hour and hence bring down cost of energy for the consumer. Key takeaways from the simulation results are as follows:

- The DSLM performance shows a positive correlation with consumer cooperation.
- The performance seen in the study is indicative, and dependant on distribution of LD, OT, and ST.
- The scheme exhibits a drop in load drawn from the grid, in a range of 3.5–6 % for a modest consumer cooperation of 25%, for LS distribution of OT.
- There is a significant reduction in mean power drawn from grid during two segments of consumer load profile, uphill shoulder and peak/trough.
- The DSLM performance is significant for left skewed (LS) distribution for OT; LS distribution has members of OT with small values, and even small shift in plug-in time contributes to drop in power drawn from the grid.
- The least DSLM performance is seen in case of right skewed (RS) distribution for OT; RS distribution has members of OT with large values, and shift in plug-in time contributes negligibly to drop in power drawn from the grid.

References

1. Alizadeh M, Scaglione A, Thomas RJ (2012) From packet to power switching: digital direct load scheduling. *IEEE J Sel Areas Commun* 30(6):1027–1036
2. Wang S, Wu J, Zhang Y (2018) Consumer preference enabled intelligent energy management for smart cities using game theoretic social tie. *Int J Distrib Sens Netw* 14(4):1550147718773235. <https://doi.org/10.1177/1550147718773235>
3. Mohsenian-Rad AH, Wong VWS, Jatskevich J, Schober R, Leon-Garcia A (2010) Autonomous demand-side management based on game-theoretic energy consumption scheduling for the future smart grid. *IEEE Trans. Smart Grid* 1(3):320–331
4. Shailendra B, Singh S, Karande O, Chaturvedi S, Dhariwal S, Mohan V (2011) Architecture for smart grid based consumer end solution. In: 13th international conference on advanced communication technology (ICACT2011), pp 88–92
5. Costanzo GT, Zhu G, Anjos MF, Savard G (2012) A system architecture for autonomous demand side load management in smart buildings. *IEEE Trans. Smart Grid* 3(4):2157–2165
6. Dharme A, Ghatol A (2006) Demand side management quality index for assessment of DSM programs. In: 2006 IEEE PES Power systems conference and exposition, PSCE'06. IEEE vol 2006, pp 1718–1721
7. Dheeru D, Taniskidou EK (2017) UCI machine learning repository. <http://archive.ics.uci.edu/ml>
8. Efron B, Tibshirani RJ (1994) An introduction to the bootstrap. CRC Press
9. Kuhl ME, Lada EK, Steiger NM, Wagner MA, Wilson JR (2006) Introduction to modeling and generating probabilistic input processes for simulation. In: Proceedings of the 38th conference on winter simulation, ser. WSC '06. Winter simulation conference, pp. 19–35. <http://dl.acm.org/citation.cfm?id=1218112.1218120>

A New Line Voltage Stability Index (NLVSI) For Voltage Stability Assessment



Trinadha Burle, V. V. S. Bhaskara Reddy Chintapalli and Phanindra Thota

Abstract Power system is probably one of the most complex dynamical systems. In these systems, active and reactive power demand is increasing day by day, other way it can be said that the stress on these systems is increasing. Under these stressed conditions, they are operating at the stability limits to meet their load demand. Due to the above scenario, voltage stability problem became a major issue. For stable operation of power systems, continuous monitoring of proximity of the voltage instability is necessary. This paper presents a New Line Voltage Stability Index (NLVSI) for detecting the proximity of voltage instability of the system. In this work, constant PQ and ZIP load models are considered to study the effectiveness of the proposed index. Experimentally determined ZIP coefficients are used for ZIP load models. The proposed work is demonstrated on standard IEEE 14 bus test system. The results are compared with some existing indices to validate its feasibility. All the simulations in this work are carried out through MATLAB.

Keywords NLVSI · PMUs · SLPF · Voltage collapse · Voltage stability analysis · ZIP load model

1 Introduction

During the past two decades, the power demand has been increasing and to meet that power demand modern power systems are forced to operate at its stability limit [1, 2]. Continuous operation of power systems under such conditions leads to voltage

T. Burle (✉) · V. V. S. B. R. Chintapalli · P. Thota
Andhra University College of Engg. (A), Andhra University,
Visakhapatnam 530003, India
e-mail: trinadha.burle@gmail.com

V. V. S. B. R. Chintapalli
e-mail: chbr.elec@gmail.com

P. Thota
e-mail: phanindras.thota@gmail.com

© Springer Nature Singapore Pte Ltd. 2020
A. Kalam et al. (eds.), *Intelligent Computing Techniques for Smart Energy Systems*,
Lecture Notes in Electrical Engineering 607,
https://doi.org/10.1007/978-981-15-0214-9_57

instability or collapse. Voltage stability means to maintain the voltages at all buses within the specified limits in a power system even if it is disturbed from a given initial operating condition [3]. The major reason for voltage instability is due to non-linear loads, continuously increasing of these loads may lead to voltage fall. The power systems with load burden are associated with lack of reactive power support, low voltage profiles and heavy reactive power flows tend to blackouts. Therefore, the study of voltage collapse and voltage instability is still a major concern in power system operation and planning.

Several articles have been published in the literature in the area of voltage stability using Single Line Power Flow (SLPF) concept. Moghavvemi et al. derived a line stability index (L_{mn}) [4], Musirin et al. proposed a Fast Voltage Stability Index (FVSI) [5], using the same concept as L_{mn} . Mohamed et al. developed the line stability factor (L_{QP}) [6]. Based on the maximum power and power loss in a line, Moghavvemi et al. derived four Voltage Collapse Proximity Indicators [7]. Line Voltage reactive power index (VQI_{line}) [8] was developed by Althowibi et al. and Kanimozhi et al. derived an index NVSI for line voltage stability estimation [9]. In some of the above indices, the effect of active power change, angle difference between two buses and shunt components of the lines are neglected but not all these effects in a single through in single index. Moreover, constant PQ loads are used in the NR load flow method for calculating these indices in the analysis of voltage stability. But in any practical power system, any bus/substation may have constant impedance type loads, constant current type loads and constant power type loads or combination of any loads mentioned above. Constant impedance and constant current type loads are voltage dependent but constant power type loads are independent of voltage and hence if voltage changes at any bus the voltage dependent loads will change at that particular bus. So if only constant power type loads are used in NR load flow method will give inaccurate results.

In general, the stability studies of power systems depends on how the real load models are represented. Each real load has its own load characteristics and hence in simulation studies it is very difficult to incorporate each real load type individually. Therefore, generalized load models are required for getting the optimistic results when compared to constant power type loads. ZIP load models are one of them [10], where Z represents constant impedance type load, I represents constant current type load and P represents constant power type load. Constant impedance (Z) type load is proportional to the square of the ratio between operating voltage to the nominal voltage, constant current type load (I) varies linearly according to the ratio, constant power type loads (P) are independent of voltage.

In this paper, a New Line Voltage Stability Index (NLVSI) is derived based on the concept of SLPF. For the ease of mathematical calculations, shunts in a line are neglected. In this index, the effect of active power flow, reactive power flow and phase angle at the buses common to a line are also incorporated. For the analysis of voltage stability, ZIP load models are used instead of constant power loads. The results obtained with ZIP load model are compared with constant power load model. The proposed index has been exhibited on standard IEEE 14 bus system [11] and compared with some existing indices.

2 Existing Line Based Voltage Stability Indices

2.1 Line Stability Index (L_{mn})

Based on the concept of SLPF, by considering reactive power equation Mahmoud Moghavvemi et al. proposed an index L_{mn} . Here line charging admittance and effect of active power change are neglected and the index is given by

$$L_{mn} = (4X Q_r)/(V_s \sin(\theta - \delta))^2 \quad (1)$$

where, X = Line reactance, Q_r = Reactive power available at receiving end bus, V_s = Sending end bus voltage, θ = Line impedance angle, δ = angle difference between two bus voltages of a line.

2.2 Fast Voltage Stability Index (FVSI)

This index was developed by Ismail Musirin et al. using the same concept as L_{mn} . In this index formulation the effect of reactive power flow is considered. The line charging admittance, the effect of active power flow and the bus angles of a line are neglected. The index is given by

$$FVSI = (4Z^2 Q_r)/(V_s^2 X) \quad (2)$$

where, Z = Line impedance and the remaining parameters are as given in previous index.

2.3 Line Stability Factor (L_{QP})

A. Mohamed et al. derived a line stability factor L_{QP} using the single line power transmission system. The index is given by

$$L_{QP} = 4(X/(V_s^2))(Q_r + (X P_s^2)/(V_s^2)) \quad (3)$$

where, P_s = active power available at sending end bus and the remaining parameters are as given in L_{mn} . In this index, the effect of sending end voltage, active power and receiving end reactive power are considered. Line charging admittance, receiving end active power, and bus angle of a line are neglected.

2.4 Line Voltage Reactive Power Index (VQI_{line})

F. A. Althowibi et al. derived a line-based voltage reactive power index using the same concept as FVSI. The effect of reactive power at receiving end only considered. Active power at receiving end, shunt elements, and bus angles of a line are neglected. The index is given by

$$VQI_{line} = (4Q_r) / (|B_{sr}| |V_s|^2) \quad (4)$$

where, Q_r = Reactive power available at receiving end bus, V_s = Sending end bus voltage, B_{sr} = the susceptance of a line between sending end bus and receiving end bus.

2.5 New Voltage Stability Index ($NVSI$)

R. Kanimozhi et al. developed an index NVSI. In this index, both the effects of active power and reactive power are considered but shunt elements, resistance, and bus angles of a line are neglected. The index for a transmission line is given by

$$NVSI = (2X\sqrt{(P_r^2 + Q_r^2)}) / (2Q_r X - V_s^2) \quad (5)$$

where, P_r = active power available at receiving end bus and remaining parameters are as explained in previous section. For the system to be stable, all the above line indices should be maintained less than one.

3 Effect of Delta on Voltage

Actually at the midpoint of a transmission line, voltage will effect greatly with respect to an angle difference between two buses of a line [12]. The voltage at this point decreases with increase in angle difference and hence the impact of this voltage reduction will be on bus voltages. For the analysis purpose, a single line two bus system is considered and different cases are chosen for observing the effect of angle difference on receiving end bus voltage. They are shown graphically. Consider a single-line two bus system as shown in Fig.1, where, V_s = Sending end bus voltage, V_r = Receiving end bus voltage, δ_s = sending end bus voltage angle, δ_r = receiving end bus voltage angle, S_s = Complex power available at sending end bus, S_r = Complex power available at receiving end bus, Z = impedance of a line, R = resistance of a line, X = Reactance of a line, P_s = active power at sending end bus, Q_s = reactive power at sending end bus, P_r = active power at receiving end bus, Q_r = reactive power at receiving end bus and I_{sr} = current flowing in a line between two buses. From the Fig.1, the complex power flow at receiving end bus can be written as

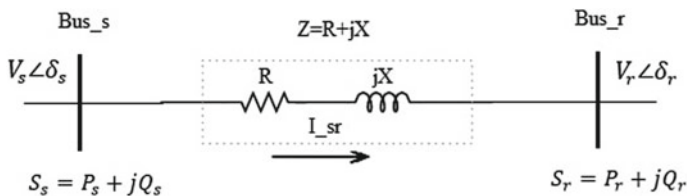


Fig. 1 Single line diagram of a two bus system without shunts

$$P_r + jQ_r = \frac{V_s V_r}{Z} \angle (\theta - \delta_s + \delta_r) - \frac{V_r^2}{Z} \angle \theta \tag{6}$$

let $\delta = \delta_s - \delta_r$ and by comparing the imaginary parts on both sides, the above equation can be written as

$$Q_r = \frac{V_s V_r}{Z} \sin(\theta - \delta) - \frac{V_r^2}{Z} \sin\theta \tag{7}$$

$$\Rightarrow V_r^2 \sin\theta - V_s V_r \sin(\theta - \delta) + ZQ_r = 0 \tag{8}$$

the roots for the above quadratic equation can be written as

$$\Rightarrow V_r = (V_s \sin(\theta - \delta) \pm \sqrt{[V_s \sin(\theta - \delta)]^2 - 4ZQ_r \sin\theta}) / 2\sin\theta \tag{9}$$

since $Z \sin\theta = X$, the above equation can be modified as

$$\Rightarrow V_r = (V_s \sin(\theta - \delta) \pm \sqrt{[V_s \sin(\theta - \delta)]^2 - 4XQ_r}) / 2\sin\theta \tag{10}$$

For the case study simulation, 17th line is randomly selected from standard IEEE 14 bus system and the data for the 17th line is given as $R = 0.12711$ pu, $X = 0.27038$ pu, $Z = 0.29877$ pu, $\theta = 64.8210$, $V_s = 1.056$ pu, $Q_r = 0.0336$ pu. From this data, Eq. (10) can be modified as

$$\Rightarrow V_r = (0.58344) \sin(\theta - \delta) + (0.5525) \sqrt{[V_s \sin(\theta - \delta)]^2 - 1.0815Q_r} \tag{11}$$

Here the following eight cases are considered for showing the effect of delta on receiving end bus voltage, Case1: V_s , Q_r fixed at given values and δ increase; Case2: V_s decrease, Q_r fixed and δ increase; Case3: V_s increase, Q_r fixed and δ increase; Case4: V_s fixed, Q_r and δ increase; Case5: V_s fixed, Q_r decrease and δ increase; Case6: V_s decrease, Q_r and δ increase; Case7: all V_s , Q_r and δ increase and Case8: V_s , Q_r decrease and δ increase.

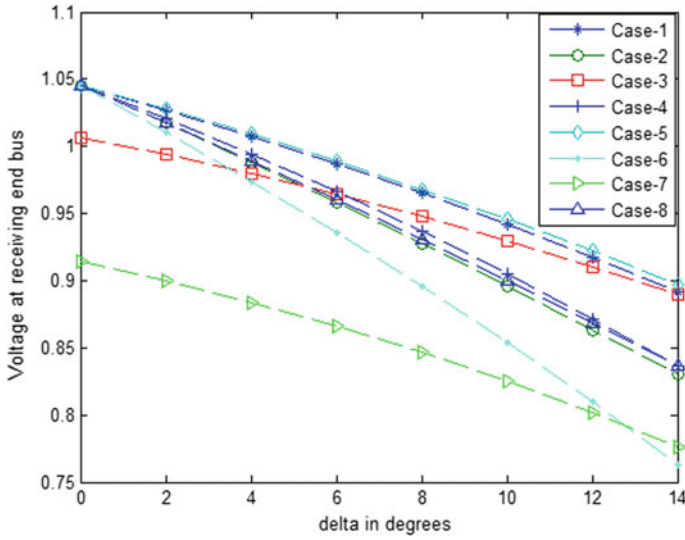


Fig. 2 Effect of delta on receiving end bus voltage for different cases

From Fig.2, it can be concluded that the receiving end bus voltage is falling as delta increases and severity may be more near the collapse point. Hence, delta should be considered in stability index definition for getting accurate voltage collapse point.

4 Proposed Index Formulation

The proposed index named as New Line Voltage Stability Index (NLVSI) is derived from Fig.1, the current entering the receiving end bus can be expressed as

$$I_{sr} = \frac{(V_s \angle \delta_s - V_r \angle \delta_r)}{Z \angle \theta} \tag{12}$$

The complex power available at receiving end bus can be written as

$$S_r = V_r \angle \delta_r \cdot (I_{sr})^* \tag{13}$$

where, $(I_{sr})^*$ is the conjugate of current reaching the receiving end bus. The complex power can also be written as

$$S_r = P_r + jQ_r \tag{14}$$

in polar form it can be expressed as

$$S_r = \sqrt{P_r^2 + Q_r^2} \angle \phi_r \quad (15)$$

where, $\phi_r = \tan^{-1} \left(\frac{Q_r}{P_r} \right)$ and therefore from Eqs. (12), (13) and (15)

$$\sqrt{P_r^2 + Q_r^2} \angle \phi_r = V_r \angle \delta_r * \frac{(V_s \angle -\delta_s - V_r \angle -\delta_r)}{Z \angle -\theta} \quad (16)$$

$$Z \sqrt{P_r^2 + Q_r^2} \angle (\phi_r - \theta) = V_s V_r \angle (\delta_r - \delta_s) - V_r^2 \angle 0 \quad (17)$$

Let $\delta_r - \delta_s = \delta$ and by comparing the real parts on both sides, we will get

$$V_r^2 - V_s V_r \cos \delta + Z \sqrt{P_r^2 + Q_r^2} \cos(\phi_r - \theta) = 0 \quad (18)$$

to get the real roots for V_r , discriminant should be greater than or equal to zero

$$(-V_s \cos \delta)^2 - 4Z \sqrt{P_r^2 + Q_r^2} \cos(\phi_r - \theta) \geq 0 \quad (19)$$

$$\Rightarrow (V_s \cos \delta)^2 \geq 4Z \sqrt{P_r^2 + Q_r^2} \cos(\phi_r - \theta) \quad (20)$$

from the above equation, finally it can be expressed as

$$(4Z |S_r| \cos(\phi_r - \theta)) / (V_s \cos \delta)^2 \leq 1 \quad (21)$$

where, $|S_r| = \sqrt{P_r^2 + Q_r^2}$ and therefore, the proposed index is

$$NLVSI = (4Z |S_r| \cos(\phi_r - \theta)) / (V_s \cos \delta)^2 \quad (22)$$

In this index, for optimistic prediction of line voltage stability, active and reactive power flow available at receiving end bus are incorporated. In addition to this, angle between two buses of a line is also included as mentioned in the previous section. Here Z and θ are the line impedance and impedance angle respectively and they are known parameters. By using Phasor Measurement Units (PMUs), $|S_r|$, ϕ_r , V_s and δ can be measured online and hence it can also be used for online voltage stability monitoring. The step-by-step procedure for identifying the proximity of voltage instability point of a line with respect to a particular load bus using proposed index is given below: *step1*: Start with the initial data of the system; *step2*: Run the NR load flow for base case loading; *step3*: Evaluate the proposed index for each line in the system using NR load flow solution for the base case; *step4*: Select one load bus (especially weak bus) in the system; *step5*: Increase the load at that particular bus and run again the NR load flow; *step6*: Re-evaluate the proposed index for each line in the system using the load flow solution; *step7*: Note down the line number and corresponding index values in a table; *step8*: Check whether the proposed index value of any line in the

system is less than one or not; *step9*: If yes repeat the steps 5–8, otherwise stop the process. The line which exhibits index value more than one is called critical line to the respective load bus. Hence if index reaching near to one, information should be given to the operator then the operator can take necessary action. For a stable system, index value for any line should be maintained less than one. The same procedure can also be applied to ZIP load case by replacing all the constant power loads with ZIP load models.

5 Representation of ZIP Load Model

ZIP load model is the voltage dependent generalized load model [10] and the mathematical representation of this model is given as

$$P_{ZIP} = P_0[Z_p(V_i/V_0)^2 + I_p(V_i/V_0) + P_p] \quad (23)$$

$$Q_{ZIP} = Q_0[Z_q(V_i/V_0)^2 + I_q(V_i/V_0) + P_q] \quad (24)$$

where P_{ZIP} and Q_{ZIP} are the active and reactive powers at operating voltage V_i ; P_0 and Q_0 are the active and reactive powers at rated voltage V_0 ; Z_p , I_p , and P_p are the ZIP coefficients for active power; and Z_q , I_q , and P_q are the ZIP coefficients for reactive power.

6 Test Case Results

In this section, IEEE 14 bus system is considered to demonstrate the proposed index for line voltage stability analysis. It is having 5 generator buses, 9 load buses, and 20 interconnected transmission lines. In this system, each load bus is considered individually and reactive load at each bus is increased step by step from its base case loading until voltage collapse point of a line is reached. The load at remaining buses is maintained at base level. The maximum loading, critical lines and line voltage stability indices values with respect to that particular bus are given in Table 1. Ranking is given to the buses based on maximum loading to identify the weak bus in the system, i.e. the bus which is having least maximum loading ability has 1st rank and highest maximum loading ability has last rank. According to the ranking, the first rank bus is the weak bus in the system. From the Table 1, it can be concluded that bus 14 is the weakest bus in the system and the corresponding reactive loading at this bus is 72 MVar. At this loading 17th line, which is connected between 9th bus and 14th bus, is the most critical line. The 20th line, which is connected between 13th bus and 14th bus, is less critical when compared to 17th line with respect to bus 14 and it is obvious from the Table 1. After identification of weak bus, by changing both

Table 1 Line stability index values at each load bus and corresponding critical lines with conventional (i.e constant power) reactive load

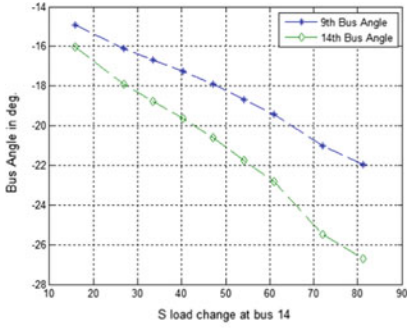
Bus no.	Maximum reactive loading in MVar	Rank	Critical line number	NLVSI	L_{mn}	FVSI	VQI_{line}	NVSI
4	258.6	9	4 (2–4)	0.9311	0.8015	0.8312	0.8312	0.7389
			10 (5–6)	0.7756	0.7756	0.7656	0.7656	0.7675
5	207.6	8	2 (1–5)	1.0727	0.8585	0.8989	0.8989	1.0413
7	146	5	8 (4–7)	1.0795	1.0795	1.0752	1.0752	1.2109
9	196.6	7	9 (4–9)	1.0529	1.0529	1.0478	1.0478	1.1589
			14 (7–8)	0.8714	0.8714	0.8714	0.8714	0.7721
10	158.8	6	11 (6–11)	0.8693	0.9749	0.9432	0.9432	0.6464
			18 (10–11)	0.9584	1.0876	1.0456	1.0456	0.8069
11	92.8	3	11 (6–11)	0.8432	1.0047	0.9545	0.9545	0.645
12	74	2	12 (6–12)	1.0091	1.0051	1.0195	1.0195	1.0038
13	95.8	4	10 (5–6)	0.7899	0.7899	0.7762	0.7762	0.8269
			13 (6–13)	0.8984	1.0464	0.9997	0.9997	0.6802
14	72	1	17 (9–14)	0.9714	1.1062	1.0622	1.0622	0.7924
			20 (13–14)	0.7943	0.9083	0.8755	0.8755	0.5621

active and reactive load simultaneously, different case studies have been performed at that bus and the corresponding results are explained in later sub sections.

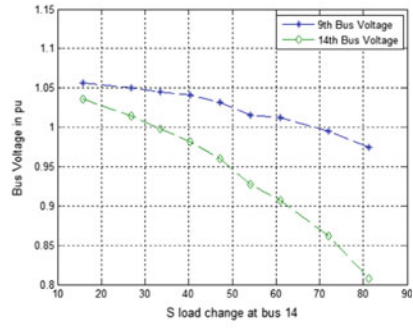
6.1 When Conventional (i.e. Constant Power) Load is Used

It is well known that simultaneous real and reactive load variations are more probable combinations in practical systems and therefore in this case both constant P & Q load at load bus 14 is increased step by step simultaneously until voltage instability point is reached. For each step, index values, voltage and angle at bus 9&14 are noted down. The corresponding graphs and table are shown in Fig. 3. The S in graphs and tables indicates that complex power load. Figure 3c shows the variation of indices for different loading conditions and from Table 2, it is clear that both active and reactive powers are increased to 64 MW & 50 MVar, respectively, from their base values. In this case, the 17th line is stressed more and its index value is 1.0213. The proposed index NLVSI is only influenced by both the real and reactive power variations, while other indices are not revealed.

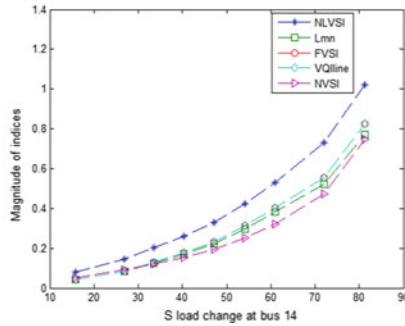
From Table 2, it is clear that the indices FVSI & VQIline are showing same performance. From Fig. 3a, it is observed that the angle difference between 9th bus and 14th bus is increasing gradually from the starting itself and it can be observed



(a) 9th and 14th bus angles Vs S load change at bus 14.



(b) 9th and 14th bus voltages Vs S load change at bus 14.



(c) Line stability indices Vs S load change at bus 14.

Fig. 3 Plots for simultaneous change of active and reactive load at bus 14 for the conventional load case

Table 2 Line index values for 17th line with S load change at bus 14 for the conventional load case

S. no	Complex load	Line number	NLVSI	L_{mn}	FVSI	VQI_{line}	NVSI
1	Base case i.e. P = 14.9 MW and Q = 5 MVar or S = 15.72 MVA	17	0.0811	0.0437	0.0445	0.0445	0.0518
2	Max. load i.e. P = 64 MW and Q = 50 MVar or S = 81.22 MVA	17	1.0213	0.7706	0.8263	0.8263	0.7457

that the voltage at bus 14 is reducing drastically when compared to 9th bus voltage, it is obvious from the Fig. 3b.

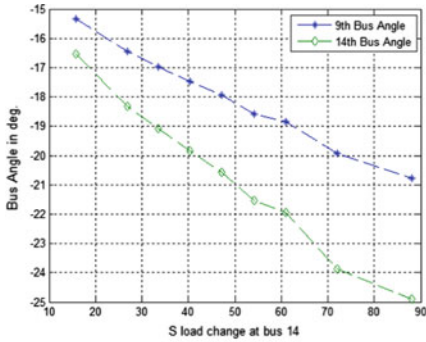
6.2 When ZIP Load Model is Used

In this section, the constant power loads at all buses are replaced with ZIP load models and at all the load buses same ZIP coefficients are used. The aggregate values of ZIP coefficients for 29 types of loads are taken from [13]. For the convenience of comparison, the load at bus 14 is varied like conventional load case. Here NR load flow solution is used and in which reference voltages are taken as rated voltages. In the first iteration, rated voltages are considered as operating voltages and next iteration onwards updated voltages are taken as operating voltages. From Eqs. (23) and (24), P_0 and Q_0 are changed from their base values, corresponding P_{ZIP} and Q_{ZIP} values are used in NR load flow method. The final solution is used in calculation of the Line stability Indices.

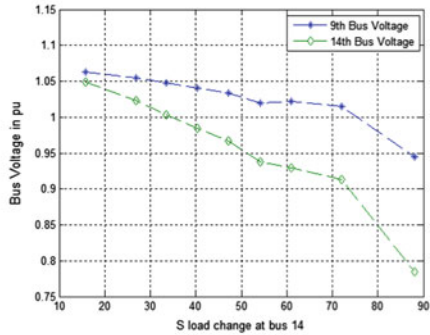
Like conventional case here also the angle difference between 9th bus and 14th bus is increasing gradually from the starting itself and it can be observed that the voltage at bus 14 is reducing drastically when compared to 9th bus voltage, it is obvious from the Fig.4b. From the Table 3, it is clear that the active load is increased to 68 MW and reactive load is increased to 56 MVar. The maximum loadability margin at bus 14 is increased compared to constant power load (i.e. Conventional load) case.

6.3 Results Comparison Between Conventional Load and ZIP Load Model

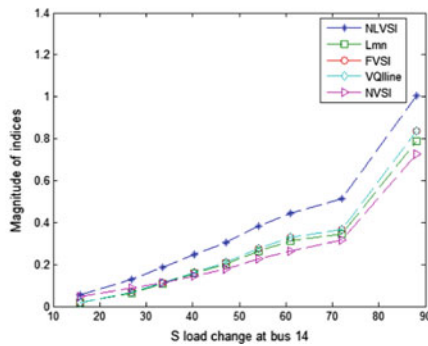
In this section, some results are compared for conventional and ZIP load models. The maximum loading capacity at weak bus (i.e. bus 14) is increased with ZIP load model when compared to conventional load model and it is obvious from Table 4, the delta limit for the critical line is also given in same table. For comparing the remaining parameters one particular loading is considered for both conventional and ZIP load models. From the Table 5, for simultaneous change of active and reactive load, it is clear that ZIP load model maintaining good voltage profile at the weak bus when compared to conventional load model. The power loss in the critical line and total power loss in the system also reduced by using ZIP load models.



(a) 9th and 14th bus angles Vs S load change at bus 14.



(b) 9th and 14th bus voltages Vs S load change at bus 14.



(c) Line stability indices Vs S load change at bus 14.

Fig. 4 Plots for both active and reactive load change at bus 14 for the ZIP load case

Table 3 Line index values for 17th line with S load change at bus 14 for the ZIP load case

S. no	Complex load	Line number	NLVSI	L_{mn}	FVSI	VQI_{line}	NVSI
1	Base case i.e. P = 14.9 MW and Q = 5 MVar or S = 15.72 MVA	17	0.0566	0.0167	0.0170	0.0170	0.0463
2	Max. load i.e. P = 68 MW and Q = 56 MVar or S = 88.09 MVA	17	1.003	0.7861	0.8358	0.8358	0.7262

Table 4 Results comparison for maximum loading at weak bus in the system

S. no.	Name of the test system	Critical line number	Conventional load		ZIP load	
			Max. loading in MVa	Delta in deg.	Max. loading in MVa	Delta in deg.
1	IEEE 14 bus system	17	81.22	4.7519	88.09	4.1032

Table 5 Results comparison for one particular loading at weak bus in the system

S. no.	Name of the test system	Loading in Mva	Conventional load			ZIP load		
			Voltage at weak bus in pu	Power loss in critical line in MW	Total power loss in the system in MW	Voltage at weak bus in pu	Power loss in critical line in MW	Total power loss in the system in MW
1	IEEE 14 bus system	72.11	0.862	3.25	26.042	0.9130	2.1150	23.608

7 Conclusion

This paper presented a New Line Voltage Stability Index (NLVSI) and the effectiveness of this index is shown by demonstrating it on IEEE 14 bus system. In this system, weak bus is identified depending on maximum acceptable load at a bus. Different case studies have been performed with constant power and ZIP load models at the weak bus, but simultaneous change of both active and reactive load case is only presented in this paper. From the results, it can be concluded that proposed index is effectively indicating the proximity of voltage instability point for both active and reactive power load change. The delta limit at maximum loading condition for both conventional and ZIP load model is shown in Table 4. The results obtained with ZIP load model are compared with conventional (i.e. Constant power) load model. From the results, it can also be concluded that when ZIP load models are used, maximum loading capability and voltage profile at the weak bus are improved and the same improvement can be appeared for remaining buses also with the increase in load at the respective buses. The power loss in the critical line and total power loss in the system are also reduced. The future scope of this work is to find out the contingency ranking in a system and it has to be compared with existing contingency rank estimation techniques.

References

1. K12-M Group, Begović J, Bright TJ, Domin S, Easterday-Mcpadden A, Girgis W, Hartmann C, Henville M, Ibrahim K, Kožmiński R, Marttila G, Michel K, Mustaphi D, Novosel B, Pettigrew M, Sachdev HS, Shuh P, Solanics J, Williams JGP, Voltage collapse mitigation report to IEEE power system
2. Bian J, Rastgoufard P (1994) Power system voltage stability and security assessment. *Electr Power Syst Res* 30(3):197–201
3. Kundur P, Paserba J, Ajarapu V, Andersson G, Bose A, Canizares C, Hatziargyriou N, Hill D, Stankovic A, Taylor C et al (2004) Definition and classification of power system stability IEEE/CIGRE joint task force on stability terms and definitions. *IEEE Trans Power Syst* 19(3):1387–1401
4. Moghavvemi M, Omar FM (1998) Technique for contingency monitoring and voltage collapse prediction. *IEE Proc-Gener Transm Distrib* 145(6):634–640
5. Musirin I, Abdul Rahman TA (2002) Novel fast voltage stability index (FVSI) for voltage stability analysis in power transmission system. In: Student conference on research and development, 2002. SCOReD 2002. IEEE, pp 265–268
6. Mohamed A, Jasmon GB, Yusoff S (1989) A static voltage collapse indicator using line stability factors. *J Ind Technol* 7(1):73–85
7. Moghavvemi M, Faruque O (1998) Real-time contingency evaluation and ranking technique. *IEE Proc-Gener Transm Distrib* 145(5):517–524
8. Althowibi FA, Mustafa MW (2010) Line voltage stability calculations in power systems. In: 2010 IEEE international conference on power and energy (PECon). IEEE, pp 396–401
9. Kanimozhi R, Selvi K (2013) A novel line stability index for voltage stability analysis and contingency ranking in power system using fuzzy based load flow. *J Electr Eng Technol (JEET)* 8(4):694–703
10. Hajagos LM, Danai, B (1998) Laboratory measurements and models of modern loads and their effect on voltage stability studies. *IEEE Trans Power Syst*, 13(2):584–592
11. Christie R (2000) Power systems test case archive. Electrical engineering. University of Washington. <https://www2.ee.washington.edu/research/pstca>
12. IITKANPUR. Power systems analysis, NPTEL. course. Electrical engineering. http://nptel.ac.in/courses/Webcourse-contents/IIT-KANPUR/power-system/ui/Course_home-2.htm
13. Bokhari A, Alkan A, Dogan R, Diaz-Aguiló M, De Leon F, Czarkowski D, Zabar Z, Birenbaum L, Noel A, Uosef RE (2014) Experimental determination of the ZIP coefficients for modern residential, commercial, and industrial loads. *IEEE Trans Power Deliv* 29(3):1372–1381

A Comprehensive Comparative Economic Analysis of ACO and CS Technique for Optimal Operation of Stand-alone HES



Sri Lakshmi E and S. P. Singh

Abstract In a hybrid energy system, there are generally more than three sources of generation to meet the given load, optimization technique optimally schedules the generation of these resources such that a given objective is met. There are many such methods to optimize a system to achieve desired results. This paper gives a comprehensive comparative economic analysis of ant colony optimization and cuckoo search technique to achieve optimal operation of hybrid stand-alone system. For the analysis, hybrid energy system having solar photovoltaic generator and wind turbines with energy storage system backed by diesel generators is used to power a remote village with no access to grid power. The comparative analysis of the two optimization methods with objective to achieve lowest per unit cost of generation is discussed.

Keywords Distributed generation · Convergence rate · Optimization

Nomenclature

$v_w(t)$	Velocity of wind w.r.t. time in m/s
v_r	Wind turbine's Rated velocity in m/s
v_{co}	Wind turbine's Cutoff velocity in m/s
v_{ci}	Wind turbine's Cut-in velocity in m/s
A	Rotors Swept area
C_p	Coefficient of Power
η_w	Efficiency associated with energy conservation system
P	Density of Air

S. Lakshmi E (✉) · S. P. Singh
Indian Institute of Technology (BHU) Varanasi, Varanasi, India
e-mail: srilakshmie.rs.eee15@itbhu.ac.in

S. P. Singh
e-mail: spsingh.eee@iitbhu.ac.in

© Springer Nature Singapore Pte Ltd. 2020
A. Kalam et al. (eds.), *Intelligent Computing Techniques for Smart Energy Systems*,
Lecture Notes in Electrical Engineering 607,
https://doi.org/10.1007/978-981-15-0214-9_58

C_p	Constant determined by the wind turbine curve
STC	Standard test condition
K_i	Solar PV module Temperature coefficient of current in $A/^\circ C$
K_V	Solar PV module Temperature coefficient of voltage in $V/^\circ C$
η_{MPPT}	MPPT device efficiency
f_{PV}	Derating factor
GSTC	Solar PV modules solar radiation (1000 W/m^2) under STC
TSTC	Solar PV modules Temperature ($25^\circ C$) under STC
T	Temperature of solar PV module in $^\circ C$
G	Amount of Solar radiation on solar PV module in kW/m^2
SOC	Battery's State of charge
SDR	Battery's Self-discharge rate
η_{RTE}	Battery's Round trip efficiency
DOD	Depth of discharge of battery
$P_b(t)$	Power supplied by the battery at time t
$P_L(t)$	Total load in kW at time t
$P_w(t)$	Wind turbine's Total output power in kW at time t
$T_{b_{min}}$	Minimum allowed time for a battery to discharge from full to empty in hours
$F(t)$	Diesel generators Hourly fuel consumption
$P_{DG}(t)$	DGs Actual power generated by at time t in kW
P_{RE}	Renewable sources Total power
P_{Rdg}	DGs Rated power of in kW
λ_L	Allowable LPSP of the load
N_w, N_{pv}, N_b, N_{dg}	No. of wind turbines, solar PV, battery, diesel generator
C_T	Total annual cost of system
C_w, C_{pv}, C_b, C_{dg}	Annual capital, operation and maintenance, replacement cost of wind turbine, solar PV, battery, and diesel
$C_{u_w}, C_{u_{pv}}, C_{u_b}, C_{u_{dg}}$	Cost of single unit of wind turbine, solar PV, battery, diesel generator
$C_{OM_w}, C_{OM_{pv}}, C_{OM_b}, C_{OM_{dg}}$	Operation and maintenance cost for wind turbine, solar PV, battery, diesel generator for a year
$N_{wmin}, N_{pvmin}, N_{bmin}, N_{dgmin}$	Min value of no. of units of wind turbines, PV panels, battery, Diesel generator
$N_{wmax}, N_{pvmax}, N_{bmax}, N_{dgmax}$	Max Values of no. of units wind turbines, PV panels, battery, Diesel generator
$P_{L_{avg}}$	Average value of the load

$P_{\text{bcap}}, P_{\text{Rpv}}, P_{\text{Rdg}}, P_{\text{Rw}}$	Rated value of each battery unit, PV unit, diesel generator unit, wind generator unit
$t_{(i,j)}$	Intensity of the pheromone deposited by each ant on the path (i, j)
$\alpha \& \beta$	Intensity control parameter and visibility control parameter
$\eta_{(i,j)}$	Visibility measure of the quality of the path (i, j) and
$l_{(ij)}$	Distance between two nodes
$S_m(i)$	Set of sessions to be observed
$\rho, \Delta \tau_{(i,j)}$	Evaporation parameter, pheromone level
$r, L\rho$	Rate of interest, life of project

1 Introduction

A distributed generation based on renewable energy resources such as wind, solar arrays, fuel cells, biogas, biomass, and micro-hydro has presented a reliable solution for many power system experts. The scope of expansion for electric power grid has fewer limitation with renewable energy sources. In order to provide power to the villages with shortfall of power located in far-flung areas, a stand-alone system with renewable energy is a viable and fitting solution. Hybrid energy system (HES) is an amalgamation of conventional energy sources and renewable energy sources (RESs). The efficient utilization of RES requires techno-economic analysis of HES [1–3]. So by using Metaheuristic optimization techniques [4], the optimal sizing and performance of HES is achieved. The basic parameters of climate such as temperature, solar irradiance, and wind speed are always changing for different locations and regions. Due to this, solar and wind turbine cannot generate stable power. In order to reduce the instability, the system is backed by the battery bank. To achieve optimum utilization of renewable energy resources, sizing optimization method provides lucrative solutions for HES installation [5].

Many novel methods for optimal design problems have been developed over the last two decades, and its application for renewable energy is a challenging problem for researchers in defining the optimal size and location of the forthcoming feeders and substation comprising of distribution network, a new possibilistic method, is developed by Ramrez and Navarro [6]. To reduce the techno-economic risks and monetary cost index, Haghifam et al. [7] developed a specialized NSGA-II algorithm. Another novel multi-objective approach is made here to minimize the expected loss of load, energy, computation time, and annualized system cost by Baghaee et al. [8]. An enhanced method is proposed by Xu et al. [9] in optimizing the charge and discharge state of battery which also reduces the total system cost. Yang et al. [10] discuss another novel approach comprising LPSP and LEC techniques in optimal sizing model for hybrid power generation. Aurn et al. [11] discuss design space approach which plays a vital role in the designing of isolated power system which optimizes

the battery integrated diesel generation systems. Rachid et al. [12] work on deterministic approach in optimizing the size of hybrid energy system along with overall cost reduction of the system. A linear programming model and simulation based method is developed by Carlos et al. [13], for sizing a HES. Where, for establishing the systems reliability, the concept of LPSP is used which also results in minimization of the system cost. Song and Irving [14] discuss the major modern heuristic optimization techniques and its integration and comparison with other methods. Based on distributed autocatalytic process, a new search methodology is introduced by Dorigo et al. [15]. It has been applied in solving the classical optimization problem. The various characteristics such as distributed communication, global data structure revision, and probabilistic transition of the ant system are also been discussed here. Cuckoo search (CS), a novel metaheuristic algorithm, is formulated by Yang and Deb [16] for solving optimization problems. Compared to other metaheuristic algorithms, it's been proved to be more robust and generic for many optimization problems. Yang and Deb [17] review the fundamental idea of cuckoo search and its recent developments along with the applications. Another efficient approach is made for multi-objective optimization, by framing a new CS technique by Yang and Deb [18] which has been verified alongside a subset of relevant test functions. Cuckoo technique emerges as the better solution over other optimization techniques under wide range of test condition. Cuckoo search algorithm also encourages hybridization with other algorithms, hence making the improvised version, an enhanced solution for diverse problems [18]. A comprehensive comparative performance analysis of ant colony algorithm and cuckoo search technique for optimal economic operation of hybrid stand-alone system is discussed in this paper. The paper is structured as follows: Mathematical modeling and objective function of hybrid stand-alone system is presented in Sect. 2. Ant colony optimization technique is explained in Sect. 3, and cuckoo search technique is discussed in Sect. 4. Comparative economic operation of hybrid stand-alone system with ACO and CS techniques is explained in Sect. 5. Finally, the conclusion of the presented work is discussed in Sect. 6 followed by references.

2 Mathematical Formulation

The hybrid energy system (HES) comprises of two or more renewable energy sources amalgamated in such a manner to provide an efficient system with an uninterrupted power supply. The hybrid energy system which is proposed here consists of wind turbine generator (WTG), solar PV, battery bank as storage, and diesel generator (DG) as shown in Fig. 1. HES is suitable for far-flung areas where connectivity to national grid is not possible. Due to the geographical location of HES, where the availability of power from renewable resources is very dynamic in nature, optimization for economic operation becomes crucial. To carry out any optimization technique, mathematical modeling of complete system for obtaining the objective function plays a

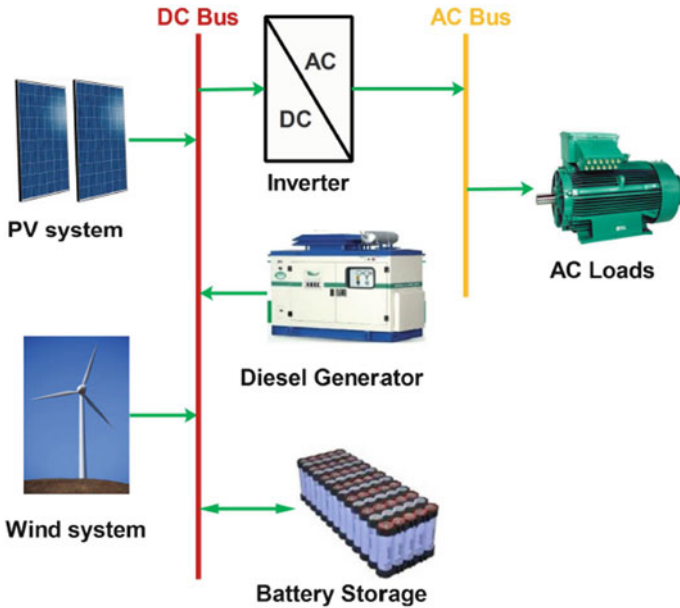


Fig. 1 Hybrid energy system

pivotal role. The following section features the mathematical formulation of numerous components of HES. The time-varying equation expresses the real-time behavior of different available sources. This represents a dynamic modeling of the system. In terms of power generation, utilization, and load demand fulfillment, the effective modeling of each component and source is very essential.

2.1 Modeling of System Components

HES comprises of solar PV module, WTGS, battery bank, and DG, as shown in Fig. 1. The real-time performance of these components can be emulated by dynamic modeling using time-varying equations. Modeling of discrete component depends on several variables in which few are nonlinear by nature. Thereby making whole HES system highly variable. Precise modeling of individual component justifies the effectiveness of HES in terms of utilization of available power source meeting the required load demand.

2.1.1 WTGS

By considering the local weather conditions, the wind turbine’s output power is calculated at any instant. The power generated at time t for a certain wind speed is calculated as follows [8]:

$$P_w(t) = \left\{ \begin{array}{ll} 0 & v_w(t) < v_{ci} \\ P_{Rw} \left(\frac{v_w(t) - v_{ci}}{v_r - v_{ci}} \right)^n N_w & v_{ci} \leq v_w(t) < v_r \\ P_{Rw} N_w & v_r \leq v_w(t) < v_{CO} \\ 0 & v_w(t) \geq v_{CO} \end{array} \right\} \tag{1}$$

Here, the value of *n* for the above equation is chosen as 1 as it lies between 1 and 3, respectively. The wind turbine’s rated power is given as

$$P_{Rw} = \frac{1}{2} \rho A C_p \eta_w v_r^3 \tag{2}$$

2.1.2 Solar PV Module

The PV module output power using metrological data can be determined as

$$P_{pv} = f_{PV} \eta_{MPPT} V_{OC} I_{SC} \tag{3}$$

The open-circuit voltage and short-circuit current of solar PV module can be assessed using the following equations:

$$I_{SC} = [I_{sc(STC)} + K_i(T - T_{STC})] G / G_{STC} \tag{4}$$

$$V_{OC} = [V_{OC(STC)} + K_v(T - T_{STC})] \tag{5}$$

Hence, the power of solar PV module is calculated as

$$P_{pv} = f_{PV} \eta_{MPPT} [V_{OC(STC)} + K_v(T - T_{STC})] \times [I_{sc(STC)} + K_i(T - T_{STC})] G / G_{STC} \tag{6}$$

2.1.3 Battery

The parameters like temperature, solar irradiance, wind speed ,etc., are volatile in nature. In order to compensate the volatile nature of renewable energy resources, a battery system is added. The SOC (state of charge) of the battery capacity is defined

as follows:

$$SOC(t) = SOC(t - 1)(1 - SDR)\eta_{RTE} - \frac{P_b(t)}{n_b} \tag{7}$$

The SOC of the battery is limited by DOD (depth of discharge) as well as battery rated capacity.

$P_b(t)$ is the power supplied by the battery at time t is calculated by the following equation [8]:

$$P_b(t) = P_w(t) + P_{pv}(t) - P_L(t) \tag{8}$$

When the combined power of wind and solar PV is more than load demand, then the battery is charged or else it discharges. During charging, $P_b(t)$ will be positive and negative during discharging. The value of SOC depends on the previous SOC, rate of charging or discharging, DOD, and rated capacity of the battery [11]. Its value increases with charging and decreases with the discharge of the battery. Power of the battery charging depends mainly on these parameters: (i) battery’s charging rate, (ii) battery’s current SOC, and (iii) available power for charging. Therefore, at any time “ t ” the charging power of the battery ($P_{b, ch}$) and discharging power of battery ($P_{b, dch}$) is minimum of the above-discussed parameters and is given as (9), (10), respectively.

$$P_{b, ch} = \min \left[\{P_w(t) + P_{pv} - P_L(t)\} \left\{ \frac{\eta_{RTE} P_{b, cap} n_b}{T_b \min} \right\} \{(\eta_{RTE} P_{b, cap} - SOC(t - 1))n_b\} \right] \tag{9}$$

$$P_{b, dch} = \min \left[\{P_L(t) - P_w(t) - P_{pv}(t)\} \left\{ \frac{\eta_{RTE} P_{b, cap} n_b}{T_b \min} \right\} \{(SOC(t) - (1 - DOD_{max})P_{b, cap})n_b\} \right] \tag{10}$$

2.1.4 Diesel Generator

To enhance the system reliability, a diesel generator (DG) is added. The power is drawn from the DG only when the load is more than the wind, solar, and rate of discharge or when the battery has reached the depth of discharge. The fuel type, hourly fuel consumption, and efficiency specify the performance of DG. Here, $F(t)$ of the DG is given as [11].

$$F(t) = aP_{Rdg} + bP_{DG}(t) \tag{11}$$

The constants “a” and “b” rely on DG’s rated capacity. Typically, for DG system rated under 20 kW, “a” and “b” are opted as 0.08415 liter/kWh and 0.246 liter/kWh, respectively. Similarly, for DG rated above 20 kW, “a” and “b” is considered as 0.0184 liter/kWh and 0.2088 liter/kWh

2.2 Operation Strategy

The primary generating sources of HES are wind energy and solar PV energy but because of fluctuating nature of power from these sources, the system is supported by battery backup and diesel generator. Whenever there is a shortfall of power from the renewable sources, the power is first drawn from the battery storage; if the required power is in excess of the current rating limit of the battery storage, then the remaining power is met by the DG. And if the power produced from the renewable sources exceeds the demanded load, then this surplus power is stored in the battery bank considering the current limits of the battery set. If there is excess of power after maximum limit of battery is reached, then this power is considered as loss to the system. Hence, P_{RE} denotes total power 'generated by RES at time t given as follows [12].

$$P_{RE} = P_w(t) + P_{pv}(t) \quad (12)$$

Here, $\Delta P_1(t)$ and $\Delta P_2(t)$ are the difference in generated power from renewables and load power (13) and difference in generated power from renewables, battery energy at time $(t - 1)$ and load power is shown in Eq. (14)

$$\Delta P_1 = P_{RE}(t) - P_L(t) \quad (13)$$

$$\Delta P_2 = P_{RE}(t) + P_{b_{dch}}(t - 1) - P_L(t) \quad (14)$$

The adapted power dispatch strategy on the basis of $\Delta P_1(t)$ and $\Delta P_2(t)$ is as follows:

- If $\Delta P_1(t) > 0$, charging of battery will begin and it will continue till SOC reaches maximum (SOC_{max}) as applicable for battery. While charging battery, it is made sure that batteries are charged only with the excess power from renewable sources after feeding the load.
- If $\Delta P_1(t) < 0$ and $\Delta P_2(t) > 0$, then the excess load demand, $\Delta P_1(t)$ after being fed from the renewable sources is met from the energy stored in the batteries till SOC reaches the maximum Depth of Discharge (DOD)
- If $\Delta P_1(t) < 0$ and $\Delta P_2(t) < 0$, after feeding the excess load from the batteries, if there is still remaining unmet load, it is fed from the diesel generators.
- If the total power from renewables, battery storage, DG are not able to meet the total load, then it is considered as loss of power supply (LPS) given as

$$LPS(t) = P_L(t) - \{P_w(t) + P_{pv}(t) + P_{b_{dch}}(t) + P_{dg}(t)\} \quad (15)$$

LPSP (loss of power supply probability) is the ratio of total LPS at time t [LPS(t)] and load demand for that period ($T = 8760$) [14].

$$LPSP = \sum_{T=1}^T LPS(t) / P_L(t) \tag{16}$$

Here, the LPSP is considered as 10% of load as the LPSP should be limited to less than or equal to allowable LPSP of load (λ_L).

2.3 Objective Function

The prime focus of this paper is to optimally size the hybrid energy system for curtailing the overall system cost by satisfying the constraints and also achieving continuous supply of power.

$$\text{Minimize, } C_T = \sum C_W + \sum C_{pv} + \sum C_b + \sum C_{dg} \tag{17}$$

$$\text{where, } C_W = C_{u_w} N_w f_{cr} + C_{OM_w} N_w \tag{18}$$

$$C_{pv} = C_{u_{pv}} N_{pv} f_{cr} + C_{OM_{pv}} N_{pv} \tag{19}$$

$$C_b = C_b N_b f_{cr} + C_{OM_b} N_b + C_{R_b} N_b \tag{20}$$

$$C_{dg} = C_{u_{dg}} N_{dg} f_{cr} + C_{OM_{dg}} \tag{21}$$

Here, the capital recovery factor (f_{cr}) is given as

$$f_{cr} = \frac{r(1+r)^{L_p}}{(1+r)^{L_p} - 1} \tag{22}$$

2.4 Constraints

To get a viable solution, a set of constraints should be fulfilled throughout the system operations owing to the operational and physical limits of the target system which are as follows.

2.4.1 Power Balance

Reliability criteria should be satisfied by the power supplied to load at any instant during the period t . The allowable LPSP of load (λL) represents the reliability. So for the considered period, LPSP should be less than λL .

$$\text{LPSP} < \lambda L \quad (23)$$

2.4.2 Design Variable

The design variables N_w, N_{pv}, N_b, N_{dg} , SOC defines the optimal operation of HES. These variables need to be varied between the min and max limits.

$$\frac{P_{L_{avg}}}{\eta_w P_{R_w}} \leq N_w \leq \frac{1.5 P_{L_{max}}}{\eta_w P_{R_w}} \quad (24)$$

$$\frac{P_{L_{avg}}}{\eta_{pv} P_{R_{pv}}} \leq N_{pv} \leq \frac{1.5 P_{L_{max}}}{\eta_{pv} P_{R_{pv}}} \quad (25)$$

$$\frac{n_h P_{L_{avg}}}{P_{b_{cap}}} \leq N_b \leq \frac{6 n_h P_{L_{avg}}}{P_{b_{cap}}} \quad (26)$$

$$1 \leq N_{dg} \leq \frac{P_{L_{avg}}}{\eta_{dg} P_{R_{dg}}} \quad (27)$$

$$0.15 \leq \text{SOC} \leq 1 \quad (28)$$

3 Ant Colony Optimization

Marco Dorigo [17] first introduces the ant colony optimization (ACO) technique which is metaheuristic in nature and used in solving the combinatorial problems. This technique is based on the actions of real ants. It is been explained that though the ants being blind, they have the ability in determining the shortest path from nest to food. The ant's deposit pheromones while moving from one point to another point on the path and the path with highest intensity of pheromone are followed by other ants as deposited amount of pheromones is the medium of communication. The following equation mentioned below define the transition rule from initial position i which is given as

$$P_m(i, j) = \begin{cases} \frac{[\tau_{ij}]^\alpha \times [\eta_{ij}]^\beta}{\sum_{k \in S_m(i)} [\tau_{ik}]^\alpha \times [\eta_{ik}]^\beta} & \text{if } j \in S_m(i) \\ 0 & \text{otherwise} \end{cases} \tag{29}$$

The quality of visibility $\eta_{(i,j)}$ is measured by

$$\eta_{(i,j)} = 1 / l_{(i,j)} \tag{30}$$

Pheromone updating takes place and is depicted by the following equation:

$$\tau_{(i,j)} \leftarrow \rho \times \tau_{(i,j)} + \Delta \tau_{(i,j)} \tag{31}$$

4 Cuckoo Search Technique

A nature-inspired metaheuristic algorithm known as cuckoo search algorithm based on the behavioral activities of the cuckoo bird [16] was introduced by Yang et al. It mainly operates on two strategies, random walk and levy flight search techniques. The probability of host bird to discover an alien egg in its own nest is done using the random walk technique and the levy flights technique explore the search space followed by a sudden 90° turn by various straight path flights. Therefore, the CS technique is found efficient in solving optimization problems and they are further briefly discussed in the upcoming subsection.

4.1 Levy Flights Technique

Levy flight technique proposes a novel solution using the best location previously obtained for a particular solution and is calculated as follows:

$$G_i^{new} = G_i^{prev} + (\chi * rand_1 * \Delta G_i^{new}) \tag{32}$$

The equation for ΔG_i^{new} is expressed by

$$\Delta G_i^{new} = \psi * \{ \sigma_x(\beta) / \sigma_y(\beta) \} * (G_i^{prev} - G^{best}) \tag{33}$$

where G_i^{new} is new solution, G_i^{prev} is previous known solution, and G^{best} is global best value.

$$\text{and } \psi = rand_x / |rand_y|^{1/\beta} \tag{34}$$

$$\sigma_x(\beta) = \left[\Gamma(1+\beta) * \left\{ \sin(\Pi\beta/2) / (\Gamma(1+\beta)/2) \right\} * \beta * 2^{\left(\frac{\beta-1}{2}\right)} \right]^{\frac{1}{\beta}} \quad (35)$$

$$\sigma_y = 1 \quad (36)$$

4.2 Random Walk Technique

This method obtains a new solution which is expressed by

$$G_i^{\text{dis}} = G_i^{\text{prev}} + K * \Delta G_i^{\text{dis}} \quad (37)$$

where value of K (coefficient of probability) is given as follows:

$$K = \begin{cases} 1 & \text{if } \text{rand}_3 < P_a \\ 0 & \text{other wise} \end{cases} \quad (38)$$

and ΔG_i^{dis} is given by

$$\Delta G_i^{\text{dis}} = \text{rand}_3 * [\text{rand}_{p_1}(G_i^{\text{prev}}) - \text{rand}_{p_2}(G_i^{\text{prev}})] \quad (39)$$

5 Comparative Analysis

For comparative performance analysis of both the optimization techniques discussed above, a remote village, where solar, wind, DG along with battery storage emulates as a HES. The metrological data of temperature, wind speed, and solar irradiation of the location with geographical coordinates 17°08'48.6''N, 77°54'47.2''E is collected for a year from National Renewable energy Laboratory to calculate the power extracted by the wind turbine generators and the solar power generators. Loads in remote villages are primarily domestic and agricultural hence are mostly dependent on the seasonal and demographical conditions. Load data for three seasons of winter, summer, and rainy are shown in Fig. 2 is collected, the primary aim is to see that the load is met by renewable energy resources, if the power generated is falling short of the demanded load, then energy is drawn from the battery bank even then if the load is not met, then the diesel generators are used leaving a margin of 10% for load shedding. The per unit system details, investment cost/start-up cost, and operation and maintenance cost of the considered energy sources are given in the following Table 1. The code for the ACO and CS algorithm to achieve optimal economic operation of HES is designed in MATLAB. The result gives the optimum number of solar panel arrays, wind turbines,

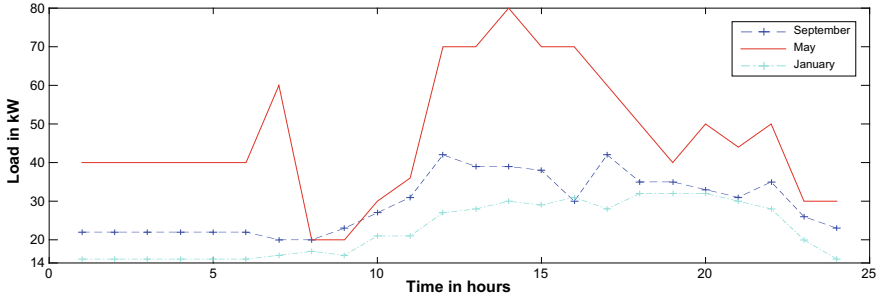


Fig. 2 Hourly seasonal load profile for months of January, May, and September

Table 1 Per unit system detail

WTG	PV	Battery	DG
<ul style="list-style-type: none"> Rated power: 5 kW Cut-in speed: 2.7 m/s Direct drive PMSG* AC generator cutout speed: 25 m/s Wind speed: 11 m/s Start-up cost (Rs./single unit): 5 lakh Operation and Maintenance cost per year (Rs./per unit): 25,000 	<ul style="list-style-type: none"> Rated power: 5 kW/200 W Open-circuit voltage: 30.8 V Monocrystalline Open-circuit current: 8.7A Optimum voltage and current: 24.5 V and 8.16 A Start-up cost (Rs./single unit): 5 lakh Operation and Maintenance cost per year (Rs./unit): 10,000 	<ul style="list-style-type: none"> Rated capacity: 100 Ah Rated voltage: 12 V Lead-acid battery Minimum SOC: 15% Round tip efficiency: 85% Start-up cost (Rs./single unit): 10,000 Operation and Maintenance cost per year (Rs./unit): 720 	<ul style="list-style-type: none"> Rated power: 5 kW Output voltage: 440 V AC generator Diesel cost (Rs./l): 55 Efficiency: 85% Start-up cost (Rs.): 1 lakh Operation and Maintenance cost per hour (Rs.): 97

battery capacity, and diesel generators to be installed in the hybrid energy system to achieve optimal economic solution shown in Table 2. The convergence characteristics of ant colony and CS optimization technique are plotted in Fig. 3. It is observed that cuckoo technique converges within 10 iterations whereas ACO technique takes more

Table 2 Optimal Sizing of HES using ACO and CS

Sources capacity	Single unit rating	No. of units		Total	
		ACO	CS	ACO	CS
Wind	5 kW	17	17	85 kW	85 kW
Solar	5 kW	16	20	80 kW	100 kW
Battery	12 v, 100 Ah	247	222	296.4 kWh	266.4 kWh
DG	5 kW	5	4	25 kW	20 kWh

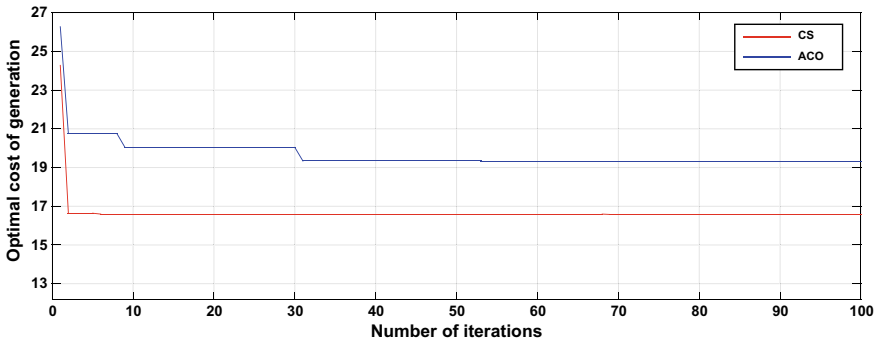


Fig. 3 Convergence characteristics of ACO and CS

number of iterations because in ACO algorithm, the newer solutions tend to follow the pheromone trail left by previous ants.

Hence, the ability of the ants to search for an optimal solution is limited. In cuckoo search algorithm, the cuckoo does levy walk to find a solution, cuckoo search technique lacks the ability to think socially, randomness in search is very high.

Using the collected meteorological and load data, the optimal number of PV strings, wind turbine, battery units, and diesel generators calculated by ant colony algorithm and cuckoo search technique are shown in Table 2. The corresponding annual cost incurred are evaluated in Table 3, for the ACO algorithm, the optimal number of solar PV string, wind turbine, battery units, and DG units are 16, 17, 247, and 5, respectively which incurs an annual expenditure of Rs. 19.39 lakhs, since the ant colony lacks the ability to search locally, the solution gets converged at the point where the pheromone deposition is higher. In case of cuckoo search technique, the optimal number of PV strings, wind turbine, battery units, and DG units are 20, 17, 222, and 4, incurring an annual expenditure of Rs. 16.82 lakhs, since the CS technique has the ability to search locally, a better solution can be obtained but with every new iteration, a new nest is created. The randomness is very high and the probability to find optimal solution reduces. Per unit cost of generation obtained with both the optimization method is shown in (Table 4). The annual energy generation of HES

Table 3 Annual cost summary of HES using ACO and CS (Rs. in lakhs)

Component	Capital per year		O and M per year		Annual total cost	
	ACO	CS	ACO	CS	ACO	CS
Wind turbine	0.403716	0.403716	4.25	3.4	4.653716	3.803716
Solar PV	0.379968	0.47496	1.6	2	1.979968	2.47496
Battery	0.117316	0.10544	1.8525	1.665	1.969816	1.77044
DG	0.023748	0.019	10.7632	8.7558	10.78695	8.7748
System	0.924748	1.003116	18.4657	15.8208	19.39045	16.82392

Table 4 Per unit cost of generation

Method of optimization	Energy delivered (kWh)	per unit cost of generation (in Rs.)
Ant colony optimization	219484	8.83
Cuckoo search technique	219491	7.66

Table 5 Annual energy generation of HES using ACO and CS

Component	Production		Fraction	
	CS	ACO	CS (%)	ACO (%)
PV array	57489	57363	26.19	26.14
Wind turbine	160656	160156	73.19	72.97
Generator	1346	1965	0.61	0.90
Total	219491	219484	100	100

Table 6 Average time taken for each iteration

Technique	Time (in sec)
Ant colony algorithm	126.46
Cuckoo search technique	58.35

using both the method is shown in Table 5 and average time for each iteration in two methods is given in Table 6 which shows that the CS takes lesser time to converge as compared to ACO algorithm.

6 Conclusion

The objective of this paper is to provide a conclusive comparative analysis of ant colony optimization and CS technique in optimizing the size of units in a hybrid stand-alone system. Convergence rate is a prime figure of merit for any optimization technique for its adoption. With this comparative analysis, the average time taken in each iteration as a unit of convergence rate is found to be substantially reduced by 53.8% with CS technique as compared to ACO technique; hence, making the CS technique the better choice for implementation. In addition to this, it is also observed that for a HES, as compared to ACO technique, with CS technique, there is reduction of 10 and 20% requirement in number of units of battery bank and DG, respectively, at the cost of 25% increase in solar array utilization. As a result of which, the capital and operation cost is curtailed by 10 and 20% in case of battery and DG, respectively. The cost constraint for solar even though increases but the overall cost of the system

is reduced by an ample amount. The results show that the CS technique emerged as front-runner in terms of quality of the solution and the time taken to optimize the problem.

References

1. Suhane P, Rangnekar S, Mittal A, Khare A (2016) Sizing and performance analysis of stand-alone wind-photovoltaic based hybrid energy system using ant colony optimization. *IET Renew Power Gener* 10(7):964–972
2. Hong Y-Y, Lian R-C (2012) Optimal sizing of hybrid wind/PV/diesel generation in a stand-alone power system using Markov-based genetic algorithm. *IEEE Trans Power Deliv* 27(2):940–950
3. Pappala VS, Erlich I, Rohrig K et al (2009) A stochastic model for the optimal operation of a wind-thermal power system. *IEEE Trans Power Syst* 24(2):940–950
4. Behera S, Sahoo S, Pati BB (2015) A review on optimization algorithms and application to wind energy integration to grid. *Renew Sustain Energy Rev Elsevier* 48:214–227
5. Yang H, Lu L, Zhou W (2007) A novel optimization sizing model for hybrid solar-wind power generation system. *Sol Energy Elsevier* 81:76–84
6. Ramírez-Rosado IJ, Domínguez-Navarro JA (2004) Possibilistic model based on fuzzy sets for the multiobjective optimal planning of electric power distribution networks. *IEEE Trans Power Syst* 19(4):1801–1810
7. Haghifam M-R, Falaghi H, Malik OP (2008) Risk-based distributed generation placement. *IET Gener Transm Distrib* 2(2):252–260
8. Baghaee HR, Gharehpetian GB, Kaviani AK (2012) Three dimensional Pareto optimal solution to design a hybrid stand-alone wind/PV generation system with hydrogen energy storage using multi-objective particle swarm optimization. In: *IEEE Second Iranian Conference on Renewable Energy and Distributed Generation*. IEEE, Tehran, Iran, pp 80–85
9. Xu L, Ruan X, Mao C et al (2013) An improved optimal sizing method for wind–solar–battery hybrid power system. *IEEE Trans Sustain Energy* 4(3):774–785
10. Yang H, Lu L, Zhou W (2007) A novel optimization sizing model for hybrid solar-wind power generation system. *Int J Sol Energy Elsevier* 81(1):76–84
11. Arun P, Banerjee R, Bandyopadhyay S (2008) Optimum sizing of battery-integrated diesel generator for remote electrification through design-space approach. *Int J Energy Elsevier* 33(7):1155–1168
12. Belfkira R, Zhang L, Barakat G (2011) Optimal sizing study of hybrid wind/PV/diesel power generation unit. *Int J Sol Energy Elsevier* 85(1):100–110
13. Nogueira CEC, Vidotto ML, Niedzialkoski RK, et al (2014) Sizing and simulation of a photovoltaic-wind energy system using batteries, applied for a small rural property located in the South of Brazil. *Int J Renew Sustain Energy Rev Elsevier* 29:151–157
14. Song YH, Irving MR (2001) Optimization methods for electric power systems, part 2, heuristic optimization methods. *IEE Power Eng J* 15(3):151–160
15. Dorigo M, Maniezzo V, Colomi A (1996) The ant system: optimization by a colony of cooperating agents. *IEEE Trans Syst Man Cybern* 26(1):29–41
16. Yang X-S, Deb S (2009) Cuckoo search via Lévy flights. In: *2009 World congress on nature and biologically inspired computing (NaBIC)*. IEEE, Coimbatore, India, pp 210–214
17. Yang X-S, Deb S (2014) Cuckoo search: recent advances and applications. *Neural Comput Appl* 24(1):169–174
18. Yang X-S, Deb S (2013) Multiobjective cuckoo search for design optimization. *Comput Oper Res* 40(6):1616–1624

Demand Response in Distribution Systems: A Comprehensive Review



Bhuvan Sharma, Nikhil Gupta, K. R. Niazi and Anil Swarnkar

Abstract The power system is growing from conventional grids to the smarter grids. The development of smart grids has facilitated the communication infrastructure between the grid and the end-user, which enables the grid to communicate with the customer and vice versa. This development motivated the researchers to gain interest in the area of Demand Response (DR). DR is capable to alleviate the economy of the distribution systems, however, its impact percolates to centralized generating stations via transmission systems. An extensive research work has been carried on DR pertaining to vital concerns such as economy, efficiency and reliability of the distribution systems. A brief review of this research is duly addressed by giving special attention to several methodologies, formulations and optimization techniques suggested and also throw some light on the issues and concerns of DR which are yet not being explored, but may provide new dimensions to operate future distribution systems.

Keywords Smart grids · Demand response · Distribution systems · Demand response programs

1 Introduction

The emergence of DR in the future smart grids is gaining importance due to its significant contribution in enhancing the efficiency, reliability and cost savings of the utility as well as customers. DR is the change in customer's energy consumption pattern from its usual consumption pattern in response to the variable electricity prices over time or the incentives paid to reduce the consumption when wholesale electricity prices are high or when system reliability is at risk [1]. The significance of

B. Sharma · N. Gupta (✉) · K. R. Niazi · A. Swarnkar
Malaviya National Institute of Technology, Jaipur, India
e-mail: bhuvansharma27@gmail.com

N. Gupta
e-mail: nikhil2007_mnit@yahoo.com

© Springer Nature Singapore Pte Ltd. 2020
A. Kalam et al. (eds.), *Intelligent Computing Techniques for Smart Energy Systems*,
Lecture Notes in Electrical Engineering 607,
https://doi.org/10.1007/978-981-15-0214-9_59

DR lies in the fact that it is the only program which motivates customers to shift their load from peak hours to off-peak hours and hence provides peak shaving as well as valley filling simultaneously. This shifting of the load from peak hours to off-peak hours due to higher electricity prices during peak hours flattens the load profile and therefore, generates elasticity in the load demand [2]. DR delivers certain financial benefits to the utility both by peak shaving as well as valley filling. Peak shaving considerably reduces the power needs to be purchased by the utility during peak hours which results in substantial economic benefit to the utility. It also provides capacity margin to the power system assets, which can defer the system upgrades for future endeavours. Valley filling, on the other hand, enables the utility to purchase cheap electricity in bulk during off-peak hours which again financially benefits the utility. Hence, adopting DR can fetch benefits for the utility not only in peak but also in off-peak periods. DR can be implemented by the utility either by following price-based or incentive-based demand response programs (DRPs). In price-based DRPs, variable prices are transmitted by the utility to the customers over the time which inspires them to change their energy consumption by shifting their loads from high price periods to low price periods while in incentive-based DRPs customers are given incentives to reduce their energy consumption during the peak hours as per the pre-signed contracts made by them with the utility. These incentives are proportional to the power reduction achieved by the customers.

Plenty of research work has been reported to seek the benefits of DR in the distribution systems. Majority of the earlier research work focuses on the impact of DR on renewable penetration, financial benefit to customers and utility, and reliability of the system, where all these have responded positively toward DR. A brief literature about the research carried is presented by arbitrarily classifying the work into four major areas, viz. the penetration of renewable DGs, operation of micro-grids, benefit to residential customers and reliability of the system by critically examining the advantages and shortcomings of various methodologies proposed. The paper also highlights the future directions of this research area considering more practical aspects and issues of DR which ought to be addressed in order to achieve more realistic solutions to operate distribution systems.

2 Background and Classification of DRPs

Power system is facing new challenges to accommodate exponentially growing load demand. Due to this growth in load demand, transmission lines become heavily loaded during peak hours which infuse congestion in the transmission network. Since we are living in a world having complex and interconnected power systems, heavy congestion along one or more tie-line(s) may lead to a grid failure, if not duly taken into consideration. There are several ways, such as network reconfiguration, optimal placement of DG units, capacitors or energy storages in distribution systems so that power flow can be managed which may relieve congestion in transmission lines. In this context, DR is a direct approach as it directly affects load demand thus manages

power flow in distribution systems. The attempt to change the consumers' energy consumption pattern in response to the variable prices of electricity over time or financial incentives, when the system's reliability is jeopardized is known as DR [3]. DR programmes can successfully provide peak shaving, valley filling and elasticity in the load profile of distribution systems. This can be achieved easily by using time-varying tariff structure to customers. However, customers' require motivation, economic, social and ethical, for being actively participating in DRPs. Different customers group or different customers in a group may behave differently. This leads to a variety of customers' responses while they curtail or shift their load demand.

DR is majorly implemented by price-based and incentive-based DRPs. In price-based DRPs, customers are motivated to change their energy consumption pattern with respect to energy prices transmitted by the utility over time. They constitutes three major programmes, viz., time of use (TOU), critical peak pricing (CPP) and real-time pricing (RTP). While, in incentive-based DRPs, customers are motivated to curtail their load demand during peak hours against the incentives credited to them. They are classified into direct load control (DLC), interruptible/curtailable service, emergency demand response program (EDRP), ancillary service markets, capacity market program and demand bidding/buy back. A few of these DRPs have been discussed below.

TOU pricing strategy consists of different electricity pricing during peak and off-peak periods in a day. The prices are kept high during peak hours while they are kept low during off-peak hours. Therefore, the customers get motivated to shift their loads from peak to off-peak hours in order to gain financial benefits. While CPP is different from the TOU in the context of defining the peak price period. The peak price period is the time interval during which power system reliability is at risk owing to generator outage or transmission line failure. Prices are kept substantially high during this period [4]. In RTP, the prices of electricity are not predetermined but they are decided on the real time wholesale market price and supply–demand conditions. RTP can be implemented either on the hourly basis or on the day-ahead basis.

In DLC, customers allow the utility to directly control their selected appliances such as electric water heaters (EWHs), air conditioners and pumps remotely. The utility can shut down or cycle the users' appliances during the peak demand or when the system reliability is jeopardized. Incentives are given to the customers for participating in the program. Interruptible/curtailable service programs are called for the customers who agree to reduce their energy consumption during the peak periods or under any contingency to gain the financial incentives. Moreover, to address the system contingencies and reliability issues EDRP is designed. Contingencies may happen due to insufficient generation at the peak time due to generator outage or transmission line failure. In this situation, utility makes the call for interruptible load programs focussing to interrupt the major industrial loads for a small duration and let them operate on their back up supply. The other option is to go for a bulk load shedding to restore the system security, stability and reliability. Incentives are given to the customers for curtailing their loads [5].

Few other incentive-based DRPs such as ancillary service markets, capacity market and demand bidding/buyback programs are also designed for customers for different applications and situations.

3 An Overview of DR

Following research has been carried out to study the impact of DR on the performance of distribution system. The literature portrays the effect of DR on the renewable penetration, economy, customer benefits and reliability of the distribution system.

Initially, researchers applied DR to reduce the curtailment of wind energy and hence increasing its penetration level so as to achieve clean and inexpensive form of energy which can be judiciously utilized to match the supply and demand. In [6] the impact of DR on increasing the wind penetration by adopting RTP has been discussed. Authors suggested that RTP is capable of reducing peak load demand during low wind periods so that majority of demand can be met through inexpensive and clean wind energy, which leads to the considerable financial benefits for both utility as well as customers. In [7], analysis of the costs and potential of DR in addition to its significance in improving wind penetration for future power system has been conducted. It was observed that per unit cost of electricity decreases drastically using DR. It has been observed that implementing DR reduces the operating cost considerably, supports the higher wind penetration and improves peak to average ratio (PAR) [8]. In [9] the impact of DR in integration to various energy storage systems was investigated with an aim to reduce the wind energy curtailment and authors concluded that compressed air energy storage, when combined with the DR gives the most promising results.

A few of the researchers worked on maximizing the micro-grid operator's (MGOs) benefit by optimally scheduling the resources and loads. Optimal scheduling of resources as well as loads in presence of DR contributes to enormous cost savings to the utility along with the customers. In [5] the authors discussed the various incentive-based DRPs and their implementation in smart grids. In [10], an optimal economic dispatch of micro-grid has been achieved by maximizing the MGO's economic benefit and minimizing the fuel cost of the conventional generators as well as power trading cost between grid and micro-grid. Authors in [11] applied incentive-based DRPs to compensate the uncertainties caused by the intermittent nature of the renewable energy and to reduce the operational cost of the MGO as well as the pollution caused by the DGs and the grid. In [12], the effect of DR on the performance of the isolated micro-grid has been studied. It has been observed that optimal energy management and application of DR can lead to reduced peak demands, less load curtailment, improved load factor, deferred system upgrades and more economic gains to the MGO. However, in [10–12] the scope of the EVs was not considered which ought to be the major loads for the distribution systems to accommodate in the near future. As EVs are non-critical as well as the major shiftable loads, not only in residential but also for commercial and industrial customers, hence, their impact

on the distribution system in the DR environment cannot be ignored. It has been observed that smart charging of plug-in electric vehicles (PEVs) in the presence of DR and battery energy storage system (BESS) can significantly address the energy management problem and hence can increase the MGO's economic benefits [13]. In [14] profit of MGO has been maximized considering the risk aversion and system frequency security constraints. It has been reported that as the customer participation in DR program increases, MGO's profit as well as system frequency security gets alleviated. In [15], work has been done to minimize the operational cost of virtual power players (VPP) by managing the energy resources intelligently. In [16] energy management of the resources using the distributed generation as well as the electric vehicles has been studied to minimize the operational cost of the network operator. EV trip reduction and trip shifting were the two unique DRPs implemented in this work.

A section of researchers also worked on analysing the impact of DR in the residential sector. The deployment of smart grids with contemporary communication infrastructure laid the foundation for the application of DR. To accomplish residential DR the advanced metering infrastructure (AMI) has been incorporated by the utility. Smart meters are installed at the residential premises to enable the communication between utility and the customers. The utility transmits the pricing signal to the customers, which motivate them to change their energy consumption patterns according to the pricing signals. Most of the literature studies residential DR in order to reduce the customer electricity bills and utility economic gains. In [2], the authors performed the optimal scheduling of the residential loads considering the different price-based DRPs combined with an interruptible load (IL) program to minimize the electricity consumption cost of the customers. In [17], a household energy system, combined with the small renewable generators and energy storage system (ESS) is deployed in presence of RTP to minimize the energy procurement cost of the grid by optimally scheduling the residential loads. In [1], the energy consumption cost of the customers has been optimized using DRPs. The results are optimized using TLBO and SFL algorithms, which indicate that the customers who opted for DR programs achieved reduced power consumption and costs (electricity bills) in comparison to the customer who did not opt for it. In [3], an energy management system (EMS) for optimization of smart grids has been proposed and it has been observed that EMS as well as DR are capable to alleviate the network constraints and reduce the cost of energy. In [18], the authors worked on minimizing the bill of the residential customers by scheduling the EVs in different modes such as vehicle-to-grid (V2G), vehicle-to-home (V2H) and vehicle-to-neighbour (V2N) in the residential DR environment. The authors focused on smart charging of EVs which can reduce the operating cost of EVs as compared to dumb charging. A few of the researchers also incorporated home energy management systems (HEMS) and intelligent residential energy management systems (IREMS) which are capable enough to automatically schedule the residential loads optimally so as to minimize the customer's electricity consumption cost. In [19] HEMS has been incorporated in the residential environment so as to schedule the home appliances automatically according to the price signals transmitted by the utility. Objective of HEMS is to optimize energy consumption pattern of users in an

efficient way to enhance the customer economic gains. In [20] the combination of PV, EV, ESS, dynamic pricing and peak-limiting DR strategies have been incorporated in presence of HEMS with an aim to reduce the consumer's electricity bill amount. However, in [19, 20], the impact of DR on other shiftable residential loads (washing machines, dish washers, electric cookers and cloth dryers) was not realized which may render less convincing results. Therefore, to obtain more realistic results the above shiftable residential loads needs to be incorporated in this research. In [21] an IREMS has been deployed with an objective to optimally schedule the loads in presence of DR and gain the significant economic benefits for the customers as well as utility. Authors in [22] proposed building energy management system (BEMS) which schedules the resources optimally to maximize the economy of the generated energy as well as to ensure customer's comfort level. To achieve this authors performed simultaneous dispatch of source, load and storage while adopting TOU, a price responsive DRP.

Efficient performance of DR depends on the effective communication between customers and utility. In [4], the authors reviewed the scope of DR globally and proposed the communication based DRP and block tariff scheme depending on the customer's income and load profile so that DR can be efficiently incorporated in the distribution system. Accurate price prediction also alleviates the DR operation as well as financial benefits of customers on electricity bills. In [23], the authors discussed the importance of prediction techniques for day-ahead price prediction. The support vector regression with genetic algorithm (SVRGA) has been proposed which is later compared with linear prediction model (LPM) as well as artificial neural network (ANN) and superiority of SVRGA over the others has been reflected. However, it has been observed that majority of the research is limited to residential sector only which denies the impact of DR on the commercial as well as industrial sector.

A few of the research works associated DR with reliability of the system. It has been observed that reliability of the system tends to improve by adopting DRPs. The efforts were made to optimize the operational cost, customer's payment, and reliability of the network by integrating DRPs with SCUC [24]. In [25], authors investigated the impact of DR on major characteristics of service reliability in a residential distribution network. It was concluded that the energy not served and its associated costs decreases significantly when DRPs were considered. The reliability indices such as EENS, SAIFI, SAIDI, EIC improves as the DR participation increases. Also, considering the fact that EV population will be going to increase in the near future, cost-based sizing and siting problem of the electric vehicle charging stations (EVCS) has been worked upon implementing the incentive-based DRPs [26].

4 Conclusion

This paper discusses the importance of DR in the distribution system. The work presents two different DR implementation techniques and their classifications. The previous and current research works on DR have been studied extensively and their brief review has been reported.

This work also throws some light on the future aspects of DR. It has been observed that majority of the research work for DR has been carried out considering only residential customers, however, it can be extended by considering commercial and industrial customers in the view that these customers would also be capable to penetrate power into the system via DGs and EVs in the near future primarily on the economic basis. Also, the effectiveness of DR has been considered the same for all customers under dynamic price of electricity. However, this cannot be true in practice. A more comprehensive modelling should be developed and investigated by considering annual consumption of customers, as the customers of each income group respond differently, and more precisely all customers of the same income group never respond in a unique fashion toward DR.

Though reduced electricity billing to customers participating in DRPs has been looked as their reward. But, this benefit is on account of sacrificing their comfort, especially during peak load hours. Engineering provides comfort to all living creatures. With this aspect, means should be explored to compensate against the reduced comfort levels of customers by providing monetary reward. The impact of DR may also be investigated in interconnected GENCOS system to have most economic operation in totality. This may not provide most economic operation of individual GENCO for a given hour, but shall provide most economic annual operation of all GENCOS due to the advantage associated with almost constant power dispatches.

References

1. Derakhshan G, Shayanfar HA, Kazemi A (2016) The optimization of demand response programs in smart grids. *Energy Policy* 94:295–306
2. Nan S, Zhou M, Li G (2018) Optimal residential community demand response scheduling in smart grid. *Appl Energy* 210:1280–1289
3. Cecati C, Citro C, Siano P (2011) Combined operations of renewable energy systems and responsive demand in a smart grid. *IEEE Trans Sustain Energy* 2(4):468–476
4. Hussain M, Gao Y (2018) A review of demand response in an efficient smart grid environment. *Electr J* 31(5):55–63
5. Khajavi P, Abniki H, Arani A (2011) The role of incentive based demand response programs in smart grid. In: 2011 10th international conference on environment and electrical engineering (EEEIC). IEEE, pp. 1–4
6. Roscoe AJ, Ault G (2010) Supporting high penetrations of renewable generation via implementation of real-time electricity pricing and demand response. *IET Renew Power Gener* 4(4):369–382
7. Klobasa M (2010) Analysis of demand response and wind integration in Germany's electricity market. *IET Renew Power Gener* 4(1):55–63

8. Zhou X, Shi J, Kang G (2017) Optimal demand response aiming at enhancing the economy of high wind power penetration system. *J Eng* 2017(13):1959–1962
9. Bitaraf H, Rahman S (2018) Reducing curtailed wind energy through energy storage and demand response. *IEEE Trans Sustain Energy* 9(1):228–236
10. Nwulu NI, Xia X (2017) Optimal dispatch for a microgrid incorporating renewables and demand response. *Renew Energy* 101:16–28
11. Aghajani G, Shayanfar H, Shayeghi H (2017) Demand side management in a smart micro-grid in the presence of renewable generation and demand response. *Energy* 126:622–637
12. Solanki BV, Raghurajan A, Bhattacharya K, Canizares CA (2017) Including smart loads for optimal demand response in integrated energy management systems for isolated microgrids. *IEEE Trans Smart Grid* 8(4):1739–1748
13. Alharbi T, Bhattacharya K (2017) Optimal scheduling of energy resources and management of loads in isolated/islanded microgrids. *Can J Electr Comput Eng* 40(4):284–294
14. Vahedipour-Dahraie M, Rashidizadeh-Kermani H, Najafi HR, Anvari-Moghaddam A, Guerrero JM (2017) Stochastic security and risk-constrained scheduling for an autonomous microgrid with demand response and renewable energy resources. *IET Renew Power Gener* 11(14):1812–1821
15. Sousa T, Morais H, Vale Z, Faria P, Soares J (2012) Intelligent energy resource management considering vehicle-to-grid: a simulated annealing approach. *IEEE Trans Smart Grid* 3(1):535–542
16. Soares J, Morais H, Sousa T, Vale Z, Faria P (2013) Day-ahead resource scheduling including demand response for electric vehicles. *IEEE Trans Smart Grid* 4(1):596–605
17. Yang Q, Fang X (2017) Demand response under real-time pricing for domestic households with renewable dgs and storage. *IET Gener Transm Distrib* 11(8):1910–1918
18. Pal S, Kumar R (2018) Electric vehicle scheduling strategy in residential demand response programs with neighbor connection. *IEEE Trans Ind Inform* 14(3):980–988
19. Ghazvini MAF, Soares J, Abrishambaf O, Castro R, Vale Z (2017) Demand response implementation in smart households. *Energy Build* 143:129–148
20. Erdinc O, Paterakis NG, Mendes TD, Bakirtzis AG, Catalão JP (2015) Smart household operation considering bi-directional EV and ESS utilization by real-time pricing-based DR. *IEEE Trans Smart Grid* 6(3):1281–1291
21. Arun S, Selvan M (2018) Intelligent residential energy management system for dynamic demand response in smart buildings. *IEEE Syst J* 12(2):1329–1340
22. Wang F, Zhou L, Ren H, Liu X, Talari S, Shafie-khah M, Catalão JP (2018) Multi-objective optimization model of source-load-storage synergetic dispatch for a building energy management system based on tou price demand response. *IEEE Trans Ind Appl* 54(2):1017–1028
23. Pal S, Kumar R (2016) Price prediction techniques for residential demand response using support vector regression. In: 2016 IEEE 7th power India international conference (PIICON). IEEE, pp. 1–6
24. Dadkhah A, Vahidi B (2017) On the network economic, technical and reliability characteristics improvement through demand-response implementation considering consumers' behaviour. *IET Gener Transm Distrib* 12(2):431–440
25. Safdarian A, Degefa MZ, Lehtonen M, Fotuhi-Firuzabad M (2014) Distribution network reliability improvements in presence of demand response. *IET Gener Transm Distrib* 8(12):2027–2035
26. Simorgh H, Doagou-Mojarrad H, Razmi H, Gharehpetian GB (2017) Cost-based optimal siting and sizing of electric vehicle charging stations considering demand response programmes. *IET Gener Transm Distrib* 12(8):1712–1720

Stochastic Operational Management of Grid-Connected Microgrid Under Uncertainty of Renewable Resources and Load Demand



Sonam Parashar, Anil Swarnkar, K. R. Niazi and Nikhil Gupta

Abstract This work presents the operational management of microgrid under intermittency of non-dispatchable DGs and load. A single bus AC microgrid installed with a mix of dispatchable and non-dispatchable DGs is considered as a test system. A new stochastic approach is proposed to capture the randomness of the non-dispatchable DGs. A short-term operational problem for microgrids is formulated and solved by using Modified Elephant Herding Optimization (MEHO). The results obtained by implementing the proposed stochastic approach are presented, analyzed, and compared with the deterministic approach and the significant effects on the operational management of the microgrid are manifested.

Keywords Wind power · PV power · Battery energy storage · Stochastic modeling · Modified Elephant Herding Optimization (MEHO)

1 Introduction

Operational management of microgrids is an important issue in achieving various techno-economic challenges. Operational management of microgrids is widely focused on the scheduling of the available generating sources following the load demand of the system over a finite time horizon. The increasing non-dispatchable DGs penetration creates an uncertain environment for microgrid operational management. It is a very challenging task for a system operator to take various planning

S. Parashar (✉) · A. Swarnkar · K. R. Niazi · N. Gupta
Malaviya National Institute of Technology, Jaipur, India
e-mail: sonam_ee@yahoo.com

A. Swarnkar
e-mail: mnit.anil@gmail.com

K. R. Niazi
e-mail: krn152001@yahoo.co.in

N. Gupta
e-mail: nikhil2007_mnit@yahoo.com

and operational decisions under the uncertainty or without knowing the information about the power generation and consumer load. The uncertain generation and load may create some serious technical and economical disasters in operation management of microgrids such as mismatch of demand and generation, mismatch of frequency, and economic losses. Thus, it is necessary to model the uncertainty of the intermittent generation and load for the smooth operation of microgrids and to achieve various techno-economic and environmental benefits. In the literature, deterministic scheduling of microgrids is widely attempted using traditional optimization techniques and various evolutionary computation such as Genetic Algorithm (GA), Particle Swarm Optimization (PSO), Improved Bat Algorithm (IBA), Gray Wolf Optimization (GWO), and Modified Elephant Herding Optimization (MEHO) [1–7]. However, it has been noticed that very less work is reported on stochastic or probabilistic scheduling of the microgrid. Stochastic scheduling of the microgrid is attempted, where expected total cost of the microgrid is minimized for all generated scenarios; these scenarios are obtained by modeling of uncertain data of intermittent sources [8–11]. A probabilistic constrained approach is implemented in [12] to capture the randomness of renewable resources and load. Some other methods are also available in the literature to model the uncertain renewable sources and wind power [13–15]. Chen et al. implemented time series and FNN to model the wind and solar power [13]. A probabilistic scenario generation with roulette wheel selection is presented to forecast the renewable resources and load demand for the volt/VAR planning of microgrids [14]. A probabilistic approach using probabilistic distribution function is used to model uncertain wind and solar power [15]. It has been observed from the literature that the probabilistic scenario generation and reduction methods are widely used to capture the uncertainty of the renewables. These methods require a lot of computational efforts and may be less efficient. By addressing these shortcomings, a new stochastic model is proposed in this paper to model the uncertain renewable generation and load demand that requires less computational efforts and will be more efficient with higher probability to reach the realistic renewable generation and load demand scenario. Also, a recently proposed optimization technique, MEHO is explored to solve the problem.

2 Stochastic Modeling of Renewable Generation and System Load

2.1 Stochastic Modeling of Wind Power Generation

Wind speed is uncertain and varies with different geographical conditions. It is a random variable following a certain type of probabilistic density function (PDF). Generally, wind speed follows Weibull distribution function [9, 14, 15]. In this work, an hourly stochastic wind power generation is modeled using Weibull distribution function which is a well-fitted PDF for wind speed and is given below:

$$F(v) = \frac{B}{A} \left(\frac{v}{A}\right)^{B-1} e^{-\left(\frac{v}{A}\right)^B} \tag{1}$$

where A and B are the shape index and scale index, respectively. v is the random variable representing wind speed.

Weibull PDF is fitted to an hourly annual historical data [14] to obtain shape and scale index parameters. The N_w no. of random samples using Eq. (1) for each hour are drawn for wind speed. The hourly wind power generation for each sample is calculated using piecewise function given below.

$$P_{w,t} = \begin{cases} 0 & v_t < v_{in} \text{ OR } v_t > v_{out} \\ P_{wr,t} \times \frac{(v_t - v_{in})}{(v_r - v_{in})} & v_{in} \leq v_t \leq v_r \\ P_{wr,t} & v_r \leq v_t \leq v_{out} \end{cases} \tag{2}$$

where $P_{w,t}$ and $P_{wr,t}$ are the forecasted and rated wind power at time t , respectively. v_{in} , v_{out} , v_r , and v_t are the cut-in, cut-out, rated, and forecasted wind speed.

A set of wind power generation called wind power scenarios ($P_w \in N_w$) for each N_w sample is obtained having ($\rho_w \in N_w$) probabilities.

2.2 Stochastic Modeling of PV Power Generation

Mainly, solar irradiation is modeled using Normal or Gaussian distribution function [14]. In this paper, solar irradiation is modeled as Normal distribution function and is shown by

$$F(x) = \frac{1}{\sqrt{2\pi\sigma^2}} e^{-\frac{(x-\mu)^2}{2\sigma^2}} \tag{3}$$

where x is a random variable denoting variable solar radiation to be modeled, μ and σ are the mean and standard deviation of the solar irradiation historical data, respectively.

The Normal PDF is fitted to the hourly annual solar irradiation data. Also, the hourly mean and standard deviation are calculated from the historical data. The N_{PV} random samples are drawn for each hour using Eq. (3). The hourly PV power is calculated using Eq. (4).

$$P_{pv,t} = \eta \times S \times x \times L \tag{4}$$

where $P_{pv,t}$ is the hourly PV power output η (%) is the efficiency of the solar cell array, S is the area of the array in m^2 , and L is the power loss coefficient.

A set of PV power generation called PV power scenarios ($P_{pv} \in N_{pv}$) for each N_{pv} sample is obtained having ($\rho_v \in N_{pv}$) probabilities.

2.3 Stochastic Modeling of System Load Demand

The system load demand is also modeled as a Normal PDF as discussed in the previous section. An hourly load (P_d, t) is modeled having N_D random samples drawn from Eq. (4) ($P_d \in N_d$) with corresponding probabilities ($\rho_d \in N_d$).

2.4 Combined Stochastic Modeling of the System

As discussed in the previous sections, for each hour, wind power, solar power, and load demand have forecasted scenarios or set of values namely $P_{w,t}$, $P_{pv,t}$ and $P_{d,t}$, respectively, with corresponding probabilities ρ_w , ρ_{pv} and ρ_d . Thus, the modeled system will have $N_w \times N_{pv} \times N_d$ possible scenario states with a probability of $\rho_w \times \rho_{pv} \times \rho_d$ for each hour. In this study, equal number of random samples are considered for wind, PV, and load, i.e., $N_w = N_{pv} = N_d = 365$.

2.5 Tournament Selection Based Scenarios Sampling

In this work, Tournament selection method is used for the scenarios sampling. Tournament selection method is a probabilistic method and chooses the most probabilistic scenario state from the pool of the competitor scenarios states. This method is a more accurate method as compared to the other scenario sampling methods available in the literature [8, 9, 15]. The method calculates the combined probability of the randomly selected independent events and chooses the most probabilistic individual scenario states as an outcome. From the previous sections, hourly scenarios and possible states of the whole system are obtained for 24 h. Each hour has a number of scenarios and $N_w \times N_{pv} \times N_d$ possible states with corresponding probabilities. The Tournament selection method randomly selects the hourly possible states [$P_{w,t}$, $P_{pv,t}$, $P_{d,t}$] and calculates their corresponding combined probability $\rho_w \times \rho_{pv} \times \rho_d$. The scenario state having the highest probability is chosen as the forecast of wind power, solar power, and load demand.

3 Problem Formulation

3.1 Objective Function

The objective of the operational management of microgrid is to minimize the total cost of the microgrid. Hence, the objective function for the operational management problem of the microgrid for a time horizon T may be defined as

$$\text{minimize TC} = \sum_{t=1}^T \left[\sum_i [(a_i + (b_i \times P_{i,t}))] + \sum_n C_n \times P_{n,t} + \sum_j C_j \times P_{j,t} + \sum_i \text{SUC}_{i,t} + \text{SDC}_{i,t} \right] + C_{\text{grid},t} \times P_{t,\text{grid}} \tag{5}$$

where TC is the total cost of the microgrid in \$, a and b are the cost coefficients of dispatchable DGs, C_n and C_j are the cost coefficients in \$/kW of the non-dispatchable DGs and battery energy storage, respectively; $C_{\text{grid},t}$ is the hourly grid price in \$/kW, $P_{i,t}$, $P_{n,t}$, $P_{j,t}$ and $P_{\text{grid},t}$ are the output power of the dispatchable DGs non-dispatchable DGs and battery energy storage at t th hour and hourly exchange of power from utility grid, respectively. $\text{SUC}_{i,t}$ and $\text{SDC}_{i,t}$ are the start-up cost and shut-down cost of the dispatchable DGs at t th hour, respectively.

3.2 Constraints

1. Power balancing constraints: The constraint ensures that at each hour, the total generation of the system including the generation from dispatchable DGs, non-dispatchable DGs, and battery energy storage should be equal to the system load demand.

$$P_{\text{gen},t} = P_{\text{load},t} \tag{6}$$

where $P_{\text{gen},t} = P_{i,t} + P_{n,t} + P_{j,t} + P_{\text{grid},t}$.

2. State of Charge (SOC) constraints of battery energy storage: At each hour, SOC of the BES should remain in predefined limits for the satisfactory operation and longevity of BES.

$$\text{SOC}_{j,t}^{\min} < \text{SOC}_{j,t} < \text{SOC}_{j,t}^{\max} \tag{7}$$

where SOC is the state of charge of BES.

Also, SOC of the battery at each hour can be calculated using Eqs. (8–9)

$$\text{Charging state : } \text{SOC}_j(t + 1) = \text{SOC}_j(t) + \Delta t \times (P_{j,t}) \times \eta_c \tag{8}$$

$$\text{Discharging state : } \text{SOC}_j(t + 1) = \text{SOC}_j(t) - \frac{(\Delta t \times (P_{j,t}))}{\eta_d} \tag{9}$$

where η_c and η_d are the charging and discharging efficiency of BES.

3. Power limiting constraint: The power output of each DG, BES, and utility grid should be in a predefined limit.

$$P_{i,t}^{\min} < P_{i,t} < P_{i,t}^{\max} \tag{10}$$

$$P_{j,t}^{\min} < P_{j,t} < P_{j,t}^{\max} \tag{11}$$

$$P_{\text{grid},t}^{\min} < P_{\text{grid},t} < P_{\text{grid},t}^{\max} \tag{12}$$

4 Solution Methodology

In this work, the Modified Elephant Herding Optimization (MEHO) algorithm is implemented to solve the problem formulated in Sect. 3.1. MEHO is a recently proposed optimization algorithm [6] that suggests some modifications in Elephant Herding Optimization introduced by Wang et al. [5]. The algorithm is modeled by capturing the behavior of the herd of the elephants having different clans where each clan is lead and followed by its matriarch and their calves, respectively, and it is capable to solve such type of real-word complex problems and is imposed by many equality, inequality, and dynamic constraints.

5 Simulation Results and Discussion

In this work, a single-bus grid-connected AC microgrid is considered which is installed with Microturbine (MT), Fuel Cell (FC), Wind Turbine (WT), Solar (PV), and a Lithium Ion Battery Energy Storage (BES). The energy rating of BES is 1000 Kwh, η_c and η_d are taken as 0.9. The depth of discharge of BES is assumed as 90%. Initially, BES is assumed to be fully charged. The various cost coefficients and power limits of the considered Distributed Energy Resources (DERs) are shown in Table 1 [11, 13].

The parameters of the WT are $P_{wr} = 1000$ kW, $v_{in} = 3$ m/s, $v_{out} = 30$ m/s, and $v_r = 12$ m/s. The parameters of the PV source are $\eta = 15.7\%$, $L = 0.75$, and $S = 7000$ m².

Table 1 Distributed generator, BES, and utility grid data

S. no.	Type	Min. power (kW)	Max. power (kW)	Bid (\$/Kw)	a (\$/Kw)	b (\$/Kw)	Startup/shutdown cost (\$)
1.	MT	100	3000	–	30	0.13	150
2.	FC	100	1000	–	80	0.50	30
3.	WT	–	–	0.082	–	–	–
4.	PV	–	–	0.122	–	–	–
5.	BES	–500	500	0.07	–	–	–
6.	Utility grid	–1000	1000	–	–	–	–

The system has a peak load of 4000 kW. The Time of Use (TOU) grid prices for selling and purchasing the power to/from the utility grid are considered as 0.055\$/kWh (if load factor ≤ 0.5), 0.072 \$/Kwh (if $0.5 < \text{load factor} \leq 0.75$) and 0.122 \$/kWh (if load factor > 0.75). It is assumed that non-dispatchable DGs are always in on state and generate the forecasted power. Figure 1a shows the deterministic output power of the wind and PV [14]. Figure 1b shows the deterministic load factor of the load demand for the considered system [15].

In order to study the stochastic scheduling over the deterministic scheduling of grid-connected microgrid, the test system discussed above is considered. A Modified Elephant Herding Pptimization algorithm is implemented to solve the formulated problem for two types of scheduling, i.e., deterministic scheduling and stochastic scheduling. The parameters of MEHO, α and β are set to 0.8 and 0.1, respectively. The population of elephants in a clan is taken as 60, and the maximum number of iterations is considered as termination criterion which is set to 30. The wind power, PV power, and load demand of the system are forecasted using the proposed stochastic approach discussed in Sect. 2 and are shown in Fig. 2a and Fig. 2b, respectively.

Figure 3 shows the comparison of the total cost of the microgrid obtained after minimizing the formulated objective function in Sect. 3.1. Figure 4a and Figure 4b shows the deterministic and stochastic scheduling of the microgrid, respectively.

It has been observed from Fig. 3 that the stochastic scheduling manifested the significant effects on daily scheduling of the microgrid as a reduction in TC by 15.65% in stochastic scheduling over deterministic scheduling is noticed which is worthy of attention for operational planning of the microgrid.

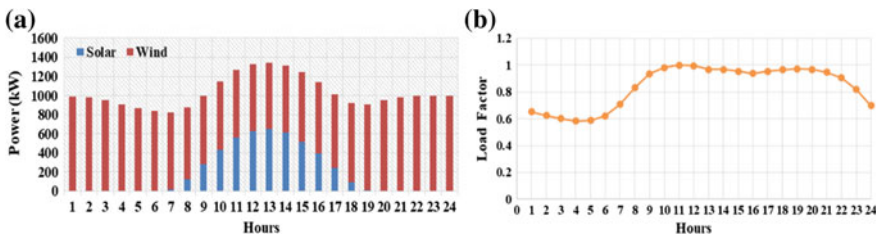


Fig. 1 a Deterministic PV and wind power b Deterministic load factor of the system

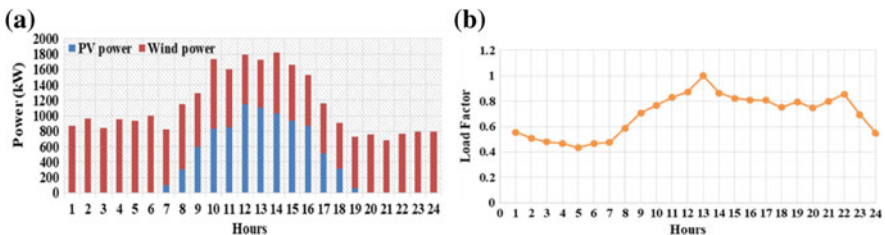


Fig. 2 a Forecasted PV and wind power b Stochastic load factor of the system

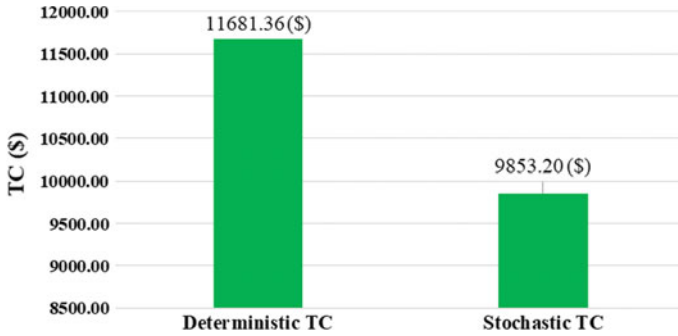


Fig. 3 Cost comparison of TC

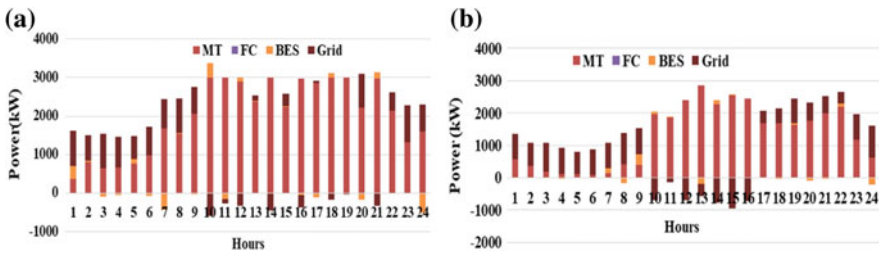


Fig. 4 a Deterministic scheduling of DERs and utility grid b Stochastic scheduling of DERs and utility grid

6 Conclusion

In this work, stochastic scheduling of microgrid is presented. A new stochastic model to predict the uncertain renewable resources and system load demand is developed and discussed. A recently proposed optimization technique MEHO is explored to solve the formulated problem. The study reveals a significant impact of stochastic scheduling over the deterministic scheduling which results in a noteworthy reduction in the total cost of the microgrid. It may be concluded that the proposed stochastic model can forecast more realistic renewable generation and load demand that may be very useful for better decision-making for optimal operational management strategies of microgrid.

References

1. Liyuan P, Ruihuan L, Fen Z (2014) Study on economic operation for micro-grid based on scenario and PSO. In: IEEE international conference on power system technology. POWERCON, Chengdu, China
2. Ahn S-Ju, Nam S-R, Choi J-H, Moon S-II (2013) Power scheduling of distributed generators for economic and stable operation of a microgrid. *IEEE Trans Smart Grid* 4(1):398–405
3. Zhao B, Shi Y, Dong X (2014) Short-term operation scheduling in renewable-powered microgrids: a duality-based approach. *IEEE Trans Sustain Energy* 5(1):209–217
4. Khodaei A (2014) Microgrid optimal scheduling with multi-Period islanding constraints. *IEEE Trans Power Syst* 29(3):1383–1392
5. Wang GG, Deb S, Coelho LDS (2015) Elephant herding optimization. In: Proceedings of 3rd international symposium on computational and business intelligence. Bali, Indonesia, pp 1–5
6. Parashar S, Swarnkar A, Niazi KR, Gupta N (2017) Modified elephant herding optimisation for economic generation co-ordination of DERs and BESS in grid connected micro-grid. *J Eng* 2017(13):1969–1973
7. Parashar S, Swarnkar A, Gupta N, Niazi KR (2017) An efficient AI-based approach for dynamic scheduling of grid connected microgrid. In: International conference on advanced computing and communication systems IEEE. Coimbatore, India
8. Su W, Wang J, Roh J (2014) Stochastic energy scheduling in microgrids with intermittent renewable energy resources. *IEEE Trans Smart Grid* 5(4):1876–1883
9. Talari S, Yazdanejad M, Haghifam M (2015) Stochastic-based scheduling of the microgrid operation including wind turbines, photovoltaic cells, energy storages and responsive loads. *IET Gener Transm Distrib* 9(12):1498–1509
10. Gholami A, Shekari T, Aminifar F, Shahidehpour M (2016) Microgrid scheduling with uncertainty: the quest for resilience. *IEEE Trans Smart Grid* 7(6):2849–2858
11. Farzin H, Firuzabad MF, Aghtaie MM (2017) Stochastic energy management of microgrids during unscheduled islanding period. *IEEE Trans Ind Inf* 13(3):1079–1087
12. Nguyen TA, Crow ML (2016) Stochastic optimization of renewable-based microgrid operation incorporating battery operating cost. *IEEE Trans Power Syst* 31(3):2289–2296
13. Chen SX, Gooi HB, Wang MQ (2012) Sizing of energy storage for microgrids. *IEEE Trans Smart Grid* 3(1):142–151
14. Meena NK, Swarnkar A, Gupta N, Niazi KR (2016) Stochastic volt/var planning and operation for microgrids with renewable. *Int J Electr Energy* 4(3):159–164
15. Atwa YM, El-Saadany EF, Salama MMA, Seethapathy R (2010) Optimal renewable resources mix for distribution system energy loss minimization. *IEEE Trans Power Syst* 25(1):360–370

Real-Time High-Speed Novel Data Acquisition System Based on ZYNQ



Himanshu Tyagi, Nagendra P. Gajjar, Mainak Bandyopadhyay
and Arun Chakraborty

Abstract Continuous acquisition along with streaming of analog signals at high sampling rates of order of 100 MS/s is a difficult task due to both memory and network bottlenecks. At such high sampling rates the data acquisition system follows the model of storing and forwarding the data. This needs large size on board memory. Commercially available platforms are not only quite expensive but also provide limited configuration freedom to the end developers. In order to develop a custom data acquisition device, a platform with high-speed ADCs, large onboard RAM, and embedded controller is needed. Presently, Xilinx ZYNQ offers a system on chip (SOC) based solution with strongly coupled ARM processor and FPGA. The benefit of such architecture is that the processor can handle configuration management and the FPGA can be available for handling critical time-bound tasks. The present work focuses on development of continuous high-speed acquisition system based on Zynq SOC with user-configurable options. For development of the prototype, Zynq board with two onboard ADC modules and 512 MB RAM is selected. The ADCs although support maximum sampling up to 125 MS/s, acquisition at such high rate will lead to large file sizes which will be difficult to handle and analyze. The developed system is developed for two modes, offline acquisition and live streaming over Ethernet interface. In the offline mode, the acquisition will operate at highest sampling rate of 125 Ms/s and the file will be saved locally on the Linux OS on ZYNQ. In run time streaming, the data will be transferred over the Ethernet interface to a host system. In this mode, the data is saved in chunks which are defined by the client software. In continuous streaming of data to host, the effective sampling rates were found to be of order of 30 MSps. The server program is being performed using a C program which communicates to the ARM processor. The client program is developed using

H. Tyagi (✉) · N. P. Gajjar
Institute of Technology, Nirma University, Ahmedabad, India
e-mail: 16mecrex01@nirmauni.ac.in

H. Tyagi · M. Bandyopadhyay · A. Chakraborty
ITER-India, Institute for Plasma Research, Gandhinagar, India

© Springer Nature Singapore Pte Ltd. 2020
A. Kalam et al. (eds.), *Intelligent Computing Techniques for Smart Energy Systems*,
Lecture Notes in Electrical Engineering 607,
https://doi.org/10.1007/978-981-15-0214-9_61

Python open-source libraries with Qt-based GUI. In this paper, the details of the system design, architecture, benchmarking, software flow, and analysis of results are mentioned.

Keywords SoC · ZYNQ · FPGA · Data acquisition

1 Introduction

Data acquisition systems are important for any experimental system in order to characterize the physical events. High-speed acquisition is needed in multiple areas where signal of interest has high-frequency contents such as optical signals and spectroscopic signals. Some of the areas are physics-based diagnostics [1], wireless systems [2], and many other areas.

Development of any such acquisition system needs three primary components, namely ADCs, memory, and a controller. The controller must be efficient enough to provide the requisite signals to ADC and memory so that the operation of sampling and storing the data sample is performed within required time. Another paradigm is the software interface in the DA systems which act as an interface for passing on the configuration parameters and acquired data. In present work, the focus has been laid to develop the software interface based on open-source programming languages such as C and Python. The server application is developed on C and the client interface is based on Python.

Commercial platforms based on LXI [3], PCI [4] interface are available at lower sampling rates and are expensive. One of the main motivations of present work is to develop a better and configurable system at low cost.

The present work is focused on developing a low-cost configurable data acquisition system (DAS) which can be widely adopted for diagnostic applications. The paper is organized as follows: Sect. 2 covers the hardware details and comparison with commercial solutions, Sect. 3 covers the block diagram details of the developed DAS, and Sect. 4 covers the operational flow and software interface of the DAS. Sections 5 and 6 provide the results and conclude the paper.

2 Overview of the Hardware Platform and Contemporary Solutions

In order to achieve the required parameters for the developed DAS, the first step is to identify the correct platform for development. Figure 1 shows the block diagram of a generic DAS. For this purpose, a variety of ADC module and embedded platforms were studied. ZYNQ was selected as the embedded platform. ZYNQ is presently latest family of FPGA-based embedded platforms launched by Xilinx and has extended the amalgamation of FPGA and processor. In earlier available families

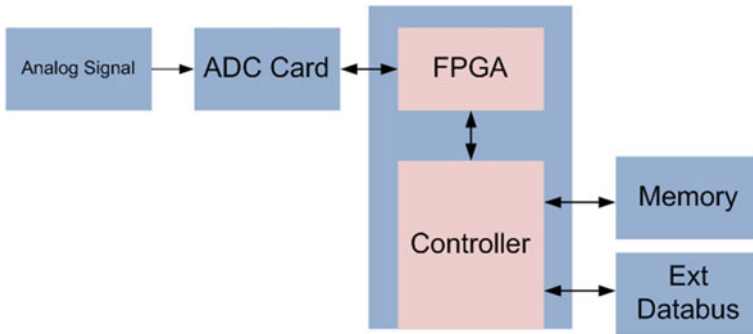


Fig. 1 Generic data acquisition system

of FPGA, the concept of soft processor in form of Microblaze was generally used when the developer felt the need. With the induction of hard processor in silica, the interface is more rugged and supports high speed transfers.

In terms of the front end component, the ADC module determines the maximum sampling speed achievable by the system. For the current development, ADC LTC2145-14 [5] was selected which supports two channels with 14 bit resolution and simultaneous sampling up to 125 MSps. The data from ADC is transferred to the processor via AXI interface [6]. For the development, Red Pitaya [7] based developmental board was selected. Red Pitaya platform supports all the needed features such as ZYNQ controller, high-speed ADCs, and 4 GB of onboard RAM. Hence, it provides all the resources for developing the targeted application. It has a Linux interface and can be controlled/accessed by USB and Ethernet via SSH protocol. The user can develop custom logic for the FPGA and interface it with the ARM controller as per application requirement. The user can take benefit of the SOC architecture and utilize the available analog front end resources for various engineering applications. The most important aspect of SOC development is utilizing AXI bus interface.

In terms of available platforms, LXI and PCI interfaces are available but at lower sampling rates. Agilent platform with LXI [8] supports up to 20 MSps sampling rate only. NI PCR R [9] series digitizer card although supports 100 MSps sampling but is quite expensive.

Some previous solution developed based on FPGA such as [10, 11] had some limitations in terms of configurability and lack of client interface.

3 Firmware Design of Data Acquisition System

Figure 2 depicts the overall design implemented in the PL and PS side. With the introduction of IP integrator [12] in Vivado, the practice of creating custom IPs for each function and then integrating them in the main block diagram has made hardware programming more efficient and fast. Each block is written in Verilog and

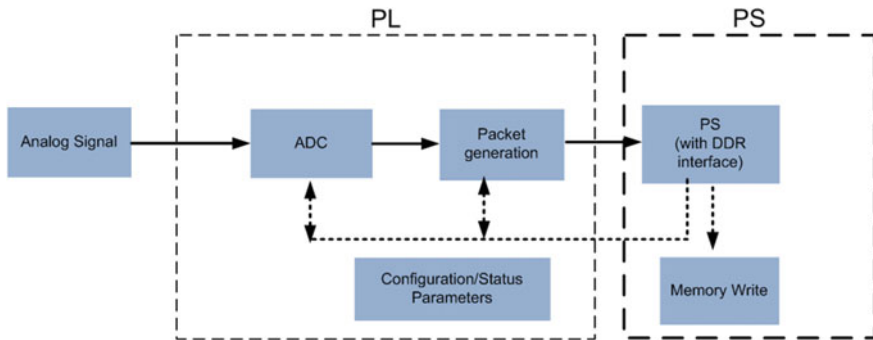


Fig. 2 Hardware design within the PL and PS part of ZYNQ

customized as an IP package. After dividing the functions to be implemented in PL and PS, the development can be initiated. As shown in Fig. 2, the PL is responsible for interfacing the ADC with the required timing signals and streaming the data with AXI stream bus to an encapsulating IP where the data is transferred to the PS side. The ADC block is written with the help of IP manager and code reference from [13, 14] is taken with necessary modifications as required from targeted application.

The PS then transfers the data to onboard memory which is read by the C-based server program. The PS is also responsible for transferring configuration parameters from client side and allocating the memory size of the block to be read at each instance. In the development, two modes were followed

- Standalone Mode: Here, the client program is specifying the memory size to be acquired and the file is created locally on the Zynq platform itself. The file is later retrieved to the host system for analysis.
- Streaming mode: In this mode, the client specifies the size of chunk and number of chunks to be acquired. The data is then transferred over TCP/IP to client and saved on host system. In this case, the network acts as a bottleneck.

The detail of operational flow is described in Sect. 4.

4 Software Interface for Data Acquisition System

The highest available sampling rates are 125 MSps and at such rate, standard available instrumentation bus interfaces are not capable of transferring data. Considering each sample of 14 bits each,

Net throughput is $14 \times 125 \times 10^6 = 1.75 \times 10^9$ bit/s

Available capacity of 1 Gbps Ethernet = 1.07×10^9 bit/s

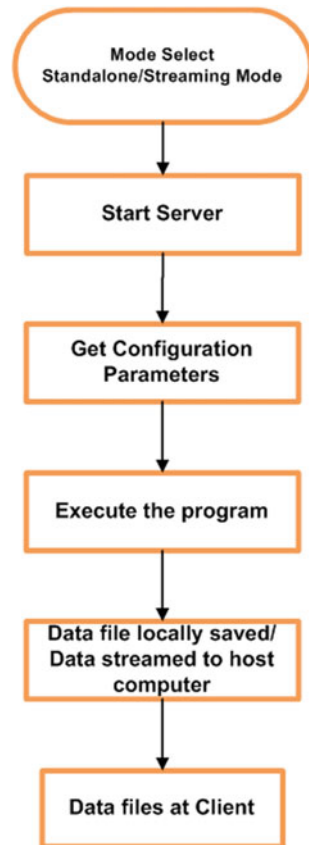
The above calculations point to the limitation posed by real-time streaming over Ethernet interface. This is called for defining two operating modes of the developed DAS.

Figure 3 shows the overall flowchart of the software flow. The operational mode is selected at the beginning which programs the required bit file in FPGA. After the C-based server program is executed, it waits for the configuration parameters from client interface. The client program was developed using simple C program and Python with Qt [15] GUI interface.

The configuration parameters are different for standalone mode and streaming mode. For streaming mode, the packet size is fixed which is transferred as a TCP/IP packet to the host system. The numbers of packets are configured at client side after which the connection is terminated and server goes in waiting mode. Since the data is streamed, the network acts as an averaging system and limits the data transfer rate. From practical observations, the data rate is observed at ~30 MS/s. Hence for streaming mode, the maximum supported analog bandwidth is of order of 10 MHz which is a significant bandwidth.

For standalone mode, the data buffer size is decided by client varying from 1 to 10 MS which gives the duration of acquisition as 8–80 ms. Larger size files can also be created depending upon the need of experiment.

Fig. 3 Flowchart of process within the processor



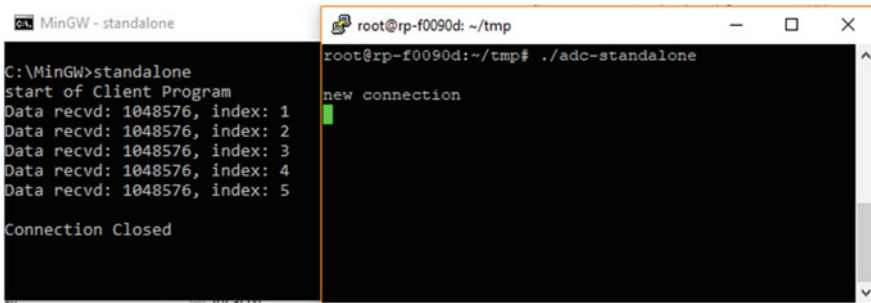


Fig. 4 Client-server communication on terminal

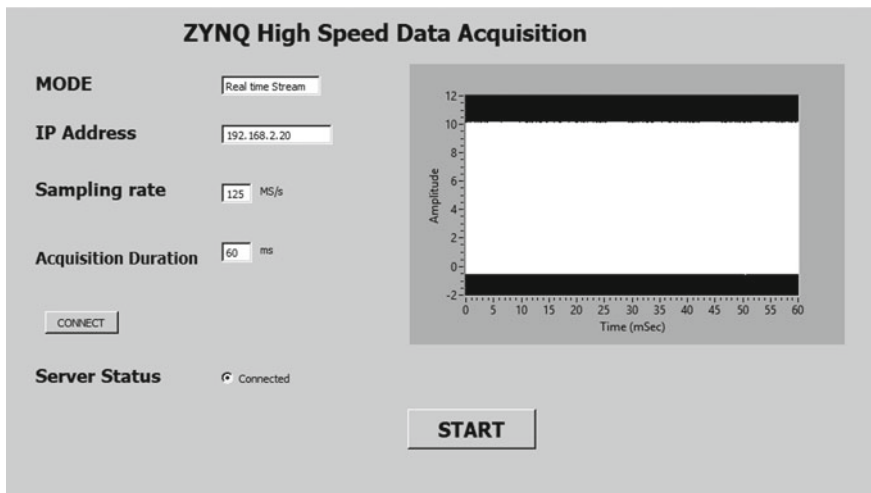


Fig. 5 Python-based GUI for client application

Figure 4 shows the client and server communication together. 1 MS size of data is received at client side with five different chunks. Figure 5 shows the Qt-based GUI developed with Python in back end. The data received from the server is saved to a file and retrieved in the GUI.

5 Results and Discussion

Figure 5 shows the acquired data plotted in Python-based GUI. The data in standalone mode was captured at full rate at various buffer sizes. Coming to the file storage options, binary and text are widely used formats. Test file although human readable occupy larger footprint for storage. Binary files on other hand allow for lesser size

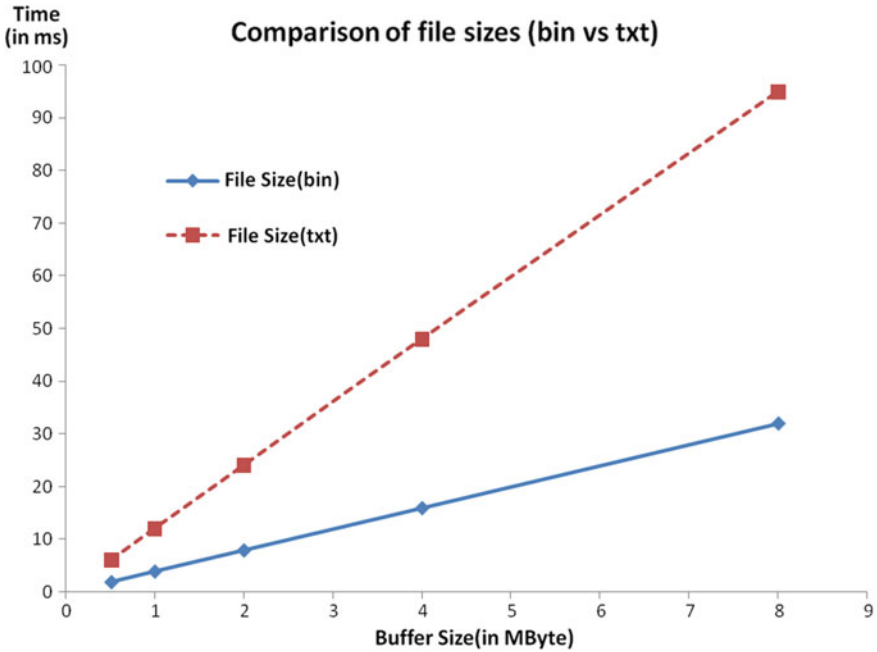


Fig. 6 File comparison for bin and text formats

footprint but are not readable by humans. During the development of present work, the file formats were compared in terms of their footprints for various buffer sizes. A clear advantage of binary files is observed as shown in Fig. 6. The files were written using `fprintf()` and `fwrite()` functions available in C language.

The `fwrite()` function logs the entire data block at once from one memory location to another instantly while the `fprintf()` function works in a serial manner.

6 Conclusion

The present work was motivated from exploring advance features of ZYNQ architecture for applications to the area of fast data acquisition. The work covered the development of client-server interface for a system on chip-based solution for data acquisition requirements. This also establishes the usage of ZYNQ platform for variety of applications

References

1. Wojenski1a A, Pozniaka K (2015) Fast data acquisition measurement system for plasma diagnostics using GEM detectors. In: First EPs conference on plasma diagnostics—1st ECPD
2. Zheng W (2014) Design of FPGA based high-speed data acquisition and real-time data processing system on J-TEXT tokamak. *Fusion Eng Des* 89(6):698–701
3. LXI interface. <http://www.lxistandard.org/about/LXI-Core-Features.aspx>. Accessed 15 Sept 2018
4. PXI interface. <https://www.electronics-notes.com/articles/test-methods/pxi/pxi.php>. Accessed 15 Sept 2018
5. LTC2145-14 ADC, ADC LTC. <http://www.analog.com/en/products/ltc2145-14.html>. Accessed 15 Sept 2018
6. AXI, ARM, AMBA AXI and ACE Protocol Specification: AXI3, AXI4, and AXI-Lite, ACE and ACE-Lit. <http://www.arm.com/products/system-ip/amba/>. Accessed 15 Sept 2018
7. RED Pitaya, RedPitaya, RedPitaya Open Source Instrument. <http://www.redpitaya.com/>. Accessed 15 Sept 2018
8. LXI interface platform. <https://www.keysight.com/en/pc-100000676%3Aeeps%3Apgr/data-acquisition-daq?nid=-33257.0&cc=IN&lc=eng>. Accessed 15 Sept 2018
9. NI R series cards. <http://sine.ni.com/nips/cds/view/p/lang/en/nid/13897>. Accessed 15 Sept 2018
10. Khedkar AA, Khade RH (2017) High speed FPGA-based data acquisition system. *Microprocess Microsyst* 49:87–94
11. Kandadai V, Sridharan M (2017) A comprehensive embedded solution for data acquisition and communication using FPGA. *J Appl Res Technol* 15:45–53
12. IP integrator. <https://www.xilinx.com/products/design-tools/vivado/quicktake-videos/using-ip-integrator.html>. Accessed 15 Sept 2018
13. Potonik A, Red pitaya FPGA project 4. <http://antonpotocnik.com/?p=519284>. Accessed 15 Sept 2018
14. <http://pavel-demin.github.io/red-pitaya-notes/>. Accessed 15 Sept 2018
15. QT. <https://www.qt.io/>. Accessed 15 Sept 2018

Exergetic Analysis of Glazed Photovoltaic Thermal (Single-Channel) Module Using Whale Optimization Algorithm and Genetic Algorithm



Sourav Diwania, Anmol Gupta, Anwar S. Siddiqui and Sanjay Agrawal

Abstract Photovoltaic thermal (PV-T) system gains greater attention in the last four decades because of its quality to produce both electrical and thermal energy simultaneously and unites the electrical and thermal components in a single unit over the conventional photovoltaic system and solar thermal system which are capable of producing electricity and thermal energy, respectively. There are various parameters which affects the performance of the PV-T system such as dimensions of the channel (duct), depth of the tedlar, thickness of insulation layer, solar cell fabrication technology, velocity of fluid flowing through the channel, temperature of the fluid at the inlet and outlet of the channel ,and cell temperature but in this paper, only four of the above parameters have been considered for optimization study. But in the proposed work, only four parameters such as air channel length (L_M), depth of the air duct (d), fluid velocity through the duct (V_F), and temperature of the air at the inlet of duct (T_{in}) have been considered for optimization using two dissimilar optimization algorithms such as whale optimization algorithm (WOA) and genetic algorithm (GA). The outcomes show that an improvement around 31.147% in exergy efficiency and 41.29% in thermal efficiency of glazed PV-T (single-channel) module is observed using WOA technique when compared with GA. Furthermore, WOA is better in contrast to GA because of faster rate of convergence in identifying the parameters.

Keywords Exergy efficiency · Photovoltaic thermal (PV-T) · Whale optimization algorithm (WOA)

S. Diwania (✉) · A. S. Siddiqui
Department of Electrical Engineering, JMI, New Delhi 110025, India
e-mail: souravdiwania123@gmail.com

A. Gupta
Department of Electrical and Electronics Engineering, KIET, Ghaziabad 201206, India

S. Agrawal
SOET, IGNOU, New Delhi 110068, India

© Springer Nature Singapore Pte Ltd. 2020
A. Kalam et al. (eds.), *Intelligent Computing Techniques for Smart Energy Systems*,
Lecture Notes in Electrical Engineering 607,
https://doi.org/10.1007/978-981-15-0214-9_62

1 Introduction

In today's scenario, the demand for renewable energy is increasing day by day because the energy generated from conventional energy sources is not pollution-free. Apart from all the renewable energy sources available, solar photovoltaic is most popular because of the availability of sunlight in most part of the globe. A PV system converts sunlight into electricity while solar thermal converts sunlight into heat, but a PV-T system converts sunlight into heat and electricity simultaneously. A channel or duct is used below the PV panel in which air/water is used as a circulating fluid or cooling medium to assimilate the heat energy from the PV panel by conductive or convective process in order to enhance the electrical efficiency of the system. It was reported in the literature that electrical efficiency of the solar cell decreases with increase in temperature of upper surface of solar cell. The crucial factor about the popularity of PV-T collector is the low efficiency of the solar cell that varies from 6 to 16% at the temperature of 25 °C but in some of the countries the ambient temperature rises up to 35 °C. The rising of temperature decreases the module efficiency therefore, the extraction of heat energy from the backend surface of PV module is necessary. Depending upon the type of cooling medium, PV-T system is classified as PV-T air collector, PV-T water collector, and PV-T combi system in which both air and water are used as cooling medium. From the last three decades, a lot of research and development is done in this field in order to reduce the cost and complexity of the PV-T system. In this direction, Wolf [1] performed the experimental investigation on PV-T system and individual solar PV and solar thermal system. The PV-T is installed in Boston, USA to supply a single family residence. The area of designed collector is 50 m² and the collector is of non-concentrating type as shown in Fig. 1.

Crystalline silicon technology is used in the fabrication of solar PV array. From the outcomes obtained from the experimental investigation, it was concluded that that PV-T system is technically feasible and cost-effective as compared to the individual system used for electricity and thermal production. An active cooling system was designed by Teo [2] in which parallel array of cooling ducts was attached with back side of PV panel. The results obtained from the experimental analysis show

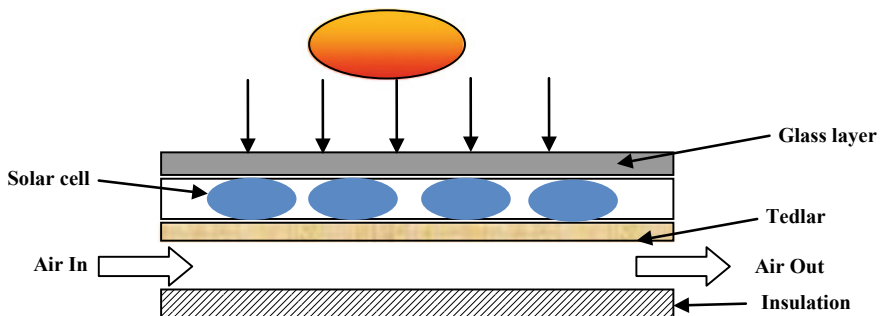


Fig. 1 PV-T air collector

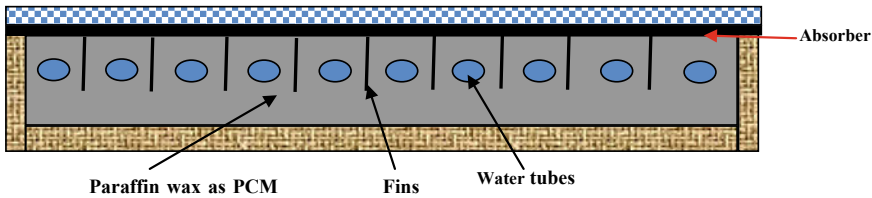


Fig. 2 PV-T water collector system with PCM

that the electrical efficiency of the system was enhanced by 4–5% with the active cooling system. Kalogirou et al. [3] reviewed the applications of various solar thermal collectors. The author discussed the latest advancement in the PV-T technology, i.e., application of phase changing materials (PCM) in the channel so that better thermal and electrical performance of the PV-T system is achieved. PCMs are used in the cooling medium due to its high latent heat of fusion, it increases the thermal absorbing capacity of cooling medium and keep the temperature fluctuations under the controlled range. Stropnik et al. [4] discussed the advantage of using PCM in the cooling medium as shown in Fig. 2. It was concluded that the average electricity production in the city of Ljubljana was enhanced by around 7.3% by mixing PCM in the cooling medium. Certain design modifications such as use of additional glass cover (upper glaze), use of thin metallic sheets and fins in the channel, etc., were also adopted by various researchers around the globe because these design modifications help in achieving the better the performance of the PV-T system. An additional glass cover (glaze) is used above the PV surface in order to trap more heat energy due to which thermal efficiency of the system improves significantly. It was reported that thermal output of the glazed PV-T system is almost double that of unglazed PV-T but decreases the electrical energy output [5]. Apart from this, there are certain disadvantages of the glazing such as edge shedding and increased temperature of the surface which leads to reduction in electrical output [6] and increases the sensitivity of photovoltaic module toward reflection losses and leads to the formation of hot spots.

The reflection losses are then reduced by using antireflective coating and hence improves the electrical efficiency of the system as compared to an ordinary glass cover [7]. Since there are a lot of design parameters which affect the performance of PV-T system. Therefore, optimization of parameters using soft computing techniques proved be very efficient in the designing of the system. In this direction, Singh et al. [8] use the genetic algorithm (GA) approach to optimize the parameters of single-channel photovoltaic thermal air collector. The outcomes demonstrate that the thermal and electrical performance of the system enhances significantly when the parameters were optimized using GA as compared to un-optimized system. In another study, the author [9] investigates the performance of the system with multi-objective function using genetic algorithm for the climatic conditions of New Delhi (India). Singh and Agrawal [10] implemented the hybrid GA-FS approach to the single-channel PV-T and the performance is compared with GA and un-optimized

system. The objective function during the course of optimization is exergy efficiency. The conclusions drawn from the outcomes showed that the exergetic performance of the PV-T system is significantly enhanced using GA-FS approach as compared to GA and an un-optimized system. Singh et al. [11] worked upon evolutionary algorithm approach to optimize the parameters of glazed PV-T module and concludes that the performance of the system is improved when compared with un-optimized system.

2 System Description

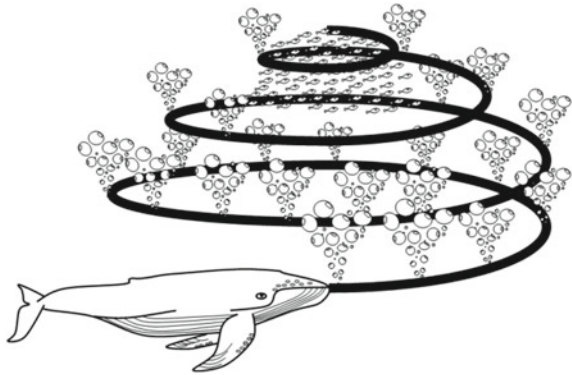
In the proposed work, two different algorithms such as whale optimization algorithm (WOA) and genetic algorithm (GA) have been implemented on a single-channel glazed hybrid PV-T air collector system to find out the optimum value of parameters in order to maximize the exergetic performance of the system. There are various parameters which affect the performance of the PV-T system such as dimensions of the channel (duct) below the panel, depth of the tedlar, thickness of insulation layer, type of solar cell fabrication technology, velocity of fluid flowing through the channel, temperature of the fluid at the inlet and outlet of the channel, and temperature at the upper surface of the PV panel but in this paper, only four of the above parameters have been considered for optimization study. These four parameters were air channel length (L_M), depth of the air duct (d), fluid velocity through the duct (V_F), and temperature of the air at the inlet of duct (T_{in}). The overall exergy efficiency is considered as an objective function. The exergy efficiency, thermal efficiency, and electrical efficiency of the system are calculated according to the thermal modeling given by Agrawal and Tiwari [12].

3 Tool Used for Optimization

In this paper, two dissimilar optimization algorithms such as whale optimization algorithm (WOA) and genetic algorithm (GA) have been used to optimize the parameters of glazed PV-T (single-channel) module. WOA is a recently developed algorithm which was based upon the hunting behavior of humpback whales. WOA is introduced in 2016 by Mirjalili and Lewis [13]. For feeding themselves, humpback whale kills the little fishes close to the upper water surface. During this process, they formed a spiral or nine-like structure of bubbles in order to encircle its prey. They go down to 12 m and formed spirals of water bubbles to confuse the fishes and then swim up toward the surface as shown in Fig. 3.

This foraging behavior of humpback whales is called bubble-net feeding method. The movement of whale is classified in two ways, one in which whale goes down, make bubbles, and then goes up and second method includes different stages: coral loop, lobtail, and capture loop. When one of the whales updates its position to reach an optimal location, other whales are also attracted toward that and updated their

Fig. 3 Bubble-net feeding behavior of humpback whales [13]



positions according to Eq. 1.

$$\vec{D} = \left| \vec{P} \cdot \vec{Y}^*(t) - \vec{Y}(t) \right| \tag{1}$$

$$\vec{Y}(t + 1) = \vec{Y}^*(t) - \vec{D} \cdot \vec{Q} \tag{2}$$

\vec{P} and \vec{Q} are coefficients, \vec{Y}^* is the position vector of best position obtained so far, and \vec{Y} is the position vector. The P and Q vectors are calculated as follows:

$$\vec{Q} = 2 \cdot \vec{a}\vec{r} - \vec{a} \tag{3}$$

$$\vec{P} = 2 \cdot \vec{r} \tag{4}$$

where \vec{a} decreased from 2 to 0. The searching location dimension of whale is based upon the number of tuning variables. Since four design parameters have been considered for optimization, so a hypercube for searching space can be considered in which either optimal position or area around optimal position is the target of whale. The optimal location for whale will be that for which value of exergy the set of searching space parameters will be highest among nearby searching space positions. The flow chart which explains the proposed work is shown in Fig. 4.

4 Result and Discussion

The optimization is performed on the data for a day taken from Indian Meteorological Department, Pune for New Delhi India climatic conditions as shown in Table 1. We have compared the results obtained by optimizing the parameters with WOA with the results obtained when the parameters were optimized using genetic algorithm (GA) using the same input data.

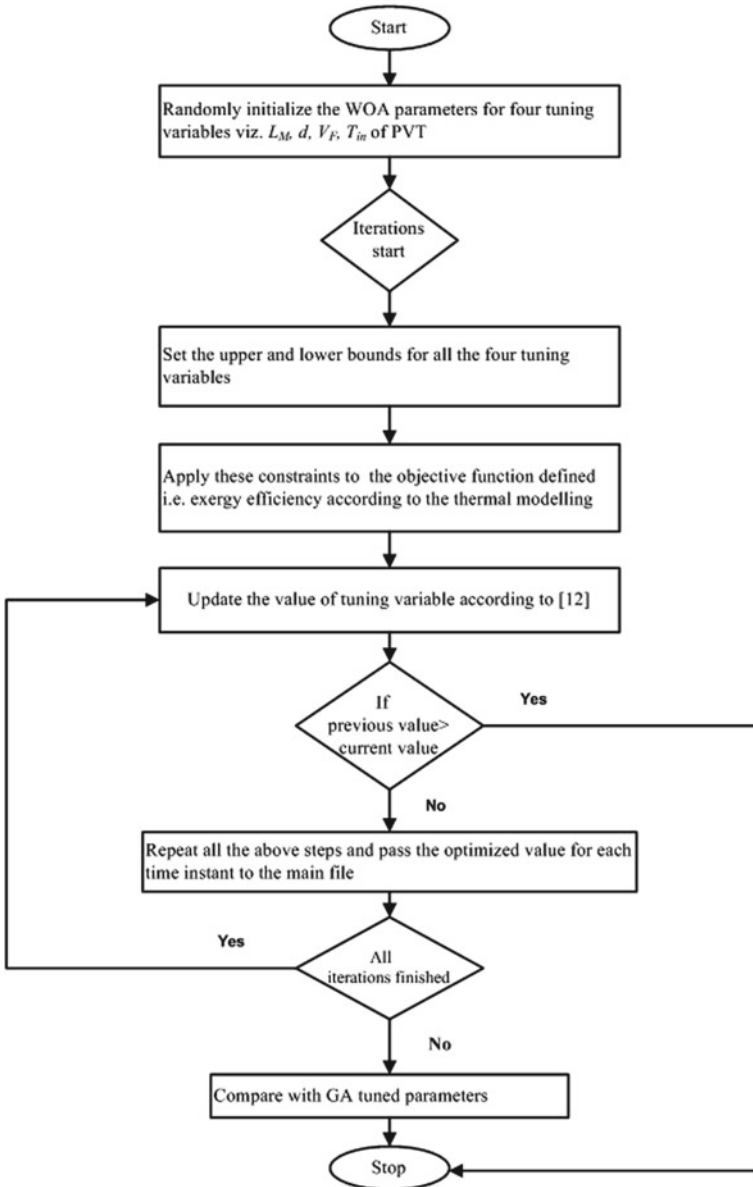


Fig. 4 Flow chart for WOA algorithm

Table 1 Input data taken from IMD, Pune

Daytime (h)	Intensity of sunlight (W/m ²)	Ambient temperature (°C)
08:00	132.99	7.90
09:00	355.56	7.90
10:00	554.69	7.90
11:00	680.73	6.60
12:00	726.74	6.40
13:00	733.85	7.70
14:00	656.08	10.60
15:00	500.00	13.00
16:00	311.46	15.00
17:00	106.42	16.50

The optimization techniques are used to solve nonlinear complex programming problems as in this work and good optimization is validated only if the iterations convergence reaches earlier and no further variation in the results is observed.

The results show that the iterations converge at a faster rate when WOA is used as an optimization technique and also it takes very less time for the identification of optimum value of design parameters for the Glazed PV-T module. The convergence curve is shown in Fig. 5. WOA optimization is best in terms of convergence rate when compared with GA. The optimization curve shows that the iteration is converging after 32 iterations in case of WOA whereas, in case of GA, it is converging after 60 iterations.

For the proposed study, exergy efficiency is considered as an objective function. Exergy efficiency is high-grade electrical energy obtained from the PV-T system. Figure 6 demonstrates that pattern for exergy efficiency is increasing from 08:00 to 13:00 h and maximum when the intensity is maximum. When the intensity of

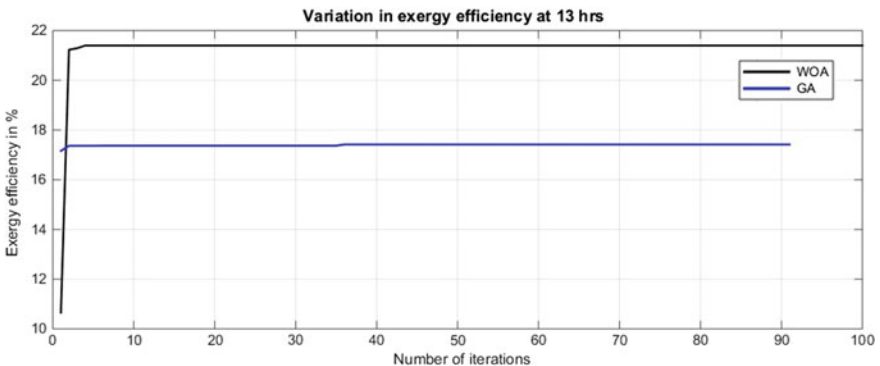


Fig. 5 Convergence curve of WOA and GA at 13 h

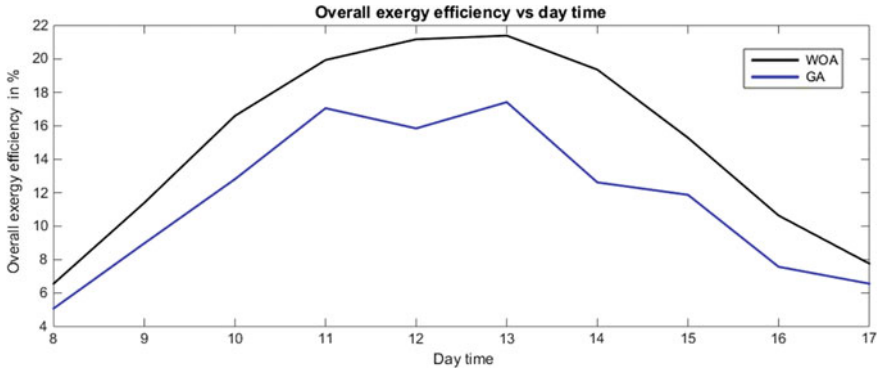


Fig. 6 Overall exergy efficiency of glazed PV-T module using WOA and GA

sunlight is decreasing, i.e., from 13:00 to 17:00 h, the exergy efficiency is decreasing. From the optimization curve, it is observed that exergy efficiency obtained when the parameters were optimized using WOA is 15.0119% and by using GA, the exergy efficiency is 11.58211%. Hence, from the results, significant improvements in the exergy efficiency of the system were observed using WOA.

The variation in thermal performance of the glazed PV-T system with time is shown in Fig. 7. The observations from the plot demonstrate that the thermal efficiency is maximum when the intensity of sunlight is maximum (i.e., around 12–13 pm) and thermal efficiency is minimum when the intensity of sunlight is minimum. The outcomes show that significant improvement in thermal efficiency was observed when the parameters were optimized using WOA.

The deviation in overall thermal efficiency with time is shown in Fig. 8. The outcomes demonstrate that the calculated value of overall thermal efficiency of the PV-T system is 43.67272% by using WOA while the calculated value of overall thermal efficiency is 33.30057% by using GA at the optimized values of parameters. The

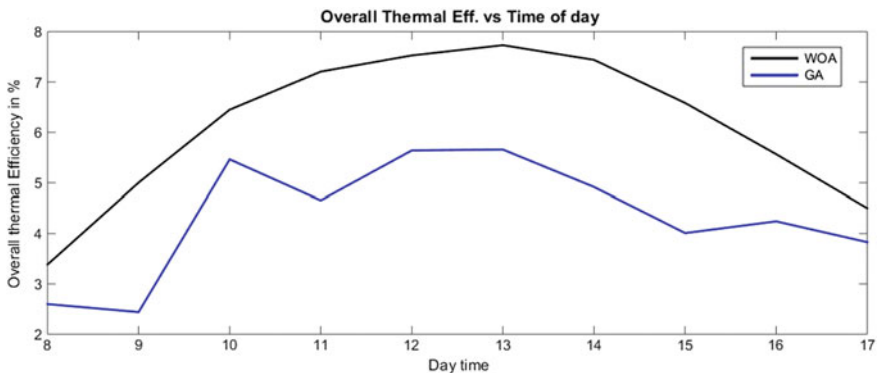


Fig. 7 Thermal efficiency of glazed PV-T module using WOA and GA

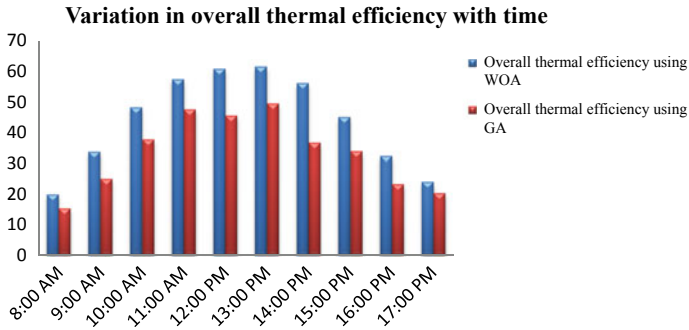


Fig. 8 Comparison of thermal efficiency using WOA and GA

outcomes demonstrate that an improvement of around 31.147% in overall thermal efficiency was observed when the parameters of glazed PV-T were optimized using WOA.

5 Conclusion

In this paper, two different optimization techniques have been implemented to glazed PV-T (single-channel) module to optimize its four variable parameters. For this purpose, the exergy efficiency of the system is considered as objective function. The outcomes of the proposed analysis demonstrate that exergy efficiency and thermal efficiency of the PV-T system were significantly enhanced by optimizing the parameters using WOA. The optimum value of exergy efficiency at the optimized value of parameters is shown in Appendix. The results show that an improvement of around 31.147% in overall thermal efficiency and 41.29% in exergy efficiency was observed when the parameters were optimized using WOA. The proposed work concludes that WOA is proved to be an efficient technique for optimizing the parameters of glazed PV-T (single-channel) module as its convergence rate is faster as compared to GA.

Appendix: Optimized Value of Parameters

Parameter to be optimized	WOA	GA
Length of the air channel, L_M (m)	0.3	0.27948
Air channel depth, d (m)	0.1	0.00092
Fluid velocity at the inlet, V_F (m/s)	1.5	1.37070

(continued)

(continued)


Parameter to be optimized	WOA	GA
Temperature of fluid at inlet, T_{in} (°C)	4.98	3.62050

References

1. Wolf M (1976) Performance analysis of combined heating and photovoltaic power systems for residences. *Energy Convers* 16:79–90
2. Teo HG, Lee PS, Hawlader MNA (2012) An active cooling system for photovoltaic modules. *Appl Energy* 90:309–315
3. Kalogirou SA, Karellas S, Braimakis K, Stanciu C, Badescu V (2016) Exergy analysis of solar thermal systems and processes. *Prog Energy Combust Sci* 56:106–137
4. Stropnik R, Stritih U (2016) Increasing the efficiency of PV panel with the use of PCM. *Renew Energy* 97:671–679
5. Zondag HA (2012) Flat plate PV–thermal collectors and systems: a review. *Renew Sustain Energy Rev* 12(4):891–959
6. Pascal A, Wolfgang E, Hubert F, Matthias R, Anton S, Henrick S, Roadmap/A European guide for the development and market introduction of PV thermal technology, contract no-502775(SES6)
7. Rajeb O, Dhaou H, Jemni A (2015) Parameters effect analysis of a photovoltaic thermal collector: case study for climate conditions of Monastir. *Tunis Energy Convers Manag* 89:409–419
8. Singh S, Agrawal S, Tiwari A, Al-Helal IM, Awasti DV (2015) Modeling and parameter optimization of hybrid single channel photovoltaic thermal module using genetic algorithms. *Sol Energy* 113:78–87
9. Singh S, Agrawal S, Tiwari GN, Chauhan D (2015) Application of genetic algorithm with multi-objective function to improve the efficiency of glazed PVT system for New Delhi (India) climate conditions. *Sol Energy* 117:153–166
10. Singh S, Agrawal S (2015) Parameter identification of the glazed photovoltaic thermal system using genetic algorithm-fuzzy system (GA-FS) approach and its comparative study. *Energy Convers Manag* 105:763–771
11. Singh S, Agrawal S, Gadh R (2015) Optimization of single channel glazed PVT array using evolutionary algorithm (EA) and carbon credit earned by the optimized array. *Energy Convers Manag* 105:303–312
12. Agrawal S, Tiwari A (2011) Experimental validation of glazed hybrid micro-channel solar cell thermal tile. *Sol Energy* 85(11):3046–3056
13. Mirjalili S, Lewis A (2016) The whale optimization algorithm. *Adv Eng Softw* 95:51–67

An 8-Bit Charge Redistribution SAR ADC



Yahya Mohammed Ali Al-Naamani, K. Lokesh Krishna  and A. Krishna Mohan

Abstract A power-efficient and moderate resolution Successive Approximation Register (SAR) ADC design is implemented in this paper. ADC is an important electronic circuit in biomedical electronic systems. Low-power operation and compacted chip size are the essential requirements of various biomedical systems. Also to precisely detect the various natural signals originating from the human body, resolution is of utmost importance. Among the different ADC designs available, SAR-type ADC has shown superior capabilities in terms of low-power operation, better resolution, a small form factor, and less die area. This proposed paper comprises of capacitive type Digital-to-Analog Converter (DAC) based on charge distribution method, SAR logic implemented using basic logic gates, and low-power operated comparator circuit. The inner blocks of the proposed architecture were designed and simulated in CMOS 130 nm N-well technology operated with V_{DD} of 1.2 V supply. The simulated Integral Nonlinearity error (INL) and Differential Nonlinearity error (DNL) are between 0.2/−0.03 LSB and 0.41/−0.22 LSB, respectively. The proposed ADC exhibits SNDR (signal-to-noise plus distortion ratio) of 42.3 dB and reside in a die area of 0.106 mm².

Keywords Resolution · CMOS · Differential · Flip-flop · Clock · Transient and capacitive

1 Introduction

Rapid improvements in integrated circuit design technologies have made electronic systems such as digital audio workstation based sound recording, digital imaging systems, high performance data acquisition systems, TV tuner cards, software-defined

Y. M. A. Al-Naamani
Department of ECE, Mewar University, Gangarar, Rajasthan, India

K. Lokesh Krishna (✉) · A. Krishna Mohan
Department of Electronics and Communication Engineering, S.V. College of Engineering,
Tirupati, Andhra Pradesh, India
e-mail: kayamlokesh78@gmail.com

© Springer Nature Singapore Pte Ltd. 2020
A. Kalam et al. (eds.), *Intelligent Computing Techniques for Smart Energy Systems*,
Lecture Notes in Electrical Engineering 607,
https://doi.org/10.1007/978-981-15-0214-9_63

radios, aircraft wireless communications, medical imaging and diagnostic equipment, spectrum analyzers, high-speed signal generators, 4G long-term evolution systems, high speed, high-frequency digital storage oscilloscopes, and fiber optic applications to be used in every part of day-to-day activities. The physical information for measurement purposes is continuous in nature. These informations or data are low peak valued or high peak valued, non-quantized, and successively fluctuate with changes in time. Currently, with the advances in digital signal processing systems, extreme processing of data is carried out in digital area only. Benefits such as easier data storage, design becomes simpler as exact values of current and voltages are not prerequisite, highly precise and accurate, logic can be reprogrammed several times, and finally, it becomes easier for an electronic circuit to distinguish an original signal and a noisy signal. Hence, it becomes very much vital, to convert to digital output so that the received physical input signal can be monitored and measured accurately.

The transformation of analog signal to digital signal and vice versa is performed using a data converter circuit. Data converter circuits are very important and essential blocks in applications related to measurement of physical data and wireless communications. The main purpose of a converter circuit is to change the given analog voltage signal to digital voltage output signal or a digital signal to an analog signal output voltage. Therefore, these converter circuits act as key interface circuits between analog and digital processing circuits and digital and analog processing circuits. In specific, there are two different categories of converter circuits such as (i) Digital-to-Analog Converter (DAC) and (ii) Analog-to-Digital Converter (ADC). An ADC circuit converts a given input signal (which is continuous both in amplitude and time) into corresponding output signals (which is discrete-time quantized magnitude). By and large, different ADC architectures exist, that can be utilized for wide variety of applications such as both in wireless communication systems and in biomedical systems. The choice of the selection of accurate and precise converter architecture is based on various design parameters. However, single converter architecture cannot be used for all the wide applications. Hence, selecting the proper converter architecture involves assuming trade-offs between various design parameters such as signal-to-noise ratio, total harmonic distortion, conversion time, silicon area, integral nonlinearity, resolution, packaging, operating temperature range, dynamic performance, differential nonlinearity, static performance, chip cost, and channel count. Lastly, the vital parameters to be well thought out in the design of any ADC circuit are high sampling rate, ultralow power operation, and linear circuit operation.

Successive Approximation Register converter architectures are the best choice and more regularly used in the design of biomedical systems with sample rate under 50 MS/s and for medium resolution levels between 6 and 16 bits. The performance specifications of SAR converter architecture can be improved by technological scaling of transistors and incorporating changes at the architectural design of the logic. Depending upon the resolution, SAR ADCs operate with several comparison cycles

to complete one-bit conversion. Due to this, they are operated at limited speed. The recent advances in feature sizes, i.e., (W/L) ratio of CMOS transistors have led to operate at several tens of megasamples per second to very low gigasamples per second, while simultaneously consuming low power. SAR ADCs offer better resolution, low power consumption, high speed, and have very less latency. These better features make SAR architecture specifically suited for challenges that arise in critical applications such as in implanted biomedical devices and in energy harvester applications.

Y. Lin et al. described a subrange SAR ADC architecture implemented in 90 nm CMOS of resolution 9-bits and with an operating speed of 150-MS/s [1]. Y. Cho et al. explained the complete design and implementation of 9-bit SAR ADC, which utilizes a comparator using offset voltage cancelation technique and digital calibration for error correction [2]. K. L. Krishna et al. described a unique hybrid ADC implemented using a flash ADC operating at 1 GS/s and a SAR architecture operating at low power. The simulated results reveal that it operates at high speed and consumes low power at better resolution levels [3]. SAR architecture based on split-CDAC which includes on-chip digital calibration techniques, an internal clock signal to compensate for PVT variations, and comparator offset voltage cancelation technique is presented by Yoshioka et al. [4]. A linear and power-efficient switching scheme utilized in asynchronous SAR architecture is presented in [5]. Speed and resolution are improved by using a low leakage latched dynamic cell in SAR logic. Harpe et al. presented the complete design and implementation of a moderate resolution level and low-power operated asynchronous SAR architecture for low energy wireless radios [6]. The complete linearity analysis of a split-type DAC technique based on conventional charge redistribution switching method and V_{cm} -based switching method is described by Zhu et al. [7]. A 10-bit pipelined ADC employing techniques namely pipeline stage scaling algorithm, capacitor ratio independent conversion scheme, and a nested gain boosting technique is presented by Murshed et al. [8]. In this proposed work, ultralow power SAR architecture is designed and simulated in 130 nm N-well CMOS technology.

The main summary of the presented work is as follows: The block diagram details and its explanation are shown in Sect. 2. Section 3 presents the design and implementation of the inner blocks of the proposed SAR architecture. The achieved simulation results are presented in Sect. 4. Lastly, Sect. 5 gives the conclusions.

2 8-Bit SAR ADC Architecture

A conventional diagram of SAR converter architecture is presented in Fig. 1. In its simplest form, the architecture comprises of a CMOS comparator, a DAC utilizing charge redistribution technique, and an 8-bit SAR logic. Because of the presence of charge redistribution technique, the sample and hold process is integrally present in the circuit. Due to its fast conversion time and easier fabrication, charge redistribution DACs are frequently used in many applications. Also, they operate at very less power

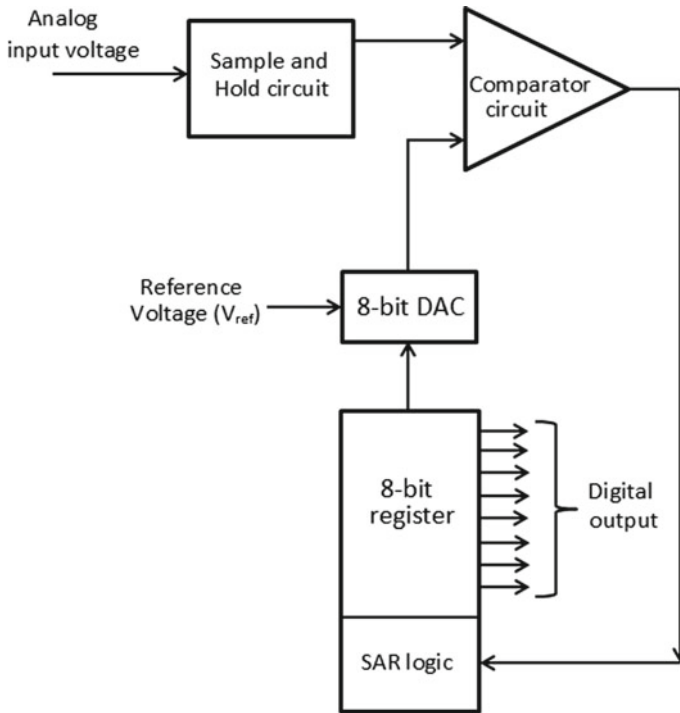


Fig. 1 Block diagram of 8-bit SAR architecture

and generate less mismatch errors compared to the resistive operated DAC circuits. The occupied die area of the SAR ADC can be greatly minimized by decreasing the total capacitor size in a capacitive-based DAC. SAR architecture is the appropriate choice for ultralow power applications such as in portable wireless devices and biomedical devices. It employs a successive binary search algorithm to find the closest digital word to match the input analog data. In this proposed work, 8-bit resolution is considered. During the first clock pulse, the SAR logic is set to midscale, i.e., 10,000,000, so that the DAC output produces an analog output. The obtained output voltages of the proposed SAR logic and the 8-bit DAC are compared and output polarity is determined. This determines the value of MSB. If the given input voltage (V_{in}) is higher than the DAC voltage (V_{DAC}), then logic 1 is allocated to the MSB bit, else logic 0. During the next clock pulse, once again the comparison is performed. If analog input voltage is greater than the DAC voltage, then once again the next MSB bit is assigned with logic 1, else logic 0. Similarly, the comparison process continues until all the bit conversion is completed.

3 Implementation of Inner Blocks

The architecture consists of an inherent sample and hold circuit (S/H), dynamic CMOS comparator, a DAC based on charge redistribution, and 8-bit successive approximation logic.

3.1 S/H Circuit

The benefit of using the charge distributive capacitive type DAC architecture is that it makes obtainable inbuilt sample and hold function. The concept is to use binary-weighted capacitor values to describe different resolution levels; the largest capacitor in the circuit produces the largest current, and therefore corresponds to the MSB; similarly, the value of smallest capacitor corresponds to the LSB. Figure 2 shows the operation of sample mode of operation, while the hold mode of operation is shown in Fig. 3. The 8-bit capacitive DAC utilized in the SAR architecture comprises of an array of eight capacitors that are appropriately selected according to the binary-weighted values, i.e., $C, C/2, C/4, C/8, C/16, C/32, C/64,$ and $C/128$ plus one dummy LSB capacitor. The last two capacitors connected at the LSB side have a value of $C/128$ so that the total equivalent capacitances of the nine capacitors are $2C$. In this circuit, the 11 switches are implemented by bootstrapped MOS transistor technology.

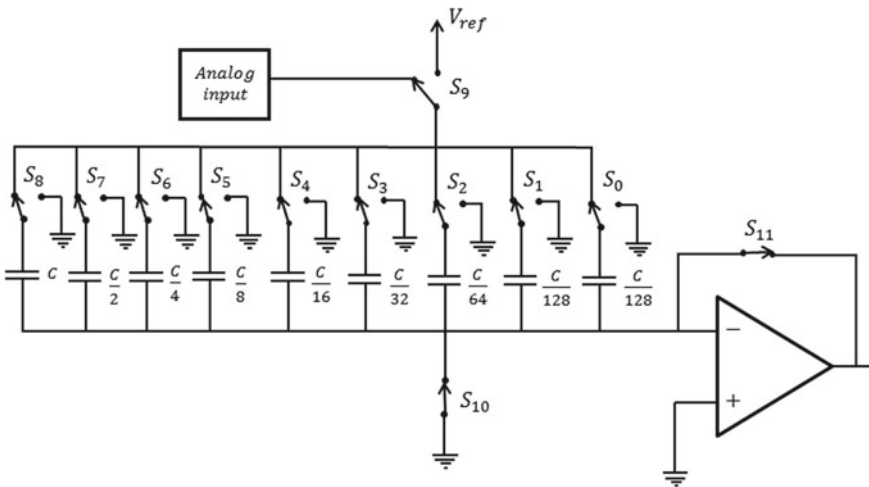


Fig. 2 Sample mode schematic diagram

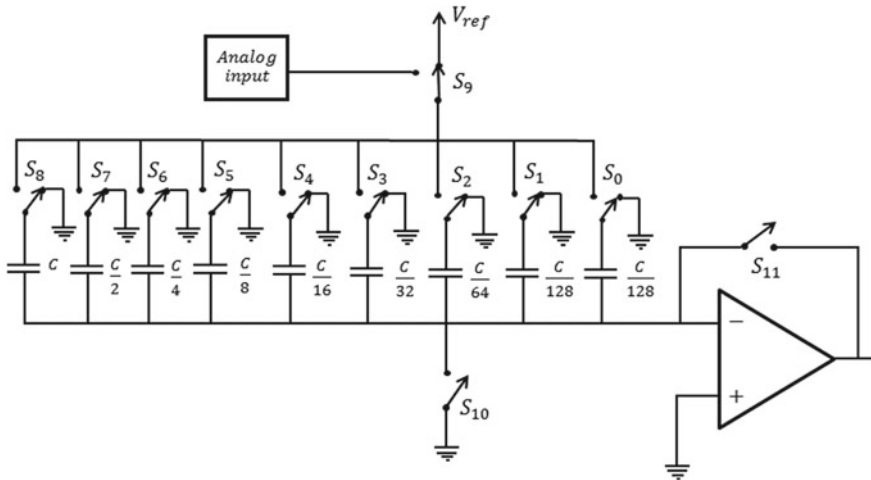


Fig. 3 Hold mode schematic diagram

3.2 Comparator

The objective of a comparator circuit is to compare the continuous input signal at one terminal with a known reference dc voltage (V_{ref}) at the other terminal, and produces a digital logic at the output terminal. A wide variety of designs are available to implement a comparator circuit. The proposed SAR ADC design utilizes dynamic comparator circuit architecture because they exhibit better performance characteristics such as very high input impedance, low offset voltage, rail-to-rail output swing, low power consumption, and higher sampling speed. They employ positive feedback so that any small input voltage difference between the input terminals can be converted to full-scale digital output in short time of operation. The comparator circuit consists of two cross-coupled differential pairs with an inverter latch placed above. The threshold voltage of the comparator can be varied by changing the (W/L) ratio of the transistors present at the input side. Figure 4 shows the schematic diagram of comparator circuit.

During the reset period of operation, i.e., $CLCK = \text{low}$, the output nodes of the cross-coupled inverters (transistors M_3 and M_9) are at the potential V_{DD} through the reset transistors M_6 and M_9 . Similarly, during the evaluation phase, i.e., $CLCK = V_{DD}$, the transistor M_T is switched ON. The transistors forming the input differential pair M_1 and M_2 starts to discharge the drain node voltages with a different time constant proportional to the each applied input voltage from voltage V_{DD} to zero. When the voltages of one of the either drain nodes of transistors M_1 and M_2 drops to $[V_{DD} - V_{in}]$, then the transistors M_3 and M_4 in the cross-coupled connection switches ON and this starts the necessary positive feedback required for comparator action. As

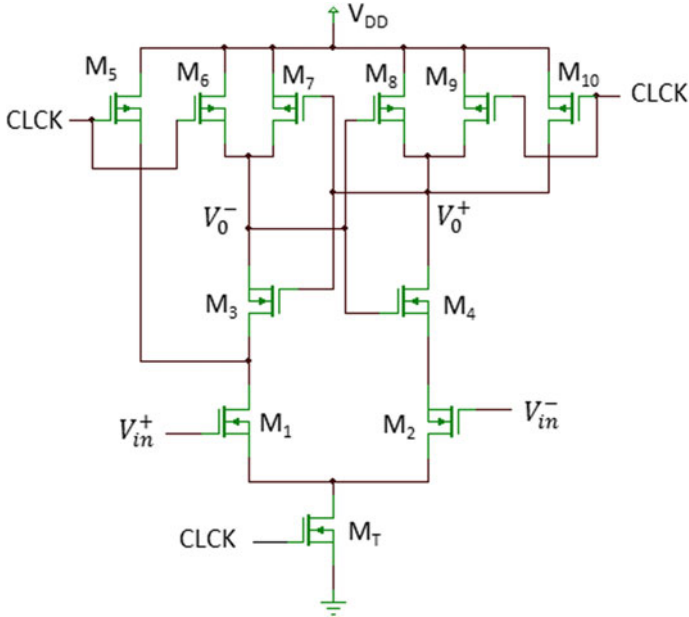


Fig. 4 Comparator circuit diagram

soon as the output node voltage reaches to $[V_{DD}-V_{tp}]$, the transistors M_6 and M_9 are also switched ON, still further augmenting the effect of positive feedback and aiding the regeneration of a small input differential voltage to full swing differential output voltage. Due to this, latch-regeneration time reduces significantly, circuit operates faster, and operating power is also lowered.

4 Simulation Results

The proposed 8-bit SAR architecture has been simulated using Cadence specter tool in 130 nm CMOS technology. Figure 5 presents the simulated results of the dynamic comparator circuit. The power consumption being a very vital parameter depends on the performance of the CMOS comparator. The comparator was simulated with $V_{DD} = 1.2$ V, clock frequency = 1 MHz, and input voltage = 1 V.

Since SAR logic is realized using digital components, they consume less power compared to the analog circuits. The obtained simulated waveforms of the proposed 8-bit SAR architecture are displayed in Fig. 6.

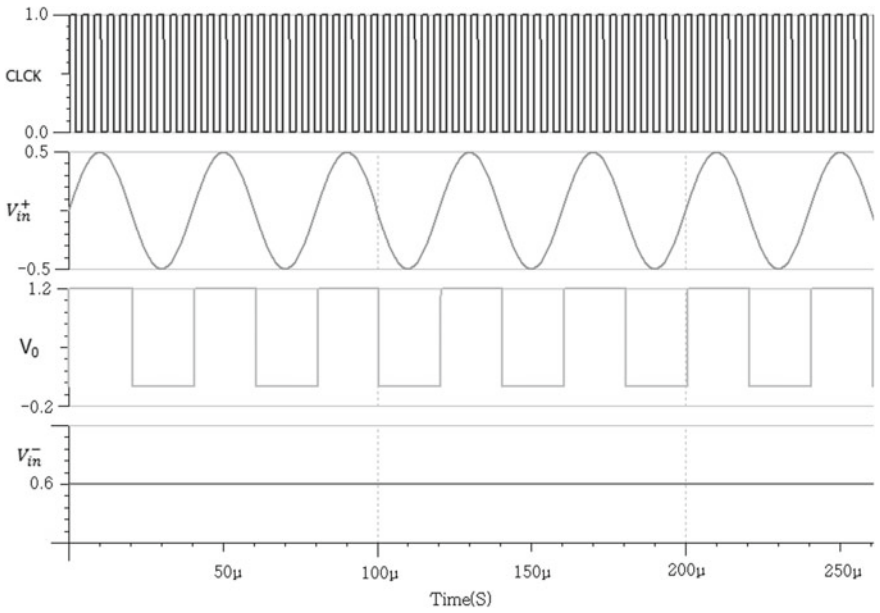


Fig. 5 Simulated results of comparator circuit

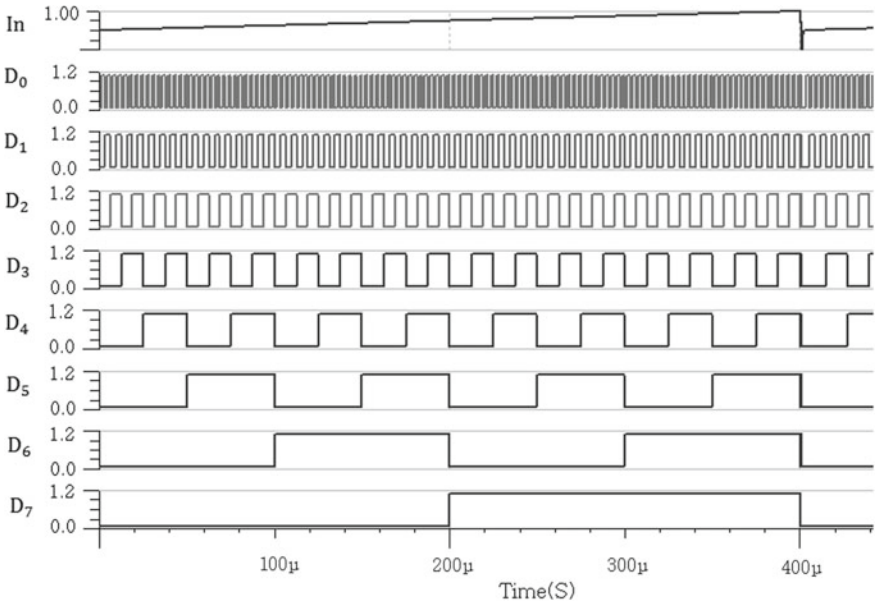


Fig. 6 Simulated waveforms of SAR architecture

5 Conclusion

An ultralow power SAR architecture operating at 8-bit resolution levels is described in this paper. The designed architecture uses a capacitive type DAC based on charge redistribution. The main advantages of the capacitive type based charge redistribution are the inherent sample and hold circuit, higher operating speed, and reduced offset mismatch errors. Also, SAR architecture is suitable for sampling levels ranging from few Ksps to Msps. The complete circuit is operated at a voltage $V_{DD} = 1.2$ V and the power dissipation is found to be $18.8 \mu\text{W}$. The architecture is implemented in 130 nm N-well CMOS technology and occupies a die area of 0.106 mm^2 . The ADC exhibits no missing codes and it is monotonic; the measured INL and DNL is found to be less than 0.34 LSB and 0.25 LSB, respectively. From the simulated results, the SAR ADC operates with low power, higher speed, and better resolution; hence, it can be used in applications such as in design of biomedical electronic systems.

References

1. Lin Y, Liu C, Huang G, Shyu Y, Liu Y, Chang S (2013) A 9-bit 150 MS/s subrange ADC based on SAR architecture in 90 nm CMOS. *IEEE Trans Circuits Syst-I: Regul Pap* 60(3):570–581
2. Cho Y, Jeon Y, Nam J, Kwon J (2010) A 9-bit 80 MS/s successive approximation register analog to digital converter with a capacitor reduction technique. *IEEE Trans Circuits Syst-II: Express Briefs* 57(7):502–506
3. Krishna KL, Ramashri T (2014) VLSI design of 12-bit ADC with 1 Gsps in $0.180 \mu\text{m}$ CMOS integrating with SAR and two-step flash ADC. *J Theor Appl Inf Technol* 68(1):27–35
4. Yoshioka M, Ishikawa K, Takayama T, Tsukamoto S (2010) A 10-bit 50 MS/s $820 \mu\text{W}$ SAR ADC with on-chip digital calibration. *IEEE Trans Biomed Circuits Syst* 4(6):410–416
5. Zhu Z, Qiu Z, Liu M, Ding R (2015) A 6-to-10-Bit (0.5–0.9)V reconfigurable 2-MS/s power scalable SAR ADC in $0.18 \mu\text{m}$ CMOS. *IEEE Trans Circuits Syst-I: Regul Pap* 62(3):689–696
6. Harpe PJA et al (2011) A 26 mW 8-bit 10 MS/s asynchronous SAR ADC for low energy radios. *IEEE J Solid-State Circuits* 46(7):1585–1595
7. Zhu Y et al (2014) Split-SAR ADCs: improved linearity with power and speed optimization. *IEEE Trans VLSI Syst* 22(2):372–383
8. Murshed AM, Krishna KL, Saif MA, Anuradha K (2018) A 10-bit high speed pipelined ADC. In: 2018 international conference on inventive systems and control (ICISC), pp 1253–1258

Analysis of Triple-Threshold Technique for Power Optimization in SRAM Bit-Cell for Low-Power Applications at 45 Nm CMOS Technology



Sudershan Kumar, Shaifali Ruhil, Neeraj KR. Shukla and Shilpi Birla

Abstract As the technology node is shrinking from micron to sub-micron and to deep sub-micron, the device size of semiconductor components is getting smaller and smaller to achieve greater functionality. It has been established that the power consumption in the technology >100 nm is largely dominated by the active power dissipation. The technology <100 nm (more transistors on a single chip area), the active power dissipation is no longer a power dominant component as compared to static power dissipation. At the lower CMOS technology nodes, the threshold voltage of the devices also decreases. Therefore, the devices have become more noise sensitive (bit-cell) which affects the stability of the systems profoundly and degrade the overall system performance. The threshold voltage reduction also challenges the device sub-threshold leakage current and noise margin. To address this issue, this work presents the triple- V_{th} CMOS transistors approach which have different threshold voltages. It is found that the read/write data stability is improved by 10% at the cost of area overhead of one transistor.

Keywords CMOS · Noise margin · SRAM · System on chip · Threshold voltage

1 Introduction

Since the last few decades, CMOS devices have been scaled down to achieve the higher speed and performance with optimal power distribution [1]. CMOS circuitry, when scaled beyond 100 nm technology has a lower V_{th} and an extrinsic thin gate oxide (T_{ox}) to maintain a better control between the switching speed of CMOS and the current drive through the device while dealing with the short-channel effects of the device. The lower V_{th} of the device offers a sharp increment in sub-threshold leakage current that result in an increase in the leakage power of the device. Also, the thin

S. Kumar · S. Ruhil (✉) · N. KR. Shukla
The NorthCap University, Gurgaon, India
e-mail: shaifali.ruhil04@gmail.com

S. Birla
Manipal University Jaipur, Jaipur, Haryana, India

© Springer Nature Singapore Pte Ltd. 2020
A. Kalam et al. (eds.), *Intelligent Computing Techniques for Smart Energy Systems*,
Lecture Notes in Electrical Engineering 607,
https://doi.org/10.1007/978-981-15-0214-9_64

oxide layer of the scaled device also results in an increase in the gate-tunneling current [2]. Thin gate oxide (T_{ox}) gives larger current drive at low supply voltage to overcome short channel effect as Drain Induced Barrier Lowering (DIBL), ultra thin gate oxide along eminent electric field results in substantial increment in gate direct tunneling surpassing drain induced barrier lowering and feeble inversion leakage [3]. Due to technology scaling below 90 nm, the SRAM standby leakage has become a major threatening issue. To overcome the growing leakage challenge in the CMOS devices, the dynamic leakage current reduction at the product level is mainly done through (i) using sleep transistors to turn-off the circuit in the standby mode and (ii) increasing threshold voltage by reversing the body bias of NMOS and PMOS [4]. To maximize the battery lifespan of a portable device, various designs, circuits or architectural level techniques have been adopted to minimize the power intake. Scaling down the supply voltage will reduce the dynamic power quadratically and leakage power got reduced along with the decrease in the supply voltage [5]. Ultra-Dynamic Voltage Scaling is one more approach to reduce energy intake by adjusting the system supply voltage [6]. This paper provides an overview of different technologies (45, 90, 180 nm) and various design methodologies (such as multi threshold, body biasing, Power gating, clock gating, re-mapping, radiation-harden techniques) on SRAM memory and then characterization of SRAM cell as per the specification or requirements of low-power.

A new design technique for the low leakage SRAM is presented, the methodology is founded on the non-zero delay of interconnection of word-line, bit-line of the SRAM cell. By using the proposed methodology, the leakage power of the bit cell is optimized up to 40% [2]. In deep submicron technology, gate leakage has turned out to be the dominant source of leakage as it is increasing with technology scaling. By using two extra PMOS/NMOS devices which change the gate voltages of the transistors, results show 66.5% reduction in total leakage at 65 nm technology [3]. The write power of SRAM is generally greater than the read power by using two tail transistors in pull-down path. The leakage power of the SRAM cell is reduced by 18% when compared to conventional 6T SRAM cell and 29% faster also [7]. Scaling down the supply voltage is an efficient way for ultra-low- power operation [8]. ST-based SRAM bit cell which are worthy for ultra-low-voltage applications, built-in feedback mechanism in the projected ST bit cell can be efficient for process-tolerant, low-voltage SRAM procedure in future nano scaled technology [5, 9]. An 8T sub-threshold SRAM has improved write margin, better variation tolerance, speed optimization of 52% in read bit line discharge time, and it is 20% faster than the conventional SRAM [10]. Voltage scaling proficiency is used to optimize the total power in SRAM with the trade-off of size of the sense amplifier and its statistical offset. For this trade-off, a conception of sense amplifier redundancy is introduced which reduced the statistical offset error [11]. An enhanced SNM with the reduced leakage power of conventional 6T SRAM circuitry, a new 9T SRAM cell was proposed with separate data access for read and write mechanism for the SRAM circuitry. The stability of the SRAM cell is also optimized [12, 13]. A new 7T read SNM free SRAM is developed to overcome the SNM problem in the conventional SRAM and the area problem in the 8T conventional SRAM. The 7T SRAM cell reduces the area overhead

from 13 to 30% [14]. A strong data stability and optimized leakage power consumption are achieved by using the multi-threshold technique for designing the 6T CMOS SRAM circuitry [15, 16]. The power is optimized by using various techniques such as Dual-Rail technique which is implemented on the technology above 32 nm, a dual threshold transistor is also used to design the SRAM circuitry which are specified for low power consumption applications [6]. The SRAM circuitry which is designed for the purpose of high speed operations uses small voltage swing on the bit-lines during the write operation. Scaling on the various levels will affect the delay and power of SRAM [17]. The work in this paper demonstrates several dual-threshold voltage circuit techniques which will be helpful to reduce sub-threshold leakage current during the standby mode of SRAM for combinational logic blocks [18, 19]. The sleep transistor technique to design a 6T SRAM cell is the best technique by which we can achieve a high leakage power optimization during the standby mode of operation in the SRAM [20].

2 Approach

Design of 6T SRAM with Triple-V_{th} is similar in structure with the conventional 6T SRAM and the area is also similar to the conventional SRAM. The only difference is that we use a High-V_{th}, Low-V_{th}, and a standard V_{th} transistor in place of conventional transistors used in conventional 6T SRAM.

These multi-threshold transistors are very useful for the reduction of the leakage power of the complete SRAM bit cell.

3 Analysis and Result

3.1 Data Stability

See Figs. 1, 2 and 3.

3.2 Read Noise Margin

Read Noise Margin values are plotted as shown in Fig. 4 for different cells with V_{IL} (maximum allowable input to be considered as logic '0'), V_{IH} (minimum allowable voltage to be considered as logic '1'), NML (Noise Margin low) and NMH (Noise Margin High)

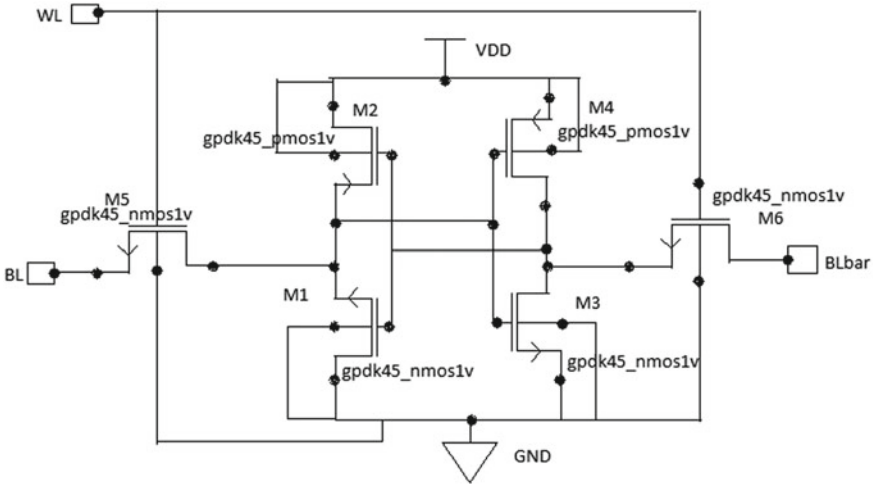


Fig. 1 Conventional 6T SRAM with standard threshold voltage transistor [14]

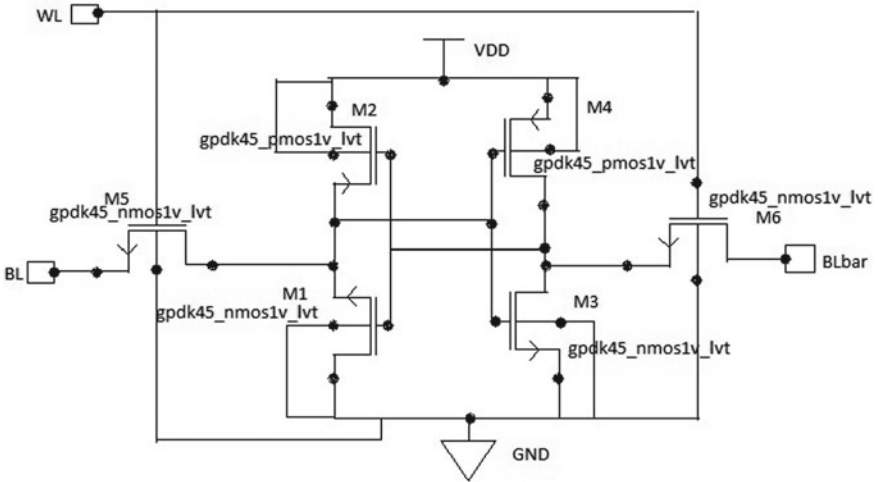


Fig. 2 6T SRAM with triple-Vth technique

3.3 Write Noise Margin

See Figs. 5, 6 and 7.

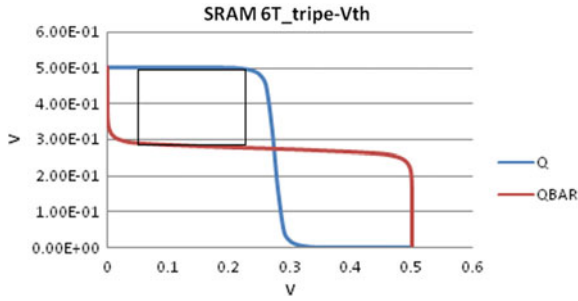


Fig. 3 Stability curve for conventional 6T and Tri-Vth 6T

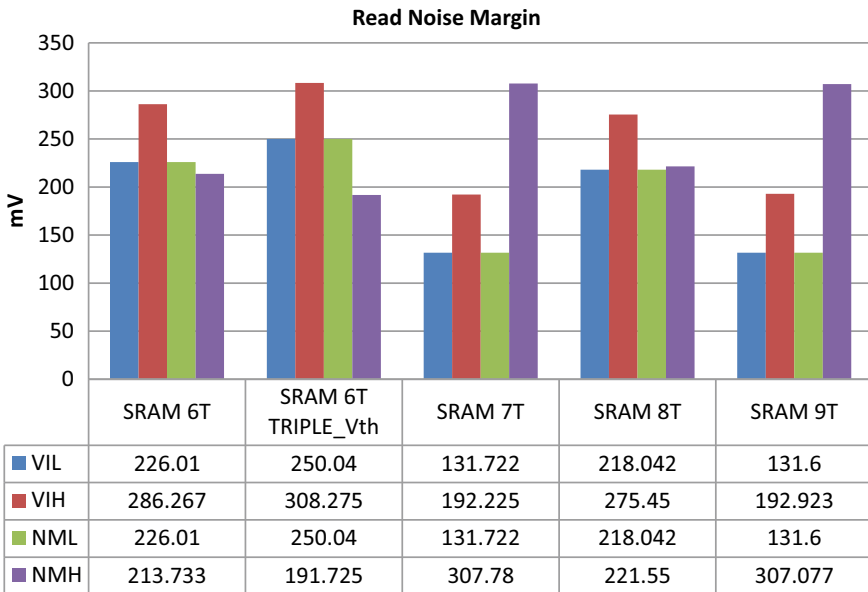


Fig. 4 Read noise margin

3.4 Average Power and Leakage Power

The transistor with Low threshold works faster and hence consumes more power, whereas high Vth transistor works slower than low-Vth transistor and consumes low power. Leakage currents that are raised by the separate transistors are extremely sensitive to process variations.

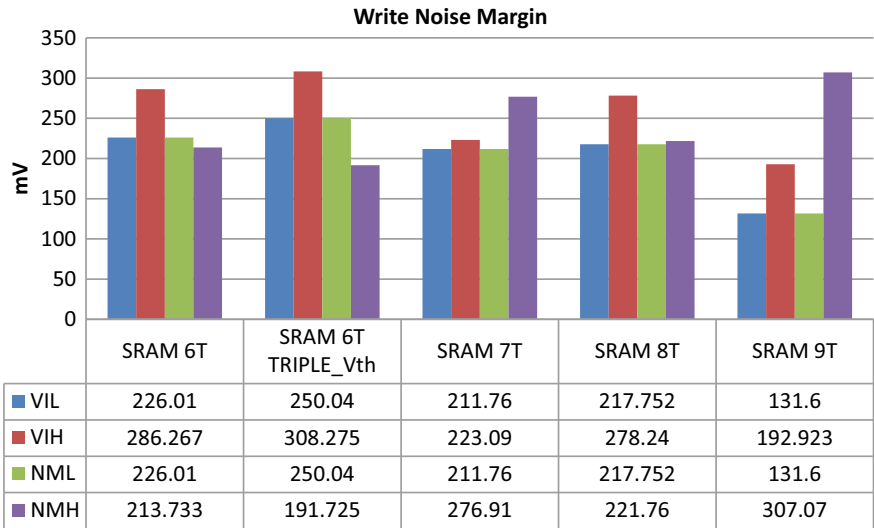


Fig. 5 Write noise margin

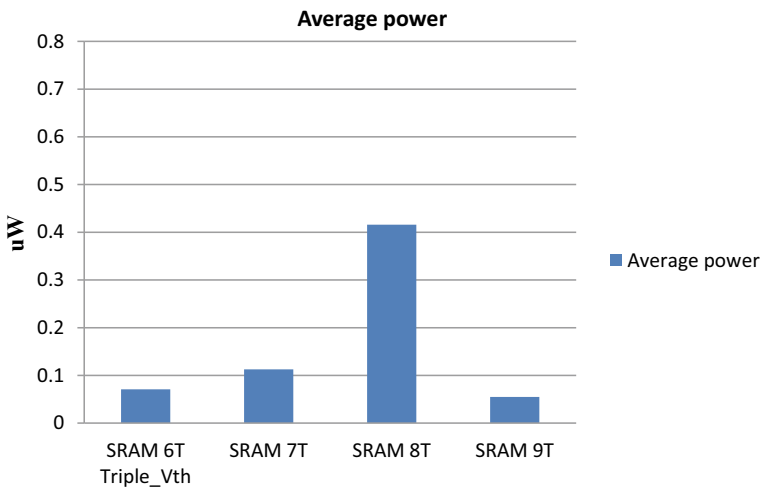


Fig. 6 Average power

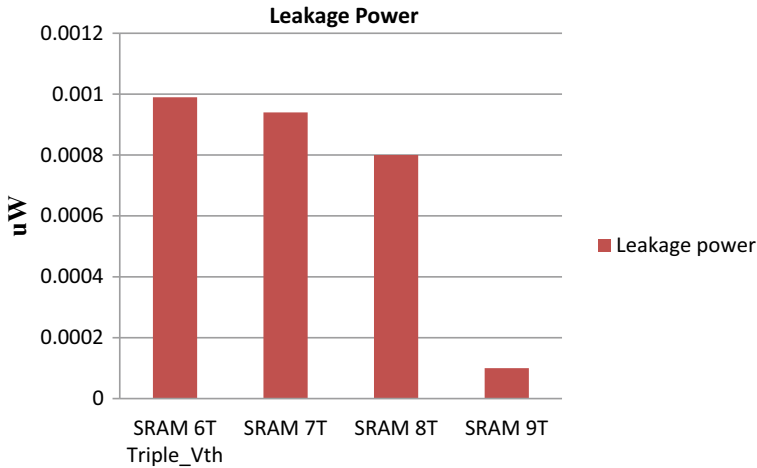


Fig. 7 Leakage power

4 Conclusion

With the triple- V_{th} approach used in 6T, 7T and 8T SRAM cells, a better write ability is achieved. Data stability is better in tri- V_{th} 8T and 9T and also they have less leakage power. On increasing the channel length of the transistor, the device read stability may degrade. The read/write data stability is improved by 10% on using triple- V_{th} approach with an area tradeoff as an additional transistor is used in the SRAM bit cell. Therefore the size of bit cell may increase due to that additional transistor. The leakage power of the cell is reduced in SRAM using 9T in comparison to 6T SRAM by 10%. Average power is also optimized in 9T SRAM as in 6T SRAM.

References

1. Dhanumjaya K, Giri Prasad MN, Padmaraju K, Raja Reddy M (2013) Design of low power SRAM in 45 nm CMOS technology. *Int J Eng Res Appl* 1(4):2040–2045
2. Amelifard B, Fallah F, Pedram M (2007) Leakage minimization of SRAM cells in a dual- V_t and dual- t_{ox} technology. *IEEE Trans Very Large Scale Integr Syst*, 1–10
3. Elakkumanan P, Thondapu C, Sridhar R (2005) DG-SRAM: a low leakage memory circuit. *IEEE*, pp 167–170
4. Lakshminarayanan S et al (2009) Standby power reduction and SRAM cell optimization for 65 nm technology. In: *IEEE quality electronic design conference on 10th international symposium 2009*, San Jose, pp 471–475
5. Kulkarni JP, Roy K (2011) Ultralow-voltage process-variation-tolerant Schmitt-trigger-based SRAM design. *IEEE Trans. Very Large Scale Integr (VLSI) Syst* 20(2):319–332
6. Birla S, Shukla NK, Pattanaik M, Singh RK (2010) Device and circuit design challenges for low leakage SRAM for ultra low power applications. *Can J Electr Electron Eng* 1(7):156–167

7. Sharma R, Antil R, Kumar K (2015) Comparative study of 6T and 8T SRAM using tanner tool. *IJCSMC* 4(1):211–221
8. Zhang Xi et al (2016) Analysis of 7/8-nm Bulk-Si FinFET technologies for 6T-SRAM scaling. *IEEE Trans Electron Devices* 63(4):1502–1507
9. Ahmad Sayeed et al (2016) Single-ended schmitt-trigger-based robust low-power SRAM Cell. *IEEE Trans Very Large Scale Integr Syst* 24(8):2634–2642
10. Kim TH, Liu J, Kim CH (2007) An 8T subthreshold SRAM cell utilizing reverse short channel effect for write margin and read performance improvement. In: *IEEE custom integrated circuits conference*, San Jose, pp 241–244, 16–19 Sept 2007
11. Verma N, Chandrakasan AP (2008) A 256 kb 65 nm 8T subthreshold SRAM employing sense-amplifier redundancy. *IEEE J Solid-State Circuits* 43(1):141–149
12. Yang Younghwi et al (2015) Single-Ended 9T SRAM cell for near-threshold voltage operation with enhanced read performance in 22-nm FinFET technology. *IEEE Trans Very Large Scale Integr Syst* 23(11):2748–2752
13. Liu Z, Kursun V (2008) Characterization of a novel nine-transistor SRAM cell. *IEEE Trans Very Large Scale Integr Syst* 16(4): 488–492
14. Koichi Takeda et al (2006) A read-static-noise-margin-free SRAM cell for low-VDD and high-speed applications. *IEEE J Solid-State Circuits* 41(1):113–121
15. Jiao H, Kursun V (2012) Low power and robust ground gated memory banks with combined write assist techniques. In: *IEEE Faible Tension Faible Consommation*, Paris, pp 1–4
16. Kao JT, Chandrakasan AP (2000) Dual-threshold voltage techniques for low-power digital circuits. *IEEE J Solid-State Circuits* 35(7):1009–1018
17. Burange RA, Agrawal GH (2013) An overview and analysis of low power SRAM design. *Int J Appl Inf Syst* 33–35
18. Sajitha Banu S, Yogesh R, Kamalam S (2015) Design of low power 6T SRAM 8*8 array using gateway transistor. *Int J Adv Res Educ Technol* 2(4):125–128
19. Yadav Shivani et al (2012) Low power SRAM design with reduced read/write time. *Int J Inform Comput Technol* 3(3):195–200
20. Shivhare E, Shukla NK (2011) Active power optimization in a conventional 6T-SRAM for embedded mobile/multimedia applications. *Int J Advanc Sci Technol* 2(3):55–62

Low Power Adder Circuits Using Various Leakage Reduction Techniques



Shreya Upadhyay, Sugandha Tiwari, Shilpi Birla and Neha Singh

Abstract Due to scaling which is a remarkable feature of CMOS, the power consumption in ICs having CMOS devices includes a major factor of leakage power. As per Moore's Law, the transistor count should be doubled in every 18 months as the density is increasing continuously. With the growing technology, the smallest feature size in CMOS ICs is now decreased to 7 nm and below within a span of few decades. As the size of transistors is getting reduced, some limitations have also been observed in CMOS circuits which are undesirable such as a drastic increase in leakage current which results in an increase in leakage power. Different techniques being proposed by various people that are helpful in reducing leakage current. This paper presents the implementation of three techniques for the reduction of leakage power in 1-bit adder and 4-bit full adder. The techniques used are Transistor stack technique, Sleep Transistor Technique and Super Cutoff CMOS Technique (SCCMOS). The above-mentioned techniques have been analyzed using the HSPICE Software with supply voltage varying from 0.9 to 0.5 V using 45 nm technology. The three techniques are being compared with respect to power reduction.

Keywords SCCMOS technique · Leakage power · Threshold voltage · Sleep transistor technique · Transistor stacking technique

1 Introduction

Since the exclusive feature of Scaling came into existence the scaling of the device and power utilization of the device varies a lot. In present scenario of miniaturization of the devices leakage power becomes a crucial factor in investigating the device power consumption. As we advance towards miniaturization the overall chip power

S. Upadhyay · S. Tiwari (✉) · S. Birla · N. Singh
Department of Electronics and Communication Engineering,
Manipal University Jaipur, Jaipur, India
e-mail: sugandha.tiwari@hotmail.com

S. Upadhyay
e-mail: ushreya18@gmail.com

© Springer Nature Singapore Pte Ltd. 2020
A. Kalam et al. (eds.), *Intelligent Computing Techniques for Smart Energy Systems*,
Lecture Notes in Electrical Engineering 607,
https://doi.org/10.1007/978-981-15-0214-9_65

utilization comprises of mainly leakage power. Furthermore, the existence of leakage current is still there when the device is in the standby state which makes leakage power the most critical factor in CMOS VLSI circuits. In present scenario the nanoscaled transistor's leakage current mostly depends on two major factors: Length of the gate and its oxide thickness [1, 2].

Dynamic power is majorly depends on the square of the supply voltage so to minimize it, scaling of supply voltage is must. This reduction of supply voltage affects the performance of the circuit. Due to an increase in the operating speed of the device, the reduction in supply voltage exponentially increases the subthreshold leakage current, and hence the leakage current rises and becomes responsible for increment of power dissipation [3]. Thus, the present demand is of lowering the dynamic power dissipation of the devices in nanoscaled devices. Different techniques have been suggested from time to time by researchers to fulfill the abovementioned criteria [1]. This paper discusses the implementation of three techniques which reduce leakage power. The techniques are Stack Transistor Technique, Sleep Transistor Technique, and Super Cutoff CMOS Technique in 1-bit full adder and 4-bit full adder.

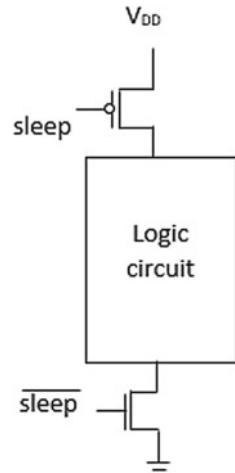
2 Literature Review

Various new techniques have been proposed by the researchers to reduce power consumption in the circuits and various techniques have been experimented and implemented to make low power circuits [1]. Three of those techniques are discussed below.

2.1 *Sleep Transistor Technique*

The most used technique to reduce the subthreshold leakage power is sleep transistor technique which is also called gated-GND and gated- V_{DD} . In this technique, extra transistors known as sleep transistors are inserted between the supply voltage of the device and ground. These sleep transistors control the power supply to turn off the circuit. The turning on of the sleep transistors during the active state provides low resistance in the conduction path and the sleep transistors does not affect the performance of the circuit [4, 5]. Since these transistors remain in off condition during the standby mode of operation, it provides large resistance in the conduction path which reduces the leakage current in the circuit [6]. By using this technique leakage power can be minimized. Sleep technique is applied to both pull-up PMOS transistor and pull-down NMOS transistor as given in Fig. 1.

Fig. 1 Sleep technique

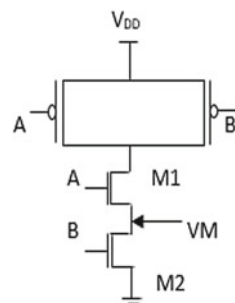


2.2 Stack Transistor Technique

The transistor stack is another technique which is used to reduce leakage power in a circuit and it works both in active mode and in standby mode. The subthreshold leakage current through a stack of series-connected transistors is exponentially related to the threshold voltage of the device, and the threshold voltage changes due to the body effect. From these two effects, the subthreshold leakage can be reduced by turning off more than one transistor in the stack which is known as the “stacking effect” or “self-reverse bias” [7, 8]. The stacking device has lesser leakage current than the leakage of a single transistor with two times the channel length. The transistors introduced over the lower transistor will be having an upper threshold voltage due to the voltage difference between the source and body terminal. This decreases the V_{DS} of the higher transistor as the intermediate node has some positive voltage.

The transistors M1 and M2 are turned off as shown in Fig. 2, due to the small drain in current the voltage at the middle node (V_M) is positive. The positive voltage at the intermediate node results in the following effects:

Fig. 2 Stack transistor technique

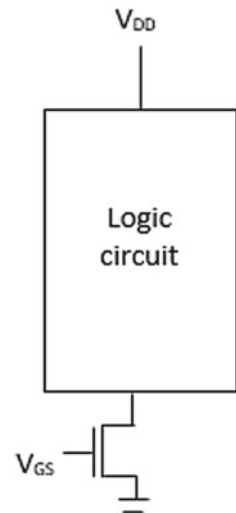


- (1) Due to the positive voltage present at source V_M , the gate to source voltage (V_{GS1}) of transistor M1 becomes negative, and the subthreshold current reduces significantly [3].
- (2) Due to $V_M > 0$, body to source voltage (V_{BS1}) of transistor M1 becomes negative, which increases the threshold voltage of M1, and consequently minimizes the subthreshold leakage [3].
- (3) Due to $V_M > 0$, the voltage between the drain and the source of M1 decreases, which increases the threshold voltage of M1 and reduces the subthreshold leakage.

2.3 Super Cutoff (SCCMOS) Technique

Super Cutoff CMOS Technique (SCCMOS) is used for minimizing the subthreshold leakage current and thus the power dissipation occurs. In this the gate terminal of the sleep transistor is given the voltage more than V_{DD} or less than ground voltage during idle periods by using a bias voltage [9]. In this technique, the Low- V_{TH} cutoff NMOS, whose V_{TH} is lower than V_{TH} of the full adder circuit, is introduced in series to the logic circuits. The low V_{TH} satisfies high-speed operation of the logic circuits [7]. Figure 3 shows SCCMOS technique where Low- V_{TH} cutoff NMOS is applied below the logic circuit (Fig. 4).

Fig. 3 SCCMOS technique



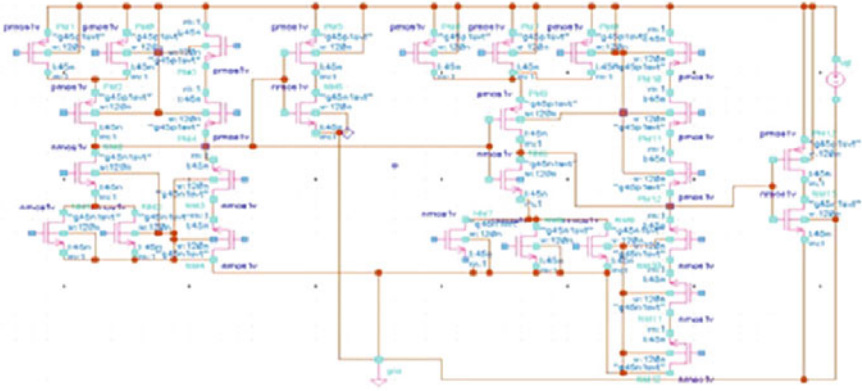


Fig. 4 1-bit full adder circuit

3 Implementation of Adder Circuit

3.1 1-Bit Full Adder

A full adder is a logical circuit that adds binary numbers and gives sum and carries as output. The abovementioned three leakage reduction techniques are applied to 1-bit full adder and their circuit-level diagrams are as shown below. Figure 5 shows the schematic of Sleep Transistor technique where 1 PMOS is added above the pull-up network and 1 NMOS is added below the pull-down network of 1-bit full adder.

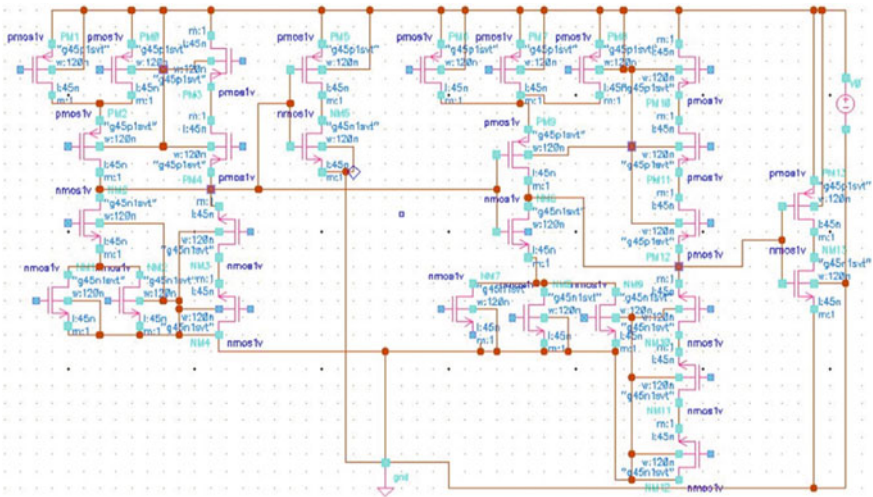


Fig. 5 Implementation of sleep transistor technique in 1-bit full adder

Figure 6 shows the schematic application of Stack Transistor technique in 1-bit full adder where 2 NMOS stacks are turned off to lower the leakage power. Figure 7 shows the schematic application of SCCMOS technique in 1-bit full adder where 1 NMOS is added below the pull-down network of the full adder and voltage lower than V_{TH} is supplied to it.

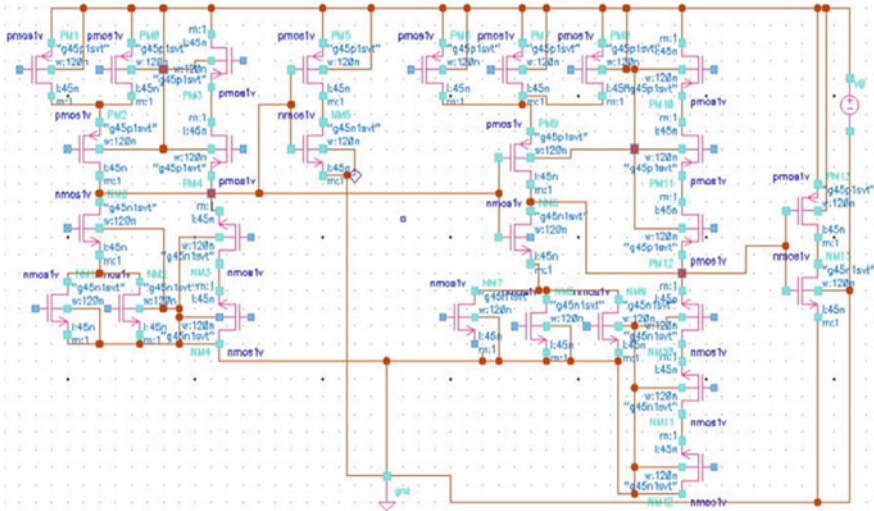


Fig. 6 Implementation of stack transistor technique in 1-bit full adder

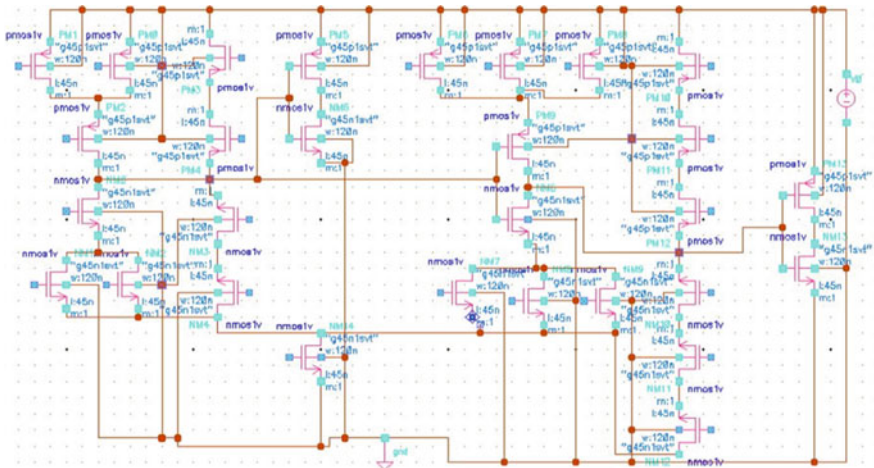


Fig. 7 Implementation of SCCMOS technique in 1-bit full adder

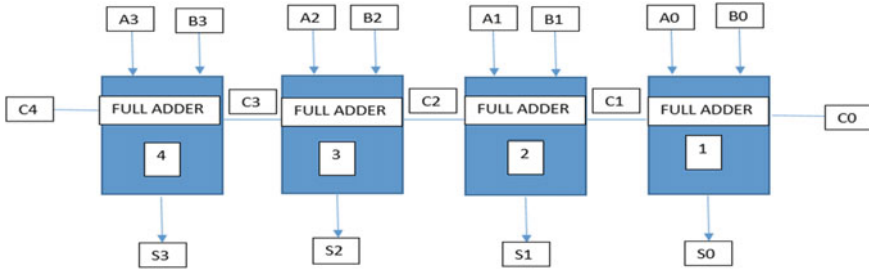


Fig. 8 4-bit ripple carry adder using 1-bit full adder

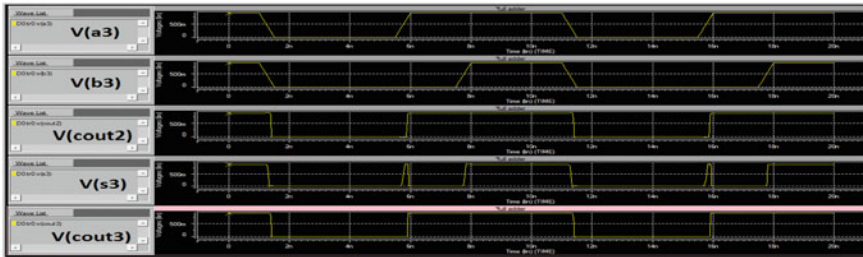


Fig. 9 Simulated output waveform of the fourth stage of 4-bit ripple carries adder

3.2 4-Bit Ripple Carry Adder

A 4-bit full adder is made up of four 1-bit adders giving output as 4 sums and 1 carry [10] (Fig. 8).

On simulating the circuit of 4-bit full adder on applying leakage power reduction techniques, output waveforms were obtained which are shown below. The following figures show the waveform of the last stage of the 4-bit full adder using different leakage reduction technique on application of leakage reduction techniques having inputs a3, b3, and cout2 (which is the previously generated carry) and the outputs s3 and Cout3 (Figs. 9, 10, 11 and 12).

4 Simulation and Analysis

The effect of varying input voltage from 0.5 to 0.9 V on power consumption for the abovementioned techniques in 1-bit full adder and 4-bit Ripple carry adder is shown in Figs. 13 and 14. In both the adders we can analyze that the sleep technique has minimum power consumption.

Table 1 shows power consumption in different techniques in 1-bit full adder and 4-bit ripple carry adder. All the techniques are simulated in 45 nm CMOS technology in

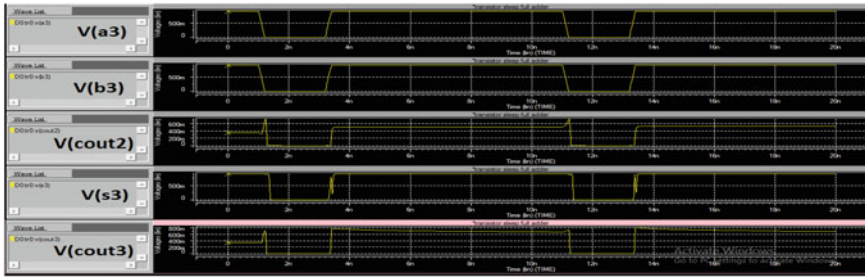


Fig. 10 Simulated output waveform of the fourth stage of 4-bit full adder on applying sleep transistor technique

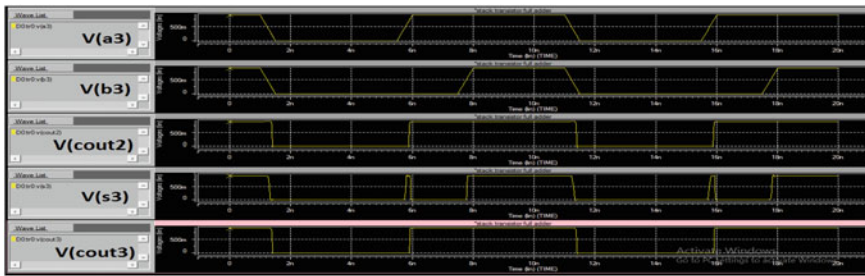


Fig. 11 Simulated waveform of the fourth stage of 4-bit full adder on applying stack transistor technique

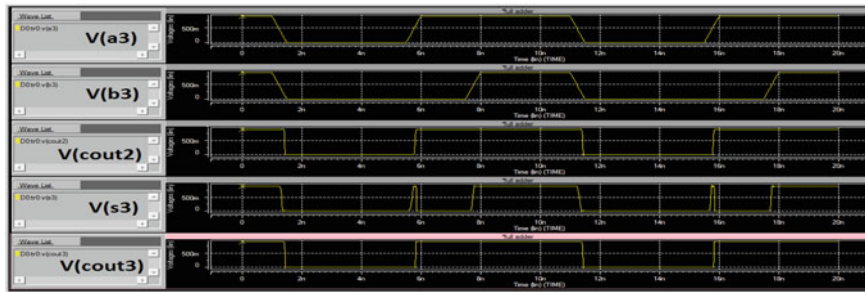


Fig. 12 Simulated output waveform of the fourth stage of 4-bit full adder on applying SCCMOS technique

Hspice software. The analysis concludes that in 1-bit full adder power consumption comes out to be 10.1089 nW at 0.9 V supply voltage which has been reduced by 1.83 times using sleep transistor technique, 1.29 times using stack transistor technique and 1.3347 times using SCCMOS technique, whereas in 4-bit ripple carry adder power consumption which comes out to be 73.5254 nW at 0.9 V supply voltage which has

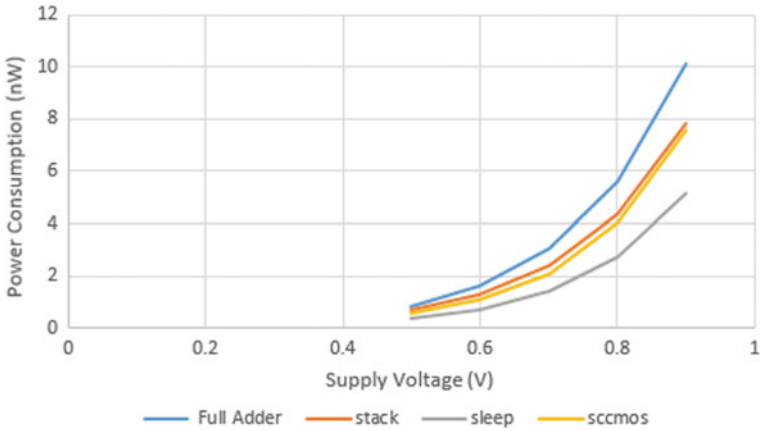


Fig. 13 Power consumption versus supply voltage for different techniques in 1-bit full adder

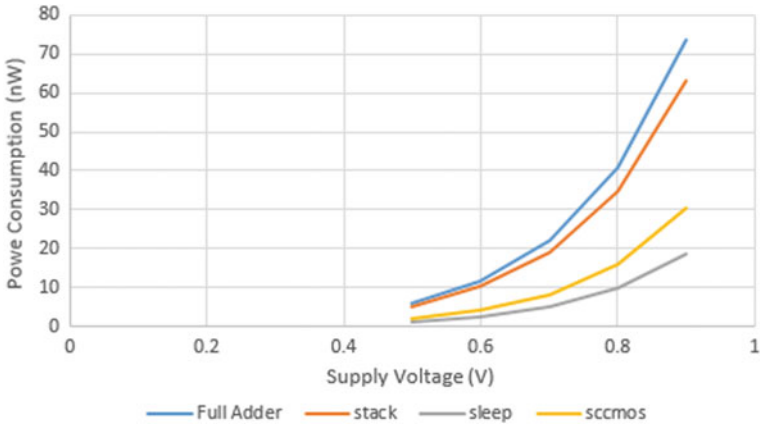


Fig. 14 Power consumption versus supply voltage for different techniques in 4-bit ripple carry adder

been reduced by 3.95 times using sleep transistor technique, 1.16 times using stack transistor technique and 2.42 times using SCCMOS technique.

5 Conclusion

We hereby note that reduction in power consumption was the most prominent in Sleep Transistor technique. For 1-bit Full Adder, power reduction comes out to be

Table 1 Power consumption of the abovementioned techniques at varying voltages

Circuit	Power consumption (nW)				
	Vdd = 0.5 V	Vdd = 0.6 V	Vdd = 0.7 V	Vdd = 0.8 V	Vdd = 0.9 V
1-bit full adder	0.854	1.6297	3.0458	5.5933	10.1089
Sleep transistor technique in 1-bit full adder	0.3511	0.7119	1.4084	2.7226	5.498
Stack transistor technique in 1-bit full adder	0.674	1.2791	2.378	4.3447	7.8158
SCCMOS technique in 1-bit full adder	0.5506	1.0722	2.0892	4.016	7.5739
4-bit ripple carry adder	6.2098	11.8474	22.147	40.6771	73.5254
Sleep transistor technique in 4-bit full adder	1.383	2.712	5.248	9.9714	18.6005
Stack transistor technique in 4-bit full adder	5.3315	10.1648	18.9884	34.8528	62.9602
SCCMOS technique in 4-bit full adder	2.2027	4.2888	8.357	16.0642	30.2961

10.1089 nW whereas sleep technique has 5.1498 which is lower than other techniques. For 4-bit ripple carry adder, power reduction comes out to be 73.5254 nW whereas sleep technique has 18.6005 which is lower than other techniques.

These techniques can be used for various circuits like multipliers, carry look-ahead adder, etc. for low power consumption.

References

1. Gupta RK, Rathi M (2017) Comparison of various leakage power reduction techniques for full adder circuit
2. Kang S, Leblibici Y (2013) CMOS digital integrated circuits: analysis and design. Tata McGraw Hill
3. Yeo K-S, Roy K (2004) Low-voltage, low-power VLSI subsystems. McGraw Hill
4. Chandrakasan AP, Brodersen RW (1995) Low power digital CMOS design. Kluwer Academic Publishers, Boston
5. Fujita T, Hatori F (2015) A comprehensive study on power reduction techniques in deep submicron technologies. Int J Eng Res Appl: 517–521
6. Sneha Naga Shilpa P, Mahender Reddy E, Jayakrishna P (2013) Low power Cmos full adder design with sleep transistor for submicron VLSI technologies, vol 2
7. Kalyani P, Satishkumar P (2013) Various low power techniques in Cmos circuits, vol 3

8. Nagar A, Parmar V (2014) Implementation of transistor stacking technique in combinational circuits. *IOSR J VLSI Signal Process* 4:01–05
9. Kawaguchi H, Nose K, Sakurai T (2000) A super cut-off CMOS (SCCMOS) scheme for 0.5-V supply voltage with picoampere stand-by current. *IEEE J Solid-State Circ* 35:1498–1501
10. Morris Mano M (2001) *Digital design*, 3rd edn

A Nature-Inspired Metaheuristic Swarm Based Optimization Technique BFOA Based Optimal Controller for Damping of SSR



Rajeev Kumar, Rajveer Singh and Haroon Ashfaq

Abstract In the proposed paper, an innovative method for damping of sub-synchronous resonance in a series capacitor compensated line has been investigated. A nature-inspired metaheuristic swarm based optimization technique BFOA is applied over the optimal control theory for damping and mitigation of sub-synchronous oscillations, with a FACT controller (SVS) connected at the midpoint of a series capacitor compensated network. The analysis has been carried out using IEEE first benchmark model and the entire test system has been simulated using MATLAB software, the simulation results include the eigenvalue analysis which explicitly shows that the application of BFOA on the optimal control theory, the problem of SSR is effectively minimized. Further the time domain analysis for the response curve of rotor angle (Mech-Delta 5) also shows the effectiveness of the proposed BFOA based optimal controller. All the time domain parameters viz., rise time, settling time, overshoot, and peak time is improved by the application of optimal controller which is further improved by the application of BFOA over optimal controller.

Keywords BFOA · Eigen value · Optimal control theory · Static var system · Sub-synchronous resonance · Torsional oscillations · Time domain analysis

1 Introduction

The use of series capacitors in transmission line definitely helps in the improvement of power transfer capability as well as transient and steady state stability limits of power systems and it is also economical compared to the addition of new lines. However, the Series compensated lines having capacitance C have a tendency to produce series resonance at frequencies below the fundamental power frequency. This is called sub-synchronous resonance [1–4]. SSR problem results due to the interaction

R. Kumar (✉) · R. Singh · H. Ashfaq
Department of Electrical Engineering, Jamia Millia Islamia, New Delhi 110025, India
e-mail: rajeev.kumar@kiet.edu

© Springer Nature Singapore Pte Ltd. 2020
A. Kalam et al. (eds.), *Intelligent Computing Techniques for Smart Energy Systems*,
Lecture Notes in Electrical Engineering 607,
https://doi.org/10.1007/978-981-15-0214-9_66

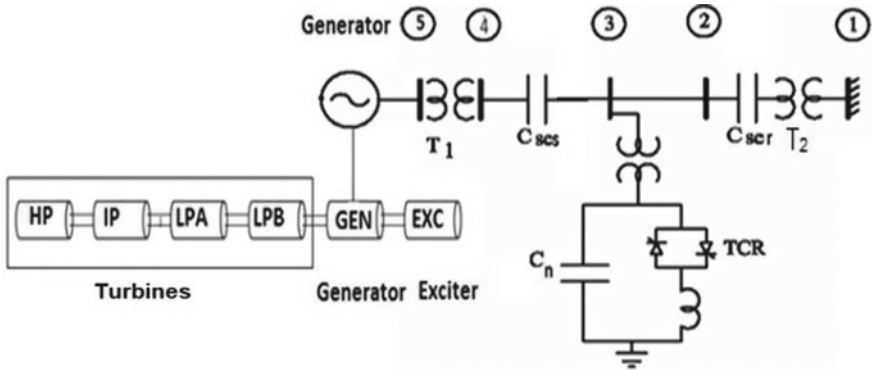


Fig. 1 Study system

between series capacitor compensated electrical network and the mechanical spring-mass system of the turbine generator at sub-synchronous frequencies which can lead to turbine generator shaft failure and electrical instability of the system. This phenomenon is known as sub-synchronous resonance (SSR). Therefore, when going for the series capacitor compensation the chances of SSR must be carefully examined using some well-defined techniques proposed by IEEE and the required counter measures must be exercised to avoid the SSR, if the analysis reveals a potential SSR problem. A number of techniques for damping and control of SSR have been suggested in the past [2–5]. Excitation controller [6] and several series and shunt FACT controllers such as STATCOM, TCSC, and SVS have been proposed and tested [7] to avoid the torsional oscillations caused by SSR. Out of these, SVS has become popular in the modern power system because of its potential to operate as reactive power (var) compensator (generation and absorption).

In the proposed paper BFOA based optimal Controller has been used to mitigate the problem of SSR in the power system, the power system model used is a modified IEEE first benchmark model (FBM) with SVS connected at the mid of the line [8] so as to achieve the optimum performance.

The purpose of the paper is to expose the potential of BFOA algorithm in damping and control of SSR when implemented with optimal control theory and compare the effectivity of both the controllers in the mitigation of the low frequency torsional oscillations.

2 System Configuration

The system (Fig. 1) considered is a modified IEEE first benchmark model consisting of an alternator supplying bulk power to an infinite bus over 400 kV, The length of the line is considered as 600 km, for which the shunt parameters are duly considered. The series compensation has been provided at both the ends of the line. A fixed

capacitor thyristor controlled reactor type SVS is located at the mid of the line that provides continuously controllable reactive power at its terminal.

The different subsystems of the model are described in [7].

3 Development of Overall System Model

The entire system model has been developed by associating the differential equations of each constituent subsystems model developed earlier in [7] to result in state space model equation of the entire system.

4 Application of Optimal Control Theory

The equation that we have developed for the overall system is similar to the standard equation used in the optimal control theory.

$\dot{x} = Ax(t) + Bu(t) + Fw$ is the standard form of equation used in the optimal control theory [9].

5 Optimal Parameter Selection Using BFOA

5.1 A Brief Overview of BFOA

Bacteria Foraging Optimization Algorithm (BFOA), proposed by Passino, is one of the metaheuristic nature-inspired evolutionary optimization algorithms. Evolutionary algorithms influenced by the law of natural selection have solved many real-world optimization problems. All the evolutionary algorithms have almost three things in common like the process involves initialization, selection, and reproduction. A fitness function generally used to rank the health of each population and based on which appropriate selections are made. After this selection the unhealthy population those having low fitness function are eliminated and new population is formed for further evaluation and selection. One such evolutionary algorithm based on swarm behavior is Bacterial Foraging Optimization Algorithm (BFOA). The algorithm as suggested by Passino in the year 2002, was based on the foraging properties of the *E-Coli* bacteria and mimics their behavior in searching nutrients for their survival. Bacteria searches for their food in a way to optimize their energy gained per unit time. They also communicate with each other via signals. The way by which the bacteria moves by making the small steps in search of the food is known as chemotaxis and the key idea of BFOA is copying the chemotactic movements of hypothetical bacterium in the search space. This movement is classified into two steps namely

“swimming” (if the movement is in forward direction referred to as) and “tumbling” (if is in reverse direction referred to as). Swimming and tumbling occur alternately in bacteria’s search for nutrients. The nutrients represent the solution in the case of optimization problems. A virtual bacteria is nothing but one of the trial solutions regarded as a search agent which moves on a problem search space (objective function surface) to get the global optimum position. The algorithm and flow chart of BFO is described in [10].

6 Results and Discussions

6.1 Case Study with 60% Series Compensation

The System data is taken from [11]. The system is delivering $P_g = 800$ MW, the eigenvalues for different system modes for 20% change in the reference voltage (considered as a step input disturbance to the system) have been computed for the system with SVS only, with the application of the optimal controller and optimal plus BFOA with and without natural damping at 60% compensation level.

Case 1. Natural damping considered is zero. A perturbation of 20% change in the reference voltage is considered, the eigenvalues for different system modes obtained are given in Table 1.

The various system response curves (viz. Rotor angle, HP-IP torque, and SVS Susceptance) for step input disturbance (20% change in the reference voltage) with SVS only, optimal controller, and optimal controller plus BFOA is shown in Figs. 2, 3 and 4, respectively. The time-domain results for the rotor angle (Mech-Delta 5) curve shown in Fig. 2 is given below in Table 2 shows all the time domain parameters viz., rise time, settling time, overshoot, and peak time have been improved by the use of the optimal controller which is further improved by the application of BFOA on the optimal controller.

Table 1 System Eigenvalues for case 1 at 60% compensation level

MODE Mech.	With SVS only	With optimal controller	With optimal controller and BFO
Mode 5	$4.9296e-5 \pm 298.18i$	$-0.41984 \pm 298.18i$	$-0.42990 \pm 298.18i$
Mode 4	$-1.3000e-1 \pm 203.02i$	$-6.9124 \pm 202.95i$	$-7.0198 \pm 202.95i$
Mode 3	$-0.096318 \pm 160.77i$	$-8.5361 \pm 160.80i$	$-8.6401 \pm 160.80i$
Mode 2	$-0.017522 \pm 127.06i$	$-6.2103 \pm 128.50i$	$-6.3110 \pm 128.50i$
Mode 1	$0.0982 \pm 99.6781i$	$-8.1250 \pm 98.6839i$	$-8.2252 \pm 98.6840i$
Mode 0	$-1.6621 \pm 14.5739i$	$-3.1593 \pm 13.4312i$	$-3.2598 \pm 13.4312i$

Case 2. Natural damping considered is 0.0322. A perturbation of 20% change in the reference voltage is considered, the eigenvalues for different system modes obtained are given in Table 3.

The various system response curves (viz., rotor angle, HP-IP torque, and SVS susceptance) for step input disturbance (20% change in the reference voltage) with SVS only, optimal controller, and optimal controller plus BFOA is shown in Figs. 5, 6 and 7, respectively. The time-domain results for the rotor angle (Mech-Delta 5) curve shown in Fig. 5 is given below in Table 4 shows all the time domain parameters viz., rise time, settling time, overshoot, and peak time have been improved by the use of the optimal controller which is further improved by the application of BFOA on the optimal controller.

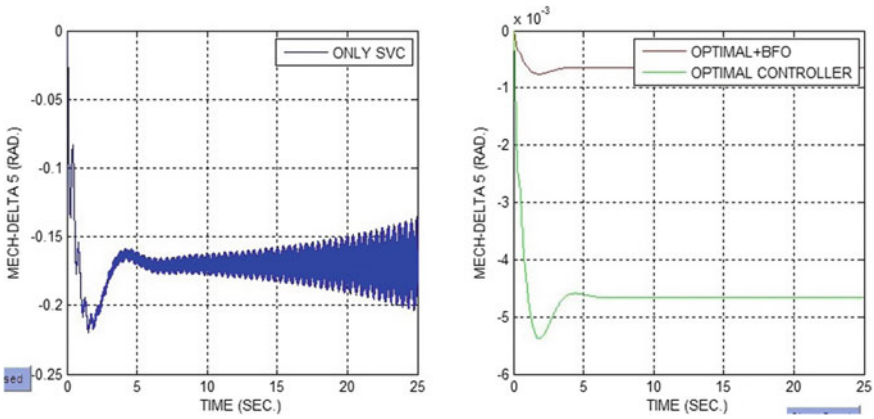


Fig. 2 Mech Delta 5 (Rad) for case 1 at 60% compensation

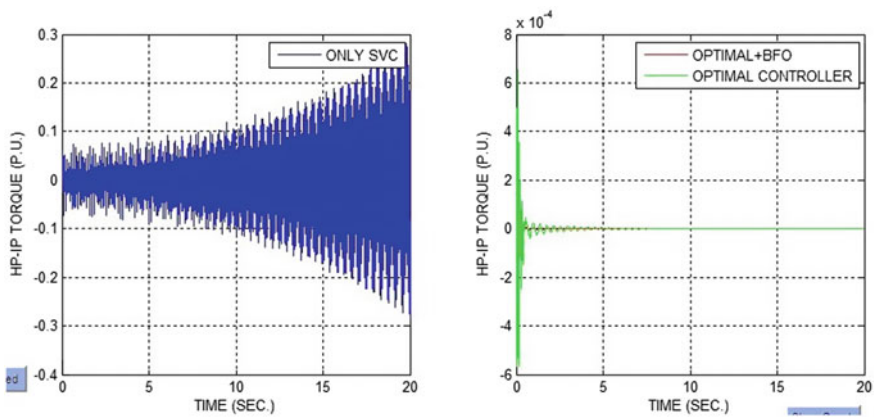


Fig. 3 HP-IP torque (p.u.) for case 1 at 60% compensation

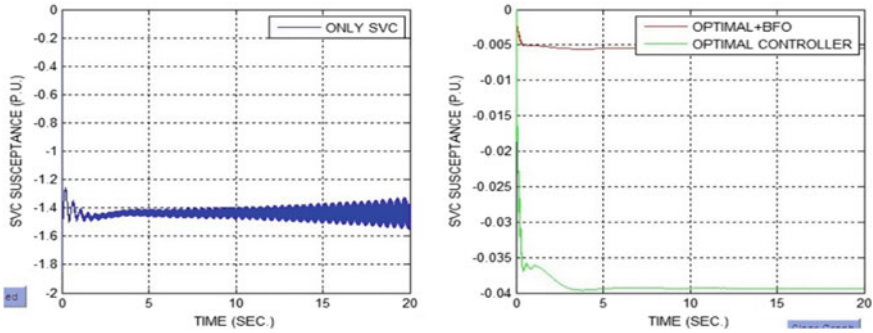


Fig. 4 SVC susceptance (p.u.) for case 1 at 60% compensation

Table 2 Time domain analysis for the rotor angle curve for case 1 at 60% compensation

Mech-Delta 5 Spec.	With SVS only time (s)	With optimal controller time (s)	With optimal controller and BFO time (s)
Rise- time	0.55774	0.78061	0.7706
Settling- time	24.998	3.3696	3.3348
Over- shoot	19.002	16.12	15.45
Under- shoot	0	0	0
Peak- time	1.56	1.84	1.82

Table 3 System eigen values for case 2 at 60% compensation level

Mode Mech.	With SVS only	With optimal controller	With optimal controller and BFO
Mode 5	$-4.4281 \pm 298.14i$	$-4.4478 \pm 298.14i$	$-4.5480 \pm 298.14i$
Mode 4	$-3.4796 \pm 202.96i$	$-7.4854 \pm 202.88i$	$-7.5917 \pm 202.88i$
Mode 3	$-2.4078 \pm 160.66i$	$-8.7372 \pm 160.69i$	$-8.8409 \pm 160.69i$
Mode 2	$-10.738 \pm 126.57i$	$-12.030 \pm 127.92i$	$-12.531 \pm 127.92i$
Mode 1	$-1.6293 \pm 99.7485i$	$-8.2377 \pm 98.8839i$	$-8.3378 \pm 98.8840i$
Mode 0	$-2.5670 \pm 14.5373i$	$-3.8490 \pm 13.3442i$	$-3.9492 \pm 13.3387i$

7 Conclusion

In the proposed paper the potential of BFOA based optimal controller is investigated for damping of the electro-mechanical torsional oscillations in a given series compensated power system. The load flow study is carried out for calculating the operating point. The eigenvalue analysis is done for the system at $P_g = 800$ MW with and without natural damping at a compensation level of 60% to evaluate the dynamic performance of the series compensated line and the unstable torsional system modes are

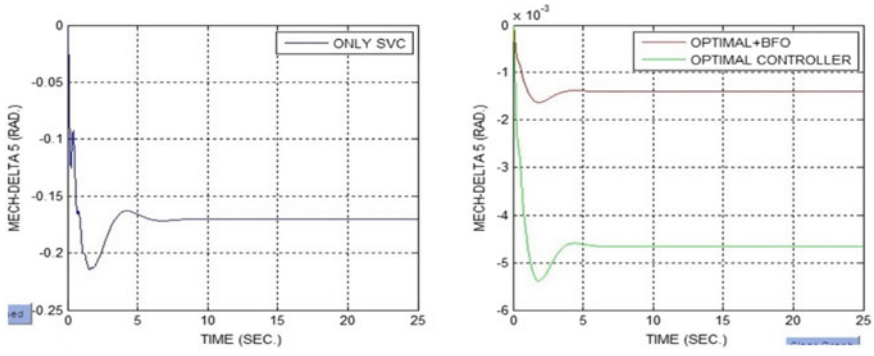


Fig. 5 Mech-Delta 5 (Rad) for case 2 at 60% compensation

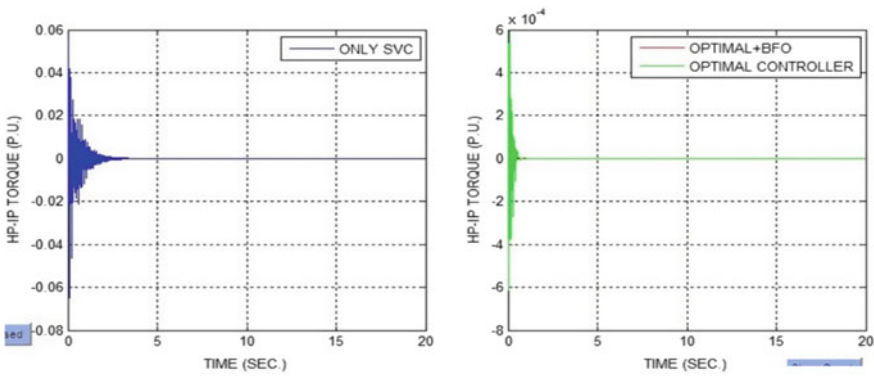


Fig. 6 HP-IP torque (p.u.)

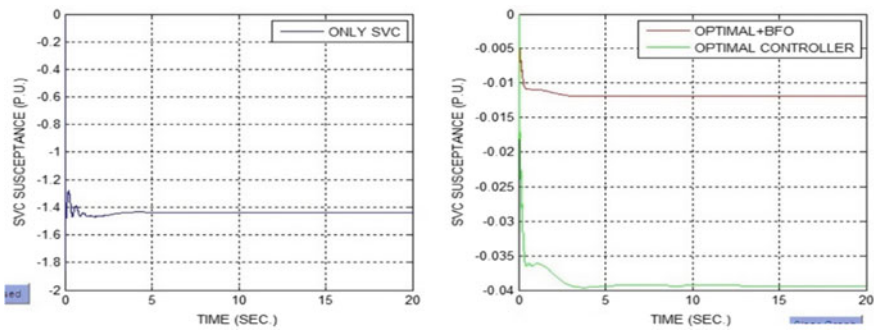


Fig. 7 SVC susceptance (p.u.)

Table 4 Time domain analysis for the rotor angle curve for case 2 at 60% compensation

Mech-Delta 5 Spec.	With SVS only time (s)	With optimal controller time (s)	With optimal controller BFO time (s)
Rise- Time	0.5531	0.78956	0.7706
Settling- Time	5.2026	3.3761	3.3348
Over- shoot	25.869	16.28	15.45
Under- shoot	0	0	0
Peak- time	1.56	1.86	1.82

investigated. Time-domain analysis is also made for the response curve of the rotor angle (Mech-Delta 5) with the application of BFOA based optimal controller. The effectiveness of the proposed BFOA based control strategy is clear from the results of the eigenvalues of the system states. The results of the time-domain analysis are also seen from the response curve of the rotor angle (Mech-Delta 5) which shows the effectiveness of the proposed BFOA based optimal controller. All the time-domain parameters viz., rise time, settling time, overshoot, and peak time are improved by the application of optimal controller which is further improved by the application of BFOA over optimal controller. The responses for the SVS susceptance, mechanical angle of the generator shaft, and HP-IP turbine torque are shown. A similar response is also obtained for other system modes too. To illustrate the comparative effectiveness of the proposed controllers the system is disturbed by 20% change in the reference voltage. The natural damping of the system is considered to be zero so that effect of the control strategies can be examined effectively. The simulation results show that the proposed BFOA optimized SVS control strategy utilizes the effectiveness of BFOA to optimize SVS control signals to improve the system eigenvalues and time-domain response.

References

1. Padiyar KR (2009) FACTS controller in power transmission and distribution. New Age International, New Delhi, India
2. Padiyar KR (1999) Analysis of sub-synchronous resonance in power system. Kluwer, Norwell, MA
3. Kundur P (1996) Power system stability and control. McGraw-Hill, New York
4. Anderson PM, Agrewal BL, Van Ness JE (1990) Sub-synchronous resonance in power system. IEEE Press, New York
5. Farmer RG, Suchwalb AL (1977) Navajo project report on sub-synchronous resonance in power system. IEEE Trans Power Appar Syst PAS-96(4)
6. Wang L (1991) Damping of torsional oscillation using excitation control of synchronous generator: IEEE second benchmark model investigation. IEEE Trans Energy Convers 6(1):1810–1818
7. Kumar N, Dave MP (1996) Applications of auxiliary controlled static var system for damping sub-synchronous resonance in power system. Electr Power Syst Res 37:189–201

8. Yu Huang Z, Ooi BT (2002) Power transfer capability of long transmission line with midpoint sited FACTS and HVDC. *IEEE Trans Power Eng Rev* 22(5):51–53
9. Kothari DP, Nagrath IJ (2007) *Modern power system analysis*, 3rd edn. Tata McGraw Hill Publishing Company Limited
10. Abdul-Ghaffar HI, Ebrahim EA, Azzam M (2013) Design of PID controller for power system stabilization using hybrid particle swarm-bacteria foraging optimization. *WSEAS Trans Power Syst* 8(1). E-ISSN: 2224-350X
11. Gupta SK, Kumar N, Gupta AK (2002) Damping sub-synchronous resonance in power systems. *IEE Proc Gener Trans Distrib* 149(6):679–688

New Fuzzy Divergence Measures, Series, Its Bounds and Applications in Strategic Decision-Making



Ram Naresh Saraswat and Neha Khatod

Abstract In this paper, we have introduced a series of fuzzy divergence measures with proof of its validity. Some bounds of fuzzy divergence measure in terms of well-known divergence using new f-divergence measure, fuzzy set, and inequalities are studied. These relations may be interested in the literature of Information Theory and Fuzzy Mathematics. Application of proposed series of fuzzy divergence in strategic decision-making.

Keywords New f-divergence · Inequalities · Information divergence measures · Fuzzy set · Generalized fuzzy divergence measures · Strategic decision-making etc.

MSC2010 62B99 · 94A15 · 94A17

1 Introduction

Let $\Gamma_n = \{P = (p_1, p_2, \dots, p_n) \mid p_i \geq 0, \sum_{i=1}^n p_i = 1\}$, $n \geq 2$ be the set of all complete finite discrete probability distributions. The domain of information theory and statistics contains wide information and divergence measures. Jain and Saraswat [1] and [2] and its particular cases which are interesting in areas of information theory and statistics is given by

$$S_f(P, Q) = \sum_{i=1}^n q_i f\left(\frac{p_i + q_i}{2q_i}\right) \quad (1)$$

where $f : \mathfrak{R}_+ \rightarrow \mathfrak{R}_+$ is a convex function and $P, Q \in \Gamma_n$. Shannons's [3] Entropy is one of the key for measure of information. Zadeh [4] introduced entropy as a degree of

R. N. Saraswat · N. Khatod (✉)
Department of Mathematics & Statistics, Manipal University Jaipur,
Jaipur 303007, Rajasthan, India
e-mail: maheshwarineha20@yahoo.com

R. N. Saraswat
e-mail: saraswatramn@gmail.com

© Springer Nature Singapore Pte Ltd. 2020
A. Kalam et al. (eds.), *Intelligent Computing Techniques for Smart Energy Systems*,
Lecture Notes in Electrical Engineering 607,
https://doi.org/10.1007/978-981-15-0214-9_67

fuzziness. Fuzzy information is measured by an essential concept of Fuzzy entropy. The fuzziness of a set can be measured by measuring the fuzzy entropy of the set. Kapur [5] discusses that both fuzzy entropy and probabilistic entropy can measure uncertainty. While the former utilizes the fuzziness of information, the latter uses the information provided by a probability distribution only. The fuzzy sets as proposed by Zadeh [4] has a range of usefulness in areas of speech recognition, pattern recognition, feature selection, fuzzy aircraft control, image processing, bioinformatics, decision-making, etc. Uncertainty can be of two types

- (i) Probabilistic uncertainty
- (ii) Fuzzy uncertainty.

In Information Theory, Shannon [3] defined entropy with probability distribution. The measure of divergence has first introduced by Kullback and Leibler [6]. Divergence measure is simply a measure of the degree to which the probability distribution that has been assumed, deviates from the correct one. Other sets of probabilities like discrimination, distance, etc., can have their own measures of divergence which can find enormous applications in areas of decision-making and various other studies. Zadeh [4] in 1965 has proposed the fuzzy sets (FSs) theory as Probability theory. Fuzzy divergence presented by Bhandari and Pal [7] gives information about fuzzy measure for discrimination between two fuzzy sets A & B . It has found broad applications in the fields of signal and image processing, pattern recognition, fuzzy clustering, etc.

Here we give some examples of information divergence measures as following:

- Fuzzy chi-square divergence

$$\chi^2(A, B) = \sum_{i=1}^n \left[\frac{[\mu_A(x_i)]^2}{\mu_B(x_i)} \right] + \left[\frac{[1 - \mu_A(x_i)]^2}{1 - \mu_B(x_i)} - 1 \right] \tag{2}$$

- Fuzzy relative arithmetic-geometric divergence

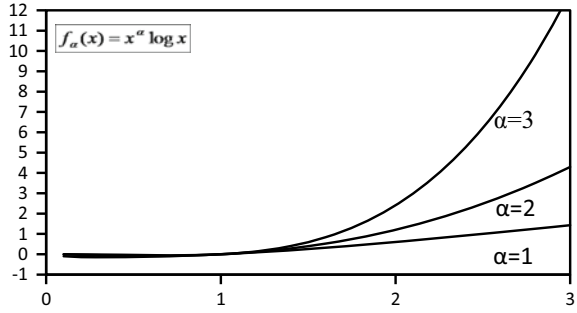
$$G(A, B) = \sum_{i=1}^n \left[\frac{\frac{\mu_A(x_i) + \mu_B(x_i)}{2} \log\left(\frac{\mu_A(x_i) + \mu_B(x_i)}{2\mu_A(x_i)}\right)}{\left(\frac{2 - \mu_A(x_i) - \mu_B(x_i)}{2}\right) \log\left(\frac{2 - \mu_A(x_i) - \mu_B(x_i)}{2(1 - \mu_A(x_i))}\right)} \right] \tag{3}$$

2 New Information Divergence Measures

In the following section, we shall evaluate the new information measures with the aid of the below convex function. Consider the function $f : (0, \infty) \rightarrow R$ given by (Fig. 1)

$$f_\alpha(x) = x^\alpha \log x, \quad \alpha = 1, 2, 3, 4 \dots \tag{4}$$

Fig. 1 Graph of convex function $f_\alpha(x)$



$$f'_\alpha(x) = x^{\alpha-1}(\alpha \log x + 1)$$

$$f''_\alpha(x) = x^{\alpha-2}[\alpha(\alpha - 1) \log x + 2\alpha - 1] \tag{5}$$

The function $f_\alpha(x)$ is always convex and normalized $f(1) = 0$. Applying in the following new f-divergence property

$$S_{f_\alpha}(P, Q) = \begin{cases} \sum_{i=1}^n q_i \left(\frac{p_i+q_i}{2q_i}\right)^\alpha \log\left(\frac{p_i+q_i}{2q_i}\right) \\ \sum_{i=1}^n \left(\frac{p_i+q_i}{2}\right) \log\left(\frac{p_i+q_i}{2q_i}\right), & \text{if } \alpha = 1 \end{cases}$$

Then we get new fuzzy divergence measure

$$S_{f_\alpha}(P, Q) = \left\{ \begin{array}{l} \sum_{i=1}^n \mu_B(x_i) \left(\frac{\mu_A(x_i)+\mu_B(x_i)}{2\mu_B(x_i)}\right)^\alpha \log\left(\frac{\mu_A(x_i)+\mu_B(x_i)}{2\mu_B(x_i)}\right) = Z_n^\alpha(A, B) \\ \sum_{i=1}^n \left[\left(\frac{\mu_A(x_i)+\mu_B(x_i)}{2}\right) \log\left(\frac{\mu_A(x_i)+\mu_B(x_i)}{2\mu_B(x_i)}\right) \right. \\ \left. + \left(\frac{2-\mu_A(x_i)-\mu_B(x_i)}{2}\right) \log\left(\frac{2-\mu_A(x_i)-\mu_B(x_i)}{2\mu_B(x_i)}\right) \right] = Z_n^1(A, B) \end{array} \right\}$$

3 Series of Fuzzy Divergence Measures

Now let the function $f : (0, \infty) \rightarrow R$ and If $\alpha = 1 \forall x > 0$. in Eq. (4), Thus, we now have the series of convex functions as stated below.

$$x \log x, \quad x^2 \log x, \quad x^3 \log x, \quad x^4 \log x, \dots \tag{6}$$

Further, we can say that if $f_1(x), f_2(x), f_3(x), f_4(x) \dots$ are convex functions, then the following function $c_1 f_1(x) + c_2 f_2(x) + c_3 f_3(x) + c_4 f_4(x) \dots$ is also a convex function.

Where $c_1, c_2, c_3, c_4 \dots$ are positive constants and at least one c_i is not equal to zero.

Now taking $c_1 = 1, c_2 = 1, c_3 = \frac{1}{2!}, c_4 = \frac{1}{3!} \dots$

$$\text{And } f_1(x) = x \log x, f_2(x) = x^2 \log x, f_3(x) = x^3 \log x, f_4(x) = x^4 \log x, \dots \tag{7}$$

We have the next series of convex function

$$x \log x + x^2 \log x + \frac{1}{2!} x^3 \log x + \frac{1}{3!} x^4 \log x + \dots = x \log x \left[1 + x + \frac{x^2}{2!} + \frac{x^3}{3!} \dots \right]$$

$$g(x) = x \log x \cdot \exp(x) \tag{8}$$

where $\exp\{.\}$ is the exponential function which when applied it to the following new f-divergence property

$$Z_n^r(P, Q) = \sum_{i=1}^n \frac{(p_i + q_i)}{2} \log \left(\frac{p_i + q_i}{2q_i} \right) \exp \left(\frac{p_i + q_i}{2q_i} \right) \tag{9}$$

we get new fuzzy divergence measure

$$= \sum_{i=1}^n \left[\frac{[\mu_A(x_i) + \mu_B(x_i)]}{2} \log \left(\frac{\mu_A(x_i) + \mu_B(x_i)}{2\mu_B(x_i)} \right) \exp \left(\frac{\mu_A(x_i) + \mu_B(x_i)}{2\mu_B(x_i)} \right) \right. \\ \left. + \frac{[2 - \mu_A(x_i) - \mu_B(x_i)]}{2} \log \left(\frac{2 - \mu_A(x_i) - \mu_B(x_i)}{2[1 - \mu_B(x_i)]} \right) \exp \left(\frac{2 - \mu_A(x_i) - \mu_B(x_i)}{2[1 - \mu_B(x_i)]} \right) \right]$$

If $\alpha = 2 \forall x > 0$ in Eq. (4).

Divergence measure $g(A, B)$ is the combination of arithmetic and triangular divergence measures.

Likewise, we get, $c_1 = 1, c_2 = 1, c_3 = \frac{1}{2!}, c_4 = \frac{1}{3!} \dots$ and (10)

$$f_1(x) = x^2 \log x, f_2(x) = x^3 \log x, f_3(x) = x^4 \log x, f_4(x) = x^5 \log x \tag{11}$$

We have the following new series of convex function

$$x^2 \log x + x^3 \log x + \frac{1}{2!} x^4 \log x + \frac{1}{3!} x^5 \log x \dots$$

$$\begin{aligned}
 &= x^2 \log x \left[1 + x + \frac{x^2}{2!} + \frac{x^3}{3!} \dots \right] \\
 &= x^2 \log x \cdot \exp(x)
 \end{aligned}
 \tag{12}$$

Then we attain the subsequent divergence measure of new f-divergence class

$$= \sum_{i=1}^n q_i \frac{(p_i + q_i)^2}{4q_i^2} \log \left(\frac{p_i + q_i}{2q_i} \right) \exp \left(\frac{p_i + q_i}{2q_i} \right)
 \tag{13}$$

Applying fuzzy

$$\begin{aligned}
 &\sum_{i=1}^n \left[\mu_B(x_i) \frac{[\mu_A(x_i) + \mu_B(x_i)]^2}{4\mu_B(x_i)^2} \log \left(\frac{\mu_A(x_i) + \mu_B(x_i)}{2\mu_B(x_i)} \right) \exp \left(\frac{\mu_A(x_i) + \mu_B(x_i)}{2\mu_B(x_i)} \right) \right. \\
 &\quad \left. + [1 - \mu_B(x_i)] \frac{[2 - \mu_A(x_i) - \mu_B(x_i)]^2}{4[1 - \mu_B(x_i)]^2} \log \left(\frac{2 - \mu_A(x_i) - \mu_B(x_i)}{2[1 - \mu_B(x_i)]} \right) \exp \left(\frac{2 - \mu_A(x_i) - \mu_B(x_i)}{2[1 - \mu_B(x_i)]} \right) \right]
 \end{aligned}
 \tag{14}$$

Similarly, by selecting appropriate constants and convex functions, it will achieve a resulting series of convex functions

$$f_k * (x) = x^k \log x \cdot \exp(x), \quad k = 1, 2, 3, 4 \dots
 \tag{15}$$

and the subsequent series of divergence measures of new f-divergence class

$$N_k * (P, Q) = \sum_{i=1}^n \frac{(p_i + q_i)^k}{2^k q_i^{k-1}} \log \left(\frac{p_i + q_i}{2q_i} \right) \exp \left(\frac{p_i + q_i}{2q_i} \right) \quad k = 1, 2, 3, 4 \dots
 \tag{16}$$

Applying fuzzy

$$\begin{aligned}
 N_k * (A, B) &= \sum_{i=1}^n \left[\frac{[\mu_A(x_i) + \mu_B(x_i)]^k}{2^k [\mu_B(x_i)]^{k-1}} \log \left(\frac{\mu_A(x_i) + \mu_B(x_i)}{2\mu_B(x_i)} \right) \exp \left(\frac{\mu_A(x_i) + \mu_B(x_i)}{2\mu_B(x_i)} \right) \right. \\
 &\quad \left. + \frac{[2 - \mu_A(x_i) - \mu_B(x_i)]^k}{2^k [1 - \mu_B(x_i)]^{k-1}} \log \left(\frac{2 - \mu_A(x_i) - \mu_B(x_i)}{2[1 - \mu_B(x_i)]} \right) \exp \left(\frac{2 - \mu_A(x_i) - \mu_B(x_i)}{2[1 - \mu_B(x_i)]} \right) \right]
 \end{aligned}
 \tag{17}$$

It is apparent from the above graph that the convex function $N_k * (x)$ gives a steeper slope as the value of k increases. Further, $f_k(1) = 0$, so that $N_k * (P, P) = 0$ and the convexity of the function $f_k(x)$ confirm that the measure (5) is nonnegative. Thus, we can say that the measure (5) is convex and nonnegative in the probability distributions pair $P, Q \in \Gamma_n$.

Theorem 3.1 $N_k * (A, B)$ is a valid fuzzy divergence measure.

- (a) $N_k * (A, B) \geq 0$
- (b) $N_k * (A, B) = 0$ if $\mu_A(x_i) = \mu_B(x_i), \forall i = 1, 2, \dots, n$
- (c) $N_k * (A, B)$ reach the maximum value for the following cases $A = (0, 1), B = (1, 0)$ or $A = (1, 0), B = (0, 1)$, gives the required results, i.e., $0 \leq N_k * (A, B) \leq 1$
- (d) It follows the condition of the convexity of $N_k * (A, B)$.

$$\frac{\partial^2 N_k * (A, B)}{\partial \mu_A^2(x_i)} > 0 \quad \text{and} \quad \frac{\partial^2 N_k * (A, B)}{\partial \mu_B^2(x_i)} > 0, \quad k > 0$$

Thus, $N_k * (A, B)$ is a convex function of fuzzy sets A and B and, therefore, in view of the definition of fuzzy divergence measure of Bhandari and Pal [7] is a valid fuzzy divergence measure.

By putting value of $k = 1, 2, 3, 4 \dots$ in Eq. (16) we get the following information divergence measures in Eqs. (18) (19) and so on.

$$N_1 * (P, Q) = \sum_{i=1}^n \frac{(p_i + q_i)}{2} \log\left(\frac{p_i + q_i}{2q_i}\right) \exp\left(\frac{p_i + q_i}{2q_i}\right) \tag{18}$$

$$N_2 * (P, Q) = \sum_{i=1}^n \frac{(p_i + q_i)^2}{4q_i} \log\left(\frac{p_i + q_i}{2q_i}\right) \exp\left(\frac{p_i + q_i}{2q_i}\right) \tag{19}$$

Hence, we get some new other fuzzy divergence measure which is the following:

$$\begin{aligned} &N_1 * (A, B) \\ &= \sum_{i=1}^n \left[\frac{[\mu_A(x_i) + \mu_B(x_i)]}{2} \log\left(\frac{\mu_A(x_i) + \mu_B(x_i)}{2\mu_B(x_i)}\right) \exp\left(\frac{\mu_A(x_i) + \mu_B(x_i)}{2\mu_B(x_i)}\right) \right. \\ &\quad \left. + \frac{[2 - \mu_A(x_i) - \mu_B(x_i)]}{2} \log\left(\frac{2 - \mu_A(x_i) - \mu_B(x_i)}{2[1 - \mu_B(x_i)]}\right) \exp\left(\frac{2 - \mu_A(x_i) - \mu_B(x_i)}{2[1 - \mu_B(x_i)]}\right) \right] \tag{20} \end{aligned}$$

and so on.

Therefore, we can conclude that the measure $N_k * (P, Q)$ is made up of generalized series of combinations of and arithmetic and triangular divergence measure.

4 Some New Other Fuzzy Information Divergence Measures

In the following section, we shall come up with some new information divergence measures using the convexity property of divergence measures. Since the addition of two convex functions is also a convex function, hence we have the resulting convex functions.

$$x \log x + x^2 \log x = x \log x(1 + x) \tag{21}$$

$$x^2 \log x + x^3 \log x = x^2 \log x(1 + x) \tag{22}$$

... and so on.

The resulting divergence measures are attained using a new f-divergence measure which is given by

$$N_1(P, Q) = \frac{1}{4} \sum_{i=1}^n \frac{(p_i + 3q_i)(p_i + q_i)}{q_i} \log\left(\frac{p_i + q_i}{2q_i}\right) \tag{23}$$

$$N_2(P, Q) = \frac{1}{8} \sum_{i=1}^n \frac{(p_i + 3q_i)(p_i + q_i)^2}{q_i^2} \log\left(\frac{p_i + q_i}{2q_i}\right) \tag{24}$$

Hence, we get some new other fuzzy divergence measures which are the following:

$$\begin{aligned} N_1(A, B) &= \frac{1}{4} \sum_{i=1}^n \left[\frac{[\mu_A(x_i) + 3\mu_B(x_i)][\mu_A(x_i) + \mu_B(x_i)]}{\mu_B(x_i)} \log\left(\frac{\mu_A(x_i) + \mu_B(x_i)}{2\mu_B(x_i)}\right) \right. \\ &\quad \left. + \frac{[4 - \mu_A(x_i) - 3\mu_B(x_i)][2 - \mu_A(x_i) - \mu_B(x_i)]}{[1 - \mu_B(x_i)]} \log\left(\frac{2 - \mu_A(x_i) - \mu_B(x_i)}{2[1 - \mu_B(x_i)]}\right) \right] \end{aligned} \tag{25}$$

... and so on.

Likewise, we can create several series of different divergence measures by making use of the properties of convex functions. The additional results of these divergence measures shall be discussed later.

5 New Information Divergence and Their Relation with Other Well-Known Divergence Measures

In the following section, we shall derive inequalities related to new and well-known divergence measure.

Proposition 5.1 Let $\mu_A(x_i)$ and $\mu_B(x_i)$ fuzzy sets defined on $A, B \in \Gamma_n$, then we have the relation

$$\Rightarrow Z_n^\alpha(A, B) \leq AT(A, B)$$

Proof

$$x^\alpha \log x < x, \quad \forall x > 0 \tag{26}$$

Put $x = \frac{\mu_A(x_i) + \mu_B(x_i)}{2\mu_B(x_i)}$ in Eq. (26), we get

$$\left(\frac{\mu_A(x_i) + \mu_B(x_i)}{2\mu_B(x_i)} \right)^\alpha \log \left(\frac{\mu_A(x_i) + \mu_B(x_i)}{2\mu_B(x_i)} \right) < \frac{\mu_A(x_i) + \mu_B(x_i)}{2\mu_B(x_i)}$$

Multiply by $\mu_B(x_i)$ and taking the summation

$$\begin{aligned} & \sum_{i=1}^n \mu_B(x_i) \left[\left(\frac{\mu_A(x_i) + \mu_B(x_i)}{2\mu_B(x_i)} \right)^\alpha \log \left(\frac{\mu_A(x_i) + \mu_B(x_i)}{2\mu_B(x_i)} \right) \right] \\ & \leq \sum_{i=1}^n \mu_B(x_i) \left(\frac{\mu_A(x_i) + \mu_B(x_i)}{2\mu_B(x_i)} \right) \end{aligned} \tag{27}$$

Put $x = \frac{2 - \mu_A(x_i) - \mu_B(x_i)}{2[1 - \mu_B(x_i)]}$ in Eq. (26), we get

$$\left(\frac{2 - \mu_A(x_i) - \mu_B(x_i)}{2[1 - \mu_B(x_i)]} \right)^\alpha \log \left(\frac{2 - \mu_A(x_i) - \mu_B(x_i)}{2[1 - \mu_B(x_i)]} \right) \leq \frac{2 - \mu_A(x_i) - \mu_B(x_i)}{2[1 - \mu_B(x_i)]}$$

Multiply by $[1 - \mu_B(x_i)]$ and taking the summation

$$\begin{aligned} & \sum_{i=1}^n [1 - \mu_B(x_i)] \left[\left(\frac{2 - \mu_A(x_i) - \mu_B(x_i)}{2[1 - \mu_B(x_i)]} \right)^\alpha \log \left(\frac{2 - \mu_A(x_i) - \mu_B(x_i)}{2[1 - \mu_B(x_i)]} \right) \right] \\ & \leq \sum_{i=1}^n [1 - \mu_B(x_i)] \left(\frac{2 - \mu_A(x_i) - \mu_B(x_i)}{2[1 - \mu_B(x_i)]} \right) \end{aligned} \tag{28}$$

Adding the Eqs. (27) and (28), we get

$$= \sum_{i=1}^n \left[\mu_B(x_i) \left(\frac{\mu_A(x_i) + \mu_B(x_i)}{2\mu_B(x_i)} \right)^\alpha \log \left(\frac{\mu_A(x_i) + \mu_B(x_i)}{2\mu_B(x_i)} \right) + [1 - \mu_B(x_i)] \left(\frac{2 - \mu_A(x_i) - \mu_B(x_i)}{2[1 - \mu_B(x_i)]} \right)^\alpha \right]$$

$$\log\left(\frac{2 - \mu_A(x_i) - \mu_B(x_i)}{2[1 - \mu_B(x_i)]}\right) \leq \sum_{i=1}^n \left[\frac{[\mu_A(x_i) + \mu_B(x_i)]}{2\mu_B(x_i)} + \frac{[2 - \mu_A(x_i) - \mu_B(x_i)]}{2} \right]$$

$$\Rightarrow Z_n^\alpha(A, B) \leq AT(A, B) \tag{29}$$

where $Z_n^\alpha(A, B)$ and $AT(A, B)$ are new fuzzy divergence measure and arithmetic divergence measures.

Corollary if $\alpha = 1, 2, 3, \dots$ we get the following relations

$$\begin{aligned} Z_n^1(A, B) &= \sum_{i=1}^n \left[\mu_B(x_i) \left(\frac{\mu_A(x_i) + \mu_B(x_i)}{2\mu_B(x_i)} \right) \log\left(\frac{\mu_A(x_i) + \mu_B(x_i)}{2\mu_B(x_i)} \right) \right. \\ &\quad \left. + [1 - \mu_B(x_i)] \left(\frac{2 - \mu_A(x_i) - \mu_B(x_i)}{2[1 - \mu_B(x_i)]} \right) \log\left(\frac{2 - \mu_A(x_i) - \mu_B(x_i)}{2[1 - \mu_B(x_i)]} \right) \right] \\ &\leq \sum_{i=1}^n \left[\frac{[\mu_A(x_i) + \mu_B(x_i)]}{2\mu_B(x_i)} + \frac{[2 - \mu_A(x_i) - \mu_B(x_i)]}{2} \right] \\ Z_n^1(A, B) &= \sum_{i=1}^n \left[\left(\frac{\mu_A(x_i) + \mu_B(x_i)}{2} \right) \log\left(\frac{\mu_A(x_i) + \mu_B(x_i)}{2\mu_B(x_i)} \right) \right. \\ &\quad \left. + \left(\frac{2 - \mu_A(x_i) - \mu_B(x_i)}{2} \right) \log\left(\frac{2 - \mu_A(x_i) - \mu_B(x_i)}{2[1 - \mu_B(x_i)]} \right) \right] \\ &\leq \sum_{i=1}^n \left[\frac{[\mu_A(x_i) + \mu_B(x_i)]}{2} + \frac{[2 - \mu_A(x_i) - \mu_B(x_i)]}{2} \right] \end{aligned} \tag{30}$$

but we know

$$\begin{aligned} G(A, B) &= \sum_{i=1}^n \left[\left(\frac{\mu_A(x_i) + \mu_B(x_i)}{2} \right) \log\left(\frac{\mu_A(x_i) + \mu_B(x_i)}{2\mu_A(x_i)} \right) \right. \\ &\quad \left. + \left(\frac{2 - \mu_A(x_i) - \mu_B(x_i)}{2} \right) \log\left(\frac{2 - \mu_A(x_i) - \mu_B(x_i)}{2(1 - \mu_A(x_i))} \right) \right] \\ &\Rightarrow G(B, A) \leq AT(A, B) \end{aligned}$$

Replace A by B

$$\begin{aligned} Z_n^1(B, A) &= \sum_{i=1}^n \left[\left(\frac{\mu_B(x_i) + \mu_A(x_i)}{2} \right) \log\left(\frac{\mu_A(x_i) + \mu_B(x_i)}{2\mu_A(x_i)} \right) \right. \\ &\quad \left. + \left(\frac{2 - \mu_A(x_i) - \mu_B(x_i)}{2} \right) \log\left(\frac{2 - \mu_A(x_i) - \mu_B(x_i)}{2[1 - \mu_A(x_i)]} \right) \right] \\ &\leq \sum_{i=1}^n \left[\frac{[\mu_A(x_i) + \mu_B(x_i)]}{2} + \frac{[2 - \mu_A(x_i) - \mu_B(x_i)]}{2} \right] \end{aligned} \tag{31}$$

Adding Eqs. (30) and (31) we get the following results

$$T(A, B) = \frac{1}{2}[G(A, B) + G(B, A)] \leq 2AT(A, B)$$

where $T(A, B)$ Arithmetic-Geometric divergence and $AT(A, B)$ Arithmetic divergence.

6 Application of Proposed Series of Fuzzy Divergence Making in Strategic Decision-Making

The applications of the fuzzy divergence measure have been specified in different areas in recent years: Ghosh et al. [8] in automated leukocyte recognition; Bhandari et al. [9], Fan et al. [10], and Bhatia and Singh [11] in image thresholding; Poletti et al. [12] in bioinformatics. The proposed divergence measure provides an application in strategic decision-making.

We assume that there be existent a set $I = \{I_1, I_2, I_3, \dots, I_m\}$ of m alternate inputs and a set of n attributes (strategies) given by $C = \{C_1, C_2, C_3, \dots, C_n\}$. The decision maker has to find the best alternative from the set I corresponding to set C of n attributes (strategies).

The computational process for solving the fuzzy strategic decision-making problem contains the below steps:

1. Make a fuzzy decision matrix.

$$\begin{array}{cccc}
 & C_1 & C_2 & \cdots & C_n \\
 I_1 & x_{11} & x_{12} & \cdots & x_{1n} \\
 I_2 & x_{21} & x_{22} & \cdots & x_{2n} \\
 \vdots & \vdots & \vdots & & \vdots \\
 I_m & x_{m1} & x_{m2} & \cdots & x_{mn}
 \end{array}$$

$$W = [w_1, w_2, \dots, w_n]$$

2. Construct a normalized fuzzy decision matrix. The normalized value n_{ij} is calculated as

$$n_{ji} = x_{ji} / \sqrt{\sum_{j=1}^m x_{ji}^2}, \quad j = 1, 2, \dots, m, \quad i = 1, 2, \dots, n. \quad (32)$$

3. Construct a weighted normalized fuzzy decision matrix, Weighted normalized value

$$v_{ji} = w_i n_{ji} \quad j = 1, 2, \dots, m, \quad i = 1, 2, \dots, n. \quad (33)$$

where the weighted matrix for each strategy is as follows: $W = [1, 1, 1, 1, 1]$ and the weight of i -th attribute is w_i .

4. Calculate the fuzzy positive ideal solution A^+ and negative ideal solution A^- using the formulae

$$A^+ = \{v_1^+, v_2^+, \dots, v_n^+\} = \left\{ \max_j v_{ij} / i \in C \right\},$$

$$A^- = \{v_1^-, v_2^-, \dots, v_n^-\} = \left\{ \max_j v_{ij} / i \in C \right\} \tag{34}$$

respectively, where C is associated with the set of different strategies.

5. By using the proposed measure (17) define the separation of each option contribution from the fuzzy positive ideal solution A^+ and negative ideal solution A^- , respectively.
6. By using the formula, define the relative closeness of each alternate to positive ideal solution

$$N_k^*(A_i) = \frac{N_k^*(A^-, A_i)}{(N_k^*(A^-, A_i) + N_k^*(A^+, A_i))} \quad i = 1, 2, \dots, n. \tag{35}$$

7. Now according to the closeness coefficient, give rank the preference order of all alternatives.

Now the application of the proposed measure $N_k^*(A, B)$ with TOPSIS technique is considered in Table 1 by using the fuzzy decision matrix. Corresponding to the fuzzy decision matrix given in Tables 1 and 2 presents the normalized/weighted fuzzy decision matrix using the formulae (32) and (33). Table 3 shows the fuzzy positive A^+ and negative ideal solutions A^- using formulae (34) (Tables 4 and 5).

The distance that is minimum to the fuzzy positive ideal solution A^+ and is maximum to the fuzzy negative ideal solution A^- is the optimum solution. The values that are derived from the relative closeness of every option to the positive

Table 1 Fuzzy decision matrix

	C_1	C_2	C_3	C_4	C_5
I_1	0.5	0.2	0.6	0.9	0.4
I_2	0.4	0.6	0.8	0.3	0.6
I_3	0.8	0.3	0.5	0.7	0.2
I_4	0.6	0.4	0.2	0.8	0.9
I_5	0.9	0.5	0.3	0.4	0.7

Table 2 Normalized/weighted normalized decision matrix

	$\mu_{I_j}(C_1)$	$\mu_{I_j}(C_2)$	$\mu_{I_j}(C_3)$	$\mu_{I_j}(C_4)$	$\mu_{I_j}(C_5)$
I_1	0.3356	0.2108	0.5108	0.6082	0.2933
I_2	0.2685	0.6325	0.681	0.2027	0.4399
I_3	0.5369	0.3162	0.4256	0.473	0.1466
I_4	0.4027	0.4216	0.1703	0.5406	0.6599
I_5	0.604	0.527	0.2554	0.2703	0.5133

Table 3 Fuzzy positive A^+ and negative A^- ideal solutions

	$\mu_{I_j}(C_1)$	$\mu_{I_j}(C_2)$	$\mu_{I_j}(C_3)$	$\mu_{I_j}(C_4)$	$\mu_{I_j}(C_5)$
A^+	0.6082	0.681	0.5369	0.6599	0.604
A^-	0.2108	0.2027	0.1466	0.1703	0.2554

Table 4 Calculated numerical values of $N_k^*(A^+, A_i)$ for $k > 0$

	$k = 1$	$k = 2$	$k = 5$	$k = 10$	$k = 20$
$N_k^*(A^+, A_1)$	2.765	33.021	279.363	11058.819	19541785.852
$N_k^*(A^+, A_2)$	3.351	7.483	64.673	2538.023	4662068.081
$N_k^*(A^+, A_3)$	5.153	13.253	203.5	21622.221	260602284.970
$N_k^*(A^+, A_4)$	2.27	4.977	40.844	1487.5	2200971.673
$N_k^*(A^+, A_5)$	1.731	3.432	17.382	230.182	45873.752

Table 5 Calculated numerical values of $N_k^*(A^-, A_i)$ for $k > 0$

	$k = 1$	$k = 2$	$k = 5$	$k = 10$	$k = 20$
$N_k^*(A^-, A_1)$	1.597	2.892	10.727	84.95	6277.538
$N_k^*(A^-, A_2)$	2.996	6.005	34.277	619.19	243317.882
$N_k^*(A^-, A_3)$	1.323	2.259	6.232	25.368	434.961
$N_k^*(A^-, A_4)$	1.862	3.385	12.648	104.959	9412.736
$N_k^*(A^-, A_5)$	1.586	2.805	9.122	55.098	2501.001

ideal solution A^+ using formula (35) and their ranks are shown in Table 6. According to the coefficient of closeness, the ranks of the partiality order of these options $I_j (j = 1, 2, 3, 4, 5)$ is determined. Therefore, we conclude by taking different values of k , the ranking of the alternatives get changed but the finest choice is unaffected. So I_5 is the superior alternative.

Table 6 Computed values of relative divergence measure $N_k^*(A_i)$ for $i = 1, 2, 3, 4, 5$

	$k = 1$	$k = 2$	$k = 5$	$k = 10$	$k = 20$
$N_k * (A_1)$	0.3661	0.0805	0.03697	0.007623	3.211E-04
$N_k * (A_2)$	0.472	0.4452	0.3441	0.1931	0.001279
$N_k * (A_3)$	0.2042	0.1456	0.02971	0.001171	1.66E-06
$N_k * (A_4)$	0.4506	0.4048	0.2364	0.06591	0.004258
$N_k * (A_5)$	0.4781	0.4497	0.3464	0.1961	0.0517

7 Conclusion

In the current paper, we have achieved some series of fuzzy divergence measures by using new f -divergence measure properties with proof of validity. We have recommended generalized series of combinations of arithmetic and triangular divergence measure. We have derived inequalities relating to new and well-known divergence measure. And finally, the application of introduced fuzzy divergence measure is used in strategic decision-making.

References

1. Jain KC, Saraswat RN (2013) Some bounds of information divergence measure in term of relative arithmetic-geometric divergence measure. *Int J Appl Math Stat* 32(2):48–58
2. Jain KC, Saraswat RN (2012) A New information inequality and its application in establishing relation among various f -divergence measures. *J Appl Math Stat Inform* 8(1):17–32
3. Shannon CE (1948) A mathematical theory of communication. *Bell Syst Tech J* 2:623–659
4. Zadeh LA (1965) Fuzzy sets. *Inf Control* 8(3):338–353
5. Kapur JN (1997) Measures of fuzzy information. Mathematical Science Trust Society, New Delhi
6. Kullback S, Leibler RA (1951) On information and sufficiency. *Ann Math Stat* 22(1):79–86
7. Bhandari D, Pal NR (1993) Some new information measures for fuzzy sets. *Inf Sci* 67:204–228
8. Ghosh M, Das D, Chakraborty C, Ray AK (2010) Automated leukocyte recognition using fuzzy divergence. *Micron* 41:840–846
9. Bhandari D, Pal NR, Majumder DD (1992) Fuzzy divergence, probability measure of fuzzy event and image thresholding. *Inf Sci* 13:857–867
10. Fan S, Yang S, He P, Nie H (2011) Infrared electric image thresholding using two-dimensional fuzzy entropy. *Energy Procedia* 12:411–419
11. Bhatia PK, Singh S (2013) A new measure of fuzzy directed divergence and its application in image segmentation. *Int J Intell Syst Appl* 4:81–89
12. Poletti E, Zappelli F, Ruggeri A, Grisan E (2012) A review of thresholding strategies applied to human chromosome segmentation. *Comput Methods Programs Biomed* 108:679–688

Mutual Coupling Reduction of Biconvex Lens Shaped Patch Antenna for 5G Application



Ribhu Abhusan Panda, Udit Narayan Mohapatro and Debasis Mishra

Abstract This paper is an attempt to highlight the reduction of mutual coupling by implementing a simple structure rectangular strip. The proposed antenna consist of two patches and both are the modification of conventional circular patch. The structure resembles the biconvex lens structure. To reduce mutual coupling a simple strip of copper has been implemented between the two patches. The maximum distance between the two arches of the patches is equal to the wavelength λ which can be computed by taking the corresponding design frequency of 15 GHz. The frequency 15 GHz has been assigned for 5G communication. As mutual coupling is an unwanted thing for the efficient utilization of patch antenna with more than one patch so a simple structure has been implemented in the space which is greater than 0.5λ .

Keywords Biconvex patch · 5G · Mutual coupling · HFSS · Directivity · Antenna gain

1 Introduction

In the past few years, many antennas have been developed to exploit the benefit of small size and wideband. In the year 2016 the metamaterial substrate has been used to reduce the mutual coupling between the high packet patch array [1]. In the year 2012 the mutual coupling has been reduced by using waveguide metamaterials [2]. The adverse effect of mutual coupling will take place if several antennas are closely

R. A. Panda (✉) · D. Mishra
Department of Electronics and Telecommunication Engineering,
V.S.S. University of Technology, Burla, Odisha, India
e-mail: ribhupanda@gmail.com

D. Mishra
e-mail: debasisuce@gmail.com

U. N. Mohapatro
Department of Electronics and Communication Engineering, GIET, Gunupur, Odisha, India
e-mail: uditnarayanmohapatro@gmail.com

© Springer Nature Singapore Pte Ltd. 2020
A. Kalam et al. (eds.), *Intelligent Computing Techniques for Smart Energy Systems*,
Lecture Notes in Electrical Engineering 607,
https://doi.org/10.1007/978-981-15-0214-9_68

packed. This will reduce the efficiency of the antenna by reducing the bandwidth [3]. To reduce this mutual coupling many methods have been implemented. EBG (Electronic Bandgap Structures) have been implemented to overcome this problem [4–7]. By implementing strip, slot and via, a significant amount of mutual coupling has been reduced without effecting the radiation pattern [8]. The motivation to do the perturbation to the conventional circular patch antenna is the work which have been done in the year 2016 [9–12]. The log-periodic implementation of this biconvex and perturbed circular patch also has been done in the year 2016 [13, 14]. Here the same biconvex patch has been implemented but as a combination of two patches separated by a distance which is greater than 0.5λ . In recent years the mutual coupling has been reduced for the conventional patches but in this paper, an attempt to reduce the mutual coupling by implementing the perturbed strip for the modified circular patch leading to biconvex patch.

2 Design of the Proposed Antenna

2.1 Rotman Lens Equations and Proposed Modification

The proposed patch design—The conventional circular patch has been modified and the resultant structure is treated as a biconvex patch which has maximum distance between two arcs is λ which is equal to 20 mm. The separation between the two patches has been taken as 20 mm which is greater than $0.5\lambda = 10$ mm coaxial probe feed has been implemented by having the radius of outer probe $r = 2$ mm and the inner pin $r' = 0.35$ mm. The dimensions of the patch and the perturbed strip have been shown in Fig. 1.

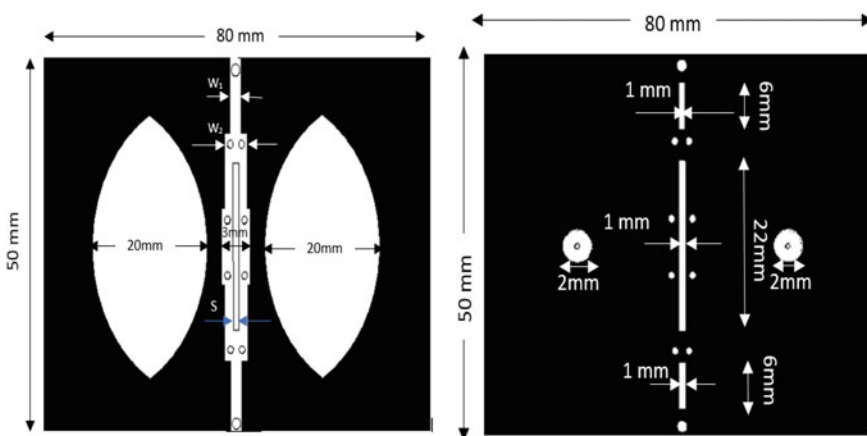


Fig. 1 Design of the proposed patch structure (left) and ground plane with slots (right)

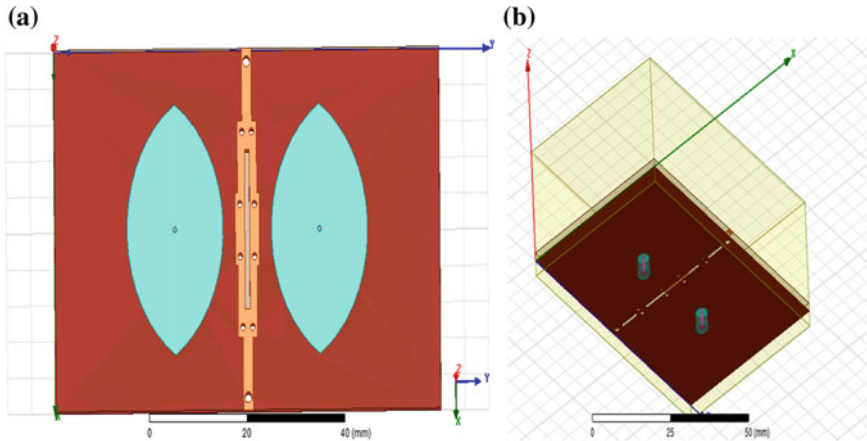


Fig. 2 Design of the proposed antenna using HFSS **a** front view **b** back view

2.2 Design of the Perturbed Strip

The perturbed strip has been implemented which has basically three parts—(i) strip (ii) slot, and (iii) via. The strip consists of three parts, the narrow width $W_1 = 1$ mm, the medium width $W_2 = 2$ mm, and the large width $W_3 = 3$ mm. The second vital part of the perturbed strip is the slot having the slot width $S = 1$ mm. The ground plane has been implemented with three slots having equal width 1 mm with different lengths shown in the Fig. 2.

3 Design and Simulation of Proposed Antenna

3.1 Substrate Material and Height

The substrate material is chosen to be FR4 Epoxy which is easily available for fabrication. It is having a dielectric constant of 4.4. The substrate is having the dimension $80\text{ mm} \times 50\text{ mm}$. The height of the substrate has been chosen as 1.6 mm which can support up to 18 GHz by the formula [15–18].

$$f_t = \frac{150}{h\pi} \left[\left\{ \sqrt{\frac{2}{\epsilon_r}} - 1 \right\} \left\{ \sqrt{\tan^{-1}(\epsilon_r)} \right\} \right] \tag{1}$$

3.2 Design of the Proposed Antenna

The proposed antenna has been designed using Ansys Electromagnetic Solution HFSS (High Frequency Structure Simulator) which uses the finite element method. Wave Port has been assigned to each face of the probe feed. So, there are two ports and based upon this S_{11} and S_{12} with S_{21} and S_{22} are calculated.

3.3 Results from Simulation of the Proposed Antenna

The simulation results include S-Parameters, VSWR, gain, directivity, and the surface current distribution. Main aspect is to verify the S_{11} , S_{12} , S_{21} , and S_{22} . As there are two ports so four S-Parameters (S_{11} , S_{12} , S_{21} , and S_{22}) have to be taken into account (Figs. 3 and 4).

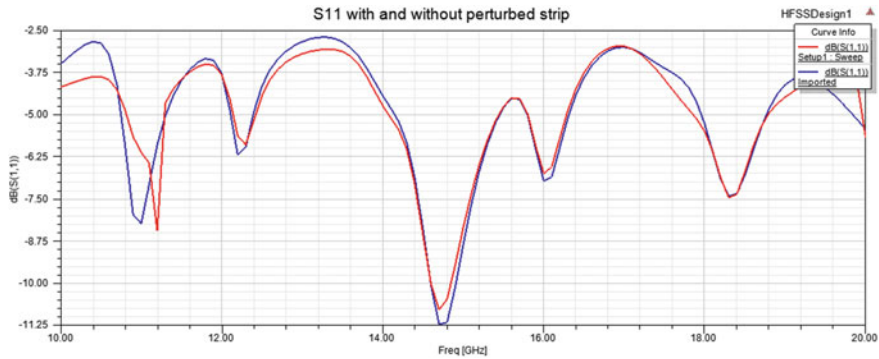


Fig. 3 Comparison of S_{11} with perturbed strip (blue) and without perturbed strip (red)

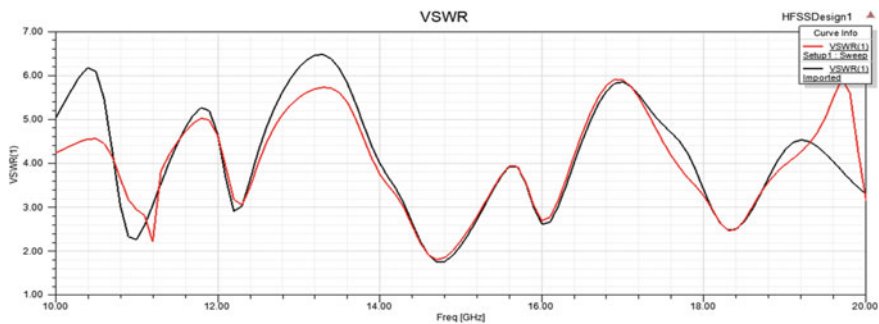


Fig. 4 Comparison of VSWR with perturbed strip (black) and without perturbed strip (red)

From the simulation results, the VSWR for the proposed antenna is coming as 1.8 without the perturbed strip and 1.71 with the perturbed strip. Ideally VSWR should be less than 2 and for the proposed antenna this condition is matched.

From the Fig. 5 it is obvious that in the 14–15 GHz Range the transmission coefficient S_{12} with the perturbed strip has less value compared to the proposed antenna without strip. The edge to edge distance is 10 mm which is 0.5λ [18]. Similarly, the S_{21} result is also compared. From the simulation result it is obvious that by implementation of the perturbed strip the mutual coupling reduces and the resonant frequency comes in the desired range (Figs. 6, 7, 8, 9, 10 and 11).

For 5G communication, the 15 GHz frequency band has been allocated [19]. This frequency is higher than that of the frequency for 3G and 4G LTE network. At this frequency the parameters like S-parameter, VSWR, gain, directivity, and radiation efficiency are measured (Table 1).

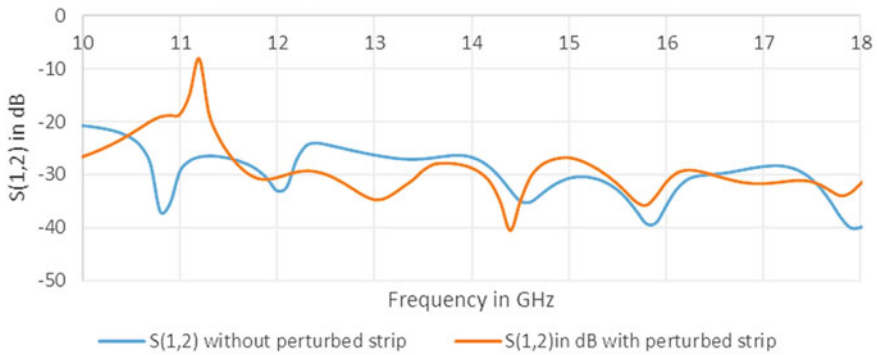


Fig. 5 Comparison of S_{12} with and without perturbed strip

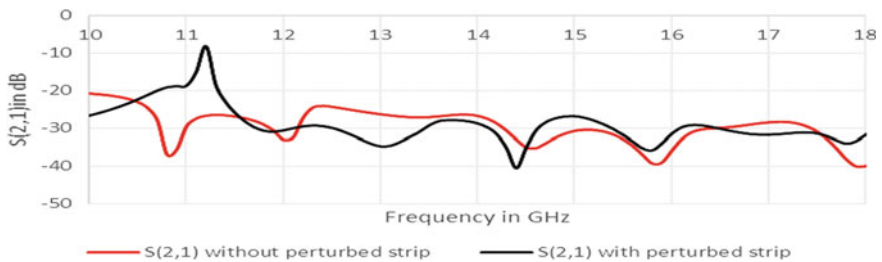


Fig. 6 Comparison of S_{21} with and without perturbed strip

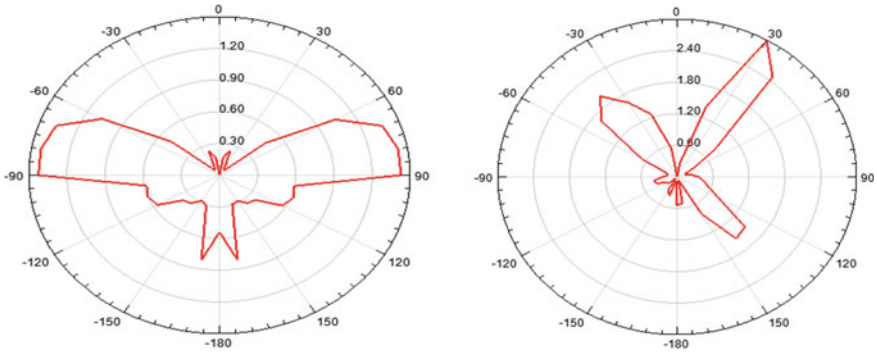


Fig. 7 Radiation pattern of Gain at $\Phi = 0^\circ$ (left) $\Phi = 90^\circ$ (right)

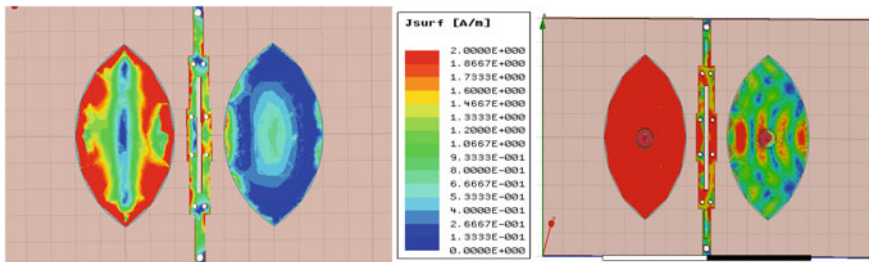


Fig. 8 Surface current distribution of proposed patch antenna (with perturbed strip)

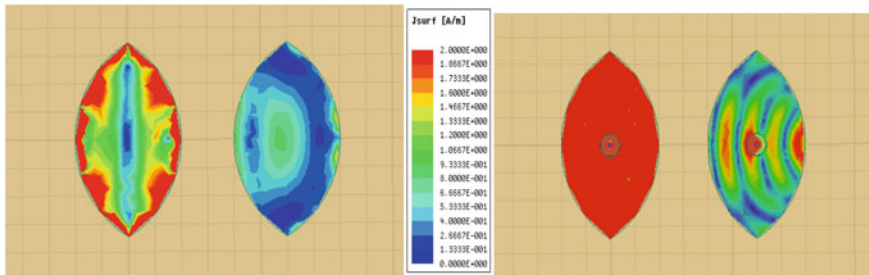


Fig. 9 Surface current distribution of proposed patch antenna (without perturbed strip)

4 Conclusion

The proposed antenna has been designed for 5G communication and the mutual coupling has been reduced by implementing perturbed strip. The radiating waves which are adversely affecting the gain and directivity are obstructed by the implementation of slots in the ground plane. Overall a significant amount of mutual coupling has been reduced for the biconvex patch without affecting the radiation pattern.

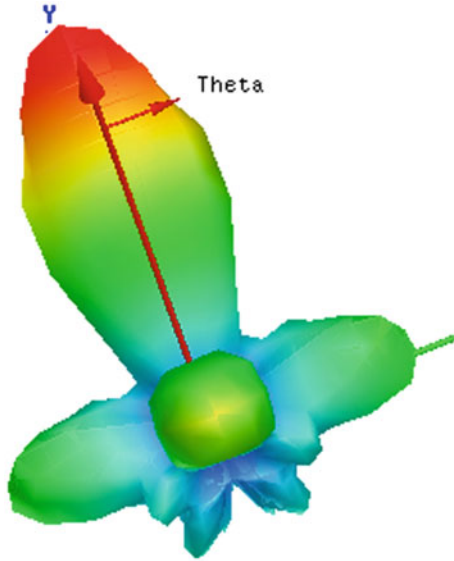


Fig. 10 3D radiation pattern

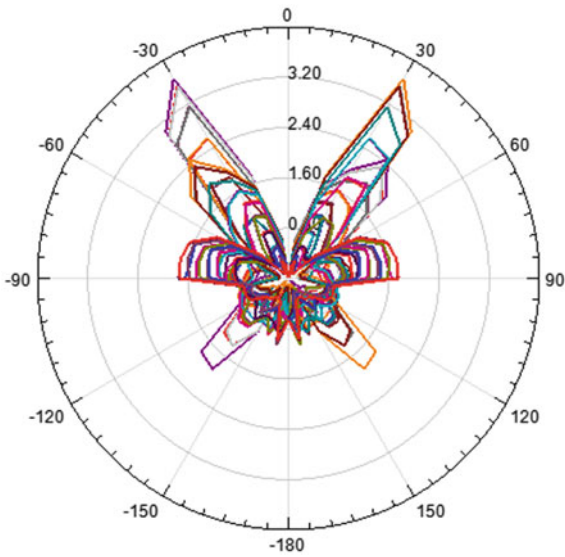


Fig. 11 Directivity of the proposed antenna

Table 1 Parameters for the band 1 for 5G communication

Parameters →	Resonant frequency (GHz)	S_{11} dB	S_{12} dB	S_{21} dB	S_{22} dB	Gain dB	Directivity dB	Radiation efficiency
Without perturbed strip	14.5	-11.2	-35.17	-35.17	-11.1	4.71	5.67	0.82
With perturbed strip	14.68	-11.2	-40.59	-40.59	-11.22	4.71	5.67	0.82

References

1. Qamar Z, Naeem U, Khan SA, Chongcheawchamnan M, Farhan Shafique M (2016) Mutual coupling reduction for high-performance densely packed patch antenna arrays on finite substrate. *IEEE Trans Antennas Propag* 64(5)
2. Yang XM, Liu XG, Zhou XY, Cui TJ (2016) Reduction for high-performance densely packed patch antenna arrays on finite substrate. *IEEE Trans Antennas Propag* 64(5)
3. Ludwig A (1976) Mutual coupling, gain and directivity of an array of two identical antennas. *IEEE Trans Antennas Propag* AP-24(6):837–841
4. Yang F, Rahmat-Samii Y (2003) Microstrip antennas integrated with electromagnetic band-gap (EBG) structures: a low mutual coupling design for array applications. *IEEE Trans Antennas Propag* 51(10):2936–2946
5. Schuhler M, Wansch R, Hein MA (2008) Reduced mutual coupling in a compact antenna array using periodic structures. In: *Proceedings of LAPC, Loughborough, U.K.*, pp 93–96
6. Farahani HS, Veysi M, Kamyab M, Tadjalli A (2010) Mutual coupling reduction in patch antenna arrays using a UC-EBG superstrate. *IEEE Antennas Wirel Propag Lett* 9:57–59
7. Coulombe M, Farzaneh KS, Caloz C (2010) Compact elongated mushroom (EM)-EBG structure for enhancement of patch antenna array performances. *IEEE Trans Antennas Propag* 58(4):1076–1086
8. Emadeddin A, Shad S, Rahimian Z, Hassani HR (2017) High mutual coupling reduction between microstrip patch antennas using novel structure. *Int J Electron Commun (AEÜ)* 71:152–156
9. Panda RA, Mishra SN, Mishra D (2016) Perturbed elliptical patch antenna design for 50 GHz application. In: *Lecture notes in electrical engineering*, vol 372, pp 507–518. Springer India, New Delhi
10. Panda RA, Mishra D, Panda H (2016) Biconvex patch antenna with circular slot for 10 GHz application. In: *SCOPEs 2016, IEEE*, pp 1927–1930
11. Panda RA, Panda H (2016) Bi-convex patch antenna with probe feed for 5.9 GHz WLAN application. *IJARECE* 5(9):2273–2276
12. Panda RA, Mishra D, Panda H (2018) Biconcave lens structured patch antenna with circular slot for Ku band application. In: *Lecture notes in electrical engineering*, vol 434, pp 73–83. Springer Nature, Singapore
13. Panda RA, Panda H, Mishra D (2016) Log periodic implementation of biconvex patch antenna. *IJERMT* 5(3):10–16
14. Panda RA, Mishra D (2016) Log-periodic waning crescent patch antenna for X-band applications. *IJRSR* 7(3):9483–9887
15. Balanis CA (2005) *Antenna theory: analysis and design*, 3rd edn. Wiley, New York
16. Kraus JD, Marhefka RJ, Khan AS (2006) *Antennas for all applications*, 3rd edn. TMH, Chap. 14
17. Pozar DM (1998) *Microwave engineering*, 2nd edn. Wiley, New York ch. 1
18. Gupta KC, Garg R, Bahl I, Bhartia P (1996) *Microstrip lines and slotlines*. Artech House, Norwood, MA Chap. 2
19. <https://www.comsoc.org/blog/latest-update-5g-ieee-communications-society>

Analysis of Anti-Islanding Protection Methods Integrated in Distributed Generation



Vikram Singh, Manoj Fozdar, Ajeet Kumar Singh and Satyendra Singh

Abstract The increase in electricity demand has given the Distributed Generation (DG) technology a boost in the power system. DG units are increasing expeditiously and majority of them are connected with distribution network in order to feed power in the local load and network as well. However, in order to do the maximum utilization of DGs few issues have to be discussed. Islanding condition is a standout amongst the most vital issue in this context. This paper discusses the various anti-islanding protection methods followed by a comparison between one of the active method with its improved variant on the basis of certain parameter.

Keywords Anti-islanding · Non-detection zone · Slip mode frequency shift · Quality factor

1 Introduction

Recently, more focus is shifted toward nonconventional, i.e., renewable sources such as wind, solar, fuel cells, etc., because of the increase in consumption of energy all over the world and the depletion of nonrenewable energy resources. Since the past decade, nonconventional energy sources have been comprehensively utilized as Distributed Generation (DG) as they are eco-friendly and cause less CO_2 emission and therefore have less impact on the environment. Thus, the concept of DG introduces a transformation from centralized generation of power to DG. But, the introduction of DG creates some issues related to the stability and power quality in nearby utility. It may result in certain protection related problems which may include selectivity prob-

V. Singh (✉)

Swami Keshvanand Institute of Technology, Jaipur 302017, India

e-mail: vikramsingh.ee.99@gmail.com

M. Fozdar · S. Singh

Malaviya National Institute of Technology, Jaipur 302017, India

A. K. Singh

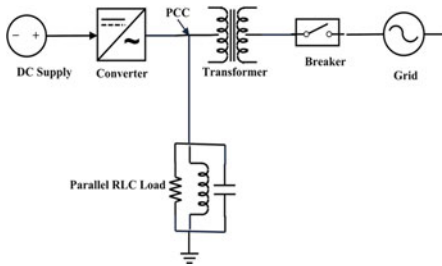
KIET Group of Institutions, Ghaziabad 201206, India

© Springer Nature Singapore Pte Ltd. 2020

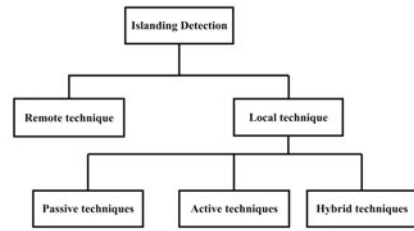
A. Kalam et al. (eds.), *Intelligent Computing Techniques for Smart Energy Systems*,

Lecture Notes in Electrical Engineering 607,

https://doi.org/10.1007/978-981-15-0214-9_69



(a) Configuration used for understanding anti-islanding features of grid connected inverters



(b) Islanding Detection Techniques

Fig. 1 Configuration used for understanding anti-islanding and classification of Islanding techniques

lem during faults, failed auto reclosing and sensitivity problems created by reduced fault current due to impact of DG. The most problematic issue in the present scenario is islanding condition. The condition of islanding is an electrical phenomenon that occurs when the energy supplied by the main utility gets interrupted due to several factors but DG continues to energize some or the entire load [1]. Islanding can be intentional as well as unintentional. Whereas intentional/planned islanding can be used for repair/maintenance purposes and could potentially bring benefits to the owner of DG by giving additional revenue due to increased power supplied in case of power outage, unintentional islanding is not desirable as there are various issues associated with it [2]. As per IEEE 1547, IEEE 929–2000, and IEC 62116 Standards [3], grid-connected DER systems have to detect fault situation for the purpose of safety and detach itself within a fixed interval of time, ranging from 0.1–2 s, which depends on the relevant standard and on the category of fault. The main ideology of identifying a situation of islanding is to observe the output parameters of DG such as, frequency, voltage, power, etc., and determine whether condition of islanding has occurred or not from shift in the values of these parameters. Islanding detection methods can be broadly classified as remote and local methods. Local methods are further classified as active, passive and hybrid methods as indicated in Fig. 1a.

2 Passive Methods

Passive techniques measure current, voltage, harmonics, and phase information at the point of common coupling (PCC) or DGs terminals, in order to identify whether an islanding has occurred or not [5–8]. The values of these parameters differ highly when the system is islanded. The most difficult thing in using passive detection techniques is setting an appropriate threshold that can effectively determine the difference between islanded condition and natural power system variations. Appropriate pre-

Table 1 DG system response to abnormal voltages [4]

Voltage range (%)	Disconnection time (sec)
$V \leq 50$	0.16
$50 \leq V \leq 88$	2
$110 \leq V \leq 120$	1
$V \geq 120$	0.16

cautions need to be considered while setting the threshold value for the purpose of discriminating islanding from other perturbations present in the system as small value of threshold setting can lead to nuisance tripping and high value of threshold setting can lead to failure of islanding detection (Table 1).

1. Rate of change of frequency (df/dt): This islanding detection technique relies on the frequency at the PCC to detect islanding. Deviation in frequency depends on the mismatch in reactive power [9, 10]. Under normal operation, i.e., in grid-connected mode, since there is no mismatch between consumed and generated reactive power, there is no deviation in the frequency. However, in islanding mode there is a mismatch between reactive power developed by DG and the reactive power consumed by the local load in the island. Depending on the ratio of the mismatch, the frequency will depart to a certain level. In case, there is a large mismatch, then the frequency will depart beyond a predefined value of threshold and the relay will trip followed by the disconnection of DG.
2. Voltage Phase Jump Detection (PJD): PJD method involves observation of error in phase between output current of inverter and voltage at the PCC [11]. The waveform of PCC voltage and output current of inverter are kept in synchronization by utilizing an analog or digital PLL. When the islanding occurs, the PCC voltage deviates from the grid voltage in order to compensate for the difference in power and also to manage the phase angle of the load. However, the output current of inverter remains invariable as it follows the PLL waveform. This leads to a jump in voltage phase as indicated in Fig. 2b. The phase error is measured and once the phase error exceeds a certain threshold value condition of islanding is detected.
3. Voltage Imbalance and Total Harmonic Distortion (THD): In this method, two criteria of islanding detection is discussed, viz., Voltage imbalance and Total Harmonic Distortion of current. VU at DG terminals is defined by

$$VU = \frac{V_{NS}}{V_{PS}} \quad (1)$$

where V_{NS} is negative sequence component of DG output and voltage V_{PS} is positive sequence component of DG output voltage. Also, as a result of disconnection of main utility change of loading occurs. This can lead to variation in the harmonics of current. Total Harmonic Distortion of current is given by

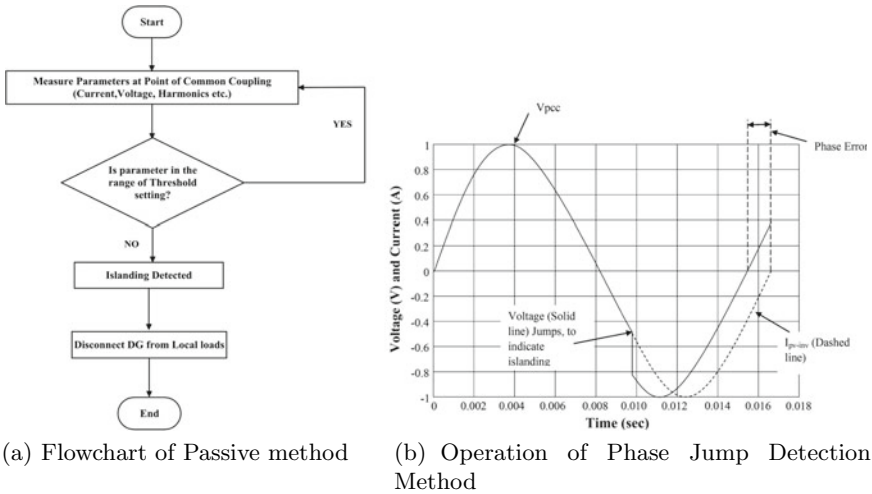


Fig. 2 Flowchart of Passive method and operation of PJD

$$THD = \frac{\sqrt{\sum_{h=2}^H I_h^2}}{I_1} \times 100 \tag{2}$$

where I_h is the root mean square value of h th harmonic component and I_1 is the root mean square value of fundamental component. When islanding occurs DG takes control of the local load. As a result, the loading of DG is immediately modified. This immediate shift results into voltage fluctuations and can also lead to current harmonics. At every interval of time, voltage unbalance of 3- ϕ voltages and total harmonic distortion of phase current are calculated. These calculated values are then compared with threshold.

3 Active Methods

Active islanding detection techniques are based on intentionally injecting disturbances with power systems operation. Islanding can be identified even in case of exact match between load and generation with the help of active methods, which would not be possible with passive techniques [12, 13]. The basic concept behind these techniques is that a little disturbance can cause a considerable shift in parameters of the system when the islanding phenomenon occurs, though the effect of disturbance will be small before islanding phenomenon occurs, i.e., when the DG is operating in parallel to the grid (Fig. 3).

1. Impedance Measurement Method: For direct measurement, an inductor is connected across supply voltage in parallel and the reduction in supply voltage and short-circuit current is utilized to evaluate the impedance of source of the power system. But, in case of indirect method a signal of large frequency is introduced into the terminals of DG with the help of voltage divider. This signal of large frequency gets more powerful when the main utility is cut off [14].
2. Slip Mode Frequency Shift (SMS): SMS is an inverter based method of islanding detection that utilizes a positive feedback control to make the source inverter unstable the source inverter when an island condition occurs. The difference in phase between the voltage at PCC and output current of inverter is made to be zero normally in a PV inverter (i.e., unity pf). However, with SMS method, rather of being controlled to zero, this phase difference between voltage and current of the inverter is designed as a function of the frequency of PCC voltage. SMS curve can be given by the following equation:

$$\theta = \theta_m \left(\frac{\pi (f^{(k-1)} - f_n)}{2 (f_m - f_n)} \right) \tag{3}$$

where θ_m is maximum value of phase shift that exist at frequency f_m , f_n is nominal frequency, and $f(k - 1)$ is the frequency of prior cycle.

3. Improved SMS (I-SMS) Method: For the purpose of eliminating the limitations of the SMS method, a modified version of it with an additional phase shift called I-SMS is recommended as (Fig. 4)

$$\theta_{I-SMS} = n(f - f_g) + F(f - f_g)\theta_0 \tag{4}$$

where, n and θ_0 are constants, $F(f - f_g)$ is signum function of frequency error.

$$F(f - f_g) = \begin{cases} 1 & f \geq f_g \\ -1 & f < f_g \end{cases} \tag{5}$$

Due to the added phase shift in I-SMS method when the frequency of grid is at its nominal value f_g , it still remains and aid to accelerate the frequency positive feedback. As a result, the islanding detection technique becomes more reliable. In order to examine the islanding detection, a parallel RLC load is considered. The resulting phase angle of current advancing the voltage is given by

$$\theta_{load} = \tan^{-1} \left(R \left(\omega C - \frac{1}{\omega L} \right) \right) \tag{6}$$

or

$$\theta_{load} = \tan^{-1} \left(Q_f \left(\frac{f}{f_0} - \frac{f_0}{f} \right) \right) \tag{7}$$

where, Q_f - Load Quality Factor and, f_0 Resonant frequency. The Quality Factor Q_f , for a parallel RLC circuit is given by

$$Q_f = R\sqrt{\frac{C}{L}} \tag{8}$$

4 Simulation Results

In order to demonstrate the design feasibility of the I-SMS method, a SIMULINK model of the utility-connected converter system is designed in MATLAB R2013a to carry out a digital simulation and authenticate the efficacy of the I-SMS technique.

Table 2 indicates the simulated run time for different values of Quality factor, Q_f of a DG inverter to illustrate all possible values for a distribution line. The run-on time is defined as the time instant between the main utility disconnection and the instant the inverter gets tripped to stop feeding the RLC loads. For $Q_f < 2.5$ the average tripping time is less whereas, in case of RLC circuit with $Q_f > 2.5$ the identification time is larger. As the value of load Quality Factor is raised, it can be seen that run-on times are enhanced. Depending on the values of Run-on Time for Slip Mode Frequency Shift (SMS) and Improved Slip Mode Frequency Shift (I-SMS) method, a comparison has been made between them by plotting a graph taking Quality factor, Q_f as abscissa and Run-on time as ordinate (Fig. 5).

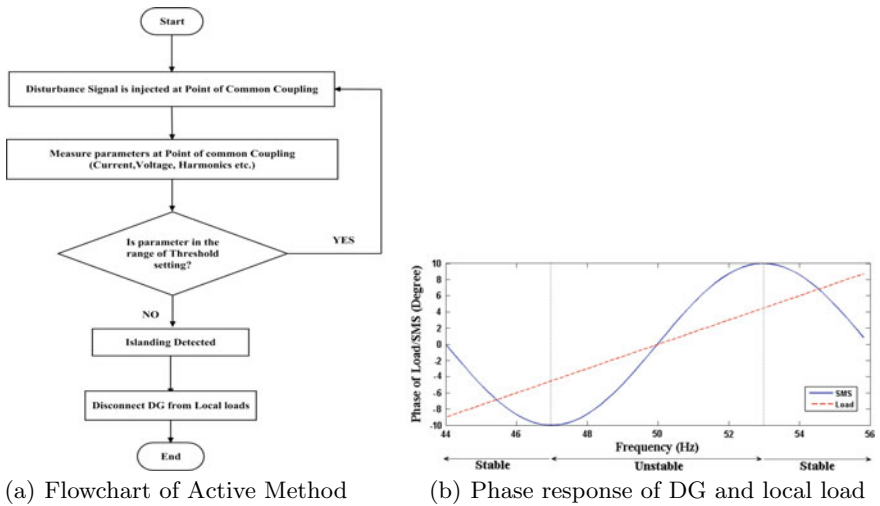
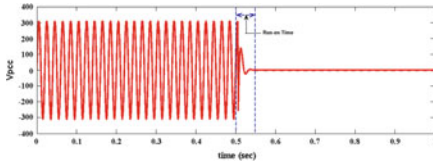
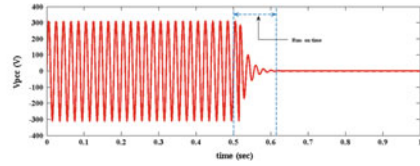


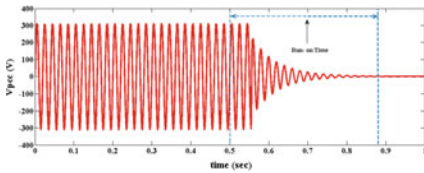
Fig. 3 Flowchart of Active Method and phase response of DG and local load



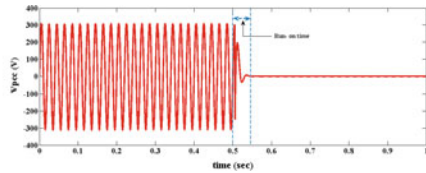
(a) Converter output voltage with I-SMS and parallel RLC load ($Q_f = 1.0, f_0 = 50$ Hz)



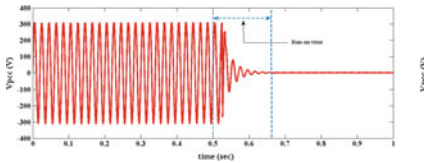
(b) Converter output voltage with I-SMS and parallel RLC load ($Q_f = 3.0, f_0 = 50$ Hz)



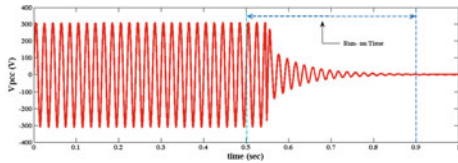
(c) Converter output voltage with I-SMS and parallel RLC load ($Q_f = 10.0, f_0 = 50$ Hz)



(d) Converter output voltage with SMS and parallel RLC load ($Q_f = 1.0, f_0 = 50$ Hz)



(e) Converter output voltage with SMS and parallel RLC load ($Q_f = 3.0, f_0 = 50$ Hz)



(f) Converter output voltage with SMS and parallel RLC load ($Q_f = 10.0, f_0 = 50$ Hz)

Fig. 4 Converter output voltage with I-SMS and SMS for different values of Quality factor

Fig. 5 Run-on time versus quality factor for SMS and I- SMS

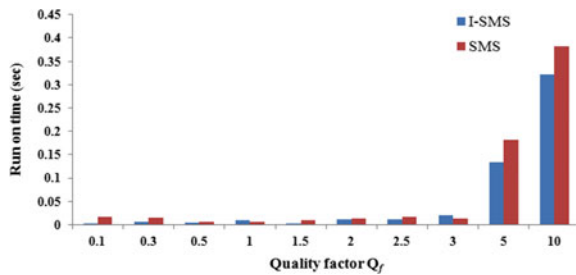


Table 2 Simulated run-on time for SMS and I-SMS

Q_f	L (mH)	C (μF)	Run-on time SMS (sec)	Run-on time I-SMS (sec)
0.1	1833.4	5.526	0.0165	0.0021
0.3	611.16	16.57	0.0158	0.0057
0.5	366.6	27.63	0.00652	0.00378
1.0	183.35	55.26	0.0052	0.0103
1.5	122.23	82.89	0.01007	0.00024
2.0	91.67	110.52	0.01295	0.01097
2.5	73.34	138.15	0.01672	0.01203
3.0	61.10	165.8	0.01289	0.01982
5.0	36.67	276.31	0.1823	0.1342
10.0	18.33	552.62	0.3821	0.3224

5 Conclusion

This paper portrays and analyzes different techniques of islanding detection. These techniques can be divided into two categories relying upon their position in the DG system, namely, local techniques and remote techniques. A MATLAB/SIMULINK model of SMS which is one of the active method is investigated and has been compared with I-SMS, which is the improved version of SMS on the basis of run-on time (a parameter) for different load quality factor Q_f and it is observed that due to the additional shift in phase introduced in I-SMS method, the islanding detection effectiveness is guaranteed and it also requires less time to detect islanding as compared to SMS method. This shows the robustness of I-SMS method and its role in reducing the run-on time and increasing the speed of islanding detection.

References

1. IEEE recommended practice for utility interface of photo-voltaic (PV) systems (2000) IEEE standards coordinating committee on photo-voltaic, IEEE Std 929–2000
2. Chiang W-J, Jou H-L, Wu J-C, Wu K-D, Feng Y-T (2010) Active islanding detection method for the grid-connected photovoltaic generation system. *Electr Power Syst Res* 80(4):372–379
3. Test Procedure of Islanding Prevention Measures for Utility Interconnected Photovoltaic Inverters (2008) IEC Std 62116
4. IEEE standard for interconnecting distributed resources with electric power systems (2003) IEEE Std 1547, pp 1–28, 28 July 2003
5. Kunte R, Gao W (2008) Comparison and review of islanding detection techniques for distributed energy resource. In: 40th North American power symposium, pp 18
6. Moradzadeh M, Rajabzadeh M, Bathaee SMT (2008) A novel hybrid islanding detection method for distributed generations. In: Third international conference on electric utility deregulation and restructuring and power technologies, pp 22902295

7. Lee S, Park J (2010) New islanding detection method for inverter-based distributed generation considering its switching frequency. *IEEE Trans Ind Appl* 46:2089-2098
8. Yu B, Matsui M, Yu G (2010) A correlation based islanding detection method using current magnitude disturbance for PV system. *IEEE Trans Ind Electron* 58, 2935-2943
9. Bugdal R, Dysko A, Burt GM, McDonald JR (2006) Performance analysis of the ROCOF and vector shift methods using a dynamic protection modeling approach. In: 15th international conference on power system protection. Bled, Slovenia
10. Freitas W, Xu W, Affonso CM, Huang Z (2005) Comparative analysis between ROCOF and vector surge relays for distributed generation applications. *IEEE Trans Power Deliv* 20(2):1315–1324
11. Xu M, Melnic RVN, Borup U (2004) Modeling anti-islanding protection devices for photovoltaic systems, 29(15):2195–2216
12. Mahat P, Bak-Jensen B (2008) Review of islanding detection methods for distributed generation. In: 3rd international conference on electric utility deregulation and restructuring and power technologies, pp 2743-2748
13. Mahat P, Chen Z, Bak-jensen B (2011) Review on islanding operation of distribution system with distributed generation. In: Power and energy society general meeting, p 1–8
14. Ropp ME, Begovic M, Rohatgi A, Kern G, Bonn R (2000) Determining the relative effectiveness of islanding detection methods using phase criteria and non-detection zones. *IEEE Trans Energy Convers* 15(3):290–296

Color Image Watermarking with Watermark Hashing



Neha Singh, Sandeep Joshi and Shilpi Birla

Abstract Color images are extensively used, published, and exchanged through internet. The need to establish ownership of digital images has resulted in the development of many image watermarking techniques. Many of these techniques are based on Singular Value Decomposition (SVD) of images. But, the major issue with SVD based watermarking is that it can be fooled easily to reproduce false data. This paper uses SVD with three different hashing techniques to counter this issue. These techniques for hash value generation are compared with respect to imperceptibility and their recovery when two copies of 128-bit hash values are embedded in addition to the watermark itself. The hash value of the claimed watermark at the receiver end will be first verified with the extracted value. If verified, the watermark is extracted. Experiments show that the PSNR of the watermarked image is nearly 41.5 dB for Lena image, irrespective of the method used for hashing. Embedding two copies of 128-bit unique hash value of the watermark exhibits an average correlation of 0.7966 during retrieval of watermark after authenticating it.

Keywords Digital image watermarking · Hashing · Singular value decomposition · SHA256 · MD5

1 Introduction

Digital image watermarking (DIW) is quite a successful tool to establish authorship of images for copyright protection. The importance of techniques for establishing ownership has grown with the growth of digital media and the use of internet for their exchange or display. DIW embeds some author information in the form of a

N. Singh (✉) · S. Joshi · S. Birla
Manipal University Jaipur, Jaipur 303007, Rajasthan, India
e-mail: neha.singh@jaipur.manipal.edu

S. Joshi
e-mail: sandeep.joshi@jaipur.manipal.edu

S. Birla
e-mail: shilpi.birla@jaipur.manipal.edu

© Springer Nature Singapore Pte Ltd. 2020
A. Kalam et al. (eds.), *Intelligent Computing Techniques for Smart Energy Systems*,
Lecture Notes in Electrical Engineering 607,
https://doi.org/10.1007/978-981-15-0214-9_70

text, string, image, logo, etc., as watermark, into the cover images. This additional data is required to be embedded such that, it does not bring in perceptible changes in the cover. At the same time, hiding should be robust enough to resist various malicious and non-malicious image manipulations. The imperceptibility of watermarking technique is measured in terms of Peak Signal to Noise Ratio (PSNR) and robustness is measured in terms of correlation of the extracted watermark and the original watermark.

There have been several DIW techniques in the literature based on Discrete Wavelet Transform (DWT) and Singular Value Decomposition (SVD). Most of these techniques have been able to embed the watermark imperceptibly and resist the general image processing operations like histogram equalization, filtering, noise, histogram equalization, compression, etc. This is because singular values exhibit high stability against variation in them caused due to addition of weighted watermark. But, the major weakness of SVD is that, if during reconstruction, singular vectors of the original image are replaced by singular vectors of some other image, the reconstructed image will closely resemble the other image. This gives rise to ambiguity in the originally embedded watermark for SVD based DIW techniques that use singular vectors as key for reconstruction of watermark from the extracted singular values. The previous work [1] highlights the major ambiguity issues with SVD based DIW techniques.

To solve this issue of extraction of the false watermark, hashcode of the original watermark is embedded into the cover along with the watermark itself. During extraction of embedded information, close match of the extracted data and hash value of the claimed watermark signifies that the claimed watermark is the original one. This paper presents the experiments performed to study the effect on PSNR of the watermarked image due to embedding hash values generated by simple bit-by-bit XORing, MD5, and SHA-256.

The paper is organized as follows: Sect. 2 presents a quick refresher about the image transforms used in the presented work, SVD, and DWT. Section 3 presents three hashing techniques under consideration: Thresholding, MD5, and SHA256. Section 4 outlines the embedding and extraction procedures used for experiments and presents results and discussions. Finally, Sect. 5 concludes the study.

2 Background

2.1 Singular Value Decomposition (SVD)

SVD [2] is a generalization of the eigen-decomposition which can be used to analyze rectangular matrices unlike eigen-decomposition, which is defined only for squared matrices. The main idea of SVD is to decompose a rectangular matrix, A , into two orthogonal matrices and one diagonal matrix, such that,

$$A = U * S * VT \quad (1)$$

where U is the orthogonal column-wise normalized eigenvectors of the matrix AA^T , called the left singular vectors of A ;

V is the orthogonal column-wise normalized eigenvectors of the matrix $A^T A$, called the right singular vectors of A ;

S is the diagonal matrix of the square root of Eigenvalues, called singular values.

SVD has been used for image compression, denoising, forensics, watermarking, etc. [3]. Most of SVD based non-blind watermarking techniques update the S matrix of the cover image with either the weighted watermark or its weighted singular values. During recovery, the Singular values are extracted from the watermarked image, but singular vectors need to be supplied. This calls for verification of the singular vectors used for reconstruction of the extracted watermark [1].

2.2 Discrete Wavelet Transform (DWT)

The wavelet analysis method is a time-frequency analysis method which selects the appropriate frequency band adaptively based on the characteristics of the signal. Then the frequency band matches the spectrum which improves the time-frequency resolution. In the wavelet space, a function is represented with an infinite series of wavelets, whose most of the energy is confined in a finite interval. The transform contains frequencies from a certain frequency band only.

3 Hashing Techniques

Hashing algorithms have been lately used for password security, image authentication, and watermarking. These algorithms are one-way functions, which means that one can get the output from the input but input cannot be retrieved from the output. A hashing algorithm generates a fixed sized output for an input message of arbitrary size, based on the message itself. This fixed sized output is called the hash value, the hashcode or the message digest, which serves as a fingerprint of the message. Possibly, the simplest hash function generator uses bit-by-bit XOR. The result obtained for bit-by-bit XORing of two message blocks is further XORed with the next block, and so on. The resulting hash value denotes the parity at each bit position, respectively, for all blocks.

MD5 is one of the well-known and widely used hashing algorithms which produces a one-way 128 bits hash value which is used for authentication of the message. This 128-bit MD5 hash is a sequence of 32 hexadecimal digits. This algorithm divides the input message into data blocks of 512 bits each, where extra bits are padded is required. Each block is further divided into 16 words of 32 bits each. To begin with,

MD5 initialized four constants referred to as, $A = 01234567$, $B = 89abcdef$, $C = fedcba98$, and $D = 76543210$. Each message block is processed with 64 operations, grouped in four rounds of 16 operations each. Each round is based on a nonlinear function, modulo addition, and left rotation. A different function is used in each round, where the functions are defined as follows:

$$F(B, C, D) = (B \text{ AND } C) \text{ OR } (\text{NOT } B \text{ AND } D) \quad (2)$$

$$G(B, C, D) = (B \text{ AND } D) \text{ OR } (C \text{ AND } \text{NOT } D) \quad (3)$$

$$H(B, C, D) = B \text{ XOR } C \text{ XOR } D \quad (4)$$

$$I(B, C, D) = C \text{ XOR } (B \text{ OR } \text{NOT } D) \quad (5)$$

Longer hash values of 32-bytes or 256-bit are generated using Secure Hash Algorithm (SHA)-256 to provide better security against collision attacks. This technique too divides the information into blocks of 512 bits or 64 bytes to be processed in 64 rounds. The initial hash value $H(0)$ is obtained by taking the fractional parts of the square roots of the first eight primes.

It is experimented and shown in [4] that complexity of MD5 and SHA256 is the same and MD5 consumes less time. Many others works [5–9] have used hashing as a fragile watermark to detect manipulations in the cover image, especially in scanned text pdf document [6], satellite images [7, 8], and medical images [9].

4 Experiments and Results

To conduct experiments for the choice of hashing technique, the watermark is embedded into 1-level DWT coefficients and two copies of hash values of the embedding watermark are embedded in four-level DWT coefficients. To ensure recovery of hidden hash values, the hash value bits are embedded into high energy regions of the image. So, HH coefficients of one-level DWT of the cover image undergoes multiple level DWT further to embed two copies of unique hash value obtained for watermark.

Tests were conducted on the cover images shown in Fig. 1a for the embedding of watermarks shown in Fig. 1b.

The watermark is embedded into singular values of one-level HH band coefficients, by replacing singular values of HH band with those of the watermark. For maximum payload, watermark is assumed to be of the same size as one-level HH band. Thus, for cover images of 512×512 , the watermark is taken for size 256×256 . The singular vector matrices U and V for authentication are used to generate two respective binary sequences as corresponding hash values using the three techniques in Sect. 3. The individual hash is 256 bits in length. To add randomness to these

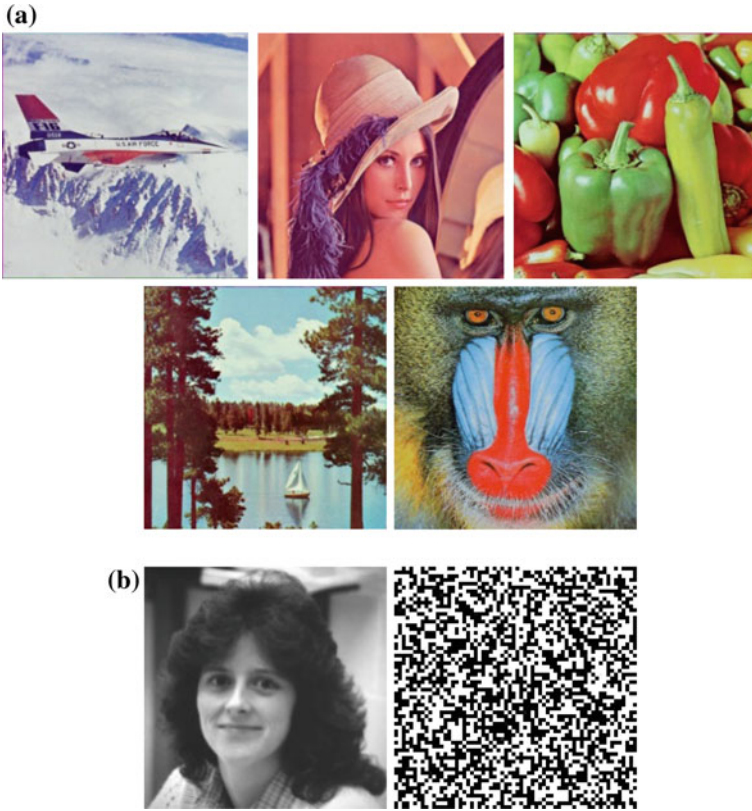


Fig. 1 a Cover images b watermark images

binary hash values the two sequences are EX-ORed together and finally EX-ORed with a random binary sequence generated with a secret key.

In order to embed the hash value in four-level coefficients, the maximum size of hash value is 128. The watermark embedding and extraction procedures are depicted in Fig. 2a and b, respectively.

To overcome ambiguity in deciding if the extracted watermark was originally used for embedding or not, authentication of vectors being used for reconstruction is required. This is done with the help of verification of hash value of these vectors. The unique hash value of the watermark image originally embedded, is generated using one of the three different techniques summarized in the previous section and embedded blindly as hidden data. The claimed watermark is verified for its hashcode with respect to the hidden info to allow to proceed for extraction of watermark.

Hash values of the orthogonal matrices to be verified is a random and unique binary string, such that, the attacker is not able to predict it. To find the best suitable

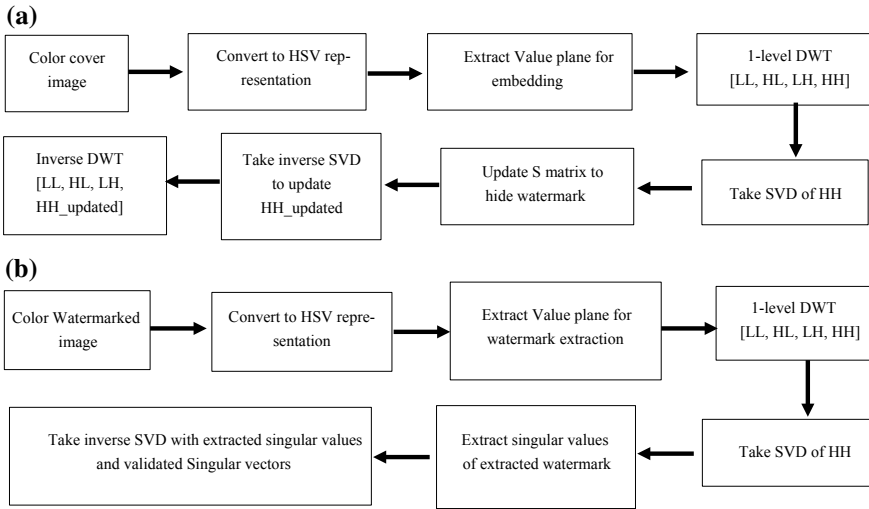


Fig. 2 a Watermark embedding b watermark extraction

coefficients for embedding 256-bit binary hash for the watermark was generated using hashing. Two copies of this string are embedded into the band other than HH band, where watermark is embedded. Table 1 shows PSNR of the image when two copies of hash values are embedded into four-level LL and HH bands for each of one-level LL, HL, and LH band of the cover image. The highest PSNR was obtained for LL band, so the hash value is embedded in this band only. For all the bands, the hash value was retrieved successfully with 100% accuracy, as is clear with a correlation coefficient of 1 in Table 1.

Table 2 compares different hashing techniques with respect to PSNR of the watermarked image and recovery of hash values. The PSNR of the watermarked images obtained (after embedding two copies of hash generated and watermark itself) using the three techniques are quite close, within 0.12 dB, for a fixed length of the hash

Table 1 PSNR for different locations of hash bits embedding for Lena image as cover

1-level DWT band for hash value embedding	PSNR (dB)	Correlation of extracted hash value bits with original hash value	
		From 4-level LL band	From 4-level HH band
LL	42.3484	1	1
HL	41.7490	1	1
LH	41.7946	1	1
HH	41.7641	1	1

Table 2 Comparison of three hashing techniques w.r.t. PSNR and recovery of hash values

Hashing method for U and V matrices	Hash value full length (number of bits)	Number of bits randomly chosen	PSNR (dB)	Correlation of extracted hash value from	
				LL band	HH band
Thresholding w.r.t median	256	128	41.6418	0.7504	0.8280
MD5	128	128	41.5704	0.7148	0.7996
SHA256	256	128	41.6880	0.7967	0.7964








value. The hash embedded in the four-level HH band is recovered with higher correlation as compared to that extracted from LL band. The high correlation coefficient of the recovered hash value ensures that the watermark is verified before extraction. The highest average correlation of 0.7966 is obtained for SHA-256 technique.

Use of different watermarks with the fixed hash length for embedding affected the PSNR of the watermarked image but the difference was less than 1 dB. Table 3 shows PSNR obtained for different combinations of cover and watermarked images. Higher PSNR is obtained for the random watermark shown in Fig. 2b for all cover images. The number of bits randomly selected from the hash value, to be embedded in the cover image, is taken as 16 bits. The hash is fully recovered for all cover image and watermark images except for Aircraft cover image which gives a correlation of 0.8783 dB and 0.7460 dB for the hash value extracted from four-level LL and HH band, respectively.

5 Conclusions

False positive problem is a major issue to be addressed for SVD based image watermarking techniques. This paper presents experiments conducted to hide the hash value of the original watermark into DWT coefficients and analyze the effect of the choice of hashing technique on PSNR of the watermarked image. The PSNR is achieved sufficiently high that the changes are imperceptible. The experiment is carried out with the maximum hash length. However, it is expected that with reducing hash length, PSNR will improve along with higher correlation between extracted and original hash value for verification. But smaller length of hash makes it easy to get collision. Therefore, it is better to compromise with the PSNR and use longer hash values. Thus, SHA-256 is the most suitable choice for generating hash values for embedding to ensure best PSNR and fair recovery of hash value originally embedded.

Table 3 PSNR for different watermarks for different cover images

Cover image	Watermark	PSNR (dB)	Watermark	PSNR (dB)
		43.4034		43.7074
		43.2591		43.5482
		39.2177		39.3809
		37.1346		37.2651
		31.0551		31.1276

References

1. Singh N, Joshi S, Birla S (2017) False watermark extraction and rewatermarking issues with image watermarking techniques. *Indian J Sci Technol* 10(7):1–6
2. Singh N, Joshi S, Birla S (2019) Suitability of singular value decomposition for image watermarking. In: *Proceedings of IEEE 6th international conference on signal processing and integrated networks (SPIN)*, pp 983–986. IEEE, India
3. Rowayda A (2012) Sadek: SVD based image processing applications: state of the art, contributions and research challenges. *Int J Adv Comput Sci Appl* 3(7):26–34
4. Rachmawati D, Tarigan JT, Ginting ABC (2018) A comparative study of message digest (MD5) and SHA256 algorithm. *J Phys Conf Series* 978

5. Afzali N, Manochehri K (2016) A novel robust watermarking algorithm for image tamper detection. *Int J Comput Sci Netw Secur* 16(11):16–19
6. Mahmoud A, Maharmeh HA, Al-Ahmad H (2015) A new watermarking algorithm for scanned colored PDF files using DWT and hash function. In: *Proceedings of IEEE international conference on information and communication technology research*, pp 140–143. IEEE, UAE
7. Kunhu A, Al-Ahmad H (2013) A new watermarking algorithm for color satellite images using color logos and hash functions. In: *Proceedings of 5th international conference on computational intelligence, communication systems and networks*, pp 251–255. IEEE, Latvia
8. Kunhu A, Al-Ahmad H (2013) Multi watermarking algorithm based on DCT and hash functions for color satellite images. In: *9th IEEE international conference on innovations in information technology—innovations '13*, pp 30–35. IEEE, UAE
9. Kunhu A, Al-Ahmad H, Taher F (2017) Medical images protection and authentication using hybrid DWT-DCT and SHA256-MD5 hash functions. In: *24th IEEE international conference on electronics, circuits and systems*, pp 397–400. IEEE, Batumi

Global Neighbourhood Algorithm Based Event-Triggered Automatic Generation Control



Pankaj Dahiya, Pankaj Mukhija and Anmol Ratna Saxena

Abstract The present work studies global neighbourhood algorithm (GNA) to tune/optimize proportional–integral–derivative with filter (PIDN) controller parameters for the stability of frequency in a one area thermal power system. The integral of time multiplied absolute error is chosen as the performance index for the controller tuning. For effective communication, periodic event triggered scheme is considered. The effects of delay introduced by the communication channel is also considered. Hence, delay dependent stability using Lyapunov theory is also investigated. Finally, simulations are performed to confirm the effectiveness of the obtained optimized gains using GNA.

Keywords Global neighbourhood algorithm · Linear matrix inequalities · Automatic generation control · Lyapunov theory

1 Introduction

Maintaining frequency to predefined range or active power balance in a power utility is recognized as automatic generation control (AGC) problem. Modern power system is a very complex structure consisting of distributed power generation sources. Where, communication channels acts as backbone of the AGC scheme [1]. Dedicated communication lines are not suggested because of the disadvantages such as high

P. Dahiya (✉)

Research Scholar, Electrical and Electronics Engineering Department, National Institute of Technology Delhi, Delhi, India

e-mail: pankajdahiya@nitdelhi.ac.in

P. Mukhija · A. R. Saxena

Electrical and Electronics Engineering Department, National Institute of Technology Delhi, Delhi, India

e-mail: pankajmukhija@nitdelhi.ac.in

A. R. Saxena

e-mail: anmolsaxena@nitdelhi.ac.in

© Springer Nature Singapore Pte Ltd. 2020

A. Kalam et al. (eds.), *Intelligent Computing Techniques for Smart Energy Systems*,

Lecture Notes in Electrical Engineering 607,

https://doi.org/10.1007/978-981-15-0214-9_71

cost and rigidity. On the other hand, open channel is unreliable due to presence of delays, packet dropout and limited bandwidth [2]. For effective utilization of bandwidth, event-triggered control (ETC) has been given a greater attention in the recent past. Moreover, ETC has also been implemented for AGC scheme in [3–6]. In [3], an event-based output feedback PI controller is implemented for multi-area AGC system. Along with PI controller, supplementary adaptive dynamic programming is implemented for multi-area AGC scheme [4]. In [5], a sliding mode controller is implemented for multi-area AGC scheme. An event-based state feedback controller is implemented for an isolated area consisting of wind-diesel generator [6].

Because of robust and simple structure, PID controllers are very much used in AGC implementation [7–11]. Tan in [7] proposed PID controller tuning for AGC system using internal model control design method. In [8], PID controller is designed for AGC scheme by expansion of controller transfer function through Laurent series. Zhang et al. [9] designed PID controller considering communication delay in form of linear matrix inequalities (LMIs). LMIs based approach is used to obtain an optimized PID controller for multi-area AGC scheme in [11]. A new modified structure of PID controller, having low pass filter with filter coefficient “N” in the derivative term is implemented in [12, 13]. This PID controller with filter (PIDN), eliminates the high-frequency noise added due to sampling. So, for a system employing sampled data or event-based PID controller, should be fitted with the low-pass filter in derivative term.

To attain frequency regulation in AGC system, tuning of the controller gain is very important. A number of heuristic algorithms have been proposed in the literature and used in AGC for the tuning of the controller parameters. In [12], a new algorithm named Jaya algorithm has been used for the tuning of PIDN controller. In [14], the authors used teaching learning based optimization (TLBO). The authors in [13] proposed differential search algorithm. The results in [12–14] have been compared with other algorithms such as particle swarm optimization, TLBO, differential evolution algorithms, etc. PID controllers give better response compared to PI controllers [13, 14], but till date, no attempt has been made for designing event based PID controller for AGC system.

Recently, a heuristic algorithm named global neighbourhood algorithm (GNA) has been proposed [15], and is used in [16] for automatic voltage regulator problem. The algorithm looks promising for PID controller tuning for AGC system. Hence, in this paper, a PIDN-structured ETC parameters are optimized using GNA.

The organization of the paper is given as: in section II, description and state-space model (SSM) of a one area thermal power system with PIDN controller is done. In next section first, objective function used is defined. Then, GNA implementation to AGC system is described. Finally, a theorem in terms of LMIs is derived to find delay dependent stability as well as maximum value of trigger parameter “ σ ”. Model is simulated for the obtained controllers and results are presented and discussed in section IV. In the last section, conclusions are drawn.

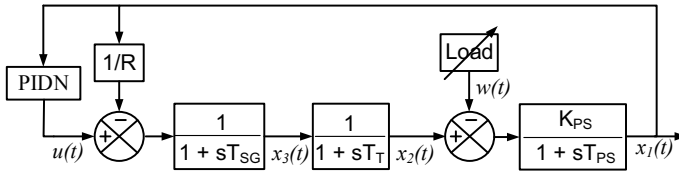


Fig. 1 one area thermal AGC system

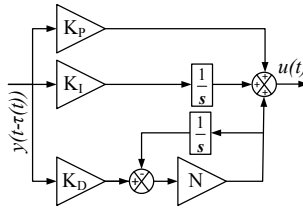


Fig. 2 Structure of PIDN controller

2 AGC System Modelling

The transfer function model of conventional one area thermal AGC system implemented with PIDN controller is shown in Fig. 1 and PIDN controller structure having PID gain “ K_P, K_I, K_D ” and filter coefficient “ N ” is shown in Fig. 2. The SSM of one area AGC system without controller is expressed in Eq. (1).

$$\begin{aligned} \dot{x}(t) &= Ax(t) + Bu(t) + Fw(t) \\ y(t) &= Cx(t) \end{aligned} \tag{1}$$

$$\begin{aligned} \text{where, } x(t) &= [x_1(t) \ x_2(t) \ x_3(t)]^T, \ A = \begin{bmatrix} -\frac{1}{T_{PS}} & \frac{K_{PS}}{T_{PS}} & 0 \\ 0 & -\frac{1}{T_T} & \frac{1}{T_T} \\ -\frac{1}{RT_{SG}} & 0 & -\frac{1}{T_{SG}} \end{bmatrix}, \\ B &= \begin{bmatrix} 0 & 0 & \frac{1}{T_{SG}} \end{bmatrix}^T, \ F = \begin{bmatrix} -\frac{K_{PS}}{T_{PS}} & 0 & 0 \end{bmatrix}^T \text{ and } C = [1 \ 0 \ 0] \end{aligned}$$

where A, B, C and F are the AGC system matrices and the states $x_1(t), x_2(t)$ and $x_3(t)$ are the deviations in frequency, generator power and steam output, respectively. Further, T_{SG}, T_T and T_{PS} are the time constants of speed governor, turbine and power system, respectively. Whereas, R and K_{PS} are the speed droop of the governor and gain of the power system. The SSM of closed loop AGC system, i.e., with PIDN controller can be obtained by defining virtual vector $z(t) = [z_1^T(t) \ z_2^T(t) \ z_3^T(t)]^T$, where $z_1(t), z_2(t)$ and $z_3(t)$ are $x(t), \int y(t)dt$ and a dummy state variable, respectively. The system equation with controller can be represented as Eq. (2).

$$\begin{aligned} \dot{z}(t) &= \bar{A}z(t) + \bar{B}K\bar{C}z(t) + \bar{F}w(t) \\ y(t) &= \bar{C}z(t) \end{aligned} \tag{2}$$

where,

$$\bar{A} = \begin{bmatrix} A & 0 & 0 \\ C & 0 & 0 \\ NC & 0 & -N \end{bmatrix}, \bar{C} = \begin{bmatrix} C & 0 & 0 \\ 0 & I & 0 \\ NC & 0 & -N \end{bmatrix}, \bar{B} = [B^T \ 0 \ 0]^T \tag{3}$$

$$\bar{F} = [F^T \ 0 \ 0]^T, K = [K_P \ K_I \ K_D] \text{ and } \bar{C} = [C \ 0 \ 0]$$

3 Problem Formulation

3.1 Objective Function

For the tuning of PIDN controller using an heuristic algorithm, an objective function must be constructed. In AGC problem, the major performance index includes the change of frequency should return to the nominal point and integral of change in frequency should be minimum. Therefore, here Integral time absolute error (ITAE) is used as the objective function “J”. Mathematically it can be expressed as $J = \int_0^t t \cdot |x_1(t)| \cdot dt$.

3.2 Global Neighbourhood Algorithm (GNA)

GNA is one of the latest heuristic optimization algorithm proposed by Alazzam and Lewis [15]. It is a gradient free, iterative algorithm used to obtain the optimal values in complex problems. It works on the assumption that probability of finding the optimal solution is more in the neighbourhood of the best solution found in previous iteration.

3.3 Delay/Sampling Time Dependent Stability

Event-based scheme for AGC system, as shown in Fig. 3, is introduced. Now, system Eq. (2) becomes

$$\begin{aligned} \dot{z}(t) &= \bar{A}z(t) + \bar{B}K\bar{C}z(t_k h) + \bar{F}w(t) \\ y(t) &= \bar{C}z(t) \end{aligned} \tag{4}$$

To transmit the output, event generator monitors the output $y(t)$ using an sample and hold circuit regularly, at sampling interval of ‘h’ s. The error $e_y(t)$ and $e_z(t)$ are

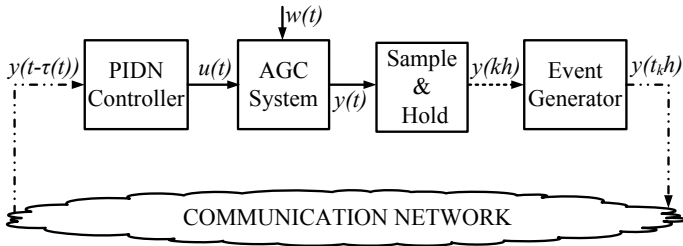


Fig. 3 Block diagram of the proposed AGC system

taken as

$$e_y(t) = y((k + l)h) - y(kh) \tag{5}$$

$$e_z(t) = z((k + l)h) - z(kh) \tag{6}$$

The output $y(t)$ will be modified and transmitted to the controller if the error violates Eq.(7), where $\sigma \in [0, 1)$ and $l = 1, 2, \dots$ and $\bar{\Omega} > 0$.

$$e_y(t)^T \bar{\Omega} e_y(t) \leq \sigma y((k + l)h)^T \bar{\Omega} y((k + l)h) \tag{7}$$

Now AGC scheme SSM Eq.(4) can be modified as Eq.(8), with initial condition $z(t_0) = z_0, \forall t \in [-\bar{h}, 0]$ where \bar{h} is maximum allowable delay bound (MADB) which equals $h + \bar{\tau}$, $\bar{\tau}$ is maximum delay and $\tau(t)$ is as defined in [3], also $e_z(t)$ is similar to $\hat{x}_k(t)$ in [3] and Eq.(7) can be modified as Eq.(9).

$$\begin{aligned} \dot{z}(t) &= \bar{A}z(t) + \bar{B}K\bar{C}z(t - \tau(t)) + \bar{B}K\bar{C}e_z(t) + \bar{F}w(t) \\ y(t) &= \bar{C}z(t) \end{aligned} \tag{8}$$

$$e_z(t)^T \Omega e_z(t) \leq \sigma z(t - \tau(t))^T \Omega z(t - \tau(t)), \quad \forall \Omega > 0 \tag{9}$$

Theorem 1 For a given trigger parameter σ and PID controller gain K , filter coefficient N , the AGC system Eq.(8) is stable. If there exist matrices $P, R, Z, \Omega > 0, N = [N_1^T \ N_2^T \ N_3^T \ N_4^T]^T$ and $M = [M_1^T \ M_2^T \ M_3^T \ M_4^T]^T$, such that following LMIs satisfy for error Eq.(6) and $r = 1, 2$:

$$\begin{bmatrix} \Phi_{11} & * & * & * & * & * & * \\ \Phi_{21} & \Phi_{22} & * & * & * & * & * \\ \Phi_{31} & \Phi_{32} & \Phi_{33} & * & * & * & * \\ \Phi_{41} & \Phi_{42} & -M_4 & -\Omega & * & * & * \\ \psi_1^r & \psi_2^r & \psi_3^r & \psi_4^r & -Z & * & * \\ \bar{F}^T P & 0 & 0 & 0 & 0 & 0 & * \\ \sqrt{\bar{h}}Z\bar{A} & \sqrt{\bar{h}}Z\bar{B}K\bar{C} & 0 & \sqrt{\bar{h}}Z\bar{B}K\bar{C} & 0 & \sqrt{\bar{h}}Z\bar{F} & -Z \end{bmatrix} < 0 \tag{10}$$

where $\Phi_{11} = P\bar{A} + \bar{A}^T P + R + N_1 + N_1^T$, $\Phi_{31} = N_3 - M_1^T$, $\Phi_{21} = \bar{C}K^T\bar{B}^T P + N_2 - N_1^T + M_1^T$, $\Phi_{32} = -N_3 + M_3 - M_2^T$, $\Phi_{22} = \sigma\Omega - N_2 + M_2 - N_2^T + M_2^T$, $\Phi_{33} = -R - M_3 - M_3^T$, $\Phi_{41} = \bar{C}K^T\bar{B}^T P + N_4$, $\Phi_{42} = -N_4 + M_4$, $\psi_i^1 = \sqrt{h}N_i^T$, $\psi_i^2 = \sqrt{h}M_i^T$, $i = \{x \in \mathbb{N} | x < 5\}$

Proof Choose Lyapunov function as

$$V(t) = z^T(t) Pz(t) + \int_{t-\bar{h}}^t z^T(s) Rz(s) ds + \int_{t-\bar{h}}^t \int_s^t \dot{z}^T(v) Z\dot{z}(v) dv ds \quad (11)$$

with $P, R, Z > 0$. Differentiating Eq. (11), leads to

$$\dot{V}(t) = 2z^T(t)P\dot{z}(t) + z^T(t)Rz(t) - z^T(t-\bar{h})Rz(t-\bar{h}) + \bar{h}\dot{z}^T(t)Z\dot{z}(t) - \int_{t-\bar{h}}^t \dot{z}^T(v)Z\dot{z}(v)dv \quad (12)$$

Introducing free weighting matrices N and M and using Schur complement lemma [17], the proof is completed.

4 Case Study

In this section, simulation results obtained for the one area thermal power system are discussed. The parameters for the power system under consideration are given in Table 1 and the corresponding model is shown in Fig. 1.

Two different test cases with periodic sampling time $h = 1$ ms and $h = 100$ ms are considered for simulations. The cases are as follows.

4.1 Case I

Applying GNA with $h = 1$ ms, the obtained controller parameters are $K_P = 1.8776$, $K_I = 3.243$, $K_D = 0.4652$, $N = 223.478$ and the optimized ITAE is found to be

Table 1 Area parameters

Parameters	$T_{PS}(s)$	K_{PS}	$T_T(s)$	R	$T_{SG}(s)$
Area	20	120	0.3	2.4	0.08

Table 2 MADB for different values of σ

σ	0	0.1	0.2	0.3	0.4	0.5	0.6	0.64
\bar{h} (ms)	96.7	58.3	44.4	33.5	23.4	14.3	4.4	1

Fig. 4 Frequency response for 1% load disturbance at $h = 1$ ms and different values of delays

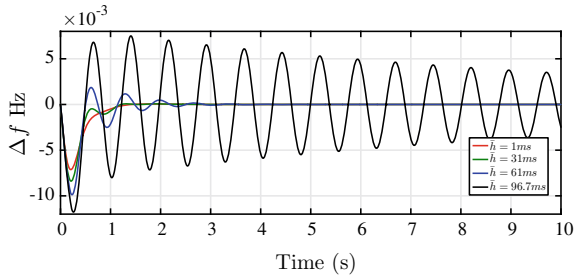


Fig. 5 Frequency response for 1% load disturbance at $h = 1$ ms and $\sigma = 0$ & 0.2

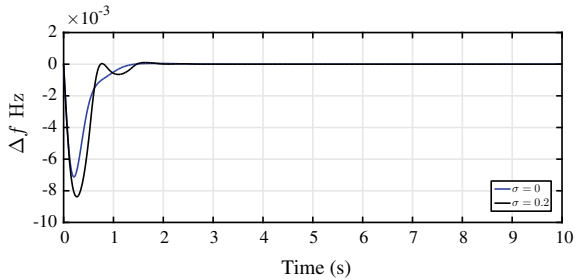
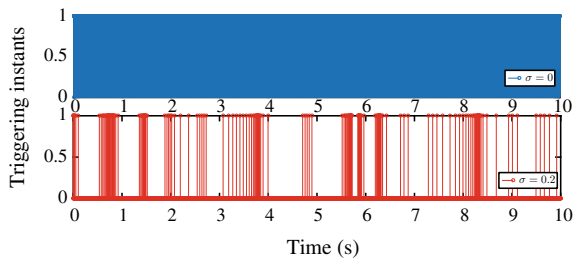


Fig. 6 Samples release instants for $\sigma = 0$ & 0.2



1.202×10^{-3} . Thereafter, using Theorem 1, for $\sigma = 0$, \bar{h} is found to be 96.7 ms, and for $h = 1$ ms, σ_{\max} is found to be 0.64. For different values of σ , corresponding \bar{h} values are given in Table 2. Now, the system is simulated to check stability, taking $h = 1$ ms and different time delay $\tau = 0, 30, 60$ and 95.7 ms and the time responses for 1% load disturbances are shown in Fig. 4. The responses show that for the obtained delay bound, system frequency deviation is stable for the applied step disturbance. For effective utilization of bandwidth, σ may also be varied up to σ_{\max} , which results in decrease of the sampled data sent to stabilize the system. To show the effectiveness of ETC, the model is simulated for $\sigma = 0$ & 0.2. The corresponding frequency deviation and samples release instants are shown in Figs. 5 and 6, respectively. The results shows numbers of samples sent, decreases from 10,000 samples to only 215 samples, as σ increases from 0 to 0.2.

Table 3 MADB for different values of σ

σ	0	0.1	0.2	0.3	0.4	0.5	0.6	0.7	0.8	0.9	0.92
\bar{h} (ms)	174	114	92	80	69	57	45	31	20	4	1

Fig. 7 Samples release instants for $\sigma = 0$ & 0.18

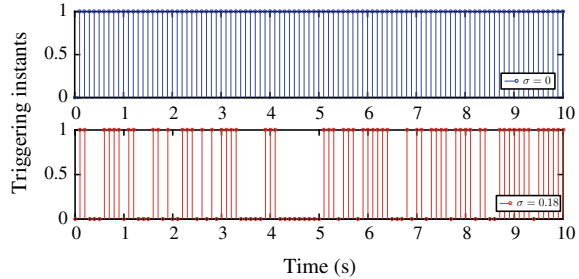
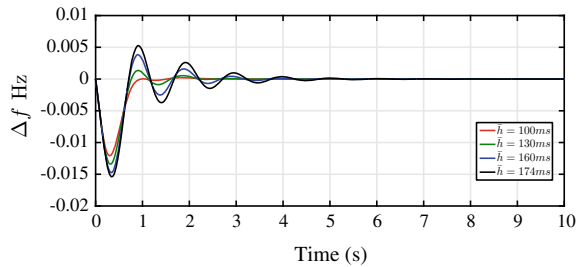


Fig. 8 Frequency response for 1% load disturbance at $h = 100$ ms and different values of delays

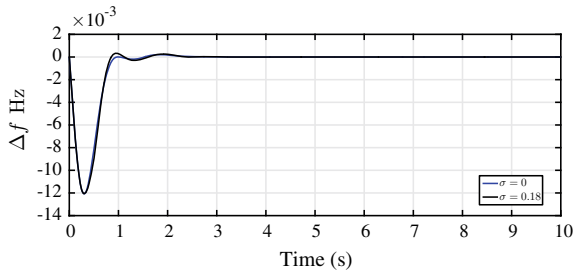


4.2 Case II

Again Applying GNA with $h = 100$ ms, the obtained controller parameters are $K_P = 0.9459$, $K_I = 1.7967$, $K_D = 0.2672$, $N = 101.3124$. Then by applying Theorem 1, for $\sigma = 0$ value of \bar{h} is found to be 174 ms, for $h = 100$ ms value of σ_{max} is found to be 0.18 and for $h = 1$ ms value of σ_{max} is found to be 0.92 ms. For different values of σ , corresponding \bar{h} values are given in Table 3. Again, the system is simulated for stability, taking $h = 100$ ms and different time delay $\tau = 0, 30, 60$ and 74 ms and the time responses for 1% load disturbances are shown in Fig. 8. The responses show that for the obtained delay bound system frequency deviation is stable for the applied step disturbance.

For effective utilization of bandwidth, the model is again simulated for $\sigma = 0$ & 0.18. The corresponding frequency deviation and samples release instants are shown

Fig. 9 Frequency response for 1% load disturbance at $h = 100$ ms and $\sigma = 0$ & 0.18



in Figs. 9 and 7, respectively. The results shows without much distortion in frequency deviation, numbers of samples sent, decreases to only 61 samples from 100 samples, as σ increases from 0 to 0.18.

5 Conclusions

In this article, PIDN controller is implemented, with event-based triggering, for the frequency regulation of one area thermal power system. The controller parameters are tuned using a new heuristic algorithm named GNA and ITAE is used as objective function. The results shows, GNA can be successfully applied for solving real-time AGC problem. Simulation studies also shows network bandwidth can be conserved without much deviation from desired response by using periodic event-based sampling.

References

1. Jiang L, Yao W, Wu QH, Wen JY, Cheng SJ (2012) Delay-dependent stability for load frequency control with constant and time-varying delays. *IEEE Trans Power Syst* 27(2):932–941
2. Dahiya P, Mukhija P, Saxena AR (2016) Stability criteria for load frequency control systems with communication delays and packet dropout. In: 1st IEEE international conference on power electronics, intelligent control and energy systems (ICPEICES-2016), pp 1–4
3. Wen S, Yu X, Zeng Z, Wang J (2016) Event-triggering load frequency control for multiarea power systems with communication delays. *IEEE Trans Ind Electron* 63(2):1308–1317
4. Dong L, Tang Y, He H, Sun C (2017) An event-triggered approach for load frequency control with supplementary ADP. *IEEE Trans Power Syst* 32(1):581–589
5. Su X, Liu X, Song Y-D (2017) Event-triggered sliding mode control for multi-area power systems. *IEEE Trans Ind Electron* 64(8):6732–6741
6. Dahiya P, Mukhija P, Saxena AR (2018) Design of sampled data and event-triggered load frequency controller for isolated hybrid power system. *Int J Electr Power Energy Syst* 100, 331–349. <http://www.sciencedirect.com/science/article/pii/S014206151731195X>
7. Tan W (2010) Unified tuning of PID load frequency controller for power systems via IMC. *IEEE Trans Power Syst* 25(1):341–350

8. Padhan DG, Majhi S (2013) A new control scheme for PID load frequency controller of single-area and multi-area power systems. *ISA Trans* 52(2), 242–251. <http://www.sciencedirect.com/science/article/pii/S0019057812001656>
9. Zhang C-K, Jiang L, Wu QH, He Y, Wu M (2013) Delay-dependent robust load frequency control for time delay power systems. *IEEE Trans Power Syst* 28(3):2192–2201
10. Anwar MN, Pan S (2015) A new PID load frequency controller design method in frequency domain through direct synthesis approach. *Int J Electr Power Energy Syst* 67, 560–569. <http://www.sciencedirect.com/science/article/pii/S0142061514007510>
11. Singh VP, Kishor N, Samuel P (2017) Improved load frequency control of power system using LMI based PID approach. *J Frankl Inst* 354(15), 6805–6830. <http://www.sciencedirect.com/science/article/pii/S0016003217304258>
12. Singh SP, Prakash T, Singh V, Babu MG (2017) Analytic hierarchy process based automatic generation control of multi-area interconnected power system using jaya algorithm. *Eng Appl Artif Intell* 60, 35–44. <http://www.sciencedirect.com/science/article/pii/S0952197617300088>
13. Guha D, Roy PK, Banerjee S (2017) Study of differential search algorithm based automatic generation control of an interconnected thermal-thermal system with governor dead-band. *Appl Soft Comput* 52, 160–175. <http://www.sciencedirect.com/science/article/pii/S1568494616306305>
14. Sahu RK, Panda S, Rout UK, Sahoo DK (2016) Teaching learning based optimization algorithm for automatic generation control of power system using 2-DOF PID controller. *Int J Electr Power Energy Syst* 77, 287–301. <http://www.sciencedirect.com/science/article/pii/S014206151500513X>
15. Alazzam A, Lewis HW (2013) A new optimization algorithm for combinatorial problems. *Int J Adv Res Artif Intell* 2(5):63–68
16. Gözde H, Taplamac MC, Ar M (2017) Simulation study for global neighborhood algorithm based optimal automatic voltage regulator (AVR) system. In: *ICSG Istanbul*, pp 46–50
17. Wu M, He Y, She JH (2010) *Stability analysis and robust control of time-delay systems*. Springer, New York

A Review on Voltage and Frequency Control of Micro Hydro System



Priya Singh Bhakar, Saumendra Sarangi and Kirti Gupta

Abstract Modern technology developed in renewables has opened a door to utilize micro hydro as one of the major sources of energy in micro-grid in terms of capital investment and sustainability. With such developments, frequency and voltage variation in micro-grid arise as a major concern where conventional control technique fails. This has driven the idea to develop electronic load controller to dump extra power hence minimizing the frequency variations. As the efficiency is reduced using such methods, batteries are applied in micro hydro to store the dumped power. However, to improve both voltage and frequency, combination of ELC and STATCOM are developed. Further, in order to improve the system performance, modifications in ELC corresponding to the load configuration were developed and proved to be beneficial. To improve the efficiency of the system, water heaters, pump loads, or other low wattage apparatus are also used. This paper presents a survey on various frequency and voltage control techniques available in small hydro system with their merits and demerits. The investigations on various problems demand further development.

Keywords Isolated asynchronous generator · Electronic load controller · Integrated and decoupled configuration · Ballast load · Distributed ELC

1 Introduction

The progressive development of civilization with sustained growth in industries can only be achieved with ample energy production. In order to meet the demand of electrical energy with depletion of fossil fuel reserve, alternate sources of generation

P. S. Bhakar

Indian Institute of Technology Ropar, Nangal Road, Rupnagar, Punjab, India
e-mail: priyabhakar1995@gmail.com

S. Sarangi · K. Gupta (✉)

National Institute of Technology Uttarakhand, Srinagar, Uttarakhand, India
e-mail: kirti.gupta.eee17@nituk.ac.in

S. Sarangi

e-mail: usomsam@gmail.com

© Springer Nature Singapore Pte Ltd. 2020

A. Kalam et al. (eds.), *Intelligent Computing Techniques for Smart Energy Systems*,
Lecture Notes in Electrical Engineering 607,
https://doi.org/10.1007/978-981-15-0214-9_72

are being extensively studied in last two decades [1, 2] and found that resources like wind, small hydro, solar, etc., are feasible [3]. However, the flow of wind and solar insolation in photovoltaic are unpredictable, which makes them variable in nature; hence, the deployment of hydro felt quite encouraging [4]. This has led hydropower as one of the leading renewable energy sources contributing 71% of total renewable electricity all over the world.

In comparison to existing hydro stations, small hydro is beneficial in few aspects as hundreds of massive concrete barriers, rocks, and huge construction is done across the river to build large dams which flooded large fertile land, displaced many inhabitants [5, 6]. The dam for micro hydro systems is very small and produces sufficient electric energy for far-flung and rural areas [7]. Such power plant mainly employs asynchronous generator for their working. However, voltage and frequency regulation of IAGs is poor and causes underutilization.

The frequency control of asynchronous generators in micro hydro can be achieved in two ways: speed governor system and Electronic Load Controllers (ELC). Governor control modulate frequency by varying the turbine flow in accordance with the load demand. However for a small hydro station, governor systems are proved to be complex, bulky in construction, costly, and require routine maintenance which leads to the use of ELC for frequency regulation in small hydro. ELC uses power electronic devices, which improves the time response and causes reduction of cost (about one-tenth of the governor) for active power balance in the system.

Electronic load controllers work to minimize the difference between generated and consumed power by dumping the surplus active power; regulates the system frequency. It senses the frequency and connects the dump load to maintain the load constant on the generator. Earlier resistive loads were connected with ELCs, where surplus power was dissipated as heat energy. With the advancement in technology, the energy loss is minimized and effectively utilized; SPV with MPPT technique, PV arrays, wind, Battery Energy Storage Systems (BESS), diesel generator as a backup with micro hydro, and a combination of two or more micro hydros to constitute a micro-grid are a few available arrangements.

The voltage regulation of SEIG can be achieved by using switched capacitors, static VAR compensators, and static compensators (STATCOM). A switched capacitor scheme is less costly; however, it regulates the voltage in steps. SVC schemes that mostly use either thyristor switched capacitor or thyristor controlled reactor use large capacitors and reactors. STATCOM uses a Voltage Source Inverter (VSI) to control the voltage. The innovation of devices like gate turn off thyristor that provides full on/off control or fast-acting devices like insulated gate bipolar transistor has replaced SVC with STATCOM. Various topologies for voltage control are presented in this paper.

The combined frequency and voltage regulation of IAGs using ELC and STATCOM is also achieved for integrated or decoupled manner in micro hydro systems. Integrated configuration uses a single controller for both voltage and frequency regulation while the decoupled configuration uses separate voltage and frequency control. Several control algorithms related to the working of ELC and STATCOM have been

developed. Algorithms like instantaneous reactive power theory based algorithm, adaptive noise cancelation filter based algorithm, and proportional resonant control algorithm are used in micro hydro systems.

2 Voltage and Frequency Regulation in Micro Hydro System

The use of asynchronous generator in micro hydro system imposes challenges in the regulation of voltage and frequency. The basic idea behind this survey is to address the issues threatening the voltage and frequency regulation in micro hydro for achieving a milestone of stable operation of generator with minimum losses. The most important factor that affects these goals hard to achieve is the management of the load demand.

Frequency control on the load side in micro hydro systems working autonomously is remunerative by exercising ELC. An IGBT switch which is hitched during the operation of ELC whose triggering depends upon the frequency variations is employed as a chopper [8]. Voltage and current sensors are employed to detect the fluctuation in the generator parameters and any variation from desired; the switch is triggered to dump the excess power. Voltage regulation in micro hydro is done by static VAR compensators, SVC, solid-state SVS, and STATCOM. STATCOM with fast-acting devices like IGBTs, MOSFETs, and GTOs is used to provide sufficient voltage regulation.

A classification of the combined voltage and frequency control in micro hydro has been shown in Fig. 1. IGBT switches in place of diodes or thyristors to allow the bidirectional flow of energy in the converter are exercised by improved ELC configuration and the converter itself acts as load balancer, harmonic eliminator, and reactive power compensator. The input power was earlier converted into the demand and dump power due to the nonavailability of storage devices. With the innovation

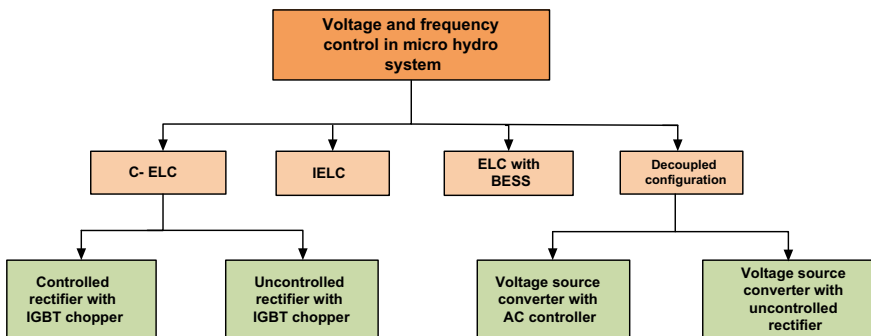


Fig. 1 Combined voltage and frequency control in micro hydro

of battery energy storage system, the application of ELC with BESS instead of a dumping load has eliminated power shortage while securing the energy balance. Regular replacement of batteries after certain time duration produced toxic disposals which emphasized on further amendment in ELC.

The conventional ELC shown in Fig. 2 has a disadvantage of having high total harmonic distortion which can be slashed out by using thyristor bridge rectifier instead of diode rectifier with an additional thyristor firing circuitry to trigger the switches. A battery storage system in Fig. 3 ameliorates the conversion efficiency and reduces noise and vibrations in IAG to supply peak load demands while providing bidirectional power flow. However replacement of batteries produces toxic disposals even multiplying the capital investment.

The reactive power demand of the consumer loads in the above configuration is the drawback in micro hydro system which can be compensated by using static compensator in parallel to the load. STATCOM maintains the reactive power balance ultimately regulating the voltage of the system.

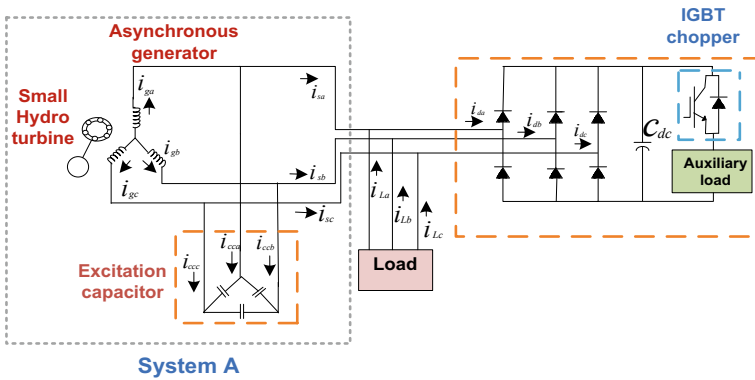
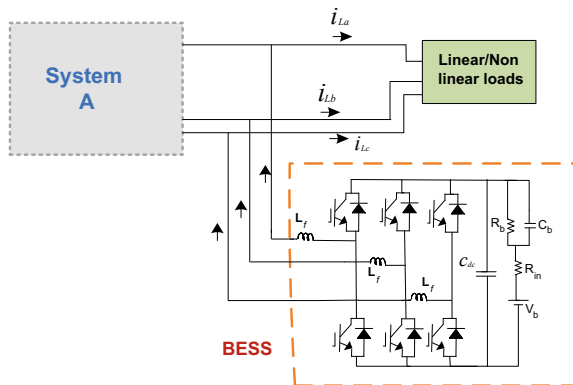


Fig. 2 Block diagram of the conventional ELC

Fig. 3 Block diagram of ELC with BESS



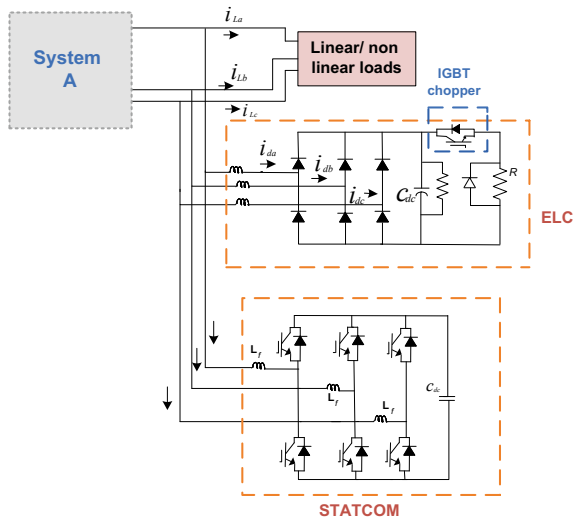


Fig. 4 Pictorial view of decoupled load controller

Both STATCOM and conventional ELC are independently used in the decoupled load controller to modulate voltage and frequency as shown in Fig. 4.

3 Classification of ELC on the Basis of Loading

The configuration of electronic load controller depends upon the type of loads, i.e., three-phase three-wire or three-phase four-wire loads that generally categorize the controller into three-leg or four-leg IGBT based converter. These loads are single phase or three phase, linear or nonlinear that are further classified as static/dynamic and balanced/unbalanced.

Three-phase three-wire loads do not require any neutral connection either from the star connected capacitor bank or from any transformer. All the main architectures with this kind of load along with their specifications, merits, demerits, and applications are provided in Table 1.

Three-phase four-wire loads require a neutral connection as listed in Table 2. A micro hydro system can also feed static or dynamic loads [9–11]. Further, the voltage and frequency controller gets divided into a configuration of different number of legs depending on the application of load [12, 13]. Frequency regulation, control over wastage of available water, and managing the electricity distribution are a few functions performed by fuzzy controller employed in micro hydro systems guaranteeing the closed-loop stability, a better solution to low-efficiency methods [14]. To attain the frequency in the prescribed limits at a faster rate, many intelligent controllers using the concept of artificial intelligence are used to reduce the system losses [15].

Table 1 Main architectures with three-phase three-wire loads

Paper	Specifications	Merits/applications	Demerits
8	Controller modeled as variable impedance; Integrated configuration	Less costly	T.H.D. is very high
14	Parallel connection of synchronous and induction generator; STATCOM	<ul style="list-style-type: none"> • ELC is not used • Additional circuitry for synchronization is not required 	<ul style="list-style-type: none"> • Frequent maintenance is required • It has bulky construction
16	Decoupled configuration, ELC, STATCOM	<ul style="list-style-type: none"> • Provides reactive power compensation • Better voltage and frequency regulation 	Additional circuitry for generating signals for STATCOM is required
23	Incremental conductance based algorithm; Bidirectional, solar PV array, and BESS	<ul style="list-style-type: none"> • Peak load demands are fulfilled by BESS • Maintains stable and continuous power generation 	System complexity and cost increases

Table 2 Main architectures with three-phase four-wire loads

Paper	Specifications	Merits/applications	Demerits
17	ELC (three-leg IGBT based CC-VSC) with non-isolated T transformer	<ul style="list-style-type: none"> • Less sensitive to load perturbations and fast response • Mitigation of triplen harmonics and derating of the device 	Complex circuitry
18	Least mean square algorithm; Integrated, Neural network based ELC	<ul style="list-style-type: none"> • Losses due to harmonics and derating of generators are reduced • Provides improved power quality 	Zigzag transformer currents are huge under light load conditions
24	Integrated, VFC (three-leg IGBT VSC), zigzag/star transformer, DSP	<ul style="list-style-type: none"> • Provides neutral current compensation • Isolation between generator and load 	Tuning of PI controllers is a difficulty
25	Indirect current control; Two back-to-back connected PWM controlled VSC, MPT, BESS	<ul style="list-style-type: none"> • Bidirectional active and reactive power flow • Provides mitigation of zero sequence currents 	<ul style="list-style-type: none"> • System complexity increases • Uses large circuitry

The voltage and frequency regulation was collectively obtained using STATCOM and ELC for which an additional firing circuitry was as described in Tables 1 and 2 [15–25].

The control strategy initially started with a resistance to dump the surplus power. Methods were developed to find an alternative for the resistive loads. Seeing the power demand during peak load conditions, a power backup was provided by the configuration employing BESS.

4 Discussion

Methods were developed to improve the efficiency of the system employing ELC

- A centralized control strategy has been invented for frequency modulation with enhanced efficiency where ELC and pump loads are connected in parallel which are controlled by observing the rate of change of frequency as shown in Fig. 5.
- Owing to the disadvantage of power wastage, a method to avoid electronic load controller is to divert the excess water coming to the penstock to the fields for irrigation and other purposes.
- Until now, ELC or conventional ELC dissipates the surplus power in dump load in the form of heat energy which can be effectively utilized by transferring it for domestic consumption.

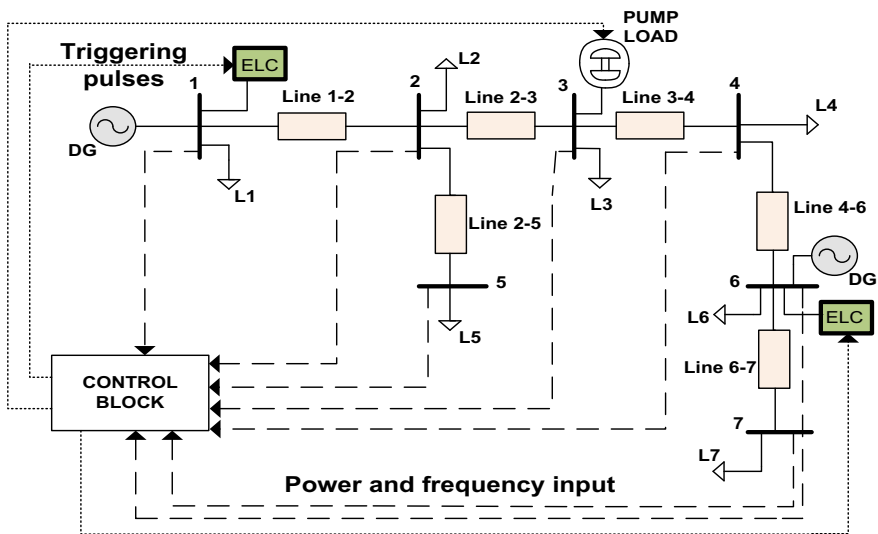


Fig. 5 Single line diagram of the centralized control strategy

5 Conclusion

The frequency regulation in autonomous micro hydro system is a challenging task for which the excess power is needed to be managed properly. Electronic load controller is the new technology developed which dissipates the surplus power as heat. To minimize power losses in ELC, electric power instead of being dumped is utilized in one or the other way. Pump loads, water heaters, etc., are alternatives used in unreachable places in order to improve the quality of life of people living there. Distributed ELC is also an option providing separate ELC for all the houses such that the dumped power can be utilized for running low wattage apparatus for household purposes.

This review shows the need for further modification in controllers to minimize the total harmonic distortion in the load current. Also there is a scope for upgrading the efficiency of the system while using a control technique for frequency modulation with minimum power losses.

References

1. Alghuwainem SM (1999) Steady-state analysis of an isolated self-excited induction generator driven by regulated and unregulated turbine. *IEEE Trans Energy Convers*: 718–723
2. Adhau SP (2009) A comparative study of micro hydro power schemes promoting self sustained rural areas. In: 1st international conference on sustainable power generation and supply, pp 1–6
3. Sarkar N, Bannerjee S, Aikat K, Ghosh SK (2012) Bioethanol production from agricultural wastes: an overview. *Renew Energy*: 19–27. <https://doi.org/10.1016/j.renene.2011.06.045>
4. Camara MB, Barakat G, Nichita C, Dakyo B (2009) Simulation of a doubly-fed induction generator with hydro turbine for electrical energy production. In: 8th international symposium on advanced electromechanical motion systems and electric drives joint symposium, pp 1–3
5. Adhau SP, Adhau PG, Moharil RM (2010) Reassessment of irrigation potential for micro hydro generation. In: IEEE international conference on sustainable energy, pp 1–5
6. Andreica M, Exteberria-Otadui I, Roye D, Bacha S (2008) Micro-hydro water current turbine control for grid connected or islanding operation. In: PESC record—IEEE annual power electronics specialists conference, pp 957–962
7. Murthy SS, Chilipi RR, Bhuvaneswari G, Singh B, Madishetti S (2014) Design and implementation of dynamic electronic load controller for three-phase self-excited induction generator in remote small-hydro power generation. *IET Renew Power Gener* 8:269–280
8. Singh B, Tandon AK, Goel M, Murthy SS (2006) A steady state analysis on voltage and frequency control of self-excited induction generator in micro-hydro system
9. Singh B, Kasal GK, Chandra A, Al-Haddad K (2008) An independent active and reactive power control of an isolated asynchronous generator in 3-phase 4-wire applications. In: IEEE annual power electronics specialists conference, pp 2057–2063
10. Kumar Kasal G, Singh B (2008) VSC with zig-zag transformer based decoupled controller for a pico hydro power generation. In: Annual IEEE India conference, pp 441–446
11. Singh B, Al-Haddad K, Chandra A, Rajagopal V (2010) Development of electronic load controller for IAG based standalone hydro power generation. In: Annual IEEE India conference: green energy, computing and communication, pp 3–6
12. Scherer LG, de Camargo RF (2011) Frequency and voltage control of micro hydro power stations based on hydraulic turbine's linear model applied on induction generators. *Power electronics conference*, pp 546–552. <https://doi.org/10.1109/cobep.2011.6085209>

13. Singh B, Rajagopal V (2011) Neural-network-based integrated electronic load controller for isolated asynchronous generators in small hydro generation. *IEEE Trans Ind Electron*: 4264–4274
14. Becker Tischer C, Camargo R, Giuliani Scherer L, Tibola J (2017) Proportional-resonant control applied on voltage regulation of standalone SEIG for micro-hydro power generation. *IET Renew Power Gener*: 593–602
15. Dahal R, Adhikary B, Jha SK (2016) Performance of droop based load controller in inter-connected micro hydro power plants. In: International conference on the developments in renewable energy technology. <https://doi.org/10.1109/icdret.2016.7421502>
16. Seema, Singh B (2016) Intelligent control of SPV-battery-hydro based microgrid. <http://ieeexplore.ieee.org/document/7914506/>
17. Singh B, Rajagopal V (2012) Digital control of voltage and frequency of induction generator in isolated small hydro system. In: IEEE international conference on power electronics, drives and energy systems, pp 1–7 <https://doi.org/10.1109/pedes.2012.6484407>
18. Goel PK, Kishore N, Murthy SS, Singh B (2011) Isolated wind—hydro hybrid system using cage generators and battery storage. *IEEE Trans Ind Electron*: 1141–1153
19. Singh B, Gupta S, Murthy SS (2003) An improved electronic load controller for self-excited induction generator in micro-hydel applications. *Ind Electron Conf Proc* 3:2741–2746. <https://doi.org/10.1109/IECON.2003.1280681>
20. Singh B, Al-Haddad K, Chandra A, Kasal GK (2008) Voltage and frequency controller for an autonomous micro hydro generating system. In: IEEE power and energy society general meeting: conversion and delivery of electrical energy in the 21st century, pp 1–9. <https://doi.org/10.1109/pes.2008.4596127>
21. Nababan S, Blaabjerg F, Muljadi E (2012) An overview of power topologies for micro-hydro turbines. In: IEEE international symposium on power electronics for distributed generation systems, pp 737–744
22. Singh B, Sharma S (2012) Stand-alone single-phase power generation employing a three-phase isolated asynchronous generator. *IEEE Trans Ind Appl* 48:2414–2423
23. Adetona O, Keel LH, Garcia E (2000) A new method for the control of discrete nonlinear dynamic systems using neural networks. *IEEE Trans Neural Netw* 11
24. Salhi I, Doubabi S (2010) Fuzzy control of micro hydro power plants. In: IET international conference on power electronics, machines and drives, pp 1–6
25. Syan S, Biswal GR (2015) Frequency control of an isolated hydro power plant using artificial intelligence. In: IEEE workshop on computational intelligence: theories, applications and future directions, pp 1–5. <https://doi.org/10.1109/wci.2015.7495537>

Performance Analysis of Solar and Plug-in Electric Vehicle's Integration to the Power System with Automatic Generation Control



Subhranshu Sekhar Pati, Tapas Kumar Panigrahi and Aurobindo Behera

Abstract Plug-in electric vehicle (PEV) is one of the essential constituents of the smart grid. The loading of PEVs to the grid hinders stability, as the size and complexity increases. This work prescribed a smart grid scenario with the incorporation of renewable energy and PEVs. Here, Automatic Generation Control (AGC) is introduced to maintain the system frequency at the scheduled level through a Proportional–Integral–Derivative controller with n-filter (nPID) tuned by Jaya algorithm. Two-area interconnected system considered consists of thermal, hydro, and photo-voltaic (PV) sources with PEVs in each area. To check the system performance, dynamic loading of $\pm 5\%$ in either area for a duration of 80s has been considered. To validate the efficiency of the proposed system, diverse controller schemes such as PI, PID, and nPID are deliberated. A noteworthy improvement in the response time is observed, owing to the effective tuning of the controller for upholding system stability.

Keywords Automatic generation control (AGC) · Jaya algorithm · Integral of time multiplied absolute error (ITAE) · Plug-in electric vehicle (PEV)

1 Introduction

Now around the world, the prime focus of power generation is from renewable energy, predominantly, from PV cells owing to its widespread advantages over conventional energy sources. The operational efficiency and maintenance cost of PV plant has been improving significantly in recent years. Moreover, solar technology can also be

S. S. Pati

International Institute of Information Technology Bhubaneswar, Bhubaneswar 751003, Odisha, India

T. K. Panigrahi

Parala Maharaja Engineering College, Berhampur 761003, Odisha, India

A. Behera (✉)

Cambridge Institute of Technology, Ranchi 835103, Jharkhand, India
e-mail: C115002@iiit-bh.ac.in

© Springer Nature Singapore Pte Ltd. 2020

A. Kalam et al. (eds.), *Intelligent Computing Techniques for Smart Energy Systems*,
Lecture Notes in Electrical Engineering 607,
https://doi.org/10.1007/978-981-15-0214-9_73

703

used as storage medium, because of the smooth conversion of power from one form to other via suitable power electronics converter and advance controlling algorithm like MPPT [1]. In spite of the increase in power generation from PV plant, most of the power still comes from thermal and hydro units. Thus, in a highly complex interconnected power network, frequency, and transaction of power between areas through tie line should be maintained at scheduled level. In this case, AGC plays a major role of maintaining the frequency and tie-line power within permissible limits [2, 3].

The study of AGC is further extended with the implementation of the aggregate model of PEVs by many researchers [4, 5]. The PEV technology can be switched to generator mode thus supplying energy to grid or motoring mode for charging the battery. So these dynamic interactions of the grid with PEVs need to be examined and analyzed adequately. Thus, the authors have decided to implement the PEVs with power rating of ± 5 KW each in this work for the study of AGC.

However, to achieve the system response at a satisfactory level, diverse controllers can be used. Some of the commonly used controllers are PID, nPID, and fractional-order PID (FOPID). Generally, the gain parameters are properly optimized with the help of suitable optimization technique such as Particle Swarm Optimization (PSO), Differential Evolutionary (DE), Teaching Learning Based Optimization (TLBO), Chaotic Optimization (CO) [6], and Jaya algorithm. In the proposed study, Jaya algorithm is considered for optimal tuning of controller parameters as it is simple yet effective optimization technique.

2 Proposed System Study

With the advancement of technology and the negative impact of fossil fuel, use of PEVs increases in an incremental manner across the globe. To examine the system performance, two equal areas with different sources named as thermal, hydro, PV, and PEV have been considered, as shown in Fig. 1. In thermal model, boiler dynamics (BD) is taken to realize the exact working model of a boiler in a thermal power station. Moreover, appropriate nonlinearities such as Generation rate Constraint (GRC) and Governor Dead Band (GDB) are implemented in both thermal and hydro units. GDB of 0.05% for thermal and 0.02% for hydro is considered for this study. Likewise GRC of 3% is taken for thermal plant and 270% for rising the generation as well as 360% lowering the generation is reflected in proposed hydro plant [7]. Now, most of the power utilities use solar harvesting technology such as PV in distributed generation (DG) mode. To simulate a practical PV model, MPPT controlled units are considered in either area. Although the DGs generate green power which is easier to synchronize with the grid, it will add new complexities and challenges in the existing power network. Two thousand numbers of PEVs are used in each area, also the Jaya-optimized nPID controller is used in the proposed study for sustaining the desired system state.

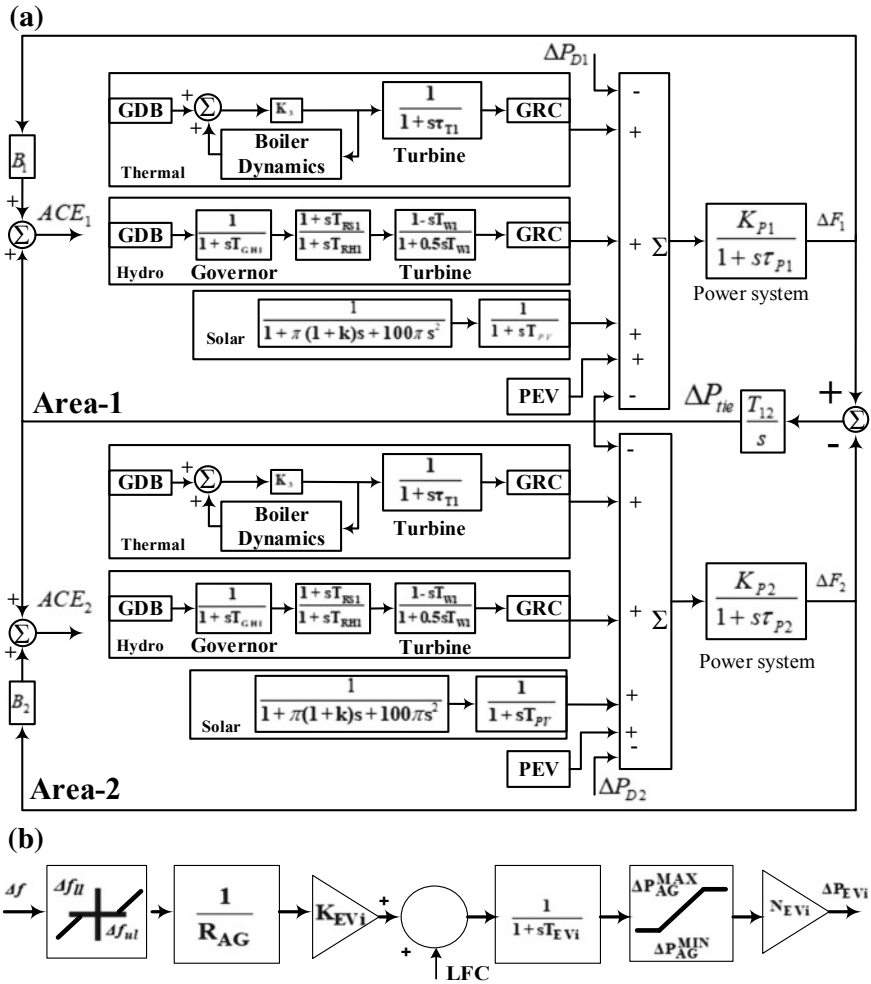
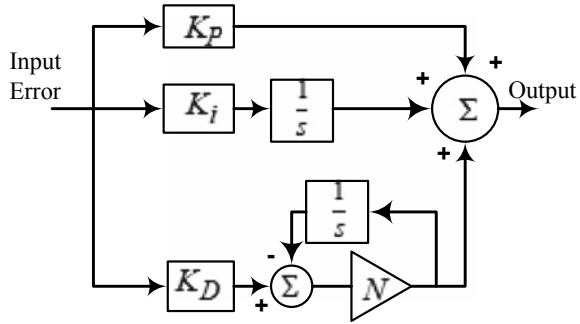


Fig. 1 Block diagram representation of the a Multi-source system; b PEV

3 Selection of Controller and Objective Function

A simple PID controller with an additional filter coefficient (N) constitutes an nPID controller. In this present study, nPID controller with parameters such as K_P , K_i , K_D and N shown in Fig. 2 has been selected for investigation. The input to the controller is the summation of error signals which are to be minimized by the control action of the nPID controller [8]. The output of the controller is fed to the governor-turbine system in the respective areas. The transfer function of the nPID controller is depicted in Eq. (1).

Fig. 2 Block diagram of nPID controller



$$TF_{nPID} = \left[K_P + K_i \left(\frac{1}{s} \right) + K_D \left(\frac{N_s}{s + N} \right) \right] \tag{1}$$

For this optimization problem, Integral Time Absolute Error (ITAE) is used owing to its suitability and efficacy of assisting the controller for producing an adequate control action [9, 10].

$$J = ITAE = \int_0^{t_{sim}} (|\Delta F_1| + |\Delta F_2| + |\Delta P_{tie}|).t. dx \tag{2}$$

Here, ΔF_1 and ΔF_2 are the fluctuations of frequency in area-1 and 2, respectively, and ΔP_{tie} is the change in tie line power. Along with the formulation of objective function, maximum and minimum value of the gain parameters is also considered in the system.

4 Jaya Optimization Technique

Jaya algorithm is an effective and influential algorithm proposed by Rao [11, 12], used for constrained as well as unconstrained problems. The algorithm is so designed that, the solution for given set of problem always move closer to best solution and restrict the solution not to go toward worst solution. The algorithm is devoid of any algorithm-specific control parameter. The algorithm is analyzed against evolutionary-based algorithm and swarm intelligence based algorithm and found that, the performance is better over other traditional algorithms.

The steps of this algorithm are quite simple and easy to implement with optimum accuracy. $X_{j,k,i}$ is the current set of parameters, whereas, r_1 and r_2 are random numbers in the interval [0, 1]. From Eq. (3), modified solutions $X'_{j,k,i}$ is produced through the interaction of $X_{j,k,i}$ with $X_{j,best,i}$ and $X_{j,worst,i}$.

$$X'_{j,k,i} = X_{j,k,i} + r_{1,j,i} [X_{j,best,i} - |X_{j,k,i}|] + r_{2,j,i} [X_{j,worst,i} - |X_{j,k,i}|] \tag{3}$$

Algorithm 1 Jaya Algorithm

Initialization process: Initialize the variables, population size and Set the termination criteria.
top:
 Categorized the best $X_{j,best,i}$ and worst $X_{j,worst,i}$ solution among the population.
New population generated:The current solution $X_{j,k,i}$ is revised to produce new solution $X'_{j,k,i}$ depending on best and worst solutions, by using Eq. (3).
Check the new solution:
if $J(X') \leq J(X)$ **then**
 Accept $X'_{j,k,i}$ and replace the previous parameters.
else
 No change is allowed.
check the termination criteria:
if Nos of iteration (Itr) $<$ (Itr_{max}) **then**
 goto \rightarrow **top**.

Here, j is the number of controller parameters, i is the population size and k represents the number of iterations completed.

5 Result and Analysis

The 2-area nonlinear system has sources such as thermal, hydel, and wind plants along with PEV. Here, nPID controller is implemented and IWD is adopted for the purpose of tuning the controller parameters. The range of controller parameters is: $0 < K_P, K_i, K_D < 2$; $0 < n < 500$. The system is tested with a dynamic load fluctuation of $-5, +3, +7$ and -8% is considered, at $t = 0, 30, 50$ and 60 s respectively as presented in Fig. 3. Similar analysis, as in [13], has been performed to obtain the results discussed in this section. The IWD tuned parameters for PI, PID and nPID controllers are given in Table 1.

Results in graphical format for the applied disturbance is presented in Fig. 4 and the mathematical analysis of the performance parameters such as overshoot (OS) and

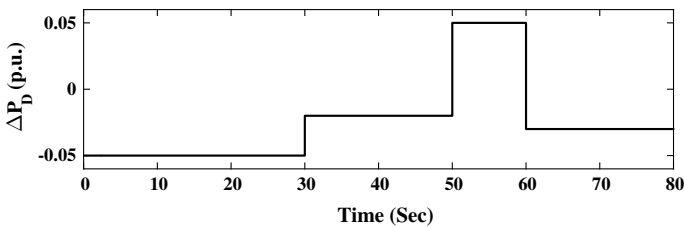


Fig. 3 Dynamic load variation considered for testing the system

Table 1 The PI, PID and nPID controller parameter tuned by Jaya algorithm

Controller/Optimization technique	Optimum controller parameter			
	K_P	K_i	K_D	N
PI: Jaya	1.9521	1.9128	–	–
PID: Jaya	1.5565	1.1962	0.5529	–
nPID: Jaya	1.2639	1.1194	0.8465	439

Table 2 System Response parameters ΔF_1 , ΔF_2 and ΔP_{tie} for different values of ΔP_D in a dynamic loading condition

Various operating conditions	Controller/Optimization technique	Settling Time (2%) T_s (S)			Overshoot/Undershoot (OS/US) ($\times 10^{-4}$)		
		ΔF_1	ΔF_2	ΔP_{tie}	ΔF_1	ΔF_2	ΔP_{tie}
$\Delta P_D = -5\%$ at $t = 0$ s	No controller	18.35	14.52	22.76	10.23	9.645	2.238
	PI:Jaya	8.828	8.969	9.821	38.73	31.21	4.051
	PID:Jaya	3.593	4.595	8.822	16.12	14.70	1.459
	nPID:Jaya	3.204	2.433	7.083	9.827	9.253	0.705
$\Delta P_D = +3\%$ at $t = 30$ s	No controller	18.66	13.29	19.25	-4.065	-3.970	-0.858
	PI:Jaya	7.128	7.971	10.27	-19.44	-17.57	-1.926
	PID:Jaya	2.914	4.385	7.180	-5.769	-5.516	-0.447
	nPID:Jaya	1.826	3.262	4.690	-3.638	3.569	-0.226
$\Delta P_D = +7\%$ at $t = 50$ s	No controller	NA	NA	NA	-20.72	-18.02	-4.537
	PI:Jaya	4.399	6.132	6.894	-27.80	-23.53	-2.836
	PID:Jaya	4.482	8.036	7.891	-34.67	-28.59	-3.379
	nPID:Jaya	4.027	5.731	6.435	-19.96	-17.61	-1.536
$\Delta P_D = -8\%$ at $t = 60$ s	No controller	19.61	18.46	19.63	31.88	24.21	7.097
	PI:Jaya	5.327	7.021	8.69	38.53	31.02	4.017
	PID:Jaya	6.691	8.823	9.54	49.63	36.35	5.024
	nPID:Jaya	4.479	5.853	8.27	26.99	23.28	2.133

settling time (T_s) for either case is presented in Table 2. A comparative assessment of fault response for nPID, to that of no controller, PI and PID is done in Fig. 4 and Table 2 to provide clarity of observation.

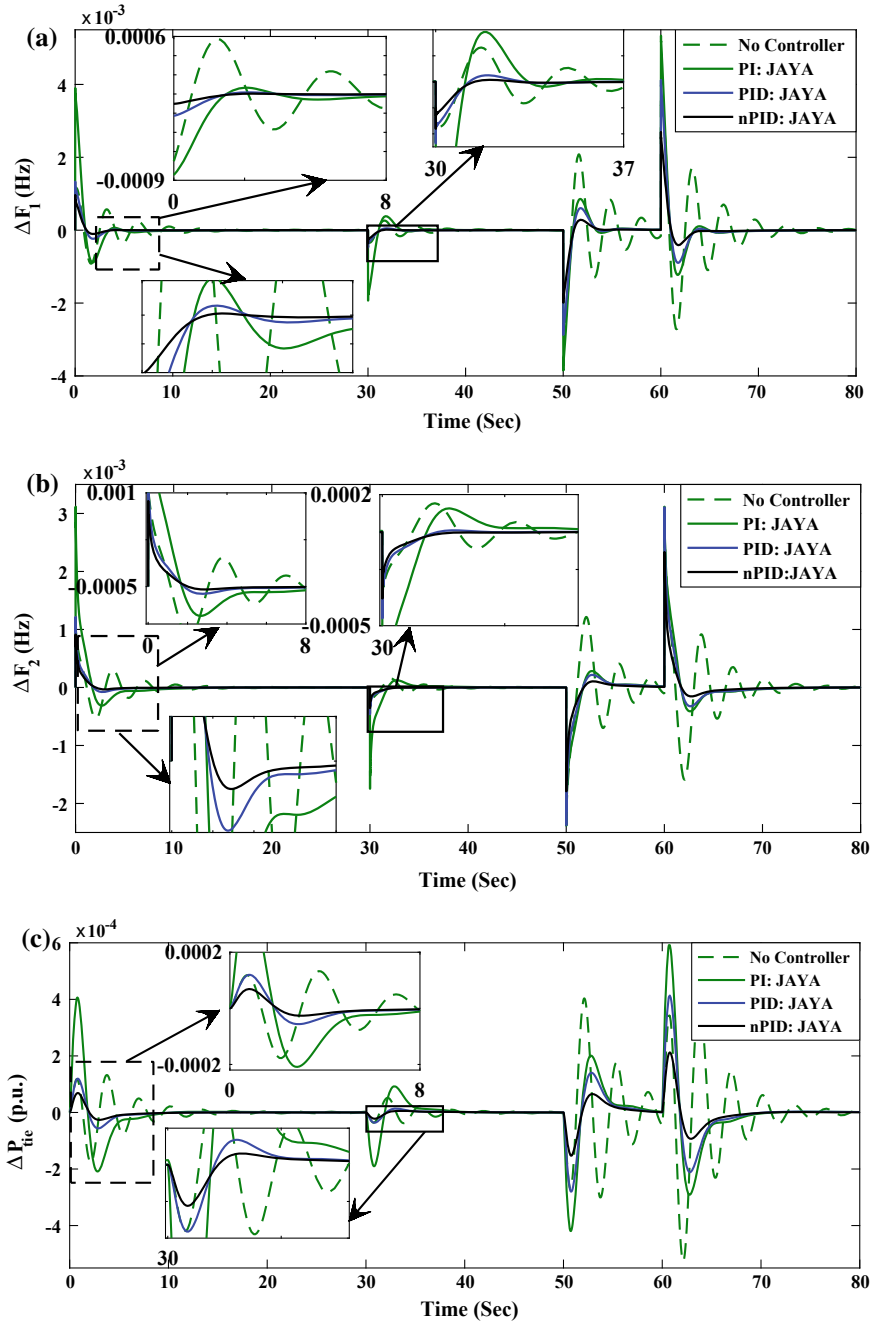


Fig. 4 Dynamic load variation considered for testing the system

6 Conclusion

The work presents an extensive analysis of the multi-source PEV system with nPID controller tuned by Jaya algorithm. The effectiveness of the approach can be observed by the extent to which the system response is stabilized, even with a large and dynamic load deviation of $\pm 5\%$. The major observations from the analysis of multi-source PEV system, which is highly nonlinear and complex in nature, can be listed as

1. The suggested nPID controller tuned by Jaya algorithm is highly efficient even under severe and continuous load variations.
2. The Jaya algorithm owing to its parameter-free operation reaches an optimum result in least possible time. Thus, producing fast response of the system for any load disturbance.

Acknowledgements This work is inspired by the integration of wind turbine as a power source to a system with PEV as presented in [13].

7 Appendix

System Parameters:

Governor gain: $\tau_{g1} = 0.2$, $\tau_{g2} = 0.3$; Turbine gain: $\tau_{t1} = 0.5$, $\tau_{t2} = 0.6$;
 Power system gain: $H_1 = 5$, $D_1 = 0.6$, $H_2 = 4$, $D_2 = 0.9$; Droop characteristics:
 $R_1 = 0.05$, $R_2 = 0.0625$; Feedback gain: $B_1 = 29.6$, $B_2 = 16.9$; Tie line gain:
 $a_{12} = -1$, $T_{12} = 0.545$.

PEV Parameters:

Droop coefficient: $R_{AG} = 2.4$, EV gain: $K_{EVi} = 1$, time constant: $T_{EVi} = 1$, number of electric vehicles: $N_{EVi} = 2000$.

References

1. Hasanien HM (2016) An adaptive control strategy for low voltage ride through capability enhancement of grid-connected photovoltaic power plants. *IEEE Trans Power Syst* 31(4):3230–3237
2. Bevrani H (2009) Robust power system frequency control. Springer, Berlin
3. Elgerd OI (2000) Electric energy systems theory an introduction. McGraw-Hill Book Company, New York, NY
4. Izadkhast S, Garcia-Gonzalez P, Frás P, Bauer P (2017) Design of plug-in electric vehicle's frequency-droop controller for primary frequency control and performance assessment. *IEEE Trans Power Syst* 32(6):4241–4254
5. Debbarma S, Dutta A (2017) Utilizing electric vehicles for LFC in restructured power systems using fractional order controller. *IEEE Trans Smart Grid* 8(6):2554–2564
6. Farahani M, Ganjefar S, Alizadeh M (2012) PID controller adjustment using chaotic optimisation algorithm for multi-area load frequency control. *IET Control Theory Appl* 6(13):1984–1992

7. Sahu RK, Gorripotu TS, Panda S (2016) Automatic generation control of multi-area power systems with diverse energy sources using teaching learning based optimization algorithm. *Eng Sci Technol, Int J* 19:113–134
8. Gorripotu TS, Sahu RK, Panda S (2015) AGC of multi-area power system under deregulated environment using redox flow batteries and interline power flow controller. *Eng Sci Technol* 18:555–578
9. Behera A, Panigrahi TK, Sahoo AK, Ray PK (2018) Hybrid ITLBO-DE optimized fuzzy PI controller for multi-area automatic generation control with generation rate constraint. *Smart computing and informatics. Smart innovation, systems and technologies, vol. 77* Springer, Berlin
10. Panigrahi TK, Behera A, Sahoo AK (2017) novel approach to automatic generation control with various non-linearities using 2-degree-of-freedom PID controller. *Energy Procedia* 138:464–469
11. Rao RV (2016) Jaya: A simple and new optimization algorithm for solving constrained and unconstrained optimization problems. *Int J Ind Eng Comput* 7:19–34
12. Rao RV, Saroj A (2017) A self-adaptive multi-population based Jaya algorithm for engineering optimization. *Swarm Evol Comput* 37:1–26
13. Pati SS, Behera A, Panigrahi TK (2020) Plug in electric vehicle-wind integrated multi-area automatic generation control tuned by intelligent water drops algorithm. In: *Intelligent systems design and applications. ISDA 2018, Advances in intelligent systems and computing, vol 940*. Springer, Berlin, pp 240–250

A Bibliographical View on Research and Developments of Photovoltaic and Thermal Technologies as a Combined System: PV/T System



Anmol Gupta, Sourav Diwania, Sanjay Agrawal, Anwar S. Siddiqui and Yash Pal

Abstract In this hybrid photovoltaic thermal (PV/T) system, air or water is utilized as a circulating fluid which helps in maintaining electrical efficiency as well as utilization of thermal energy (space heating, crop drying, etc.) at the output. In this article, a review of innovative work in the field of PV/T system and thermal modelling of PV/T collector is presented. The thermal model having different equations for PV-integrated flat plate collector, energy balance for air or water heating system stored thermal energy, the instantaneous energy efficiency and the instantaneous exergy efficiency has been presented. Analytical articulations for different thermal parameters and electrical parameters, considering energy balance for several segments or components of PV/T collector is obtained. Various optimization techniques used in the field of PV/T collector, in view of the exergy concept is also presented.

Keywords Exergy efficiency · Photovoltaic thermal · Optimization · Genetic algorithm

NOMENCLATURE

α_t	Absorptivity of glass
b	Width of PV/T collector (m)
L	Length of PV/T collector (m)
dx	Small length (m)

A. Gupta (✉)
KIET Group of Institutions, Ghaziabad, UP, India
e-mail: anmol.gupta@kiet.edu

A. Gupta · Y. Pal
National Institute of Technology, Kurukshetra, Haryana, India

S. Diwania · A. S. Siddiqui
Jamia Millia Islamia, New Delhi, India

S. Agrawal
SOET, IGNOU, New Delhi, India

© Springer Nature Singapore Pte Ltd. 2020
A. Kalam et al. (eds.), *Intelligent Computing Techniques for Smart Energy Systems*,
Lecture Notes in Electrical Engineering 607,
https://doi.org/10.1007/978-981-15-0214-9_74

A_c	Area of the solar cell (m^2)
I_{sl}	Solar radiation intensity ($W\ m^{-2}$)
η_c	Efficiency of the solar cell (%)
$C_{a/w}$	Specific heat of air/water ($J\ kg^{-1}\ K$)
$m_{a/w}$	Mass flow rate of air/water in the channel (kg/s)
$Q_{U,N}$	Useful heat gain for N no. of channels (kWh)
h_{p1}	Penalty factor due to the presence of solar cell material, glass and EVA
T_a	Ambient temperature ($^{\circ}C$)
T_c	Solar cell temperature ($^{\circ}C$)
T_{bs}	Temperature of the back surface ($^{\circ}C$)
T_{aw}	Temperature of air/water ($^{\circ}C$)
α_c	Absorptivity of solar cell
β_c	Packing factor of solar cell
h_t	Heat transfer coefficient of tedlar (W/m^2K)
τ_g	Transmittivity of glass
U_{ca}	An overall heat transfer coefficient from the solar cell to ambient (W/m^2K)
U_t	Convective heat transfer coefficient through the tedlar (W/m^2K)
h_{p2}	Penalty factor due to the presence of an interface between tedlar and working fluid

1 Introduction

Hybrid PV/T technology is a combination of both solar thermal and solar photovoltaic technology. A solar photovoltaic system changes sunlight into electric power while solar thermal changes sunlight into heat yet a PV/T system converts sunlight into heat and electricity simultaneously. The temperature of the PV module increases tremendously when light radiations of certain intensity fall on it, causing reduction in electrical efficiency. It is found that for every $1^{\circ}C$ rise in temperature of PV surface, it will cause 0.4–0.5% decrement in its electrical efficiency.

PV/T system has gained greater attention in the last four decades because of its quality to generate both electric power/energy and thermal energy all the while and joins the electrical and thermal parts in one element over the conventional PV system and solar thermal system. The application areas of PV/T technology are space heating, water heating, drying, integration of photovoltaic thermal in buildings, etc. [1] (Fig. 1).

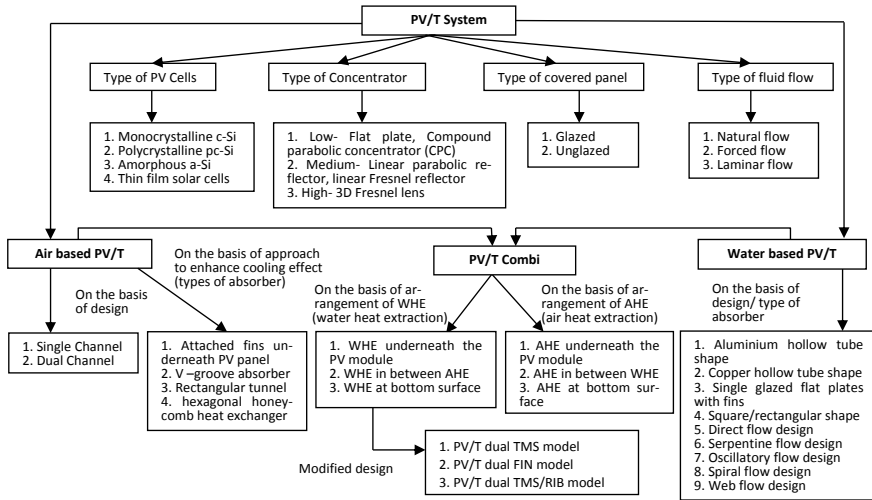


Fig. 1 Classification of PV/T system in view of various literatures

2 PV/T Air Collector

A considerable number of researches have been conducted in the designs of PV/T air collector because its performance is affected by several parameters such as position, dimensions of air duct, input temperature, velocity of flowing air into channel and surface roughness of air duct. A channel or duct is applied below the PV panel in which air is used to absorb the heat energy from the solar cell by conductive or convective process so as to improve the electrical efficiency of the system. The critical factor about the popularity of PV/T is the low efficiency of the cell that varies from 6% to 16% at the temperature of 25 °C but in some of the countries, the ambient temperature rises up to 35 °C. The rising of temperature decreases the module efficiency, hence heat removal from the module is necessary [2].

Hegazy [3] presented four different designs of PV/T collectors based on airflow and investigated the thermal, electrical and overall performance as shown in Fig. 2. The comparative study shows that system-(c) gives appropriate result as it converts solar energy in the form of high-grade electrical energy and low-grade thermal energy, and also it is simple to install in rural areas. Wolf [4] performed the analysis of PV/T system and individual solar PV and solar thermal system and concluded that exergy analysis is a valuable method for the evaluation and comparison of various solar systems.

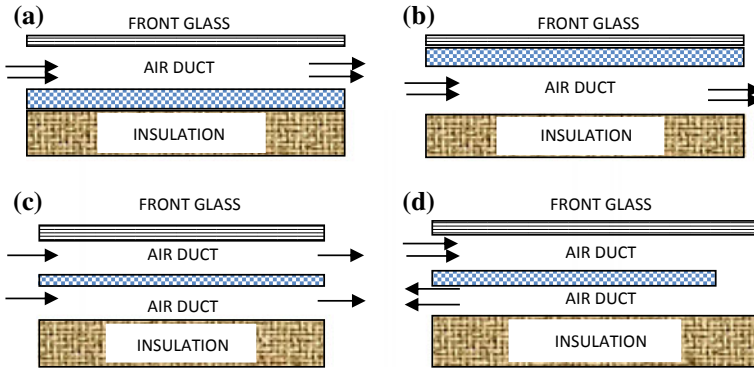


Fig. 2 Cross-sectional view of common designs of PV/T air collector

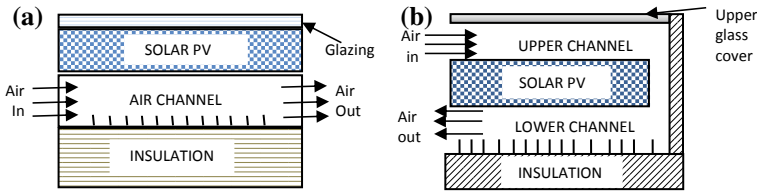


Fig. 3 Cross-sectional view of single-pass and double-pass PV/T air collector with fins

2.1 Effect of Glazing

The overall energy output or thermal energy output can be maximized by using glass cover above the PV surface to trap the extra heat energy which will increase the thermal energy output almost double that of unglazed PV/T, but decreases the electrical energy output [5] (Fig. 3).

2.2 Effect of Adding Thin Metallic Sheets (TMS) and Fins

Tripanagnostopoulos et al. [6] presented a study of PV/T air collectors and suggested that the surface roughness and thin metallic sheets (TMS) used in the air channel are the cost-effective and simple methods for heat removal from the PV panel. Mojumdera et al. [7] experimentally observed the electrical and thermal efficiencies of the system with TMS as 13.75 and 56.19%, respectively.

2.3 Effect of Packing Factor

Packing factor refers to the area of the module covered by the solar cell to the left blank and it affects the output power and operating temperature of the photovoltaic module. Vats et al. [8] found that with an increase in packing factor, the temperature at the output of the channel increases by absorbing the higher amount of thermal energy. Hence, the temperature of the PV module increases which causes a decrease in electrical efficiency. At lower packing factor, the absorber area is less, hence the electrical efficiency is further reduced.

3 PV/T Water

PV/T air has the main problem of temperature issue because an air-based system cannot work effectively at high-temperature areas as there are constraints of low heat capacity, low density, etc.; instead of air, water can carry maximum heat so researchers work in the field of PV/T water. In some areas, during summer season the ambient temperature is very high and for the PV/T air standard, operating is at 20 °C temperature so PV/T water is preferred due to its higher density [9] (Fig. 4).

Huang et al. [10] relate the performance of conventional solar water heater system with a new design which is a combination of the photovoltaic and thermal solar system and evaluated electrical efficiency of 9%. Ji et al. [11] fabricated a flat box aluminium alloy PV for large contact area with a circulation water heating system and the experimental results are obtained with its electrical efficiency of 10.15%, thermal efficiency of 45% and daily total energy of 52%. Chow et al. [12] designed and presented a PV/T system having aluminium alloy flat box collector. In this work, electrical efficiency of the system is 10% with a thermal efficiency of 45–48% for closed circuit and thermal efficiency of 49–52% for open circuit.

The logical articulation of PV/T water heater in steady flow rate of hot water is acquired by Tiwari et al. [13]. Ibrahim et al. [14] executed simulation on seven types of water absorbers. The spiral flow configuration indicates the best result, it has the highest thermal efficiency and parallel cell efficiency of 50.12% and 11.98%, respectively. Dupeyrat et al. [15] investigated the impact of water flow in a flat plate PV/T having single glazing and found thermal efficiency as 79%, electrical efficiency

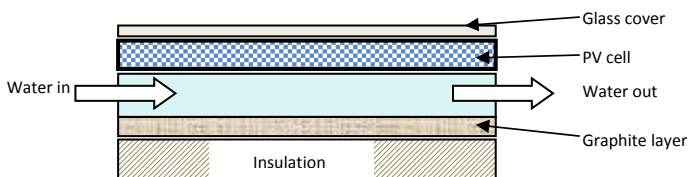


Fig. 4 Cross-sectional view of PV/T water system

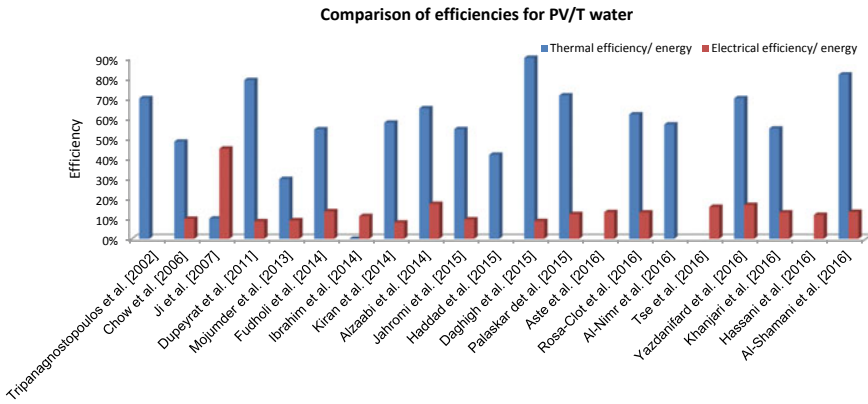


Fig. 5 Comparison of thermal and electrical efficiency for PV/T water system

as 8.8% and in totality, the efficiency is 88% for the propelled configuration. Liang et al. [16] composed a PV/T water collector combined with graphite; it produced the highest electrical efficiency of 7.2% and essential energy saving efficiency of 45%. Yazdanpanahi et al. [17] numerically estimated exergy efficiency of PV/T considering pressure drop in flow channels and maximum efficiency of 13.95% is observed experimentally. Yazdanifard et al. [18] presented mathematical modelling and simulation of flat plate PV/T water system with and without glass cover. It is found that PV/T system with glazing has better energy efficiency (Fig. 5).

4 PV/T Combi

To improve the absorption process on photovoltaic and to get maximum performance of the overall system, the combination of various types of coolant media are utilized (Fig. 6).

PV/T combi achieved better overall energy efficiency, particularly in the generation of electrical energy since heat is removed from the photovoltaic module by integrating both air and water media [19]. Six PV/T combi system designs based on

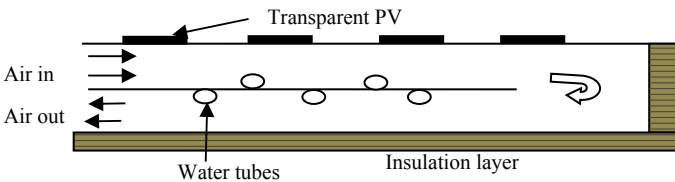


Fig. 6 Cross-sectional view of PV/T-combined system

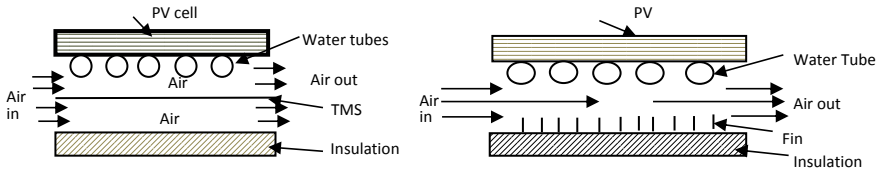


Fig. 7 Cross section of PV/T/dual solar system with TMS modification and with fins

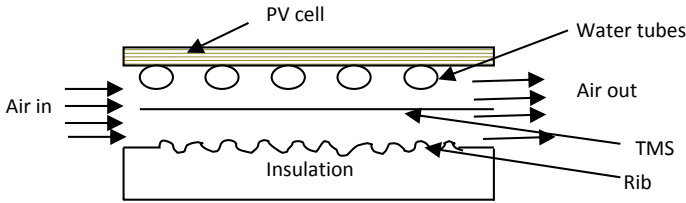


Fig. 8 Combination of TMS with ribs on opposite air channel

the arrangement of air-type and water-type absorber are presented and their performances are observed by Tripanagnostopoulos [20]. Tripanagnostopoulos et al. [21] worked on PV/T combi unit with slight modifications in the air heat extraction unit.

A thin metallic sheet (TMS) is placed between the air channel and the modification is named as PV/T/dual-TMS. This result in a temperature rise of TMS leads to an increase in temperature of the circulating air and hence the thermal efficiency improves (Fig. 7).

A fin plate element is used throughout the length of the air duct and the modification is named as PV/T/dual-fin. This results in increasing the temperature of the air at the output which will further help in improving the thermal efficiency. In the PV/T/dual-TMS/RIB model, ribs are used on opposite channel wall. This model combines the advantages of the above two models mentioned (Fig. 8).

5 Modelling of PV/T Collector

The transfer of heat can take place by means of three mechanisms: conduction, convection and radiation. Heat transfer coefficients of different modes are essential for analysis [22, 23].

Energy balance for solar cells of the PV module (for glass—tedlar PV module)—

$$\tau_g[\alpha_c\beta_c + \alpha_t(1 - \beta_c)]I_{s,l}bdx = [U_{ca}(T_c - T_a) + U_t(T_c - T_{bs})]bdx + \eta_c\alpha_c\tau_g\beta_cI_{s,l}bdx \tag{1}$$

Energy balance for the back surface of tedlar—

$$U_t(T_c - T_{bs})bdx = h_t(T_{bs} - T_{aw})bdx \quad (2)$$

Energy balance for air/water flowing below the tedlar—

$$\left[m_{a/w} C_{a/w} \frac{d}{dx} T_{aw} \cdot dx \right] + [U_{wa}(T_{aw} - T_a) * bdx] = h_t(T_{bs} - T_{aw})bdx \quad (3)$$

Thermal efficiency of PV/T collector—

$$\eta_{th} = \frac{Q_{u,N}}{bLI_{sl}} \quad (4)$$

Electrical Efficiency of PV/T collector—

$$\eta_{el} = \eta_o[1 - \beta_0(T_c - T_o)] \quad (5)$$

where η_o —efficiency at standard test condition, β_0 —temperature coefficient, T_o —outlet temperature

Overall thermal energy gain—

$$\sum Q_{overall,thermal} = \sum Q_{thermal} + \frac{\sum Q_{Electrical}}{\eta_{c,power}} \quad (6)$$

Overall Exergy gain—

$$\sum Exg_{thermal} = Q_{thermal} \left[1 - \frac{T_a + 273}{T_{awout} + 273} \right] \quad (7)$$

$$\text{Exergy Efficiency } \eta_{EXG} = \left(\frac{Exg_{outflow}}{Exg_{inflow}} \right) \times 100 \quad (8)$$

6 Optimization Using Soft Computing

Optimization using soft computing techniques is proved to be very efficient to evaluate the design parameters of PV/T air and water collector. Singh et al. [24] optimized the parameters of a single-channel hybrid photovoltaic thermal air collector using the genetic algorithm (GAs). The overall exergy efficiency of the system is found to be 16.88% at the optimized value of parameters. Singh and Agrawal [25] work on improving the results of GA approach by using the fuzzy-based rules. The overall exergy efficiency with GA-FS approach is observed as 15.82% which is much better than an optimized system with GAs and an unoptimized system. Singh et al. [26] used Evolutionary Algorithm (EA) for parameter optimization of glazed SCPV/T.

An annual carbon emission reduction of around 88% is observed than unoptimized system. Sobhnamayan et al. [27] presented an optimized PV/T water collector system in view of the exergy concept. To optimize exergy efficiency, genetic algorithm is utilized for the given PV/T water collector system. Maximum exergy efficiency of 11.36% is experimentally obtained with optimum inlet velocity and pipe diameter.

7 Conclusion

The PV/T system is in the emerging phase and at present, there is vast acceptability for facilitating development as well as advancement in the presently available PV/T system. Numerous researchers are in this field to enhance the performance of the ordinary air and water PV/T system; whereas, some researchers have presented a small number of innovative ideas in the field of PV/T as heat pipe, nanofluid and phase change materials. The purpose of the review of traditional PV/T systems, so that bibliophile will be assessed advancement in the field of PV/T. Summary of essential PV/T methods and additional attributes of thermal and electrical systems like efficiency, exergy and energy is obtained towards the finish of each section, in order to obtain real facts with respect to technical improvement in PV/T systems initially. Apart from the advantages, further research is required to optimize cost, improvement in efficiency and technological design development.

References

1. Said Z, Arora S, Bellos E (2018) A review on performance and environmental effects of conventional and nanofluid-based thermal photovoltaics. *Renew Sustain Energy Rev*
2. Baskar P, Edison G (2013) A review of mathematical models for performance analysis of hybrid solar photovoltaic—thermal (PV/T) air heating systems. *Adv Mater Res*
3. Hezagy A (2000) Comparative study of the performance of four photovoltaic thermal solar air collectors. *Energy Conserv Manag* 41:861–881
4. Wolf M (1976) Performance analysis of combined heating and photovoltaic power systems for residences. *Energy Convers* 16:79–90
5. Zondag HA (2008) Flat plate PV–thermal collectors and systems: a review. *RSER* 12(4):891–959
6. Tripanagnostopoulos Y, Nousia TH, Souliotis M (2000) Low cost improvement to building integrated air cooled hybrid PV-thermal systems. In: *Proceedings of 16th European PV solar energy conference*, vol 2, pp 1874–1899
7. Mojumdera JC, Changa WT, Onga HC, Leong KY, Al-Mamoon A (2016) An experimental investigation on performance analysis of air type PV thermal collector system integrated with cooling fins. *Energy Build* 130:272–285
8. Vats K, Tomar V, Tiwari GN (2012) Effect of packing factor on the performance of a building integrated semitransparent photovoltaic thermal (BISPVT) system with air duct. *Energy Build*
9. Sathe TM, Dhoble AS (2017) A review on recent advancements in photovoltaic thermal techniques. *Renew Sustain Energy Rev*
10. Huang BJ, Lin TH, Hung WC, Sun FS (2001) Performance evaluation of solar photovoltaic thermal systems. *Sol Energy* 70:443–448

11. Ji J, Lu J-P, Chow T-T, He W, Pei G (2007) A sensitivity study of a hybrid photovoltaic/ thermal water-heating system with natural circulation. *Appl Energy* 84:222–237
12. Chow TT, Ji J, He W (2006) Photovoltaic-thermal collector system for domestic application. *J Sol Energy Eng* 129:205–209
13. Tiwari A, Dubey S, Sandhu GS, Sodha MS, Anwar SI (2009) Exergy analysis of integrated photovoltaic thermal solar water heater under constant flow rate and constant collection temperature modes. *Appl Energy* 86:2592–2597
14. Ibrahim A, Othman MY, Ruslan MH, Alghoul MA, Yahya M, Zaharim A (2009) Performance of photovoltaic thermal collector (PV/T) with different absorbers design. *WSEAS Trans Environ Dev* 5:321–330
15. Dupeyrat P, Ménézo C, Rommel M, Henning H-M (2011) Efficient single glazed flat plate photovoltaic–thermal hybrid collector for domestic hot water system. *Sol Energy* 85:1457–1468
16. Liang R, Zhang J, Ma L, Li Y (2015) Performance evaluation of new type hybrid photovoltaic thermal solar collector by experimental study. *Appl Therm Eng* 75:487–492
17. Yazdanpanahi J, Sarhaddi F, Mahdavi Adeli M (2015) Experimental investigation of exergy efficiency of a solar photovoltaic thermal (PVT) water collector based on exergy losses. *Sol Energy* 118:197–208
18. Yazdanifard F, Ebrahimi-Bajestan E, Ameri M (2016) Investigating the performance of a water-based photovoltaic thermal (PV/T) collector in laminar and turbulent flow regime. *Renew Energy* 99:295–306
19. Abdul Hamid S, Yusof Othman M, Sopian K, Zaidi SH (2014) An overview of photovoltaic thermal combination (PV/T combi) technology. *Renew Sustain Energy Rev*
20. Tripanagnostopoulos Y, Nousia TH, Souliotis M (2001) Proceeding of the 17th European PV solar energy conference. Munich, Germany, pp 2515–2518
21. Tripanagnostopoulos Y (2007) Aspects and improvements of hybrid photovoltaic/thermal solar energy systems. *Sol Energy*
22. Sarhaddi F, Farahat S, Ajam H, Behzadmehr A, Mahdavi Adeli M (2010) An improved thermal and electrical model for a solar photovoltaic thermal (PV/T) air collector. *Appl Energy*
23. Tiwari A, Sodha MS (2006) Performance evaluation of solar PV/T system: an experimental validation. *Sol Energy* 80(7):751–759
24. Singh S, Agrawal S, Tiwari A, Al-Helal IM, Awasti DV (2015) Modeling and parameter optimization of hybrid single channel photovoltaic thermal module using genetic algorithms. *Sol Energy* 113:78–87
25. Singh S, Agrawal S (2015) Parameter identification of the glazed photovoltaic thermal system using Genetic Algorithm- Fuzzy System (GA-FS) approach and its comparative study. *Energy Convers Manag* 105:763–771
26. Singh S, Agrawal S, Gadh R (2015) Optimization of single channel glazed PV/T array using Evolutionary algorithm (EA) and carbon credit earned by the optimized array. *Energy Convers Manag* 105:303–312
27. Sobhnamayan F, Sarhaddi F, Alavi MA, Farahat S, Yazdanpanahi J (2014) Optimization of a solar photovoltaic thermal (PV/T) water collector based on exergy concept. *Renew Energy* 68:356–365

UPM-NoC: Learning Based Framework to Predict Performance Parameters of Mesh Architecture in On-Chip Networks



Anil Kumar and Basavaraj Talawar

Abstract Conventional Bus-based On-Chips are replaced by Packet-switched Network-on-Chip (NoC) as a large number of cores are contained on a single chip. Cycle accurate NoC simulators are essential tools in the earlier stages of design. Simulators which are cycle accurate performs gradually as the architecture size of NoC increases. NoC architectures need to be validated against discrete synthetic traffic patterns. The overall performance of NoC architecture depends on performance parameters like network latency, packet latency, flit latency, and hop count. Hence we propose a Unified Performance Model (UPM) to deliver precise measurements of NoC performance parameters. This framework is modeled using distinct Machine Learning (ML) regression algorithms to predict performance parameters of NoCs considering different synthetic traffic patterns. The UPM framework can be used to analyze the performance parameters of Mesh NoC architecture. Results obtained were compared against the widely used cycle accurate Booksim simulator. Experiments were conducted by varying topology size from 2×2 to 50×50 with different virtual channels, traffic patterns, and injection rates. The framework showed an approximate prediction error of 5% to 6% and overall minimum speedup of $3000 \times$ to $3500 \times$.

Keywords Network-on-Chip · Machine Learning · Support Vector Regression · Booksim · Performance · Latency · Hop count · Traffic pattern

A. Kumar (✉) · B. Talawar
Systems, Parallelization and Architecture Research Lab (SPARK-Lab), Department of Computer Science and Engineering, National Institute of Technology Karnataka, Surathkal, Mangalore, India
e-mail: anilkumar.cs14f05@nitk.edu.in

B. Talawar
e-mail: basavaraj@nitk.edu.in

© Springer Nature Singapore Pte Ltd. 2020
A. Kalam et al. (eds.), *Intelligent Computing Techniques for Smart Energy Systems*,
Lecture Notes in Electrical Engineering 607,
https://doi.org/10.1007/978-981-15-0214-9_75

1 Introduction

NoCs have become the standard communication platform for Multiprocessor System-on-Chips (MPSoCs) and in Chip Multiprocessors (CMPs). It coherently uses the shared On-Chip resources, provides higher bandwidth and modular design for verification and fabrication. NoC architectures are tested using simulators before fabrication. There are different Cycle accurate NoC simulators available viz. Booksim2.0 [7], Noxim [2], SICOSYS [11], Nirgam [6], Nocsim [17] to explore the Micro-architectural design space of NoCs before fabrication. Booksim2.0 is a leading NoC simulator which is widely used by most researchers. It offers network parameters such as routing algorithm, flow control, topology, and router micro-architecture including buffer management, allocation schemes, etc. System operational speed and overall performance of NoC architecture depends on performance parameters like network latency, flit latency, packet latency, and hop count [8].

Large NoC architectures are time-consuming to complete the simulation. Hence, there is a need for a faster method to explore NoC architectures. Figure 1 shows the simulation time of Booksim simulator varying from 6 seconds to 10 days for Mesh topology with uniform traffic pattern and architectural size ranging from 2×2 to 56×56 .

Simulation time of NoC is linearly dependent on architectural size and resources [7]. Experiments were conducted to verify the association between performance parameters and size of NoC architecture. It was observed that performance parameters also are linearly dependent on NoC architecture size which is explained in the results section.

The significant contribution of our work is proposing a Unified Performance Model which can be used to predict the performance parameters of discrete synthetic traffic patterns by training the datasets obtained from Booksim simulator. The UPM is designed using widely used ML regression algorithm like Support Vector

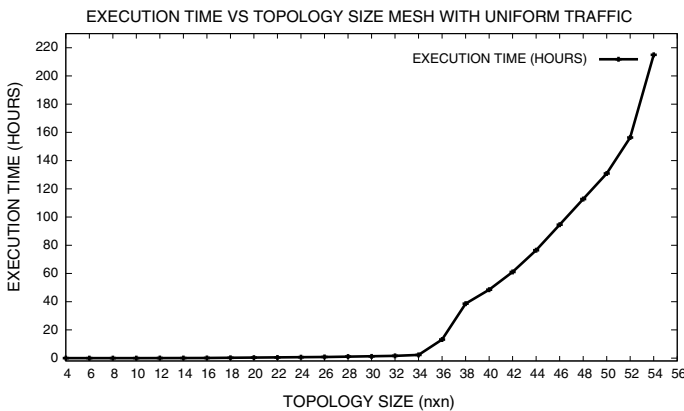


Fig. 1 Booksim simulation time for k-ary 2-dimensional Mesh networks ($k = 2-56$)

Regression (SVR). It can be used to configure different NoC architectures. The proposed framework shows a speedup of minimum $3000\times$ to $3500\times$ for single traffic pattern over the Booksim simulator.

The rest of the paper is organized as follows: Sect. 2 describes the related work, Sect. 3 specifies Experimental Procedure, Sect. 4 presents the results and Sect. 5 concludes this paper.

2 Related Work

2.1 Learning Models Used in Different Aspects of NoC

Lu et al. [10] used reinforcement learning to allocate tasks like the selection of core and temperature of the router to be used. The algorithm updated based on feedback obtained from previously provided prediction. Results showed that the proposed technique was swift in scheduling and reduced the temperature on an average of 4.3°C for a 49-core processor.

Ebranhimi et al. [4] proposed an adaptive routing algorithm based on minimal and nonminimal paths for On-Chip networks using Reinforcement Learning. It provided a large pair of source and destination switches. The congestion information was collected via a fully distributed approach with a small number of bits per link. Selection function finally chose a less congested output channel.

Wang et al. [16] proposed a self-tuning framework which assists in building NoC which can deliver high performance with a change in data traffic. Traffic flows were recorded and dominated flows were identified. These flows were later optimized by reconfiguring the network layer made of configurable switches.

Qian et al. [12, 13] used SVR model for evaluating Network-on-Chip latency performance. This work differs from state of the art NoC analytical models. The classical queuing theory was used to compute the average channel waiting time and Booksim generated training data was used to analyze NoC latency.

Das et al. [3] proposed a robust design development methodology to boost the energy efficiency of 3D NoC architectures. Online ML algorithm was utilized combining the benefits of small world networks and machine learning techniques [1]. The proposed model achieved a reduction of 35% EDP over conventional 3D Mesh.

Most of the works in this area concentrate on smaller sizes of the Mesh topology and on limited traffic patterns. The proposed regression-based UPM framework predicts performance parameters for six synthetic traffic patterns the Mesh topology and size was varying from 2×2 to 50×50 .

3 Design Strategy

3.1 Detailed Layout of Unified Performance Model

UPM consists of six submodels namely uniform traffic pattern model, tornado traffic pattern model, transpose traffic pattern model, shuffle traffic pattern model, bitrev traffic pattern model, and bitcom traffic pattern model. These, in turn, consists of four performance parameters such as Average Network Latency(ANL), Average Packet Latency(APL), Average Flit Latency(AFL), and Average Hop Count(AHC). Each model works independently by considering training dataset obtained from Booksim2.0 simulator. This is later validated using the Booksim2.0 simulator results in the testing phase. All six submodels works in a similar manner. The Outline of the UPM framework is shown in Fig. 2. Results obtained from these six submodels are fed into UPM. This framework gives the desired predicted output once the calibrations are done. The detailed structure of individual submodel is shown in Fig. 3.

Submodels were tested against various regression algorithms like Artificial Neural Networks, SVR and different generalized Linear regression algorithms. Among all the comparisons SVR gave the optimum results. SVR is predominantly used regression algorithm [5]. It has two implementations namely ϵ -SVR and ν -SVR. The fundamental aim of regression algorithms is to form a function that approximates the target values precisely using a set of input values. SVR is used to identify a mapping function between input and output values [15]. The results have been tested with both the variants of SVR algorithm. In ϵ -SVR, ϵ stands for insensitive loss function which is employed to solve the problem of quadratic optimization. The value of ϵ need to be set prior to the training of the SVR model, nevertheless, it is hard to forecast the value of ϵ in most problems. To overcome this limitation, ν -SVR [14] is used where ν indicates a lower bound on the number of support vectors and an upper bound on the fraction of training samples. The kernels used in the framework are linear and radial basis function(RBF). RBF works for both linear and nonlinear data. There are other parameters for SVR like C which controls the trade-off between the margin and the size of the slack variables and γ which is kernel coefficient

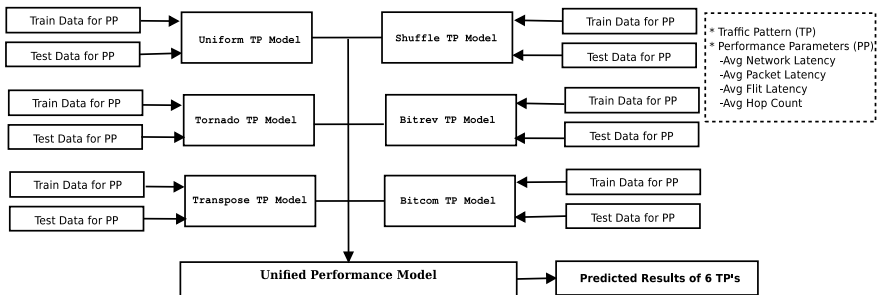


Fig. 2 Outline of unified performance model for mesh topology

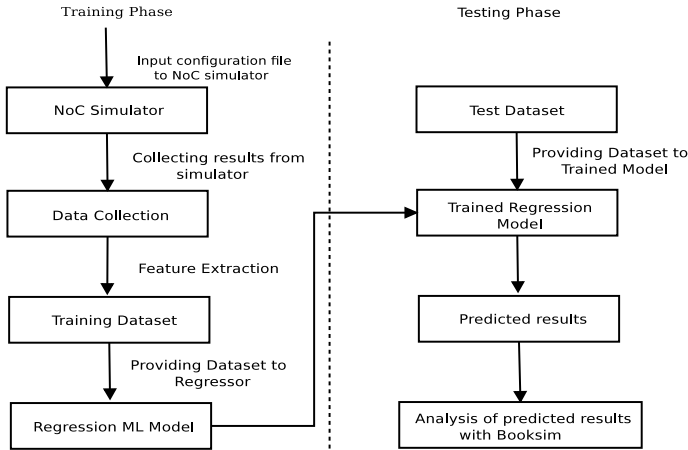


Fig. 3 Independent Learning submodel for different Traffic Patterns

for ‘*RBF*’ and ‘*linear*’. Higher the values of *gamma* algorithm trying fitting data as per the training dataset. Experiments were conducted to test datasets with different available kernels for SVR namely linear, RBF, and Polynomial to check whether dataset works for all the kernels. It was witnessed that the algorithm worked efficiently for ‘*rbf*’ and ‘*linear*’ kernels. Various combinations of (ϵ, C, γ) and (ν, C, γ) were used in all our experiments.

3.2 Data Collection Using Booksim Simulator

The system specifications used for data collection and configuration details of Booksim simulator are shown in Table 1. Among the results acquired we considered topology size, virtual channel, traffic pattern, and injection rates as input features. ANL, AFL, APL, and AHC were considered as output features.

Each traffic pattern generates the traffic non-identically. Uniform and tornado traffic patterns generate traffic for all size of NoC architectures. Data for uniform and tornado was collected by varying architectural size, virtual channels, and injection rate as specified in Table 1. Shuffle, transpose, bitrev and bitcom traffic patterns generate traffic for architectures sizes only in powers of 2 (2, 4, 8, 16, 32, ...). Data for these traffic patterns are also collected in a similar manner using Table 1.

Table 1 Booksim network and system configuration details

Booksim network configuration details	
Topology type	Mesh
Traffic pattern (TP)	Uniform, Tornado, Shuffle, Transpose, Bitrev, and Bitcom
Network size	$2 \times 2, 3 \times 3, 4 \times 4 \dots 50 \times 50$ for Uniform, Tornado TP $2 \times 2, 4 \times 4, 8 \times 8 \dots 64 \times 64$ for Shuffle, Transpose, bitrev, and bitcom TP
Number of virtual channels	2, 3, 4, 5
Buffer size	10
Packet size	20
Sample period	100000 cycles
Injection rates	0.002, 0.0025, 0.003,.....,0.09
Routing algorithm	Deterministic XY routing algorithm
System configuration for mesh topology	
Processor	Intel Xeon CPU E5-2650 V2
Frequency	2.6 Ghz
Memory	64 GB

3.3 Generation of Dataset

Data is collected independently for each network size, traffic pattern, etc., as stated above using Booksim simulator. This data is divided into training and testing datasets which we further use in UPM framework. For uniform and tornado 32% (2×2 to 17×17) of data was considered as training data and remaining 68% (18×18 to 50×50) of data was used to test data and to validate UPM framework in a later stage.

For shuffle, transpose, bitrev, and bitcom training dataset consist of data associated with injection rates ranging from 0.004 to 0.009. Testing data comprises of remaining data with injection rates ranging from 0.002 to 0.0035.

4 Results and Discussion

4.1 Experimental Results

Verification of Analytical Model The correlation study of performance parameters with NoC architectural size was conducted, and the results showed that performance parameters increase linearly with the increase in the architectural size of NoC. Figure 4 justifies Average Network Latency and Average Hop Count obtained from Booksim increase linearly. Similar results were observed for Average Flit

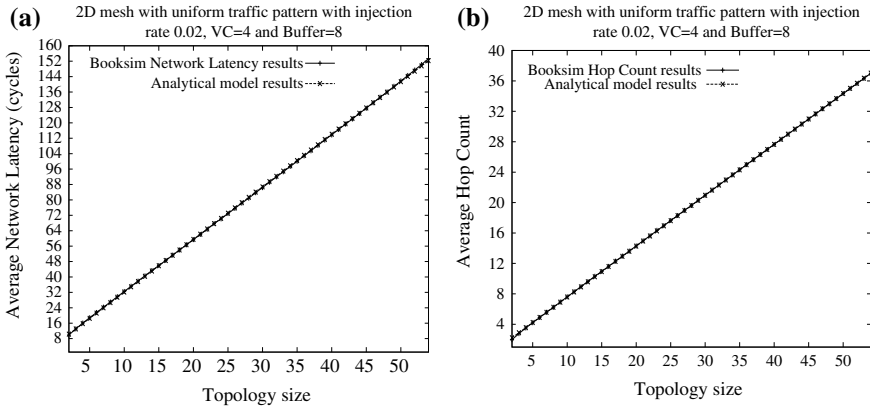


Fig. 4 Comparison of performance parameters between Booksim simulator versus Analytical model for Mesh topology, where **a** Average Network Latency, **b** Average Hop Count with injection rate 0.02, VC = 4, respectively

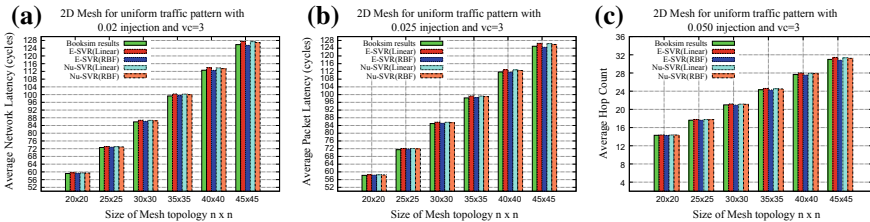


Fig. 5 Comparison of UPM framework against Booksim simulator results for Mesh Topology with Uniform traffic pattern **a** Average Network Latency, **b** Average Packet Latency, and **c** Average Hop Count with injection rates 0.02, 0.025, 0.050 and VC = 3 respectively

Latency and Average Packet Latency. Average Network Latency follows the linear curve $4.8625 + 2.7303 * (architecture_size)$, Average Hop count follows the linear curve $0.8832 + 0.66929 * (architecture_size)$, Average Flit latency follows $5.3495 + 2.7040 * (architecture_size)$ and Average Packet latency follows the curve $4.4962 + 2.6643 * (architecture_size)$. These results were obtained for Mesh topology with an injection rate of 0.02, virtual channel 4 and buffer size 8. Similar results were found for different injection rates and traffic patterns.

UPM for Mesh topology Experiments were conducted using the Booksim configuration and system configuration as shown in Table 1. UPM framework was used to predict performance parameters like ANL, AFL, APL, and AHC which is explained in detail for each traffic pattern.

Uniform traffic pattern submodel is fed with the testing data from 17×17 to 50×50 . Figure 5 shows a comparison of ANL, APL, and AHC of Booksim results against UPM. For better vision we have represented only a few results, similar accuracy was found for remaining architecture sizes. It is observed that this submodel

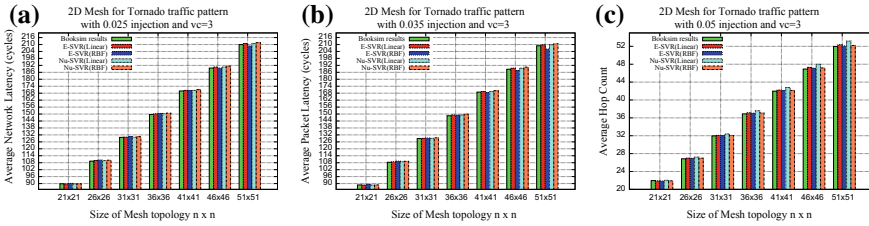


Fig. 6 Comparison of UPM against Booksim simulator results for Mesh Topology with Tornado traffic pattern **a** Average Network Latency, **b** Average Packet Latency and **c** Average Hop Count with injection rates 0.025, 0.035, 0.05, and VC = 3, respectively

gave the highest accuracy of 97.5% for ν -SVR with Linear kernel and MSE of 0.025. It was observed that the least accuracy of 94.1% with MSE 0.059 for ϵ -SVR with RBF kernel.

Tornado traffic pattern submodel is tested with from 21×21 to 50×50 . Figure 6 shows a comparison of ANL, APL, and AHC of Booksim results against UPM. It is observed that this submodel gave the highest accuracy of 95.9% for ν -SVR with RBF kernel and MSE of 0.041. It was also seen that the least accuracy of 90% with MSE 0.1 for ν -SVR with Linear kernel.

The graphs of shuffle, transpose, bitrev and bitcom are similar to the above shown graphs. Shuffle showed a maximum accuracy of 99.98% using ν -SVR with Linear kernel and least accuracy of 97.8% using ν -SVR with RBF kernel. Transpose showed a maximum accuracy of 95.7% using ϵ -SVR with RBF kernel and least accuracy of 93% using ν -SVR with Linear kernel. Bitrev showed a maximum accuracy of 92.8% using ν -SVR with RBF kernel and least accuracy of 89.3% using ϵ -SVR with Linear kernel. Bitcom showed a maximum accuracy of 90.5% using ν -SVR with RBF kernel and least accuracy of 88% using ν -SVR with Linear kernel.

Complete MSE values for each submodel with both ϵ -SVR and ν -SVR considering Linear and RBF kernel are shown in Table 2. Similar results were obtained for AFL by considering all traffic patterns and bitcom traffic pattern also showed the same behavior for all performance parameters.

UPM framework gave the highest accuracy of 94.8% using ν -SVR with RBF kernel and least accuracy of 93.4% using ν -SVR with Linear kernel. This result is evident from Table 2.

4.2 Validation

The testing dataset which was formulated for six traffic patterns earlier is used to check the effectiveness of several traffic patterns and UPM framework. It was observed that the UPM framework demonstrated an overall accuracy of 94.8% with MSE 0.052.

Table 2 Mean Square Errors of Different submodels and UPM framework

Mean square errors of UPM framework and submodels								
Traffic patterns	MSE of submodels				MSE of UPM framework			
	ϵ -SVR (LINEAR)	ϵ -SVR (RBF)	ν -SVR (LINEAR)	ν -SVR (RBF)	ϵ -SVR (LINEAR)	ϵ -SVR (RBF)	ν -SVR (LINEAR)	ν -SVR (RBF)
Uniform	0.0428	0.059	0.025	0.036	0.062	0.061	0.066	0.052
Tornado	0.061	0.072	0.100	0.041				
Transpose	0.067	0.043	0.07	0.048				
Shuffle	0.00029	0.00032	0.0002	0.022				
Bitrev	0.107	0.084	0.0843	0.072				
Bitcom	0.098	0.11	0.12	0.095				

Table 3 Timing Comparison of Booksim simulator with UPM for Mesh topology

Timing comparison of booksim simulator with UPM framework for different synthetic traffic patterns					
Traffic Pattern	Size of the topologies used for testing	Time consumed by booksim simulator		Time consumed by individual submodels	Time consumed by UPM
		In Seconds	In Hours	In seconds	In seconds
Uniform	17×17 to 50×50	4955542	1376.54 [57.36 days]	2.53	114
Tornado	20×20 to 50×50	1128230	313.4 [13.06 days]	1.19	
Transpose	$2 \times 2, 4 \times 4 \dots 32 \times 32$	4833.438	1.34	2.91	
Shuffle	$2 \times 2, 4 \times 4 \dots 32 \times 32$	4179	1.16	0.91	
Bitrev	$2 \times 2, 4 \times 4 \dots 64 \times 64$	44172	12.42	52.08	
Bitcom	$2 \times 2, 4 \times 4 \dots 64 \times 64$	40104	11.14	53.59	

4.3 Runtime Comparison

Experiments were conducted using the system configuration as shown in Table 1 for Mesh topology. Table 3 shows the timing comparison of Booksim simulator against different submodels and UPM framework. Total time taken to complete the execution of all architectural sizes with different traffic patterns was 6.18×10^6 in seconds, 1716 in hours or 71.5 days for Booksim simulator. UPM framework took 114 seconds to predict all performance parameters of different traffic patterns. Each submodel, in turn, took an average of 18.8 seconds time to complete the execution.

5 Conclusion

Unified Performance Model (UPM) is proposed to predict performance parameters of different synthetic traffic patterns for Mesh topology. It is designed using Machine Learning SVR Regression algorithm. Two well-known variants of SVR namely ϵ -SVR and ν -SVR are adopted in our work. The datasets were verified against different available kernels of SVR like ‘linear’, ‘radial basis function’ and ‘polynomial’. It was observed that ν -SVR with RBF kernel provided the best results with error rate of 5.2%. Individual datasets were created for each traffic pattern for network size ranging from 2×2 to 50×50 and these datasets were split into training and testing datasets. The designed UPM-NoC framework predicts different performance parameters namely Average Network Latency, Average Packet Latency, Average Flit Latency, and Average Hop Count. It showed an overall accuracy of 94% to 95% for Mesh architecture. UPM framework works contrary to the conventional cycle accurate simulators in terms of execution time. It shows a minimum speedup of $3000 \times$ against Booksim simulator.

Our target is to extend the framework for power and area model. The future work also concentrates on the remaining regular and irregular topologies with Real time traffic.

Acknowledgements This work is an extension of our earlier work in Eleventh International Conference on Contemporary Computing (IC3), 2018 paper title “Machine Learning Based Framework to Predict Performance Evaluation of On-Chip Networks” [9].

References

1. Boyan J, Moore AW (2000) Learning evaluation functions to improve optimization by local search. *J Mach Learn Res* 1, 77–112
2. Catania V, Mineo A, Monteleone S, Palesi M, Patti D (2015) Noxim: an open, extensible and cycle-accurate network on chip simulator. In: 26th IEEE international conference on application-specific systems, architectures and processors, ASAP 2015, Toronto, ON, Canada, pp 162–163. <https://doi.org/10.1109/ASAP.2015.7245728>
3. Das S, Doppa JR, Kim DH, Pande PP, Chakrabarty K (2015) Optimizing 3d noc design for energy efficiency: a machine learning approach. In: 2015 IEEE/ACM international conference on computer-aided design (ICCAD). IEEE, pp 705–712
4. Ebrahimi M, Daneshmand M, Farahnakian F, Plosila J, Liljeberg P, Palesi M, Tenhunen H (2012) Haraq: congestion-aware learning model for highly adaptive routing algorithm in on-chip networks. In: 2012 IEEE/ACM sixth international symposium on networks-on-chip. pp 19–26. <https://doi.org/10.1109/NOCS.2012.10>
5. Friedman J, Hastie T, Tibshirani R (2001) The elements of statistical learning, vol 1. Springer series in statistics, New York
6. Jain L, Al-Hashimi B, Gaur M, Laxmi V, Narayanan A (2007) Nirgam: a simulator for noc interconnect routing and application modeling. In: Design, automation and test in Europe conference. pp 16–20
7. Jiang N, Balfour J, Becker DU, Towles B, Dally WJ, Michelogiannakis G, Kim J (2013) A detailed and flexible cycle-accurate network-on-chip simulator. In: 2013 IEEE international symposium on performance analysis of systems and software (ISPASS), IEEE. pp 86–96

8. Kiasari AE, Lu Z, Jantsch A (2013) An analytical latency model for networks-on-chip. *IEEE Trans Very Large Scale Integr (VLSI) Syst* 21(1):113–123
9. Kumar A, Talawar B (2018) Machine learning based framework to predict performance evaluation of on-chip networks. In: 2018 eleventh international conference on contemporary computing (IC3), IEEE. pp 1–6
10. Lu SJ, Tessier R, Bureson W (2015) Reinforcement learning for thermal-aware many-core task allocation. In: Proceedings of the 25th edition on great lakes symposium on VLSI, GLSVLSI '15, ACM, New York, NY, USA. pp 379–384. <https://doi.org/10.1145/2742060.2742078>
11. Puente V, Gregorio J, Beivide R (2002) Sicosys: an integrated framework for studying inter-connection network performance in multiprocessor systems. In: Proceedings. 10th euromicro workshop on parallel, distributed and network-based processing, pp 15–22. <https://doi.org/10.1109/EMPDP.2002.994207>
12. Qian ZL, Juan DC, Bogdan P, Tsui CY, Marculescu D, Marculescu R (2016) A support vector regression (svr)-based latency model for network-on-chip (noc) architectures. *IEEE Trans. Comput-Aid Des Integr Circuits Syst* 35(3):471–484
13. Qian Z, Juan DC, Bogdan P, Tsui CY, Marculescu D, Marculescu R (2013) Svr-noc: a performance analysis tool for network-on-chips using learning-based support vector regression model. In: Proceedings of the conference on design, automation and test in Europe, EDA Consortium. pp 354–357
14. Schölkopf B, Smola AJ, Williamson RC, Bartlett PL (2000) New support vector algorithms. *Neural Comput* 12(5):1207–1245
15. Smola AJ, Schölkopf B (2004) A tutorial on support vector regression. *Stat Comput* 14(3):199–222. <https://doi.org/10.1023/B:STCO.0000035301.49549.88>
16. Wang X, Mak T, Jiang MY, Daneshmand M, Palesi M (2013) On self-tuning networks-on-chip for dynamic network-flow dominance adaptation. In: 2013 Seventh IEEE/ACM international symposium on networks-on-chip (NoCS), pp 1–8. <https://doi.org/10.1109/NoCS.2013.6558418>
17. Whelihan D, Schmit H (2003) The nocsim simulator

Comparison of Performance Analysis of Optimal Controllers for Frequency Regulation of Three-Area Power System



Preeti, Vivek Shrivastava, Vikas Singh Bhadoria and Harish Pulluri

Abstract The purpose of this paper is to present the solution of load frequency regulation problem of three-area power system comprising of thermal turbines in each control area. The controllers namely proportional integral (PI), proportional integral derivative (PID) controller, fractional order proportional integral derivative (FOPID) controller, and sliding mode controller (SMC) have been used to solve the automatic generation control problem in the present work. The gains of these controllers have been tuned using disrupted oppositional learned gravitational search algorithm (DOGSA) which exhibit the features of exploration and exploitation of the search space to obtain more optimal solution. The optimal controller gains minimize the deviations in frequency and tie-line power of the system under study. From simulation results, it has been deduced that the optimized sliding mode controller shows improved performance in terms of settling time, peak overshoot/undershoot, damping ratio and fitness function value as compared to other tuned conventional controllers.

Keywords Automatic generation control · Disruption · Opposition learning

1 Introduction

In an interconnected power system, generation has to vary with varying load demand. Whenever the load is more than the generation, the frequency and speed of generator

Preeti (✉)

Shri Vishwakarma Skill University, Palwal, Haryana, India

e-mail: preetiednith@gmail.com

V. Shrivastava

National Institute of Technology, Delhi, India

V. S. Bhadoria

ABES Engineering College, Ghaziabad, UP, India

H. Pulluri

Geethanjali College of Engineering Technology, Hyderabad, India

© Springer Nature Singapore Pte Ltd. 2020

A. Kalam et al. (eds.), *Intelligent Computing Techniques for Smart Energy Systems*,

Lecture Notes in Electrical Engineering 607,

https://doi.org/10.1007/978-981-15-0214-9_76

falls and vice versa. This disparity between the power generation and demand is tackled using the automatic generation control (AGC) to attain intended level of frequency and tie-line power independent of change in power demand by the consumers in a control zone. For execution of AGC, the parameters namely frequency, tie-line power and output of each alternator are checked constantly. Based on these examined values and reference information, area control errors (ACEs) [1] are calculated. The controllers in the system sense these ACEs and give appropriate control signal to the alternators to synchronize with the varying power demand [2]. The difficulty faced in this process is the optimal tuning of the controller parameters.

Many researchers [3–5] have worked towards the solution of AGC problem using different control methodologies. From the literature survey of the work of various researchers, it has been inferred that the optimization algorithms based controller exhibit better performance in comparison to the conventional and manually tuned control methods. The concerns with the classical controllers are their optimal tuning and inefficiency to handle large size systems. These limitations are overcome by the use of optimization algorithms in which the performance criterion constituting the fitness function is minimized or maximized to achieve the optimal values of the controller. In the recent past, a more robust control technique known as sliding mode control (SMC) has been implemented to solve AGC for two-area power systems [6, 7] which overcome the limitations posed by the conventional control methodologies. In these research articles, genetic algorithm (GA) and particle swarm optimization (PSO) has been used to fine-tune SMC gains. However, GA and PSO sometimes get trapped in local minima and exhibit the slow convergence of the fitness function. Thus, keeping in view the need for a robust controller, an efficient optimization technique having advantages of good speed of response and enhanced exploration is needed to attain the optimal values of controller gains. In the recent past, gravitational search algorithm based on Newton's law of motion has been introduced in [8]. But sometimes it saturates to local minima. To overcome this, two operators: opposition [9] and disruption operators [10] have been added to improve the exploration and exploitation capability, respectively, of the algorithm and a new hybrid algorithm known as disrupted oppositional learned gravitational search algorithm (DOGSA) is obtained [11, 12].

In this paper, the issue of AGC is explained utilizing established controllers to be specific: integral (I), proportional integral (PI), proportional integral derivative (PID) and fractional order proportional integral derivative (FOPID) control, and sliding mode control (SMC). The controller parameters are tuned through DOGSA for superior performance of the framework under load perturbations. The execution of parameters tuned controllers is exhibited on three region interconnected power system. In light of certain execution lists like settling time, peak overshoot/undershoot, and damping ratio, the dynamic execution of the power system is contrasted for various control procedures.

2 Three-Area System Under Study

In the present work, the interconnected power system comprising of three control areas and thermal turbine in each control area shown in Fig. 1 has been considered for solving the problem of frequency regulation. The Fig. 1 also depicts the different state variables, inputs, and disturbances used for state space analysis of the system.

The detailed structure of I, PI, PID, FOPID, and SMC controller can be referred from [2, 11–13].

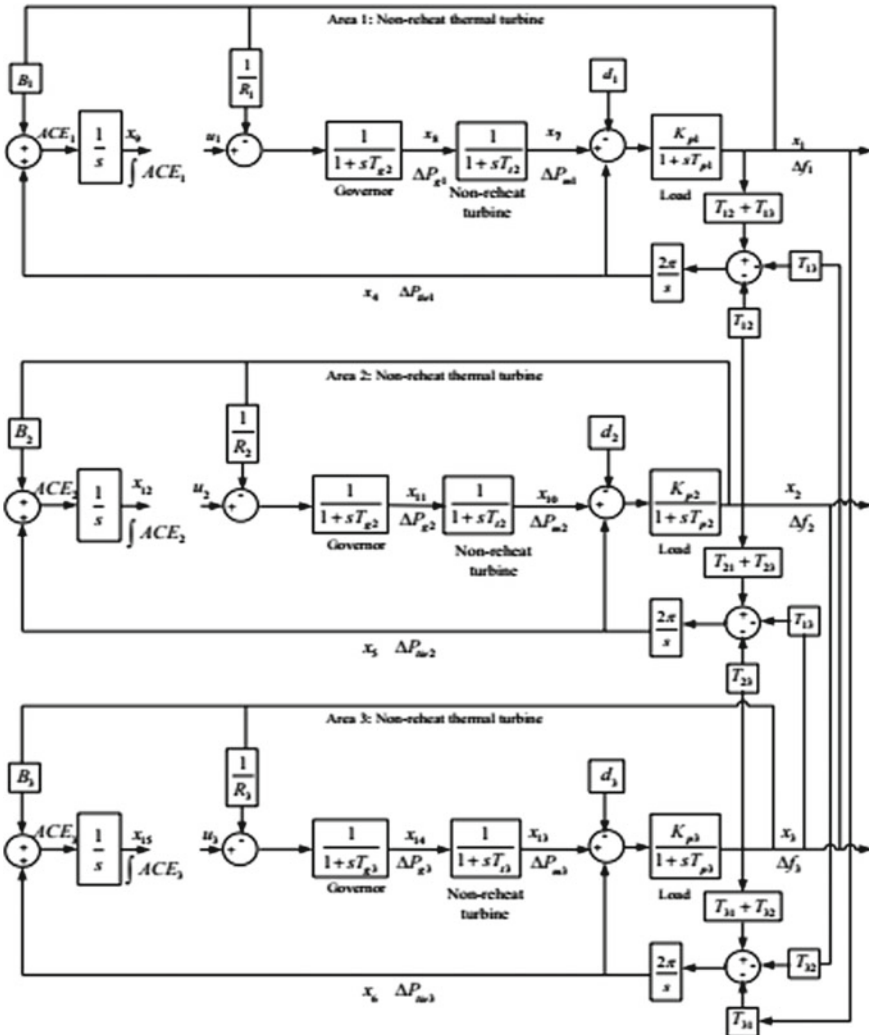


Fig. 1 Transfer function diagram of three-area power system

3 Optimization of Controller Gains

The optimal tuning of the controller parameters implies to achieve the tuned gains which help in attaining the minimum deviations in frequency and tie-line power. Also, the chattering problem in SMC also needs to be diminished. This is achieved by designing a fitness function comprising of integral square error and minimizing it. The values of controller gains giving the minimum fitness function value will be the optimal values giving the desired dynamic response when the system is subjected to load variation. In present work, the fitness functions considered are the following:

$$ff_1 = \sum_{\substack{j,k=1 \\ j \neq k}}^n \int (\Delta f_k^2 + \Delta P_{tiejk}^2) dt \quad (1)$$

$$ff_2 = \sum_{\substack{j,k=1 \\ j \neq k}}^n \int (\Delta f_k^2 + \Delta P_{tiejk}^2 + \Delta u_k^2) dt \quad (2)$$

The fitness function ff_1 aims to reduce the frequency (Δf_k) and tie-line power (ΔP_{tiejk}) fluctuations. The second fitness function ff_2 aims to diminish the chattering in the control input (Δu_k) of the SMC in addition to ff_1 parameters. The n is the aggregate number of control regions in the power system.

To minimize the objective functions given in (1) and (2), the hybridized DOGSA has been used whose detailed mathematical equations and algorithm steps are given in [2, 11–13]. The steps of DOGSA is summarized below:

1. Initialize the controller parameters randomly.
2. Generate the opposition population as follows:

$$\tilde{x} = x + h - l \quad (3)$$

where x is initial population gain, h is higher bound and l is the lower bound value of the controller gain.

3. Calculate the value of the fitness function for every parameter value in initial as well as the opposite population. Select N gains with minimum fitness value from initial and opposite population.
4. Evaluate the mass of every individual agent in selected N gains as

$$M_i(t) = \frac{J_i(t) - w(t)}{(b(t) - w(t)) \times \sum_{j=1}^q m_j(t)} \quad (4)$$

where $b(t)$ and $w(t)$ are the best and worst values of fitness function.

5. Compute the force and acceleration of each controller gain as

$$F_{ij}^d(t) = G(t) \times \left(\frac{M_i(t) \times M_j(t)}{R_{ij}(t) + \varepsilon} \right) \times (x_j^d(t) - x_i^d(t)) \tag{5}$$

$$a_i^d(t) = \sum_{j=1, j \neq i}^n rand_j \times G(t) \times F_{ij}^d(t) \tag{6}$$

6. The velocity and position of every individual in the population are upgraded.
7. Disrupt the gain's position satisfying the disruption condition.
8. The steps from 3 to 8 are repeated until the ceasing measure, i.e., the most extreme number of iteration is reached.

4 Results and Discussion

In this segment, the examination of three-area interconnected power system is performed to analyze the viability of the DOGSA tuned controllers in automatic generation control. Here, the fitness functions ff_1 and ff_2 are minimized using DOGSA algorithm considering a load of 0.01 p.u MW in all the areas. The performance indices of fitness function ff_1 for I/PI/PID/FOPID controllers and ff_2 for SMC controller improved by the DOGSA is depicted in Figs. 2 and 3.

The DOGSA optimized I, PI, PID, and FOPID controllers attains the fitness function ff_1 value of 0.012179, 0.014258, 0.00961, and 0.004806 in 4, 6, 6, and 7

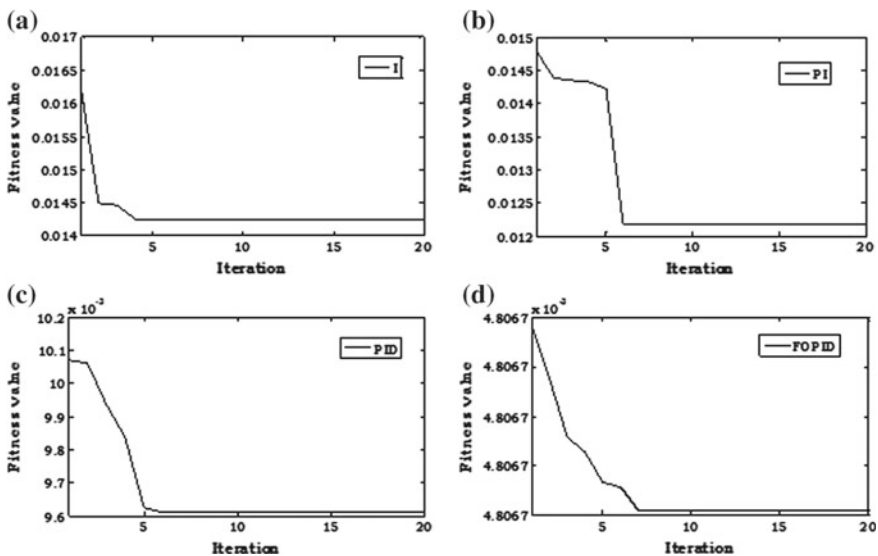


Fig. 2 Performance indices of DOGSA optimized **a** I controller, **b** PI controller, **c** PID controller, and **d** FOPID controller

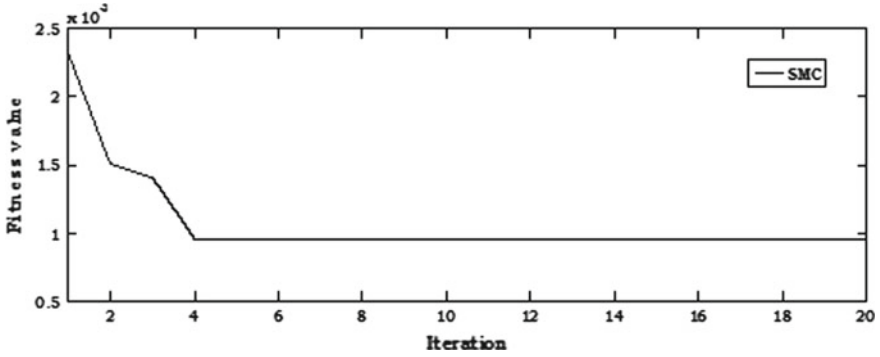


Fig. 3 Performance index of DOGSA optimized SMC controller

Table 1 Performance parameters of three-area power system with DOGSA tuned controllers

Factors		Integral	Proportional Integral	PID	FOPID	SMC
Damping ratio		0.0532	0.0229	0.0228	0.0090	0.1007
Δf_1	OS	0.003945	0.0000	0.0000	0.0000	0.001631
	US	- 0.02807	- 0.02475	- 0.02176	- 0.01409	- 0.003475
	ST	9.92	24.64	10.06	7.83	7.31
Δf_2	OS	0.00385	0.0000	0.0000	0.0000	0.0009959
	US	- 0.02803	- 0.02854	- 0.01747	- 0.01359	- 0.002409
	ST	9.92	21.95	10.82	7.2	6.82
Δf_3	OS	0.003777	0.0000	0.0000	0.0000	0.00169
	US	- 0.028	- 0.02474	- 0.0173	- 0.01352	- 0.003792
	ST	12.49	27.2	10.5	7.83	7.60
ΔP_{tie1}	OS	0.000006821	0.001861	0.0006802	0.0002548	0.0000
	US	- 0.0001479	0.0000	- 0.001715	- 0.0000656	- 0.0002629
	ST	21.89	42.86	14.03	11.35	11.16
ΔP_{tie2}	OS	0.0000149	0.0000	0.000976	0.0001041	0.000672
	US	- 0.00000037	- 0.003641	- 0.0002849	- 0.0001089	- 0.00002693
	ST	22.69	38.86	25.16	20.82	10.11
ΔP_{tie3}	OS	0.000133	0.00178	0.0007579	0.0001593	0.0001526
	US	- 0.000006451	0.0000	- 0.0004107	- 0.0002016	- 0.0000423
	ST	27.49	46.86	26.11	9.27	7.6
Obj		0.012179	0.014258	0.00961	0.004806	0.000958

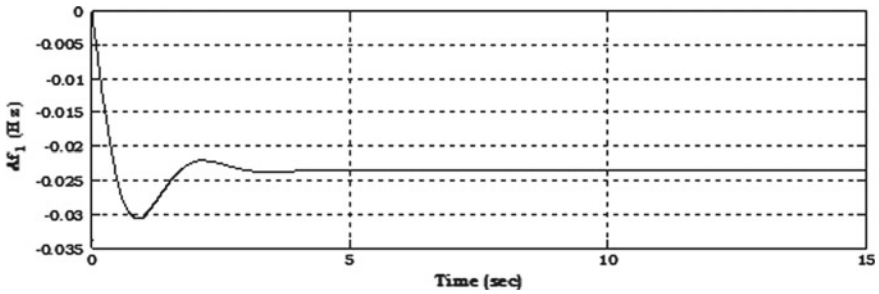


Fig. 4 Frequency deviation of area 1 without controller

iterations. The frequency deviation of area 1 of three-area system without controller is shown in Fig. 4 from which it is evident that deviation achieves steady state value of -0.02353 and does not reach the zero steady state. The dynamic response of area 2 and area 3 are same as of area 1 and the tie-line power is zero.

Figure 5 shows the control input signal to area 1 using pole placement and DOGSA optimized SMC controller for fitness function ff_2 . It is evident from Fig. 5 that the DOGSA tuned SMC generated control signal is smooth and optimized SMC gives smooth and deprived of chattering control signal.

Figures 6a, b demonstrate the output of deviation in frequency of area 1 and deviation in tie-line power of area 1. The performance parameters obtained using DOSA optimized controllers are presented in Table 1. The simulation results displayed in Figs. 6a, b and Table 1 uncovers that the DOGSA tuned SMC controller gives comparably better transient execution.

Looking at the execution of three-area power system with DOGSA optimized controllers from Figs. 2, 3, 4, 5 and 6, and Table 1, it is uncovered that the optimized SMC controller offers improved responses when contrasted with alternate controllers.

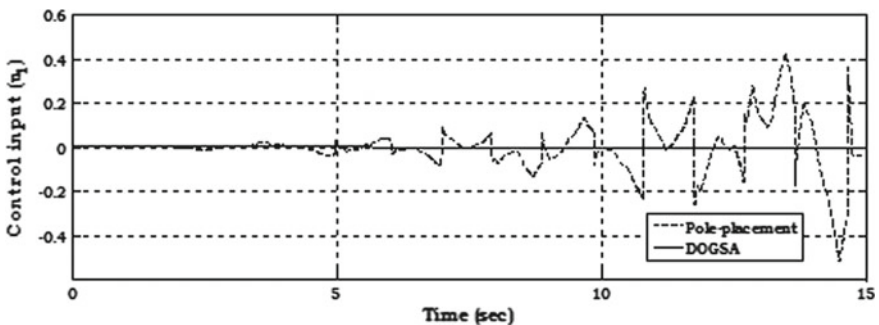


Fig. 5 Tuned SMC generated control input signal

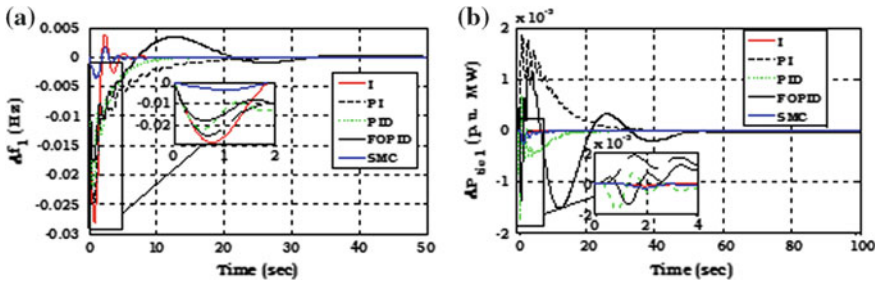


Fig. 6 a Frequency deviation of area 1 b Tie-line power deviation of area 1

5 Conclusion

The automatic generation control problem of three-area power system has been solved using DOGSA optimized I, PI, PID, FOPID, and SMC controller. The controller gains optimized using DOGSA effectively reduces the settling time, peak overshoot/undershoot, and damping ratio of the dynamic responses of the frequency deviations and tie-line power deviations in the system. It is concluded from the simulation results that amongst all the controllers, optimized SMC shows superior performance depicted in terms of different performance criterion of dynamic responses as compared to other controllers considered in the present study.

References

1. Nasiruddin I, Bhatti TS, Hakimuddin N (2015) Automatic generation control in an interconnected power system incorporating diverse source power plants using bacteria foraging optimization technique. *Electr Power Compos Syst* 43(2):189–199
2. Dahiya P, Sharma V, Naresh R (2015) Solution approach to automatic generation control problem using hybridized gravitational search algorithm optimized PID and FOPID controllers. *Adv Electr Comput Eng* 15(2):23–34
3. Ibraheem Kumar P, Kothari DP (2005) Recent philosophies of automatic generation control strategies in power systems. *IEEE Trans Power Syst* 20(1):346–357
4. Shayeghi H, Shayanfar HA, Jalili A (2009) Load frequency control strategies: a state-of-the-art survey for the researcher. *Energy Convers Manag* 50(2):344–353
5. Pandey SK, Mohanty SR, Kishor N (2013) A literature survey on load-frequency control for conventional and distribution generation power systems. *Renew Sustain Energy Rev* 25:318–334
6. Al-Hamouz Z, Al-Duwaish HN, Al-Musabi N (2011) Optimal design of a sliding mode AGC controller: application to a non-linear interconnected model. *Electr Power Syst Res* 81(7):1403–1409
7. Al-Hamouz Z, Al-Duwaish HN, Al-Musabi N (2011) Particle swarm optimizing sliding mode controller. US Patent US2011/0257800 A1
8. Rashedi E, Nezamabadi-pour H, Saryazdi S (2009) GSA: A gravitational search algorithm. *Inf Sci* 179(13):2232–2248
9. Rahnamayan S, Tizhoosh HR, Salama MMA (2007) A novel population initialization method for accelerating evolutionary algorithms. *Comput Math Appl* 53(10):1605–1614

10. Sarafrazi S, Nezamabadi-Pour H, Saryazdi S (2011) Disruption: a new operator in gravitational search algorithm. *Sci Iran* 18(3):539–548
11. Dahiya P, Sharma V, Naresh R (2017) Hybridized gravitational search algorithm tuned sliding mode controller design for load frequency control system with doubly fed induction generator wind turbine. *Optim Contr Appl Met* 38(6):993–1003
12. Dahiya P, Sharma V, Naresh R (2016) Automatic generation control using disrupted oppositional based gravitational search algorithm optimized sliding mode controller under deregulated environment. *IET Gener Transm Dis* 10(16):3995–4005
13. Dahiya P, Sharma V, Naresh RN (2015) Optimal generation control of interconnected power system including DFIG-based wind turbine. *IETE J Res* 61(3):285–299

Optimal DG Allocation in a Microgrid Using Droop-Controlled Load Flow



Ankit Uniyal and Saumendra Sarangi

Abstract With increasing autonomy of the microgrid and the growing load, DG allocation is a mandatory exercise. When output of DGs are droop controlled, their bus location and corresponding droops may affect the system voltage and frequency profile. To analyse such a system, droop-based load flow is required. In the present work, optimal placement of droop-based DGs is done in an islanded/autonomous radial microgrid system with an objective to minimise deviations of voltage and frequency from the nominal values. The problem is formulated as a bi-objective optimization problem and is solved using a multi-objective heuristic-based optimization technique, namely, NSGA-II and FSM. The proposed analysis is carried out for an IEEE 33 bus radial distribution system modified as an autonomous microgrid. The results show the applicability of the proposed analysis.

Keywords Distributed generation (DG) · Fuzzy satisfying method (FSM) · Load flow · Microgrid · Non-dominated sorted genetic algorithm (NSGA-II)

1 Introduction

The present power system is experiencing various changes both in structure and operation. The most prominent ones being the growing load demand with time and the increasing intermittency in generation, owing to rise in penetration level of renewable energy sources. The renewable energy sources being pollution-free and non-exhausting have numerous applications. The distributed generation system (DG) is one such application which forms a vital part of the modern concept of smart distribution grid [1]. A DG is a source of power which may be only active, only reactive or both [2]. The massively rising load demand across the globe is one such vital factor.

A. Uniyal (✉) · S. Sarangi
National Institute of Technology, Srinagar, Uttarakhand, India
e-mail: ankit2011uniyal@gmail.com

S. Sarangi
e-mail: usomsam@gmail.com

© Springer Nature Singapore Pte Ltd. 2020
A. Kalam et al. (eds.), *Intelligent Computing Techniques for Smart Energy Systems*,
Lecture Notes in Electrical Engineering 607,
https://doi.org/10.1007/978-981-15-0214-9_77

To meet such exponentially rising power demands, DGs allocation in the existing grid is a necessity. However, the allocation of DGs is a momentous challenge concerned to meet the safety and technical constraints of the grid [3]. The DG placement in the distribution system is a complex optimization problem dealing with optimisation of multiple objectives related to maximisation of power quality, voltage profile, power system reliability, stability, security, etc. and minimization of power losses in the system, line loading, power prices and related costs etc. [4, 5]. The massive penetration of renewable-based DGs in the power grids has enabled them to get operated without the aid of power from fossil fuel-based centrally located power generation systems in form of low voltage modular grids called autonomous microgrids (AMGs) which have emerged as the most beneficial power providing solutions for islands, hilly terrains etc. [6, 7]. In spite of numerous benefits, there are some issues with renewable-based AMGs related to voltage and frequency fluctuations due to imbalance of generation and load. In the present times, the renewable-based generation sources are interfaced with the grid via power electronic devices. Such power electronic interfaces provide P-f and Q-V drooping characteristics to these DGs. Thus frequency (f) and voltage (V) change with change in the active and reactive power supplied by these DGs [8, 9]. The optimal planning of DGs in the distribution system has been included in many works. Authors in [10] used an analytical 2/3 rule for optimal DG allocation in radial systems. In [11] a power loss sensitivity analysis was carried out to allocate DG in a practical distribution system with the objective of minimization of power losses. The analytical method for optimal DG allocation was used for minimization of power losses in [12] and improvement of line loss reduction and voltage profile indices in [13]. Authors in [14] placed stochastically modelled wind and solar DG using Monte Carlo simulation and fuzzy theory.

In [15], authors have done optimal planning to allocate DGs based on PV, small scale hydro (SSH) and wind. Chu-Beasley Genetic Algorithm is used to determine optimal buses for allocation and PSO is used to determine optimal size. In [16] authors have used PSO to calculate optimal placement of wind-based DG in the radial distribution systems with an objective to minimise the real power losses in the system and voltage profile improvement. Sadeghi and Kalantar [17] have used Rayleigh probability distribution function to model uncertainty of wind speed on 9-bus test distribution system. The objective function used here included cost of energy loss, energy not supplied cost and purchased energy from transmission system and DG owners. Srinivasa Rao and Kalyan Raj [18] have modelled power flow of self-excited and doubly fed wind generators at different speeds. Authors in [19] compared optimal DG allocation methods in radial distribution system based on sensitivity-based approaches. They used index vector, voltage sensitivity and combined power loss sensitivity methods at unity and 0.9 power factor lagging. All the above works have not used voltage and frequency constraints for the optimal DG allocation in the system.

The present work is a novel attempt to optimally allocate droop-controlled DGs in an autonomous microgrid considering deviations of voltage and frequency from the nominal values as the dual objectives with varying load requirements. A multi-objective problem is formulated in the present work and is solved using a heuristic

optimization technique, namely, Non-Dominated Sorted Genetic Algorithm (NSGA-II). The analysis has been carried out at various load levels on IEEE 33 bus system [19] modified as an AMG. The DGs has been assumed to be of droop controlled. The backward–forward sweep load flow is modified for droop-controlled DGs in the droop-controlled load flow. The analysis has been done using MATLAB® [20].

2 Problem Formulation

The present problem is related to allocation of DGs in the AMG with increasing system load. In present autonomous system entire load is met by the DGs, so as system load rises it is quite obvious to add DGs in the system. The Q-V characteristics at three different droops are shown in the Fig. 1a. As droop increases, more deviations are observed and voltage limit is violated with droop n_{q3} . Thus selecting an appropriate droop for a DG is important. The P-f droop characteristics at loads exceeding generation are shown in Fig. 1b. Another observation done through the present work is that the value of $\text{del}F$ and $\text{del}V$ changes with DG bus location. Hence, an optimal bus location which minimises the voltage and frequency deviation is also an important criteria for DG allocation. Taking into account the above factors, the present problem is formulated as a multi-objective optimization as follows:

$$\text{Min } (\text{del}V1 \text{ and } \text{del}F)$$

subjected to the following constraints:

$$|V_{min}| \leq |V| \leq |V_{max}| \tag{1}$$

$$|I_i| \leq |I_{i,max}| \tag{2}$$

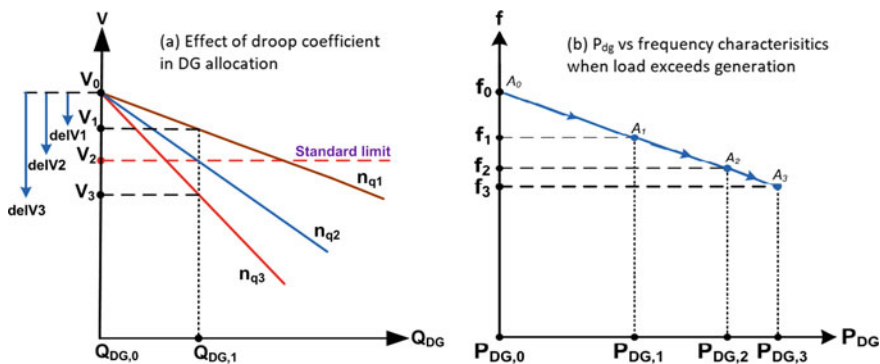


Fig. 1 Droop characteristics of DG

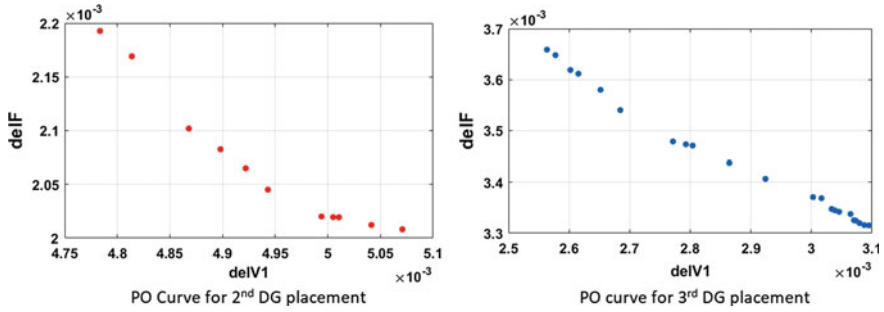


Fig. 2 Pareto optimal curve for second and third DG placement

$$|P_{dg,min}| \leq |P_{dg}| \leq |P_{dg,max}| \tag{3}$$

$$|Q_{dg,min}| \leq |Q_{dg}| \leq |Q_{Ldg,max}| \tag{4}$$

$$|F_{min}| \leq |F| \leq |F_{max}| \tag{5}$$

where V , V_{min} and V_{max} are the voltage at each bus, minimum and maximum voltage limits, respectively. V_{min} and V_{max} are taken as 0.9 pu and 1.05 pu, respectively. I_i and $I_{i,max}$ are the branch current and maximum branch current, respectively. $P_{dg,min}$ is minimum active power of DG and $P_{dg,max}$ is the maximum active power of DG. $P_{dg,min}$ and $P_{dg,max}$ are taken as 1 KW and 1.5 MW, respectively. $Q_{dg,min}$ is the minimum reactive power of DG and $Q_{dg,max}$ is the maximum reactive power of DG. $Q_{dg,min}$ and $Q_{dg,max}$ are taken as 1 KVAR and 1.5 MVAR, respectively. F , F_{min} and F_{max} are the frequency, minimum and maximum frequency limits, respectively. F_{min} and F_{max} are taken as 0.95 pu and 1.05 pu, respectively.

3 Methodology

The methodology used in solving the present problem has three important segments. First one is distribution system load flow involving droop-controlled DGs, second is multi-objective heuristic optimization technique NSGA-II and third one is FSM.

3.1 Droop-Controlled Load Flow (DCLF)

In order to incorporate the V and f parameters due to droop-controlled DGs in the load flow, a droop-controlled load flow is used in the present work. The first bus is

assumed to be the virtual bus whose V and f determines the V and f of the entire system [8, 9].

According to IEEE Std. 1547.7 [8], the power electronic interfaced DGs exhibit drooping P-f and Q-V characteristics and the DGs output contributions to the grid are based on their individual droop coefficients (droop gains). For smaller droop coefficients, more power is contributed by DG and vice versa.

In Fig. 1b, A_0 to A_1 , A_1 to A_2 and A_2 to A_3 , respectively, represents the steps followed during DCLF by a DG to reach final value of active power to be supplied by it. As the iterations are increased the step size in terms of power supplied by the DG P_{dg} decreases, i.e. $P_{DG,3} - P_{DG,2} < P_{DG,2} - P_{DG,1} < P_{DG,1} - P_{DG,0}$. Finally P_{dg} and f are settled to $P_{DG,3}$ and f_3 , respectively, i.e. point A_3 . Similarly reactive power is shared by the DG according to the Q-V characteristics. The algorithm for DCLF is implemented in the present problem as suggested by authors in [8, 9].

3.2 Non-Dominated Sorted Genetic Algorithm

NSGA is a genetic algorithm technique which is modified to solve multiple optimization problem [21, 22], but due to some criticism, it was adapted to NSGA-II which is a better version of NSGA. In this technique, Pareto optimal front is obtained which is nothing but a set of solutions generated after non-domination sorting and crowding distance calculation. Non-dominated individual is the one which dominates others, i.e. if the objective functions of it are no worse than the other and at least in one of the objective functions it is better than the other.

3.3 Fuzzy Satisfying Method

Fuzzy satisfying method [23] is a membership function-based method to select the most optimum solution out of the Pareto front. In this method, for each solution in the Pareto front x_i , a membership function is defined as $\mu_{f,i}$. If $\mu_{f,i} = 1$, solution completely satisfies the decision-maker with respect to a particular objective function. If $\mu_{f,i} = 0$, solution completely dissatisfies the decision-maker with respect to that objective function. Different types of membership functions can be used like exponential, linear, etc. In the present problem, a linear type membership function has been assumed. A conservative decision is achieved when solution of minimum satisfaction is maximum over all the objective functions. Thus, the final solution is achieved using Max-Min conceptual formulation.

4 Results and Discussions

The system configuration used was of Intel I3, 6 GB RAM, 2.53 GHz. For NSGA-II population size, number of iterations, probability of crossover and mutation are taken as 400, 80, 0.7 and 0.4, respectively. The IEEE 33 bus microgrid in island/autonomous

Table 1 Optimal DG allocation for 33 bus systems

P_L (KW, pu)	1114.5, 2.23	1857.5, 3.71	2600.5, 5.2	3343.5, 6.68
Q_L (KVAR, pu)	690, 1.38	1150, 2.3	1610, 3.22	2070, 4.4
Load levels (%)	30	50	70	90
No. of DGs (Bus)	2 (1, 15)	3 (1, 15, 12)	4 (1, 15, 12, 8)	5 (1, 15, 12, 8, 9)
m_p, n_q	-0.01	-0.01	-0.01	-0.01
P_{dg}, Q_{dg} (p.u.)	1.0382, 0.8967	1.065, 0.9326	1.0751, 0.9461	1.0803, 0.9518
	1.1908, 0.4833	1.325, 0.6631	1.3753, 0.7305	1.4017, 0.7590
	-, -	1.325, 0.7043	1.3753, 0.7717	1.4017, 0.8097
	-, -	-, -	1.3753, 0.7717	1.4017, 0.8097
	-, -	-, -	-, -	1.4017, 0.8097
f (pu)	0.9981	0.9967	0.9962	0.9960
$delV1$ (pu)	2.56E-06	1.86E-04	2.56E-04	3.61E-04
$delF$ (pu)	5.17E-06	4.41E-06	4.16E-06	4.75E-06

mode with base KVA as 500 and base KV as 12.66 is used. The system has initially a DG installed at bus 1 for supplying loads less than 30% of full load. As loads are increased to 30, 50, 70 and 90%, number of DGs allocated to sustain the increased load are 2, 3, 4 and 5, respectively. Bus 1 is assumed as slack bus or virtual bus whose frequency is considered as the standard frequency of the grid.

Table 1 shows the load levels of the system, various DG locations obtained using the optimization technique and their corresponding sizes using DCLF as per new power flow requirement in the system. Before load level below 30%, there was only one DG at bus 1. When P, Q load is increased to 30%, second DG is obtained at bus 15 with droop coefficients as -0.01 . Now the P, Q generations by both the DGs is adjusted by the DCLF to 1.0382 pu and 1.1908 pu for P-type while 0.8967 pu and 0.4833 pu for Q-type. Similarly, the new DGs for increased 50, 70 and 90% of the total load are obtained at buses 12, 8 and 9, respectively, with identical droops of -0.01 .

The frequency values were obtained as 0.9981 pu, 0.9967 pu, 0.9962 pu and 0.9960 pu for 30, 50, 70 and 90% load levels, respectively. From the results, the frequency values are well within the specified limits. The voltage profile at all load levels is shown using Fig. 3. It is observed that with more DGs inclusion in the system voltages are improved towards 1 pu mark. The Pareto optimal curves for the DG placements are shown in Figs. 2 and 4.

5 Conclusion

In this work, optimal DG allocation is proposed for an IEEE distribution system modified as an autonomous microgrid. The DGs are assumed to be droop controlled so DCLF is used in the analysis. The minimum deviation of voltage and frequency from the nominal values are the objectives considered in the analysis.

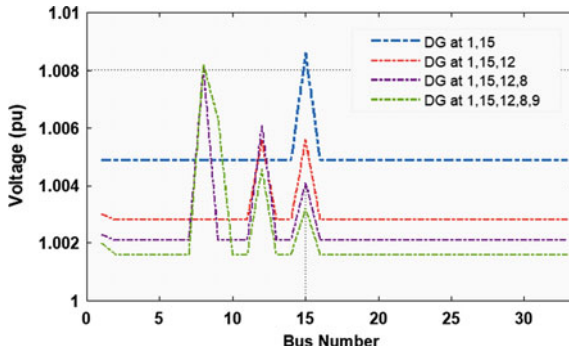


Fig. 3 Voltage profile with DG

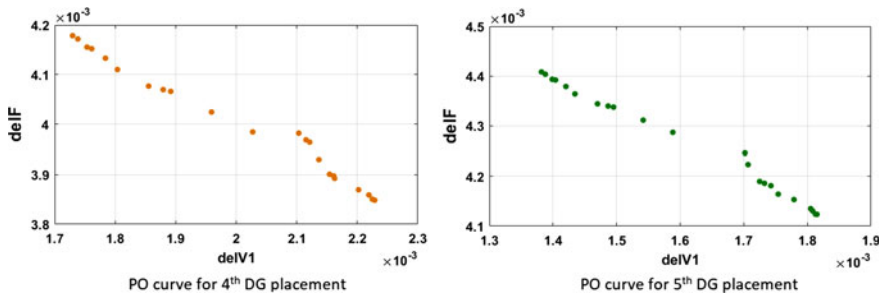


Fig. 4 Pareto optimal curve for fourth and fifth DG placement

Based on the results, it is concluded that the present multi-objective optimization problem is solved using heuristic-based NSGA-II and FSM techniques and optimal DG bus locations and their corresponding droops are obtained for minimum delF and delV1 fulfilling the Pareto optimality criteria. The frequency and voltage profile are well within the standard limits. It is also observed that to supply increased load with more DG allocations, the voltage profile is improved.

Thus, through the present analysis, it is concluded that DG allocation in the droop-controlled environment has supplied the increased system load, kept the voltage and frequency profile within prescribed limits and improved the bus voltages.

References

1. Brown RE (2008) Electric power distribution reliability. CRC Press
2. Kansal S, Kumar V, Tyagi B (2013) Optimal placement of different type of DG sources in distribution networks. *Electr Power Energy Syst* 53:752–760
3. Sahoo NC, Ganguly S, Das D (2013) Recent advances on power distribution system planning: a state-of-the-art survey. *Energy Syst* 4:165–193

4. Alarcon-Rodriguez A, Ault G, Galloway S (2010) Multi-objective planning of distributed energy resources: a review of the state-of-the-art. *Renew Sustain Energy Rev* 14:1353–1366
5. Chiradeja P, Ramakumar R (2004) An approach to quantify the technical benefits of distributed generation. *IEEE Trans Energy Convers* 19(4):764–773
6. Lasseter RH, Paigi P (2004) Microgrid: a conceptual solution. In: *Proceedings of Power Electronics Specialists Conference Germany*, pp 1–6 (2004)
7. Integrating Renewable Electricity on the grid. A report by APS panel on public affairs. <https://www.aps.org/policy/reports/popareports/upload/integratingelec.pdf>
8. Hameed F, Hosani MA, Zeineldin HH (2019) A modified backward & forward sweep load flow method for islanded radial microgrids. *IEEE Trans. Smart Grid* 10(1):910–918
9. Díaz G, Aleixandre JG, Costo J (2016) Direct backward/forward sweep algorithm for solving load power flows in AC droop-regulated microgrids. *IEEE Trans Smart Grid* 7(5):2208–2217
10. El-Khattam W, Salama MAA (2004) Distributed generation technologies, definitions and benefits. *Electr Power Syst Res* 71:119–128
11. Kashem MA., Le AD, Negnevitsky M, Iedwich G (2008) Distributed generation for minimization of power losses in distribution systems. In: *IEEE PES society general meeting* (2008)
12. Wang C, Nehrir MH (2006) Analytical approaches for optimal placement of DG sources in power systems. *IEEE Trans. Power Syst.* 19(4):2068–2076
13. Iyer H, Ray S, Ramakumar R (2006) Assessment of distributed generation based on voltage profile improvement and line loss reduction. In: *IEEE PES transmission and distribution conference and exhibition*, pp 1171–76 (2006)
14. Hadian A, Haghifam M (2010) Placement of DG with stochastic generation. In: *IEEE/PES transmission and distribution conference and exposition*, pp 1–7 (2010)
15. Grisales LF, Grajales A, Montoya OD, Hincapie A, Granada, M (2015) Optimal location and sizing of distributed generators using a hybrid methodology and considering different technologies. In: *IEEE 6th Latin American symposium on circuits & systems (LASCAS)*, pp 1–4
16. Kansal S, Sai BBR, Tyagi B, Kumar V (2015) Optimal location and sizing of distributed generators using a hybrid methodology and considering different technologies. In: *IEEE 6th Latin American symposium on circuits & systems (LASCAS)*, pp 1–4
17. Sadeghi M, Kalantar M (2014) Probabilistic analysis of wind turbine planning in distribution systems. In: *IEEE 19th electrical power distribution networks conference (EPDC)*, pp 13–18
18. Srinivasa Rao R, Kalyan Raj K (2015) Power flow modeling of wind generators and study of their impact on the distribution system during different wind speeds. In: *International conference on electrical electronics signals communication and optimisation (EESCO)*, pp 1–6
19. Murthy VVSN, Kumar A (2013) Comparison of optimal DG allocation methods in radial distribution systems based on sensitivity approaches. In: *Electrical power and energy systems*, vol 53, pp 450–467 (2013)
20. MATLAB R2013a 1994-2013 The Math Works
21. Deb K, Pratap A, Agarwal S, Meyavivan T (2002) A fast elitist multi-objective genetic algorithm: NSGA-II. *IEEE Trans Evol Comput* 6(2):182–197
22. Srinivas N, Deb K (1994) Multiobjective optimization using nondominated sorting in genetic algorithms. *Evol Comput* 2(3):221–248
23. Soroudi AR, Ehsan M (2010) Multi-objective planning model for integration of distributed generations in deregulated power systems. *Iran J Sci Technol B: Eng* 34, B3:307–324

A Comparative Study of Classification Algorithms for Predicting Liver Disorders



Rashi Bhardwaj, Rajat Mehta and Prakash Ramani

Abstract In this era of technological advancements, the focus is on applying different machine learning and deep learning algorithms to solve real-life problems. The current condition of the health sector is one of the major problems which can be solved to a great extent by applying these algorithms. Some examples in the field of medicine where these algorithms are being applied are—prediction of diabetes, cardiovascular diseases, and cancer. Our aim is to predict liver disorders in patients. There are several essential deciding factors which are used for classification. For this purpose, a comparative study of classification algorithms has been performed for the classification of patients into two categories, i.e., having or not having a liver disorder. The algorithms used for comparison are Decision Tree, Random Forest Tree, Naïve Bayes, k-Nearest Neighbor (kNN), Support Vector Machine (SVM), Artificial Neural Networks (ANN), and Extreme Gradient Boost (XGBoost). Among all the classification algorithms, XGBoost results in the highest accuracy.

Keywords Decision tree · Random forest tree · Naïve Bayes · k-nearest neighbor · Support vector machine · Artificial neural networks · Extreme gradient boost

1 Introduction

Around 10 lakh patients of liver cirrhosis are newly diagnosed every year in India. TNN [1] Liver disease is the tenth most common cause of death in India as per the World Health Organization. Liver disease may affect every 1 in 5 Indians. Liver

R. Bhardwaj (✉) · R. Mehta · P. Ramani
Manipal University Jaipur, Jaipur, Rajasthan, India
e-mail: rashib2497@gmail.com

R. Mehta
e-mail: rjtmehta99@gmail.com

P. Ramani
e-mail: prakash.ramani@jaipur.manipal.edu

© Springer Nature Singapore Pte Ltd. 2020
A. Kalam et al. (eds.), *Intelligent Computing Techniques for Smart Energy Systems*,
Lecture Notes in Electrical Engineering 607,
https://doi.org/10.1007/978-981-15-0214-9_78

Cirrhosis is the 14th leading cause of deaths in the world and could be the 12th leading cause of deaths in the world by 2020. Hepatocellular carcinoma (HCC), or a cancer in the liver, is the second most common cause of death due to malignancy in the world.

The problem which has been identified is that deaths due to liver disorders are increasing year by year worldwide. Liver disorders are caused due to many factors. Mayo Clinic Staff [2] Parasites and viruses can infect the liver (for example, Hepatitis B, Hepatitis C), causing inflammation that reduces liver function, increased alcohol consumption, immune system abnormality, obesity, etc.

The need of the hour is to build a fast and efficient system which correctly classifies on the basis of history of the patient and other parameters if the patient has a liver disease or not. If a model can be prepared which gives great accuracy, it will be easier for doctors for faster classification. If this identification and diagnosis are successful, the patient can be treated well before his/her problem increases and takes his/her life. This will help in further reducing the number of deaths worldwide per year due to liver disorders such as—hemochromatosis (a hereditary disease associated with too much iron in the liver), cirrhosis, liver cancer, etc. With the help of this, the required resources could be allocated in advance to prevent liver disorders in people. Also, by spreading awareness about the causes and effects of liver disorders, the number of deaths due to liver problems can be reduced.

The problem undertaken here is a binary classification problem which will give the result in the form of a binary answer, i.e., a person has a liver disorder or does not have a liver disorder. The dataset used for the prediction of liver disorders in patients is the Indian Liver Patient Dataset (ILPD) [3] which has been collected from the UCI Machine Learning Repository. It consists of a total of 11 attributes out of which 10 attributes are the major causes of liver disorders seen in patients and they are considered as important factors for prediction since these are the parameters which are the deciding factors for classifying patients into one of the two categories mentioned above.

The last attribute of the dataset is the selector field which consists of only two values—either 1 or 2. It is used to split the dataset into two sets—one comprising of all those patients having a liver disorder (selector field 1) and the other one comprising of all those patients who do not have liver disorder (selector field 2).

2 Literature Review

The initial work on liver disorder prediction was done by Ramana et al. [4] and they evaluated particular classification algorithms for the classification of two different liver patient datasets—the ILPD and the BUPA Liver Disorders [5] datasets. The classification algorithms considered were Backpropagation Neural Network Algorithm, Naïve Bayes classifier, Support Vector Machines, and C4.5. These algorithms were evaluated on the basis of four criteria which are Accuracy, Precision, Sensitivity, and Specificity.

Following this research, in order to find out the reason for the difference in classification accuracies of several classifiers with different datasets, they analyzed the populations of liver patients belonging to USA and India [6]. ANOVA and MANOVA analyses were carried out on these datasets. Observations showed that the reason for difference in classifiers performance was that liver patients of both countries were having huge differences.

Modified Rotation Forest algorithm was proposed in their further research which is a combination of multiple classification algorithms that generally give better results as compared to individual classifiers [7]. Classification algorithms were chosen from different categories and feature selection technique was applied.

Using data mining algorithms and techniques to analyze medical data is Medical Data Mining (MDM). Bahramirad et al. [8] applied 11 classification algorithms to two different datasets and a comparison was done on the basis of performance of the classifiers against each other in terms of accuracy, recall, and precision.

Computational intelligence techniques for liver patient classification were presented by Gulia et al. [9]. For this purpose, evaluation of classification algorithms including Support Vector Machine, J-48, Random Forest, Multilayer Perceptron, and Bayesian Network was done. This paper implemented the construction of hybrid models and a comparative study for improving prediction accuracy of liver patients. They also made the use of feature selection technique to get a subset of the dataset and then applied the abovementioned algorithms.

Support vector machine was used by Hashem et al. [10] for classifying liver diseases by utilizing two liver patients datasets with distinct feature combinations, thus leading to an evaluation of the SVM classifier by measuring the performance in terms of accuracy, sensitivity, error rate, specificity, and prevalence.

Pakhale et al. [11] used techniques like C4.5, Random Forest (RF), Multilayer Perceptron (MLP), Classification and Regression Technique (CART), and applied all these techniques on liver patient data collected from UCI repository. In this paper, they used ensemble model to develop a robust classification model which resulted in a higher classification accuracy as compared to its individual model. Information gain feature selection technique was applied.

In the paper by Babu et al. [12], K-means clustering algorithm was applied for partitioning of data from which identification of some mis-clustered objects was done and they were removed from the ILPD dataset. The new dataset (NDS) which consisted of 373 patient records was supplied to classifiers such as Naïve Bayes, K-NN and C4.5, and observed Accuracy, Precision, Sensitivity, and Specificity. In this analysis, evaluation of performance was done using tenfold cross validation.

Jin et al. [13] investigated and analyzed the classification algorithms such as Decision Tree, Naïve Bayes, k-NN and Multilayer Perceptron used previously in a study, and additionally analyzed the Random forest and Logistic proposed by them. For the purpose of comparing the algorithms in various types of evaluation criteria like precision, recall, specificity, and sensitivity, they used WEKA tool widely known as a quite useful tool for data mining.

Naïve Bayes and Support Vector Machine (SVM) algorithms were used by Vijayarani et al. [14]. Two essential performance comparison factors, i.e., classification

accuracy and execution time were used and the results showed that the execution time of SVM was more than Naïve Bayes but it gave a much better accuracy than Naïve Bayes.

Pahareeya et al. [15] utilized techniques like SVM, Multiple Linear Regression, Multilayer Feed Forward Neural Network, Random Forest, Genetic Programming, and J-48 on the unbalanced ILPD dataset. For balancing it, they used under sampling and oversampling. Throughout the study, tenfold cross validation was performed.

In the paper by Olaniyi et al. [16], two different models of ANN, viz., backpropagation and radial basis function were employed to solve the problems of diagnosing liver diseases. The dataset used for this paper was the BUPA liver disorder dataset obtained from the UCI machine learning repository.

3 Methodology

3.1 Data Collection

The dataset used here is the ILPD Dataset which has been taken from UCI machine learning repository. It contains 10 important attributes used for liver disorder classification and one class field. The total number of records in this dataset is 583. Out of the total number of records, 416 are liver patient records and 167 are non-liver patient records.

3.2 Data Preprocessing

- ★ There are some records in the dataset which have missing values and these were replaced by the mean value of their respective columns.
- ★ Encoding Categorical Data—In this case, the gender attribute of the dataset has two values—male and female—which are converted into 1 and 0, respectively, so that these values can be applied conveniently to the model.
- ★ Feature Scaling—Done so that one independent variable does not dominate another independent variable. It is done to standardize the range of independent variables.

3.3 Applying Different Classification Algorithms

Here, seven different classification algorithms, viz., Decision Tree, Random Forest Tree, Naïve Bayes, kNN, SVM, ANN and XGBoost have been applied. These algorithms are applied on the training set (70%) and tested on the test set (30%) to get the different accuracies in each case. For ANN one hidden layer is used with input and output layer. It is trained with a batch size of 5 for 200 epochs with “tanh” as activation function. For kNN, five-nearest neighbors are considered.

3.4 Predicting the Test Set Results

For this binary classification problem, the prediction of test set results is done based on different models. The output obtained here is in the form of a confusion matrix which helps to calculate the accuracy of the test set. K-Fold cross validation, in this case, tenfold cross validation has also been applied to improve the model performance in each case and make the analysis much more relevant by reducing the variance in the accuracies and giving their mean as results.

3.5 Comparison of Models

Accuracy has been used as a metric to compare the performance of different classification algorithms. First, a comparison is done based on the accuracies obtained from the test set and second after applying tenfold cross validation.

4 Results and Discussion

Given below is the formula for calculating the accuracy using true positives, true negatives, false positives, and false negatives.

$$\text{Accuracy} = \frac{\text{number of true positives} + \text{number of true negatives}}{\text{number of true positives} + \text{false positives} + \text{false negatives} + \text{true negatives}}$$

Table 1 contains values from the confusion matrices of each classification algorithm and based on these, the accuracy is calculated. Since the data in training and test set is split randomly, the value of true positives is lesser than true negatives as the number of patients with no liver disease are more in the test set.

Table 1 Values from confusion matrices

Algorithms	True positives	True negatives	False positives	False negatives
ANN	8	115	7	45
DT	26	91	31	27
KNN	13	97	25	40
NB	53	47	75	0
RFT	19	100	22	34
SVM	0	122	0	53
XGB	5	113	9	48

Table 2 Accuracies obtained on the test set

Classification algorithms	Accuracy (%)
ANN	70.28
DT	66.85
KNN	62.85
NB	57.14
RFT	68
SVM	69.71
XGB	67.42

Fig. 1 Comparison graph of the test set accuracies

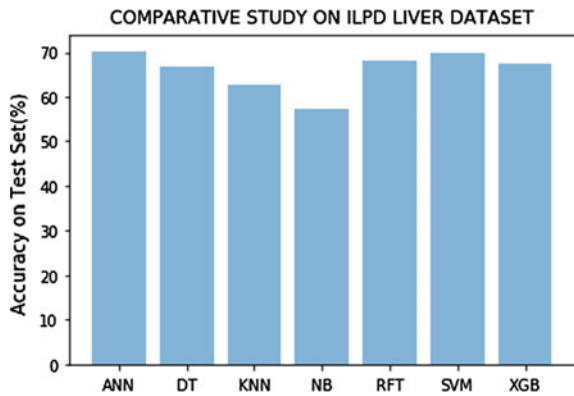


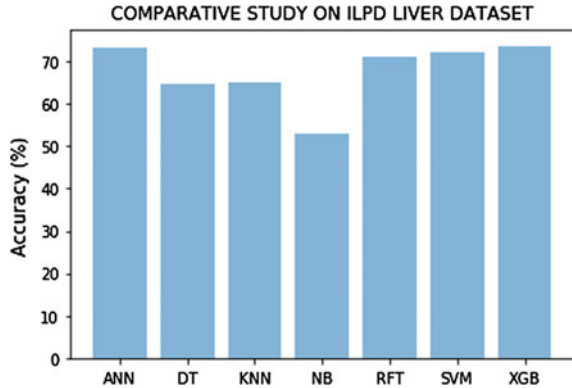
Table 3 Accuracies obtained by applying K-fold cross validation

Classification algorithms	Accuracy (%)
ANN	73.298
DT	64.595
KNN	65.107
NB	52.892
RFT	71.071
SVM	72.071
XGB	73.749

On the basis of confusion matrices, the highest accuracy on the test dataset is achieved by ANN and then SVM. Table 2 and Fig. 1. show comparison and visualization of the accuracies on the test set.

The evaluation of the different models was then done using the tenfold cross validation which gives the mean of the accuracies. The best accuracy obtained was **73.749%** using **XGBoost** algorithm. Both **XGBoost** and **ANN** gave good accuracies as compared to other algorithms for the classification of liver disorders as shown in Table 3 and Fig. 2.

Fig. 2 Comparison graph of accuracies after tenfold cross validation



5 Conclusion and Future Work

Classification techniques as applied here will have a very wide application since they will help the doctors with faster and more accurate classification so that patients can be provided with a better and faster treatment. Faster diagnosis will lead to saving many lives and reducing the threat to patients caused due to various liver disorders and their harmful effects.

Collection of more data from hospitals where the patients get their tests conducted for diagnosis of liver disorders can be done. The test reports contain all the attributes specified in the dataset such that this model can be applied in thousands of patients to give better results. Construction of hybrid models could also be a possible solution for improving the results in the future.

References

1. TNN (2017) Is liver disease the next major lifestyle disease of India after diabetes and BP? <https://timesofindia.indiatimes.com/life-style/health-fitness/health-news/is-liver-disease-the-next-major-lifestyle-disease-of-india-after-diabetes-and-bp/articleshow/58122706.cms?> Accessed 16 Aug 2018
2. Mayo Clinic Staff (2018) Liver disease. <https://www.mayoclinic.org/diseases-conditions/liver-problems/symptoms-causes/syc-20374502>. Accessed 18 Aug 2018
3. UCI Machine Learning Repository (2012) Indian Liver Patient Dataset (ILPD). [https://archive.ics.uci.edu/ml/datasets/ILPD+\(Indian+Liver+Patient+Dataset\)](https://archive.ics.uci.edu/ml/datasets/ILPD+(Indian+Liver+Patient+Dataset)). Accessed 20 March 2018
4. Ramana BV, Babu MSP, Venkateswarlu NB (2011) A critical study of selected classification algorithms for liver disease diagnosis. *Int J Database Manag Syst* 3(2):101–114. <https://doi.org/10.5121/ijdms.2011.3207>
5. UCI Machine Learning Repository (2007) Liver disorders data set. <https://archive.ics.uci.edu/ml/datasets/liver+disorders>. Accessed 20 March 2018
6. Ramana BV, Babu MSP, Venkateswarlu NB (2012) A critical comparative study of liver patients from USA and INDIA: an exploratory analysis. *Int J Comput Sci Issues (IJCSI)* 9(3):506–516

7. Ramana BV, Babu MSP, Venkateswarlu NB (2012) Liver classification using modified rotation forest. *Int J Eng Res Dev* 17–24
8. Bahramirad S, Mustapha A, Eshraghi M (2013) Classification of liver disease diagnosis: a comparative study. *Ib: Second international conference on informatics and applications*, pp 42–46. <https://doi.org/10.1109/icoia.2013.6650227>
9. Gulia A, Vohra R, Rani P (2014) Liver patient classification using intelligent techniques. *Int J Comput Sci Inf Technol* 5(4):5110–5115
10. Hashem EM, Mabrouk MS (2014) A study of support vector machine algorithm for liver disease diagnosis. *Am J Intell Syst* 4(1):9–14
11. Pakhale H, Xaxa DK (2016) Development of an efficient classifier for classification of liver patient with feature selection. *Int J Comput Sci Inf Technol* 7:1541–1544
12. Babu MP, Ramjee M, Katta S, Swapna K (2016) Implementation of partitional clustering on ILPD dataset to predict liver disorders. In: 7th IEEE international conference on software engineering and service science, pp 1094–1097. <https://doi.org/10.1109/icseess.2016.7883256>
13. Jin H, Kim S, Kim J (2014) Decision factors on effective liver patient data prediction. *Int J Bio-Sci Bio-Technol* 6(4):167–178. <https://doi.org/10.14257/ijbsbt.2014.6.4.16>
14. Vijayarani S, Dhayanand S (2015) Liver disease prediction using SVM and Naïve Bayes algorithms. *Int J Sci Eng Technol Res* 4(4):816–820
15. Pahareeya J, Vohra R, Makhijani J, Patsariya S (2014) Liver patient classification using intelligence techniques. *Int J Adv Res Comput Sci Softw Eng* 4(2):295–299
16. Olaniyi EO, Adnan K (2013) Liver disease diagnosis based on neural networks. *Adv Comput Intell* 48–53

Performance Analysis of Fabricated Buck-Boost MPPT Charge Controller



Neeraj Tiwari, Amit Saraswat, Ravi Soni and Suchi Rawat

Abstract This paper presents a performance analysis of a MPPT charge controller designed for two different atmospheric conditions, i.e., clear sky day and cloudy day. The experiments are also performed in different atmospheric conditions such as partial cloudy day and fully cloudy day. The developed power electronic converter works as buck and boost regulator with MPPT algorithm. The comparative results shows, the MPPT charge controller can extract 91% more energy from Solar Photo-voltaic power plant compare to without an MPPT charge controller. The experimental results are satisfactory and demonstrate that developed charge controller is better and cost-effective.

Keywords MPPT · Photo voltaic system · P and O algorithm · Power electronic converter

1 Introduction

In the present scenario to fulfill the demand for pollution free electrical energy renewable energy sources are the best substitute among the present energy sources. The petroleum is more and more costly, also it pollutes the atmosphere. The solar energy is the best alternative among other energy sources. It is clean and abundant in nature. But due to low conversion efficiency of PV cells, the installation cost of solar photovoltaic (SPV) system is high. Different authors presented and focused towards the improvement of solar cell conversion efficiency, nowadays researchers claim that organic cells have a good conversion efficiency of about 37%. MPPT charge controller plays an important role. MPPT can extract maximum electrical

N. Tiwari (✉) · R. Soni

Department of Electrical Engineering, Poornima University, Jaipur, Rajasthan, India
e-mail: neerajtiwari1407@gmail.com

A. Saraswat

Department of Electrical Engineering, Manipal University Jaipur, Jaipur, Rajasthan, India

S. Rawat

Poornima Institute of Engineering and Technology, Jaipur, Rajasthan, India

© Springer Nature Singapore Pte Ltd. 2020

A. Kalam et al. (eds.), *Intelligent Computing Techniques for Smart Energy Systems*,
Lecture Notes in Electrical Engineering 607,
https://doi.org/10.1007/978-981-15-0214-9_79

power from SPV system by load matching concept. In the solar cell characteristics it has been seen that I–V characteristics of solar cell vary with the variation of sunlight intensity and temperature [1]. Thereby instant change in sunlight intensity and temperature of atmosphere results fluctuation on voltage. In the past different algorithms were presented by many authors. But most popular algorithms used in MPPT charge controller is P and O.

This paper deals with the performance analysis of designed and developed MPPT charge controller. A number of algorithms for MPPT charge controller have been presented in the literature by different authors. Among them perturbation and observation is perhaps the most widely used algorithm which is also known as the hill climbing method [2], the second popular algorithm is an incCond method [3], the ripple based method for determining the MPP, [4, 5] and the constant voltage method [6, 7]. The main function of the maximum power point tracking charge controller is to draw the maximum power from the solar PV array by load matching technique. MPPT Charge controllers not only extract maximum power from PV cells but also prevents the battery from overcharging and deep discharging [7–11]. During the installation of solar power plants with MPPT charge controller, study of Solar array specification is necessary.

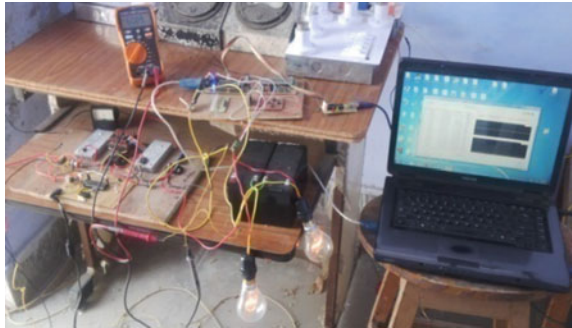
2 Experimental Setup

For analyzing the performance of the Buck-Boost Converter (BBC) power electronic convertor, in the experimental setup, the output of the convertor is connected to two 100 W bulbs. The input port is connected to 170 W SPV panel. In the experiment it has been observed that when the bulb load is directly connected to the SPV panel then it glows low as compared to the load connected to MPPT circuit. MPPT is connected between SPV energy source and load as shown in Figs. 1 and 2. As shown in Fig. 1, when a 200 watts bulb load is connected to SPV panel without MPPT controller then load gets only 38.16 V as indicated by digital multimeters while when the load is connected with MPPT charge controller multimeter shows the voltage across load to

Fig. 1 Load connected to SPV cells without MPPT controller



Fig. 2 Load connected to SPV Cells with MPPT controller



be 60.89 as shown in Fig. 2. This shows that the MPPT charge controller is boosting the voltage and power level.

3 Experimental Result

To see the performance of designed BBC power electronic convertor. The data were collected on different days under different weather conditions with an MPPT charge controller and without an MPPT charge controller. The various results are presented below. The data collection were done under partially cloudy day, on date 24-02-2017. On this date load is connected via the MPPT charge controller. The maximum power calculated across the load is 16 W and voltage reaches to 50 V. While without MPPT charge controller, maximum value of voltage measured across the load is 38.12 V. The results obtained on this day has been shown in Fig. 5. The data collection were done from 01:18 PM to 04:20 PM. Figures 3, 4 and 5 show the variation in power, voltage, and current with respect to time, respectively.

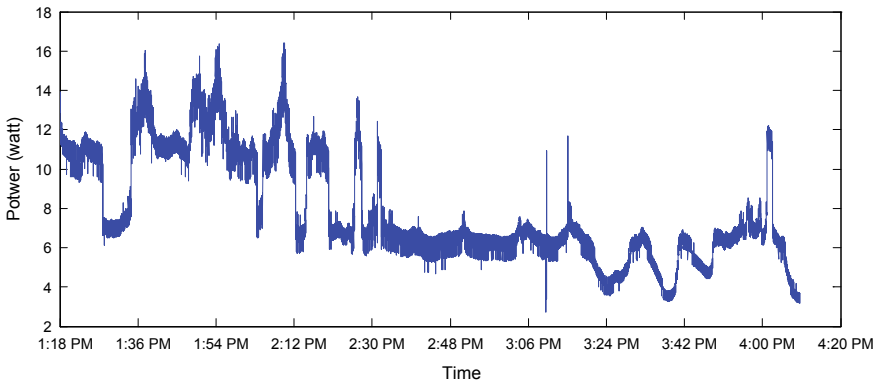


Fig. 3 Variation in power with respect to time across load on date 24-02-2017

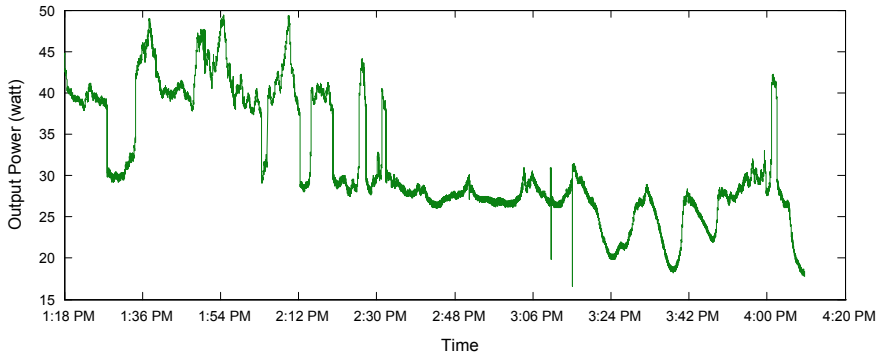


Fig. 4 Variation in voltage with respect to time across load on date 24-02-2017

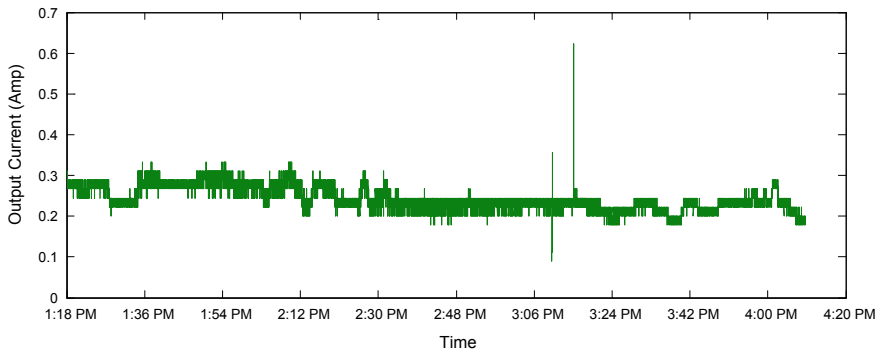


Fig. 5 Variation in current with respect to time across load on date 25-02-2017

The data were collected on date 25-02-2017 under fully cloudy condition. In this day the load was directly connected via the MPPT charge controller. here it is observed that the maximum value of voltage is 75 V and the value of current is 0.38 A the next experiment was performed under partially cloudy day when load is directly connected to SPV cells. The data collection were done on date 25-02-2017 and varies in power, voltage, and current were recorded from 11:20 AM to 03:40 PM and the obtained results are shown in Figs. 5, 6 and 7. Here it is observed that the maximum value of power and voltage measured across the load is 12.2 watts and 42.8 V.

The data were collected on date 26-02-2017, for the calculation of improved solar energy getting across load via MPPT charge controller as compared to solar energy getting without an MPPT charge controller. In this experimental setup, two 100 W bulb load was connected in parallel. And data collection was done via a simple microcontroller-based interfacing circuit. The front end is developed on VB.net as shown in Fig. 8. The comparative results obtained are shown in Fig. 9. It has been observed that the system with MPPT charge controller can extract 91% more solar energy as compared to a system without an MPPT charge controller. Comparative

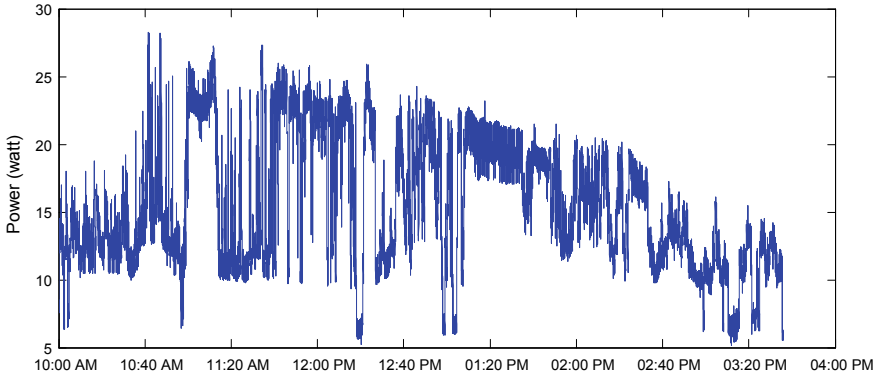


Fig. 6 Power versus time, across load on date 25-02-2017

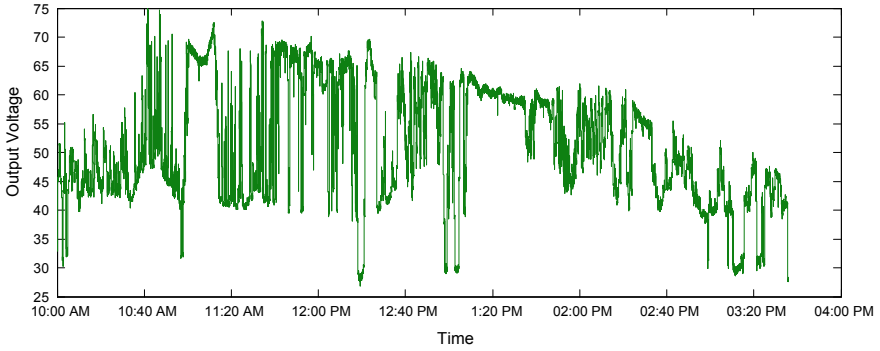


Fig. 7 Output voltage versus time across load on date 25-02-2017

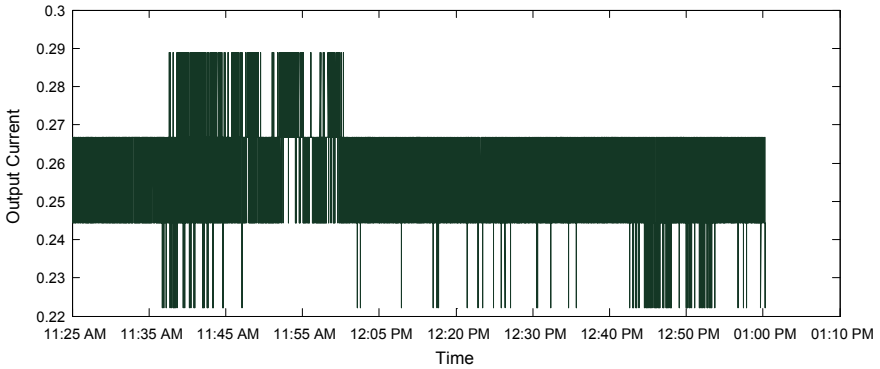


Fig. 8 Output current versus time across the load on date 26-02-2017

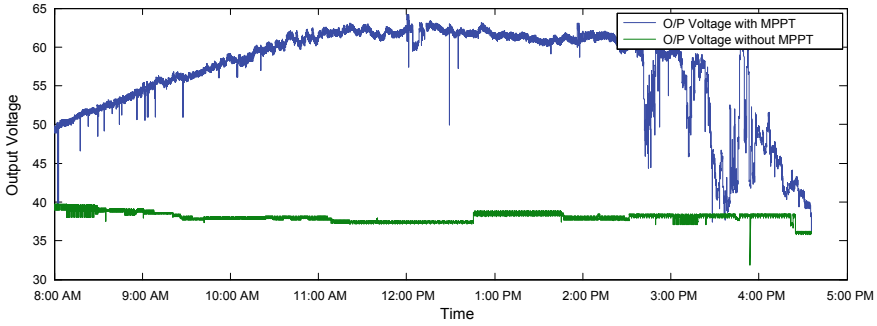


Fig. 9 Variation in voltage across the load with MPPT and without MPPT w.r.t time

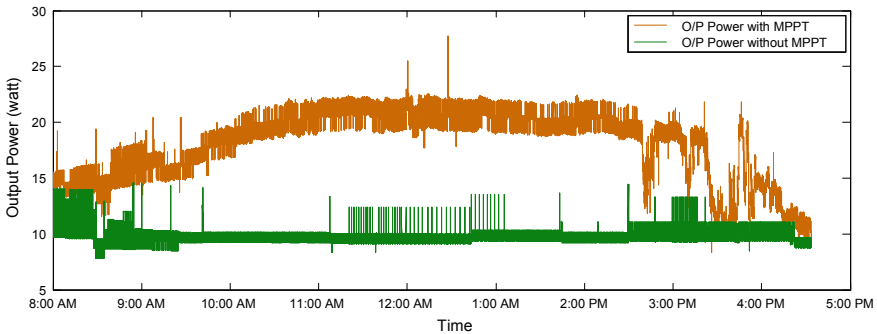


Fig. 10 Variation in power across the load with MPPT and without MPPT with respect to time

variations in power, voltage, and current across the load with designed BBC charge controller and without BBC charge controller are shown in Fig. 10. The data collection were done from 8:00 AM to 5:00 PM.

As shown in Fig. 11, when the bulb load is connected via BBC-MPPT charge controller the measured voltage is above 40 V while the voltage across the load is 38 V when the load is directly connected to SPV cells. The main function of MPPT charge controller is to boost up the out voltage level so that maximum power can be obtained across load. The comparative variation in power is shown in Fig. 11. In this figure it can be seen that the power getting across load with MPPT charge controller is above 15 W while without MPPT charge controller the power across load is approximately 10 W within the whole day.

The variation in current is shown in Fig. 11, the measured current value flowing through the load is 0.34 A when the load is connected via a developed BBC-MPPT charge controller while the current value measured across load without BBC-MPPT charge controller is 0.26 A. In the Fig. 11, some disturbances can be seen after 2.40 PM. This disturbance comes due to the cloudy condition in the sky.

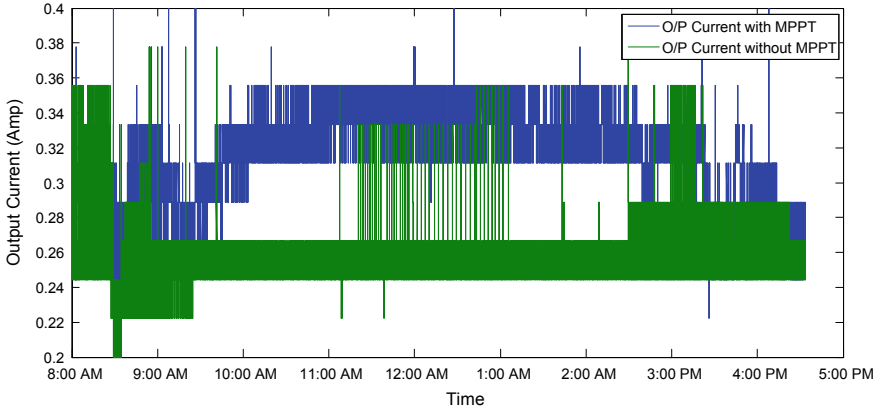


Fig. 11 Variation in current across the load with MPPT and without MPPT w.r.t to time

4 Conclusion

The data collection has been done in different environmental conditions such as cloudy days, partially cloudy day, and clear sky day with different experimental setup the load is connected with BBC-MPPT charge controller and without BBC-MPPT charge controller. It has been observed that the designed MPPT charge controller can increase the output solar energy by up to 91.6% under a clear sky day. The designed MPPT charge controller is cheaper than the MPPT charge controller available in the market. It's designing cost is Rs. 550. The designed BBC-MPPT power electronic convertor is also helpful to increase the efficiency of SPV power Plants.

References

1. Koutroulis E, Kalaitzakis K, Voulgaries Nicholas C (2001) Development of a microcontroller based photovoltaic maximum power point tracking control system. *IEEE Trans. Power Electron* 16(1):46–54
2. Femia N, Petrone G, Spagnuolo G, Vitelli M (2005) Optimization of perturb and observe maximum power point tracking method. *IEEE Trans Power Electron* 20(4):963–973
3. Young-Hyok J, Doo-Yong J, Jun-Gu K, Jae-Hyung K, Tae-Won L, Chung-Yuen W (2011) A real maximum power point tracking method for mismatching compensation in PV array under partially shaded conditions. *IEEE Trans Power Electron* 26(4):1001–1009
4. Yang Du (2011) Battery-integrated boost converter utilizing distributed MPPT configuration for photovoltaic systems. *Sol Energy* 85:1992–2002
5. Balakrishna S, Thansoe Nabil A, Rajamohan G, Kenneth AS, Ling CJ (2006) The study and evaluation of maximum power point tracking systems. In: *International conference on energy and environment 2006 (ICEE)*, pp 17–22
6. Lokanadham M (2012) Incremental conductance based maximum power point tracking (MPPT) for photovoltaic system. *Int J Eng Res Appl (IJERA)* 2(2):1420–1424

7. Wu TF, Shen CL, Nein HS, Li GF (2005) A Single phase 3 W inverter with grid connection and active power filtering based on nonlinear programming and fast zero detection algorithms. *IEEE Trans Power Electron* 20:218–226
8. Saha S, Sundarsingh VP (1996) Novel grid-connected photovoltaic inverter. *IEE Proc Gener Transm Distrib* 143:219–224
9. Villalva MG, Ruppert E (2009) Analysis and simulation of the P&O MPPT algorithm using a linearized photovoltaic array model. In: *Proceedings 35th annual conference of the IEEE industrial electronics society, IECON*, p 231–236
10. Mao M-Q, Su J-H, Zhang G-R et al (2005) Simulation of large-scale photovoltaic grid-connected systems. *J Hefei Univ Technol* 28:1069–1072
11. Gonzalez R, Lopez J, Sanchis P, Marroyo L (2007) Transformerless inverter for single-phase photovoltaic systems. *IEEE Trans Power Electron* 22:693–697

Performance Improvement of Cycloconverter Fed Induction Machine Using Shunt Active Power Filter



Vishnu Goyal and Sulochana Wadhawani

Abstract The cycloconverter is able to vary voltage and frequency simultaneously to control the induction machine at rated air gap flux. Due to switching operation and phase control approach of cycloconverter, it produces harmonics in supply current and demands additional reactive power from the supply. The shunt active power filter is developed to compensate the harmonic currents and reactive power demand. A fuzzy logic based controller is used to generate the reference current of the active power filter by using hysteresis band current control technique. Therefore, active power filter improves the Total Harmonic Distortion (THD) and supply power factor of the cycloconverter fed induction machine. This paper presents MATLAB/Simulation of fuzzy logic based shunt active power filter to improve the performance of cycloconverter fed induction machine.

Keywords Cycloconverter · Interharmonics · Reactive power compensation · Shunt active power filter · Fuzzy logic controller · Hysteresis band current controller · Voltage source converter

1 Introduction

Cycloconverter fabricates the output voltage waveforms at the desired frequency from the input ac voltages simply by perpetually turning on and turning off the thyristors. Therefore, cycloconverter produces harmonics in supply current at the frequencies, which are dependent on input as well as output frequencies of cycloconverter. These harmonic currents introduce voltage distortion in the electric system, which produce several problems related to the electric power quality [1, 2]. In addition, due to phase commutation, cycloconverter always consumes lagging reactive power from

V. Goyal (✉)

Electrical Engineering Department, Manipal University Jaipur, Jaipur, Rajasthan, India
e-mail: vishnu.goyal@jaipur.manipal.edu

S. Wadhawani

Electrical Engineering Department, MITS, Gwalior, Madhya Pradesh, India
e-mail: sulochana_wadhawani1@rediffmail.com

© Springer Nature Singapore Pte Ltd. 2020

A. Kalam et al. (eds.), *Intelligent Computing Techniques for Smart Energy Systems*,
Lecture Notes in Electrical Engineering 607,
https://doi.org/10.1007/978-981-15-0214-9_80

Table 1 Different harmonic components and its frequency range [4–6]

S. no.	Harmonic components	Frequency range (Hz)
1	DC component	$f = nf_1$ for $n = 0$
2	Sub-harmonics	$f > 0$ and $f < f_1$
3	Super-harmonics	$f > f_1$
	Harmonics	$f = nf_1$
	Interharmonics	$f \neq nf_1$

f_1 = Fundamental frequency (Hz) and n = Integral greater than zero

the supply, irrespective of the load displacement factor (lagging or leading) and the direction of real power flow [3]. Different harmonic frequencies are defined in Table 1 over a frequency range. In this paper, an Shunt Active Power Filter (SAPF) is developed to filter the harmonic components and compensate the reactive power demand of the cycloconverter fed induction machine; henceforth, it improves the displacement factor of the supply.

2 Input Current of Cycloconverter

In three-phase to single-phase cycloconverter, positive and negative group converters are used to accomplish positive and negative half cycle of the load current. Thyristors of cycloconverter are triggered by an appropriate firing sequence to synthesize the single-phase load current at desired frequency by consecutive segments of three-phase input currents. Hence, the input currents become discontinuous. Single-phase load current is given by Eq. (1).

$$i_0 = i_A + i_B + i_C \tag{1}$$

where i_0 is load current and i_A , i_B , and i_C are three-phase input currents.

Three separate and independent circuits of three-phase to single-phase cycloconverter are used for synthesis of the balance three-phase load current. Each input phase current is divided into three segments, which are supplied to individual output phase through separate circuits of the cycloconverter. Three segments of input current of phase A are denoted by i_{Aa} , i_{Ab} , and i_{Ac} , which are supplied to three output phases through separate circuits of cycloconverter. Input current of phase A is given by Eq. (2), here a , b , and c denote three output phases of the cycloconverter. Hence, the input phase currents of cycloconverter become near to continuous for three-phase balance load. Therefore, certain harmonic components of input current cancel one another when three-phase balance load is connected through the cycloconverter.

$$i_A = i_{Aa} + i_{Ab} + i_{Ac} \tag{2}$$

2.1 Harmonic Analysis of Input Current

The characteristic harmonic frequencies, which are independent of circuit configuration of cycloconverter, are given by Eqs. (3) and (4) for single- and three-phase output, respectively.

$$f_{ch} = f_i \pm 2nf_o \quad (3)$$

$$f_{ch} = f_i \pm 6nf_o \quad (4)$$

Moreover, the harmonic frequencies, which are dependent on the circuit configuration of cycloconverter for three-pulse cycloconverter, are given below.

For a single-phase output

$$f_H = |[3(2n - 1) \pm 1]f_i \pm (2N + 1)f_o| \quad \text{and} \quad f_H = |[6n \pm 1]f_i \pm 2Nf_o| \quad (5)$$

For three-phase output

$$f_H = |[3(2n - 1) \pm 1]f_i \pm 3(2N + 1)f_o| \quad \text{and} \quad f_H = |[6n \pm 1]f_i \pm 6Nf_o| \quad (6)$$

In which, f_{ch} is characteristic harmonics frequency, f_H is circuit dependent harmonic frequency f_i and f_o are input and output frequency of cycloconverter, n is an integer from unity to infinity, and N is zero to infinity. In case of six-pulse cycloconverter, harmonics of triple multiple of input frequency are eliminated, the harmonic frequencies of input current are given by Eqs. (7), (8) for single-phase and three-phase load, respectively.

$$\text{For a single-phase output} \quad f_H = |[6n \pm 1]f_i \pm 2Nf_o| \quad (7)$$

$$\text{For three-phase output} \quad f_H = |[6n \pm 1]f_i \pm 6Nf_o| \quad (8)$$

3 Harmonic Analysis of Input Current of Cycloconverter Fed Induction Machine

The block diagram of fuzzy logic based shunt active power filter of cycloconverter fed induction machine is shown in Fig. 1. Cycloconverter supplies electrical power at variable voltage and frequency to adjust the speed of the induction machine [7].

Simulation is carried out for six-pulse cycloconverter fed induction machine at 10 Hz frequency and phase A input current of the cycloconverter as shown in Fig. 2

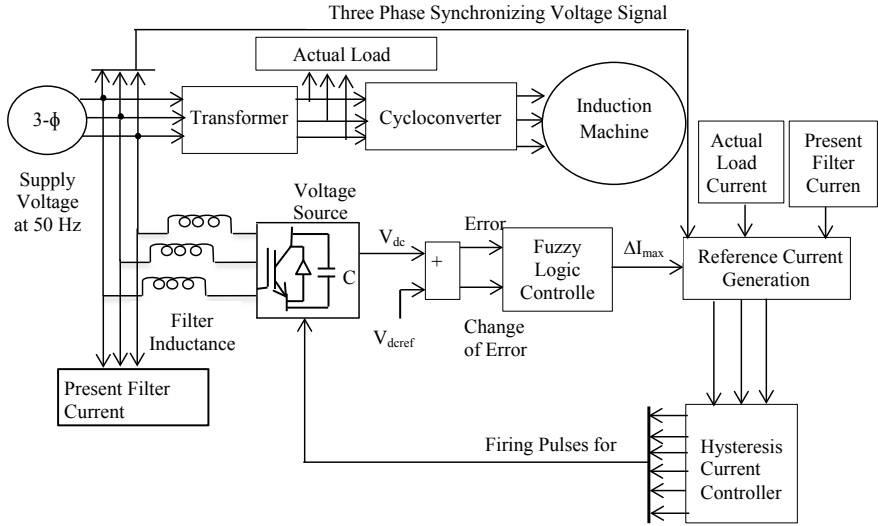


Fig. 1 Block diagram of cycloconverter fed induction machine with fuzzy logic based shunt active power filter

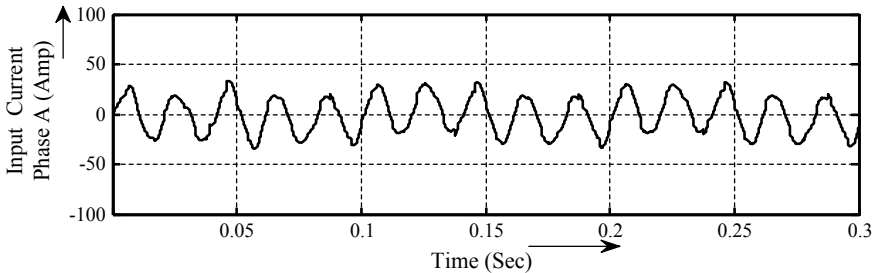


Fig. 2 Phase A input current of cycloconverter fed induction machine

THD of the input current of cycloconverter is found to be 16.91%. Harmonic frequencies of input current with their amplitude and phase are shown in Table 2. It can be observed that total harmonic distortion of supply current is higher than the acceptable level of the grid and the magnitude of harmonics is independent of the frequency of harmonic components. Table 2 shows that few higher order harmonics in supply current has higher magnitude and ignores the lower order harmonics, which has lower magnitude. Moreover, the phase angle of the fundamental component of the input current is -26.1° in this case. It shows that the supply side power factor of cycloconverter is lagging. The magnitude of subharmonic frequency is higher, which is difficult to filter by passive filter circuit. Therefore, a suitable active power filter is required to develop for filter harmonic components from supply current and compensate the reactive power demand.

Table 2 Harmonic analysis of input current of cycloconverter

S. no	Harmonic frequencies (Hz)	Amplitude of harmonic (% of fundamental)	Harmonics phase in (degree)
1	10	27.2	-7.8
2	50 (Fund.)	100	-26.1
3	70	10.6	-64.7
4	130	8.7	37.0
5	170	2.3	53.7
6	190	3.46	79.5
7	250	3.7	100.3
8	310	2.3	-25.0
9	430	2.27	67.6

4 Design Shunt Active Power Filter

Active power filters are superior in filtering performance compared to traditional passive filters due to smaller in physical size, more flexible, and less sensitive for frequency variation [8]. Therefore, shunt active power filter is generally used to improve the harmonics of different nonlinear loads including cycloconverter load [9].

4.1 Voltage Source Converter

The Voltage Sourced Converter (VSC) is used as active power filter to compensate the harmonic currents of cycloconverter, which is connected just across the cycloconverter. The turn off power switches, IGBTs are used in converter power circuit with antiparallel diodes to operate the converter as rectifier as well as inverter as shown in Fig. 3. A capacitor maintains the balance of real power flow between supply and load during transient operation and ac side inductor compensates the reactive power demand by load. Therefore, it improves the supply current harmonics and input displacement factor. DC voltage across the capacitor always has single polarity with reversible dc current. Therefore, it is capable to transfer power in both directions.

Voltage source converter can control the magnitude, phase angle, and frequency of the ac side voltage using appropriate switching. When instantaneous current flows from ac source to dc through the diodes; the converter operates as rectifier, on the other hand, reverse current flow from dc to ac source through IGBT switches and converter operates as inverter. DC side capacitor requires a controller to maintain a

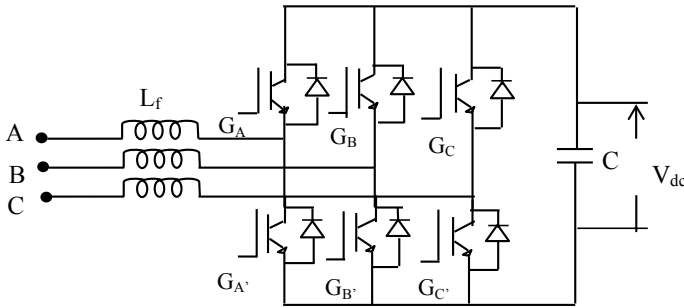


Fig. 3 Three-phase voltage source converter

constant dc voltage at reference voltage with minimum ripple. In recent years, fuzzy logic controller has become popular because it deals with imprecise inputs, does not need an accurate mathematical model, and capable to handle nonlinearity of the system.

4.2 Fuzzy Logic Based Controller

Fuzzy logic is an alternative technology that develops computer program, based on human intelligence and nature of human thinking. In fuzzy logic system, the control action is determined from assessment of a set of simple linguistic rules. The fuzzy logic system can be developed by exploring the knowledge about the system in the form of IF and THEN rules, and the order of the rules is not essential but all probable rules are evaluated in parallel. The internal structure of the fuzzy controller is shown in Fig. 4.

4.2.1 Fuzzification

The voltage across capacitor is compared with the reference voltage, which gives the error (e) and hence calculates the change of error (ce). Signals of e and ce are used from the real system as input of the fuzzy controller. The numerical value of these inputs are changed to membership function with seven fuzzy sets, which are defined

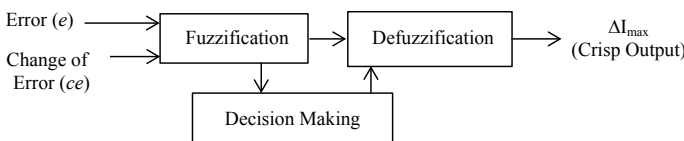


Fig. 4 Internal structure of the fuzzy logic controller

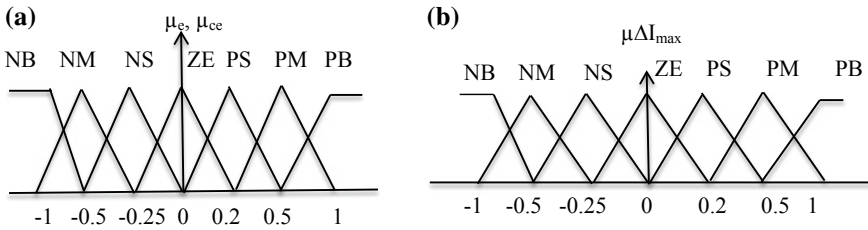


Fig. 5 Membership function of **a** Error (e) and change of error (ce) **b** change in maximum value of line current

Table 3 Rule-based fuzzy label for output variable

ce	e						
	NB	NM	NS	ZE	PS	PM	PB
NB	NB	NB	NB	NB	NM	NS	ZE
NM	NB	NB	NB	NM	NS	ZE	PS
NS	NB	NB	NM	NS	ZE	PS	PM
ZE	NB	NM	NS	ZE	PS	PM	PB
PS	NM	NS	ZE	PS	PM	PB	PB
PM	NS	ZE	PS	PM	PB	PB	PB
PB	ZE	PS	PM	PB	PB	PB	PB

as NB (Negative Big), NM (Negative Medium), NS (Negative Small), ZE (Zero), PS (Positive Small), PM (Positive Medium), and PB (Positive Big). Normalized triangular membership functions are used in fuzzification. The membership function of input variables (error and change of error) and output variable (change in maximum value of the line current) are shown in Fig. 5a, b. X-axis parameters define the universe of discourse and Y-axis parameters define the membership function.

4.2.2 Rule Matrix

There are seven fuzzy sets for each input and output variables, therefore, rule base matrix is a (7×7) square matrix as shown in Table 3 [10], in which error is defined by row of the matrix and change of error is defined by column. Corresponding to error and change of error, controller sets ΔI_{max} as output.

4.2.3 Defuzzification

Defuzzification is the process to convert the fuzzy outputs into crisp value to control the real system. The Centroid of Area (COA) method of defuzzification is used

because it finds the point where a vertical line would slice the aggregate set into two equal masses and considers the rules, which are applied below as well as at the maximum label of membership function. The output of fuzzy controller is provided to Hysteresis Band Current Controller (HBCC) to generate the corresponding firing pulses for VSC, therefore, VSC develops compensating currents at the harmonic frequencies but opposite in phase.

4.3 Hysteresis Band Current Control Technique

The HBCC technique is used to generate firing pulses for SAPF to achieve higher accuracy, stability, and fast response. HBCC requires synchronizing signal from supply to generate firing pulses at supply frequency. These synchronizing signals are multiplied by the output of fuzzy logic controller to obtain the reference line current [11]. The actual input current of cycloconverter is subtracted from the reference line current to find the reference current for SAPF. This reference filter current deducts the present filter current to determine the error signal. This error signal is then fed to the relay, which is defined by hysteresis band surrounding the reference current and maintains the filter current within a band limits.

4.4 Simulation of Cycloconverter Fed Induction Machine with Shunt Active Power Filter

Simulation of cycloconverter fed induction machine with fuzzy logic based shunt active power filter is shown in Fig. 6. This simulation is carried out at 10 Hz output frequency of cycloconverter with the supply frequency of 50 Hz for steady-state load as well as dynamic load that changes at the simulation time of 0.2 s. Three-phase output voltages of cycloconverter are shown in Fig. 7.

Corresponding electromagnetic torque and rotor speed of induction machine at 10 Hz supply fed by cycloconverter are shown in Fig. 8. Phase A supply voltage with actual input current of cycloconverter fed induction machine without SAPF is shown in Fig. 9a and with SAPF is shown in Fig. 9b, respectively.

In Fig. 9, it can be observed that the phase angle between supply voltage and current of cycloconverter is completely compensated in addition, the waveform of supply current is also improved. Consumed active and reactive powers of cycloconverter fed induction machine without and with SAPF are shown in Fig. 10 and Fig. 11, respectively. It is seen that the consumed reactive power of cycloconverter is completely compensated by SAPF. Performance parameters magnitude, phase angle, and its THD of the supply current of cycloconverter fed induction machine are shown in Table 4.

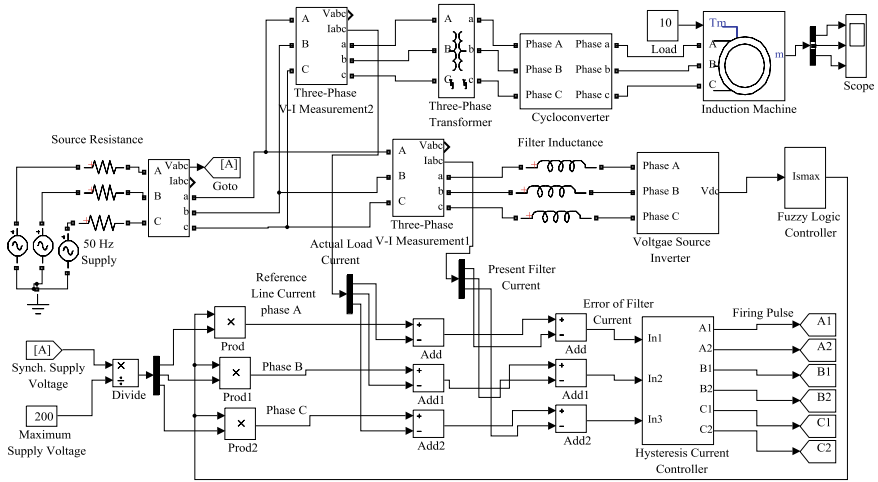


Fig. 6 Simulation of the cycloconverter fed induction machine with shunt active power filter

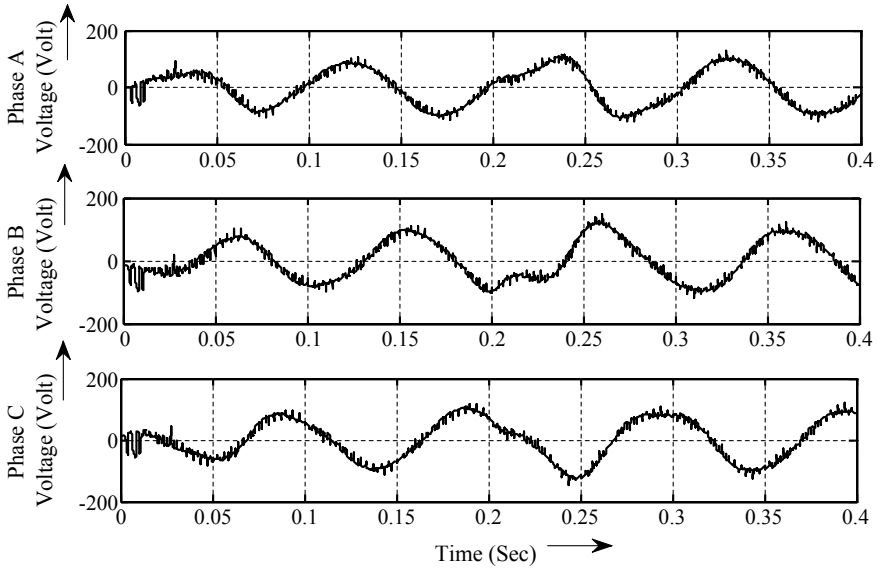


Fig. 7 Three-phase output voltages of cycloconverter for 10 Hz

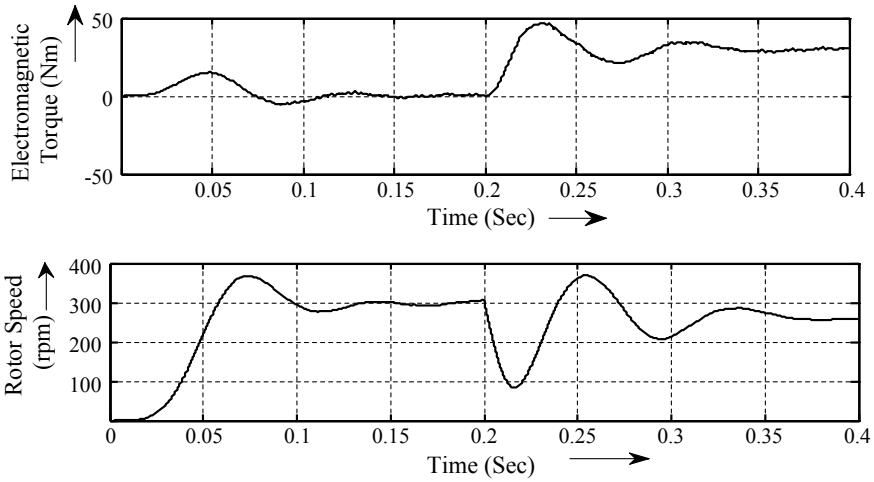


Fig. 8 Electromagnetic torque and rotor speed of cycloconverter fed induction machine with shunt active power filter

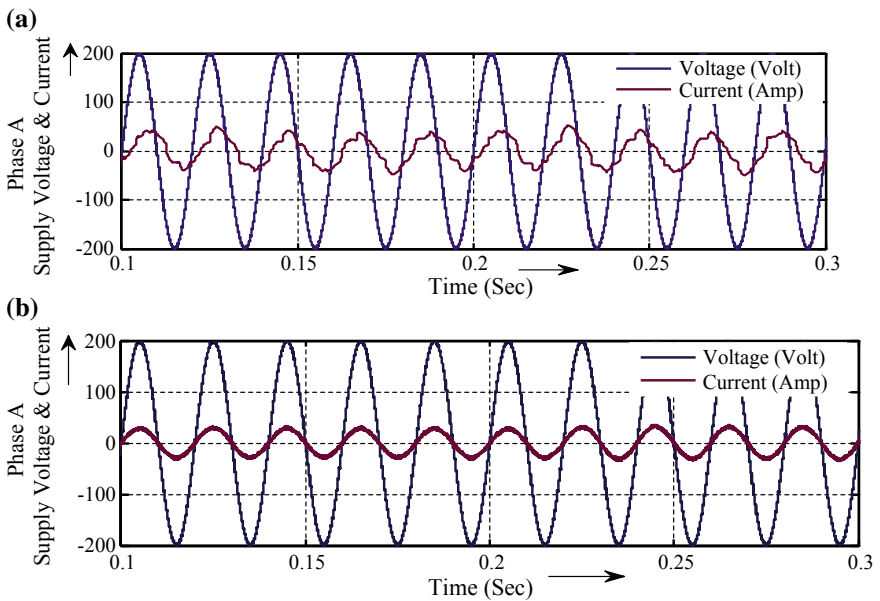


Fig. 9 a Phase A supply voltage and actual input current without SAPF, **b** phase A supply voltage and line current with SAPF

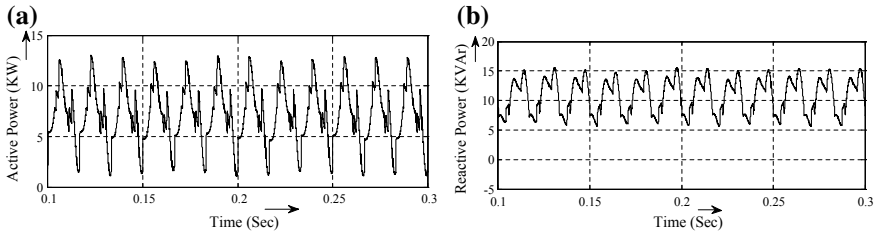


Fig. 10 Active and reactive power consumed by cycloconverter fed induction machine without SAPF

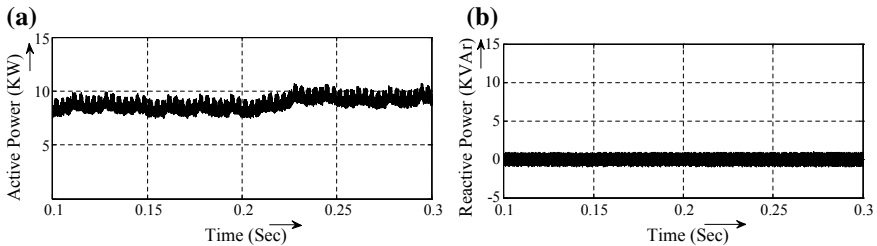


Fig. 11 Active and reactive power consumed by cycloconverter fed induction machine with SAPF

Table 4 Compare actual input current with and without SAPF

	Actual input current without SAPF	Actual input current with SAPF
Magnitude (Amp)	27.0	20.2
Phase (Deg.)	-48.4	-0.1
THD (%)	16.91	2.12

5 Conclusion

Cycloconverter injects harmonics in supply current and draws additional reactive power from the supply mains. SAPF improves THD of the supply current of cycloconverter fed induction machine from 16.91 to 2.12%. The phase angle of the input current is also improved from -48.4° to -0.1° . Fluctuation of active power consumption by cycloconverter is suppressed to acceptable label and reactive power consumption is totally compensated by SAPF. Hence, cycloconverter fed induction machine with SAPF performs similar to a resistive load, which draws the fundamental component of load current in phase with ac mains voltage.

References

1. Chen CS, Lee YD, Hsu CT, Ting DS, Shen CC (2007) Power quality assessment of hot strip mill with cycloconverter drive systems. *Ind Appl* 23:9–16
2. Liu Y, Heydt GT, Chu RF (2005) The power quality impact of cycloconverter control strategies. *IEEE Trans Power Deliv* 20(2):1711–1718
3. Xiaojun Z, Lin Z, Xiaoli S (2004) One-cycle control three-phase four-wire active filter with four-leg. *J Chongqing Univ* 27(3):77–80
4. Zhezhelenko I, Sayenko Y, Baranenko T (2007) Frequency converters as generators of interharmonics. In: 9th international conference, electrical power quality and utilization, Barcelona, 9–11, October, pp 9–11
5. Syam P, Bandyopadhyay G, Nandi P, Chattopadhyay A (2004) Simulation and experimental study of interharmonic performance of a cycloconverter-fed synchronous motor drive. *IEEE Trans Energy Convers* 19(2):325–332
6. Syam P, Nandi P, Chattopadhyay A (2002) Improvement in power quality and a simple method of subharmonic suppression for a cycloconverter-fed synchronous motor drive. *Electron Power Appl, IEEE Proc* 149(4):292–303
7. Khalil RM, Al-kababjie M (2007) Modelling and simulation of multi-pulse cycloconverter fed ac induction motor and study of output power factor. *Al-Rafidain Eng* 15(1):1–14
8. Udgave RS, Atre YR, Active filters with control based on the P-Q theory. In: *IOSR Journal of Electronics and Communication Engineering (IOSR-JECE)*, Second International Conference on Emerging Trends in Engineering, ISSN: 2278-2834, ISBN: 2278-8735, pp 27–30
9. Wang M, Li Y, Tan B, Wei B (2006) Harmonic analysis and suppression methods study of cycloconverter-feed synchronous motor drive system. *IEEE Int Conf Power Syst Technol*
10. Ogbuka CU, Eng M, Agu MU (2009) A modified approach to induction motor stator voltage and frequency control. *Pac J Sci Technol* 10(1):44–51
11. Jain SK, Agrawal P, Gupta HO (2002) Fuzzy logic controlled shunt active power filter for power quality improvement. In: *Proceedings of institute of electrical engineers, electrical power applications* 149(5)

Comparative Analysis of Speaker Recognition System Based on Voice Activity Detection Technique, MFCC and PLP Features



Akanksha Kalia, Shikar Sharma, Saurabh Kumar Pandey,
Vinay Kumar Jadoun and Madhulika Das

Abstract Due to rapid advancement in technology, speaker recognition systems become more robust and user friendly. The idea is to study and analyse the speech signal based on feature extraction method. This paper compares the performance of Mel-Frequency Cepstral Coefficient (MFCC) and PLP feature extraction with voice activity detection (VAD) technique. Vector Quantisation approach is used for features matching to select the combination which gives highest accuracy.

Keywords Speaker recognition systems · Mel-frequency cepstral coefficients (mfcc) · PLP · Voice activity detection (vad)

1 Introduction

The speech signal is capable of conveying different types and levels of information to the listener. At the primary levels, speech simply conveys a message intended. Additionally, the complete information (i.e. gender, identity and emotion ect.) of the speaker is also identified by the speech. The aim of this system is to characterize the identity of the speaker from the received speech signal. In practice, it is quite difficult to derive speech anatomy from the speech waveform. Hence, we generally use

A. Kalia · S. Sharma
National Institute of Technology Hamirpur, Hamirpur 177005, HP, India
e-mail: akanksha2kalia@gmail.com

S. K. Pandey (✉)
Indian Institute of Technology Patna, Patna 801106, Bihta, India
e-mail: saurabh.rjit@gmail.com

V. K. Jadoun · M. Das
National Institute of Technology Delhi, Delhi 110040, India
e-mail: vjadounmnit@gmail.com

M. Das
e-mail: madhulikadas86@gmail.com

features derived from the waveform based on the various production and perception models.

In the recent past, many works have been proposed by the researchers in this area. Some of them are discussed as follows: Hermans [1] described the perceptual linear predictive (PLP) analysis of speech. Gudnason and Brookes [2] developed a novel feature set for speaker identification. The analysis has shown that a standard speaker identification system can be improved significantly. Zhou et al. [3] have presented a comparison between the performance of MFCC (Mel-Frequency Cepstral Coefficients) and LFCC (Linear frequency cepstral coefficients) for speaker Recognition. Authors of Ref. [4] have introduced automatic speaker recognition (ASR) system based on Mel-Frequency Cepstrum Coefficients (MFCC) and Gaussian Mixture Models (GMM) to develop a security control access gate. This paper [5] presented Feature Extraction Methods Linear Predictive Codes (LPC), Perceptual Linear Prediction (PLP), Mel-Frequency Cepstral Coefficients (MFCC) in Speech Recognition problem. Selvan et al. [6] proposed an improved strategy for Text Dependent Speaker Recognition System for Security Applications. Jensen and Tan [7] proposed an STFT-based algorithm for cepstral feature estimation of mel-frequency cepstral features. Deepak and Prasanna [8] exploited the Foreground Speech Segmentation features using Glottal Closure Instants and Mel Cepstral Coefficients. Daly et al. [9] have implemented a recognition-based system models with MFCC, PLP, Jitter, and Shimmer. In this paper [10], BARIS EROL et al. have presented a novel method for Automatic Data-Driven Frequency-Warped Cepstral Feature Design for Micro-Doppler Classification.

Feature extraction and the classification are the two main stage for speaker recognition process. The features are extracted from the speech signal. There are various methods available in the literature for feature extraction. The preferably used methods for feature extraction are MFCC (Mel-Frequency Cepstral Coefficient), LPC (Linear Predictive Coding), LPCC (Linear Predictive Cepstral Coefficient), etc. [11]. MFCC is one of the most robust and efficient feature extraction method. It has two kinds of filters which are linearly spaced at below 1000Hz and logarithmically spaced above 1000Hz. In this paper, a comparative Analysis of Speaker Recognition System based on Voice Activity Detection technique, MFCC, and PLP features has been discussed.

The organization of the paper is given as: Section II discuss the Methodology. Results and Discussion are presented in next section. In the last section, conclusions are drawn.

2 Methodology

The process of identification of the true person from the characteristics of voice is known as speaker or voice recognition. Speaker recognition systems can be divided into two-step process, i.e., identification and verification. Further which is divided into two modules of feature extraction and feature matching. In feature extraction

process, unique features from the voice signal are extracted which is used for identification of the person. The second step is feature matching which involves the procedure to identify the extracted voice features with the database of the already known speakers. The efficiency of the system depends on various parameters that present a challenge to speaker recognition technology.

2.1 Voice Activity Detection (VAD)

Voice activity detection is a technique used in front end processing which facilitates the speech-based applications. The performance of speech processing depends on various features required for voice and data applications. In our approach, we have used a Voice Activity Detector based on Energy, Zero-Crossing Rate (ZCR) [12] and have compared its accuracy with a normal amplitude threshold based truncation. ZCR is an estimate of frequency and signifies the rate of change of signal from positive to negative. Voiced part has higher energy and lower ZCR than the unvoiced part. For truncation, the signal is first normalized and then compared with amplitude threshold to extract the voiced part. Figure 1 shows the actual signal applied in the system which is furthermore diversified after the inclusion of VAD as shown in Fig. 2. The third waveform (Fig. 1) shows truncated signal based on amplitude threshold values. The Fig. 3 shows the signal received after applying truncation and VAD technique.

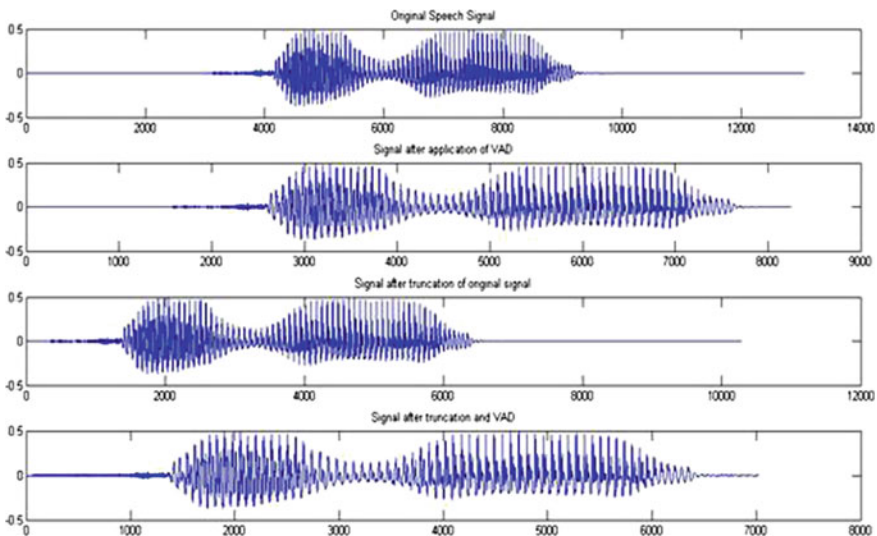


Fig. 1 First graph shows the original signal. Second graph shows signal after application of VAD, the third shows truncated signal based on amplitude threshold and the fourth shows signal after truncation and VAD both applied to original signal

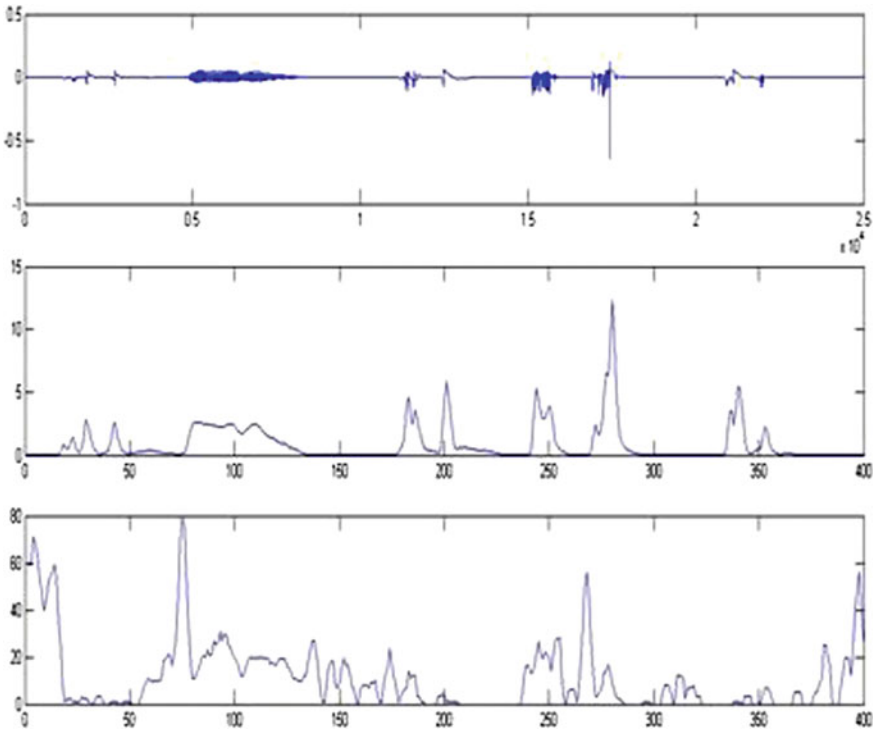


Fig. 2 Subplot 1 shows the noisy sample. Subplot 2 depicts energy vector and subplot 3 depicts the Zero crossing rate. The purple box shows the actual voiced part

2.2 MFCC

In this approach, 13 MFCC coefficients are extracted. Considering that speech signal is short term stationary, frame size of 15 ms and frame shift of 5 ms is used with a hamming window. 20 filter bank channels were used with a pre-emphasis coefficient of 0.97 and range of filter banks was 0–5000. This range was selected as it is observed that the energy of the speech signal is considerable in this frequency range.

2.3 Vector Quantization

For feature matching and dimensionality reduction, Vector Quantization technique is used. The high dimensional data (about 160 frames) is represented by 16, 32 and 64 centroids. LBG algorithm was used for clustering. This was used to build speaker-specific vector quantization codebook.

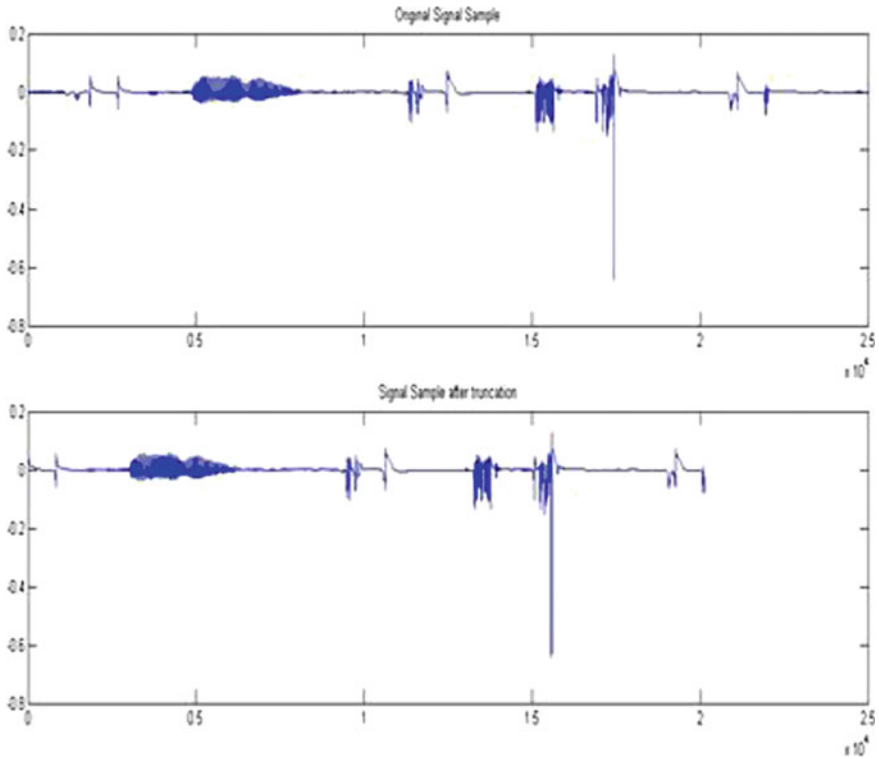


Fig. 3 Problematic sample after truncation

2.4 Perceptual Linear Predictive (PLP)

The basic idea behind the introduction of PLP Coefficients is the use of a perpetual front end to determine Linear Prediction Cepstral Coefficients and has been applied in different ways to improve speech detection and coding, including echo cancellation, noise reduction and reverberation suppression. PLP technique takes into account critical-band spectral resolution, equal loudness curve, and intensity loudness power law [13].

2.5 Database

A database which consists of word zero spoken by 49 persons is collected using MATLAB voice recorder. Sampling rate is fixed at 16 and 12500 KHz and stored it in .wav format. Each person is asked to utter the word twice. The first is used as training data and the second is used as test data for the respective speaker.

3 Results and Discussion

Problematic samples: The sample shown in Fig. 2 is an example of a noisy sample which impedes the working of the voice activity detector. In such cases, noise is seen to have more energy than the voiced section contrary to the normal notion. Also, the ZCR for voiced and unvoiced parts is comparable and cannot be used for detection. The result of normal truncation method includes the noisy part as well and this further decreases the accuracy of the Speaker recognition system.

The accuracy of various tests is measured in terms of number of correct identifications made by the system. Speaker identification was done based on PLP and MFCC features with vector quantization for feature matching. Number of centroids is 16, 32, and 64 for the tests. The accuracy was highest for $k = 64$, hence it was considered for further experiments. The accuracy of the various combinations tried is given below: MFCC with vector Quantization, where k is the number of centroids used.

From Tables 1 and 2, it is evident that MFCC features lead to more accurate results than PLP features. Also in case of MFCC, amplitude-based truncation method leads to most accurate results.

Table 1 Accuracy results for MFCC features with VQ

Method of VAD	Accuracy of detection for $k = 64$
None	79.59
Truncation	89.79
Energy and ZCR based	83.67
VAD based on truncation, ZCR and energy threshold	81.63

Table 2 Accuracy results for PLP with vector quantization

Method of VAD	Accuracy of detection for $k = 64$
None	81.6326
Truncation	67.34
Energy and ZCR based	67.34
VAD based on truncation, ZCR and energy threshold	63.26

4 Conclusions


Human speech signal has speaker-related differences that include linguistic, semantic, articulatory, and acoustic. There are also anatomical differences in vocal tract and learned speaking habits of the speaker. All these features are to be taken into account to develop a robust and applicable to real-life scenario, efficient VAD techniques must be designed which can take into account the large noise peaks in the signals. Also a combination of features can be used instead of single features.

References

1. Hermansky H (1990) Perceptual linear predictive (PLP) analysis of speech. *J Acoust Soc Am* 87(4), 1738–1752
2. Gudnason J, Brookes M, (2008) Voice source cepstrum coefficients for speaker identification. In: IEEE International Conference on Acoustics, Speech and Signal Processing, ICASSP 2008. IEEE, PP 4821–4824
3. Zhou X, Garcia-Romero D, Duraiswami R, Espy-Wilson C, Shamma S (2011) Linear versus mel frequency cepstral coefficients for speaker recognition, In: IEEE workshop on automatic speech recognition and understanding (ASRU). IEEE, pp 559–564
4. Maesa A, Garzia F, Scarpiniti M, Cusani R (2012) Text independent automatic speaker recognition system using mel-frequency cepstrum coefficient and gaussian mixture models. *J Inf Secur* 3(04):335
5. Dave N (2013) Feature extraction methods LPC, PLP and MFCC in speech recognition. *Int J Adv Res Eng Technol* 1(6):1–4
6. Selvan K, Joseph A, Babu KA (2013) Speaker recognition system for security applications. In: IEEE recent advances in intelligent computational systems (RAICS). IEEE, pp 26–30
7. Jensen J, Tan Z-H (2015) Minimum mean-square error estimation of mel-frequency cepstral features—a theoretically consistent approach. *IEEE/ACM Trans Audio, Speech Lang Process (TASLP)* 23(1):186–197
8. Deepak K, Prasanna S (2016) Foreground speech segmentation and enhancement using glottal closure instants and mel cepstral coefficients. *IEEE/ACM Trans Audio, Speech Lang Process (TASLP)* 24(7):1204–1218
9. Daly I, Hajaiej Z, Gharsallah A (2017) Speech analysis in search of speakers with MFCC, PLP, jitter and shimmer. In: 2017 International conference on advanced systems and electric technologies (IC_ASET). IEEE, pp 291–294
10. Erol B, Amin MG, Gurbuz SZ (2018) Automatic data-driven frequency-warped cepstral feature design for micro-doppler classification. *IEEE Trans Aerosp Electron Syst* 54(4):1724–1738
11. Campbell JP (1997) Speaker recognition: A tutorial. *Proc IEEE* 85(9):1437–1462
12. Bachu R, Kopparthi S, Adapa B, Barkana B (2008) Separation of voiced and unvoiced using zero crossing rate and energy of the speech signal. In: American society for engineering education (ASEE) Zone conference proceedings, pp 1–7
13. zohra Chelali F, Djeradi A, Djeradi R (2011) Speaker identification system based on PLP coefficients and artificial neural network. *Environments*, 1, 2

Nonintrusive Load Monitoring: Making Smart Meters Smarter



DeepRaj Bedi  and Vineet Sharma

Abstract Recent advancements in smart metering have put interest in load monitoring techniques which can provide consumers with better understanding of load in their environment. Electrical meters with NILM technology are used by utility companies to survey the specific uses of electrical power in different homes. Once, Equipment's running in the environment are learnt, we can play with its features. The system can intelligently understand if the equipment which needs attention by the user, is in knowledge. It will inform the user with precautions to give attention and this can save consumer's energy and appliance, both. This all can be integrated into a single energy meter without adding any cost for IoT appliances. Whereas, System will be capable enough to predict if the appliance is working in the mode of operation it was designed to work, or not. Also, keeping a check on its service requirement and sometimes even recognizing which part is producing ambiguity and hence saving customer from technician's extra service fees.

Keywords NILM · Energy disaggregation · Load monitoring · Security · Appliance health

1 Introduction

1.1 Need for NILM in Smart Meters

You cannot improve what you cannot measure and that is the problem where the increasing adoption of Smart Meters (SMs) in energy distribution networks are planning to address so that the utility providers (UPs) will be able to monitor the grid more accurately. With the addition of NILM in a meter, both consumer and utility are at benefit. Consumer gets to know where it is consuming energy, Which appliance is most energy demanding and which appliance is not working properly, whereas

D. Bedi (✉) · V. Sharma
Manipal University Jaipur, Jaipur 303007, Rajasthan, India
e-mail: deepbedi31@gmail.com

© Springer Nature Singapore Pte Ltd. 2020
A. Kalam et al. (eds.), *Intelligent Computing Techniques for Smart Energy Systems*,
Lecture Notes in Electrical Engineering 607,
https://doi.org/10.1007/978-981-15-0214-9_83

utility knows which customer is responsible for disturbing power factor at its end and at what time power scheduling as per the load is to be done as per the daily data collected out of those meters, Which results in better customer utility relation.

2 Working of NILM and Challenges with It

NILM employs machine learning and pattern recognition algorithms through which appliance signatures are read. This field has been increasing during the last years after the release of a number of public data sets designed specifically for these purposes as well as a Python toolkit enabling comparison of various algorithms. The NILM methods can be considered as signal processing and time series analysis strategies. Over the last years, many methods have been proposed and have succeeded in substantial advances. These methods refer to the extraction of appliance level data from a single measuring point. It uses an appliance database of some known devices and data is compared with the signal measured by the meters to conclude which signatures best match. The frequency and the resolution of the A/D converter has a significant role in the attempt to disaggregate appliances with low consumption or similar power with other devices. Therefore, low frequency approaches are not capable of identifying small loads. Improved sampling rate improves both the number of recognized appliances and the accuracy of detection. A realistic example is given on the following Fig. 1, where the appliance signature of three devices is given and is asked to extract information about their use on an aggregate energy signal.

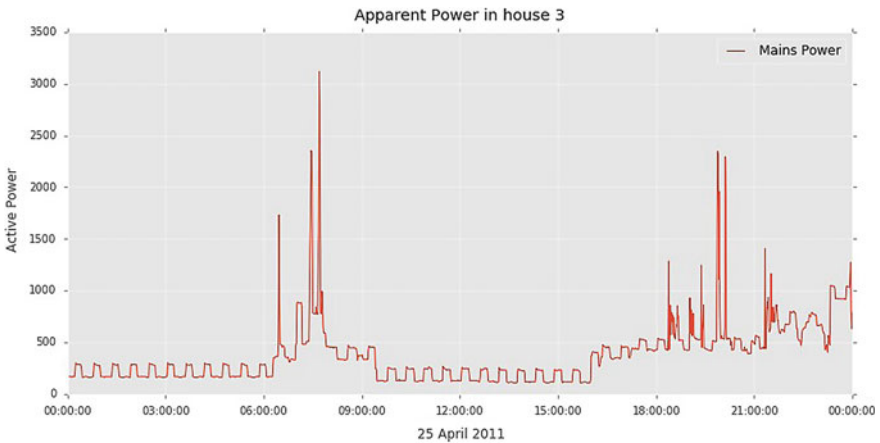


Fig. 1 Aggregate energy signal on a household

2.1 Data Acquisition

Smart meters measure the alternating current (I), voltage (V) and apparent power (S), measured in Volt-Amperes: V.I) which is the product of current by voltage. There are other measurements derived from the previous ones: real power (P , measured in watts: W) is the transference of energy in the net, regardless of the direction. It is also called the power or average power. Additionally, there are other advanced measures such as electric characteristic, harmonic distortion, electromagnetic interference (EMI), and transients. NILM: disaggregate this total amount to each appliance. Next to this, it is necessary to emphasize the sampling rate of the data collected, as it determines the type of information that could be extracted from the electrical signals. There are two main groups of data collected based on this criteria.

Another approach is to work on already acquired data sets and train the module as per it. If the same signature comes, NILM easily predicts the appliance and the energy it is consuming. High sampling rate: The data is collected at a sampling frequency of 1 Hz or more. This kind of data allows to extract some features in the consumption which are only present at the sampling rates. In some cases these very high sampling rates only can be achieved with special hardware. Low sampling rate: This group includes frequencies of sampling lower than 1 Hz down minutes or even hours. This kind of sampling rate is the most common in the smart meters which can be bought nowadays. NILM works fine if provided with high frequency sampling that puts concern for faster A/D converter and fast processing of microprocessor. Extra RAM capabilities are also needed. In Fig. 2, is the trainer interface where different equipment like washing machine, oven, and iron box can be added and corresponding to it data can be accumulated and trainer can be trained.

3 Proposal

3.1 Security Feature to Safeguard Consumer as Well as Appliance

Once the signature for certain appliance is known by software based on NILM, it can analyze its working in the environment. Say, if consumer turns ON the iron box in the morning and later forgets to turn it OFF and leaves the premises, NILM trainer knows that Iron box is being set to ON position from say past 1 h as repeated curve is repeated in its background and It will inform the consumer to give its attention to certain load running from past 1 h as shown in Fig. 3. Thus, saving consumer from any loss due to damage of appliance or fire hazardous, whereas appliance is saved from getting damaged and turned OFF at right time.

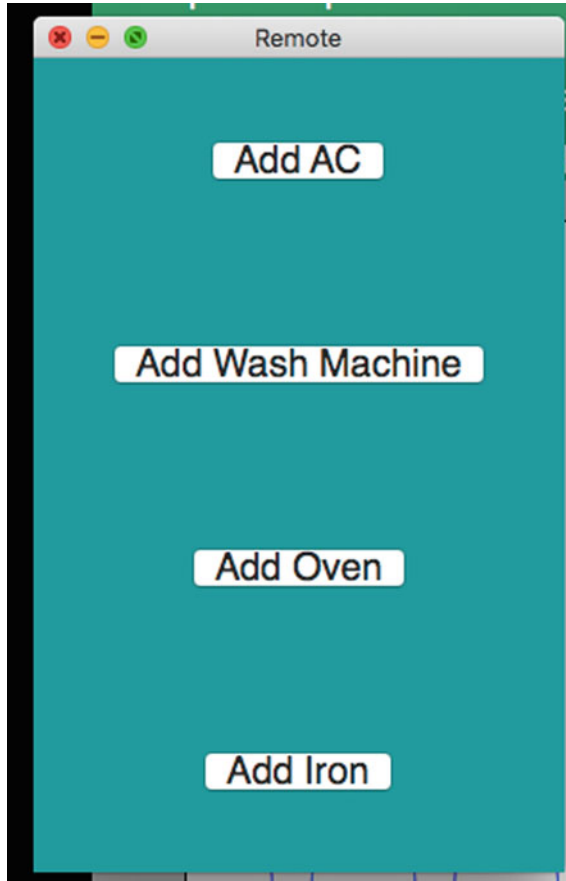


Fig. 2 Training the module trainer with data sets

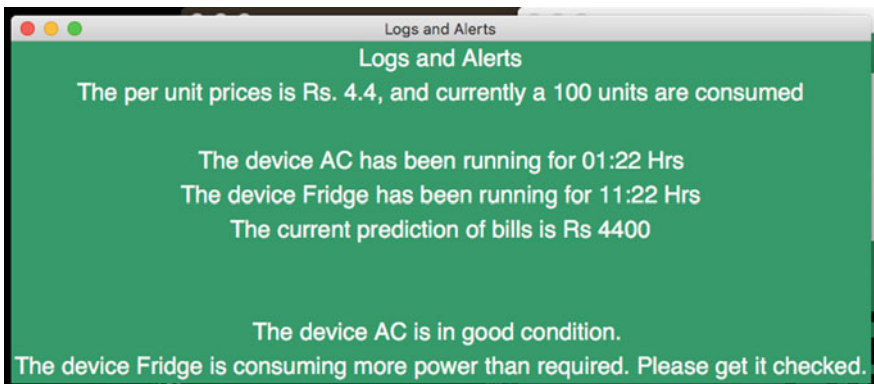


Fig. 3 Logger depicting the billed amount as per consumption, running alert and health functioning of appliance

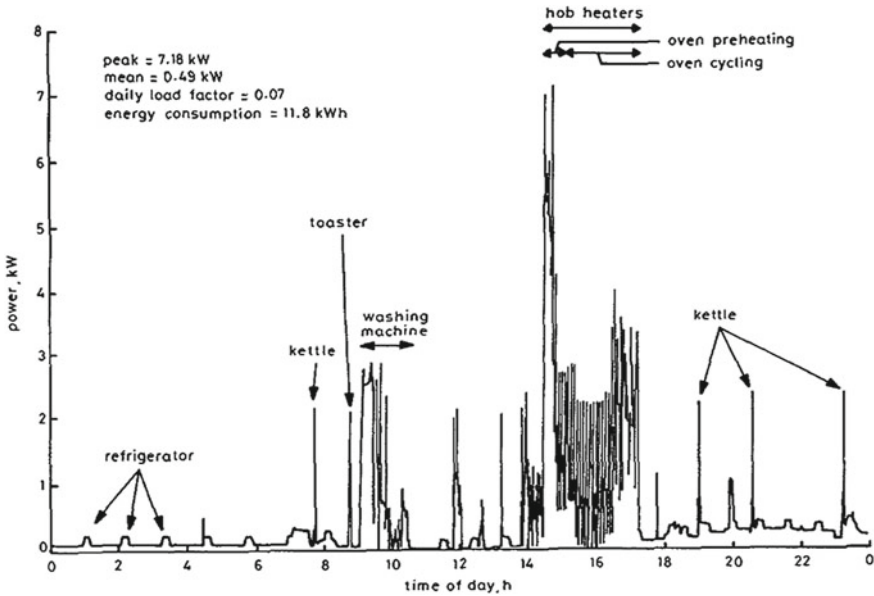


Fig. 4 Curve for different appliances shows the curve for electric oven taking extra clicks to ignite (depicted by arrow \longleftrightarrow)

3.2 NILM to Predict Appliance Health

NILM is trained for the general working signature curve of appliances. There may be scenario where appliances are not working as it should be. NILM will predict the error in the signature curve and intimate the consumer that appliance is lacking the capabilities to work as designed. Say, Electric burner generally needs 15 clicks to set up but it is taking double the required as depicted by curve, NILM will judge the pattern for repeated occurrence and inform the user that it needs repair. Imagine, user does not require any repair person to check for errors, hence saving the fees to be paid to the repairer for just checking error, below is the analysis curve fed to trainer in Fig. 4, which will intimate the consumer about the electric oven wrong functioning.

4 Conclusion

NILM has lots of application out of which we worked on security features and device health prediction. Integrating with the smart meter will help both consumer and utility. The consumer can have better knowledge about where most of the energy is being spent and which appliance is working abnormally. Whereas, for utility,

complaints like meter faulty or thefts can be checked by matching the data provided by smart meter. In India, where 60% of fire are caused by short circuits and allied electricity problems, maybe due to consumer negligence can be avoided as smart meter will be continuously checking for load at run and giving alert to consumer accordingly. Whereas, consumer can replace the faulty part for the appliance and save on electricity bills.

Stabilization of Chaotic Systems Using Robust Optimal Controller



Madhulika Das and Vinay Kumar Jadoun

Abstract In this paper, a robust optimal controller is proposed to stabilize chaotic systems. Chaos is a highly nonlinear system. A small change in parameters shows different characteristics. Robust controller is suitable to stabilize the chaotic system. To minimize the control effort the optimal controller is incorporated with the robust controller. Optimal controller based on state-dependent Riccati equation is designed for known part of the system to minimize the control effort. Whereas robust controller is designed to tackle the uncertain part of the system. The proposed controller is employed to the Lorenz chaotic system. In simulation, the proposed controller is compared with the existing robust controller.

Keywords Robust control · Optimal control · Chaotic system · Lorenz system

1 Introduction

Chaos is a very worrying nonlinear phenomenon. It exhibits unpredictable and irregular dynamics depending on its initial conditions, that is, a small change in the initial states can lead to extraordinary perturbation in the system states. In the recent past different chaotic system was proposed such as Lorenz system, Chua's circuit, Chen system [1] and the complex behaviour were also studied. Moreover, in many engineering application chaotic behaviour is discussed such as lasers, Colpitts oscillators, nonlinear circuits, communication [2], and so on. In 1990, chaos control was first considered by Ott et al. [3], till then chaos control is extremely investigated by many researchers. Many control strategy such as sliding mode control [4], adaptive control [5], backstepping control [6], observer-based control [7], were developed to control the chaotic system.

M. Das (✉) · V. K. Jadoun
National Institute of Technology Delhi, Narela, Delhi-40, India
e-mail: madhulikadas@nitdelhi.ac.in

V. K. Jadoun
e-mail: vjadounmnit@gmail.com

© Springer Nature Singapore Pte Ltd. 2020
A. Kalam et al. (eds.), *Intelligent Computing Techniques for Smart Energy Systems*,
Lecture Notes in Electrical Engineering 607,
https://doi.org/10.1007/978-981-15-0214-9_84

Chaotic system is highly sensitive to its parameters. A small change occurred due to parameter variegate or external disturbance varies the performance of the system. So, robust controllers are the first choice to stabilize a chaotic system. Among all the robust controller sliding mode controller is highly popular for its robustness to the matched uncertainties [8]. In the sliding phase, it inherently nullifies the effect of matched uncertainty. A SMC is mainly designed to tackle the uncertainty. Therefore, the amount of control input requires to control a system is not taken in account. Unnecessary high-control gain rises the cost of controller as well as it leads to instability. Moreover, very high controller gain may saturate the actuator leading to failure of the control scheme.

To overcome this problem, optimal controller is incorporate with the sliding mode controller which introduces a new controller named as optimal sliding mode controller (OSMC) [9]. Optimal controller is easily incorporated with the sliding mode controller by designing integral sliding surface. In the field of optimal controller linear quadratic regulator (LQR) [10] is highly popular due to its simplicity. But the main drawback of LQR technique is that it cannot be applied directly to nonlinear systems. So, several suboptimal methods have been proposed in the literature. Among them state-dependent Riccati equation (SDRE) [11] is a popular choice due to its simple numerical analysis. SDRE technique is used to design the optimal control for nonlinear system similar as LQR technique is used to define the optimal feedback control for linear systems. In the case of SDRE technique the weighting matrices are dependent on the states of the system. Another drawback of the sliding mode controller is chattering which is also seen in OSOSMC. The sign function in control input causes chattering. A common an efficient method to reduce chattering is to design a higher order sliding mode controller [12].

2 Problem Statement

The mathematical model of three-dimensional chaotic system is considered as

$$\begin{aligned}\dot{x}_1(t) &= f(x_1, x_2, x_3) - \alpha x_1 \\ \dot{x}_2(t) &= x_1 \cdot g(x_1, x_2, x_3) + x_3 \cdot \Psi(x_1, x_2, x_3) - \beta x_2 \\ \dot{x}_3(t) &= x_1 \cdot h(x_1, x_2, x_3) - x_2 \cdot \Psi(x_1, x_2, x_3) - \gamma x_3\end{aligned}\tag{1}$$

where x_1, x_2, x_3 are state variables and α, β, γ are nonnegative known constant. Each of the four function $f(\cdot), g(\cdot), \Psi(\cdot)$ are considered as smooth function, which belongs to \mathbb{R}^3 .

After adding the control input $u(t)$ and the uncertainty $\Delta f(x_1, x_2, x_3)$ in the same channel of the system (1), it can be rewritten as follows:

$$\begin{aligned}
 \dot{x}_1(t) &= f(x_1, x_2, x_3) - \alpha x_1 + \Delta f(x) + u(t) \\
 \dot{x}_2(t) &= x_1 \cdot g(x_1, x_2, x_3) + x_3 \cdot \Psi(x_1, x_2, x_3) - \beta x_2 \\
 \dot{x}_3(t) &= x_1 \cdot h(x_1, x_2, x_3) - x_2 \cdot \Psi(x_1, x_2, x_3) - \gamma x_3
 \end{aligned}
 \tag{2}$$

The above equation can be rewritten as

$$\dot{x}(t) = A(x)x + Bu(t) + \xi(x)
 \tag{3}$$

where $x(t) = \begin{bmatrix} x_1(t) \\ x_2(t) \\ x_3(t) \end{bmatrix}$, $A(x) = \begin{bmatrix} \alpha & f(x)/x_2 & 0 \\ g(x_1, x_2, x_3) & -\beta & \Psi(x_1, x_2, x_3) \\ h(x_1, x_2, x_3) & -\Psi(x_1, x_2, x_3) & -\gamma \end{bmatrix}$,
 $B = \begin{bmatrix} 1 \\ 0 \\ 0 \end{bmatrix}$ and $\xi(x) = \begin{bmatrix} \Delta f(x) \\ 0 \\ 0 \end{bmatrix}$

The objective of the proposed control method is to design a robust optimal controller based on second-order sliding mode controller for the chaotic system affected by matched uncertainties. The design of proposed controller is divided into two steps, (1) optimal controller $u_1(t)$ design for the known part of nonlinear system based on state-dependent Riccati equation, (2) second-order sliding mode controller $u_2(t)$ is designed to tackle the uncertain part of the system control. So the control can be written as

$$u(t) = u_1(t) + u_2(t)
 \tag{4}$$

3 Optimal Controller Design

Neglecting the uncertain part of the system, (3) is written as

$$\dot{x}(t) = A(x)x + Bu(t)
 \tag{5}$$

The performance index J is selected to minimize control input $u_1(t)$ is

$$J = \int_0^\infty [x(t)^T Q(x)x(t) + u(t)^T R(x)u(t)]dt
 \tag{6}$$

where $Q(x) \in \mathbb{R}^{3 \times 3}$ and $R(x) \in \mathbb{R}^1$ are weighting matrices which are the function of states. The control law $u_1(t)$ is defined as

$$u_1(t) = -R^{-1}(x)B^T P(x)x(t) = K(x)x(t)
 \tag{7}$$

where $K(x) = -R^{-1}(x)B^T P(x)$, $P(x)$ is solution of the state-dependent Riccati equation [11].

$$\dot{P}(x) = A(x)^T P(x) + P(x)A(x) + Q(x) - P(x)BR^{-1}(x)B^T P(x) = 0 \quad (8)$$

4 Design of Sliding Mode Controller

The purpose of designing sliding mode controller is to tackle unknown part of the system. For the stabilization of uncertain chaotic system with least control effort the SMC is combined with the optimal control methodology. While designing integral sliding surface [9] optimal control can be incorporated easily with the optimal control. But the conventional sliding mode controller is effected by chattering. The sign function in the control input is the reason of chattering. Second-order sliding surface is designed to minimize the chattering. The second-order sliding surface is designed in two section. In the first part, an integral sliding manifold is designed.

$$s(t) = C \left[x(t) - \int_0^t \dot{\varphi}(\tau) d\tau \right] \quad (9)$$

where

$$\dot{\varphi}(t) = A(x)x(t) + Bu_1(t) \quad (10)$$

from (3), it is determined as follows

$$\dot{s}(t) = C [Bu_2(t) + B\xi(t)] \quad (11)$$

In the proposed integral sliding manifold, knowledge of initial condition is not needed. But the system has some reaching phase. For finite-time convergence, terminal sliding manifold is established based on the proposed integral sliding manifold.

$$\sigma(t) = s(t) + \lambda \dot{s}(t)^{\frac{p}{q}} \quad (12)$$

where λ is the switching gain

$$\lambda > 0 \quad (13)$$

in addition p, q meet the following conditions

$$p, q \in \{2n + 1 : n \text{ is an integer}\} \quad (14)$$

and

$$1 < \frac{p}{q} < 1.5 \quad (15)$$

The constant plus proportional reaching law [13] formulates to

$$\dot{\sigma}(t) = -\eta_1 \text{sgn}(\sigma(t)) - \varepsilon_1 \sigma(t) \tag{16}$$

where $\eta_1 > 0$ and $\varepsilon_1 > 0$.

Further

$$\begin{aligned} \dot{\sigma}(t) &= \dot{s}(t) + \lambda \frac{p}{q} \dot{s}(t)^{\frac{p}{q}-1} \ddot{s}(t) \\ &= \lambda \frac{p}{q} \dot{s}(t)^{\frac{p}{q}-1} \left(\frac{q}{\lambda p} \dot{s}(t)^{2-\frac{p}{q}} + \ddot{s}(t) \right) \end{aligned} \tag{17}$$

As parameters p, q satisfy (14) and (15), the following conditions are also meet [14]

$$\begin{aligned} \dot{s}(t)^{\frac{p}{q}-1} &> 0 \quad \text{for} \quad \dot{s}(t) \neq 0 \\ \dot{s}(t)^{\frac{p}{q}-1} &= 0 \quad \text{only for} \quad \dot{s}(t) = 0 \end{aligned} \tag{18}$$

Again, from (13)–(15) and (18), the term $\lambda \frac{p}{q} \dot{s}(t)^{\frac{p}{q}-1}$ in (17) can be substituted by a scalar $\eta_2 > 0$ for $\dot{s}(t) \neq 0$. So, (17) is defined as written as

$$\dot{\sigma}(t) = \eta_2 \left(\frac{q}{\lambda p} \dot{s}(t)^{2-\frac{p}{q}} + \ddot{s}(t) \right) \tag{19}$$

Substituting the value of $\dot{\sigma}(t)$ from (19), (16) can be expressed as

$$\begin{aligned} \eta_2 \left(\frac{q}{\lambda p} \dot{s}(t)^{2-\frac{p}{q}} + \ddot{s}(t) \right) &= -\eta_1 \text{sgn}(\sigma(t)) - \varepsilon_1 \sigma(t) \\ \text{or, } \frac{q}{\lambda p} \dot{s}(t)^{2-\frac{p}{q}} + \ddot{s}(t) &= -\eta \text{sgn}(\sigma(t)) - \varepsilon \sigma(t) \end{aligned} \tag{20}$$

where $\eta = \frac{\eta_1}{\eta_2} > 0$ and $\varepsilon = \frac{\varepsilon_1}{\eta_2} > 0$. Then (20) can be rewritten as

$$\ddot{s}(t) = -\eta \text{sgn}(\sigma(t)) - \varepsilon \sigma(t) - \frac{q}{\lambda p} \dot{s}(t)^{2-\frac{p}{q}} \tag{21}$$

Differentiating (11) formulates as

$$\ddot{s}(t) = G [B\dot{u}_2(t) + B\dot{\xi}(t)] \tag{22}$$

Using (21) and (22), the switching control law is defined as

$$u_2(t) = - \int_0^t (CB)^{-1} \left[\frac{q}{\lambda p} \dot{s}(\tau)^{2-\frac{p}{q}} + \eta \text{sgn}(\sigma(\tau)) + \varepsilon \sigma(\tau) \right] d\tau \quad (23)$$

Parameters η and ε are designed such a way that $|GB\dot{\xi}(t)| < \eta$ [15].

5 Simulation Results

In simulation result, the effectiveness of the proposed controller is depicted by stabilizing the Lorenz chaotic system by using the proposed controller. Obtained simulation result is compared with already exists sliding mode controller.

Lorenz system is defined by the following equations [16]:

$$\begin{aligned} \dot{x}_1(t) &= -10x_1(t) + 10x_2(t) \\ \dot{x}_2(t) &= 28x_1(t) - x_2(t) - x_1(t)x_3(t) \\ \dot{x}_3(t) &= -\frac{8}{3}x_3(t) + x_1(t)x_2(t) \end{aligned} \quad (24)$$

where $x_1(t)$, $x_2(t)$, $x_3(t)$ are state variables The chaotic behaviour of the Lorenz system is shown in Fig. 1

The Lorenz system can be controlled by using control input in either states $x_1(t)$, or $x_2(t)$. Here the control input and disturbance $\Delta f(x)$ are associated with the state $x_1(t)$. The system (24) is rewritten as

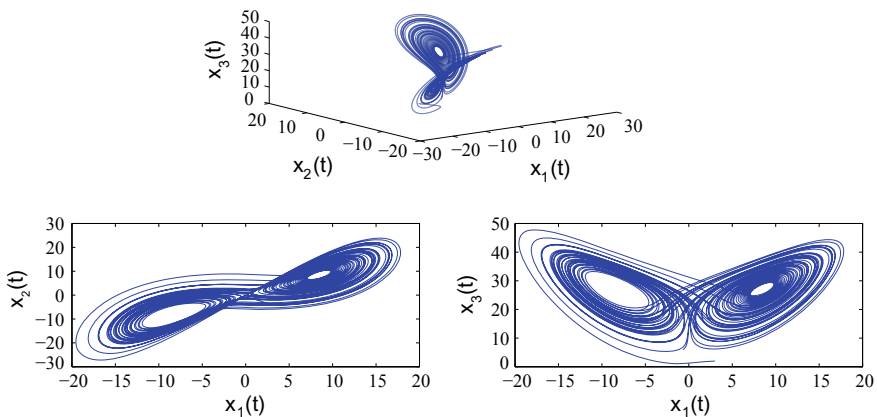


Fig. 1 Lorenz system state-space trajectory

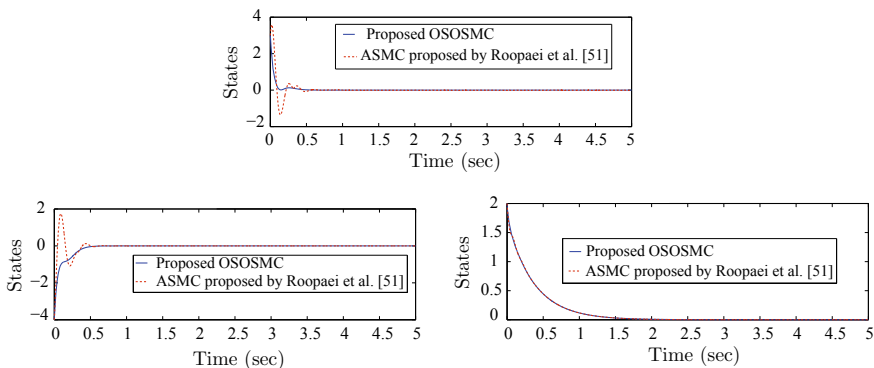


Fig. 2 Convergence of states using proposed OSOSMC and ASMC proposed by Roopaei et al. [16]

$$\begin{aligned}
 \dot{x}_1(t) &= -ax_1(t) + ax_2(t) + u(t) + \Delta f(x) \\
 \dot{x}_2(t) &= rx_1(t) - x_2(t) - x_1(t)x_3(t) \\
 \dot{x}_3(t) &= -bx_3(t) + x_1(t)x_2(t)
 \end{aligned}
 \tag{25}$$

The performance index are chosen as

$$J = \int_0^\infty \left(x^T(t) \begin{bmatrix} 1 & 0 & 0 \\ 0 & 1 & 0 \\ 0 & 0 & 1 \end{bmatrix} x(t) + u^T(t)u(t) \right)
 \tag{26}$$

Using the SDRE-based optimal control the feedback control $u_1(t)$ is found as $u_1(t) = -R^{-1}B^T P(x)x$ where $R = 1$, $B = [1 \ 0 \ 0]^T$, and $P(x)$ is the solution of the SDRE defined in (8). Design parameter of the integral and terminal sliding mode controller are chosen as follows:

$$C = [1 \ 0 \ 0], \quad p = 7, \quad q = 5 \quad \text{and} \quad \lambda = 0.2$$

Convergence of states is shown in the Fig. 2. States obtained by employing the proposed OSOSMC and adaptive sliding mode controller (ASMC) proposed by Roopaei et al. [16] is compared here. From this figure, it can be claimed that convergence time for the states are more or less same for the both of the controller.

In Fig. 3, the characteristic of the proposed OSOSMC and ASMC proposed by Roopaei et al. [16] is highlighted. From this figure it can be claimed that proposed controller is capable to reduce but the required control energy and chattering, Though the convergence time for the states is same.

To validate the claim more clearly, total variance (TV) [17] and control energy (second norms of $u(t)$) is calculated for the zero to five seconds with sampling time 0.01 seconds for both the controller. The control indices are shown in Table 1.

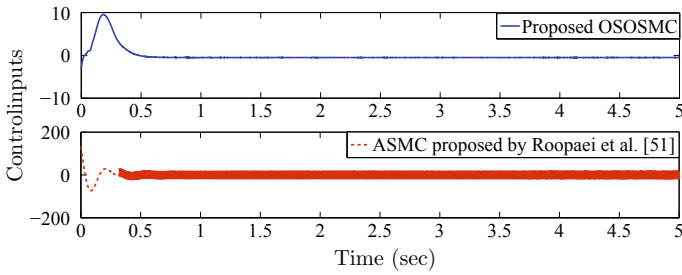


Fig. 3 Characteristic of control inputs [16]

Table 1 Control indices for both the controller

Methods	Total variance (TV)	Control energy
ASMC [16]	6074.00	438.00
Proposed OSOSMC	25.29	36.00

6 Conclusion

The paper proposed a robust optimal controller to stabilize an uncertain chaotic system. The optimal controller based on the state-dependent Riccati equation is designed to tackle the known part of the system. System uncertainties and disturbance have impact on the performance of chaotic systems. To ensure the robustness an integral sliding surface is designed to combine the optimal control with the sliding mode control. To design integral sliding mode control law information about initial condition is not needed. For finite reaching a non singular terminal sliding manifold is designed based on integral sliding manifold. A second-order sliding mode is formed by designing a terminal sliding surface based on the integral sliding surface. It reduces the harmful chattering phenomenon present in first order sliding mode. The proposed OSOSMC is employed to Lorenz chaotic system affected by uncertainties and compared with already developed sliding mode control method.

References

1. Yu W (1999) Passive equivalence of chaos in lorenz system. *IEEE Trans Circuits Syst I: Fundam Theory Appl* 46(7):876–878
2. Chan S-C, Tang WKS (2009) Chaotic dynamics of laser diodes with strongly modulated optical injection. *Int J Bifurc Chaos* 9(10):3417–3424
3. Ott E, Grebogi C, Yorke JA (1990) Controlling chaos. *Phys Rev Lett* 64:1196–1199
4. Wang H, Han ZZ, Xie QY, Zhang W (2009) Sliding mode control for chaotic systems based on LMI. *Commun Nonlinear Sci Numer Simul* 14(4), pp 1410–1417
5. Chang K-M (2008) Adaptive control for a class of chaotic systems with nonlinear inputs and disturbances. *Chaos, Solitons Fractals* 36(2):460–468

6. Yongguang Y, Suochun Z (2003) Controlling uncertain lü system using backstepping design. *Chaos, Solitons Fractals* 15(5):897–902
7. Solak E, Morgül Ö, Ersoy U (2001) Observer-based control of a class of chaotic systems. *Phys Lett A* 279(1–2), 47–55
8. Edwards C, Spurgeon SK (1998) Sliding mode control: theory and applications. Taylor and Francis
9. Young KD, Özgüner Ü (1997) Sliding-mode design for robust linear optimal control. *Automatica* 33(7):1313–1323
10. Lewis FL, Vrabie DL, Syrmos VL (2012) Optimal control. Wiley
11. Cloutier JR, Stansbery D (2002) The capabilities and art of state-dependent riccati equation-based design. In: Proceedings of the 2002, American control conference, 2002, vol 1, pp 86–91
12. Laghrouche S, Plestan F, Glumineau A (2007) Higher order sliding mode control based on integral sliding mode. *Automatica* 43(3):531–537
13. Hung J, Gao W, Hung J (1993) Variable structure control: a survey. *IEEE Trans Ind Electron* 40(1):2–22
14. Komurcugil H (2012) Adaptive terminal sliding-mode control strategy for DC-DC buck converters. *ISA Trans* 51(6):673–681
15. Wang Y, Zhang X, Yuan X, Liu G (2011) Position-sensorless hybrid sliding-mode control of electric vehicles with brushless DC motor. *IEEE Trans Veh Technol* 60(2):421–432
16. Roopaei M, Sahraei BR, Lin T-C (2010) Adaptive sliding mode control in a novel class of chaotic systems. *Commun Nonlinear Sci Numer Simul* 15(12):4158–4170
17. Skogestad S (2003) Simple analytic rules for model reduction and PID controller tuning. *J Process Control* 13(4):291–309

Jaya Algorithm Based Optimal Allocation of Distributed Energy Resources



Manoj Kumawat, Nitin Gupta, Naveen Jain and R. C. Bansal

Abstract In this study, energy demand growth with environment issues is considered towards the environment-friendly planning of smart distribution network. Therefore, Distributed Energy Resource (DERs) can be located to supply the required system energy demand. This paper presents Jaya algorithms that can deal with the placement of DERs with most effectively in radial distribution networks. This algorithm is a powerful optimization method which can be easily handled in the single-phase without any algorithms-specific control parameter. The strength of the proposed strategy is validated on two distribution networks as IEEE 33-bus and 69-bus test systems. The results are compared with already established methods as suggested in the literature. The result would be proved that the proposed approach is a robust approach that enhances the network performance by diminishing the demand for the distribution load within the constraints of the system.

Keywords Backward/forward power flow · Distributed energy resource · Jaya algorithm · Smart distribution system

1 Introduction

In the present scenario, conventional power systems are producing various types of problems such as voltage deviations, high capital cost, static-, dynamic-, and transient- stability problems, overloaded lines, high levels of resistive losses, service

M. Kumawat (✉)

Department of Electrical and Electronics Engineering, MCE, Motihari 845401, India
e-mail: mnit2010pee117@gmail.com

N. Gupta

Department of Electrical Engineering, MNIT Jaipur, Jaipur 302017, India

N. Jain

Department of Electrical Engineering, CTAE, MPUAT, Udaipur 313001, India

R. C. Bansal

Department of Electrical and Computer Engineering, University of Sharjah, Sharjah, UAE

© Springer Nature Singapore Pte Ltd. 2020

A. Kalam et al. (eds.), *Intelligent Computing Techniques for Smart Energy Systems*,
Lecture Notes in Electrical Engineering 607,
https://doi.org/10.1007/978-981-15-0214-9_85

805

interruptions, and high amount of emissions [1]. Moreover, the regulatory commission is focused on environmental issues which object to reduce the pollutants content in the atmosphere by decreasing the percentage of fossil fuel from the power plant and increase the percentage of renewable sources in distribution system [2]. In addition to this issue, technological innovations under upcoming economy introduced the renewed interest in distributed energy resources (DERs) to supply the incremental demand of the distribution system in the deregulated power system.

An innovative and environment-friendly approach is to generate electric power locally at the distribution network using distributed sources such as solar photovoltaic, wind turbines, small hydropower generation, fuel cells, biomass, and capacitor. This type of power generation is called distributed generation. Moreover, resources are used to provide the energy, named as distributed energy resources (DERs) [1]. These technologies have their limitations and advantages [3]. However, besides the several restrictions, the DERs contributes in the diversification of DERs to enhance the energy security, increases the potential for service quality, reduces the operating cost of peak load and competitive policies, supports for uncertainty in the electricity market, and decreases the cost and losses of the system [4]. Hence, DERs' penetration into the distribution system would be required to improve system performance. Moreover, unplanned allocation of the DERs may be distorted to the distribution system. Therefore, the planning is important to avoid the mortification of distribution service.

In [5–10], the various optimization algorithms were applied to minimizing power loss by optimized DERs allocation in the radial distribution network. However, the analytical based optimization algorithms conversion at a single point. Therefore, the distribution system planner has not considered the planning of multiple DGs in the large-scale distribution system. Further, the swarm optimization technique has been applied for the optimistic location of the different type of distributed generators in the radial distribution networks.

A genetic algorithm is a mature heuristic method. However, it takes high processing time and even fails to converge in some applications [5]. Therefore, hybrid heuristic algorithms have been applied to compensate for the negative impact of the other algorithm. Hybrid swarm-based algorithms have obtained the minimum energy loss whenever constraints of distribution are also satisfied at every location of DERs [6]. However, the efficiency and computational time are inversely proposals in any hybrid approach.

Further, a single evolutionary method is suitable whenever the computational time also significantly essential to obtain the optimal solution for DERs planning. However, the particle swarm optimization (PSO) has exploration and greater diversity in any dimensional population(s). Moreover, the PSO algorithm obtained the fastest conversion speed by the momentum effect on particles. The heuristic algorithms are widely used for distributed generation planning to minimize the losses by tuning some algorithms-specific control parameters [7]. However, Teaching Learning-Based Optimization (TLBO) is a control parameter-less algorithms as applied in [8] to the simultaneous placement of DERs on standard distribution system while considering multilevel load scenario. Further, a Jaya algorithm is also algorithms-specific control

parameters less method which operates in a single phase as compared to the TLBO. Therefore, this algorithm is simple to apply with a powerful effort to search the global solution.

This paper is presenting a Jaya algorithm for DERs planning on two IEEE standard radial distribution systems. Simultaneous allocation of DGs and SCs in 33 and 69 bus distribution systems usually enhanced the loss reduction with satisfied all constraints of the distribution system. Comparison with a recently published article [8] shows the strength of the applied method. The salient features of the paper are given below:

- (1) Jaya algorithm is the specific parameter-less method which can be applied with the simple process to achieve admirable outcomes.
- (2) The energy demand of the radial distribution systems is addressed using the optimal allocation of the distribution resources in multilevel load pattern.

2 Problem Description

The optimal allocation of DERs by minimizing the energy losses would be enhanced the benefits of the system with better bus voltage profile. However, a nonoptimal allocation may produce an unpredictable voltage profile which is a cause of poor power quality. Therefore, the node voltage of the distribution system should be laid in the specified boundary.

$$F = \max \left[\rho \left(\sum_{i=1}^{n_l} P_{\text{loss},bi} * t - \sum_{i=1}^{n_l} P_{\text{loss},ai} * t \right) \right] \quad \forall i \in n_l \quad (1)$$

where, $P_{\text{loss},bi}$, and $P_{\text{loss},ai}$ is the power losses of the distribution system in each load level in the absence and presence of DERs.

2.1 Boundary Limit of Node Voltage

$$V_{\text{min}} \leq V_{m_i} \leq V_{\text{max}} \quad (2)$$

The lower limit of node voltage V_{min} is 0.95 p.u. and the upper restriction of node voltage V_{max} is 1.05 p.u.

2.2 Power Balance

In the system, the total generation of power from the distributed energy resources and grid must be equal to the addition of demand and losses of the network.

$$S_{\text{Grid}} + \sum_{i=1}^{n_b} S_{\text{DER}} - \sum_{i=1, j=j+1}^{n_b} B_{ij}^2 \cdot Z_{ij} = \sum_{i=1}^{n_b} S_D \quad (3)$$

2.3 Distribution Thermal Limit

The thermal capacity must be considered as constraints because the line of the network should be capable of carrying the current at a given condition.

$$S_{ij, \text{max}} \geq S_{ij} \quad \& \quad S_{ji, \text{max}} \geq S_{ji} \quad (4)$$

2.4 DERs Generation

The unit size of DGs and SCs should always be operated in the specified standard of the distribution system.

$$P_i^{\min} < P_{DG_{s_i}} \leq P_i^{\max} \quad (5)$$

$$Q^{\min} < Q_{SC_{s_i}} \leq Q^{\max} \quad (6)$$

3 Description of the Jaya Algorithm

Jaya algorithm is a simple optimization algorithm [9]. The process of the algorithm is used the best and worst solution of each step of the process to optimize the solution in best direction. It means, the solution should move towards or close to the best, to best result and away from the worst result. Therefore, this algorithm has optimized the problem with perfect consistency in very less computation time.

The Jaya algorithm has different characteristic as compared to other optimization techniques. Each algorithm has required a specific parameter to obtain the best solution. The value of the specific parameters is varied according to the application of

algorithms. However, Jaya method does not require any algorithm-specific parameter for neither constraints nor unconstraint problems. Therefore, Jaya algorithm is a parameter-less method. The process of Jaya is different from Teaching Learning-Based Optimization (which uses two phases: Teaching and Learning), whenever Jaya algorithm requires only one phase. Therefore, the applied algorithm consumes less computation time. In a comparison of TLBO, the Jaya algorithm can be handled effortlessly on any constrained or unconstrained problem for optimization. This algorithm is greedy to get success, so it always tries to get a best, to best solution and tries to avoid the worst solution or failure. Hence, it makes every effort to become victorious and to reach the best solution. Therefore, this algorithm is known as ‘Jaya’ (‘Jaya’ is a Sanskrit word which means ‘Victory’). In addition to this, it is very easier to understand and simpler to apply.

The step-by-step process of Jaya algorithm implemented to optimizing the DERs penetration at optimized siting in the distribution system is expressed as follows:

Step 1. Initialize the population and decision parameter for Jaya algorithm as:

- Parameters for Decision: S_z, S_t (S_z : DER Size, S_t : DER Site)
- Number of design variables: d_n (Number of DERs for planning)
- Number of Population: m
- Iteration: $itr = 100$ (number of generations)
- DG/SC size Limit: U_L —Upper limit, L_L —Lower Limit

$$L_L < S_z < U_L$$

(U_L and L_L would be assigned as per the requirement of the distribution network and geographic condition)

- Define the objective function $f(X)$: Minimize $f(X)$ where $f(X)$ is the objective function which will compute the annual loss reduction.

Step 2. Randomly assign the decision parameter of DERs for every population which can be expressed such as:

For Size of DERs	For Siting of DERs
$Cand \cdot S_z = \begin{pmatrix} x_{1,1} & x_{1,2}, \dots, x_{1,d_n} \\ x_{2,1} & x_{2,2}, \dots, x_{2,d_n} \\ \dots & \dots & \dots & \dots \\ x_{m,1} & x_{3,2}, \dots, x_{N_p,d_n} \end{pmatrix}$	$Cand \cdot S_t = \begin{pmatrix} x_{1,1} & x_{1,2}, \dots, x_{1,d_n} \\ x_{2,1} & x_{2,2}, \dots, x_{2,d_n} \\ \dots & \dots & \dots & \dots \\ x_{m,1} & x_{3,2}, \dots, x_{N_p,d_n} \end{pmatrix}$

Step 3. Evaluate the objective function on the randomly generated candidate’s data values and calculate the annual energy losses of the system as $Solution_{\alpha\beta}$ (where $\alpha = 1, 2, \dots, m$ and $\beta = 1, 2, \dots, d_n$).

Step 4. At the iteration itr , according to the solution of entire candidates, select a particle that gives the best solution and assigns it as $Best_\beta$ and also find another particle, which calculates the worst result assigned as $Worst_\beta$. Further, applying the following equation on the candidate’s data:

$$\begin{aligned}
 Cand \cdot S_{zitr}^{new} = Cand \cdot S_{zitr}^{old} + \underbrace{r_1(\text{Best}_\beta - |Cand \cdot S_{zitr}^{old}|)}_{\text{Term}_1} - \underbrace{r_2(\text{Worst}_\beta - |Cand \cdot S_{zitr}^{old}|)}_{\text{Term}_2}
 \end{aligned}
 \tag{7}$$

$$\begin{aligned}
 Cand \cdot S_{iitr}^{new} = Cand \cdot S_{iitr}^{old} + \underbrace{r_1(\text{Best}_\beta - |Cand \cdot S_{iitr}^{old}|)}_{\text{Term}_1} - \underbrace{r_2(\text{Worst}_\beta - |Cand \cdot S_{iitr}^{old}|)}_{\text{Term}_2}
 \end{aligned}
 \tag{8}$$

where, r_1 and r_2 are two random numbers, which explore the search area for the best solution. The part of the above equation ‘‘Term₁’’ designates the leaning of the solution to move closer to the best solution, and another part ‘‘Term₂’’ indicates the tendency of the result to away from the worst solution. The above equation uses the absolute value of the candidate’s decision parameters which may also increase the exploration capability of the Jaya algorithm.

Step 5. Apply the backward–forward load flow function on new calculated candidates. If $Cand \cdot S_{zitr}^{new}$ gives a better result than $Cand \cdot S_{zitr}^{old}$, then accept the new selected particle otherwise remain as previously generated candidate’s decision parameters.

Step 6. Afterward, apply the constraint handling mechanism and check limits of the updated decision parameters, whenever it is not satisfied, then again it generates S_z and S_t of the learner randomly. Further, assure the modified DER has not repeated location. Moreover, if it is repeated then it removes the duplicity of them by generating a new S_t randomly.

Step 7. Terminate/Stop, if the maximum number of iterations itr is reached then show the optimal result. Else, the accepted function values of each iteration itr are maintained and these values become the input to the next iteration. With this input, go to step 4 and run the whole process until stopping criteria is not satisfied.

4 Simulation Results

In this section, Jaya algorithm is validated on the standard 33-bus [10], and 69-bus [10] radial distribution network and results are compared with well established Improved Teaching Learning-Based Optimization (ITLBO) [8] which is distinguished in case I for each test system.

The annual load profile is classified in light (L), nominal (N), and peak (P) load level. The light load is 50% of nominal load, and peak load level is 160%. The light load level is present for 2000 h and a nominal load level for 5260 h. Moreover, the peak load level contains only 1500 h. The backward/forward power flow method is applied for power load flow of the distribution system.

Table 1 Optimal performance parameter for test system 1 (33-bus)

Particular	Node (DGs in kW)	Node (SCs in kVAr)
Light load level	13(395), 30(510), 24(524)	30(500), 25(200), 14(200)
Nominal load level	13(789), 30(1027), 24(1055)	30(1000), 25(400), 14(400)
Peak load level	13(1092), 30(1299), 24(572)	30(1300), 25(300), 14(500)

Table 2 Performance comparison for 33 bus system

Cases	Load level	P_{loss} (kW)	V_{min} (p.u.)	Annual E_{loss}	
				MWh	Reduction (%)
I	Light	3.02	0.9963	191.83	90.52
	Nominal	11.94	0.9911		
	Peak	81.99	0.9500		
II	Light	2.97	0.9963	169.75	91.61
	Nominal	11.94	0.9910		
	Peak	67.34	0.9656		

4.1 Test System 1: 33 Bus Radial Distribution Network

The details of the standard 33-bus distribution network are given in [10], has been applied to corroborate the Jaya algorithm. The DERs have got the optimal penetration for each load level after 100 autonomous trails. Further, the applied algorithm achieved more diminution of annual energy losses. The optimal performance parameters are determined by the Jaya algorithm which is shown in Table 1.

Case II used the performance parameter of the applied method. Further, Table 2 shows the comparison of system performance between case 1 and case II.

Figure 1 demonstrates the node voltage profile for different load level in the system. There is a significant improvement in bus voltage profile as prevailed by the applied method. In the second case, losses are low from the case I for each load level. Therefore, it depicts the most affirmative assess of DERs is obtained by the applied algorithm.

4.2 Test System 2: 69 Bus Radial Distribution Network

A 69-bus distribution network [10] is considered as the secondary system. The best allocation of the DERs for this network is obtained after 100 trails of the Jaya algorithm which are shown in Table 3. Further, it attains the maximum diminution of annual energy losses.

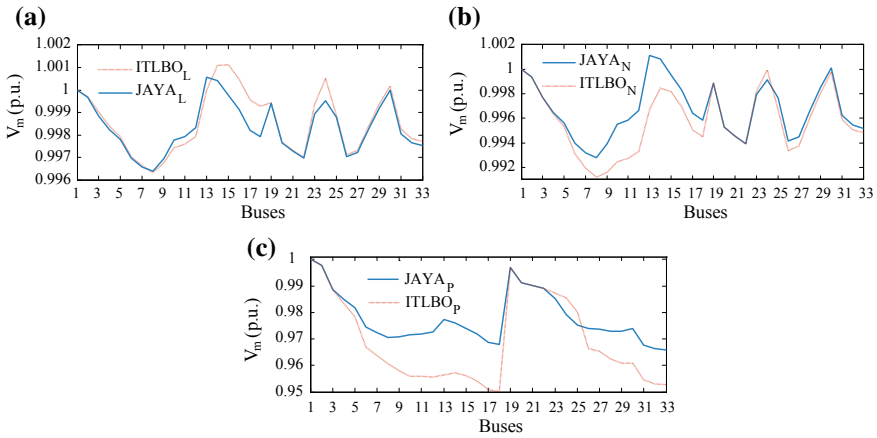


Fig. 1 The comparison of the node voltage profile of the standard 33 bus system **a** light load level **b** nominal load level **c** peak load level

Table 3 Optimal performance parameter for test system 2 (69-bus)

Particular	Node (DGs in kW)	Node (SCs in kVAr)
Light load level	19(200), 10(251), 61(836)	19(100), 10(200), 61(600)
Nominal load level	19(380), 10(523), 61(1672)	19(300), 10(300), 61(1200)
Peak load level	19(488), 10(300), 61(1899)	19(200), 10(200), 61(1300)

The performance parameter is obtained by an applied method which is used to improve the system performance. Further, Table 4 shows the comparison of system performance between case 1 and case II.

Figure 2 is depicted the comparison of node voltage profile for all load level of the network. The Jaya algorithm has achieved a significant improvement in the node voltage profile of all load level.

Table 4 Performance comparison for 69 bus system

Cases	Load level	V_{min} (p.u.)	P_{loss} (kW)	Annual E_{loss}	
				MWh	Reduction (%)
I	Light	0.9971	1.082	134.16	94.08
	Nominal	0.9943	4.331		
	Peak	0.9500	72.81		
II	Light	0.9971	1.142	128.16	94.34
	Nominal	0.9942	4.554		
	Peak	0.9533	67.95		

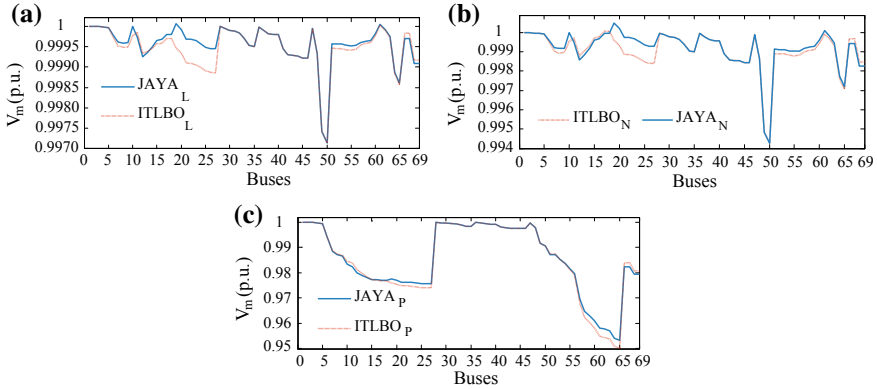


Fig. 2 Node voltage profile of test system 2 **a** light load level **b** nominal load level **c** peak load level

Further, it accomplishes the maximum diminution of annual energy losses in every test system and corresponding their load level from ITLBO. Therefore, the Jaya algorithm achieved the best result without tuning of any control parameter of the algorithm.

5 Conclusion

Integrating DERs in the radial distribution network is accomplishing popularity in restructured power system due to the significant positive impacts. In this work, a Jaya algorithm is applied which is a generic simple and parameter-less method. This method is used to optimize the best location of DERs and optimistic penetration level of the DERs in the medium voltage distribution network under the different load conditions. The application results of the proposed method using Jaya algorithm have better performance as compared to Improved Teaching Learning-Based Optimization in all test cases. The applied method is well screened for each case for its reliability and robustness.

References

1. Rahman HA, Majid MS, Jordehi AR, Kim GC, Hassan MY, Fadhil SO (2015) Operation and control strategies of integrated distributed energy resources: a review. *Renew Sustain Energy Rev* 51:1412–1420
2. Kumawat M, Gupta N, Jain N, Bansal RC (2017) Optimally allocation of distributed generators in three-phase unbalanced distribution network. *Energy Procedia* 142:749–754
3. Akorede MF et al (2010) A critical review of strategies for optimal allocation of distributed generation units in electric power systems. *Int R Electr Eng (Part B)* 5(2):593–600

4. Kumawat M, Gupta N, Jain N, Bansal RC (2018) Optimal planning of distributed energy resources in harmonics polluted distribution system. *Swarm Evol Comput* 39:99–113
5. Kanwar N, Gupta N, Niazi KR, Swarnkar A (2015) Improved meta-heuristic techniques for simultaneous capacitor and DG allocation in radial distribution networks. *Int J Electr Power Energ Syst* 73:653–664
6. Sattianadan D, Sudhakaran M, Dash SS, Vijayakumar K (2013) Cost/ loss minimization by the placement of DG in distribution system using GA and PSO—a comparative analysis. *Int R Electr Eng* 8(2):769–775
7. Kumawat M, Gupta N, Jain N, Saxena D (2015) Optimal distributed generation placement in power distributed networks: a review. In: *International conference on electrical, electronics, signals, communication and optimization*, pp 1–6
8. Kanwar N, Gupta N, Niazi KR, Swarnkar A (2015) Simultaneous allocation of distributed resources using improved teaching learning-based optimization. *Energy Convers Manag* 103:387–400
9. Rao R (2016) Jaya: a simple and new optimization algorithm for solving constrained and unconstrained optimization problems. *Int J Ind Eng Comput* 7(1):19–34
10. Acharya N, Mahat P, Mithulananthan N (2006) An analytical approach for DG allocation in the primary distribution network. *Int J Electr Power Energ Syst* 28(10):669–678

Bayesian Game Model: Demand Side Management for Residential Consumers with Electric Vehicles



Akash Talwariya, Santosh Kumar Sharama, Pushpendra Singh and Mohan Kolhe

Abstract This paper proposes the game theory enabled approach for the integration of electric vehicles for demand side management (DSM). Demand side management is very complex with conventional approaches. In order to the efficient mechanism of a game theory enabled approach may resolve the complexity. With the increased penetration level of electric vehicles it will be difficult to control grid-to-vehicle integration. The Bayesian game theory provides the solution of such problems in an organized manner. In the presence of distributed energy resources, Electric vehicles will play an important role to stabilize the grid integration. Electric Vehicles consume power during off-peak load period and inject power to grid during peak load period to minimize peak to average ratio (PAR).

Keywords Smart grid · Demand side management · Bayesian game model · Electric vehicles

1 Introduction

This paper evolves an approach based on game theory for efficient energy tariff with different price functions during normal and peak hour consumption. Information about electric energy price is provided through a communication network operated by DSM center [1]. Two broad conditions (i) Intelligent Electronic Devices (IED's) and (ii) Real time price mechanism, are required to galvanize the DSM [2]. IED's are having the capability to communicate with local appliances as well as the utility [3]. The real time price mechanism is a method to provide information about energy price to consumers on hourly basis [4]. Most of the consumers are only interested in their

A. Talwariya (✉) · P. Singh
JK LakshmiPat University, Jaipur, India
e-mail: akash.talwariya@gmail.com

S. K. Sharama
Rajasthan Technical University, Kota, India

M. Kolhe
University of Agder, Kristiansand, Norway

© Springer Nature Singapore Pte Ltd. 2020
A. Kalam et al. (eds.), *Intelligent Computing Techniques for Smart Energy Systems*,
Lecture Notes in Electrical Engineering 607,
https://doi.org/10.1007/978-981-15-0214-9_86

benefits, incentive-based tariff is a methodology used to motivate the consumers for DSM, mostly used price mechanisms are time of use, stepwise power tariff, two-part tariffs, real time pricing, critical time pricing, etc. [5]. Domestic consumers with EV's (Electric Vehicle's) get attention of most researchers. EV's charging and discharging schedule manage peak to average power consumption ratio.

Demand side management is a complex problem which includes distribution network operator, consumers with DG installations, consumers, consumers with EV's, and utilities. There are numerous approaches for the electrocution of DSM which are game theory, machine learning, IoT, artificial intelligence, fuzzy logic controller's, Genetic algorithm, etc.

This research paper proposes the demand side management using game theory. Energy tariff game based on the degree of information shared is categorized into two types, complete information game, and incomplete information game or Bayesian game. All information about payoff's of participated consumers are shared is classified as complete information game.

In order to maximize the things, a part of information about payoff's is not shared by the consumer, to optimize the issue Bayesian game model is design [6]. For the implementation of Bayesian game model, participating agents are consumers, distributed network operators (DNO), EV's, solar photovoltaic systems and small wind generators. Results obtained from the proposed approach focuses the benefits of consumers by reducing the peak to average consumption ratio.

2 System Model

Smart grid with N domestic consumers, one energy producer and demand side management center is shown in Fig. 1. To schedule the energy consumption of domestic

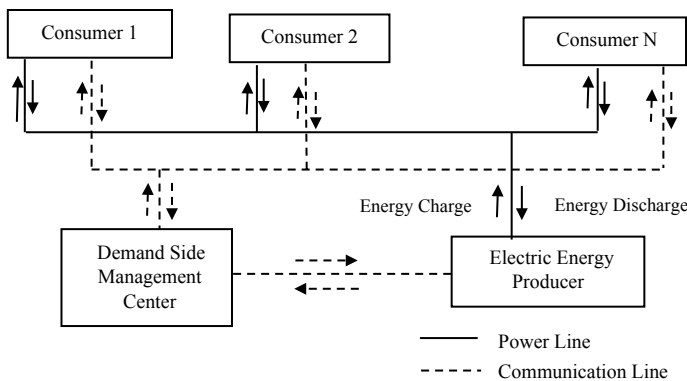


Fig. 1 Energy consumption management scenario

consumers and share the information with other consumers. Some assumptions are taken:

- i. Each consumer is connected with IED's.
- ii. Each consumer having electric vehicles.

Demand side management center is the control center of the grid which collects the information about consumption design tariff structure and informed to consumers through communication network. Grid is designed with an assumption that each consumer have EV's which could supply energy to grid as per the instructions of DSM center [7]. The set of consumers is denoted by $\underline{N} = \{1, 2, \dots, n, \dots, N\}$ and time \underline{T} is divided into different slots and denoted by $\underline{T} = \{1, 2, \dots, t, \dots, T\}$.

2.1 Energy Consumption Cost Model

Let energy consumption of household consumer $n \in \underline{N}$ is E_n^t in time slot $t \in \underline{T}$ and the total consumption for user n is calculated as

$$E_n = \sum_{t \in \underline{T}} E_n^t \quad (1)$$

The total energy consumption for all residential consumers in time slot $t \in \underline{T}$, E_t^r can be formulated as

$$E_t^r = \sum_{n \in \underline{N}} E_n^t \quad (2)$$

The total energy consumed during charging of electric vehicles E_t^c is formulated as

$$E_t^c = \sum_{n \in \underline{N}} E_n^t \quad (3)$$

Similarly, let $E_{n,t}^d$ represents the energy discharge to the grid with EV's in time slot $t \in \underline{T}$ and total energy discharge to the grid for all EV's is

$$E_t^d = \sum_{n=1}^N E_{n,t}^d \quad (4)$$

To encourage the consumers for managing the demand, a tariff structure based on incentives for consumers is design. It manage the peak to average energy consumption ratio:

$$C_t = \alpha_t(E_t) + \beta_t \quad (5)$$

where α_t , β_t are the coefficient of energy cost $\alpha_t > 0$ and $\beta_t \geq 0$, and directly proportional to total energy consumed.

The cost of energy consumed by the consumer n th in a day is formulated as

$$C_n = \sum_{t=1}^T T_t(E_t)(E_t^r + E_t^c) \quad (6)$$

2.2 Payoff Model for EV's

The fundamental objective of consumers procuring EV's is traveling, thus users will give preference to traveling and then the excess amount of energy is injected to grid [8]. Let, consumer n have EV with storage capacity Q_n and EV expend Q_n^v on road for primary fulfillment. If the consumer has excess energy in EV's when consumer goes back to home, consumer can discharge the remaining energy to grid. Let, n th consumer have Q_n^d energy discharge to grid in a day, then the total energy of the EV for n th consumer is denoted as:

$$Q_n = Q_n^v + Q_n^d \quad (7)$$

A reasonable discharge model is required to motivate the consumers for discharging during peak hours. Discharging model is required, if all consumers will discharge electricity in a certain time to maximize their benefits will damage the stability of the system and enhancing the overall power losses. Therefore, energy price for discharging is continuous and decreasing function. In addition, the price of injected period should be higher to the price of purchasing to provide benefit to consumers. Therefore, the price model for discharging on incentive mechanism is formulated as:

$$I_t^d(E_t^d) = \alpha_t^d E_t^d + \beta_t^d \quad (8)$$

where α_t^d and β_t^d are coefficient of discharging cost and varied time slots, $\alpha_t^d < 0$ and parameter $0 < \beta_t^d < \beta_t$. Therefore, the total utility function of EV's for consumer n in the whole day is formulated as:

$$U_n(E_n^d, E_{-n}^d) = \sum_{t=1}^T (I_t^d(E_t^d)E_{n,t}^d) + Q_n^v \quad (9)$$

where $E_{-n}^d = [E_1^d, \dots, E_{n-1}^d, E_{n+1}^d, \dots, E_N^d]$ is denoted all consumers cost except E_n^d . $\sum_{t=1}^T E_{n,t}^d = Q^d$ and $E_{n,t}^d \leq E_n^{d\max}$, where $E_n^{d\max}$ is the maximum discharged energy with EV's in one hour.

On the basis of the analysis of consumption cost and discharge function, total cost of domestic consumer n can be formulated as:

$$H_n(E_n^d, E_{-n}^d) = C_n - U_n(E_n^d, E_{-n}^d) \tag{10}$$

3 Bayesian Game for Household Consumers

Bayesian game theory is based on uncertainty about the payoff's of other consumers [9]. Bayesian game has two factors: type of player and probability distribution of the players. Type of consumer on the bases of the degree of information shared is the set of $J_n = \{J_1, \dots, J_n, \dots, J_N\}$ and the probability of type of household consumers can be defined by probability function:

$$p_n(J_{-n}|J_n) = \frac{p(J_{-n}, J_n)}{\sum p(J_{-n}, J_n)} \tag{11}$$

Payoff of the consumer n with type J_n is:

$$E_n(J_n) = \sum_{J_{-n} \in J_n} p_n(J_n, X_n(J_n), X_{-n}(J_{-n})) \cdot p(J_{-n}|J_n) \tag{12}$$

where, $X_n(J_n) = [X_n^c(J_n), X_n^d(J_n)]$ denotes the charging and discharging approach of consumer n with type J_n , while $X_{-n}(J_{-n}) = [X_{-n}^c(J_{-n}), X_{-n}^d(J_{-n})]$ denotes the strategy of competitor's for the type J_{-n} .

The Bayesian game is designed to maximize the profit by scheduling the approach $X_n(J_n)$ on the basis of the competitor's approach $X_{-n}(J_{-n})$. Therefore, the function $X_n(J_n)$ is converted into $X_n^*(J_n)$, then $[X_n^*(J_n), X_{-n}^*(J_{-n})]$, is called Nash Equilibrium of Bayesian game model, which is mathematically expressed as:

$$E_n[X_n^*(J_n), X_{-n}^*(J_{-n})] \geq E_n[X_n(J_n), X_{-n}(J_{-n})] \tag{13}$$

Nash equilibrium of Bayesian game is designed on the bases of the following algorithm (Fig. 2).

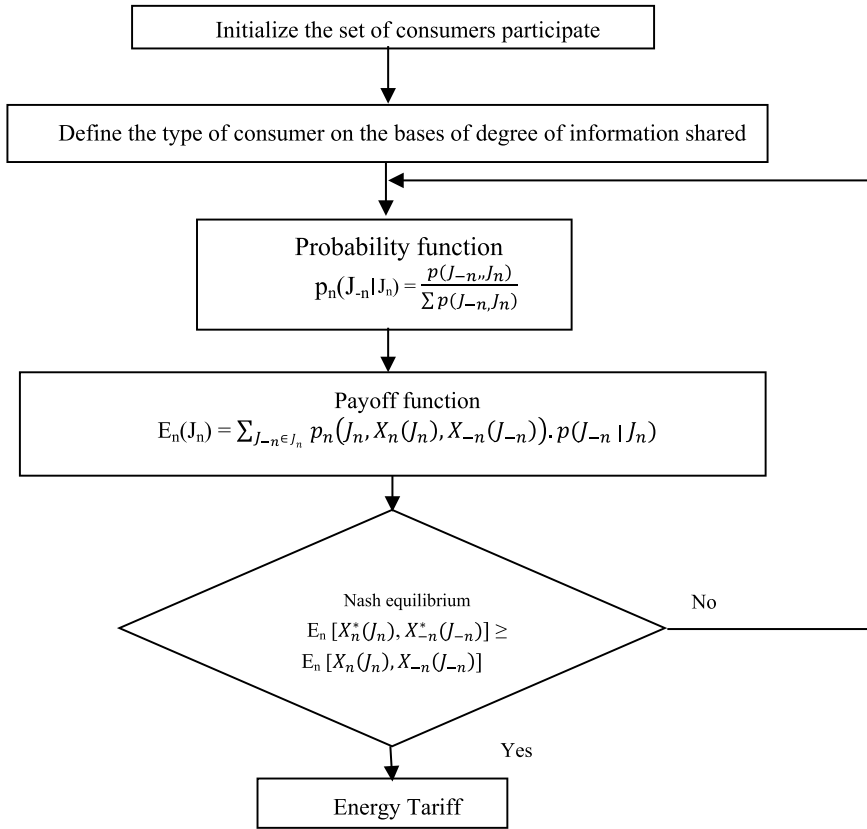


Fig. 2 Algorithm of bayesian game nash equilibrium

4 Simulation Results

A simulation-based on the proposed methodology is designed in MATLAB and effectiveness of the results are shown in this section. Suppose that there are 50 users and each user has an EV and IED's. Demand is managed for a day and one day is divided in 24 slots each slot is indicating 1 hour duration. Figure 3 denotes that from time 00:00 to 5:00 and at time 24:00 energy consumption is very less and it is defined as baseload consumption period, from time 06:00 to 15:00 and time 23:00 energy consumption is moderate and from time 15:00 to 22:00 energy consumption is very high and denoted as peak energy consumption period. As load curve defines that from duration 00:00 to 05:00 energy consumption is less and consumers can allowed to charge EV's, and during peak load period from 15:00 to 22:00 consumers are allowed to discharge their excess amount of energy to grid. In simulation parameters of purchase and selling are taken from [10] as shown in Table 1.

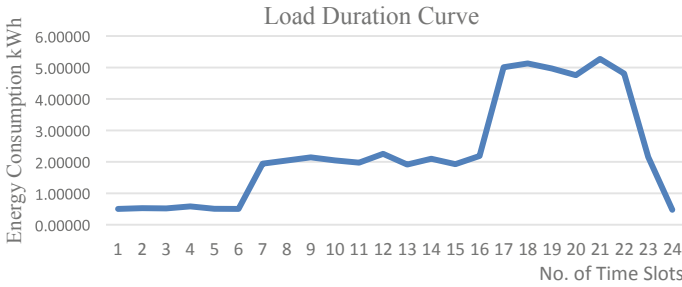


Fig. 3 Average consumption curve of N user's

Table 1 Parameters of consumption and EV's discharge in simulation

Time slot	0:00–5:00	5:00–15:00 and 22:00–24:00	15:00–22:00
α_t	0.0002	0.0003	0.0004
β_t	0.053	0.111	0.179
α_t^d	-	-0.0006	-0.0005
β_t^d	-	0.098	0.132

Table 1 shows the constraints value for energy consumption cost function (5) and EV's energy discharging function constraints (8). α_t^d negative value shows the decreasing function. Average energy consumption curve after applying game theory is shown in Fig. 4 represents the energy consumption during time 15:00 to 22:00 is reduced from 5.27 to 4.76 kWh.

Energy consumption cost is calculated and denoted in Fig. 5 with and without Bayesian game model shows that without game electricity cost of all consumers are more as compared to the cost of applying game. Average energy consumption cost during baseload hours are reduced from 5.3083 \$ to 2.9699, average moderate energy consumption cost is reduced from 8.2379 \$ to 5.8995 \$, and average peak hour consumption cost is reduced from 12.600 \$ to 10.2622 \$. Average cost without game is 8.4132 \$ reduced to 6.074807 \$ by applying Bayesian game model is providing benefit to the consumers.

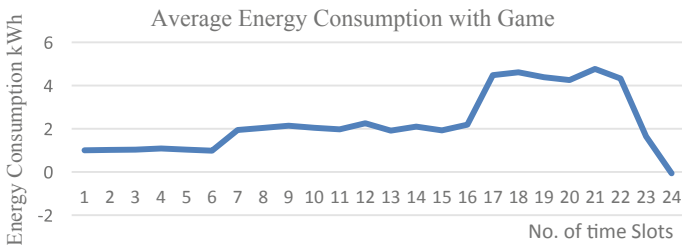


Fig. 4 Energy consumption after applying game theory

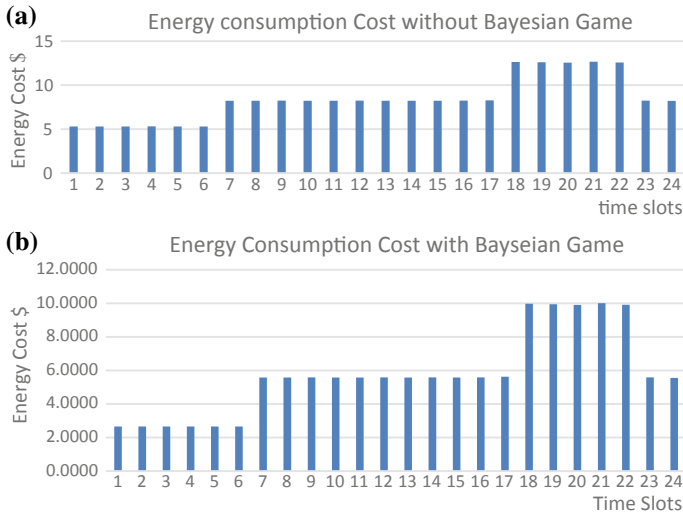


Fig. 5 Energy consumption cost **a** without Bayesian game **b** with Bayesian game

5 Conclusion

Game theory is applied for the feasibility of DSM to provide benefits to participating agents. Bayesian game is modeled for domestic consumers with incomplete information about the payoff's of other consumers. This paper highlights the effect of EV's on DSM, the proposed model focused on the methodology to inject energy to grid during peak hour consumption and absorb during baseload duration. Simulation results describe that peak to average energy consumption ratio is reduced from 2.34 to 2.29 and average energy consumption cost is reduced from 8.4132 \$ to 6.0748 \$. Therefore, the Bayesian game model is beneficial for both consumers and utilities.

References

1. Logenthiran T, Srinivasan D, Shun TZ (2012) Demand side management in smart grid using heuristic optimization. *IEEE Trans Smart Grid* 3(3):1244–1252
2. Zhou J, Hu RQ, Qian Y (2012) Scalable distributed communication architectures to support advanced metering infrastructure in smart grid. *IEEE Trans Parallel Distrib Syst* 23(9):1632–1642
3. Morello R, De Capua C, Lipari G, Lugarà M, Morabito G (2014) A smart energy meter for power grids. In: 2014 IEEE international instrumentation and measurement technology conference (I2MTC 2014), May 12–15 2014, Montevideo, Uruguay, pp 878–883
4. Lin B, Liu X (2013) Electricity tariff reform and rebound effect of residential electricity consumption in China. *Energy* 59:240–247
5. Gelazanskas L, Gamage KA (2014) Demand side management in smart grid: a review and proposals for future direction. *Sustain Cities Soc* 11:22–30

6. Mondal A, Misra S, Obaidat MS (2017) Distributed home energy management system with storage in smart grid using game theory. *IEEE Syst J* 11(3):1857–1866
7. Chen H, Li Y, Louie RH, Vucetic B (2014) Autonomous demand side management based on energy consumption scheduling and instantaneous load billing: an aggregative game approach. *IEEE Trans Smart Grid* 5(4):1744–1754
8. Eksin C, Deliç H, Ribeiro A (2015) Demand response management in smart grids with heterogeneous consumer preferences. *IEEE Trans Smart Grid* 6(6):3082–3094
9. Liu X, Gao B, Wu C, Tang Y (2016) Bayesian game-theoretic energy management for residential users in smart grid. In: *IEEE international conference on cyber technology in automation, control, and intelligent systems (CYBER)*, pp 67–71
10. Liu X et al (2017) Demand-side management with household plug-in electric vehicles: a bayesian game-theoretic approach. *IEEE Syst J*

Classification of Power System Disturbances Using Support Vector Machine in FPGA



Vivek Patel

Abstract Support vector machine (SVM) is a standard classification technique used to envisage accuracy of extracted data in the power system. A real time implementation of SVM is yet at premature phase, because of requirement of advance parallel calculation of features. In this paper, Software simulation of SVM using MATLAB and Hardware Co-simulation of SVM in FPGA is designed to classify power quality (PQ) disturbances. Initially IEEE 13 bus system is designed in PSCAD to generate various type of transient signals, caused by heavy load switching and capacitive switching. Here, three different statistical features are extracted for feature classification namely Means, Variance, and Standard Deviation of the signal. A Xilinx system generator block sets are used to simulate SVM using radial basis kernel (RBF) function. Simulation result, reveals that the FPGA based SVM classification system is fast and predicts high classification accuracy.

Keywords Support vector machine · FPGA · Capacitive switching · Load switching

1 Introduction

In the last 2–3 decades' evaluation of power system network main context was to control the frequency of power system fluctuating near 50 Hz, with the advancement of technology, use of an electrical instrument like an electrical machine, computer, etc., has increased. Therefore, uses of these devices increases the electrical load on the power system generally in day time, causing this voltage level of power system go down and expected to be boost. A capacitor bank is used for increasing the voltage level. When the capacitor bank is switched on then the voltage level increases along with switching transient. The line to ground (L-G) fault is most usual of all fault line to line, double line to ground, and 3-phase fault and this initiates the transient in voltage and current waveforms [1]. These transient are very dangerous for electrical

V. Patel (✉)
MNNIT, Allahabad, Uttar Pradesh, India
e-mail: royal.vivekk@gmail.com

© Springer Nature Singapore Pte Ltd. 2020
A. Kalam et al. (eds.), *Intelligent Computing Techniques for Smart Energy Systems*,
Lecture Notes in Electrical Engineering 607,
https://doi.org/10.1007/978-981-15-0214-9_87

825

system and due to this severe problem comes and this also affect the power system components, so it is essential to know which transient comes in power system and which can be suppressed.

There are plenty of literature that exist for classification with the objective of exploring SVM. As SVM is a strong candidate for pattern classification, Support Vector Machine (SVM) is a technique which can classify these transient data. It is one of the most reliable and good performance algorithm used widely in the field of linear, as well as nonlinear classification and regression problems [2, 3].

In the scientific community, most of the SVM related study is based on software up-gradation; various algorithms have been developed and tested on the software. Nevertheless, the first significant work of hardware implementation on SVM has been reported by Anguita [4]. D. Anguita has proposed a digital architecture for SVM training and classification using linear and RBF kernel functions, But the proposed hardware architecture utilized a lot of resources and not the desired computation time. The Maximum frequency obtained by D. Anguita was 35.3 MHz. Author Khan keeps away from the fixed-point computations for implementing testing phase of linear SVM by using logarithmic number system, but faced problems in converting real number to their equivalent logarithmic number [5, 6].

In the rest part of the paper, a basic of SVM is described in Sect. 2. Software Implementation of SVM and Hardware Implementation of Linear SVM discussed in Sect. 3. In Sect. 4, simulation result has been discussed in detail and the conclusion is given in Sect. 4.

2 Support Vector Machine

Support vector machine is one of the most powerful techniques of classification and regression initialized in the 1990s by Vapnik. SVM is basically a binary classifier but it can classify sample or data of multiclass, as well as it makes possible to solve linear as well as nonlinear classification or regression problems.

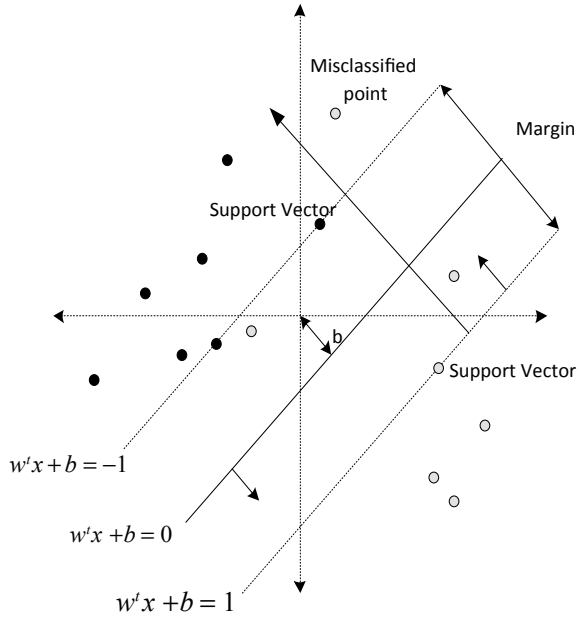
2.1 Linear SVM

The objective of linear SVM is to separate the hyperplane optimally with a large margin. Now assume a set of feature vector of training samples x_i which is to be separable linearly and have been tagged in class1 and class2 which shown in Fig. 1. Most of the data classify correctly but some data point falls into margin, called as slack variables [7].

So the decision function of the Linear SVM is defined as follows:

$$D(x) = \text{sign}(w^T x + b) \quad (1)$$

Fig. 1 SVM optimal separating hyperplane



We get Optimal hyperplane by solving dual Lagrangian problem in Eq. (2):

$$\begin{aligned}
 \text{Maximize } L_d(\alpha) &= \sum_{i=1}^N \alpha_i - \frac{1}{2} \sum_{i,j=1}^N y_i y_j \alpha_i \alpha_j x_i^T x_j & (2) \\
 \text{Subject to } &\begin{cases} 0 \leq \alpha_i \leq C \\ \sum_{i=1}^N \alpha_i y_i = 0 \end{cases}
 \end{aligned}$$

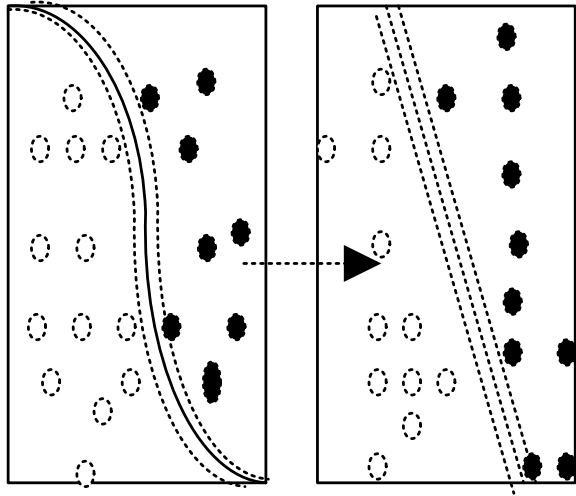
where W is a vector with real values and b is a constant, α_i is Lagrange multipliers, and y_i is the class label, which is either +1 or -1 value.

$$w = \sum_{i=1}^{SV} \alpha_i x_i y_i \quad b = y_i - w^T x_i$$

2.2 Nonlinear SVM

Practically in classification problem mostly it is not practicable to separate the data linearly in original space. SVM can get better of this problem by transfer vector x

Fig. 2 Nonlinear SVM mapping



from input space to higher dimension space $\Theta(x)$, where this conversion takes place by using Hilbert conversion, one where linear separation may be possible which is shown in Fig. 2.

Decision function of Nonlinear SVM can be expressed as given by the following Eqs. (3) and (4):

$$D(x) = \text{sign}\left(\sum_{j=1}^{sv} \alpha_j y_j K(x_j, x) + b\right) \tag{3}$$

$$b = y_j - \sum_{j=1}^{sv} \alpha_j y_j K(x_j, x) \tag{4}$$

when dot product replaced with the kernel function, then it accepts the algorithm to apposite the hyperplane with large margin and it is feasible to achieve nonlinear SVM classification [5].

Some kernel function:

polynomial kernel of degree p : $K(X, Y) = (X \cdot Y - 1)^p$

Radial basis function (RBF) kernel: $K(X, Y) = e^{-\frac{\|X-Y\|^2}{\sigma}}$

Hyperbolic tangent: $K(X, Y) = \tanh(\lambda X \cdot Y - \delta)$

When the kernel function is applied, then there is no necessity to map the input data into higher dimensional space.

3 Power System Transient

A transient in power system can be defined as the reaction of an electrical network to an abrupt change in network conditions, either intentional or unintentional, (e.g., fault, switching action, Islanding or lightning strike). A transient is a usual part of the operation where power system changes from one steady state condition to another. It occurs for very small duration (μs to ms) but it can be in large magnitude. The factors that affect the transient magnitude and characteristics are electrical source, transmission lines, other transmission components like capacitor banks and switching components.

Here, to analyze the transient events a 13 bus power system model has been Simulated in PSCAD software as shown in Fig. 3. It consists of 120 kV, 50 MVA and 50 Hz grid connected to the main transformer through bus B1. Three distributed generations (DGs), i.e., two wind plants connected at bus B9, B12 and one PV at bus B10 along with six loads at different busses are connected. Each load having same rating; 10 MW, 4 MVAR, and the busses are separated by a distance of 10 km using pi section distribution line. Here, power quality disturbance is created like, capacitive switching in Fig. 4, load switching in Fig. 5, fault signal in Fig. 6, and islanding in Fig. 7.

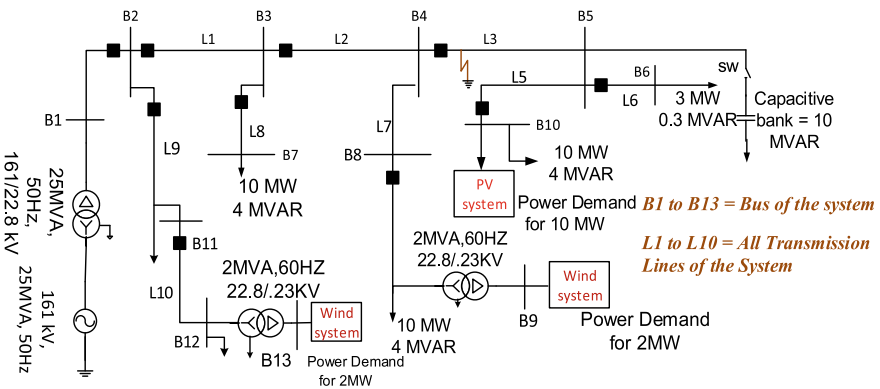


Fig. 3 PSCAD Simulated 13 bus model

Fig. 4 Capacitor switching transients

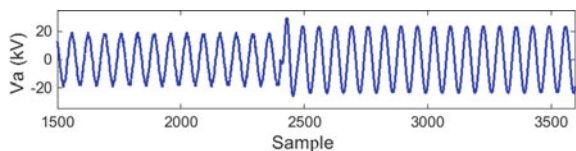


Fig. 5 Load switching transients

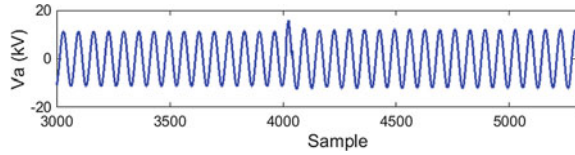


Fig. 6 Fault transient

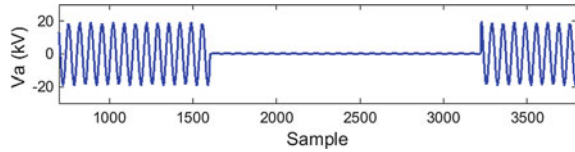
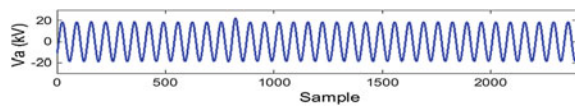


Fig. 7 Islanding at zero power mismatch



4 SVM Implementation

4.1 Software Simulation of SVM in MATLAB

MATLAB software has been used for SVM implementation, the feature of four class data has been taken and labeled the corresponding class for the training phase. Now for testing phase similar data have been taken and labeled the corresponding class, and then run the program and get the accuracy and computation time for SVM classification.

4.1.1 Feature Extraction of Different Classes

The Power Quality disturbance signals and islanding signal simulated in PSCAD (V46) software. There are 40 sets of data generated for each separate event. Therefore, the total ($4 * 40 = 160$) datasets are used for training data. The following four different statistical features are extracted for feature classification.

- First Feature: Variance of the signal
- Second Feature: Mean of the signals
- Third Feature: Standard Deviation
- Fourth Feature: Coefficients of the Variance.

Figure 8 reveals the procedural stages for classification of Power Quality (PQ) disturbances for the same training and testing data. The above result shows that SVM is a standard pattern classification technique to classify the disturbances into a different class. Hence, boundary plots, being procured by SVM, showing four distinct

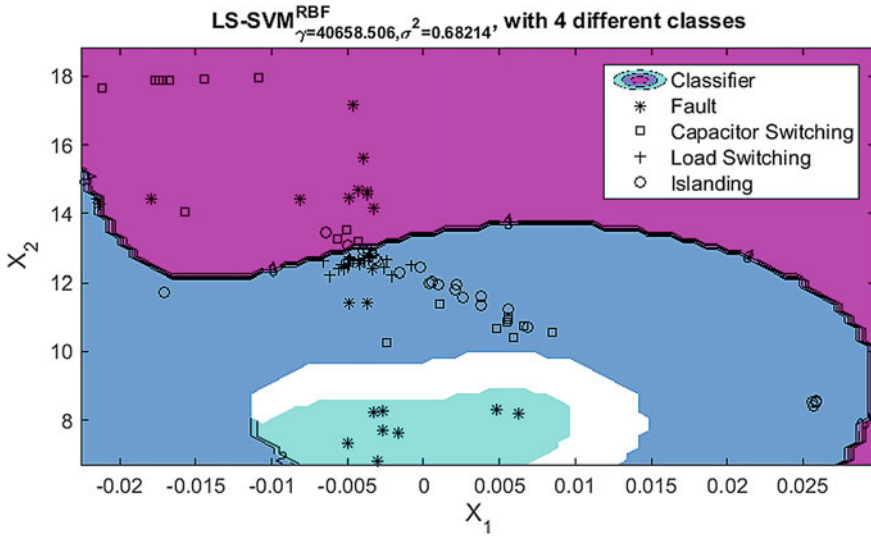


Fig. 8 Boundary plot of SVM of the fault and capacitive switching

regions for four different classes of PQ disturbances such as load switching, capacitor switching, L-G fault, and islanding. The hyperplanes separate all the different classes from each other clearly. The detection accuracy of the radial basis function (RBF Kernel) SVM model implemented for classification among four different classes is obtained to be 98%, and it takes more computation time for classification is 0.847 s.

4.2 Hardware Co-simulation of SVM in FPGA

There are plenty of literature that exist for classification with the objective of exploring SVM. As SVM is a strong candidate for pattern classification, the attempt is made for real time implementation through FPGA. Prior to real time implementation accomplishment of the co-simulation of FPGA for disturbance classification is carried out, which is the main focus for the classification accuracy for two-class problems. The SVM implementation through FPGA is segregated into two parts such as linear kernel as well as nonlinear kernel.

4.2.1 Linear SVM Using System Generator

The proposed architecture diagram of FPGA for linear SVM is given in Fig. 9. The feature vectors (training datasets) of both class1 and class2 loaded in FPGA's internal memories, as long as the classification data or test data points are streamed through the test data units into the FPGA. The dot product multiplication builds the decision

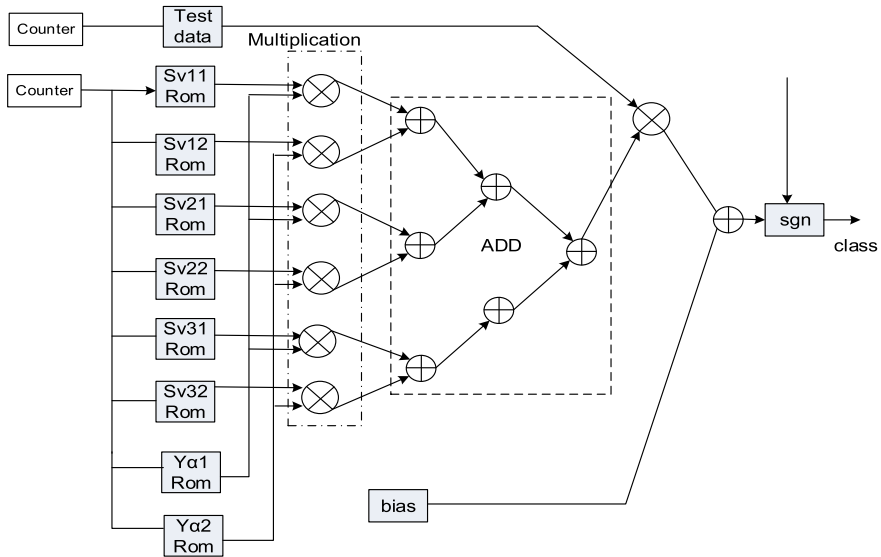


Fig. 9 Linear SVM classifier architecture

function with training dataset and Lagrange multipliers, where all the multiplication is done in parallel. The adder tree in linear SVM architecture builds the decision function $g(x)$ accompanied by parameter bias b [7].

To design hardware architecture, a series and parallel method have been used with MATLAB System Generator block. Every array of a row of matrix SV is placed in SV11–SV32 outputs, which operates by counter1. Test data are in block Test data1 to Test data2 operating by counter 2 with the period of 50 (number of support vector of class1 and class2) [8–11].

In order to make easier mathematical operation, the dot product of vector α and y into a vector $y\alpha$ is preferable to converge. A new vector $y\alpha$ placed in yalpha ROM and addressed by same as SV ROMs. Block Multi 1 to Multi 8 and Add0 to Add5 perform inner product between test data and support vectors; the remaining operation is the sum of this values, that is done serially and add Bias b , which is shown in Fig. 9 From PSCAD Simulated 13 bus Model we capture the PQ disturbance signal load switching and capacitive switching signal and extract the feature like mean, variance, and standard deviation of the signal. And put this data in system generator SV ROMs. We have used three different feature for two-class classifications.

4.2.2 Nonlinear SVM using System Generator

For the simulation of nonlinear SVM, we used the same feature which is used in Linear SVM, but the decision function of nonlinear SVM with Gaussian kernel function is given in Eq. (5) [11–13]:

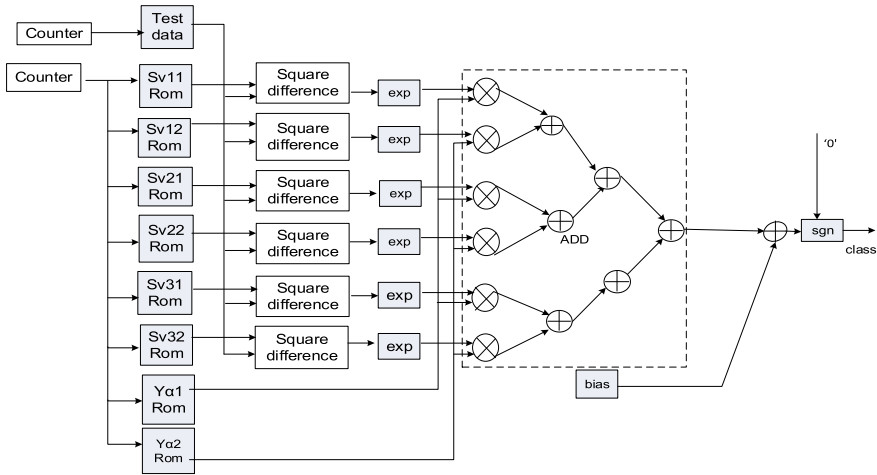


Fig. 10 Hardware architecture for the computation of $\alpha_i y_i e^{-\frac{\|X-Y\|^2}{\sigma}}$

$$d(x) = \sum_{i=1}^{SV} \alpha_i y_i \exp(-\gamma \|x - x_i\|^2) + b \tag{5}$$

Figure 10 shows for computation of $\alpha_i y_i K(x_i, x)$ in nonlinear Gaussian SVM, as long as another part is same as linear SVM.

5 Simulation Result

Whenever implementing SVM classifier in hardware architecture, it is essential to perform the training phase of SVM initially. In simulation we have taken two-class data of capacitive switching and fault and labeled the corresponding class for training sample of SVM. We named 1 for class1 and -1 for class2. We have taken 100 samples from each class1 were 75 samples were taken for training and 25 samples for testing from each class. After vector multiplication and addition.

The classification result of Nonlinear SVM, where 0-23 sample time shows the delay, in this simulation given 50 test sample date in SV rom having 1-25 of class1 data and 26-50 for class2, when the output is greater than zero then it is class1 and when less than zero then it means class2, some data was misclassified, on the basis of this calculated accuracy in linear SVM is 80% and in the nonlinear case it is 92%. Simulation results of SVM are given in Table 1.

Table 1 Hardware co-simulation results of SVM

SV	System generator (linear SVM two class) with $C = 0.02$		System generator (nonlinear two class) with $\gamma = 0.00008$	
	Class1 25 test sample	Class2 25 test sample	Class1 25 test sample	Class2 25 test sample
No. of misclassified	5		2	
Bias	-0.01		0.002	
Accuracy	80%		92%	
Computation time	0.437 s		0.603 s	
Maximum Frequency	20 kHz		20 kHz	

6 Conclusion

This paper demonstrates that the SVM is able to classify the faults, and capacitor switching data point with high accuracy. The Two class FPGA based SVM having, classification accuracy of linear SVM & computation time is 80% and 0.437 s, respectively, and classification accuracy of Nonlinear SVM & computation time is 92% and 0.603 s, which is less than the computation time taken by MATLAB is 0.837 s and MATLAB classification Accuracy is 90% that shows good performance of the hardware architecture.

References

1. Sharmeela C, Mohan MR, Uma G, Baskaran J (2006) A novel detection and classification algorithm for power quality disturbances using wavelet. *Am J Appl Sci* 3(10):2049–2053
2. Song X, Wang H, Wang L (2014) FPGA implementation of a support vector machine based classification system and its potential application in smart grid. In: 11th international conference on information technology: new generations, pp 397–402
3. Thorat P, Turkane S (2012) Detection of capacitor switching transients and L-G fault transients by implementing wavelet transform. *IOSR J Electr Electron Eng (IOSR-JEEE)* 2(5):39–42, ISSN: 2278-1676
4. Anguita D et al (2003) A digital architecture for support vector machines: theory, algorithm, and FPGA implementation. *Neural Netw IEEE Trans* 14(5):993–1009
5. Khan FM et al (2004) Hardware-based support vector machine classification in logarithmic number systems. *Circuits Syst* 5:5154–5157
6. Pina-Ramirez O et al. (2006) An FPGA implementation of linear kernel support vector machines. In: IEEE international conference on the reconfigurable computing and FPGA's, San Luis, pp 1–6
7. Saurav S, Saini AK, Singh S, Saini R (2015) VLSI architecture of pairwise linear SVM for facial expression recognition. In: 2015 international conference on advances in computing, communications and informatics (ICACCI), pp 521–527, 28 Sept 2015

8. Mahmoodi D, Soleimani A, Khosravi H, Taghizadeh M (2011) FPGA Simulation of linear and nonlinear support vector machine. *J Softw Eng Appl* 4:320–328
9. Meyer-Baese U (2007) *Digital signal processing with field programmable gate arrays*. Springer Verlag, Berlin
10. Ganapathiraju A et al (2004) Applications of support vector machines to speech recognition. *IEEE Trans Signal Process* 52(8):2348–2355
11. Jiang Y, Virupakashappa K, Oruklu E (2017) FPGA implementation of support vector machine classifier for ultrasonic flaw detection. In: 2017 midwest symposium on circuits and systems (MWSCAS), pp 180–183
12. Kumar S, Manikandan J, Agrawal VK (2017) Hardware implementation of support vector machine classifier using reconfigurable architecture. In: 2017 international conference on advances in computing, communications and informatics (ICACCI), pp 45–50
13. Saini R, Saurav S, Gupta DC, Sheoran N (2017) Hardware implementation of SVM using system generator. In: 2017 2nd IEEE international conference on recent trends in electronics, information & communication technology (RTEICT), pp 2129–2132

Designing a Smart System for Air Quality Monitoring and Air Purification



Palak Gandhi, Kartik Upadhyay, Ashwani Kumar Yadav and Vaishali

Abstract Rise in the air pollution is a matter of concern as it slowly degrades the health of a person. This increase in pollution has led to the monitoring of air quality to analyze the ill effects it may have on health. Recent reports by WHO have listed 13 cities from India among the top 20 most polluted cities of the world. In this paper, we have explained the design and results of a low cost automatic air purifier system which can help deal with the ambient air pollution and curb it for healthier life. It also discusses the various filters and sensors which can be used to remove and control the air pollution and monitor the quality of air. The filters have been put to test in a polluted environment and the results show that even when any one of the filters is used the quality of air improves to a certain level but when both the filters are used together, the results are enhanced.

Keywords Air pollution · Air quality index · Air purifier · Filters and sensors

1 Introduction

There has been a rapid growth in air pollution in the last few decades. Sixteen cubic meters of exhaust gas are produced by burning one liter of gas in vehicles, the main content of which is nitrogen dioxide [1]. It was reported by WHO in 2014 that there was only one person out of every ten breathe clean air [2]. With 2.51 million deaths in the year 2015 India has been ranked number one in pollution-related deaths of which 1.24 lakh deaths were caused by indoor air pollution based on the reports by the Lancet commission on pollution and deaths. This is mostly due to the use of cow dung and wood as fuel sans ventilation [3]. Air pollution both indoor and outdoor has been responsible for around 6.5 million deaths throughout the world [4]. It potentially raises alarm for people who commute via two wheeler and rickshaw

P. Gandhi · K. Upadhyay · A. K. Yadav (✉) · Vaishali
ASET, Amity University Rajasthan, Jaipur, India
e-mail: ashwaniy2@gmail.com

P. Gandhi
e-mail: gandhipalak.123@gmail.com

© Springer Nature Singapore Pte Ltd. 2020
A. Kalam et al. (eds.), *Intelligent Computing Techniques for Smart Energy Systems*,
Lecture Notes in Electrical Engineering 607,
https://doi.org/10.1007/978-981-15-0214-9_88

pullers [5]. A recent report by WHO lists 14 cities of India out of the 15 most polluted cities of the world in terms of PM_{2.5} levels and 13 cities of India out of 20 cities in the world in terms of PM₁₀ levels [6].

According to WHO PM_{2.5} (Particulate Matter), PM₁₀, and nitrogen dioxide (NO₂), sulfur dioxide (SO₂) and Ozone (O₃) are the pollutants which have adverse effects on health [7]. In September 2014 India came out with an Air Quality Index (AQI) system which was recommended by Indian Institute of Technology (IIT) Kanpur and a group of experts. They have allotted categories to levels of pollutants in the air indicated using various colors. In addition to the pollutants listed by WHO it also includes NH₃, CO, and Pb. The categories are good, satisfactory, moderate, poor, very poor, and severe [8]. Currently there are 342 stations installed in the country which are spread across 127 cities in 26 states and 4 union territories [9]. According to WHO report the acceptable level of PM_{2.5} is 10 µg/m³ annual mean and PM₁₀ is 20 µg/m³ annual mean [2].

Keeping the above-mentioned scenario in mind we have come up with a low cost automated air purifier system which is discussed in the paper.

2 Filters and Sensors

2.1 Filters

The filters that have been used in the system are as follows.

Pre-filter. Pre-filter is placed before HEPA filter or activated carbon filter to remove large particles from the air such as hair, mold, and large dust particles which reduce the efficiency of subsequent filters. Hence pre-filter expand the life of HEPA filter. Pre-filter is made of fiberglass and polysynthetic [10].

HEPA filter. HEPA stands for High-Efficiency Particulate Air. This filter traps 99.97% of particles which are more than or equal to 0.3 µm in size [11]. They are made up of randomly arranged fibers of fiberglass. The size of pores of HEPA filter ranges from 0.5 to 2.0 Åµm.

Activated Carbon Filter. Activated carbon filter removes hazardous elements from the air and keep it odor free. The phenomenon used is adsorption. The porosity of the activated carbon is proportional to its capacity to adsorb hazardous elements [12]. The smaller the size of particles of activated carbon the more is the adsorption rate and hence better performance. The hazardous elements may degrade our health [13]. It is used in combination with HEPA filter to produce the maximum results.

Air Ionizer. Air ionizer is a negative ion generator circuit that is used to charge the particles of the air with the help of emitters which are mounted on the circuit. It operates at 230 V. The emitter releases electrons in the air. Electrons are excited with the help of high electric field produced at the tip of the sharp-pointed needle which is proportional to the voltage produced at the tip of the needle. The high electric field produced at the tip is used to polarize the molecules of air around the needle and force them to accept the electrons by the phenomenon called dipole polarization [14]. Ions

produced by $1 \mu\text{A}$ of current is equal to $6.28 \times 10^{23} \times 10^{-6}$ where 6.28×10^{23} is the Avogadro's number [15]. These cations target the positively charged pollutants like pollen grains, dust particles, smoke, etc. as a result of which the particles become neutral and settle down and can be easily trapped by the filters [16].

Corona discharge occurs in the conductors which are surrounded by air and through which a high voltage is passing usually in the range of 2–6 kV. The corona can be minimized using a needle that is rounded at the end or using a corona ring [17, 18].

The air ionizer that has been used in the project has been designed using 30 units of $0.01 \mu\text{F}$ capacitors and 30 units of 1N4007 diode and 3 units of 1M1 resistor and 1 unit of 2M2 resistor. The circuit is connected to AC mains power supply which is 230 V. The circuit is basically a multiplier circuit which increases the voltage to reach around 4 kV. A sharp end needle is mounted to the air ionizer which works as an emitter and releases electrons at 4 kV which charges the air molecules around it [19]. The circuit in Fig. 1 has been designed using proteus 7 professional showing the circuit of air ionizer that has been integrated in the project.

The ion generator circuit has been described using a section of it with the help of Figs. 2 and 3.

It is a basic full-wave rectifier circuit that would convert AC current to DC current. Initially, both the capacitors C1 and C2 in the figure are discharged. It is a basic full-wave rectifier circuit that would convert AC current to DC current. Initially, both the capacitors C1 and C2 in the figure are discharged. In the first half cycle the AC current flows through the circuit and D1 is forward biased as in Fig. 2, so the current charges the capacitor C1 to the peak value of the input that is $\sqrt{2}$ times the AC input

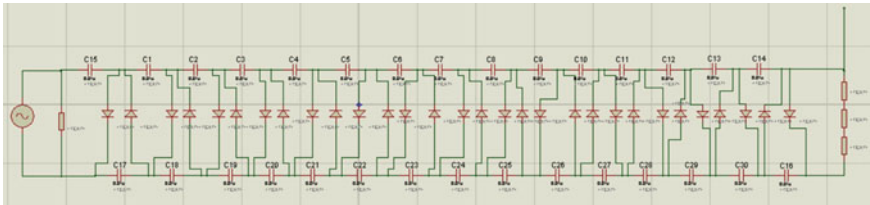


Fig. 1 Simulation circuit of air ionizer

Fig. 2 Current flow during first half cycle

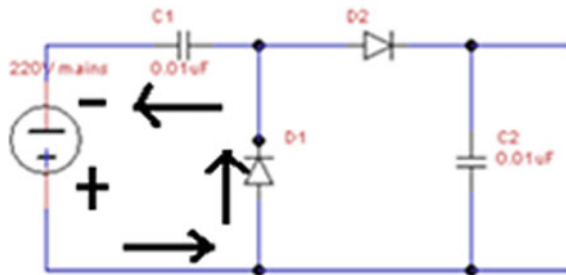
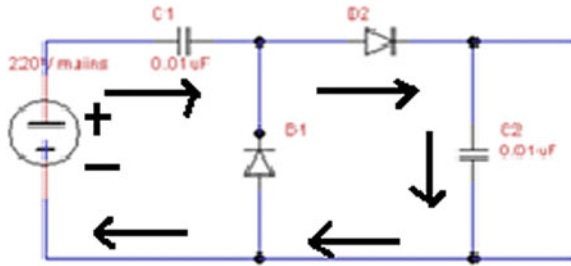


Fig. 3 Current flow during second half cycle



supply of 230 V. In the second half cycle Fig. 3 the capacitor C2 is charged while D2 conducts current as it is in forward bias.

During the second half cycle when D2 is in forward bias the input voltage and charge across capacitor C1 are now in series due to which they add up to 650.54 (325.27 + 325.27 V). Thus this process is repeated in the same way for 15 pairs of capacitors and diodes and hence at the last stage 4 kV is produced which is enough for the excitation of electrons which are emitted out from the emitter. The circuit hence is used to multiply the voltage without a transformer. The needle used in the air ionizer is usually made of tungsten material.

2.2 Comparison of Various Filters Used in the Air Purifiers

Table 1 lists all the filters that are used for air purification around the world.

2.3 Sensors

The sensors that are used in the project are as follows.

MQ-135. A hazardous gas detection apparatus for the environment, suitable for ammonia, aromatic compounds, sulfur, benzene vapor, smoke, and other gases harmful gas detection, gas-sensitive element test concentration. Air quality sensor is for detecting a wide range of gases, including NH_3 , NO_x , alcohol, benzene, smoke, and CO_2 . Ideal for use in office or factory, simple drive, and monitoring circuit [26].

GP2Y1010AU0F. GP2Y1010AU0F is a dust sensor using optical sensing system. An infrared emitting diode (IRED) and a phototransistor are diagonally arranged in this device. It detects the reflected light of dust in air. It is effective in detecting very fine particle like the cigarette smoke. In addition to that it can distinguish smoke from house dust by pulse pattern of output voltage [27].

Table 2 lists all the other sensors which are used in the designing of the air purifier.

Table 1 Various filters

S. no.	Filters	Descriptions
1	HEPA filter	High-Efficiency Particulate air (HEPA) is used to remove particles whose size is in sub-micron [20]
2	Activated carbon filter	Activated carbon filter is used to adsorb particles as it passes through it. The pores of the filter chemically react with the particles and trap them
3	Ionic filter	They generate negative ions and the ions attract positively charged dust particles because of which they become heavy and settle down and are picked up by the filters
4	Ultraviolet light air purifier	This filter kills the pathogens by breaking the bond in their DNA using a source of ultraviolet light [21]
5	Ozone	Ozone air purifier produces ozone to kill contaminants. But health experts do not recommend the use of ozone producing air purifier because it has some health hazards [22]
6	Electrostatic precipitator (ESP)	It consists of two oppositely charged plates, negative one is used to charge the dust particles and positive one is used to collect them using electromagnetic force [23, 24]
7	Pre-filter	It is used before HEPA filter in order to trap pollutants which are larger in size
8	Charged media filter	They use charged metallic screens which is stuffed between two filters which are fibrous. A drop in voltage affects the efficiency of the filter [25]

3 Proposed Model

The proposed model is an intelligent air purifier that would be switched on in the presence of the air pollution. The air quality needs to be checked continuously with the help of sensors MQ-135 and GP2Y1010AU0F.

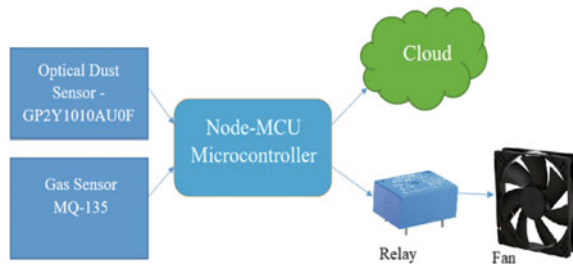
The microcontroller used in this model is NodeMCU which has an embedded Wi-Fi module ESP8266. The data sensed by the sensors is processed by NodeMCU and uploaded to cloud. As the pollutant level exceeds the preset threshold limit NodeMCU instructs the relay which in turn switches on the fan. The polluted air hence is drawn into the purifier and is passed through the filters. The fan and the air ionizer are operated at 230 V. The entire structure has been encased in a thick cardboard box. The readings from the cloud can be accessed to analyze the quality of the surrounding air.

Figure 4 shows the proposed model. The direction of the arrow indicates the direction of flow of data and instructions.

Table 2 Various sensors

S. no.	Sensor name	Detects	Temperature range (°C)	Operating voltage (V)
1	MQ-2	Methane, butane, LPG, smoke	-20 to 55	5
2	MQ-7	Carbon monoxide	-20 to 55	Alternating 5 and 1.4
3	MQ-131	Ozone	-20 to 55	6
4	MQ-135	Air quality (benzene, alcohol, smoke)	-20 to 55	5
5	MQ-303A	Alcohol, ethanol, smoke	-20 to 55	0.9
6	MQ-309A	Carbon monoxide, flammable gases	-20 to 55	Alternating 0.2 and 0.9
7	MICS-2714	Nitrogen dioxide	23 to 50	5
8	MICS-5914	Ammonia	23 to 50	5

Fig. 4 Block diagram of the proposed model



4 Results

The results have been shown with the help of Table 3. The readings are uploaded to the cloud platform Think Speak each time the sensor senses the level of pollutants in the air has exceeded the preset threshold limit. The threshold limit has been decided depending on the surrounding environment. It can be changed if the pollutant level exceeds than before. The result in the table shows that after the introduction of the filters viz a viz pre-filter, HEPA filter, Activated carbon filter and air ionizer the level of pollutants in the air decreases and hence we get a cleaner air to breathe.

5 Conclusion

Based on the results obtained, it can be concluded that the proposed system is able to reduce the indoor air pollution to the good category of the AQI and is also saving electricity as it only switches on when pollution level exceeds.

Table 3 Sensors readings

S. no.	Dust sensor readings (μm)		Gas sensor readings (ppm)	
	Without filters	With filters	Without filters	With filters
1	318	123	337	161
2	316	113	328	154
3	280	106	315	147
4	277	98	308	136
5	270	87	301	123
6	265	80	296	115
7	254	74	289	98
8	234	66	285	83
9	219	61	278	71
10	203	52	270	62

6 Future Scope

There is a scope for lot of work in the field of air purification. Drastic actions need to be taken to control the rise of air pollution. Further a larger system can be built to remove the air pollution on a larger scale from the cities which may make use of sensitive sensor to detect the slightest of pollutants in the air.

References

1. Dyvak M, Darmorost I, Shevchuk R, Manzhula V, Kasatkina N (2018) Correlation analysis traffic intensity of the motor vehicles and the air pollution by their harmful emissions. In: 2018 14th international conference on advanced trends in radioelectronics, telecommunications and computer engineering (TCSET). IEEE, pp 855–858
2. Ambient air pollution: a global assessment of exposure and burden of disease: a report by WHO (2016)
3. Prasad R (2017) Most pollution-linked deaths occur in India. The Hindu report. <http://www.thehindu.com/sci-tech/energy-and-environment/india-ranked-no-1-in-pollution-related-deaths-report/article19887858.ece>. Accessed 13 Apr 2018, 20 Octo 2017
4. Gordon S, Mortimer K, Grigg J, Balmes J (2017) In control of ambient and household air pollution-how low should we go? *Lancet Respir Med* 5(12):918–920
5. Varun J, Goel M, Maity M, Naik V, Ramjee R (2018) Scalable measurement of air pollution using cots Iot devices. In: 2018 10th international conference on communication systems & networks (COMSNETS). IEEE, pp 553–556
6. PTI, India had 14 out of world's 20 most polluted cities in terms of PM2.5 levels in 2016, says who. The Hindu report. <http://www.thehindu.com/sci-tech/energy-and-environment/14-out-of-worlds-20-most-polluted-cities-in-india-who/article23745178.ece>. Accessed 02 July 2018
7. Ambient air pollution: pollutants. WHO report. <http://www.who.int/Airpollution/Ambient/Pollutants/En/>. Accessed 11 Apr 2018

8. Ministry of Environment, Forest and Climate Change, Government has made serious efforts to deal with air pollution. Press Information Bureau Government of India. <http://Pib.Nic.In/Newsite/Pmleases.aspx?Mincode=30>. Accessed 21 Apr 2018
9. Chakrabarti A (2016) Ambient air quality monitoring stations. Perfect pollution services blog. <http://www.ppsthane.com/Blog/Ambient-Air-Quality-Monitoring-Stations>. Accessed 15 Aug 2016
10. Sheng H (2017) Architecture amidst Smog. Master of architecture theses. Dept. School of Architecture, Syracuse Univ. New
11. Hepa standards explained. Airmaega. <https://Airmega.com/What-Is-A-Hepa-Filter/>. Accessed 15 July 2018
12. Tang Y-M, Kostecki JC, Graeve EG (1994) Agglomerated activated carbon air filter. US Patent 5,332,426A 26 Jul 1994
13. Sarah. Activated carbon filters: what they are & how they work. Allergy and air. <https://Learn.Allergyandair.Com/Activated-Carbon-Filters/>. Accessed 18 Apr 2018, 7 May 2014
14. Mifflin M (2018) What does an air purifier's ionizer do. The spruce report. <https://www.TheSpruce.Com/Air-Purifier-Ionizer-Uses-1907078>. Accessed 07 Apr 2018
15. Joannou C (2003) Portable ion generator and dust collector. US Patent 2,003,014,778,4A1 07 Aug 2003
16. What is an air ionizer?. Air Oasis. <http://www.airoasis.com/knowledgebase/air-ionizer-benefits/>. Accessed 05 July 2018
17. Corona discharge. https://en.wikipedia.org/wiki/corona_discharge. Accessed 08 July 2018
18. Kim H-J, Han B, Woo CG, Kim Y-J (2017) Ozone emission and electrical characteristics of ionizers with different electrode materials, numbers, and diameters. IEEE Trans Ind Appl 53(1):459–465
19. Swagatam, Make a room air ionizer circuit. Homemade circuit projects blog. <https://www.homemade-circuits.com/Make-Room-Air-Ionizer-Circuit-Get/>, 13 Nov 2013
20. Tsai P, Malkan SR (2002) Hepa filter. US Patent 6,428,610B 06 Aug 2002
21. Sham JC, Kunavongvorakul K (2002) Ultraviolet air purifier. US Patent 6,464,760,B1 15 Oct 2002
22. The 5 most common types of air purifiers. Allergy and air. <https://learn.allergyandair.com/Types-Of-Air-Purifier>. Accessed 02 July 2018
23. Boll RH (1968) Electrostatic precipitator. US Patent 3,400,513,A, 10 Sep 1968
24. Morita K, Sakai T (1994) Electrostatic precipitator machine for charging dust particles contained in air and capturing dust particles with coulomb force. US Patent 5,290,343A 01 Feb 1994
25. Pick W (1990) Pleated charged media air filter. US Patent 4,978,372A 18 Dec 1990
26. Datasheet. <https://www.olimex.com/products/components/sensors/snsmq135/resources/snsmq135.pdf>. Accessed 13 Apr 2018
27. Datasheet. https://www.sparkfun.com/datasheets/sensors/gp2y1010au_e.pdf. Accessed 12 July 2018

Activation Map Networks with Deep Graphical Model for Semantic Segmentation



Cheruku Sandesh Kumar, Ratnadeep Roy, Sanyog Rawat and Archek Praveen Kumar

Abstract In this research semantic segmentation by the deep convolutional neural network is used. Segmentation of contextual information with the use of patch-patch between the regions and background. The patch-patch context is done with the help of conditional random fields with CNN pairwise potential functions to identify the semantic correlation of adjacent patches. Efficient piecewise training of deep graphical model is then assigned to eschew continuous CRF inference through background propagation. For Patch-background context capturing the network is designed with the help of multi-scale image input and slide pyramid pooling for the efficient performance. In the CRF model we have used both unary and pairwise potential functions. The simulation results are verified in the semantic segmentation dataset like MATLAB contextual modeling. The proposed technique will give better accuracy. The evaluation metrics of invented method has been done in terms of pixel accuracy. The model achieves outperforming innovation than the other algorithms like Deeplab and DPN on semantic segmentation.

Keywords Feature extraction · Deep learning · Fully convolutional neural networks · Dense CRF · Contextual models · Semantic segmentation · SS-semantic segmentation

C. S. Kumar (✉) · R. Roy
ASET, Amity University, Noida, India
e-mail: sandeshkumarc7@gmail.com

R. Roy
e-mail: roy.ratnadeep@gmail.com

S. Rawat
ASET, Manipal University, Manipal, India
e-mail: sanyog.rawat@gmail.com

A. P. Kumar
Malla Reddy College of Engineering for Women, Secunderabad, India
e-mail: archekpraveen@gmail.com

1 Introduction

Image SS has a category label for image pixel that plays an important role in the complete scene of understanding an image. The related approaches like CNNs have pixel-level labeling [15–17]. There are many CNNs methods FCNNs [16, 17] is widely used because it has good computational efficiency, dense prediction, and end to end training. Contextual information or data has the main cues for scene understanding areas. The spatial context is applied in semantic compatibility relations between one object and its adjacent objects/stuff where compatibility relation is a point of co-occurrence of visual patterns. Considering on a highway, a bottle on a stool, context encodes incompatibility relations which would be the example for a boat on the highway. The relations can have good scales for assumption, object part-to-part relation, and part-to-part object relations. Contextual information is mainly useful in finding cue for isolated object that has visual uncertainty. The spatial context is a broad area of research and has given in [18].

In our findings, we try to explore spatial context to obtain good results of semantic segmentation. Spatial context has patch-to-patch and patch-to-background context. The patch-to-patch context has semantic relationships on visual patterns of two stuffs of an image. Patch-to-background context had semantic relations in image patch and whole background region. In our research we have explored contextual relations based on CRF. CNNs pairwise potential captures semantic correlation on nearby patches. Researchers in the past had used CNN-Sparse CRF [17, 19, 20].

In our model, we used CNN-Dense CRF technique to refine our samples of resolution prediction to sharpen the object boundaries. CNN-Dense CRF uses Potts-Model-Based pairwise potentials for local smoothness of images. Pairwise potentials are log-linear functions for semantic compatibility in image regions. CRF pairwise is to develop coarse-level prediction. CRF and Potts-model-based pairwise potential are combined to obtain good results for semantic segmentation. Figure 2 shows the prediction of our method. The patch-background context is traversed in this regard. CNN based techniques of multi-scale image network give good output when compared to recent semantic segmentation methods [15]. In this model the use of multi-scale networks to encode background data and then slide window on activation maps is applied to encapsulate intelligence from background regions of various sizes. Generally pairwise potentials have rich computational inference in CRF training. The piecewise learning of CRF ignores continuous inference on back-propagation learning of deep model.

2 Context Deep CRFs

The design of deep CRF model is given below. Let us consider $i \in I$ one original image and $j \in J$ labeling mask that is label configuration of every node in the CRF graph. As we know, the energy of a function is given by $E(j, i; \theta)$ model prognostic

j . The networks are denoted by that the classifiers need to study [19]. As per the probability theory, the conditional likelihood for the given image is as follows:

$$P(j/i) = \frac{1}{S(i)} \exp[-E(j, i)] \tag{1}$$

where ‘ S ’ is the partition function and is known as:

$$S(i) = \sum_j \exp[-E(j, i)].$$

As we knew that energy function is a set of unary and pairwise potentials and is given in the below equation.

$$E(j, i) = \sum_{K \in k} \sum_{l \in M_K} K(j_c, i_c) + \sum_{T \in t} \sum_{(c,d) \in F_T} T(j_c, j_d, i_{cd}) \tag{2}$$

Here K is unary potential function. To resolve the expression, we assume multiple types of unary potential k . M_K denotes set of nodes of potential K . Next T is a pairwise ‘ t ’ is pairwise potentials. F_T edges of potential T . i_c and i_{cd} associates to node and edge.

3 Pairwise Potential Functions

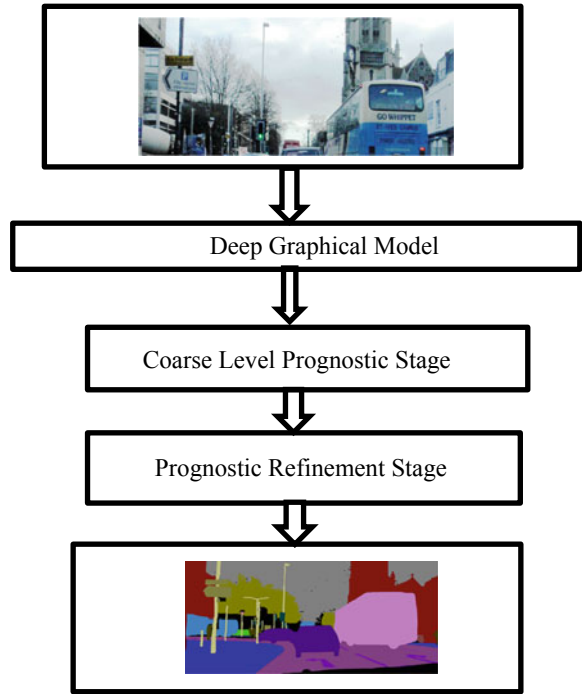
Pairwise potential function in comparison with unary potentials by stack activation map net [1–4]. Pairwise potential is given below:

$$T(j_c, j_d, i_{cd}; \theta_T) = -w_{c,d,j_c,j_d}(i; \theta_T) \tag{3}$$

Here w_{c,d,j_c,j_d} output pairwise net.

Node pair (c, d) to labeled with class value (j_c, j_d) for the original image i . θ_T Corresponds Convolution Neural Network for potential T . The pairwise net have H^2 . [6, 17] This invention of pairwise potential nodes semantic each feasible (j_c, j_d) by CNNs. After coarse-level prediction, still we have to accomplish a refine stage to get the end high resolution prognostic in Fig. 1. In our invention we applied dense CRF technique at the stage of prediction refinement [10–14].

Fig. 1 Prognostic proposed approach



4 Prognostic Process

The two-stage prediction that is coarse-level prediction and prediction refinement are shown in the Fig. 2 below to get last high-resolution prediction [5, 6]. In coarse stage we proposed the deep graphical model and the main purpose of refinement stage is to sharpen the object boundary.

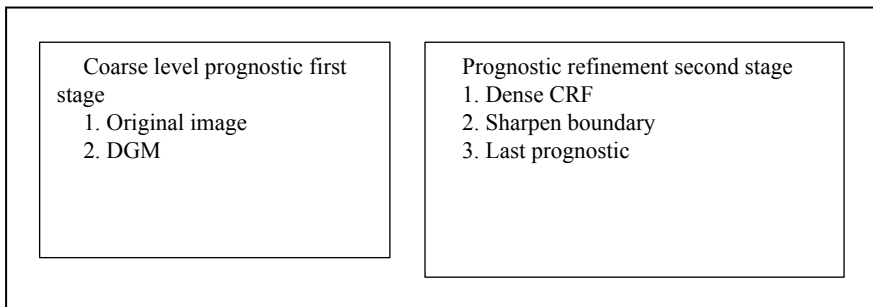


Fig. 2 Two stage prognostic process [16]

5 Prognostic Consummation Phase

Generating a score map to the coarse prediction is done by marginal distribution, can be get by mean field inference. The size of the input image, we first bilinear upsample. Use dense CRF technique for post-processing [16] to scarp. Boundary refinement is done by post-processing. The low-resolution prediction, upsample the refinement model to the last prediction [17, 20], do bilinear upsample. Refinement methods example coarse training deconvolution networks multiple coarse for fine learning [7–9]. Refinement approach is used for performance improvement. Practically we got improvement in refine approach on Matlab contextual modeling.

6 Practical Experiments with Validation Set on Matlab Contextual Modeling

The simulation of the introduced technique is verified on challenging SS test sets. They are MATLAB contextual modeling that unfolds different kind of scene images like counting indoor and outdoor scenes, etc. The simulation of the proposed technique got outperforming performance on the above stated test sets. The execution is done in MATLAB contextual modeling of visual object classes' data set. The comparison has been done for various techniques with outstanding performance. The proposed model is trained using images that gave accuracy score of 75.1%, outperforming other techniques. The accuracy scores are shown in Table 1.

The original dataset contains 1464, 1449, and 1456 images for training, validation, and testing , respectively. The prognostic results of the proposed method are tested on Matlab contextual modeling. Figure 3 shows—original image and prognostic.

7 Conclusion

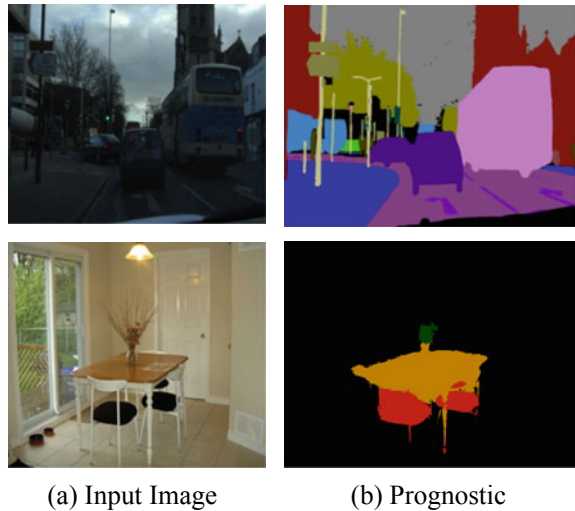
In this research, we jointly used FCNN and CRF technique to investigate context information to get efficient SS. This can be done by CNN related pairwise potentials to model semantic relationships between regions of an image. The practical results were simulated in couple of datasets mentioned in this research which gave state of the art performance. The technique introduced is well suited for all other SS related works.

In all, classification accuracy rates are generated and the best results are selected for design of DGM. Hence after many experimental techniques, Deeplab gave the best classification accuracy of 72.6%, DPN gave the best classification accuracy of 74.1%, and DGM gave accuracy score of 75.1% outperforming among other techniques.

Table 1 Category outcomes via MATLAB contextual modeling

Method	Classifier	Classification Accuracy (%)									
		Road	Pedestrian	SignSymbol	Building	Bus	Car	Chair	Table	Potted	TrafficLight
DeepLab	Dense CRF	72.6	36.6	59.9	48.4	69.2	70.1	29.7	58.9	58.7	70.2
DPN	Dense CRF	73.2	56.5	63.2	51.4	74.1	69.1	30.9	60.2	59.8	71.6
Deep graphical model	Dense CRF	74.2	62.1	67.2	56.2	66.1	69.9	38.1	59.9	61.3	75.1

Fig. 3 Prognostic examples of our approach to MATLAB contextual modeling



DGM brings the state of the art designs to the general humans. At last this work consists of extensive work on pre-processing, front-end processing, back end processing, and post-processing in the design of a DGM for SS.

References

1. Winn J, Shotton J (2006) The layout consistent random field for recognizing and segmenting partially occluded objects. In: Proceedings of IEEE conference on computer vision and pattern recognition
2. Heesch D, Petrou M (2010) Markov random fields with asymmetric interactions for modelling spatial context in structured scene labeling. *J Signal Process Syst*
3. Simonyan K, Zisserman A (2015) Very deep convolutional networks for large-scale image recognition. In: Proceedings of international conference on learning representations
4. Krähenbühl P, Koltun V (2012) Efficient inference in fully connected CRFs with Gaussian edge potentials. In: Proceedings of advances in neural information processing systems
5. Nowozin S, Lampert C (2011) Structured learning and prediction in computer vision. *Found Trends Comput Graph Vis*
6. Eigen D, Fergus R (2015) Predicting depth, surface normals and semantic labels with a common multi-scale convolutional architecture. In: Proceedings of the IEEE international conference on computer vision
7. Noh H, Hong S, Han B (2015) Learning deconvolution network for semantic segmentation. In: Proceedings of international conference computer vision
8. Hariharan B, Arbeláez P, Girshick R, Malik J (2014) Hypercolumns for object segmentation and fine-grained localization. In: Proceedings of IEEE conference on computer vision and pattern recognition
9. Besag J (1977) Efficiency of pseudolikelihood estimation for simple Gaussian fields. *Biometrika*
10. Nowozin S, Rother C, Bagon S, Sharp T, Yao B, Kohli P (2011) Decision tree fields. In: Proceedings of international conference on computer vision

11. Jancsary J, Nowozin S, Sharp T, Rother C (2012) Regression tree fields an efficient, non-parametric approach to image labeling problems. In: Proceedings of IEEE conference on computer vision and pattern recognition
12. Liu C, Yuen J, Torralba A (2011) Sift flow-dense correspondence across scenes and its applications. *IEEE T Pattern Anal Mach Intell*
13. Kumar CS, Roy R, Gupta M, Sharma A, Kumar AP, Sharma A (2016) Velocity estimation and speed tracking through segmentation. *Int J Control Theory Appl (IJCTA)* 9(23):101–106
14. Kumar CS, Roy R, Kumar AP, Gupta M (2016) Segmentation on moving shadow detection and removal by symlet wavelet for vehicle detection. In: IEEE international conference on computing for sustainable global development (INDIACom)
15. Farabet C, Couprie C, Najman L, LeCun Y (2013) Learning hierarchical features for scene labeling. *IEEE T Pattern Anal Mach Intell*
16. Long J, Shelhamer E, Darrell T (2015) Fully convolutional networks for semantic segmentation. In: Proceedings of IEEE conference on computer vision and pattern recognition
17. Chen L, Papandreou G, Kokkinos I, Murphy K, Yuille AL (2015) Semantic image segmentation with deep convolutional nets and fully connected CRFs. In: Proceedings of international conference on learning representations
18. Heitz G, Koller D (2008) Learning spatial context-Using stuff to find things. In: Proceedings of European conference on computer vision
19. Schwing AG, Urtasun R (2015) Fully connected deep structured networks
20. Zheng S, Jayasumana S, Romera-Paredes B, Vineet V, Su Z, Du D, Huang C, Torr P (2015) Conditional random fields as recurrent neural networks. In: Proceedings of international conference computer vision

Grey Wolf Optimized PI Controller for Hybrid Power System Using SMES



Sandeep Bhongade and Ritu Verma

Abstract This paper emphasizes on load frequency control of hybrid power system using SMES technology. The hybrid power system includes solar panels, wind panels and diesel engine generator along with a microgrid for power generation. Whenever a load change occurs in the system, frequency deviation occurs. In order to mitigate the deviation occurred in the system, a PI controller is optimized. Parameters of controller are optimized using Grey Wolf Optimization technique. SMES is used for the purpose of energy storage and its impact on the frequency stability has studied. Steady state stability analysis has been carried out for two cases viz. during off-peak load and peak load conditions. The system is simulated under different operating conditions and results obtained shows the supremacy of the controller.

Keywords Grey Wolf optimization (GWO) · Hybrid power system (HPS) · LFC · SMES

1 Introduction

Due to the degradation of fossil fuels, renewable sources such as solar, wind and hydro plants plays a vital role to meet the required energy consumption. These clean energy sources have an application of providing power to the off-grid area, where the extension of power system is not possible. These renewable energy sources have various advantages such as low running cost, less maintenance, ease of use and nonhazardous. Solar and wind power plant can act as a stand-alone energy conversion system and supplies power to the domestic locations [1, 2]. Solar panels can be mounted on small scale and possess good flexibility of installation. Due the variation of light in accordance with time, output power is variable. Similarly, as the wind speed is random in nature, power output is also variable. The stochastic nature of

S. Bhongade (✉) · R. Verma
SGSITS, Indore, India
e-mail: bhongadesandeep@gmail.com

R. Verma
e-mail: ritumits3@gmail.com

© Springer Nature Singapore Pte Ltd. 2020
A. Kalam et al. (eds.), *Intelligent Computing Techniques for Smart Energy Systems*,
Lecture Notes in Electrical Engineering 607,
https://doi.org/10.1007/978-981-15-0214-9_90

these sources results in various technical problems such as voltage and frequency deviation. In order to minimize this deviation various techniques are employed in the system such as controllers, power system stabilizers and LQR. In this paper frequency deviation due to the operation of hybrid power system has been discussed [3]. Whenever a load change occurs then frequency of the system deviates from its nominal value. In order to mitigate this deviation energy storage systems are employed, which possess the capacity of handling multifunctional tasks as backup powers, active and reactive power injection from/to the grid [4]. SMES have higher conversion efficiency, fast response time, injecting and storing real or reactive power endorses it as a viable solution [5].

2 Hybrid Power System

Hybrid power system is designed for the generation of electrical power and independent of large grid but includes number of power sources or microgrids. They take advantage of transferring AC power to higher voltage with minimum power loss. Microgrids are small scale power system, which consists of renewable energy sources such as solar, wind, etc. energy storage, power electronic interfaces, and system load. It acts as a local source of supply which is connected to a centralized grid but able to function independently. Microgrid with hybrid renewable energy sources operate in two modes viz. stand-alone (off-grid) or grid-connected (on grid). A typical hybrid power system contains a combination of-

- (i) Power generation sources
- (ii) Energy storage system
- (iii) Power conditioning system
- (iv) Controllers

2.1 Mathematical Modelling of HPS

The mathematical modelling of the hybrid power system has been carried out. Figure 1 represents the model of microgrid connected hybrid power system [3].

A linear model of the power systems, where the dynamics of a diesel power plant, SMES is considered for study. For smooth operation of hybrid power system, load generation balance should be maintained. For proper controlling, an error signal is given to the system which is the difference between the change in load demand (ΔP_D) and change in net power (ΔP_T) [3].

$$\Delta P_T = \Delta P_{PV} + \Delta P_W \pm \Delta P_{DEG} \pm \Delta P_{SMES} \quad (1)$$

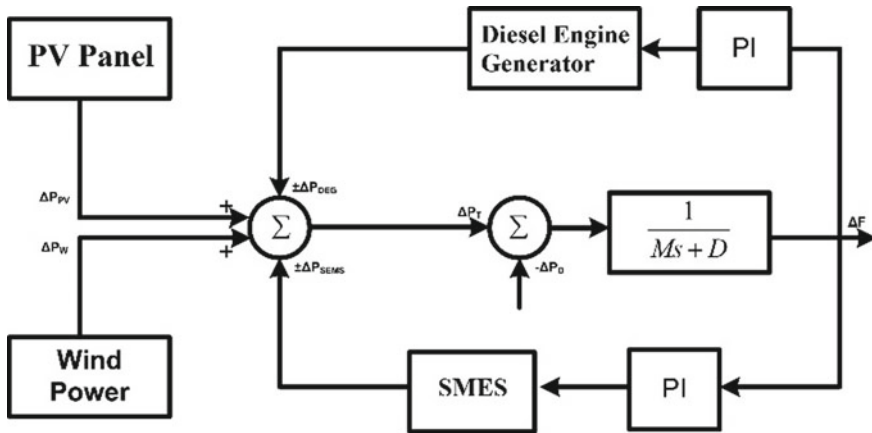


Fig. 1 Model of hybrid power system [3]

$$\Delta P_S = \Delta P_T - \Delta P_D \tag{2}$$

where ΔP_S is net power controlling error.

And the frequency deviation is given by ΔF ,

$$\Delta F = \frac{K_{PS}}{1 + T_{PS}} \cdot \Delta P_S \tag{3}$$

Transfer function of system frequency deviation to per unit power deviation is,

$$\Delta F = \frac{1}{D + sM} \cdot \Delta P_S \tag{4}$$

$$D = \frac{1}{K_{PS}} \text{ and } M = \frac{T_{PS}}{K_{PS}}$$

where M is equivalent inertia constant (p.u) and D is Damping constant (p.u)

SMES

An SMES unit is a DC current device which stores energy in the magnetic field. When DC current flows through the superconducting wire, a magnetic field is created due to the large magnets (Fig. 2).

Due to the superconducting nature, energy stored for a long time duration may be used either to inject active power into the grid or to absorb the surplus power available in the grid. The SMES unit is able to damp out oscillation. The major advantage of SMES coil is to discharge a large amount of rated power into the system with a short duration of time [5]. The large superconducting coil is kept at cryogenic temperature and the temperature is maintained by a cryostat which contains helium or nitrogen liquid vessels. When the coil is on standby, a bypass switch is used to reduce energy

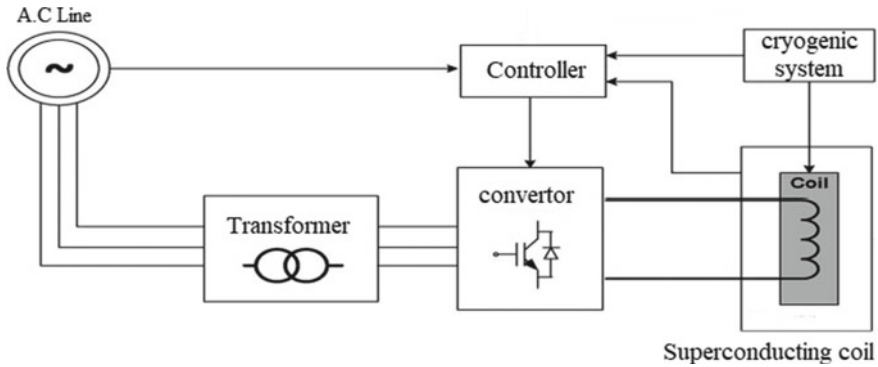


Fig. 2 Configuration of SMES unit

losses. A power conditioning system (PCS) is required to transfer the power from SMES to grid according to the requirement.

DC voltage is given below,

$$E_d = 2V_d \cos \alpha - 2I_d RC \quad (5)$$

where

E_d is DC voltage applied to the inductor, α is firing angle in degrees, I_d is current flowing through the inductor and RC is equivalent commutating resistance.

Charging and discharging of SMES Coil is done by varying the commutation angle. When the load of the system increases, the frequency falls from the nominal value in order to maintain the frequency, generation has to be increased. Thus, SMES discharges power into the system and acts in inverter mode, i.e., α is less than 90° . Similarly, when the load of the system reduces, frequency increases as the large amount of power is available in the system, thus, SMES absorbs that energy and operates in charging mode or in convertor mode, i.e., α is greater than 90° [6].

3 Grey Wolf Optimization

This optimization technique was proposed by Mirjalili in 2013 [7]. GWO algorithm mimics the leadership hierarchy and hunting mechanism of one of the most successful predators, grey wolves in nature [7]. Four types of grey wolves such as alpha, beta, delta and omega are employed for simulating the leadership hierarchy. A pack of around 10–12 wolves is led by a leader, i.e., alpha wolves and the subordinates respect the decision of the leader. Tuning of PI controller depends upon two parameters (K_P and K_I) to regulate the change in frequency error (Δf). PI controller is selected for minimizing the deviation in frequency and its optimal values are determined using GWO.

In order to achieve optimum system response, the integral time square error method is used [1]:

$$F(X) = \text{ITES} = \int_0^{t_{\text{sim}}} t * (\Delta f)^2 dt \quad (6)$$

where X is the variable in terms of the value of K_p and K_i .

4 Simulation Results and Analysis

This section presents the simulation results of HPS. A 2 MW system has been considered for the study. Simulation is carried out with the scenario of HPS employing PV panel, wind power, diesel engine generator with or without SMES. Following system has been analyzed for two cases (i) during off-peak load (ii) during peak load.

The steady state stability analysis of hybrid power system is carried out through step load change during the maximum and minimum power consumption period. The system response is analyzed with or without SMES. Simulink model has simulated for a time period of 30 s.

Case (1)—During Peak Load

In this case, wind and solar power variations are assumed to be absent. When the load of the system changes, frequency deviation takes place. Consider the step load change of 0.1 p.u is occurred as peak load. With the sudden change in load demand, i.e., as the peak load change occurs, system frequency falls below a predefined limit. In order to maintain the system frequency within the desired limit, energy storage system plays the role. SMES unit which acts as a storage device starts providing the additional energy to the system to meet the required demand. Thus, SMES is operating under discharging mode and result shows that the response of the system is fast and deviation is minimized. The effect in frequency response with and without SMES using Grey wolf optimized controller is shown below.

(1) HPS without SMES:

At $t = 5$ s when sudden load change occurs in the system frequency deviates and is minimized by grey wolf optimized PI controller shown in Fig. 4 and best fitness value for the optimized controller is shown in Fig. 3.

(2) HPS with SMES:

When sudden load change occurs in the system SMES starts acting in inverter mode, i.e., starts injecting power to the system so as the maintain the required demand and frequency deviation with respect to this load change is shown in Fig. 6 and best fitness value for grey wolf tune PI controller is given (Fig. 5).

Fig. 3 Best fitness obtained with respect to iteration

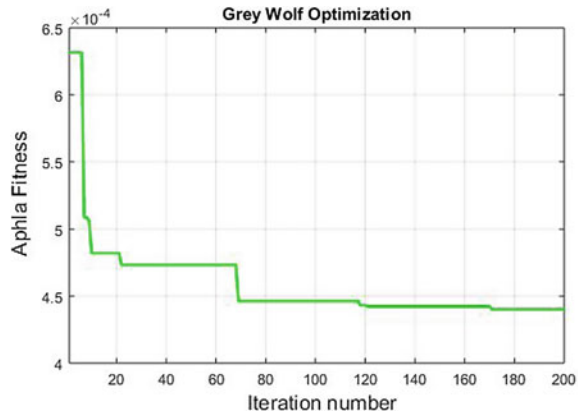


Fig. 4 Change in frequency without SMES

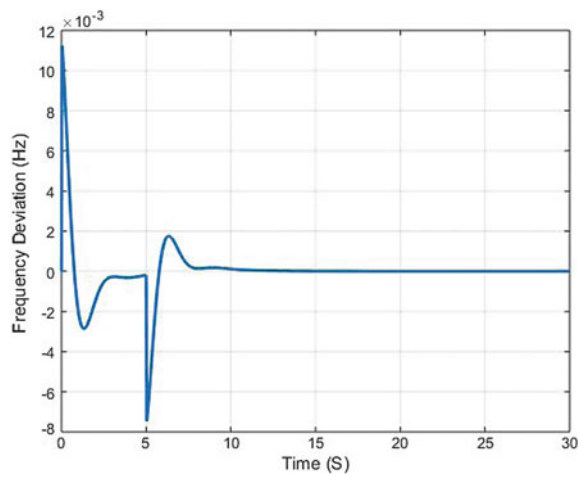


Fig. 5 Best fitness obtained with respect to iteration

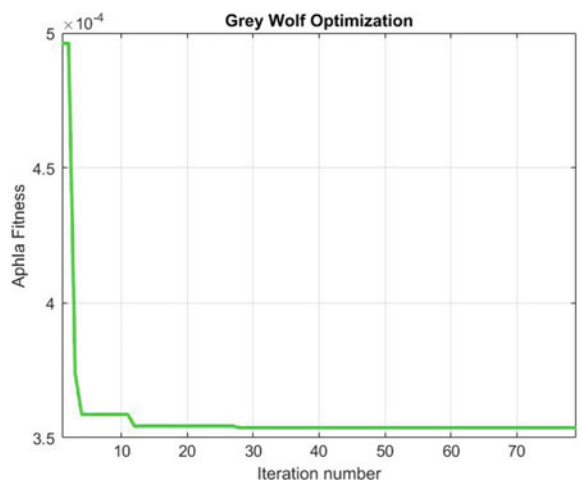
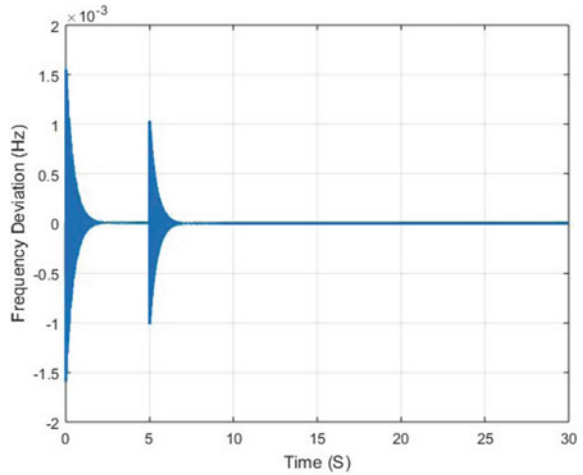


Fig. 6 Change in frequency



Case (2)—During the Off-Peak Load

Similar conditions as above are applied here but during off-load condition. A step load change of 0.05 p.u. is occurred in the system and system response with or without considering SMES is shown. When the load demand decreases, frequency of the system increases above the nominal value. As a result surplus amount of power is available in the system, which is absorbed by the SMES unit. Here SMES act as a charging unit. The result of the system with or without SMES has shown below:

- (1) HPS without SMES

Case (2) studies show the mitigation in frequency deviation (Fig. 8) due to the tuned PI controller whereas, Fig. 8 shows the best fitness value (Fig. 7).

Fig. 7 Best fitness obtained so far

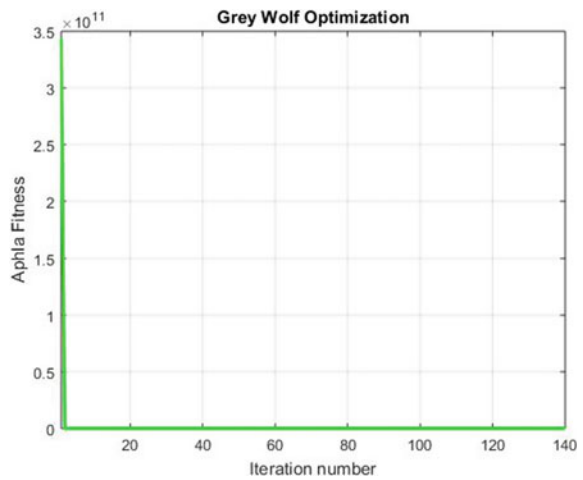


Fig. 8 Frequency deviation

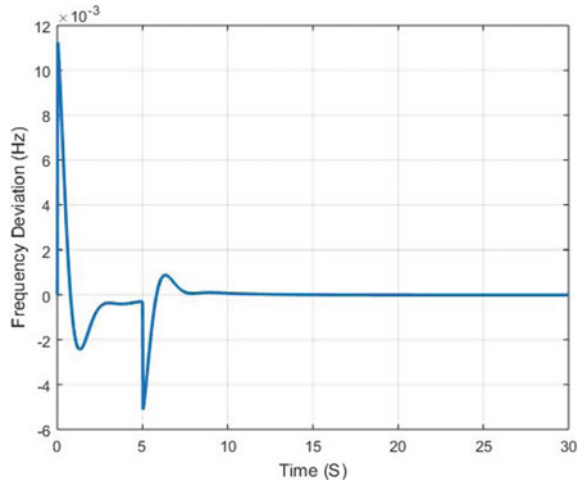
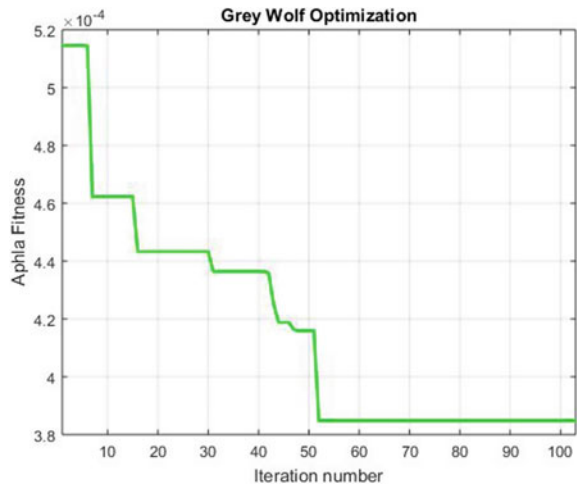


Fig. 9 Best fitness with respect to iteration



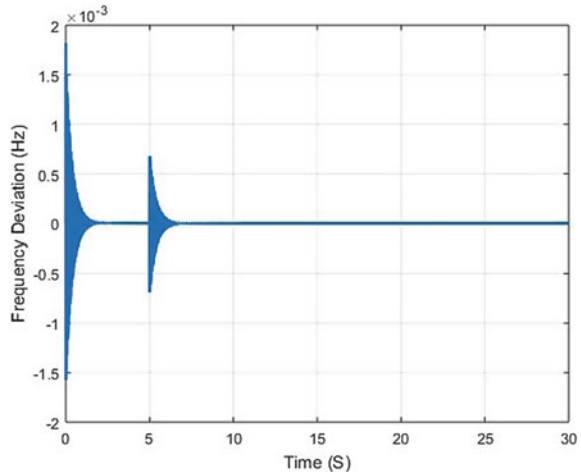
(2) HPS with SMES

Effect of GWO optimized PI controller is shown in Fig.10 which shows the mitigation of frequency deviation occurred in the system along with its best fitness value (Fig. 9).

5 Conclusion

Steady state stability analysis of hybrid power system using SMES technology has been carried out. GWO is used to tune the parameters of the PI controller. The performance of the system has been represented through simulation results, with

Fig. 10 Change in frequency



step load change. Results obtained shows that the SMES plays an important role in the mitigation of frequency deviation. With the emergence of smart grid, SMES is receiving more attention in the area of power system due to several applications such as fast response, large storage capacity and power handling capacity. Since the modern era involves renewable energy sources for power generation, it provides clean energy and pollution free environment. Therefore, it is shown that the several advantages of renewable energy hybrid power system along with SMES makes this system an important structure for power and energy system.

References

1. Tummala AS (2017) Optimal load frequency control of electric vehicle based micro-grid using Grey Wolf Optimization. In: International conference on computing of power, energy & communication-ICCPEIC-2017, vol 6
2. Singh S, Singh M, Chanana S, Raveendhra D (2014) Operation and control of a hybrid wind-diesel-battery energy system connected to micro-grid. In: International conference on control and automation, robotics and embedded system
3. Singh S, Verma RK, Shakya AK (2017) Frequency regulation of microgrid connected hybrid power system with SMES. *Technol Econ Smart Grids Sustain Energy*
4. Singh S, Joshi H, Chanana S, Verma RK (2014) Impact of superconducting magnetic energy storage on frequency stability of an isolated hybrid power system. In: *Computing for sustainable global development*. IEEE
5. Ali MH et al (2010) An overview of SMES applications in power and energy systems. *IEEE Trans Sustain Energy* 1(1):38–47
6. Singh S, Singh M, Chanana S, Semwal S (2015) Frequency regulation of isolated hybrid wind/diesel, power generation with fuel cell system. *Lecture notes in electrical engineering*, vol 326. Springer, pp 853–862
7. Mirjalili S, Mirjalili SM, Lewis A (2014) Grey Wolf optimizer. In: *Advances in engineering software*

JAYA-Evaluated Frequency Control Design for Hydroelectric Power System Using RFB and UPFC



Akhilesh Panwar, Gulshan Sharma, Ibraheem Nasiruddin and R. C. Bansal

Abstract The present paper discusses an early attempt to investigate and propose the various control actions such as integral derivative (ID), integral double derivative (IDD) and proportional integral derivative (PID) with gains evaluated via a new and powerful evolutionary technique known as JAYA algorithm to maintain the equilibrium between power generation and demand of the hydroelectric power system, and hence to reach system frequency in minimum time for variation in system demand. At first, the enactment of JAYA-ID, JAYA-IDD and JAYA-PID founded designs are assessed for standard demand change in one of the areas of a connected electric power system and the comparative assessment is carried out on the acquired value of inverse time multiplied absolute error (ITAE). The assessment of hydroelectric power system is carried out in terms of obtained gains, minimized error value and power responses to demonstrate the efficacy of the proposed design. The obtained assessment shows the advancement of JAYA-PID over other evaluated designs. However, still the hydroelectric power responses struggle with higher overshoot, unacceptable settling time and error in reaching steady state. This is due to slow responding of hydroturbines and hence the unified power flow control (UPFC) in series with tie line and support from redox flow battery (RFB) is further used in the hydroelectric power system to improve the assessment significantly. Further enrichment in the hydroelectric power responses is realized by again calculating the gains of PID via JAYA algorithm with positive contribution from RFB and UPFC.

A. Panwar (✉)

Department of Electrical Engineering, Institute of Technology, Nirma University,
Ahmedabad 382481, India
e-mail: akhileshpanwar01@gmail.com

G. Sharma

Department of Electrical Power Engineering,
Durban University of Technology, Durban 4001, South Africa

I. Nasiruddin

Department of Electrical Engineering, Jamia Millia Islamia University, New Delhi, India

R. C. Bansal

Department of Electrical and Computer Engineering, University of Sharjah,
Sharjah 27272, UAE

© Springer Nature Singapore Pte Ltd. 2020

A. Kalam et al. (eds.), *Intelligent Computing Techniques for Smart Energy Systems*,
Lecture Notes in Electrical Engineering 607,
https://doi.org/10.1007/978-981-15-0214-9_91

Keywords LFC · JAYA algorithm · RFB · UPFC · ID · IDD · PID

1 Introduction

The electric power system is escalating year by year to cater to the demands of needy and developing society considering the bounds on carbon dioxide emission by aiming towards power generation via cleaner energy sources in order to set the equilibrium between the generations and future demands. The power delivery industries are moving towards wind power, solar power, tidal power, geothermal power as well as hydropower for future energy generation and many advancements are going in the design and control strategies of renewable-based generation technologies. However, the hydropower plants are well developed as compared to other renewable technologies and can play a major role in meeting the energy demands in future. As the power generation shifts towards hydropower plants, it will be difficult to set the minute-by-minute equilibrium between generations and system demands as the time constants of hydroturbines are higher as compared to thermal turbines, and basically they are more slower compared to thermal turbines to respond for change in system demand and hence result in frequency variations and may lose the system stability completely. The equilibrium between power generation and system demand are met via load frequency control (LFC) strategy which maintains the balance among these quantities and hence keeps the electric system frequency close or near to original value as well as the tie-power exchange among interconnected areas as per the defined value [1, 2]. To meet the requirements of LFC, the control design founded on conventional design was the primary pain taken by the researchers worldwide and become unsuccessful to meet the standards of LFC due to evaluation of controller gains via trial and error technique. The recent advancement and development of artificial intelligence techniques such as fuzzy logic, genetic algorithm, particle swarm optimization, and hybrid bacteria foraging algorithm are explored and proposed by various researchers in order to provide a more advanced and effective control design for LFC, but still there is a scope of improvement and hence the new and strong optimization technique such as JAYA algorithm is always welcome in the LFC studies in order to select the gains of control design as well as to meet the requirement of LFC [3]. Further, it is also observed that LFC studies are narrow to thermal generations and very less care is taken for hydroelectric power system.

On the other side, the enrichment in power electronics industries and successful design and development of flexible alternating current transmission system (FACTS) led to its efficacious installation in the electric power system. The FACTS such as redox flow battery (RFB) is having zero time constant and is quick enough to inject the stored power in the system in case of quick alteration in the system demand. However, due to increased cost of RFB, it is not advisable to install RFB in every area of interconnected electric power system. Unified power flow controller (UPFC) is also a member of the FACTS family, is much cheaper and can be installed in series with the existing tie line and can significantly enhance the system stability [4]. In the light of the above discussion, this paper is set as follows:

1. To propose several architectures of conventional design, i.e. ID, IDD and PID with gains assessed via strong optimization algorithm, i.e. JAYA.
2. To assess the JAYA-ID, JAYA-IDD and JAYA-PID for standard system demand and to assess their performance using obtained ITAE for LFC.
3. The obtained ITAE through JAYA-PID is quite promising in comparison to other designs but still, the LFC performance of hydroelectric systems lacks in reducing the frequency and tie-power overshoots, settling time and slow movement towards steady-state condition.
4. Hence, the UPFC installed in series with the existing tie line and RFB in area-2 of the system model for further enhancement.
5. At last, the gains of PID via JAYA are again calculated with support from UPFC and RFB for standard system demand change and the enhancement in LFC performance is observed. Also, the value of filter coefficient (N) is optimized and it further results in more improvement in responses of LFC.

2 Studied Model

To assess the ability of JAYA-ID, JAYA-IDD and JAYA-PID, an interconnected hydroelectric system with hydroturbines in both areas is used for the analysis.

The RFB dynamics in area-2 and UPFC in the form of first-order gain and time constant, well-known as a transfer function, is incorporated in series with the existing tie line of the studied model. The model of the system with RFB and UPFC is given in Fig. 1. The exhaustive mathematical modelling of UPFC and RFB is not included due to space limitations.

3 JAYA-Optimized LFC Designs

In this study, the performance of various control designs is assessed by first developing the objective function (OF) on the basis of area control error (ACE). ACE combines the frequency and tie-power deviations in single quantity in a linearized form. The ITAE is considered as OF for this study as it has proficiency in settling time reduction, peak overshoot reduction which is hard enough to achieve via other error criterions such as integral of squared error (ISE) and integral of absolute error (IAE).

The OF (J_n) for the present LFC problem is as follows:

$$J_n = \int_0^{T_{sim}} (ACE) \cdot t \cdot dt \tag{1}$$

The aim of JAYA optimization is to attain the ITAE minimum considering the following limitations:

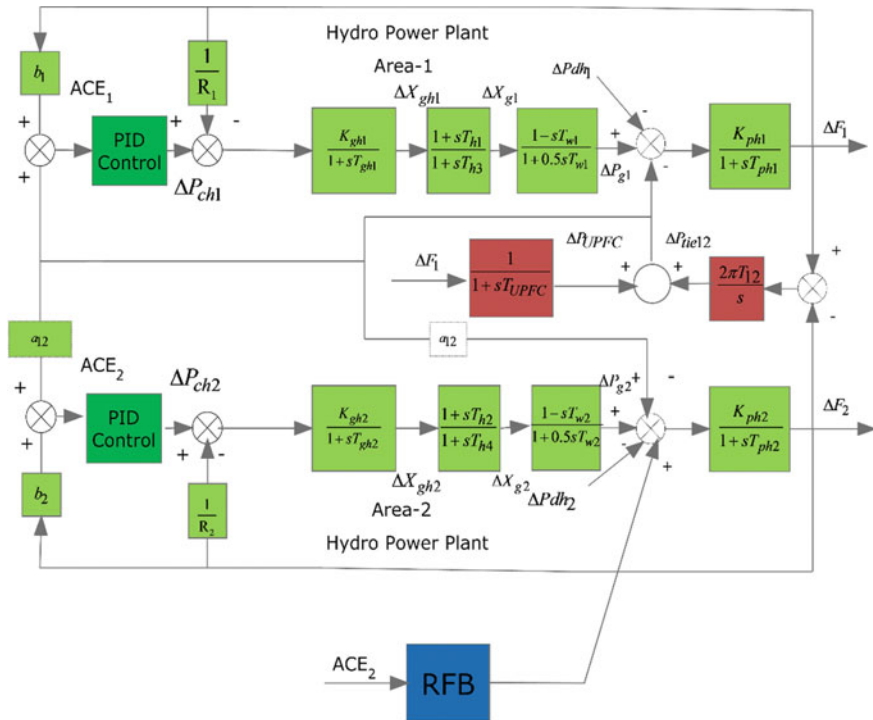


Fig. 1 Studied model

$$\begin{aligned}
 K_{pn}^{\min} &\leq K_{pn} \leq K_{pn}^{\max} \\
 K_{in}^{\min} &\leq K_{in} \leq K_{in}^{\max} \\
 K_{dn}^{\min} &\leq K_{dn} \leq K_{dn}^{\max}
 \end{aligned}$$

where K_{pn} , K_{in} and K_{dn} indicate the proportional, integral and derivative gains, respectively. The maximum and minimum range for all these parameters is considered between -3.0 and 3.0 as it will help the algorithm to provide you the desired results in minimum time. The JAYA optimization technique [3] is chosen to evaluate the various control parameters. The execution steps of the JAYA optimization in the form of a flow chart is given in Fig. 2. The algorithm is run fifty times and the best solution obtained is used as the final control parameters for the several control designs for LFC. Further, the value of filter coefficient (N) is also optimized via JAYA and it results in a significant enhancement in LFC.

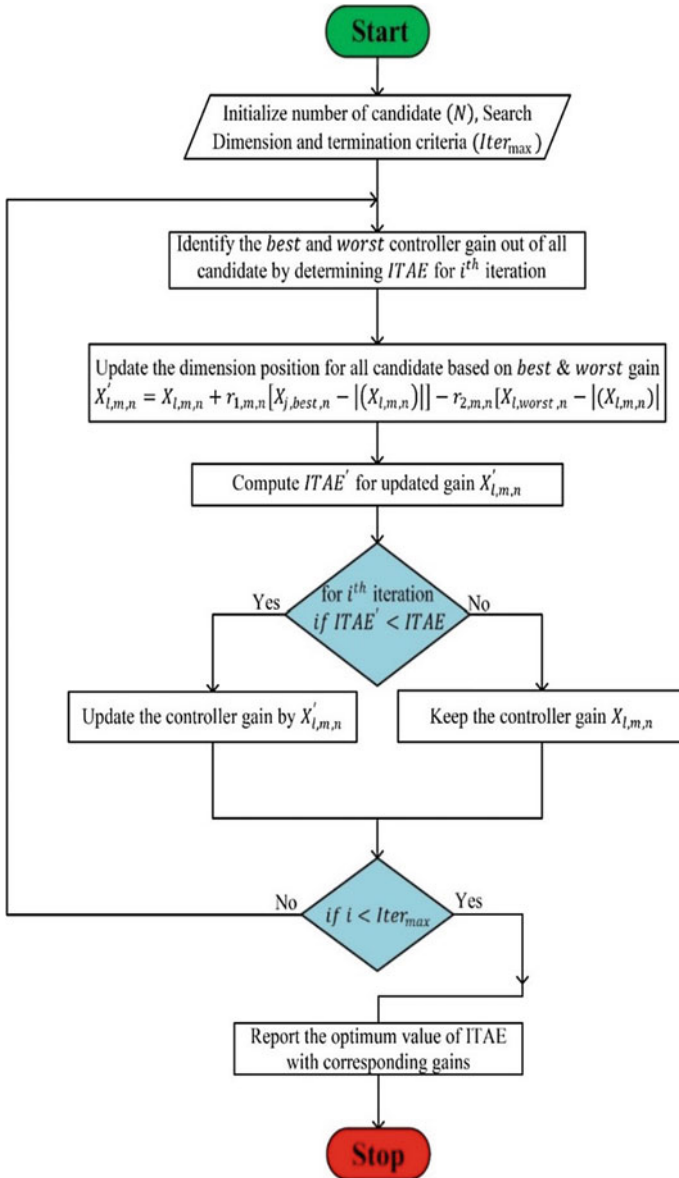


Fig. 2 Execution methodology of JAYA

4 Result Analysis

In this work, an early attempt is made to investigate the dynamics of LFC of hydro-electric power system as well as to find the suitable LFC design which can set the equilibrium between the power generation and changing system demand for such type of system. Limited work on the studied model is available in the past literature of LFC as the time constant of hydroturbines are higher as compared to thermal turbines, and it results in increased overshoot, continuous oscillations and challenging for the frequency and tie-power responses to reach steady state for standard change in the system demand. The architecture based on conventional control is the preferred choice not only in the power industry but also in various control industries due to its simplicity. Hence, the structure is kept the same and the conventional design is combined with the new and powerful optimization technique, i.e. JAYA, to evaluate the parameters of various studied designs such as ID, IDD and PID. In the first step, the gains of ID, IDD and PID are achieved for 1% change in the system demand via JAYA and a comparative analysis is carried out considering the obtained gains, ITAE value and in terms of frequency and tie-power responses. Table 1 shows the various obtained parameters for various LFCs. The ITAE reduction (4.910032) achieved with JAYA-PID in comparison to JAYA-ID (7.191476) and JAYA-IDD (7.187137) demonstrates the control and efficacy of the JAYA-PID LFC. The LFC responses of ΔF_1 , ΔF_2 (frequency deviations of areas-1 and 2) and ΔP_{tie12} (tie-power deviation) are shown in Fig. 3a–c. It is also observed that the performance of JAYA-PID LFC with the optimized value of N is showing promising performance in comparison to other LFCs and there is a great reduction in ITAE, i.e. 4.503048. However, there is still scope of improvement in LFC responses and hence the dynamics of UPFC and RFB is incorporated in the studied model. The LFC assessment is checked for alteration in the standard system demand and the performance of JAYA-PID+N is compared with JAYA-PID+N+UPFC+RFB. There is a slight increase in the value of ITAE (5.870145) as compared to ITAE obtained earlier. This is due to the fact that PID gains are the same as it is considered for JAYA-PID+N. However, the great reductions in system responses are obtained and shown in Fig. 3d–f.

Table 1 Evaluated gains of LFC designs via JAYA

LFC designs	Kp	Ki	Kd	Kd1	N	ITAE
ID	–	0.037278	0.620617	–	–	7.191476
IDD	–	0.037174	–1.215430	0.589348	–	7.187137
PID	0.343769	0.047195	–0.437454	–	–	4.910032
PID+N	0.426382	0.048893	–0.391059	–	4	4.503048
PID+N+RFB+UPFC	0.426382	0.048893	–0.391059	–	4	5.870145
PID+N+RFB+UPFC (Recalculated)	2.000000	2.000000	–0.743502	–	2	0.627759

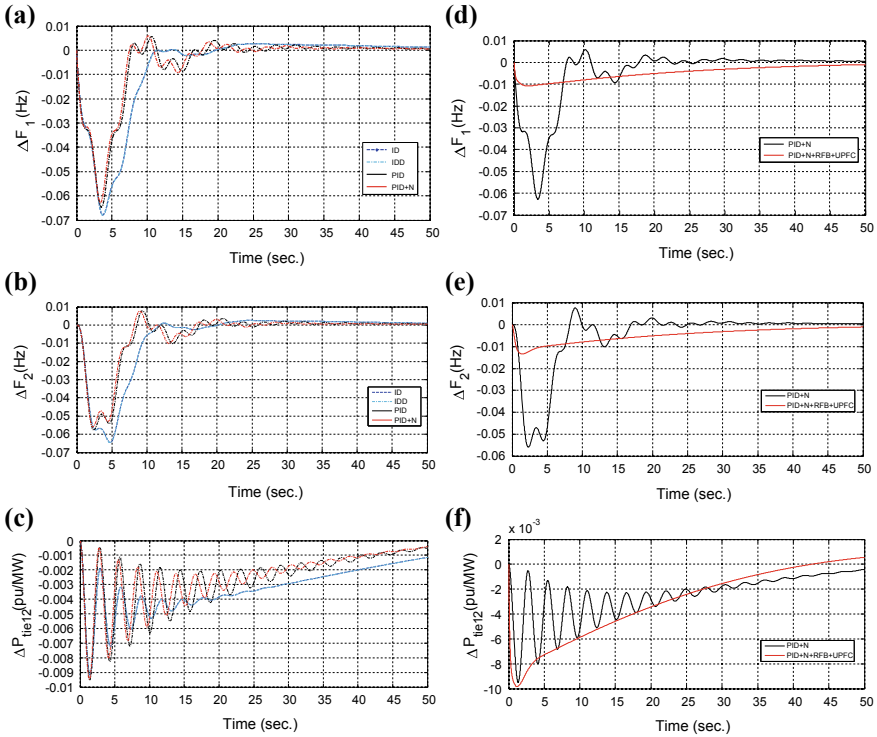


Fig. 3 a–f LFC responses for standard load change in area-1, i.e. 1%

Hence, at last, the gains of PID+UPFC+RFB+N are recalculated via JAYA and the significant reduction in the value of ITAE is achieved, i.e. 0.627759. The obtained gains as well as ITAE are shown in Table 1 and the LFC responses are shown in Fig. 4a–c. It is also observed from the power responses that there is a noticeable reduction in the overshoot and settling time enhancements via JAYA-PID+N with the UPFC+RFB combination. This is due to the fact that these energy storage technologies have lesser time constant resulting in significant enhancement in LFC.

5 Conclusion

This work is intended to design the JAYA-optimized PID controller with filter coefficient for satisfactory operation of hydro-dominated power system under step-power demand and to show its efficacy over other designs by obtaining the acceptable values of the objective function (ITAE). The response is further improved after incorporating fast-acting series-connected UPFC in tie line and power injection through RFB. The improvement in system responses such as decreased overshoot with fast settling

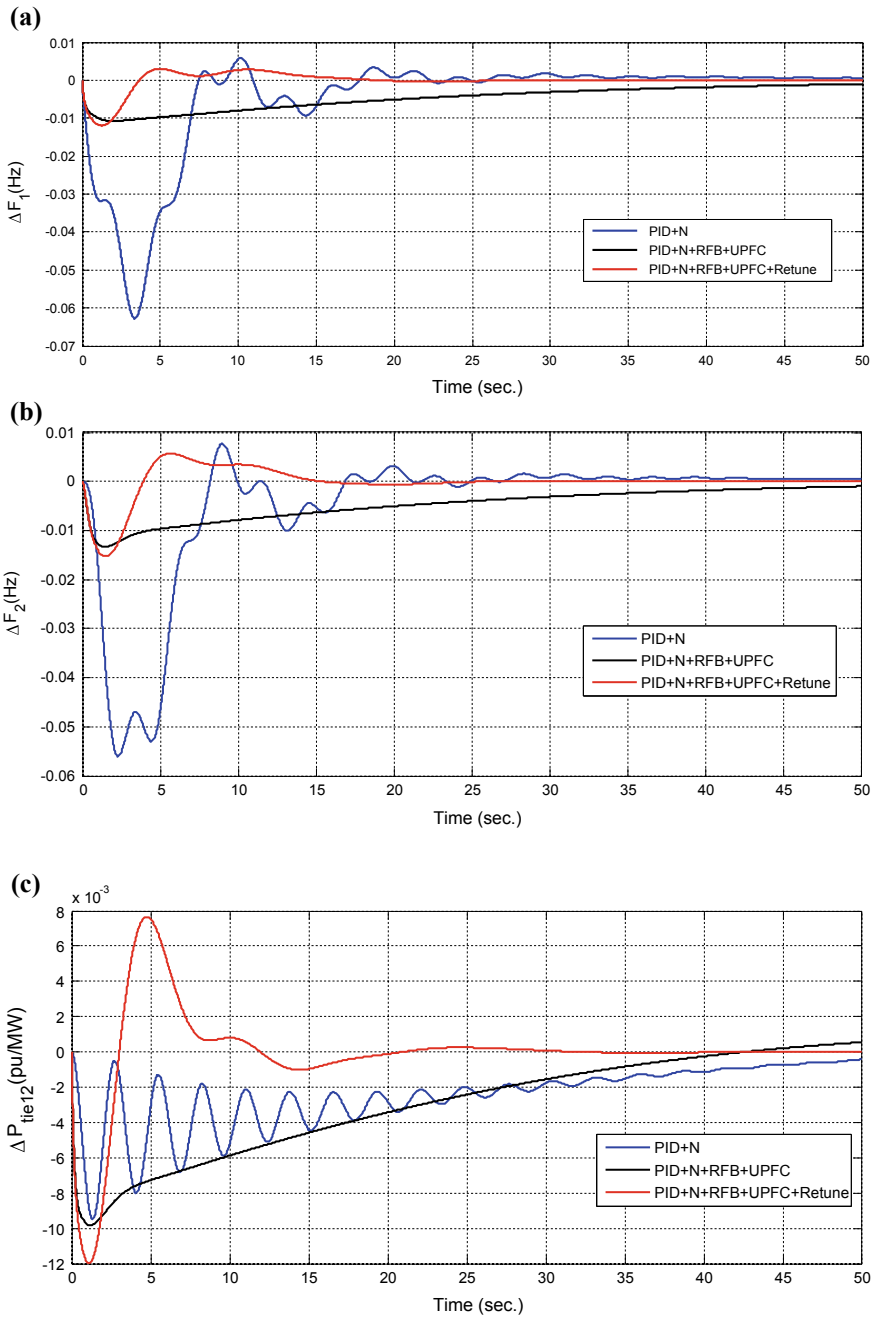


Fig. 4 a-c LFC responses for standard load change in area-1, i.e. 1%

time and zero steady-state error is achieved with the proposed design. Finally, the controller parameters are redesigned via JAYA for step power demand considering the combined effect of UPFC and RFB and the perceptible improvement in frequency control is observed for hydro-dominated power system. In conclusion, it can be said that the proposed frequency control technique is simple yet effective and provides suitable performance for such type interconnected power system.

References

1. Ibraheem, Niazi KR, Sharma G (2014) Study on dynamic participation of wind turbines in AGC of power system. *Electr Power Compon Syst* 4(1):44–55
2. Sharma G, Ibraheem, Niazi KR (2015) Optimal AGC of asynchronous power systems using output feedback control strategy with dynamic participation of wind turbines. *Electr Power Compon Syst* 43(4):384–398
3. Venkata RR (2016) Jaya: a simple and new optimization algorithm for solving constrained and unconstrained optimization problems. *Int J Ind Engg Comput* 7:19–34
4. Sahu RK, Gorripotu TS, Panda S (2015) A hybrid DE-PS algorithm for load frequency control under deregulated power system with UPFC and RFB. *Ain Shams Engg J* 6:893–911

A Human Face-Shaped Microstrip Patch Antenna for Ultra-Wideband Applications



Anandhi Dharmarajan, Pradeep Kumar and Thomas J. O. Afullo

Abstract This paper presents the design and simulation of a compact human face-shaped microstrip patch antenna that can operate from 5.9 to 11.2 GHz. The antenna has an elliptical patch with a human face to achieve the wideband characteristics. The bandwidth of the proposed antennas is further improved by using the concepts of Defected Ground Structure (DGS). The slots are inserted in the ground plane for improving the bandwidth. The proposed antenna is simulated and optimized in CST Microwave studio and the simulation results prove that the antenna can operate at a wide range of frequencies from 5.9 to 11.2 GHz. The proposed antenna is compact in size and provides wide bandwidth, high gain, high efficiency, etc. Return loss characteristics, antenna gain, radiation efficiency, and radiation patterns are presented in the paper.

Keywords Patch antenna · Defected Ground Structure (DGS) · Ultra-Wideband (UWB) antenna

1 Introduction

Microstrip patch antennas are smaller in size, have various shapes (rectangular, triangular, or circular), easy to etch in PCB, have low fabrication cost, and so are the choice for mobile communication systems. But these antennas suffer from narrow impedance bandwidth and low gain [1]. There have been various techniques to increase the bandwidth of the antenna such as increasing the thickness of the substrate, decreasing the substrate dielectric constant [2], employing electromagnetic bandgap structures [3, 4], and using defected ground structures [5, 6]. Most of these antennas are made by adding additional structure so that their structures become more complex.

A. Dharmarajan · P. Kumar (✉) · T. J. O. Afullo
Discipline of Electrical, Electronic and Computer Engineering, University of Kwazulu Natal,
King George V Avenue, Durban 4041, South Africa
e-mail: pkumar_123@yahoo.com

© Springer Nature Singapore Pte Ltd. 2020
A. Kalam et al. (eds.), *Intelligent Computing Techniques for Smart Energy Systems*,
Lecture Notes in Electrical Engineering 607,
https://doi.org/10.1007/978-981-15-0214-9_92

Ultra-Wideband (UWB) technology has attracted much attention in modern telecommunication systems as it can transmit a lot of data (high bandwidth) over a short distance without using too much power. In 2002, the Federal Communication Commission (FCC) has allotted bandwidth from 3.1 to 10.6 GHz for license-free use and named as ultra-wideband [7]. Researchers are continuously working on the design of microstrip antennas for ultra-wideband applications. Recently, ultra-wideband antennas are given using different technologies [8–10].

This paper uses Defected Ground Structure (DGS) where slots or defects are integrated on the ground plane of microwave planar circuits thus modifying the continuity of the ground plane [11, 12]. These slots are placed under the transmission line so that it can provide better coupling with the line. This improves the bandwidth of the antenna so that it can cover the UWB frequencies. The slots in the ground plane also help in reducing the return loss. The geometry of the antenna is also an important key factor in the design and therefore the antenna designed is a compact antenna. The proposed antenna is smaller in size and has wide bandwidth compared to [13, 14] which is larger in size and has narrow bandwidth. The elliptical patch antenna also has wide bandwidth compared to [15]. The presented antenna also provides high gain and efficiency. The paper is structured as follows. Section 2 explains the antenna structure. Section 3 presents the return loss characteristics, antenna gain, radiation efficiency, and radiation patterns. The conclusion is given in Sect. 4.

2 Antenna Geometry

The proposed antenna is shown in Fig. 1. Figure 1a, Fig. 1b, and Fig. 1c present the top view, bottom view, and side view of the antenna, respectively. It has an elliptical patch with a human face embedded in the patch. The antenna is designed on a 38.2 mm × 25.2 mm FR4 substrate with dielectric constant of 4.4 and substrate thickness of 1.6 mm. A thin 50 Ω microstrip line of width 3.058 mm and length 10 mm feeds the antenna. The elliptical patch is made of copper foil and has a width of 15.6 mm and a height of 28.6 mm. The ground plane is modified as shown in Fig. 1b. Two slots are provided in the ground plane to increase the bandwidth of the antenna. The ground plane has a width of 25.2 mm and a height of 9.5 mm. Both the ground and the patch have a very small thickness. The elliptical patch antenna without the human face and slots provides a very narrow bandwidth. The addition of human face with eyes and nose reduces the reflection coefficient and improves the bandwidth. The mouth in the structure further improves the bandwidth of the antenna. The addition of head and eyebrows significantly decreases the reflection coefficient and improves the bandwidth significantly. The elliptical patch is modified to have a human face in which the eyebrows have a width of 6 mm and a height of 0.4 mm. The head has a width of 12 mm. The mouth has a width of 8 mm and a height of 2 mm. The eye has a width of 4 mm. The nose has a width of 1 mm and a height of 6 mm. The entire optimized dimensions are shown in Table 1.

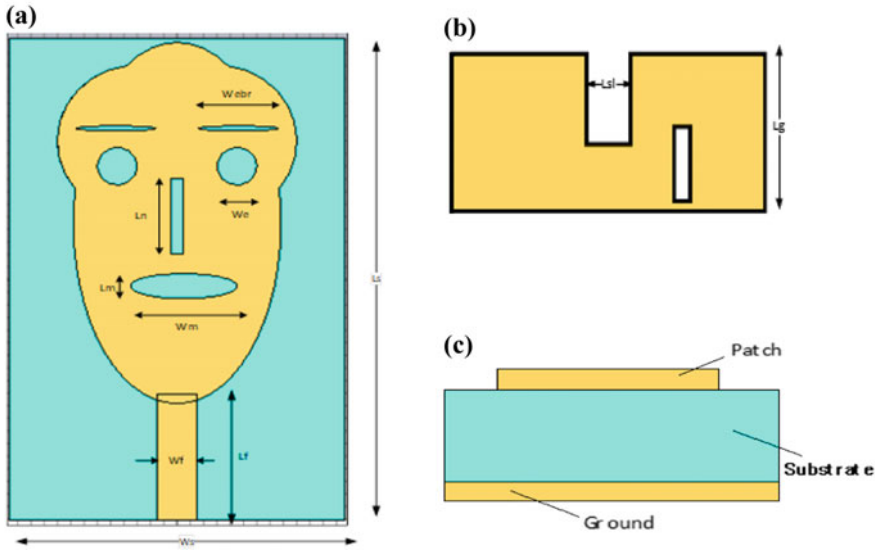


Fig. 1 Geometry of the proposed antenna **a** top view, **b** bottom view, **c** side view

Table 1 Antenna dimensions

Parameter name	Value (mm)	Description
Ls	38.2	Substrate length
Ws	25.2	Substrate width
Lf	10	Feedline length
Wf	3.05	Feedline width
Wm	8	Mouth width
Ln	1	Nose length
We	1	Eye width
Lm	2	Mouth length
Webr	6	Eyebrow width
Ws	3.4	Slot width
Lsl	5.2	Slot length
Lg	9.5	Ground length

3 Simulation Results

The antenna is simulated using CST microwave studio and the results for the reflection coefficient plot with elliptical patch and elliptical patch with slots are discussed. S11 denotes the power that is reflected back from an antenna and it is also known by reflection coefficient. Figure 2 shows the S11 plot for the elliptical patch antenna with no slots in the ground plane. The reflection coefficient is -16 dB with a –

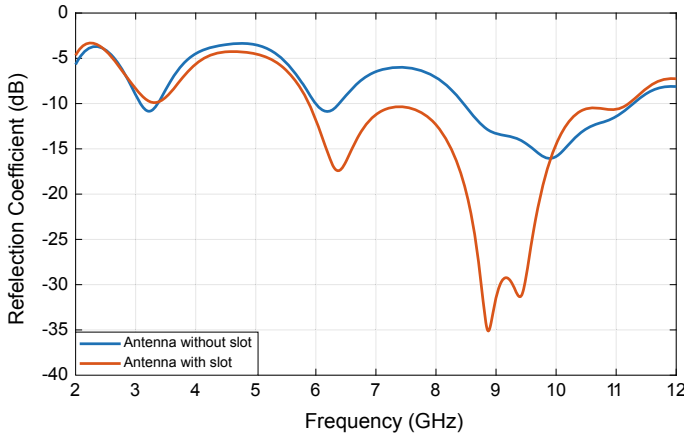


Fig. 2 Reflection coefficient of the antenna

Table 2 Reflection coefficient and bandwidth for various antenna structures

Antenna structure	S11 (dB)	Bandwidth (GHz)
No slots and no face	-17	8.4–10
No face and two slots	-26.17	7.6–10.7
Two slots, human face with eyes and nose	-25	7.6–10.7
Two slots, human face with eyes, nose, and mouth	-29.7	7.6–10.8
Two slots, human face with eyes, mouth, nose, and eyebrows	-35.11	5.9–11.2
No slots, human face with eyes, mouth, nose, and eyebrows	-16	8.4–11.2

10 dB bandwidth of 2.8 GHz. Figure 2 also shows the S11 plot for the elliptical patch antenna with two slots in the ground plane. The return loss is -35.11 dB with a -10 dB bandwidth of 5.3 GHz. From Table 2, it is evident that the human face in the elliptical patch with eyes, nose, mouth, and eyebrows is necessary to achieve the wide bandwidth with reduced reflection coefficient of -35.11 dB. Figure 3 shows the radiation pattern of the antenna without DGS for $f = 8$ GHz and $f = 10$ GHz. Figure 4 shows the radiation pattern of the antenna with DGS (two slots in the ground plane) for $f = 8$ GHz and $f = 10$ GHz. It is observed that the patterns are not stable with the frequency. Future work will be done to achieve stable patterns. Table 3 shows the maximum gain, maximum directivity, radiation efficiency, and total efficiency of the antenna at various frequencies. It is seen that the gain and directivity is maximum at $f = 10$ GHz. Table 4 shows the comparison of human face antenna with the other existing antennas. It is seen that the designed antenna is compact in size which provides high gain and minimum reflection coefficient.

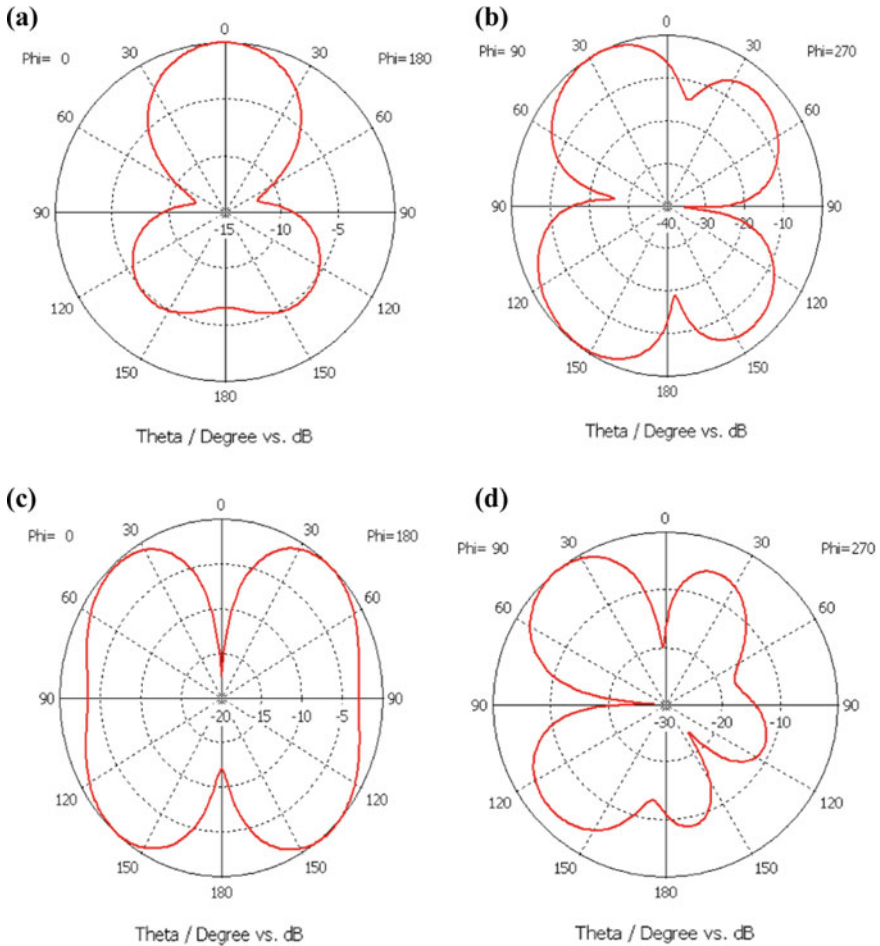


Fig. 3 Radiation pattern for antenna without slots **a** $f = 8 \text{ GHz}$, $\phi = 0^\circ$, **b** $f = 8 \text{ GHz}$, $\phi = 90^\circ$, **c** $f = 10 \text{ GHz}$, $\phi = 0^\circ$, **d** $f = 10 \text{ GHz}$, $\phi = 90^\circ$

4 Conclusion

An elliptical human face patch antenna with eyes, nose, eyebrows, and nose with DGS is designed. The proposed antenna has a wide bandwidth from 5.9 to 11.2 GHz and is found to be higher than the antenna without DGS (8.4–11.2 GHz). The antenna designed is suitable for UWB applications. The design of the antenna is simple, and the antenna is easy to fabricate and is compact. The antenna shows high gain and wide bandwidth characteristics. In future work, the antenna will be designed to cover the entire UWB band with polarization diversity.

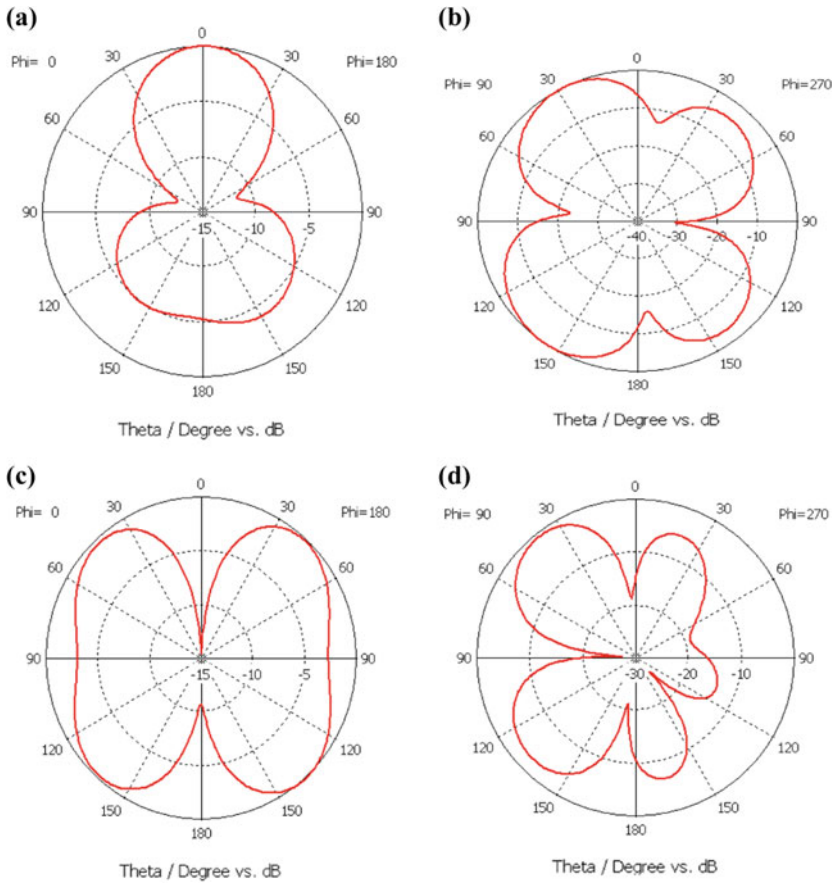


Fig. 4 Radiation pattern for antenna with DGS (two slots) **a** $f = 8$ GHz, $\phi = 0^\circ$, **b** $f = 8$ GHz, $\phi = 90^\circ$, **c** $f = 10$ GHz, $\phi = 0^\circ$, **d** $f = 10$ GHz, $\phi = 90^\circ$ and $f = 10$ GHz

Table 3 Gain, radiation efficiency, total efficiency, and directivity at various frequencies

Frequency	$f = 2$ GHz	$f = 4$ GHz	$f = 6$ GHz	$f = 8$ GHz	$f = 10$ GHz	$f = 12$ GHz
Gain (dB)	-0.0154	2.720	4.377	3.778	6.219	5.570
Radiation efficiency (dB)	-1.929	-0.4820	-0.7422	-0.4294	-0.0499	-0.1508
Total efficiency (dB)	-4.437	-2.271	-0.8475	-0.4915	-0.4738	-1.077
Directivity (dBi)	1.913	3.202	5.119	4.207	6.268	5.721

Table 4 Comparison of human face antenna with existing antennas

Reference	[16]	[17]	[18]	[19]	Proposed antenna
Max. gain (dB)	3	1.49	7.362	3.778	6.219
Bandwidth (%)	140	77	142	119	70
size (mm)	40 * 40	20 * 18	70 * 82	30 * 30.82	25.2 * 38.2
Min. reflection coff. (dB)	-30	-16	-26.02	-28.4908	-35

References

- Balanis CA (2005) Antenna theory analysis & design, 3rd edn. Wiley, New York
- Yi XH, Wu T, Wang Y, Tentzeris MM (2015) Sensitivity modeling of an RFID-based strain-sensing antenna with dielectric constant change. *IEEE Sens J* 15(11):6147–6155
- Majid HA, Abd Rahim MK, Hamid MR (2015) Wideband antenna with reconfigurable band notched using EBG structure. *Prog Electromagn Res Lett* 54:7–13
- Kurra L, Abegaonkar MP, Basu A, Koul SK (2016) FSS properties of a uni-planar EBG and its application in directivity enhancement of a microstrip antenna. *IEEE Antennas Wirel Propag Lett* 15:1606–1609
- Patel R, Desai A, Upadhyay T (2018) An electrically small antenna using defected ground structure for RFID, GPS and IEEE 802.11 a/b/g/s applications. *Prog Electromagn Res Lett* 75:75–81 (2018)
- Desai A, Upadhyaya T, Patel R, Bhatt S, Mankodi P (2018) Wideband high gain fractal antenna for wireless applications. *Prog Electromagn Res Lett* 74:125–130
- Siwiak K, McKeown D (2004) Ultra-wideband radio technology. Wiley, Hoboken, NJ
- Kumar P, Masa-Campos JL (2016) Dual polarized monopole patch antennas for UWB applications with elimination of WLAN signals. *Adv Electromagn* 5(1):46–52
- Kumar P (2017) Design of low cross-polarized patch antenna for ultra-wideband applications. *Int J Comm Antenna Prop* 7(4):265–270
- Prashnath KV, Hadalgi PM (2018) Design of compact UWB antenna for wireless applications. In: AIP conference proceedings, vol 1989 (1)
- Guha D, Biswas S, Kumar C (2014) Printed antenna designs using defected ground structures: a review of fundamentals and state-of-the-art developments. In: Forum for electromagnetic research methods and application technologies (FERMAT), pp 1–13
- Mabaso M, Kumar P (2018) A dual band patch antenna for bluetooth and wireless local area networks applications. *Int J Microw Opt Technol* 13(5):393–400
- Thatere A, Arya D, Zade PL (2017) Wi-Fi microstrip antenna with DGS. In: 2017 innovations in power and advanced computing technologies, pp 1–6 (2017)
- Kannadhasan S, Shagar AC (2017) Design and analysis of U shaped micro strip patch antenna. In: 2017 third international conference on advances in electrical, electronics, information, communication and bio-informatics (AEEICB), pp 1–4 (2017)
- Maiti S, Rajak SK, Mukherjee A (2014) Design of a compact ultra wide band microstrip patch antenna. In: Fifth international conference on computing, communications and networking technologies, pp 1–3
- Ibrahim AA, Abdalla MA (2016) Compact size UWB antenna with multi-band notched characteristics for wireless applications. In: 2016 IEEE international symposium on antennas and propagation, pp 1–2 (2016)
- Ullah MA, Ashraf FB, Alam T, Alam MS, Kibria S, Islam MT (2016) A compact triangular shaped microstrip patch antenna with triangular slotted ground for UWB application. In: 2016 international conference on innovations in science, engineering and technology, pp 1–4 (2016)

18. Senapati M, Kumar P, Bara V (2016) Design of microstrip patch antenna for application in UWB region. In: 2016 10th international conference on intelligent systems and control, pp 1–3 (2016)
19. Singh GP, Kumar M, Saxena R, Ansari JA (2017) Bandwidth analysis of boomerang slot rectangular microstrip patch antenna. In: 2017 2nd international conference on telecommunication and networks, pp 1–4

Scheduling Energy Storage to Provide Balancing During Line Contingency at High Wind Penetration



Bal Krishna, Anjali Jain and Ajay Bharadwaj

Abstract Decarbonization of electrical sector increases the penetration of nonfossil fuel-based energy resources in power system. These resources are intermittent in nature which result in frequent demand–supply imbalance. Moreover, operational constraints of conventional generating units and technical limits of network restrict required amount of balancing from supply side. This necessitates the integration of flexible resources to increase system reliability by reducing gap between demand and supply. In this context, a battery energy storage system is integrated as flexible resource. This framework is modeled on RTS-24 bus system with 40% wind penetration using mix-integer linear programming (MILP). A security-constrained unit commitment (SCUC) is performed with (N-1) line contingency. This results in improved demand–supply balance along with reduced wind curtailment.

Keywords Energy storage · Load following · Microgrid · Outage mitigation · Uncertainty

Nomenclature

Sets and Indices

$u \in U$	Dispatchable Generating Units
T	Set for time interval indexed by t
b, n	Index for bus, node
$w \in W$	Wind units
$s \in ST$	Storage units

B. Krishna · A. Bharadwaj
Swami Keshvanand Institute of Technology, Management and Gramothan, Jaipur, India
e-mail: research.balkrishna@gmail.com

A. Jain (✉)
Malaviya National Institute of Technology, Jaipur, India
e-mail: anjaliain025@gmail.com

© Springer Nature Singapore Pte Ltd. 2020
A. Kalam et al. (eds.), *Intelligent Computing Techniques for Smart Energy Systems*,
Lecture Notes in Electrical Engineering 607,
https://doi.org/10.1007/978-981-15-0214-9_93

u_b	Index for dispatchable units u connected at bus b
w_b	Index for wind units w connected at bus b
s_b	Index for storage units s connected at bus b

Parameters

C_u^{op}	Operating Cost of unit u (\$/MWh)
$\overline{P}_u/\underline{P}_u$	Maximum/minimum Power limits of unit u
η_s^c/η_s^d	Charging/discharging efficiency of storage unit s
SOC_s^+/SOC_s^-	Maximum/minimum limit of charge for storage unit s
RP_u^+/RP_u^-	Limits for ramp-up/ramp-down rate of unit u (MW/h)
MU_u/MD_u	Minimum up/minimum downtime of unit u (hour)
S_u^+/S_u^-	Start-up/shutdown ramp limits of unit u (MW/h)
C_u^s/C_u^d	Start-up/shutdown cost of unit u (\$)
$\gamma_{b,n}$	Admittance of line between bus b and node n
$P_{w,t}^A$	Available wind generation of unit w at time t (MW)
L_b^t	Total load at bus b at time t (MW)
$\text{lim}_{b,n}$	Line limits between bus b and node n (MVA)
S_{base}	Base value of apparent power
VLS	Value of load shed (\$/MWh)

Variables

C_{gen}	Cost of generation (\$)
$P_{u,t}$	Power generation of unit u at time t
$H_{u,t}^{on}/H_{u,t}^{off}$	Total on/off-hours of unit u at time t
$P_{w,t}/P_{w,t}^c$	Wind power generation/curtailment of unit w at time t
$L_{b,t}^s$	Load shedding at bus b at time t (MW)
$P_{s,t}^c/P_{s,t}^d$	Charging/discharging power of storage units s at time t (MW)
$SOC_{s,t}$	Charging status of storage units s at time t (MWh)
$l_{s,t}/m_{s,t}$	Charging/discharging binary variable for storage unit s (1-charging/discharging)
$v_{u,t}$	Unit commitment binary variable for unit u (1-on, 0-off)
$\alpha_{u,t}/\beta_{u,t}$	Start-up/shutdown binary variable for unit u
$\delta_{b,t}$	Load angel of bus b at time t
$Fl_{b,n,t}$	Power flow at time t from line connected between bus b and node n

1 Introduction

The increased concern toward decarbonization and sustainable energy drive the power sector toward high penetration of green energy resources such as solar and wind. However, their inherent variability due to weather dependency causes high intermittency in their generation profile. This intermittency poses many challenges to system operator in meeting demand–supply balance.

The benefits of wind generation get undermined when hybridizing wind energy with thermal systems due to operational constraints of thermal units [1]. High penetration of wind energy makes the net load more variable and requires high system flexibility [2]. Wind curtailment and load shedding are two major performance specifications to measure system reliability [3]. The power plant operator decides the unit commitment (UC) in the presence of flexible resources when large-scale wind units are integrated into the grid.

Energy storage systems (ESS) can improve the system flexibility and participate in UC by providing multiple grid services such as energy arbitrage, peak shaving, and frequency response [4]. Co-optimization of dispatchable generating units and ESS can reduce the operational cost and improves the system reliability [5]. The operating cost can be minimized by reducing the load shedding and RE curtailment. This can be done by reserving the energy at off-peak load time and utilizing that energy during peak load time. Storage devices such as compressed air energy storage, pumped storage, ultra-capacitor, flywheel, and battery storage are widely used and can be compared with respect to their technical characteristics to provide grid services [2–6]. A study has been done to determine various strategies to provide reserve from wind and storage where storage participates to mitigate the wind volatility [7].

A pump hydro station is used to flatten the net load variations caused by intermittency and anti-peaking characteristics of wind and later, the smoothed net load is distributed among dispatchable thermal units [8]. A study on single-area power system shows the effectiveness of ESS to provide frequency regulation services [9].

In [10], the particle swarm optimization is used to minimize the operating cost and bring out economic benefits in day-ahead multi-objective dispatching problem consisting CGs with wind and pumped storage units. In [11], temporal and spatial uncertainty of wind and solar is captured by Robust UC formulation incorporating large-scale storage devices. In [12], ESS is used to improve operational flexibility of the system.

Operational complexity increases during any contingency while performing security constraints unit commitment (SCUC). Considering all operational limits of dispatchable units and network security limits, this paper performs day-ahead SCUC to improve the system performance in terms of reduced wind curtailment and load shedding by the incorporation of energy storage with wind generating units. The system is simulated in general algebraic modeling system (GAMS) using mixed-integer linear programming (MILP) and scheduled for 24-h time horizon. Performance of system is analyzed with line outage (N-1) contingency.

2 Problem Formulation

Two cases are studied in this paper. Case-I: SCUC without any contingency, Case-II: SCUC with line contingency. Both the cases are further analyzed for 40% wind penetration with and without energy storage system.

2.1 Objective Function

The objective function (1) minimizes the total generation cost while maintaining the reliability of the system. Three costs are considered under generating cost namely operating cost, start-up cost, and shutdown cost. Penalty for load shed is also added in objective function to improve the reliability by minimizing penalty with other operational costs.

$$\text{Min}C_{gen} = \sum_{u,t} P_{u,t} C_u^{op} + \sum_{u,t} C_u^s \alpha_{u,t} + \sum_{u,t} C_u^d \beta_{u,t} + \sum_{b,t} L_{b,t}^s VLS \quad (1)$$

2.2 Operating Constraints

Up-Ramp and Down-Ramp Limits

The ramp rate is the rate of change of output over a period. The up- and down-ramp limits of thermal unit are explained in (2) and (3).

$$P_{u,t} - P_{u,t-1} \leq RP_u^+ v_{u,t-1} + S_u^+ \alpha_{u,t} \quad \forall u, t \quad (2)$$

$$P_{u,t-1} - P_{u,t} \leq RP_u^- v_{u,t} + S_u^- \beta_{u,t} \quad \forall u, t \quad (3)$$

Unit Status

Unit running status can be analyzed by (4). Equation (5) ensures that any unit cannot undergo in start-up and shutdown mode simultaneously.

$$\alpha_{u,t} - \beta_{u,t} = v_{u,t} - v_{u,t-1} \quad \forall u, t \quad (4)$$

$$\alpha_{u,t} + \beta_{u,t} \leq 1 \quad (5)$$

Generation Power Limit

Generating units generate power within its minimum/maximum power limits (6).

$$\underline{P}_u v_{u,t} \leq P_{u,t} \leq \overline{P}_u v_{u,t} \quad \forall u, t \quad (6)$$

Unit Minimum Up and Downtime

Every generating unit needs to fulfill its specified minimum up and minimum downtime due to thermal constraints that can be ensured as explained in (7) and (8).

$$[H_{u,t-1}^{on} - MU_u][v_{u,t-1} - v_{u,t}] \geq 0 \quad \forall u, t \quad (7)$$

$$[H_{u,t-1}^{off} - MD_u][v_{u,t} - v_{u,t-1}] \geq 0 \quad \forall u, t \quad (8)$$

Security Constraints

In DC-optimal power flow, power flow through transmission lines depends on power angle defined by delta (9). The p.u. value of the power flow should be limited by p.u. capacity of line (10).

$$Fl_{b,n,t} = \gamma_{b,n}(\delta_{b,t} - \delta_{n,t}) \quad \forall b, n, t \quad (9)$$

$$-\lim_{b,n} /S_{base} \leq Fl_{b,n,t} \leq \lim_{b,n} /S_{base} \quad \forall b, n, t \quad (10)$$

2.3 Wind Generation Constraints

Wind generating station generates the wind energy and curtails the excess amount that cannot be integrated with coordination to balance the overall system as given in (11).

$$P_{w,t} + P_{w,t}^c \leq P_{w,t}^A \quad \forall w, t \quad (11)$$

2.4 Storage Constraints

ESS stores the excess power to deliver during generation deficiency. Its operation can be explained by (12). Status of charge and charging/discharging powers are constraint by (13) to (15). Equation (16) ensures its nonsimultaneous charging and discharging.

$$SOC_{s,t} = SOC_{s,t-1} + (P_{s,t}^c \eta_s^c - P_{s,t}^d / \eta_s^d) \Delta t \quad \forall s, t \quad (12)$$

$$\underline{SOC}_s \leq SOC_{s,t} \leq \overline{SOC}_s \quad \forall s, t \quad (13)$$

$$\underline{P}_s^c l_{s,t} \leq P_s^c(t) \leq \overline{P}_s^c l_{s,t} \quad \forall s, t \quad (14)$$

$$\underline{P}_s^d m_{s,t} \leq P_s^d(t) \leq \overline{P}_s^d m_{s,t} \quad \forall s, t \quad (15)$$

$$l_{s,t} + m_{s,t} \leq 1 \quad (16)$$

2.5 Power Balance

In case of penetration of wind and integration of storage, the overall power at any bus is given by (17).

$$\sum_{u \in u_b} P_{u,t} + \sum_{w \in w_b} P_{w,t} + L_{b,t}^s + \sum_{s \in s_b} P_{s,t}^d - \sum_{s \in s_b} P_{s,t}^c - L_{b,t} = \sum_{n \in b} Fl_{b,n,t} S_{base} \quad (17)$$

3 Data and Result Analysis

3.1 Data

IEEE RTS-24 bus system is considered for this study consisting of 12 conventional generating units with total capacity 3375 MW including two nuclear, six coal-based, three oil-based, and one hydro generating units. The hourly load curve is shown in Fig. 1. To simulate wind generating units, 30 years historical data has been taken from [13]. Hourly wind generation profile of a day is developed by performing Monte Carlo Simulation considering Weibull distribution and is shown in Fig. 1.

3.2 Result Analysis

To examine the system performance at high wind penetration with the role of storage in improving reliability, two cases with three different conditions have been considered; Case-I: SCUC without contingency and Case-II: SCUC with (N-1) line contingency.

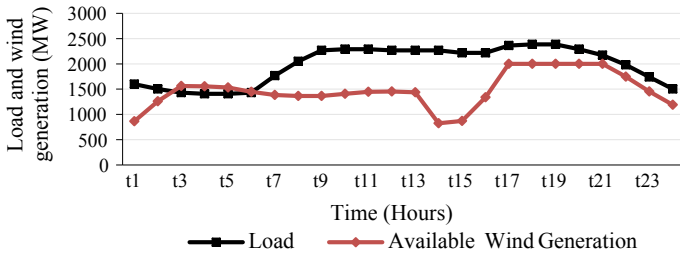


Fig. 1 Hourly load and available wind generation curve

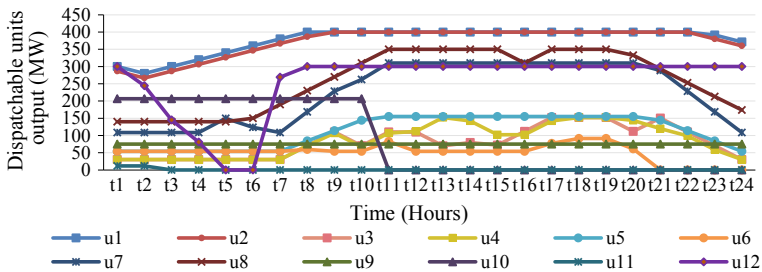


Fig. 2 Dispatch of dispatchable units in SCUC

Case-I: SCUC Without Contingency

Scheduling Dispatchable Units only

In this case, generating units are scheduled for 24 h without wind integration. Generation at different buses with dispatch profile as shown in Fig. 2 is capable to meet load.

Scheduling Units with Wind Penetration

In this case, 40% wind penetration is introduced. Wind units having capacity 400 MW each are connected at bus no. 10, 13, 14, 15, and 23. Results depict that there is significant load and wind curtailment with 105 MW and 6934 MW, respectively, as operational constraints of dispatchable generating units limit them to provide required balancing. Variation of net load, load curtailment, and output of dispatchable units is shown in Fig. 3.

Scheduling Dispatchable Units and Wind Units with Energy Storage

To improve the reliability of system, battery energy storage is integrated with wind units having 40 MWh energy capacity of each. Incorporation of storage decreases the load shedding to zero with 422 MW decline in wind curtailment as shown in Fig. 4.

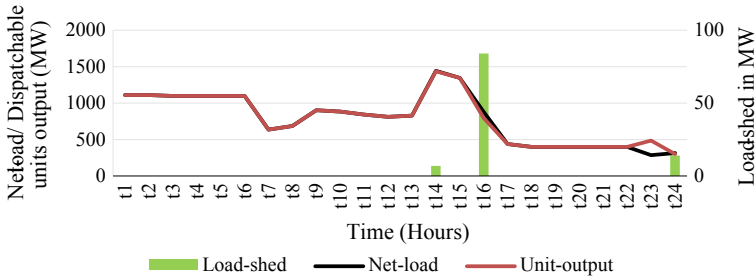


Fig. 3 Load shedding at 40% wind penetration

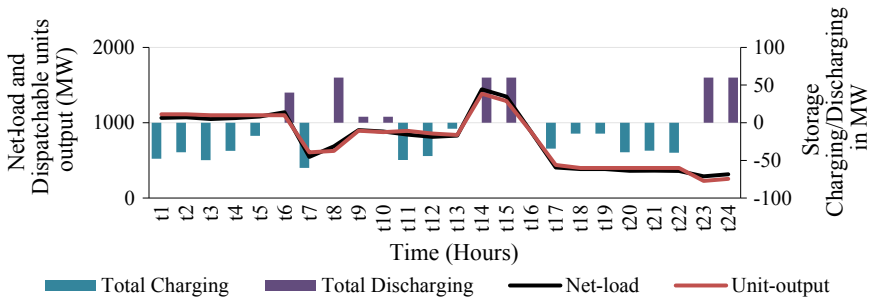


Fig. 4 Storage charging/discharging to improve reliability

Case-II: SCUC with (N-1) Line Contingency

All the three conditions studied in Case-I are again examined with a line contingency, i.e., outage of line connected between bus no. 13 and 23 (capacity 500 MVA).

Scheduling Dispatchable Units only

The system is capable to meet the load requirement even with (N-1) contingency. Figure 5 demonstrates the results of system study with (N-1) contingency at line 13–23.

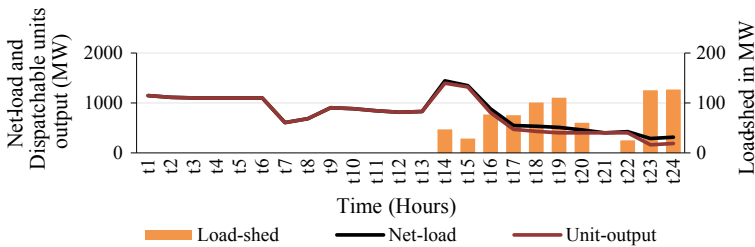


Fig. 5 Load shedding at line contingency with 40% wind penetration

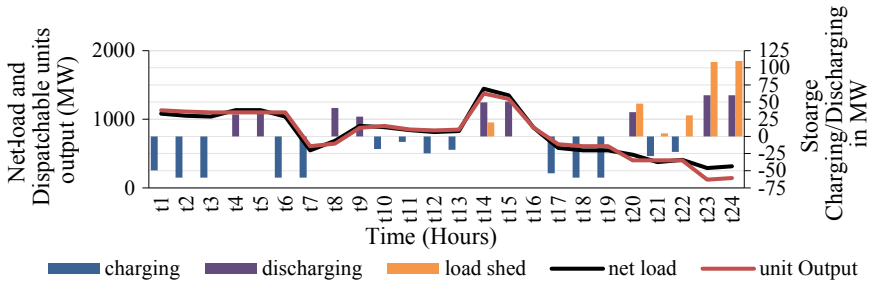


Fig. 6 Storage charging/discharging to improve reliability at line contingency

Scheduling Units with Wind Penetration

Line contingency in presence of high wind penetration causes an indicative amount of load shed of 776 MW as shown in Fig. 5 with 7372 MW wind curtailment in a day.

Scheduling Dispatchable Units and Wind Units with Energy Storage

Figure 6 indicates that integration of storage decreases the load shedding and wind curtailment significantly as 455 MW and 172 MW, respectively.

4 Conclusion

Energy generated by wind is highly intermittent due to weather dependency. To reduce the variability created by wind integration, the introduction of energy storage system as a flexible resource is necessary. SCUC in presence of high wind penetration is performed. The overall reliability and performance of system are compared here for with storage and without storage cases. The same study is conducted and analyzed during line contingency. The line outage results in more wind curtailment and load shedding. Results indicate that participation of storage makes the entire system more reliable by reducing both wind and load curtailment.

References

1. Wang C et al (2013) A consideration of the wind power benefits in day-ahead scheduling of wind-coal intensive power systems. *IEEE Trans Power Syst* 28(1):236–245
2. Badakhshan S et al (2017) Security-constrained unit commitment with integration of battery storage in wind power plant. In: 2017 IEEE power & energy society innovative smart grid technologies conference (ISGT), Washington, DC, pp 1–5
3. Bakirtzis EA et al (2017) Storage management by rolling unit commitment for high renewable energy penetration. In: 2017 IEEE Manchester PowerTech, Manchester, pp 1–6

4. Beaudin M et al (2010) Energy storage for mitigating the variability of renewable electricity sources: an updated review. *Energy Sustain Dev* 14(4):302–314
5. Bruninx K, Delarue E (2017) Improved energy storage system & unit commitment scheduling. In: 2017 IEEE Manchester PowerTech, Manchester, pp 1–6
6. Eyer J et al (2010) Technical Report Energy storage for the electricity grid: benefits and market potential assessment guide. SANDIA National Laboratory, US, February
7. Jian X et al (2016) Unit commitment considering reserve provision by wind generation and storage. In: 2016 IEEE PES Asia-Pacific power and energy engineering conference (APPEEC), pp 8–12
8. Sheng S, Sun X (2014) “A new unit commitment model considering wind power and pumped storage power station,” *electronics, computer and applications*. In: 2014 IEEE workshop on electronics, computer and applications, Ottawa, ON, pp 743–746
9. Zhang F et al (2017) Assessment of the effectiveness of energy storage resources in the frequency regulation of a single-area power system. *IEEE Trans Power Syst* 32(5):3373–3380
10. Shi N et al (2016) Unit commitment and multi-objective optimal dispatch model for wind-hydro-thermal power system with pumped storage. In: IEEE Power Electronics and Motion Control Conference (PEMC-ECCE Asia), pp 1489–1495
11. Lorca Á et al (2017) Multistage robust unit commitment with dynamic uncertainty sets and energy storage. *IEEE Trans Power Syst* 32(3):1678–1688
12. Falugi P, Konstantelos I, Strbac G (2018) Planning with multiple transmission and storage investment options under uncertainty: a nested decomposition approach. *IEEE Trans Power Syst* 33(4)
13. NREL. NREL’s PVWatts Calculator (2017). <http://pvwatts.nrel.gov/India/>. Accessed 16 February 2018

Multilevel Inverter Topologies in Renewable Energy Applications



**Prakash Kumar, Maneet Kour, Sunil Kumar Goyal
and Bhuwan Pratap Singh**

Abstract In recent decades, multilevel inverters (MLIs) have gained attention in grid-connected and stand-alone applications. The increasing dependence on electrical power and uneven distribution of energy reserves needs suitable converter design to meet low demand efficiently. MLIs have reduced harmonics and are best suited for domestic as well as industrial applications. With the current improvements in renewable energy systems (RES), uses of traditional MLI topologies are thwarted because of their issues in performance like low power quality, low efficiency, and uneconomical structure. These confinements in the performance issues of traditional MLI topologies have pulled in the researchers toward developing new hybrid type of MLI topologies. In the present article, a detailed analysis of such current hybrid MLI topologies is given based on certain indices covering both qualitative and quantitative performance. Due concentration has been given to widely review the impact of MLIs in grid associated renewable energy applications, for example, photovoltaic (PV) frameworks, wind energy conversion systems (WECS) as well as microgrids.

Keywords Multilevel inverter · Reduced component count topologies · Classical topologies · Renewable energy systems · Point of common coupling

P. Kumar
Department of Electrical Engineering, Amity University, Patna 801503, India
e-mail: prakash.ucertu@gmail.com

M. Kour
Government College of Engineering and Technology, Jammu, Jammu 181122, India
e-mail: maneet.1556@gmail.com

S. K. Goyal (✉) · B. P. Singh
Department of Electrical Engineering, Manipal University Jaipur, Jaipur 303007, India
e-mail: sunilkumar.goyal@jaipur.manipal.edu

B. P. Singh
e-mail: halobhuwan@gmail.com

© Springer Nature Singapore Pte Ltd. 2020
A. Kalam et al. (eds.), *Intelligent Computing Techniques for Smart Energy Systems*,
Lecture Notes in Electrical Engineering 607,
https://doi.org/10.1007/978-981-15-0214-9_95

1 Introduction

The concept of MLI is dated back to 1975 and was put forward by Baker and Banister. Throughout the years, MLIs have been widely used in numerous modern applications, for example, medium voltage (MV) high-power drives [1, 2], electric vehicles (EV) [3, 4], dynamic voltage restorer (DVR) [5] active power filters [6], unified power flow controller (UPFC) [7], microgrids [8], power line conditioner [9], distribution static compensator (DSTATCOM) [10], stand-alone or grid-connected photovoltaic (PV) frameworks [11–14], and various different applications. The uses of two-level voltage source inverters (VSIs) were for the most part limited to low voltage (LV) and applications involving medium power because of the power rating and voltage imperatives on power semiconductor gadgets. Likewise, these pulse width modulation (PWM) inverters experienced high amount of losses during switching owing to switching operation on high frequencies. Such confinements offered ascend to the idea of multilevel inverter (MLI) which alludes to age of voltage levels higher than two levels at inverter output by utilizing a variety of power semiconductor gadgets, dc voltage sources, and capacitors [15]. The first MLI topology was called cascaded inverter, giving stepped AC voltage as the output. In 1980, a new type of VSI topology was patented called the neutral point clamped (NPC). The disadvantages of this topology are unbalanced dc-link voltage and necessity of a large number of clamping diodes [16]. A new type of MLI called the flying capacitor (FC) was proposed in 1992. In this topology, the flying capacitor is employed as clamping device but an increased number of storage capacitors are used for high-voltage applications [16, 17]. Among them, the cascaded H-bridge (CHB) is a suitable choice for application in high voltages owing to its control simplicity. But, CHB additionally has a restriction because of its prerequisite of huge number of isolated dc voltage sources.

Recently, many hybrid inverter topologies have been proposed by researchers, derived from classical topologies for eliminating various power quality problems and meeting high grid standards in a sparing way. Reduced component count (RCC) topologies using H-bridge [18–23] have isolated blocks for level generation and polarity, while topologies not using H-bridge [24–30] comprise of series associated unit cells having the ability to generate bipolar waveforms. Topologies using H-bridge are largely appropriate for applications in LV. On the contrary, topologies without H-bridge are utilized as a part of medium voltage (MV) applications. Barbosa et al. presented active neutral point clamped (ANPC) converter by putting together the features FC and NPC [31]. Batschauer et al. put forth three-phase hybrid MLI for applications in MV; using a traditional three-phase VSI connected in series with a half-bridge inverter at every phase, thus reducing prerequisite of dc sources to a significant extent. Due to increase in renewable power generation over the past decades, researches are going on in the application of MLIs in grid-connected as well as stand-alone renewable energy systems (RES) to improve substantially the power quality [32–38]. J. C. Wu and C. W. Chou put forth a solar power generation

system comprising of seven-level inverter and boost converter [39]. In 2015, a single-phase inverter with operation in five levels was proposed, constituting a half-bridge inverter and a three-level diode clamped inverter, which had a high fault tolerance limit and a reduced number of switch count [40].

The presented article reviews different MLI topologies and breaks down their consistently developing effect on renewable energy applications. In Sect. 2, classical MLI topologies are discussed. Section 3 illustrates the recently developed hybrid MLIs. In Sect. 4, an elaborate review on renewable power applications of MLIs is provided and concluding remarks are presented in Sect. 5.

2 Classical MLI Topologies

2.1 Neutral Point Clamped MLI (NPC MLI)

In a five-level NPC MLI [15, 41], the dc-link voltage is divided equally in the capacitors which are connected in series. The capacitors have a high capacitance value, which is equal. The dc bus middle point serves as the reference point. Four pairs of unidirectional switches are present and every switch is clamped indirectly to a voltage level of $V/4$, with the help of clamping diodes, thus reducing the voltage rating of switches. NPC MLI does not show redundancy when it comes to phases. NPC MLI is among the generally utilized topology in MV high-power applications because of its simple control as well as minimal cost hardware execution. It discovers widespread use in DSTATCOM, UPFC, FACTS, mechanical drives, and numerous applications using low frequencies. In spite of its many points of interest, NPC MLI extensively experiences different issues, for example, uneven distribution of power among switches and unequal use of semiconductor. These deficiencies confined the utilization of NPC MLI to voltage levels of five or seven (Figs. 1, 2, and 3).

Fig. 1 NPC MLI

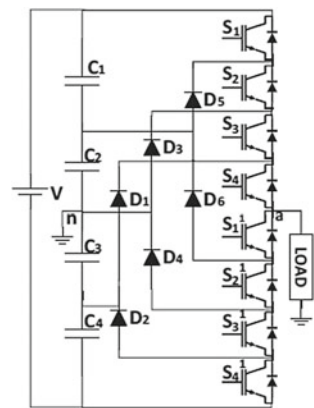


Fig. 2 FC MLI

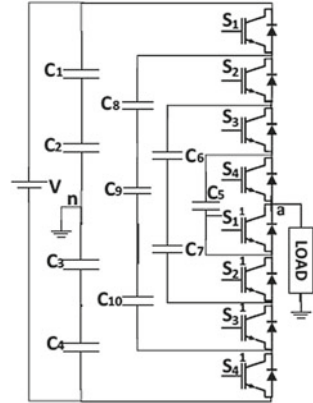
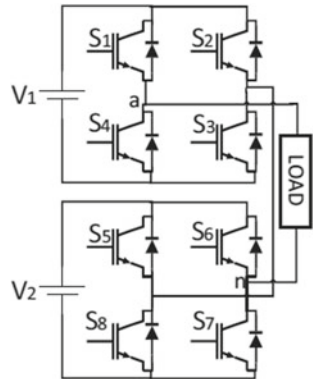


Fig. 3 CHB MLI



2.2 Flying Capacitor MLI (FC MLI)

In a single-phase five-level FC MLI [15, 41, 42], four number of dc-link capacitors having same value of capacitance as well as voltage rating are present. These capacitors split the dc bus voltage into four equal parts. Eight unidirectional power switches are also present. The clamping or flying capacitors clamp each switch voltage to one dc-link capacitor voltage. In this topology, every switch has an equal voltage rating. The main characteristic of FC MLI is that the inner voltage levels are quite redundant, which can be utilized for charge balancing in clamping capacitors. Phase redundancies are regularly utilized, so as to keep up the equivalent charge or voltage levels among clamping capacitors. The utilization of high-frequency switching is too prescribed keeping in mind the balancing of charge levels among clamping capacitors. This configuration is broadly applicable as a part of high-frequency MV traction drives. As of late, multicell converters employing flying capacitors are additionally presented [43].

2.3 Cascaded H-Bridge MLI (CHB MLI)

A single-phase CHB MLI has two cells connected in series, each cell comprising of an H-bridge, for five-level. Every H-bridge consists of an isolated dc source and four unidirectional switches, generating three levels of voltage as output. The redundancies in symmetric CHB MLI can be eliminated by properly selecting unequal dc sources. Thus, higher voltage levels can be obtained and the need for a larger number of dc sources can be diminished. These asymmetric topologies employ the common usage of binary and trinary sequences for the selection of dc source. The merits of a seven-level asymmetric CHB MLI is that redundancy is eliminated and generation of two additional voltage levels as compared to five-level CHB MLI. But, this characteristic is acquired with the loss of modularity which becomes its primary disadvantage.

Symmetrical CHB MLI configuration is exceptionally modular and a simplified pulse generating scheme is required, while employing minimal count of components for the production of voltage level in any number. Consequently, it is generally utilized as a part of battery controlled applications, stand-alone PV systems, grid-tied systems, and in numerous other utilities. The principal limitations of symmetrical CHB MLI configuration are the prerequisite of large count of isolated dc supplies.

3 RCC Topologies for LV Applications

3.1 Developed Cascaded MLI (DC MLI)

Proposed by Babaei et al. [44], it includes a number of unit cells arranged in cascade connection for the generation of high levels of voltage and different blocks for polarity and level generation. Its features also include modularity, asymmetric and symmetric structure, and reduced switch count. For implementation at nine-level, DC MLI requires eleven switches along with four dc sources. For generating higher voltage, authors have suggested connecting n basic units in series with every unit comprising of three dc voltage sources and five switches. The implementation of H-bridge converts the unipolar waveform at the output into a bipolar waveform (Figs. 4, 5, and 6).

3.2 Cascaded Sub-multilevel Inverter (CSMLI)

This topology was introduced by Kangarlu and Babaei [19], in view of an arrangement of sub-multilevel inverters connected in series. For implementation at 13-level, this configuration utilizes symmetrical dc sources. Herein, one zero voltage level and six positive levels are produced by the series connection of two sub-MLI cells. The

Fig. 4 DC MLI

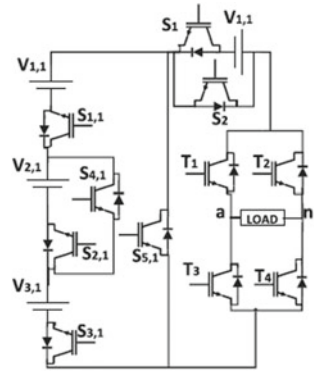


Fig. 5 CS MLI

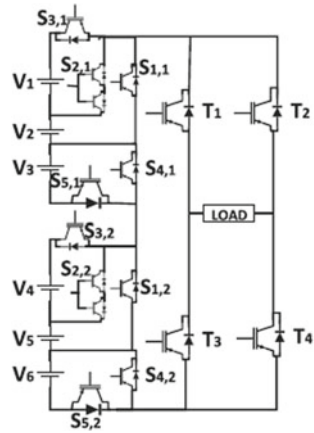
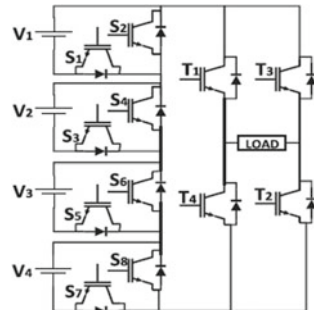


Fig. 6 MLDCLI



H-bridge is utilized as polarity generator. The above-stated topology has appeared predominant over asymmetrical CHB MLI as far as reduced IGBT count for a given voltage level is considered, but the number of switches to be used increases. Favorable characteristics of the above configuration are symmetric and asymmetric structure, isolated polarity, and level generation, modularity, decrease in the count of driver circuits, lowered THD in output as well as reduced losses.

3.3 Multilevel DC-Link Inverter (MLDCLI)

Su [20] presented another sort of RCC multilevel inverter comprising of half-bridge cells connected in series for level generation. The polarity generation block constitutes an H-bridge. Every half-bridge cell has an individual confined dc type of supply in addition to two correlative switches. For an inductive load, it is guaranteed that H-bridge switches in all cases be switched off at zero value of voltage, while they are turned on at both voltage zero as well as zero current. This characteristic brings down the losses during switching in H-bridge. Another critical feature of MLDCLI is that high-voltage rated switches have lower frequency of switching while low-voltage rated switches have higher frequency of switching. In spite of its many advantages, primary disadvantage of this type of topology is the high value of voltage rating of the switches in H-bridge. This restrains its application in medium level power LV range (under 100 kW).

4 MLIs in Renewable Energy Applications

4.1 Photovoltaic Systems

The PV inverters being implemented in industrial applications include different configurations which are either transformer-based or transformer-less. A few topologies, like, half H-bridge, full H-bridge, and H5 have been derived from H-bridge [45]. J. Chavarria et al. tentatively approved for both uniform as well as nonuniform irradiance levels, an energy balance control method for seven-level cascaded grid-connected inverter [46]. For a single-phase grid-connected PV system, a boost current MLI was presented by P. G. Barbosa et al. [47]. The proposed system achieved high power quality and efficiency as high as 96%. A CHB MLI, implementing space vector modulation method was put forth [48]. The proposed system ensured unity power factor for grid injected power, balanced dc-link voltages, and distributed MPPT. L. V. Nguyen et al. presented a virtual prototype for distributed control of MLI, in a grid-tied system, and analyzed its effect on fault tolerance capability and redundancy [49]. A modified cascaded MLI was put forth by Wu et al. [50] and results were compared to standard CHB inverter, to highlight its feasibility and merits. Latran and Teke

[51] presented a detailed study of different multilevel multifunctional grid-connected inverter (ML-MFGCI) topologies in both single and three-phase configurations. Various control strategies to improve power quality were also discussed. A 3-KWp 15-level cascaded inverter was implemented by S. Alexander, for grid-connected as well as stand-alone applications and the same was examined for different modulation algorithms [52].

4.2 Wind Energy Conversion System (WECS)

Samuel et al. [53] performed interfacing of a 2 MW wind generator and grid, with the use of CHB MLI for enhanced power quality at PCC. For a large grid-connected wind turbine alternator, a control scheme showing high tolerance limit to faults was presented, employing CHB MLI [54]. X. Yuan et al. proposed a high-power MV inverter configuration for a grid-connected WECS [55]. The above topology eliminated the need for a bulky and costly frequency transformer and was a combination of H-bridge inverter and NPC MLI. A low voltage ride through (LVRT) for three-level NPC inverter was performed, connected to WECS, and the thermal performances and various losses were examined [56, 57]. Keeping in mind the compensation of the ripple power in MLI connected to grid, a proportional—integral—resonant controller was put forth, resulting in size reduction of dc-link capacitor [58]. The simulations have demonstrated the great execution of the control technique and converter configuration with reduction in dc-link ripple voltage. Madariaga et al. [59] critically reviewed the current trends for an offshore grid integrated WECS. M. A. Parker et al. investigated different PWM control strategies in case of modular converter configurations for implementation in offshore WECS [60]. An extensive survey on current situation of ac transmission systems based on low frequencies and connection to large wind plants, particularly offshore ones is exhibited in [61].

4.3 Battery Storage Energy Systems (BSES)

BSES require large current and low-voltage devices. Hagiwara M et al. presented a push-pull PWM converter for the same, having prerequisites of a transformer for boosting the output voltage [62]. For implementing in grid-connected applications, the same transformer serves as a grid transformer. Hawke et al., [63] put forth a system which actualized a single-NPC MLI interface for the connection of many fuel cells (FC) to MV grid. The system achieved independent control of power at each source, flexibility in operation, increase in output power, source availability, and balancing of thermal power. An extensive review on different FC technologies along with the principle of operation, merits, demerits, transportation, suitability for grid-connected implementation, transportation as well as industrial usage has been

presented [64]. It is suggested that RCC models are used for reliable and monetary operation of grid associated FC systems.

5 Conclusion

In the article presented, an inclusive review of different classical as well as recently proposed RCC hybrid MLI configurations has been put forth. The article will help the readers to differentiate among various topologies conceptually. The various advantages and disadvantages, as well as the utilization of these topologies, are summarized clearly. This will be exceptionally useful for the analysts to legitimize the choice of a specific topology in their researches. Moreover, a detailed analysis on the impact of MLIs in grid integrated RESs is presented. Researchers will be able to think of other economical solutions as well as the various research gaps.

References

1. Veenstra M, Rufer A (2005) Control of a hybrid asymmetric multilevel inverter for competitive medium-voltage industrial drives. *IEEE Trans Ind Appl* 41(2):655–664
2. Akagi H (2011) Classification, terminology, and application of the modular multilevel cascade converter (mmcc). *IEEE Trans Power Electron* 26(11):3119–3130
3. Tolbert LM, Peng FZ (1998) Multilevel converters for large electric drives. In: APEC '98 thirteenth annual applied power electronics conference and exposition, vol 2. IEEE, pp 530–536 (1998)
4. Zheng Z, Wang K, Xu L, Li Y (2014) A hybrid cascaded multilevel converter for battery energy management applied in electric vehicles. *IEEE Trans Power Electron* 29(7):3537–3546
5. Al-Hadidi H, Gole A (2006) Minimum power operation of cascade inverter based dynamic voltage restorer
6. Varschavsky A, Dixon J, Rotella M, Morán L (2010) Cascaded nine-level inverter for hybrid-series active power filter, using industrial controller. *IEEE Trans Ind Electron* 57(8):2761–2767 (2010)
7. Wang J, Peng FZ (2004) Unified power flow controller using the cascade multilevel inverter. *IEEE Trans Power Electron* 19(4):1077–1084
8. Hamzeh M, Ghazanfari A, Mokhtari H, Karimi H (2013) Integrating hybrid power source into an islanded mv microgrid using chb multilevel inverter under unbalanced and nonlinear load conditions. *IEEE Trans Energy Convers* 28(3):643–651
9. Peng FZ, McKeever JW, Adams DJ (1997) A power line conditioner using cascade multilevel inverters for distribution systems. In: IAS '97. Conference Record of the 1997 IEEE Industry Applications Conference Thirty-Second IAS Annual Meeting, vol 2. IEEE, pp 1316–1321
10. Srikanthan S, Mishra MK (2010) Dc capacitor voltage equalization in neutral clamped inverters for DSTATCOM application. *IEEE Trans Industr Electron* 57(8):2768–2775
11. Buticchi G, Barater D, Lorenzani E, Concari C, Franceschini G (2014) A nine level grid-connected converter topology for single-phase transformerless PV systems. *IEEE Trans Industr Electron* 61(8):3951–3960
12. Xiao B, Hang L, Mei J, Riley C, Tolbert LM, Ozpineci B (2015) Modular cascaded h-bridge multilevel PV inverter with distributed MPPT for grid-connected applications. *IEEE Trans Ind Appl* 51(2):1722–1731

13. Rahim NA, Selvaraj J (2010) Multistring five-level inverter with novel PWM control scheme for PV application. *IEEE Trans Industr Electron* 57(6):2111–2123
14. Villanueva E, Correa P, Rodriguez J, Pacas M (2009) Control of a single-phase cascaded h-bridge multilevel inverter for grid-connected photovoltaic systems. *IEEE Trans Industr Electron* 56(11):4399–4406
15. Rodriguez J, Lai JS, Peng FZ (2002) Multilevel inverters: a survey of topologies, controls, and applications. *IEEE Trans Industr Electron* 49(4):724–738
16. Ebrahimi J, Babaei E, Gharehpetian GB (2012) A new multilevel converter topology with reduced number of power electronic components. *IEEE Trans Industr Electron* 59(2):655–667
17. McGrath BP, Holmes DG (2007) Analytical modelling of voltage balance dynamics for a flying capacitor multilevel converter. In: 2007 IEEE power electronics specialists conference. IEEE, pp 1810–1816
18. Rixin L, Maja HT, Juan S (2010) Analysis and suppression of a common mode resonance in the cascaded H-bridge multilevel inverter. In: IEEE energy conversion congress and exposition, 4564–4568
19. Kangarlu MF, Babaei E (2013) A generalized cascaded multilevel inverter using series connection of sub multilevel inverters. *IEEE Trans Power Electron* 28(2):625–636
20. Su GJ (2005) Multilevel dc-link inverter. *IEEE Trans Ind Appl* 41(3):848–854
21. Lezana P, Aceiton R (2011) Hybrid multi-cell converter: topology and modulation. *IEEE Trans Industr Electron* 58(9):3938–3945
22. Nami A, Zare F, Ghosh A, Blaabjerg F (2011) A hybrid cascade converter topology with series-connected symmetrical and asymmetrical diode-clamped h-bridge cells. *IEEE Trans Power Electron* 26(1):51–65
23. Hinago Y, Koizumi H (2010) A single-phase multilevel inverter using switched series/parallel dc voltage sources. *IEEE Trans Industr Electron* 57(8):2643–2650
24. Mokhberdorani A, Ajami A (2014) Symmetric and asymmetric design and implementation of new cascaded multilevel inverter topology. *IEEE Trans Power Electron* 29(12):6712–6724
25. Babaei E, Laali S, Alilu S (2014) Cascaded multilevel inverter with series connection of novel h-bridge basic units. *IEEE Trans Industr Electron* 61(12):6664–6671
26. Babaei E, Hosseini S, Gharehpetian G, Haque MT, Sabahi M (2007) Reduction of dc voltage sources and switches in asymmetrical multilevel converters using a novel topology. *Electr Power Syst Res* 77(8):1073–1085
27. Kala P, Arora S (2017) A comprehensive study of classical and hybrid multilevel inverter topologies for renewable energy applications. *Renew Sustain Energy Rev* 76:905–931
28. Gupta KK, Jain S (2014) A novel multilevel inverter based on switched dc sources. *IEEE Trans Industr Electron* 61(7):3269–3278
29. Gupta KK, Jain S (2014) Comprehensive review of a recently proposed multilevel inverter. *IET Power Electron* 7(3):467–479
30. Chattopadhyay SK, Chakraborty C (2014) A new multilevel inverter topology with self-balancing level doubling network. *IEEE Trans Industr Electron* 61(9):4622–4631
31. Barbosa P, Steimer P, Meysenc L, Winkelkemper M, Steinke J, Celanovic N (2005) Active neutral-point-clamped multilevel converters. In: 2005 IEEE 36th power electronics specialists conference. IEEE, pp 2296–2301 (2005)
32. Agrawal R, Jain S (2017) Comparison of reduced part count multilevel inverters (rpcmlis) for integration to the grid. *Int J Electr Power Energy Syst* 84:214–224
33. Chakraborty A (2011) Advancements in power electronics and drives in interface with growing renewable energy resources. *Renew Sustain Energy Rev* 15(4):1816–1827
34. Veena P, Indragandhi V, Jayabharath R, Subramaniaswamy V (2014) Review of grid integration schemes for renewable power generation system. *Renew Sustain Energy Rev* 34:628–641
35. Zeng Z, Yang H, Zhao R, Cheng C (2013) Topologies and control strategies of multi-functional grid-connected inverters for power quality enhancement: a comprehensive review. *Renew Sustain Energy Rev* 24:223–270
36. Patrao I, Figueres E, González-Espín F, Garcerá, G (2011) Transformerless topologies for grid-connected single-phase photovoltaic inverters. *Renew Sustain Energy Rev* 15(7):3423–3431 (2011)

37. Li Q, Wolfs P (2008) A review of the single phase photovoltaic module integrated converter topologies with three different dc link configurations. *IEEE Trans Power Electron* 23(3):1320–1333
38. Mahela OP, Shaik AG (2017) Comprehensive overview of grid interfaced solar photovoltaic systems. *Renew Sustain Energy Rev* 68(316–332):3
39. Wu JC, Chou CW (2014) A solar power generation system with a seven-level inverter. *IEEE Trans Power Electron* 29(7):3454–3462
40. Sivakumar K et al (2015) A fault-tolerant single-phase five-level inverter for grid independent PV systems. *IEEE Trans Industr Electron* 62(12):7569–7577
41. Colak I, Kabalci E, Bayindir R (2011) Review of multilevel voltage source inverter topologies and control schemes. *Energy Convers Manag* 52(2):1114–1128 (2)
42. Meynard T, Foch H (1992) Multi-level conversion: high voltage choppers and voltage source inverters. In: *PESC '92 Record. 23rd annual IEEE power electronics specialists conference*. IEEE, pp 397–403
43. Shukla A, Ghosh A, Joshi A (2011) Natural balancing of flying capacitor voltages in multi-cell inverter under pd carrier-based PWM. *IEEE Trans Power Electron* 26(6):1682–1693
44. Babaei E, Laali S, Bayat Z (2015) A single-phase cascaded multilevel inverter based on a new basic unit with reduced number of power switches. *IEEE Trans Industr Electron* 62(2):922–929
45. Islam M, Mekhilef S, Hasan M (2015) Single phase transformerless inverter topologies for grid-tied photovoltaic system: a review. *Renew Sustain Energy Rev* 45:69–86
46. Chavarria J, Biel D, Guinjoan F, Meza C, Negroni JJ (2013) Energy-balance control of PV cascaded multilevel grid-connected inverters under level-shifted and phase-shifted PWMs. *IEEE Trans Industr Electron* 60(1):98–111
47. Barbosa PG, Braga HAC, Rodrigues MDCB, Teixeira EC (2006) Boost current multilevel inverter and its application on single-phase grid-connected photovoltaic systems. *IEEE Trans Power Electron* 21(4):1116–1124
48. Liu Y, Ge B, Abu-Rub H, Peng FZ (2014) An effective control method for three-phase quasi-z-source cascaded multilevel inverter based grid-tie photovoltaic power system. *IEEE Trans Industr Electron* 61(12):6794–6802
49. Nguyen LV, Tran HD, Johnson TT (2014) Virtual prototyping for distributed control of a fault-tolerant modular multilevel inverter for photovoltaics. *IEEE Trans Energy Convers* 29(4):841–850
50. Wu F, Li X, Feng F, Gooi HB (2015) Modified cascaded multilevel grid-connected inverter to enhance european efficiency and several extended topologies. *IEEE Trans Industr Inf* 11(6):1358–1365
51. Latran MB, Teke A (2015) Investigation of multilevel multifunctional grid connected inverter topologies and control strategies used in photovoltaic systems. *Renew Sustain Energy Rev* 42:361–376
52. Alexander S et al (2016) Development of solar photovoltaic inverter with reduced harmonic distortions suitable for Indian sub-continent. *Renew Sustain Energy Rev* 56(C):694–704
53. Samuel P, Gupta R, Chandra D (2011) Grid interface of wind power with large split winding alternator using cascaded multilevel inverter. *IEEE Trans Energy Convers* 26(1):299–309
54. Parker MA, Ng C, Ran L (2011) Fault-tolerant control for a modular generator-converter scheme for direct-drive wind turbines. *IEEE Trans Industr Electron* 58(1):305–315
55. Yuan X, Chai J, Li Y (2012) A transformer-less high-power converter for large permanent magnet wind generator systems. *IEEE Trans Sustain Energy* 3(3):318–329
56. Ma K, Blaabjerg F (2014) Modulation methods for neutral-point-clamped wind power converter achieving loss and thermal redistribution under low-voltage ride-through. *IEEE Trans Industr Electron* 61(2):835–845
57. Sotoodeh P, Miller RD (2014) Design and implementation of an 11-level inverter with facts capability for distributed energy systems. *IEEE J Emerg Sel Top Power Electron* 2(1):87–96 (4)
58. Yuan X (2014) A set of multilevel modular medium-voltage high power converters for 10-mw wind turbines. *IEEE Trans Sustain Energy* 5(2):524–534

59. Madariaga A, Martin J, Zamora I, De Alegria IM, Ceballos S (2013) Technological trends in electric topologies for offshore wind power plants. *Renew Sustain Energy Rev* 24:32–44
60. Parker MA, Ran L, Finney SJ (2013) Distributed control of a fault-tolerant modular multilevel inverter for direct-drive wind turbine grid interfacing. *IEEE Trans Industr Electron* 60(2):509–522
61. Ruddy J, Meere R, O'Donnell T (2016) Low frequency ac transmission for offshore wind power: a review. *Renew Sustain Energy Rev* 56:75–86
62. Hagiwara M, Akagi H (2014) Experiment and simulation of a modular push-pull PWM converter for a battery energy storage system. *IEEE Trans Ind Appl* 50(2):1131–1140
63. Hawke JT, Krishnamoorthy HS, Enjeti PN (2014) A family of new multiport power sharing converter topologies for large grid-connected fuel cells. *IEEE J Emerg Sel Top Power Electron* 2(4):962–971
64. Kirubakaran A, Jain S, Nema R (2009) A review on fuel cell technologies and power electronic interface. *Renew Sustain Energy Rev* 13(9):2430–2440

A Review on Demand Side Management Forecasting Models for Smart Grid



Sweta Singh and Neeraj Kanwar

Abstract There has been excessive stress on the present resources owing to the ever-increasing demand of electricity. The population needs to be satisfied with their electricity demands, and the grid is being overused and therefore has become more fragile owing to the increasing electricity demand with the increasing population. Thus, the reliability as well as the efficiency of the grid has been affected. Therefore, the research to explore more ways in improving the efficiency and stability of the grid in a sustainable manner has occupied the center stage and therefore the coinage of new term, i.e., smart grid. One can define smart grid as an automation of electric grid with the current ICT that aims toward efficient management of electricity generation networks. One of the main features of smart grid is that of demand response (DR) which may be defined as the changes in the electricity usage pattern from their normal usage in response to the changing electricity pricing over time or to incentivize the payments which are designed to encourage users to decrease their usage at times of higher wholesale market price. The DSM activities are supported by the communication infrastructure, intelligent devices, sensors, and processors. This capability results in modification of load profiles and thereby helps the consumers in achieving financial gains and at the same time proper electricity usage. Energy savings and therefore reduced greenhouse gas emissions are also achieved through such process capabilities. DSM provides management of energy balance within the network and also helps in realizing the importance of intermittent renewable energy sources.

Keywords Demand side management · Smart grid · Load forecasting · Demand response · Renewable energy

1 Introduction

The need of electricity is increasing continuously day by day resulting stress in on the resources. This increased population results in higher number of electricity demands with increased electricity appliances for making the grid more fragile, which affects

S. Singh · N. Kanwar (✉)

Department of Electrical Engineering, Manipal University Jaipur, Jaipur, India

e-mail: neeraj.kanwar@jaipur.manipal.edu

© Springer Nature Singapore Pte Ltd. 2020

A. Kalam et al. (eds.), *Intelligent Computing Techniques for Smart Energy Systems*,

Lecture Notes in Electrical Engineering 607,

https://doi.org/10.1007/978-981-15-0214-9_96

efficiency and reliability of the grid. To improve the reliability and efficiency of power network in a sustainable and stable manner, in which grid networks play huge important role through out the research. The initiative has been taken to improve the grid network management strategy based on the concept of smart grid. For efficient management toward electricity network the integration of ICT is required with electric grid with an automation of smart grid [1]. In smart grid demand response (DR) is one of the main features. DR is defined as the changes in electric energy by end user in their regular consumption pattern to reduce the electricity price [2]. Grid network is enabled by communication infrastructure, intelligent devices, and processors to support DSM activities. This opportunity provides financial gains to the consumers by modifying load profile. DSM provides benefits of intermittent renewable energy sources through real-time data [3, 4]. DSM addition in power system provides flexibility to the management in the network.

In literature review DSM would augment the integration energy sources, wherein the dynamic pricing encourages consumers to use electricity from the renewable energy sources, when the electricity pricing mechanism is high. The main reason in evolution of electricity market is strict environment regulations and increasing demand of electricity with a need to exploit the underlying untapped potential in DSM [5]. This would need a new infrastructure based on the smart grid having an integral feature of data exchange and control through AMI. DSM techniques also contend with the renewable energy sources, energy storage system, and regular power plant thereby restructuring the electricity market. In a survey of energy industry in Germany, it was found that the balancing requirements had been increased with increased renewable energy sources penetration [6]. DSM has more significance works like controlling electricity consumption, supporting integration of renewable energy sources using ancillary services, hence, balancing the system. For the German power system, DSM can help in reduce the green energy wastage and provide better integration. It also enhancing the efficiency of power system and also conduce toward lesser load shedding [6]. It has been analyzed that in Germany maximum of 8 GW of renewable energy sources integration can be used with DSM potential in households and commercial sector [7]. The researcher was found that DSM assisted the wind energy integration in power system and also led to reduce the financial problem in Ireland [8]. It is also predicted that DSM through its induce reduction can help in elimination of expansion of generation facilities in energy consumption. It also assists the primary and secondary services based on the frequency control. It would lead to the participation of prosumer a heading to enhance the security and reliability of the power system [9]. The deployment of distributed resources program leads uncertainty in realizable benefits from DSM in the case of shortage of suitable data [10]. It is also anticipated that the average electricity demand gets reduced by 12.65% with the introduction of time of use tariffs (TOU) in 500 households of Sweden [11]. It was concluded that based on survey of 15 experiments; it was observed that the residential consumer depends on electricity price. They reduce their consumption based on the response to higher electricity pricing [12]. The demand gets reduced in summer by 3.3% peaks leading to a drop of 179 MW [13]. In a survey of 5000 Irish households, it was observed that the information played a vital role in achieving

demand response. In a detailed survey of 14,000 customers, it was stimulated that in even though a small, the time-based pricing response in Ontario [14]. It was also observed that for 483 households a significant pricing is achieved in California for different pricing [15].

The modern electricity market has been adopted the newer policy reforms to achieved high electricity markets and smart grid technology to serving multiple objectives [16]. In present scenario, the number of flexible loads owned by residential consumer is high in developed nation as compared to developing nation. In some countries where the number of flexible is less and per capita consumption is low, the technique provides both the utility with certainty with the implementation of feasible DSM technique. The other designing technique is accounted based on the demand, which is availability of RES and their energy profile. This encourages consumers to consume energy whenever available from RESs. Now, it is important for developing nations to develop a strategic plan to mitigate the issue of sustainable development focus on climate change.

2 Load Forecasting

Electric power load forecasting (LF) is a discipline which explores the relation between things and development change rule with the help of electric power systems, economical, meteorological, and other historical data [16]. To the more development electric power load should be reestimated and speculation [17]. Accuracy short-term LF can reduce the generating cost with stable and safe power grid [18]. The data of the grids are explosive with the popularity of smart meters and sensors. LF technology has been greatly developed for the continuous progress of modern technology and development of smart grid. Present scenario the modern forecasting technique has been divided into traditional forecasting and modern forecasting.

2.1 Traditional Forecasting Method

Multiple Linear Regressions

Multiple linear regressions (MLR) are a method that predicts quantitatively the power load. Variation of load affects the dependent and independent variables for finding the relation between them with the variation of historical data to determine the future load value [19]. Mathematical representation of MLR is

$$y(t) = b_0 + b_1x_1(t) + \dots + b_nx_n(t) + \theta(t) \quad (1)$$

On the basis of diversity and uncertainty of load factors, MLR has different cases to understand the proper way of analysis. The MLR is a method which describes

the quantitative relations between variables having statistical significance, but due to low accuracy it is not suitable for load forecasting.

Stochastic Time Series Method

Stochastic times series method (STS) is a time series method which extracts the basic special events, weather sensitive load component from the historical load records, residual that random load component can look into the STC. Stochastic time series can look some models such as autoregression (AR), moving average (MA), autoregression–moving average (ARMA), and autoregressive integrated moving average (ARIMA).

Autoregression (AR)

In this model linear combination is assumed to solve the previous load data. Mathematical representation of model by Liu et al. [20] is written as

$$L_k = - \sum_{i=1}^m a_{ik} L_{k-1} + w_k \tag{2}$$

Moving Average (MA)

The current value of function $y(t)$ is expressed in terms of MA modeling technique as combination of current and previous value of noise series [21]. The mathematical representation of model is expressed below

$$Y(t) = a(t) - \phi_1 \alpha(t - 1) - \phi_1 \alpha(t - 1) - \dots - \phi_q \alpha(t - q) \tag{3}$$

Autoregressive–Moving Average (ARMA)

In this model, the linear model is considered in terms of previous value of load and previous value of interference [22].

The mathematical model of ARMA is represented as below

$$Y(t) = \phi_1 y(t - 1) + \dots + \phi y(p - t) + \dots + \alpha(t - 1) + \dots + \phi_q \alpha(t - q) \tag{4}$$

Autoregressive Integrated Moving Average (ARIMA)

ARIMA is explained the nonstationary random process, which represented by mathematically as below

$$\phi(B)\Delta^d y(t) = (B)\alpha(t) \tag{5}$$

All methods of STS require very small amount of load data when it operates, when the data will have big change faces huge error. So, this method only suitable for relatively uniform data for the situation of load changes in same way.

Exponential Smoothing Exponential smoothing (ES) is a classical prediction method which predicts the historical load data and uses Rahman and Mogharam model for analysis the fitting function. This model only prefers recent data when it operates but if input data is not suitable then the result is deviated by large value. The mathematical modeling is represented as

$$Y(t) = \beta(t)^T f(t) + e(t) \quad (6)$$

In the case of traditional forecasting methods, they do not have ability to express large amount of data. During the development of smart grid, the load data become more precise in the case of complicated load data. Traditional load forecasting method is proposed for big data.

2.2 Modern Forecasting Method

Artificial Neural Network

ANNs are calculated with “neuron” interconnection relationship by sending signals or information for predicting the model [22]. It has reasoning, autonomous learning, memory, and calculation features but the rate of convergence of ANN is slow. Hong Xie et al. have described a model based on the neural network and rough set. In order to determine the input variables of the model predictions the short-term load forecasting has been used to identify the influence of variables using rough set theory [23].

Fuzzy Theory

Fuzzy theory has powerful nonlinear mapping, strong adaptability, and robustness to solve nonlinear function by extracting data from large amount of data. Generally, it is used to solve complex power system network prediction [24]. It has two methods to solve the problem either by data training or online forecasting [25]. Jinzeng Cheng has designed the cluster analysis and fuzzy reason methods and described the ability data analysis for leaning the uncertainty [26].

Support Vector Machine (SVM)

SVM solves quadratic programming problem such as small sample, nonlinear, high dimension, and local minimum problem based on statistical learning theory which structured on risk minimization problem [27]. But it required large number of training data, which make the processor slow. Yuan-Cheng Li proposed the complementary and advantages of the rough set theory of SVM based on the kind of prediction system [28]. Chen explained the comparison analysis of traditional BP neural network results, a higher accuracy has been found in SVM [29].

Combination Method

Factors affecting the load data and change have increased exponentially with the advancements in the domain of smart grid. Therefore, requirements of LF have been found to be met with difficulty by a single load forecasting method. This is particularly true for LF in a big data environment. To meet the aforementioned objectives, combination methods have been proposed for the big data environment. Such combination methods must be able to refine the load data and forecast accurately. A cloud computing MapReduce model was formulated by Wang et al. [30] for the big data environment. With the simulations, linear regression forecasting model based on subblock data was formulated. It was revealed that the proposed model was able to minimize the LF time and certain predictions were obtained with greater accuracy. In another study, cloud computing technique was integrated with the smart grid load data. The computational speed as well as the accuracy of prediction was reported to be enhanced.

3 Comparative Study of Forecasting Techniques

Mean absolute percentage error (MAPE) was used as a comparison technique by the researchers to compare most of the proposed technologies. Equation (7) can be used for the calculation of MAPE:

$$MAPE = \left[\sum_{i=1}^n |Y_i - y_i| / y_i \right] / n \times 100\% \tag{7}$$

The accuracy of the modern methods was found to be higher than that of the traditional ones. Values of MAPE for different forecasting models have been tabulated in Table 1.

This can be attributed to the fact that the modern forecasting models are more suitable for processing of input data that is of nonlinear nature. Further, such methods have the capability to deal with the increased complexity possessed by the smart grids.

Table 1 Values of MAPE for different forecasting models

Methods	MAPE (%)
ARIMA	4.5
ARMA	4.77
ANN	1.59
FL	2.21
SVM	2.71
MLR	3.8
ARIMA and SVM	3.86

4 Challenges and Conclusion

With the advancements in big data and smart grid technology development, it has now become feasible to accurately capture the load data as well as the environment and meteorological data. However, still some challenges exist related to LF and DSM in contextual framework of smart grid. One of the major hurdles for achieving effective DSM is the lack of infrastructure pertaining to communication as well as intelligent sensing devices. Another problem is to obtain standardized model for fusion and management of data because of existing different technology agreements on the user side. Storage time is another limitation to the big data environment. Deviations in the information related to the facility records arise as a result of error in weather forecasting models. Serious problems also include that of effective identification of suitable data after deletion of erroneous data. Usage patterns differ from consumers to consumers which ultimately affects the effectiveness of DSM and LF.

DSM leads to the development of smart grid that is safe and stable to operate. Various forecasting models have been highlighted in this paper and it was revealed that AI-based methods have superior accuracy to other traditional methods. It is quintessential to comprehend various forecasting models and to address the aforementioned challenges for effective DSM implementation.

References

1. Saffre F, Gedge R (2010) Demand-side management for the smart grid. In: Network operations and management symposium workshops (NOMS Wksp), pp 300–303
2. Lee M, Aslam O, Foster B, Kathan D, Kwok J, Medearis L, Palmer R, Sporborg P, Tita M (2013) Assessment of demand response and advanced metering. Federal Energy Regulatory Commission, Tech Rep
3. Masters GM (2013) Renewable and efficient electric power systems. Wiley
4. Siano P (2014) Demand response and smart grids—a survey. *Renew Sustain Energy Rev* 30:461–478
5. Korkas CD, Baldi S, Michailidis I, Kosmatopoulos EB (2016) Occupancy-based demand response and thermal comfort optimization in microgrids with renewable energy sources and energy storage. *Appl Energy* 163:93–104
6. Paulus M, Borggrefe F (2011) The potential of demand-side management in energy-intensive industries for electricity markets in Germany. *Appl Energy* 88(2):432–441
7. Stötzer M, Hauer I, Richter M, Styczynski ZA (2015) Potential of demand side integration to maximize use of renewable energy sources in Germany. *Appl Energy* 146:344–352
8. Finn P, Fitzpatrick C (2014) Demand side management of industrial electricity consumption: promoting the use of renewable energy through real-time pricing. *Appl Energy* 113:11–21
9. Wang Q, Zhang C, Ding Y, Xydis G, Wang J, Østergaard J (2015) Review of real-time electricity markets for integrating distributed energy resources and demand response. *Appl Energy* 138:695–706
10. Nolan S, O'Malley M (2015) Challenges and barriers to demand response deployment and evaluation. *Appl Energy* 152:1–10
11. Bartusch C, Wallin F, Odlare M, Vassileva I, Wester L (2011) Introducing a demand-based electricity distribution tariff in the residential sector: demand response and customer perception. *Energy Policy* 39(9):5008–5025

12. Faruqui A, Sergici S, Sharif A (2010) The impact of informational feedback on energy consumption—a survey of the experimental evidence. *Energy* 35(4):1598–1608
13. Di Cosmo V, Lyons S, Nolan A (2014) Estimating the impact of time-of-use pricing on Irish electricity demand. *Energy J* 117–136 (2014)
14. Herter K, Wayland S (2010) Residential response to critical-peak pricing of electricity: California evidence. *Energy* 35(4):1561–1567
15. Shen B, Ghatikar G, Lei Z, Li J, Wikler G, Martin P (2014) The role of regulatory reforms, market changes, and technology development to make demand response a viable resource in meeting energy challenges. *Appl Energy* 130:814–823
16. Wang B, Li Y (2010) Demand side management planning and implementation mechanism for smart grid. *Electr Power Autom Equip* 12:19–24
17. Niu D, Wang Y, Wu DD (2010) Power load forecasting using support vector machine and ant colony optimization. *Expert Syst Appl* 37(3):2531–2539
18. Li R, Liu Y, Li JH, Gu XP, Niu DX, Liu YQ (2005) Study on the daily characteristic load forecasting based on the optimized algorithm of decision tree. *Zhongguo Dianji Gongcheng Xuebao* 25(23):36–41
19. Peng P, Peng JH (2011) Research on the prediction of power load based on multiple linear regression model. *J Saf Sci Technol* 7(9):158–161
20. Liu K, Subbarayan S, Shoultz RR, Manry MT, Kwan C, Lewis FI, Naccarino J (1996) Comparison of very short-term load forecasting techniques. *IEEE Trans Power Syst* 11(2):877–882
21. Moghram I, Rahman S (1989) Analysis and evaluation of five short-term load forecasting techniques. *IEEE Trans Power Syst* 4(4):1484–1491
22. Zhao H, Tang Z (2016) The review of demand side management and load forecasting in smart grid. In: 12th world congress intelligent control and automation (WCICA) 2016, pp 625–629
23. Xie H, Cheng HZ, Zhang GL, Niu DX, Yang JF (2003) Applying rough set theory to establish artificial neural networks for short term load forecasting. *Proc Csee* 11
24. Srinivasan D, Lee MA (1995) Survey of hybrid fuzzy neural approaches to electric load forecasting. In: *Systems, man and cybernetics, 1995, IEEE international conference on intelligent systems for the 21st century*, vol 5, pp 4004–4008
25. Zhao XY, Ma LL (2013) Applying rough set theory to establish artificial neural networks model for short term incidence rate forecasting. *Appl Mech Mater* 347, 2937–2941 (Trans Tech Publications)
26. Zhao H, Tang Z (2016) The review of demand side management and load forecasting in smart grid. In: *Intelligent control and automation, WCICA, 2016*, pp 625–629
27. Niu DX, Gu ZH, Xing M, Wang HQ (2006) Study on forecasting approach to short-term load of SVM based on data mining. *Zhongguo Dianji Gongcheng Xuebao* 26(18):6–12
28. Li Y, Li B, Fang T (2004) An approach to forecast short-term load of support vector machines based on rough sets. In: *Intelligent control and automation, WCICA, 2004*, vol 6, pp 5180–5184
29. Zhao H, Tang Z (2016) The review of demand side management and load forecasting in smart grid. In: *Intelligent control and automation (WCICA)*, pp 625–629
30. Wang B, Zhao S, Zhang S (2014) A distributed load forecasting algorithm based on cloud computing and extreme learning machine. *Power Syst Technol* 38(2):526–531

Detection of Suspicious Activity in ATM Booth



Anjali Saini, Mushtaq Ahmed and Kartikey Sharma

Abstract This paper focuses on safety and security issues in Automated Teller Machine (ATM) counters, which includes detection of covered faces, person wearing helmet, more than one person at ATM at a time, person in drunken state, people fighting, etc. We use combine method of Viola–Jones Algorithm and modified Circle Hough Transform for helmet detection. Results show better decision rates and attained high precision and low false positive rate.

Keywords Video surveillance · Viola–Jones · Circular hough transform · Multiple object detection · Helmet detection · ATM security

1 Introduction

In recent trends, use of automatic video surveillance [1] systems has increasingly enhanced for security and monitoring ATM machines. Efficient mechanism for detecting suspicious activities is desirable for law enforcement, and security of ATM machine.

Object detection and behavior analysis provide quick and efficient decision-making [2–4]. Video surveillance system detects objects and analyzes their behavior to refine output for righteous decision. We focus only two suspicious activities

- Multiple person detection
- Helmet detection inside the ATM machine counter.

A. Saini · M. Ahmed (✉)
Department of Computer Science and Engineering MNIT Jaipur, Jaipur, India
e-mail: mahmed.cse@mnit.ac.in

A. Saini
e-mail: 2015pcp5290@mnit.ac.in

K. Sharma
Centre for Converging Technologies U.O.R Jaipur, Jaipur, India
e-mail: kartikey.sharma34@yahoo.com

© Springer Nature Singapore Pte Ltd. 2020
A. Kalam et al. (eds.), *Intelligent Computing Techniques for Smart Energy Systems*,
Lecture Notes in Electrical Engineering 607,
https://doi.org/10.1007/978-981-15-0214-9_97

Background subtraction [5–7] is needed for extracting object images in video processing. This is also useful in detecting objects from images taken by static camera [5]. Object detection is a procedure of finding an instance of a real-world object such as head, nose, mouth, and eyes in a given face.

When a person is considered as an object in an image can be detected using the Histogram with oriented gradient [8] features and trained support vector machine [9]. For this, an image is divided into distinct segments and from which features are extracted for analysis. Depending upon features, identification of more than one person can be processed using the modified Viola–Jones algorithm [10]. Hough transform descriptor confine features of a particular shape such as a circle within an image and features can be specified in some parametric form [11].

1.1 Video Surveillance

Video surveillance is an effective method for detecting suspicious activities. The term surveillance implies scrutinization or inspection of a specific area for detection of any suspicious activity by an individual or a group. Multiple footages from different angles help in making accurate decision to distinguish threats or any criminal activity [12, 13]. Some of the application of the video surveillance system includes traffic monitoring, event surveillance, public safety, outdoor perimeter security, etc.

1.2 Overview

Section 1 initiates the description of the proposed framework by a brief introduction pertaining to the need and other related issues regarding the methods used in designing the system. Section 2 describes the various propositions by the researchers over the past 5 years in Helmet Detection and Activity Detection. Section 3 dives into a brief background of the ATM and kinds of suspicious activities that can take place inside the ATM booth. Sections 4 and 5 present us the various algorithms and approaches used for the implementation of the detection system. Section 6 shows the results and remarks of our proposed work and a comparative analysis in accordance with the classical method. Section 7 concludes the work and describes the future scope of the model.

2 Related Work

A few past years, people were able to withdraw money from banks only during their opening hours. Over the years, there has been a proliferation of ATM frauds across the world. ATM machine has lots of advantages such as flexibility of cash withdrawals to

the customer withdraw money anywhere and at any time but also have disadvantages such as theft of personal information, physical attacks, and murder attempt in ATM [14–16]. To resolve from such suspicious activities various techniques have been proposed.

Doungmala and Klubsuwa [17], described a technique that combined two methods for helmet detection for achieving better decision rates and low false positive rates. Face detection using Haar-like features is used for detecting person without helmet or with helmet and Circle Hough Transform technique for detection among person without helmet and half helmet.

Tamilselvan and Monika [18], described a way for intelligent video surveillance with the implication of finding behavioral anomalies. They claimed efficient approach for anomaly detection in crowded scenes. Foreground segmentation is applied to input frames divided into nonoverlapping cells and features are extracted based on size, motion, and texture.

Silva et al. [8] showed how to detect helmet on motorcyclists using image classifiers and descriptors. Motorcycle accidents have been increasing and helmet is an essential safety equipment of motorcyclists, but many of the motorcyclists do not use helmet. Compulsion of wearing helmet is needed to protect motorcyclists in case of an accident. They also used Circular Hough Transform and Histogram of oriented gradients descriptor to extract the attributes from the image. Multilayer perceptron classifier is used to achieve results and compared with other algorithms accomplishing an accuracy rate of 91.37.

Dalal and Bill [9], In this paper a circle/circular detection algorithm is proposed, based upon modified Circular Hough Transformation and applied for helmet detection in the surveillance system of ATM. Circular arcs and geometric features are used to verify the existence of the helmet in the set and centroid information They proposed framework for the surveillance systems of banks and ATM's, which can provide primary warning to concerned authority when any person tries to hide his/her face information from the surveillance camera during withdrawal of money.

3 Background

Exponential increase in the use of ATM over the past few years eventually resulted in rise of fraudulent activities and thefts inside the ATM counter. Further information on these criminal exercises is described in these subsections.

3.1 Automated Teller Machine

A few years back, it was not possible to withdraw money anywhere and at any time. Now, It is possible with the help of an ATM. An Automated Teller Machine (ATM) is an electronic banking outlet, which acquiesces customers to complete basic

transactions without the assistance of a branch representative [10]. Over the years, there has been a proliferation of ATM frauds in our society. Keeping aside the fact that ATM offers a lot of beneficial services like flexibility of cash withdrawals and transactions, it also hatches certain disadvantages like theft of personal information, physical attacks, and criminal activities [19]. Therefore, to suppress or put an end to these illegal exercises in the ATM counter, this system is proposed.

3.2 *Suspicious Activities in ATM Booth*

Suspicious activity is recognized as a behavioral exercise that demonstrates crime [12, 20, 21]. ATM booth threats can be broadly categorized into three major classes which are as follows:

- Card and currency related
- Logical attacks
- Physical attacks

We significantly focused on activities that manoeuvre threats. Such activities can be multiple customers on a single machine, drunken person, and person wearing helmet.

4 Multiple Object Detection

Moving object detection in digital image sequence involves identification of the presence of an object in consecutive frames [3, 16, 22]. Video surveillance is one of the applications among them, which is used to detect changes in the scenes. There are various techniques for detecting moving objects such as background subtraction, temporal differencing [23] and so on [6, 24, 25]. However, we applied modified Viola–Jones algorithm for multiple object detection.

4.1 *Viola–Jones Algorithm*

The system is designed by training a cascade of classifiers to identify faces in image inputs.

Haar-like Features: Haar features represent characteristics that are similar to facial elements. A 24*24 subwindow is passed over the image input, Haar feature considers adjacent rectangular regions at specific locations during detection in the window over the image in search of features, then the pixel intensities of these regions are summed up and manipulated with respect to pixel intensities of other regions. While considering the variations of size such as 2-pixel features and 4-pixel features, the difference calculated after manipulations categorizes subsections of the image. Over

Fig. 1 Different categories of Haar features

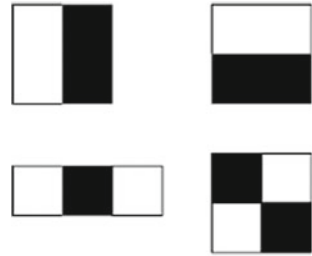


Fig. 2 Location of corresponding features on human face



the course of this process over 160,000+ features are extracted but only relevant features are considered for calculations [10] (Figs. 1 and 2).

Integral Image: The basic idea behind integral image [10] calculation of area of a particular patch instead of calculating all pixel values. By using corner values of this patch and processing those values through a series of calculations.

Adaboost Classifier: The classifier is employed to eliminate redundant features. It will select relevant features from the 160,000+ features, after identifying all these features weight is assigned to these features and a linear combination of these features is used to decide whether the input is a face or not. Weak classifier is a relevant feature which is extracted by Adaboost [8]. It ends up with 2500 features and these features are used to form a strong classifier.

Cascade of Classifiers: For every 24*24 window, we evaluate 2500 features that are obtained after the termination of AdaBoost classifier. Instead of evaluating 2500 features for every 24*24 window, we generate these features into several stages. Suppose the first stage comprises a total of 10 features, similarly second stage consists of 10 different features and in this manner successive stages are formed until a total count of 2500 features is attained, input image is passed through this cascade and if it passes the first stage, then there is a possibility of presence of facial elements. Therefore, the input is then promoted on to the second stage for confirmation of facial features. However, if the input image fails at the first stage itself the process is terminated with a notification on absence of face; thus, input is eliminated.

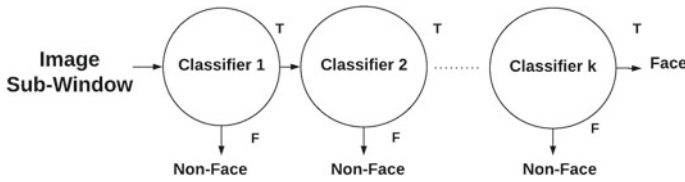


Fig. 3 Stages in cascade of classifiers

4.2 Approach Used for Multiple Person Detection

Figure 3 shows the proposed algorithm steps for multiple person detection.

Video acquired by the surveillance camera [1] is taken as an input for the proposed algorithm. This video is then preprocessed through various steps for conversion into multiple frames of sufficient size and type for efficient processing in further steps. The processed frames consists of RGB images which raise complexity of the algorithm, thus these images are converted into gray scale [26] and then brightness adjustment is done for remapping image intensity values and other preprocessing operations are applied on the frames for reduction of noise. After performing all the above steps Viola–Jones algorithm is applied for detection of people and for a face count. If count value is greater than 1, it indicates detection of more than one person which is considered as suspicious activity [15]. If count value is less than or equal to 1, it indicates that everything is normal (Figs. 4 and 5).

5 Helmet Detection

The technique used here for helmet detection is Circle Hough Transform [17]. Hough transform is a method for estimating the parameters of arbitrary shapes from it's boundary points. Classical Hough Transform [27, 28] can locate regular curves like circles, straight lines, ellipse, etc. and it is required that curve can be described in some parametric form.

5.1 Circle Hough Transformation

Hough transform is applied after edge detection and for edge detection canny edge detector is used. Canny edge detection[38] is a common multistage algorithm designed to be an optimum edge detector while suppressing noise. It takes as input a grayscale image and produces an image demonstrating the positions of tracked intensity discontinuities as output.

Fig. 4 Multiple person detection

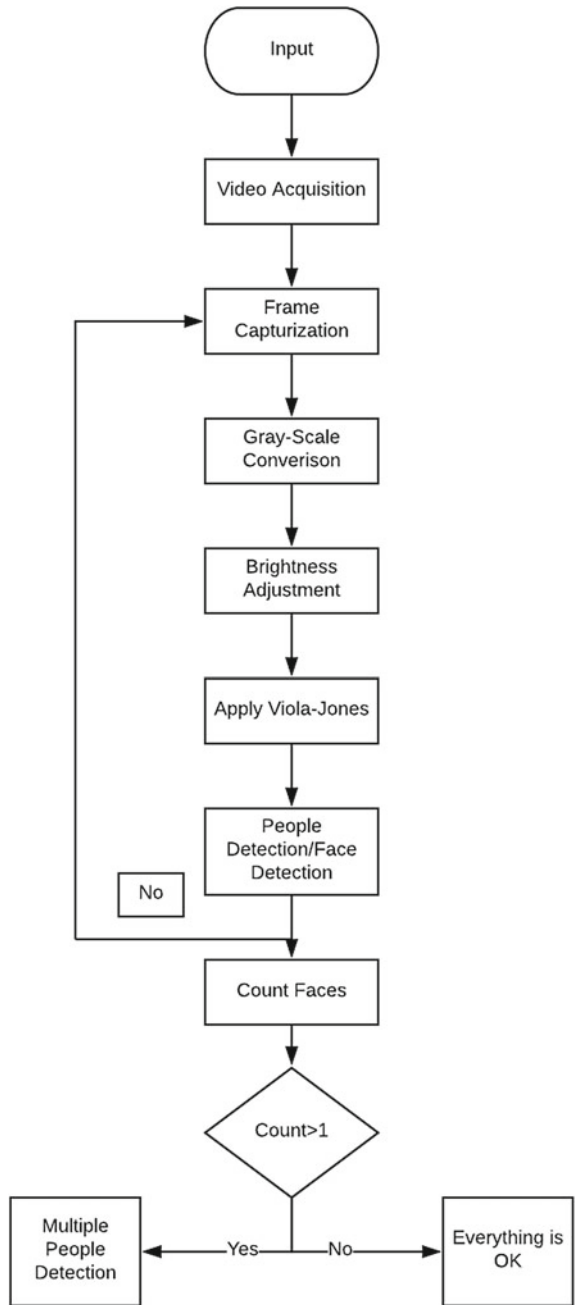
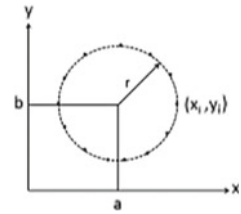


Fig. 5 Circle in parameter space



The parametric equation of the circle can be written as

$$(x_i - a)^2 + (y_i - b)^2 = r^2 \tag{1}$$

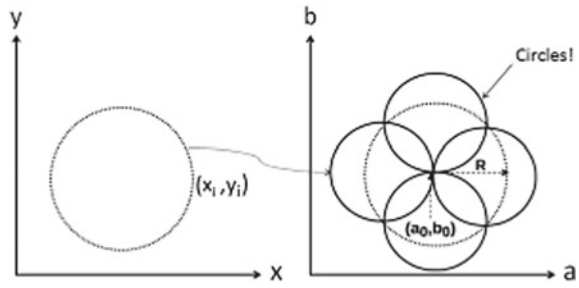
where parameter a and b denote the center of the circle and r is the radius. The equation of the circle can be rewritten as

$$a = x_i - r \cos\theta \tag{2}$$

$$b = y_i - r \sin\theta \tag{3}$$

The curve obtained in the transform space for each point will be right circular cone. Points of intersection of the cones deliver the parameters required for circle detection [11]. So, the aim of using Hough Transform is to search for triplet of parameters (a, b, r) which inclines the points (xi, yi). In the same manner, the transform is applied on every point on the circle. The resultant output will be a combination of voted circles. The point of intersection of these voted circles accords the center of the required circle that is (a0, b0). This point is attained by seeking the local maximum of the accumulator space. The darker circles specify a set of edge points in the image. Each edge point of these circles devotes a circle of radius R to an output accumulator space marked by the dotted circles. The “a” value represents the x-axis, “b” value represents the y-axis, while the z-axis is the radii in the parameter space of the circle. At the coordinates which belong to the perimeter of the drawn circle, we increment the value in our accumulator matrix which essentially has the same size as the parameter space. In this way for each edge point in the input image drawing circles with the desired radii and incrementing the values in the accumulator. When the process is over with every edge point and every desired radius, the attention is turned to the accumulator. The numbers in the accumulator will represent the number of circles passing through the individual coordinates. Thus, the highest numbers correspond to the center of the circle in the image. To increase the performance of Circular Hough Transform, the edge orientation information is used (Figs. 6 and 7).

Fig. 6 Voting and accumulation in parameter space



5.2 Approach Used for Helmet Detection

As mentioned above in Chap. 4, the approach used for helmet detection is similar to multiple people detection in some manners. For example, the process is initiated by acquiring a video input from the video surveillance camera. This video is then preprocessed through various steps for conversion into frames of a particular spatial resolution at a fixed frame rate. Then, for efficient processing of applied algorithms, these RGB frames are converted into grayscale images.

Before any further proceedings of the input, segmentation is applied. The aim of segmentation is to significantly change the representation of an image into something that is meaningful and easier to analyze [4, 29–31]. After segmentation, the input is passed on to Canny Edge Detector for extraction of boundaries of objects present in the image and further reduction of noise.

Upon termination of the Hough Transform a Region of Interest(ROI) is captured and thus the remaining measures required for final detection of presence/absence of helmet are performed in the ROI [17, 21]. After ROI extraction, Viola–Jones algorithm is applied to search for available facial features, if the resultant output of the algorithm reports availability of facial features then it means, presence of person’s head. Otherwise, if the algorithm reports unavailability of facial features then it is regarded as presence of a helmet, which is denoted as suspicious activity.

6 Results Analysis

The proposed algorithm was tested on different video sequences. The images were gained at a fixed frame rate of 16 fps and 640*480 pixels spatial resolution. The proposed method executes in real time on a standard desktop computer, even though the fact that it was programmed in MATLAB. However, its been tested on 50 different input sets and positive results were attained more than 45 times. As we can see in the results below, abnormal activities are perfectly detected.

Figure 8: The proposed system was able to detect the person count and also checks for availability of helmet inside the ATM booth. Here it identifies that two persons

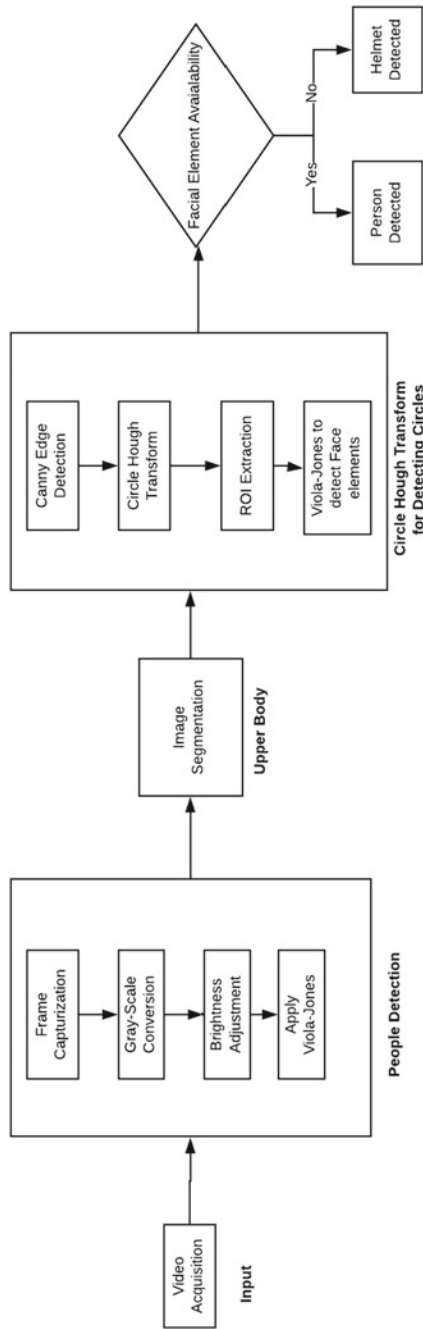
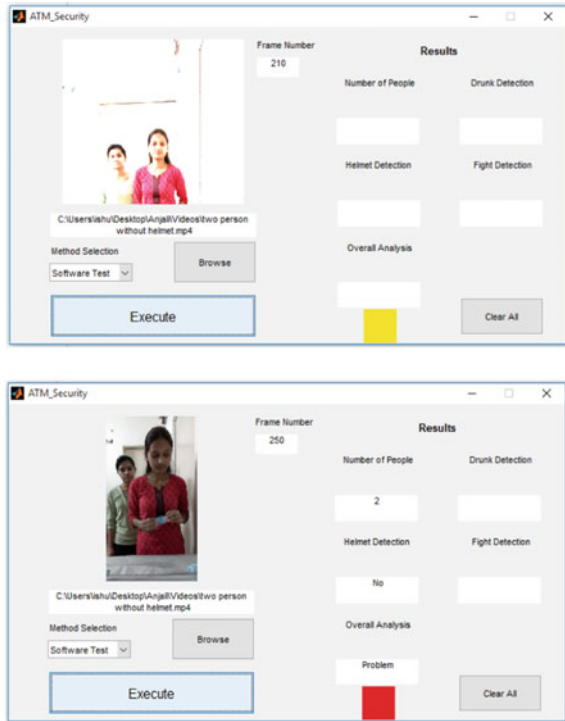


Fig. 7 Helmet detection

Fig. 8 Multiple person detection



present inside ATM booth and there is no availability of helmet. This activity is considered as suspicious activity.

Figure 9: shows a single person wearing helmet and this is considered as suspicious activity.

Figure 10: After detecting ROI of this circular area, Viola–Jones algorithm is applied for detecting facial features availability, if facial features are available then it is considered as normal activity, if facial features are unavailable, then it is regarded as suspicious activity.

Figure 11: shows the comparison between modified Viola–Jones algorithm and classic Viola–Jones algorithm. For this purpose, we assign fixed frame rate of 16, fixed 640*480 pixels spatial resolution, and also same time duration for each video. When optimization takes place the frame rate changes for each video. In both these cases, we used 500 sample frames for detecting suspicious activities. The resultant graph shows that the modified Viola–Jones algorithm is better than classic Viola–Jones algorithm because at the same frame rate modified Viola–Jones algorithm takes less time compared to classic Viola–Jones algorithm.

Table 1 shows the analyzed results of different videos for multiple activities. With a fixed frame rate that is 16, fixed 640*480 pixels spatial resolution, and also fixed time duration for each video. During optimization, the frame rate changes for each video

Fig. 9 Single person helmet detection

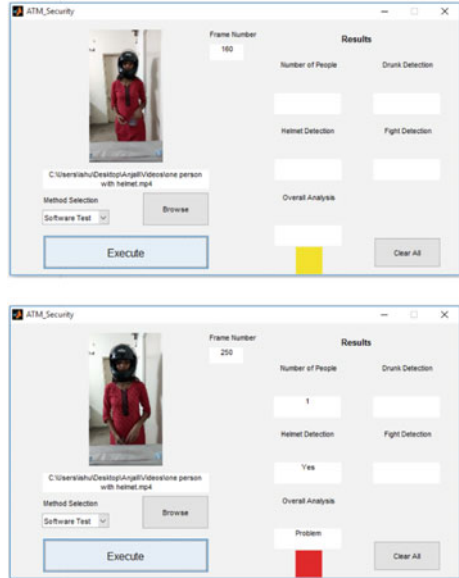


Fig. 10 ROI extraction and head detection

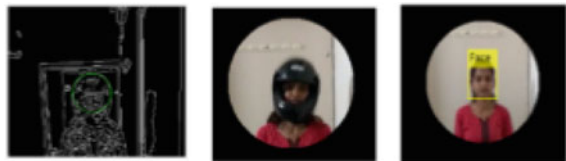


Fig. 11 Comparison between MVJA and VJA

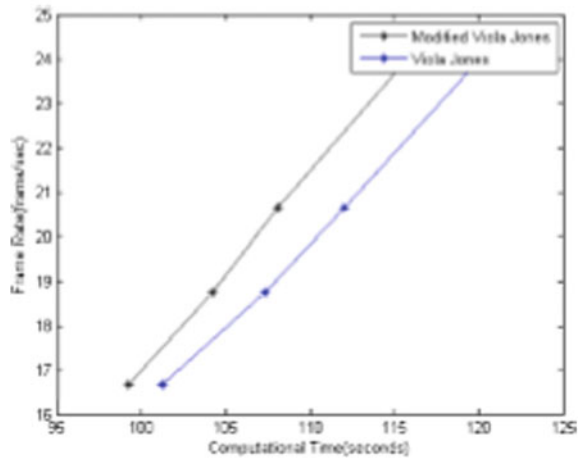


Table 1 Computational analysis of different videos

Activity	Frame rate during optimization	Computational time (s)
One person without helmet	16.6830	93.5089
One person with helmet	16.6960	99.2675
Two person without helmet	17.6325	100.2365

Table 2 Accuracy and comparison with classical method

Input	Problem	Accuracy(%)	Approach(Solution)
Video data set(25)	Multiple person detection	98	Modified Viola–Jones algorithm
Video data set(25)	Helmet detection	96	Modified circle hough transform

resulting in a change in computational time. In every video input, we worked on 500 sample frames for detection of suspicious activity. Computational times marks the difference between one person without the helmet and with a helmet. The proposed framework will take more time in case of a person wearing a helmet than a person without the helmet, similarly takes more time for detecting the presence of multiple people rather than a single person.

Table 2, after performing the above analysis, we conclude that the accuracy percentage of modified Viola–Jones algorithm for multiple person presence detection is 98% and the accuracy percentage for helmet detection is 96%.

7 Conclusion

This research primarily focuses on building an ingenious framework that imparts high-class security in ATM booth. Depending on the activities carried out by the customer in the ATM booth, the system will address suspicious activities spontaneously. The aim of developing this proposed framework is to obviate ATM crime by using computer vision and machine learning techniques. Different angles of entrance and standing positions of the customer and the environmental brightness conditions are challenging issues in this analysis. The proposed system will be able to detect suspicious activities such as overcrowding situations and a person wearing helmet. In case of a suspicious event, a message will be sent to the concerned authority. The urgency of developing such security system arose due to the rise in criminal activities in ATM booth. The proposed system is essential for enhancing ATM security. Furthermore, it can be analyzed to work upon affine transformation, for more stability in random angled image inputs and selection of ROI from the images.

References

1. Haritaoglu I, Harwood D, Davis LS (2000) W4: real-time surveillance of people and their activities. *IEEE Trans Pattern Anal Mach Intell* 22:809–830
2. Badal T, Nain N, Ahmed M (2017) Multi-object trajectory coupling using online target specific decision making, pp 1–6. <https://doi.org/10.1109/ISBA.2017.7947702>
3. Badal Tapas, Nain Neeta, Ahmed Mushtaq (2018) Online multi-object tracking: multiple instance based target appearance model. *Multimed Tools Appl.* <https://doi.org/10.1007/s11042-018-5781-3>
4. Gaikwad K, Patil DM (2013) Human activity detection and recognition algorithm from video surveillances. *Int J Tech Explor Learn* 2319–2135
5. Bayona A, SanMiguel CJ, Jose MM (2010) Stationary foreground detection using background subtraction and temporal difference in video surveillance. In: *IEEE 17th international conference on image processing*
6. Elhabian SY, El-Sayed KM (2008) Moving object detection in spatial domain using background removal techniques, state of the art, recent patents on computer science, pp 32–54
7. Patil S (2013) Moving object detection using statistical background subtraction for a rotating camera. *Int Monthly Ref J Res Manag Technol*
8. Silva E, Veloso RR, Aires KRT, Veras RMS (2014) Helmet detection on motorcyclists using image descriptors and classifiers. In: *IEEE 27th SIBGRAPI conference on graphics, patterns and images (SIBGRAPI)*
9. Dalal N, Bill T (2005) Histograms of oriented gradients for human detection. *IEEE computer society conference on computer vision and pattern recognition*
10. Viola P, Jones M (2001) Rapid object detection using a boosted cascade of simple features. In: *IEEE computer society conference on computer vision and pattern recognition*
11. Wen C et al (2003) The safety helmet detection for ATM's surveillance system via the modified Hough transform. In: *IEEE 37th annual international Carnahan conference on security technology proceedings*
12. Charara N, Jarkass I, Sokhn M, Mugellini E, Khaled OA (2012) Automatic detection of abnormal behavior in video-surveillance. In: *International conference on image, signal and vision computing, Oslo Norway, 2012*
13. Mahadevan V, Li W, Bhalodia V, Vasconcelos N (2010) Anomaly detection in crowded scenes. In: *IEEE computer society conference on computer vision and pattern recognition (CVPR)*
14. Aviv DG (1997) Abnormality detection and surveillance system, U.S. Patent No. 5
15. Kotikalapudi UK (2007) Abnormal event detection in video. M.Tech Thesis IISC
16. <http://projekter.aau.dk/projekter/files/63453522/main.pdf-Detecting> (unusual activities in surveillance video)
17. Doungmala P, Klubsuwan K (2016) Helmet wearing detection in Thailand using Haar like feature and circle hough transform on image processing. In: *IEEE international conference on computer and information technology (CIT)*
18. Tamilselvan S, Monika B Anomalous events detection in frequent sequence video via object segmentation using motion pixel compensation and gradient
19. Kausalya K, Chitrakala S (2012) Idle object detection in video for banking ATM applications. *Res J Appl Sci Eng Tech* 5350– 5356
20. Sujith B (2014) Crime detection and avoidance in ATM: a new framework. *Int J Comput Sci Inf Tech*
21. Cui L, Li K, Chen J, Li Z (2011) Abnormal eventdetection in traffic video surveillance based on local features 362–366
22. Aslani S, Homayoun M (2013) Optical flow based moving object detection and tracking for traffic surveillance. *Int J Electr Comput Energy Electron Commun Eng* 7:789–793
23. Canny J (1983) Finding edges and lines in images. Technical Report, Cambridge, MA, USA
24. Jadhav JJ, Patil YR (2015) Moving object detection for video surveillance system. In: *International journal of computer applications national conference on emerging trends in advanced communication technologies (NCETACT)*

25. Lipton AJ, Fujiyoshi H, Patil RS (1998) Moving target classification and tracking from real-time video. In: IEEE workshop applications of computer vision, pp 8–14
26. Himani SP, Darshak GT, Udesang KJ (2014) A survey on object detection and tracking methods. *Int J Innov Res Comput Commun Eng*
27. Rhody H, Chester F (2005) Hough circle transform. Carlson center for image. Science Rochester Institute of Technology
28. Ioannou D, Duda W, Laine F (1991) Circle recognition through a 2D Hough Transform and radius histogramming. *Image Vis Comput* 17:15–26
29. Niu W, Long J, Han D, Wang YF (2004) Human activity detection and recognition for video surveillance. In: IEEE International Conference on multimedia and expo (ICME), pp 719–722
30. Wang Y, Huang K, Tan T (2007) Human Activity Recognition Based on R Transform. In: IEEE computer society conference on computer vision and pattern recognition
31. Vinayak GU, Samvatsar M (2012) A review on object detection in dynamic background using image segmentation. *Int J Eng Res Appl* 232–236
32. Mandal R, Choudhury N (2016) Automatic video surveillance for theft detection in ATM machines: an enhanced approach. In: IEEE 3rd international conference on computing for sustainable global development (INDIACom)
33. <https://www.slideshare.net/automated-teller-machine>
34. Turk MA, Pentland AP (1991) Face recognition using Eigen -faces. In: IEEE conference on computer vision and pattern recognition, pp 586–591
35. Sonoda S, Tan JK, Kim H, Ishikawa S, Morie T (2011) Moving objects detection at an intersection by sequential background extraction. In ICCAS, pp 1752–1755
36. Sonoda S, Tan JK, Kim H, Ishikawa S, Morie T (2011) Moving objects detection at an intersection by sequential background extraction. ICCAS, pp 1752–1755
37. Thongkamwitoon T, Aramvith S, Chalidabhongse TH (2004) An adaptive real-time background subtraction and moving shadows detection. In: IEEE conferences on multimedia, pp 1459–1462

Mitigation of Power Quality for Wind Energy Using Transmission Line Based on D-STATCOM



Sourabh Kumar Jain and Amit Soni

Abstract The power quality is the most essential issue for any customer, who needs to be concerned. This paper deals with the effect of using Distributed Static Compensator (D-STATCOM) on Power Quality (PQ) issues associated with Electrical Power System supplied using Wind Energy Source. For this study, we have developed a control scheme in which a D-STATCOM is used. The performance for this system is observed by using a MATLAB/SIMULINK having D-STATCOM connected to the bus. The results are recorded by incorporating FACTS devices to the system at appropriate location to identify the improvement in overall system performance. Active and reactive power control is studied for the existing power system under the periphery of norms and guidelines given for PQ improvement. The measurement considered over here is active power and reactive power. The results obtained for the proposed scheme reveals the considerable improvement in the PQ for the transmission line.

Keywords Power quality · MATLAB · D-STATCOM · Wind energy sources · Transmission line

1 Introduction

Due to an increase in population and industrialization, meeting the additional demand for electricity is a major challenge for the generation [1, 2]. To meet the demands of the load new alternative renewable energy should be used which will also ensure pollution free environment and complete the guideline of environmental protection rules [3, 4]. Renewable energy sources such as wind and solar power have to reduce the existing conventional power system.

S. K. Jain (✉)

Department of Electrical Engineering, Pacific Academy of Higher Education & Research University, Udaipur, Rajasthan, India
e-mail: jain.sourabh05@gmail.com

A. Soni

Department of Electrical Engineering, Manipal University Jaipur (MUJ), Jaipur, Rajasthan, India
e-mail: amit.soni@jaipur.manipal.edu

© Springer Nature Singapore Pte Ltd. 2020

A. Kalam et al. (eds.), *Intelligent Computing Techniques for Smart Energy Systems*,
Lecture Notes in Electrical Engineering 607,
https://doi.org/10.1007/978-981-15-0214-9_98

927

In the integration of existing electrical power, the wind power system induce the problem of electrical quality such as voltage regulation. The quality of electricity is always customer-centric, which is very much affected by the operation of the measurement. In this proposal one of the flexible transmission systems, i.e., D-STATCOM has been added which is very beneficial in reducing the quality of power quality. D-STATCOM grants electricity to the public generator connected to the grid and makes it responsive for the load. This fluctuation also provides integrated or solar energy to maintain the actual power source under the air. Due to this reactive power absorbed and affect voltage of IG, causing a magnet. It changes the active power of generator. Therefore, such a proper scheme is adopted in the wind power system, allowing it to allow proper control under normal conditions, as well as to control the active power generation and increasing grid conditions and also a battery power storage system. This paper tried to resolve PQ problems, with demand of load and environment friendly renewable energy resources. D-STATCOM control scheme [5] is being used for the hybrid connected to the grid which is following the energy system to improve the quality of electricity. If there is any change or sudden change in the system or grid, the voltage profile suddenly responses to the changes and causes short circuit in a point. The system responses it rapidly and stabilizes the voltage, which maintains the power quality [6–9].

2 Proposed Work

This paper deals with the effect of using Distributed Static Compensator (D-STATCOM) on Power Quality (PQ) issues associated with Electrical Power System supplied by using Wind Energy Source. For this study, we have developed a control scheme in which a D-STATCOM is used. The performance for this system is observed by using a MATLAB/SIMULINK having FACT device connected to the bus (Fig. 1). The relation for voltage rise will be given as [10–12]:

$$u = \frac{s_{\max} (r \cos \theta - x \sin \theta)}{u^2} \quad (1)$$

The active and reactive power is given as:

$$P = VI \cos \phi \quad (2)$$

$$Q = VI \sin \phi \quad (3)$$

This research is based on the MATLAB/Simulink for the power quality improvement of the transmission system using wind power source, with data collected from

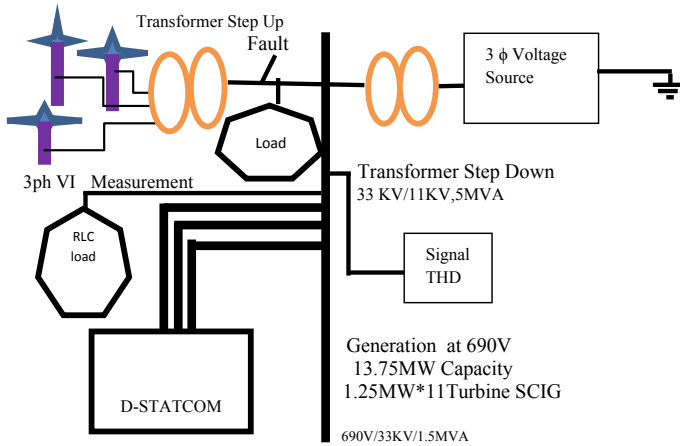


Fig. 1 Single line diagram for the transmission system using D-STATCOM with wind energy source

the Windmill Dewas, Madhya Pradesh. This work reveals the analysis evaluation for some power quality issues and solution using D-STATCOM [13, 14].

3 Result and Discussion

In this proposed model Fig. 2, three-phase voltage source is connected to the three-phase transformer which is interconnected to the three-phase voltage and current measurement source. In this, the simulation setup consists of 11 wind generating units of capacity 1.25 MW each. The power generated by each is stepped up to 33 kV voltage level and is finally distributed through 11 kV line in connection with grid (see Table 1). In this, we have connected a D-STATCOM. The performance for this system is observed by using a MATLAB/SIMULINK having D-STATCOM connected to the bus [15]. The results are recorded by incorporating FACTS devices to the system at appropriate location to identify the improvement in overall system performance. Real and reactive power control is studied for the existing power system under the periphery of norms and guidelines given for PQ improvement. The measurement considered over here is active power, reactive power, and harmonics parameters. The results obtained for the proposed scheme reveals the considerable improvement in the PQ for the transmission line. Also showed single line diagram of proposed work in Fig. 1. The Simulation model used is drawn as shown below.

Case 1—The graph at the top in Fig. 3 reflects the feeder line power factor 0.4 s of the course during the simulation time period. Across the auxiliary capacitors and

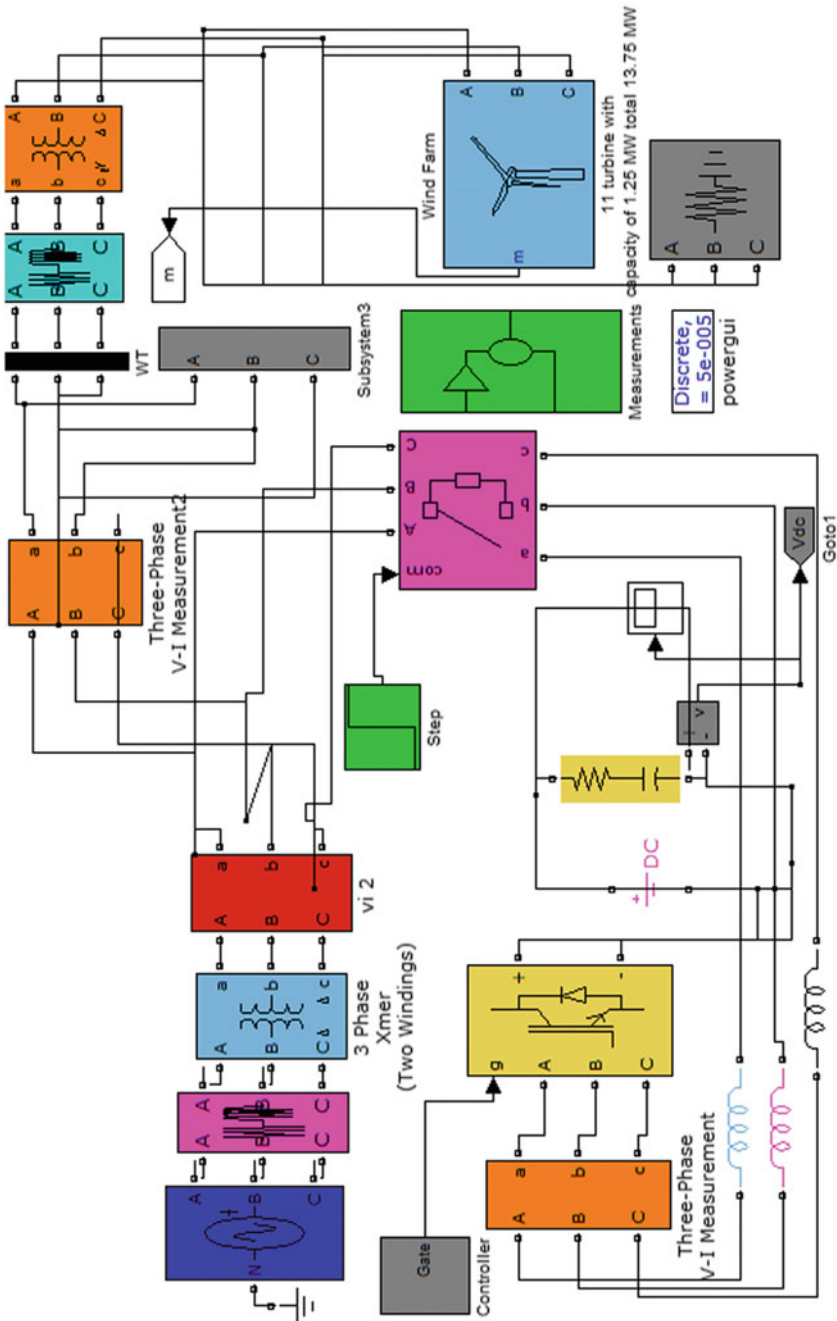


Fig. 2 Simulation model of wind energy generation using FACTS device D-STATCOM

Table 1 Simulated parameters for the proposed system

Generating data	
Wind speed	Cut in 3 m/s
Rated speed	12 m/s
Cut out speed	25 m/s
Generation (RPM)	1250 KW, 1590 RPM
Stator resistance	0.004873 Ω
Rotor resistance	0.004467 Ω
Transformer data at generating end	690 V/33 kV; 1.5 MVA, 50 Hz
Magnetizing resistance	500 p.u.
Transformer data at transmission side	33 kV/11 kV; 5 MVA, 50 Hz
Transmission parameter	
R1; R0	(0.128; 0.533)
L1; L0	(1.15e-3; 3.41e-3)
C1; C0	(11.46e-009; 5.24e-009)

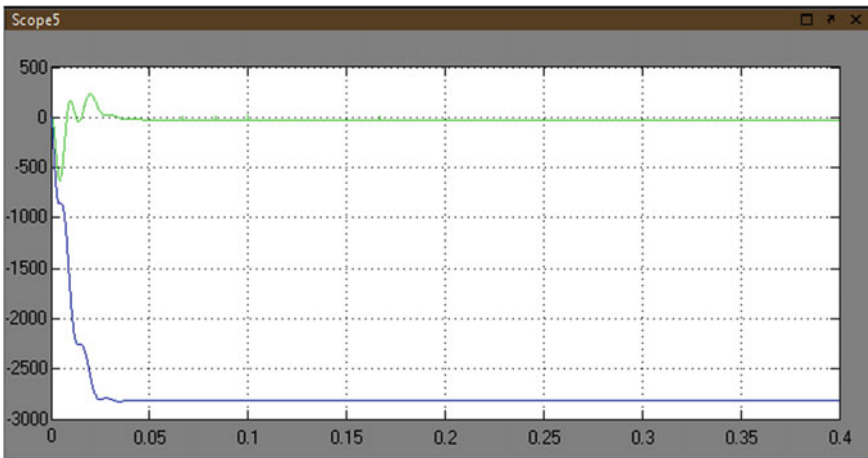


Fig. 3 Real and reactive power

each of the links there is individual voltage in DC links. Figure 3 also reflects the feeder line power factor, and the feeder line p and Q values.

Real and reactive power control is studied for the existing power system under the periphery of norms and guidelines given for PQ improvement. According to the results the reactive power decreases from 0 to 0.03 s. After 0.03 s it flows constantly throughout the system. Similarly, at 0–0.01 s the active power increases but there are

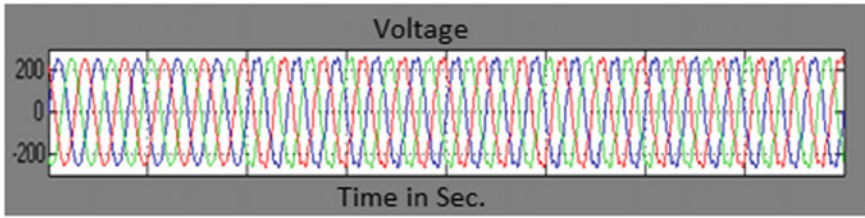


Fig. 4 Voltage versus time graph

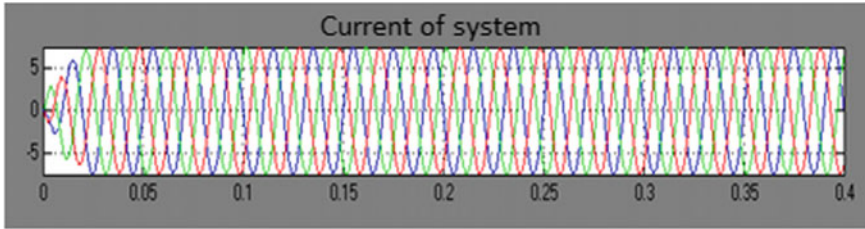


Fig. 5 Current versus time graph

sudden changes from 0.01 to 0.03 s and from -500 to 100 VA. After experiencing changes and reaching again the value 0, the active power flows constantly.

Case 2—The scope is connected to VI measurement, which shows that the voltage flows continuously throughout the circuit in all the three-phase. But there are sudden changes in the current graph. The current increases from 0 to 6 amp in 0.025 s and then it flows continuously as shown in Fig. 4. Figures 4 and 5 show the voltage source after mitigation and the waveforms of a current source, by elevating the contents of the harmonics the voltage and current of D-STATCOM become sinusoidal.

But there are sudden changes in the current graph. The current increases from 0 to 6 amp in 0.025 s and then it flows continuously.

Case 3—At full capacity, D-STATCOM supplies the reactive power to the machine. And wind turbine cannot recover voltage itself after creating fault. The improve voltage profile during default is observed because of the use of D-STATCOM which also causes improvement in its terminal voltage.

These are the voltages and currents of D-STATCOM. Here the sinusoidal voltage and the Distortion current are shown. The Source current is injected by the distorted current. For making the sinusoidal sources current harmonics are eliminated. But the current level is constant at 0.1 s. After 0.1 s the current starts fluctuating from its maximum and minimum value (Fig. 6).

Similarly at 0–0.1 s the current travels from its maximum to the minimum value (Fig. 7). But after 0.1 there is sudden fluctuation in the current graph and the current increases from 0 to 6 amp in 0.025 s and then it flows continuously.

This is observed that, when D-STATCOM is incorporated in the system, reactive power (Q) reaches its steady state within a few milliseconds (Fig. 8). D-STATCOM

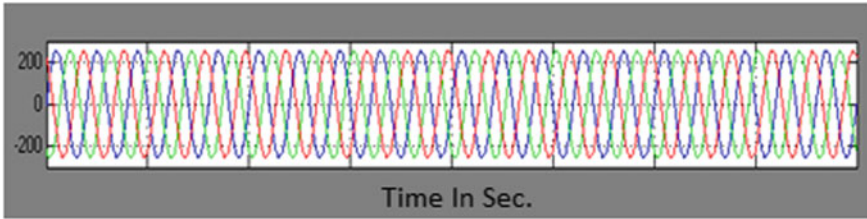


Fig. 6 Voltage versus time graph after D-STATCOM operation

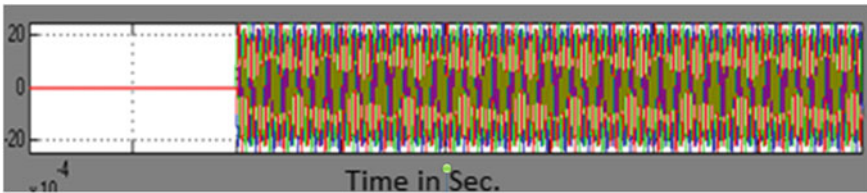


Fig. 7 Current versus time graph after D-STATCOM operation

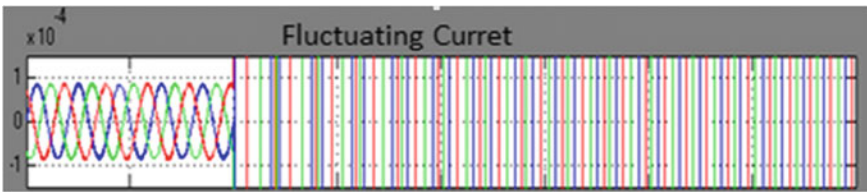


Fig. 8 Fluctuating current

has shown the efficiency and effectiveness of active and reactive power compensation, hence it makes and D-STATCOM to be an interesting power quality improvement device. Also the simulation study shows that the D-STATCOM provides a better improvement in reactive power and system oscillation.

4 Conclusion

The new D-STATCOM system is incorporated in this research which is specially designed for the PQ issues mitigation. In this system of the D-STATCOM, for the mitigation of reactive power and voltage variation-current control model is used. Similarly, for voltage stabilizer, a mode of voltage control is used. It is used in the dips compensation application which generally comes from the supply network.

The scheme for the simulation shows that D-STATCOM performance is satisfactory which provides the result in improving the problem of power quality. At full capacity D-STATCOM operates which supplies the machine the required reactive power which is remaining. It should be noted that the wind turbine voltage and load bus is not able to recover itself even after clearing the fault. The improve voltage profile during fault condition is observed because of the use of D-STATCOM which also causes improvement in its terminal voltage.

Acknowledgement Authors thank Suzlon Energy wind farm, Dewas, Madhya Pradesh, India for providing all practical data for this proposed research.

References

1. Jovitha J, Subha R (2004) Power quality enhancement in distribution system. In: 13th national power system conference. Indian Institute of Technology (IIT), pp 749–754
2. Muljadi E, Sallan J, Sanz M, Butterfield CP (1999) Investigation of self-excited induction generators for wind turbine applications. In: Thirty-fourth IAS annual meeting industry applications conference record, pp 509–515
3. Hara Y, Masada E, Miyatake M, Shutoh K (2000) Application of unified power flow controller for improvement of power quality. In: Power engineering society winter meeting, pp 2600–2606
4. Slootweg JG, Kling WL (2002) Modeling of large wind farms in power system simulations. In: Power engineering society summer meeting, pp 503–508
5. Tavakkoli A, Ehsan M, Batahiee SMT, Marzband M (2008) A simulink study of electric arc furnace power quality improvement by using STATCOM. In: IEEE international conference on industrial technology, pp 1–6
6. Geibel D, Degner T, Hardt C, Antchev M, Krusteva A (2009) Improvement of power quality and reliability with multifunctional PV-inverters in distributed energy systems. In: International conference on electrical power quality and utilization, pp 1–6
7. Hu Y, Chen Z (2009) STATCOM's effects on stability improvement of induction generator based wind turbine systems. In: Conference on power and energy engineering, pp 1–4
8. Aggarwal M, Gupta SK, Kasal G (2010) D-statcom control in low voltage distribution system with distributed generation. In: 3rd international conference on emerging trends in engineering and technology (ICETET), pp 426–429
9. Yahiya AA, Uzair AR (2016) Performance analysis of DVR, D-STATCOM and UPQC for improving the power quality with various control strategies. In: IEEE biennial international conference on power and energy systems, towards sustainable energy, PESTSE, pp 1–4
10. Pradeepa S, Uma Rao K, Deekshit R (2013) Comparative study of different series compensation configurations for voltage sag mitigation in multimachine system. In: IET fifth international conference on advances in recent technologies, pp 295–300
11. Gawande SP, Kubde NA, Joshi MS, Sudame BS (2012) Reactive power compensation of wind energy distribution system using distribution static compensator. In: IEEE 5th India international conference on power electronics, pp 1–5
12. Dehini R, Benachaiba C, Bassou A (2013) Simulation of distribution static compensator (D-STATCOM) to improve power quality. Springer, Arab J Sci Engg 3051–3058
13. Roy NK, Hossain MJ, Pota HR (2011) Voltage profile improvement for distributed wind generation using D-STATCOM. In: IEEE power and energy society general meeting

14. Hingorani NG Overview of custom power application. Hingorani Power Electronics, 26480 Weston drive, Los Altos Hills, CA 94022
15. Jain SK, Soni A (2017) Analysis of power quality improvement for wind energy generation using STATCOM. JARDCS. ISSN 1943-023X, Scopus, Elsevier, pp 136–141

Performance Evaluation of Solar Power Plant



Amit Rai, Ashish Shrivastava and K. C. Jana

Abstract The growing energy demand of the world is now looking for the new, clean and viable energy source. The greenhouse gas emission and limited stock of coal, is now phasing out thermal power plants. The potential answer to this requirement is renewable energy. The solar power is abundantly available worldwide, especially in equatorial regions. In this work, a location which has the equatorial climatic condition is selected and a solar power plant potential is estimated. The annual yield, capacity factor, performance ratio, payback period and net saving are the different parameters which are analyzed to estimate the full potential of the plant.

Keywords Photovoltaic (PV) · Net present value (NPV) · Cost of electricity (COE) · System advisor model (SAM)

1 Introduction

The rising demand for energy and the implications of the thermal power plant has provided a way forward to renewable energy worldwide. Currently, the share of fossil fuels in energy generation has the highest percentage and renewable energy has the lowest share [1]. But this large share of fossil fuels is also adding a large number of pollutants in the environment [2, 3]. Due to these pollutants life mortality is decreasing [4]. This decrease in life expectancy and increasing diseases have a negative effect on the countries economy. All the stated reasons are increasing promotion and research in renewable energy generation systems.

Solar power plants do not have greenhouse emission. The decreasing cost and increasing efficiency of solar panels, is making the solar energy more attractive choice with other renewable energy options [5]. This distributed generation needs potential assessment before installation. Different researchers have analyzed the solar

A. Rai (✉) · K. C. Jana
Indian Institute of Technology (ISM), Dhanbad, India
e-mail: rai.amit21@gmail.com

A. Shrivastava
Manipal University Jaipur, Jaipur 303007, Rajasthan, India

© Springer Nature Singapore Pte Ltd. 2020
A. Kalam et al. (eds.), *Intelligent Computing Techniques for Smart Energy Systems*,
Lecture Notes in Electrical Engineering 607,
https://doi.org/10.1007/978-981-15-0214-9_99

photovoltaic plants with the different hybrid combination and with battery backup [6], analysing different parameters like the cost of electricity (COE), net present cost (NPC), operation and maintenance cost (O&M) and return on investment (RoI). With these researches, it can be seen that assessment is an important role before the installation of the solar power plant [7].

This integration of renewable energy in the grid will also add uncertainty in the generation. The solar plant will create power, according to the irradiance incident on its surface [8]. Any variation in the irradiance will create a generation disturbance. To mitigate this issue different control strategies are also proposed, like integrating batteries in the system and converters to smooth out the supply and proper calculation of radiation [9].

This paper analyses the solar plant viability with SAM [10], for Sri Ganganagar, Rajasthan. The location of the selected area is 29°N latitude and 73.85°E longitude. The average yearly temperature is 28.5 °C of the location. The solar plant of 220 kW DC capacity is considered for implementation. In an analysis [10], annual generation, monthly generation of the plant, energy yield and plant capacity is analyzed in the technical section. In economical section, the cost of electricity (COE), the net present value (NPV) and net saving with the system with the payback period are estimated. For proper working different methods are analyzed to improve the grid connectivity of the system.

2 Methodology and Input Parameters

The proposed system is analysed with the System Advisor Model (SAM) of National Renewable Energy Laboratory (NREL) of U.S.A. This professional software provides an insight into the proposed solar plant with all its key parameters. The plant capacity is taken as 220 kW DC power. In Table 1 all the input parameters of location and solar panel are given.

Table 1 Input parameters

Location input	Value
Latitude	29.95° N
Longitude	73.85° E
Temperature	28.5°
Irradiance	5.21 kWh/m ² /day
<i>Solar plate input</i>	<i>Value</i>
Nominal efficiency	19%
Vmp	54.7 Vdc
Imp	5.7 Adc
Voc	64.4 Vdc
Isc	6.1 Adc

Table 2 Performance outcomes

Metric	Value
Annual energy (year 1)	336,092 kWh
Capacity factor (year 1)	17.50%
Energy yield (year 1)	1,531 kWh/kW
Performance ratio (year 1)	0.73
Levelized COE (nominal)	8.28 ¢/kWh
Levelized COE (real)	6.55 ¢/kWh
Electricity bill without system (year 1)	\$825,733
Electricity bill with system (year 1)	\$791,886
Net savings with system (year 1)	\$33,848
Net present value	\$88,064
Payback period	14.1 years
Net capital cost	\$452,346
Debt	\$452,346

3 Result and Discussion

The simulation of the solar plant with the above input has given the output, shown in Table 2. The total energy production in one year is 336092 kWh with 17.5% capacity factor and performance ratio of 73%, which is comparable with the established plants in similar climatic zones. This shows that the proposed plant is feasible in terms of energy-generation.

The cost of electricity is 8.28 cents per kWh, which has shown its cost-effectiveness. The payback period is 14.1 years and the project lifetime is 25 years, which implies that this plant has high return on investment (RoI).

The electricity production of the solar plant depends on solar irradiance and temperature of the place. The energy production is highest in the month of February and March as these months have high irradiance and low temperature. In April to August production is lower than expected as these months have a high temperature, which will reduce the efficiency of the solar panels, shown in Figs. 1 and 2, in which blue line is for irradiance and the orange line is for DC power output.

The solar plant has different kind of losses, like soiling, wiring, panel and inverter, which is shown in Fig. 3.

4 Conclusion

In this work, a solar plant of 220 kW is analysed for its feasibility, for Sri Ganganagar, Rajasthan. The outcome of the simulation provides the pre-implementation insight for the plant. The capacity factor and performance ratio of the plant is 17.5% and

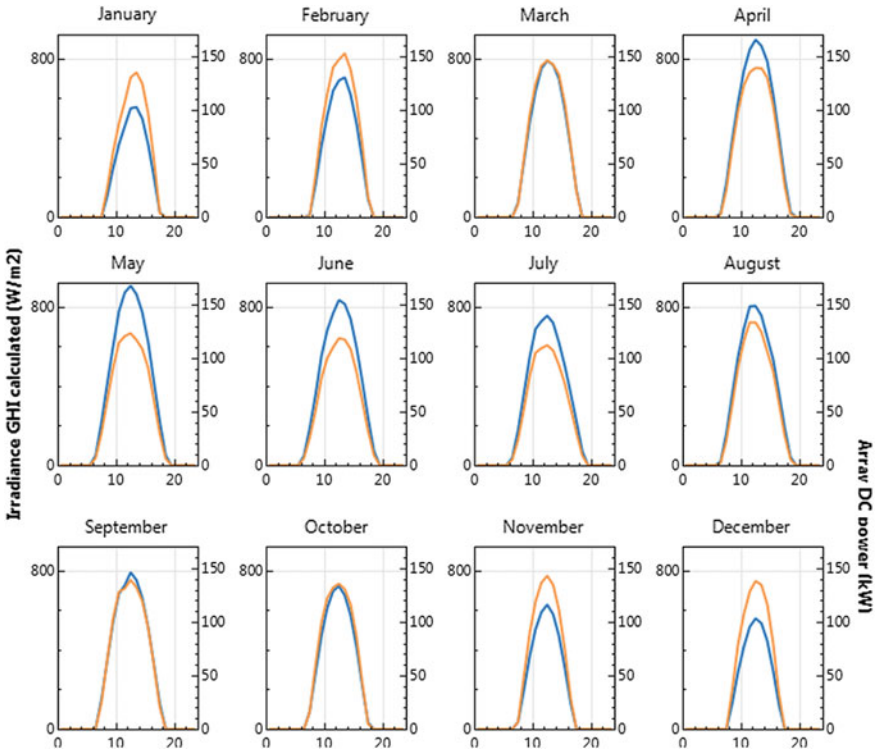
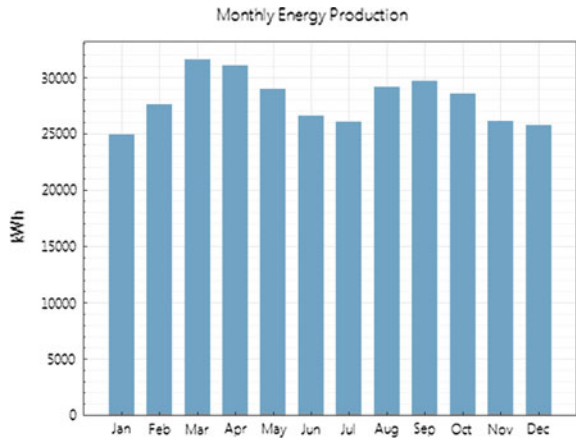


Fig. 1 Monthly irradiance and DC output of the plant

Fig. 2 Monthly energy production of plant



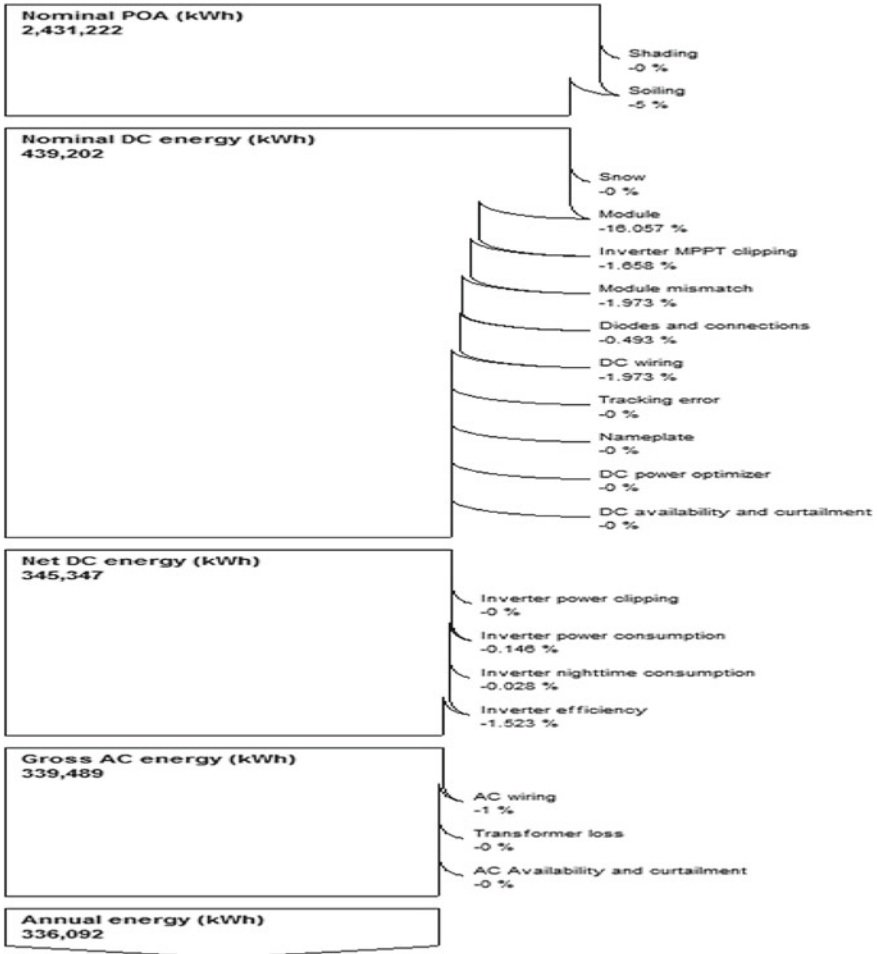


Fig. 3 Losses of the plant

73%, respectively, which is comparable to established power plants worldwide. The payback period and net saving of the plant is also reflecting the financial viability of the project. Moreover, it will also reduce pollutant emission and hence will improve the environment and life expectancy of the people.

References

1. IEA. Renewables information: overview (2017) International energy agency
2. Intergovernmental panel on climate change (2007) Climate change. Synthesis report. Cambridge University Press, Cambridge, UK

3. Intergovernmental panel on climate change (2007) Climate change. Mitigation of climate change. Cambridge University Press, Cambridge, UK
4. Correia AW, Pope CA III, Dockery DW, Wang Y, Ezzati M, Dominici F (2013) The effect of air pollution control on life expectancy in the United States: an analysis of 545 us counties for the period 2000 to 2007. *Epidemiology* 24(1):23–31
5. Timilsina G, Kurdgelashvili L, Narbel P (2011) A review of solar energy: markets, economics and policies. The World Bank Development Research Group, Environment and Energy Team
6. Brandoni C, Bosnjakovic B (2016) HOMER analysis of the water and renewable energy nexus for water-stressed urban areas in Sub-Saharan Africa. *J Clean Prod* 1–14
7. Türkay BE, Telli AL (2011) Economic analysis of standalone and grid connected hybrid energy systems. *Renew Energy* 36:1931–1943
8. Stoffel T (2015) A review of measured/modeled solar resource uncertainty. In: Proceedings sandia pv performance modeling workshop (29 Jan 2015)
9. McArthur LJB, Hay JE (1980) An assessment of the techniques for determining the distribution of diffuse solar radiance for the sky hemisphere. *Sol Energy* 25:573–574
10. System Advisory Model (SAM)

GWO Based PID Controller Optimization for Robotic Manipulator



Sandeep Tripathi, Ashish Shrivastava and K. C. Jana

Abstract The robotic manipulator application is used in the various processes like automation and medical industries for pick, place, and path positioning purpose. These systems are time varying and nonlinear, as a result the performance is a primary issue for this type of systems. In this work tracking of trajectory for robotic manipulator is obtained with different soft computing techniques. The optimal value PID is obtained through Gray Wolf Optimization (GWO) and this value is compared with another optimization which is Antlion (ALO). The obtained results are demonstrated on performance indices of time domain. The final simulation results show that GWO with integral time absolute error gives the best optimal value for PID controller than ALO.

Keywords Ant lion optimization · Gray wolf optimization · PID controller · Two-link robotic manipulator

1 Introduction

In this rapidly growing world, robotics play a major role in human comfort. Various processes such as medical and automation industries widely use such type of devices which manipulate material without human indulgence. The robotic manipulator is also used in various automation industries where human presence is hazardous. The robotic manipulator is used in all these types of industries, and hence requires very precise and accurate measurement. As robotic manipulators are highly non-linear systems, its use in automation industries requires very accurate measurement. It is

S. Tripathi (✉) · K. C. Jana
Indian Institute of Technology (ISM), Dhanbad, India
e-mail: trisandeep@gmail.com

K. C. Jana
e-mail: kartickjana@gmail.com

A. Shrivastava
Manipal University Jaipur, Jaipur 303007, Rajasthan, India
e-mail: rewa.ashish@gmail.com

© Springer Nature Singapore Pte Ltd. 2020
A. Kalam et al. (eds.), *Intelligent Computing Techniques for Smart Energy Systems*,
Lecture Notes in Electrical Engineering 607,
https://doi.org/10.1007/978-981-15-0214-9_100

also necessary to ensure that the manipulators follow the exact trajectory with utmost precision [1]. With the considerable growth in control engineering, the conventional controller like PID controller is the first choice due to simple design, easy implementation, quick response, and low steady state error [2, 3].

In this proposed paper, the robotic manipulator is simulated, controlled, and optimized so as to minimize the error in the following trajectory [4]. The error occurs due to external disturbances like noise or maybe due to the friction and other manipulator parameters that are uncertain. Due to these parameters being unknown, it is difficult to model the system and measure them precisely [5]. Firstly, the control equations of robotic manipulator are modeled and simulated in MATLAB. After designing the system a reference trajectory is provided to the system and the output is analyzed and it is observed that the output trajectory does not exactly follow the input trajectory. This difference between the input and output trajectory is called error and this error occurs due to nonlinear behavior of system that cannot be properly evaluated but can be minimized using PID controller. Various new metaheuristic Optimization techniques like Particle Swarm optimization [6], Whale optimization algorithm (WOA) [7], Ant lion Optimization (ALO) [8–10], and Gray Wolf Optimization (GWO) are used [11, 12], Multi-objective gray wolf optimizer [13], for error minimization of various nonlinear system application can be used.

So, in this paper, Ant lion optimization (ALO) and Gray wolf optimization (GWO) are considered for error optimization and to find the best suited PID controller parameter. Once the system is optimized, their error performance is compared. For error performance comparison, two time domain errors like Integral Square Error (ISE) and Integral time Absolute Error (ITAE) are taken [14, 15].

2 Modeling of Robotic Manipulator

The two-link robotic manipulator (RM) model is used [1, 11] in this paper. Equation (1) shows the relationship between links, position, and torque of manipulator. Table 1 shows the relevant parameter of manipulator. Figure 1 shows a two-link robotic manipulator

Table 1 Parameters of manipulator

Parameters	Joint 1 of RM	Joint 2 of RM
Mass	0.392924 kg	0.094403 kg
Acceleration due to gravity (g)	9.81 m/s ²	9.81 m/s ²
Length	0.2032 m	0.1524 m
Center of gravity to joint distance	0.104648 m	0.081788 m
Length wise centroid inertia link	0.0011411 kg-m ²	0.0020247 kg-m ²
Joints friction	0.141231 N-m/radian/s	0.3530776 N-m/radian/s

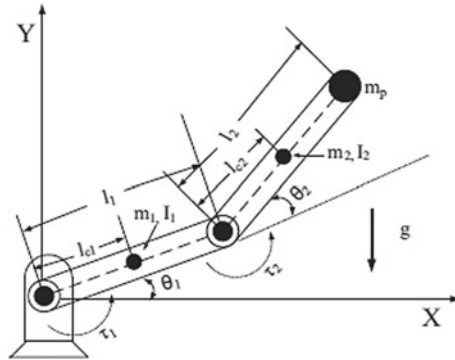


Fig. 1 Two-link planar robotic manipulator

$$\begin{bmatrix} Q_{11} & Q_{12} \\ Q_{21} & Q_{22} \end{bmatrix} \begin{bmatrix} \ddot{\theta}_1 \\ \ddot{\theta}_2 \end{bmatrix} + \begin{bmatrix} P_1 \\ P_2 \end{bmatrix} + \begin{bmatrix} f_1 \\ f_2 \end{bmatrix} + \begin{bmatrix} g_{1q} \\ g_{2q} \end{bmatrix} = \begin{bmatrix} \tau_1 \\ \tau_2 \end{bmatrix} \tag{1}$$

where

$$Q_{11} = l_1 + l_2 + m_1 l_{c1}^2 + m_2 l_1^2 + m_2 l_{c2}^2 + m_{33} l_2^2 + m_{33} l_1^2 + 2m_2 l_1 l_{c2} \cos \theta_2 + 2m_{33} l_1 l_2 \cos \theta_2$$

$$Q_{12} = l_2 + m_2 l_{c2}^2 + m_{33} l_2^2 + m_2 l_1 l_{c2} \cos \theta_2 + m_{33} l_1 l_2 \cos \theta_2$$

$$Q_{22} = l_2 + m_2 l_{c2}^2 + m_{33} l_2^2, \quad Q_{21} = Q_{12}$$

$$P_{11} = -m_2 l_1 l_{c2} (2\dot{\theta}_1 + \dot{\theta}_2) \dot{\theta}_2 \sin \theta_2 - m_{33} l_1 l_2 (2\dot{\theta}_1 + \dot{\theta}_2) \dot{\theta}_2 \sin \theta_2$$

$$P_{21} = m_2 l_1 \dot{\theta}_1^2 l_{c2} \sin \theta_2 + m_{33} l_1 \dot{\theta}_1^2 l_2 \sin \theta_2, \quad g_{2q} = m_2 l_{c2} g \cos(\theta_1 + \theta_2) + m_{33} l_2 g \cos(\theta_1 + \theta_2)$$

m_{33} is mass of payload and it is constant and its value is 0.14174 kg.

where

θ_1 and θ_2 are the position of the link. τ_1 and τ_2 are control output.

m_1 and m_2 are arm 1 & arm 2 mass. l_1 and l_2 are arm 1 and arm 2 length.

l_{c1} and l_{c2} are the lengths of arm 1 and arm 2 where the center of gravity lies.

b_1 and b_2 are coefficient of friction at joints.

f_1 and f_2 are the dynamic friction coefficients of joint 1 & joint 2.

3 Trajectory for Manipulator

The trajectory tracking which is polynomial in nature is considered as follows:(2).

$$\theta_{desired} = \theta_{initial} + \left(6 \frac{t^5}{t_s^5} - 15 \frac{t^4}{t_s^4} + 10 \frac{t^3}{t_s^3}\right)(\theta_{final} - \theta_{initial}) \tag{2}$$

where $\theta_{desired}$ is the joint 1 and joint 2 desired position independently; $\theta_{initial} = 0$ is joint 1 and joint 2 initial positions; $\theta_{final} = \pi/2$ is the final position of Link1; $\theta_{final} = \pi/6$ is final position of joint 2 and, t_s which is 2 s is the time when both links approaches its end position [3].

4 PID Controller

As the output trajectory does not exactly follow the input trajectory, the error has to be minimized. This error is minimized using a conventional PID controller used in manipulator control as shown in Fig. 2. PID controller transfer function is shown in Eq. (3).

$$K_p + \frac{K_i}{s} + K_D s = \frac{K_p s + K_i + K_D s^2}{s} \tag{3}$$

$$u = K_p + K_i \int e.dt + K_D \frac{de}{dt} \tag{4}$$

Where,

K_p = Gain Proportional, K_i = Gain Integral, K_D = Gain Derivative, e = Tracking error

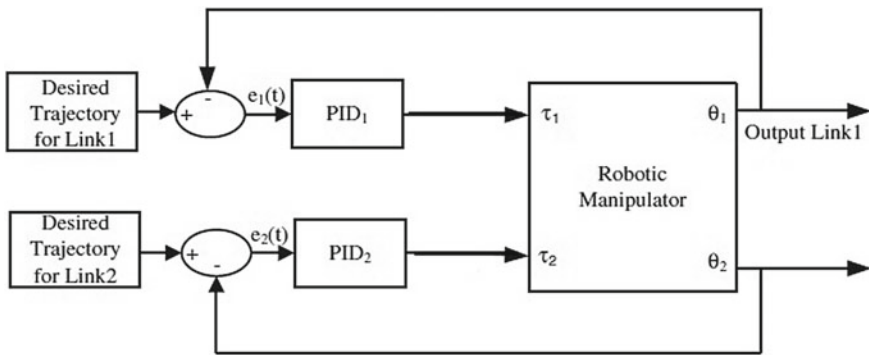


Fig. 2 PID controller structure for manipulator

5 Optimization Technique

This part of the paper presents a brief description of the used optimization techniques. The time domain fitness function is considered for controller parameter tuning which is subjected to minimization of controller parameter and the time domain error in predefined bounds. In this paper, ISE and ITAE are chosen as error functions, as shown in Eqs. (5) and (6) [10].

$$ISE = \int e^2(t)dt \tag{5}$$

$$ITAE = \int t|e|dt \tag{6}$$

5.1 GWO Optimization

When Gray wolf optimization (GWO) is a metaheuristic optimization which is based on wolf hunting behavior, this new technique was introduced by Mirjalili et al. [11]. The Gray wolves are categorized into four groups viz. alpha (α), beta (β), delta (δ), and omega (ω), in the lowering order of dominance. In searching process GWO starts with random generation of population of gray wolves. In each iteration, the α , β , and δ pack determines the approximate position and distance from the prey. This encirclement continues until the distance between prey stops changing or the satisfactory condition is met. The mathematical model of GWO algorithm is based on social structure and hunting style (tracking, encircling and attacking) of a gray wolf.

According to the mathematical modeling of gray wolf, (α)alpha is considered as the first best fittest, beta (β) as the second best fittest, and delta (δ) as the third best fittest solution. The rest of the solution is considered to be omega (ω). The hunting is primarily guided by α , and β , then δ and ω are followed.

The first step in hunting is encircling the prey and mathematically it is given in Eqs. (7) and (8).

$$\vec{F} = \left| \vec{G} \cdot \vec{X}_{pos}(t) - \vec{Y}(t) \right| \tag{7}$$

$$\vec{Y}(t + 1) = \vec{X}_{pos}(t) - \vec{B} \cdot \vec{F} \tag{8}$$

$$\vec{B} = 2\vec{a} \cdot r_1 - \vec{a} \tag{9}$$

$$\vec{G} = 2 \cdot \vec{r}_2 \tag{10}$$

Here t is iterations \vec{B} , \vec{G} are coefficient vectors given in Eqs. (8) and (9). \vec{X}_{pos} is the position of prey and \vec{Y} is the gray wolf position. Values of \vec{a} are decreasing from 2 to 0 over the iteration. The $r1$ and $r2$ have the value within $[0, 1]$ limit.

We choose the first best three solutions (α) alpha, (β) beta, and (δ) delta and they update their position according to the best search solution. The mathematical formula for this is [8].

$$\vec{D}_\alpha = \left| \vec{G}_1 \cdot \vec{X}_\alpha - \vec{Y} \right|, \vec{D}_\beta = \left| \vec{G}_2 \cdot \vec{X}_\beta - \vec{Y} \right|, \vec{D}_\delta = \left| \vec{G}_3 \cdot \vec{X}_\delta - \vec{Y} \right| \tag{11}$$

$$\vec{Y}_1 = \vec{Y}_\alpha - \vec{B}_1 \cdot (\vec{D}_\alpha) \tag{12}$$

$$\vec{Y}_2 = \vec{Y}_\beta - \vec{B}_2 \cdot (\vec{D}_\beta), \vec{Y}_3 = \vec{Y}_\delta - \vec{B}_3 \cdot (\vec{D}_\delta) \tag{13}$$

$$\vec{Y}(t + 1) = \frac{\vec{Y}_1 + \vec{Y}_2 + \vec{Y}_3}{3} \tag{14}$$

The (α) alpha, (β) beta, and (δ) delta wolves encircle around the prey and update their position within the circle. The parameter emphasizes on exploration and exploitation, while parameter emphasizes on convergence and divergence from the prey. As value of \vec{B} tends to zero, $|\vec{B}|$ also tends to zero ($|\vec{B}| < 1$) and next best position is found between current position of wolves and prey. The iteration continues until the prey stops moving. For Tracking, if $|\vec{B}| > 1$, gray wolves diverge from the prey to find the fitter prey. Vector help in exploration and in avoiding local optima by giving weights to prey. Value of \vec{C} is chosen randomly and it also shows the effect of obstacles in the path of wolves. The algorithm is terminated when the end criteria are met.

6 Simulation and Result Analysis

MATLAB/SIMULINK software version R2016a is used for simulation. A simulink model developed for Eq. (1).The simulation time is taken as $t_s = 2$ s.

The fitness functions which are chosen — ISE and ITAE for the error as shown in Eqs. (5), (6) [15]. The single fitness function F combines two functions (23)–(24) of both the joints. The fitness function is mainly used to reduce the error difference between desired and present outputs.

$$f_1 = \int e_1^2(t)dt + \int e_2^2(t)dt \tag{23}$$

$$f_2 = \int t|e_1|dt + f_2 = \int t|e_2|dt \tag{24}$$

$$F = w * f \tag{25}$$

The optimized value of K_p , K_i , K_d , ISE, and ITAE and the Fitness Values are provided in the Tables 2 and 3.

As from Table 2 the fitness functions of GWO for ISE error is 6.8516×10^{-5} and for ALO 0.0001128.

From Table 3 where we choose ITAE as a fitness function, GWO gives 0.0093997 optimized value of fitness function as compared to 0.013442 for ALO. Figures 3 and 4 show the GWO response for ISE and ITAE error.

ALO response for ISE and ITAE error is shown in Figs. 5 and 6, respectively.

Table 2 Parameter of K_p , K_i , and K_d when ITAE as an error

Parameter	GWO		ALO	
	Joint 1	Joint 2	Joint 1	Joint 2
Proportional gain	85.27767	40.75586	89.86733	45.8469
Integral gain	64.41897	82.68774	95.04659	94.4587
Derivative gain	44.07892	62.05974	23.47598	38.3612
ITAE	0.004686	20.00480	0.01665	0.006525
Fitness value	0.0093997		0.013442	

Table 3 Parameter of K_p , K_i , and K_d when ISE as an error

Parameter	GWO		ALO	
	Joint 1	Joint 2	Joint 1	Joint 2
Proportional gain	45.61079	72.14704	94.91267	41.4415
Integral gain	95.06732	96.27777	98.21718	85.4008
Derivative gain	19.19369	26.67798	51.31193	43.7064
ISE	5.446×10^{-5}	1.477×10^{-5}	0.0001298	3.058×10^{-5}
Fitness value	6.8516×10^{-5}		0.0001128	

Fig. 3 ISE response of GWO

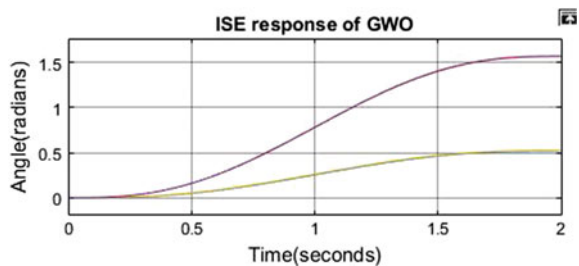


Fig. 4 ITAE response of GWO

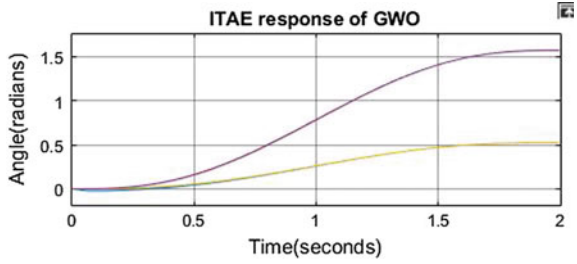


Fig. 5 ISE response of ALO

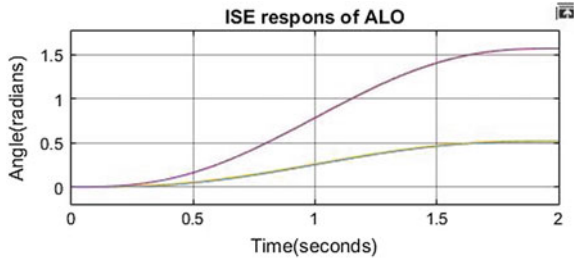
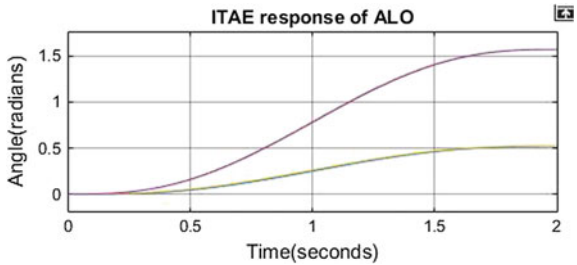


Fig. 6 ITAE response of ALO



7 Conclusion

The optimization gains and fitness function values of the two PID controllers have been compared in this paper for GWO and ALO. This result analysis provides ease in selection of proper parameter values for proper system designing, with better performance and minimum error.

It is suggested that GWO gives the least optimized values of 0.0093997 for ITAE and 6.8516e-05 for ISE as compared to ALO which gives 0.0001128 for ISE and 0.013442 for ITAE. Henceforth, GWO optimization technique is best suited for suitable designing of PID controller for a robotic manipulator.

References

1. Sharma R, Gaur P, Mittal AP (2015) Performance analysis of two-degree of freedom fractional order PID controllers for robotic manipulator with payload. *ISA Trans* 58:279–291
2. Sharma R, Rana KPS, Kumar V (2014) Performance analysis of fractional order fuzzy PID controllers applied to a robotic manipulator. *J Expert Syst Appl* 41(9):4274–4289
3. Tripathi S, Panday H, Gaur P (2013) Robust control of inverted pendulum using fuzzy logic controller. In *Proceedings of student conference on engineering and systems (SCES)*, Allahabad, India, pp 1–6
4. Sharma R, Rana KPS, Kumar V (2014) Comparative study of controller optimization techniques for a robotic manipulator. In: *Proceedings of third international conference on soft computing for problem solving, advances in intelligent systems and computing*, pp 379–393, Springer India, Berlin
5. Kim TH, Maruta I, Sugie T (2008) Robust PID controller tuning based on the constrained particle swarm optimization. *Automatica* 44(4):1104–1110
6. Kennedy J, Eberhart RC (1995) Particle swarm optimization. In *Proceedings of IEEE international conferences neural networks*, Perth, Australia, November 1995, pp 1942–1948
7. Mirjalili Seyedali, Lewis Andrew (2016) The whale optimization algorithm. *Adv Eng Softw* 95:51–67
8. Mirjalili S (2015) Ant lion optimizer. *J Adv Eng Softw* 83:80–98
9. Dorigo M, Maniezzo V, Colomi A (1996) The ant system: optimization by a colony of cooperating agents. *IEEE Trans Syst Man Cybern* 26(1):29–41
10. Mehta S, Nischal MM (2015) Ant lion optimization for optimum power generation with valve point effects. *Int J Res Appl Sci Eng Technol* 3(X):1–6
11. Mirjalili S, Mirjalili SM, Lewis A (2014) Gray wolf optimizer. *Adv Eng Softw* 69:46–61
12. Gupta E, Saxena A (2016) Grey wolf optimizer based regulator design for automatic generation control of interconnected power system. *Cogent Eng* 3(1)
13. Mirjalili S, Saremi S, Mirjalili SM, Coelho LD (2016) Multi-objective grey wolf optimizer: A novel algorithm for multi-criterion optimization. *J Expert Syst Appl* 47(1):106–119
14. Yadav AK, Gaur P, Tripathi S (2015) Design and control of an intelligent electronic throttle controlsystem. In *2015 International Conference on Energy Economics and Environment (ICEEE)*, pp 1–5
15. Kealy T, O'Dwyer A (2003) Analytical ISE calculation and optimum control system design. *Irish signals and systems conference, University of Limerick, Ireland*

A 26 W Power Supply Based on Luo Converter with Improved Power Factor and Total Harmonic Distortion



Amit Agrawal, Ashish Shrivastava, Amit Rai and K. C. Jana

Abstract A 26 W power supply is proposed in this research paper to glow an LED (light emitting diode) load. It is based on single-stage single-switch circuit, which used power factor corrected (PFC) positive Luo converter to maintain the power quality. The converter is operating in continuous conduction mode (CCM) to get constant load voltage. To stabilize the whole system, a PI (proportional integral) is designed and used to generate control signal. Theoretical verification of system stability is done with the help small signal state-space averaging technique. The simulation model of proposed power supply is performed in MATLAB sim-power toolbox. A constant output of voltage 65 V and current 0.4 A is achieved with better power quality parameters as power factor (PF) and total harmonic (THD). The quality parameters satisfy the standards of IEC 61000-3-2.

Keywords Continuous conduction mode (CCM) · Luo converter · Power factor (PF) · SSA modeling · Stability · State-space analysis · THD

1 Introduction

In the past two decades, the light emitting diode (LED) has become the best choice for researchers and industrial people because it is full of tremendous properties like long lifetime, durability, flicker-less start, high luminous efficiency, low maintenance, vibration resistant, small size, environment friendliness, effortlessly dimmable, robust, etc. [1, 2]. Also these LEDs are very much helpful in biomedical apparatus, outdoor lighting, LCD backlight, automobile industry, railway signals, aircraft lightings, traffic light, detective system, etc. [3]. Even the cost of LED is

A. Agrawal (✉)

ABES Engineering College, Ghaziabad, UP 201009, India
e-mail: amit.stm@gmail.com

A. Shrivastava

Manipal University Jaipur, Rajasthan 303007, India

A. Rai · K. C. Jana

Indian Institute of Technology (ISM), Jharkhand, Dhanbad 826004, India

© Springer Nature Singapore Pte Ltd. 2020

A. Kalam et al. (eds.), *Intelligent Computing Techniques for Smart Energy Systems*,
Lecture Notes in Electrical Engineering 607,
https://doi.org/10.1007/978-981-15-0214-9_101

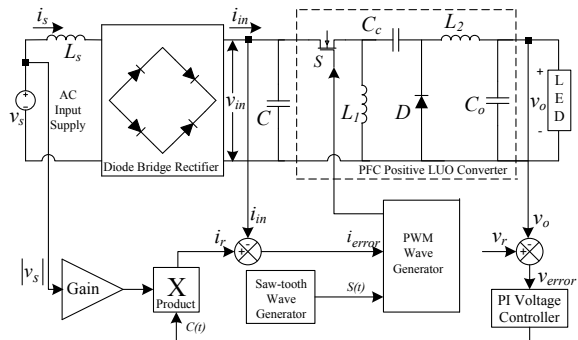
high compared to a fluorescent lamp, still it is economical because of its longer lifespan [4]. To get constant voltage, ac signal to dc signal conversion is required. The conventional circuits are able to achieve the desired output but power quality issues are still present. As per standard the power factor must be more than 0.9 [5]. The proposed power supply comes under IEC 61000-3-2 Class-C category [6]. To enhance the power quality the optimized controller and power factor correction scheme can be used [7]. As per the literature, the circuit size, cost, and complication of controller design in two-stage converter are lesser than single stage [8, 9].

In this paper, a novel power supply is proposed to get constant voltage. Further, it can be used to glow LED light. A simple controller design is used with single-stage converter to stable the whole system. The optimized values of parameters are used in PI controller to generate control signal which is responsible for duty cycle. The theoretical results of proposed model are achieved with the help of small-signal average modeling technique. The MATLAB tool is used to simulate the proposed model where the switching frequency is considered as 60 kHz to reduce the size and cost of inductor.

2 Proposed Model: A Power Factor Corrected (PFC) Power Supply Based on Luo Converter

The detail block diagram of proposed power supply is shown in Fig. 1. To get pulsating dc signal (v_{in}) from input ac mains (v_s), a DBR (diode bridge rectifier) is used. Further a PFC Luo converter is cascaded to get constant dc output (v_o) from pulsating dc input. A comparator takes output signal and reference signal to generate error signal (v_{error}). The PI controller's output is converted into reference current (i_r) and compared with input current (i_{in}) to get error current (i_{error}). This error current is further compared with saw-tooth wave signal to generate small-signal pulse width modulated (PWM) signal which controls the duty ratio (D) of n-channel MOSFET switch (S) with 60 kHz of switching frequency (f_s).

Fig. 1 Proposed power supply based on Luo converter



3 Components Selection of Power Supply

The proposed power supply is based on Luo converter running in continuous conduction mode (CCM) to run LED light. The selection of components is the key to operate converter in CCM and system stability. Few criterions are needed to consider before design the model as the component's behavior is considered as ideal and the load is considered as a pure resistor. The output capacitor (C_o) must be very high with input frequency of 60 Hz. As we have taken CCM of the converter, the allowed ripple current must not exceed above 100% of the average load current. Few standard equations are taken to calculate the parameters of the proposed model.

The duty cycle of the switch is given as

$$D = v_o / (v_{in} + v_o) \quad (1)$$

The minimum inductance value is calculated below to run the converter in continuous conduction mode (CCM) [10, 11].

$$L_{1(\text{minimum})} = L_{2(\text{minimum})} = (1 - D)v_o / 2Df_s I_o \quad (2)$$

Both the capacitor's value (C_c and C_o) is given as follows [12].

$$C_c = i_o D / f_s \Delta v_{C_c} \quad (3)$$

$$C_o = i_o / 2\omega \cdot \Delta v_{C_o} \quad (4)$$

The components are calculated from Eqs. (1) to (4) and listed in Table 1.

4 System Loop Gain Analysis

For stability analysis, the system loop gain is achieved with the help of small signal averaging technique. These converters may behave in CCM, BCM or DCM [12, 13]. It is a mathematical tool by which the complex converter systems are easily analyzed. This technique is based on averaging of state-space matrices those are achieved through Kirchhoff's current and voltage laws. The state matrices are calculated for both cases as switch-on and switch-off, mentioned below. After that average state matrices are evaluated and mentioned below.

$$A = \begin{bmatrix} 0 & 0 & (D-1)/L_1 & 0 \\ 0 & 0 & D/L_1 & -1/L_2 \\ (1-D)/C_c & -D/C_c & 0 & 0 \\ 0 & 1/C_o & 0 & -1/RC_o \end{bmatrix}; B = \begin{bmatrix} D/L_1 \\ D/L_2 \\ 0 \\ 0 \end{bmatrix} \quad (5)$$

Table 1 Parameters of proposed power supply

Parameters	Formulated value	Selected value
AC main input voltage (v_s)	–	220 V
Frequency of AC mains (ω)	–	60 Hz
Output voltage (v_o)	–	65 V
Frequency of switch (f_s)	–	55 kHz
Peak voltage on coupling capacitor (v_{Cc})	311.08 V	311.08 V
Maximum ripple on the coupling capacitor $\Delta v_{Cc} = 10\%$ of v_{Cc}	31.12 V	31.12 V
Maximum ripple on output capacitor $\Delta v_{Co} = 4\%$ of v_{Co}	2.6 V	2.6 V
Duty ratio of the switch at 270 V of input supply	0.145	–
Value of duty cycle for ac mains input of 90 V	0.338	–
Duty ratio (D)	–	0.161
Load current I_o	0.4 A	0.4 A
Inductor L_1 for CCM	7.69 mH	10 mH
Inductor L_2 for CCM	7.69 mH	10 mH
Average inductor current (I_{L1})	0.14 A	0.14 A
Average inductor current (I_{L2})	0.40 A	0.40 A
Coupling capacitor C_c	37.63 nF	50 nF
Output capacitor C_o	353.53 μ F	400 μ F
V_{OSC} (Oscillator voltage)	–	3.5 V
v_r (Reference voltage)	–	2.5 V

The small-signal model can be achieved by using equation below.

$$d\hat{x}(t)/dt = A \cdot \hat{x}(t) + B \cdot \hat{v}(t) + \{(A_1 - A_2) \cdot X + (B_1 - B_2) \cdot V\} \hat{d}(t) \quad (6)$$

Now, the value of all matrices is placed in the above equation. The final equation is solved and written as below.

$$\begin{aligned} \begin{bmatrix} d\hat{i}_{L1}(t)/dt \\ d\hat{i}_{L2}(t)/dt \\ d\hat{v}_{Cc}(t)/dt \\ d\hat{v}_{Co}(t)/dt \end{bmatrix} &= \begin{bmatrix} 0 & 0 & (D-1)/L_1 & 0 \\ 0 & 0 & D/L_1 & -1/L_2 \\ (1-D)/C_c & -D/C_c & 0 & 0 \\ 0 & 1/C_o & 0 & -1/RC_o \end{bmatrix} \begin{bmatrix} \hat{i}_{L1} \\ \hat{i}_{L2} \\ \hat{v}_{Cc} \\ \hat{v}_{Co} \end{bmatrix} \\ &+ \begin{bmatrix} D/L_1 \\ D/L_2 \\ 0 \\ 0 \end{bmatrix} \hat{v}_i(t) + \left\{ \begin{bmatrix} 0 & 0 & 1/L_1 & 0 \\ 0 & 0 & 1/L_2 & 0 \\ -1/C_c & -1/C_c & 0 & 0 \\ 0 & 0 & 0 & 0 \end{bmatrix} \begin{bmatrix} I_{L1} \\ I_{L2} \\ V_{Cc} \\ V_{Co} \end{bmatrix} + \begin{bmatrix} 1/L_1 \\ 1/L_2 \\ 0 \\ 0 \end{bmatrix} V_i \right\} \hat{d}(t) \quad (7) \end{aligned}$$

The output capacitor is attached with load in parallel. So output load voltage follows the capacitor voltage which is derived in the frequency domain as below after taking Laplace of Eq. (7).

$$\hat{v}_{Co}(s) = \frac{(RL_2 D^2(1-D) + RL_1 D(1-D)^2 + RL_1^2 C_c D s^2) \hat{V}_i(s) + ((RDL_2(1-D) + RL_1(1-D)^2 + RC_1 L_1^2 s^2)(V_{Cc} + V_{in}) - RDL_1 L_2 (I_{L1} + I_{L2}) s) \hat{d}(s)}{RL_1^2 L_2 C_c C_o s^4 + L_1^2 L_2 C_c s^3 + RL_1 (L_1 C_c + L_2 C_o (D^2 - D + 1)) s^2 + L_1 L_2 (D^2 - D + 1) s + RL_1 (1-D)^2} \quad (8)$$

The $G_{vd}(s)$ is defined for control-to-output Transfer Function (TF) as $G_{vd}(s) = \left. \hat{V}_o(s) / \hat{d}(s) \right|_{\hat{V}_{in}(s)=0}$.

$G_{vd}(s)$ is calculated with the help of components listed in Table 1 and written below.

$$G_{vd}(s) = \frac{4.7 * 10^{-7} s^2 - 1.3 * 10^{-3} s + 783.0}{3.0 * 10^{-15} s^4 + 4.9 * 10^{-14} s^3 + 5.2 * 10^{-6} s^2 + 8.6 * 10^{-5} s + 1.1} \quad (9)$$

The TF of PWM generator is defined as $G_{PWM}(s) = \left. \hat{d}(s) / \hat{V}_{error}(s) \right| = 1 / V_{osc}$

The $G(s)$ is taken as the loop gain of the system when the compensated network is not attached in the feedback path, considered as $G(s) = G_{vd}(s) * G_{PWM}(s) * v_r / v_o$

$$G(s) = \frac{7.49 * 10^{-7} s^2 - 1.95 * 10^{-3} s + 1175.01}{8.12 * 10^{-13} s^4 + 1.35 * 10^{-11} s^3 + 1.40 * 10^{-3} s^2 + 2.32 * 10^{-2} s + 297.0} \quad (10)$$

5 Model Stability Without Controller in Feedback

In the MATLAB environment, the Bode plot is drawn for this loop gain ($G(s)$) and presented by Fig. 2. From plot, the value of gain margin (GM) 19.5 and the value of phase margin (PM) 1.08° indicate the practical instability of system because to fulfill the stability criterion the PM must be higher than 45° [14].

6 Controller Design and Analysis of Stability System with Compensation Network

In this section, a control scheme is discussed which generates the control signal according to the difference between output and reference signal. It is associated with the feedback path of the model to stabilize the system.

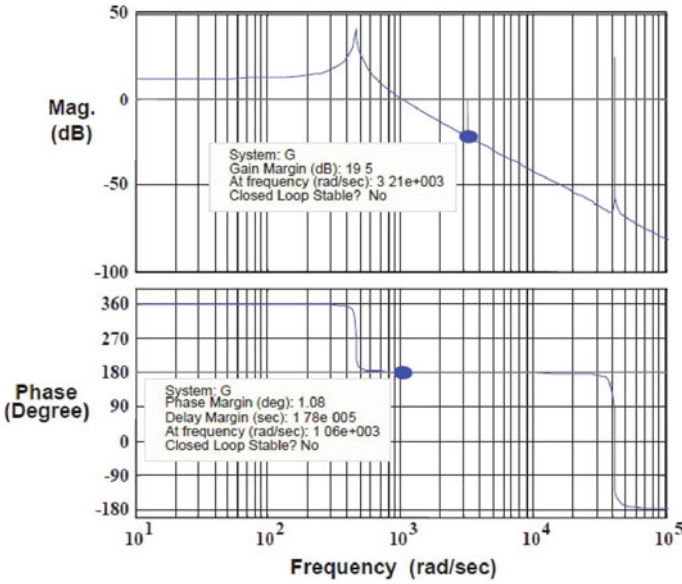


Fig. 2 Bode plot of loop gain $G(s)$

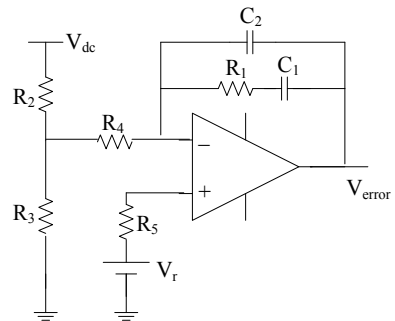
6.1 Proportional Integral (PI) Controller

The compensation network which is using as PI controller is shown by Fig. 3. The error signal is considered as $v_{error} = v_r - v_o$.

The control signal is defined below, where K_p and K_i are the gains.

$$I_c(n) = I_c(n - 1) + K_p\{v_{error}(n) - v_{error}(n - 1)\} + K_i v_{error}(n) \quad (11)$$

Fig. 3 PI controller used as compensator



6.2 Compensator's Component Design

The compensator is drawn by Fig. 3 and its transfer function is derived below.

$$C(s) = (1 + sR_1C_1) / sR_2 \cdot ((C_1 + C_2) + sR_1C_1C_2) \quad (12)$$

With the help of standard formulas, all the parameters are calculated. Those are mentioned by Eqs. (13)–(19). To achieve the mathematical values bandwidth (B.W.) is taken 20 Hz and over-voltage protection (ΔV_{ovp}) is taken 3 V [13].

$$R_2 = \Delta V_{ovp} / 30 \mu\text{A} \quad (13)$$

$$R_3 = R_2 v_r / (v_o - v_r) \quad (14)$$

$$R_1 = R_3 v_r / (V_{osc} - v_r) \quad (15)$$

$$f_o = 1 / (2\pi \sqrt{L_2 C_o}) \quad (16)$$

$$f_z = 0.75 f_o \quad (17)$$

$$C_1 = 1 / (2\pi R_1 f_z) \quad (18)$$

$$C_2 = 1 / (2\pi (R_2 || R_3) B.W.) \quad (19)$$

With help of all components, the TF of the compensated network is calculated as below.

$$C(s) = 7.60 * 10^{-3} s + 1 / (3.45 * 10^{-3} s^2 + 1.86s) \quad (20)$$

6.3 Model with Proposed Compensated Network: Stability Analysis

A compensated network is proposed and designed having transfer function ($C(s)$). The new system loop gain ($G_c(s)$) is calculated and written below.

$$G_c(s) = \frac{5.36 * 10^{-9} s^3 - 1.41 * 10^{-5} s^2 + 8.93s + 1175}{s(2.80 * 10^{-15} s^5 + 1.55 * 10^{-12} s^4 + 4.83 * 10^{-6} s^3 + 2.68 * 10^{-3} s^2 + 1.07s + 552.4)} \quad (21)$$

Figure 4 depicts 10.6 db of gain margin with 90.8° of phase margin for $G_c(s)$.

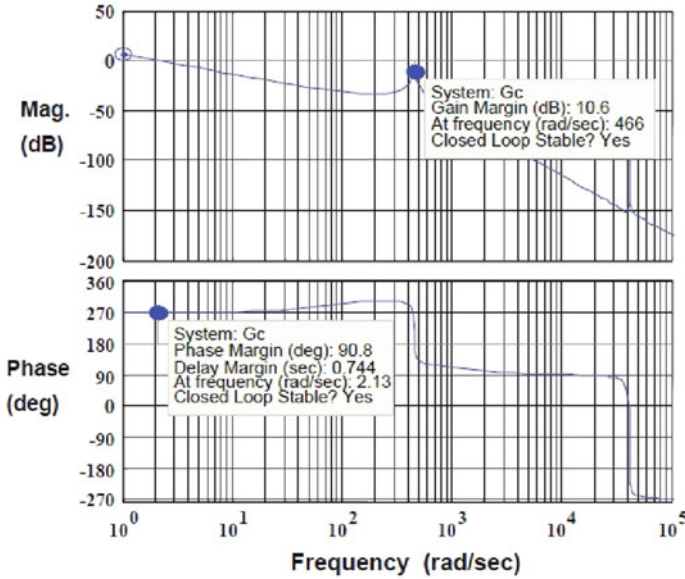


Fig. 4 Bode plot of system loop gain $G_c(s)$

7 Simulated Circuit Diagram and Analysis

The circuit is simulated in the MATLAB version-R2013a as shown by Fig. 5. As per the diagram supply from AC mains is converted into constant DC voltage with help of diode bridge rectifier and filter capacitor. Further the desired constant voltage is achieved by cascading PFC Luo converter. The converter parameters are designed in such way so it can operate in CCM. A PI controller is used in the MATLAB toolbox in place of compensation network. The repeating sequence is used as saw-tooth wave having frequency of 55 kHz. The control signal helps to generate the i_{ref} which goes into relational operator further to get PWM pulse. This pulse controls the duty ratio.

8 Results Analysis

The waveform of output voltage (V_o) and output current (I_o) are shown in Fig. 6 along with the waveforms of input ac voltage, current, and inductor current extracted at 220 V of AC mains supply. The output load voltage and power quality parameters are also extracted at AC inputs of 90–270 V. The power quality parameters like PF and THD along with output voltage and current at different input supply are listed in Table 2. The power factor is maintained at more than 0.92 and THD is less than 0.25%. It justifies the proposed controller and PFC technique used to stabilize the system and to get constant power supply with better power quality.

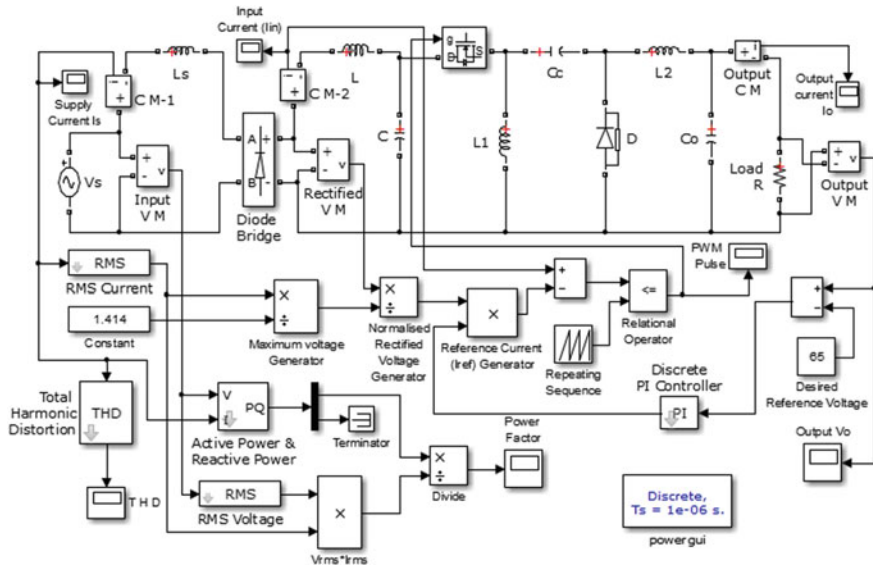


Fig. 5 Simulated circuit diagram in MATLAB

Fig. 6 The waveforms of model parameters

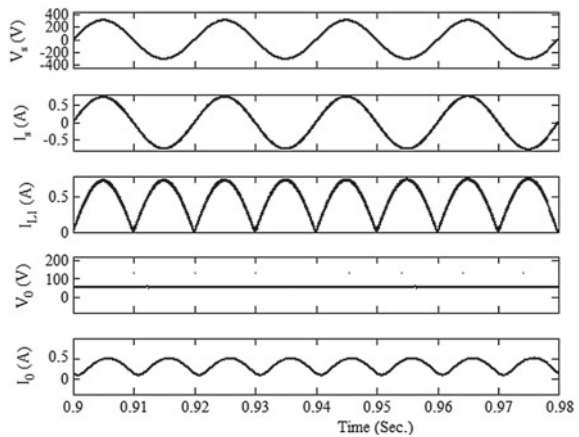


Table 2 Power quality parameters of proposed power supply based on Luo circuit

V_s (V)	I_s (A)	V_o (V)	I_o (A)	PF	THD (%)
110	0.27	64.8	0.39	0.92	0.62
150	0.18	65.2	0.40	0.93	0.56
190	0.16	65.8	0.42	0.93	0.56
220	0.14	65.3	0.45	0.96	0.42
260	0.11	66.2	0.41	0.97	0.25

9 Conclusions

In this paper, a power supply with a rating of 26 W, 65 V is proposed. It is based on Luo converter and its components are designed in such way so it can operate in CCM. With help of small-signal modeling and MATLAB, the Bode plot of system loop gain is calculated to check the stability and to justify the need of controller. The proposed circuit is simulated in the MATLAB sim-power toolbox and waveforms are extracted at universal input supply. The results show better power factor and THD with constant output voltage at all input supply. The PF and THD are under the limit of IEC 61000-3-2 Class-C equipment.

References

1. Xingming L, Jing Z (2008) An intelligent driver for light emitting diode street lighting. In: Proceedings of the world automation congress (WAC). pp 1–5
2. Simpson RS (2003) Lighting control technology and applications. Focal Press, Burlington, MA, USA
3. Chen CC, Wu CY, Wu TF (2006) LED back-light driving system for LCD panels. In: Proceedings of the IEEE applied power electronics conference and exposition. pp 381–385
4. Wu CY, Wu TF, Tsai JR, Chen YM, Chen CC (2008) Multistring LED backlight driving system for LCD panels with color sequential display and area control. *IEEE Trans Ind Electron* 55(10):3791–3800
5. Limits for Harmonic Current Emissions, International Electrotechnical Commission Standard, IEC-61000-3-2 (2004)
6. Weir B, Cathell F (2008) LED streetlight demands smart power supply. *Power Electron Technol* 34(2):34–39
7. Broeck H, Sauerländer G, Wendt M (2007) Power driver topologies and control schemes for LEDs. In: Proceedings of the IEEE APEC. pp 1319–1325
8. Agrawal A, Shrivastava A, Jana KC (2019) A universal input, single stage AC-DC LED driver for an auditorium light. *J Circuit Syst Comput* 28(4)
9. Ye Z, Greenfeld F, Liang Z (2008) A topology study of single-phase offline ac/dc converters for high brightness white LED lighting with power factor pre-regulation and brightness dimmable feature. In: Proceedings of the 34th annual conference IEEE industrial electronics. pp 1961–1967
10. Shrivastava A, Singh B (2013) Power factor-corrected DCM-based electronic ballast. *Electr Eng* 95(4):403–411
11. Gatto G, Marongiu I, Mocci A, Serpi A (2013) An improved averaged model for boost dc–dc converters. In: Proceedings of the IECON, Vienna. pp 412–417
12. Agrawal A, Shrivastava A, Jana KC (2018) Uniform model and analysis of PWM DC-DC converter for discontinuous conduction mode. *IETE J Res* 64(4):569–581
13. Erickson RW (1997) Fundamentals of power electronics, 1st edn. Chapman and Hall, New York
14. Singh B, Shrivastava A (2014) Buck converter based power supply design for low power light emitting diode lamp lighting. *IET Power Electron* 7(4):946–956

Optimal Strategic Bidding Using Intelligent Gravitational Search Algorithm for Profit Maximization of Power Suppliers in an Emerging Power Market



Satyendra Singh, Manoj Fozdar and Ajeet Kumar Singh

Abstract In the assessment of the features of strategic bidding choice issues, this paper proposes a novel procedure that optimizes strategic bidding using Intelligent Gravitational Search Algorithm (IGSA) for profit maximization of power suppliers in an emerging power market. In this paper, two approaches are suggested. One suggests using the inverse agents in the assessment procedure of GSA. It empowers improved investigation of the exploration space and avoids trapping of the solution in a local optimum result. Another is a new gravity constant control procedure to avoid repetitive calculation and enhance the speed of convergence. The suggested procedure has been tested on the IEEE 30-bus system. The experimental solutions of both result qualities in terms of profit and calculation efficiency demonstrate the efficacy and strength of IGSA to other approaches such as Shuffled Frog Leaping Algorithm (SFLA), Particle Swarm Optimization (PSO), Genetic Algorithm (GA), and Monte Carlo (MC).

Keywords Electricity market · Intelligent gravitational search algorithm · Market clearing price · Strategic bidding

1 Introduction

With the deregulation of the power industry, deregulated electricity markets have been set up in numerous nations. However, the rising power markets have an assortment of new issues, for example, oligopolistic nature of the market, bidding behavior of power

S. Singh (✉) · M. Fozdar
Malaviya National Institute of Technology Jaipur, Rajasthan, India
e-mail: satyendagur@gmail.com

M. Fozdar
e-mail: mfozdar.ee@mnit.ac.in

A. K. Singh
KIET Group of Institutions, Ghaziabad, India
e-mail: ajeetksingh@yahoo.co.in

suppliers, mishandling of market power, flexibility in demand and cost, etc. [1]. In deregulated power market, power pool has risen as a famous type of power market where the members such that the power providers and the consumers submit their bids and the operation of the arrangement is administered through an Independent System Operator (ISO) [2]. Each member of market bids with the motivation behind upgrading its profit. Ideally, in a fully competitive market, power providers should bid at, or near, their marginal production cost to amplify result. Knowing their expenses, practical limitations and their expectation of market and opponents behavior, power providers, confront the issue for developing the greatest optimal bid [3].

Various procedures dependent on Lagrangian Relaxation (LR) [4, 5] and Game theory [6–8] have been suggested. Furthermore, heuristic [9–11], and metaheuristic [12–14] methodologies have been incorporated to resolve the diverse strategic bidding issues in the literature. Joint strategies dependent on LR and stochastic dynamic programming have been presented in [4]. The strategic bidding issue is comprehended by Genetic Algorithm [9, 10]. Particle Swarm Optimization (PSO) was utilized toward comprehensive strategic bidding issue in [11]. In this methodology, traditional and disintegration-based PSO were utilized, and an important correlation between the two variations was introduced. Fuzzy adaptive configuration effort was established in PSO [12] for doing the strategic bidding issue. Fuzzy basis presentations are investigated in metaheuristic techniques to adjust the key limitations of the technique for healthier arrangement feature. Utilization of Shuffled Frog Leaping Algorithm (SFLA) in Strategic bidding issue has been investigated in [13]. In this examination, characteristics of memetic calculation and PSO are consolidated to defeat untimely combination and unfortunate arrangement quality. A bilevel advancement issue was created in [14]. A consolidated use of PSO with Simulated Annealing (SA) technique has been investigated in [15], in that work, the authors asserted that the aftereffect of this amalgam methodology was exceptionally viable.

It is concluded from the above literature that some modifications in the heuristic techniques are needed further to acquire the goal of optimal result. Accepting this as a point of worry mass associations and law of gravity are connected in Gravitational Search Algorithm (GSA) to find optimal outcome by an arrangement of agents, and the execution of the agents is controlled through their masses [16]. As per the research of literature [16, 17] GSA possesses solid search capability, and its rate of convergence is quicker than PSO and GA. The initialization of population parameter is configured randomly in GSA, and the activity approach of reinforcement agents is at first dependent on randomness [18]. Moreover, in the GSA the way of an agent is determined dependent on the total force acquired by every other agent. However, if the estimation of gravitational mass is too small, it won't just neglect to enhance the accuracy of the calculation, yet also devour a lot of calculation time [19]. Therefore, in the perspective of referenced over, this paper proposes a new strategy named optimal bidding strategy utilizing Intelligent Gravitational Search Algorithm (IGSA) for profit maximization of power suppliers in an emerging power market. To create the ordinary GSA more appropriate for bidding strategy issues, two sorts of modification are proposed in this paper:

1. The search space for the given issue is investigated more broadly by utilizing GSA after the presentation of oppositional population based learning (OBL).
2. Control the gravity coefficient to stay away from excessive precision mathematics and enhance the techniques overall search capability.

2 Problem Formulation

With the end goal to outline the proposed strategic bidding issue, it is supposed that there is one generator in each Traditional Power Supplier (TPS). In addition, there is just a single power provider at each generator transport. Each power provider cost function can be figured as follows [17, 20].

$$G_{cf,x}(D_{pg,x}) = a_x D_{pg,x} + b_x (D_{pg,x})^2 \quad (1)$$

where, a_x and b_x are coefficients of cost for the x th power supplier and $D_{pg,x}$ is the dispatch of the power generation for the x th power supplier.

It is vital to observe that all the power providers prescribe their offer and submit them to the ISO by means for a straight supply bidding model as the going with structure [17, 20].

$$B_x(D_{pg,x}) = \phi_x + \pi_x D_{pg,x} \quad x = 1, 2, \dots, TPS \quad (2)$$

where ϕ_x and π_x are bidding parameters which must be nonnegative. In the wake of getting the offers from the power providers, ISO matches the output of generation with aggregate required interest from the framework, and afterward limits the acquiring cost. It is noticed that conditions (3) to (5) ought to be fulfill the power dispatch while considering power balance limitation (4) and power imbalance requirements (5).

$$\phi_x + \pi_x D_{pg,x} = R \quad (3)$$

$$\sum_{x=1}^{TPS} D_{pg,x} = Q_f(R) \quad (4)$$

$$D_{pg,x,min} \leq D_{pg,x} \leq D_{pg,x,max} \quad (5)$$

where R is the market clearing price, $Q_f(R)$ is Forecasted load by the ISO. Suppose $Q_f(R)$ is

$$Q_f(R) = C_d - k * R \quad (6)$$

where, C_d is fixed demand and $k = 0$ is demand price elasticity. The explanation of condition (3), (4) when (5) is ignored.

$$R = \frac{C_d + \sum_{x=1}^{TPS} \frac{\phi_x}{\pi_x}}{k + \sum_{x=1}^{TPS} \frac{1}{\pi_x}} \tag{7}$$

$$D_{pg,x} = \frac{R - \phi_x}{\pi_x} \tag{8}$$

If the solution of $D_{pg,x}$ in (8) exceeds its maximum limits, $D_{pg,x}$ is set according to (5).

Optimal strategic bidding of TPS for profit maximization can be expressed as

$$\begin{aligned} & \text{Maximize} \\ & F(\phi_x, \pi_x) = R * D_{pg,x} - G_{cf,x}(D_{pg,x}) \end{aligned} \tag{9}$$

Subject to: conditions (1), (7), and (8).

In a sealed bid focused power marketplace, information about bidding data for next period is mysterious. Thus, individuals don't have data about other individuals' bided information. In any case, last period bidding data information is accessible; in light of this data, estimation of MCP is possible. Each part attempts to assess diverse individuals bidding coefficients, anyway this is troublesome. So from each part's point of view, the bidding coefficient seeks after a normal joint distribution with following probability density function (pdf). For each supplier pdf is

$$\text{pdf}(\phi_x, \pi_x) = \frac{1}{2 * 3.14 * \sigma_x^{(\phi)} \sigma_x^{(\pi)} \sqrt{1 - \rho_x^2}} \times \exp \left\{ -\frac{1}{2(1 - \rho_x^2)} \left[\left(\frac{\phi_x - \mu_x^{(\phi)}}{\sigma_x^{(\phi)}} \right)^2 + \left(\frac{\pi_x - \mu_x^{(\pi)}}{\sigma_x^{(\pi)}} \right)^2 - \frac{2\rho_x(\phi_x - \mu_x^{(\phi)})(\pi_x - \mu_x^{(\pi)})}{\sigma_x^{(\phi)} \sigma_x^{(\pi)}} \right] \right\} \tag{10}$$

where $\mu_x^{(\phi)}$, $\mu_x^{(\pi)}$, $\sigma_x^{(\phi)}$ and $\sigma_x^{(\pi)}$ are coefficients of the combined distribution, ρ_x is correlation coefficient between ϕ_x and π_x . The peripheral distributions of ϕ_x and π_x are together normal with mean values of $\mu_x^{(\phi)}$, $\mu_x^{(\pi)}$, and standard deviations $\sigma_x^{(\phi)}$ and $\sigma_x^{(\pi)}$, respectively. Rely upon last bidding hour information; these appropriations can be resolved [20]. Mutual delivery of ϕ_x and π_x is characterized through probability distribution function, through the objective task (9) subject to conditions (1), (7) and (8) is a stochastic optimization issue.

3 Intelligent GSA

In this work, two modification in original GSA [16] is proposed to obtain better optimal solution of the problem mentioned in aforementioned section. Following are the modifications proposed.

3.1 Opposition Phenomenon in GSA

Oppositional population based learning phenomenon has been introduced by [18]. In that work, the authors have thought about the existing and conflicting specialists to improve estimation of existing operator outcome. It is presumed that an opposing operator gives healthier ideal arrangements contrasted with that of random specialist arrangements. The opposing operator’s positions ($o\alpha_i$) are totally characterized by segments of α_i .

$$o\alpha_i = [o\alpha_i^1, \dots, o\alpha_i^d, \dots, o\alpha_i^n] \tag{11}$$

where $o\alpha_i^d = L_i^d + U_i^d - \alpha_i^d$ with $o\alpha_i^d \in [L_i^d, U_i^d]$ is the location of i^{th} conflicting agent $o\alpha_i$ in the d^{th} dimension of oppositional populace.

Now the best result of condition (9) is measured as fitness task (fit_i). On the IGSA beginning an iterative procedure, a mutual populace of is created through all the limitation is fulfilled. Choice methodologies are utilized to choose the N figure of fittest operators from the combined populace arrangement of $\{\alpha, o\alpha\}$ produced existing population α .

$$\alpha_i(z) = \begin{cases} o\alpha_i(z) & \text{if } fit(o\alpha_i(z)) > fit(\alpha_i(z)) \\ \alpha_i(z) & \text{otherwise} \end{cases} \tag{12}$$

3.2 Update Mode of Gravity Constant

In the ordinary GSA, gravity constant reduce with the expansion of the quantity of iteration. In the perspective of this, IGSA refresh the gravity constant [19] as indicated by

$$G(z) = G \times \left(1 - \frac{iter}{Total \ iter}\right) + \frac{iter}{Total \ iter} \tag{13}$$

The explanation methodology as a flowchart is specified in Fig. 1.

4 Results and Discussion

The proposed IGSA has been tested to determine profit maximization of competitive power suppliers in IEEE 30-bus system and its performance is compared with traditional called Monte Carlo (MC) [20] and well as some heuristic and metaheuristics algorithms viz. binary coded GA [10], PSO [11] and SFLA [13], method. The simulations were performed in MATLAB 2014a on a 3.20 GHz, Core i5, 4GB RAM PC. Data of generator cost of the system has been taken from [20]. The tuning parameters of the proposed IGSA algorithm for profit maximization of power suppliers is taken

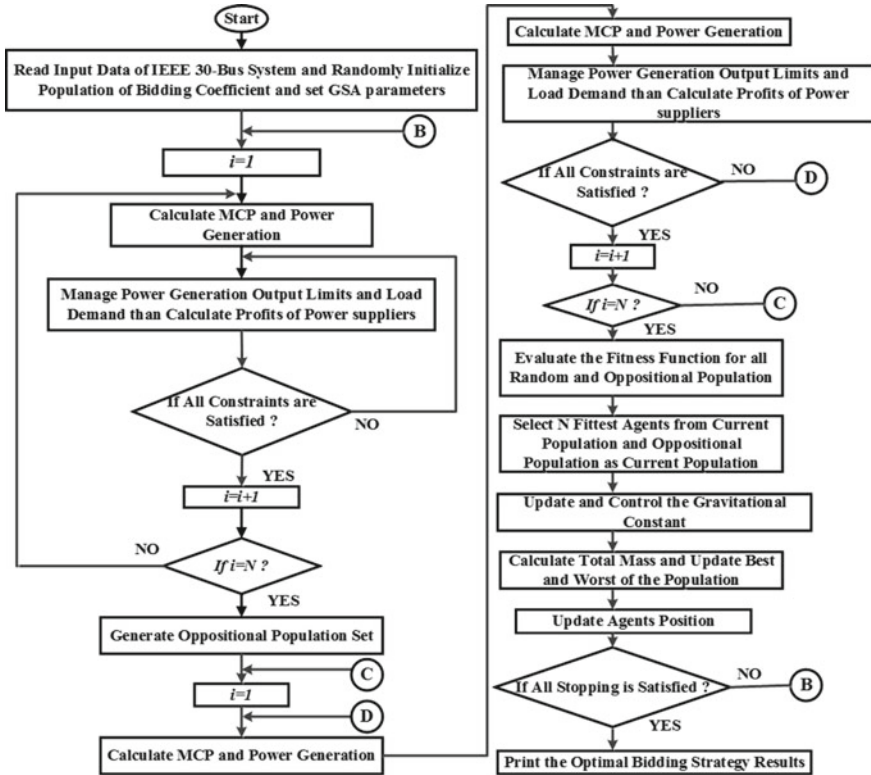


Fig. 1 Flowchart for IGSA

from [16]. The forecasted demand on the period of the bidding is 500 MW as the value of k is taken as 0. The interdependency between bidding coefficients ϕ_x and π_x facilitates to keep one coefficient fixed and trace the other using an optimization approach [20]. In this paper, the value ϕ_x has been kept fixed and their value is presented in Table 1. The best values of π_x for diverse generators using suggested IGSA, SFLA, PSO, GA and MC are given in Table 1.

By optimal tuning of IGSA parameters for fixed number of trials, the optimal values of bidding coefficients obtained using the proposed IGSA is listed in Table 1. This Table also shows the bidding coefficients obtained using other methods like SFLA, PSO, GA, and MC. Using optimal bidding factors obtained using suggested IGSA method in Table 1, the optimal bidding results for suppliers in terms of individual power output, market clearing price (MCP), individual and overall profits. These results are presented in Table 4 and it deduced that the results obtained using proposed IGSA method is far better than those obtained using other literature methods like SFLA, PSO, GA, and MC. In Table 2, it is cleared that the overall profit obtained using IGSA method is \$ 491.47, \$ 1685.4, \$ 1781.74 and \$ 2178.97 more than those obtained using SFLA, PSO, GA, and MC respectively. Moreover, the

Table 1 Optimal bidding coefficients for suppliers

Suppliers	Bidding coefficients limits					
	ϕ_x	π_x				
		IGSA	SFLA [13]	PSO [11]	GA [10]	MC [20]
1	2	0.035667	0.021004	0.001092	0.001045	0.15800
2	1.75	0.104615	0.090472	0.050953	0.048786	0.04745
3	1	0.577099	0.263450	0.181976	0.174234	0.13099
4	3.25	0.074792	0.054320	0.024283	0.023250	0.02458
5	3	0.217273	0.108594	0.072791	0.069694	0.05614
6	3	0.217273	0.108594	0.072791	0.069694	0.05614

Table 2 Optimal bidding results for suppliers

Suppliers	IGSA		SFLA [13]		PSO [11]		GA [10]		MC [20]	
	D_{pg} (MW)	Profit (\$)	D_{pg} (MW)	Profit (\$)	D_{pg} (MW)	Profit (\$)	D_{pg} (MW)	Profit (\$)	D_{pg} (MW)	Profit (\$)
1	160	1252.7	160	1097.16	160	772.41	160	741.45	160	557
2	101	698.3	96.76	581.93	100.83	340.10	101.2	321.32	91.3	249
3	34.42	250.5	29.73	196.19	32.35	125.06	32.68	119.33	38.8	103
4	100	634.5	100	537.32	100	280.36	100	261.01	100	200
5	52.27	320	56.75	285.94	53.40	136.32	53	125.56	54.90	94
6	52.27	320	56.75	285.94	53.40	136.32	53	125.56	54.90	94
$\sum Profit$		3475.97		2984.50		1790.57		1694.23		1297
MCP		10.43		9.45		6.88		6.69		6.08
$\sum (D_{pg})$		500		499.99		499.99		499.99		499.99

individual profits obtained using IGSA is better than other methods. This profit is obtained using MCP and IGSA has better MCP. Other than this, the error among total generated power and load is zero for IGSA method and thus shows the robustness of the proposed method.

The cause of receiving excellence results using IGSA method is that in IGSA, population parameter is configured randomly and the activity approach of reinforcement agents is at first dependent on randomness. If the random guess is not far away from the optimal result, can solution in a quick convergence. Due to these reasons, the convergence features for IGSA technique is fast during the initial period and spreads to the improved best result with the lapse of time, thus not stuck in local minima.

5 Conclusion

In this paper, an intelligent gravitational search algorithm is suggested to solve the strategic bidding issue for profit maximization of power suppliers. Two enhancements are suggested in this paper, one is OBL, and another is a new approach to update gravity constant. To validate the effectiveness and efficacy of the suggested procedure, the IGSA has been tested on the IEEE 30-bus system. The experimental outcomes show that the IGSA outperforms the other reported techniques in terms of result quality and profit, and reduce process time-consumption. This is because the deployment of oppositional operators in the assessment technique of GSA enables improved examination of the search space. This circumvents trapping of the exploration of the GSA algorithm in the local optima. Another is updating gravity constant control methodology to maintain a strategic distance from the inadequate precision calculation and enhance the calculation's wide-reaching search capability.

References

1. Bhattacharya K, Bollen MH, Daalder, J.E.: Operation of restructured power systems. Springer Science & Business Media (2012)
2. Rajaraman R, Alvarado F (2003) Optimal bidding strategy in electricity markets under uncertain energy and reserve prices. PSERC Publication pp 03–05
3. David AK (1993) Competitive bidding in electricity supply. In: IEE proceedings C-Generation, transmission and distribution, vol 140, pp 421–426. IET
4. Ni E, Luh PB, Rourke S (2004) Optimal integrated generation bidding and scheduling with risk management under a deregulated power market. *IEEE Trans Power Syst* 19(1):600–609
5. Steeger G, Rebennack S (2017) Dynamic convexification within nested benders decomposition using lagrangian relaxation: an application to the strategic bidding problem. *Eur J Oper Res* 257(2):669–686
6. Ferrero R, Rivera J, Shahidehpour S (1998) Application of games with incomplete information for pricing electricity in deregulated power pools. *IEEE Trans Power Syst* 13(1):184–189
7. Park JB, Kim BH, Kim JH, Jung MH, Park JK (2001) A continuous strategy game for power transactions analysis in competitive electricity markets. *IEEE Trans Power Syst* 16(4):847–855
8. Lai M, Tong X, Yang H, Bing P (2009) Dynamic bidding analysis in power market based on the supply function. *Comput Math Appl* 58(1):25–38
9. Wen F, David A (2001) Strategic bidding for electricity supply in a day-ahead energy market. *Electr Power Syst Res* 59(3):197–206
10. Azadeh A, Ghaderi SF, Nokhandan BP, Sheikhalishahi M (2012) A new genetic algorithm approach for optimizing bidding strategy viewpoint of profit maximization of a generation company. *Expert Syst Appl* 39(1):1565–1574
11. Yucekaya AD, Valenzuela J, Dozier G (2009) Strategic bidding in electricity markets using particle swarm optimization. *Electr Power Syst Res* 79(2):335–345
12. Bajpai P, Singh S (2007) Fuzzy adaptive particle swarm optimization for bidding strategy in uniform price spot market. *IEEE Trans Power Syst* 22(4):2152–2160
13. Kumar JV, Kumar DV (2014) Generation bidding strategy in a pool based electricity market using shuffled frog leaping algorithm. *Appl Soft Comput* 21:407–414
14. Shivaie M, Ameli MT (2015) An environmental/techno-economic approach for bidding strategy in security-constrained electricity markets by a bi-level harmony search algorithm. *Renew Energy* 83:881–896

15. Soleymani S (2011) Bidding strategy of generation companies using pso combined with sa method in the pay as bid markets. *Int J Electr Power Energy Syst* 33(7):1272–1278
16. Rashedi E, Nezamabadi-Pour H, Saryazdi S (2009) Gsa: a gravitational search algorithm. *Inf Sci* 179(13):2232–2248
17. Singh S, Fozdar M (2017) Generation bidding strategy in a pool-based electricity market using oppositional gravitational search algorithm. In: 2017 14th IEEE India council international conference (INDICON). IEEE, pp 1–6
18. Tizhoosh HR (2005) Opposition-based learning: a new scheme for machine intelligence. In: 2005 and international conference on intelligent agents, web technologies and internet commerce, international conference on computational intelligence for modelling, control and automation, vol 1. IEEE, pp 695–701
19. Sun Y, Tang Z, Lu J, Du P (2013) Optimal multilevel thresholding using improved gravitational search algorithm for image segmentation. In: Proceedings 2013 international conference on mechatronic sciences, electric engineering and computer (MEC). IEEE, pp 1487–1490
20. Wen F, David AK (2001) Optimal bidding strategies and modeling of imperfect information among competitive generators. *IEEE Trans Power Syst* 16(1):15–21

Synchrophasor Measurements Assisted Naïve Bayes Classification Based Real-Time Transient Stability Prediction of Power System



Divya Rishi Shrivastava, Shahbaz Ahmed Siddiqui and Kusum Verma

Abstract Synchrophasor measurements assisted real-time wide area monitoring and control of power system is a challenging task. Transient stability status of a power system following a disturbance is an important aspect of wide-area monitoring. This paper presents methodology of PMU-assisted Naïve Bayes classification to predict transient stability state of power system following a disturbance. The optimum PMU placement is obtained using Integer Linear Programming (ILP). The input given to the classifier is Frequency records prior to fault through first six cycle consecutive data obtained from optimally placed PMU following a large disturbance and output is the stability status of the power system. The proposed methodology is tested on New England IEEE 39-bus test system implemented on DiGSILENT Power Factory and Python. The results obtained for unobserved operating conditions shows the proposed methodology predicts the real-time stability status of the system and with less computational effort.

Keywords Power system stability · PMU · Classification algorithms

1 Introduction

Power Systems today are functioning with constricted security boundaries. This drives them towards large wide-area disturbances. Regardless of available efforts on field operation and planning, any disturbance may lead to grid failure [1, 2]. Further down such scenarios response-based control actions are required based on location and nature of the disturbance. It becomes commanding to establish firm and precise methodology to estimate transient instability by using sufficient data to approximate the severity of disruption within few cycles after the onset of disturbance. Then after emergency remedial actions may be implemented within sufficient time to make

D. R. Shrivastava (✉) · S. A. Siddiqui
Manipal University Jaipur, Jaipur 303007, India
e-mail: divyarishi.shrivastava@jaipur.manipal.edu

K. Verma
MNIT Jaipur, Jaipur 302017, India

© Springer Nature Singapore Pte Ltd. 2020
A. Kalam et al. (eds.), *Intelligent Computing Techniques for Smart Energy Systems*,
Lecture Notes in Electrical Engineering 607,
https://doi.org/10.1007/978-981-15-0214-9_103

majority of the system stable [3]. The first step implied for wide-area monitoring is that it should be completely observable under contingency conditions. PMUs are the measurement devices that gives time-stamped global positioning system synchronized real time status of power system. These devices gives voltage magnitude, voltage phasor angle, current, frequency, and rate of change of frequency [4]. It becomes important to have optimal placement of PMUs at significant locations so as to have real-time monitoring of power system state [5–7]. Real-time transient stability analysis involves using the available PMU data to estimate the instability status following a disturbance. This data carries sufficient information regarding status of power system in response to a probable disturbance. Hence, it becomes most promising to have synchrophasor measurement assisted real-time monitoring in power grid [8].

Various methods are available in the literature to forecast the transient stability state. In [9–12], PMU measurements assisted ANN-based methods by taking different input features are presented for predicting stability of the power system. The Support Vector Machine (SVM) and Decision Tree (DT) based methods are also applied to accurately predict the status of the power system [2, 13, 14]. These methods can predict the transient stability of the power system in real-time frame. However, it is equally important for the methods available in literature such that how fast the status of transient stability is predicted.

In this paper, a methodology is proposed to predict status of power system transient stability representing PMU-assisted classification method. The synchrophasor measurement devices at key locations in power system give frequency data of all the installed locations. Frequency data prior to fault through first six-cycle consecutive data is used for all predictions. This data is then used to train naïve Bayes classifier and is then used to predict the transient instability status of unobserved system state. The available prediction can then be used to implement control actions to avoid system collapse. A comparative result with simple perceptron classifier is also made. The presented methodology is tested on New England IEEE 39 Bus test system implemented on DIGSILENT Power Factory and Python. The result shows the effectiveness of proposed methodology.

2 Naïve Bayes Classifier

The Naïve Bayes classifier is a probabilistic classifier that computes the probabilities of each predictive trait of the data fit into each class in order to make prediction of probability distribution over all classes [15]. In this classifier, the “class” variable C (which can be predicted) is the root and the “attribute” variables X_i are the leaves. Parameter estimation is done by the method of maximum likelihood. Let there be m classes: C_1, \dots, C_m and observed attribute values $X : x_1, \dots, x_n$. The classifier predicts X belongs to Class C_i if

$$P(C_i|X) > P(C_j|X) \text{ for } 1 \leq j \leq m, j \neq i \quad (1)$$

where each class probability is given by

$$P(C_m|x_1, \dots, x_n) = \alpha P(C_m) \prod_i P(x_i|C_m) \tag{2}$$

where α is scaling factor dependent only on x_1, \dots, x_n ,

And is given by

$$\alpha = \frac{1}{P(X)} = \frac{1}{\sum_m P(C_m)P(X|C_m)} \tag{3}$$

The classifier combines the above model with a decision rule called maximum a posteriori or MAP decision rule. After the model has been trained, it can be implemented to classify new data for which the class variable C is unobserved. Classifier learning can handle noisy data as well and can give probabilistic forecasts when appropriate [15, 16].

3 Proposed Methodology

This paper presents, a methodology that predicts transient stability status within a few cycles of a disturbance in real time. The proposed methodology is shown in Fig. 1.

The algorithmic steps for the proposed methodology are presented in the subsection.

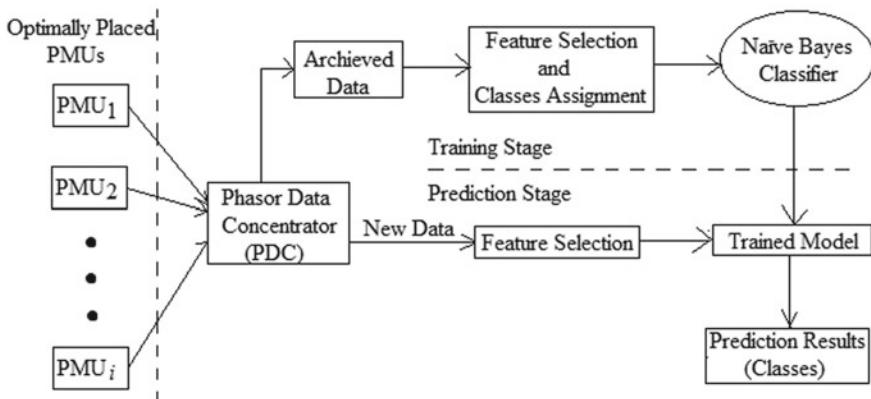


Fig. 1 Proposed methodology

3.1 Optimal PMU Placement Formulation

Optimum PMU location identification is carried out so as to have a complete power system observability under disturbances. Here, Integer Linear Programming (ILP) [5–7] a graph-theoretic technique is applied to achieve desired objective. Measurements done at installed locations are called direct measurements else are referred as pseudo measurements. In the algorithm, the placement variable assumes value “1” for a bus i as well as for if bus i is associated to bus j , else assumes “0”.

3.2 Data Generation

The purpose is to have an archived database of power system. Here database is created for large set of operating conditions with disturbances. The disturbance considered are 3 phase faults at dissimilar locations with different operating conditions as

1. System Load is randomly varied from 90 to 110% of the baseload with each load is individually randomly varied.
2. 3 phase fault is considered at dissimilar locations and for respective loading conditions
3. The time-domain simulation is carried out for respective operating condition along with disturbance.
4. Frequency data prior to fault through consecutive data before and after fault clearing is recorded.
5. The database is separated into training and testing set.

3.3 Feature Selection and Target Assignment

In this paper, frequency data after fault clearing is considered as input features. This frequency from optimally installed PMU in the power system is used as an input attribute to the classifier. The initial variations in frequency data after fault clearance are signatures of stable or unstable system and hence carries information about the transient state. The status of the system in terms of transient stability or instability can be taken by analyzing if at least one generator goes out of step. Under these conditions local frequency of buses will, therefore, reflect the status of the system. Target (classes) is transient stability status of the system with “0” as stable and “1” as unstable.

3.4 Training, Testing and New Data

Data generated with 3 phase faults at different locations for a large set of operating conditions are used to train the classifier. These large set of operating conditions were created with 90–110% load variation of the base load in steps of 1% change. Also, each individual load in the system were randomly varied. The installed PMU at optimal locations is reading the time-stamped frequency for each operating condition through faulted locations. The database generated is then divided into training dataset and testing dataset. To check how the trained classifier performs, new frequency dataset is then created and given to trained model to have monitoring of the test system.

3.5 Proposed Synchrophasor Measurement Assisted Naïve Bayes Classifier

In this paper, PMU-NB Classifier based approach is presented to predict the transient stability status of the power system in real-time. By predicting the transient stability status of the system, remedial actions can be implemented to secure the system the maximum. The optimally allocated PMUs streams the time-stamped frequency data which is used as input to the classifier. The projected approach is presented in Fig. 1.

4 Simulation and Results

The methodology is verified on New England 39 Bus test system [17], which contains 10 generators and 34 transmissions with 12 transformers. All the dynamic simulations are carried out on DIgSILENT Power Factory [18] and classifier was implemented on Python [19].

4.1 Optimal PMU Placement

The optimum PMU placement was carried out and the available results are depicted in Table 1. A total of 15 PMUs are installed in the test system in order to have complete

Table 1 Optimal PMU placement result

Test system	Optimum no. of PMU	Optimal locations
New England 39 bus system	15	3, 8, 16, 24, 26, 28, 30, 31, 32, 33, 34, 35, 36, 37, 38

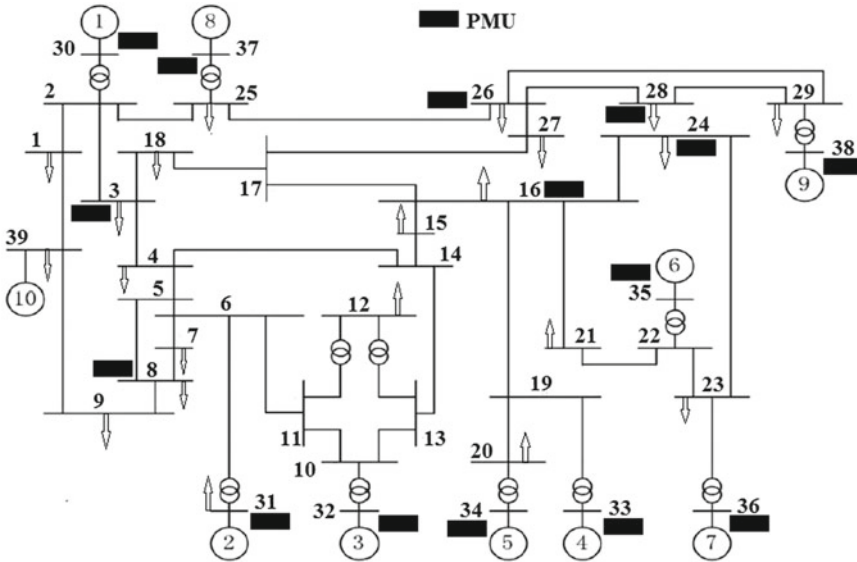


Fig. 2 Optimal PMU positions for New England IEEE 39 bus system

system observability under contingency conditions. The considered contingency in this paper is three-phase faults with line outage clearance. The bus at which PMUs are installed are also shown in Fig. 2.

4.2 PMU-Naïve Bayes Based Real-Time Transient Stability Prediction

The synchrophasor measurements from PMU are created in the form of archived data to be used for offline training of Naïve Bayes classifier. The classifier is then tested for effectiveness with data streamed in from PMUs and results are obtained. The system under study is New England IEEE 39 Bus System with different operational conditions with single line outages and random load variations. In this paper, these synchrophasor measurements created are with 90–110% load variation of the base case in steps of 1% change. The generated data is then used for training and testing process. Total of 1000 operating conditions are generated, 600 are used for training and 400 used for testing. The classifier is then subjected to test for unknown data so as to evaluate its performance. For all conditions, three-phase fault is applied at 0 s and the FCT is set between 6 cycles to 12 cycles. The frequency of observed buses are observed and recorded ranging from FCT – 18 to FCT + 6 cycles. It can also be said that first 18 cycle frequency data from and 6 cycles prior to fault initiation is recorded from optimally installed PMUs. This range is so selected so as to ensure

Table 2 Performance evaluation of classifier for new data

Case no.	Loading (% of base case)	Stability status/predicted ^a	Testing time
1002	104 (Line 01–02 removed)	0/0	0.000409
1003	104 (Line 02–25 removed)	1/1	0.000362
1004	105 (Line 23–24 removed)	1/1	0.000290
1005	105 (Line 09–39 removed)	0/0	0.000262
1006	106 (Line 05–06 removed)	1/1	0.000262

^aStable: 0 and Unstable: 1

the classifier is learning all three phases as: healthy (pre-fault), during fault and after fault clearing. The bus frequency values are also observed. Each case is assigned a class of stable (0) and unstable (1) based on bus frequency values at the end of simulation. All the simulation for data generation is carried out in DIGSILENT [18] and classifier is implemented in Python [19].

For testing performance evaluation, the stability status of the system for new bus frequency 6-cycle post-fault data set is also predicted and shown in Table 2. The results show the excellent performance of the classifier.

5 Conclusion

The timely detection of power system instability is a significant step undertaken to ensure implementation of emergency remedial actions. The paper proposes a new methodology to predict the real-time power system instability. The proposed methodology accurately predicts the status of power system which can contribute to implementing control actions. The important aspect of proposed methodology is it has been trained with pre-fault, during fault, and post-fault consecutive frequency synchrophasor data from optimally placed PMUs. This enables the methodology to forecast the status of power system for new data accurately. The proposed PMU-NB Classifier methodology shows excellent performance in predicting the status of the power system after disturbance and its suitability for real-time predictions.

References

1. Begovic M, Novosel D, Karlsson D, Henville C, Michel G (2005) Wide-area protection and emergency control. *Proc IEEE* 93(5):876–891
2. Xu Y, Dong ZY, Meng K, Zhang R, Wong KP (2011) Real-time transient stability assessment model using extreme learning machine. *IET Gener Transm Distrib* 5(3):314–322
3. Adamiak MG, Apostolov AP, Begovic MM, Henville CF, Martin KE, Michel GL, Phadke AG, Thorp JS (2006) Wide area protection—technology and infrastructures. *IEEE Trans Power Delivery* 21(2):601–609

4. Phadke AG (1993) Synchronized phasor measurements in power systems. *IEEE Comput Appl Power* 6(2):10–15
5. Gou B (2008) Optimal placement of PMUs by integer linear programming. *IEEE Trans Power Syst* 23(3):1525–1526
6. Gou B (2008) Generalized integer linear programming formulation for optimal PMU Placement. *IEEE Trans Power Syst* 23(3):1099–1104
7. Shrivastava DR, Siddiqui SA, Verma K (2017) Optimal PMU placement for coordinated observability of power system under contingencies. In: *IEEE international proceedings on circuits and systems*. IEEE, Trivandrum, pp 334–339
8. Gomez O, Rios MA (2015) Real time identification of coherent groups for controlled islanding based on graph theory. *IET Gener Trans Distrib* 9(8):748–758
9. Hashiesh F, Mostafa HE, Khatib A, Helal I, Mansour MM (2012) An intelligent wide area synchrophasor based system for predicting and mitigating transient instabilities. *IEEE Trans Smart Grid* 3(2):645–652
10. Lin CW, Su MC, Tsay SS, Wang YJ (1999) Application of a novel fuzzy neural network to real-time transient stability swing prediction based on synchronized phasor measurements. *IEEE Trans Power Syst* 14:685–692
11. Siddiqui SA, Verma K, Niazi KR, Fozdar M (2015) Real-time identification of generator coherent groups through synchrophasor measurements and ANN. In: *IEEE INDICON India conference proceedings*. IEEE, New Delhi, pp 1–5
12. Siddiqui SA, Verma K, Niazi KR (2018) Real-time monitoring of post-fault scenario for determining generator coherency and transient stability through ANN. *IEEE Trans Ind Appl* 54(1):685–692
13. Gomez FR, Rajapakse AD, Annakkage UD, Fernando IT (2011) Support vector machine-based algorithm for post-fault transient stability status prediction using synchronized measurements. *IEEE Trans Power Syst* 26(3):1474–1483
14. Rovnyak S, Kresinger S, Thorp J, Brown D (1994) Decision trees for real-time transient stability prediction. *IEEE Trans Power Syst* 9(3):1417–1426
15. Russell S, Norvig P (2003) *Artificial intelligence a modern approach*, 2nd edn. Prentice Hall Series in Artificial Intelligence, Pearson New Jersey
16. Rennie JDM, Shih L, Teevan J, Karger DR (2003) Tackling the poor assumptions of Naïve Bayes text classifiers. In: *20th International Proceedings on Machine Learning*, Washington DC
17. User manual, DIGSILENT Power Factory (2017)
18. <https://www.digsilent.de/en/>
19. <https://www.python.org/>

Device Modeling and Characteristics of Solution Processed Perovskite Solar Cell at Ambient Conditions



Anupam Agrawal, Shahbaz Ahmed Siddiqui, Amit Soni
and Ganesh D. Sharma

Abstract The power conversion efficiency (PCE) of perovskite solar cell (PSC) reached 22.1% at lab scale which is comparable with first and second-generation solar cells. This has attracted a lot of attention toward this alternative solar cell that can be manufactured with low-cost materials, easy manufacturing method, and less toxic material than traditional solar cells. In lab scale, PSCs are prepared and characterized in nitrogen-filled chamber due to stability issues (sensitive to moisture and heat). For large-scale production, it is not possible to make nitrogen-filled production units. Therefore, manufacturing at nitrogen-filled chamber of PSC is a major barrier for large-scale production. So, this is an attempt to prepare and characterize PSC at ambient conditions. Although PSCs are sensitive to moisture and heat.

Keywords Perovskite solar cell · Spin coating · Device fabrication

1 Introduction

Over 80% of the energy in the world is derived from fossil fuels [1], which produce carbon dioxide. With the present trend in consumption of electricity, it is expected that the demand for energy will be doubled and that of electricity will be quadrupled [2]. This future challenge is combined with the fast depleting conventional fuel-based

A. Agrawal (✉) · A. Soni
Department of Electrical Engineering, Manipal University Jaipur, Jaipur, Rajasthan, India
e-mail: anupamagrawal123@gmail.com

A. Soni
e-mail: amit.soni@jaipur.manipal.edu

S. A. Siddiqui
Department of Mechatronics Engineering, Manipal University Jaipur, Jaipur, Rajasthan, India
e-mail: shahbazahmed.siddiqui@jaipur.manipal.edu

G. D. Sharma
Department of Physics, LNM Institute of Information Technology, Jamdoli, Jaipur, Rajasthan, India
e-mail: gdsharma273@gmail.com

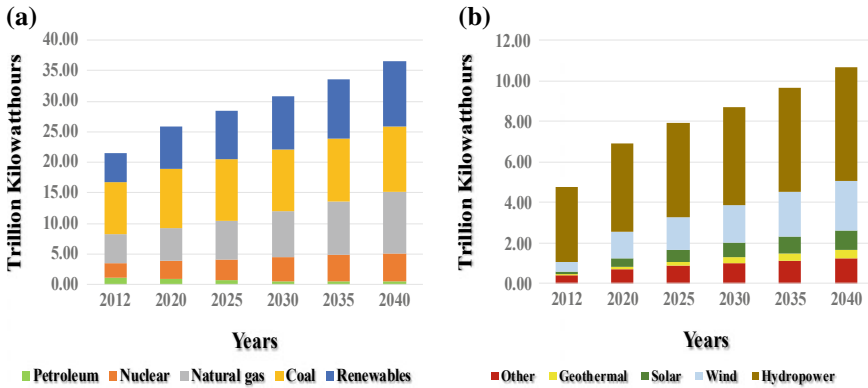


Fig. 1 a Projected overall generation of electricity across the world by all fuels including renewable sources (2012–2040) [3], b Projected overall generation of electricity across the world by all renewable sources (2012–2040) [3]

energy sources and the risk of environmental change. Therefore, it has motivated the advancement of non-conventional energy technologies. Of the possible renewable energies (i.e., solar, wind, biomass, tidal, and geothermal energy), solar energy is a promising alternative source of energy for our energy-starved planet. US Energy Information Administration provides the scenario of global net electricity generation by all fuels and renewable fuels from year 2012–2040 in International Energy Outlook 2016 as shown in Fig. 1a and b, respectively [3].

Photovoltaic (PV) cells used for electricity generation must show certain qualities such as minimal cost of raw materials, easy manufacturing process, high efficiency, simple installation of PV panel, and long life [4]. Unfortunately, there is no such PV-cell is available that can meet all the above necessities.

From last few years, researchers have focused on the improvement of cost-effective PV and feasible non-silicon PV-cells technologies. The third-generation PV cells are emerged as the most promising alternative of silicon-based PV cell. Dye-sensitized solar cells (DSSCs), quantum dots, conjugated polymers, organic solar cells (OSCs), and perovskites solar cells (PSCs) fall under third-generation PV cells. Perovskite-based PV cells are still an emerging technology. However, the diverse qualities of PSC such as high absorption coefficient, long carrier diffusion length, tunable band-gap, and gradual improvement in efficiency within last few years, makes it an exceptionally fascinating technology [5, 6].

In a very short period, the device power conversion efficiencies (PCEs) have rapidly increased more than six times from 3.8% [7] to exceed 21% [8]. To summarize the chronological developments of PSCs [9–14] and the key landmarks in the developments are represented in Fig. 2. In this paper, we demonstrate the fabrication of PSC (FTO/TiO₂/CH₃NH₃PbI₃/spiro-OMeTAD/Al) at ambient conditions. It also includes a detailed description of materials used, preparation and methodology

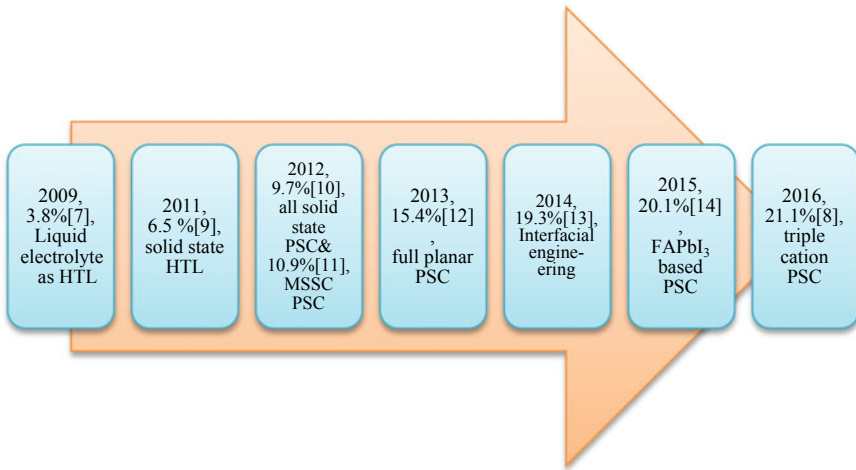


Fig. 2 The chronological developments of PSCs

of different layers, current-voltage characteristics, and ultraviolet-visible spectrum analysis.

2 Methodology

Our work focuses on third-generation solar cell which will work on an enabling and realization of PSCs through the development of inorganic–organic materials. It is based on a multidisciplinary approach where device physics, organic and inorganic chemistry, material science, and experimental setup are combined synergistically.

2.1 Materials

Titanium dioxide which is used as electron transport layer was brought from Sigma Aldrich. For the preparation of mesoporous (mp) TiO₂ paste, acetylacetone and Triton X-100 both from Merck were purchased. Methylammonium thiodyplumbate(II) precursor solution 40 wt% in DMF used as active layer was purchased from Sigma Aldrich. Then hole transport layer, i.e., spiro-OMeTAD, 3–4% in H₂O, high conductivity grade was taken from Sigma Aldrich. A solution of spiro-OMeTAD is prepared by mixing with chlorobenzene from Merck, 4-tert-butylpyridine, Li-TFSI, and acetonitrile were purchased from Sigma Aldrich. Finally, Aluminum granule of Alfa company, high purity was used as top electrode.

2.2 Preparation of Layers

2.2.1 Electron Transport Layer

For the mp-TiO₂ layer, in 100 mg of TiO₂ powder 0.5 mL of ultrapure water was mixed after that 10.0 μL of acetylacetone and 5 μL of Triton X-100 were dropped and mixed for 30 min. Then, the solution was left in vacuum-filled desiccator for 12 h to suppress the formation of bubbles in the solution.

2.2.2 Active Layer

Heat the 60 μl of CH₃NH₃PbI₃ solution for at least 2 h at 70 °C to allow for complete re-dissolution of solutes. Keep the CH₃NH₃PbI₃ solution at room temperature to cool down before deposition.

2.2.3 Hole Transport Layer

Initially, 36.1 mg powder of spiro-OMeTAD in 0.5 mL of chlorobenzene was mixed with a solution of 14.4 μL of 4-tert-butylpyridine in 260 mg of Li-TFSI and 0.5 mL of acetonitrile. Then resultant solution was left for 12 h in vacuum-filled desiccator.

2.3 Device Fabrication

First, Fluorine doped tin oxide (FTO) conductive substrates were put in an ultrasonic bath for cleaning with double distilled water at 50°C for 5 min then with acetone and ethanol for 5 min each at 0 °C. Finally, FTO conductive substrates dipped in DI water and dried with hot air. Second, the obtained mp-TiO₂ paste was coated on the FTO substrate by spin coater at 5000 rpm for 30 s and the substrate is placed on the hot plate at 100°C for 10 min. Third, again place the substrate into spin coater, dispense 30–50 μl CH₃NH₃PbI₃ solution and start spinning at 4000 rpm for 30 s. Then place the substrate onto the hotplate and anneal for 120 °C for 12 min. Fourth, dispense 35 μl of the Spiro-OMeTAD solution onto CH₃NH₃PbI₃ film and rotate at 2000 rpm for 30 s. Put the resultant substrate in desiccator for 12 h so that spiro-OMeTAD oxidized. Fifth, deposition of Al contact onto the sample as top electrodes by vapor deposition technique and finally PSC achieved. A schematic illustration of the fabrication of the FTO/TiO₂/CH₃NH₃PbI₃/spiro-OMeTAD/Al PV cells energy band diagram showing how PSCs operate is shown in Fig. 3 and Fig. 4, respectively.

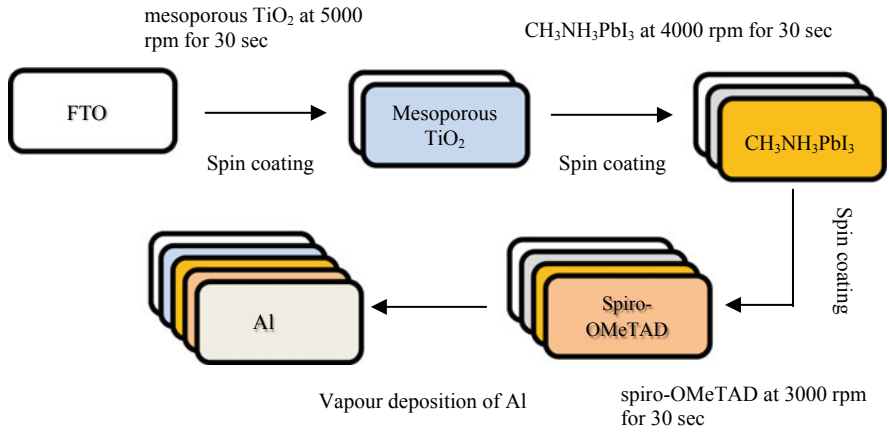


Fig. 3 Schematic illustration of the fabrication of PSC

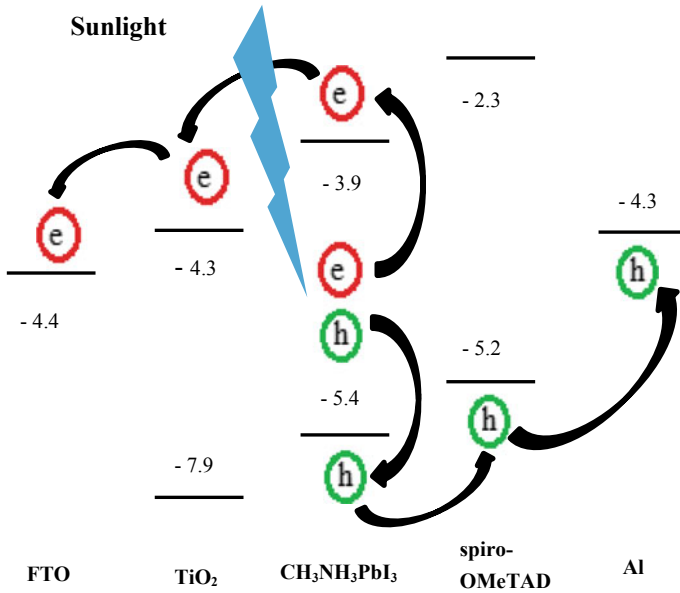
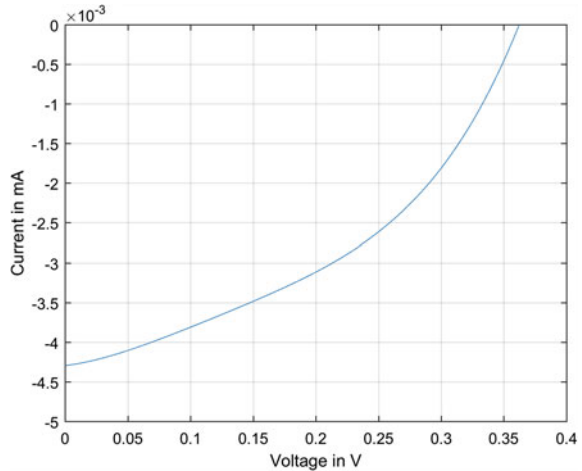


Fig. 4 Schematic energy band diagram showing how perovskite solar cells operate

Fig. 5 I–V characteristics of FTO/TiO₂/CH₃NH₃PbI₃/spiro-OMeTAD/Al solar cell under illumination



3 Characterization

The characterization of fabricated PSC (FTO/TiO₂/CH₃NH₃PbI₃/spiro-OMeTAD/Al) was carried out with current-voltage measurement (I–V measurement) and ultraviolet-visible analysis (UV-Vis).

3.1 I–V Measurement

I–V characteristics of the PSC were measured on a Keithley 2400 that applied a voltage and measured response current with the help of LabVIEW software. For I–V curve, the substrate was placed in a DC 350 W xenon solar simulator under AM 1.5 illuminations (100 mW/cm²) and Keithley applied voltage from –0.1 V to 1.0 V. Finally I–V curve was achieved shown in Fig. 5. PSC fabricated on TiO₂ film shows V_{oc} of 0.362 V, I_{sc} of 0.00429 mA.

3.2 UV-Visible Analysis

The UV-visible absorption spectrum of the different films was obtained using a Shimadzu UV-vis. Absorbance is a measure of the amount of light absorbed. Absorbance is on the vertical axis and wavelength of the light is on horizontal axis. Higher the value of absorbance, the even more a specific wavelength is being absorbed. The absorption spectrum is obtained by subtracting the transmittance and reflectance portion of light from the incident light. UV-visible absorption spectrum of the different films is shown in Fig. 6. In Fig. 6d absorption spectrum of solar cell shows

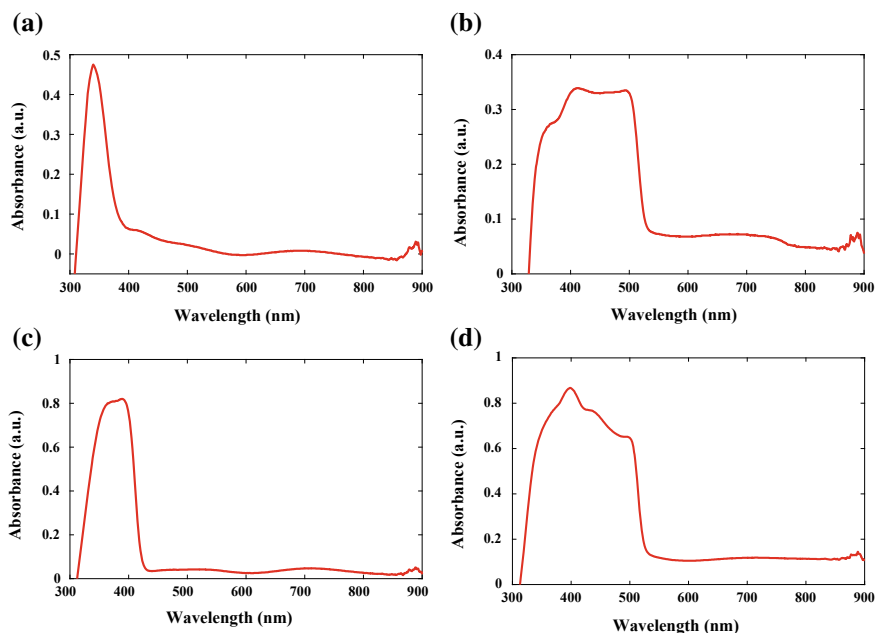


Fig. 6 Absorption spectrum of film: **a** TiO_2 , **b** $\text{CH}_3\text{NH}_3\text{PbI}_3$, **c** spiro-OMeTAD, **d** complete cell

maximum absorption range is between wavelength 350 nm to 510 nm and maximum peak obtained at wavelength 400 nm.

4 Summary

We successfully designed PSC at ambient conditions using TiO_2 as ETM and spiro-OMeTAD as HTM based on aluminum counter electrode with FTO/ TiO_2 / $\text{CH}_3\text{NH}_3\text{PbI}_3$ /spiro-OMeTAD/Al structure. As shown in methodology section, a detailed manufacturing process has been made with parameters for achieving PSC. Although the efficiency of our PSC is lower than the other reported PSCs. The main reason behind the low efficiency is stability problem (i.e., moisture and heat) and these are the biggest obstacle right now for making them commercialized. It would also be interesting to investigate alternative materials for every layer in the PSC structure, to try to optimize the cell and see if other materials reduce degradation problem.

References

1. IE Agency (2013) World energy outlook 2013 factsheet. World Energy Outlook. <http://www.World-energyoutlook.org>
2. Soria A, Szabo L, Russ P, Suwala W, Hidalgo I, Purwanto A (2006) World energy technology outlook 2050. European Commission, Joint Research Centre 21
3. U Energy. Information Administration, International energy outlook 2016. <http://www.eia.gov>
4. Sampaio PGV, González MOA (2017) Photovoltaic solar energy: conceptual framework. *Renew Sustain Energy Rev* 74:50–601
5. Ansari MIH, Qurashi A, Nazeeruddin MK (2018) Frontiers, opportunities, and challenges in perovskite solar cells: a critical review. *J Photochem Photobiol C* 35:1–24
6. Tonui P, Oseni SO, Sharma G, Yan Q, Mola GT (2018) Perovskites photovoltaic solar cells: an overview of current status. *Renew Sustain Energy Rev* 91:1025–1044
7. Kojima A, Teshima K, Shirai Y, Miyasaka T (2009) Organometal halide perovskites as visible-light sensitizers for photovoltaic cells. *J Am Chem Soc* 131(17):6050–6051
8. Saliba M, Matsui T, Seo JY, Domanski K, Correa-Baena JP, Nazeeruddin MK, Grätzel M (2016) Cesium-containing triple cation perovskite solar cells: improved stability, reproducibility and high efficiency. *Energy Environ Sci* 9(6):1989–1997
9. Im JH, Lee CR, Lee JW, Park SW, Park NG (2011) 6.5% Efficient perovskite quantum-dot-sensitized solar cell. *Nanoscale* 3(10), 4088–4093
10. Kim HS, Lee CR, Im JH, Lee KB, Moehl T, Marchioro A, Grätzel M (2012) Lead iodide perovskite sensitized all-solid-state submicron thin film mesoscopic solar cell with efficiency exceeding 9%. *Sci Rep* 2:591
11. Lee MM, Teuscher J, Miyasaka T, Murakami TN, Snaith HJ. (2012) Efficient hybrid solar cells based on meso-superstructured organometal halide perovskites. *Science* 1228604
12. Liu M, Johnston MB, Snaith HJ (2013) Efficient planar heterojunction perovskite solar cells by vapour deposition. *Nature* 501(7467):395
13. Zhou H, Chen Q, Li G, Luo S, Song TB, Duan HS, Yang Y (2014) Interface engineering of highly efficient perovskite solar cells. *Science* 345(6196):542–546
14. Yang WS, Noh JH, Jeon NJ, Kim YC, Ryu S, Seo J, Seok SI (2015) High-performance photovoltaic perovskite layers fabricated through intramolecular exchange. *Science* 348(6240):1234–1237

Control and Remote Sensing of an Irrigation System Using ZigBee Wireless Network



Jay Praful Chheda and Vikash Kumar Boradak

Abstract Cropping systems concerns are increasing significantly in semi-arid and arid areas. In order to maximize the productivity while saving water, the barrier of site-specific irrigation management can be solved. This is done by using in-field distributed sensor-based irrigation system. The main aim of this paper is to highlight the details and instrumentation of various controls. They are variable rate irrigation, wireless sensor network. For monitoring the real-time in-field sensing and control of a site-specific precision linear-move irrigation system a software is used. According to the soil property map, six in-field sensor stations are used to monitor the field conditions. The report of these monitoring data is periodically sampled and transmitted to base station. Geo-referenced location of sprinklers is updated timely with the help of logic programmable controllers [1]. ZigBee communication enables the interfacing of communication signals from sensor network and irrigation controller to the base station. Stable remote access to field conditions and monitoring and real-time control of variable rate irrigation controller is achieved. A graphic user interface-based software is used for this.

Keywords WPAN—Wireless Personal Area Network · Personal computer (PC) · ZDO—ZigBee Device Object · Wireless sensor network (WSN) · Simple mail transfer protocol (SMTP) · Automation · Control systems · Measurement · Portable radio communication · Sensors · Water resources · SHT71 · ADC · CMOS · LM35

J. P. Chheda · V. K. Boradak (✉)
Department of Electrical Engineering, Manipal University Jaipur, Jaipur, Rajasthan, India
e-mail: vikaskumar.boradak@jaipur.manipal.edu

J. P. Chheda
e-mail: chheda_jay@yahoo.in

© Springer Nature Singapore Pte Ltd. 2020
A. Kalam et al. (eds.), *Intelligent Computing Techniques for Smart Energy Systems*,
Lecture Notes in Electrical Engineering 607,
https://doi.org/10.1007/978-981-15-0214-9_105

989

1 Introduction

In semi-arid and arid areas, irrigation is an essential practice and efficient water applications and management are major concerns. Water applications are used in self-propelled center pivot and linear move irrigation systems. Environmental impacts, application efficiencies, and yields can be improved by site-specific irrigation management. While saving water, quality and yield can be increased by the development of distributed in-field sensor-based site-specific irrigation system. But the seamless integration of sensor fusion, irrigation control, data interface, software design, and communication can be challenging.

Microcontrollers operating at low cost and data networks are useful in managing the coordination of control and instrumentation data. Reusability of common hardware and communication protocol can be materialized by adopting a standard interface for sensors and actuators. The installation and maintenance costs shoot up by the application of a hard-wired system from in-field sensing stations to base station. Normal farming operations get disrupted by hard-wiring the system for long distances and may not be acceptable to growers. Dynamic mobility and cost-free relocation provide a wireless data communication system. Wireless communication products used by consumers are established with a radio frequency technology incorporated in it. It provides numerous opportunities to use wireless signal communication in agricultural systems.

According to the IEEE 802.15.4-2003 [2], ZigBee is a specification for a suite of high-level communication protocols by applying small and low-power WPANs [3]. This can be related to the wireless headphones connected with the cell phones via short-range radio. ZigBee technology in comparison with other WPANs such as Bluetooth is less complex and cheaper. Radio frequency applications requiring low data rate, long battery life, and secure networking use ZigBee technology [1, 4].

The sensor-based rate irrigation operating at variable conditions prefer ZigBee module operations in this project. It functionalizes development, testing, and usage of an integrated distributed wireless sensor network. A reduction in installation and maintenance costs is possible with the WSN which eliminates the need of hard-wiring the sensor stations. Unlike the WLAN, WSN uses an ad hoc network, i.e., a mobile wireless network. These ad hoc networks due to their mobility and self-configuration find applications in agricultural operations as they are suitable for a distributed sensor network. The brief analysis and study of the design, construction, and testing of various controls is the ultimate objective of this paper. These controls include WSN, remote valve control, motor control, and user-friendly software for real-time in-field sensing and control.

2 Materials and Methods

2.1 Conceptual System Design

In-field WSN is illustrated with a conceptual system layout in Fig. 1. A base station, irrigation control station and two in-field sensing stations are put in use field conditions related to soil moisture, humidity and air temperature are monitored through the in-field sensing stations [5]. Wireless transmission of in-field sensory data is given to the base station. A user-friendly decision-making program is used for the processing of in-field sensory data from the base station to the irrigation control station. This control station regulates the operation control of valves and motors. Module containing controller, data converter, and memory provide row data to ZigBee module to make wireless network. A process unit is needed to satisfy the operations of the individual nodes and to reduce hardware cost, a common control unit is required [6].

Command to generate control signals given from the decision-making algorithm and analysis of whole network is done through the base station. Storage of sensor data from in-field sensing nodes and provision of inter-connectivity is given by a PC-interface.

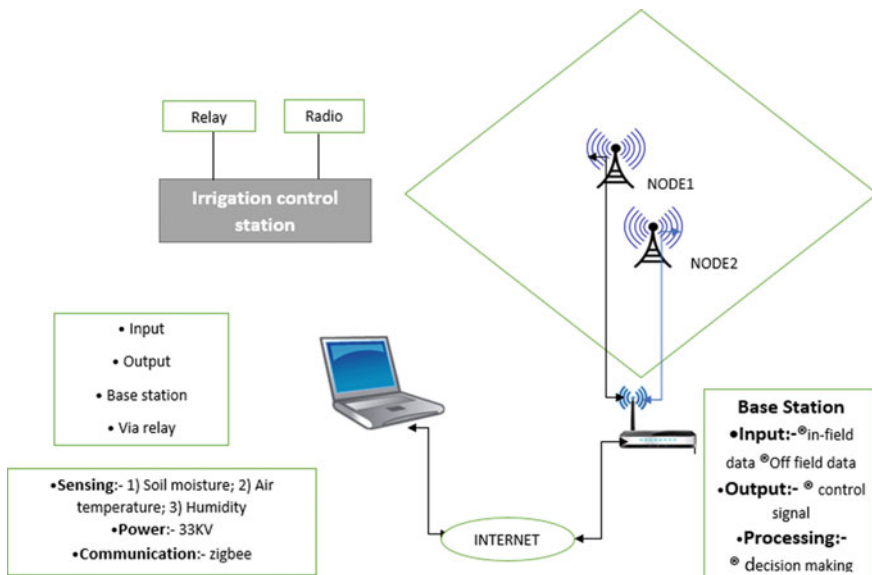


Fig. 1 Conceptual system layout of in-field wireless network [2]

2.2 Sensor-Based In-field Station

The main components used majorly in this station’s operation are three different types of sensors, controllers with data converters, and wireless data communication module (Fig. 2).

2.2.1 Interface-Based Sensing

The sensing-based operation is performed by connecting an analog output and digital outputs on either side. Trouble of voltage range discrepancy occurs due to the fact of us using same power supply for analog output with sensors and data converters (Fig. 3).

2.2.2 I2c-Bus [9]

Transmission of information among devices connected to the bus is done via two wires, namely, Serial data wire and serial clock wire. Observing the functionality of the system, device can operate as a transmitter or receiver by recognizing from its unique address. Initiation of data transfer and generation of clock signals are performed by the master device and this establishment satisfies the normal operation.

Fig. 2 Block diagram of in-field sensing station [7]

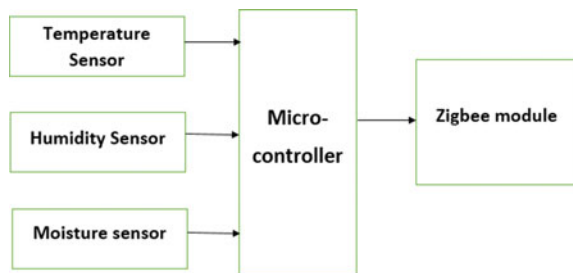
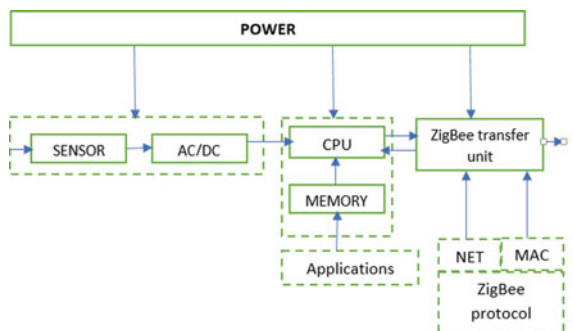


Fig. 3 Block diagram of sensor interface with analog output [8]



2.2.3 Humidity-Based Sensor [10]

A calibrated digital output is generated from a module comprising humidity and multi-sensor chip known as the SHT71. For high reliability and long-term stability CMOS process with patented micromachining is applied. For the sensing of humidity a capacitive polymer sensing element and a bandgap temperature sensor is incorporated in the device. These sensors are coupled to a serial interface circuit and an ADC converter.

2.2.4 Soil Moisture-Based Sensor [11]

For the measurement of the conductivity of soil and keeping it low cost, a simple designed circuit is used rather than a standard soil moisture sensor. This operation functions when the soil is wet. The copper wires get short and output senses and indicate by jumping to a high position. The absence of conductivity between copper wires indicates that the soil is dry.

2.2.5 Temperature-Based Sensor

A direct proportional operation between the device output and Celsius temperature is governed by LM35 precision integrated-circuit temperature sensors. The major disadvantage of Kelvin-based temperature sensor is that it cannot subtract a large constant voltage from its output to obtain scaling in centigrade. No need of providing any external calibration or trimming to support typical accuracies of $\pm 1/4$ °C at room temperature and $\pm 3/4$ °C over a full temperature range.

2.3 *Irrigation Control Station*

Irrigation control station consists of a wireless communication module, driver circuit, valves, and AC motor. Functioning of motors and valves is controlled via input signaling conditions (Fig. 4).

2.3.1 Driver Circuit

This circuit provides major prevention for microcontrollers from high surge current and voltage by providing isolation between them. Motor control board being a single-layer board is used for the routing on the bottom layer. With a threshold range of AC current to 2 A and for remaining tracks a maximum of 25 mA, there is successful application in both signal and power nets. Keeping the current rating in loop, the output nets of AC signal are with 150 mil track.

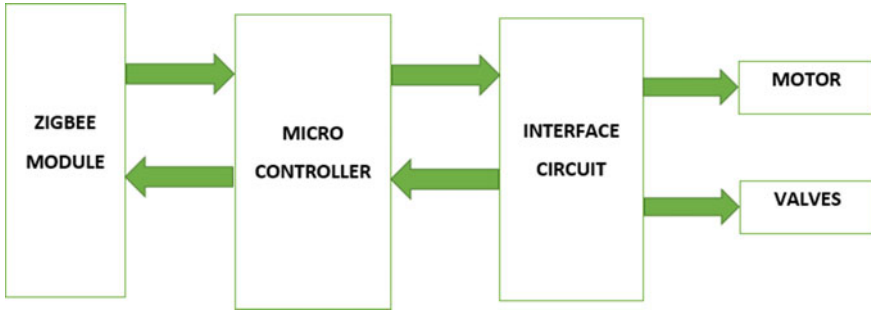


Fig. 4 Block diagram of irrigation control station [12]

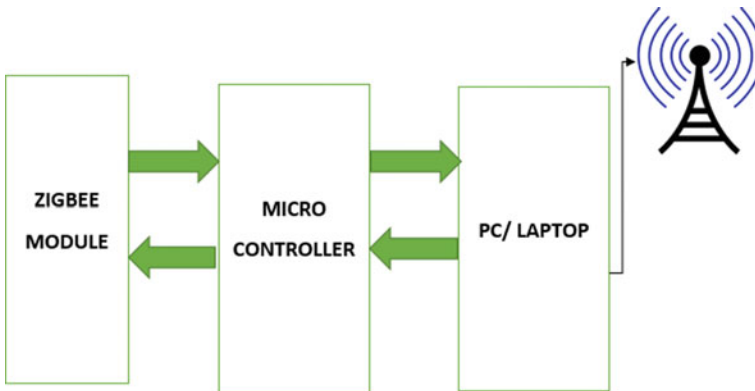


Fig. 5 Block diagram of base station [13]

2.4 Base Station

Command to generate control signals given from the decision-making algorithm and analysis of whole network is done through the base station. Storage of sensor data from in-field sensing nodes and provision of inter-connectivity are given by a PC-interface (Fig. 5).

2.5 Graphical User Interface (Gui)

In contrast with the text-based interfaces, typed command labels or text navigation, the GUI offers graphical icons and visual indicators to represent the information and actions defined by the user. Direct manipulation of graphical elements is the driving force to describe anything an application displays to the user. It is the primary way

you interact with the hardware and allows it to interact with you. GUI is being implemented using Visual Basic6.

This module has the following functionality:

- (1) Node Setting
- (2) Mode Setting
- (3) Current Status
- (4) Node and Motor Control.

Flexibility of changing the threshold values of temperature, humidity, and soil moisture can be materialized through node setting. Selection of either manual mode or auto-mode is done through mode setting. The display text boxes show the current status of infield sensor nodes (Figs. 6 and 7).

Fig. 6 Main graphical user interface (GUI) window

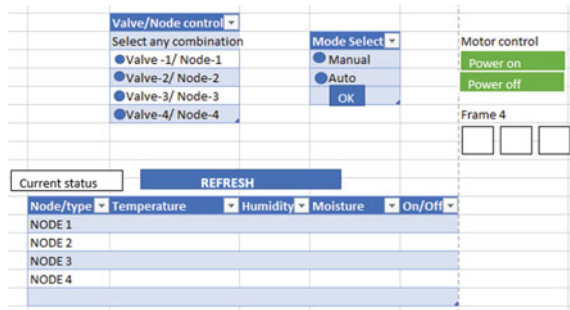
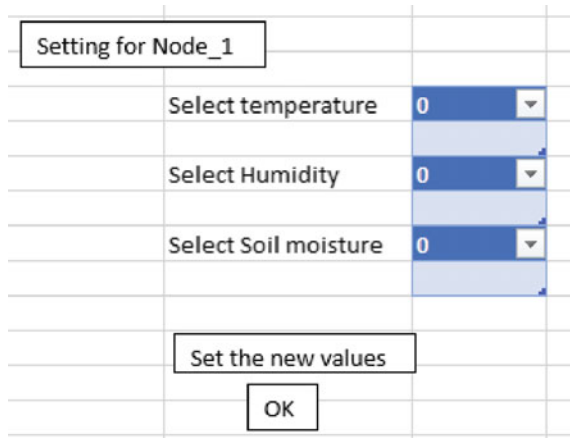


Fig. 7 Node setting GUI window



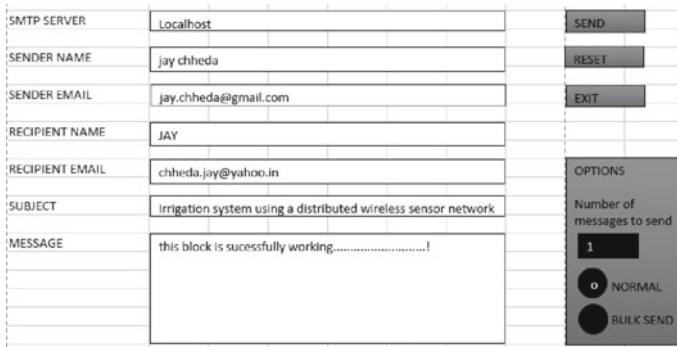


Fig. 8 E. Mail transfer GUI window

2.6 Mail Transfer

Having a graphical user interface, mail transfer makes a connection with the local SMTP server with logical addressing mode. This checks the availability of port number 25 connected to SMTP server. Execution is done through mail-id communication (Fig. 8).

2.6.1 Data Acquisition

In order to get the computer data processed in an easy way, data acquisition samples the real-world physical conditions and conversions into digital numeric values which are used. It typically involves the conversion of analog waveforms into digital values for processing. In this project data from in-field sensing station is stored in two different files. This finds applications in software programs developed using various general-purpose programming languages. Data acquisition is implemented with Visual Basic Language.

3 Application and Observations

This project includes two in-field sensing stations, one base station and one control station. Action of base station is to sense and generate control signals for motor and valves. Incorporation of the ability to set different threshold values is possible through signaling via computer. Functioning of data logging and mailing section have been checked using 5–6 email-ids.

FILE	EDIT	FORMAT	VIEW	HELP		FILE	EDIT	FORMAT	VIEW	HELP
31	60	0				31	60	24		
31	60	20				31	60	26		
31	60	20				31	60	22		
31	60	0				31	60	26		
31	60	0				31	60	24		
31	60	0				31	56	24		
31	60	0				31	60	24		
31	60	0				31	56	26		
31	60	0				31	60	26		
31	60	0				31	60	26		
31	60	0				31	56	26		
31	60	0				31	56	26		
31	60	0				31	56	28		
31	60	0				31	56	26		
31	60	0				31	56	28		
31	60	0				31	56	26		
31	60	0				31	56	24		
31	60	0				31	56	26		
31	75	0				31	56	26		
31	60	0				31	56	24		

4 Limitation

Operation of ZigBee module is limited to 10–12 m range which is comparatively less for an irrigation system. Usage of excess current causes a reduction in battery life and needs more batteries. Manual mode of mailing is operational instead of automatic. A simple comparator circuit is used instead of a soil moisture sensor. This circuit comprises only two states, thus we cannot find out water level present in the soil.

5 Conclusion and Future Work

A wireless irrigation system comprising ZigBee technology is helpful in building low-power and low-cost wireless irrigation system. The main force driving this phenomenon is the requirement of low power consumption. The interface provides large operations to user to set the conditions according to his/her requirement. A thorough checkup starting from circuit level to system design is done and it can accessible through the internet. Mails are periodically updated with the stipulated data.

Certain discrepancies are still not resolved. However, appropriate actions have been planned and charted to ease out the operations. Mail transfer can be automatically operated with certain algorithm. These in-field sensing stations are powered by an external battery which can be converted into solar-powered wireless in-field sensing station. This can be implemented through better energy management in wireless station.

References

1. <https://www.radio-electronics.com/info/wireless/zigbee/zigbee.php>
2. Kim Y, Evans RG, Iverson WM (2007) Remote sensing and control of an irrigation system using a distributed wireless sensor network. IEEE
3. Baronti P, Pillai P, Chook VWC, Chessa S, Gotta A, Hu YF (2007) Wireless sensor network: a survey on the state of the art and the 802.15.4 and ZigBee standard. Sci Direct
4. Wheeler (2007) Commercial application of wireless sensor networks using ZigBee, communication magazine. IEEE
5. Wang Ning, Zhang Naiqian, Wang Manhua (2006) Wireless sensors in agriculture and food industry—recent development and future perspective. Sci Direct Comput Electron Agric 50:1–14
6. <https://www.pocket-lint.com/smart-home/news/129857-what-is-zigbee-and-why-is-it-important-for-your-smart-home>
7. Ranade P, Takale SB (2016) Smart irrigation system using FPGA based wireless sensor network
8. Improving sensor to ADC analog interface design
9. <https://www.ncbi.nlm.nih.gov/pmc/articles/PMC4063076/>
10. <https://www.epa.gov/watersense/soil-moisture-based-control-technologies>
11. <https://www.elprocus.com/temperature-sensors-types-working-operation/>
12. <http://embeddedprojectsworld.blogspot.com/2013/11/intelligent-automatic-plant-irrigation.html>
13. https://en.wikipedia.org/wiki/File:Base_station_2_channel_block_diagram.png, <https://www.elprocus.com/i2c-bus-protocol-tutorial-interface-applications/>

Analysis and Classification of Maximum Power Point Tracking (MPPT) Techniques: A Review



Bhuwan Pratap Singh, Sunil Kumar Goyal and Shahbaz Ahmed Siddiqui

Abstract In recent scenario, Photovoltaic system (PVS) in grid-connected mode is an emerging tool for electricity generation throughout the world to overcome the effects of conventional fossil fuel-based electricity generation on environment. However, apart from tremendous benefits of using this technology, there are various issues and challenges also associated with the integration of this technology to the electric utility grid. Various researchers are working and have proposed numerous solutions, by the implementation of which, the performance of the system could be improved and the impacts on the electric utility grid could be minimized. Out of those the Maximum Power Point Tracking Technique (MPPT Technique) is most popular and widely used solution. After doing an extensive study of various previously and recently developed techniques, the concept behind using MPPT techniques and its benefits are presented in this article. A comparative analysis based on 32 different algorithms developed and implemented for maximum power point tracking purpose is presented at the end of the article. The comparison is presented on the basis of performance and requirements for the implementation purpose.

Keywords PVS · MPPT · DGs · LVRT · RES · Grid integration · Electric utility

1 Introduction

The effects of fossil fuel-based power generation on environmental and climate change present serious challenges to the society as well as global environment [1]. The PVS is a process of generating electricity directly by the energy received from the sunlight. The operation of solar PVS is classified into two modes, i.e., stand-alone

B. P. Singh (✉) · S. K. Goyal · S. A. Siddiqui
Manipal University Jaipur, Jaipur, Rajasthan, India
e-mail: halobhuwan@gmail.com

S. K. Goyal
e-mail: sunilkumar.goyal@jaipur.manipal.edu

S. A. Siddiqui
e-mail: shahbazahmed.siddiqui@jaipur.manipal.edu

© Springer Nature Singapore Pte Ltd. 2020
A. Kalam et al. (eds.), *Intelligent Computing Techniques for Smart Energy Systems*,
Lecture Notes in Electrical Engineering 607,
https://doi.org/10.1007/978-981-15-0214-9_106

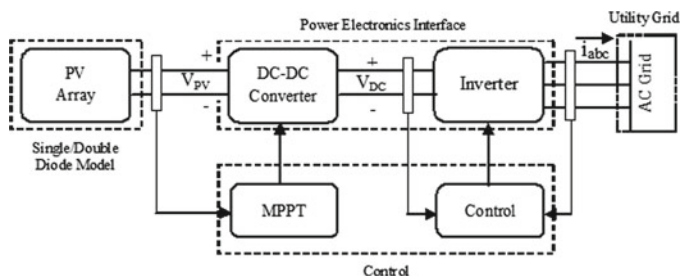


Fig. 1 Basic components of grid-connected PVS

mode and grid-connected mode. In stand-alone mode it feeds electricity directly to the connected load; however, in grid-connected mode it feeds electricity to the electric utility grid. There is one more mode which comes into picture after encouragement given by the respective governments of the countries throughout the world. In this mode, the solar PVS feeds electricity to the electric utility grid as well as to the locally connected load through net-metering (NEM) or feed-in-tariff (FIT). In Fig. 1 the major components generally used in the grid integration of solar PVS are represented [1]. The basic configuration of solar PVS in grid-connected mode comprises the following devices: PV array, a DC–DC converter, a DC–AC converter (inverter), maximum power point tracking device (MPPT), and a control equipment along with a low pass filter. The MPPT device is generally employed with the power converter to optimize the utilization of large PV arrays. The implementation of MPPT device is possible in different ways: either with the DC–DC converter or with the inverter or sometimes with both.

To fully furnish the details of various previously and recently developed MPPT techniques an attempt has been made and a critical analysis is provided on each method.

2 Introduction to MPPT Techniques

The use of MPPT becomes essential in order to ensure the optimum operation of solar PVS, i.e., the system operates at its MPP. The nonlinear behavior of MPP complicates the tracking algorithm as the solar irradiance and ambient temperature are continuously variable in nature. The objective of implementing MPPT is to automatically determine the output voltage or output current of PVS under the specific irradiance and temperature; this is the point where the PV array produces maximum output power. Implementation of MPPT algorithm and analysis of these environmental variations as well as P–V characteristic allow us to ensure that the PVS is operating at its MPP.

In [2], a single-stage three-phase PVS is proposed by the authors to enhance the capability of MPPT; this system is also found capable to meet demand and produce electricity under partial shaded conditions. An MPPT method is proposed by the authors in [3] on the basis of controlling the AC/DC converter which is connected to the PV array output, as it acts as a continuous input power load.

3 Types of MPPT Techniques

In last few decades, many researchers have been working on MPPT techniques for solar PVS. The numerous methods have been developed so far by the researchers which may be classified into two main categories: (A) Conventional methods and (B) Soft computing methods. Perturb and Observe (P&O), Hill Climbing (HC), Incremental Conductance (IncCond), Fractional Open Circuit (FOC), Fractional Short Circuit (FSC), and Global MPPT techniques are come under conventional methods.

Moving toward soft computing methods, the knowledge-based systems are Fuzzy Logic Control (FLC) and Artificial Neural Networks (ANN) algorithms. Before their implementation, it is essential to provide detailed knowledge. The most severe drawback associated with FLC-based algorithm is that the rules once defined cannot be changed [4, 5].

There are many other old and recently developed algorithms also available in the literature which can be used to track MPP, the comparative study of these 32 techniques (not included all) and their classification is shown in Table 1.

3.1 Conventional Methods

3.1.1 Perturb and Observation (P&O) Algorithm

In solar PVS, the Perturb and Observe (P&O) is one of the most popular and widely used methods among all available methods to track MPP. In P&O, voltage perturbations are required to produce which can determine the tracking direction after calculating the required PV power which is calculated on the basis of sensor inputs [6]. There may be a continuously rise or fall in output power of PV cells depending upon produced voltage perturbations. As a result this algorithm produces oscillations around global MPP, since voltage perturbations help it to continuously keep tracking the global MPP [4]. However, P&O is found comparatively less complex, even though, as far as high power applications are concerned, this method is not preferable.

As far as the limitations of P&O are concerned then it greatly suffers from the production of high perturbation rate around the global peak as well as increased power oscillations.

Table 1 Comparative analysis of various MPPT techniques

S no.	Name of MPPT technique	Tracking speed	Convergence speed	Partial shading handling	PV array dependency	Efficiency	Hardware implementation
1	P&O	Slow	Varies	N	Independent	Varies	Easy
2	Modified P&O with fixed Perturb	Slow	Slow	NA	Independent	Varies	NA
3	Conv. P&O with adaptive Perturb	Fast	Fast	N	Independent	Varies	Medium
4	Modified P&O with adaptive Perturb	Fast	Fast	N	Independent	Varies	Medium
5	PSO	Slow	Fast	Y	Dependent	Medium	Medium
6	IncCond	Slow	Varies	N	Independent	Medium	Medium
7	Fuzzy logic	Medium	Fast	Y	Dependent	High	Complex
8	ANN	Fast	Fast	Y	Dependent	High	Complex
9	Short-circuit current	Slow	Medium	N	Dependent	Medium	Medium
10	Open-circuit voltage	Slow	Medium	N	Dependent	Low	Easy
11	Open-circuit voltage pilot PV cell method	Fast	Fast	Y	Dependent	Low	Medium
12	Best fixed voltage	Fast	Fast	N	Dependent	Medium	Medium
13	Hill climbing	Slow	Slow	N	Dependent	Low	Easy
14	Global MPP	Slow	Slow	Y	Dependent	Low	Easy
15	Genetic algorithm	Slow	Slow	Y	Independent	High	Complex
16	Nonlinear method	Fast	Fast	N	Independent	Low	Easy
17	Differential evaluation	Medium	Fast	Y	Independent	Varies	Medium
18	Fibonacci series	Slow	Medium	Y	Independent	Varies	Medium

(continued)

Table 1 (continued)

S no.	Name of MPPT technique	Tracking speed	Convergence speed	Partial shading handling	PV array dependency	Efficiency	Hardware implementation
19	Direct MPPT	Medium	Medium	Y	Dependent	Medium	Medium
20	Artificial Bee colony	Fast	Fast	Y	Dependent	Medium	Medium
21	Ant colony optimization	Medium	Fast	Y	Dependent	Varies	Medium
22	Firefly algorithm	Fast	Fast	Y	Independent	Low	Easy
23	Random search	Fast	Fast	Y	Independent	Low	Easy
24	Temperature gradient (TG) algorithm	Fast	Fast	Y	Dependent	Low	NA
25	Temperature parametric (TP) method	Fast	Fast	Y	Dependent	Low	NA
26	Feedback voltage or current method	Slow	Slow	N	Dependent	Low	NA
27	P-N junction drop voltage tracking technique	Fast	Fast	Y	Dependent	High	Medium
28	Look-up table	Fast	Medium	Y	NA	Varies	NA
29	Load current or load voltage maximization	Slow	Slow	N	Dependent	Low	NA
30	Linear current control	Slow	Slow	N	Dependent	Varies	NA
31	The only current photovoltaic	Slow	Varies	Y	Independent	Low	NA
32	PV Output senseless (POS) control	Slow	Varies	Y	Independent	Low	NA

3.1.2 Incremental Conductance (IncCond) Algorithm

In IncCond algorithm, the slope of PV characteristics is reformed based on the conductance value obtained from the ratio of incremental conductance to the instantaneous conductance of the PV module. As a result duty cycle is generated for the converter [7, 8]. In order to minimize the tracking error in this algorithm, several approaches have been followed by the researchers out of which an improved IncCond is presented in [7] with variable step size. The duty cycle is generated as per the following relation [7].

$$D(k) = D(k - 1) \pm N^* \left| \frac{P(k) - P(k - 1)}{V(k) - V(k - 1)} \right| \quad (1)$$

where “k” denotes the value of iteration, “P” denotes the power, “D” stands for duty cycle, “V” stands for voltage, and “N” denotes the scaling factor.

3.1.3 Hill Climbing (HC) Algorithm

Among all available classical methods to track MPP; Hill Climbing is the oldest technique which is widely used due to its proven effectiveness and simplicity. First of all, the values for voltage and current are obtained by the sensors and then the duty cycle is suitably adjusted based on the calculated power. Once a certain number of duty cycles are achieved depending upon whether the duty cycle is increasing or decreasing, the converter will become able to react at global MPP. The authors in [9] presented a precise tracking algorithm by testing HC technique with interleaved boost converter under uniformly variable irradiation condition. The below relations are given to calculate the extracted maximum power from PV:

$$P_g(max) = \frac{P_l(max)}{\eta} \quad (2)$$

$$P_g(max) = k_2 V_L^2 \quad (3)$$

where the generated power is “ $P_g(max)$ ” and the controlling factor $k_2 = 1/\eta R_\eta$.

3.2 Soft Computing Methods

Several works have been done over the last decades to find out the best suitable technique for solving nonlinear problems and it has been found that soft computing-based MPPT techniques are the key choice for this purpose. The methods used under these techniques assure faster convergence and high reliability. Numerous tracking algorithms have been developed and implemented based on soft computing because

of the existence of some natural drawbacks with conventional methods. An extensive survey is presented in this section on various soft computing methods. These methods have been employed successfully in the past to extract maximum power.

3.2.1 Fuzzy Logic Control (FLC) Based Algorithm

Fuzzy Logic Control is well known for its firmness, it is a regulation based technique, various nonlinear optimization problems can be solved with this technique. It is preferable for implementation because of its unique advantages as it provides convenient user interface, implementation is less complex and qualified validation along with flexible operation. However, it has been found that FLC is highly effective when implemented along with some other soft computing technique instead implemented alone. That is why, it is less observed that FLC is implemented alone in tracking. Artificial Neural Network (ANN), Genetic Algorithm (GA) and some other conventional methods are generally used in combination with FLC for the implementation.

Following equations are used in general practices to determine the error component as well as error difference because reduction in error component is generally reported in the approaches.

$$E(j) = \frac{P(j) - P(j - 1)}{I(j) - I(j - 1)} \quad (4)$$

$$C_E(j) = E(j) - E(j - 1) \quad (5)$$

where “j” denotes the iteration number, the change in error is denoted by “C_E”, “E” refers to error, “P” refers the power, and “I” refers the current.

3.2.2 Artificial Neural Network-Based Algorithm

ANN is a technique which has the capability to think of its own as it is derived from the behavior of neurons and is an algorithm based on artificial intelligence. However, to train the neurons that are present in the algorithm much knowledge is needed and essential [10, 11]. It is generally advisable to implement ANN in combination with some other conventional MPPT method for tracking MPP. The reason behind this is its enlarged optimization scope.

Experimentations are performed for variation in solar irradiations (under steady change and partial shaded conditions) and results are presented with better convergence with series parallel, bridge link, and total cross ties configurations. The accuracy of solar PVS is tested and it has been found from the obtained results in a unique approach that performance of ANN extremely depends on the weights of the hidden layers [11]. The formula used to calculate these hidden layer weights of the neuron is

$$w(j + 1) = w(j) - \frac{\alpha \delta(j - 1)}{\delta w(j)} \quad (6)$$

where “j” is the iteration number, “ α ” is the constant, “w” denotes the age of weight of the hidden layer and “ δ ” indicates the change in weight.

3.2.3 Genetic Algorithm (GA)

In case when a wide stochastic search is needed, Genetic Algorithm (GA) has been found as key choice for MPP tracking. Collaborative product customization [12], fuel flow rate in transport aircraft [13], remanufacturing process planning and scheduling [14], and power grid wind disaster management [15] are some of the areas of application where GA is recently implemented.

A novel MPPT technique capable under all partial shaded conditions are proposed in [16] which is based on GA. The algorithm is tuned for required yields by fixing the properties of GA like cross over and mutation to 10% and 80%, respectively. However, the drawback associated with the methods based on GA is large initial population; hence, it is advisable for this method to implement along with some other conventional method to ensure the improved liability of the system [14, 15].

3.2.4 Particle Swarm Optimization (PSO) Based Algorithm

An exhaustive literature including the application along with the basic operating principles of conventional particle swarm optimization (PSO) to track MPP is presented in [17]. The PSO algorithm becomes an excellent choice for the implementation in nonlinear optimization problems because of its potential. It derives its ability to search from the responses of swarms, flocks, and insects. The initial particles that are involved can be chosen randomly inside the boundary limits is the intrinsic idea behind PSO and this is the fact that over the past few decades, PSO has been found one of the most preferable optimization techniques for MPPT application.

The PSO is also implemented in combination with conventional P&O technique by Sundareswaran et al. in [17]. Experiments performed to extract global MPP and improved the inability of tracking. In [18] Babu et al. have used reflecting impedance method for selecting the values and eliminated the randomness in initial duty cycle.

3.3 Comparative Study

After an exhaustive review of 18 various publications, 9 important parameters have been assessed to produce a comparative analysis of 32 different MPPT techniques.

These 32 techniques include both conventional and soft computing techniques and are analyzed based on nine important and common parameters. The comparative

analysis has been presented in Table 1 which included 32 recent and old MPPT techniques. The criterion on the basis of which the analysis has been produced are (1) tracking speed, (2) convergence speed, (3) partial shading handling capability, (4) pv array dependency, (5) efficiency, and (6) hardware implementation. The requirements may vary according to these conditions so, the categorization presented above may not be the final conclusion to achieve better response in dynamic and steady-state; however, a fair comparison is presented.

4 Conclusion

In last few decades, the field of MPPT in grid-connected PVS is increasingly attracting the interest of those researchers who are continuously working toward the performance enhancement along with improvement in efficiency of the grid-connected PVS. The MPPT is utilized and implemented in the grid-integrated system mainly to extract maximum power from the sunlight so that the system works at maximum overall efficiency. In this article, an effort has been made to focus on how the maximum power can be extracted from the sunlight by implementing some tracking algorithm despite the complexity level in implementation. Moreover, the most widely used 32 tracking algorithms including conventional and recently developed are cited in the article. The selection and citation mainly focused on the advantages, disadvantages, implementation requirements and complexity level for implementation in each and every tracking algorithm. Additionally, it is also most important to remark that every technique imposes limitations and compromises on the regulations of the system by itself independent of the size of power plant and type of the technique used. Such as, if a solar PVS is installed to generate few hundreds of watts. So, ANN technique is not advisable to implement irrespective of its accuracy over other techniques. Therefore, before the implementation, one should keep in mind the trade between revenue and tracker costs, in addition to additional clearance.

References

1. Saad NH, El-Sattar AA, Mansour AEAM (2016) Improved particle swarm optimization for photovoltaic system connected to the grid with low voltage ride through capability. *Renew Energy* 85:181–194
2. Ghoddami H, Yazdani A (2011) A single-stage three-phase photovoltaic system with enhanced maximum power point tracking capability and increased power rating. *IEEE Trans Power Deliv* 26(2):1017–1029
3. Koutroulis E, Blaabjerg F (2012) A new technique for tracking the global maximum power point of PV arrays operating under partial-shading conditions. *IEEE J Photovolt* 2(2):184–190
4. Salam Z, Ahmed J, Merugu BS (2013) The application of soft computing methods for MPPT of PV system: a technological and status review. *Appl Energy* 107:135–148
5. Ishaque K, Salam Z (2013) A review of maximum power point tracking techniques of PV system for uniform insolation and partial shading condition. *Renew Sustain Energy Rev* 19:475–488

6. Femia N, Petrone G, Spagnuolo G, Vitelli M (2005) Optimization of perturb and observe maximum power point tracking method. *IEEE Trans Power Electron* 20(4):963–973
7. Hsieh GC, Hsieh HI, Tsai CY, Wang CH (2013) Photovoltaic power-increment-aided incremental-conductance MPPT with two-phased tracking. *IEEE Trans Power Electron* 28(6):2895–2911
8. Veerachary M, Senju T, Uezato K (2001) Maximum power point tracking control of IDB converter supplied PV system. *IEE Proc Electric Power Appl* 148(6):494–502
9. Karatepe E, Hiyama T et al (2009) Artificial neural network-polar coordinated fuzzy controller based maximum power point tracking control under partially shaded conditions. *IET Renew Power Gener* 3(2):239–253
10. Boumaaraf H, Talha A, Bouhali O (2015) A three-phase NPC grid-connected inverter for photovoltaic applications using neural network MPPT. *Renew Sustain Energy Rev* 49:1171–1179
11. Dou R, Zong C, Nan G (2016) Multi-stage interactive genetic algorithm for collaborative product customization. *Knowl Based Syst* 92:43–54
12. Baklacioglu T (2016) Modeling the fuel ow-rate of transport aircraft during flight phases using genetic algorithm-optimized neural networks. *Aerosp Sci Technol* 49:52–62
13. Zhang R, Ong S, Nee AY (2015) A simulation-based genetic algorithm approach for remanufacturing process planning and scheduling. *Appl Soft Comput* 37:521–532
14. Zhang B, Li X, Wang S (2015) A novel case adaptation method based on an improved integrated genetic algorithm for power grid wind disaster emergencies. *Expert Syst Appl* 42(21):7812–7824
15. Ramaprabha R, Mathur B (2012) Genetic algorithm based maximum power point tracking for partially shaded solar photovoltaic array. *Int J Res Rev Inf Sci (IJRRIS)* 2
16. Ishaque K, Salam Z, Amjad M, Mekhilef S (2012) An improved particle swarm optimization (pso)-based MPPT for PV with reduced steady-state oscillation. *IEEE Trans Power Electron* 27(8):3627–3638
17. Sundareswaran K, Palani S et al (2015) Application of a combined particle swarm optimization and perturb and observe method for MPPT in PV systems under partial shading conditions. *Renew Energy* 75:308–317
18. Babu TS, Rajasekar N, Sangeetha K (2015) Modified particle swarm optimization technique based maximum power point tracking for uniform and under partial shading condition. *Appl Soft Comput* 34:613–624

A Study and Comprehensive Overview of Inverter Topologies for Grid-Connected Photovoltaic Systems (PVS)



**Bhuwan Pratap Singh, Sunil Kumar Goyal, Shahbaz Ahmed Siddiqui
and Prakash Kumar**

Abstract Global environmental concerns and the advancements in power electronics technology leading the application of Photovoltaic Systems (PVS) in the distribution generation (DG). For generating electric power through the energy received from the Sun, solar PVS is an emerging technology. It is playing a key role to consume solar energy as much as possible. Electric power is generated by the PV array in form of DC. This DC power before utilization for domestic or industrial uses must be converted into AC. If the PVS is grid-connected then the inverter requires high efficiency, maximum power point tracking, total harmonic distortion of currents injected into the grid must have low and the power injected into the grid must be controlled. The employed control schemes decide the performance of the inverter which is connected to the grid. In this paper, all aspects related to grid-connected inverter are presented that includes historical evolution of the inverter topologies, standards and specifications, summary of inverter types, and classification of inverter topologies. Also, a discussion has been presented based on the number of power processing stages required in the system to feed electrical power into the grid.

Keywords PVS · Grid-connected inverter · VSI · CSI · DC–DC converter

B. P. Singh (✉) · S. K. Goyal
Department of Electrical Engineering, Manipal University Jaipur, Jaipur, Rajasthan, India
e-mail: halobhuwan@gmail.com

S. K. Goyal
e-mail: sunilkumar.goyal@jaipur.manipal.edu

S. A. Siddiqui
Department of Mechatronics Engineering, Manipal University Jaipur, Jaipur, Rajasthan, India
e-mail: shahbazahmed.siddiqui@jaipur.manipal.edu

P. Kumar
Department of Electrical Engineering, Amity University, Patna, Bihar, India
e-mail: prakash.ucertu@gmail.com

© Springer Nature Singapore Pte Ltd. 2020
A. Kalam et al. (eds.), *Intelligent Computing Techniques for Smart Energy Systems*,
Lecture Notes in Electrical Engineering 607,
https://doi.org/10.1007/978-981-15-0214-9_107

1009

1 Introduction

The increasing power demand throughout the world and environmental benefits of using PVS are gaining more visibility toward PVS to supply electrical power directly to the utility grid [1]. The main drawback why PVS have not so far been installed into the grid is its cost. It has relatively high cost, if compared to the conventional energy sources. However, solid-state inverter is the key technology for placing PVS into the grid. The cost of PV modules is now decreasing these days due to rise in production capacity of PV modules which has the major component in the high cost of PVS in the past. In order to get reduced overall cost of the system, the most challenging issue these days is the cost of the inverter which is connected to the grid. To make PVS more attractive, it becomes necessary to reduce the cost per watt of grid-connected inverter [2].

A DC/DC converter is required to connect PVS to the electric utility grid together with a DC/AC inverter. Typically used inverters are either Voltage Source Inverter (VSI) or a Current Source Inverter (CSI). The application of VSI is gaining interest throughout the world day by day in grid-connected PVS. Therefore, the main constraint in these inverters is high efficiency, also it is the serious constraint for the effective application of these inverters in the grid-connected PVS [3]. The design of VSI control system must be fast and accurate in order to ensure the proper operation of the PVS in the grid-connected mode. As a result, in order to achieve appropriate performance of the grid-connected PVS and for the actual tracking as per the anticipated command, an appropriate VSI control system is needed. In a grid-connected PVS, grid-connected inverter controls the current injected to the grid as a result DC-link voltage is maintained to its reference value also, active and reactive powers are regulated which is to be delivered to the grid [4].

Therefore, main focus in this paper has been placed on inverter solutions which are new, innovative as well as cheap. It has been found in the high diversity within the inverter itself and some new configurations of the system. Further, the study follows an overview of historical as well as some new inverter topologies for interfacing modules connected in PVS to the electric utility grid. Various approaches are discussed to recognize the most appropriate topology for PV inverters, and, finally, a conclusion is given.

2 Evolution of Grid-Connected Inverter Topologies for PVS

An inverter is used to convert the DC output power received from solar PV array into AC power of 50 Hz or 60 Hz. It may be high-frequency switching based or transformer based, also, it can be operated in stand-alone, by directly connecting to the utility or a combination of both [5]. In order to have safe and reliable grid interconnection operation of solar PVS, the inverter is the key technology. The generation of high-quality AC power is required for the electric utility system at reasonable cost, for

which inverter is essential. The high-frequency power electronics-based switching devices with PWM are used to meet these requirements [6]. There are five possible topologies of inverter family in grid-connected PVS as shown in Fig. 1, viz., (a) centralized inverters, (b) string, (c) multi-string, (d) AC-module inverters, and (e) cascaded inverters [7].

The advantages and disadvantages based on the comparative study of the various publications [8–14] are presented in Table 1.

Fig. 1 Inverter topologies in grid-connected PVS: **a** Centralized, **b** String, **c** Multi-string, **d** AC-module and **e** Cascaded inverter topology

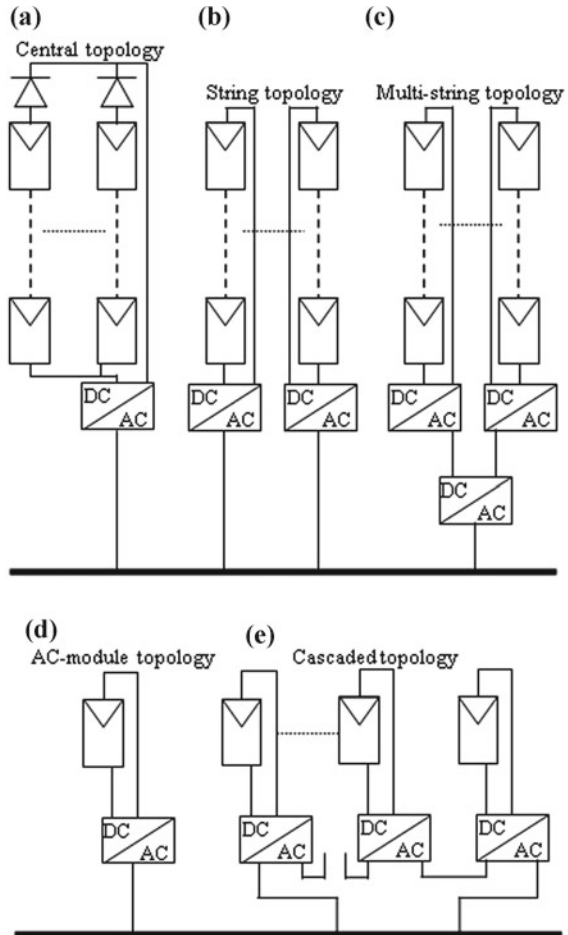


Table 1 Advantages and disadvantages of various inverter topologies

Inverter topology	Advantages	Disadvantages	Power rating
Centralized	Monitoring and maintenance is easy, low cost and use of high voltage and high power applications	Application of HVDC cables leads to high DC losses, high power losses due to centralized MPPT, string diodes and modules mismatch. Not flexible in design with low reliability, cost is high and in case of failure whole plant will get into shut down mode	Up to several Mega-Watts
String	Reduced energy losses due to partial shading, no losses in string diodes, low cost, reliable and flexible in design. Individual MPPT's may be employed for each string	Cost is higher than the central inverter, applicable in low power ratings, reduced efficiency because of high voltage amplification as a result the cost of per kW production increases	3-5 kilo-Watts per string
Multi-string	Reduced energy losses due to partial shading, no losses in string diodes, DC-DC converter can amplify the voltage, individual control can be provided for each string, optimum monitoring of PVS and due to local MPPT high energy can be revealed	Cost per kW production increases due to the application of both DC/AC and DC/DC converters, losses increases inside the DC-DC converter and reduced reliability because all the strings are connected to the single inverter	5 kilo-Watts
AC modules	No energy losses due to modules mismatch and partial shading, flexible and expandable, low cost and maximum power can be extracted from the PV modules	If the fault is not easy then whole inverter has to be replaced, very high cost, because of additional thermal stress the lifetime of the power electronic devices reduced, overall efficiency is less and inverter has to amplify the very small voltage also which is the main challenge for the designers	Up to 500 Watts
Cascaded inverters	There are several converters connected in series in cascaded inverters; thus, in medium and large grid-connected PVS, the high voltage or high power obtained from the combination of several modules would support this topology	In order to offer the advantage of individual MPPT module, each PV module has its own DC/DC converter to create a high DC voltage, this high DC voltage is then fed to a simplified DC/AC inverter	Up to several Mega-Watts

2.1 *Centralized Inverters*

The centralized inverters were the first topology as illustrated in Fig. 1a with that a large number of PV modules interfaced to the grid [15]. Each PV module generating a sufficiently high voltage and is divided into series to form string as a result further amplification of the voltage is avoided. Further, these strings were then connected in parallel along with string diode to achieve high power levels.

The PV modules and inverter were tied with the high-voltage DC cables in this centralized inverter, which is considered as the limitation related to this topology. Also, the increased power losses in centralized MPPT, increased mismatch loss between inverter and PV modules, nonflexible design, and increased losses in the string diodes are the severe limitations of this topology. The benefits of mass production could not be achieved due to these factors. The grid-connected stage comprising poor power quality and many current harmonics as it was ordinarily line commutated. This was the occasion to evolve a new inverter topology as to overcome the large amount of harmonics and comprises the evolving standards which also overcome power quality issue.

2.2 *String Inverters and AC-Modules*

The string inverters and the AC-module are the two technologies which are widely used in recent days also termed as present technology [15]. The string inverter is nothing but the reduced version of the centralized inverter as illustrated in Fig. 1b, where the inverter is connected to a single string of the PV modules [16]. The voltage amplification here can be avoided because of enough high input voltage. For European system, it requires only 16 PV modules approximate and the total open-circuit voltage of whole system may reach 720 V for 16 PV modules. However, the voltage in normal operation is as low as 450–510 V. If for voltage amplification, a line frequency transformer or a DC–DC converter is used then there is also the possibility to connect some PV modules in series also. Individual MPPTs can be applied for each string and there would be no losses accompanying with string diodes. As a result increased overall efficiency could be achieved as compared to the centralized inverter with reduced cost because of mass production.

On the other hand as illustrated in Fig. 1d, in the AC module, PV module and the inverter are integrated into one electrical equipment [16]. As there is only one PV module so, it maintains optimal adjustment between the inverter and the PV module and removes the mismatch losses. Also, there is a possibility of an easy enlarging of the system because of modular structure. The inherent feature of this topology is that it can become a “plug and play” device so that anyone can use it without any knowledge regarding electrical installation.

On the other hand, increased complexity in the topology may lead to reduced overall efficiency along with increase in price per watt due to the necessity of high

voltage amplification. However, to keep low manufacturing cost as well as retail prices, the AC-module is proposed to be mass produced.

2.3 *Multi-string Inverters and Cascaded Inverters*

The multi-string is the further development of the string inverter as illustrated in Fig. 1c, in which several strings are interfaced to a single DC–AC inverter with their own DC–DC converter [16, 17]. Since every string can be controlled separately therefore, this is beneficial over centralized system, since every string can be controlled individually. Hence, with few modules, an operator may start his/her own PVS connected to the grid. With the possibility of plugging a new string into the existing platform with a DC–DC converter, further developments can be easily achieved as a result a flexible design is hereby achieved with high efficiency [18–20]. To develop an inverter which is capable to amplify very low voltage, 0.5–1.0 V and 100 W per meter square, up to required voltage level for the grid is the main challenge for the designers. Also, at the same time, it should reach high efficiency, that is why the new converter technology is required these days. The cascaded inverter depicted in Fig. 1e in which several converters have been connected in series to achieve high power or high voltage from the combination of several modules. These parameters would have supported this topology in medium and large grid-connected PVS.

3 Power Processing Stages-Based Inverters

There are broadly two categories of the inverters according to their power processing stages: single-stage inverters (SSI) and multiple-stage inverters (MSI).

3.1 *SSI: Single-Stage Inverter*

Multiple functions are to be performed by the single-stage inverter, such as voltage amplification function, controlling of currents to be injected into the grid, and the maximum power point tracking process. The double peak power is also handled by the design of single-stage inverter as per the below equation

$$p_{\text{grid}} = 2 P_{\text{grid}} \text{Sin}^2(\omega_{\text{grid}}t) \quad (1)$$

where P_{grid} denotes peak grid power and ω_{grid} denotes grid frequency.

A huge weight is added to the inverter by the application of low-frequency transformer in single-stage inverter (operating at low frequency), also, the peak efficiency

losses of 2% are introduced [21]. On the other hand, the most efficient, light in weight and cost-effective converter design is transformer-less or high-frequency transformer based converter design. The line frequency transformers are increasingly replacing by these transformers.

3.2 MSI: Multiple-Stage Inverter

There are more than one power processing stages involved in multistage inverter. The function of DC–AC conversion is executed by the last stage of power processing while the voltage amplification function is performed the first and intermediate stages, the galvanic isolation function is also performed by the intermediate stages in some of the inverters. In [22] a multiple-stage inverter with buck-boost converter is presented. As there is no transformer implemented so it is an example of non-isolated type with input DC voltage of very low range [22]. Another isolated topology is presented in [22] with multiple-stage buck-boost converter, in which transformer is implemented of very high frequency which works on a very low DC voltage. The sine wave of rectified current in both the aforesaid topologies received in the first stage and at the line frequency is transformed into the full sine wave which is switched by the second stage CSI. In both SSI and MSI, the power decoupling process is essential in order to filter out the voltage spikes and to allow the DC component of the input PV source. This decoupling is accomplished by the high capacitance which is offered by a bulky electrolytic capacitor.

4 Conclusion

To adopt PV inverter technology interconnected with the grid in domestic as well as industrial application, the most severe issues are their cost and efficiency. The cost is not only determined by the rated power of the inverter. The variation in technology is found from manufacturer to manufacturer which ultimately leads efficiency differences, variations in size, reliability, weight, etc. These factors have also the same impact on the costing of an inverter. The emerging topologies these days are advanced topologies like energy storing and harmonic filtering devices, power switching which also leads lower cost and higher overall efficiency of power conversion, also, with reduced number of devices. Some standards have been covered in this review which is essential for an inverter to fulfill before implementing in grid-connected PVS. This includes focussing on detection of islanding as well as injection of DC currents into the grid and power quality. The next part focuses on the large areas of PV modules which are connected to the grid through centralized inverters to present historical summary used in the past. In this part many shortcomings are included due to which string inverters came into picture as an emerging technology. Naturally, it was developed by adding more strings, individual DC–DC converter and MPPT

connected to each string and a common DC–AC inverter is connected to them. Thus, the multi-string inverters were highlighted. This has been believed as one of the possible solutions from future perspective. Development of the AC-module was the trend which has been seen in this field, where each PV module along with its own DC–AC inverter is interfaced to the grid.

References

1. Benner JP, Kazmerski L (1999) Photovoltaics gaining greater visibility-IEEE. *Spectrum* 36(9)
2. Standard I (2004) 61000-3-2: 2004, limits for harmonic current emissions. International Electrotechnical Commission, Geneva
3. Libo W, Zhengming Z, Jianzheng L (2007) A single-stage three-phase grid-connected photovoltaic system with modified MPPT method and reactive power compensation. *IEEE Trans Energy Convers* 22(4):881–886
4. Engel S, Riggers K, De Doncker RW (2009) Digital repetitive control of a three-phase at-top-modulated grid tie solar inverter. In: 13th European conference on power electronics and applications, 2009. EPE'09. IEEE, pp 1–10
5. Chinnaiyan VK, Jerome J, Karpagam J (2013) An experimental investigation on a multilevel inverter for solar energy applications. *Int J Electr Power Energy Syst* 47:157–167
6. Eltawil MA, Zhao Z (2010) Grid-connected photovoltaic power systems: technical and potential problems: a review. *Renew Sustain Energy Rev* 14(1):112–129
7. Xiao B, Hang L, Mei J, Riley C, Tolbert LM, Ozpineci B (2015) Modular cascaded H-bridge multilevel PV inverter with distributed MPPT for grid-connected applications. *IEEE Trans Ind Appl* 51(2):1722–1731
8. Abdel-Gawad H, Sood VK (2014) Overview of connection topologies for grid-connected pv systems. In: 2014 IEEE 27th Canadian conference on electrical and computer engineering (CCECE). IEEE, pp 1–8
9. Mahela OP, Shaik AG (2017) Comprehensive overview of grid interfaced solar photovoltaic systems. *Renew Sustain Energy Rev* 68:316–332
10. Chowdhury ASK, Razzak MA (2013) Single phase grid-connected photovoltaic inverter for residential application with maximum power point tracking. In: 2013 2nd international conference on informatics, electronics and vision (ICIEV 2013). IEEE, pp 1–6
11. Sastry J, Bakas P, Kim H, Wang L, Marinopoulos A (2014) Evaluation of cascaded H-bridge inverter for utility-scale photovoltaic systems. *Renew Energy* 69:208–218
12. Islam M, Mekhilef S, Hasan M (2015) Single phase transformerless inverter topologies for grid-tied photovoltaic system: a review. *Renew Sustain Energy Rev* 45:69–86
13. Latran MB, Teke A (2015) Investigation of multilevel multifunctional grid connected inverter topologies and control strategies used in photovoltaic systems. *Renew Sustain Energy Rev* 42:361–376
14. Chong B, Zhang L (2013) Controller design for integrated PV-converter modules under partial shading conditions. *Sol Energy* 92:123–138
15. Calais M, Myrzik J, Spooner T, Agelidis VG (2002) Inverters for single-phase grid-connected photovoltaic systems-an overview. In: 2002 IEEE 33rd annual power electronics specialists conference, 2002. PESC'02, vol 4. IEEE, pp 1995–2000
16. Lysen E, Vigotti R (1998) The international energy agency photovoltaic power systems implementing agreement. *Renew Energy* 15(1–4):60–65
17. Meinhardt M, Cramer G (2000) Past, present and future of grid connected photovoltaic-and hybrid-power-systems. In: IEEE power engineering society summer meeting, 2000, vol 2. IEEE, pp 1283–1288

18. Wilk H, Ruoss D, Toggweiler P (2002) Innovative electrical concepts. International Energy Agency Photovoltaic Power Systems, IEA PVPS, pp 7–07
19. Wuest M, Toggweiler P, Riatsch J (1994) Single cell converter system (SCCS). In: IEEE photovoltaic specialists conference-1994, 1994 IEEE first world conference on photovoltaic energy conversion, 1994, conference record of the twenty fourth, vol 1. IEEE, pp 813–815
20. Riatsch J, Stemmler H, Schmidt R (1997) Single cell module integrated converter system for photovoltaic energy generation. In: European conference on power electronics and applications, vol 1. Proceedings Published by Various Publishers, pp 1–071
21. Attanasio R, Cacciato M, Gennaro F, Scarcella G (2008) Review on single-phase PV inverters for grid-connected applications. In: 4th IASME/WSEAS, international conference on energy, environment, ecosystems and sustainable development (EEESD'08). Algarve, Portugal
22. Saha S, Sundarsingh V (1996) Novel grid-connected photovoltaic inverter. IEEE Proc Gener Trans Distrib 143(2):219–224

IOT Based Smart Writer



Chirag Agarwal and Bhawna Singh

Abstract This Paper is a massive step towards digital India, because digital India does not only include new innovative ideas, but a major part of digital India targets to upgrade existing paper-based infrastructure to a digital medium. The basic idea is to build a *CNC based printing machine* that would help in printing technology. Things are gradually moving towards smarter technology which involves digital signature, new and different ideas in printing technology, and many more. The paper will also help the students involved in art and designing industry to use the real sketching feature (which means that the sketching has been done from one's hand). This paper represents an *Arduino platform project* which requires a software prototype that would help to run the device in a faster and efficient manner. So an application software would be developed using Internet of Things(IOT) to introduce some new features for more advanced technology. This software would help us to control the device from anywhere through our smartphones. The different government organizations require too much flow of documents from one department to another. So here we introduce our android/iOS application which would contain a digitalized signature of a personnel in an encrypted manner. A speech to text converter would be fit inside the device, exclusively for visually impaired personnels which would help them in examinations. The most significant part of this paper represented by the project is that it would consist of a hand scanner, which would help in printing the words in a manner that would be the exact replica of the person's own handwriting.

Keywords Hand sketching feature · Digital signature · Words in the own handwriting

This paper would be a great in leading innovation and "Make in India" initiative.

C. Agarwal (✉) · B. Singh
Manipal University Jaipur, Jaipur, India
e-mail: agarwalchirag35@gmail.com

B. Singh
e-mail: bs2811@gmail.com

© Springer Nature Singapore Pte Ltd. 2020
A. Kalam et al. (eds.), *Intelligent Computing Techniques for Smart Energy Systems*,
Lecture Notes in Electrical Engineering 607,
https://doi.org/10.1007/978-981-15-0214-9_108

1019

1 Technical Details of the Paper

1.1 *Origin of Idea*

Origin of the idea is when we came across some physically disabled people who were unable to do their own jobs. It was very painful to see that the students who were willing to read and write could not do so. So here comes the idea of speech to text through our machine to help such people. The governing body of an organization has many tasks to perform on daily basis which involves many documentation tasks, putting signatures on different documents. These tasks, when piled up together for the signature from different heads of the department become difficult for them to sign on all the documents one by one and the movement of these documents to different departments is also way too time-consuming. So, here we introduce our application which would make the scenario of such kind of environment, easy to handle.

1.2 *Definition of the Problem*

The biggest problem in big organizations is that it involves a lot of paperwork, which is all done in the offline mode. Our idea is to make the society work in a smarter and digital environment. A person has to run from one department to another for the signatures of various directors and heads. Our idea is that each department in an organization has its own authorization of signatures which one (only the employee of that organization) can access through a password via an application downloaded in their personal computers or smartphones. In this way he does not have to go here and there and just sitting from his place he can get various permissions, stamps, and signatures from a particular department. The other issue is that our government is trying their best to give equal opportunities to the physically disabled people to help them in the best way in their learning process. We are introducing our machine which would help them to compete with others in a fair manner (especially in examinations) through the speech to text mechanism.

2 Objectives

2.1 *Printing*

It would involve digital signature, new and different ideas in printing technology, and many more. The project will also help the people involved in art and design industries to use the real sketching feature from this CNC machine. Printing on project cover papers, phone covert-shirt printing, etc.

2.2 Android/IOS Development

Application software will be introduced which will control the functioning of the device.

2.3 App to Machine Communication

The communication will completely be wireless and operated by Gcode files.

2.4 Speech to Text Conversion

Exclusively for physically challenged people. A convertor is to be installed along with the device which would convert human voice to words.

2.5 Signature Printing and Encryption

The key objective is to build a machine which would help us to print different jobs or own important documents from anywhere in the world and the printed document will be the exact replica of the original copy, we will also protect the job printing using a password which will authorize the authenticity of the user and will also provide security to the user.

3 Workplan

3.1 Literature Survey

We have studied many reports and surveys on CNC machine and our idea is to take this machine to a higher platform.

3.2 Writer Installation

In the installation process, we will assemble the parts like stepper motors, servo motors, and Arduino board which will try to make the connections in a more simplified way.

3.3 Arduino Programming

In the programming process, we will program on the Arduino software and will try to make the coding in the best possible manner that would help in meeting the demands as proposed in this project.

3.4 Mobile App Development

An application software would be developed that will have the access to the device from our PC's and smartphones directly.

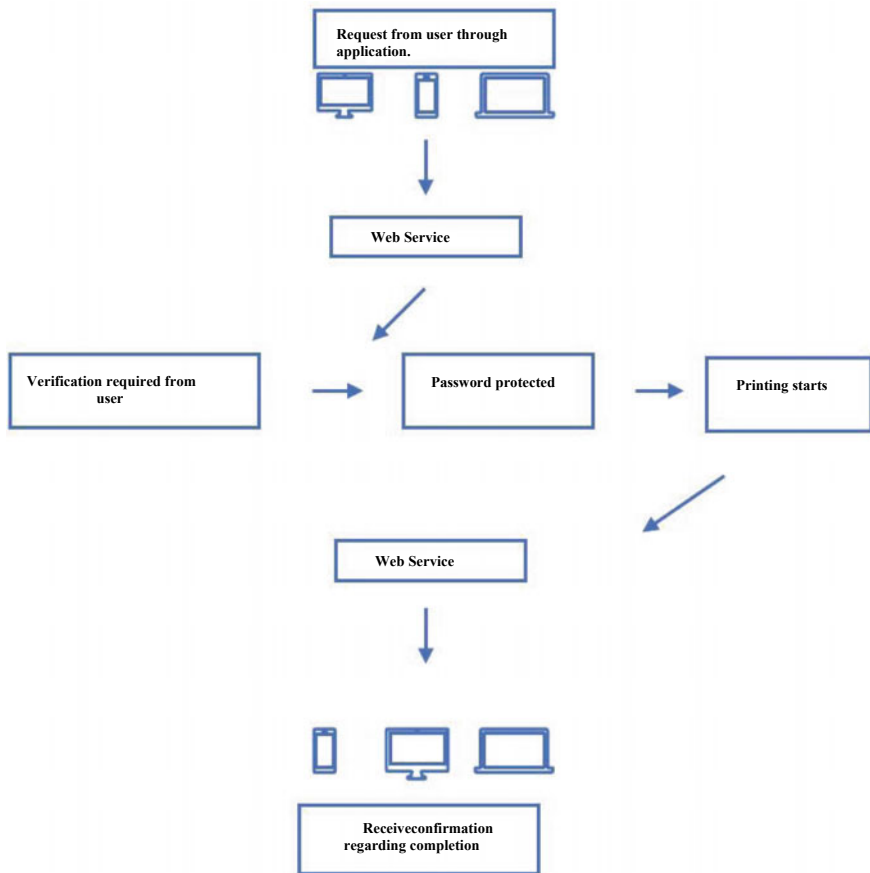
3.5 Paper Representation

The annual report of the paper would be finalized and submitted after the completion.

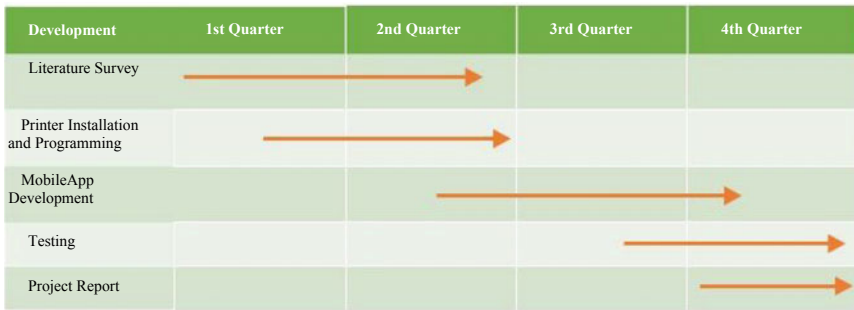
4 Methodology

The machine will be working purely from Arduino C programming. It would also consist of the features of an IOT device. The next task would be developing an application software which would run by the Python Programming. The framework of this project will be based on the different features which involve digital signature, speech to text Conversion, sketching, and many more. These features would be applied through the knowledge of machine learning.

5 Organization of the Work Elements



6 Time Schedule Chart



7 Technologies Used

- 7.1 Knowledge of Embedded and IOT Devices
- 7.2 PCB Designing and Project Installation
- 7.3 Arduino C programming
- 7.4 Raspberry Pi
- 7.5 Android/IOS App Development

A beta version will be deployed and tested by the development team. Once we are satisfied with the results, the project will be handed over to the Govt. for deployment. We will, of course, help in deployment.

8 Conclusion

The paper, thus is a big step towards the simplification of society and implementation of Digital India. It aims mostly at the development of digital infrastructure and providing universal literacy. Our paper can be the possible outcome of the problems as mentioned earlier. The device would consist of modern technology, which makes it different and better from other devices available in the market.

References

1. https://playground.arduino.cc/uploads/Main/arduino_notebook_v1-1.pdf
2. https://en.wikipedia.org/wiki/Numerical_control
3. <https://www.quora.com/How-does-a-CNC-machine-work>

Design and Implementation of Arduino Based Control System for Power Management of Household Utilities



Mahipal Bukya, Aayush Bajaj, Peeyush Garg and Amit Saraswat

Abstract Electricity is an important part of homes and industries. The power demand in our country is increasing rapidly, so the management and efficient utilisation of power are imperative. The efforts were made to provide reliable power supply facility to society as well as industry. In the present scenario, the major portion of domestic power is provided by the conventional power resources but renewable energy resources are taking over the conventional energy resources. The utilisation of solar cell based energy resources are increasing exponentially, so the conventional power sources and solar energy resources are used in hybrid mode especially for running the household utilities. The solar system is preferred over the conventional source due to its economical and environmentally friendly nature. The conventional sources are preferred over the solar energy sources when the solar cell-based system is not able to give sufficient power. This paper will analyse the impact of the solar as well as conventional power management using Arduino based control system for household utilities. The Arduino based hardware is designed to use solar power optimally. The voltage sensor will measure the battery voltage and display it on LCD. Then the battery voltage is logically used by Arduino based control unit to run the household utilities.

Keywords Conventional power source · Solar power source · Hybrid system · Arduino based control unit · Household utilities

1 Introduction

An outline is given here about the energy management in building which dynamically manages its conventional power and the solar power utilisation. These are used for optimal uses of solar power and to reduce the consumption of conventional power. It allows you to reduce your total energy expenditure of conventional power

M. Bukya (✉) · A. Bajaj · P. Garg · A. Saraswat
Department of Electrical Engineering, Manipal University Jaipur, Jaipur, India
e-mail: mahipalbhukya@gmail.com

© Springer Nature Singapore Pte Ltd. 2020
A. Kalam et al. (eds.), *Intelligent Computing Techniques for Smart Energy Systems*,
Lecture Notes in Electrical Engineering 607,
https://doi.org/10.1007/978-981-15-0214-9_109

1025

without compromising comfort and safety. It can be ensured building security, building utilities, automatically controlling air conditioning and lighting, safety, water by reducing the amount of conventional power.

As 15–25% of electrical energy gets wasted due misuse of appliances. Mostly, the electrical appliances or loads are plugged-in but it is not in use. On a larger level like hospitals, institutions like schools and colleges, commercial complexes and residential areas electrical loads are forgotten unplugged for no reason and the misuse of power continues. So it is a waste of time and money. To make the best use of electrical energy, solar as well as convectional power management using Arduino based control system for household utilities is required. In this context many researchers have developed smart home management systems in order to facilitate and improve the living standards of human beings.

2 Environmental Impact of Conventional Energy Resources

In the present system, the generation of conventional power is more as compared to the power generation from renewable energy sources. The conventional power generation is produced from coal, petroleum, nuclear and natural gas that contain hydrocarbon. The consumption of world's total electrical energy is 132,000 terawatt-hours (TWh) in 2012 was a very large amount 3,044.4468 KWh per capita [1]. Only India has been generated about 880 billion units of electrical energy in 2012 of which 66% came from conventional energy sources and 12% from non-conventional sources [2]. These resources on combustion give out gases such as CO₂ and methane, which are responsible for global warming. Pollution not only occurs by their usage but also during their process of extraction, refining, transportation and storage of such resources. The conventional power generation is responsible for the pollution, for the environment protection we have to reduce the dependency on conventional resources. So alternative resources are like solar power, wind power, tidal, etc. use these sources and make renewable hybrid integration and generate more renewable power connected to the grid and reduce the dependency on conventional power generation [3, 4].

3 Solar Power and Scope in India

Solar power is a clean and abundant source of energy which makes it a promising choice over the conventional sources of power. Solar energy can be used in the form of thermal as well as photovoltaic route which converts solar energy into electricity that can be used for generation of electricity. India has great potential to generate solar energy.

India is located in the sunny belt of earth, and it is benefit to generate solar energy. Due to geographical location and sunny belt earth, receives solar radiation almost for the duration of the year, which amounts to nearly 3,000 h of sunshine. This is

Table 1 Statewise solar power generation

S. No.	State	Photovoltaic capacity (CNIW)	Solar thermal capacity (MW)
1.	Rajasthan	43	400
2.	Gujarat	722	45
3.	Maharashtra	133	–
4.	Karnataka	10	–
5.	Andhra Pradesh	20.5	–
6.	Uttarakhand	4	–
7.	Punjab	5	–
8.	Haryana	7.8	–
9.	Uttar Pradesh	11	–
10.	Jharkhand	16	–
11.	Chhattisgarh	4	–
12.	Madhya Pradesh	7.25	–
13.	Odisha	11	–
14.	Tamil Nadu	12	–
Total		1006.55	445

equal to more than 5,000 trillion kWh. almost every part of India receives 4–7 kWh of solar radiation per sq metres [5]. Solar energy is neat and pollution less. When it is in use, it will not release CO₂ and other gases which pollute the air. Hence, it is very suitable for the country, the population of India is very high as compared to the other countries in the world. So it needs to manage the electrical power utilisation and require innovative ideas to explore the energy resource to generate power which is environment-friendly. Table 1 shows state wise solar power generation [5–7].

4 Experimental Setup

The project module is the combination of conventional energy and solar energy. The solar panel is used for generation of solar energy and conventional energy is taken from supplied electricity board. A 12 V DC battery is used to store the solar energy. I have connected three relays as switching power between battery and conventional source which is further connected to an LCD and Arduino UNO both on separate PCB. An inverter circuit board with IC SG3525 is used to convert 12 V DC of battery to 220 V AC of load. IC ULN2003 is used to feed signals to relay from Arduino UNO. For load, three LED light bulbs are used. Basic components such as resistors, connecting wires and pins are used as per requirement as shown in Fig. 2.

The results were observed at various stages as per the voltage level of the battery (Figs. 1 and 3).

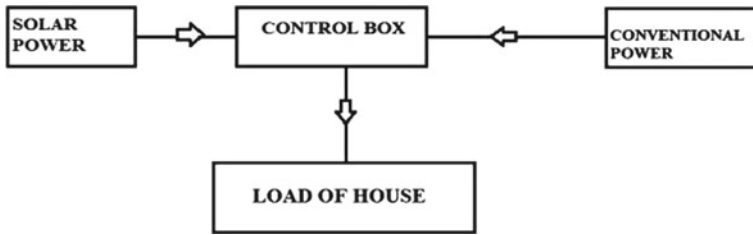


Fig. 1 Block diagram of power management system

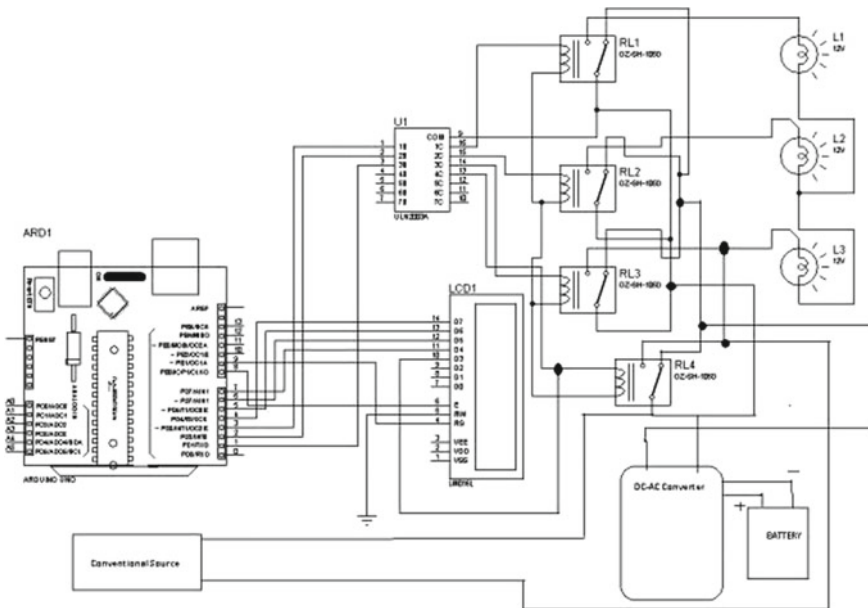


Fig. 2 Circuit diagram of power management system

5 Results and Discussion

Case-I: When the voltage level of battery is greater than 12 V. All three lamps load are supplied by solar panel through inverter. Power supplied by electricity board is zero. For this case 1 1 1 are displayed on LCD screen as shown in Fig. 4.

Case-II: When the voltage level of battery is less than 12 V and greater than 11.5 V. Two lamps load are supplied by solar panel through inverter and one lamp is powered by electricity board. For this case 0 1 1 are displayed on LCD screen as shown in Fig. 5.

Case-III: When the voltage level of the battery is less than 11 V and greater than 10.5 V. one lamp load is supplied by solar panel through inverter and two lamps are

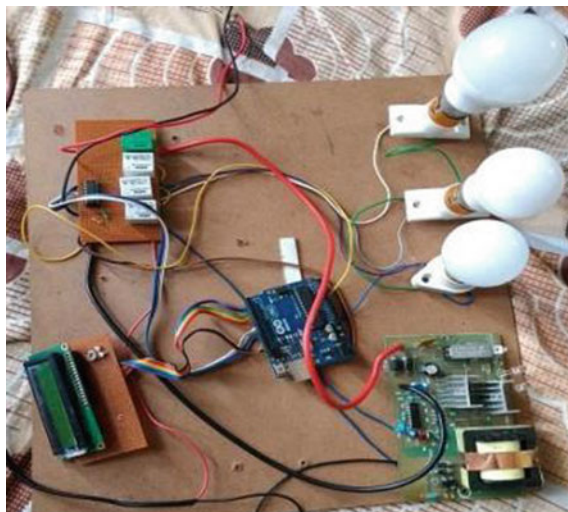


Fig. 3 Real time experimental setup



Fig. 4 First battery level range

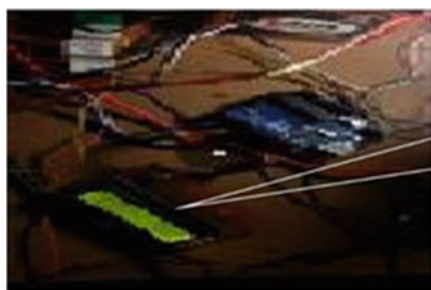


Fig. 5 Second battery level range

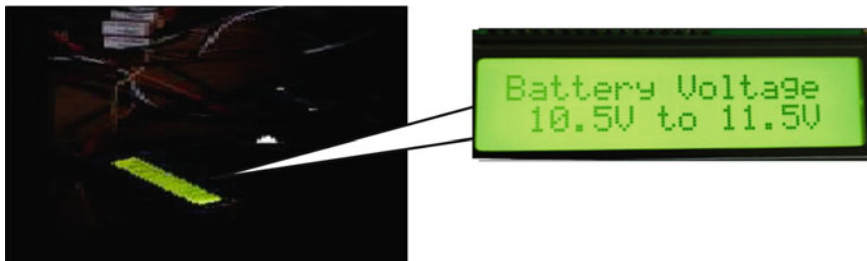


Fig. 6 Third battery level range

powered by electricity board. For this case 0 0 1 are displayed on LCD screen as shown in Fig. 6.

Case-IV: When the voltage level of the battery is less than 10.5 V. All Three lamps load are supplied by electricity board For this case 0 0 0 are shown in LCD screen in Fig. 7. All outputs are summarized in Table 2.

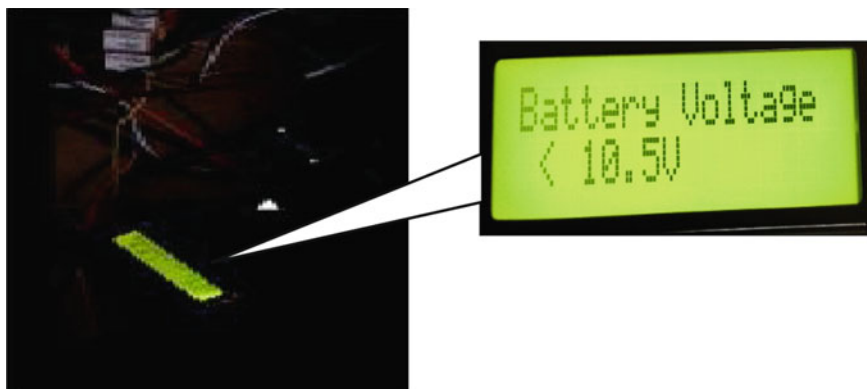


Fig. 7 Fourth battery level range

Table 2 Power consume with PV and without PV system from electricity board in 10 h

Load (W)	Power consume with PV system	Power consume without PV system	% power saving
0	0	0	0
10	0.040 W	0.10 W	60
20	0.13 W	0.20 W	35
30	0.2625 W	0.30 W	12.5

6 Conclusion

Due to an increasing electrical energy demand in home and industries, it is necessary to generate solar power and require power management system in home and industries to mitigate the demand. It has been designed and implemented Arduino based control system for power management of household utilities, the designed project module is very effective for power management. It is economic and delivers reliable power to the household's light duty appliances. The designed system was working properly by sharing the power to the domestic load with the conventional power supply system. As per the analysis this designed power management system saved the conventional power up to 12–40%, depending on the connected load.

References

1. Mahipal B, Phulia M, Bhargava G, Sharma S, Singh CS, Singla P (2015) Novel method of integrating solar-wind-tidal power with grid. *Adv Res Electr Electron Eng* 2(7):18–22. Print ISSN: 2349-5804; Online ISSN: 2349-5812
2. Government of India, The National Electricity Plan. Ministry of New and Renewable Energy, Jan 2012
3. Kadioğlu S, Tellioglu Z (1996) Using of energy sources and environmental effects. In: TMMOB 1st energy symposium. Ankara, Turkey, November
4. Unal O, Karagoz S, Ulger G, Yuce E, Erkul S (2008) How expensive the global warming. In: 2nd international economics conference. Eskisehir, Turkey
5. Singh BR, Singh O (2016) Future scope of solar energy in India. *SAMRIDDHI: J Phys Sci, Eng Technol* 8. <https://doi.org/10.18090/samriddhi.v8i1.11408>
6. Mahipal B, Venugopal Rao P, Swetha T, Babu Naik G, Kumar CN (2013) A new technique to find the effect of active power loading on voltage stability and algorithm to improve voltage stability of radial and meshed power systems. *J Inf Eng Appl* 3(5)
7. Bhukya M, Kumar CN (2014) Text book on power system voltage stability: for radial and meshed power systems (ISBN 978-3-659-22276-4, LAP LAMBERT Academic Publishing, Germany)

Interfacing Python with DIgSILENT Power Factory: Automation of Tasks



Divya Rishi Shrivastava, Shahbaz Ahmed Siddiqui and Kusum Verma

Abstract The DIgSILENT Power Factory is an engineering tool for the analysis of distribution, transmission, and industrial electrical power systems. “DIgSILENT” is an acronym for “**D**igital **S**imuLation of **E**lectrical **N**eTworks”. This software is an advanced integrated and interactive package dedicated to electrical power system and control analysis so as to achieve planning and operational optimization objectives. The package can be interfaced with programming languages and software for performing tasks for better utility. Python is a high-level programming language with legible syntax and comes with open-source license. This paper brings the methodology for interfacing of Python with DIgSILENT Power Factory for automation of tasks. The paper provides various code snippets for interfacing Python with software package and task automation.

Keywords Power system · DIgSILENT Power Factory · Python interpreter

1 Python Interpreter

In Power Factory, no Python interpreter is preinstalled. An installation of Python interpreter is mandatory and can be downloaded from www.python.org/downloads/. The interpreter comes with both 32-bit and 64-bit versions and has to be used for Power Factory 32-bit and Power Factory 64-bit, respectively with default settings [1–3]. Wherein *powerfactory.pyd* interfaces with *PowerFactory API*. Figure 1 shows the snapshot for configuring Python 3.6 with Power Factory. The next step is to create new Python script.

D. R. Shrivastava (✉) · S. A. Siddiqui
Manipal University Jaipur, Jaipur 303007, India
e-mail: divyarishi.shrivastava@jaipur.manipal.edu

K. Verma
MNIT Jaipur, Jaipur 302017, India

© Springer Nature Singapore Pte Ltd. 2020
A. Kalam et al. (eds.), *Intelligent Computing Techniques for Smart Energy Systems*,
Lecture Notes in Electrical Engineering 607,
https://doi.org/10.1007/978-981-15-0214-9_110

1033

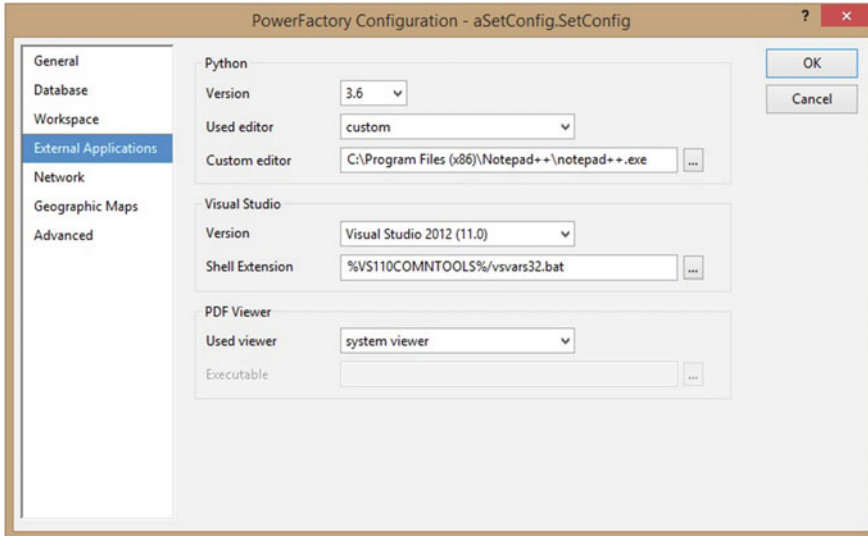


Fig. 1 Configuring Python 3.6 with Power Factory [2]

2 Python Power Factory Module

Power Factory can now be imported from system into Python as shown in Fig. 2. The code snippet provided imports powerfactory and assigns *pf* as its name. This name so provided is the short abbreviation and can now be used instead of powerfactory in current Python script. Here, it is to be understood that the user can use any short name instead of *pf* and then has to use it wherever needed. This code snippet gives access to Python PowerFactory module.

3 Python Power Factory Module Usage

Now, it becomes important to enter into Power Factory environment and for that, the following code snippet can be used as shown in Fig. 3. Python requires “.” operator for gaining access in objects for their element parameters. Using “app”, we can now

```

1  import os,sys
2  DIG_PATH='C:\Program Files\DIGSILENT\Power Factory 2017 SP2'
3  import powerfactory as pf
  
```

Fig. 2 Code snippet for importing Power Factory and assigning name as pf


```

1 import os,sys
2 DIG_PATH='C:\Program Files\DIGSILENT\Power Factory 2017 SP2'
3 import powerfactory as pf
4 app = pf.GetApplication()

```

Fig. 3 Code snippet for gaining access in powerfactory environment

```

1 import os,sys
2 DIG_PATH='C:\Program Files\DIGSILENT\Power Factory 2017 SP2'
3 import powerfactory as pf
4 app = pf.GetApplication()
5 app.ResetCalculation()
6 # Setting all scales to 1.
7 Loads=app.GetCalcRelevantObjects('*.*.ElmLod')
8 APL=[322,500,233.8,522,7.5,320,329,158,628,274,247.5,308.6,224,139,281,206,283.5,9.2,1104]
9 # APL is real power component of Load
10 AQL=[2.4,184,84,176,88,153,32.3,30,103,115,84.6,-92.2,47.2,17,75.5,27.6,26.9,4.6,250]
11 # AQL is quadrature power component of Load
12 iter=0
13 for Load in Loads:
14     Load.scale0=1
15     Load.plini=APL[iter]
16     Load.qlini=AQL[iter]
17     iter+=1

```

Fig. 4 Code snippet for changing loads one by one

globally access powerfactory functionality. For an example, Fig. 4 shows a code snippet for scaling loads to unity and then assigning loads one by one iteratively for New England 39 Bus system [1, 2, 4, 5]. Similarly, we can print output directly into csv files using Python extensions as shown in Fig. 5. In this code snippet, first a function is created for getting time and variable as output. Then, at the desired location, results are exported in csv file. The available code snippet is for dynamic simulation.

It is to be understood that the desired location can be created pre-hand in the script itself or it can create the directory externally. Adding or creating a desired location internally within a script can be done by following code snippet shown in Fig. 5. In the given code, it is ensured that first column gets time data and subsequent column can be appended by desired data, respectively, to be mentioned in the code. Tasks like fault initiation and fault clearance at specified time can also be implemented as shown in Fig. 6.

```

1  def setupSimulation(comInc, comSim):
2      comInc.iopt_sim = "rms"
3      comInc.iopt_show = 0
4      comInc.iopt_adapt = 0
5      comInc.ipolate=0
6      comInc.dtgrd = 1/60
7      comInc.tstart = -0.1
8      comSim.tstop = 10
9  def runSimulation(comInc, comSim):
10     app.EchoOff()
11     comInc.Execute()
12     app.EchoOn()
13     comSim.Execute()
14  def addShcEvent(obj, sec, faultType):
15     faultFolder = app.GetFromStudyCase("Simulation Events/Fault.IntEvt")
16     event = faultFolder.CreateObject("EvtShc", obj.loc_name)
17     event.p_target = obj
18     event.time = sec
19     event.i_shc = faultType
20     shcBus = app.GetCalcRelevantObjects("Bus 05.ElmTerm") [0]
21     time1 = 0 # event time = 0 sec
22     clearTime1 = 12/60 # Fault cleared in 12 cycles
23     faultType1 = 0 # 3ph shc
24     faulClear1 = 4 #Fault type 4 is fault clearing
25     # Ends
26     comInc = app.GetFromStudyCase("ComInc")
27     comSim = app.GetFromStudyCase("ComSim")
28     comInc.Execute()
29     clearSimEvents()
30     setupSimulation(comInc, comSim)
31     addShcEvent(shcBus, time1, faultType1)

```

Fig. 5 Code snippet for fault initiation and clearance at specified time

4 Conclusion

DIgSILENT Power Factory is a software package dedicated to electrical power system and control utility so as to achieve optimal planning and operational objectives. The paper provides various code snippets for interfacing Python with Power Factory package. For tasks like entering powerfactory environment, changing load one by one iteratively, fault initiation and clearance at specified timings, and exporting result into csv files are successfully carried out in the paper in the form of code snippets. These snippets can be used as it is or can be modified by the user as per the requirements.

```

1 def get_dynamic_results(elm_name,var_name):
2     # get network element of interest
3     element=app.GetCalcRelevantObjects(elm_name)[0]
4     # load results from file
5     app.ResLoadData(elmres)
6     # find colom in results file that holds result of interest
7     col_index=app.ResGetIndex(elmres,element,var_name)
8     # get number of rows (points in time) in the result file
9     n_rows=app.ResGetValueCount(elmres,0)
10    # read results and time and store them in lists
11    time=[]
12    var_values=[]
13    for i in range(n_rows):
14        time.append(app.ResGetData(elmres,i,-1)[1])
15        var_values.append(app.ResGetData(elmres,i,col_index)[1])
16
17    return time,var_values
18    PATH1=('G:/DRS/Data Folder')
19    if not os.path.exists(PATH1): os.makedirs(PATH1)
20    # Select to add Bus Voltage Angles in Degrees
21    # Calling get_dynamic_results
22    t,bus1_deg=get_dynamic_results('Bus 01.ElmTerm','m:phiu')
23    t,bus2_deg=get_dynamic_results('Bus 02.ElmTerm','m:phiu')
24    t,bus3_deg=get_dynamic_results('Bus 03.ElmTerm','m:phiu')
25    t,bus4_deg=get_dynamic_results('Bus 04.ElmTerm','m:phiu')
26    .....so on
27    # store Bus Voltage Angles in Degrees in CSV file
28    with open('G:/DRS/Data Folder/Bus_voltage_Angles.csv','w',newline='') as csvfile:
29        csvwriter=csv.writer(csvfile)
30        csvwriter.writerow(['t','bus1_deg','bus2_deg','bus3_deg','bus4_deg',.....])
31        for row in zip(t,bus1_deg,bus2_deg,bus3_deg,bus4_deg,.....):
32            csvwriter.writerow(row)

```

Fig. 6 Code snippet exporting results in csv file

References

1. User manual, DIGSILENT Power Factory (2017)
2. <https://www.digsilent.de/en/>
3. <https://www.python.org/>
4. Technical reference documentation python function reference, DIGSILENT Power Factory (2017)
5. Shrivastava DR, Siddiqui SA, Verma K (2017) Optimal PMU placement for coordinated observability of power system under contingencies. In: IEEE international proceedings on circuits and systems. IEEE, Trivandrum, pp 334–339

Recent Development in Perovskite Solar Cell Based on Planar Structures



Anupam Agrawal, Shahbaz Ahmed Siddiqui, Amit Soni
and Ganesh D. Sharma

Abstract Perovskite materials can revolutionize the solar energy industry due to their unique features and most importantly, the efficiency of perovskite solar cell (PSC) has been enhanced to above 21% (with TiO₂ mesoporous structure) within few years. There are increasing studies focusing on the area of planar structures (n-i-p and p-i-n) of PSC because of its processibility for large-scale production. Particularly, p-i-n (inverted) structure has attracted attention because it overcomes the drawback of mesoporous and n-i-p (regular) structure of PSCs and reached the power conversation efficiency (PCE) above 20%. In this paper, we present the introduction and classification of photovoltaic (PV) technologies, a brief description of the planar structure of PSCs, and recent improvement in the inverted structure of PSCs.

Keywords Photovoltaic technology · Planar structure · p-i-n structure

1 Introduction

Individuals require more energy to make better living surroundings because of rise in population, technologic, and economic development. A few years back, fuelwood, animal residues, and agricultural waste were utilized. With progressing time, natural gas, coal, petroleum, etc., are consuming very rapidly to fulfill the energy necessities.

A. Agrawal (✉) · A. Soni

Department of Electrical Engineering, Manipal University Jaipur, Jaipur, Rajasthan, India

e-mail: anupamagrawal123@gmail.com

A. Soni

e-mail: amit.soni@jaipur.manipal.edu

S. A. Siddiqui

Department of Mechatronics Engineering, Manipal University Jaipur, Jaipur, Rajasthan, India

e-mail: shahbazahmed.siddiqui@jaipur.manipal.edu

G. D. Sharma

Department of Physics, LNM Institute of Information Technology, Jamdoli, Jaipur, Rajasthan, India

e-mail: gdsharma273@gmail.com

© Springer Nature Singapore Pte Ltd. 2020

A. Kalam et al. (eds.), *Intelligent Computing Techniques for Smart Energy Systems*,

Lecture Notes in Electrical Engineering 607,

https://doi.org/10.1007/978-981-15-0214-9_111

Usage of commercial fuels are causing a progression of environmental issues, for example, environmental change, worldwide temperature alteration, air contamination, and acid rain [1–3]. To overcome the above issues, improvement of renewable energy technologies is required, keeping in mind the end goal to manage the political, financial, and ecological difficulties that are associated with producing electricity. With the help of photovoltaic (PV) cells, the conversion of solar energy into electricity is considered one of the most encouraging technology among all renewable energies.

The PV solar energy is standout among the most developing businesses everywhere throughout the globe, and so as to keep that speed, new improvements have been rising with regards to material utilization, energy utilization to fabricate the materials, device outline, manufacturing technologies, and novel ideas to upgrade the worldwide efficiencies of the solar cells [4–6].

As indicated in [7, 8], there is a range of PV cell technologies (using different types of materials) in the commercial places and a significantly large number will be accessible in the near future. Figure 1 shows different types of PV solar cells and also indicates the different generations of PV cell technologies with their advantages (A) and disadvantages (D). A new material class, quantum dot solar cell (QDSC), organic solar cell (OSC), and PSC, can address the issues like consumption of fossil fuels and environmental challenges, with the end goal that minimal cost PV modules may turn into a reality. Among these materials, PSCs have been given much consideration by scientists because of its simple fabrication steps, low cost, and most vital, its efficiency growth within the 8 years of extensive research.

In the PV solar cells, perovskite materials have become the most popular because of their distinctive qualities, for example, optimal bandgap, high absorption coefficient, and high defect tolerance. These qualities lead to the stunning increment in PCE from 3.8% [9] to above 22% [10] in few years. From last few years, several research have been carried out on planar structure [11] and mesoporous structure [12] of PSCs based on n-type TiO_2 layer used as electron transport layer (ETL). The efficiency achieved by these architectures were remarkable. Still, mesoporous structure and n-i-p structure show some hindrances. Recently, p-i-n structure [13] that utilizes p-type materials as bottom and n-type materials as top charge transport layer have become another emerging structure. The whole concept of this structure is derived from OSCs. The p-i-n structure of PSCs have shown efficiencies greater than 20% and overcame the difficulties of mesoporous structure and n-i-p structure.

The quick advancement in the area of planar structure of PSC has now made it essential to survey the present scenario of planar structure of PSCs by concentrating on p-i-n structure and their materials, so as to update and encourage the upcoming research works. This paper is summarized as development and basics on planar structures of PSCs, surveying current development on p-i-n structure of PSCs including efficiency, device structure, open-circuit voltage, and fill factor.

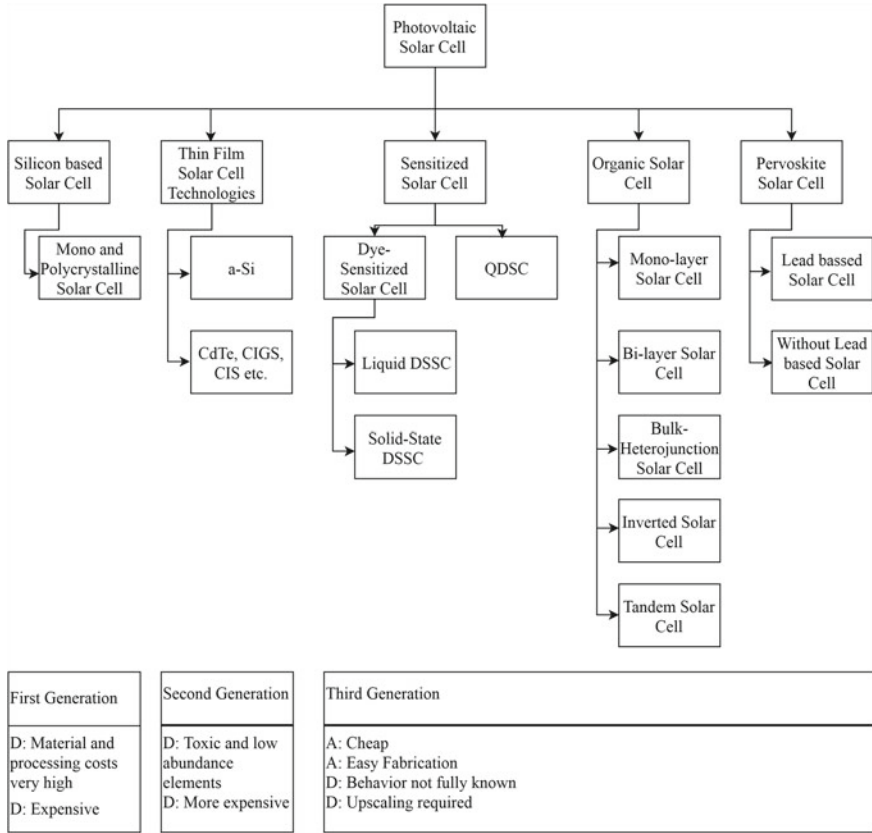


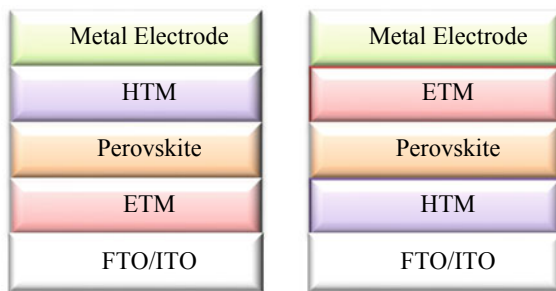
Fig. 1 Schematic representation of the different generations of the PV cell technologies

2 Planar Structure

In 2013, Sum and Snaith individually reported that the PSCs based on methylammonium showed ~100 nm for $\text{CH}_3\text{NH}_3\text{PbI}_3$ and ~1000 nm for $\text{CH}_3\text{NH}_3\text{PbI}_{3-x}\text{Cl}_x$ long charge carrier diffusion lengths [14, 15]. Then, Dong et al. in 2015, found that single crystals of $\text{CH}_3\text{NH}_3\text{PbI}_3$ reached >175 μm diffusion lengths [16]. Further research proved that perovskites show ambipolar behavior. It means that the perovskite materials are capable of transporting both charges (holes and electrons) between the two electrodes [14]. All of these outcomes showed that a planar structure of PSC was feasible.

In 2013, Guo et al. reported the first effective demonstration of the planar structure showing PCE of ~4% [17]. This PCE of planar structure reported at that time was poor because of poor absorption of the perovskite layer and lower film quality [17]. Development occurred in same year, 2013, Snaith et al. achieved 15.4% PCE with the help of dual-source vapor deposition [11]. After that, the PCE of the planar structure

Fig. 2 Planar structures of PSCs: **a** n-i-p structure and **b** p-i-n structure



reached $\geq 19\%$ with the help of interface engineering [18]. Above results proved that the planar structure might reach similar PCE as the mesoporous structure.

The planar structure can be categorized on the basis of contact layer (either HTL or ETL) that is used on the bottom. Hence, it can be separated into two structures, n-i-p structure and p-i-n structure shown in Fig. 2a, b, respectively. Today's most researcher is working on p-i-n structure because it overcomes the demerits of mesoporous structure and n-i-p structure and shows comparable results. In mesoporous structures, TiO_2 scaffold is achieved by sintering process having temperature greater than 450°C . This will ultimately lead to high cost of device and also not suitable with flexible substrates. The TiO_2 -based n-i-p structures are usually affected with a large degree of J-V hysteresis due to charge accumulation induced by ion migration in the perovskite layer [19, 20]. While, p-i-n structures have shown flexibility, processing at low temperature, and negligible effect of J-V hysteresis.

3 The Inverted Planar Structure

This structure is derived from OSCs. The charge transport layers used in OSCs were effectively moved into PSCs. Most researchers have reported negligible hysteresis in the p-i-n structure of PSC when fullerene was used as ETL [21–23]. The p-i-n structure of PSCs have shown less hysteresis due to following reasons: (i) the ion migration may be blocked by trap states which are made from fullerene halide radical [24]. (ii) with the help of pinholes and grain boundaries, fullerenes possibly diffuse into the perovskite material [25], which results in enlarged interface area of perovskite and fullerene. Hence, the structure becomes same as that of the mesoporous structure of PSCs with decreased hysteresis. (iii) the electron could be extracted more efficiently with fullerenes [26], consequently preventing charge accumulation at the boundary and reducing the hysteresis.

The device structure of first planar p-i-n structure of PSCs is derived from OSCs [17]. The most commonly used organic charge transport layers, i.e., PEDOT:PSS and fullerene derivative were directly employed in a PSC as an HTL and ETL, respectively. In 2013, suitable selection of fullerene derivative and optimization of processing conditions of the perovskite layer led to an effective PCE of 3.9%. Later,

Table 1 Development of the p-i-n structure of PSCs

S.No	Device structure (HTL/ETL)	PCE (%)	V _{OC} (V)	J _{SC} (mA/cm ²)	FF
1	PEDOT:PSS/PC ₆₁ BM/BCP [17]	3.9	0.60	10.32	0.63
2	PEDOT:PSS/PC ₆₁ BM [27]	7.4	0.91	10.8	0.76
3	NiO _x /PC ₆₁ BM/BCP [28]	7.8	0.92	12.43	0.68
4	PEDOT:PSS/PC ₆₁ BM/TiO _x [26]	9.8	0.94	15.8	0.66
5	PEDOT:PSS/PCBM/C ₆₀ /BCP [29]	10.1	0.88	15.9	0.722
6	PEDOT:PSS/P3TMAHT [30]	11.28	0.899	17.10	0.741
7	PEDOT:PSS/PCBM/bis-C ₆₀ [31]	11.8	0.92	17.5	0.73
8	PEDOT:PSS/PEIE [30]	12.01	0.899	17.32	0.77
9	PEDOT:PSS/PCBM/TIPD [32]	12.95	0.89	22.57	0.645
10	PEDOT:PSS/PCBM/Rhodamine101/ LiF [33]	13.2	1.01	17.72	0.73
11	PEDOT:PSS/PCBM [34]	13.3	0.9	18.5	0.80
12	PEDOT:PSS/PCBM/PDINO [35]	14.09	0.95	18.8	0.78
13	PEDOT:PSS/PCBM/PN4 N [36]	15.0	1.00	20.61	0.72
14	PEDOT:PSS/C ₆₀ /Bphen [37]	15.4	1.02	20.9	0.722
15	PEDOT:PSS/PC ₆₁ BM/ZnO [38]	15.9	0.97	20.5	0.801
16	NiO _x /ZnO [39]	16.1	1.01	21.0	0.76
17	PEDOT:PSS/PCDTBT/PC ₆₁ BM/LiF [40]	16.5	1.05	21.9	0.72
18	PEDOT:PSS/PC ₆₁ BM/ZnO [41]	16.8	1.02	22.0	0.74
19	NiO & PCBM/PCBDAN [42]	17.2	1.08	20.71	0.77
20	PTAA:F4-TCNQ/Teflon/C ₆₀ /BCP [43]	18.1	1.05	22.8	0.756
21	NiMgLiO/PCBM/Ti(Nb)O _x [44]	18.3	1.083	20.4	0.827
22	NiO _x /PCBM/TiAcac [45]	18.36	1.076	22.14	0.776
23	NiO _x /PCBM/ZrAcac [45]	18.69	1.079	22.17	0.781
24	NiO/C ₆₀ /SnO ₂ [46]	18.8	1.12	21.8	0.77
25	PTAA/IDIC/C ₆₀ /BCP [47]	19.5	1.11	22.96	0.765
26	PTAA:F4-TCNQ/PS plastic foam/C ₆₀ /BCP [43]	19.6	1.07	22.9	0.803
27	PTAA:F4-TCNQ/PS/C ₆₀ /BCP [43]	20.3	1.10	22.9	0.806
28	PTAA/choline chloride/C ₆₀ /BCP [48]	20.59	1.13	22.99	0.791

Sun and his team achieved thick and dense perovskite film by using two-step sequential deposition into the planar structure and improved the PCE to 7.41% [27]. After 2014, several efforts that include film formation, interface engineering, etc., were made to increase the efficiency. The main development of the p-i-n structure of PSCs is summarized in Table 1.

4 Summary

The p-i-n structure of PSCs has reached efficiency above 20% that is comparable to the n-i-p structure and mesoporous structure of PSCs. The p-i-n structure of PSCs have advantages such as compatible to roll-to-roll production, high stability, and negligible effect of hysteresis. It is however by no means claimed as comprehensive survey but it gives recent progress of planar p-i-n structures of PSCs including details of device structure, efficiency, open-circuit voltage, short-circuit current density, and fill factor. Overall, planar p-i-n structure of PSC can emerge as efficient and stable structure as compared to the other structures of PSC.

References

1. Peng J, Lu L, Yang H (2013) Review on life cycle assessment of energy payback and greenhouse gas emission of solar photovoltaic systems. *Renew Sustain Energy Rev* 19:255–274
2. Bhattacharya T, Chakraborty AK, Pal K (2014) Effects of ambient temperature and wind speed on performance of monocrystalline solar photovoltaic module in Tripura, India. *J Sol Energy* 2014
3. Tyagi V, Rahim NA, Rahim N, Jeyraj A, Selvaraj L (2013) Progress in solar PV technology: research and achievement. *Renew Sustain Energy Rev* 20:443–461
4. Jager-Waldau A (2006) European photovoltaics in worldwide comparison. *J Non-Cryst Solids* 352(9–20):1922–1927
5. Parida B, Iniyana S, Goic R (2011) A review of solar photovoltaic technologies. *Renew Sustain Energy Rev* 15(3):1625–1636
6. Razykov TM, Ferekides CS, Morel D, Stefanakos E, Ullal HS, Upadhyaya HM (2011) Solar photovoltaic electricity: current status and future prospects. *Sol Energy* 85(8):1580–1608
7. Lacerda JS, van den Bergh JC (2016) Diversity in solar photovoltaic energy: implications for innovation and policy. *Renew Sustain Energy Rev* 54:331–340
8. Gangopadhyay U, Jana S, Das S (2013) State of art of solar photovoltaic technology. In: *Conference papers in science*, vol 2013. Hindawi
9. Kojima A, Teshima K, Shirai Y, Miyasaka T (2009) Organometal halide perovskites as visible-light sensitizers for photovoltaic cells. *J Am Chem Soc* 131(17):6050–6051
10. Saliba M, Matsui T, Seo JY, Domanski K, Correa-Baena JP, Nazeeruddin MK, Zakeeruddin SM, Tress W, Abate A, Hagfeldt A et al (2016) Cesium containing triple cation perovskite solar cells: improved stability, reproducibility and high efficiency. *Energy Environ Sci* 9(6):1989–1997
11. Liu M, Johnston MB, Snaith HJ (2013) Efficient planar heterojunction perovskite solar cells by vapour deposition. *Nature* 501(7467):395

12. Kim HS, Lee CR, Im JH, Lee KB, Moehl T, Marchioro A, Moon SJ, Humphry-Baker R, Yum JH, Moser JE et al (2012) Lead iodide perovskite sensitized all-solid-state submicron thin film mesoscopic solar cell with efficiency exceeding 9%. *Sci Rep* 2:591
13. Meng L, You J, Guo TF, Yang Y (2015) Recent advances in the inverted planar structure of perovskite solar cells. *Acc Chem Res* 49(1):155–165
14. Xing G, Mathews N, Sun S, Lim SS, Lam YM, Gratzel M, Mhaisalkar S, Sum TC (2013) Long-range balanced electron-and hole-transport lengths in organic-inorganic $\text{CH}_3\text{NH}_3\text{PbI}_3$. *Science* 342(6156):344–347
15. Stranks SD, Eperon GE, Grancini G, Menelaou C, Alcocer MJ, Leijtens T, Herz LM, Petrozza A, Snaith HJ (2013) Electron-hole diffusion lengths exceeding 1 micrometer in an organometal trihalide perovskite absorber. *Science* 342(6156):341–344
16. Dong Q, Fang Y, Shao Y, Mulligan P, Qiu J, Cao L, Huang J (2015) Electron hole diffusion lengths $>175 \mu\text{m}$ in solution grown $\text{CH}_3\text{NH}_3\text{PbI}_3$ single crystals. *Science* 376:5760
17. Jeng JY, Chiang YF, Lee MH, Peng SR, Guo TF, Chen P, Wen TC (2013) $\text{CH}_3\text{NH}_3\text{PbI}_3$ perovskite/fullerene planar-heterojunction hybrid solar cells. *Adv Mater* 25(27):3727–3732
18. Zhou H, Chen Q, Li G, Luo S, Song TB, Duan HS, Hong Z, You J, Liu Y, Yang Y (2014) Interface engineering of highly efficient perovskite solar cells. *Science* 345(6196), 542–546
19. Xiao Z, Yuan Y, Shao Y, Wang Q, Dong Q, Bi C, Sharma P, Gruverman A, Huang J (2015) Giant switchable photovoltaic effect in organometal trihalide perovskite devices. *Nat Mater* 14(2):193
20. Chen B, Yang M, Zheng X, Wu C, Li W, Yan Y, Bisquert J, Garcia Belmonte G, Zhu K, Priya S (2015) Impact of capacitive effect and ion migration on the hysteretic behavior of perovskite solar cells. *J Phys Chem Lett* 6(23):4693–4700
21. Heo JH, Han HJ, Kim D, Ahn TK, Im SH (2015) Hysteresis-less inverted $\text{CH}_3\text{NH}_3\text{PbI}_3$ planar perovskite hybrid solar cells with 18.1% power conversion efficiency. *Energy Env Sci* 8(5), 1602–1608
22. Meng X, Bai Y, Xiao S, Zhang T, Hu C, Yang Y, Zheng X, Yang S (2016) Designing new fullerene derivatives as electron transporting materials for efficient perovskite solar cells with improved moisture resistance. *Nano Energy* 30:341–346
23. Bai Y, Xiao S, Hu C, Zhang T, Meng X, Li Q, Yang Y, Wong KS, Chen H, Yang S (2017) A pure and stable intermediate phase is key to growing aligned and vertically monolithic perovskite crystals for efficient pin planar perovskite solar cells with high processibility and stability. *Nano Energy* 34:58–68
24. Xu J, Buin A, Ip AH, Li W, Voznyy O, Comin R, Yuan M, Jeon S, Ning Z, McDowell JJ et al (2015) Perovskite-fullerene hybrid materials suppress hysteresis in planar diodes. *Nat Commun* 6:7081
25. Shao Y, Xiao Z, Bi C, Yuan Y, Huang J (2014) Origin and elimination of photocurrent hysteresis by fullerene passivation in $\text{CH}_3\text{NH}_3\text{PbI}_3$ planar heterojunction solar cells. *Nat Commun* 5:5784
26. Docampo P, Ball JM, Darwich M, Eperon GE, Snaith HJ (2013) Efficient organometal trihalide perovskite planar-heterojunction solar cells on flexible polymer substrates. *Nat Commun* 4:2761
27. Sun S, Salim T, Mathews N, Duchamp M, Boothroyd C, Xing G, Sum TC, Lam YM (2014) The origin of high efficiency in low-temperature solution processable bilayer organometal halide hybrid solar cells. *Energy Environ Sci* 7(1):399–407
28. Jeng JY, Chen KC, Chiang TY, Lin PY, Tsai TD, Chang YC, Guo TF, Chen P, Wen TC, Hsu YJ (2014) Nickel oxide electrode interlayer in $\text{CH}_3\text{NH}_3\text{PbI}_3$ perovskite/PCBM planar-heterojunction hybrid solar cells. *Adv Mater* 26(24):4107–4113
29. Wang Q, Shao Y, Dong Q, Xiao Z, Yuan Y, Huang J (2014) Large fill-factor bilayer iodine perovskite solar cells fabricated by a low-temperature solution-process. *Energy Environ Sci* 7(7):2359–2365
30. Zhang H, Azimi H, Hou Y, Ameri T, Przybilla T, Spiecker E, Kraft M, Scherf U, Brabec CJ (2014) Improved high-efficiency perovskite planar heterojunction solar cells via incorporation of a polyelectrolyte interlayer. *Chem Mater* 26(18):5190–5193

31. Liang PW, Liao CY, Chueh CC, Zuo F, Williams ST, Xin XK, Lin J, Jen AKY (2014) Additive enhanced crystallization of solution-processed perovskite for highly efficient planar-heterojunction solar cells. *Adv Mater* 26(22):3748–3754
32. Li C, Wang F, Xu J, Yao J, Zhang B, Zhang C, Xiao M, Dai S, Li Y, Tan Z (2015) Efficient perovskite/fullerene planar heterojunction solar cells with enhanced charge extraction and suppressed charge recombination. *Nanoscale* 7(21):9771–9778
33. Sun K, Chang J, Isikgor FH, Li P, Ouyang J (2015) Efficiency enhancement of planar perovskite solar cells by adding zwitterion/LiF double interlayers for electron collection. *Nanoscale* 7(3):896–900
34. Savva A, Burgues-Ceballos I, Choulis SA (2016) Improved performance and reliability of p-i-n perovskite solar cells via doped metal oxides. *Adv Energy Mater* 6(18), 1600285
35. Min J, Zhang ZG, Hou Y, Ramirez Quiroz CO, Przybilla T, Bronnbauer C, Guo F, Forberich K, Azimi H, Ameri T et al (2014) Interface engineering of perovskite hybrid solar cells with solution-processed perylene-diimide heterojunctions toward high performance. *Chem Mater* 27(1):227–234
36. Xue Q, Hu Z, Liu J, Lin J, Sun C, Chen Z, Duan C, Wang J, Liao C, Lau WM et al (2014) Highly efficient fullerene/perovskite planar heterojunction solar cells via cathode modification with an amino-functionalized polymer interlayer. *J Mater Chem A* 2(46):19598–19603
37. Chen CW, Kang HW, Hsiao SY, Yang PF, Chiang KM, Lin HW (2014) Efficient and uniform planar-type perovskite solar cells by simple sequential vacuum deposition. *Adv Mater* 26(38):6647–6652
38. Bai S, Wu Z, Wu X, Jin Y, Zhao N, Chen Z, Mei Q, Wang X, Ye Z, Song T et al (2014) High-performance planar heterojunction perovskite solar cells: preserving long charge carrier diffusion lengths and interfacial engineering. *Nano Research* 7(12):1749–1758
39. You J, Meng L, Song TB, Guo TF, Yang YM, Chang WH, Hong Z, Chen H, Zhou H, Chen Q et al (2016) Improved air stability of perovskite solar cells via solution-processed metal oxide transport layers. *Nat Nanotechnol* 11(1):75
40. Lin Q, Armin A, Nagiri RCR, Burn PL, Meredith P (2015) Electro-optics of perovskite solar cells. *Nat Photonics* 9(2):106
41. Zhang LQ, Zhang XW, Yin ZG, Jiang Q, Liu X, Meng JH, Zhao YJ, Wang HL (2015) Highly efficient and stable planar heterojunction perovskite solar cells via a low temperature solution process. *J Mater Chem A* 3(23):12133–12138
42. Xie J, Yu X, Sun X, Huang J, Zhang Y, Lei M, Huang K, Xu D, Tang Z, Cui C et al (2016) Improved performance and air stability of planar perovskite solar cells via interfacial engineering using a fullerene amine interlayer. *Nano Energy* 28:330–337
43. Wang Q, Dong Q, Li T, Gruverman A, Huang J (2016) Thin insulating tunneling contacts for efficient and water-resistant perovskite solar cells. *Adv Mater* 28(31):6734–6739
44. Chen W, Wu Y, Yue Y, Liu, J, Zhang W, Yang X, Chen H, Bi E, Ashraful I, Gratzel M, et al (2015) Efficient and stable large-area perovskite solar cells with inorganic charge extraction layers. *Science* 1015
45. Chen W, Xu L, Feng X, Jie J, He Z (2017) Metal acetylacetonate series in interface engineering for full low-temperature-processed, high-performance, and stable planar perovskite solar cells with conversion efficiency over 16% on 1 cm² scale. *Adv Mater* 29(16):1603923
46. Zhu Z, Bai Y, Liu X, Chueh CC, Yang S, Jen AKY (2016) Enhanced efficiency and stability of inverted perovskite solar cells using highly crystalline SnO₂ nanocrystals as the robust electron-transporting layer. *Adv Mater* 28(30):6478–6484
47. Lin Y, Shen L, Dai J, Deng Y, Wu Y, Bai Y, Zheng X, Wang J, Fang Y, Wei H et al (2017) -conjugated lewis base: Efficient trap-passivation and charge extraction for hybrid perovskite solar cells. *Adv Mater* 29(7):1604545
48. Zheng X, Chen B, Dai J, Fang Y, Bai Y, Lin Y, Wei H, Zeng XC, Huang J (2017) Defect passivation in hybrid perovskite solar cells using quaternary ammonium halide anions and cations. *Nat Energy* 2(7):17102